www.jresm.org

Research on Engineering Structures and Materials

Volume 11
Issue 6
December 2025

P-ISSN: 2148-9807 E-ISSN: 2149-4088

The International Journal of **Research on Engineering Structures and Materials (RESM**) is a peer-reviewed open access journal (p-ISSN: 2148-9807; o-ISSN: 2149-4088) published by MIM Research Group. It is published in February, April, June, August, October, and December.

The main objective of RESM is to provide an International academic platform for researchers to share scientific results related to all aspects of mechanical, civil, and material engineering areas.

RESM aims the publication of original research articles, reviews, short communications technical reports, and letters to the editor on the latest developments in the related fields.

All expenditures for the publication of the manuscripts are most kindly reimbursed by *MIM Research Group*. Thus, authors do not need to pay for publishing their studies in the journal.

The scope of the journal covers (but not limited to) behavior of structures, machines and mechanical systems, vibration, impact loadings and structural dynamics, mechanics of materials (elasticity, plasticity, fracture mechanics), material science (structure and properties of concrete, metals, ceramics, composites, plastics, wood, etc.,), nano-materials performances of new and existing buildings and other structural systems, design of buildings and other structural systems, seismic behavior of buildings and other structural systems, repair and strengthening of structural systems, case studies and failure of structural systems, safety and reliability in structural and material engineering, use of new and innovative materials and techniques in energy systems and mechanical aspects of biological systems (biomechanics and biomimetics).

The topics covered in JRESM include:

- Structural Engineering
- Mechanical Engineering
- Material Engineering
- Earthquake Engineering
- Nano-technology
- Energy Systems (Focus on Renewable)
- Biomechanics and Biomimetics
- Environment (Material and Engineering System Related Issues)
- Computer Engineering and Data Science (Material and Engineering System-Related Issues)

Abstracting and Indexing
Please visit http://www.jresm.org for more information.

Graphics and Design

Mehmet Yılmaz myilmaz@jresm.net

RESEARCH on ENGINEERING STRUCTURES & MATERIALS

Research Group

RESEARCH on ENGINEERING STRUCTURES & MATERIALS

Editorial Board

Editor in Chief		
Hayri Baytan Özmen	Usak University	Türkiye
Editors		
Antonio F. Miguel	University of Evora	Portugal
Michele Barbato	University of California Davis	USA
Mehmet Palancı	Arel University	Türkiye
Francesco D'Annibale	University of L'Aquila	Italy
Chitaranjan Pany	Vikram Sarabhai Space Centre	India
Badrinarayan Rath	Wollega University	Ethiopia
Taymaz Tabari	Jagiellonian University	Poland
Tamer Saracyakupoglu	İstanbul Gelisim University	Türkiye
Ivan Banović	University of Split	Croatia
Rayah Nasr Al-Dala'ien	Al-Balqa Applied University	Jordan
Balasubramanian Ramesh	Dhanalakshmi Srinivasan University	India
Abbasali Sadeghi	Islamic Azad University	Iran
Srinivasan Anandhan	National Institute of Technology Karnataka	India
Huatian Zhao	Imperial College London	UK
Majid Pouraminian	Islamic Azad University	Iran
Blessen Skariah Thomas	National Institute of Technology Calicut	India
Ibrahim Alshaikh	University of Science and Technology	Yemen
Seyed Reza Samaei	Islamic Azad University Science and Research Branch	Iran
Uzair Aslam Bhatti	Hainan University	China
Tian Su	Shandong University of Technology	China
Pawel Skruch	AGH University of Krakow	Poland
Haris M. Khalid	University of Dubai	United Arab Emirates

Editorial Office

Publishing Manager		
Mehmet Yılmaz	MIM Research Group	Türkiye
Production Editor		
Damla Yalçıner Çal	MIM Research Group	Türkiye
Language Editors		
Gaye Kuru	Uşak University	Türkiye
Mete Çal	MIM Research Group	Türkiye

Editorial Board Members		
Farid Abed-Meraim	Arts et Metiers ParisTech	France
P. Anbazhagan	Indian Institute of Science	India
Raffaele Barretta	University of Naples Federico II	Italy
R.S. Beniwal	Council of Scientific and Industrial Research	India
Antonio Caggiano	University of Buenos Aires	Argentina
Noel Challamel	University of South Brittany	France
Abdulkadir Çevik	Gaziantep University	Türkiye
J. Paulo Davim	University of Aveiro	Portugal
Hom Nath Dhakal	University of Portsmouth	UK
Ali Faghidian	Islamic Azad University	Iran
S. Amir M. Ghannadpour	Shahid Beheshti University	Iran
Ali Goodarzi	Harvard University	USA
Jian Jiang	National Institute of Standards and Technology	USA
Ramazan Karakuzu	Dokuz Eylül University	Türkiye
Arkadiusz Kwiecien	Cracow University of Technology	Poland
Stefano Lenci	Universita Politecnica delle Marche	Italy
Silva Lozančić	University of Osijek	Croatia
Fabio Mazza	University of Calabria	Italia
Yuan Meini	North University of China	China
Stergios A. Mitoulis	University of Surrey	UK
Vinayagam Mohanavel	Anna University	India
Ehsan Noroozinejad Farsangi	Kerman Graduate University of Technology	Iran
Alaa M. Rashad	Shaqra University	Saudi Arabia
Mohammad Mehdi Rashidi	University of Tongji	China
Pier Paolo Rossi	University of Catania	Italy
Neritan Shkodrani	Polythecnic University of Tirana	Albania
Y.B. Yang	National Taiwan University	Taiwan

Advisory Board Members

A. Abdelbary	Alexandria University	Egypt
A. Karthik	SRM Institute of Science and Technology	India
A. Suresh Kumar	Kalasalingam Academy of Research and Education	India
A.A.A. Sheha	Petrogulfmisr Oil Company	Egypt
Aashish Roy	University of Bouira	Algeria
Abbasali Sadeghi	Islamic Azad University	Iran
Abde lbaki Chikh	Ibn Khaldoun University of Tiaret	Algeria
Abdelhalim Bensaada	University of Yahia Fares of Medea	Algeria
Abdel-Hamid Ismail Mourad	United Arab Emirates University	United Arab Emirates
Abdelkader Fidjah	University of Djelfa	Algeria
Abdellah Douadi	Ferhat Abbas University of Setif 1	Algeria
Abdel-Nasser Sharkawy	South Valley University	Egypt
Abdul HaseebWani	Presidency University	India
Abdul Razak Abdul Karim	Senior Lecturer at Universiti Malaysia Sarawak	Malaysia
Abdullah Khan	The University of Agriculture Peshawar	Pakistan
Abhilash P. P.	Kalasalingam Academy of Research and Education	India
Abid Ustaoglu	Bartın University	Türkiye
Abou-bakr Cherki	Ecole Nationale Supérieure des Mines de Rabat	Morocco
Abrham Gebre	Silesian University of Technology	Poland
Adel Al-Azzawi	Al-Nahrin University	Iraq
Adeniyi Ganiyu Adeogun	Kumamoto University	Japan
Adil Mahdi Jabbar	Wasit University	Iraq
Afonso R.G. Azevedo	University of Hassan II Casablanca	Morocco
Ahmad Zaki	Universitas Muhammadiyah Yogyakarta	Indonesia
Ahmed Abdulwahhab	University of Technology Baghdad	Iraq
Ahmed Ghazy	Zagazig University	Egypt
Ahmed Maamoun	McMaster University	Canada
Ahmed Tareq Noaman	University of Anbar (tekrar)	Iraq
Ahmet Demir	Bolu University	Türkiye
Ahmet Devlet Ozcelik	Eskisehir Osmangazi University	Türkiye
Aicha Rouabeh	Ziane Achour University of Djelfa	Algeria
Ajibola Ibrahim Quadri	Aristotle University of Thessaloniki	Greece
Akhil Raj Gaius Yallamelli	Amazon Web Services Inc.	USA
Aktham Alani	University of Fallujah	Iraq
Alaa M. Rashad	Building Materials Research and Quality Control Institute	Egypt
Alaa Salman	University of Baghdad	Iraq
Aleksandar Ašonja	General Directorate of State Airports	Türkiye
Aleksandar Savić	University of Belgrade	Serbia
Aleksandar Vencl	University of Belgrade	Serbia
Ali Abbar Khleif	University of Technology	Iraq
Ali Abdulhameed	University of Baghdad	Iraq

Ali Bagherkhani	Shiraz Univ. of Technology	Iran
Ali Elgohary	Tanta University	Egypt
Ali Goodarzi	Harvard University	USA
Ali Mahmood	Tunis El Manar University	Tunisia
Ali Raza	University of Engineering and Technology	Pakistan
Ali Sadiq Al-Ithari	University of Kufa	Iraq
AliaJasem	S. S. Tegnoor Degree College	India
Alpay Tamer Erturk	Kocaeli University	Türkiye
Alper Incesu	Karabuk University	Türkiye
Alyaa Abd Alsalm	University of Technology – Iraq	Iraq
Amad Ud Din	Fatima Jinnah Women University	Pakistan
Amdjed Islam Dali	SETS International	Saudi Arabia
Amdulla Mehrabov	Azerbaijan State University of Economics	Azerbaijan
Ameer Baiee	University of Babylon	Iraq
Amirhossein Bahadori	Islamic Azad University	Iran
Amirreza Sadeghi	University of Birjand	Iran
Amiya Pandit	University College Dublin	Ireland
Ammar Tawashi	Dept. of Structural Eng., Al-Baath University	Syria
Ana A. Márquez	Universidad de Guanajuato	Mexico
Andi Yusra	Universitas Teuku Umar	Indonesia
Andriy Huts	Rzeszow University of Technology	Poland
Anjishnu Biswas	Indian Institute of Technology Guwahati	India
Ankang Kan	Shanghai Maritime University	China
Anthony N. Papathanassiou	University College of Engineering Villupuram	India
Arash Rahimi	University of Perugia	Italy
Arif Tuncal	Istanbul Gelisim University	Türkiye
Arife Kübra Yontar	Ondokuz Mayis University	Türkiye
Arulkirubakaran D.	Adhi College of Engineering and Technology	India
Arun K.K.	Kumaraguru College of Technology Coimbatore-641049	India
Arun Kumar K.	Mangalam College of Engineering	India
Arvind Kumar Cholker	Matrusri Engineering College	India
Ary A. Hoyos-Montilla	Construction School at Universidad Nacional de Colombia	Colombia
Ashhad Imam	National Institute of Technology Jamshedpur	India
Ash-Shu'ara MarafaSalman	Kwara State University	Nigeria
Asimina Athanatopoulou	University of Semnan	Iran
Assal Hussein	University of Diyala	Iraq
Atike İnce Yardımcı	Uşak University	Türkiye
Ayad Al-Rumaithi	University of Baghdad	Iraq
Ayoub Souileh	Mohammed V University	Morocco
Ayse Aytac	Kocaeli University	Türkiye
Ayse Pınar Demir	Usak University	Türkiye
Azad A. Mohammed	University of Sulaimani	Iraq
AzhagarsamyS	SRM Institute of Science and Technology	India
Azzura Ismail	Universiti Tun Hussein Onn Malaysia	Malaysia

B.P.R.V.S. Priyatham	GMR Institute of Technology	India
Badrinarayan Rath	Wollega University	Ethiopia
Bao Chao	Ningxia University	China
Bashir Olaniyi Sadiq	Kampala International University	Uganda
Bengi Gözmençanlı	Independent Researcher	Türkiye
Berrin İkizler	Ege University	Türkiye
Bharath Vveda Shantha Murthy	RNS Institute of Technology	India
Bhavya Kadiyala	Parkland Health	USA
Bilge Demir	Karabuk University	Türkiye
Billel Rebai	Abbes Laghrour University	Algeria
Breetha Yesudhas Jayakumari	Chennai Institute of Technology	India
Brijesh Singh	National Council for Cement and Building Materials	India
Bulent Imamoglu	Gedik University	Türkiye
C. Chella Gifta	National Engineering College, Kovilpatti (Tamil Nadu)	India
Cagri Yardimci	Usak University	Türkiye
Can Gönenli	Ege University	Türkiye
Canan Kandilli	Usak University	Türkiye
Caroline S. Sobhy	Fayoum University	Egypt
Catur Harsito	Universitas Sebelas Maret	Indonesia
Cesare Biserni	Alma Mater-University of Bologna	Italy
Chaitanya Vasamsetty	Elevance Health	USA
Chau-Khun Ma	Universiti Teknologi (UTM)	Malaysia
Chella Gifta Christopher	National Engineering College Kovilpatti	India
Chetan Jaiprakash Chitte	Dumlupınar University	Türkiye
Chinenye Elizabeth Okere	Federal University of Technology	Nigeria
Chitaranjan Pany	Structural Engineering Entity	India
Chowdhury Bin Zahid Zubayer	Islamic University of Technology (IUT)	Bangladesh
Christopher Fapohunda	Federal University Oye-Ekiti	Nigeria
Chuanjin Yu	Southwest Jiaotong University	China
Claudia Naldi	University of Bologna	Italy
Çiğdem Çırak Karakaş	Cankiri Karatekin University	Türkiye
Damilola Oyejobi	University of Botswana	Botswana
Daniel Cruze	Mohamed Sathak A J College of Engineering	India
Davide Forcellini	Universitat Politècnica de Catalunya – BarcelonaTech (UPC)	Spain
Davies Isobo Nelson	Ninevah University	Iraq
Debasis Rooj	Deakin University	Australia
Debasish Sen	Ahsanullah University of Science and Technology	Bangladesh
Deep Tripathi	University of Sherbrooke	Canada
Deniz Uner	Middle East Technical University	Türkiye
Desy Setyowulan	Ege University	Türkiye
Dheerendra Singh	Indian Institute of Technology Bombay Powai	India
Dhergham Al-Hamdani	Al-Furat Al-Awsat Technical University	Iraq

Dhinesh Balasubramanian	Mepco Schlenk Engineering College	India
Dhirendra Patel	Washington State University	USA
Dia M. Ali	Andhra University	India
Dilay Uncu	Manisa Celâl Bayar Üniversitesi	Türkiye
Dipankar Das	Tripura University	India
Diyar Qader	University of Kirkuk	Iraq
Dmitry Chernov	UENF – State University of the Northern Rio de Janeiro	Brazil
Dr. Madeva Nagaral	Hindustan Aeronautics Limited	India
Dulce Franco Henriques	Instituto Politécnico de Lisboa	Portugal
E.R. Teixeira	University of Minho	Portugal
Ebrahim Sharifi Teshnizi	Ferdowsi University of Mashhad	Iran
Edwin Klu	Virginia Tech	USA
Egemen Teomete	Dokuz Eylul University	Türkiye
Elavenil S.	Vellore Institute of Technology	India
Elizaldo Dominguesdos Santos	Universidade Federal do Rio Grande (FURG)	Brazil
Elton Hala	Polytechnic University of Tirana	Albania
Emanuele Vincenzo Arcieri	Mechanical Engineering Research Institute, Russian Academy of Sciences	Russia
Emin Erdem	Pamukkale University	Türkiye
Emre Kemer	Usak University	Türkiye
Enea Mustafaraj	Epoka University	Albania
Ercan Isik	Bitlis Eren University	Türkiye
Erdal Emre Çeçen	Metropolitan University Tirana	Albania
Eric M. Lui	Syracuse University	USA
Erion Bukaci	Polytechnic University of Tirana	Albania
Esmaeil Zavvar	University of Tabriz	Iran
Esra Özer	Tokat Gaziosmanpasa University	Türkiye
Essam Mohamed	South Valley University	Egypt
Faruk Mert	Gazi University	Türkiye
Fatih Ahmet Senel	Suleyman Demirel University	Türkiye
Fatma Zohra Benabid	Housing & Building National Research Center	Egypt
Fatoş Koç	University of Baghdad	Iraq
Federico Scafati	University of L'Aquila	Italy
Ferhat Yıldırım	GMR Institute of Technology	India
Firas Hussein	Ruhr University Bochum	Germany
Flavia Zinani	Universidade Federal do Rio Grande do Sul (UFRGS)	Brazil
Fokruddin Ahmad	Andhra University College of Engineering	India
G. Velmurugan	Excel Engineering College	India
Gajendra Kumar	Amity University Uttar Pradesh	India
Gaurav Dhadse	G. H. Raisoni Institute of Engineering and Business Management Jalgaon Maharashtra	India
Gautham Kishore Reddy G.	Vignan Institute of Technology and Science	India
Ghanim Al-Zubaidy	University of Baghdad	Iraq
Ghasan Fahim Huseien	Universiti Teknologi Malaysia (UTM)	Malaysia
Giovanni Garofalo	ISAE-SUPAERO	France

Gopi Krishnan P.	Dr. N G P Institute of Technology	India
Gökhan Gece	Bursa Teknik Üniversitesi	Türkiye
Guobo Wang	Wenzhou University	China
Gururaj Hatti	KLS VDIT	India
Gustavo Bosel Wally	Federal University of Rio Grande do Sul	Brazil
Guy Louarn	CNRS – Université de Nantes	France
Güneş Harman	Yalova University	Türkiye
Gür Emre Güraksın	Afyon Kocatepe University	Türkiye
H. C. Ananda Murthy	Adama Science & Technology University	Ethiopia
Habibe Demir	İskenderun Technical University	Türkiye
Hadeel Khalid Awad	University of Baghdad	Iraq
Hadj Bekki	University Ibn Khaldoun of Tiaret	Algeria
Haithem Boumediri	Institut des Sciences et des Techniques Appliquées (ISTA)	Morocco
Hakan Sarikaya	Uşak University	Türkiye
Hakan Ulker	Bursa Teknik University	Türkiye
Halil Murat Enginsoy	Canakkale Onsekiz Mart University	Türkiye
Halil Yalcin Akdeniz	The University of Melbourne	Australia
Halit Cetiner	Isparta University	Türkiye
Hamid Saberi	University of Eyvanekey	Iran
Hamide Tekeli	Süleyman Demirel University	Türkiye
Hamoon Fathi	Sanandaj	Iran
Hanaa Humadi	University of California, Davis	USA
Hasan Ulus	Selcuk University	Türkiye
Hashem Jahangir	University of Birjand	Iran
Hasibullah Azizi	Kalaniketan Polytechnic College	India
Hayder Kamil Shanbara	Al-Muthanna University	Iraq
Hayri B. Ozmen	Usak University	Türkiye
Hemadri Prasad Raju	Sree Vidyanikethan Engineering College	India
Hicham Lotfi	Ibn Zohr University	Morocco
Hidayatul Fitri	STAIN Teungku Dirundeng Meulaboh	Indonesia
Hilton Ahmad	Universiti Tun Hussein Onn Malaysia)	Malaysia
Hintsa G. Gebremariam	Addis Ababa University	Ethiopia
Hossein Jarrahi	University of Birjand	Iran
Hossein Kabir	University of Babylon	Iraq
Houlei Zhang	Nanjing University of Science and Technology	China
Hussein Hamada	Al-Qalam University College	Iraq
Hussein Talab Nhabih	University Malaysia Perlis	Malaysia
Hüseyin Ersen Balcıoğlu	Uşak University	Türkiye
Hüsnügül Yılmaz Atay	Izmir Kâtip Celebi University	Türkiye
I Gede Gegiranang Wiryadi	Universitas Mahasaraswati Denpasar	Indonesia
Ibrahim Raheem	University of Georgia	USA
Ibrahim Saad Agwa	Suez University	Egypt
Ibrahim Sabry	Benha University	Egypt
Ibrahim Sharaky	Taif University	Saudi Arabia
Ikram Kouidri	Tahar Moulay University of Saida	Algeria
Iman Hani	University of Babylon	Iraq

Indra Mawardi	Politeknik Negeri Lhokseumawe	Indonesia
Irakli Premti	Polytechnic University of Tirana	Albania
Irina Volokitina	Karaganda Industrial University	Kazakhstan
Isabel Milagre Martins	Laboratório Nacional de Engenharia Civil	Portugal
Issam Aouari	University of Bouira	Algeria
Ivan Kraus	University of Osijek	Croatia
Ivana Barišić	Josip Juraj Strossmayer University of Osijek	Croatia
Ivana Štimac Grandić	University of Rijeka	Croatia
İbrahim Öz	Ahi Evran University (Kırşehir Ahi Evran University)	Türkiye
İbrahimoğlu İbrahimoğlu	Papilon Savunma	Türkiye
J. Aravind Kumar	FLAME University	India
J. D. Chaitanya Kumar Jagarapu	Koneru Lakshmaiah University	India
J. Eswari	Kwara State University	Nigeria
J. Jenix Rino	Anna University	India
J. Jeyanthi	Mepco Schlenk Engineering College	India
J. Paulo Davim	University of Aveiro	Portugal
Jack Widjajakusuma	University of Pelita Harapan	Indonesia
Jagansivamani	Sona College of Technology	India
Javad Vaziri	Universiti Teknologi Malaysia	Malaysia
Jayalalitha Subbaiah	SASTRA Deemed University	India
Jayaseelan Veerasundaram	Saveetha Engineering College	India
Jessemazadu	Federal University Wukari	Nigeria
Jesús Castro	Pontifical Catholic University of Peru	Peru
Jianzhuang Xiao	Tongji University	China
Jinxu Mo	Yangtze University	China
Jojok Widodo Soetjipto	Universitas Jember	Indonesia
Josephine Chang Hui Lai	Petrogulf Misr Oil Company	Egypt
Juan Llorca-Schenk	University of Alicante	Spain
Jun Zhang	Ningbo Tech University	China
K. Ashwini	Yalova University	Türkiye
Kabiru Mustapha	Kwara State University	Nigeria
Kadir Günaydın	GE Aviation	USA
Kamel Chaoui	Badji Mokhtar University	Algeria
Kamran Asemi	Islamic Azad University	Iran
Kanish Kapoor	Dr B R Ambedkar National Institute of Technology	India
Kannan Srinivasan	Saiana Technologies Inc.	USA
Kaplan Kaplan	Kocaeli University	Türkiye
Karthikeyan Parthasarathy	LTIMindtree	India
Katarina Rogulj	University of Split	Croatia
Kavendra Pulkit	NIT Kurukshetra	India
Kh. Hosseinzadeh	Babol Noshirvani University of Technology	Iran
Khairi Supar	University of Mustansiriyah	Iraq
Khairul NizarIsmail	Universiti Malaysia Perlis	Malaysia
Kiran Devi	SGT University	India
Kirollos Sobhy	Babol Noshirvani University of Technology	Iran
Kirti Kanta Sahoo	Kalinga Institute of Industrial Technology (KIIT) Deemed to be University	India

Konstantinos Kalfas	University of Texas at Tyler	USA
Kourosh Mehdizadeh	Islamic Azad University	Iran
Kourosh Nazari	Islamic Azad University	Iran
Krishna Murari Pandey	National Institute of Technology	India
Krzysztof Grzyb	National Institute of Metrology	Thailand
Lavanya Prabha	SRM Easwari Engineering College	India
Lawrence Zahemen Tuleun	University of Ilorin	Nigeria
Lemecha Geleto Wariyo	Addis Ababa University	Ethiopia
Leonid Dvorkin	National University of Water and Environmental Engineering	Ukraine
Leticia Florespulido	Universidad Autónoma de Tlaxcala	Mexico
Lilesh Gautam	Malaviya National Institute of Technology	India
Lim Siong Kang	Universiti Tunku Abdul Rahman	Malaysia
Liyana Jamaludin	Universiti Malaysia Perlis	Malaysia
Lomesh Mahajan	Dr. Babasaheb Ambedkar Technological University	India
Lubna Abdulkhaleq	National and Kapodistrian University of Athens	Greece
Luiz Rocha	Federal University of Rio Grande do Sul	Brazil
LyamineBriki	University of Batna2	Algeria
M. Jafaryar	Conservatoire National des Arts et Métiers	France
M. Kalil Rahiman	Saveetha School of Engineering	India
M.Helen Santhi	University of Split	Croatia
Madhu Puttegowda	Malnad College of Engineering	India
Madhulika Sinha	University of Bergamo	Italy
Magdalini Titirla	University of Illinois	USA
Maher Jebur	University of Baghdad	Iraq
MaherChakhari	UNISTRAPG	Italy
Mahesh Gopal	Wollega University	Ethiopia
Mahesh Raut	G.H. Raisoni Institute of Engineering and Technology	India
Maheswaran Chellapandian	Mepco Schlenk Engineering College	India
Maheswaran Muthiah	K.S. Rangasamy College of Technology	India
Mahmoud Mokhtar	Indian Institute of Technology Bombay	India
Mahmudul Hasan Moon	Eskisehir Technical University	Türkiye
Majid M.A. Kadhim	University of Babylon	Iraq
Majid Pouraminian	University of San Marino	San Marino
Marco Breccolotti	University of Perugia	Italy
Maria Julieta Mateos Ochoa	National Autonomous University of Mexico	Mexico
Maria Richert	AGH University of Science and Technology	Poland
Maridula Thakur	Himachal Pradesh University	India
Marina Sunara	University of Split	Croatia
Marthin Dody Josias Sumajouw	Sam Ratulangi University	Indonesia
Marva Ghazimanesh	Jadavpur University	India
Marwa Enneffati	Laboratoire MOLTECH-Anjou, Université d'Angers	France
Marzieh Naseralmemar	Islamic Azad University	Iran
Matthew Martianus Henry	Bina Nusantara University	Indonesia
Md. Golam Kibria	University of Rajshahi	Bangladesh

Md. Saiful Islam	Universiti Putra Malaysia	Malaysia
Md. Zia Ul Haq	Panjab University	India
Mehdi Khorasani	Isfahan University of Technology	Iran
Mehdi Panji	Islamic Azad University	Iran
Mehmet Ada	Usak Üniversitesi	Türkiye
Mehmet Cemal Genes	Eastern Mediterranean University	Northern Cyprus
Mehmet Kaya	Yozgat Bozok University	Türkiye
Mehrab Nodehi	University of California	USA
Melika Mahmoodabadi	Islamic Azad University	Iran
Mengtao Liang	Xi'an Jiaotong University	China
Mert Göksüzoğlu	Sampa Automotive	Türkiye
Mevlüt Gürbüz	Ondokuz Mayıs University	Türkiye
Mihir Mishra	Texas A&M University	USA
Mihira Acharya	Indian Institute of Technology Bhubaneswar	India
Milica Vasić	Centre for Materials Institute for Testing of Materials	India
Mohamed Bouamama	Mechanics Research Center (CRM)	Algeria
Mohamedi M. Mjahidi	The University of Dodoma	Tanzania
Mohammad Afrazi	Duke University	USA
Mohammad Fayez Saded	Ferhat Abbas University Sétif 1	Algeria
Mohammad Hossein Razmkhah	Semnan University	Iran
Mohammad Iai Biajawi	Universiti Malaysia Pahang Al-Sultan Abdullah	Malaysia
Mohammad Lesani	University of Tehran	Iran
Mohammad Naeim Moradi	Amirkabir University of Technology	Iran
Mohammad Sadegh Shahidzadeh	Behbahan Khatam Alanbia University of Technology	Iran
Mohammad Saleh Baradaran	Islamic Azad University	Iran
Mohammad Salim Kaiser	International University of Business Agriculture and Technology	Bangladesh
Mohammadreza Baghoolizadeh	Shahrekord University	Iran
Mohammed Al-Alusi	University of Anbar	Iraq
Mohammed AL-Ezzi	Universiti Tenaga Nasional	Malaysia
Mohammed Bentahar	University Business Academy	Serbia
Mohammed JalalAl-Ezzi	University of Bilad Al-Rafidain	Iraq
Mohammed Kadhim	Mustansiriyah university	Iraq
Mohammed Kamal Ali	University of Kirkuk	Iraq
Mohammed Salam Shuaib	Kogi State University	Nigeria
Mohammed Salman	University of Fallujah	Iraq
Mohammed Sarhan	Rivers State University	Nigeria
Mohan G.	University of Garmian	Iraq
Mohd Ataullah Khan	Mahindra University	India
Mohd Nasim	IPS Academy	India

Mohd Syahrul Hisyam Mohd Sani	Universiti Teknologi MARA Jengka Campus Pahang Branch	Malaysia
Mohsen Hajizamani	Graduate University of Advanced Technology	Iran
Moosa Mazloom	Shahid Rajaee Teacher Training University	Iran
Morchid Fatima Ezzahrae	Saveetha School of Engineering	India
Moslem Paidar	Islamic Azad University	Iran
Mostafa Akbari	Technical and Vocational University	Iran
Motahhareh Nezafat Tabalvandani	Islamic Azad University	Iran
Mouhammed Lafta	University of Technology	Iraq
Mounika Ganta	Vignana Bharathi Institute of Technology	India
Muhammad AminuAhmad	Kaduna State University	Nigeria
Muhammad Anggara Adji Prasetiya	Universitas Sriwijaya	Indonesia
Muhammad Bilal Khan	GIK Institute	Pakistan
Muhammad Hamza	Jawaharlal Nehru Technological University Hyderabad	India
Mukaila Anifowose	Federal Polytechnic Offa	Nigeria
Murat Aydin	Ontario Tech University	Canada
Murk Chohan	Begum Nusrat Bhutto Women University, Sukkur	Pakistan
Murtala Namakka	Universiti Malaysia Sarawak	Malaysia
Mushriq Al-Shamaa	University of Baghdad	Iraq
Mustafa Akpolat	Munzur University	Türkiye
Mustafa H. Omar	Bilad Alrafidain University College	Iraq
Mustafa Ozgunler	Mimar Sinan Fine Arts University	Türkiye
Mustaqqim Abdul Rahim	University Malaysia Perlis	Malaysia
Mutiu Akinpelu	Kwara State University	Nigeria
Mutluhan Akin	Nevşehir Hacı Bektaş Veli University	Türkiye
Muttaqin Hasan	Syiah Kuala University	Indonesia
N. Arunachelam	Mepco Schlenk Engineering College	India
N. Gurumoorthy	PSNA College of Engineering and Technology	India
N.L.N. Kiran Kumar	Sri Venkateswara University	India
N.Venkata Sairam Kumar Namepalli	R.V.R & J.C College of Engineering	India
Nabil Bella	Tahri Mohamed University of Bechar	Algeria
Nadhim Hamah Sor	Ondokuz Mayıs University	Türkiye
Nagaraj Ekabote	KLE Technological University	India
Nahida Nazim Musayeva	Gazi University	Türkiye
Naser Hassan	Tikrit University	Iraq
Natt Makul	Phranakhon Rajabhat University	Thailand
Navdeep Singh	Dr B R Ambedkar National Inst. of Tech.	India
Naveen Kumar Suniya	MBM University	India
Naveen S.	National Institute of Technology	India
Nazime Seda Şaşmaz Karacan	Usak University	Türkiye
Nebab Mokhtar	Université Hassiba Ben Bouali de Chlef	Algeria

Neeraj S.N.	India affiliated to Visvesvaraya Technological University	India
Nermin Demirkol	Kocaeli University	Türkiye
Nghia P. Tran	Islamic Azad University	Iran
Nguyen Van-Toan	Industrial University of Ho Chi Minh City	Vietnam
Nhlanhla Nyembe	University of the Witwatersrand	South Africa
Nikhil Bharat	National Institute of Technology	India
Nilesh Masne	GESCOEMSR	India
Ninu Praseetha N. S.	Addis Ababa University	Ethiopia
Nisha Aggarwal	Maharaja Agrasen Institute of Technology	India
Nitin Kumar	Universiti Tun Hussein Onn Malaysia	Malaysia
Nizirwan Anwar	Universitas Esa Unggul	Indonesia
O. Philip Oladijo	Botswana International University of Science and Technology	Botswana
Ola Mazen Makki	University of Al-Qadisiyah	Iraq
Oladimeji Olatunji Ojo	Federal University of Technology	India
Olatunji Abolusoro	Tshwane University of Technology	South Africa
Oleg V. Devitsky	Federal Research Centre Southern Scientific Centre of the Russian Academy of Sciences	Russia
Oleksii Hrechanyi	Zaporizhzhia National University	Ukraine
Olfa Maalej	Mustansiriyah University	Iraq
Olufemi Oni	University of North Dakota	USA
Olumoyewa D. Atoyebi	Landmark University	Nigeria
Oluwatobi Dayo-Olupona	University of the Witwatersrand	South Africa
Omer Fayadh	Al-Nahrin University	Iraq
Orhan Gülcan	General Electric Aerospace	USA
Oritonda Muribwathoho	Cape Peninsula University of Technology	South Africa
Orkun Yılmaz	National Institute of Technology	India
Osama Zaid	Institute of Material Technology	India
Osman M. Ramadan	Cairo University	Egypt
Owen Tamin	Universiti Malaysia Sabah	Malaysia
OzgurAvsar	Eskisehir Technical University	Türkiye
Özgür Demircan	Chemical and Energy Engineering, Universiti Teknologi Malaysia	Malaysia
P. Manoj Kumar	KPR Institute of Engineering and Technology	India
P. Marimuthu	SASTRA Deemed to be University	India
P. V. Ramana	Malaviya National Institute of Technology	India
P.N.L. Pavani	Gyeongsang National University	South Korea
P.S.Shreyas	School of Mechanical Engineering	India
Pardhasaradhi Kasinikota	National Institute of Technology	India
Parmo Parmo	UIN Sunan Ampel Surabaya	Indonesia
Partheeban Pachaivannan	Chennai Institute of Technology	India
Peng Gao	University of Massachusetts Lowell	USA
Peter P. Ikubanni	Landmark University	Nigeria
Peyman Beiranvand	Razi University	Iran
Peyman Maleki	Ayatollah Boroujerdi University	Iran
Piya Chotickai	Kasetsart University	Thailand

Pooja Sharma	Dr. Yashwant Singh Parmar University of Horticulture and Forestry	India
Pooya Arezoomand Langarudi	Islamic Azad University	Iran
Prakash Somani	Malaviya National Institute of Technology	India
Priyanka Malhotra	Chitkara University	India
Puneet Sharma	UiT The Arctic University of Norway	Norway
Qasim M. Shakir	University of Kufa	Iraq
Qiang Ou	Chongqing University	China
Qichao Jin	Xi'an Jiaotong University	China
R. Ralegaonkar	Department of Civil Engineering at VNIT	India
R.L. Lija	Department of Civil Engineering	India
R.S. Jangid	Indian Institute of Technology Bombay	India
Rachid Zegait	SASTRA Deemed to be University	India
Rahul Kesharwani	Indian Institute of Technology Patna	India
Raif Sakin	Balıkesir University	Türkiye
Rajaa Abdulsada	National Authority for Nuclear, Radiological, Chemical and Biological Control	Egypt
Rajani Priya Nippatla	Kellton Technologies Inc	India
Rajasekhar Kondarajasekhar	Nigerian Defence Academy	Nigeria
Rajesh Kumar	KPR Institute of Engineering and Technology	India
Rajesh M.	Hindustan Institute of Technology and Science	India
Ramaswamy Palanivel	Alaivani College of Technology	India
Rami Sldozian	University of Technology- Iraq	Iraq
Ramnarayan Sahu	Rajeev Gandhi Technical University	India
Rana Alrubaye	National Institute of Technology, Patna	India
Rana Falah	University of Babylon	Iraq
RanaAl-khadaar	University of Baghdad	Iraq
Rasheed Abdulwahab	Wollega University	Ethiopia
Rathish Kumar Pancharathi	National Institute of Technology Warangal	India
Ravichandran M.	K.Ramakrishnan College of Engineering	India
Ravikumar Jayabal	SIMATS	India
Rayeh Nasr Al-Dala'ien	Universiti Tenaga Nasional	Malaysia
Renu Dalal	Guru Gobind Singh Indraprastha University, Delhi	India
Revathi Srinivasan	Mepco Schlenk Engineering College	India
Riadh Bennai	University Hassiba Benbouali of Chlef	Algeria
Rianti Dewi Sulamet-Ariobimo	Universitas Trisakti	Indonesia
Roberto Nascimbene	School of Advanced Studies IUSS Pavia	Italy
Rosendo Romero-Andrade	SSN College of Engineering	India
Royal Madan	Chandigarh University	India
Rupesh Kumar Dhondy	Osmania University	India
Rusul Mansoor Al-Amri	University of Kerbala	Iraq
S. Ali Faghidian	Islamic Azad University	Iran
S. Gholizadeh	University of Cape Town	South Africa
S. Prasanth	Sabaragamuwa University of Sri Lanka	Sri Lanka

S.R.R. Teja Prathipat	National Institute of Technology Warangal	India
Saba Jawad	Bilad Al-Rafidain University	Iraq
Sabah Fartosy	University of Mustansiriyah	Iraq
Sachin Kumar	SKITM-Sat Kabir Institute of Technology and Management	India
Sadanand Paneru	Tribhuwan University	Nepal
Saeid Foroughi	Selçuk University	Turkey
Sahar Ismail	Saint Joseph University of Beirut	Lebanon
Sai Krishna Pinnamaneni	University of Texas at Arlington	USA
Saiful Hasan	Jamia Millia Islamia	India
Saifullah Shahen	Hochschule Neu-Ulm	Germany
Saifulnizan Jamian	Indian Institute of Technology	India
Sajjad Hassanpour Kasanagh	Middle East Technical University	Türkiye
Salah Bouzina	University of Constantine	Algeria
Salmabanu Luhar	National Taipei University of Technology	Taiwan
Salwa Elakeili	University of Benghazi	Libya
Sam Saham	Tarbiat Modares University	Iran
Saman Mansouri	Universiti Malaysia Sarawak	Malaysia
Saman Saadatfar	Islamic Azad University	Iran
Samer Adeeb	National Institute of Technology Puducherry	India
Samia Bouzouaid	Kasdi Merbah University	Algeria
Samuel Awe	Automotive Components Floby AB	Sweden
Sandra Juradin	Independent Researcher	Croatia
Sangeetha Palanivelu	SSN College of Engineering	India
Sanjeeb Prasad Panday	Tribhuvan University	Nepal
Sarmila Sahoo	Heritage Institute of Technology Kolkata	India
Sasikumar Palanisamy	K. Ramakrishnan College of Technology	India
Sastri M. V. S. S.	Vasavi College of Engineering	India
Saumen Mandal	National Institute of Technology Karnataka	India
Seema Gupta Bhol	KIIT University	India
Sefiu Bello	Kwara State University	Nigeria
Selcuk Selimli	University of Karabük	Türkiye
Sercan Serin	Osmaniye Korkut Ata University	Türkiye
Serdar Gungor	Bilecik Şeyh Edebali University	Türkiye
Serkan Elcin	Pamukkale University	Türkiye
Seyed Reza Samaei	Islamic Azad University	Iran
Seyedeh Yasaman Samaei	Imamkhomeini Internaional University	Iran
Seymur Bashirzade	Azerbaijan University Architecture and Construction	Azerbaijan
Shahazadi Begum	Baba Institute of Technology and Sciences	India
Shahrul Niza Mokhatar	Faculty of Civil Engineering & Built Environment	Malaysia
Shaise K. John	College of Engineering Trivandrum	India
Shakir Musa	Al-Furat Al-Awsat Technical University	Iraq
Shanshan Jin	Beijing University of Civil Engineering and Architecture	China
Shaohong Cheng	Univ. of Windsor	Canada
Sharmin Reza Chowdhury	Civil Eng.Dept. Ahsanullah University of Science and Technology	Bangladesh

Sharmistha Shee Kanrar	Federal University of Technology	Nigeria
Shashi Prakash Dwivedi	G. L. Bajaj Institute of Technology & Management	India
Shaymaa Naser	University of Kufa	Iraq
Sheelan Hama	University of Anbar	Iraq
Shimol Philip	Universiti Tun Hussein Onn Malaysia	Malaysia
Shoulong Zhang	Harbour Engineering Research Institute Co. Ltd.	China
Shuaib Ahmed Wadho	Usak University	Türkiye
Siti Aisyah Nurjannah	Universitas Sriwijaya	Indonesia
Sivakumar N.	University of Alberta	Canada
Solomon Olalere Ajamu	Ladoke Akintola University of Technology	Nigeria
Somayyeh Pourbakhshian	Islamic Azad University	Iran
Somya Ranjan Patro	Indian Institute of Technology Delhi	India
Sonachalam M.	Arvind Gavali College of Engineering	India
Sonal Thakkar	Nirma University	India
Sophia Immanuel	National Institute of Technology Tiruchirappalli	India
Soumia Hammache	Mohamed Khider University of Biskra	Algeria
Sridhar G.	National Institute of Technology Karnataka	India
Srinivasan Anandhan	National Institute of Technology Karnataka	India
Stefania Sica	University of Sannio	Italy
Subash Thanappan	KAAF University College	Ghana
Subramanyam Boyapati	American Express	USA
Suliman Khan	NFC Institute of Engineering and Fertilizer Research	Pakistan
Sumanth Ratna Kandavalli	New York University	United States
Sumit Kumar Baral	Jagannath University	India
Sunday Chukwuemeka	Projects Dev. Inst.	Nigeria
Surajit Kumar Paul	Indian Institute of Technology	India
Suriati Sufian	Universiti Teknologi PETRONAS	Malaysia
Suriyaprakash Rajadesingu	SRM Institute of Science and Technology	India
Suseela Alla	Vignan's Foundation for Science, Technology & Research	India
Susmita Naskar	University of Southampton	United Kingdom
Syed Nasir Abbas	University of Sargodha	Pakistan
T.V. Reshma	GITAM School of Technology	India
Taha Rashid	Monastir University	Tunisia
Talha Jamshaid	Islamia University of Bahawalpur	Pakistan
TalhaTaskanat	Erciyes University	Türkiye
Tamer Saracyakupoglu	TUSAŞ Academy	Türkiye
Tankiso Lawrence Ngake	Walter Sisulu University	South Africa
Taqiy Eddine Boukelia	Mechanical Engineering, University of Jijel	Algeria
Tarun Kumarrajak	Northern Technical University	Iraq
Tasnia Ahmed	Military Institute of Science and Technology	Bangladesh
Tebatso Gorgina Moape	University of South Africa	South Africa
Teotino Gomes Soares	Universidade Oriental Timor Lorosa'e	Timor-Leste (East Timor)
Thaer Alrudaini	University of Basrah	Iraq

Thayathip Thongtan	Faculty of Earth and Space Sciences, Autonomous University of Sinaloa	Mexico
Thi Loanpham	Hai Phong University	Vietnam
Thirusubramanian Ganesan	Cognizant Technology Solutions	USA (şirket)
Thomás L. Resende	Federal University of Jequitinhonha and Mucuri Valleys	Brazil
Thomas Salonikios	Institute of Engineering Seismology and Earthquake Engineering	Greece
Toufik Sebbagh	University of Skikda	Algeria
Tri Rochmadi	Universitas Alma Ata	Indonesia
Tuan Anh Nguyen	Thuyloi University	Vietnam
Tuqa Mahdi	Bilad Al-Rafidain University	Iraq
Uchechi Eziefula	University of Agriculture and Environmental Sciences	Nigeria
Upendra K.Mallela	Aerospace Vertical Largy Services Limited	India
Usama Naeem	University of Basrah	Iraq
Utsav Koshti	Nirma University	India
Uwemedimo Nyong Wilson	Azerbaijan National Academy of Sciences	Azerbaijan
Vafa Morsali	Islamic Azad University	Iran
Vedat Arda Küçük	Çankırı Karatekin University	Türkiye
Venkatesh Chava	CVR College of Engineering	India
Venkatesh Rathinavelu	Saveetha Institute of Medical and Technical Sciences	India
Vera Ilyina	IG KarRc Ras Russian Academy of Sciences	Russia
Víctor I.Fernandez-Davila	Shri Shankaracharya Institute of Professional Management and Technology	India
Victor Rizov	University of Architecture	Bulgaria
Vijayasarathy Rathanasalam	ATRIA Institute of Technology	India
Vikas B. Magdum	KLS Gogte Institute of Technology	India
Vina Kamila	Mulawarman University	Indonesia
Vincent Sam Jebadurai	Department of Civil Engineering, Karunya Institute of Technology and Sciences	India
Vineeth Kumart V.	Siddaganga Institute of Technology	India
ViniciusPepe	Mechanical Engineering, University Ritter dos Reis	Brazil
Vishwash B.	Indian Institute of Science	India
Vivek Srivastava	SGT University	India
Wael Shaheen	University of Baghdad	Iraq
Wahyu Dwi Lestari	University of Pembangunan Nasional Veteran Jawa Timur	Indonesia
Waleed A. Abbas	University of Technology	Iraq
Xiaojian Wang	Xinjiang University	China
Xinyue Wang	Dalian University of Technology	China
Y. Bouras	Victoria University	Australia
Yahaya Ismail	University of Abuja	Nigeria
Yamini SreevalliI	Vellore Institute of Technology	India
Yang Feng	Xi'an Jiaotong University	China
Yang Yang	Southeast University	China
Yaser Acikbas	Uşak Üniversitesi	Türkiye
Yassine Zelmat	University Abdelhamid Ibn Badis	Algeria

Yonatan Ayele Abera	Dilla University	Etihopia
Yuliang Chen	Guangxi University of Science and Technology	China
Yunika Kirana Abdul Khalik	Tikrit University	Iraq
Yunusa Haruna	Beihang University	China
Yuvaperiyasamy M.	Saveetha School of Engineering	India
Yuvaraj K.	University of Relizane	Algeria
Zafer Kaya	Yildiz Technical University	Türkiye
Zahid Iqbal Khan	Çanakkale Onsekiz Mart Üniversitesi	Türkiye
Zaim Omar	Universiti Sains Malaysia	Malaysia
Zainab Tolu Giwa	Kwara State University	Nigeria
Zainorizuanmohd Jaini	Universiti Tun Hussein Onn Malaysia	Malaysia
Zeynep Ekincioğlu Küzeci	Kırşehir Ahi Evran Üniversitesi	Türkiye
Zikriye Ozbek	Canakkale Onsekiz Mart University	Türkiye
Ziyauddin Seikh	Aliah University	India

In This Issue

Research Article
2731 **Subitha Thirupathi, Sasikumar Palanisamy, Venkateshan Asokan**
Enhancing sustainability in construction: Exploring the self-healing mechanisms of bio-concrete

Research Article
2745 **P. Sangeetha, R. Prithvi, Ashwin Kumaran V, Murali B, Yaashika M**
Structural behavior of deficient hollow steel columns strengthened using GFRP

Research Article
2761 **Mohammed Layth Abbas, Erhan Güneyisi**
Compressive behavior and code-based evaluation of normal weight and lightweight concrete filled composite steel tubes

Research Article
2777 **Ganesh S. Ingle, Shailendra Banne, Darshan Gaidhankar, Kshitij Dhawale, Dinesh Aswar**
Numerical analysis of surface settlement with saturated zone during urban tunnelling

Research Article
2797 **Mutiu Adelodun Akinpelu, Abdullateef Olamilekan Amao, Ash-Shu'ara Marafa Salman, Daniel Sunday Gabriel**
Sustainable self-compacting concrete: A study on the combined effects of waste glass powder and metakaolin as cement replacements

Research Article
2821 **Debendra Nath Choudhury, S.K Panda**
Effect of ADG-NH2 functionalized graphene on fracture and impact resistance of carbon fiber reinforced composites

Research Article
2837 **Pooja Damodaran, Yuvaperiyasamy Mayilsamy**
Strength and characterization studies on nano-silica and steel fibre reinforced bacterial concrete: An eco-friendly and sustainable approach

Research Article
2849 **Safia Mebarek Haddad, Mebarek Belaoura**
Impact of recycled concrete powders on the behavior of high-performance concrete in fresh and hardened states

Research Article
2863 **Noor Sadie Saleh, Jamal M. Rzaij**
Influence of samarium oxide mixing on the structural and optical properties of tin oxide thin films prepared by pulsed laser deposition

Research Article
2879 **P. Sangeetha**
Effects of web openings on axial compression in cold-formed steel lipped channel columns

Research Article
2891 **Shahazadi Begum, Shaik Yajdani**
Mechanical and durability studies on different grades of concrete using cinder aggregates

Research Article
2905 **Bindhu Bernard, Kavitha Madhu**
Characterizing rheological properties and rutting risk of VG30 and PMB 40 binders with warm mix additives

Research Article
2919 **Sasikumar Palanisamy, Subitha Thirupathi**
A study on flexural behaviour and strengthening of fibre reinforced concrete beams using microorganisms

Research Article
2941 **K C Vishwanath, Nagabhushana N, Bharath V, Virupaxi Auradi, Rajendra P, Madeva Nagaral, Manjunath Vatnalmath, Mohammed Kareemullah, Nagaraj Namdev, Abhishek Bhattacherjee, Balaraj V**
Mechanical and fractography behavior of nano and micro boron carbide particles reinforced Al2014 alloy composites for aerospace applications

Research Article
2953 **Rayana Harika, Panugalla Rama Rao, Sankar Boomibalan, Arunkumar Kadarkarai, Rameshkumar Deivasigamani**
Durability and microstructure of ternary binder geopolymer concrete: A comprehensive study

Research Article
2965 **Vidhya Ramesh, Gajalakshmi Pandulu, Nisha Khanam, Oh Chai Lian**
Compressive strength prediction of ecofriendly recycled aggregate concrete: A machine learning approach

Research Article
2983 **Rifkah, Saloma, Siti Aisyah Nurjannah**
Compressive and tensile strength of fly ash based lightweight geopolymer concrete with variation of Na_2SiO_3 and NaOH using expanded polystyrene

Research Article
2999 **Ghazwan F. Khudhair, Waleed A. Abbas**
Properties of sustainable concrete incorporating cold-bonded lightweight aggregate manufactured from expired cement, biopolymer, and various waste

Research Article
3019 **Leilei Zhu, Jiren Li, Houlei Zhang**
Experimental study on energy-saving effect of alternate temperature system with cold storage unit

Research Article
3035 **Amdjed Islam Dali, Sami Zerari, David Gandreau**
In-situ investigation of earthen building materials in the Ksour of the Ziban region, Algeria: A comparative study between Chetma and Lichana

Research Article
3051 **Shcherban Pavel Sergeyevich, Potapov Boris Vasilievich, Karagadyan Artur Nairievich**
Detection of defects in steel oil and gas operating pipelines using a neural network, based on the results of optical diagnostics

Research Article
3069 **Vudata Harsha Sai, Lingeshwaran N, P. K. Prasanna, George Fernandez Raj A, P. Jayanthi**
Flexural behavior of GFRP rebars and steel rebars with polypropylene fibers and fly ash-based concrete

Research Article
3087 **Teuku Farizal, Teuku Budi Aulia, Dian Febrianti, Roni Agusmaniza, Muhammad Arrie Rafshanjani Amin**
Effect of areca catechu fiber and superplasticizer interaction on the optimization of concrete compressive strength using the Box-Behnken design statistical approach

Research Article
3111 **Ruwaida Kareem Khoman, Haider M. Owaid**
Development of sustainable high performance self-compacting concrete incorporating natural and waste pozzolanic materials

Research Article
3133 **Tidjar Boudjemaa, Khelafi Hamid, Bella Nabil, Bennaceur Saïd, Lammari Khelifa, Benabdelfattah Mohamed, Hadj Djelloul Nasser Dine, Slimani Abdeldjalil, Dahbi Abdeldjalil**
Solar energy-driven heat treatment of concrete and mortar in desert environments: A case study of Bechar region, Algeria

Research Article
3149 **Sudhir Sharma, Pushpendra Kumar Sharma**
Initial setting time of cement using sugarcane juice as an admixture

Research Article
3167 **Aicha Rouabeh, Issam Aouari, Baizid Benahmed, Mehmet Palanci**
Improved PGA and PGV estimation in soft soils for earthquake engineering applications

Research Article
3187 **Hammad D. Merie, Diyar N. Qader, Baraa T. Kamel, Muyasser Mohammed Jomaa**
Buckling resistance of layered reinforced concrete columns: Experimental evaluation of normal and lightweight thermo-stone aggregate configurations

Research Article
3207 **A. Senthilkumar**
Prediction and performance enhancement of R600a refrigerator adopting machine learning algorithms

Research Article
3225 **Loan Thi Pham, Thi Hoai Thu Nguyen, Jie Yi Huang**
Experimental study on anisotropic mechanical properties of 3D reinforced concrete with discrete polyethylene fibers

Research Article
3245 **Md Hasan Ruhan Rabbi, Md Abdur Rahaman, Fatema Akter, Md Mezbah Uddin**
Investigation of electro-mechanical and corrosion behavior of leaded copper

Research Article
3261 **Asma Mecheter, Faris Tarlochan**
Packaging optimization for reducing bruising in pears

Research Article
3279 **Wissam A Ismaeel, Ali Ahmed Mohammed**
A systematic review of physical and environmental indicators for BIM implementation in construction and demolition waste management

Research Article
3289 **Chandra Sekhar Malla, Mukunda Rao D, Sunil Nandipati**
Performance and environmental impact analysis of alkali activated slag and OPC concretes with polypropylene fiber in sustainable construction

Research Article
3309 **Kaushal Sharma, Kiran Devi, Neeraj Saini**
Mechanical properties and optical efficiency of light-transmitting concrete using plastic optical fibre and industrial wastes

Research Article
3327 **S.M. Fahad Hossen Munna, Md Mezbah Uddin**
CFD analysis on horizontal axis tidal current turbine

Research Article
3341 **Rabiâ Abdeldjebar, Abdelghani Idder, Lahbib Lahmar, Lakhdar Missoum, Abderrahmane Moulay Ali**
Artisanal lime as a low-carbon stabilizer for enhanced stabilized earth blocks in sustainable earthen structure rehabilitation

Research Article
3357 **Anton Nekrylov**
Experimental determination of glass units strength under point load from temporary installation tools for blinds and sun protection systems

Research Article
3375 **Shukran Hikmat Faraj, Mohammed J. Kadhim**
Effect of PVA and basalt fibers on enhancing the structural and thermal behavior of cement panels

Research Article
3393 **Ravikiran Kamath B., Sudheer M.**
Fabrication and mechanical behavior of Kevlar® fabric-reinforced epoxy matrix composites modified by potassium titanate whiskers

Research Article
3405 **Carlos Proaño, Michael Rodríguez, Alex Andrango, Juan Quilumba, Leslie Paspuel, Jason Guevara, Ana G. Haro-Baez**
Evaluation of the physical and mechanical properties of pressed blocks and Caramelo blocks used in infill masonry for framed structures

Review Article
3427 **Othmane Karrame, Mohammed Aqil, Mohammed Ammari, Laïla Ben Allal**
Comparative bibliometric and AI-Enhanced analysis of dredged sediments, plant residues, and plastic fibers as eco-friendly additives for sustainable concrete, toward an integrated AI framework

Free access to tables of content, abstracts and full text of papers for web visitors.

Copyright © 2025

Research on Engineering Structures & Materials
MIM Research Group Publications
P-ISSN: 2148-9807
E-ISSN: 2149-4088
http://www.jresm.org

ABSTRACTING / INDEXING

The international journal of Research on Engineering Structures and Materials (RESM) is currently Abstracted/Indexed by Asos Indeks, CiteFactor, Cosmos, CrossRef, Directory of Research Journal Indexing, Engineering Journals (ProQuest), EZB Electronic Journal Library, Global Impact Factor, Google Scholar, International Institute of Organized Research (I2OR), International Scientific Indexing (ISI), Materials Science & Engineering Database (ProQuest), Open Academic Journals Index, Publication Forum, Research BibleScientific Indexing Service, Root Indexing, Scopus, Ulakbim TR Index (Tubitak), Universal Impact Factor and under evaluation by many other respected indexes.

Check web site for current indexing info, www.jresm.org

Research on Engineering Structures & Materials
www.jresm.org
Research Group

Research Article

Enhancing sustainability in construction: Exploring the self-healing mechanisms of bio-concrete

Subitha Thirupathi [*,1,a], Sasikumar Palanisamy [2,b], Venkateshan Asokan [3,c]

[1]*Dept. of Civil Eng., Avinashilingam Institute for Home Science and Higher Education for Women, Avinashilingam University, Tamil Nadu-641043, India*
[2]*Dept. of Civil Eng., K.Ramakrishnan College of Technology, Trichy – 621112, India*
[3]*Dept. of Civil Eng., Sri Muthukumaran Institute of Technology, Anna University, Tamilnadu, India*

Article Info

Article History:

Received 05 Nov 2024
Accepted 03 Feb 2025

Keywords:

Microbiologically induced calcite precipitation;
Microorganisms;
Self-healing;
Steel fibre reinforced concrete

Abstract

This study evaluates the self-healing efficiency of bio-concrete incorporating Bacillus megaterium (067) and Bacillus licheniformis (598), combined with Steel Fibre Reinforced Concrete (SFRC), for sustainable construction. Concrete specimens were prepared with bacterial concentrations of 103, 105, and 107 cells/ml, alongside steel fibre additions of 1%, 1.5%, and 2% by weight. Artificial cracks were introduced, and the healing performance was assessed through visual and microstructural analyses. Mechanical properties, including compressive, split tensile, and flexural strengths, were systematically tested. Results showed significant enhancements, with compressive strength improving by up to 18% and crack widths reducing by over 60% due to microbiologically induced calcite precipitation (MICP). Scanning Electron Microscopy (SEM) confirmed calcite deposition within cracks, validating bacterial involvement in self-healing. This research highlights the potential of integrating bacteria into SFRC to improve mechanical durability and self-healing, offering an innovative path toward eco-friendly and resilient construction materials.

© 2025 MIM Research Group. All rights reserved.

1.Introduction

Concrete is a fundamental component in Civil Engineering due to its high compressive strength, ready availability, and adaptability to various environmental conditions. However, it is inherently weak in tensile strength, which limits its use without reinforcement [1]. Under high loads, freezing and thawing cycles, and environmental fluctuations, concrete inevitably experiences cracking, compromising structural elements' durability and lifespan [2]. Key mechanical properties of concrete include compressive strength (CS), split tensile strength (STS), flexural strength (FS), and impact resistance (IR) [3]. Despite advances in reducing greenhouse gas emissions in construction, concrete remains susceptible to cracking due to shrinkage, salt crystallization, and chemical expansion [4,5]. These cracks permit the infiltration of aggressive agents, significantly reducing concrete's water resistance and durability [6]. At the same time, chloride ions in coastal regions can accelerate steel reinforcement corrosion, further weakening structures [7,8]. self-healing concrete bacteria can perform better in corrosive environmental conditions and seawater salinity, urease producing bacteria used and the mechanism of healing process. Research has shown that Bacillus subtilis bacteria can effectively heal microcracks in concrete exposed to corrosive environments, thereby improving its durability and mechanical properties [9]. Additionally, studies on bio-concrete in marine applications have demonstrated its enhanced self-healing ability in submerged and tidal conditions, particularly under sustained loading. Furthermore, the use of

*Corresponding author: subitha_civil@avinuty.ac.in
[a]orcid.org/0000-0002-1646-1237; [b]orcid.org/0000-0002-9674-5319; [c]orcid.org/0009-0006-8570-0023
DOI: http://dx.doi.org/10.17515/resm2025-517ma1105rs

bio-carriers immobilized with marine bacteria has been found to positively impact the self-healing efficiency and mechanical properties of cementitious materials, further enhancing the performance of bio-concrete in challenging environments. [10].

Concrete has a natural healing ability for micro-cracks with widths below 200 μm, aiding in its resilience [11]. Studies have shown that bacterial incorporation in concrete enhances compressive strength over time, with $CaCO_3$ precipitating to fill pores and improve concrete microstructure [12]. Fibre reinforcement, particularly polypropylene fibre, has significantly reduced crack widths by bridging gaps between fibres [13]. Research has explored enhancing fibre-reinforced concrete (FRC) durability through integrating bacteria, with Bacillus subtilis being shown to improve crack healing and nutrient sources aiding the process [14, 15]. Fibre-reinforced cement Concrete (FRCC) has also demonstrated increased energy absorption capacity and tensile strength due to the post-cracking behaviour introduced by fibre additions [16-17]. Including *Bacillus* bacteria in concrete has been associated with a 23% improvement in compressive strength and the efficient healing of micro-cracks [18,19]. Studies on polypropylene fibre have further highlighted improvements in concrete's physical and chemical properties when fibres are incorporated [20, 21]. In addition to the improvements observed with polypropylene fibers, studies on self-healing concrete incorporating natural fibers have also demonstrated notable enhancements in both physical and chemical properties. These natural fibers provide to the overall strength and durability of structures while promoting self-healing mechanisms [10,22]. The integration of such fibers in bio-concrete systems further enhances crack repair and the longevity of structures, aligning with the growing trend of sustainable materials in construction [17]. Research on these innovative approaches underscores the potential for combining natural fibers with biologically active systems to create concrete that is both environmentally friendly and capable of self-repair in response to damage [23,24].

Significant advancements in the growth of healing bacterial concrete and fibre-reinforced concrete, the simultaneous incorporation of *Bacillus megaterium* (BM) and *Bacillus licheniformis* (BL) within a Steel Fibre Reinforced Concrete (SFRC) matrix represents a novel approach in the field of sustainable construction. The existing literature primarily focuses on the use of a single microbial species or conventional polypropylene fibres, which limits the crack healing efficiency and mechanical performance of bio-concrete. This study distinguishes itself by optimizing bacterial concentrations (10^3, 10^5, and 10^7 cells/ml) alongside varying steel fibre content (1%, 1.5%, and 2%) to evaluate their synergistic impact on mechanical properties and self-healing capabilities. Furthermore, the integration of microbiologically induced calcite precipitation (MICP) with SFRC has not been extensively explored. By leveraging this unique combination, this research addresses the dual challenge of enhancing the mechanical durability and self-healing efficiency of concrete. The findings are expected to contribute to the growth of resilient and biodegradable construction materials, offering a significant step toward reducing the environmental effect of the construction production while improving structural performance and service life.

2.Materials and Methods

2.1 Cement

The Ordinary Portland Cement (OPC) of 53 grade is confirmed per the Indian code [6]. The sp. gravity of cement was 3.18. The mechanical properties of cement are illustrated in Table 1.

Table 1. Mechanical and Chemical properties of cement

Mechanical Properties	Values
Initial setting time	32 min
Final setting time	472 min
Fineness	2.77%
Consistency	32%
Sp. Gravity	3.14
Chemical Properties	%
SiO_2	22

CaO	64
Al_2O_3	5.45
Fe_2O_3	3.25
MgO	3.16
Na_2O	0.78
Loss on ignition	1.32

2.2 Fine Aggregate

River sand is the most suitable material for fine sand. The sp. Gravity of 2.69 and fineness modulus of 3.47% were used as fine aggregate. According to IS code [7], an aggregate retained on an IS 4.75mm sieve is called fine sand or aggregate as shown in (Fig. 1).

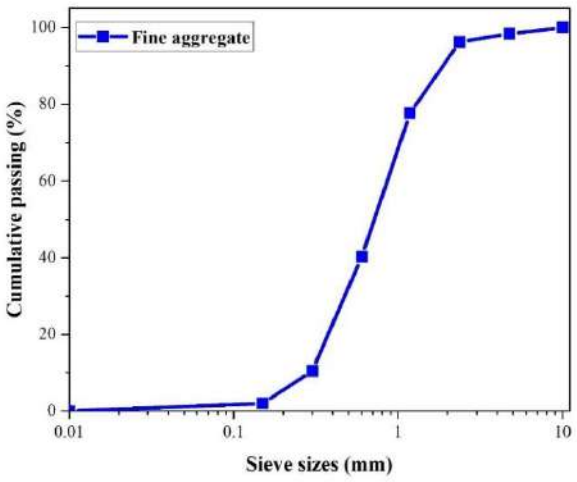

Fig. 1. Granularity diagram for fine aggregate analysis

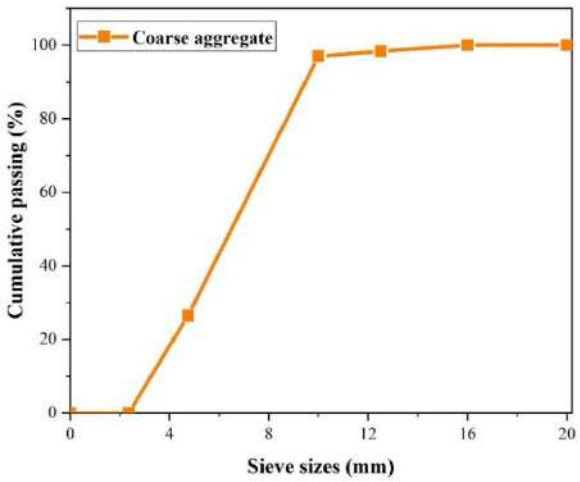

Fig. 2. Granularity diagram for coarse aggregate analysis

2.3 Coarse Aggregate

The coarse aggregate comprises granular and rough material from rocks and broken stones. In tests according to IS code [7,8], specific gravity was found to be 2.3 and water absorption at 0.68%. Granularity Diagram for Coarse Aggregate Analysis as shown in (Fig. 2).

2.4 Fly Ash

Table 2 illustrates the characteristics of fly ash, fitness, and specific gravity of 2.88 and 2.09

Table 2. Mechanical and Chemical properties of fly ash

Chemical properties	Values of fly ash %
SiO_2	46.42
Fe_2O_3	8.3
Al_2O_3	13.7
MgO	6.72
SO_3	4.45
CaO	0.16
Mechanical properties	Values for fly ash
Specific gravity	2.09
Fineness (m^2/kg)	288
Bulk density (kg/m3)	1100-1200

2.5 Silica Fume

Silica fume was purchased from the fibre regions of Chennai. The sp. gravity of silica fume was 2.63, and the properties of silica fume are illustrated in Table 3.

Table 3. Mechanical and Chemical properties of fly ash

Physical properties	Results
Physical level	Micronized powder
Odor	Odorless
Appearance	White powder form
Colour	White
The pH of 5% solution	6.9
Specific gravity	2.63
Moisture content	0.058%
Chemical properties	%
SiO_2	99.18
Al_2O_3	0.042
Fe_2O_3	0.038
TiO_2	0.001
MgO	0.000
K_2O	0.001
Na_2O	0.0022
Heavy metal Lead and Arsenic	Nil

2.6 Steel Fibre

SFRC is a composite material consisting of a concrete mix and steel fibres used as a reinforcing agent. In the concrete mix, the fibres are evenly distributed. The fibre characteristics and quantities are represented in Table 4.

Table 4. Steel fibre properties

Fibre properties	Quantity
Shape	(Deformed) Hooked end
Length	60 mm
Diameter	0.75 mm
Aspect ratio	80 (l/d)
Tensile strength	1100 N/mm^2
Unit weight	7850 kg/m^3
Elastic modulus, E	205 MPa

2.7 Chemical Admixture

Superplasticizer SP-43 was utilized in accordance with the specifications outlined in the IS codebook for concrete mix designs. This chemical admixture is designed to improve the workability of concrete without compromising its strength. It allows for the reduction of water content while maintaining or enhancing the flowability of the mix. The specific gravity of SP-43 is 1.08, indicating its density relative to water. This characteristic is important for accurately determining dosage rates and ensuring the proper balance between the admixture and other components in the mix. The correct usage of SP-43 contributes to achieving high-performance concrete with improved durability.

2.8 Concrete

This study used two natural mineral admixtures as a by-product; M40 grade concrete was used and set with a 0.3 water-cement ratio according to the Indian code [23]. Fly ash (FA) and Silica fume (SF) were used in varying proportions as a (partial replacement) for cement, such as 15% FA and 15% SF. The cultured bacteria were added to the concrete at various concentration levels, such as 10^3,10^5,10^7 cells/ml.

2.9 Bacteria Cultivation Process

Two bacterial species were obtained from a fermented mixture, and construction water samples were collected from a local construction site in Coimbatore, Tamil Nadu. A 1 ml or 1 g portion of each sample was introduced into an enriched nutrient medium and incubated at 37°C for 2 to 3 days. After sufficient bacterial growth, serial dilutions were carried out, and the cultures were transferred onto Urea agar with a pH of 9.4. The composition of the Urea agar included Urea (20 g/l), Sodium bicarbonate (2.12 g/l), NH_4Cl (10 g/l), Calcium chloride hydrate (25 g/l), and NB-Nutrient Broth (3.0 g/l). The plates were incubated for 2 to 3 days at 37°C. Following incubation, bacterial colonies showing crystal-like precipitation were identified and moved to Urea broth. Endospore staining was performed to confirm the presence of spores. The isolates were further tested for calcium carbonate precipitation by adding 2% urea and calcium chloride to the nutrient broth to maintain the ideal conditions. A 30 ml portion of this broth was inoculated with 0.6 ml of the isolated culture and incubated for 7 days at 30°C with shaking at 130 rpm. This process was repeated three times to ensure the isolates formed precipitates. The resulting calcium carbonate was filtered through Whatman filter paper, dried at 60°C for 3 hours, and weighed. Five distinct colonies were isolated using the spread plate method and sub cultured on nutrient agar slants. Nutrient agar is commonly used for growing a variety of bacteria and fungi, both in liquid and solid forms. The liquid form is referred to as Nutrient Broth, while the solidified version is called Nutrient Agar. When cooled below 45°C, the agar solidifies, providing a firm surface for bacterial growth and development. [26].

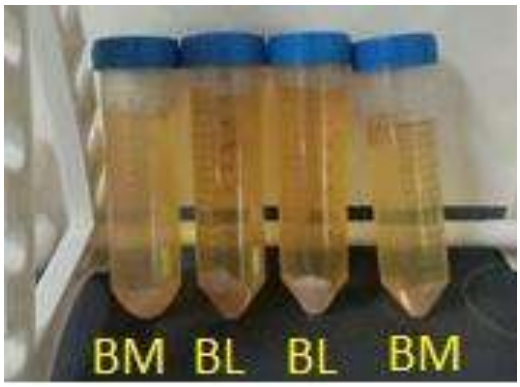

Fig. 3. Cultured *Bacillus megaterium* and *Bacillus licheniformis*

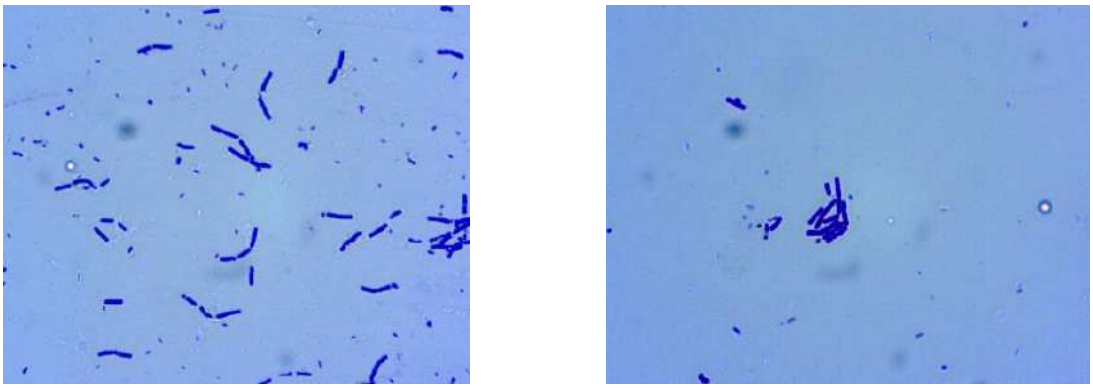

Fig. 4. Microscopic images of *Bacillus megaterium* and *Bacillus licheniformis*

3. Experimental Investigations

3.1 Proportioning of Mixes

In the trial mix design, a conventional trial mix was developed (without fibre and bacteria culture) on a trial mix to achieve a 28-day cube of 40 N/mm^2. The materials are available in the local market. The mix proportion has been determined to reach the target design strength of 48N/mm^2 without

using fibre and bacteria. By weight of cement (C), admixtures (A), fine aggregate (FA), coarse aggregate (CA), fibre, and bacteria were used in 1%,1.5%, and 2%. We could observe and evaluate the mechanical behavior of bio concrete with fibre and bacteria more effectively. The mechanical behavior of bio concrete and mixes in Table 5 were used. As for the conventional mixture, 40 N/mm^2 (without fibre and bacteria) mixing procedures were carried out as per codes [24,25].

Table 5. Bio concrete mixtures for 1m^3 volume of concrete

Materials	Quantities			
	M 1	M 2	M 3	M 4
Cement (kg)	350	350	350	350
Fly ash(kg)	65	65	65	65
Silica fume(kg)	65	65	65	65
Water	160	160	160	160
Fine aggregate (kg)	720	720	720	720
Coarse aggregate (kg)	1230	1230	1230	1230
Superplasticizer	4.2	4.2	4.2	4.2
W/c	0.36	0.36	0.36	0.36
Bacterial Sample	-	-	*B. megaterium*	*B. licheniformis*

3.2 Proportions of Test Specimens

Bio concrete is characterized by its Compressive Strength (CS), Split Tensile Strength (STS), and Flexural Strength (FS), which is prepared at various ages, like 7 days, 14 days, and 28 days. CS and STS were tested on a compression testing machine (CTM), and FS was tested on the universal testing machine (UTM) to evaluate the strength properties [27]. The specimen was cast like a 150 mm X 150 mm X 150 mm cube, a 150 mm diameter X 300 mm length cylinder, and a 500 X 100 X 100mm prism. The design target strength is achieved at 28 days of 48 N/mm^2 without fibre and bacteria. Summarizing the number of specimens and tests as shown in Table 6.

Table 6. Summarizing the number of specimens and tests

Mix Design	Specimen Shape	Specimen Size	Number of Specimens	Purpose
M1	Cube	150x150x150	3	Compressive Strength(CS)
M1	Cylinder	150x300	3	Split Tensile Strength(STS)
M1	Prism	100x100x500	3	Flexural Strength(FS)
M2	Cube	150x150x150	3	Compressive Strength(CS)
M2	Cylinder	150x300	3	Split Tensile Strength(STS)
M2	Prism	100x100x500	3	Flexural Strength(FS)
M3	Cube	150x150x150	3	Compressive Strength(CS)
M3	Cylinder	150x300	3	Split Tensile Strength(STS)
M3	Prism	100x100x500	3	Flexural Strength(FS)
M4	Cube	150x150x150	3	Compressive Strength(CS)
M4	Cylinder	150x300	3	Split Tensile Strength(STS)
M4	Prism	100x100x500	3	Flexural Strength(FS)

4. Results and Discussion

4.1 Compressive Strength

The results of this study indicate clear improvement in compressive strength with the incorporation of both steel fibers and bacterial additives in bio-concrete. Specifically, the compressive strength increased from 48.15 N/mm^2 (without fiber) to 52.38 N/mm^2 (with fiber), exceeding the target design strength of 48 N/mm^2. A further increase in compressive strength was observed when the fiber content was increased from 0% to 1.5%, with the 28-day strength reaching 52.90 N/mm^2. This demonstrates that steel fibers significantly contribute to improving the

concrete's structural integrity. The observed 9.86% increase in compressive strength is consistent with prior research, which indicates the positive effects of steel fiber reinforcement on concrete performance as shown in (Fig. 5). The addition of bacteria, particularly *Bacillus megaterium* and *Bacillus licheniformis*, further enhanced the compressive strength from 50.94 N/mm^2 to 51.45 N/mm^2 illustrated in table 7.

Fig. 5. Compressive strength test

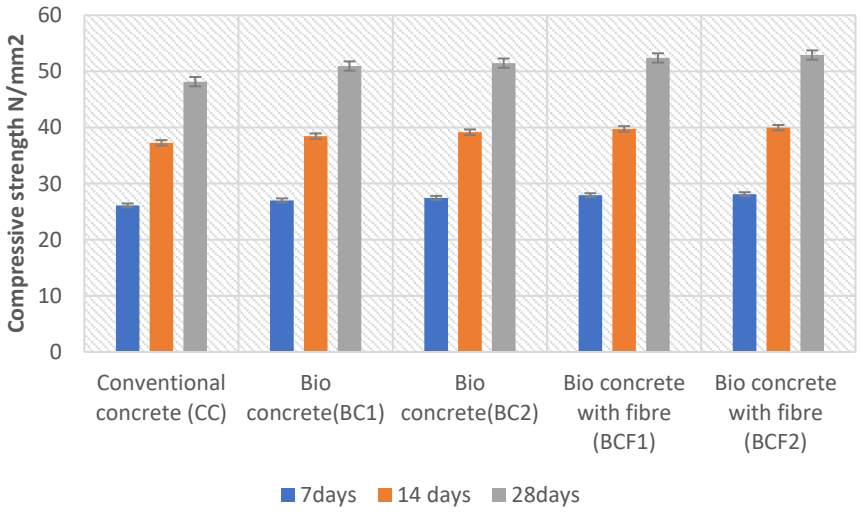

Fig. 6. Compressive strength at 7,14,28 days)

Table 7. Compressive strength result

Mix ID	% Of fibre	Average compressive strength test results in N/mm^2			% Increase over the conventional mix in 28 days
		7days	14 days	28 days	
Conventional concrete (CC)	_	26.10	37.25	48.15	-
Bio concrete (BC1) (*B. megaterium*) (10^5)	_	27.00	38.45	50.94	5.79
Bio concrete (BC2) (*B. licheniformis*) (10^5)	_	27.45	39.15	51.45	6.85
Bio concrete with fibre (BCF1) (10^5)	1.00	27.92	39.74	52.38	8.78
Bio concrete with fibre (BCF2) (10^5)	1.50	28.10	39.95	52.90	9.86

This suggests that the bacteria, likely due to their role in self-healing mechanisms, contributed to the improved durability and strength of the concrete. The optimum concentration of 10^5 cells/ml for the bacteria provided the best enhancement in compressive strength, which aligns with other studies that have highlighted the importance of bacterial concentration in bio-concrete. The optimal fiber percentage for maximum compressive strength was found to be 1.5%, reinforcing the importance of a balanced mix of fiber and bacterial additives to achieve high-strength bio-concrete [28]. The results support the hypothesis that a synergistic effect between steel fibers and bacteria can significantly improve the mechanical properties of concrete, suggesting a promising avenue for future development of self-healing, durable concrete as shown in (Fig. 6).

4.2 Split Tensile Strength (STS)

Table 8 shows different percentages of fibre and bacteria. STS of bio concrete after 7,14, and 28 days with an increase in fibre percentage from 0 to 1.5%, the 28 days split tensile strength increased from 4.85 to 6.00 N/mm^2.When the fibre percentage 1 - 1.5 % increased, the split tensile strength increased slightly from 5.9 to 6.00 N/mm^2. When the coupled effect of fibre and bacteria was added, it increased the strength from 10.10 to 23.71%. According to (Fig.7) a fibre percentage of 1.5% is the best value for the combined effect of fibre and bacteria addition for split tensile strength of 6.00 N/mm^2.The addition of bacteria and fibre increased the STS from 0 to 23.71% over the conventional concrete sample, and the optimum percentage of bacteria (10^5) cells/ml, with split tensile strength, increased from 5.68 to 6 N/mm^2 of bacteria, as shown in (Fig. 8).

Fig. 7. Split tensile strength

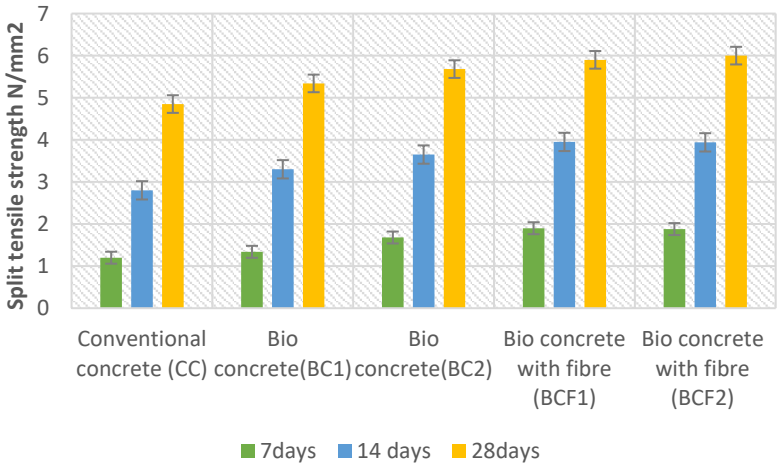

Fig. 8. Split tensile strength increased over the conventional concrete in percentage

Table 8. Split tensile strength result

Mix ID	% Of fibre	Average split tensile strength test results in N/mm²			% Increase over the conventional mix on 28days
		7days	14 days	28days	
Conventional concrete (CC)	_	1.2	2.8	4.85	-
Bio concrete(BC1) (*B. megaterium*)(10^5)	_	1.34	3.3	5.34	10.10
Bio concrete(BC2) (*B. licheniformis*) (10^5)	_	1.68	3.65	5.68	17.11
Bio concrete with fibre (BCF1) (10^5)	1%	1.90	3.95	5.90	21.64
Bio concrete with fibre (BCF2) (10^5)	1.5%	1.88	3.94	6.00	23.71

4.3 Flexural Strength (FS)

Flexural strength after 7, 14, and 28 days with different percentages of fibre and bacteria is shown in (Fig. 9) and Table 9. Increase the fibre percentage from 0 to 1.5 % in 28 days flexural strength from 8.24 N/mm² to 10.80 N/mm². With the increase in fibre percentage from 1 to 1.5%, the flexural strength increased slightly from 10.18 to 10.80 N/mm². The fibre percentage of 1.5% is the optimum value of fibre addition for a flexural strength of 10.80 N/mm².The coupled effect of fibre and the addition of bacteria for flexural strength from 0 to 31.06% over the conventional sample fibre is 1.5%, and bacterial 10^5 cells/ml optimum concentration levels as shown in (Fig.10)

Fig. 9. Flexural strength test

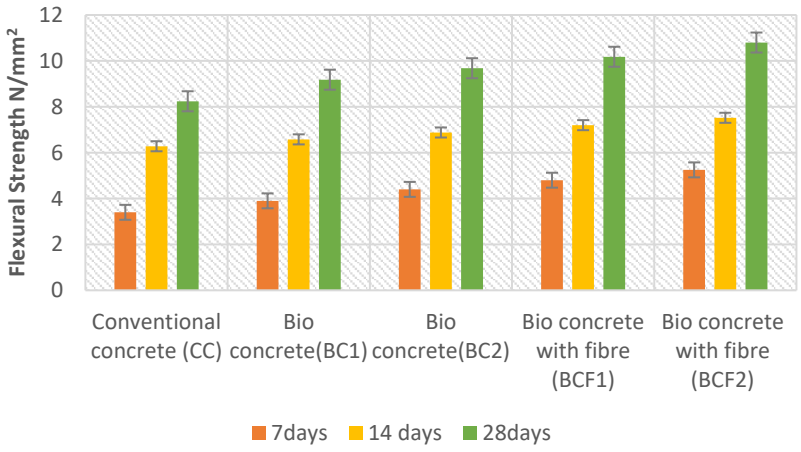

Fig. 10. Flexural strength test results at different ages (7,14, and 28 days)

Table 9. Flexural strength result

Mix ID	% Of fibre	Average split tensile strength test results in N/mm²			% Increase over the conventional mix on 28days
		7days	14 days	28days	
Conventional concrete (CC)	_	3.4	6.28	8.24	-
Bio concrete(BC1) (*B. megaterium*)(10^5)	_	3.9	6.58	9.18	11.40
Bio concrete(BC2) (*B. licheniformis*) (10^5)	_	4.4	6.88	9.68	17.47
Bio concrete with fibre (BCF1) (10^5)	1%	4.8	7.20	10.18	23.54
Bio concrete with fibre (BCF2) (10^5)	1.5%	5.25	7.52	10.80	31.06

4.4 Healing Process

The self-healing process in concrete begins soon after cracks form, and this study indicates that within the first 7 days, the cracks start to self-repair. The primary mechanism for self-healing in this context is the precipitation of calcium carbonate ($CaCO_3$). When cracks appear on the concrete surface, certain conditions (such as moisture and nutrients) trigger the bacteria within the concrete to become active, leading to the precipitation of calcium carbonate.

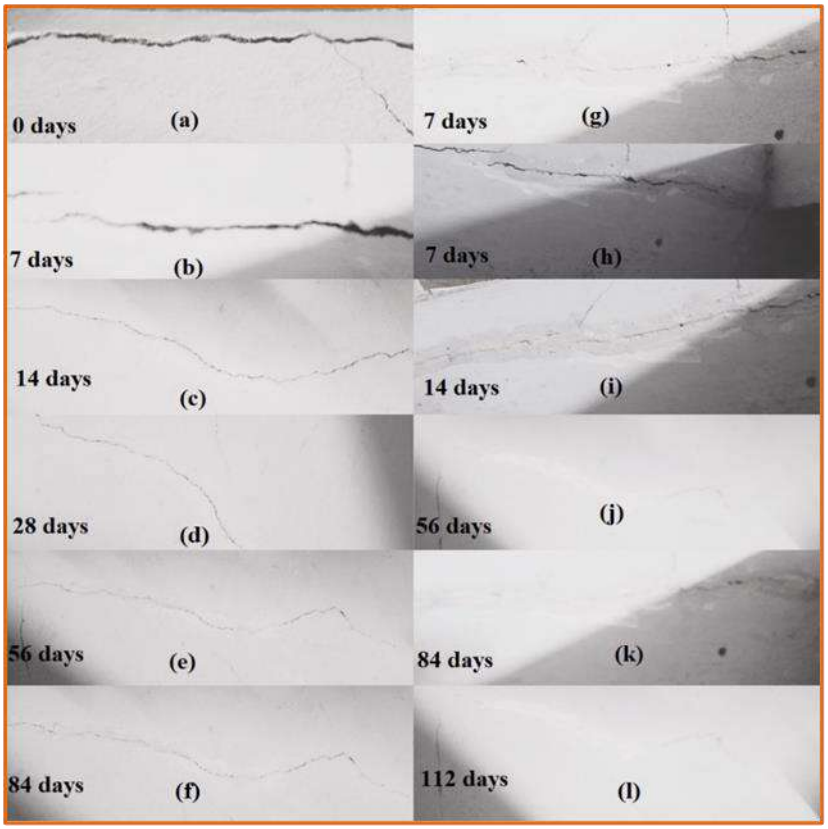

Fig. 11. Healing Process

This precipitation fills the cracks, effectively "healing" the concrete. In this case, after 112 days, the cracks in the non-bacterial concrete specimens were fully healed due to the complete deposition of calcium carbonate, as illustrated in (Fig. 11i). In the bacterial concrete specimens, however, the healing process is more gradual. After 28 days, the cracks in these specimens were only partially healed, as shown in (Fig. 11d). Over time, calcite precipitates (a form of calcium carbonate) continued to form within the cracks. By the 84-day mark, calcite was visible within the cracks of the bio concrete specimens, and by the end of 84 days, these bacterial concrete specimens had

achieved complete crack healing, as seen in (Fig. 11k). This process demonstrates the effectiveness of using bacterial-based self-healing in concrete, with bacteria promoting the formation of calcium carbonate that gradually seals the cracks, enhancing the structural integrity of the concrete over time.

5. Microstructural Analysis

Calcite precipitation in concrete specimens was observed through the activity of *Bacillus megaterium*, *Bacillus licheniformis*, and a mixture of IS 1 and IS 2. The growth of calcite crystals, interspersed with bacterial cells, was detected in the specimens, as shown in Fig. 12b, with larger crystals visible in Fig. 12c. Bacteria were found in close contact with the calcite crystals in samples 2b and 2c. The cultures of IS 1 and IS 2 significantly enhanced the strength of the structures compared to conventional bio-concrete, as shown in Fig. 13b, and traditional concrete, as seen in Fig. 12, where no crystals were visible. This absence of calcite crystals in the traditional concrete suggests that calcite-precipitating bacteria were not present in those samples [30,31]. The XRD analysis was performed at a step size of 2θ, starting at 10° and ending at 80°. The scanning was conducted in continuous mode with a fixed divergence slit at a temperature of 25°C, using Cu Kα radiation as the source. Calcite ($CaCO_3$) was detected throughout the scan range, as illustrated in Fig. 13.

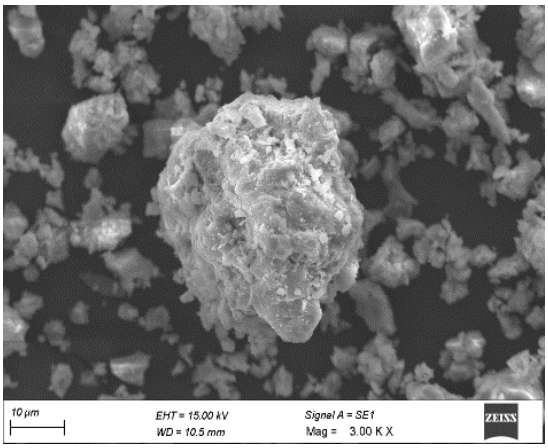

(a)

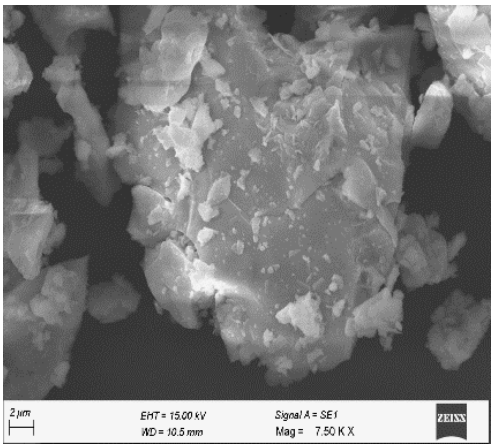

(b)

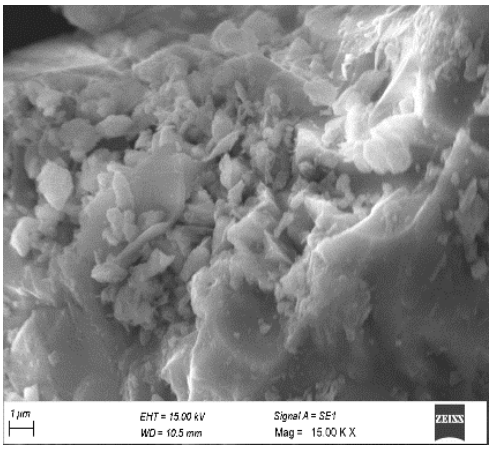

(c)

Fig. 12. SEM of (a), (b) concrete specimen with B.megaterium and B. licheniformis representing the calcite crystals, (c) concrete specimen with IS 1 and IS 2 bacterial mixture representing the presence of enlarged crystals, showing higher microbially induced calcite precipitation

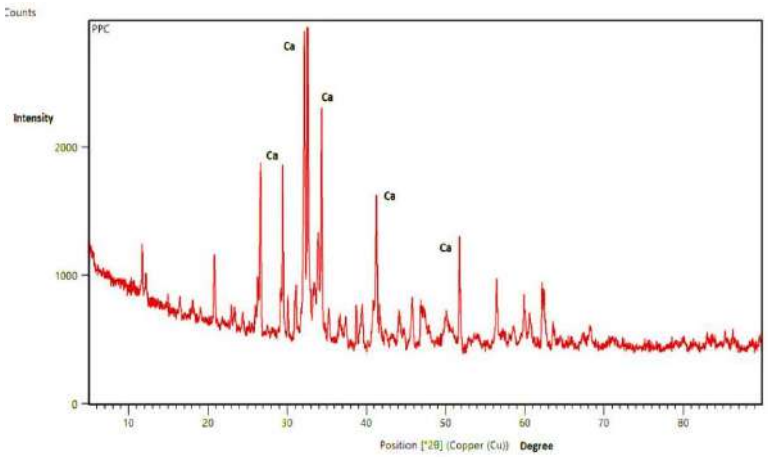

(a)

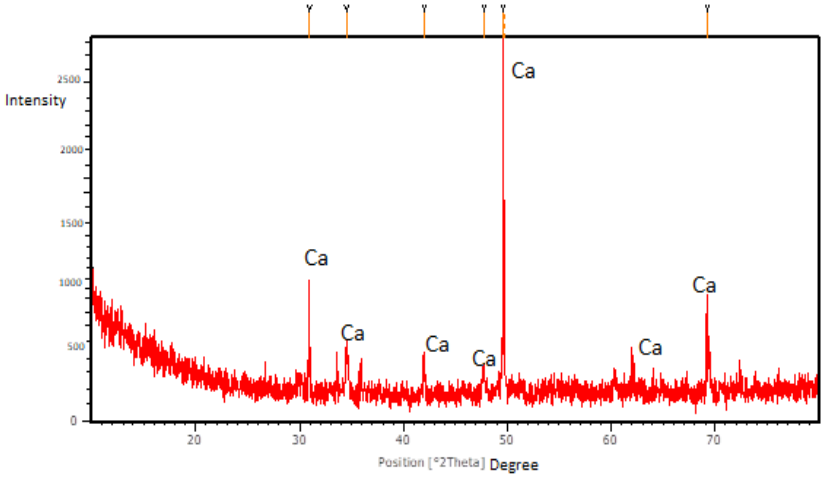

(b)

Fig. 13. XRD Analysis (a) Conventional concrete (b) Isolated Microbial concrete

6. Conclusions

This study establishes a correlation between the integration of bacterial strains and steel fibres in cementitious composites and the enhancement of both structural integrity and autonomous healing capabilities. The bio-concrete mix achieved compressive strengths of 49.25 N/mm^2 without fibres and 52.38 N/mm^2 with steel fibres, surpassing the targeted design strength of 48 N/mm^2 and outperforming traditional concrete. The self-healing efficiency of the bio-concrete was fully realized within 84 days, with approximately 60-70% strength recovery observed by day 28. Microstructural analyses, including XRD and SEM, long-established the presence of calcite ($CaCO_3$) in healed cracks, validating the role of microbiologically induced calcite precipitation (MICP) in crack healing. These findings demonstrate that standardized strains of *Bacillus megaterium* and *Bacillus licheniformis* significantly enhance both the mechanical properties and durability of bio-concrete. Further optimization of production parameters holds the potential to amplify these benefits, paving the way for the development of highly durable, sustainable construction materials.

Acknowledgement

We extend my heartfelt thanks to Avinashilingam Institute for Home Science and Higher Education for Women for completing the research work.

References

[1] Ganesh AC, Muthukannan M, Malathy R, Babu CR. Experimental study on effects of bacterial strain combination in fibre concrete and self-healing efficiency. KSCE J Civ Eng. 2019;23(10):4368-77. https://doi.org/10.1007/s12205-019-1661-2

[2] Augusto L, Borges C, Monte R, Alan D, Rambo S, De Figueiredo AD. Evaluation of post-cracking behavior of fibre-reinforced concrete using an indirect tension test. Constr Build Mater. 2019;204:510-9. https://doi.org/10.1016/j.conbuildmat.2019.01.158

[3] Bashir J, Ifrahkathwari, Aditya T, Khushpreet S. Bio concrete-the self-healing concrete. Indian J Sci Technol. 2016;9(47):1-5. https://doi.org/10.17485/ijst/2015/v8i1/105252

[4] Bundur ZB, Kirisits MJ, Ferron RD. Biomineralized cement-based materials: Impact of inoculating vegetative bacterial cells on hydration and strength. Cem Concr Res. 2015;67:237-45. https://doi.org/10.1016/j.cemconres.2014.10.002

[5] Bureau of Indian Standards. Methods of test for aggregates for specifications. IS 2720. 1963.

[6] Bureau of Indian Standards. Methods of testing for aggregates for concrete: Specific gravity, density, voids, absorption, and bulking. IS 1963b (Part 3).

[7] Bureau of Indian Standards. Methods of test for the strength of concrete. IS 516. 1959.

[8] Chalioris CE, Panagiotopoulos TA. Flexural analysis of steel fibre-reinforced concrete members. Comput Concr. 2018;22(1):11-25.

[9] Du F, Jin Z, She W, Xiong C, Feng G, Fan J. Chloride ions migration and induced reinforcement corrosion in concrete with cracks: A comparative study of current acceleration and natural marine exposure. Constr Build Mater. 2020;263:120099. https://doi.org/10.1016/j.conbuildmat.2020.120099

[10] Eidan J, Rasoolan I, Rezaeian A, Poorveis D. Residual mechanical properties of polypropylene fibre-reinforced concrete after heating. Constr Build Mater. 2019;198:195-206. https://doi.org/10.1016/j.conbuildmat.2018.11.209

[11] Philip N, R GV, Syriac T. Effectiveness of bacteria-based self-healing concrete under corrosive environment. Iran J Sci Technol Trans Civ Eng. 2024;48(6):1413-26. https://doi.org/10.1007/s40996-023-01248-x

[12] Khan MB, Shen L, Dias-da-Costa D. Self-healing behaviour of bio-concrete in submerged and tidal marine environments. Constr Build Mater. 2021;277:122332. https://doi.org/10.1016/j.conbuildmat.2021.122332

[13] Kim H, Son H, Seo J, Lee HK. Impact of bio-carrier immobilized with marine bacteria on self-healing performance of cement-based materials. Materials (Basel). 2020;13(18):4164. https://doi.org/10.3390/ma13184164

[14] Fahimizadeh M, Pasbakhsh P, Lee SM, Tan JBL, Singh RKR, Yuan P. Sustainable biologically self-healing concrete by smart natural nanotube-hydrogel system. Dev Built Environ. 2024;18:100384. https://doi.org/10.1016/j.dibe.2024.100384

[15] Kaushal V, Saeed E. Sustainable and innovative self-healing concrete technologies to mitigate environmental impacts in construction. CivilEng. 2024;5(3):549-58. https://doi.org/10.3390/civileng5030029

[16] Meraz MM, Mim NJ, Mehedi MT, Bhattacharya B, Aftab MR, Billah MM, et al. Self-healing concrete: Fabrication, advancement, and effectiveness for long-term integrity of concrete infrastructures. Alex Eng J. 2023;73:665-94. https://doi.org/10.1016/j.aej.2023.05.008

[17] Guo Y, Xiang K, Wang H, Liu X, Ye Q, Wang X. Experimental study on self-healing and mechanical properties of sisal fiber-loaded microbial concrete. Mater Res Express. 2023;10(4). https://doi.org/10.1088/2053-1591/acc718

[18] Gümü M, Arslan A. Effect of fibre type and content on the flexural behavior of high-strength concrete beams with low reinforcement ratios. Structures. 2019;20:1-10. https://doi.org/10.1016/j.istruc.2019.02.018

[19] Han J, Zhao M, Chen J, Lan X. Effects of steel fibre length and coarse aggregate maximum size on mechanical properties of steel fibre-reinforced concrete. Constr Build Mater. 2019;209:577-91. https://doi.org/10.1016/j.conbuildmat.2019.03.086

[20] Krishnapriya D, Venkatesh Babu DL, Prince Arulraj GP. Isolation and identification of bacteria to improve the strength of concrete. Microbiol Res. 2015;174:48-55. https://doi.org/10.1016/j.micres.2015.03.009

[21] Liu H, Huang H, Wu X, Peng H, Li Z, Hu J, et al. Effects of external multi-ions and wet-dry cycles in a marine environment on autogenous self-healing of cracks in cement paste. Cem Concr Res. 2019;120:198-206. https://doi.org/10.1016/j.cemconres.2019.03.014

[22] Luhar S, Suthar G. A review paper on self-healing concrete. J Civ Eng Res. 2015;5(3):53-8.

[23] Palin D, Wiktor V, Jonkers HM. Autogenous healing of marine-exposed concrete: Characterization and quantification through visual crack closure. Cem Concr Res. 2015;73:17-24. https://doi.org/10.1016/j.cemconres.2015.02.021

[24] Qin Y, Zhang X, Chai J, Xu Z, Li S. Experimental study of compressive behavior of polypropylene-fibre-reinforced and polypropylene-fibre-fabric-reinforced concrete. Constr Build Mater. 2019;194:216-25. https://doi.org/10.1016/j.conbuildmat.2018.11.042
[25] Sasikumar P, Govindh MA, Subitha T. A study on the flexural behaviour and self-healing of fibre reinforced bacterial concrete beams. Asian J Civ Eng. 2024. https://doi.org/10.1007/s42107-024-01201-x
[26] Subitha T, Manju R, Kumaresan K. Development of bacterial consortia from traditional lime mortar for the preparation of sustainable and strength-enhanced concrete: A solution for heavy metal toxic concrete. Glob Nest J. 2023;25:180-4.
[27] Subitha T, Manju R, Sasikumar P. Sustainable and strength-enhanced concrete using microbial consortia. Rev Constr. 2024;23(2):403-12. https://doi.org/10.7764/RDLC.23.2.403
[28] Subitha T, Manju R. Reduction of heavy metal toxicity in cement using microorganisms. Rev Chim. 2023;74(2):20-7.
[29] Sasikumar P, Govindh MA, Subitha T. A study on the flexural behaviour and self-healing of fibre reinforced bacterial concrete beams. Asian J Civ Eng. 2024. https://doi.org/10.1007/s42107-024-01201-x
[30] Subitha T, Manju R. Experimental investigation on strength properties of concrete with metal slag and plastic granules. AIP Conf Proc. 2022;2446:060004. https://doi.org/10.1063/5.0108162
[31] Padmanabhan G, Subitha T, Kishore KS. Influence of eco-sand drains on the performance of consolidation characteristics founded on soft clay deposits. Lect Notes Civ Eng. 2021;152. https://doi.org/10.1007/978-981-16-1831-4_17
[32] Vijay K, Murmu M. Effect of calcium lactate on compressive strength and self-healing of cracks in microbial concrete. Front Struct Civ Eng. 2019;13(3):515-25. https://doi.org/10.1007/s11709-018-0494-2
[33] Vijay K, Murmu M. Effect of calcium lactate and Bacillus subtilis bacteria on properties of concrete and self-healing of cracks. Int J Struct Eng. 2020;10(3):20-2. https://doi.org/10.1504/IJSTRUCTE.2020.108528
[34] Wiktor V, Jonkers HM. Bacteria-based concrete: From concept to market. Smart Mater Struct. 2016;25:084006. https://doi.org/10.1088/0964-1726/25/8/084006
[35] Zhu H, Hu Y, Li Q, Ma R. Restrained cracking failure behavior of concrete due to temperature and shrinkage. Constr Build Mater. 2020;224. https://doi.org/10.1016/j.conbuildmat.2020.118318
[36] Kayondo M, Combrinck R, Boshoff WP. State of the art review on plastic cracking of concrete. Constr Build Mater. 2019;225:886-97. https://doi.org/10.1016/j.conbuildmat.2019.07.197

Research on Engineering Structures & Materials
www.jresm.org
Research Group

Research Article

Structural behavior of deficient hollow steel columns strengthened using GFRP

P. Sangeetha [*,a], R. Prithvi [b], Ashwin Kumaran V [c], Murali B [d], Yaashika M [e]

Department of Civil Engineering, Sri Sivasubramaniya Nadar College of Engineering, Chennai-603 110, Tamil Nadu, India

Article Info

Article History:

Received 21 Nov 2024

Accepted 02 Feb 2025

Keywords:

Hollow steel columns;
Axial compression;
Vertical and horizontal slits;
GFRP wrapping;
Load carrying capacity;
Failure mode

Abstract

This study investigates the axial compression behavior of hollow steel columns (HSCs) with and without defects, specifically horizontal and vertical slits, and strengthened using Glass Fiber Reinforced Polymer (GFRP) wrapping. Twelve specimens were tested for failure under axial compression. The parameter varied in the study are circular and square sections and type of slit. Experimental and finite element analyses (FEA) were performed to evaluate the structural performance of intact and defective columns. The load-carrying capacity HSC with a horizontal slit was increased by 20 % when compared to the control specimen without a slit. GFRP wrapping was applied in three plies to enhance load-bearing capacity by 50 % and mitigate the effects of structural deficiencies. The results demonstrated that GFRP significantly improved the axial load capacity and ductility of the columns, particularly in defective specimens, by reducing stress concentrations around the slits. Failure modes were analyzed, showing delayed local buckling, reduced plastic hinge formation, and controlled rupture or delamination of GFRP layers. FEA simulations in ANSYS replicated the experimental behavior accurately with a minimal error of less than 5%, providing insights into stress distribution, load–axial deflection characteristics, and failure mechanisms. This study underscores the effectiveness of GFRP wrapping as a strengthening technique for improving the performance and reliability of deficient CHSCs.

© 2025 MIM Research Group. All rights reserved.

1. Introduction

During Hollow steel columns are commonly used in structural applications due to their high strength and efficiency in load-bearing. Deficiencies in hollow steel columns can arise from various factors, including manufacturing defects, wear and tear, or intentional modifications like slits for utility passages. These defects can lead to stress concentrations and local buckling, reducing the columns' load-carrying capacity and overall stability. The defects such as vertical and horizontal slits can significantly impair their structural performance. There were many techniques available to strengthen the hollow steel tube. FRP composites are extensively applied in structural engineering due to their superior strength-to-weight ratio, corrosion resistance, and adaptability. They are widely used in the retrofitting and strengthening of structural members. FRP commonly enhances flexural and shear capacities. In columns, it provides confinement, boosting axial strength and ductility. For dapped ends and corbels, FRP reinforcement alleviates stress concentrations and cracking, thereby increasing the load-carrying capacity. One promising solution to enhance the strength and stability of these deficient columns is to use glass fiber-reinforced polymer (GFRP) for strengthening. The advantages of GFRP wrapping compared to other techniques are listed in Table 1. GFRP has been extensively researched as a retrofitting material due to its high strength-to-

*Corresponding author: sangeethap@ssn.edu.in
[a]orcid.org/0000-0002-7630-011X; [b]orcid.org/0009-0003-9314-9428; [c]orcid.org/0009-0003-3045-1320; [d]orcid.org/0009-0008-3641-5204; [e]orcid.org/0009-0007-4203-1058
DOI: http://dx.doi.org/10.17515/resm2025-541st1121rs

weight ratio, corrosion resistance, and ease of application. Researchers have found that GFRP wrapping can effectively improve the structural performance of deficient columns. Mohammad et al. [1], experimental and numerical studies have been conducted on the structural behaviours of steel square hollow section (SHS) compression members with initial horizontal or vertical deficiencies, which were reinforced using Carbon Fiber Reinforced Polymer (CFRP) sheets. Similarly, another study by Rao et al. [2] demonstrated that GFRP strengthening enhanced the stiffness and delayed the onset of buckling in deficient hollow steel columns. The effect of CFRP strengthening of the deficient steel SHS columns was studied under axial compression and reported that CFRP wrapping improves the strength of column and reduces the local deformation at the places of deficient [3]. Experimental and numerical investigation on vertical and horizontal deficient SHS columns strengthened with CFRP was done and found that strength lost due to deficient was regained and delay the local buckling after strengthening [4]. The effects of axial loading, stiffness, axial displacement, the position and shape of deficient region on the length of steel SHS columns, and slenderness ratio are examined through a detailed parametric study by Shahraki et al. [5]. Comparative studies have been conducted to evaluate the effectiveness of various strengthening techniques, including the use of GFRP by Lin et al. [6] & sangeetha et al. [7, 8]. Compared the performance of steel-plated and GFRP-strengthened hollow steel columns and highlighted that GFRP retrofitting was more effective in reducing local deformations and distributing stresses uniformly.

Table 1. Comparison of strengthening methods for hollow steel columns

Method	Advantages of Present Method (GFRP Wrapping)
Concrete Filling	Lightweight and offers confinement with minimal weight addition.
Internal Steel Reinforcements	Easier to retrofit and avoids complex fabrication.
External Steel Plates	Corrosion-resistant, no welding required, and aesthetically better.
CFRP Wrapping	Cost-effective for large applications and provides better ductility.
Steel Jacketing	Lightweight, corrosion-resistant, and easier to retrofit.
Concrete Filling	Lightweight and offers confinement with minimal weight addition.

The effectiveness of CFRP composites and steel plates in retrofitting deficient steel SHS columns under axial compression was studied [9]. The study found that CFRP and steel plates reduce stress in damaged regions and enhance load-bearing capacity, but CFRP outperformed steel plates due to issues like increased weight and welding challenges. Eight specimens were tested and simulated, showing CFRP's superior ability to compensate for cross-section reduction. The failure mode of the CFRP-confined rectangular concrete-filled stainless steel tube stub columns was studied [10]. First, the local rupture of CFRP occurred, and the local buckling failure of the concrete-filled stainless-steel tube was present. The bearing capacity of the CFRP-confined concrete-filled stainless steel tube stub columns was stronger than that of concrete-filled stainless steel tube specimens because of the strong restraint capacity of CFRP. The study explored [11] the effect of CFRP strengthening on the structural behavior of square hollow section steel members having an initial deficiency under combined axial and lateral load. To study the effects of the strengthening, 17 specimens were tested under four loading scenarios, with 12 specimens strengthened using CFRP sheets. Finite Element Analysis (FEA) has been widely used to model and predict the behavior of GFRP-strengthened columns. In the study by Sharma and Singh [12], FEA models were developed to simulate the performance of deficient columns with different GFRP configurations. The models were validated through experimental testing, agreeing with the observed structural responses. The stiffness and strength parameters acquired from 27 numerical simulations were assessed for

Square Hollow Section (SHS) profiles with rectangular apertures, which were subjected to axial displacements and found that the FEA model was effective with a minimal error of 10% [13].

Despite the extensive research on strengthening hollow steel columns, existing studies primarily focus on CFRP wrapping, steel jacketing etc. over the deficient hollow steel columns. Moreover, limited attention has been given to the combined effects of deficiencies, such as vertical and horizontal slits, on the structural behavior of hollow steel columns strengthen with GFRP wrapping.

2. Materials and Methods

2.1 Material Properties

The coupon test was conducted to evaluate the material properties, from the test, the following details were observed: yield stress at 267 N/mm^2, ultimate stress at 475 N/mm^2, modulus of elasticity at 2.04x10^5 N/mm^2, and elongation after fracture at 48 mm. According to the manufacturer's data for GFRP sheets, the adopted thickness of 1 mm, tensile strength of 1724 MPa, tensile modulus of 76 GPa, elongation after fracture at 2.8%, and mass density of 2500 kg/m^2.

2.2 Experimental Study

The experimental investigation involved subjecting GFRP-wrapped hollow steel columns with and without slits to axial compression to evaluate their load-carrying capacity and deformation behavior. Specimens included circular and square hollow sections with vertical and horizontal slits, both strengthened and unstrengthened with three plies of GFRP wrapping. The columns were tested under monotonic axial loading using a universal testing machine (UTM) at a constant displacement rate. Axial displacement and axial strain were noted using a dial gauge and strain indicator respectively.

Totally Twelve hollow deficient columns were tested to failure under axial compression. The specimens were grouped into four groups such as group A (Unwrapped GFRP Circular section) which includes specimens without any deficient, specimen with vertical deficient and specimens with horizontal deficient. Group B (Wrapped GFRP Circular section), without any deficient, with vertical deficient and with horizontal deficient. Similarly, Unwrapped GFRP Square section and the wrapped GFRP Square section are grouped as group C and group D respectively. Table 1 provides the detailed dimensions of the hollow deficient columns. The vertical deficient (slit) is made parallel to the axis of the column, located at the mid-height of the specimen and the horizontal deficient (slit) is made perpendicular to the column's axis, also centered at mid-height. The dimensions of the horizontal and vertical slit on the hollow specimens are given in Table 2 as (b_s x d_s) which is 50 mm x 15 mm and 15 mm x 50 mm respectively.

Table 2. Description of specimens

Category	Specimen	D/B	t_s	H	t_f	No. of plies
				mm		
Group A	DSCC-NS-NW	76.5	1.8	624	-	-
	DSCC-HS-NW	76.5	1.8	625	-	-
	DSCC-VS-NW	76.5	1.8	623	-	-
Group B	DSCC-NS-GFRP	76.5	1.8	626	1	3
	DSCC-HS-GFRP	76.5	1.8	625	1	3
	DSCC-VS-GFRP	76.5	1.8	624	1	3
Group C	DSSC-NS-NW	76.5	1.8	623	-	-
	DSSC-HS-NW	76.5	1.8	626	-	-
	DSSC-VS-NW	76.5	1.8	627	-	-
Group D	DSSC-NS- GFRP	76.5	1.8	623	1	3
	DSSC-HS- GFRP	76.5	1.8	624	1	3
	DSSC-VS- GFRP	76.5	1.8	625	1	3

To ensure optimal bonding between the GFRP sheets and steel columns, each specimen was sandblasted to remove any rust, oxides, or other contaminants, and cleaned using acetone to obtain a smooth surface. A two-part epoxy resin for bonding GFRP to steel was applied over the prepared surface. For GFRP wrapping, sheets were positioned around the slit region of the columns by covering the whole column including the deficient portion fully. The 3-plies of GFRP fibers wrapping were done for all specimens. GFRP were oriented circumferentially around the column to maximize lateral confinement, counteracting potential buckling in the weakened regions. Once applied, all wrapped specimens were left to cure at room temperature for 48 hours. Fig. 2 shows the specification of the circular and square hollow deficient specimens before testing.

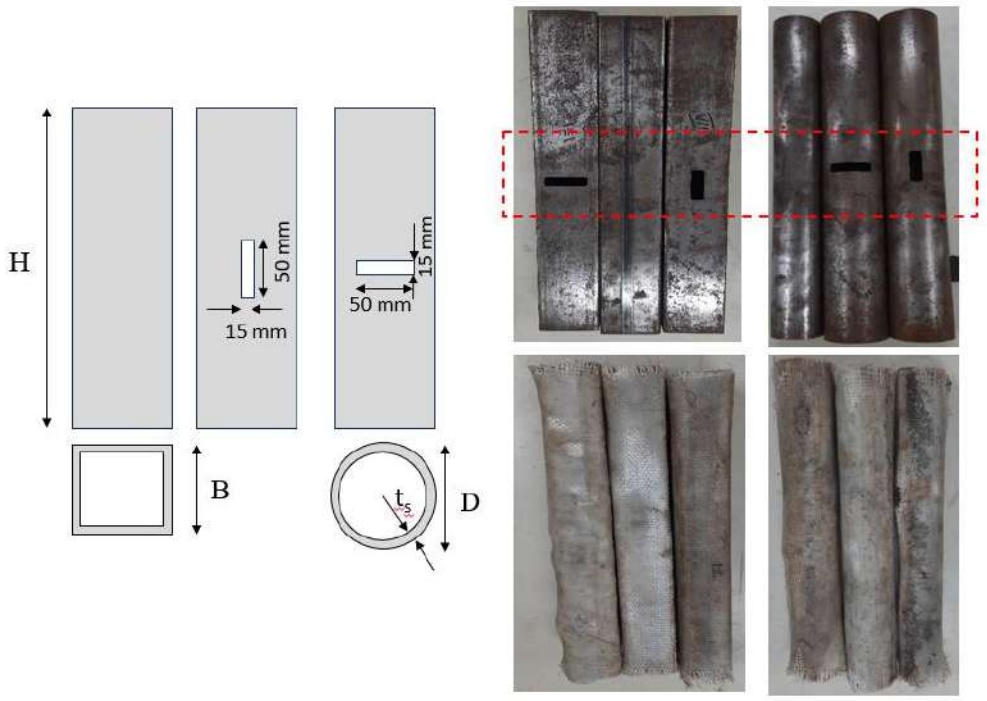

Fig. 2. Specification details of Deficient HSC with and without slit

Table 2. Experimental results and its observation

Specimen	Ultimate load[kN]	Axial deformation[mm]	Observed failure
DSCC-NS-NW	53.0	5	Material yielding + Local buckling
DSCC-HS-NW	73.6	5.8	Local bucking + Yielding near the slit
DSCC-VS-NW	58.1	5.3	Local buckling
DSCC-NS-GFRP	108.0	5.2	Local buckling +Tearing of FRP
DSCC-HS-GFRP	135.0	5.3	Local buckling +Tearing of FRP near slit
DSCC-VS-GFRP	120.0	5.8	Local buckling +Tearing of FRP near slit
DSSC-NS-NW	48.0	2.3	Inward /outward + Local buckling near the slit
DSSC-HS-NW	64.0	2.6	Inward /outward + Local buckling near the slit
DSSC-VS-NW	53.0	2.4	Inward /outward + Local buckling near the slit
DSSC-NS- GFRP	100.0	5.2	Inward /outward + Local buckling with GFRP tearing
DSSC-HS- GFRP	125.0	6.6	Inward /outward + Local buckling with GFRP tearing near the slit
DSSC-VS- GFRP	110.0	6.4	Inward /outward + Local buckling with GFRP tearing near the slit

A universal testing machine (UTM) with a maximum load capacity of 600 kN was used. Specimens were positioned vertically between two steel plates to ensure uniform load application. A dial

gauge with the least count of 0.01 mm was placed along the column height to monitor axial deformation. Strain gauges of 20 mm gauge length were attached near the slit regions to capture local strain distribution. The axial compressive load was applied at a controlled displacement rate of 0.02 mm/min until failure. The schematic diagram of the testing arrangement and specimens under loading in UTM is shown in Fig. 3. Table 2 lists the observations of the tested specimens. The table shows that GFRP wrapping provided a substantial enhancement, with HS-GFRP specimens demonstrating the highest ultimate load in both circular (135 kN) and square sections (125 kN). The ultimate load for DSCC-HS-GFRP (135.0 kN) increased by approximately 83% compared to DSCC-NS-NW (73.6 kN). Similarly, the square column DSSC-HS-GFRP (125.0 kN) showed significant improvement over DSSC-HS-NW (64.0 kN), highlighting the effectiveness of GFRP confinement. GFRP provided enhanced confinement, delaying local buckling and increasing load resistance. However, tearing of the GFRP wrap near slits was observed under peak loads, highlighting areas for material improvement or enhanced application techniques.

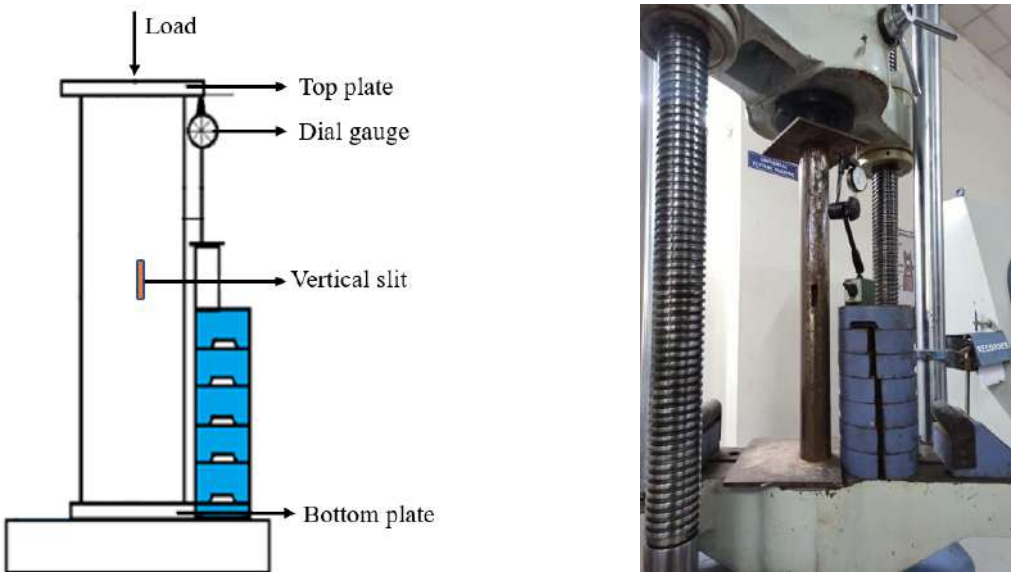

Fig. 3. Arrangement for testing of columns and its schematic diagram

2.3 Analytical Study

The Finite Element Analysis (FEA) was performed using ANSYS version 2024 software, as it is a highly capable FEA tool that excels in modeling complex structures. It offers accurate nonlinear material modeling, reliable meshing, and efficient solver options to simulate real-world behaviors. The steel columns were modelled using SOLID186 elements to capture plasticity and buckling behavior, while GFRP layers were represented using SHELL181 elements to simulate orthotropic material properties and failure criteria. Material properties derived from experimental tests, including yield stress at 267 N/mm^2, ultimate stress at 475 N/mm^2, Poisson's ratio of 0.3 for steel & tensile strength of 1724 N/mm^2 and elastic modulus of 1724 N/mm^2 for GFRP was given as input for FEA model. Boundary conditions included fixed supports and displacement-controlled axial loading, with bonded contact defining the steel-GFRP interface. The bond state between the steel substrate and the GFRP wrapping plays a critical role in the load-carrying capacity and failure behavior of specimens. The perfect bond assumption was validated by experimental evidence and numerical stress distributions. The bonded-contact model in the current FEA analysis was supported by experimental evidence and stress transfer patterns. It provides an accurate and reliable representation of the steel-GFRP interaction for the studied specimens, with minimal impact on the overall accuracy of the load predictions. Using the coinciding nodes option in ANSYS the connection between the SOLID and SHELL elements was made and it is an efficient and accurate way to model perfectly bonded interfaces. It enables seamless load transfer and realistic simulation of confinement effects, making it ideal for studying GFRP-wrapped steel or concrete columns under axial loads. The finite element model of the specimen DSCC – NS-NW, DSCC – NS – GFRP, DSSC – HS – NW & DSSC – HS – GFRP are shown in Fig. 4. The finite element model used a finer mesh (2 – 3

mm) for hollow steel column with or without slit and GFRP layers have meshed with element sizes matching their thin geometry (0.5–1 mm per ply). One end of the column is fixed to prevent all translations and rotations ($U_x = U_y = U_z = 0$; displacements in all directions are zero). Applying axial compression at the opposite end, while lateral displacements at the loaded end are constrained. This study utilized nonlinear static analysis in ANSYS to simulate the behavior of hollow steel columns under axial compression. The Newton-Raphson iterative method was employed to solve the nonlinear equations, ensuring accurate convergence through force and displacement criteria. Incremental load steps were applied to capture progressive nonlinear effects, such as material yielding, stress redistribution, and buckling near the slit regions. The experimental results revealed that the tearing of GFRP sheets was predominantly driven by stress concentrations at the slits and areas of local buckling, highlighting the role of GFRP wrapping in delaying failure. The finite element analysis successfully replicated these failure modes, validating the use of the Hashin failure criteria to capture the behavior of the GFRP under axial compression. The FEA results closely matched experimental outcomes, with a minimal error of 3.5% in load-carrying capacity predictions and consistent failure patterns. This approach validated the reliability of the chosen methodology in capturing material and geometric nonlinearities, stress redistribution, and the interaction between steel and GFRP wrapping.

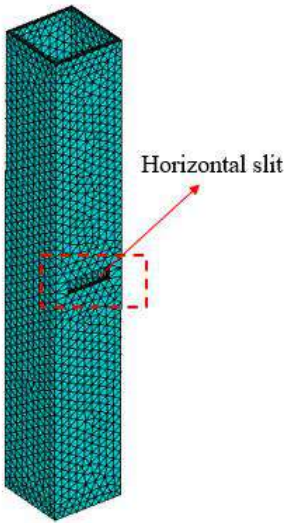

Fig. 4. Mesh model of a deficient hollow column- DSSC-HS-NW

3. Results and discussions

3.1 Load – Axial Compression Behavior of Group A Specimens

The load-axial compression curve of the circular column without a slit, with a vertical slit and with a horizontal slit was shown in Fig. 5. It was noted that the circular columns with vertical slits DSCC – VS – NW show reduction in both stiffness (33 %) and load-bearing capacity. The stiffness is measured by calculating the deflection under an applied load. This may be due to the vertical slit running parallel to the axis of the column, creating a stress concentration along the slit's edges and introducing a weak zone in the load path. This orientation disrupts the distribution of axial stresses, causing the column to be more vulnerable to buckling. The specimen with horizontal slits DSCC – HS – NW primarily affects the column's flexural stiffness and contributes to buckling due to bending or shear forces. Thus, the introduction of either vertical or horizontal slits reduces the ultimate load-bearing capacity of circular columns. However, columns with vertical slits exhibit a more pronounced reduction due to the alignment of the slit along the load path, which leads to a faster decline in the load-bearing capacity of the column.

The failure observed in columns with vertically slit is typically localized around the slit, with local buckling occurring along the slit edges. This causes a rapid loss in load-carrying capacity, resulting in brittle or semi-brittle failure characterized by significant deflection in the slit. Whereas, a column with a horizontally slit fails typically due to a combination of local buckling and yielding near the

slit region. This type of slit often leads to flexural deformation, causing the column to fail in a more ductile manner compared to vertical slits. Fig.6 shows the circular column specimens with vertical and horizontal slits after testing and compared to the control specimen without any deficiency.

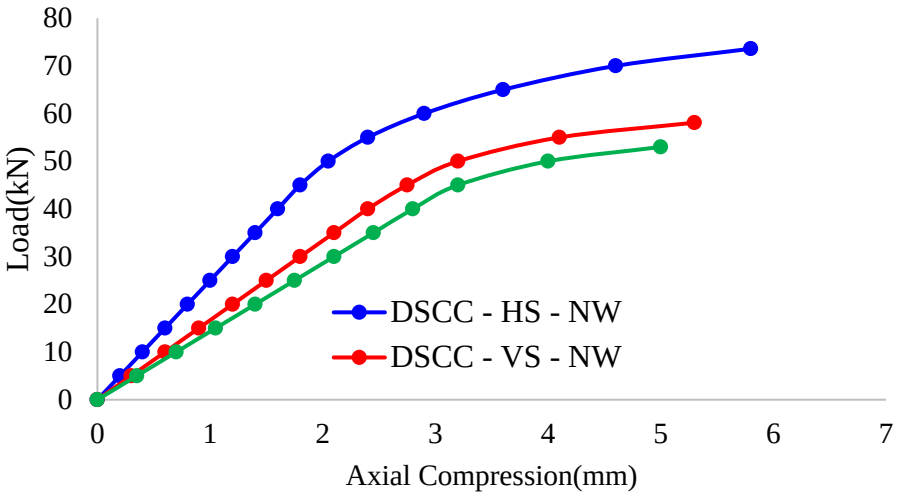

Fig. 5. Load – axial compression behavior of Group A specimens

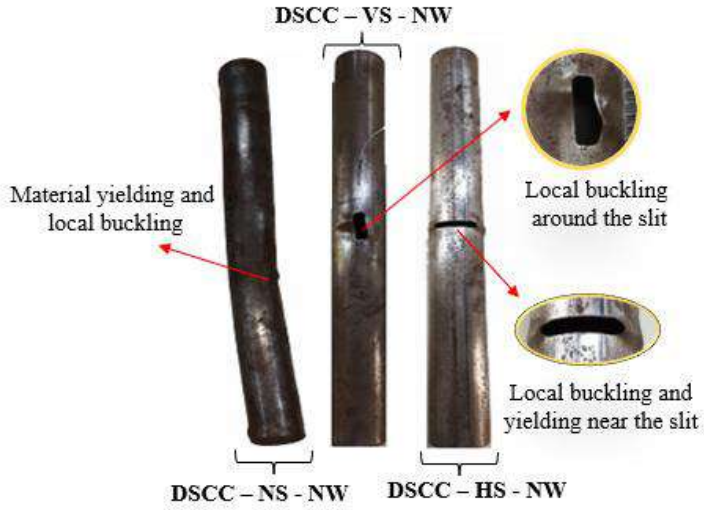

Fig. 6. Circular column specimen with and without deficient after test

3.2 Load – Axial Compression Behavior of Group B Specimens

The load–axial compression behavior of the GFRP-wrapped circular column without a slit, with a vertical slit and with a horizontal slit was shown in Fig. 7. It was noted that GFRP confinement circular column (DSCC – NS – GFRP) increases axial stiffness and allows the column to carry a higher load. The wrapping resists lateral expansion of the steel under compression, allowing the specimen to reach a higher peak load than unwrapped columns without deficiency. In specimen DSCC – HS – GFRP, the horizontal slits do not directly interrupt the load path, the addition of GFRP wrapping further improves load capacity by reinforcing the column's integrity and restricting deformation near the slit. This results in a higher peak load compared to unwrapped columns with horizontal slits. GFRP wrapping acts as a reinforcing layer over the vertical slit, helping to bridge the discontinuity and preventing stress concentrations along the slit edges. The enhancement in resistance of GFRP-wrapped hollow steel columns arises not from the direct compressive resistance of GFRP but from its ability to confine, restrain, and redistribute stresses in the steel. This results in an improved load-bearing capacity compared to unwrapped columns with vertical slits.

Fig.8 shows the column specimens after testing. From the test column specimens, it was observed that local buckling with tearing of the GFRP sheet around the vertical and horizontal slit.

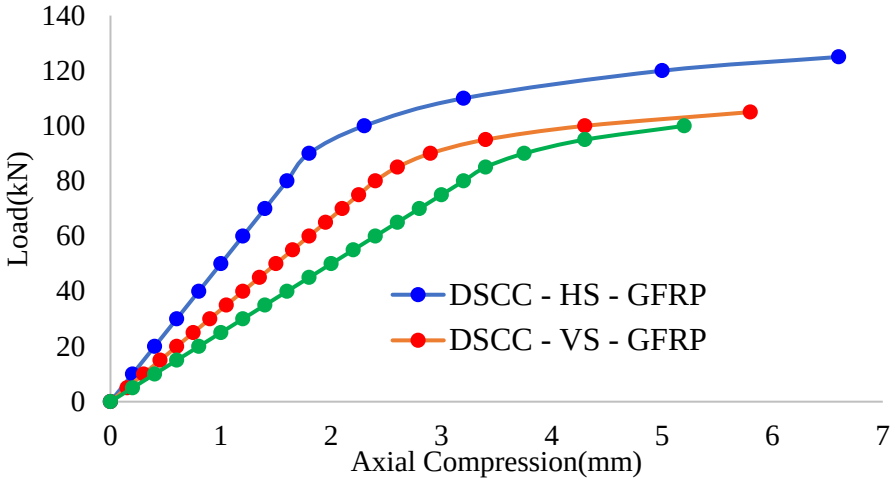

Fig. 7. Load – Axial compression behavior of Group B specimens

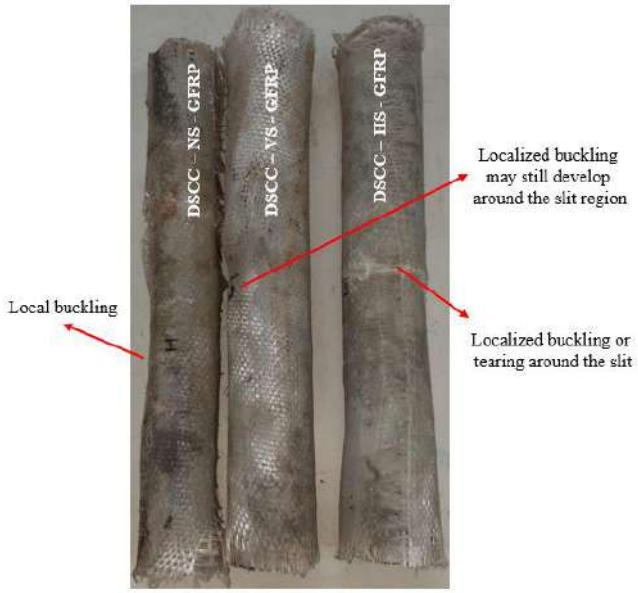

Fig. 8. Failure mode of the GFRP wrapped circular column with and without deficient

3.3 Load – Axial Compression Behavior of Group C Specimens

Fig. 9 shows the load–axial compression behavior of the unwrapped square column with or without deficiency. It is inferred from the curve, that the load-carrying capacity of DSSC-HS-NW is 25 % more than the control specimen DSSC-NS-NW. This may be due to the redistribution of load; the presence of a horizontal slit alters the load path and improves the load-carrying capacity. Similarly, the increase in the load-carrying capacity of 9 % was recorded for specimen DSSC-VS-NW as compared to DSSC-NS-NW. All the square hollow specimens fail mainly by inward and outward local buckling and also observed slight distortion around the vertical and horizontal slit. Fig. 10 shows the failure model of the unwrapped square hollow deficient column. The parameters investigated in Figure 10 are buckling patterns, with a focus on identifying regions of local and global buckling to understand the slit configurations which influence failure modes in specimens DSSC-NS-NW, DSSC-HS-NW, and DSSC-VS-NW. Another key parameter is the effect of slit orientation, comparing horizontal slits in DSSC-HS-NW and vertical slits in DSSC-VS-NW to evaluate their impact on stress concentration and load redistribution. Additionally, deformation

mechanisms are studied, with inward and outward buckling prominently observed in DSSC-HS-NW and DSSC-VS-NW, which indicates the slit orientation influences the overall failure mechanism.

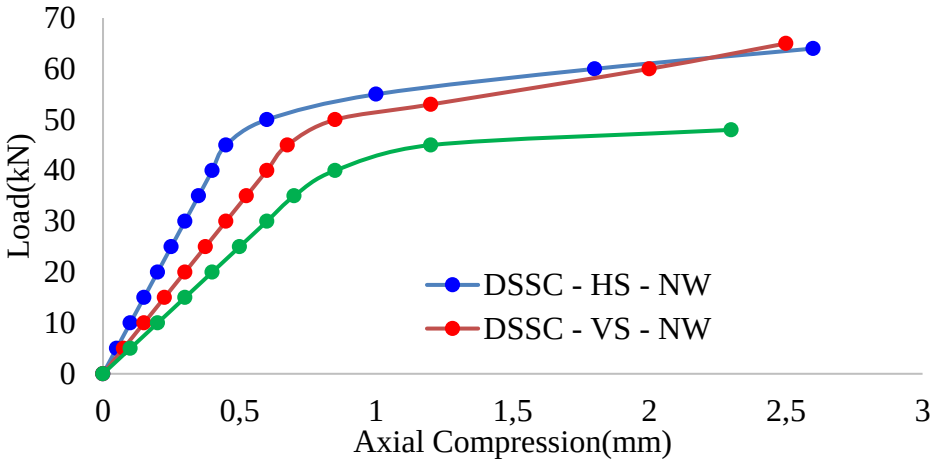

Fig. 9 Load – axial compression behavior of Group C specimens

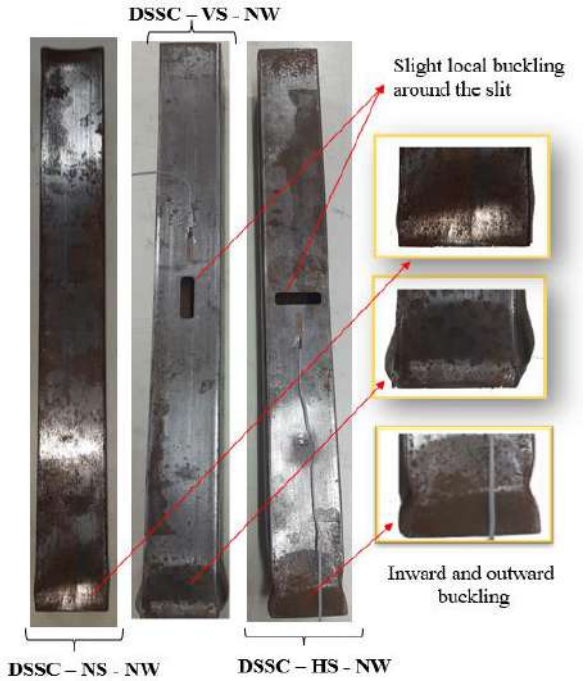

Fig. 10. Buckling pattern of the square column deficient column

3.4 Load – Axial Compression Behavior of Group D Specimens

The square hollow columns wrapped with GFRP in this study exhibited distinct behavior compared to their unwrapped counterparts. All the square columns, including DSCC-NS-GFRP, DSCC-HS-GFRP, DSCC-VS-GFRP, DSSC-NS-GFRP, DSSC-HS-GFRP, and DSSC-VS-GFRP, were strengthened by wrapping three plies of GFRP sheets using epoxy resin. Figure 11 illustrates the load-axial compression behavior of GFRP-wrapped square hollow columns with and without deficiencies. The load-carrying capacity increased significantly, with wrapped specimens showing an improvement of approximately 50%, regardless of the presence of vertical or horizontal slits. The GFRP wrapping enhanced stiffness and effectively mitigated local buckling. Notably, the confinement provided by GFRP around horizontal slits, as observed in DSCC-HS-GFRP and DSSC-HS-GFRP, was more effective than that around vertical slits, such as in DSCC-VS-GFRP and DSSC-VS-GFRP, attributed to the fiber orientation aligning favorably with the stress distribution. During axial loading, tearing of

the GFRP sheets was observed in regions of local buckling and near the slit areas, indicating critical stress concentrations and localized failure and it is shown in Fig. 12.

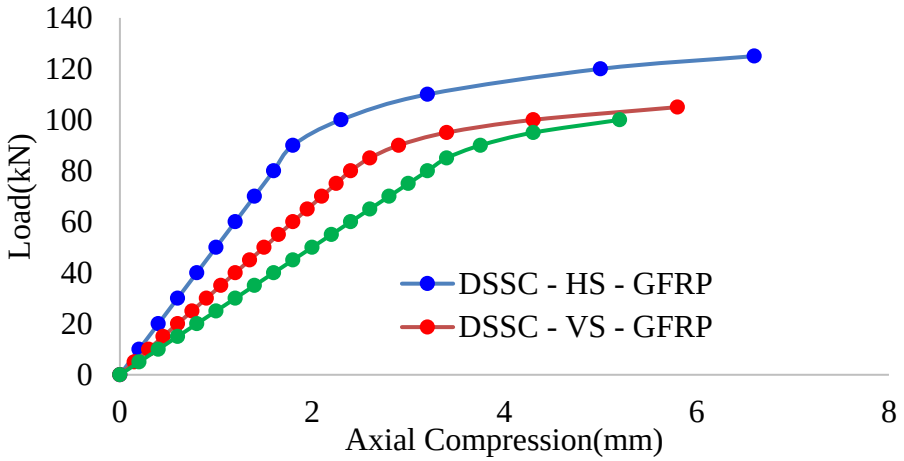

Fig. 11. Load – axial compression behavior of square Group D specimens

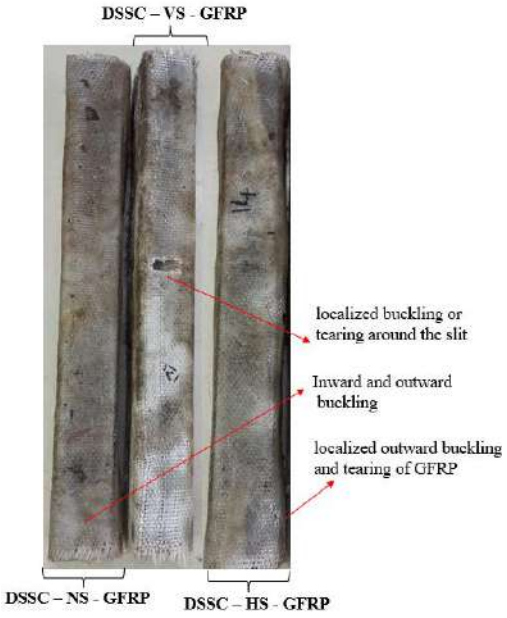

Fig. 12. Failure mode of the square hollow deficient column with GFRP wrapping

3.5 Effect of GFRP Wrapping

Bar chart comparison between the unwrapped and 3 plies of GFRP-wrapped deficient column with no slit, horizontal slit and vertical slit for the circular and square section was shown in Fig. 13. From the chat it was noted that a percentage increase in the load carrying capacity of GFRP wrapped specimen is approximately twice than that of unwrapped specimen. Thus, the confinement using GFRP is found to be an effective repair technique for deficient hollow pipes/tubes. It is also observed that the circular section was found to be more effective for wrapping than the square due to the presence of the edges. GFRP wrapping on the square column will be effective with the provision of a small corner radius.

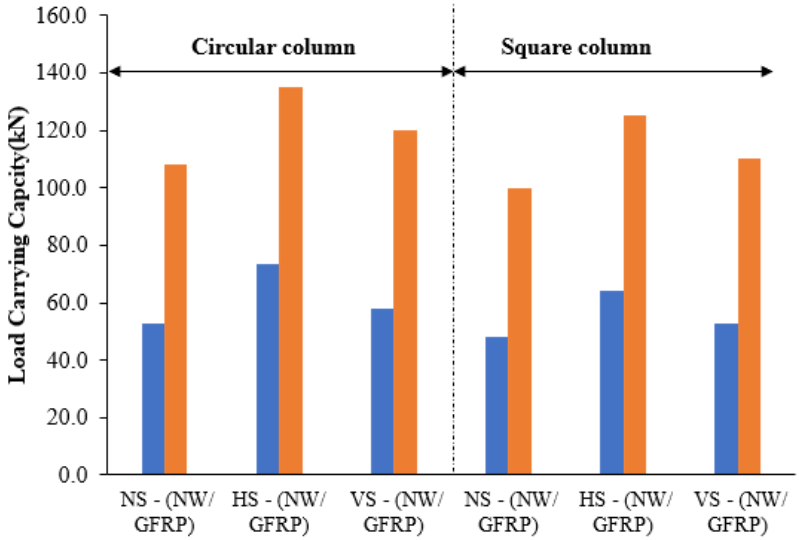

Fig. 13. Loading carrying capacity of wrapped and unwrapped deficient column

3.6 Compression Between the Experimental and FEA Model

The FEA models developed in this study can predict the failure as similar to that of experimental failure. The circular hollow column specimen and square hollow column without wrapping fail mainly by local buckling, yielding and inward and outward bucking respectively [14]. The comparison between the failure of the experimental and FEA model is illustrated in Fig. 14 & Fig.15. The colored regions in the FEA analysis (Fig.14) reveal stress patterns and failure mechanisms in circular hollow columns. For unwrapped specimens (DSCC-NS-NW, DSCC-VS-NW, and DSCC-HS-NW), red zones indicate stress concentrations and local buckling, with horizontal slits (DSCC-HS-NW) showing the most severe stress disruption. Wrapped specimens (DSCC-NS-GFRP, DSCC-VS-GFRP, and DSCC-HS-GFRP) exhibit more uniform stress distribution, delayed buckling, and reduced stress intensities near slits. GFRP wrapping is particularly effective in confining stress around horizontal slits due to fiber alignment, enhancing load capacity and mitigating failure. Similarly, FEA model for deficient hollow steel square columns was compared with or without GFRP wrapping (Fig.15).

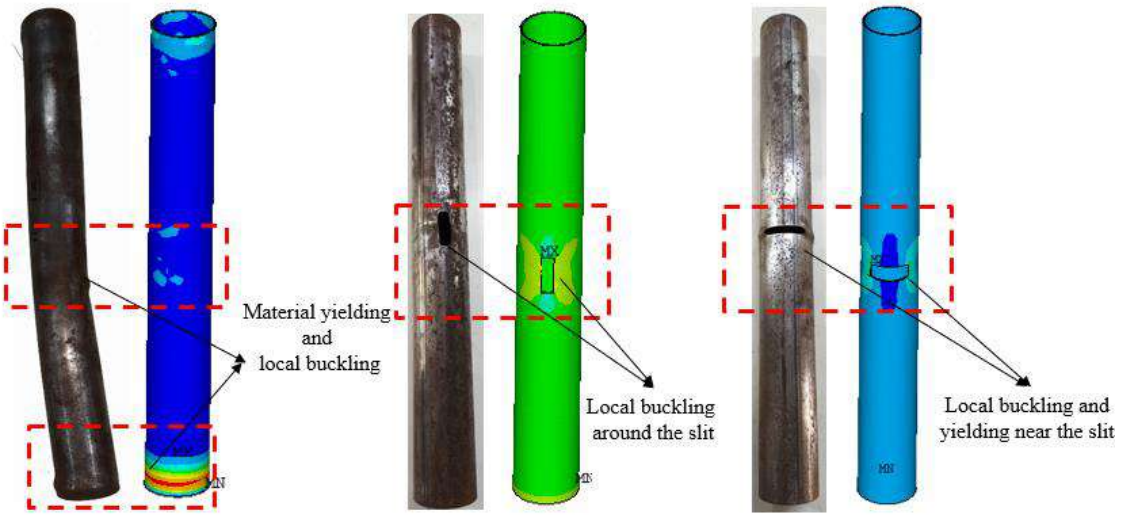

(a)DSCC-NS-NW (b) DSCC-VS-NW (c) DSCC-HS-NW

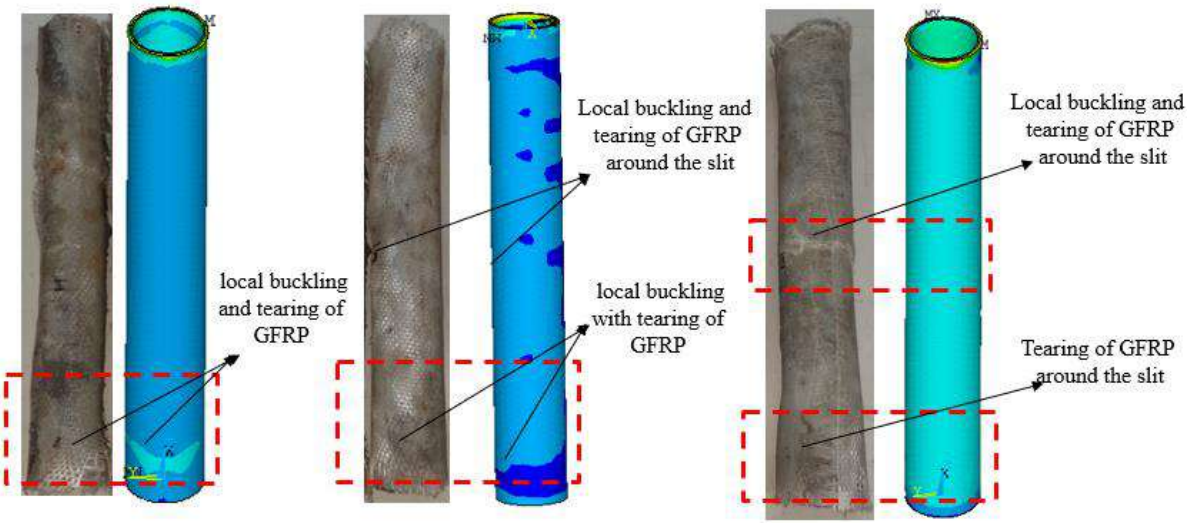

(d) DSCC-NS-GFRP (e) DSCC-VS-GFRP (f) DSCC-HS-GFRP

Fig. 14. Comparison between the failure mode of Experimental and FEA model of circular hollow column

In DSSC-NS-NW, the red zones at the middle and bottom of the column correspond to material yielding and localized inward and outward buckling. In DSSC-HS-NW (horizontal slit), the stress is concentrated around the slit, with local inward and outward buckling forming due to stress redistribution. The DSSC-VS-NW (vertical slit) specimen shows stress concentration along the slit edges, leading to local buckling near the slit. Whereas in DSSC-NS-GFRP, the stress distribution is more uniform, and localized buckling is delayed due to the confinement provided by the GFRP. The DSSC-VS-GFRP specimen shows improved stress redistribution around the vertical slit, with reduced buckling intensity compared to the unwrapped columns. From Fig.14 & Fig.15, it was observed that a good correlation between the experimental and numerical models was achieved.

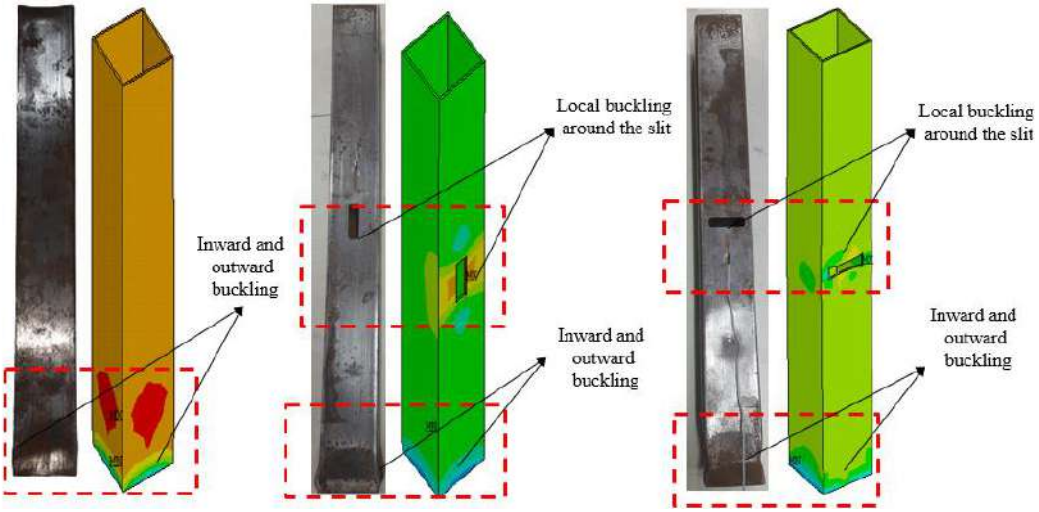

(a) DSSC-NS-NW (b) DSSC-VS-NW (c) DSSC-HS-NW

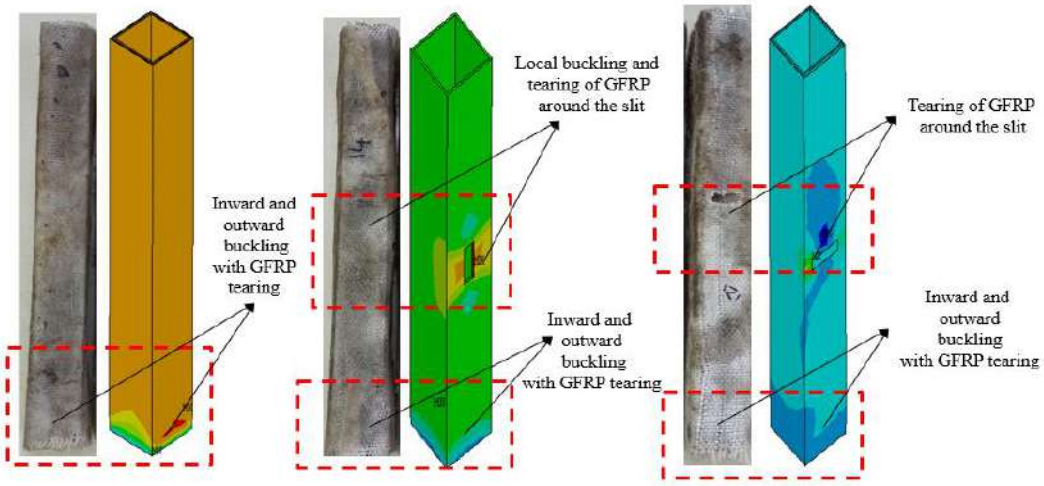

(d) DSSC-NS-GFRP (e) DSSC-VS-GFRP (f) DSSC-HS-GFRP

Fig. 15. Comparison between the failure mode of Experimental and FEA model square hollow column

3.7 Strength of Hollow Deficient Column with or Without GFRP Wrapping As Per AISI Code

The design strength of steel columns without GFRP wrapping is calculated using the provisions of AISI-S100[15], which provides a well-established framework for evaluating the axial load-carrying capacity of cold-formed steel members. The equations in AISI-S100 consider nominal material properties, such as the yield strength (F_y), and geometric characteristics, including effective cross-sectional area (A_e) and slenderness effects. For columns, the design strength (N_{AISI}) is determined based on whether the column slenderness (λc) falls within the inelastic or elastic buckling range, as defined by the critical slenderness parameter. These calculations provide a baseline strength for steel columns without external reinforcement. When GFRP wraps are introduced, the confinement effect and additional strength provided by the composite material lead to a significant enhancement in the column's load-carrying capacity. The contribution of GFRP wrapping is quantified by comparing the experimentally or numerically determined ultimate strength of the wrapped column to the unwrapped column's baseline strength calculated using AISI-S100. This approach highlights the strengthening effect of GFRP wraps and validates their efficiency in improving the performance of steel columns under axial loads. The design strengths are calculated using AISI - S100 [15] for steel hollow columns were calculated using Eq. [1-4]. The strength obtained from the experimental, FEA model and AISI design equation are summarized in Table 3.

$$N_{AISI} = A_e P_n \tag{1}$$

$$P_n = \left(0.658^{\lambda_c{}^2}\right) F_y \; for \; \lambda_c \leq 1.5 \tag{2}$$

$$P_n = \left(\frac{0.877}{\lambda_c{}^2}\right) F_y \; for \; \lambda_c > 1.5 \tag{3}$$

$$\lambda_c = \sqrt{\frac{F_y}{F_e}} \tag{4}$$

The strength of the column obtained from the FEA model overestimates by 3.5% as compared to experimental values. The FEA model tends to overestimate strength due to idealized material properties, assumptions of perfect bonding, and the omission of real-world imperfections such as geometric flaws and progressive damage. The mean and coefficient of variance between the N_{EXP} and N_{FEA} are 0.97 and 0.014 respectively. From Table 2, it was also found that the strength calculated using AISI for the hollow deficient column was 12.7**%** lower than experimental results due to its conservative approach and simplified assumptions made as ideal material properties.

The design strength was also calculated without considering the confinement effect of GFRP wrapping on the hollow column with or without vertical and horizontal slits. The mean and coefficient of variance between the N_{EXP} and N_{AISI} are 1.15 and 0.045 respectively.

Table 3. Comparison between hollow column strength of Experimental, FEA and AISI

Specimen	Ultimate Load			$\frac{N_{EXP}}{N_{FEA}}$	$\frac{N_{EXP}}{N_{AISI}}$
	N_{EXP} (kN)	N_{FEA} (kN)	N_{AISI} (kN)		
DSCC-NS-NW	53.2	55.3	46.4	0.96	1.14
DSCC-HS-NW	73.6	75.3	58.9	0.98	1.25
DSCC-VS-NW	58.1	59.5	52.3	0.98	1.11
DSCC-NS-GFRP	108.2	112.2	94.0	0.96	1.15
DSCC-HS-GFRP	135.3	139.5	120.2	0.97	1.12
DSCC-VS-GFRP	120.2	125.4	105.0	0.96	1.14
DSSC-NS-NW	48.7	51.3	41.3	0.94	1.16
DSSC-HS-NW	64.5	67.2	57.6	0.96	1.11
DSSC-VS-NW	53.2	54.2	47.7	0.98	1.11
DSSC-NS- GFRP	100.2	102.3	91.0	0.98	1.10
DSSC-HS- GFRP	125.9	127.2	112.5	0.98	1.11
DSSC-VS- GFRP	110.3	112.1	88.0	0.98	1.25
Mean				0.97	1.15
COV				0.014	0.045

4. Conclusions

Based on the experimental and FEA investigations, the following specific conclusions are drawn:

- The presence of vertical and horizontal slits in circular hollow steel columns (DSCC specimens) and square hollow steel columns (DSSC specimens) results in a redistribution of stress, altering the load path and influencing the local buckling around the slit edges. The axial load-carrying capacity of unwrapped DSCC-NS-NW and DSSC-NS-NW specimens was 53.0 kN and 48.0 kN, respectively. The reduction in capacity was attributed to localized stress concentrations around the slit edges.
- Columns with vertical slits (e.g., DSCC-VS-NW and DSSC-VS-NW) showed greater reductions in axial load capacity (by 9.2% and 10.4%, respectively, compared to their horizontal slit counterparts) due to the stress redistribution along the column height, which intensifies buckling behavior.
- GFRP wrapping significantly improved axial strength and stiffness in deficient columns. For example, the DSCC-NS-GFRP column exhibited a 103.8% increase in axial load capacity compared to its unwrapped counterpart, reaching 108.0 kN. Similarly, DSSC-NS-GFRP showed an increase of 108.3%, reaching 100.0 kN. The three-ply GFRP wrapping redistributed stresses effectively, delayed local buckling, and enhanced ductility by preventing sudden failure
- Failure mechanisms of unwrapped columns differ by geometry: unwrapped circular columns failed by localized material yielding and buckling near the slit, while square columns exhibited inward and outward buckling at the slit. In GFRP-wrapped columns, failure modes transitioned to delamination, tearing of the GFRP sheets, and combined global and local buckling, as observed in DSCC-HS-GFRP and DSSC-HS-GFRP specimens.
- The FEA model predicted the load-carrying capacities of hollow deficient columns with high accuracy, showing a minimal error of 3.5% when compared to experimental results. For instance, the predicted capacities for DSCC-NS-NW and DSSC-NS-NW were 51.3 kN and 46.3 kN, closely matching experimental results of 53.0 kN and 48.0 kN, respectively.
- The AISI estimates for load-carrying capacities were conservative, with predictions 12.7% lower than experimental results. For example, the estimated capacity for DSSC-NS-GFRP was 87.3 kN, compared to the experimental value of 100.0 kN. This conservatism highlights the

need for further refinement of AISI guidelines when considering hollow deficient columns with or without GFRP wrapping.

These findings underline the significant role of slit orientation, geometry, and GFRP confinement in governing the axial load capacity and failure modes of hollow steel columns, providing a reliable experimental and numerical foundation for future design improvements.

List of Notations

HSC	Hollow steel column
DSCC	Deficient Steel circular column
DSSC	Deficient steel square column
NS	No slit
VS	Vertical slit
HS	Horizontal slit
NW	No wrap
GFRP	Glass fiber-reinforced polymer
CFRP	Carbon fiber reinforced polymer
UTM	Universal testing machine
FEA	Finite element analysis
N_{AISI}	Design strength in kN
N_{Exp}	Experimental strength in kN
N_{FEA}	Numerical strength in kN

Appendix

1. Determine the Critical Slenderness Ratio (λ_c):

$$\lambda_c = \sqrt{\frac{F_y}{F_e}}$$

Where; F_y: Yield strength of steel (assumed 257 MPa or N/mm^2), F_e: Elastic buckling stress derived using Euler's formula.

The elastic buckling stress Fe is given as:

$$F_e = \frac{\pi^2 E}{\left(\frac{KL}{r}\right)^2}$$

For simplicity in the AISI equation, λ_c is already pre-calculated as an input parameter, based on geometry and material properties.

2. Use Appropriate P_n Equations

From the AISI-S100 design standards:

For $\lambda_c \leq 1.5$*:*

$$P_n = \left(0.658^{(\lambda c)^2}\right) F_y$$

For $\lambda_c \geq 1.5$*:*

$$P_n = \left(\frac{0.877}{\lambda c^2}\right) F_y$$

3. Calculated the Net Area (A_c)

D= 76.5mm (Outer diameter), t_s = 1.8mm (thickness)

$$A_c = \frac{\pi(76.5-2(1.8))^2}{4} = \frac{\pi(72.9)^2}{4} = 4177.25\ mm^2$$

4. Calculate nominal axial strength (P_n)

Given F_y= 257 N/mm^2 and assuming $\lambda_c \leq 1.5$ for this specimen:

$$P_n = \left(0.658^{(\lambda c)^2}\right) F_y$$

Use, $(\lambda c)^2 = 1.2$ (example for DSCC-VS-GFRP)

$P_n = (0.658)^{1.2} \times 257 = 0.490 \times 257 = 125.93$ N/mm^2

5. Calculate the Ultimate Strength from AISI Formula:

Using $N_{AISI} = A_c . P_n$:
$N_{AISI} = 4177.25 \times 125.93 = 105.0$ KN

6. Compare Experimental Strength from AISI Formula:

Specimen	N_{EXP} (KN)	N_{FEA}(KN)	N_{AISI}(KN)	N_{EXP}/N_{FEA}	N_{EXP}/N_{AISI}
DSCC-VS-GFRP	120.2	125.4	105.0	0.96	1.14

Acknowledgement

The authors would like to thank the management of Sri Siva Subramaniya Nadar College of Engineering for giving the needed facilities to complete this research work.

References

[1] Ghaemdoust MR, Narmashiri K, Yousefi O. Structural behaviours of deficient steel SHS short columns strengthened using CFRP. Constr Build Mater. 2016;126:1002-1011. https://doi.org/10.1016/j.conbuildmat.2016.09.099
[2] Rao S, Kumar P, Singh R. Strengthening of hollow steel columns using glass fiber reinforced polymer. J Struct Eng. 2017;143(3):04016206.
[3] Shahraki M, Sohrabi MR, Azizyan GR, Narmashiri K. Strengthening of deficient steel SHS columns under axial compressive loads using CFRP. Steel Compos Struct. 2019;30(1):69-79.
[4] Ghaemdoust MR, Narmashiri K, Yousefi O. Structural behaviors of deficient steel SHS short columns strengthened using CFRP. Constr Build Mater. 2016;126:1002-1011. https://doi.org/10.1016/j.conbuildmat.2016.09.099
[5] Shahraki M, Sohrabi MR, Azizyan GR, Narmashiri K. Experimental and numerical investigation of strengthened deficient steel SHS columns under axial compressive loads. Struct Eng Mech. 2018;67(2):207-217.
[6] Lin J, Wang C, Xu J. Comparative study on the strengthening of hollow steel columns using steel plates and GFRP. Thin-Walled Struct. 2019;144:106286.
[7] Sangeetha P, Sumathi R. Behaviour of glass fibre wrapped concrete columns under uniaxial compression. Int J Adv Eng Technol. 2010;1(1):74-83.
[8] Palanivelu S, Moorthy D, Subramani G, Dhayanithi JR. Strength enhancement of cold-formed steel tubular column using GFRP strip subjected to axial compression. Građev Mater Konstrukcije. 2021;64(4):251-260. https://doi.org/10.5937/GRMK2104251P
[9] Shahraki M, Darmiyan HM. Structural behaviours of strengthened deficient steel square hollow section columns under axial compressive loads. Innov Infrastruct Solut. 2023;8:1-13. https://doi.org/10.1007/s41062-022-00955-0
[10] Tang H, Liu R, Zhao X. Axial compression behaviour of CFRP-confined rectangular concrete-filled stainless steel tube stub column. Front Struct Civ Eng. 2021;15:144-1159. https://doi.org/10.1007/s11709-021-0762-4
[11] Keykha AH. Carbon-fibre strengthening of deficient hollow steel sections under combined loading. Proc Inst Civ Eng Struct Build. 2019;172(8):609-620. https://doi.org/10.1680/jstbu.17.00150
[12] Sharma A, Singh P. Finite element analysis of GFRP-strengthened hollow steel columns with slits. J Constr Steel Res. 2020;170:106169.
[13] Latour M, Di Benedetto S, Francavilla AB, Elettore G, Rizzano G. Stiffness and strength of square hollow section tubes under localised transverse actions. Metals. 2023;13(10):1767. https://doi.org/10.3390/met13101767
[14] Sangeetha P. Analysis of FRP wrapped concrete columns under uniaxial compression. J Sci Ind Res. 2007;66(3):235-242.
[15] American Iron and Steel Institute (AISI). Specification for the design of cold-formed steel structural members. AISI S100-2007. 2007.

Research on Engineering Structures & Materials
www.jresm.org

Research Article

Compressive behavior and code-based evaluation of normal weight and lightweight concrete filled composite steel tubes

Mohammed Layth Abbas [*,1, a], Erhan Güneyisi [2, b]

[1]*Department of Civil Engineering, University of Technology- Iraq, 10066 Baghdad, Iraq*
[2]*Department of Civil Engineering, Harran University, 63300 Şanlıurfa, Türkiye*

Article Info

Article History:

Received 04 Dec 2024
Accepted 07 Feb 2025

Keywords:

Compressive behavior;
Concrete filled steel tube;
Design code;
Lightweight concrete;
Normal weight concrete

Abstract

The application of lightweight aggregate concrete as a core material for concrete-filled steel tube (CFST) composite columns offer various advantages such as lower self-weight and thermal conductivity, higher fire resistance and durability as well as more resistance against the earthquake loading. In this study, the axial strength of steel tubes filled with normal weight concrete (NWC) and lightweight concrete (LWC) were evaluated by applying two widely used design codes, American Concrete Institute (ACI) and Eurocode 4 (EC4). The assessment included circular steel tubes with variable diameter-to-thickness (D/t) ratios of 30, 60, and 90, coupled with steel yielding strengths of 185, 275, and 450 MPa, while keeping constant wall thickness and length-to-diameter (L/D) ratio. Twelve distinct LWC combinations from the literature, each having verified compressive strength, were employed as infill materials for the steel tubes. A total of 108 results of the ultimate axial strengths predicted by the ACI and EC4 were then investigated and compared to assess their accuracy and applicability to tubes filled with NWC and LWC. A statistical analysis was also conducted to determine the effectiveness of the investigated variables. The findings showed that variations in the D/t ratio had a substantial effect on the ultimate strength of circular steel tube columns filled with NWC and LWC with a contribution rate about 85% according to the statistical evaluation of the ACI and EC4 equations, which is slightly higher in the former. Moreover, the strength predictions by using the EC4 formula gave greater as compared to those obtained by the ACI, ranging from 29 to 54%.

© 2025 MIM Research Group. All rights reserved.

1. Introduction

Composite columns, which have been extensively utilized in engineering fields, provide exceptional ductility and strength characteristics and their development has been the focus of intensive research over the last few decades. When comparing typical reinforced concrete columns to concrete filled steel tube (CFST) columns, noticeable disparities regarding ductility and energy absorption capability are evident [1–4]. Since CFST sections are among the best composite sections and offer numerous benefits over traditional steel and reinforced concrete sections, they have grown in popularity in recent years [5]. By using the combined action of steel and concrete, the CFST sections provide resistance to applied loads. They are created by pouring concrete into a hollow steel tube section [6]. Steel tubes serve as both longitudinal and transverse reinforcement in CFST sections [7]. Because steel has a high elastic modulus, the steel tube that is located at the outside perimeter of the CFST section effectively resists tension and bending moments while also increasing the stiffness of the section. The CFST section's inner concrete core also contributes significantly to improving the section's behavior and postponing the steel tube's inward buckling [8, 9]. Additionally, CFST section's compressive strength is increased by the steel tube's effective

*Corresponding author: bce.20.13@grad.uotechnology.edu.iq
[a]orcid.org/0000-0002-2284-7056; [b]orcid.org/0000-0003-2666-2769
DOI: http://dx.doi.org/10.17515/resm2025-565me1204rs

containment of the inner concrete core [10, 11]. Therefore, in situations when the columns are subjected to high compressive stresses, CFST sections are beneficial. For a structure situated in an earthquake-prone area, the CFST section's high ductility, strength, and energy absorption capacity is crucial [12]. Another benefit of CFST sections is that its steel tube can be used as formwork during construction, which reduces the need for formwork and the amount of time needed for construction [13].

The weight-bearing capability of the column is greatly impacted by the features of the concrete and steel. The structural parts' cross sections get smaller as steel and concrete's strengths increase. Concrete in CFST columns is contained by steel, which adds to the structural benefit of CFST and increases its load capacity. Additionally, removing the permanent formwork shortens the construction period. Additionally, because of the concrete core, the use of CFST in constructions results in a delayed or inhibited local buckling of steel tube. In summary, the usage of CFST columns is advantageous due to their increased stiffness, ductility, and load carrying capacity as well as their reduction in construction time and cost [2].

CFST columns have been studied experimentally for decades [14–16]. Research has demonstrated that the characteristics and geometry of the materials are key criteria that influence CFST columns' capacity and behavior. In recent years, there have been several theoretical and practical research on circular CFST columns with a variety of diameter-to-thickness (D/t) ratios and material parameters [4,17–21].

The main parameters influencing the behavior and load-bearing capability of CFST columns are presented in a review of the currently published investigations. The behavior and load-bearing capacity were discovered to be affected by the geometrical features including length-to-diameter (L/D) ratio, D/t ratio and the geometry of specimens followed by the mechanical qualities such yield strength of steel and compressive strength of concrete [2]. The lack of understanding of the composite behavior of the concrete and steel in CFST composite columns is one of the main obstacles to their widespread adoption. According to earlier studies on CFST columns, a number of issues impede the study and design of these composite columns [22]. Due to the lack of understanding regarding the actual strength and inelastic performance of the composite columns, the widespread utilization of CFST columns is confined to specific purposes. Despite the extensive research conducted on composite columns in the past, their application has been restricted, and there is a discrepancy between the numerical predictions and the experimental results. Prior research on composite columns has mostly focused on testing different CFST composite columns without any external confinement in order to evaluate the impact of important parameters, such as concrete strength, steel grade, steel yield strength, steel tube D/t ratio, and the bond strength and characteristics at the steel-concrete interface [23].

It is noted that 75–98% of the cross-sectional area of CFST columns is made up of the concrete core. Concrete has a crucial role in determining how strong the output columns are for this. Therefore, the various designs and the availability of concrete materials must be considered while choosing the type of concrete. In this sense, normal-weight concrete (NWC) and lightweight concrete (LWC) would be a sensible option to use in the construction of such columns, especially in nations where natural resources are running low [24]. Gupta et al. [25] investigated 81 specimens to investigate the effects of steel tube diameter and D/t ratio modifications on the axial load bearing capability of the concentrically loaded circular concrete-filled steel tube columns. They found that the D/t ratio dropped with increasing steel tube confinement effectiveness. To examine the columns' failure modes, Ghannam et al. [26] tested rectangular, square and circular tubes filled with NWC and LWC. The test results revealed that the overall buckling of the CFST columns was the reason why both types of filled columns failed. Their research indicates that lightweight aggregate concrete can be used in place of regular concrete for structural purposes because of its low thermal conductivity and specific gravity. Experimental studies on the axial load bearing capacity of CFST columns pique researchers' curiosity, theoretical analysis plays an important role in engineering research and practice. In the literature, Güneyisi and Kadhim [24] assessed and analyzed the load-carrying capacity of recycled aggregate concrete-filled steel tube short columns subjected to axial compression, utilizing 1600 data evaluated based on four international design standards (AIJ,

DL/T, EC4 and ACI). The primary factors examined consist of steel tube characteristics (outside diameter, wall thickness, length, yield strength) and concrete core attributes (kind of recycled aggregate, substitution level, and compressive strength). The findings underscore EC4's enhanced efficacy in reducing data dispersion, whereas ACI demonstrated greater variability and deficiencies in addressing steel-concrete confinement effects. The inclusion of recycled aggregates negatively impacted the strength of the concrete and the anticipated N_u across all standards, with the D/t ratio modulating the influence of steel yield strength. In a recent study conducted by Luo et al. [27], the structural performance of ultra-high strength CFST stub columns subjected to combined compression and bending was investigated by using experimental and numerical methods. Twenty specimens, fabricated from steel tubes with yield stresses ranging from 813 to 1153 MPa and concrete with a compressive strength of 146.7 MPa, were subjected to diverse eccentric loads during testing. Critical experimental findings were on failure modes, ultimate load capacity, neutral axis displacements, and strain distribution within the steel tubes. Numerical models were created and confirmed with test data to examine cross-sectional stress behavior and comprehend the eccentric compression process. The research evaluated the appropriateness of design standards including EN 1994-1, AISC 360-16, AIJ-2008, and T/CECS 987–2021 for the columns. Research indicates that EN 1994-1 yields precise predictions in the absence of second-order effects, whereas AIJ-2008 enhances accuracy when these effects are taken into account. T/CECS 987–2021 significantly improves prediction accuracy following the adjustment of axial and bending capacities. Apart from the above studies, Alnemrawi and Al-Rousan [28] examined the performance of lightweight CFST columns subjected to axial compression through 48 simulated models with differing properties. The investigation tested four concrete strengths (30 to 60 MPa), three L/D ratios (3, 6, and 9), and four D/t ratios (36, 31, 26, and 21). Nonlinear finite element analysis was applied to examine load-strain relationships and failure modes. The results were juxtaposed with AISC 360-16 and EC4 design codes, revealing that AISC forecasts were conservative at low L/D ratios, whereas EC4 underestimated performance at elevated L/D ratios by as much as 28%. The results emphasize that steel tubes enhanced the mechanical properties, ductility, and strength of the columns, with failure modes determined by geometrical factors. High-strength concrete exhibited superior performance than increasing tube thickness in improving column behavior.

The structural performance of CFST columns were thoroughly examined in existing literature, with the majority of studies focusing on the use of conventional concrete as the infill material. However, limited attention has been devoted to exploring the structural behavior of lightweight concrete filled steel tube columns, leaving a significant gap in the understanding of their performance characteristics. For this, the present study aims to investigate the behavior of axially loaded normal and lightweight concrete-filled steel tube composite columns. Additionally, it is objective to identify an appropriate, viable, and precise approach to assess the predictability of two design requirements of the ACI 318 and EC4 [29, 30], including observations on their safety margins and recommendations for necessary modifications. Several factors were taken into account, including different D/t ratios of 30, 60, and 90, coupled with steel yielding strengths of 185, 275, and 450 MPa, while keeping constant wall thickness and L/D ratio. The compressive strength of the normal and lightweight concrete core with three replacement levels of fly ash and micro silica were also considered. A comparison of the analysis findings based on the two design codes was performed for the composite columns that were exposed to compressive loads.

2. Details of This Study

Two major design standards were used to assess the behavior of NWC and LWC filled steel tube columns which were exposed to axial compression, as was previously described. In order to achieve this, three steel yield strengths, f_y (185, 275, and 450 MPa), and three D/t ratios (30, 60, and 90) were specified for circular CFST columns. Nonetheless, the specimens had a constant thickness for steel tubes of 4 mm and a L/D ratio of 2.5 for each code. Fig. 1 describing the load placed on the cross section of circular CFST columns. Table 1 shows the parameters have been taken in this study.

A specific methodology was implemented to utilize the compressive strength findings of normal and lightweight concrete as a filling material to evaluate the performance of CFST columns. For the concrete core, the concrete strength utilized in this study was derived from the experimental

research of 28 days accomplished by Abbas et al. [32] as shown in Table 2. According to this study, a total of 12 normal and lightweight concrete combinations were created with respect to varied LWA, micro silica, MS (0, 10%) and fly ash, FA (0, 20%) contents. In this investigation, four batch series were examined for the axial compression capacity.

Table 1. Parameters of CFST columns applied in design codes

Diameter of steel tube (mm)	Diameter of filled concrete (mm)	Length of CFST (mm)	Diameter to thickness ratio	Area of steel (A_s) (mm^2)	Area of concrete (A_c) (mm^2)	Steel moment of Inertia (I_s) (mm^4)	Concrete moment of Inertia (I_c) (mm^4)
120	112	300	30	1457.7	9852.04	71103641	10326440
180	172	600	60	2965.7	42273.27	1.22E+09	84711312
360	352	900	90	4473.63	97314	6.31E+09	2.88E+08

The first series contains just regular and lightweight concrete. In the second and third series, micro silica and fly ash were partially substituted with 10% and 20% cement content, respectively. The fourth series involved partial substitution of MS, FA, and artificial aggregate. Their compressive strength findings, measured in cubic units, ranged from 27 to 56 MPa after 28 days. For the designation, for example, LW0MS0FA0 indicates the NWC filled steel tubes without micro silica and fly ash while LW50MS10FA0 presents steel tube filled with LWC having 50% lightweight aggregate, 10% micro silica and 0% fly ash.

Table 2. Transformation of concrete compressive strength according to EC2 [32]

Series No	Mix ID	f_c cube (MPa)	f_c' cylinder (MPa)
Series 1	L0M0F0	40.30	31.43
	L50M0F0	33.50	27.14
	L100M0F0	27.65	22.40
Series 2	L0M10F0	56.10	46.57
	L50M10F0	41.70	32.53
	L100M10F0	32.30	26.16
Series 3	L0M0F20	38.70	30.19
	L50M0F20	32	25.92
	L100M0F20	26.96	21.84
Series 4	L0M10F20	51.45	42.70
	L50M10F20	33.80	27.38
	L100M10F20	30.60	24.79

The impact of the aforementioned parameters on the ultimate compressive strength (N_u) outcomes was examined, contrasted, and thoroughly described in this work. For this, a numerical investigation was conducted into the potential use of NWC and LWC as a concrete core for CFST sections. Two distinct design codes (ACI and EC4) were used to determine the capacity (totally 108 N_u test results) for three distinct D/t ratios, steel tube yield strengths, and twelve distinct concrete core compressive strengths. Between each design code's outcomes, a convenient analysis was carried out. The study also compares and highlights the applicability and prediction capability of the equations given in the design codes for the cases of steel tube filled with both NWC and LWC. It should be noted that Eurocode 2 was used to convert the cubic compressive strength data to cylindrical compressive strength [31], which was then utilized to calculate the ultimate strength of the steel tube columns in accordance with distinct design codes.

The standardization institutions provide many expressions for various conditions. The formulas utilized in this article are those proposed by ACI 318 and EC4. This formula evaluates concrete core and steel tube separately, ignoring concrete confinement and contact. The predicted axial load capacity is expected to be less than comparable codes. The ACI code [29] employs the observing formula to calculate the directional load capacity of circular CFST columns.

$$N_u = 0.85\, f_c' A_c + f_y A_s \tag{1}$$

This relation overlooks the influence of concrete confinement and the interaction between the steel tube and concrete core. On the other hand, EC4 takes into consideration the confinement effect in addition to the contributions of the concrete core and steel tube. The coefficients of confinement for concrete (η_c) and steel tube (η_a) are applied. The triaxial state of stress increases concrete strength by η_c, while hoop stresses lower steel tube strength by ηa. EC4 proposes the following expression:

$$N_u = \left(1 + \eta_c \frac{t}{D}\frac{f_y}{f_y'}\right) f_c'\, A_c + \eta_a\, f_y\, A_s \tag{2}$$

$$\eta_c = 4.9 - 18.5\,\acute{\lambda} + 17\,\acute{\lambda}^2 \ (\eta_c \geq 0) \tag{3}$$

$$\eta_a = 0.25\,(3 + 2\,\acute{\lambda}) \quad (\eta_a \leq 1.0) \tag{4}$$

$$\acute{\lambda} = \sqrt{\frac{N_{PIR}}{N_{cr}}} \tag{5}$$

$$N_{PIR} = f_y A_s + f_c' A_c \tag{6}$$

$$N_{cr} = \frac{\pi^2 (EI)_{eff2}}{I^2} \tag{7}$$

$$(EI)_{eff2} = E_s I_s + K_e E_{c2} I_c \tag{8}$$

$$P_{0,EC4} = \left(1 + 4.9\frac{t}{D}\frac{t_y}{f_c'}\right) f_c'\, A_c + 0.75\, f_y\, A_s \ (If \acute{\lambda} = 0) \tag{9}$$

Where:

f_y': the compressive strength transferred from 100 ×100 mm cube strength;

f_y: steel tube yield strength;

A_s, A_c: concrete and steel tube cross section area, respectively

$\acute{\lambda}$: the relative slenderness;

N_{PIR}: characteristic value of the plastic resistance;

N_{cr} : the elastic critical force for the relevant buckling mode;

K_e : correction factor equals to 0.6;

I_c, I_s: second moment of inertia of concrete and steel, respectively

l: column buckling length;

E_s: elastic modulus of steel.

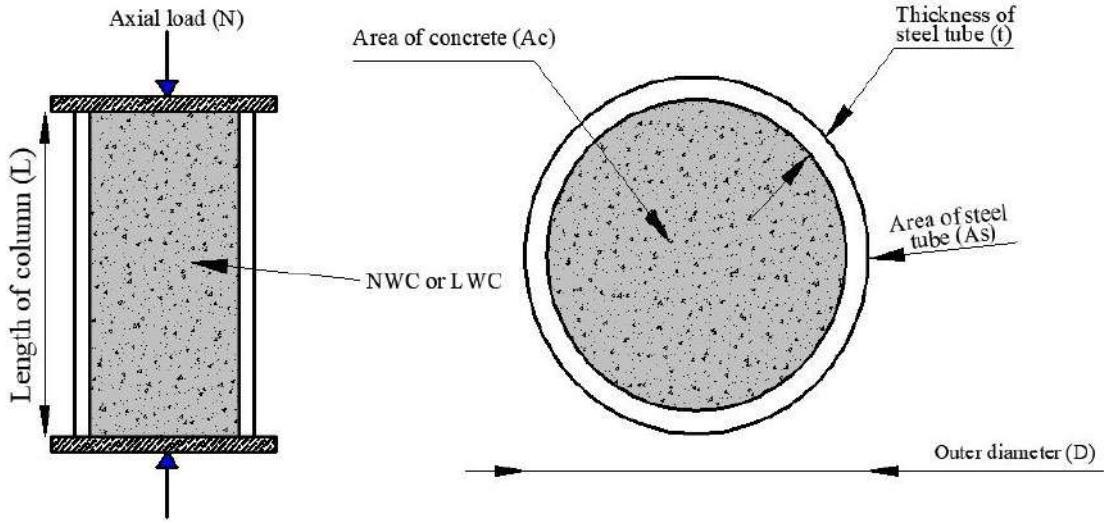

Fig. 1. Test configuration indicating the load placed across a circular CFST cross section

3. Results and Discussion

3.1 Effect of Material Strength and Type

The 28-day compressive strength of normal and lightweight concrete mixtures was applied to compute the ultimate strength of steel tube columns using ACI and EC4 techniques. Fig. 2 depicts the axial load applied capacity for the lightweight concrete and normal concrete with and without micro-silica (MS) and fly ash (FA) contents, specifically for a D/t ratio of 30 and a steel yield strength of 185 MPa. Similar results are presented in Figs. 3 and 4 for D/t ratios of 60 and 90, with steel yield strengths of 275 and 450 MPa.

The data reveal that the axial strength of steel tube filled with NWC and LWC is considerably impacted by the concrete's compressive strength. Incorporating LWA up to a 50% replacement level decreased the ultimate axial strength, which, in turn, led to decline in column ultimate strength. However, when the LWC substitution reached 100%, a fall in concrete compressive strength was found across all concrete mixtures, leading in lower ultimate strengths for CFST columns as determined by both ACI and EC4 formulas. Unlike LWC, the addition of MS often enhanced LWC compressive strength, resulting to higher ultimate strengths of the steel tube columns. The use of MS significantly improved the mixes' strength properties [32, 33], which raised the composite columns' ultimate strength, as seen in Figs 2–4. In actuality, MS is known to strengthen the transition zone and improve the link between the matrix and aggregate [34]. Regardless of MS and aggregate type, Figs. 2–4 also show that Nu decreased when the FA replaced with cement. This behavior was explained that FA developed a higher concrete strength after 28 days of water curing.

It is clear that tube columns filled with normal concrete can bear heavier weights than those loaded with LWC. For example, when evaluating conventional concrete-filled steel tube columns against their lightweight counterparts, both designed with a yield strength of 185 MPa and a diameter-to-thickness ratio of 30, the conventional columns achieved an axial strength of 533 kN as per ACI and 746 kN according to EC4. In comparison, the lightweight columns exhibited axial strengths of 457 kN and 661 kN under ACI and EC4 assessments, respectively. This disparity is attributable to the inherently higher strength of normal-weight concrete compared to lightweight concrete when all other parameters remain constant as shown in Figs. 2-4. Additionally, the ultimate strengths projected by ACI were frequently lower than those calculated from EC4. The investigation further found that raising the concrete surface area, by adjusting D/t ratios, enhances the ultimate strength, and the use of steel tubes with higher yield strengths greatly boosts the columns' ultimate strength.

3.2 Effect of Diameter to Thickness Ratio

The effects of the D/t ratio on axial strength were analyzed under controlled variables, including compressive strength and yielding steel strength (fy). For the reference mix (LW0MS0FA0), the initial axial strengths were determined as 533 kN and 746 kN according to the ACI Code and EC4, respectively, with a yielding steel strength of 185 MPa. When the D/t ratio was set to 60, the axial strength increased significantly, reaching 1678 kN for the ACI code and 2305 kN for EC4 with an increase percentage 214.82% and 208.98 %, respectively. Further increasing the (D/t) ratio to 90 resulted in axial strengths of 3427 kN and 4581 kN, with a rise percent of 542% and 514% as per the ACI and EC4, respectively. These results indicate that the axial strength of the system improves substantially with an increased (D/t) ratio, highlighting the critical influence of geometric parameters on structural performance. These findings highlight the effect of the steel tube's D/t ratio on axial ultimate strength. Between the codes, the ACI formulas yielded the lowest Nu values, impacted by the D/t ratio and yield steel tube strength. Specifically, the projected Nu values with ACI varied from 453 kN to 5865 kN, substantially lower than the 656 kN to 8187 kN range obtained using EC4. That means the ultimate strength ratings estimated using the ACI formula are lower compared to those obtained using EC4. Furthermore, it has been observed that the percentage increase in results predicted by the ACI is more pronounced compared to those of EC4 when the (D/t) ratio is increased.

In normal weight concrete filled steel tube (NWCFST), the dense concrete core provides stronger confinement due to higher lateral pressure. NWCFST rely more on the composite action between the steel tube and concrete core. In NWC, lower D/t enhances strength and confinement, making the composite action more efficient. Lightweight concrete filled steel tube (LWCFST) depend more on the steel tube, especially at high D/t ratio, because the concrete core contributes less to load resistance. In LWCFST, lower D/t also improves performance, but the gains are primarily limited to steel tube stability, as the concrete core contributes less to the overall strength. In LWCFST, the confinement effect is weaker because of the lower density and lateral pressure.

3.3 Effect of Steel Yielding Strength

The influence of f_y on axial strength was investigated while maintaining constant variables such as compressive strength and D/t ratio. Using the mix LW100MS0FA0, initial axial strengths were observed as 453 kN and 656 kN for the ACI and EC4, respectively, with a D/t ratio of 30 and f_y of 185 MPa. An increase in f_y to 275 MPa yielded axial strengths of 584 kN and 860 kN, corresponding to percentage increases of 24.58% for the ACI and 27.21% for EC4, respectively.

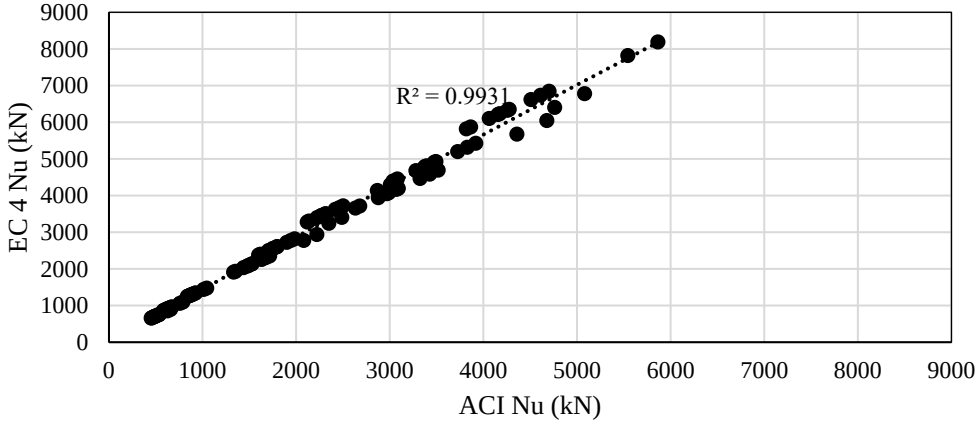

Fig. 5. Correlation between the predicted axial capacity of CFST based on the design codes

A further increase in f_y to 450 MPa resulted in a significant escalation in axial strengths, achieving 839 kN for the ACI, reflecting a percentage increase of 72.42%, and 1243 kN for EC4, corresponding to a rise of 78.42%. These findings demonstrate a strong correlation between the yielding steel strength and the axial load-carrying capacity, emphasizing the critical role of material properties in the performance of structural elements. A comparable trend is observed in Figs. 4 and 5, which depict results with identical parameters. It has been determined that the EC4 exhibits a more significant percentage increase in results compared to the ACI when variations in f_y are introduced.

Furthermore, the correlation of design codes for composite sections with various LWCs mixtures was provided in Fig. 5. The Figure showed a good correlation between the EC4 equations and the ultimate axial strength determined by ACI.

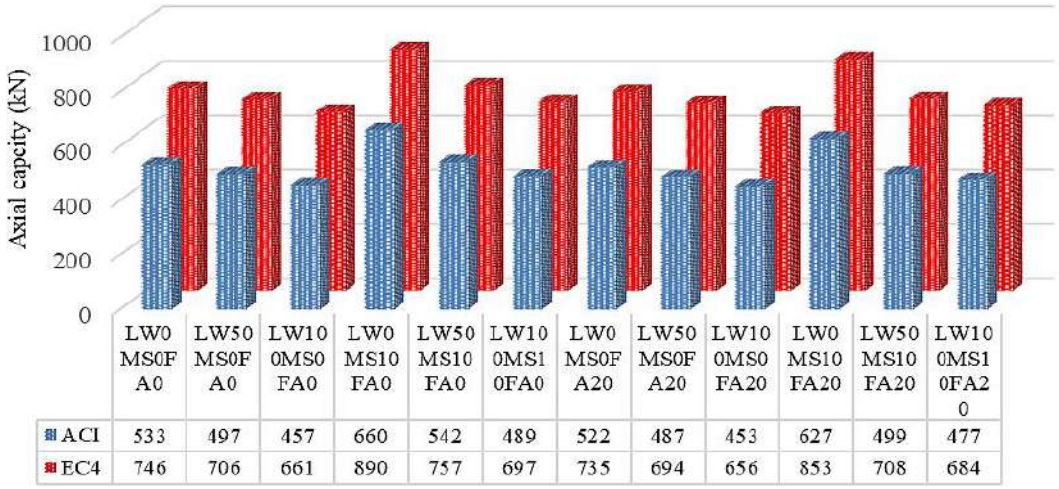

	LW0 MS0F A0	LW50 MS0F A0	LW10 0MS0 FA0	LW0 MS10 FA0	LW50 MS10 FA0	LW10 0MS1 0FA0	LW0 MS0F A20	LW50 MS0F A20	LW10 0MS0 FA20	LW0 MS10 FA20	LW50 MS10 FA20	LW10 0MS1 0FA20
ACI	533	497	457	660	542	489	522	487	453	627	499	477
EC4	746	706	661	890	757	697	735	694	656	853	708	684

(a)

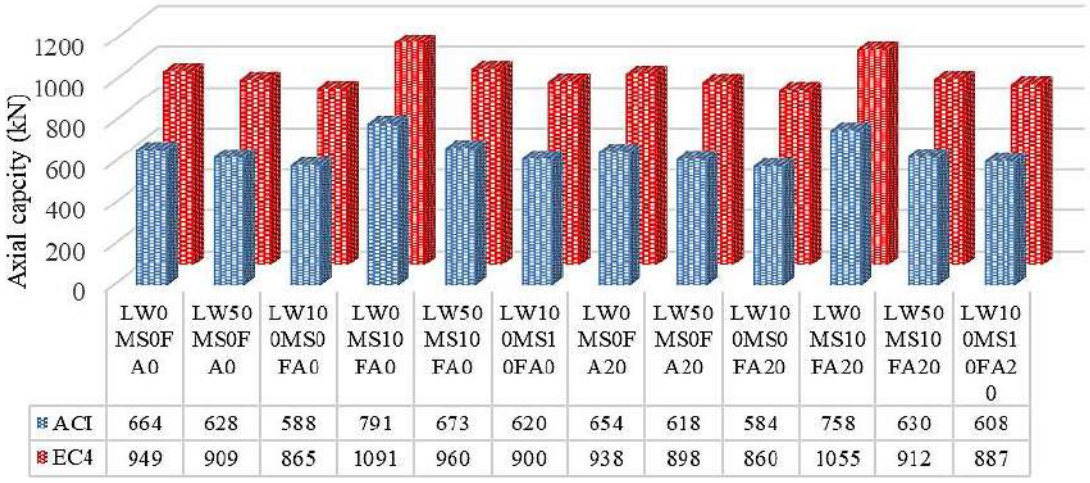

	LW0 MS0F A0	LW50 MS0F A0	LW10 0MS0 FA0	LW0 MS10 FA0	LW50 MS10 FA0	LW10 0MS1 0FA0	LW0 MS0F A20	LW50 MS0F A20	LW10 0MS0 FA20	LW0 MS10 FA20	LW50 MS10 FA20	LW10 0MS1 0FA20
ACI	664	628	588	791	673	620	654	618	584	758	630	608
EC4	949	909	865	1091	960	900	938	898	860	1055	912	887

(b)

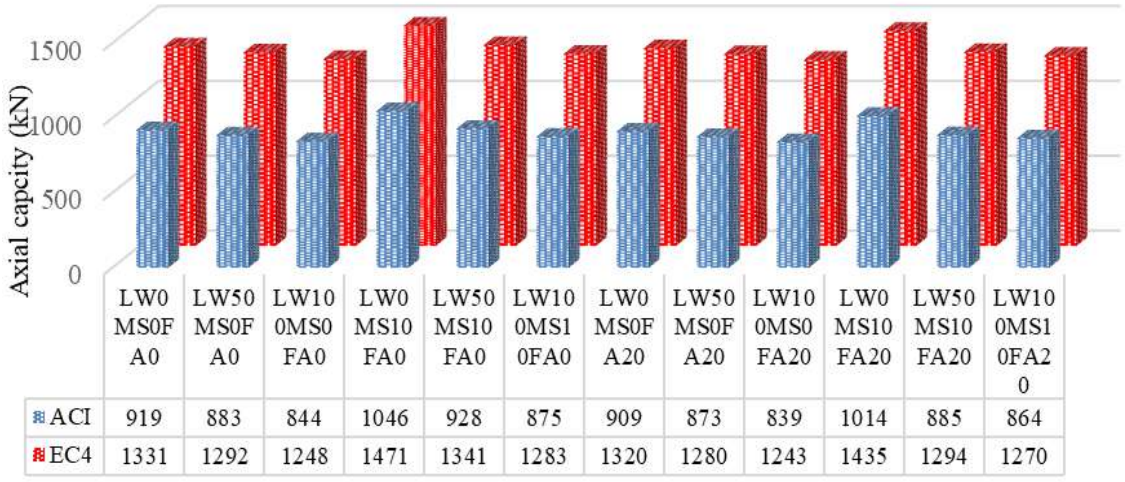

	LW0 MS0F A0	LW50 MS0F A0	LW10 0MS0 FA0	LW0 MS10 FA0	LW50 MS10 FA0	LW10 0MS1 0FA0	LW0 MS0F A20	LW50 MS0F A20	LW10 0MS0 FA20	LW0 MS10 FA20	LW50 MS10 FA20	LW10 0MS1 0FA20
ACI	919	883	844	1046	928	875	909	873	839	1014	885	864
EC4	1331	1292	1248	1471	1341	1283	1320	1280	1243	1435	1294	1270

(c)

Fig. 2. Axial compression capacity of CFST with D/t ratio of 30 and fy of a) 185, b) 275, c) 450 MPa having NWC and LWC mixtures based on ACI and EC4

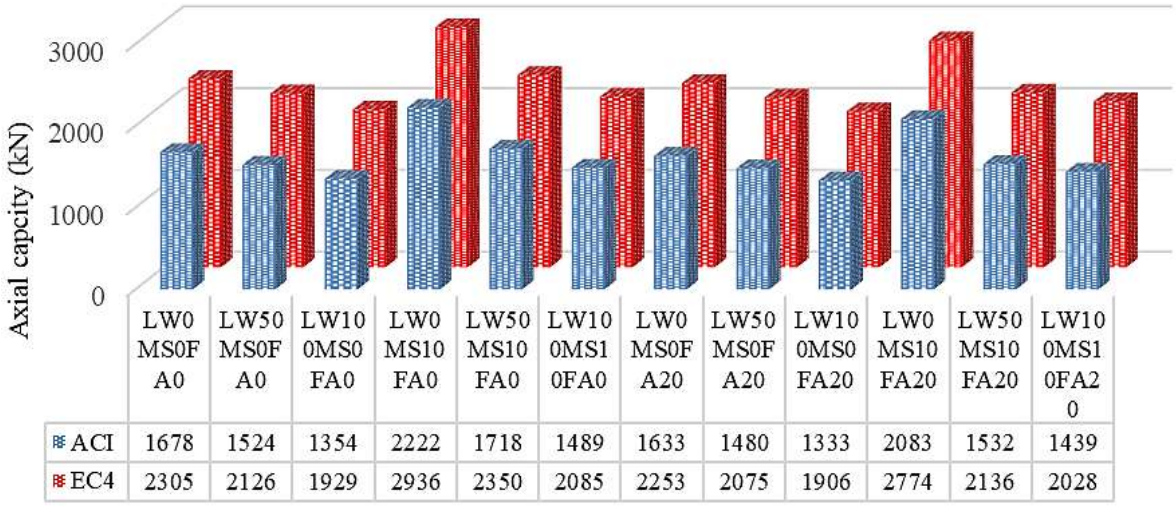

	LW0 MS0FA0	LW50 MS0FA0	LW100MS0FA0	LW0 MS10FA0	LW50 MS10FA0	LW100MS10FA0	LW0 MS0FA20	LW50 MS0FA20	LW100MS0FA20	LW0 MS10FA20	LW50 MS10FA20	LW100MS10FA20
ACI	1678	1524	1354	2222	1718	1489	1633	1480	1333	2083	1532	1439
EC4	2305	2126	1929	2936	2350	2085	2253	2075	1906	2774	2136	2028

(a)

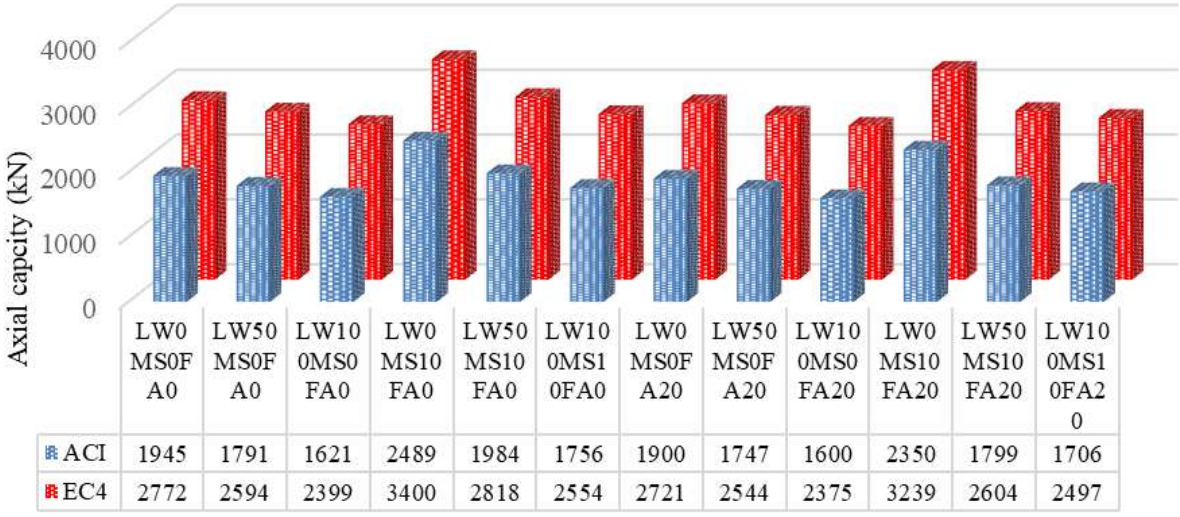

	LW0 MS0FA0	LW50 MS0FA0	LW100MS0FA0	LW0 MS10FA0	LW50 MS10FA0	LW100MS10FA0	LW0 MS0FA20	LW50 MS0FA20	LW100MS0FA20	LW0 MS10FA20	LW50 MS10FA20	LW100MS10FA20
ACI	1945	1791	1621	2489	1984	1756	1900	1747	1600	2350	1799	1706
EC4	2772	2594	2399	3400	2818	2554	2721	2544	2375	3239	2604	2497

(b)

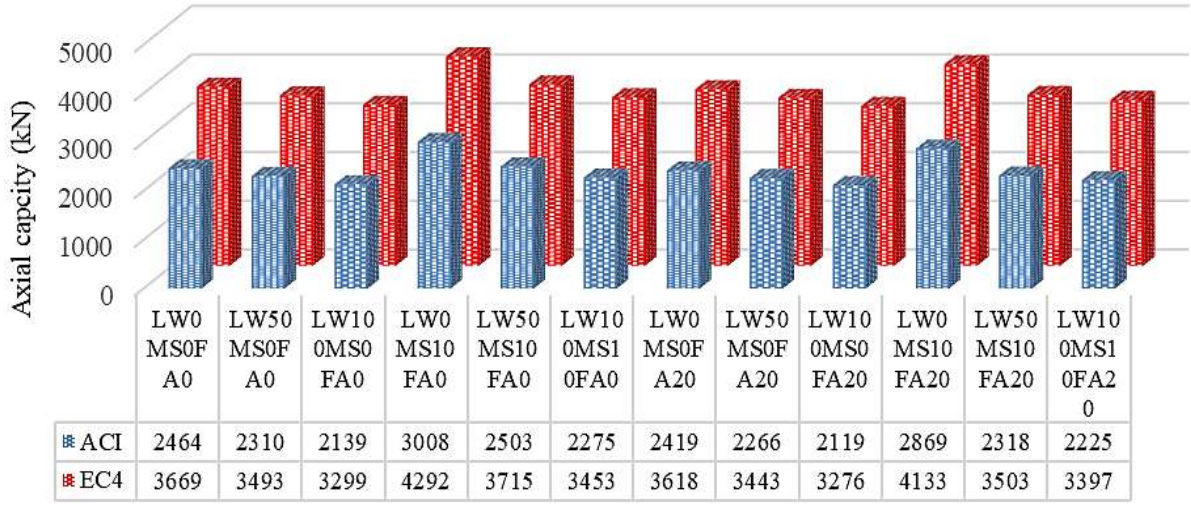

	LW0 MS0FA0	LW50 MS0FA0	LW100MS0FA0	LW0 MS10FA0	LW50 MS10FA0	LW100MS10FA0	LW0 MS0FA20	LW50 MS0FA20	LW100MS0FA20	LW0 MS10FA20	LW50 MS10FA20	LW100MS10FA20
ACI	2464	2310	2139	3008	2503	2275	2419	2266	2119	2869	2318	2225
EC4	3669	3493	3299	4292	3715	3453	3618	3443	3276	4133	3503	3397

(c)

Fig. 3. Axial compression capacity of CFST with D/t ratio of 60 and fy of a) 185, b) 275, c) 450 MPa having NWC and LWC mixtures based on ACI and EC4

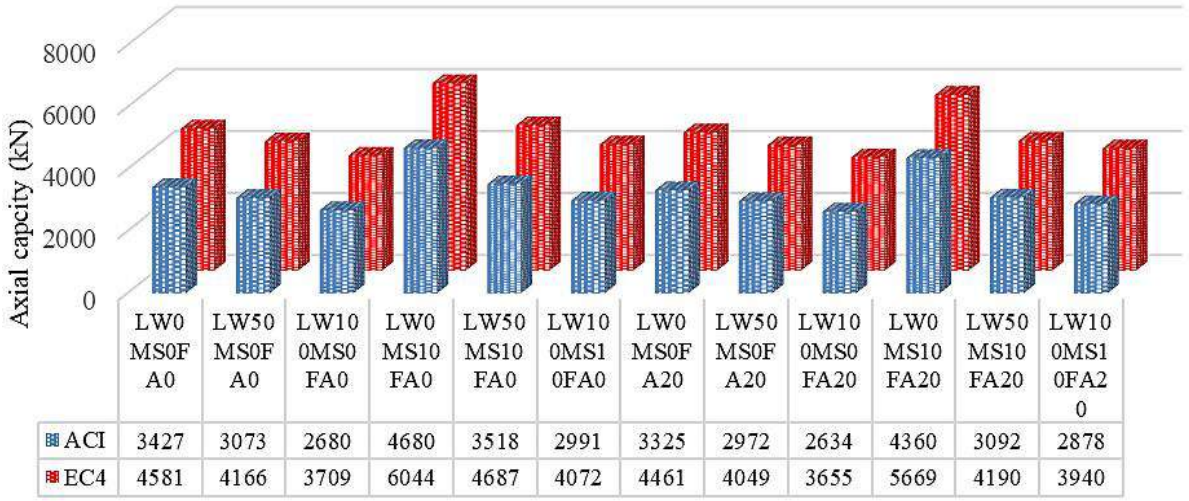

	LW0 MS0FA0	LW50 MS0FA0	LW10 0MS0 FA0	LW0 MS10 FA0	LW50 MS10 FA0	LW10 0MS1 0FA0	LW0 MS0FA20	LW50 MS0FA20	LW10 0MS0 FA20	LW0 MS10 FA20	LW50 MS10 FA20	LW10 0MS1 0FA20
ACI	3427	3073	2680	4680	3518	2991	3325	2972	2634	4360	3092	2878
EC4	4581	4166	3709	6044	4687	4072	4461	4049	3655	5669	4190	3940

(a)

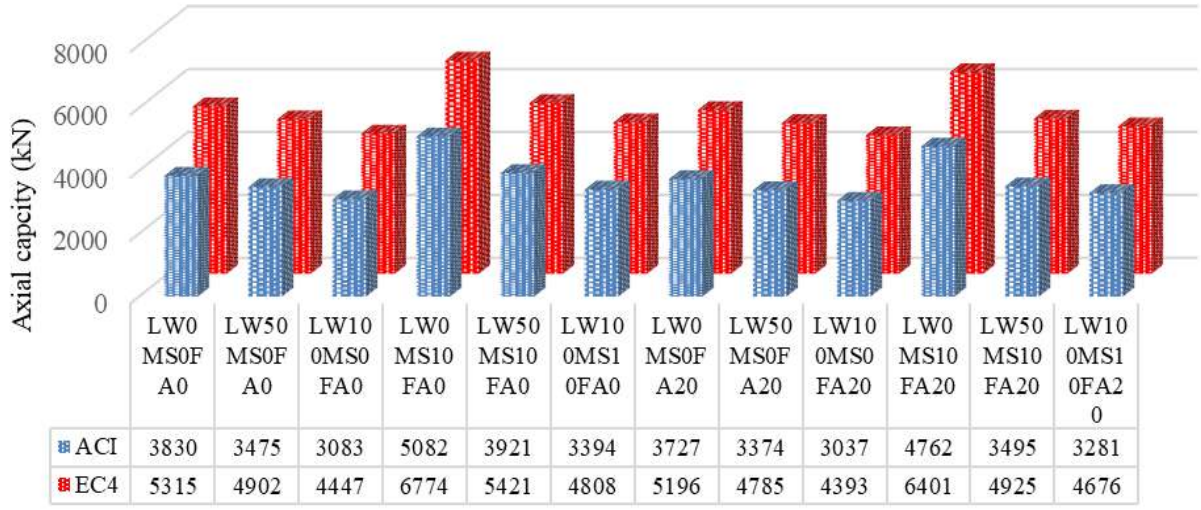

	LW0 MS0FA0	LW50 MS0FA0	LW10 0MS0 FA0	LW0 MS10 FA0	LW50 MS10 FA0	LW10 0MS1 0FA0	LW0 MS0FA20	LW50 MS0FA20	LW10 0MS0 FA20	LW0 MS10 FA20	LW50 MS10 FA20	LW10 0MS1 0FA20
ACI	3830	3475	3083	5082	3921	3394	3727	3374	3037	4762	3495	3281
EC4	5315	4902	4447	6774	5421	4808	5196	4785	4393	6401	4925	4676

(b)

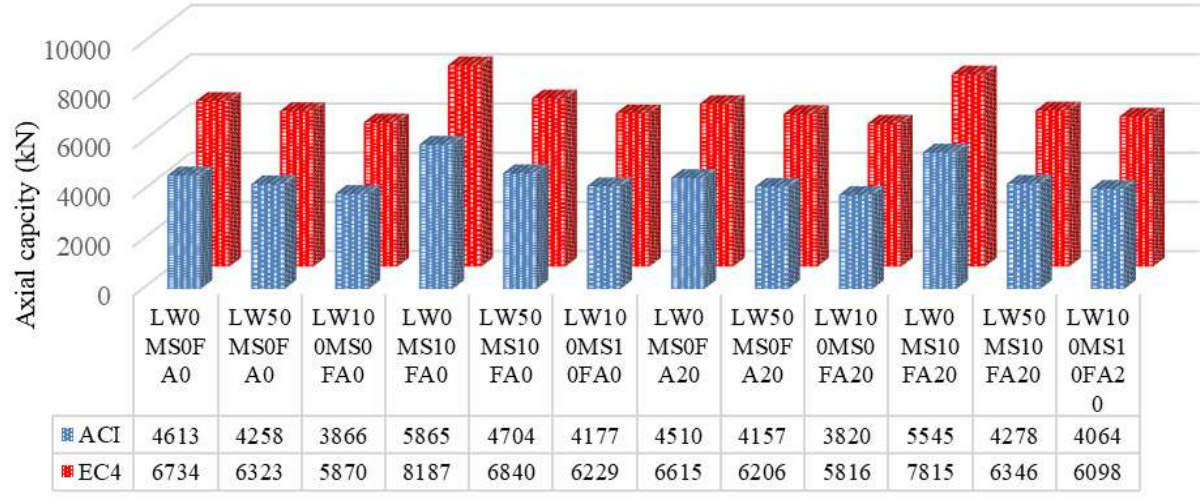

	LW0 MS0FA0	LW50 MS0FA0	LW10 0MS0 FA0	LW0 MS10 FA0	LW50 MS10 FA0	LW10 0MS1 0FA0	LW0 MS0FA20	LW50 MS0FA20	LW10 0MS0 FA20	LW0 MS10 FA20	LW50 MS10 FA20	LW10 0MS1 0FA20
ACI	4613	4258	3866	5865	4704	4177	4510	4157	3820	5545	4278	4064
EC4	6734	6323	5870	8187	6840	6229	6615	6206	5816	7815	6346	6098

(c)

Fig. 4. Axial compression capacity of CFST with D/t ratio of 90 and fy of a) 185, b) 275, c) 450 MPa having NWC and LWC mixtures based on ACI and EC4

4. Statistical Analysis

Table 3 displays the findings of the analysis of variance (ANOVA), which indicates whether or not the status of an independent variable affects the dependent variables. Minitab 19 software was used for the statistical evaluation of the GLM-ANOVA approach was used for the multiple linear regression method. Ultimate strength data from ACI (Nu) and from EC4 (Nu) were designated as dependent variables and investigated. The general linear model analysis of variance (GLM-ANOVA) was used to calculate the experimental parameter validation. However, LWA, MS, FA, f_y, and D/t were the independent criterion.

Table 3. Statistical analysis of the predicted results

Dependent variables	Independent variables	Sequential sum of squares	Computed F	P-value	Significance	Contribution (%)	R^2-value
N_u (ACI)	LWA (%)	6529976	37.02	0.000	Yes	3.129	95.8
	MS	2283458	25.89	0.000	Yes	1.094	
	FA	241797	2.74	0.101	No	0.115	
	f_y	11498839	65.19	0.000	Yes	5.51	
	D/t	179370857	1016.94	0.000	Yes	85.964	
	Error	8730993	-	-	Yes	4.184	
	Total	208655919	-	-	-	-	
N_u (EC4)	LWA (%)	8741655	25.69	0.000	Yes	2.103	96.0
	MS	3058146	17.98	0.000	Yes	0.735	
	FA	323715	1.90	0.171	No	0.077	
	f_y	34829306	102.37	0.000	Yes	8.379	
	D/t	351868129	1034.21	0.000	Yes	84.652	
	Error	16841324	-	-	Yes	4.051	
	Total	415662275	-	-	-	-	

Furthermore, while assessing the input parameters' contribution, it is evident that the D/t ratio and f_y influence the analytical outcomes' fluctuation more than the other factors. Furthermore, information on the percentage relationship between each experimental result and one or more input components is provided by the R-squared values displayed in Table 6's last column. These R squared values demonstrate a strong correlation between the input and output variables, hence confirming the significance of the analytical findings.

The statistical research shows that the D/t ratio significantly affects the axial capacity for two codes. The analysis found that this variable is the principal driver of ultimate strength values, with little effect from f_y. Table 3 shows that LWA percentage and MS have a small but considerable impact on the ultimate strength capacity values from the ACI and EC4, while FA has no effect. The D/t value has a significant impact axial strength capacity, contributing 86.0% and 84.7% for ACI and EC4, respectively.

The influence of the examined parameters and their interactions on the response is depicted in a Pareto chart, as shown in Figs. 6 and 7. This chart displays the absolute values of the standardized effects, arranged from the most impactful to the least. It also includes a reference line to identify effects that are statistically significant. The position of this reference line is determined by the chosen significance level, commonly referred to as α. The longest bar signifies the most influential factor, followed by progressively shorter bars for less impactful factors. A reference line is included to identify statistically significant factors, those bars extending beyond this line are deemed significant at a 95% confidence level. Furthermore, the Pareto chart clearly demonstrates that all analyzed parameters are statistically significant except fly ash. Among these, D/t exhibits the highest effect, followed sequentially by f_y, LWA, and MS.

Additionally, the chart provides insights into the relative significance of factor combinations. The red line in the chart represents the cumulative percentage, indicating the running total of occurrences as the progress from the highest-impact category to the lowest. Residual plots are valuable diagnostic tools for determining the validity of assumptions in regression models and other statistical analysis. They assist in determining if the model fits the data adequately and whether assumptions like as normality and constant variance hold. The normal probability plot evaluates if the residuals conform to a normal distribution. According to Figs. 8 and 9, the points align closely along a straight line, the residuals have a normal distribution, and the assumption of normality is satisfied. Residuals versus fit plot investigates whether the residuals are randomly distributed near zero across the range of fitted values. The histogram provides a visual view of the pattern of residuals. A bell-shaped curve situated at zero implies normalcy. In summarize, residual plots collectively offer a comprehensive diagnostic tool for analyzing the hypotheses of regression models. If any of the plots reveal variations from predicted trends, it may be essential to modify the model, change variables, or investigate alternate analytical approaches. Using these techniques supports the reliability and validity of statistical inferences.

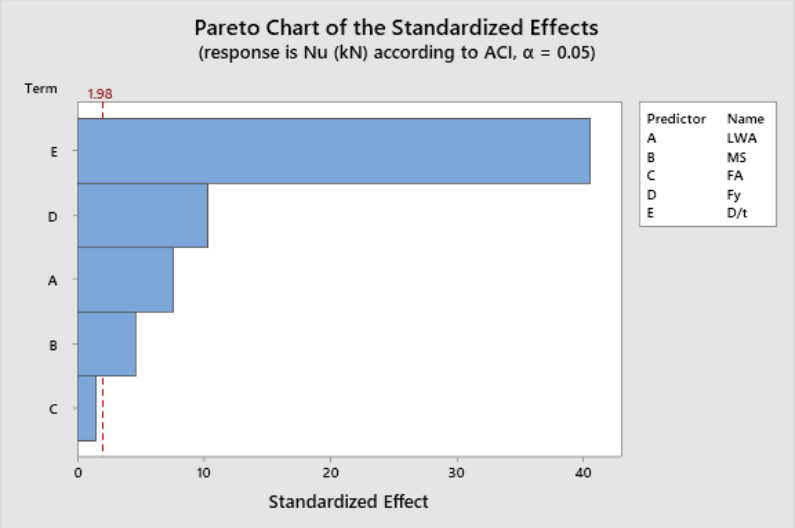

Fig. 6. Pareto chart of Nu (ACI) vs. variables

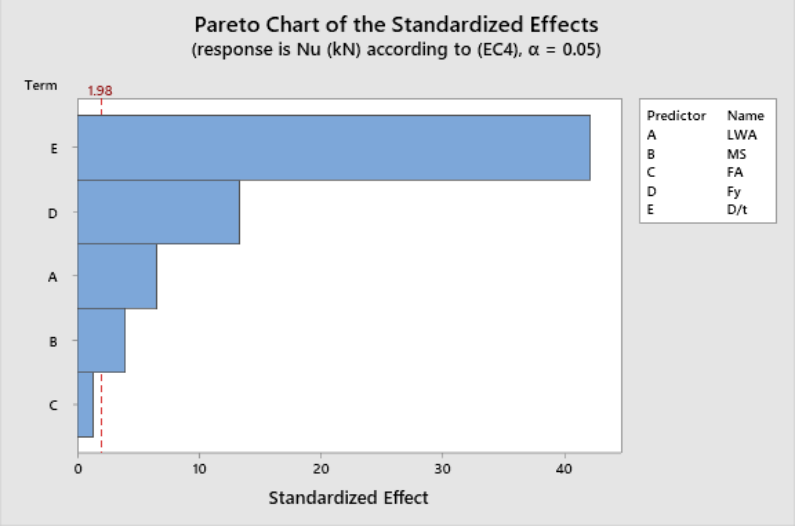

Fig. 7. Pareto chart of Nu (EC4) vs. variables

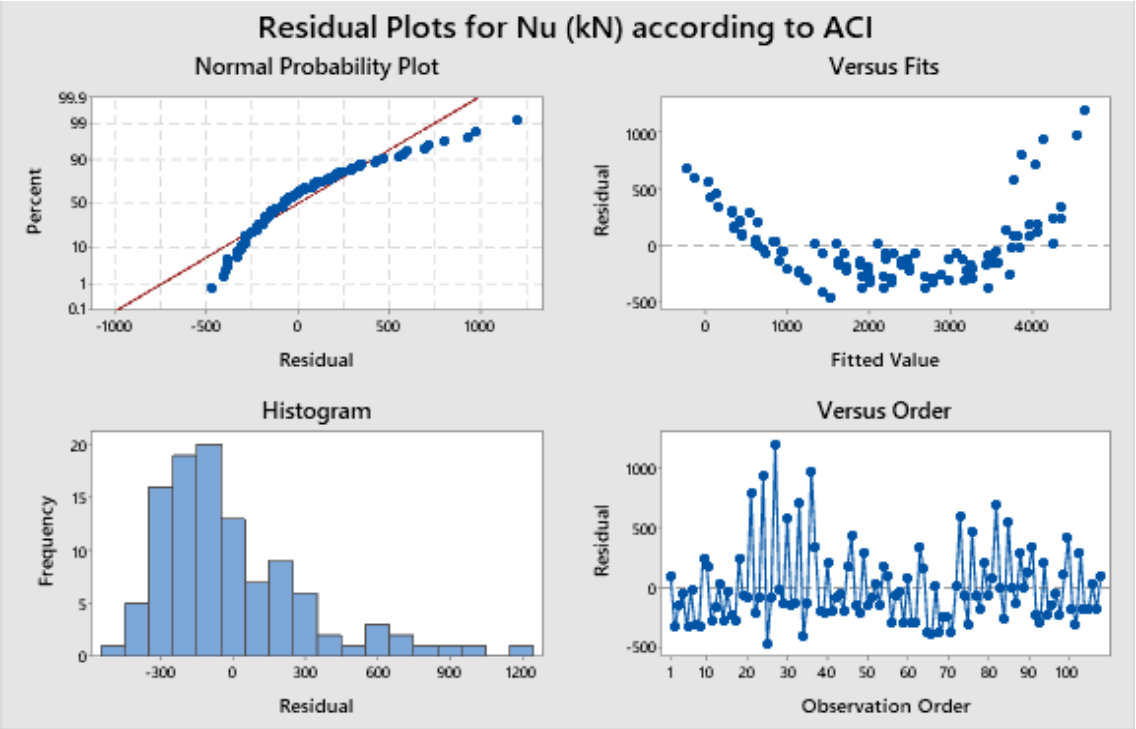

Fig. 8. Residual plots for N_u predicted by ACI

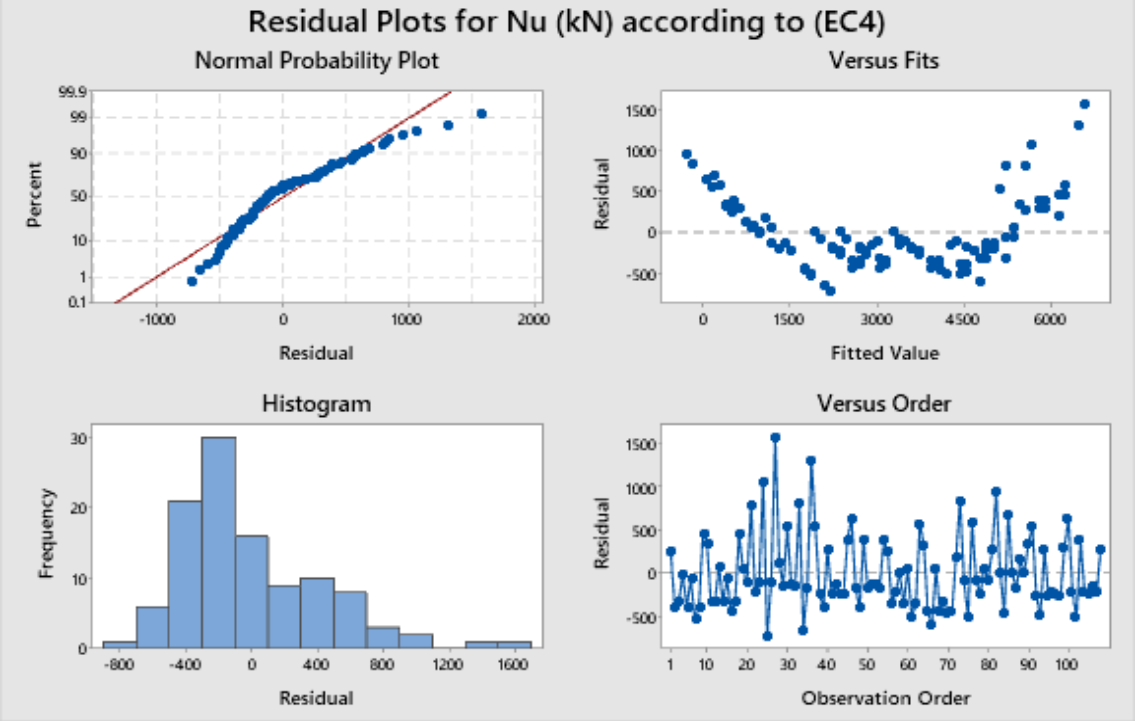

Fig. 9. Residual plots for N_u predicted by EC4

5. Conclusions

In this study, the axial strength of normal weight concrete filled steel tube (NWCFST) and lightweight concrete filled steel tube (LWCFST) were evaluated by applying ACI and EC4 with different D/t ratios and steel yielding strengths. The properties of the concrete core were also changed. The outcomes of this research led to the main crucial conclusions:

- Examining the behavior of axially loaded NWCFST and LWCFST columns requires the deployment of specialized setup, advanced equipment, and precision testing machinery. This

process involves considerable time and financial resources, making it economically impractical for widespread application. Consequently, it becomes imperative to develop an effective, feasible, and accurate methodology for evaluating the predictive capabilities of the two prominent design standards, ACI and EC4, in meeting structural performance requirements.

- The ultimate strength of circular steel tube columns filled with concrete is greatly affected by the compressive strength of the concrete and the yield strength of the steel.
- NWCFST and LWCFST columns exhibit comparable trends in their behavior, and tubular columns filled with normal concrete could bear more load than those having lightweight aggregate concrete.
- The contents of lightweight aggregate and microsilica have a substantial impact on the concrete strength and CFST columns.
- Variations in the D/t ratios demonstrate a substantial effect rather than compressive strength on the ultimate strength of circular steel tube columns filled with normal and lightweight concrete.
- The ultimate strength ratings estimated using the ACI formula are lower compared to those obtained using EC4.
- In NWCFST, the dense concrete core provides stronger confinement due to higher lateral pressure. In NWCFST, lower D/t enhances strength and confinement, making the composite action more efficient. While LWCFST depend more on the steel tube, especially at high D/t ratios, because the concrete core contributes less to load resistance. In LWCFST, lower D/t also improves performance, but the gains are primarily limited to steel tube stability, as the concrete core contributes less to the overall strength. In LWCFST, the confinement effect is weaker because of the lower density and lateral pressure.
- A high correlation exists between the ultimate strength values generated from the ACI and EC4 equations.
- The statistical evaluation showed that ultimate strength is more significantly impacted by the D/t with a contribution rate with 85% according to the statistical evaluation.
- Further study is also recommended using other codes such as American code AISC 360, Chinese code GB 50936, and Japanese code AIJ to deepen the comparative analysis and provide more comprehensive insights into the differences between these standards.

References

[1] Tsuda K, Matsui C, Mino E. Strength and behavior of slender concrete filled steel tubular columns. In: Proceeding 5th International Colloquium on Structural Stability. 1996.
[2] Zeghiche J, Chaoui K. An experimental behaviour of concrete-filled steel tubular columns. J Constr steel Res. 2005;61(1):53-66. https://doi.org/10.1016/j.jcsr.2004.06.006
[3] Mouli M, Khelafi H. Strength of short composite rectangular hollow section columns filled with lightweight aggregate concrete. Eng Struct. 2007;29(8):1791-7. https://doi.org/10.1016/j.engstruct.2006.10.003
[4] Lu ZH, Zhao YG. Suggested empirical models for the axial capacity of circular CFT stub columns. J Constr Steel Res. 2010;66(6):850-62. https://doi.org/10.1016/j.jcsr.2009.12.014
[5] Kuranovas A, Kvedaras AK. Behaviour of hollow concrete-filled steel tubular composite elements. J Civ Eng Manag. 2007;13(2):131-41. https://doi.org/10.3846/13923730.2007.9636429
[6] Hassanein MF, Kharoob OF. Compressive strength of circular concrete-filled double skin tubular short columns. Thin-Walled Struct. 2014;77:165-73. https://doi.org/10.1016/j.tws.2013.10.004
[7] Kalingarani K, Shanmugavalli B, Sundarraja MC. Axial Compressive Behavior of Slender CFST members-Analytical Investigation. Int J Innov Res Sci Eng Technol. 2014;3(1):22-5.
[8] Evirgen B, Tuncan A, Taskin K. Structural behavior of concrete filled steel tubular sections (CFT/CFSt) under axial compression. Thin-Walled Struct. 2014;80:46-56. https://doi.org/10.1016/j.tws.2014.02.022
[9] Lu FW, Li SP, Sun G. A study on the behavior of eccentrically compressed square concrete-filled steel tube columns. J Constr Steel Res. 2007;63(7):941-8. https://doi.org/10.1016/j.jcsr.2006.09.003
[10] Abed F, AlHamaydeh M, Abdalla S. Experimental and numerical investigations of the compressive behavior of concrete filled steel tubes (CFSTs). J Constr Steel Res. 2013;80:429-39. https://doi.org/10.1016/j.jcsr.2012.10.005

[11] Al-Goody A, Güneyisi EM, Ipek S. Comparison of ultimate strength results from ACI and Eurocode 4 for steel tubular columns filled with SCC. MATEC Web Conf. 2018;162(March 2021). https://doi.org/10.1051/matecconf/201816204002
[12] Niranjan BR, Eramma H. Comparison of experimental values with EC 4, ACI-318, AISC-LRFD of concrete filled steel fluted columns for concentric load. Am J Eng Res. 2014;3(5):335-44.
[13] Han LH, Li W, Bjorhovde R. Developments and advanced applications of concrete-filled steel tubular (CFST) structures: Members. J Constr steel Res. 2014;100:211-28. https://doi.org/10.1016/j.jcsr.2014.04.016
[14] Shanmugam NE, Lakshmi B. State of the art report on steel-concrete composite columns. J Constr steel Res. 2001;57(10):1041-80. https://doi.org/10.1016/S0143-974X(01)00021-9
[15] Shakir-Khalil H, Mouli M. Further test on concrete-filled rectangular hollow-section columns. Struct Eng Part A J Inst Struct Eng. 1990;68(20):405-13.
[16] Shakir-Khalil H, Zeghiche J. Experimental behaviour of concrete-filled rolled rectangular hollow-section columns. Struct Eng. 1989;67:346-53.
[17] O'Shea MD, Bridge RQ. Design of circular thin-walled concrete filled steel tubes. J Struct Eng. 2000;126(11):1295-303. https://doi.org/10.1061/(ASCE)0733-9445(2000)126:11(1295)
[18] Saisho M, Abe T, Nakaya K. Ultimate bending strength of high-strength concrete filled steel tube column. J Struct Constr Eng AIJ. 1999;523(1):133-40. https://doi.org/10.3130/aijs.64.133_4
[19] Giakoumelis G, Lam D. Axial capacity of circular concrete-filled tube columns. J Constr steel Res. 2004;60(7):1049-68. https://doi.org/10.1016/j.jcsr.2003.10.001
[20] Sakino K, Nakahara H, Morino S, Nishiyama I. Behavior of centrally loaded concrete-filled steel-tube short columns. J Struct Eng. 2004;130(2):180-8. https://doi.org/10.1061/(ASCE)0733-9445(2004)130:2(180)
[21] Han LH, Yao GH, Zhao XL. Tests and calculations for hollow structural steel (HSS) stub columns filled with self-consolidating concrete (SCC). J Constr Steel Res. 2005;61(9):1241-69. https://doi.org/10.1016/j.jcsr.2005.01.004
[22] Gourley BC, Tort C, Hajjar JF, Schiller PH. A synopsis of studies of the monotonic and cyclic behaviour of concrete-filled steel tube beam-columns. University of Minnesota Minneapolis; 2001.
[23] Fujimoto T, Mukai A, Nishiyama I, Sakino K. Behavior of eccentrically loaded concrete-filled steel tubular columns. J Struct Eng. 2004;130(2):203-12. https://doi.org/10.1061/(ASCE)0733-9445(2004)130:2(203)
[24] Kadhim IT, Güneyisi EM. Code based assessment of load capacity of steel tubular columns infilled with recycled aggregate concrete under compression. Constr Build Mater . 2018;168:715-31. https://doi.org/10.1016/j.conbuildmat.2018.02.088
[25] Gupta PK, Sarda SM, Kumar MS. Experimental and computational study of concrete filled steel tubular columns under axial loads. J Constr Steel Res. 2007;63(2):182-93. https://doi.org/10.1016/j.jcsr.2006.04.004
[26] Ghannam S, Jawad YA, Hunaiti Y. Failure of lightweight aggregate concrete-filled steel tubular columns. Steel Compos Struct An Int J. 2004;4(1):1-8. https://doi.org/10.12989/scs.2004.4.1.001
[27] Luo X, Yu X, Wei J, Li C, Yang Y, Qiao H, et al. Structural performance of ultra-high strength concrete filled high strength steel tube stub columns under eccentric loading. J Build Eng. 2024;97(September):110752. https://doi.org/10.1016/j.jobe.2024.110752
[28] Alnemrawi BR, Al-Rousan R. The Detailed Axial Compression Behavior of CFST Columns Infilled by Lightweight Concrete. Buildings. 2024;14(9):2844. https://doi.org/10.3390/buildings14092844
[29] ACI Committee 318. Building code requirements for structural concrete (ACI 318-08) and commentary. In American Concrete Institute; 2008.
[30] Eurocode 4 (2004). Design of composite steel and concrete structures. Part 1.1, General rules and rules for buildings. European Committee for Standardization British Standards Institution. Civ Eng. 2001;144(6):33-8.
[31] Standard B. Eurocode 2: Design of concrete structures-. Part. 2004;1(1):230.
[32] Abbas ML, Abbas WA, Güneyisi E. Shrinkage and thermo-mechanical properties of concretes incorporated with different substitutions of natural aggregates by cold bonded calcined attapulgite lightweight aggregates. J Build Eng. 2023;79(September):107921. https://doi.org/10.1016/j.jobe.2023.107921
[33] Güneyisi E, Gesoğlu M, Özturan T. Properties of rubberized concretes containing silica fume. Cement and Concrete Research 2004;34(12) 2309-2317. https://doi.org/10.1016/j.cemconres.2004.04.005
[34] Abbas ML, Abbas WA, Güneyisi E. Effects of using cold bonded coarse and fine calcined attapulgite lightweight aggregates on the performance properties of microsilica and fly ash blended concretes. Arab J Sci Eng. 2024;50(3):1393-419. https://doi.org/10.1007/s13369-024-08997-5

Blank Page

Research on Engineering Structures & Materials
www.jresm.org
Research Group

Research Article

Numerical analysis of surface settlement with saturated zone during urban tunnelling

Ganesh S. Ingle [*,1,a], Shailendra Banne [2,b], Darshan Gaidhankar [1,c], Kshitij Dhawale [1,d], Dinesh Aswar [3,e]

[1]*Department of Civil Engineering, Dr. Vishwanath Karad MIT World Peace University, Pune, India*
[2]*Department of Civil Engineering, Pimpri Chinchwad College of Engineering, Pune, India*
[3]*Nicmar University, Pune, India*

Article Info

Article History:

Received 19 Dec 2024
Accepted 18 Feb 2025

Keywords:

Surface settlement*;*
Analytical method*;*
Rocscience*;*
Water pocket;
Urban tunnelling

Abstract

Surface settlement assessment during urban tunnelling, especially in the presence of saturated bodies, is crucial for the safety of nearby structures and utilities. This study uses a finite element-based Rocscience (RS2) tool to obtain the surface settlement trough for the two cases, viz. tunnel hits a water pocket (saturated body) and grouted water pocket. In the case of tunnel hits a water pocket, the maximum surface settlement was found to be 31.6 mm, while for the grouted water pocket, it was 16.4 mm, which is nearly 50% less than the latter case. Furthermore, the support capacity curve findings showed that the support lining is unstable when the tunnel hits a water pocket; however, in the grouted water pocket case, the liner's safety exceeds the design factor of safety. In addition, the combined maximum surface settlement obtained by the numerical method (RS2) is validated with the O'Reilly and New method, based on Peck's classical empirical theory. It is found to be closer to it by 6%, indicating good agreement. The findings are also compared with a few analytical studies, including Limanov's, Sagaseta's and the Gonzales-Sagaseta method. Limanov's and Sagaseta's, methods showed comparable results to the present study; however, the Gonzales-Sagaseta method underestimated the results. Finally, the applicability of the RS2 method is verified by conducting the parametric study on tunnel geometry (depth and diameter), and the results compared to analytical methods. The application of predicted surface settlement guides the tunnel engineer from the future consequences regarding the destructive effects of adjacent structures and facilities, particularly in the presence of water bodies.

© 2025 MIM Research Group. All rights reserved.

1. Introduction

Tunnel projects are inherently dangerous due to the variability and unpredictability of geological conditions [1]. Tunnel construction, particularly in hilly areas, is mainly associated with complex geology and uncertainties [2]. The uncertainties in geology and hydrogeology make tunnelling very challenging. Groundwater and saturated zones are the main origins of tunnel-building issues that allow water to enter into the tunnel. Because the pressure at the excavation boundary is typically atmospheric, the tunnel function as a groundwater drain [3]. The effects of it create various problems, such as unfavourable working conditions, damage to construction equipment's, increases in the construction period, and, most notably, property losses and casualties [4,5]. Therefore, the likelihood and potential extent of water bodies, as well as the intensity of flow during tunnel construction, must be predicted in advance [6]. However, this problem may occur because of a lack of accurate information regarding the location of saturated zones/water bodies, due to

*Corresponding author: ganesh.ingle@mitwpu.edu.in
[a]orcid.org/0000-0002-2203-0011; [b]orcid.org/0000-0001-5626-5508; [c]orcid.org/0000-0003-0029-6019; [d]orcid.org/ 0009-0008-7051-2446; [e]orcid.org/0000-0002-5540-987X
DOI: http://dx.doi.org/10.17515/resm2025-571st1219

inadequate geotechnical investigations and squeezing ground conditions [4]. Therefore, prior to the construction, assessment or prediction of saturated zones/water bodies is crucial for the design and stability of tunnels [7].

Groundwater control is the prerequisite for the effective completion of tunnels [8]. Due to the saturated type of geology, India has experienced the worst disaster in the history of tunnelling. The accidental case studies, such as Bihar Chass-Nala colliery disaster, Kolkata East-West metro bowbazar accident, an artesian blowout in the Tunnel Boring Machine (TBM) driven in Dul Hasti J&K, groundwater ingress in head race tunnel of Tapovan: Vishnugad Hydroelectric Project in higher Himalayas etc. The unwanted entry of groundwater flows in the excavation area results in groundwater drawdown. This could result in ground settlement in addition to the settlement caused by the excavation effect [9,10,11,12] as well as some other environmental impacts [13]. The result of groundwater drawdown caused more than 1m ground subsidence during the construction of the Romeriksporten tunnel in Norway. Another case study reported by Yoo et al. [14] in which typical excavation under an active airport in water-bearing permeable ground resulted in significant ground surface settlements of nearly 200 mm excess on the apron area due to insufficient groundwater control. Despite the fact that the pre-grouting was carried out along the tunnel's periphery, this occurred.

The case studies discussed above highlight the significance of groundwater and settlement control during tunnelling operations in ground-water drawdown conditions [10,15]. Whereas a limited number of studies [16,17,18,19], have been conducted to characterize the ground surface settlement produced by tunnelling in water-bearing ground/saturated zones. Yoo [10] carried out a thorough investigation into the interaction of tunnelling and groundwater during tunnelling in a saturated stratum. Shen et al. [20] also did a detailed investigation on the long-term settlements behaviour of metro tunnel and found that it is caused by adjacent construction and groundwater penetration. Some of the studies [21,22,23,24] are not related to tunnelling but focuses on the lasting ground sinking instigated by dewatering in the Shanghai area. All of these scenarios demonstrate the importance of evaluation of groundwater study for proper treatment and ensuring long-term tunnel stability [7,25,26].

In fact, various methods have been used to evaluate the ground water into the tunnel. The most common are analytical, empirical, semiempirical, and numerical. Because of their simplicity, numerous analytical studies are used to compute the quantity of underground water seepage into the tunnel [5]. These studies are based on the assumption of homogeneous and isotropic rock permeability [26]. Numerical methods are complex and time-consuming in nature; despite these limitations, numerical methods have been used as a primary tool in most of the available studies because they provide more accurate results than the analytical method [5,10]. The numerical techniques can be used to simulate the heterogeneous and anisotropic conditions, as well as the interaction between groundwater and underground excavations [26]. Furthermore, the advancement in computer computational performance has resulted in the significant use of numerical techniques in tunnel engineering [13, 27]. Many numerical methods employ the finite element approach [28,29], while few studies are based on the boundary element methods, where only elements at boundaries are considered [30,31].

It is observed that numerous studies have been carried out by numerical method in tunnel engineering; this may be to obtain the tunnel- induced settlements, tunnel support stability, TBM performance, geological conditions, tunnel convergence, etc. [32]. However, the quantum of research that has been conducted to characterize the ground surface settlement trough produced by twin tunnelling, especially for water-bearing ground/saturated zones, is limited. Further numerical studies are required for predicting the ground surface settlement, especially for the saturated zone/ground. Also, the majority of the research has been conducted outside India; to investigate the impact of TBM tunnelling on Indian ground conditions, more studies/investigations are required.

The primary goal of the present study is to apply the Rocscience (RS2) tool to predict the surface settlement trough in case of twin tunnelling for two cases: when the tunnel (TBM) hits the A) hypothetical saturated zone/water pocket positioned near the 2nd tunnel crown and B) after

grouting the saturated zone (grouted water pocket). The RS2 results are validated using the empirical approach suggested by O'Reilly and New [33] and also compared to a few other analytical approaches. Finally, the applicability of the RS2 method is verified by conducting the parametric study on tunnel geometry (depth and diameter), and the results are compared with analytical methods.

2. Methodology

This study explains the investigation of surface settlement caused by urban tunnelling in the presence of a saturated body (water pocket). Fig.1 represents the detailed framework and overall approach used in the study. A thorough review of literature was carried out prior to decide the objectives of the work. Regional geology and its properties are hypothetically assumed. Twin tunnel geometry and its support system was assumed to be a composite lining consisting of a circular segmental lining as a primary support and a cement grouting layer as a secondary support by the middle and tail shield of TBM. The properties of segmental lining and steel are also assumed.

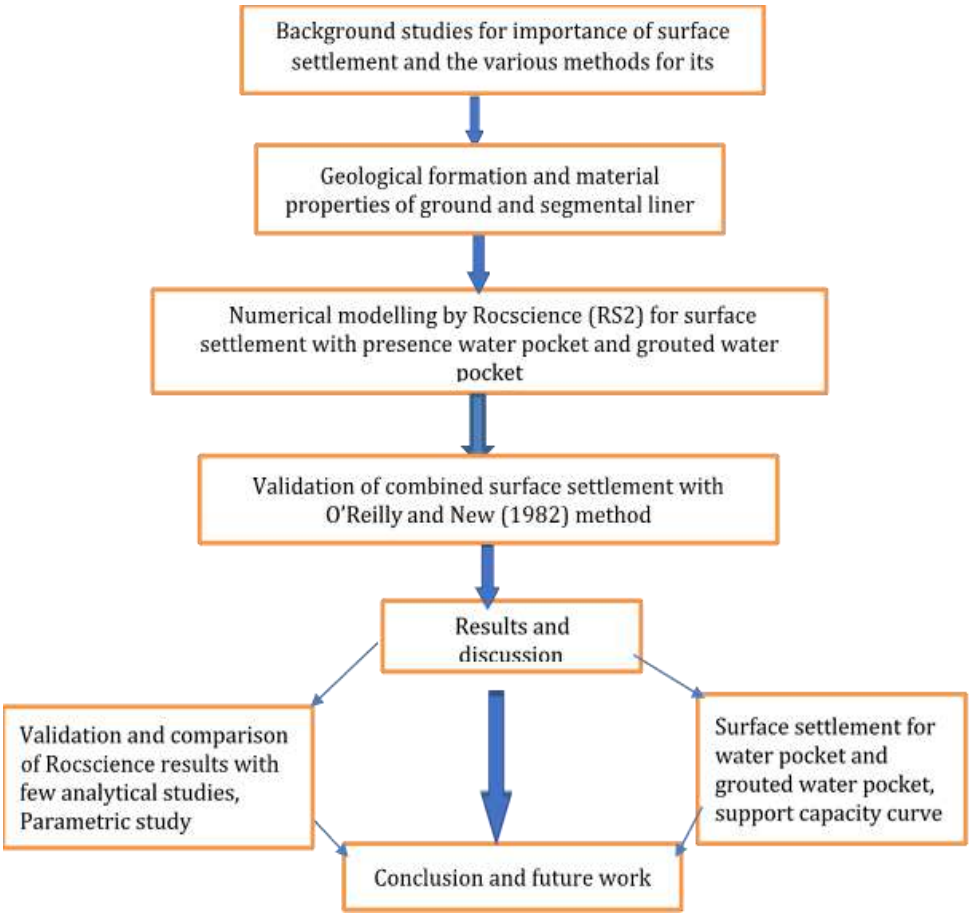

Fig. 1. Framework of the study

The surface settlement analysis was carried out in three steps. a) Numerical analysis was carried out using the FEM-based Rocscience tool (RS2) for the cases of tunnel hits to the water pocket and grouted water pocket. b) The numerical method result (combined surface settlement trough) of the grouted water pocket was validated with the empirical approach proposed by O'Reilly and New method [33], c) the numerical method result was further compared with a few analytical approaches including, Limanov's, Sagaseta's, and the Gonzales-Sagaseta method. Limanov's and Sagaseta's methods. Finally, conclusions were drawn with the comparison of numerical method with empirical and analytical methods.

3. Geology and Material Properties

Geology is one of the basic and most important aspects on which the whole tunnel support system is decided. In this study, a 2D finite element model was performed on hypothetical 5.8m diameter circular twin tunnel positioned 20m below the ground surface. The geological formation consists of eight soil layers up to 40 m depth with an average unit weight of 17kN/m^3. The borehole of the geological formation, its thickness, and the location of the tunnel are shown in Fig. 2. The borehole log data is closely related to the East-West Metro and the heritage structures in Kolkata, India.

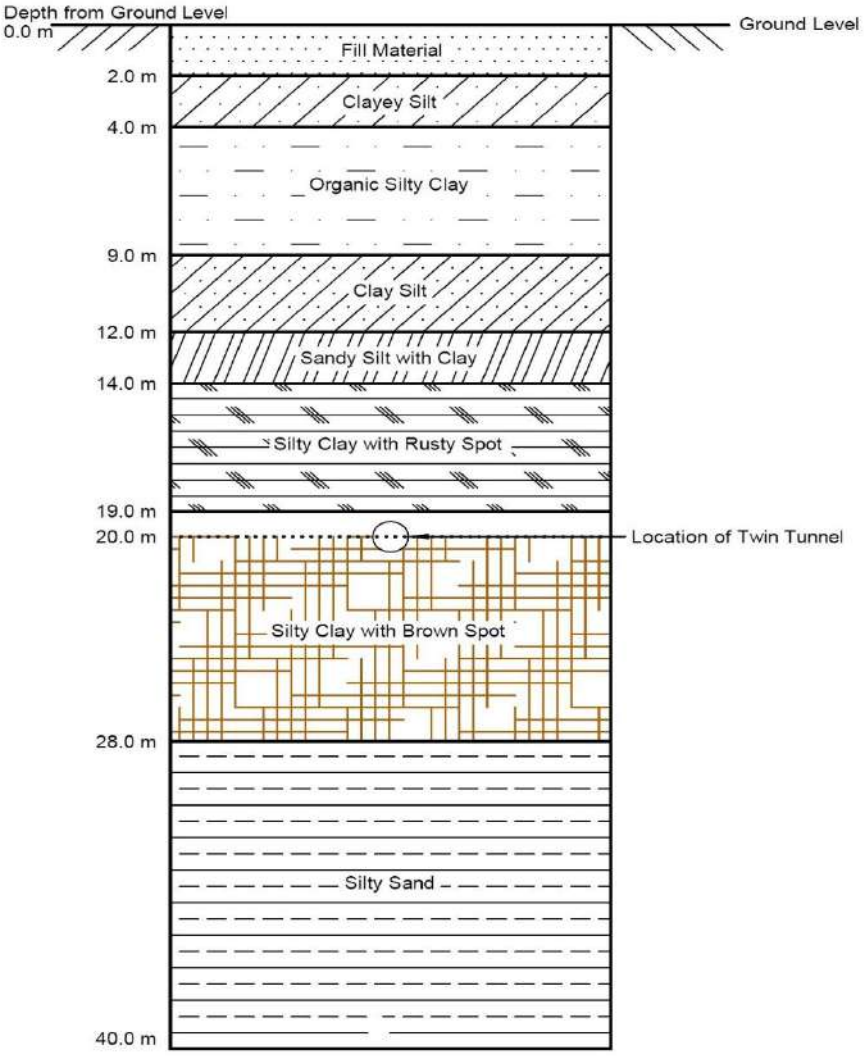

Fig. 2. Borehole of geological formations

The borehole data consists of the fill material as a topmost layer with a 0-2 m thickness below the ground surface. The second layer is clayey silt from 2 to 4 m thick, followed by organic silty clay up to 9 m thick. The clay-silt with calcareous nodules, sandy-silt with clay, and silty clay with rusty spots (loamy sandy deposits of various origins) are located at 9 m, 12m, and up to 14 m depths, respectively. In the present study, twin tunnels are considered (closely related to the East-West Metro Kolkata, India), which are located at 20 m depth below the ground level and positioned between the sixth and seventh soil layers. These layers consist of silty clay with rusty spots and silty clay with brown yellow-spots (loess), and extend up to a depth of 28 meters. The bottommost layer below 28 meters is silty sand. Table 1 shows the soil layer configuration and its elastic as well as engineering properties.

Table 1. Elastic and engineering properties of soil configuration

Soil	Soil classification	Unit Wt. (kN/m^3)	Cohesion (kN/m^3)	Friction angle (degree)	Young's Modulus (MPa)	Poisson's ratio	Permeability (m/s)	Porosity
Fill material	-	18.5	0	26	10	0.2	5×10^{-5}	0.5
Clayey silt	CL	18	0	28	15	0.3	1×10^{-7}	0.5
Silty clay with organic materials	OL	17	0	28	25	0.3	1×10^{-7}	0.5
Clay-silt with trace of calcareous modules	OH/OL	19	5	28	40	0.3	1×10^{-7}	0.5
Sandy-silt with occasional clay	SM/SC	18.5	4	30	55	0.3	5×10^{-7}	0.5
Silty clay with rusty spots	SM	19.5	5	32	63	0.3	1×10^{-7}	0.5
Silty clay with brown spots	ML/CL	19.5	5	32	65	0.3	1×10^{-7}	0.5
Silty sand	SM	19.5	0	34	100	0.3	1×10^{-7}	0.5

Table 2. Properties of concrete and steel

Parameters	Value
Type of Concrete	M50
Compressive strength (MPa)	50
Material Safety Factor	1.5
Characteristic Tensile Strength (MPa)	4.69
Design Tensile Strength (MPa)	4.15
Modulus of Elasticity shorty term or (Elastic Modulus) (MPa)	35,355
Poisson's Ratio	0.15
Unit Weight of Reinforced Concrete (MPa)	25
Steel Grade	Fe500
Characteristic Steel Strength (MPa)	500
Material Safety Factor	1.15
Design Steel Strength (MPa)	435
Ultimate Steel Strength (MPa)	545
Modulus of Elasticity (MPa)	200,000

To prepare the Rocscience (RS2) model, the tunnels are assumed to be supported by a composite lining consisting of a circular segmental lining as a primary support and a cement grouting layer as a secondary support by the middle and tail shield of TBM. The composite circular tunnel lining is made up of a 275 mm thick universal segmental ring and a 150 mm thick TBM grout. A segmental ring has an internal diameter of 5800 mm and an external diameter of 6350 mm. The space between the tunnel excavated diameter and the outer diameter of the segmental ring is filled with

Cementous grout and the sodium silicate mixture for the circular secondary lining from TBM's tail shield. Table 2 shows the properties of segmental lining and steel.

4. Numerical Modelling Using Rocscience (RS2)

In this study, numerical analysis was performed using a 2D finite element program, Rocscience (RS2). RS2 can be used to analyze and design tunnels and the support system. In the present work, the RS2 is used to predict the surface settlement trough for two cases: when the TBM hits A) the hypothetical saturated zone/water pocket positioned near the 2nd tunnel crown, and B) the grouted water pocket (after grouting the saturated zone). Fig. 3 depicts the tunnel FEM model in the presence of a water pocket/saturated zone, and Fig. 4 represents the model of twin tunnel after grouting the water pocket/saturated zone, called a grouted water pocket.

The models consist of twin tunnels with internal segment ring diameters of 5.8 m and a distance of 15m c/c. The overburden of buried tunnel is 20 m and subjected to a surface load of 40 kN/m^2. The two extreme-sided boundaries are considered at eight times the diameter of the tunnel from the tunnel centerline. The top surface is a free boundary condition, whereas the bottom surface is fixed to allow for vertical movement whereas the right and left edges of the external boundary are fixed in the X direction. The soil layers are discretized using triangular elements with three nodes and a gradation factor of 0.1. To determine the optimal mesh size, a sensitivity analysis was conducted on the mesh, which ensured accurate results while maintaining computational efficiency. A graded mesh was applied across all models, with finer mesh elements near the tunnel opening (regions of high-stress gradients) and became coarser towards the model boundaries.

In the present study, the soil layers behavior is assumed to be elasto-plastic material, and the Mohr-Coulomb (MC) model shows perfectly linear elastic-plastic behavior. It is well known that the Mohr–Coulomb failure criterion is not able to accurately reproduce the soil movements induced by excavation because it represents Young's modulus of soil in the in-situ stress state [34]. Nevertheless, most of the finite element-based numerical studies are still performed using simple constitutive models such as Mohr-Coulomb (MC). Because of the simplicity of formulation, it has more applications than other models, as well as MC model requires a limited number of input parameters determined by simple tests [35], and the calculation times tend to be lower than those of advanced soil models [36,37,38,39].

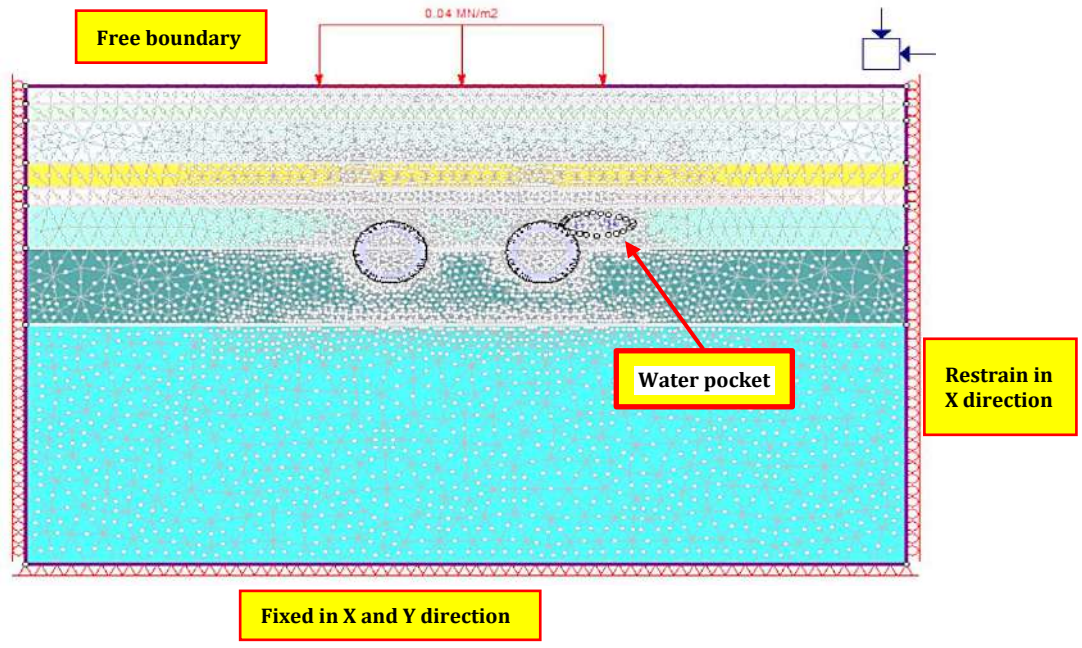

Fig. 3. FEM model in presence of water pocket (case A)

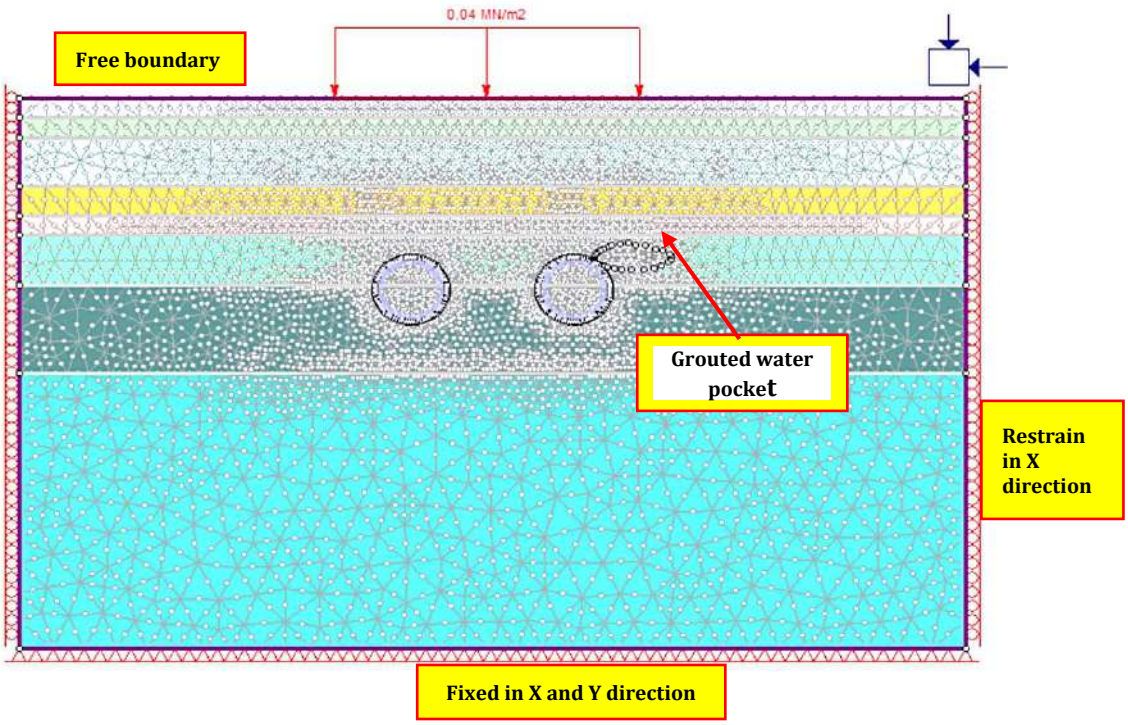

Fig.4. FEM Model in presence of grouted water pocket (case B)

The water table is considered to be 23 m below the ground surface. In the present study, the soil layers are assumed to be in undrained condition, and the short-term settlement analysis was carried out, which is mainly contributed to by construction methods. [40,41]. Settlement due to consolidation was neglected. The RS2 model considers the undrained strength and stiffness parameters, whereas the undrained Young's modulus was back- calculated based on effective shear modulus. Hence, no pore water pressure will be generated.

4.1. Modelling and Construction Sequence

The first model, case A (Fig. 3), considers a hypothetical unknown water pocket of 6 m long and 2 m thick located at the upper right corner of the 2nd tunnel. The average depth of water pocket is 14 m below the ground level. The water inside the pocket was modelled as an elastic material with a unit weight of 9.81 kN/m^3, a Poisson's ratio of 0.499, and Young's modulus of 1.1 GPa.

Table 3. Various construction stages and their features

Construction sequence	Features
Initial condition, initial ground stress	The effective stress ratio in and out of plane is considered 1.0
Excavation of 1st tunnel	The induced load factor of 0.95 from inside the tunnel, indicates 5% stress relaxation by TBM
Composite lining of 1st tunnel	combination of the primary lining (Segments) and secondary lining (grout)
Excavation of 2nd tunnel	The induced load factor of 0.95 from inside the tunnel, indicates 5% stress relaxation by TBM
Tunnel hit to water pocket	A water pocket of 6 m long and 2 m thick is located at the right top of 2nd tunnel, which is filled with water and loose soil. As the 2nd tunnel hits a water pocket at the tunnel crown, water will start entering the tunnel, causing a huge volume loss in the water pocket. This volume loss creates an empty cavity with no support, which eventually links to a huge settlement at the ground surface
Composite lining of 2nd tunnel	combination of the primary lining (Segments) and secondary lining (grout)

In the second model, case B (Fig. 4), the tunnelling was carried out after grouting the water pocket using a grouting technique having a unit weight of 24 kN/m3 and a friction angle of 31 degrees. The composite tunnel lining consists of 275mm thick segmental lining and 150 mm thick grout, which is assumed to be an elastic material with minimal seepage loss during tunnel construction. TBM grout loss during secondary lining around the tunnels is not considered. The surface settlement for both cases was determined for the following construction sequences/stages, which are presented in Table 3.

In most of the previous studies, the stress relaxation factor has been determined based on no scientific reason and merely as a hypothetical choice [42]. In contrast, the relaxation factor depends on various factors such as tunnel geometry, initial stress, soil properties, depth of the tunnel, and the length of the unsupported section at the tunnel heading. Near the working face, it is almost zero, and behind the tunnel face, it varies from 0 to 1 [42,43]. Smaller values of the relaxation factor represent smaller deformations and larger forces in the lining. In the present study, the composite lining is used behind the tunnel face, which simulates the smaller deformation and greater forces in the lining; hence the smaller stress relaxation factor is considered, i.e. 5%, and the induced load factor is 0.95.

5. Results and Discussion

The RS2 was used to analyze the tunnel surface settlement in the presence of a water pocket. For tunnel hits to the water pocket (case A) and grouted water pocket (case B), the total surface settlement and its variation along the lateral distance are obtained. The results of the grouted water pocket (case B) were validated using the empirical method suggested by O'Reilly and New [33] and compared with a few analytical approaches.

5.1. Surface Settlement in the Presence of Water Pocket

During the various construction stages, the maximum surface settlement and its variation along the horizontal distance are computed. Fig.5 shows the results of surface settlement/displacement observed for one of the construction stages namely tunnel hits to the water pocket.

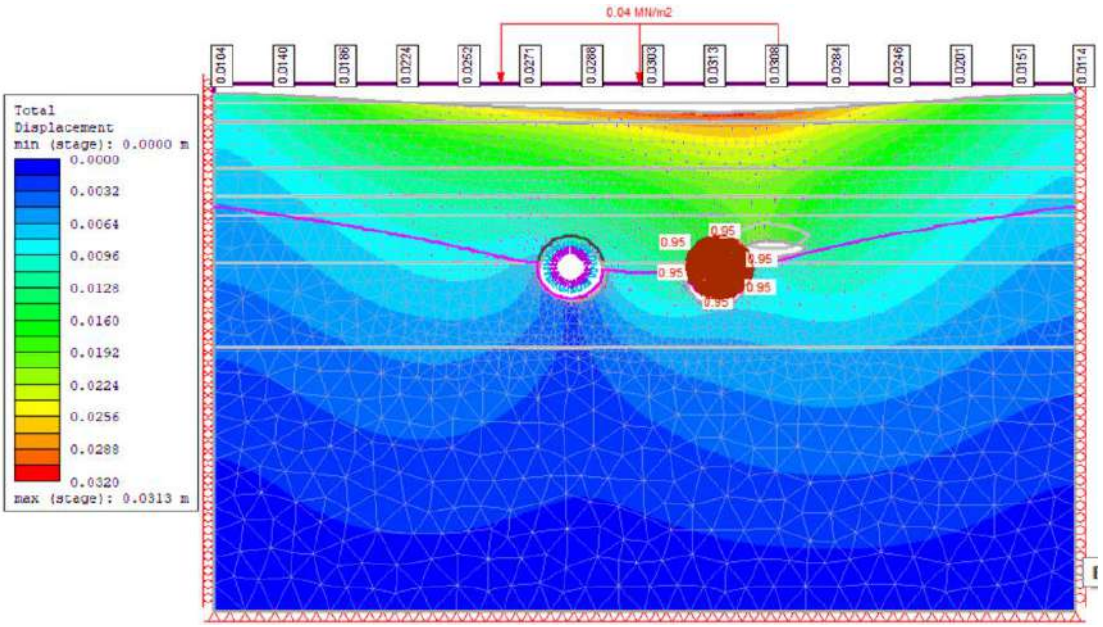

Fig. 5. Settlement at ground surface after TBM hits a water pocket

Table 4 shows the magnitude of maximum surface settlement at various construction stages for both cases. In the case of tunnel hits to a water pocket, it was found that the surface settlement of 30.3 mm occurred during the excavation stage of 2nd tunnel and that of 31.6 mm when the tunnel hits the water pocket. The maximum surface settlement was increased by 5% as compared to the

2nd tunnel excavation stage. This may be because entry of water in to the excavation area increases the effective stress and consequently increases the surface settlement.

Table 4. Maximum surface settlement for various construction stages for both the cases

Excavation stages	Surface settlement (mm)	
	Tunnel hits a water pocket	Tunnel hits a grouted water pocket
Initial (in situ) condition	0.00	0.00
Excavation of 1st tunnel	29.1	18.8
Composite lining of 1st tunnel	25.2	14.7
Excavation of 2nd tunnel	30.3	18.6
Tunnel hit to water pocket	31.6	16.4
Composite lining of 2nd tunnel	29.2	14.02

While, in the case of a grouted water pocket, the maximum surface settlement was 16.4 mm, which is nearly 50% less than the presence of water. This may be because of the pre-grouting effect of the water pocket, which controls the drawdown above the tunnel and reduces the effective stress, results in a decrease in the settlement. In both cases, the application of lining to the 2nd tunnel decreased the surface settlement; this may be because of the reduction of water flow quantity in the excavation area due to the placement of composite lining. The effect of composite lining provides superior watertightness and load bearing capacity [44]; hence the provision of composite lining applies a sufficient face pressure to push the flow towards the ground surface and reduce the water flow quantity in the excavation area.

Figs. 6 and 7 show the variation of total surface settlement (displacement) with lateral distance in cases A and B, respectively. In both cases, the surface settlement variation with horizontal distance follows a similar pattern, i.e., as the distance increases, the settlement increases as well, reaching a maximum at the crown of 2nd tunnel and further decreasing for the increment of horizontal distance. Fig. 6 shows the wider and deeper settlement trough, whereas Fig.7 shows a narrower and shallower settlement trough. This clearly shows that grouting a water pocket has a positive effect on settlement trough that are considerably narrower and shallower, with a maximum settlement of nearly 50% less than the presence of water. In the presence of a water pocket, the maximum surface settlement is observed to be 31.6 mm, which is a red trigger as it exceeds the prescribed limits (20mm) laid by EURO, the Chinese code, and British practices [45-46], causing the surface structures to be unsafe.

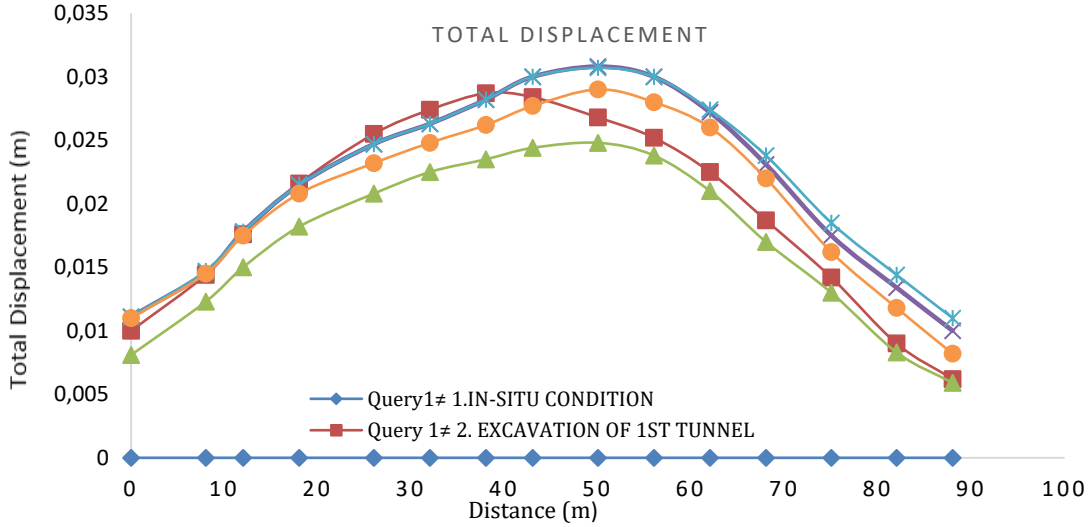

Fig. 6. Ground surface settlement variation with horizontal distance for different construction stages (case A- tunnel hits a water pocket)

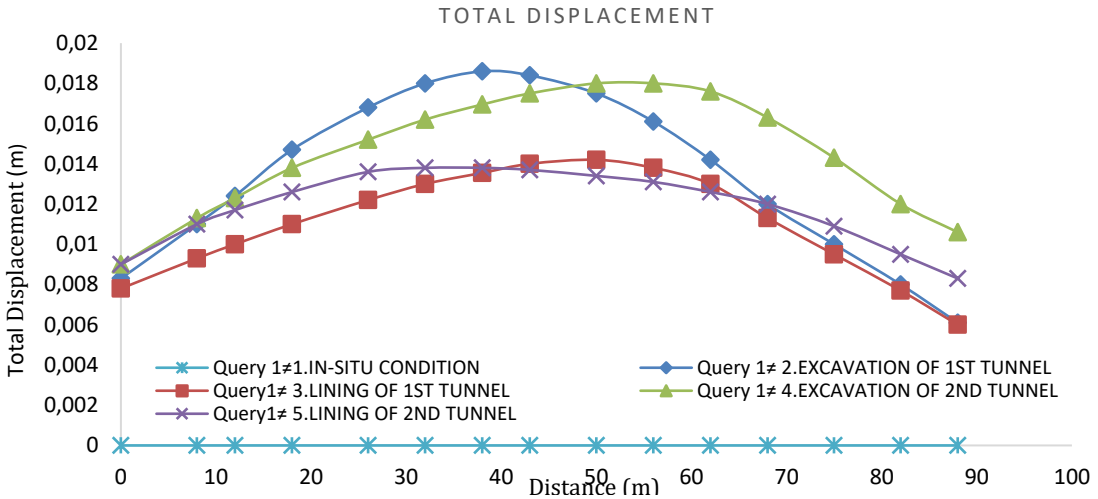

Fig. 7. Ground surface settlement variation with horizontal distance for different construction stages (case B- tunnel hits a grouted water pocket)

5.2. Support Capacity Curve

Tunnel support capacity curves are self-generated by the Rocscience program. These are the capacity envelopes of shear force, axial force, and bending moment, which provide the factor of safety of lining (concrete liner and steel sets). Figs. 8 and 9 depict the support capacity curves for cases A and B respectively.

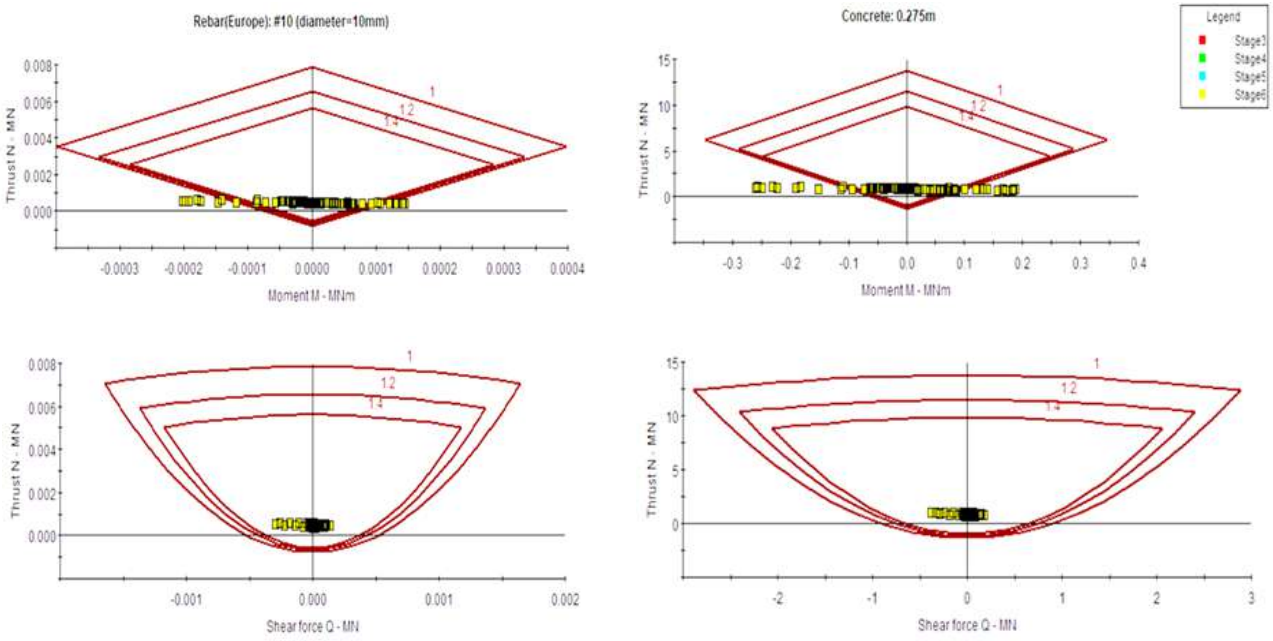

Fig. 8. Support capacity curve for case A – presence of water pocket

In the present study, the tunnels are assumed to be supported by a composite lining consisting of a circular segmental lining as a primary support and a cement grouting layer as a secondary support by the middle and tail shield of TBM. Figs. 8 and 9 show the relationship between thrust and moment, as well as thrust and shear force, which represent the liner stress and strength envelopes for both cases, respectively. This allows for the stresses induced in segmental liners and is easily envisioned in terms of strength envelopes and safety factors. The Carranza-Torres and Diederichs method is used to plot the three safety envelope factors, 1, 1.2, and 1.4, which ensure the tunnel support stability.

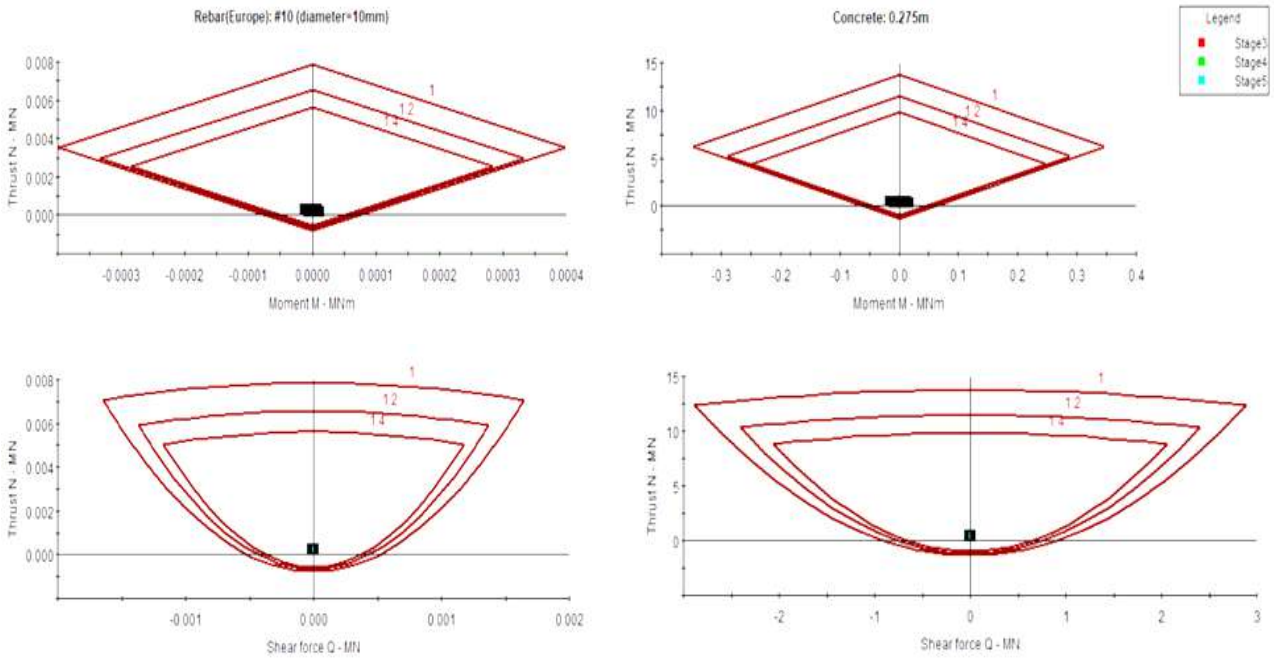

Fig. 9. Support capacity curve for case B – grouted water pocket

When the tunnel hits a water pocket, in a few stages the point nodes fall outside the envelope (Fig.8) indicating that their factor of safety is smaller than the envelope value. These findings suggest that the support lining is unstable during the stage when the tunnel hits the water pocket (saturated body), which may affect the instability of tunnel supports and the crown. For case B, Fig.9 shows that the point nodes are lying within the envelope (inside the envelope) of a factor of support safety of 1, 1.2, and 1.4 at all stages, indicating that their factor of safety is more than the envelope value. It is found that the liner's safety exceeds the design factor of safety. This demonstrated that after the water pocket is grouted, the tunnel segmental lining support will be safe.

5.3 Validation Using O'Reilly and New method

In this study, the empirical equation proposed by O'Reilly and New [33] is used to validate the results obtained by the numerical method RS2 for the case of grouted water pocket. O'Reilly and New method is based upon the first classical empirical method developed by Peck (1969) [47], which is a well-known as Gaussian distribution method. Various empirical methods, such as Attewell et al. (1986),[16], Hansmire and Cording (1972) [48], O'Reilly and New (1982) [33], Wang et al. (2016) [49] are based upon the hypothesis presented by Peck [47] but the O'Reilly and New method is widely used as a regression method and is especially used to predict the transverse surface settlement trough produced by the twin tunnels. The equation proposed by O'Reilly and New method is illustrated below;

$$S = S_{\max}\left[e^{\left(\frac{x_1^2}{2.i^2}\right)} + e^{\left(\frac{(x_{1-d})^2}{2.i^2}\right)} \right] \quad (1)$$

where, S - Theoretical settlement curve; d - Lateral c/c distance between the two tunnels; x_1 - Lateral distance from the first bored tunnel center-line; Smax - Maximum settlement (short-term) at the tunnel centerline (m). Smax is calculated by using the following equation (2)

$$Smax = 0.313x\ \frac{V_L x D^2}{i} \quad (2)$$

Where; VL - Volume loss; D - Excavated diameter of TBM Tunnel; i - Inflection point (m). For mostly cohesive soil the inflection point (i)is calculated by following;

$$i = KxZ_0 \tag{3}$$

Zo - Depth of tunnel (m); K - Coefficient, for soft clay it varies between 0.6 to 0.7

Using the O'Reilly and New [33] equation, the surface settlement is calculated for various lateral distances, and the transverse surface settlement trough for the 1st and 2nd tunnels is presented in Fig.10. The parameters (soil properties, tunnel geometry) that have been used during numerical modelling are used as the input data for the calculation of surface settlement. The addition of two overlapping curves, as presented in Fig.10, defines the total/combined settlement for twin tunnels by superpositions.Fig.11 shows the variation of combined settlement with lateral distance. The maximum combined surface settlement is found to be 13.2 mm, and the observed settlement trough is almost similar to the normal distribution (Gaussian distribution curve) demonstrated by Peck [47].

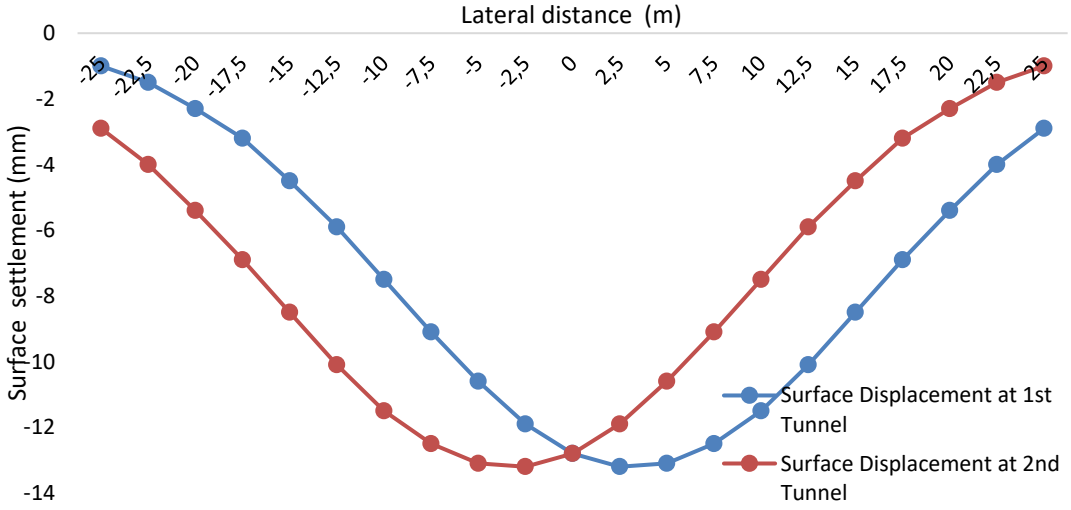

Fig. 10. Surface settlement trough for 1st and 2nd tunnel using O'Reilly and New method

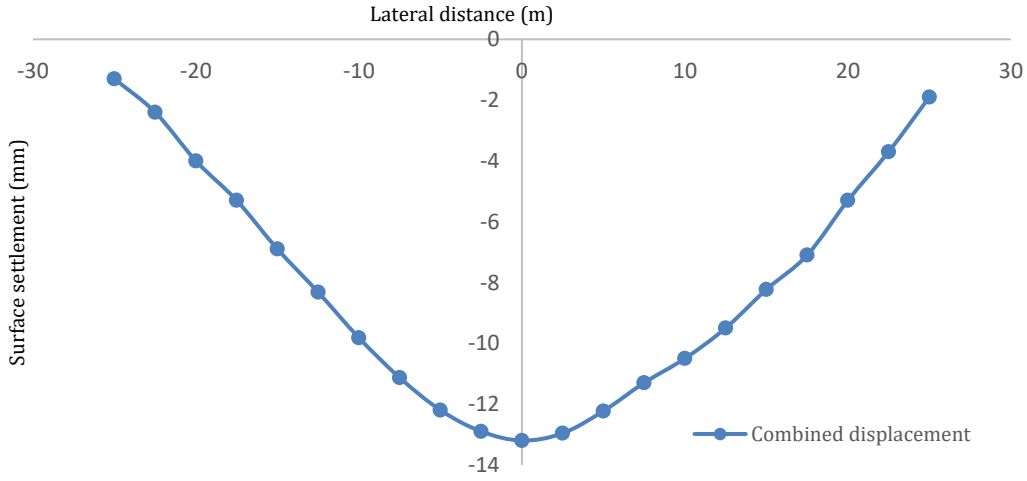

Fig. 11. Combined surface settlement trough for 1st and 2nd tunnel using O'Reilly and New method

Fig. 12 compares the combined surface settlement trough computed using numerical modelling (RS2) and the empirical equation proposed by O'Reilly and New [33]. The observed settlement trough of both techniques shows a similar pattern (Gaussian distribution curve) as observed in the analytical method proposed by Peck [47]. In the case of O'Reilly and New method, the maximum combined surface settlement is found to be 13.2 mm, whereas in the numerical method (RS2) it is

to be 14.02 mm, which is closer to the empirical method and depicts a good agreement between the results. The O'Reilly and New method underestimate the surface settlement of error by 6%. This is because the empirical method ignores the effect of creep of ground and time-dependent consolidation [41]. But the small error of 6% is tolerable and can be minimized by considering the effect of ground creep and time dependent-consolidation, as well as by enhancing the modelling approach.

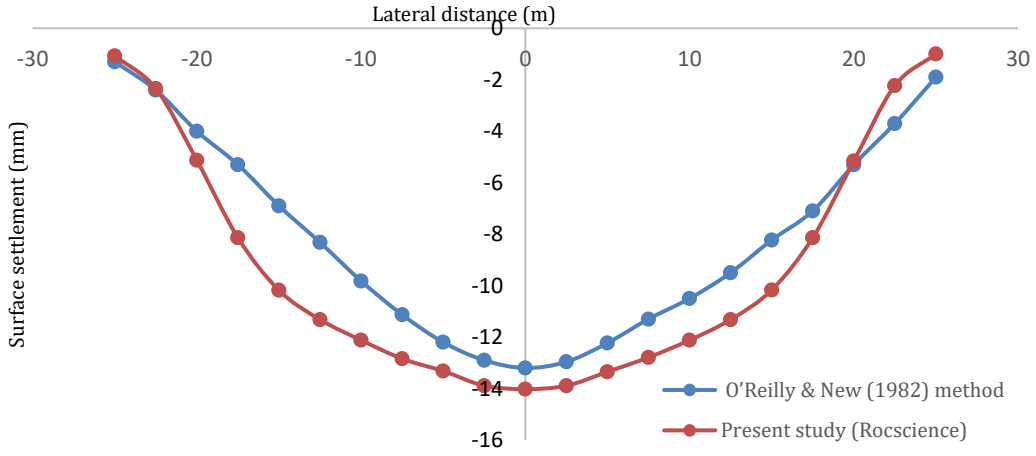

Fig. 12. Combined surface settlement trough for 1st and 2nd tunnel using numerical method (RS2) and O'Reilly and New approach

5.4 Surface Settlement Comparison with Analytical Studies

Several analytical methods have been used to predict tunnel induced surface settlement. Based on Peck's [47] hypothesis that the settlement trough is a Gaussian distribution curve, the following three analytical methods are considered:

- Limanov's method [50]
- Sagaseta's method [51]
- Gonzales-Sagaseta method [52]

Table 5 shows the analytical equations and the calculated parameters required for each method, along with the results of the maximum surface settlement.

Table 5. Analytical equations and parameters required for each method with the results of the maximum surface settlement

Sr.No.	Method	Equation	Parameters					
1	Limanov's method	$Smax = (1-\mu^2)\frac{P}{E}[\frac{4r_0\ h}{(h^2-r0^2)}]$ $P = \sigma_z\ x\ \frac{1+k_s}{2}$	Tunnel depth (h) (m)	radius (r0) (m)	ks	P (kPa)	Smax (mm)	
			20	2.9	0.65	321	11.95	
2	Sagaseta's method	$Smax = \frac{VL\ x\ D^2}{i}$	(h) (m)	VL (m3)	Smax (mm)			
			20	0.6	11.2			
3	Gonzales-Sagaseta method	$w(y) = 2 \in r_0 \left(\frac{r_0}{h}\right) 2\alpha - 1x\frac{1}{1+y^2}[1 + \rho\frac{1+y^2}{1-y^2}]$	ε	α	ρ	δ	u0 (mm)	Smax (mm)
			0.005	1.4	5.265	0.026	25	5.62

Where; Ks- lateral earth pressure; P- radial load (kPa); E- radial shrinkage strain $\in = \frac{u_0}{r_0}$; u0- uniform radial displacement; y-distance from the centerline; α-volume of compressibility, ρ - relative ellipticity

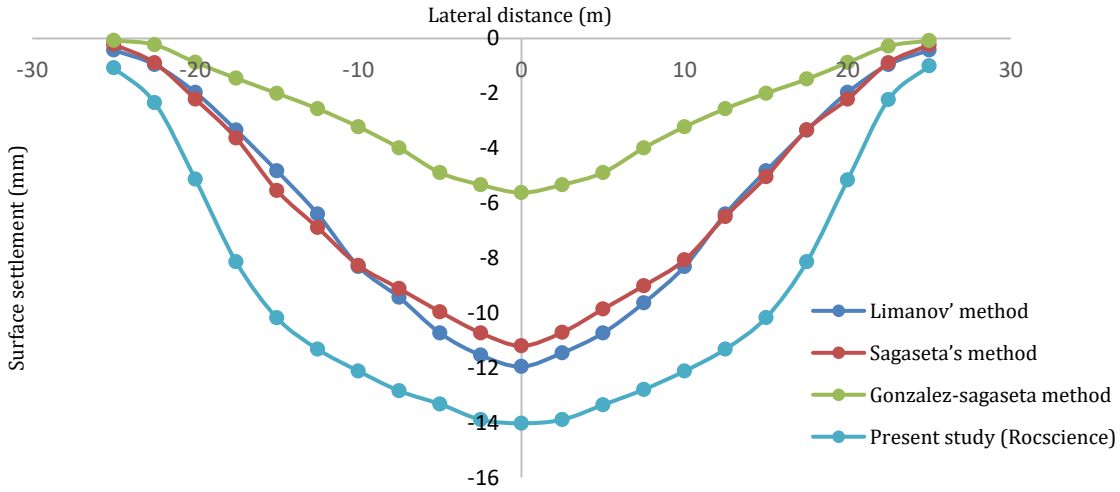

Fig. 13. Comparison of settlement trough obtained by various analytical methods with the present study (grouted water pocket)

The surface settlement trough observed using the numerical method (RS2) for the case of a grouted water pocket is compared with the abovementioned analytical methods. Fig.13 shows the comparison of the settlement trough obtained using various analytical methods and the profile obtained by the present study (RS2).

The settlement trough observed using various analytical methods and the numerical approach used in the present study exhibits a similar pattern with minor variation in the maximum surface settlement magnitude. This variation seen in the above analytical studies may be because of the assumptions and simplifications used when formulating the equations. The Gonzales-Sagaseta method underestimates the maximum surface settlement, which is almost 60% less than the present study result. While the surface settlements obtained using Limanov's and Sagasta's methods are 11.95mm and 11.2mm, respectively, which is close to the present study (14.2 mm). Limanov's and Sagasta's methods show a small error of 15% and 21%, respectively, which is tolerable and can be minimized by enhancing the modelling approach.

5.5 Parametric Study

Tunnel surface settlement can be influenced by various parameters such as soil layer parameters (cohesion, frictional angle of resistance, unit weight, Young modulus, Poisson's ratio), tunnel geometry (diameter and depth of tunnel), depth of water table, porewater pressure, support system, stress relaxation factor, etc. Chia Yu Huat et al. [53] concluded that the major parameters affecting the surface settlements are tunnel geometry, soil properties, tunnelling operation parameters, and tunnel center to center distance in the case of twin tunnels.

Many imperial and analytical methods focused on tunnel geometry and soil properties; very few methods considered the tunnelling operation parameters. In the present study, the effect of tunnel geometry (grouted tunnel), such as tunnel diameter and depth, on maximum surface settlement was evaluated and compared with the other methods while the other parameters were maintained constant.

5.5.1 Effect of Tunnel Diameter on Surface Settlement

To illustrate the effect of tunnel diameter on surface settlement, some calculations on different tunnel diameters, such as 5.0, 5.8, 7.0, 8.0, and 10.0m, are considered. The object of selecting the specific range of parameters was to compare how these parameters affected the maximum surface settlement. The RS2 analysis for maximum surface settlement was carried out for the above-specified range of tunnel diameters with a constant 20m overburden height, and the results were compared with the few analytical approaches tabulated in Table 6.

Table 6. Variation of tunnel diameter on maximum surface settlement

Sr. No.	Parameters			Maximum surface settlement (mm)			
	Diameter of tunnel D (m)	overburden height (h) (m)	h/D (m)	Present study (Rocscience)	Limanov's method	Sagaseta's method	Gonzales-Sagaseta method
1	5.0		4.0	13.43	10.64	10.07	5.33
2	5.8		3.45	14.02	11.95	11.2	5.62
3	7.0	20.0	2.85	17.01	16.7	14.1	8.46
4	8.0		2.5	19.7	21.2	17.4	10.7
5	10.0		2.0	24.4	26.33	22.9	17.2

From Fig 14, It is observed that the increase of tunnel diameter (D) significantly increases the maximum surface settlement; the same trend is also observed in analytical methods. These results are consistent with the findings [54,55,56]. This may be because a larger tunnel diameter displaces more volume of soil, consequently extending its influence zone. Within this area, soil undergoes stress redistribution, and this expanded region of stressed soil results in increased surface settlement [53].

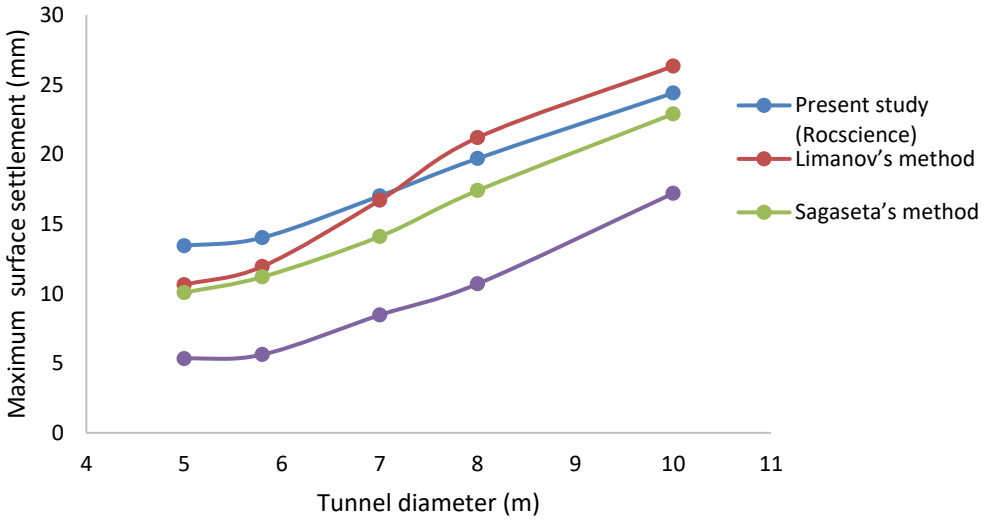

Fig. 14. Variation of tunnel diameter on maximum surface settlement and its comparison with analytical methods

In the present study, an increase of 81% in the maximum settlement has been found when the tunnel diameter increased from 5m to 10m. A similar effect was also observed in analytical methods, but the % of the increase in a settlement is more as compared to the present study (RS2). In Gonzales-Sagaseta method, the maximum settlement increased by 222% when the diameter of the tunnel increased from 5m to 10m. It indicates that decreasing the h/D ratio leads to an increase in the maximum surface settlement, but in Limanov's method, as the h/D ratio reaches lower than 3.45, the difference in settlement increment becomes higher.

5.5.2 Effect of Tunnel Depth on Surface Settlement

Tunnel depth, also called overburden, is another one of the important parameters that influence surface settlement. Many researchers studied the overburden effect for a 5.0 m increment; hence in the present study, the surface settlement was calculated for a 5.0 m tunnel depth increment (5.0 m to 25 m) by maintaining the other parameters constant with the reference model. The present study results are also compared with the analytical methods, which are presented in Table 7 and Fig. 15. It is observed that an increase in tunnel depth (h) results in a significant decrease in maximum surface settlement.

Table 7. Variation of tunnel depth (overburden) on maximum surface settlement

Sr. No.	Parameters			Maximum surface settlement (mm)			
	Overburden height (h) (m)	Diameter of tunnel D (m)	h/D (m)	Present study (Rocscience)	Limanov's method	Sagaseta's method	Gonzales-Sagaseta method
1	5.0	5.8	0.86	23.93	21.34	19.67	14.33
2	10		1.72	19.72	17.95	16.06	11.02
3	15		2.58	17.01	15.03	13.84	7.96
4	20		3.44	14.02	11.95	11.2	5.62
5	25		4.31	12.02	9.97	9.23	3.23

The observed findings are similar to the results obtained by previous studies [55,57,58,59]. Also, for an increase in the h/D ratio, the maximum surface settlement decreases. In the present study, the maximum surface settlement was found to decrease by 99% when the depth of the tunnel increased from 5m to 25 m. The analytical methods also showed a similar pattern of results, but the % of reduction in surface settlement was higher as compared to the present study. Limanov's and Sagaseta methods show almost identical and close results to the present study, while Gonzales-Sagaseta method shows the maximum settlement decreased by more than 300% when the depth of the tunnel increased from 5m to 25.0m

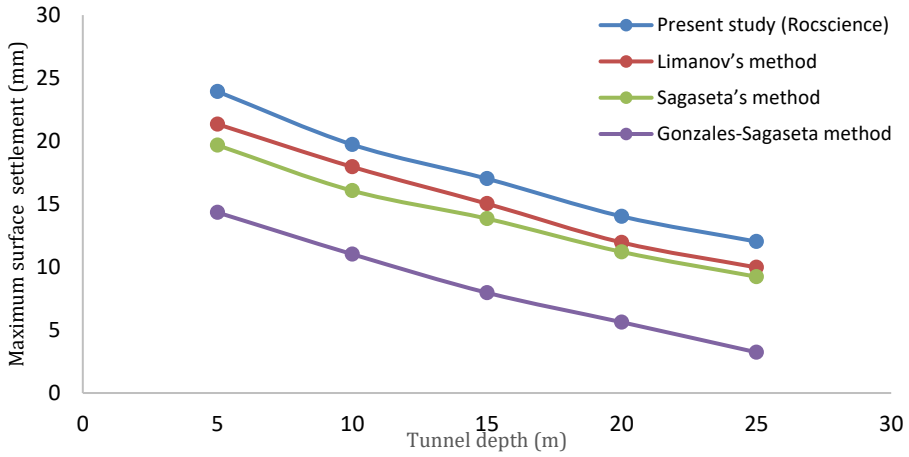

Fig. 15. Variation of tunnel depth on maximum surface settlement and its comparison with analytical methods

6. Conclusion and Future Scope of Work

6.1 Conclusion

This paper estimates the twin- tunnel induced surface settlement trough using the numerical method (RS2) for the cases of TBM hits a water pocket (case A) and a grouted water pocket (case B) during the various tunnelling construction stages. The RS2 results were validated with the empirical method developed by O'Reilly and New method. Furthermore, the results were also compared with a few analytical approaches. To ascertain the applicability of RS2 method, a parametric study is also carried out for variation of tunnel geometry (depth and diameter). The following are the main conclusions of the present study:

- In the case of tunnel hits a water pocket, the maximum surface settlement was increased by 5% as compared to the 2nd tunnel excavation stage. This may be because entry of water in the excavation area increases the effective stress and consequently increases the surface settlement.

- In the case of grouted water pocket, the maximum surface settlement was found to be 16.4 mm, which is nearly 50% less than case A (the presence of water). This may be because of the pre-grouting effect of the water pocket, which controls the drawdown above the tunnel and reduces the effective stress, resulting in a decrease in the settlement.
- The support capacity curve shows that the liner factor of safety for case A is lower than the envelope value, indicating instability during the stage of the tunnel hitting the water pocket (saturated body), whereas, for case B, the liner's safety exceeds the design factor of safety. This demonstrates that once the water pocket is grouted, the tunnel segmental lining support will be safe.
- The surface settlement trough observed by RS2 shows a similar pattern (Gaussian distribution curve) to the O'Reilly and New method, also the maximum settlement values are found to be very close to the O'Reilly and New method with a deviation of 6% only.
- The RS2 results are compared with a few analytical approaches; the Gonzales- Sagaseta method underestimates the maximum surface settlement, while Limanov's and Sagasta's methods show close results with a deviation of 17% and 25%, respectively. This error may be tolerable and can be minimised by enhancing the modelling approach.
- A parametric study indicated that increasing the tunnel diameter from 5m to 10m resulted in an 81% increase in maximum surface settlement. A similar trend was observed in analytical methods, but the % increase in settlement was higher as compared to the present study (RS2).
- When the tunnel depth was increased from 5m to 25 m, a significant 99% decrease in the maximum surface settlement was observed. The analytical methods also showed a similar pattern of results. Limanov's and Sagaseta methods reveal 114% and 113% decrease in maximum surface settlement, respectively, which is almost close to the present study.

The proposed numerical method (RS2) has been validated with the empirical method and the results are also compared with analytical methods. Therefore, the RS2 can be used to calculate the surface settlement, particularly in the presence of a water/saturated body subject to the correct modelling approach. The use of predicted surface settlement guides the tunnel engineer about the future consequences of the destructive effects of adjacent structures and facilities.

6.2 Future Scope of Work

In the present study, the fictitious water pocket is positioned close to the 2nd tunnel crown. The position of water pocket/saturated bodies can be varied, and the influence on the surface settlement can be studied. The present study results can be improved by using the more advanced models, such as Hardening Soil (HS) or Hardening Soil Small (HSs) models. The comparative study with the advanced model can be further studied. Also, the results can be verified using additional empirical, semi-empirical, or physical methods/ techniques.

Acknowledgements

The Management, Dr. Vishwanath Karad MIT World Peace University Pune is hereby acknowledged for providing the research facilities and permitting this research paper.

References

[1] Klein S, O'Carroll J. Geotechnical risk assessments for tunnelling/underground projects. 2017: 350–359.
[2] Nawani PC. Groundwater ingress in head race tunnel of Tapovan: Vishnugad Hydroelectric Project in Higher Himalaya, India. In Engineering Geology for Society and Territory 6. 2015: 941-945.
[3] Anagnostou G. Tunnel stability and deformations in water-bearing ground. Eurock 06 ISRM Symposium on Multiphysics coupling and long-term behaviour in rock mechanics Liège (Belgium). 2012. May 9 – 12.
[4] Liu Xialin. Predicting tunnel groundwater inflow by geological investigation using horizontal directional drilling technology. Advances in Civil Engineering. 2022:1-12. https://doi.org/10.1155/2022/65783.
[5] Nikakhtar L, Zare S. Evaluation of underground water flow in to Tabriz metro tunnel first line by hydro-mechanical coupling analysis. World Academy of Science, Engineering and Technology International Journal of Geotechnical and Geological Engineering. 2020; (14) 01: 1-7. https://doi.org/10.1155/2022/6578331

[6] Javadi M, Sharifzadeh M, Shahriar K. Uncertainty analysis of groundwater inflow into underground excavations by stochastic discontinuum method: Case study of Siah Bisheh pumped storage project, Iran. Tunneling and Underground Space Technology. 2016; 51:424-438. https://doi.org/10.1016/j.tust.2015.09.003
[7] Wadslin Frenelus, Hui Peng, Jingyu Zhang. Evaluation methods for ground water inflows in to rock tunnels: a state of the art-review. International Journal of Hydrology. 2021; 5(4):152-168. https://doi.org/10.15406/ijh.2021.05.00277
[8] Animateur EL.Settlement induced by tunnelling in soft ground. Tunnelling and Underground Space Technology. 2007; 22: 119-149. doi:10.1016/j. tust2006.11.001
[9] Shin JH, Potts DM, Zdravkovic. Three-dimensional modelling of NATM tunnelling in decomposed granite soil. Geotechnique.2002; 52 (3):187-200. https://doi.org/10.1680/geot.2002.52.3.187
[10] Yoo Chungsik. Interaction between tunnelling and groundwater -numerical investigation using three-dimensional stress coupled analysis. Journal of Geotechnical and Geo environmental Engineering. 2005; 131(2):240-250. https://doi.org/10.1061/(ASCE)1090-0241(2005)131:2(240)
[11] Yoo C, Kim SB.Stability analysis of urban tunnelling in difficult ground condition. Tunnelling and Underground Space Technology. 2006; 21(3-4):351-352. https://doi.org/10.1016/j.tust.2005.12.170
[12] Jordi Font-Capo, Vazquez-Sune E, Carrera J, Herms I. Groundwater characterization of a heterogeneous granite rock massif for shallow tunnelling. Geologica Acta. 2012; 10 (4): 395 http://dx.doi.org/10.1344/105.000001773
[13] Butscher C. Steady-state groundwater inflow into a circular tunnel. Tunneling and Underground Space Technology. 2012; 32:158-167. DOI: 10.1016/j.tust.2012.06.007
[14] Yoo Chingsik, Lee Young Joo, Kim Sang-Hwan, Kim Hong-Taek. Tunnel induced ground settlements in a ground water drawdown environment-A case history. Tunnelling and Underground Space Technology. 2012; 29: 69-77. https://doi.org/10.1016/j.tust.2012.01.002
[15] Kong WK. Water ingress assessment for rock tunnels: A tool for risk planning. Rock Mechanics and Rock Engineering. 2011; 44:755-765. https://link.springer.com/article/10.1007/s00603-011-0163-4
[16] Attewell PB, Yeates J, Selby AR. Ground deformation and strain equations. Soil Movements Induced by Tunneling and Their Effects on Pipeline and Structures. Glasgow: Blackie.1986: 53–66.
[17] O'Reilly MP, Mair RJ, Alderman GH. Long-term settlements over Tunnels: An eleven-year study at Grimsby. In Tunnelling'91 London: Inst. of Mining and Metallurgy. 1991:55–64. https://doi.org/10.1016/0148-9062%2892%2992317-6
[18] Bowers KH, Hiller DM, New BM. Ground movement over three years at the Heathrow Express Trial Tunnel. In Mair & Taylor (Eds.). Geotechnical aspects of underground construction in soft ground. 1996: 647–652.
[19] Anagnostou G. Urban tunnelling in water bearing ground – Common problems and soil mechanical analysis methods. 2nd Int. conf. on Soil Structure Interaction in Urban Civil Engineering. Zurich. 2002: 233– 240
[20] Shen SL, Wu HN, Cui YJ, Yin ZY. Long-term settlement behavior of the metro tunnel in Shanghai. Tunneling and Underground Space Technology. 2014; 40(1): 309–323. https://doi.org/10.1016/j.tust.2013.10.013
21] Shen SL, Tang CP, Bai Y, Xu YS. Analysis of settlement due to withdrawal of groundwater around an unexcavated foundation pit. Underground Construction and Ground Movement. 2006: 377–384. https://doi.org/10.1061/40867(199)47
[22] Xu YS, Shen SL, Bai Y (2006) State-of-art of land subsidence prediction due to groundwater withdrawal in China. Underground Construction and Ground Movement. 2006: 58–65. https://doi.org/10.1061/40867(199)5
[23] Shen SL, Xu YS.Numerical evaluation of land subsidence induced by groundwater pumping in Shanghai. Canadian Geotechnical Journal. 2011; 48(9):1378–1392. https://doi.org/10.1139/t11-049
[24] Shen SL, Ma L, Xu YS, Yin ZY. Interpretation of increased deformation rate in aquifer IV due to groundwater pumping in Shanghai. Canadian Geotechnical Journal. 2013; 50(11): 1129–1142. https://doi.org/10.1139/cgj-2013-0042
[25] Singh K, Mittal S, Kumar K. Reduction in lateral displacement of cohesionless soil box tunnel face using nails in overburden. International Journal of Geosynthetics and Ground Engineering. 2018; 4(21):1-21. https://doi.org/10.1007/s40891-018-0138-6
[26] Ghorbani A, Hasanzadehshooiili H, Eslami A, Shen W. Parametric evaluation of simultaneous effects of damaged zone parameters and rock strength properties on GRC. Advances in Civil Engineering.2021 :1-13. https://doi.org/10.1155/2021/2237918
[27] Likitlersuang S, Surarak C, Suwansawat S, Wanatowski D, Oh E, Balasubramaniam A. Simplified finite-element modelling for tunnelling-induced settlements. Geotechnical Research. 2014;1(4): 133-152. http://dx.doi.org/10.1680/gr.14.00016.
[28] Bear J. Dynamics of fluids in porous media, Dover Publications, 1972: 1-757,ISBN 0-486-65675-6.

[29] Akram MS, Noor A, Ullah MF, Ahmed L, Rehman F.Squeezing assessment along 2.84 km long headrace tunnel of a small hydropower project in KPK, Pakistan: Comparison of different methods: International Journal of Geosynthetics and Ground Engineering. 2019; 5(19):1-17. https://doi.org/10.1007/s40891-019-0167-9
[30] Panji M, Ansari B. Transient S-H wave scattering by the lined tunnels embedded in an elastic half plane. Engineering Analysis with Boundary Elements.2017; 84:220-230. https://doi.org/10.1016/j.enganabound.2017.09.002
[31] Panji M, Ansari B. Anti plane seismic ground motion above twin horse shoe-shaped lined tunnels. Innovative Infrastructure Solutions.2020; 5(7). https://doi.org/10.1007/s41062-019-0257-5
[32] Ingle GS, Niphade S.Numerical and artificial neural network analysis of tunnel liner design parameters – a comparative study. Geomechanics and Geoengineering. 2024: 1–20. https://doi.org/10.1080/17486025.2024.2354289
[33] O'Reilly MP, New BM. Settlement above tunnels in the United Kingdom- their magnitude and prediction. Proceedings of the 3rd International Symposium Brighton. 1983: 173-181. https://doi.org/10.1016/0148-9062%2883%2991768-0
[34] Alsirawan R, Sheble A, Alnmr A. Two-dimensional numerical analysis for TBM Tunneling-induced structure settlement: A proposed modeling method and parametric study. Infrastructures. 2023; 8(5): 88. https://doi.org/10.3390/infrastructures8050088
[35] Çelik S. Comparison of Mohr-Coulomb and hardening soil models numerical estimation of ground surface settlement caused by tunneling. Iğdır Üni. Fen Bilimleri Enst. Der. / Iğdır Univ. Journal of the Institute of Science & Technology. 2017; 7(4): 95-102. http://dx.doi.org/10.21597/jist.2017.202
[36] Melis M, Medina L, Rodríguez, JM. Prediction and analysis of subsidence induced by shield tunnelling in the Madrid Metro extension. Canadian Geotechnical Journal. 2002; 39:1273–1287.
[37] Möller SC. Tunnel Induced Settlements and Structural Forces in Linings. Doctoral Dissertation, Institute for Geotechnics, University of Stuttgart, Stuttgart, Germany, 2006.
[38] Mroueh H, Shahrour I. A simplified 3D model for tunnel construction using tunnel boring machines. Tunnelling and Underground Space Technology. 2008; 23(1): 38-45. https://doi.org/10.1016/j.tust.2006.11.008
[39] Migliazza M, Chiorboli M, Giani GP. Comparison of analytical method, 3D finite element model with experimental subsidence measurements resulting from the extension of the Milan underground. Computers and Geotechnics. 2009; 36 (1-2):113–124. https://doi.org/10.1016/j.compgeo.2008.03.005
[40] Ocak I, Seker SE. Calculation of surface settlements caused by EPBM tunneling using artificial neural network, SVM, and Gaussian processes Environmental Earth Sciences.2013; 70 (3): 1263-1276, 10.1007/s12665-012-2214-x
[41] Gang N, Xuzhen He, Haoding Xu, Shaoheng Dai. Tunnelling-induced ground surface settlement: A comprehensive review with particular attention to artificial intelligence technologies. Natural Hazards Research. 2024; 4(1):148-168. https://doi.org/10.1016/j.nhres.2023.11.002
[42] Mousivand M, Maleki M, Mansoori MR. Application of Convergence–Confinement Method in Analysis of Shallow Non-circular Tunnels. Geotechnical and Geological Engineering. 2017; 35:1185–1198. https://doi.org/10.1007/s10706-017-0173-4
[43] Snežana Maraš-Dragojević. Analysis of ground settlement caused by tunnel construction. GRAĐEVINAR.2012;64(7):573-581. UDK: 624.193:624.131.54
[44] De-Yang Wang, Hong-Hu Zhu, Xue-Hui Zhang, Jing-Wu Huang, Zhen-Rui Yan, Dao-Yuan Tan, Shao-Qun Lin. Structural behavior of triple-layer composite lining of a water conveyance tunnel: Insight from full-scale loading tests. Journal of Rock Mechanics and Geotechnical Engineering. 2024. In press. https://doi.org/10.1016/j.jrmge.2024.11.025
[45] Nong Xingzhong, Liang Yuehua, Ruan Yanmei. A case study of deep shaft and open face tunnelling induced excessive ground settlement in water rich strata in Guangzhou China. Frontiers in Earth Science 10.2022. https://doi.org/10.3389/feart.2022.825186
[46] Rankin WJ. Ground movements resulting from urban tunnelling: predictions and effects. Geological Society London, Engineering Geology Special Publications. 1988; 5(1): 79-92.https://doi.org/10.1144/GSL.ENG.1988.005.01.06
[47] Peck RB. Deep excavations and tunnelling in soft ground. Proceedings 7th international Conference Soil Mechanics and Foundation Engineering Mexico State-of-the-Art Volume.1969: 225-290
[48] Hansmire W, Cording E. Performance of a soft ground tunnel on the Washington Metro. In Proceedings of rapid excavation tunneling conference, Chicago.1972: 371–389.
[49] Wang F, Miao L, Yang X M, Du Y J.The volume of settlement trough change with depth caused by tunneling in sands. KSCE Journal of Civil Engineering. 2016; 20(7): 2719–2724. https://doi.org/10.1007/s12205-016-0250-x.
[50] Limaniv JA. Infolge Tunnelbau in kambrischen Tonen Leningrad Inst-Inzh. Zhelezu, Transport.1957.

[51] Sagasetta C. Analysis of underground soil deformation due to the ground loss. Geotechnique.1987; 37(3):301-330
[52] Gonzalez C, Sagaseta C.Patterns of soil deformations around tunnels application to the extension of Madrid Metro. Computers and Geotechnics. 2001; 28(6-7): 445-468. https://doi.org/10.1016/S0266-352X(01)00007-6
[53] Chia Yu Huat, Danial Jahed Armaghani, Sai Hin Lai, Hossein Motaghedi, Panagiotis G Asteris, Pouyan Fakharian. Analyzing surface settlement factors in single and twin tunnels: A review study. Journal of Engineering Research. 2024.In Press. https://doi.org/10.1016/j.jer.2024.05.009
[54] Kanagaraju R, Krishnamurthy P. Influence of tunneling in cohesionless soil for different tunnel geometry and volume loss under greenfield condition. Advances in Civil Engineering. 2020: 1–11. https://doi.org/10.1155/2020/1946761
[55] Aswathy MS, Vinoth M, Mittal A. Impact of governing factors on prediction of tunneling induced surface settlement in young alluvium deposit. Indian Geotechnical Journal. 2022; 52: 13–27. https://doi.org/10.1007/s40098-021-00561-4
[56] Agarwal J, Sarakar R. Greenfield settlements due to tunnelling using tunnel boring machine (TBM) in layered soils: a parametric study. Sadhana, Indian Academy of Sciences.2024;49 (75):1-12. https://doi.org/10.1007/s12046-023-02425-4
[57] Attewell P B and Farmer I W. Ground disturbance caused by shield tunnelling in a stiff, over consolidated clay. Engineering Geology.1974; 8(4):361-381. https://doi.org/10.1016/0013-7952(74)90028-3
[58] Golpasand MR, Nikudel M, Uromeihy Ali. Specifying the real value of volume loss (V L) and its effect on ground settlement due to excavation of Abuzar tunnel, Tehran. Bulletin of Engineering Geology and the Environment. 2016 ;75: 485-501. http://dx.doi.org/10.1007/s10064-015-0788-8
[59] Rezaei AH, Ahmadi Adli, Mohammad. The Volume Loss: Real estimation and its effect on surface settlements due to excavation of Tabriz Metro Tunnel. Geotechnical and Geological Engineering. 2020; 38: 2663–2684. https://link.springer.com/article/10.1007/s10706-019-01177-510.1007/s10706-019-01177-5.

Research on Engineering Structures & Materials
www.jresm.org
Research Group

Research Article

Sustainable self-compacting concrete: A study on the combined effects of waste glass powder and metakaolin as cement replacements

Mutiu Adelodun Akinpelu [*,1,a], Abdullateef Olamilekan Amao [1,b], Ash-Shu'ara Marafa Salman [1,c], Daniel Sunday Gabriel [2,d]

[1]Department of Civil Engineering, Kwara State University, Malete, Kwara State, Nigeria
[2]*Department of Civil Engineering, University of Calgary, Canada*

Article Info

Article History:

Received 05 Jan 2025

Accepted 10 Mar 2025

Keywords:

Self-compacting concrete;
Waste glass powder;
Metakaolin;
Microstructure

Abstract

Partial replacement of cement with eco-friendly pozzolanic materials, such as waste glass powder (WGP) and metakaolin (MK), offers a sustainable approach to improving the service life of self-compacting concrete (SCC). This study evaluates the effects of WGP and MK, individually (binary) and combined (ternary), as partial replacements for cement. Concrete mixes were assessed for workability, mechanical properties, and microstructure. Workability tests showed WGP enhances flow properties, while MK reduces them; however, their combined use at 15% replacement maintained performance. The ternary mix with 5% MK and 10% WGP (5MK+10WGP) exhibited superior mechanical properties, surpassing the control by 7.7% in compressive strength and 3.8% in split tensile strength at 56 days. SEM analysis revealed refined pores, reduced porosity, a denser microstructure, and well-formed C-S-H gels. XRD confirmed these findings with a pronounced broad hump in the 29°–34° 2θ range, indicative of well-developed C-S-H phases. This research demonstrates that incorporating 5MK+10WGP optimally balances workability, strength, and microstructure, providing a sustainable alternative for cementitious materials in SCC, reducing cement consumption, CO_2 emissions, and conserving natural resources.

© 2025 MIM Research Group. All rights reserved.

1. Introduction

The construction industry has undergone substantial transformation since the advent of self-compacting concrete (SCC) [1]. A distinguishing feature of SCC is its ability to traverse heavily reinforced sections without requiring external vibration [2]. SCC flows effortlessly under its self-weight, filling molds of complex geometries while maintaining uniformity [3-5]. The adoption of SCC reduces reliance on vibratory tools and minimizes labor expenses [6, 7]. Over the past two decades, SCC has been a focal point of research globally [8].

However, despite its advantages, concrete remains prone to durability issues, which can lead to significant structural damage over time. Insufficient strength properties often result in cracks, reduced load-bearing capacity, and, in extreme cases, structural failure, necessitating costly repairs and maintenance. These defects have been linked to infrastructure deterioration and building collapses, particularly in regions where substandard materials are used. To mitigate these risks, researchers have emphasized the importance of optimizing concrete mix designs with alternative materials that enhance both mechanical strength and durability [9-12].

*Corresponding author: mutiu.akinpelu@kwasu.edu.ng
[a]orcid.org/0000-0003-4681-9874; [b]orcid.org/0009-0001-4157-0355; [c]orcid.org/0000-0001-8067-183X; [d]orcid.org/0009-0005-6522-4667
DOI: http://dx.doi.org/10.17515/resm2025-610ma0105rs

Concrete production also demands high energy consumption, leading to significant CO_2 emissions that contribute to environmental degradation [13]. This process exacerbates climate issues through the release of greenhouse gases [14-16]. Additionally, the continuous extraction of raw materials like aggregates, cement, and natural additives depletes natural resources, increasing costs over time [17]. The increasing depletion of natural resources has driven researchers in recent decades to explore alternative, sustainable materials for construction. One effective approach is the incorporation of waste materials into concrete, reducing dependence on virgin raw materials and mitigating environmental impact. Various waste materials, including recycled aggregates from demolished concrete, waste plastics, glass, rubber, tin scraps, by-product pozzolans, and agricultural or bio-wastes, have been investigated for their potential application in concrete production [18].

Among these alternatives, supplementary cementitious materials (SCMs) have gained significant attention for their ability to partially replace cement in mortar and concrete. Several researchers have explored SCMs derived from industrial by-products and agricultural residues [19-22]. Examples of commonly used SCMs include fly ash, silica fume, coffee silver skin, ground granulated blast furnace slag (GGBS), rice husk ash (RHA), and palm oil fuel ash. The incorporation of these materials has been shown to enhance the strength and durability of concrete while also serving as an indirect method of reducing CO_2 emissions into the atmosphere [6].

However, despite their advantages, the application of SCMs in Nigeria is hindered by their limited availability due to the country's low level of industrialization. This study aims to contribute to the growing body of research on sustainable concrete materials by exploring locally available alternatives that can enhance concrete performance while promoting environmental sustainability.

Glass is widely regarded as a vital material for infrastructural development. However, its global recycling rate remains significantly low. According to Statista [23], only around 1 out of 5 metric tonnes of glass produced globally were said to be recovered. Among this production, container glass accounts for 32%. In Nigeria, recycling rates for waste glass, as well as other materials like plastic and metal, are notably low due to inadequate infrastructure, the absence of formal recycling policies, and minimal engagement from manufacturers in waste recovery programmes [24]. These factors contribute to the growing accumulation of unrecycled glass, necessitating consistent management. Reusing waste glass to manufacture new products is often impractical due to variations in its chemical composition [25-27]. As a result, unrecycled glass is typically disposed of in landfills, where it decomposes extremely slowly [28]. Being chemically inert, glass remains non-biodegradable for over a million years when buried in soil [29]. This slow decomposition rate creates environmental challenges by taking up significant dumpsite space that could be utilised for biodegradable waste. The rising volume of global glass waste highlights the need for innovative methods to effectively utilise this material [1].

One promising approach suggested by researchers is incorporating waste glass into concrete production [30, 31]. Glass primarily consists of silica (SiO_2), although its composition may vary [32, 33]. Typically, pulverised glass (depending on its particle size) is used as a substitute for fine aggregates or cement in concrete mixes [30, 34]. When used in powdered form, glass can chemically interact with cement components during hydration, influencing the qualities of the resulting hardened concrete. However, the contribution of glass powder to the workability of SCC remains a subject of debate. Bisht et al. [34] and Tanwar et al. [35] recorded that blending of cement with glass waste negatively influenced the workability of the concrete. While others suggest improved workability in glass-modified mixes, often attributed to the smoothness as well as the sharp edges of the glass particles [36, 37].

Despite its potential, glass tends to react with the calcium hydroxide from cement hydration in a process known as alkali-silica reaction (ASR), leading to the formation of ASR gel, which subsequently absorbs water, causing expansion and cracking of the concrete [38-40]. However, studies have shown that the inclusion of SCMs like fly ash and metakaolin (MK) can mitigate ASR by reacting with calcium hydroxide from cement hydration to form additional hydrates. These hydrates refine the pore structure, reduce alkali availability, and enhance the overall properties of concrete [41].

Metakaolin (MK), a calcined product of kaolinite clay processed at 600–900°C [42, 43], is widely used in cement-based composites for its ability to enhance both mechanical and durability performance [44]; mitigate ASR expansion [41, 45]. However, MK reduces concrete fluidity and workability, requiring more water in the mix [46, 47]. Its strength gains are attributed to pozzolanic reactions with calcium hydroxide, enhanced hydration, and filler effects [48].

While many studies have explored the use of waste glass powder (WGP) and metakaolin (MK) as partial replacements for cement individually, their synergistic effects as a ternary blend in self-compacting concrete (SCC) remain largely underexplored. This research seeks to fill this gap by investigating the combined influence of MK and WGP on the flow and strength properties of SCC.

1.1. Research Significance

Recent research trends have increasingly focused on using supplementary cementitious materials (SCMs), such as metakaolin, silica fumes, rice husk ash and waste glass powder (WGP), in concrete to mitigate the environmental impacts of cement production [49-51]. Numerous studies have demonstrated that incorporating WGP into conventional concrete can significantly enhance both mechanical and durability properties. However, a major concern with the use of glass in concrete is its potential to trigger harmful alkali-silica reaction (ASR) expansion. To address this issue, research has shown that SCMs like fly ash and metakaolin can effectively mitigate ASR [52-54]. Despite these findings, the combined effect of WGP and metakaolin (MK) as a ternary blend on the rheology and strength properties of self-compacting concrete remains largely unexplored. Understanding the synergistic effect of ternary blended waste glass powder (WGP) and metakaolin (MK) as partial replacements for cement will contribute to environmental protection, enhance energy conservation, promote the production of sustainable concrete, and improve concrete performance across various applications.

2. Materials and Methods

2.1. Materials

The materials utilized in this study include; cement, fine aggregate (FA), coarse aggregate (CA), waste glass powder (WGP), metakaolin (MK), superplasticizer, and potable water. The details of the physical and particle distribution properties are further discussed in section 3.3 of this paper.

- Cement**:** Portland Limestone Cement of grade 42.5 (Dangote brand), sourced from a local retailer in Malete, Kwara State, Nigeria, was used in accordance with the requirements of BS EN197-1 [55]. Fine Aggregate (FA): Fine aggregate used in the study was river sand obtained from the Asa-dam River in Ilorin, which passed through a BS 4.75 mm sieve. The sand complies with the specifications of BS EN 12620 [56].
- Coarse Aggregate (CA): The coarse aggregate used was crushed granite with a maximum size of 9.6 mm, obtained from a local supplier in Ilorin. It was retained on a BS 4.75 mm sieve and met the requirements of BS EN 12620 [56].
- Waste Glass Powder (WGP): WGP was obtained from local aluminum glass window fabricators in Ilorin, processed into fine powdered passing through a BS 0.125 mm sieve. The characterization of WGP was conducted using X-ray Diffraction (XRD), X-ray Fluorescence (XRF), and Scanning Electron Microscopy (SEM) to analyze its crystallinity, oxide composition, and morphological properties.
- Metakaolin (MK): Commercially available metakaolin, sourced from the Nigeria Building and Road Research Institute (NBRRI) in Ota, Ogun State, was used. Similar to WGP, MK was characterized using XRD, XRF, and SEM to analyze its crystallinity, oxide composition, and morphology.
- Chemical Admixture: KONKRETO SP561, a superplasticizer purchased from PURECHEM MANUFACTURING LTD, was used as water reducing admixture.
- Water: Potable water sourced from the concrete laboratory at KWASU was used for both mixing and curing. It meets the requirements of BS EN 1008 [57].

2.2. Methods

2.2.1 Physical Property Test on Materials

The physical properties of cement, metakaolin, and waste glass—such as specific gravity, fineness, standard consistency, and initial and final setting times—were assessed in line with the standards outlined in BS EN197-1 [55]. Similarly, the physical characteristics of fine and coarse aggregates, including specific gravity, bulk density, particle size distribution (via sieve analysis), fineness modulus, and water absorption, were evaluated following the requirements of BS EN 1097-6 [58].

2.2.2 Mix Proportion, Mixing and Casting of SCC Specimens

The mix design procedure adopted for this study was based on the EFNARC [59], [60] provisions, with some modifications since there is no standardized mix design procedure for SCC. Multiple trial mixes were performed in the laboratory to identify the optimal proportions that would ensure SCC with no segregation or bleeding while satisfying both fresh and hardened state performance criteria. In total, 22 SCC mix designs were developed for this research, their mix contents and labels are presented in Table 1.

Table 1. Concrete mix proportion

S/N	Mix Label	Cement (kg)	MK (kg)	WGP (kg)	Sand (kg)	Granite (kg)	Water (kg)	SP (ml)
1	Control	4.6	0.0	0.0	9.2	6.1	2.3	69.0
2	5MK	4.4	0.2	0.0	9.2	6.1	2.3	92.0
3	10MK	4.2	0.5	0.0	9.2	6.1	2.3	92.0
4	15MK	3.9	0.7	0.0	9.2	6.1	2.3	92.0
5	20MK	3.7	0.9	0.0	9.2	6.1	2.3	92.0
6	25MK	3.5	1.2	0.0	9.2	6.1	2.3	92.0
7	30MK	3.2	1.4	0.0	9.2	6.1	2.3	92.0
8	5WG	4.4	0.0	0.2	9.2	6.1	2.3	69.0
9	10WG	4.2	0.0	0.5	9.2	6.1	2.3	69.0
10	15 WG	3.9	0.0	0.7	9.2	6.1	2.3	69.0
11	20 WG	3.7	0.0	0.9	9.2	6.1	2.3	69.0
12	25 WG	3.5	0.0	1.2	9.2	6.1	2.3	69.0
13	30 WG	3.2	0.0	1.4	9.2	6.1	2.3	69.0
14	5Mk5WG	4.2	0.2	0.2	9.2	6.1	2.3	69.0
15	5MK10WG	3.9	0.2	0.5	9.2	6.1	2.3	69.0
16	5MK15WG	3.7	0.2	0.7	9.2	6.1	2.3	69.0
17	10Mk5WG	3.9	0.5	0.2	9.2	6.1	2.3	69.0
18	10MK10WG	3.7	0.5	0.5	9.2	6.1	2.3	69.0
19	10MK15WG	3.5	0.5	0.7	9.2	6.1	2.3	69.0
20	15Mk5WG	3.7	0.7	0.2	9.2	6.1	2.3	69.0
21	15MK10WG	3.5	0.7	0.5	9.2	6.1	2.3	69.0
22	15MK15WG	3.2	0.7	0.7	9.2	6.1	2.3	69.0

EFNARC [59] limits the cement content in SCC to 500 kg/m^3 to control temperature rise and thermal shrinkage cracking, while the total powder content ranges between 380–600 kg/m^3. For this design, the cement content was maintained at the maximum value of 500 kg/m^3 since no other powder was included in the control mix. The water–cement ratio was maintained at 0.5, as this falls within the acceptable limit, resulting in 250 kg of water per cubic meter of concrete.

The total aggregate weight of 1650 kg/m^3 was obtained by subtracting the weight of cement and water from the unit weight of concrete (i.e., 2400 – 500 – 250). To achieve the required workability in the fresh state, the sand fraction was increased from the recommended 55% to 60% of the total

aggregate volume, while the remaining 40% constituted the coarse aggregate (crushed granite) fraction. The superplasticizer dosage was based on the manufacturer's guidelines, which recommend a maximum of 2 liters per 100 kg of cement. The applied dosage ranged between 1.5 to 2 liters per 100 kg of cement. Typical mix design details for 0.03 m^3 of SCC, as adopted in the study, are presented in Table 1.

A laboratory drum mixer was used for blending the materials. Initially, dry ingredients including cement, metakaolin, waste glass powder, fine aggregate, and coarse aggregate were measured according to the mix design and added to the drum mixer. The mixing process was carried out in three stages: (1) the dry materials were mixed for 60 seconds, (2) 50% of the water was added and mixed till a homogenous mix is achieved, and (3) the remaining water and superplasticizer were incorporated, followed by two additional minutes of mixing. Fresh concrete tests, including slump flow, V-funnel, and L-box tests, were conducted immediately after mixing to ensure adherence to EFNARC [60] standards. The concrete was then placed into cleaned and oiled molds and allowed to set for 24 hours. A total of 396 samples were produced, comprising 198 cubes (100 × 100 × 100 mm) and 198 cylinders (100 mm Ø × 200 mm height). After a day, the concrete specimens were demolded and submerged in water for curing. Compressive strength and split tensile strength tests were carried out at 7, 28, and 56 days.

2.2.4 Fresh Property Tests of Concrete

To evaluate the workability of self-compacting concrete (SCC), several tests were conducted as follows:

- Slump Flow and T_{50cm} Slump Flow:

The filling ability of SCC containing waste glass and metakaolin was assessed through the slump flow and T_{50cm} tests as shown in Fig. 1. Concrete was poured into a standard slump cone, and the resulting flow diameter was measured. Additionally, the time taken for the concrete to spread to a 50cm diameter (T_{50cm}) was recorded. These tests were conducted in accordance with BS EN 12350-2 [61].

Fig. 1. Slump flow testing of the fresh concrete

- V-Funnel and V-Funnel at 5 Minutes:

The V-funnel test was performed to determine the flowability and viscosity of the SCC. The time taken for the concrete to flow through a funnel-shaped mold (see Fig. 2) was measured both immediately after mixing and after a 5-minute delay to evaluate any changes in flow characteristics over time. This test complied with BS EN 12350-9 [62].

Fig. 2. V-Funnel tests on fresh concrete

- L-Box Test:

The passing ability of the SCC was measured using the L-box test shown in Fig.3 . Concrete was poured into an L-shaped mold, and the ratio of the concrete height in the horizontal section to that in the vertical section was calculated. This ratio indicates the concrete's ability to flow through narrow spaces and around obstacles. The test adhered to BS EN 12350-10 [63].

Fig.3. L-Box test

2.2.5 Concrete Hardened Property Tests

- Compressive Strength Test:

Compressive strength tests were performed on three 100mm cube specimens for each mix at curing ages of 7, 28, and 56 days, following BS EN 12390-3 [64] guidelines. Concrete samples were prepared using the mix proportions detailed in Table 1. The compressive strength (f_c) of the specimens containing waste glass powder and metakaolin was calculated by dividing the maximum load at failure (Pmax) by the cross-sectional area of the cube. The load was applied at a rate of 0.5 MPa/s using a compressive testing machine.

- Split Tensile Strength test

Split tensile strength tests were performed on three cylindrical specimens with dimensions of 100mm diameter and 200mm height for each mix, conforming to BS EN 12390-6 [65]. A diametral load was applied at a rate of 0.05 MPa/s using a compression testing machine. The splitting tensile strength (f_{st}) of the concrete containing waste glass powder and metakaolin was calculated using the formula:

$$f_{st} = \frac{2P_{max}}{\pi LD} \quad (1)$$

where: P_{max} is the maximum load at failure, L is the length of the cylinder, and D is its diameter.

(a) (b)

Fig. 4. Compressive and tensile strenght test on hardened concrete specimen (a) Compressive and (b) Tensile

2.2.6 Microstructural Analysis of Concrete Specimen

- Scanning Electron Microscopy (SEM) Test for Concrete Specimen:

Concrete specimens were prepared for SEM analysis by collecting chunks from SCC cube samples tested after 28 days cutting them into smaller pieces (Fig. 5), embedding in epoxy resin, polishing with silicon carbide paper, mounting on aluminum stubs, and coating with layer of carbon to enable high-resolution imaging of the concrete microstructure.

Fig. 5. Sample preparation for SEM analysis

- X-Ray Diffraction (XRD) Test for Concrete Specimen:

Concrete specimens were prepared for XRD analysis by further crushing the cube samples tested after 28 days into smaller fragment using mortar and pestle. The fragments were then grounded into fine powder using grinder to ensure uniform particle size. The powder was subsequently sieved through a 63micromes sieve to remove any other larger particles, and then stored in an airtight container shown in Fig. 6 to prevent moisture absorption. The powdered samples were analyzed at the National Steel Raw Materials Exploration Agency, Kaduna State, where EMPYREAN DIFFRACTOMETER was used for the analysis.

Fig. 6. Powdered concrete specimen prepared for XRD analysis

3. Results and Discussion

3.1 Physical Properties of Used Materials

Table 2 presents the outcomes of the physical properties tests conducted on the binder materials, including cement, waste glass, and metakaolin. The evaluated properties cover specific gravity, standard consistency, fineness, as well as the initial and final setting times. The findings indicate that all binder materials comply with the requirements specified for SCC binder ingredients, as outlined in BS EN197-1 [55]. Similarly, the physical properties of fine and coarse aggregates, such as water absorption, fineness modulus specific gravity and bulk density are detailed in Table 2. The findings indicate that these aggregates comply with the recommended ranges for SCC production, as specified in BS EN 1097-6 [58].

Table 2. Physical properties of used materials

Property	Cement	Waste glass powder	Metakaolin	Fine aggregate	Coarse aggregate
Specific gravity	3.1	2.4	2.6	2.60	2.72
Consistency (%)	29	-	-	-	-
Fineness test (%)	2.93	64.19	46.3	-	-
Initial setting time	120	-	-	-	-
Final setting time	360	-	-	-	-
Fineness modulus	-	-	-	2.70	5.97
Water absorption	-	-	-	2.20	0.80
Bulk density(kg/m^3)	-	-	-	1585	1679

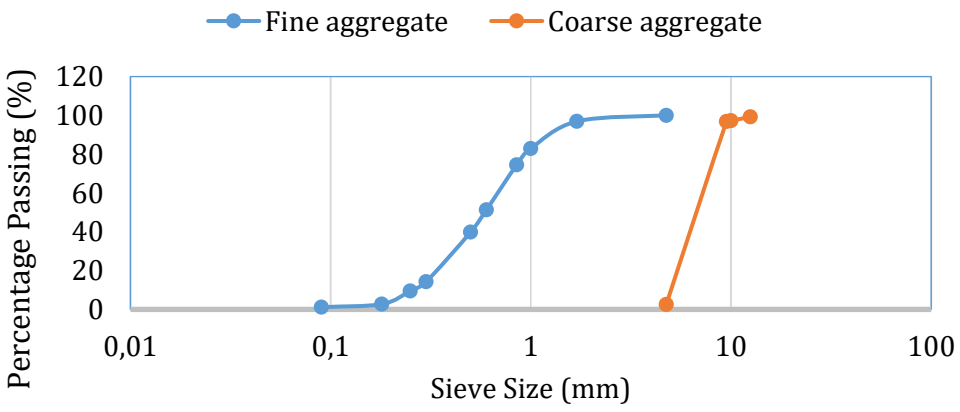

Fig. 7. Particle size distribution graph of fine and coarse aggregate

The particle size distribution curves for fine and coarse aggregates, shown in Fig. 7, provide critical parameters for assessing gradation. For fine aggregate, the coefficient of curvature (1.03) falls within the range recommended by [66], while the coefficient of uniformity (2.7) is slightly below the standard range, classifying the fine aggregate as well graded. For coarse aggregate, both the coefficient of curvature (1.2) and coefficient of uniformity (4.1) lie within the recommended ranges of ASTM C1602/C1602M [66], classifying it as well graded. These gradation characteristics indicate the suitability of both aggregates for use in SCC.

3.2 Characterization of Waste Glass and Metakaolin

The XRD diffractogram offers valuable insights into the crystalline or amorphous nature of waste glass powder and metakaolin. Fig. 8 displays the diffractograms plotted for these materials, revealing that the majority of waste glass powder and metakaolin exist in an amorphous state, with distinct Quartz (SiO2) crystals evident at certain sharp peaks. The broad hump observed in the graphs of both materials indicates their amorphous characteristics, qualifying them as pozzolanic materials. In addition, the result of the XRF showing the chemical and oxide composition of waste glass and metakaolin are presented in Table 3. The result shows a slightly lower (SiO_2 + Al_2O_3 +Fe_2O_3 (%) than ASTM C618 recommended percentage for both MK and WGP.

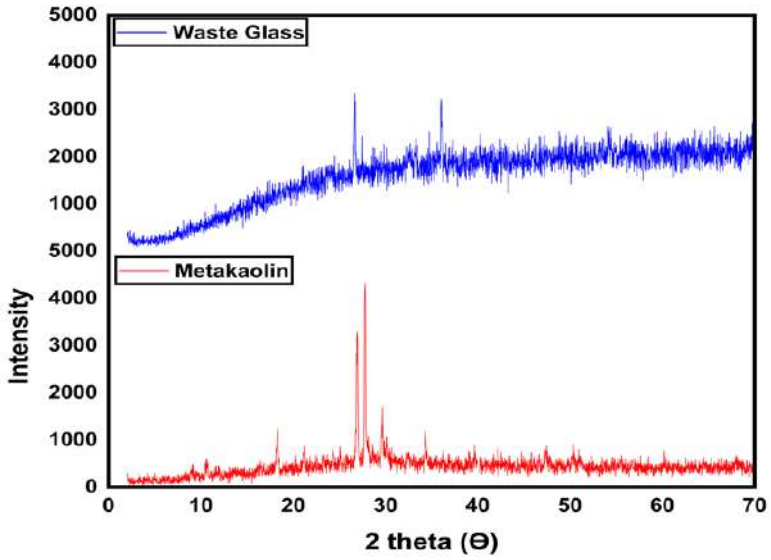

Fig. 8. XRD of materials characterization

Table 3. Chemical composition of Cement, Metakaolin and Waste glass powder (XRF results)

Composition (%)	Cement	Waste glass powder	Metakaolin
SiO_2	20.62	64.6	42.5
Fe_2O_3	3.07	1.4	9.3
Al_2O_3	5.35	2.7	15.2
SO_3(≤ 4)	-	0.1	0.5
SiO_2 + Al_2O_3 +Fe_2O_3(≥70%)		68.8	67

SEM image shows the micrograph of WG and MK at the magnification of 250. Fig. 8a and 8b shows micrograph for WGP and MK respectively. Fig. 8a shows that waste glass powder has angular irregular shape particles with smoother surfaces that are loosely packed together. Fig. 3b shows that metakaolin have particles that are closely packed with little micropores. The particles are irregular with rough surfaces and high surfaces area.

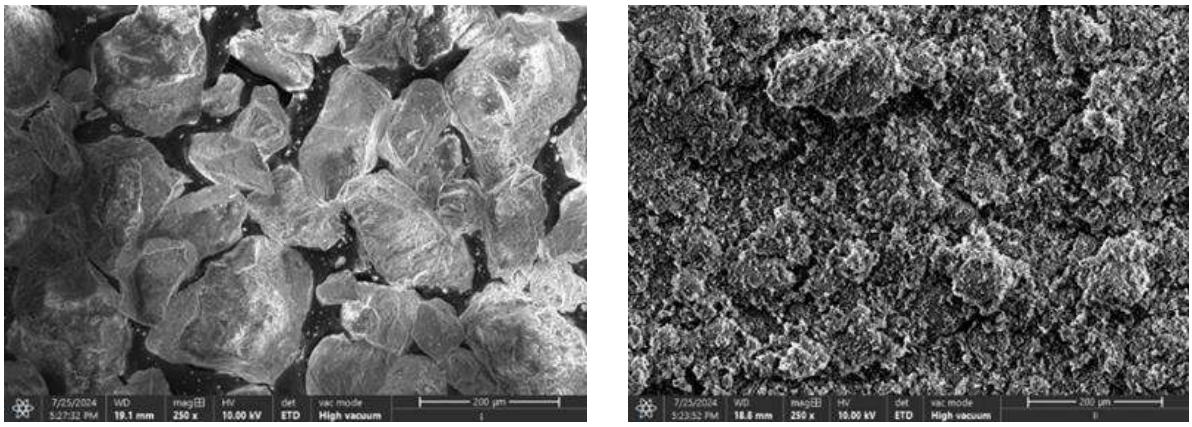

(a) (b)

Fig. 8. (a) SEM image for waste glass powder, and (b) SEM image for Metakaolin

3.3 Fresh Properties of Concrete

3.3.1 Slump Flow and T_{50cm} Slump flow

The effects of binary blends of WGP and MK with cement, as well as the ternary combination of WGP+MK with cement, on the slump flow diameter and T_{50cm} flow time are illustrated in Fig. 9. The results reveal that increasing the MK content decreases the slump flow diameter while increasing the T_{50cm} flow time, thereby reducing the overall flowability. In contrast, WGP exhibits improved slump flow diameters, and reduced T_{50cm} flow times compared to both MK and the control mix, indicating enhanced flowability. However, a reduction in flow diameter is observed when the replacement level exceeds 10%. This observation is consistent with findings by Guignone et al. [69].

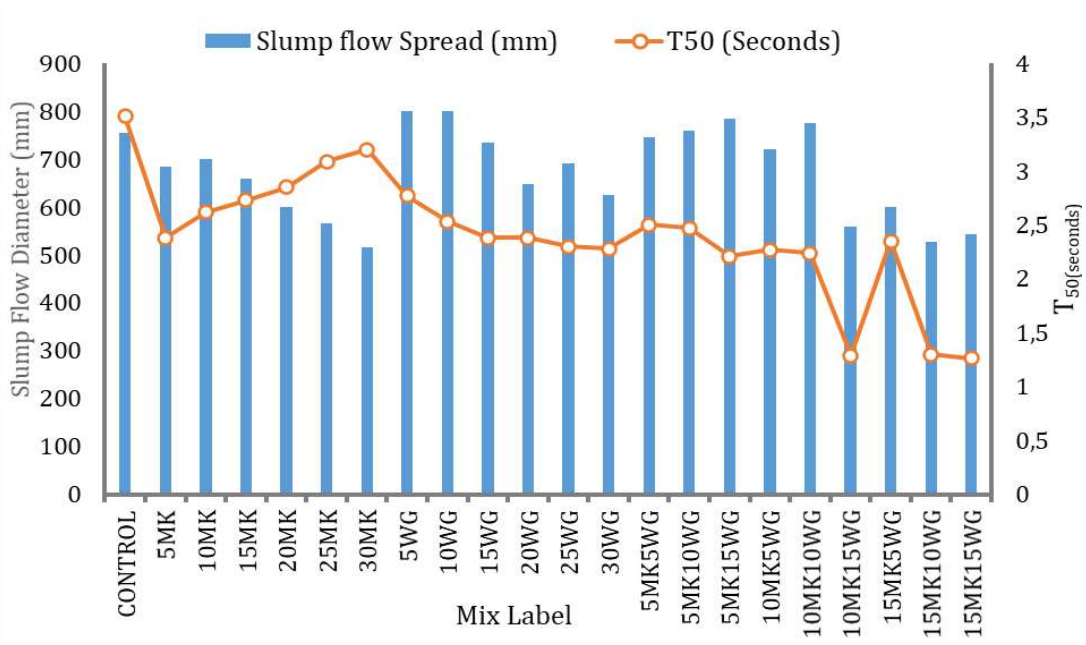

Fig. 9. Slump flow diameter and T50cm Slump flow of the SCC mixes

The ternary blend demonstrates improved slump flow diameters and lower T_{50cm} flow times at replacement levels of up to 20%, signifying better flowability. However, beyond the 20% replacement level, both the slump flow diameter and T_{50cm} flow times fall below the EFNARC [60] recommended range for flowability.

3.3.2 V-funnel and V-funnel @$T_{5minute}$

The low workability beyond 20% for the ternary blended mixtures could be due to increased surface area, higher water demand, and reduced cementitious content. The fine particles of glass powder and metakaolin absorb more water, leaving less free water for flow, while excessive replacement reduces the cement content, weakening paste cohesion. Additionally, the optimal particle packing effect diminishes at high replacement levels, leading to a stiffer mix with lower flowability.

The segregation resistance of SCC is evaluated using a V-funnel, which measures the time required for concrete to flow through a V-shaped funnel. The results presented in Fig. 10 indicate that the V-funnel flow time (Vf) for the concrete mixtures ranges between 5.6s and 7.17s, aligning with the recommended EFNARC limits, except for certain outliers among the ternary mixes. The data reveals that incorporating WGP enhances the flow properties of the mix, resulting in reduced flow times, whereas MK has the opposite effect, increasing the flow time by reducing the concrete's fluidity.

For $T_{5minutes}$, the flow times for MK and WGP mixes range between 6.26s and 9.55s, remaining within the EFNARC [60] recommended limits. Specifically, the inclusion of WGP consistently reduces $T_{5minutes}$ flow times, ranging from 8.66s at 5% WGP to 7.83s at 30% WGP. However, the flow times for MK-blended mixtures show erratic behaviour, with the 30% MK mix recording the highest $T_{5minutes}$ flow time of 9.55s, confirming MK's negative impact on concrete flow. The incorporation of WGP as part of a ternary blend with MK mitigates this effect, improving the flow time of MK-blended mixtures.

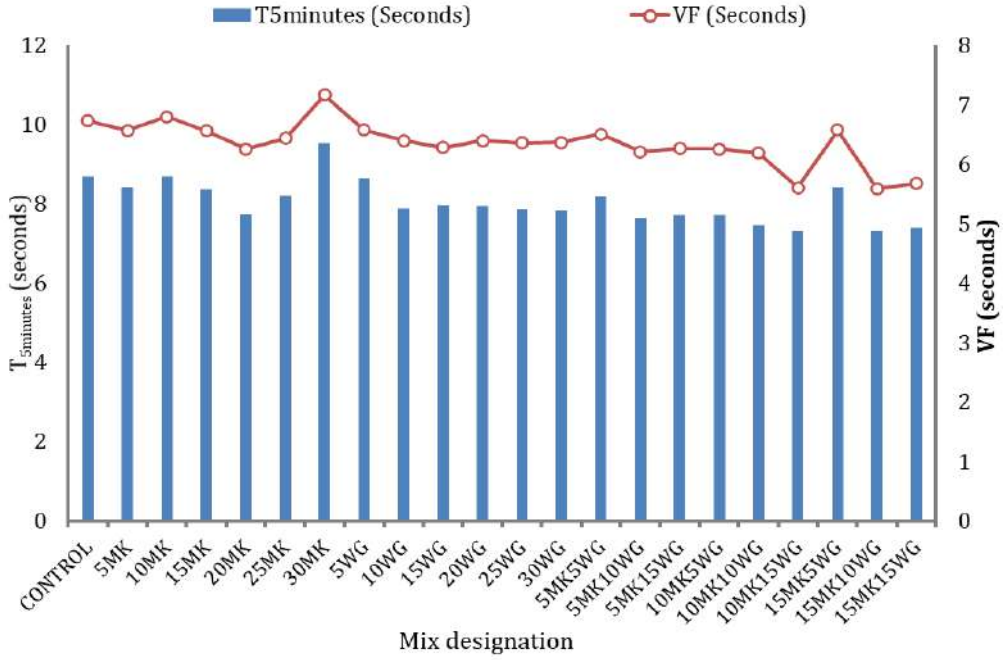

Fig. 10. V-funnel and V-funnel @ $T_{5minutes}$ of the SCC mixes

3.3.3 L- Box Result

The results of the L-box test, presented in Fig. 11, evaluate the ability of SCC to flow through and fill narrow spaces while navigating around obstacles. The blocking ratio, which represents the ability of SCC to pass through obstacles without segregation, is computed as the ratio of the final concrete height at the end of the L-box test to the initial height. This metric is crucial in evaluating the passing ability of SCC, ensuring that the mix can flow smoothly through reinforcement without blockage. The findings indicate that the blocking ratio for all binary mixes of MK and WGP ranges between 0.81 and 1, meeting the EFNARC [60] recommended values for the L-box test. Notably, the binary mixture of WGP and cement, up to a 10% replacement level, exhibits the highest blocking

ratio, demonstrating superior passing ability. However, for the ternary combination, the blocking ratio drops below the recommended range when the replacement level exceeds 20%.

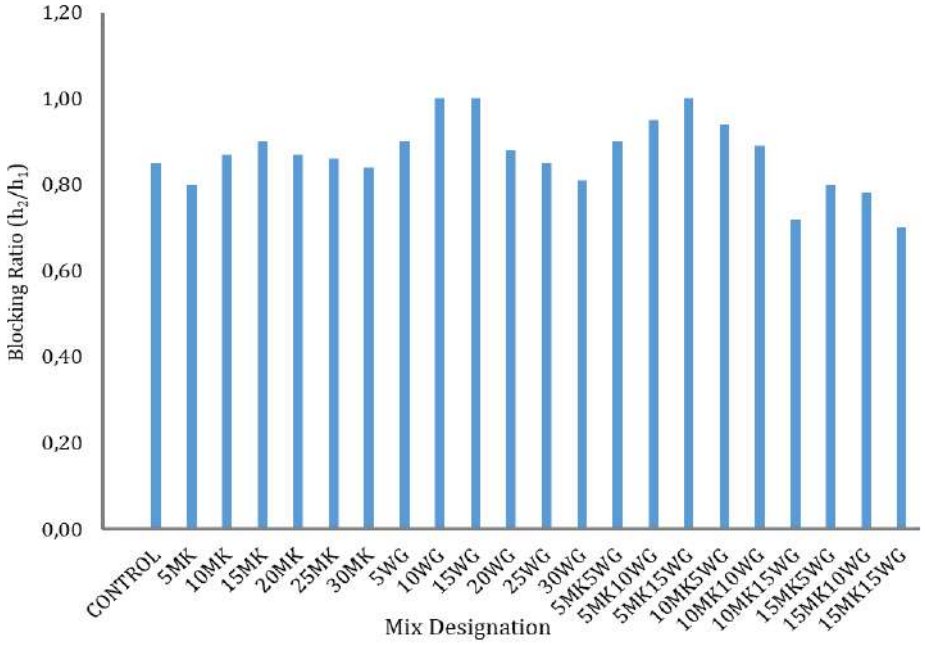

Fig. 11. L- box tests results to determine the passing ability SCC mixes

3.4 Hardened Properties of Concrete

3.4.1 Compressive Strength

The experimental results for the compressive strength of concrete samples with varying percentages of binary and ternary combinations of MK and WGP with cement are presented in Figures 12, 14, and 17. The binary blend of MK with cement, shown in Fig. 12, demonstrates that compressive strength improves with increasing MK content, reaching its peak at 15% replacement across all curing ages. This observation aligns with the findings of Chavali et al. [70] and Ofuyatan et al. [71], who identified 15% MK replacement as the optimum level for enhancing the compressive strength of concrete compared to the control mix.

At 7 days, 10MK and 15MK mixes were able to achieve strength similar to or slightly greater than the control. The improvement in compressive strength at 7 days with metakaolin (MK) replacement is primarily due to hydration acceleration and filler effects, with minimal pozzolanic contribution at this stage. MK's fine particle size and high surface area enhance nucleation, accelerating the formation of hydration products like calcium silicate hydrate (C-S-H) and boosting early-age strength. Its filler effect reduces voids, improves packing density, and refines the microstructure, further contributing to strength. While the pozzolanic reaction between MK and calcium hydroxide ($Ca(OH)_2$) begins during this period, its impact remains limited, as significant pozzolanic activity typically develops after 7 days. Beyond 15% replacement, the dilution effect becomes significant. The amount of cement available for hydration decreases, resulting in less primary C-S-H formation.

At 56 days, only the 15% metakaolin (MK) replacement surpasses the control strength, while 5% and 10% replacements show improvements but do not exceed it. This is due to the optimal balance at 15%, where pozzolanic activity and hydration synergize to produce additional calcium silicate hydrate (C-S-H), significantly densifying the matrix. At lower replacements, MK enhances the microstructure and contributes moderately through pozzolanic reactions, but the cement content remains dominant, limiting the overall strength gain. Higher replacements dilute the cement content, reducing hydration products and leaving unreacted MK, which acts as an inert material. Thus, 15% MK replacement provides the best long-term performance by maximizing both

hydration and pozzolanic contributions. A similar observation was reported by Lekhya and Kumar [72] on the utilisation of silica fume (SF) in high-performance concrete, where they noted that a 15% replacement exhibited compressive strength surpassing the control mixes at both 28 and 90 days. Almari et al. [73] also observed a 3.13% increase in compressive strength at 28 days due to a ternary blend of cement, 10% fly ash, and silica (25 kg/m^3), whereas a combination of cement, 15% metakaolin, and silica (25 kg/m^3) enhanced strength by 4.1%.

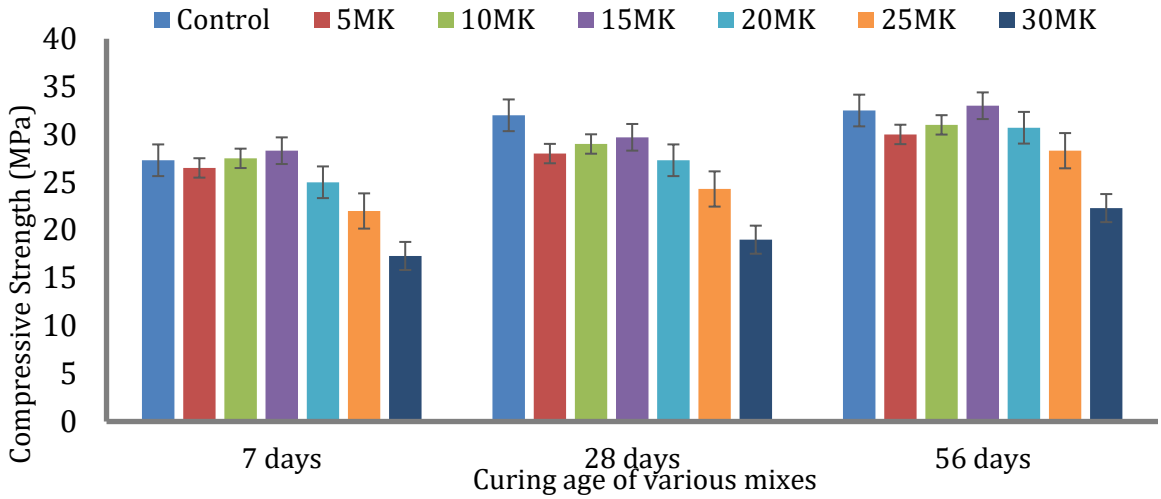

Fig. 12. Compressive strength tests result of binary blended MK with cement

The microstructural evolution of the hardened concrete samples at 56 days observed with increasing MK replacement levels is illustrated in the SEM images (Figs. 13a, 13b, and 13c). Fig. 13a (control sample) shows visible porosity and some unreacted cement particles but maintains a relatively uniform microstructure. This uniformity supports adequate hydration and structural stability. Fig. 13b reveals disrupted microstructure due to incomplete pozzolanic reactions between MK and calcium hydroxide, resulting in a less cohesive matrix. Fig. 13c, corresponding to 15% MK replacement, shows a denser and more refined microstructure with reduced porosity and improved particle packing, which likely contributes to the enhanced strength observed in mechanical tests.

The XRD patterns, presented in Fig. 14, confirm the hydration products of the hardened concrete samples. The 15% MK sample shows broader humps rather than sharp peaks in the 27°–35° 2θ range, with a noticeable intensity around 29.3° 2θ, indicating the presence of calcium silicate hydrate (C-S-H), the primary strength-giving phase. Additionally, the 15% MK sample exhibits other hydration products such as portlandite ($Ca(OH)_2$) and ettringite.

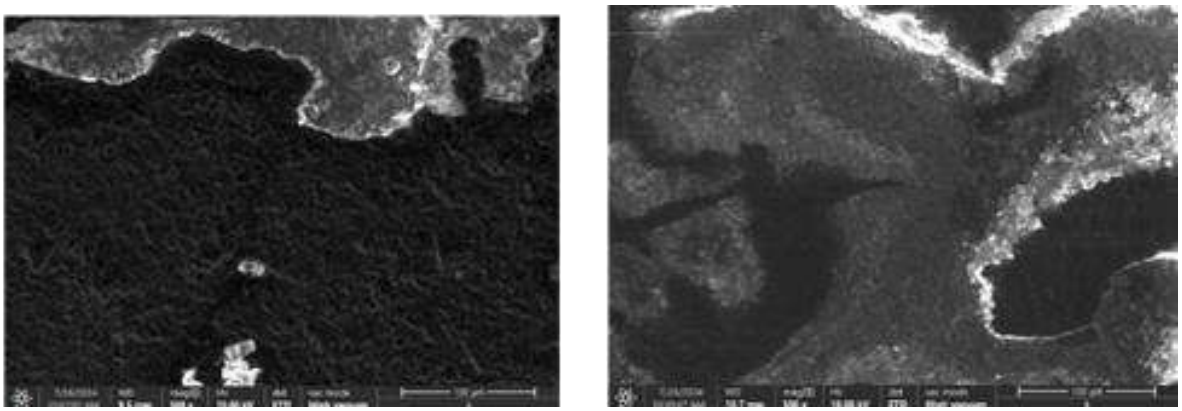

(a) (b)

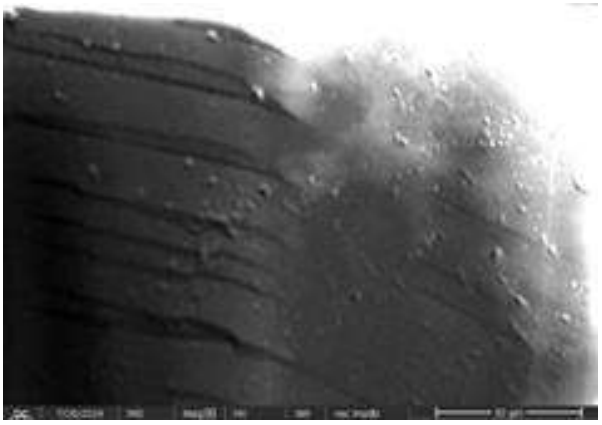

(c)

Fig 13. (a)SEM image control, (b) SEM image of 5MK, and (c) SEM image of 15MK

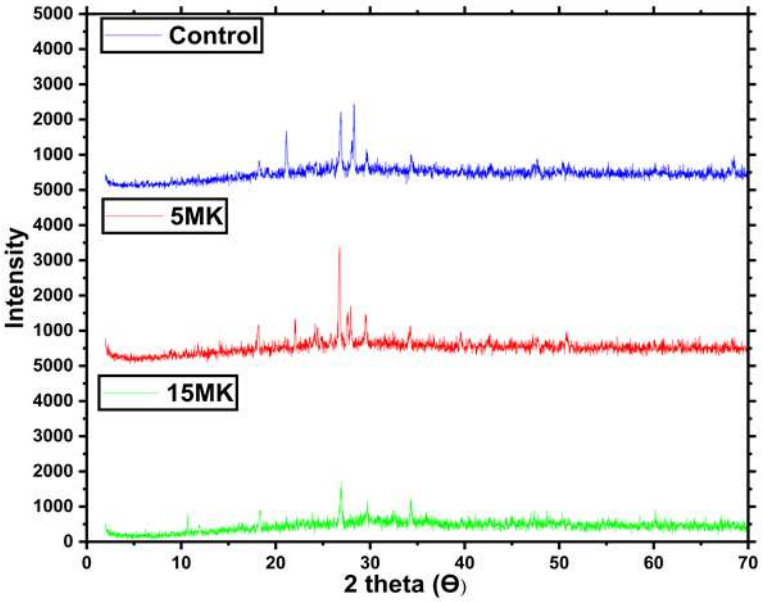

Fig. 14. XRD Comparison of various Metakaolin replacements

This more complete hydration, compared to the control (0% MK) and 5% MK samples, leads to a denser microstructure, which correlates with the improved compressive strength observed in the 15% MK mix. The enhanced C-S-H formation contributes significantly to the increased strength, supporting the role of MK in improving the mechanical properties of concrete. Fig. 15. shows a similar trend for the binary blend of WGP with cement as observed with MK, where the compressive strength increases with increasing WGP content up to 15% replacement. Beyond this point, further increases in WGP replacement led to a reduction in strength. This slightly exceeds the 10% optimum replacement level reported by Fonchou et al. [74] and Shamsudeen et al. [75].

The microstructural characteristics observed with 5% and 15% replacement of cement with WGP, relative to the control, are illustrated in the SEM images (Figs. 16a, 16b, and 16c). Fig. 16b reveals a modest enhancement in the microstructure due to the pozzolanic reaction of WGP, though the strength remains slightly below that of the control. In contrast, Fig. 16c exhibits a significantly denser and more refined microstructure, characterized by reduced porosity and increased formation of C-S-H gels. This improved microstructure underpins the superior strength achieved at the 15% replacement level compared to both the control and the 5% replacement.

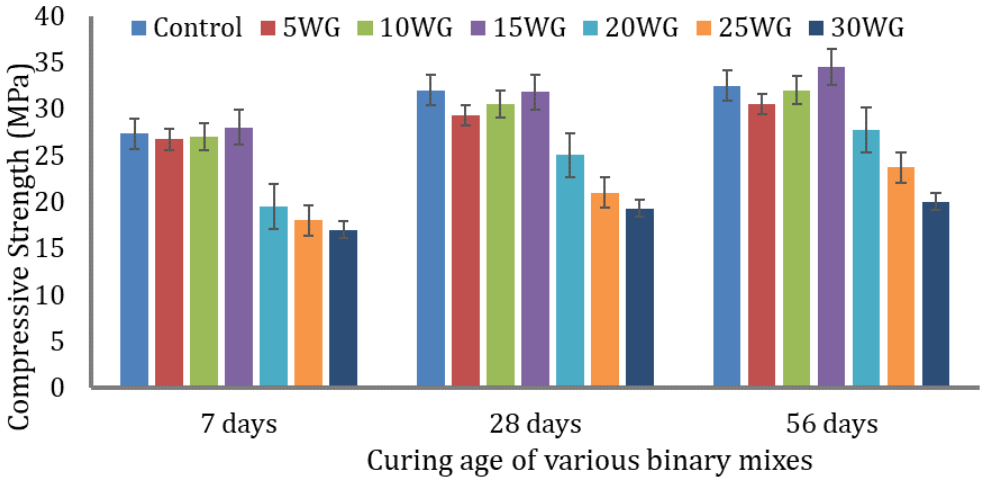

Fig. 15. Compressive strength tests result of binary blended WGP with cement

The XRD patterns of the hardened binary blends of WGP and cement for the control, 5% replacement, and 15% replacement levels are shown in Fig. 17 The 5% replacement sample exhibits a reduction in the intensity of crystalline peaks, such as portlandite, alongside a subtle broad hump, suggesting the onset of C-S-H formation. In contrast, the 15% replacement sample displays a more pronounced broad hump within the 27°–35° 2θ range, indicating more extensive or complete C-S-H formation. The reduction in crystalline peaks compared to the control signifies increased pozzolanic activity, which contributes to a denser microstructure and the higher strength observed in the sample with 15% WGP replacement.

The ternary mix 5MK+10WGP, as shown in Fig. 18, achieved the highest compressive strength among all tested concrete mixes, establishing it as the optimum replacement level. However, its early-age compressive strength was lower than that of the control mix. This behaviour aligns with findings by Guignone et al. [69], who reported that ternary blends of WGP and MK with cement could support up to 20% replacement while maintaining compressive strength.

The reduced early-age strength may be attributed to the slow nature of pozzolanic or secondary hydration reactions. These reactions depend on the availability of calcium hydroxide (CH) released during primary hydration of the cement and its interaction with amorphous silica from the pozzolans, processes which inherently progress at a slower rate [76]. However, the ternary mix of ultrafine silica fume (UFFA) and fly ash at 10% and 15% replacement (a total of 25%) in HPC achieved higher replacement level, exhibiting a significant improvement in compressive strength of around 12% at 90 days due to the extended pozzolanic reaction of SF and UFFA [72].

The SEM images of the ternary blended hardened concrete are presented in Figs. 19a, 19b, and 19c. Fig. 19b shows the densest microstructure, with well-formed C-S-H gels filling the pores, contributing to the highest strength in the mix after 56 curing days. The ternary blend of 10% WGP and 5% MK (Fig. 19b) promotes additional pozzolanic reactions, enhancing the overall matrix. Fig. 19c (10% MK and 5% WGP) displays a microstructure denser than the control but less so than the 10% WGP and 5% MK blend, with fewer visible C-S-H gels. Some micro cracks and pores remain in the 10% MK and 5% WGP ternary mix, resulting in lower strength compared to the ternary blend of 10% WGP and 5% MK. The XRD graph of the ternary blended hardened concrete is presented in Fig. 20. The 5MK10WG mix revealed a more pronounced hump in the 2θ range of 29°–34°, indicating a higher formation of C-S-H. Additionally, the reduction in the intensity of the portlandite peaks suggests more complete hydration and pozzolanic reaction, which is consistent with the SEM results, correlating with its highest strength. The 10MK5WG mix shows a moderate hump in the 2θ range of 29°–34°, indicating C-S-H formation, but it is less intense than the 5MK10WGP mix. There are also noticeable peaks for unreacted phases, which correlates with the observed lower strength compared to the 5MK10WGP mix.

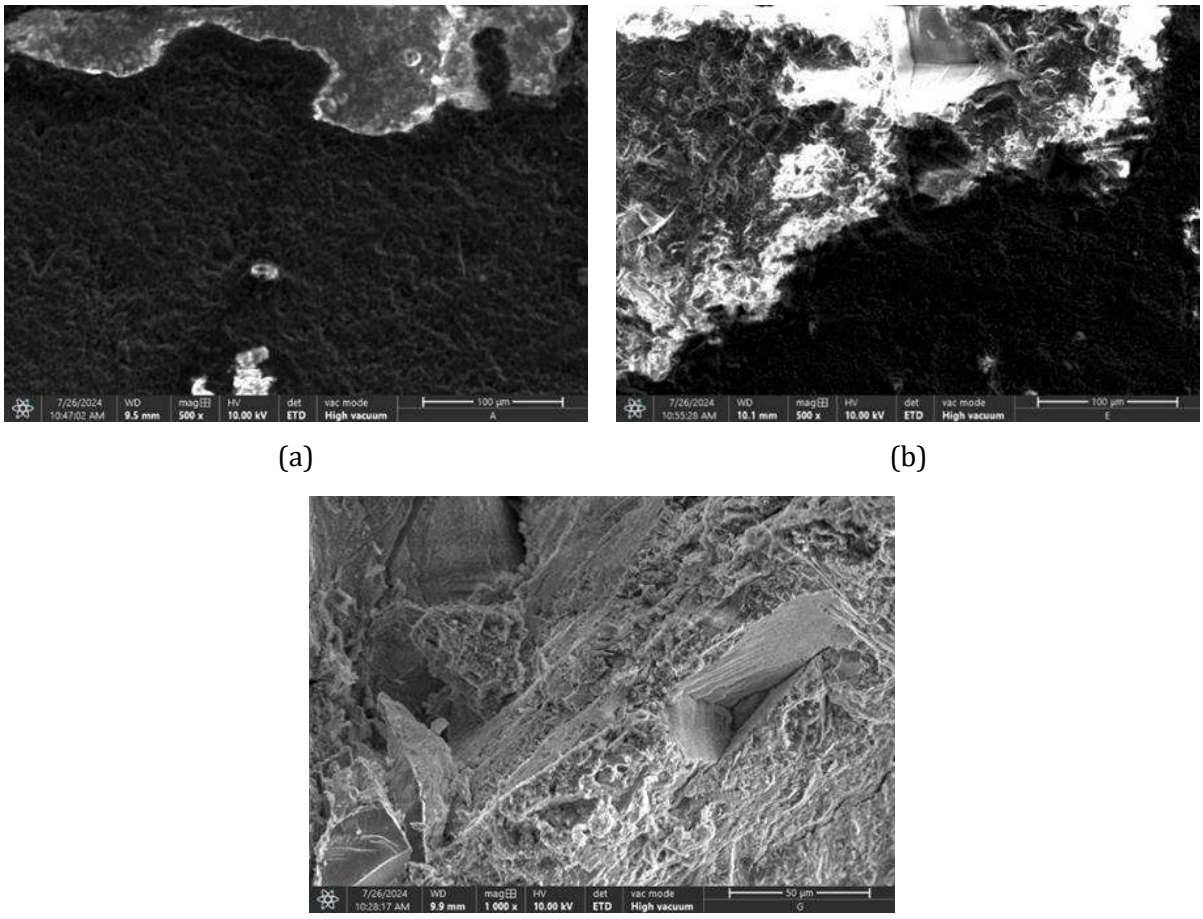

Fig 16. (a) SEM image of control, (b) SEM image of 5WGP, and (c) SEM image of 15WGP

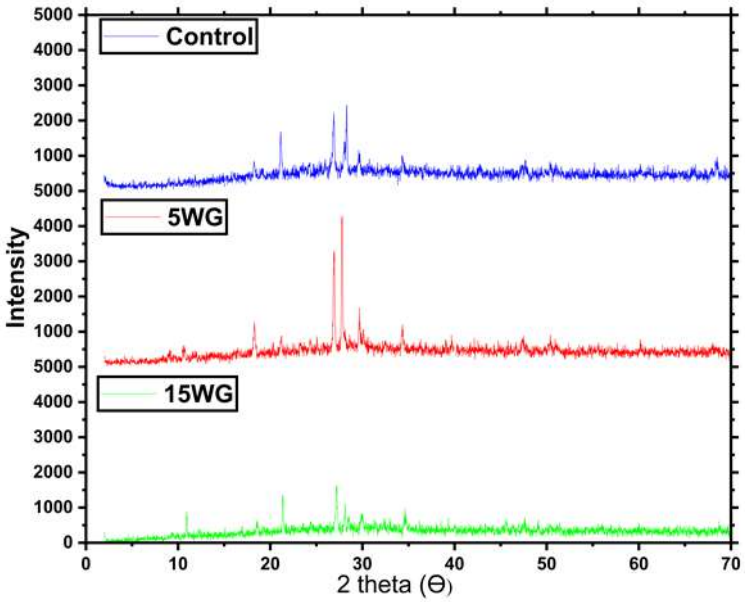

Fig. 17. XRD of various waste glass replacement

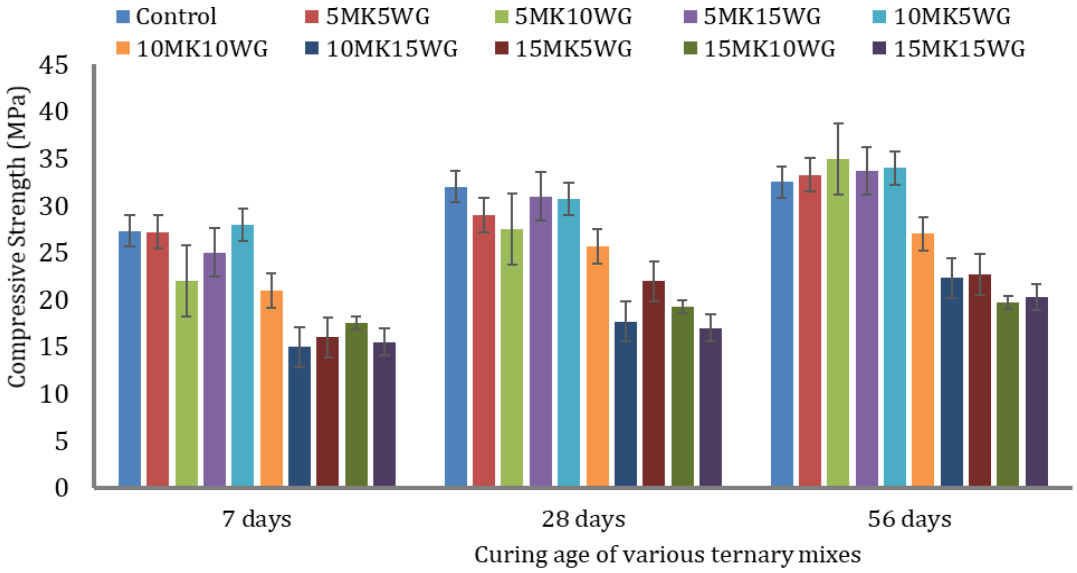

Fig. 18. Compressive strength tests result of ternary blended MK AND WGP with cement

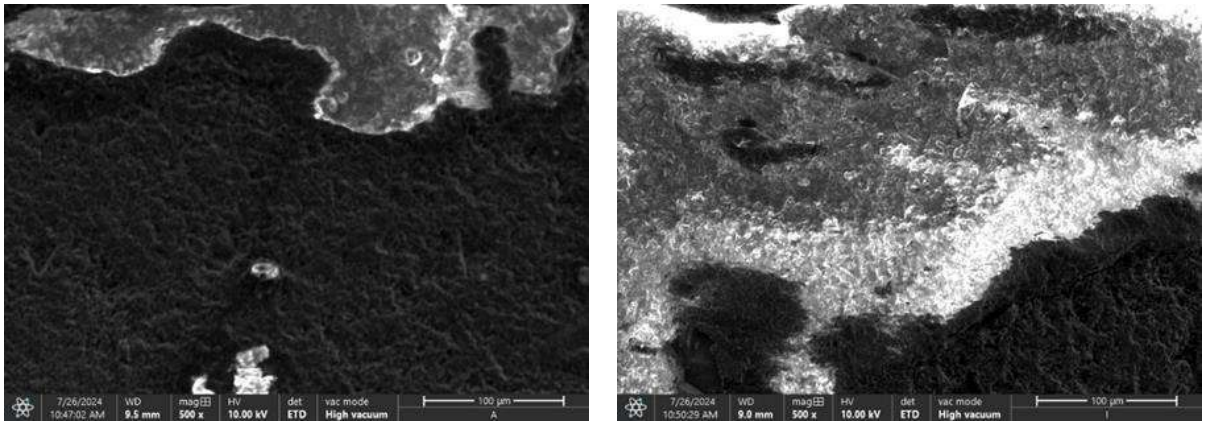

(a) (b)

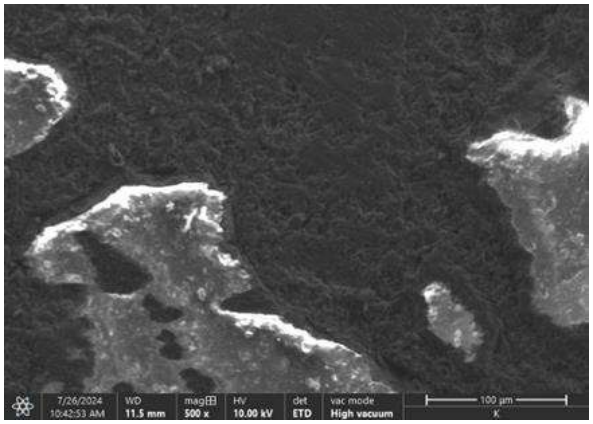

(c)

Fig. 19. (a) SEM image of control (b) SEM image of 5MK10GP, and (c) SEM image of 10MK5WGP

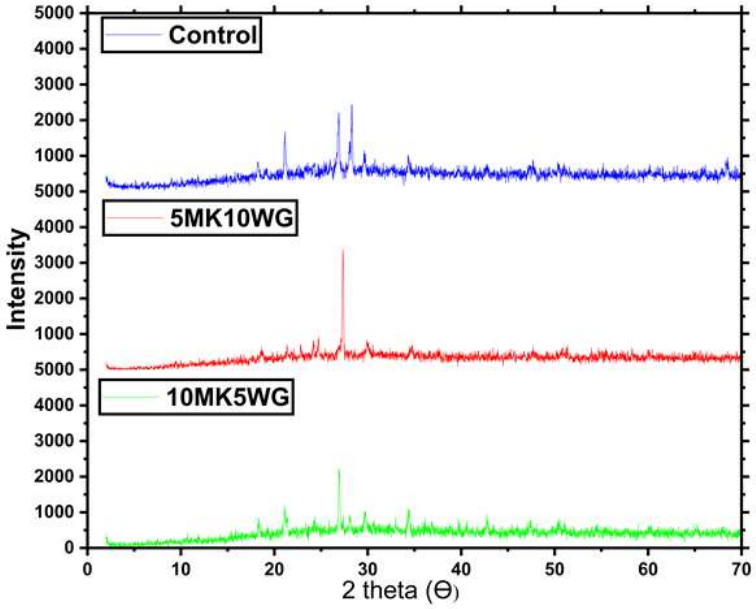

Fig. 20. XRD Graphs of ternary blended mixes

3.4.2 Split Tensile Strength

The experimental results for the split tensile strength of concrete samples containing varying percentages of binary and ternary combinations of MK and WGP with cement are illustrated in Figs. 21, 22, and 23. The results indicate that the split tensile strength improves as the curing duration increases, with all samples showing a consistent increase from 7 days to 56 days. Fig. 21 reveals that the split tensile strength rises with MK replacement up to 15%, beyond which further replacement results in a decline in strength.

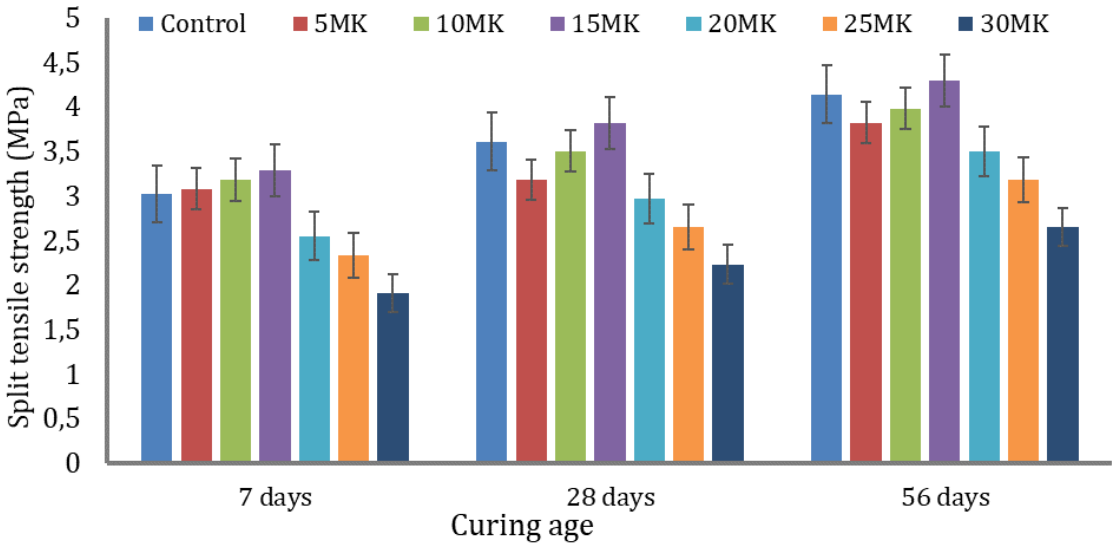

Fig. 21. Split tensile strength tests result of binary blended MK with cement

A similar pattern is evident in Fig. 22, where increasing the waste glass powder (WGP) content enhances the split tensile strength up to a 15% replacement level, after which further replacement results in a decline in strength. This partially aligns with the findings of Shamsudeen et al. [75], who identified 10% as the optimal replacement level of cement with WGP for achieving maximum split tensile strength in their study. Fig. 23 shows that the ternary mix 5MK10WG performs better having the highest split tensile strength compared to the control and other mixes, thus the optimum replacement level for the split tensile strength.

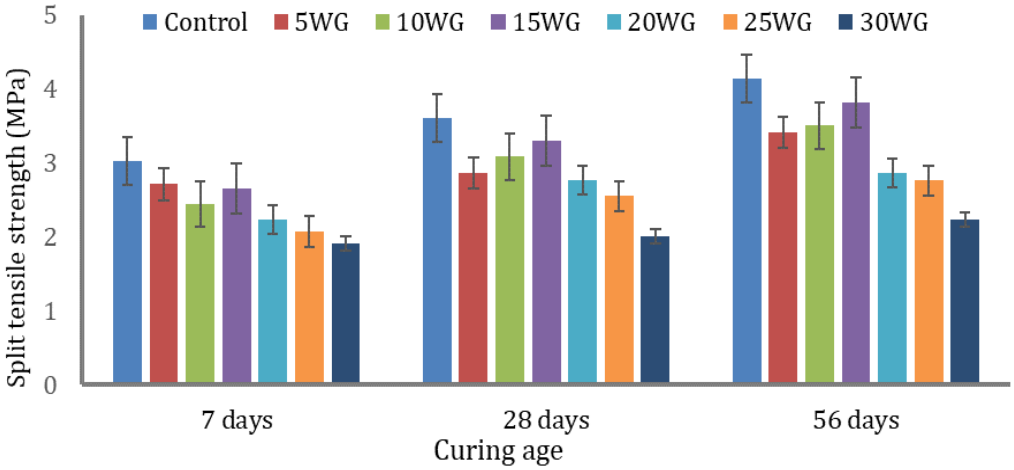

Fig. 22. Split tensile strength tests result of binary blended WGP with cement

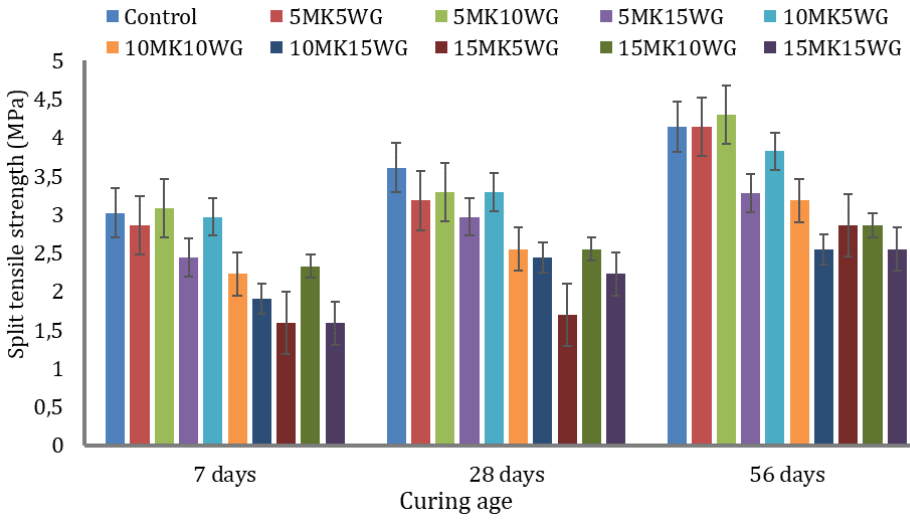

Fig. 23. Split tensile strength tests result of ternary blended MK and WGP with cement

4. Conclusions

In conclusion, the following can be drawn based on the outcomes of this research work

- XRD analysis confirmed that the Metakaolin (MK) and Waste Glass Powder (WGP) particles are predominantly amorphous and can be classified as pozzolan, though the combined Al_2O_3, SiO_2, and Fe_2O_3 content in both materials are slightly below the ASTM C618 recommended threshold.
- The mixtures with WGP exhibited higher slump values and reduced flow time compared to those containing MK, indicating greater workability. This could be attributed to microstructural properties, where MK particles are densely packed with minimal micropores, irregular shapes, rough surfaces, and high surface area, while WGP particles have angular, irregular shapes with smoother surfaces, and are more loosely packed.
- The compressive strength results reveal that 15% replacement is the optimum level for both binary and ternary combinations, with the 5MK10WGP mix achieving the highest compressive strength compared to the control and other mixes at 56 days. This performance could be attributed to enhanced pozzolanic reactions, which facilitated improved C-S-H formation and a reduction in portlandite content. The denser microstructure observed, with well-formed C-S-H gels filling pores in the 5MK10WGP mix, further validates its superior strength development.

- Although samples with 5MK10WGP was optimum in terms of both compressive and tensile strength after 90days of curing, the mix 5MK15WGP (20% replacement) also demonstrated consistently good performance at both 28 and 90 days as per compressive strength. However, the tensile strength was very low compared to 5MK10WGP samples probably due to the brittle nature of the glass material.
- The split tensile strength results also indicate that 15% replacement is the optimum level for all blended combinations, with the 15MK and 5MK10WGP mixes achieving the highest strength compared to the control at 56 days. This outcome can be linked to enhanced pozzolanic reactions, which improve the bond between aggregates and the cement matrix, as well as the denser microstructures observed in these mixes, resulting in superior tensile strength development.
- Among all the mixes, the ternary mix with 5% MK and 10% WGP (5MK+10WGP) demonstrated superior mechanical properties, surpassing the control mix by 7.7% in compressive strength and 3.8% in split tensile strength after 56 days of curing.

References

[1] Singh H, Siddique R. Long term durability assessment of self-compacting concrete made with crushed recycled glass and metakaolin. Constr Build Mater. 2023 Oct;400:132656. https://doi.org/10.1016/j.conbuildmat.2023.132656
[2] Akinpelu MA, Odeyemi SO, Olafusi OS, Muhammed FZ. Evaluation of splitting tensile and compressive strength relationship of self-compacting concrete. J King Saud Univ Eng Sci. 2019 Jan;31(1):19-25. https://doi.org/10.1016/j.jksues.2017.01.002
[3] Gill AS, Siddique R. Strength and micro-structural properties of self-compacting concrete containing metakaolin and rice husk ash. Constr Build Mater. 2017 Dec;157:51-64. https://doi.org/10.1016/j.conbuildmat.2017.09.088
[4] Sharma R, Khan RA. Durability assessment of self compacting concrete incorporating copper slag as fine aggregates. Constr Build Mater. 2017 Nov;155:617-29. https://doi.org/10.1016/j.conbuildmat.2017.08.074
[5] Silva P, de Brito J. Experimental study of the mechanical properties and shrinkage of self-compacting concrete with binary and ternary mixes of fly ash and limestone filler. Eur J Environ Civ Eng. 2017 Apr;21(4):430-53. https://doi.org/10.1080/19648189.2015.1131200
[6] Mohan A, Mini KM. Strength and durability studies of SCC incorporating silica fume and ultra fine GGBS. Constr Build Mater. 2018 May;171:919-28. https://doi.org/10.1016/j.conbuildmat.2018.03.186
[7] Pathak N, Siddique R. Effects of elevated temperatures on properties of self-compacting-concrete containing fly ash and spent foundry sand. Constr Build Mater. 2012 Sep;34:512-21. https://doi.org/10.1016/j.conbuildmat.2012.02.026
[8] Bingöl AF, Tohumcu I. Effects of different curing regimes on the compressive strength properties of self compacting concrete incorporating fly ash and silica fume. Mater Des. 2013 Oct;51:12-8. https://doi.org/10.1016/j.matdes.2013.03.106
[9] Avğın S, Köse MM, Özbek A. Damage assessment of structural and geotechnical damages in Kahramanmaraş during the February 6, 2023 earthquakes. Eng Sci Technol Int J. 2024 Sep;57:101811. https://doi.org/10.1016/j.jestch.2024.101811
[10] Isik E, Harirchian E, Bilgin H, Jadhav K. The effect of material strength and discontinuity in RC structures according to different site-specific design spectra. Res Eng Struct Mater. 2020 May;7(3):413-30.
[11] Zengin B, Aydin F. The effect of material quality on buildings moderately and heavily damaged by the Kahramanmaraş earthquakes. Appl Sci. 2023 Sep;13(19):10668. https://doi.org/10.3390/app131910668
[12] Işık E, Harirchian E, Bilgin H, Jadhav K. Seismic performance and failure mechanisms of reinforced concrete structures subject to the earthquakes in Türkiye. Sustainability. 2024 Jul;16(15):6473. https://doi.org/10.3390/su16156473
[13] Tomar R, Kishore K, Singh Parihar H, Gupta N. A comprehensive study of waste coconut shell aggregate as raw material in concrete. Mater Today Proc. 2021 Jan;44:437-43. https://doi.org/10.1016/j.matpr.2020.09.754
[14] Kishore K, Gupta N. Mechanical characterization and assessment of composite geopolymer concrete. Mater Today Proc. 2021 Jan;44:58-62. https://doi.org/10.1016/j.matpr.2020.06.319
[15] Rodrigues FA, Joekes I. Cement industry: Sustainability, challenges and perspectives. Environ Chem Lett. 2011 Oct;9(2):151-66. https://doi.org/10.1007/s10311-010-0302-2

[16] Zhang J, Liu G, Chen B, Song D, Qi J, Liu X. Analysis of CO2 emission for the cement manufacturing with alternative raw materials: A LCA-based framework. Energy Procedia. 2014 Jan;61:2541-5. https://doi.org/10.1016/j.egypro.2014.12.041
[17] Shukla A, Gupta N, Gupta A. Development of green concrete using waste marble dust. Mater Today Proc. 2020 Jan;26:2590-4. https://doi.org/10.1016/j.matpr.2020.02.548
[18] Thapa VB, Waldmann D, Simon C. Gravel wash mud, a quarry waste material as supplementary cementitious material (SCM). Cem Concr Res. 2019 Oct;124:105833. https://doi.org/10.1016/j.cemconres.2019.105833
[19] Muralidharan R, Park T, Yang HM, Lee SY, Subbiah K, Lee HS. Review of the effects of supplementary cementitious materials and chemical additives on the physical, mechanical and durability properties of hydraulic concrete. Materials. 2021 Dec;14(23):7270. https://doi.org/10.3390/ma14237270
[20] Hakeem IY, Amin M, Agwa IS, Rizk MS, Abdelmagied MF. Effect of using sugarcane leaf ash and granite dust as partial replacements for cement on characteristics of ultra-high performance concrete. Case Stud Constr Mater. 2023 Dec;19:e02266. https://doi.org/10.1016/j.cscm.2023.e02266
[21] Hakeem IY, Amin M, Agwa IS, Abd-Elrahman MH, Ibrahim OMO, Samy M. Ultra-high-performance concrete properties containing rice straw ash and nano eggshell powder. Case Stud Constr Mater. 2023 Dec;19:e02291. https://doi.org/10.1016/j.cscm.2023.e02291
[22] Ahmed MM, Sadoon A, Bassuoni MT, Ghazy A. Utilizing agricultural residues from hot and cold climates as sustainable SCMs for low-carbon concrete. Sustainability. 2024 Dec;16(23):10715. https://doi.org/10.3390/su162310715
[23] Statista. Glass recycling facts globally 2018 | Statista [Internet]. [cited 2024 Nov 14]. Available from: https://www.statista.com/statistics/1055604/key-figures-glass-recycling-globally/
[24] UNIDO. Industrial Development Report 2020 [Internet]. United Nations Industrial Development Organization; 2020 [cited 2024 Nov 14]. Available from: https://www.unido.org/resources-publications-industrial-development-report-series/idr2020
[25] Federico LM, Chidiac SE. Waste glass as a supplementary cementitious material in concrete - Critical review of treatment methods. Cem Concr Compos. 2009 Sep;31(8):606-10. https://doi.org/10.1016/j.cemconcomp.2009.02.001
[26] Kashani A, Ngo TD, Hajimohammadi A. Effect of recycled glass fines on mechanical and durability properties of concrete foam in comparison with traditional cementitious fines. Cem Concr Compos. 2019 May;99:120-9. https://doi.org/10.1016/j.cemconcomp.2019.03.004
[27] Taha B, Nounu G. Utilizing waste recycled glass as sand/cement replacement in concrete. J Mater Civ Eng. 2009 Nov;21(12):709-21. https://doi.org/10.1061/(ASCE)0899-1561(2009)21:12(709)
[28] Arabi N, Meftah H, Amara H, Kebaïli O, Berredjem L. Valorization of recycled materials in development of self-compacting concrete: Mixing recycled concrete aggregates - Windshield waste glass aggregates. Constr Build Mater. 2019 Jun;209:364-76. https://doi.org/10.1016/j.conbuildmat.2019.03.024
[29] Guo P, Meng W, Nassif H, Gou H, Bao Y. New perspectives on recycling waste glass in manufacturing concrete for sustainable civil infrastructure. Constr Build Mater. 2020 Oct;257:119579. https://doi.org/10.1016/j.conbuildmat.2020.119579
[30] Hendi A, Mostofinejad D, Sedaghatdoost A, Zohrabi M, Naeimi N, Tavakolinia A. Mix design of the green self-consolidating concrete: Incorporating the waste glass powder. Constr Build Mater. 2019 Feb;199:369-84. https://doi.org/10.1016/j.conbuildmat.2018.12.020
[31] ouldkhaoua Y, Benabed B, Abousnina R, Kadri EH. Experimental study on the reuse of cathode ray tubes funnel glass as fine aggregate for developing an ecological self-compacting mortar incorporating metakaolin. J Build Eng. 2020 Jan;27:100951. https://doi.org/10.1016/j.jobe.2019.100951
[32] Singh H, Siddique R. Utilization of crushed recycled glass and metakaolin for development of self-compacting concrete. Constr Build Mater. 2022 Sep;348:128659. https://doi.org/10.1016/j.conbuildmat.2022.128659
[33] Solanki P, Xie H. State-of-the-practice review on the field-curing methods for evaluating strength of concrete test specimen. J Civ Eng Constr. 2022 Aug;11(3):153-65. https://doi.org/10.32732/jcec.2022.11.3.153
[34] Bisht K, Kabeer KISA, Ramana PV. Gainful utilization of waste glass for production of sulphuric acid resistance concrete. Constr Build Mater. 2020 Feb;235:117486. https://doi.org/10.1016/j.conbuildmat.2019.117486
[35] Tanwar V, Bisht K, Kabeer KISA, Ramana PV. Experimental investigation of mechanical properties and resistance to acid and sulphate attack of GGBS based concrete mixes with beverage glass waste as fine aggregate. J Build Eng. 2021 Sep;41:102372. https://doi.org/10.1016/j.jobe.2021.102372
[36] Adaway M, Wang Y. Recycled glass as a partial replacement for fine aggregate in structural concrete - Effects on compressive strength. Electron J Struct Eng. 2015 Jan;14(1):116-22. https://doi.org/10.56748/ejse.141951

[37] Malik MI, Bashir M, Ahmad S, Tariq T, Chowdhary U. Study of concrete involving use of waste glass as partial replacement of fine aggregates [Internet]. 2013 [cited 2024 Nov 14]. Available from: www.iosrjen.org
[38] Rashad AM. Recycled waste glass as fine aggregate replacement in cementitious materials based on Portland cement. Constr Build Mater. 2014 Dec;72:340-57. https://doi.org/10.1016/j.conbuildmat.2014.08.092
[39] Tamanna N, Tuladhar R, Sivakugan N. Performance of recycled waste glass sand as partial replacement of sand in concrete. Constr Build Mater. 2020 Apr;239:117804. https://doi.org/10.1016/j.conbuildmat.2019.117804
[40] Tan KH, Du H. Use of waste glass as sand in mortar: Part I - Fresh, mechanical and durability properties. Cem Concr Compos. 2013 Jan;35(1):109-17. https://doi.org/10.1016/j.cemconcomp.2012.08.028
[41] Luo D, Sinha A, Adhikari M, Wei J. Mitigating alkali-silica reaction through metakaolin-based internal conditioning: New insights into property evolution and mitigation mechanism. Cem Concr Res. 2022 Sep;159:106888. https://doi.org/10.1016/j.cemconres.2022.106888
[42] Akinpelu MA, Salman A-SM, Jimoh YA, Yahaya IT, Salami HM. Impact of treatment temperature of metakaolin on strength and sulfate resistance of concrete. Res Eng Struct Mater. 2024.
[43] Bernal SA, et al. Characterization of supplementary cementitious materials by thermal analysis. Mater Struct. 2017 Feb;50(1):1-13. https://doi.org/10.1617/s11527-016-0909-2
[44] Cao Z, Shen L, Liu L, Zhong S. Analysis on major drivers of cement consumption during the urbanization process in China. J Clean Prod. 2016 Oct;133:304-13. https://doi.org/10.1016/j.jclepro.2016.05.130
[45] Rashad AM. Recycled waste glass as fine aggregate replacement in cementitious materials based on Portland cement. Constr Build Mater. 2014 Dec;72:340-57. https://doi.org/10.1016/j.conbuildmat.2014.08.092
[46] Ling G, et al. Rheological behavior and microstructure characteristics of SCC incorporating metakaolin and silica fume. Materials. 2018 Dec;11(12):2576. https://doi.org/10.3390/ma11122576
[47] Sfikas IP, Badogiannis EG, Trezos KG. Rheology and mechanical characteristics of self-compacting concrete mixtures containing metakaolin. Constr Build Mater. 2014 Aug;64:121-9. https://doi.org/10.1016/j.conbuildmat.2014.04.048
[48] Boukendakdji O, Kadri EH, Kenai S. Effects of granulated blast furnace slag and superplasticizer type on the fresh properties and compressive strength of self-compacting concrete. Cem Concr Compos. 2012 Apr;34(4):583-90. https://doi.org/10.1016/j.cemconcomp.2011.08.013
[49] Letelier V, Henríquez-Jara BI, Manosalva M, Parodi C, Ortega JM. Use of waste glass as a replacement for raw materials in mortars with a lower environmental impact. Energies. 2019 May;12(10):1974. https://doi.org/10.3390/en12101974
[50] Younes MM, Abdel-Rahman HA, Khattab MM. Utilization of rice husk ash and waste glass in the production of ternary blended cement mortar composites. J Build Eng. 2018 Nov;20:42-50. https://doi.org/10.1016/j.jobe.2018.07.001
[51] Keerio MA, Abbasi SA, Kumar A, Bheel N, Rehaman KU, Tashfeen M. Effect of silica fume as cementitious material and waste glass as fine aggregate replacement constituent on selected properties of concrete. Silicon. 2022 Jan;14(1):165-76. https://doi.org/10.1007/s12633-020-00806-6
[52] Shoaei P, Ameri F, Musaeei HR, Ghasemi T, Cheah CB. Glass powder as a partial precursor in Portland cement and alkali-activated slag mortar: A comprehensive comparative study. Constr Build Mater. 2020 Aug;251:118991. https://doi.org/10.1016/j.conbuildmat.2020.118991
[53] Figueira RB, et al. Alkali-silica reaction in concrete: Mechanisms, mitigation and test methods. Constr Build Mater. 2019 Oct;222:903-31. https://doi.org/10.1016/j.conbuildmat.2019.07.230
[54] Saha AK, Khan MNN, Sarker PK, Shaikh FA, Pramanik A. The ASR mechanism of reactive aggregates in concrete and its mitigation by fly ash: A critical review. Constr Build Mater. 2018 May;171:743-58. https://doi.org/10.1016/j.conbuildmat.2018.03.183
[55] British Standards Institution. BS EN 197-1:2011 Cement - Part 1: Composition, specifications and conformity criteria. London: BSI; 2011.
[56] British Standards Institution. BS EN 12620: Aggregates for concrete. London: BSI; 2008.
[57] British Standards Institution. BS EN 1008: Mixing water for concrete - Specification for sampling, testing and assessing the suitability of water. London: BSI; 2002.
[58] British Standards Institution. BS EN 1097-6: Tests for mechanical and physical properties of aggregates - Part 6: Determination of particle density and water absorption. London: BSI; 2022.
[59] EFNARC. The European Guidelines for Self-Compacting Concrete - Specification, Production and Use. 2005. [Online]. Available: www.efnarc.org
[60] EFNARC. Specification and Guidelines for Self-Compacting Concrete. 2002. [Online]. Available: www.efnarc.org

[61] British Standards Institution. BS EN 12350-2: Testing fresh concrete - Slump test. London: BSI; 2019. [Online]. Available: https://www.en-standard.eu/bs-en-12350-2-2019-testing-fresh-concrete-slump-test/
[62] British Standards Institution. BS EN 12350-9: Testing fresh concrete - Part 9: Self-compacting concrete - V-funnel test. London: BSI; 2010.
[63] British Standards Institution. BS EN 12350-10: Testing fresh concrete - Part 10: Self-compacting concrete - L-box test. London: BSI; 2010.
[64] British Standards Institution. BS EN 12390-3:2019: Testing hardened concrete - Compressive strength of test specimens. London: BSI; 2019. [Online]. Available: https://www.en-standard.eu/bs-en-12390-3-2019-testing-hardened-concrete-compressive-strength-of-test-specimens/
[65] British Standards Institution. BS EN 12390-6:2023: Testing hardened concrete - Split tensile strength test. London: BSI; 2023. [Online]. Available: https://knowledge.bsigroup.com
[66] ASTM International. ASTM C1602/C1602M: Standard Specification for Mixing Water Used in the Production of Hydraulic Cement Concrete. USA: ASTM; 2018.
[67] Salman AM, Akinpelu MA, Yahaya IT, Salami HM. Workability and strengths of ternary cementitious concrete incorporating calcined clay and limestone powder. Mater Today Proc. 2023 Jan;86:51-8. https://doi.org/10.1016/j.matpr.2023.02.249
[68] ASTM International. ASTM C618-23e1: Standard Specification for Coal Fly Ash and Raw or Calcined Natural Pozzolan for Use in Concrete. [Online]. Available: https://webstore.ansi.org/standards/astm/astmc61812a
[69] Guignone GC, Vieira GL, Zulcão R, Degen MK, de Moraes Mittri SH, Baptista G. Incorporation of glass powder and metakaolin as cement partial replacement to improve concrete mechanical properties and increase service life. J Compos Mater. 2020 Feb;54(21):2965-83. https://doi.org/10.1177/0021998320906873
[70] Chavali BT, Karunakar P, Tech M. Effect of varying quantities of metakaolin and fly ash on strength characteristics of concrete [Internet]. 2016. Available from: www.ijtre.com
[71] Ofuyatan OM, Olowofoyeku AM, Edeki SO, Oluwafemi J, Ajao A, David O. Incorporation of silica fume and metakaolin on self-compacting concrete. J Phys Conf Ser. 2019 Dec;1378(4):042089. https://doi.org/10.1088/1742-6596/1378/4/042089
[72] Lekhya A, Kumar NS. A study on the effective utilization of ultrafine fly ash and silica fume content in high-performance concrete through an experimental approach. Heliyon. 2024 Nov;10(22). https://doi.org/10.1016/j.heliyon.2024.e39678
[73] Alamri M, et al. Enhancing the engineering characteristics of sustainable recycled aggregate concrete using fly ash, metakaolin and silica fume. Heliyon. 2024 Apr;10(7):29014. https://doi.org/10.1016/j.heliyon.2024.e29014
[74] Fonchou WAD, Abanda A, Kenmogne F, Sali M, Doumbaye JM. Partial replacement of cement with waste glass powder in concrete for sustainable waste management: A case study of concrete incorporating sand and waste glass from the Douala City of Cameroon. Am J Mater Sci. 2023;13(1):7-21.
[75] Shamsudeen AA, Usman N, Idi MA, Gabriel U. Suitability of waste glass powder as partial cement replacement in concrete subject to chemical aggressive environment [Internet]. 2020. Available from: www.ijltemas.in
[76] Elyasigorji F, et al. Comprehensive review of direct and indirect pozzolanic reactivity testing methods. Buildings. 2023 Nov;13(11):2789. https://doi.org/10.3390/buildings13112789

Blank Page

Research on Engineering Structures & Materials
www.jresm.org

Research Article

Effect of ADG-NH_2 functionalized graphene on fracture and impact resistance of carbon fiber reinforced composites

Debendra Nath Choudhury [1,2,a], S.K Panda [*,1,b]

[1]*Department of Mechanical Engineering, IIT [BHU], Varanasi, UP - 221005, India*
[2]*Aircraft Research & Design Center, HAL, Bangalore-560037, India*

Article Info

Article History:

Received 24 Dec 2024
Accepted 13 Mar 2025

Keywords:

Composite;
CFRP;
Amine functionalized graphene;
Tensile test;
Fracture toughness;
SEM

Abstract

In this study tensile, single edge notch beam [SENB] and impact tests were done as per ASTM standards to evaluate the influence of the ADG-NH_2 functionalized Nano additives on the mode I fracture and impact resistance characteristics. This study highlights the enhancement in the Tensile strength, Mode I fracture resistance and impact strength properties of Carbon Fiber Reinforced Polymer [CFRP] composites loaded with Lower concentration of Graphene reinforcement. Five symmetrical, modified composite laminates [ADG-NH_2/Epoxy/CFRP] were fabricated using a hand layup process supported by vacuum bagging. These laminates incorporated various weight content [0.25, 0.5, 0.75, and 1%] of ADG-NH_2/Epoxy along with a neat epoxy for comparison. Notable improvements were observed in the composite properties with 0.5 wt% ADG-NH_2 graphene Nano-additive reinforcement in comparison with base epoxy CFRP composite laminates, including increase in elastic modulus by approximately 18%, rise in ultimate tensile strength by around 21%, enhanced elongation at break by roughly 19% and Improved toughness, showing a 28% gain. An enhancement of ~29 % and ~ 60% were observed for the fracture resistance [K_{IC} & G_{IC} respectively] of base epoxy resin [value of ~ 0.67 MPa $m^{1/2}$ and ~157 J/m^2 respectively] with 0.5 wt% ADG-NH_2 loading obtaining a value of ~ 0.86 MPa $m^{1/2}$ and ~251 J/m^2 respectively. Similarly, enhancement of ~ 41% was observed for the impact strength of base epoxy resin [value of ~77 J/m^2] with 0.5 wt% ADG-NH_2 loading obtaining a value of ~108 J/m^2. Morphological properties of fracture surfaces were characterized by SEM micrographs analysis.

© 2025 MIM Research Group. All rights reserved.

1. Introduction

Many engineering and industrial applications have broadened the requirement of CFRP composites due to its superior thermal properties i.e. high insulation, stability, high heat resistance, low shrinkage along with enhanced mechanical properties like good dimensional stability, high tensile strength, and modulus etc.[1–5].Nano additives like 2-D graphene sheet made of honeycomb structure arrangement SP^2 carbon atoms were used in CFRP structures to enhance mechanical, electrical, and thermal properties[6,7]. Earlier research indicated that graphene reinforced nano composites possess superior strength, stiffness and cost effective in comparison with clay, silica and carbon nano composites [8,9]. Additives like graphene nano particles enhances tensile properties and fracture stiffness of polymer composite but at the same time drastically changes the material properties i.e. weight to surface area ratio with the use of very small amount [10,11]. When a high loading content of graphene nano particles [> 1wt%] was added to the composite, fracture toughness was significantly reduced [12]. Graphene and graphene derivatives produced via chemical vapor deposition or mechanical exfoliation with several surface functionalities generally

*Corresponding author: debendranchoudhury.rs.mec18@itbhu.ac.in
[a]orcid.org/0009-0005-1059-2948; [b]orcid.org/0000-0001-8876-909X
DOI: http://dx.doi.org/10.17515/resm2025-588me1224rs

enhances the fiber matrix bonding and shows excellent properties compared to single layer graphene composites [13,14]. Surface functionalization with nano additives reduces agglomeration and further ameliorates the particle/ matrix interface [15,16]. Covalent functionalization shows more variation in material properties and excellent bonding between the functional groups and particle surfaces. Covalent bonding between the matrix and additive enables an enhanced electric charge, phonons transfer as well as mechanical loads transfer across the particle/polymer interface [17–20]. To form a strong amide bond with epoxies, amine functionalities take part in the polymerization process which is cured with amine-based hardeners and used in the majority of structural FRPs [21,22]. This functionalization found further applications such as lightening protection [23], aircraft deicing [24], sensory materials [25–29], electromagnetic interference shielding [30], thermal interface materials [31,32] or ballistic applications [33].

Various researchers also studied the effect of fracture resistance and impact strength through fictionalization of CNTs and other nano materials like silica etc. with epoxy based nano composites. In this study, fracture stiffness of the nanocomposite with graphene exhibited an approximate 53% improvement in comparison with base epoxy. The influence of SWCNTs and MWCNTs on mechanical properties, along with the advantages of surface treatment of CNTs, was examined [34,35]. It was observed that the fracture toughness of base epoxy increased by approximately 45% when reinforced with non-functionalized SWCNTs. However, increasing the SWCNT weight percentage beyond 0.3% lead to in a reduction of fracture toughness due to re-agglomeration. Whereas the strengthening mechanisms of nano-silica-reinforced epoxy polymers at a 13 wt% concentration, fabricated using a sol-gel technique [36], demonstrated a substantial increase in fracture stiffness—from 100 J/m^2 to 460 J/m^2.

The CFRP composites reinforced with ADG-NH_2 exhibit excellent potential in diverse applications due to its superior mechanical and thermal properties. However, it is crucial to thoroughly assess their performance under prolonged environmental exposure, such as humidity, temperature variations, and UV radiation. These factors significantly influence the composites' practical lifespan and overall reliability, which are essential for real-world applications. The thermal characterization studies such as thermal aging, heat resistance ensuring their thermal stability over time and interaction with various chemicals, including solvents, acids and bases ensuring their durability during chemical aggressive environments to be accessed thoroughly. Hence for the Long-term stability and durability of CFRP composites with ADG-NH_2 reinforcement the following future works such as accelerated aging test, Long- term mechanical testing including fatigue testing and dynamic mechanical analysis to be carried out which will provide better understanding of their practical lifespan and ensure reliable and efficient performance in real-world conditions.

From the previously literature review, it has been deduced that the carbon fiber shows poor wettability to the most of the polymeric matrix material. And also, it is well established that the inclusion of non-functionalized nano particles like graphene nano platelets , graphene oxide and functionalized nano particles like amino-functionalized Graphene oxide, hydroxyl graphene and carboxyl reinforced graphene] are extensively being used to augment the bulk mechanical properties. Very few literatures have used amine functionalized graphene as nano filler. Therefore, amine functionalized graphene has been used which helps in better distribution and improves the bonding between carbon fiber and aerospace grade epoxy matrix used in this study. This literature offers the novel manufacturing processing route to introduce ADG-NH_2 into the matrix, thereby focusing on better dispersion of the nano filler with the matrix. The improvement in interfacial adhesion in laminate was verified through tensile test results. This study also includes the out of plane loading performance of CFRP laminate under SENB and impact test and also corroborate it with the help of improvement in fracture resistance and impact strength properties.

This study presents the development of amine-functionalized graphene-epoxy CFRP composites, exploring various ADG-NH_2 loadings [<1 wt%]. It investigates the impact of amine functionalization on key mechanical properties, including fracture stiffness, impact resistance, tensile strength, and morphological characteristics. The paper also details the processing methodology for incorporating ADG-NH_2 into the epoxy matrix, demonstrating that its homogeneous dispersion significantly enhances the composites' overall performance.

2. Experimental Procedures

2.1 Materials

The amine functionalized graphene [product No.: ADG-NH_2] was received from M/s AdNano Technologies Private Limited, Shivamogga, Karnataka, India. Homogeneous dispersion [purity ~99%] of the amine functionalized graphene [containing 5-10 layers of graphene] with addition of [~ 2 to 5%] NH_2 on graphene in order to attain the desired exfoliation and dispersion increases the thermal and mechanical properties. Covalently functionalized graphene particles have thickness range of 5-10 nm and lateral dimension ranging between 5-10 µm with bulk density and surface area 0.1 g/cm^3 and 60-200 m^2/g respectively. [Refer Fig 1]. Bidirectional carbon fiber woven fabrics [T700], Epoxy [LY 5052] and hardener [CH 5052] were used for this study. The high strength non crimp carbon fiber fabrics [Product No.: T700] were purchased from M/s Carbonext India Private Limited. Nashik, Maharashtra, India having thickness 0.25 mm or 250 gsm.. Epoxy resin [ARALDITE LY5052] and hardener [ARADUR 5052 CH] received from M/s Singhal Chemical corporation, Meerut, UP, India were used for this study. The resin was mixed with hardener at a ratio of 100:38. Initially a baseline T700 carbon fiber fabric CFRP composite with neat epoxy were manufactured. The mould release agent was received from Mohini Organics Pvt. Ltd., Malad [West], Mumbai, Maharastra, India and an adhesive tape, release film & peel ply were purchased from Aristo Flexi pack, Daman and Diu, India. For this composite Laminate system, the nominal resin and fiber volume was of the ratio 34: 66.

2.2 Fabrication of Amine Functionalized Graphene [ADG-NH_2]/ Epoxy

As shown in Schematic representation [Refer Fig. 1], during this study all the composite laminates were prepared under similar environmental conditions. The desired Amine functionalized graphene [ADG-NH_2] solution loading content was added to solvent medium [methanol] and dispersed using a ultrasonic dispersion machine [Hielscher Ultrasonic homogenizer [Product No. UP400 ST] with 22 mm probe], for 1 hour to ensure the homogeneous dispersion of ADG-NH_2 by breaking the Vander walls attractive force of attraction between the nano particles. This process completely removes of ADG-NH_2 aggregates, enabling effective dispersion. For dispersion of ADG-NH_2, large volume of methanol solvent was used. The base epoxy was then incorporated to the ADG-NH_2 /methanol dispersion and the solution was continuously stirred. Methanol was evaporated from the ADG-NH_2-epoxy solution by using a rotorvap machine which was operated at 45° C [10 bar]. The resulting mixture was then allowed to settle down inside the oven at 45° C under the vacuum at 10 bar and methanol was completely evaporated. A mixing machine with high speed of rotation [ROSS Laboratory High shear mixer [Model 100LH], NY USA] operating at about 20 min to mix the ADG-NH_2 /epoxy. The mixtures were then allowed to settle down on the beaker stand and agglomerates were completely removed. The neat epoxy was treated similarly as the processing stage of ADG-NH_2 different Wt% filler loadings. Then the Hardener Aradur 5052 CH was mixed to the ADG-NH_2 / epoxy solution at a ratio of 100:38, which was mixed again using the mixing machine with high speed of rotation at 3000 RPM for 20 minutes. Then degassing of the suspension was carried out in a vacuum chamber [pressure ~10 bar] at 45° C for approximately 20 min while manual mixing through mechanical stirrer was carried out during the entire process. Mixture was then transferred into an open beaker at room temperature [RT] which was used for preparation of CFRP laminate.

2.3 Fabrication of Composite Laminates

Bidirectional carbon fiber was cut into 4 pieces of 300 mm x 300 mm with 0° / 90° orientation and 8 pieces of 45° /-45° orientation to prepare CFRP Laminate. For fabrication of the laminate a 15 mm thick plane aluminum plate was considered and its top face is cleaned thoroughly with MEK on which the Laminate wet Lay-up process to be carried out. A release film [300 x 300 mm^2] with 15 µm thickness was laid and on it a peel ply [30 micron] was applied. Prepared adhesive resins solution [[ADG-NH_2+ epoxy [LY 5052] + Hardener [5052 CH]] was applied on it using brush mould. Then the first carbon fiber bi-directional woven sheet [in 0° / 90° orientation] kept on the adhesive resin's solution. Then the second carbon fiber layer [at 45° /-45° orientation] was kept over the first carbon fiber layer after applying the adhesive resin solution on the first fabric uniformly with the

help of a brush. To have uniform thickness of laminates and avoid the epoxy starvation between the two carbon layers, the extra number of resins were squeezed with the help of a roller on the carbon fiber woven sheets.

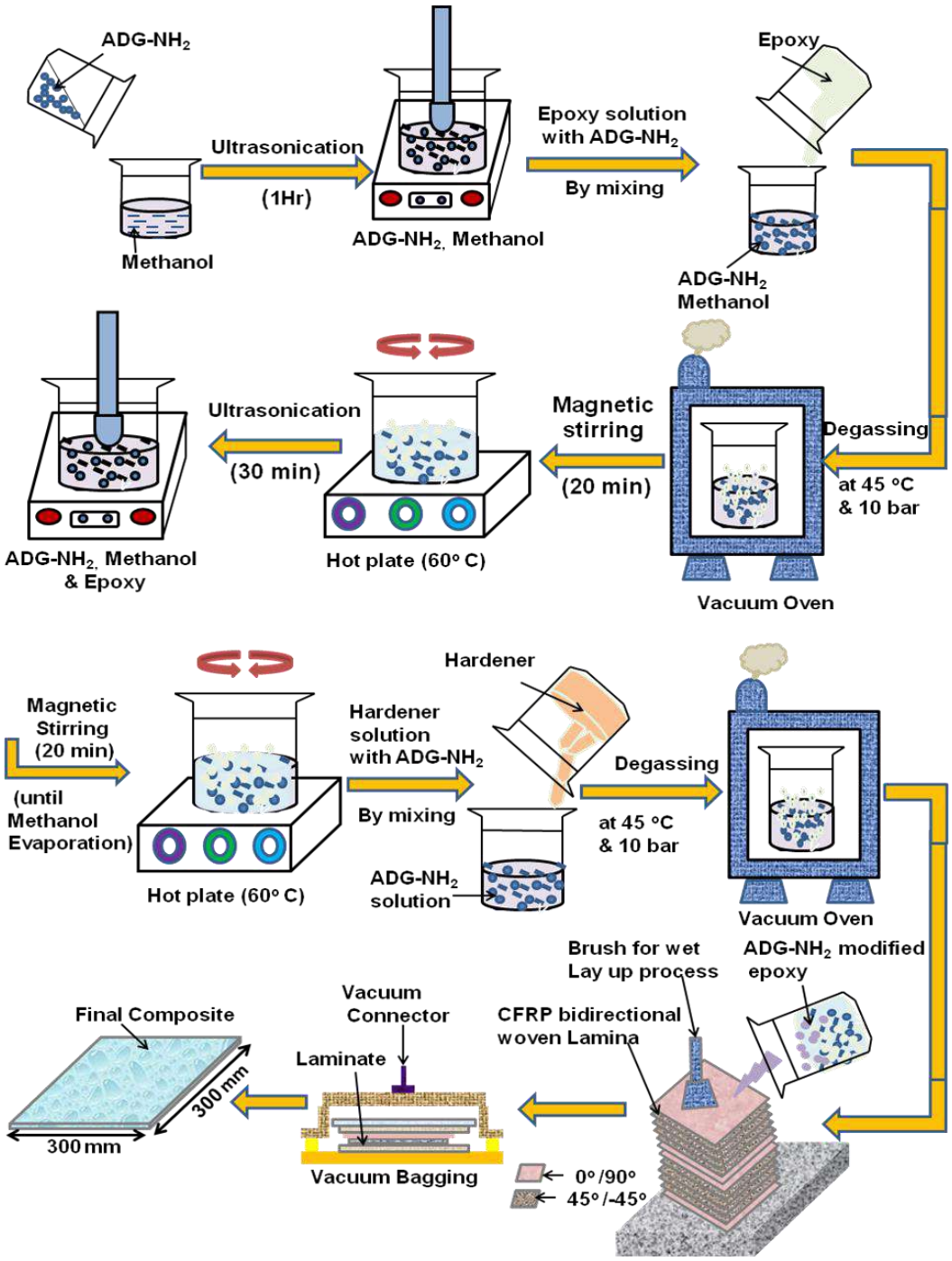

Fig. 1. Schematic diagram of processing of ADG-NH_2 and fabrication of laminated components

The third layer was kept [at 45° /-45° orientation] on the second layer and same procedure was followed. The 4th, 5th and 6th layers were kept at 45° /-45°, -45° /45° and 90° / 0° deg respectively in the same manner and the same procedure was adopted towards the preparation of twelve layers of symmetric cross plied quasi-isotropic CFRP Laminate as shown in Figure 1. After laying twelfth layer, peel ply has to be kept and on it aluminum plate has to be kept on the top. The Carbon fiber/epoxy laminate staking sequence along with fiber orientation and thickness is shown in Figure 1. During the manufacturing of the CFRPs, Vacuum Bagging Technique was used for curing of the whole stack of laminate. In this Vacuum Bagging arrangement, first a mild steel plate was taken and cleaned thoroughly with MEK which was used to form the mould base. After treating this

plate with a mould release agent, for making the mould frame Tacky tape was used, with inlet and outlet tubes. The thickness of the laminates fabricated in this entire process was between 3 to 3.5 mm which meets standard testing requirements. During this process in order to address air entrapment and void formation the laminate was cured at full Vacuum [10 bar]. The laminate was kept at this condition for 24hours curing at Room Temperature. Post curing, Laminate was again cured for 1 hr at 60° C and then again at higher temperature to 120° C for 3 hours. Similar procedure was adopted towards fabrication of other CFRP laminates with different ADG-NH_2/epoxy Wt% [0.25, 0.5, 0.75, & 1]. The average thickness of various fabricated ADG-NH_2/epoxy/CFRP composite Laminates were 3.02, 3.12, 3.23, 3.34, 3.45 mm respectively for pristine, 0.25, 0.5, 0.75 and 1 weight% ADG-NH_2/epoxy. It was noticed that due to increasing addition of ADG-NH_2 loading content the average thickness of fabricated CFRP composite laminate increases minimally. For mechanical and morphological characterization composites were cut into test specimens by means of a high-speed diamond cutter as per the testing standard requirements. The same fabrication technique and identical conditions were adopted for all neat epoxy resin base laminate to compare the performance of graphene content addition.

2.4 Methodology of Characterization Study

2.4.1 Morphology Study of ADG-NH_2 and ADG-NH_2 Enhanced CFRP Composites

To evaluate the characteristics of amine functionalized graphene [ADG-NH_2] nano characterization methodologies such as FT-IR and SEM were carried out. FT-IR spectra of the ADG-NH_2 was carried out using a Hover lab FT-IR spectrophotometer [model No HV-5500] with a 2 cm^{-1}resolution over 64 scans. The surface was checked by using a SEM [ZEISS Microscopy, Germany, [Model EVO 15] with20 kV acceleration voltage of and 2.5 mm working distance. For fractographic characterization, fracture surfaces were gold coated and images were studied using a SEM.

2.4.2 Single Edge Notch Bending Test

SENB testing was conducted to investigate the fracture properties of the modified CFRP composite as shown in Fig. 2. An UTM [kalpak instruments and controls, Pune, India, [Model No 201201] having max load carrying capacity of 50 KN and with the help of a three-point bending fixture as per ASTM D 5045 [37]. During sample preparation a V notch initial-crack of 2 mm length was generated. The laminate was subjected to normal [bending] and crack initiates along the V notch through the pre-crack. A ratio of length to depth of 4:1 and depth to thickness ratio of 2:1 was considered. The test was carried out at a speed of 10 mm/min at room temperature [25°C]. Five identical specimens were tested for each ADG-NH_2 /Epoxy/ CFRP loading wt% and results were reported. The average dimensions of the laminate samples were length x width x thickness 60x12x3 mm^3, respectively with a span length of 48 mm. The diameter of the loading roller and the support roller was 6 mm and 3 mm respectively.

By using equations 1 and 2 the critical Stress Intensity Factor [K_{IC}] and Mode I fracture toughness [G_{IC}] were evaluated as follows. K_{IC} and G_{IC} values were evaluated by conducting single edge notch bending test.

$$K_{IC} = \left\{\frac{PL}{bt^{3/2}}\right\} Y; 0 < Y < 1$$

$$Y = \frac{3(a/t)^{1/2}\left[1.99 - \left(\frac{a}{t}\right)\left(1 - \frac{a}{t}\right)[2.15 - 3.93\left(\frac{a}{t}\right) + 2.7\left(\frac{a}{t}\right)^2\right]}{2\left(1 + 2\frac{a}{t}\right)\left(1 - \frac{a}{t}\right)^{3/2}} \quad (1)$$

$$G_{IC} = \frac{(1 - v^2)K_{IC}^2}{E} \quad (2)$$

Where; K_{IC} : Critical Stress Intensity Factor [MPa m $^{[1/2]}$], G_{IC} : Critical Stress Energy Release Rate [mode I] [J/m^2], P : Critical load for crack propagation [N], L : Length of the span [mm], Y : Geometrical factor, B : Width of specimen [mm], t : Thickness of specimen [mm], a : Pre crack length

[mm], ν : Poisson's ratio for the epoxy resin [taken to be 0.3], and E: Tensile modulus obtained from fracture testing.

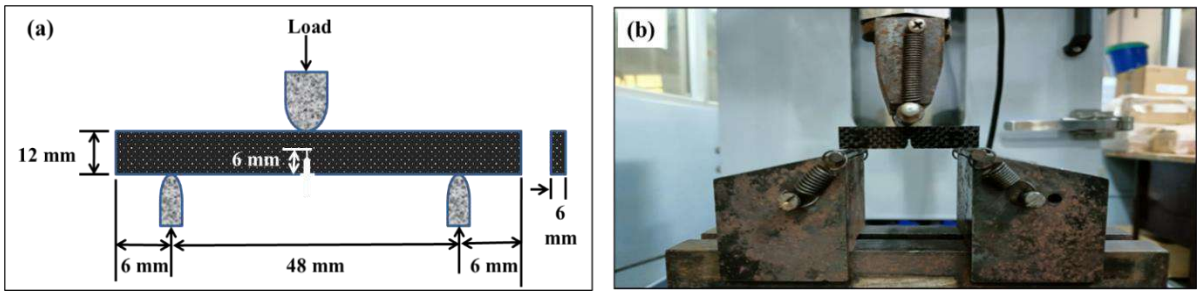

Fig. 2. (a) SENB test ADG-NH_2/epoxy/CFRP composite dimension as per ASTM D5045 and (b)SEBN Test Setup arrangement

2.4.3 Izod Impact Test

As per the ASTM-D256 [38] standard requirement, Izod Impact test specimens were prepared. The Laminate specimens were cut into beam dimensions of thickness x width x length 3 x 12.7x64 mm^3 respectively. According to the testing protocol, the specimen was kept in vertical position and fractured. The initial point of contact was maintained at a specific distance from both the clamp and the midpoint of the notch, ensuring alignment with the notch.

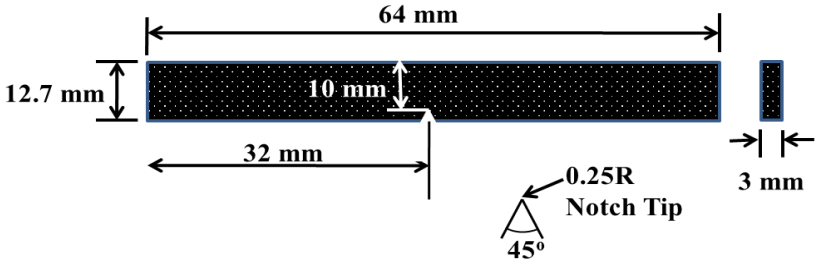

Fig. 3. Specimen dimension of ADG-NH_2/epoxy/CFRP composite impact test

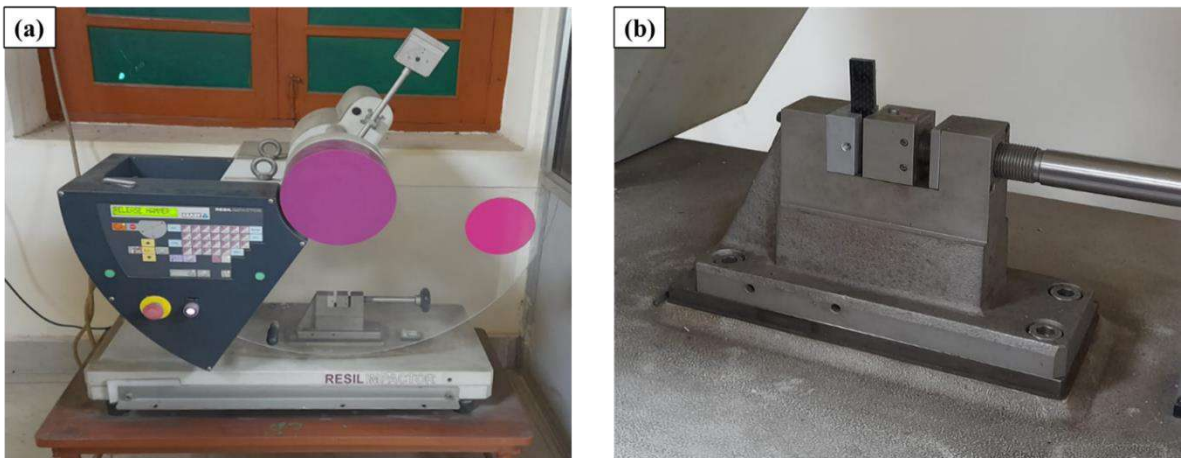

Fig.4. (a) Instron CEAST Resil Impactor (b) Izod Impact test fixture arrangement with ADG-NH2/epoxy/CFRP composite specimen

The notch has been done in a milling machine as per the requirement of the standard as per sketch Fig.3. The impact test was conducted using the RESIL IMPACTOR-50J machine from CEAST Instruments, Torino, Italy. The setup included an Izod impact fixture and a hammer with an energy capacity of 15J, expandable up to 25J [as shown in Fig. 4]. The test was done at an impact speed ranging between 2.9 m/s and 3.7 m/s to evaluate the material's impact resistance under controlled

conditions. Tests were conducted for five identical specimens with ADG-NH_2 /Epoxy/ CFRP loading wt% and then average, standard deviations were considered.

2.4.4 Tensile Test

As per ASTM D3039 standards [39] the tensile properties of ADG-NH_2/Epoxy/CFRP laminates were analysed. Specimens of (length) × (width) × (thickness) i.e 250 X25.4 X 3 mm were prepared as per standard requirements [Refer Fig. 5]. End-tabs were bonded to the rectangular specimens to evaluate the in-plane characteristics of the laminates. Rectangular shaped specimens were chosen over dog-bone-shaped specimens, which tend to split in regions where the width transitions.to mitigate stress concentration introduced by the tension test frame grips, tabs with tapered ends were attached to both sides of the specimens. UTM with 100 kN capacity and constant crosshead speed of 2 mm/min was used to carry out the tensile loading to the specimens. Testing was performed on five identical specimens for each ADG NH_2/Epoxy/CFRP loading wt%, All tests were carefully monitored and conducted at room temperature.

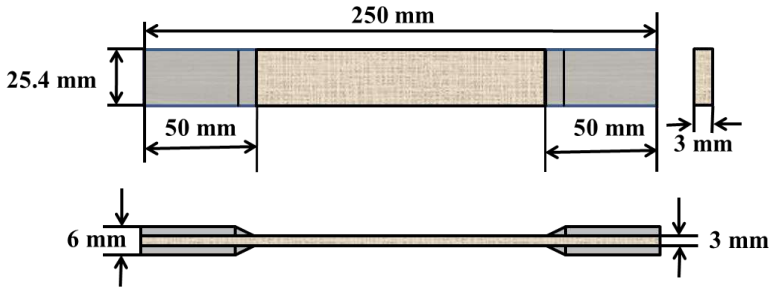

Fig. 5. Schematic diagram of Tensile Test Specimen of ADG-NH_2/epoxy/CFRP composite as per ASTM D3039

3. Results and Discussion

3.1 Morphology study of ADG-NH_2

As received ADG-NH_2 morphology study was carried out via FT-IR analysis to detect functional groups information as shown in Fig.6 [a].

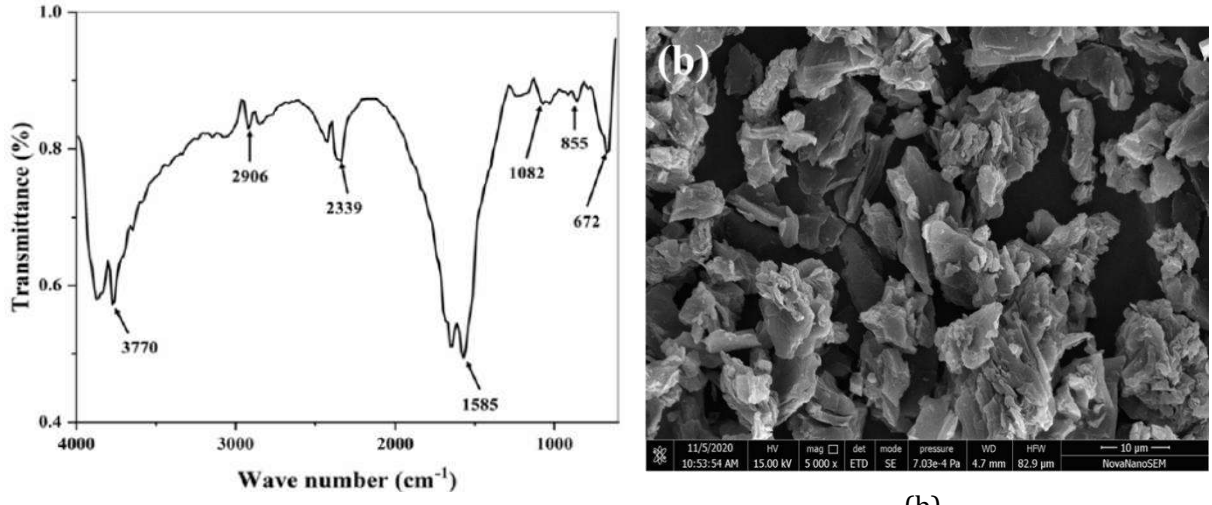

(a) (b)

Fig. 6. (a) FT-IR Spectroscopy and (b) SEM images of amine functionalized graphene [ADG-NH_2]

Micrograph analysis through SEM for the as received ADG-NH_2 with the higher magnification image was carried out [Ref Fig.6 [b]]. The lateral dimensions of functionalized graphene particles were found to be of the order of 5 to 10 µm.

3.2 Fracture toughness and Impact strength properties

CFRP composites possess excellent in-plane mechanical properties which will not be significantly affected by incorporating nano additives into the composite system. Influence of ADG-NH_2 on fracture toughness properties was evaluated by means of SENB test method. K_{IC} and G_{IC} values increase with an increment in ADG-NH_2 loading up to 0.5 wt%.

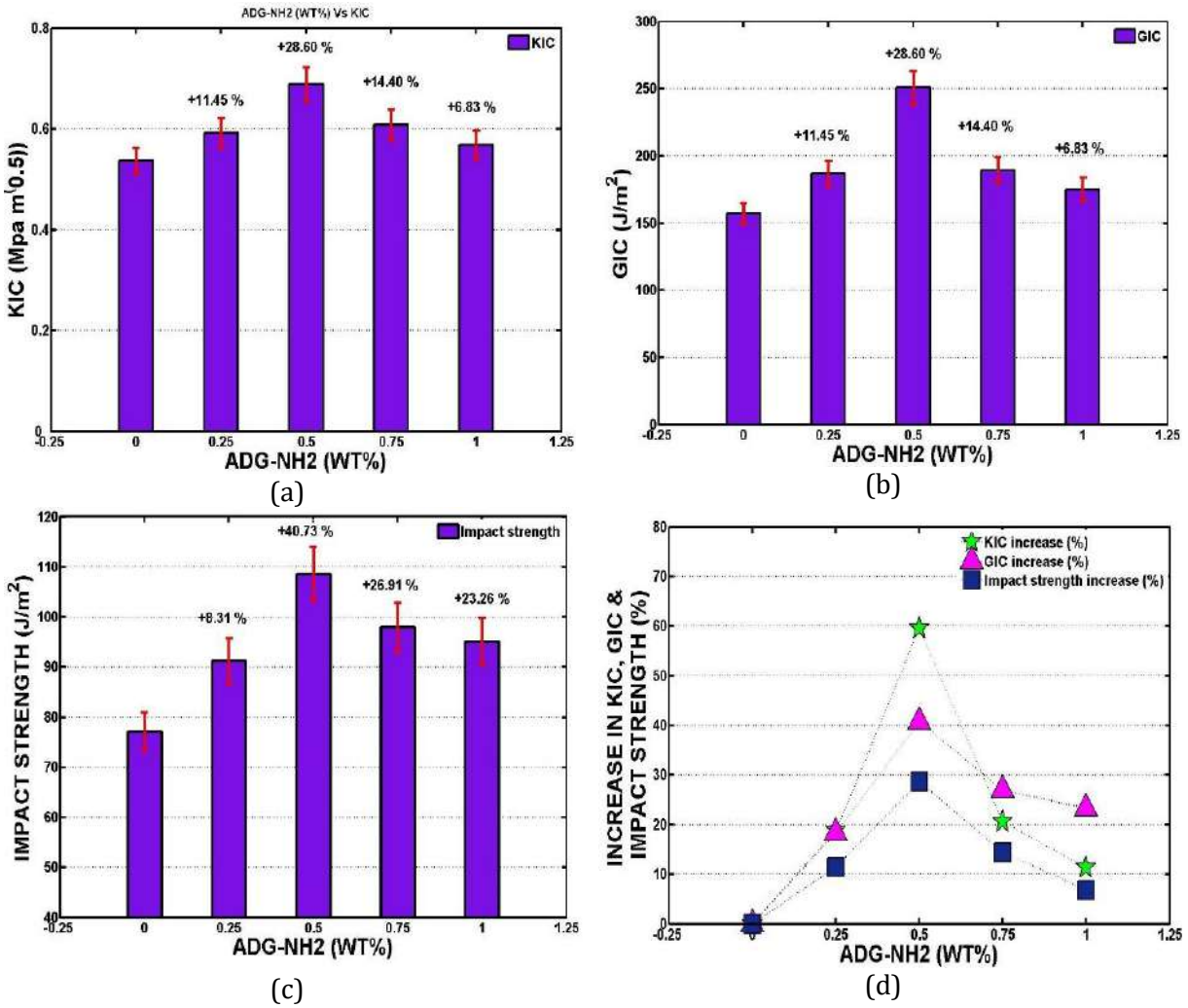

Fig. 7. Variation of (a) Critical stress intensity factor [K_{IC}] (b) Crtical strain energy release rate [G_{IC}] (c) Impact strength [Jm-2] and (d) % increase in K_{IC}, G_{IC}, Impact strength w.r.t ADG-NH_2 addittion in CFRP composite during SENB test

Table 1. Variation of KIC, GIC values observed during the SENB test and Impact strength for different ADG-NH_2 loading relative to the neat epoxy

ADG-NH_2 [wt %]	K_{IC} [MPa $m^{1/2}$]	Increase [%]	G_{IC} [Jm^{-2}]	Increase [%]	Impact strength [Jm-2]	Increase [%]
Neat	0.67± 0.07	0	157.17 ± 7.86	0	77.15± 3.86	0
0.25	0.74± 0.07	11.45	186.67 ± 9.33	18.77	91.27 ± 4.56	18.31
0.5	0.86± 0.09	28.60	250.71 ± 12.54	59.52	108.57 ± 5.43	40.73
0.75	0.76± 0.08	14.40	189.47 ± 9.47	20.56	97.91 ± 4.90	26.91
1	0.71± 0.07	6.83	174.90± 8.74	11.28	95.09 ± 4.75	23.26

Due to the enhanced chemical bonding between the matrix and ADG-NH_2 and better homogeneous dispersion under controlled environment, the fracture stiffness properties of modified laminates were increased significantly that is evident from Fig.7 and Table 1. The impact resistance properties of the ADG-NH_2 / epoxy / CFRP composites are listed in Table 1. An impact strength

value of 77.15 J/m² was observed for neat epoxy CFRP compared to the 108.57 J/m² for 0.5 wt % of ADG-NH_2 / epoxy / CFRP, an increase of nearly 40% to the neat epoxy. A notable increase in the resilience to impact for CFRP composite laminate is because the improved bonding strength of the ADG-NH_2/epoxy resins with carbon fibers.However the impact strength was reduced for ADG-NH_2 of 1 wt % which was 95.09 J/m². As the ADG-NH_2 ratio rises above 0.5 weight percent, there is noticible reduction in the impact resistive property of CFRP composites.The reduction in impact resistance is because of agglomeration that accumulates in the epoxy resin, which results in non-uniform distribution of inclusion leads to degraded adhesion between fiber and matrix [40,41].

In Table 1, The mode I fracture toughness values [K_{IC}& G_{IC}] of the ADG-NH_2/epoxy/CFRP composites were improved by the inclusion of amine functionalised graphene particles compared to neat epoxy CFRP. An enhancement in the fracture resistance values of the ADG-NH_2 / epoxy / CFRP were observed up to a ADG-NH_2 ratio of 0.5 wt % and reduces subsequently beyond 0.5 wt% but increases with respect to base structure. Compared to the neat epoxy CFRP laminate an increase of 28.6% observed in K_{IC} value for 0.5 wt % ADG-NH_2.This enhancement was observed possibly due to the better dispersion and less agglomoration of the functionalised graphene with carbon fiber composite.This homogenous dispersion will leads to better cross linking through chemical bonding between carbon fiber and epoxy . Hence, resulted to increase in Mode I fracture resistance values.

The reduction in Mode I fracture resistance and the limited enhancement in impact strength at higher ADG-NH_2 loading concentrations (0.75% and 1%) indicate ineffective cross-linking and reduced dispersion of the functionalized graphene. This phenomenon has been noted by various researchers, where excessive loading concentrations weaken the mechanical properties because of re-agglomeration and reduced effectiveness of the reinforcement [34, 42, 43].

ADG-NH_2 functionalized nano-additives improve Mode I fracture and impact resistance through mechanisms such as crack bridging, energy absorption, interfacial bonding, and crack deflection. The interaction of additives and matrix is enhanced by surface functionalization, uniform dispersion, optimized curing parameters, and advanced characterization techniques. By understanding these mechanisms and interactions, we can further optimize the performance of CFRP composites for various applications

3.3 Tensile Properties of Neat and ADG-NH_2/CFRP

The tensile properties, such as elastic modulus (E), ultimate tensile strength (UTS), elongation at break (EL), and toughness (T), which were calculated for both base epoxy and ADG-NH_2-modified CFRP. A series of ADG-NH_2 loading concentrations 0.25, 0.5, 0.75, and 1 wt% were analysed to determine their effect.

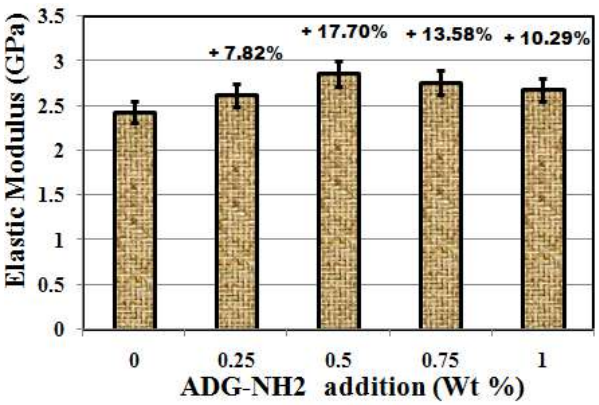

(a)

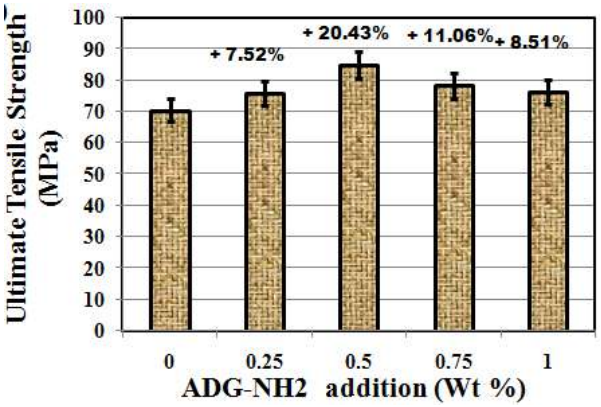

(b)

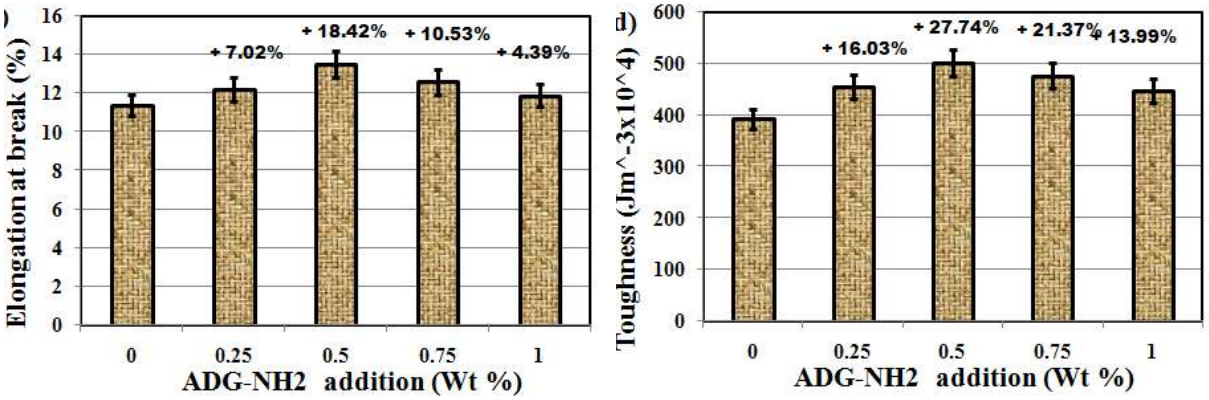

(c) (d)

Fig. 8. [a] Elastic modulus, [b] Ultimate tensile strength, [c] Elongation at break [%], [d] Toughness w.r.t ADG-NH_2 addittion in CFRP composite during tensile test

Figure 8 presents the results, indicating the mechanical properties with respect to filler concentration. The graphs represent the averages of five test samples, with error bars for each concentration. The study revealed slight improvements in tensile performance with the inclusion of amine-functionalized graphene in CFRP laminates. Detailed comparative data, along with the corresponding increments relative to the base epoxy matrix, are summarized in Table 2.

Table 2. Variation of E, UTS, % EL, and T w.r.t ADG-NH_2 addition in CFRP composite under tensile test

ADG-NH_2 [wt%]	Elastic modulus [GPa]	Increase [%]	Ultimate Tensile strength [MPa]	Increase [%]	Elongation at break [%]	Increase [%]	Toughness [J/m^{-3}] x10^4	Increase [%]
0	2.43	0.00	70.5	0.00	11.4	0.00	393	0.00
0.25	2.62	7.82	75.8	7.52	12.2	7.02	456	16.03
0.5	2.86	17.70	84.9	20.43	13.5	18.42	502	27.74
0.75	2.76	13.58	78.3	11.06	12.6	10.53	477	21.37
1	2.68	10.29	76.5	8.51	11.9	4.39	448	13.99

As shown in Figure 8[a] there was a distinct increase in the values of elastic modulus ADG-NH_2 / Epoxy weight% loading content of 0.25, 0.5, 0.75 and 1wt % to a value of 7.82 % , 17.70% , 13.58% and 10.29 % respectively with reference to neat epoxy at room temperature. As reported in Table 2, the properties of the ADG-NH_2 / Epoxy loaded laminate was increased upto 0.5 wt% w.r.t neat epoxy laminate. It shows the decreasing tendency of Elastic Modulus(E), Ultimate tensile strength(UTS), Elonagation at break(EL) and Toughness(T) beyond 0.5 weight% , However there is a substantial increase in the values with respect to pristine epoxy due to addittion of functionalised graphene particles in the CFRP. The integration of functionalized graphene into the epoxy system significantly improves the toughening mechanisms and mechanical properties of CFRP composite laminates, along with a notable increase in stiffness compared to the neat epoxy CFRP composites. Graphene, as a filler, offers an exceptionally large surface area, especially at lower ADG-NH_2 concentrations. The homogeneous dispersion of ADG-NH2 enables further efficient stress transfer, leading to enhanced tensile strength up to 0.5 wt% compared to base epoxy CFRP laminates. Specifically, the UTS values improved by 20.43% for 0.5 wt%, while EL and T increased by 18.42% and 27.74%, respectively, at the same loading level. However, at higher loading concentrations (0.75 wt% and 1 wt%), a decrease in toughness and elongation at break was observed, likely due to non-homogeneous dispersion in the CFRP matrix. The key highlights is the importance of optimal dispersion for maximizing the performance benefits of ADG-NH_2 in these composites.

3.4 Fractography Analysis of ADG-NH_2/CFRP

The fractography analysis certainly reveals the strengthneing mechanism and provides the sufficient corroboration for the fracture toughness improvement with modified ADG-NH_2 in CFRP composite laminate.However, the results clearly show that, when amine-functionalized graphene is added to CFRP composites, the fracture characteristics of the material are improved in comparison to neat carbon fiber reinforced polymer laminates [44,45]. SEM micrograph analysis was carried out to evaluate the failure mechanism and toughening mechanism of the ADG-NH_2 nano material for both neat epoxy and ADG-NH_2/ CFRP with different wt% filler content [0.25, 0.5, 0.75 and 1] [Refer Fig. 9].

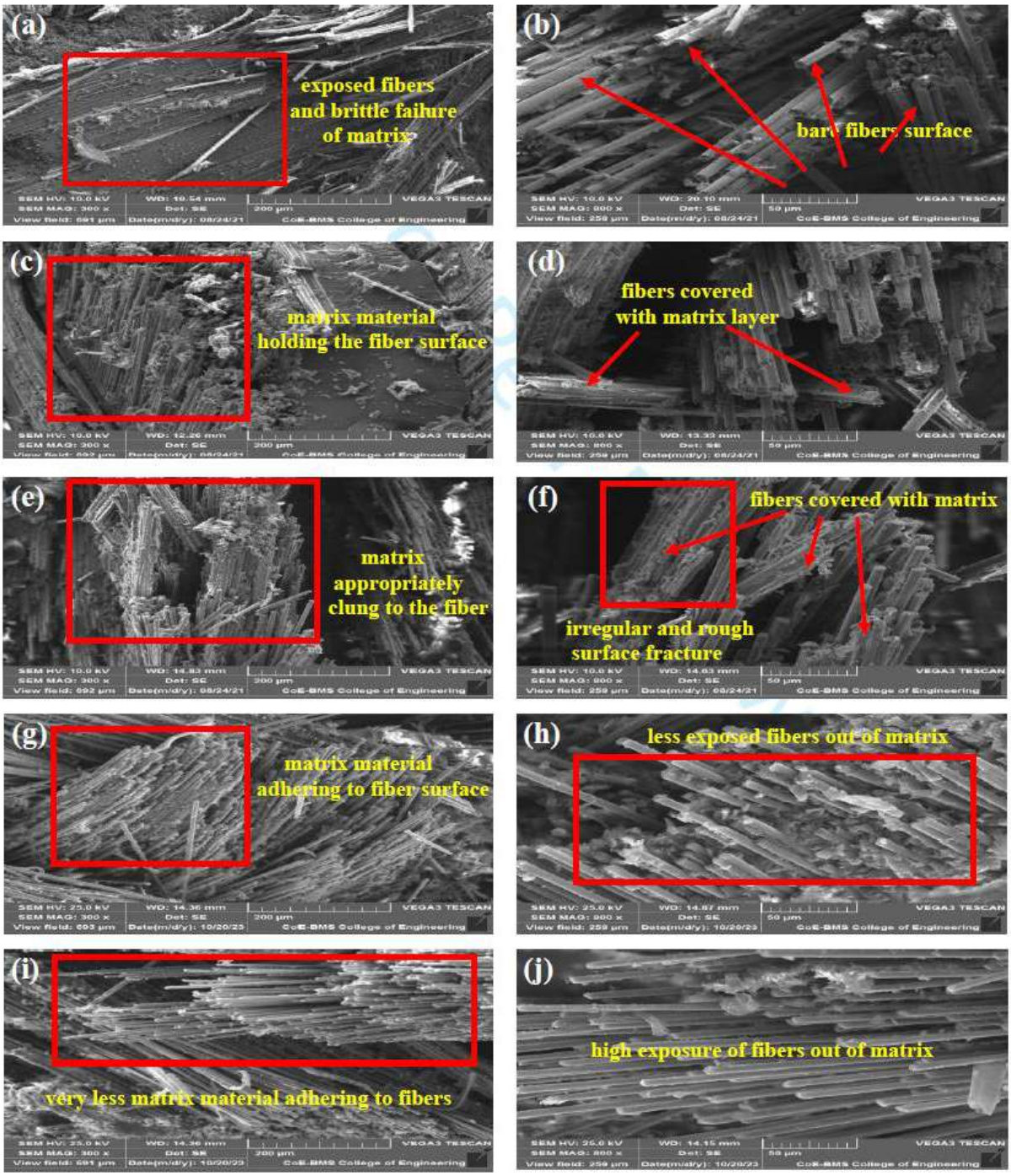

Fig. 9. SEM micrographs [a], [b] neat epoxy CFRP; [c],[d] 0.25 wt % of ADG-NH_2/CFRP; [e],[f] 0.5 wt % of ADG-NH_2/CFRP [g],[h] 0.75 wt % of ADG-NH_2/CFRP; and [i],[j] 1 wt % of ADG-NH_2/CFRP

Neat and ADG-NH_2/CFRP composites epoxy with varying filler levels [0.25, 0.5, 0.75, and 1 weight percent] were examined using SEM examination. Amine-functionalized graphene increases fracture toughness, because of its mechanical strength, surface area, wrinkled structure, and good interfacial adhesion with epoxy. The amine groups improve adhesion with the epoxy matrix also aiding uniform distribution of graphene. At higher concentrations [0.75 and 1 wt%], graphene aggregation causes stress concentration and reduced adhesion, negatively impacting performance. SEM images confirm uniform dispersion in lower concentrations but show exposed fibers and poor bonding at 1 wt%, explaining the decline in mechanical performance at higher filler contents.

SEM pictures show weak mechanical properties due to brittle fracture behavior, exposed carbon fibers, and poor bonding in neat epoxy matrix. In contrast, amine-functionalized graphene strengthens adhesion as demonstrated by the firmly bonded carbon fibers in matrix material as shown in the fractured samples in figure 9 [a], [b], [c], [d], [e] and [f] fractured samples. The sample with 0.5 weight percent graphene exhibits the best interfacial strength and rough fracture surfaces, indicating plastic deformation and crack deflection. Increased surface area and energy absorption during fracture propagation are indicated by dimples, which enhance mechanical characteristics.

Performance is adversely affected by graphene aggregation at higher concentrations [0.75 and 1 weight percent], which results in stress concentration and decreased adhesion in figure 9 [g], [h], [i] and [j]. The decrease in mechanical performance at increasing filler amounts can be explained by SEM pictures, which show exposed fibers and weak bonding at 1 weight percent but demonstrate homogeneous dispersion at lower concentrations.

4. Conclusions

In this study, the effect of amine functionalized graphene [ADG-NH_2] reinforced CFRP composites has been extensively evaluated for fracture toughness, tensile and impact resistance. The mechanical properties of various CFRP specimens with different wt% were also taken under consideration. The experimental findings have been thoroughly scrutinized, leading to the following key conclusions

- An enhancement in mechanical properties is the consequence of introduction of functionalized ADG-NH_2 to the CFRP laminate up to 1 wt% compared to neat epoxy based CFRP composites.
- For every 0.5 weight percent of ADG-NH_2 reinforced CFRP, the K_{IC} and G_{IC} values increased up to approximately 29% and 60%, respectively, but decreased at higher concentrations [0.75 wt% & 1 wt%]. Nonetheless, there is gain in the G_{IC} and K_{IC} values with respect to the base CFRP laminate.
- Compared to neat epoxy CFRP composite laminates, it was determined that 0.5% weight percentage of ADG-NH_2 graphene CFRP laminates increased impact strength by about 41%.
- The tensile characteristics of the 0.5% weight percentage of ADG-NH_2 graphene CFRP laminates showed significant improvements, with an ~18% increase in elastic modulus, ~21% enhancement in UTS, ~19% rise in EL, and ~28% boost in T compared to neat epoxy CFRP composites. These enhancements are attributed towards the superior interaction and bonding at the interface of fiber/matrix. In contrast, the neat epoxy CFRP composites exhibited weaker performance.
- Fractographic analysis demonstrates enhanced adhesion mechanisms and uniform dispersion of amine functionalization of graphene [ADG-NH_2] aiding an improvement in mechanical and thermal properties of CFRP laminate.
- Due to better mechanical properties, thermal stability and durability, ADG-NH_2 reinforced CFRP composites have various prominent industrial applications such as aerospace, automotive, construction and Sports Equipment etc. However, addressing scalability challenges such as cost-effective production, uniform dispersion, interfacial bonding, environmental impact, and regulatory compliance is crucial for their successful implementation.

5. Limitations and Scope for Future Work

During the current research study various assumptions made e.g., uniform additive dispersion, specific impact conditions, consistent hand layup process, room temperature curing etc. Hence, this research study can be extended further for testing under varied environmental test conditions such as temperature, humidity, or UV exposure, optimizing dispersion techniques, or exploring other additive concentrations, quantitative data for analyzing fracture surfaces [e.g., particle distribution, void content, or interfacial adhesion strength], and detailed statistical analyses for the experimental results should be explored in the future to gain deeper insights into the mechanical performance improvements of modified CFRP composites.

References

[1] Li N, Wang G dong, Melly SK, Peng T, Li YC, Di Zhao Q, et al. Interlaminar properties of GFRP laminates toughened by CNTs buckypaper interlayer. Compos Struct. 2019 Jan 15; 208:13-22. https://doi.org/10.1016/j.compstruct.2018.10.002

[2] Ou Y, González C, Vilatela JJ. Interlaminar toughening in structural carbon fiber/epoxy composites interleaved with carbon nanotube veils. Compos Part A Appl Sci Manuf. 2019 Sep 1; 124:105477. https://doi.org/10.1016/j.compositesa.2019.105477

[3] Sayam A, Rahman ANMM, Rahman MdS, Smriti SA, Ahmed F, Rabbi MdF, et al. A review on carbon fiber-reinforced hierarchical composites: mechanical performance, manufacturing process, structural applications and allied challenges. Carbon Letters. 2022 Aug 7; 32[5]:1173-1205. https://doi.org/10.1007/s42823-022-00358-2

[4] Bhanuprakash L, Parasuram S, Varghese S. Experimental investigation on graphene oxides coated carbon fibre/epoxy hybrid composites: Mechanical and electrical properties. Compos Sci Technol. 2019 Jul 28; 179:134-44. https://doi.org/10.1016/j.compscitech.2019.04.034

[5] Chiou YC, Chou HY, Shen MY. Effects of adding graphene nanoplatelets and nanocarbon aerogels to epoxy resins and their carbon fiber composites. Mater Des. 2019 Sep 15;178:107869. https://doi.org/10.1016/j.matdes.2019.107869

[6] Ackermann AC, Demleitner M, Guhathakurta J, Carosella S, Ruckdäschel H, Simon S, et al. Mechanical, thermal, and electrical properties of amine- and non-functionalized reduced graphene oxide/epoxy carbon fiber-reinforced polymers. Polym Compos. 2023 Aug 31; 44[8]:4937-54. https://doi.org/10.1002/pc.27461

[7] Anand Raj MK, Muthusamy S, Panchal H, Mahmoud Ibrahim AM, Alsoufi MS, Elsheikh AH. Investigation of mechanical properties of dual-fiber reinforcement in polymer composite. Journal of Materials Research and Technology. 2022 May; 18:3908-15. https://doi.org/10.1016/j.jmrt.2022.04.053

[8] Cao D, Malakooti S, Kulkarni VN, Ren Y, Liu Y, Nie X, et al. The effect of resin uptake on the flexural properties of compression molded sandwich composites. Wind Energy. 2022 Jan 20;25[1]:71-93. https://doi.org/10.1002/we.2661

[9] Mohammed Iqbal Shueb, Mohd Edeerozey Abd Manaf, Mahathir Mohamed, Noraiham Mohamad, Jeeferie Abd Razak, Nurhernida Abdullah Sani, et al. Thermal Characterization of Non-Functionalized Low Content Graphene Nanoplatelets [GNP] Added Nylon 66 Polymer. Journal of Advanced Research in Fluid Mechanics and Thermal Sciences. 2021 Dec 5; 89[1]:13-25. https://doi.org/10.37934/arfmts.89.1.1325

[10] Madarvoni S, PS Rama S. Dynamic mechanical behaviour of graphene, hexagonal boron nitride reinforced carbon-kevlar, hybrid fabric-based epoxy nanocomposites. Polymers and Polymer Composites. 2022 Jan 7; 30:096739112211072. https://doi.org/10.1177/09673911221107289

[11] Monteiro SN, Calado V, Rodriguez RJS, Margem FM. Thermogravimetric behavior of natural fibers reinforced polymer composites-An overview. Materials Science and Engineering: A. 2012 Nov 15; 557:17-28. https://doi.org/10.1016/j.msea.2012.05.109

[12] Alexopoulos ND, Paragkamian Z, Poulin P, Kourkoulis SK. Fracture related mechanical properties of low and high graphene reinforcement of epoxy nanocomposites. Compos Sci Technol. 2017 Sep 29; 150:194-204. https://doi.org/10.1016/j.compscitech.2017.07.030

[13] Wang F, Drzal LT, Qin Y, Huang Z. Mechanical properties and thermal conductivity of graphene nanoplatelet/epoxy composites. J Mater Sci. 2015 Feb 28; 50[3]:1082-93. https://doi.org/10.1007/s10853-014-8665-6

[14] Papageorgiou DG, Kinloch IA, Young RJ. Mechanical properties of graphene and graphene-based nanocomposites. Prog Mater Sci. 2017 Oct 1; 90:75-127. https://doi.org/10.1016/j.pmatsci.2017.07.004

[15] Alam A, Wan C, McNally T. Surface amination of carbon nanoparticles for modification of epoxy resins: plasma-treatment vs. wet-chemistry approach. EurPolym J. 2017 Feb 1;87:422-48. https://doi.org/10.1016/j.eurpolymj.2016.10.004

[16] Li Z, Chu J, Yang C, Hao S, Bissett MA, Kinloch IA, et al. Effect of functional groups on the agglomeration of graphene in nanocomposites. Compos Sci Technol. 2018 Jul;163:116-22. https://doi.org/10.1016/j.compscitech.2018.05.016
[17] Burger N, Laachachi A, Ferriol M, Lutz M, Toniazzo V, Ruch D. Review of thermal conductivity in composites: Mechanisms, parameters and theory. Prog Polym Sci. 2016 Oct 1;61:1-28. https://doi.org/10.1016/j.progpolymsci.2016.05.001
[18] Ma J, Meng Q, Zaman I, Zhu S, Michelmore A, Kawashima N, et al. Development of polymer composites using modified, high-structural integrity graphene platelets. Compos Sci Technol. 2014 Jan 31;91:82-90. https://doi.org/10.1016/j.compscitech.2013.11.017
[19] Ahmadi-Moghadam B, Sharafimasooleh M, Shadlou S, Taheri F. Effect of functionalization of graphene nanoplatelets on the mechanical response of graphene/epoxy composites. Materials & Design [1980-2015]. 2015 Feb 5;66[PA]:142-9. https://doi.org/10.1016/j.matdes.2014.10.047
[20] Fang H, Bai SL, Wong CP. Microstructure engineering of graphene towards highly thermal conductive composites. Compos Part A Appl Sci Manuf. 2018 Sep 1; 112:216-38. https://doi.org/10.1016/j.compositesa.2018.06.010
[21] Shen L, Zhang X, Lei Y, Liang M, Chen Y, Chen W, et al. Efficient reinforcement of epoxy resin with amine-rich rigid short-chain grafted graphene oxide. Polym Compos [Internet]. 2021 Sep 1 [cited 2024 Jun 13];42[9]:4775-85. https://doi.org/10.1002/pc.26186
[22] Costa U, Nascimento L, Almeida Bezerra W, de Oliveira Aguiar V, Pereira A, Monteiro S, et al. Dynamic Mechanical Behavior of Graphene Oxide Functionalized Curaua Fiber-Reinforced Epoxy Composites: A Brief Report. Polymers [Basel]. 2021 Jun 7;13[11]:1897. https://doi.org/10.3390/polym13111897
[23] Han JH, Zhang H, Chen MJ, Wang D, Liu Q, Wu QL, et al. The combination of carbon nanotube buckypaper and insulating adhesive for lightning strike protection of the carbon fiber/epoxy laminates. Carbon N Y. 2015 Nov 1;94:101-13. https://doi.org/10.1016/j.carbon.2015.06.026
[24] Seyyed Monfared Zanjani J, Saner Okan B, Pappas PN, Galiotis C, Menceloglu YZ, Yildiz M. Tailoring viscoelastic response, self-heating and deicing properties of carbon-fiber reinforced epoxy composites by graphene modification. Compos Part A Appl Sci Manuf [Internet]. 2018 Mar 1 [cited 2024 Jun 13];106:1-10. https://doi.org/10.1016/j.compositesa.2017.12.008
[25] Moriche R, Jiménez-Suárez A, Sánchez M, Prolongo SG, Ureña A. Graphene nanoplatelets coated glass fibre fabrics as strain sensors. Compos Sci Technol. 2017 Jul 7;146:59-64. https://doi.org/10.1016/j.compscitech.2017.04.019
[26] Reghat M, Fuss FK, Middendorf P, Bjekovic R, Hyde L, Hameed N, et al. Strain monitoring in reduced graphene oxide-coated glass fiber/epoxy composite. Polym Compos [Internet]. 2022 Nov 1 [cited 2024 Jun 13];43[11]:7913-27. https://doi.org/10.1002/pc.26918
[27] Rodríguez-González JA, Rubio-González C. Influence of graphene nanoplatelet concentration on the electrical, mechanical, and piezoresistive properties of glass fiber/epoxy composites. Polym Compos. 2022 May 1;43[5]:3276-89. https://doi.org/10.1002/pc.26616
[28] Khan T, Ali MA, Irfan MS, Khan KA, Liao K, Umer R. Resin infusion process monitoring using graphene coated glass fabric sensors and infusible thermoplastic and thermoset matrices. Polym Compos [Internet]. 2022 May 1 [cited 2024 Jun 13];43[5]:2924-40. https://doi.org/10.1002/pc.26587
[29] Pérez I, Flores S, Ortiz C, Rivero M, Corona JE, Oliva AI, et al. Processing-structure-property relationship of multilayer graphene sheet thermosetting nanocomposites manufactured by calendering. Polym Compos [Internet]. 2022 Feb 9 [cited 2024 Jun 13];43[4]:2150-62. https://doi.org/10.1002/pc.26528
[30] Hong J, Xu P. Electromagnetic interference shielding anisotropy of unidirectional CFRP composites. Materials [Internet]. 2021 Apr 2 [cited 2024 Jun 13];14[8]. https://doi.org/10.3390/ma14081907
[31] Uppin VS, Gouda PSS, Kittur MI, Andriyana A, Ang BC, Parveez B, et al. Mechanical Response of Glass-Epoxy Composites with Graphene Oxide Nanoparticles. Materials 2022, Vol 15, Page 8545 [Internet]. 2022 Nov 30 [cited 2024 Jun 13];15[23]:8545. https://doi.org/10.3390/ma15238545
[32] Domun N, Hadavinia H, Zhang T, Liaghat G, Vahid S, Spacie C, et al. Improving the fracture toughness properties of epoxy using graphene nanoplatelets at low filler content. Nanocomposites. 2017 Jul 3;3[3]:85-96. https://doi.org/10.1080/20550324.2017.1365414
[33] Nitin MS, Suresh Kumar S. Ballistic performance of synergistically toughened Kevlar/epoxy composite targets reinforced with multiwalled carbon nanotubes/graphene nanofillers. Polym Compos. 2022 Feb 1;43[2]:782-97. https://doi.org/10.1002/pc.26409
[34] Rafiee MA, Rafiee J, Wang Z, Song H, Yu ZZ, Koratkar N. Enhanced mechanical properties of nanocomposites at low graphene content. ACS nano. 2009 Dec 22;3[12]:3884-90. https://doi.org/10.1021/nn9010472
[35] Zandiatashbar A, Picu RC, Koratkar N. Mechanical behavior of epoxy-graphene platelets nanocomposites,J.Eng.Mater.Technol.,2012,134,031011. https://doi.org/10.1115/1.4006499

[36] Li Z, Wang R, Young RJ, Deng L, Yang F, Hao L, Jiao W, Liu W. Control of the functionality of graphene oxide for its application in epoxy nanocomposites. Polymer. 2013 Nov 1;54[23]:6437-6446. https://doi.org/10.1016/j.polymer.2013.09.054
[37] ASTM D. 5045-14; Standard Test Methods for Plane-Strain Fracture Toughness and Strain Energy Release Rate of Plastic Materials. ASTM: West Conshohocken, PA, USA. 2014.
[38] ASTM D 256 Standard Test Methods for Determining the Izod Pendulum Impact Resistance of Plastics. ASTM International, West Conshohocken, PA. 1998:19428-2959.
[39] ASTM D3039, "Standard Test Method for Tensile properties of Polymer Matrix Composite Materials". In Annual book of American society of Testing Materials, Vol. 15, ASTM, West Conshohocken, PA, USA, 2002
[40] Yue L, Pircheraghi G, Monemian SA, Manas-Zloczower I. Epoxy composites with carbon nanotubes and graphene nanoplatelets - Dispersion and synergy effects. Carbon N Y. 2014 Nov 1;78:268-78. https://doi.org/10.1016/j.carbon.2014.07.003
[41] Kamble Z, Behera BK, Mishra R, Behera PK. Influence of cellulosic and non-cellulosic particle fillers on mechanical, dynamic mechanical, and thermogravimetric properties of waste cotton fibre reinforced green composites. Compos B Eng. 2021 Feb 15;207:108595. https://doi.org/10.1016/j.compositesb.2020.108595
[42] Gojny FH, Wichmann MH, Fiedler B, Schulte K. Influence of different carbon nanotubes on the mechanical properties of epoxy matrix composites-a comparative study. Composites science and technology. 2005 Dec 1;65[15-16]:2300. https://doi.org/10.1016/j.compscitech.2005.04.021
[43] Johnsen BB, Kinloch AJ, Mohammed RD, Taylor AC, Sprenger S. Toughening mechanisms of nanoparticle-modified epoxy polymers. Polymer. 2007 Jan 12;48[2]:530-41. https://doi.org/10.1016/j.polymer.2006.11.038
[44] Szeluga U, Kumanek B, Trzebicka B. Synergy in hybrid polymer/nanocarbon composites. A review. Compos Part A Appl Sci Manuf. 2015 Jun 1;73:204-31. https://doi.org/10.1016/j.compositesa.2015.02.021
[45] Gheid Y, Chemami A, Gaagaia D, Aouaichia H, Gheid Y, Chemami A, Gaagaia D, Aouaichia H. Effects of seawater and acidic environment on mechanical properties of iron powder-loaded glass-epoxy composite laminates: Experimental and analytical investigation. Research on Engineering structures & Materials. 2024;11:12. https://doi.org/10.17515/resm2024.116me1207rs

Blank Page

Research on Engineering Structures & Materials
www.jresm.org
Research Group

Research Article

Strength and characterization studies on nano-silica and steel fibre reinforced bacterial concrete: An eco-friendly and sustainable approach

Pooja Damodaran [a], Yuvaperiyasamy Mayilsamy [*,b]

Saveetha School of Engineering, Saveetha Institute of Medical and Technical Sciences, Saveetha University, Chennai, Tamil Nadu, 602105, India

Article Info

Article History:

Received 02 Feb 2025

Accepted 07 Mar 2025

Keywords:

Bacillus subtilis;
Characterization;
Nano silica;
Steel fibre;
Strength

Abstract

The growing need for environmentally friendly building materials has prompted the creation of creative methods to enhance concrete's mechanical qualities and ecological sustainability. With a focus on its eco-friendliness and sustainability, this research examines the mechanical characteristics and qualities of bacterial concrete augmented with steel fibers (SF) and nano-silica (NS). NS is used at 1%, 2%, 3%, and 4% together with 1% of SF to improve the mechanical strength and durability of concrete. It is well-known for its pozzolanic activity and capacity to refine pore architectures. In this research, tests for compressive, flexural, impact, bond, and splitting-tensile strength are evaluated. Microstructural characterization conducted using techniques such as SEM with EDS on the optimized mix confirms the improved pore structure and calcite ($CaCO_3$) deposition. Comparing the findings of bacterial concrete with the control mix, the addition of 2% NS and 1% SF enhances the compressive strength by 14.17%, the splitting tensile strength by 8.69%, and the flexural strength by 12.16%. This study therefore emphasizes the possibility of combining microbiological, SF, and NS technologies to create cutting-edge green concrete solutions.

© 2025 MIM Research Group. All rights reserved.

1. Introduction

Concrete's strength, versatility, affordability, and durability make it an essential part of modern structures [1-3]. It serves as the cornerstone for the development of infrastructure everywhere. However, since cement manufacturing produces carbon dioxide emissions that make up over 7% of global CO_2 emissions, its widespread usage poses serious environmental difficulties [4]. Furthermore, there are environmental concerns associated with the mining of natural aggregates, which comprise 70–80% of the volume of concrete [5], [6]. Innovative and sustainable methods are required to reduce the environmental effect of concrete manufacturing while preserving structural performance. However, because of things like autogenous shrinkage, freeze-thaw cycles, and mechanical compressive and tensile pressures, concrete is still prone to breaking [7], [8]. The cementitious matrix may be compromised by microcracks, which allow fluids like water and chemical solutions (sulfates, chlorides, and acids) to penetrate the concrete without substantially weakening it. This may lead to the corrosion of embedded steel reinforcing [9]. Cracks affect structural safety by compromising the materials' mechanical strength and durability. Different kinds of bacteria have recently been added to concrete compositions to boost durability and fracture mending [10]. The nutrient composition of culture media and the bacterial species significantly influence urease activity and, consequently, microbial induced calcite precipitation (MICP).

*Corresponding author: yuvaperiyasamyvsb@gmail.com
[a]orcid.org/0009-0000-8028-0759; [b]orcid.org/0000-0002-9667-7192
DOI: http://dx.doi.org/10.17515/resm2025-652ma0202rs

Three primary techniques are used to introduce bacteria into concrete for self-healing: direct incorporation into the mix, encapsulation to delay activation, and surface application via spraying or injection onto cracked areas [11]. In these approaches, it is essential to supply an organic nutrient, such as yeast extract, along with a urea medium positioned near the bacteria to support cellular growth and activity. Additionally, calcification and biomineralization processes of $CaCO_3$ occur in two primary forms: autotrophic and heterotrophic $CaCO_3$ precipitation [12-15]. The typical pH of concrete mixtures is approximately 12, which limits the suitability of specific strains of alkaliphilic bacteria for $CaCO_3$ production. Bacterial precipitation is influenced by variables that modify the pH of concrete.

The ability of bacterial ureolysis to increase $CaCO_3$ precipitation capacity has been the subject of several investigations. The synthesis of the urease enzyme causes calcium carbonate to precipitate in almost all bacteria. The identification of bacterial species that maximize biomineralization and the immobilization of healing agents, such as bacteria and calcium supplies, has been the main focus of research on self-healing concrete. Rice husk concrete has been treated with Bacillus aerius to increase its durability [16]. Additionally, other bacterial strains such as Bacillus megaterium [17], [18], Bacillus sphaericus [19], and Sporosarcina pasteurii [20] have been used in self-healing concrete, with crack-width healing of around 0.3 to 0.5 mm. Bacterial spore survival is restricted during cement setting by a steady reduction in pore diameter, which falls below 1 μm, which is about the size of Bacillus spores. Because the hole size is too small for the bacteria to survive, they are rendered non-viable after seven days of cure [21]. Bacterial spore survival is restricted during cement setting by a steady reduction in pore diameter, which falls below 1 μm, which is about the size of Bacillus spores. Because the pores are too small for the bacteria to survive, they are rendered non-viable after seven days of cure [22]. By filling micropores, bacteria may increase the mechanical strength and longevity of concrete by decreasing its permeability to water and other substances. Incorporating bacteria into cement-based materials provides an economical and ecologically friendly way to extend the life of structures. Because of the cement industry's substantial carbon emissions, environmentally acceptable substitutes like fly ash and slag are required [23].

Additionally, nanoscale materials, such as NS, may enhance both the environmental sustainability and the quality of concrete [24], [25]. Incorporating fibres, whether natural or synthetic, offers another possibility for enhancing concrete performance [26-28]. SF, in particular, are compelling due to their high tensile strength and ductility, which help to prevent crack propagation and improve behavior after cracking occurs [29]. Certain studies have employed urease-based treatments to enhance concrete surface durability [30-32]. Adding bacteria to concrete has shown promise in enhancing its self-healing qualities, reducing microcracks, and boosting its overall durability [33], [34]. By forming calcium silicate hydrate (C-S-H) gels via a reaction with calcium hydroxide, NS plays a vital function in concrete technology by increasing strength. Its high-water absorption, however, may impact workability; this problem is often addressed by adding fly ash. High-performance and ultrahigh-performance concrete applications benefit greatly from this mixture as it increases flowability and early-age strength [35], [36]. A classic hybrid model (HRL) that uses recycled coarse aggregates has also been created, along with three novel sustainable hybrid deep beam models (CRV, ARC1, ARC2). Improvements in flexural toughness (up to 71%), effective stiffness (1.5–9%), and failure capacity (up to 22%) were reported. Directional cracking was considerably reduced by inclined stirrups, and the proposed models show promise for use in prestressed beams, precast walls, and constructions with numerous focused loads [37]. A new sustainable arching hybrid deep beam model has been shown, which uses recycled coarse aggregate (0%, 50%, 100% RCA) in certain places and steel fiber concrete (1% SFC) in high-stress locations. Testing of seven specimens was conducted using mid-span static loading (a/d = 1.7) with an emphasis on stiffness, ductility, failure load, and cracking behavior. Compared to conventional deep beams, the model showed significant improvements, with peak gains of 100% in toughness, 11% in stiffness, and 46% in ductility [38]. This investigation presents a hybrid sustainable deep beam model that incorporates recycled coarse aggregates (RCA) at replacement levels of 0%, 50%, and 100%. The experimental findings indicated that the introduced arched hybrid model enhanced capacity by as much as 19.7% and flexural toughness by as much as 62.1% when compared to the

traditional model. The proposed model also exhibited a flexural failure mode, establishing it as a feasible choice for sustainable precast deep beams [39].

The novelty of this study investigates a sustainable and eco-friendly approach to concrete design that integrates NS, SF, and self-healing technology. The purpose this study is to assess the effect of these components on the mechanical characteristics and self-healing capacities of the material. The research will look at various NS (1, 2, 3, and 4%) concentrations along with bacteria and 1% SF. The outcomes of this research aim to advance the creation of durable and sustainable concrete structures with improved self-healing characteristics, addressing significant challenges related to durability and environmental sustainability.

2. Materials Used and Mix Proportion

Grade 53 Ordinary Portland cement, as per IS 8112 (2013), was utilized for the experimental analysis. Specific gravity, setting time, standard consistency, compressive strength, and soundness tests were conducted following IS: 1727-1967 and IS: 4031-1968 standards. NS functioned as the binder material, improving the economic feasibility of the concrete and decreasing the CO_2 emissions associated with the final product. Table 1 displays the physiochemical characteristics of grade 53 cement and NS. Following the guidelines provided by IS 383:1970, fine aggregate from a nearby M-sand quarry was used in the investigation. In Table 2, the characteristics of the coarse and fine particles utilized in the concrete mix are shown. For mixing all of the concrete ingredients, tap water—which was considered typical and accessible on college property—was used. With their characteristics indicated in Table 3, SF was used as a reinforcing material at a weight ratio of 1% to cement to increase the strength of the concrete.

Table 1. Physiochemical properties of OPC and NS

Physiochemical Properties	OPC	NS
Specific gravity	3.18	2.3
Initial setting time (mins)	38	-
Final setting time (mins)	334	-
Standard consistency	32%	-
Soundness (mm)	0.96	-
MgO	1.31	0.21
Al_2O_3	5.02	0.004
CaO	65.00	0.05
SiO_2	22.02	99.39
SO_3	1.83	-
$CaSO_4$	3.89	-
Chlorides	0.02	0.009
LOI	1.14	0.66
Na_2O	0.20	0.48
Alkalies	0.79	-

Table 2. Properties of fine and coarse aggregates

Properties	Fine Aggregate (M-sand)	Coarse Aggregate (Granite)
Particle size (mm)	4.75	12.5
Fineness modulus	2.52	6.65
Specific gravity	2.64	2.68
Bulk density (g/cm^3)	1.59	1.56
Zone	III	-

Table 3. Properties of SF

Properties	Description
Ult. tensile strength (MPa)	900
Elastic modulus (GPa)	210
Diameter (mm)	0.5
Aspect ratio	60
Elastic modulus (GPa)	210
Length (mm)	30

2.1. Preparation of the Bacteria Culture

The preparation of a sterile and nutrient-rich medium commences with the selection of either Luria-Bertani (LB) broth or nutrient broth as the growth medium. The medium is transferred into sterilized culture bottles, which are sealed to prevent contamination. The prepared medium is autoclaved at 121°C for 15–20 minutes to eliminate unwanted microorganisms. After sterilization, it should be permitted to cool to room temperature prior to advancing to the subsequent step. Bacillus subtilis strips from the HI-media laboratory are introduced into the medium under strict aseptic conditions to initiate bacterial growth. Following inoculation, the medium is placed in a shaking incubator that is kept at 37°C and has a controlled shaking speed of 150–200 rpm to promote enough aeration and ideal bacterial growth. The bacterial culture is continuously incubated for 12 to 24 hours, which expedites its transition to an active growth phase. Bacterial growth is assessed using a spectrophotometer and optical density (OD) measurements at a wavelength of 600 nm. Maximum bacterial activity is an indication that the culture has entered the exponential (log) phase, which is indicated by an OD measurement between 0.6 and 0.8. By dilution with sterile saline or distilled water as needed, the culture is now adjusted to attain the desired concentration of 10^7 CFU/ml. After confirming the concentration by serial dilutions, the plates are spread out on nutritional agar. Bacterial colonies are counted after plates are incubated for 24 hours at 37°C to confirm the CFU/ml accuracy. After confirmation, the bacterial culture is quickly ready to be added to the concrete mixture in order to guarantee its viability. By replacing 10% of the concrete mix's water content, the bacterial solution promotes efficient integration. To make a slurry, water is combined with a 10% bacterial solution that contains 10^7 CFU/ml of Bacillus subtilis spores. The M25 grade requirements outlined in IS 10269 (2009) are met by the concrete mixture. As seen in Table 4, which contrasts the control mix with the alternative mix that incorporates steel fibers (SF), Bacillus subtilis, and nano-silica (NS) to enhance durability and self-healing properties, the mix proportions are carefully determined.

Table 4. Mix proportion

Mix ID	Cement	NS	SF	M-sand	CA	Water	B.Subtilis (10^7 CFU/ml)
N0	391	-	-	574.5	1246	192	-
N1	383.18	1%	1%	574.5	1246	172.8	19.2
N2	379.27	2%	1%	574.5	1246	172.8	19.2
N3	374.36	3%	1%	574.5	1246	172.8	19.2
N4	371.45	4%	1%	574.5	1246	172.8	19.2

3. Experimental Procedure

3.1. Mechanical Properties

This study encompasses the collection of materials, verification of properties, mixing, casting, curing, and testing conducted at 28 days, as illustrated in Figure 1. Conventional concrete and various amounts of NS and SF combined with microorganisms were used to create the specimens. Each mix ID has three samples. The compressive strength, splitting tensile strength, flexural

strength, impact strength, and bond strength of a total of 15 specimens were tested. Additionally, SEM with EDS was used to investigate six specimens.

After 28 days of the curing phase, testing was done on a 100 mm^3 cube. 100 mm diameter and 200 mm high cylindrical concrete specimens were made and tested in accordance with IS: 5816-2004, which describes how to assess the splitting tensile strength of concrete. Throughout the test, the cylinder's vertical axis received a consistent compressive force. The load was raised progressively until the specimen failed, and the highest load at failure was meticulously documented for further examination.

Prism-shaped specimens measuring 100 mm by 100 mm by 500 mm were created and subjected to four-point loading in accordance with IS: 5816-2004 instructions in order to assess the flexural strength of both conventional concrete and nano silica in steel-reinforced bacterial concrete. Following established methods, the specimens were subjected to a flexural stress until they failed. To assess the impact resistance of the mixes, the methodology recommended by ACI Committee 544.IR-56 was employed. The specimens used for this test had a diameter of 152.4mm and a thickness of 63.5mm. Each specimen underwent impact testing, with the number of blows necessary to initiate and propagate initial and final cracks documented. The test was conducted on a cube specimen measuring 150 x 150 x 150 mm^3, which contained a HYSD steel bar positioned centrally. During the test, tensile forces were applied to the steel bars, transferring tensile stress to the concrete across the bonded interface. The embedded length of the specimen was 15 cm. The slip of the bar was monitored for each applied load until failure occurred.

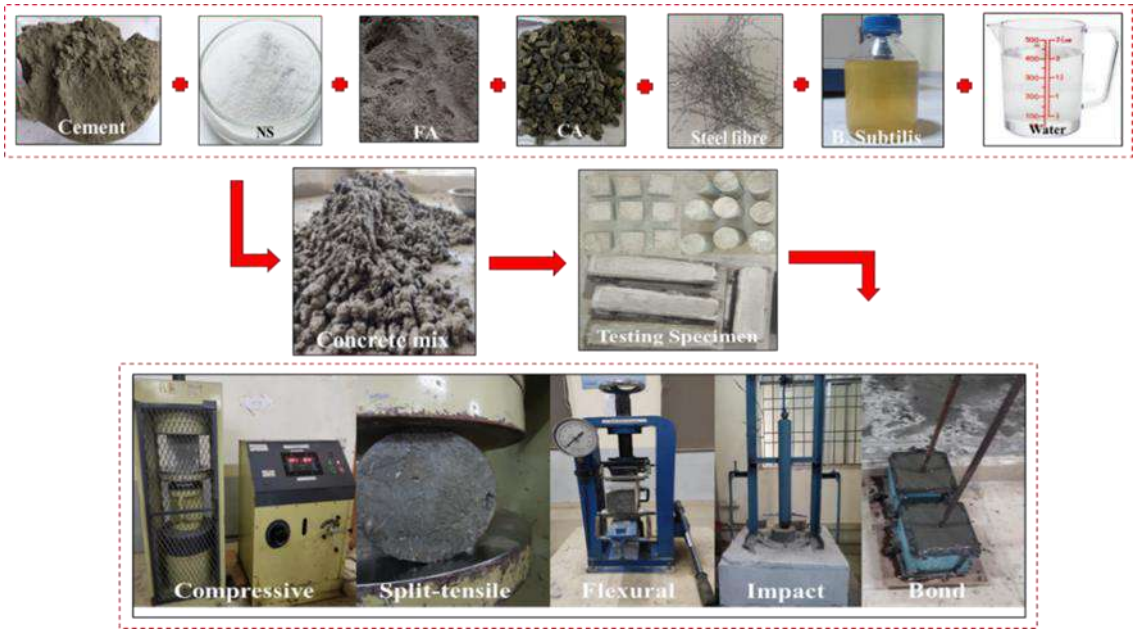

Fig. 1. Experimental procedure

3.2 Characterization Studies

To investigate the microstructure and big pores created in concrete (Optimized mix), a scanning electron microscope (SEM, JSM-IT800, JEOL, Tokyo, Japan) was used. Concrete was broken up into tiny bits using ethanol instead of the original solvent in order to avoid the concrete from hydrating during testing. The samples' conductivity was improved by applying a 20 nm coating of gold.

4. Results and Discussion

4.1. Compressive Strength

After 28 days of curing, the concrete's compressive strength was measured. The findings are shown for specimens N0 (control mix), N1, N2, N3, and N4 in Figure 2. Accordingly, N0, N1, N2, N3, and N4 have compressive strengths of 36.34 N/mm^2, 39.47 N/mm^2, 42.34 N/mm^2, 40.89 N/mm^2, and

38.9 N/mm^2. The N0 mix demonstrates the lowest compressive strength of the samples tested. Compared to N0, the N2 mix exhibits a significant strength increase of 14.17%. When NS is added, concrete's compressive strength is greatly increased. However, it is crucial to understand that there is an ideal NS concentration of 2%, beyond which the strength may begin to decline [40], [41]. In order to get optimum performance, this emphasizes the need for meticulous testing and cautious mix design. This formulation is the most successful in this series, as shown by the 14.17% improvement seen with 2% NS. Compressive strength is increased when 1% SF is added as a reinforcing agent and 2% NS is used as a cementitious material in bacterial concrete.

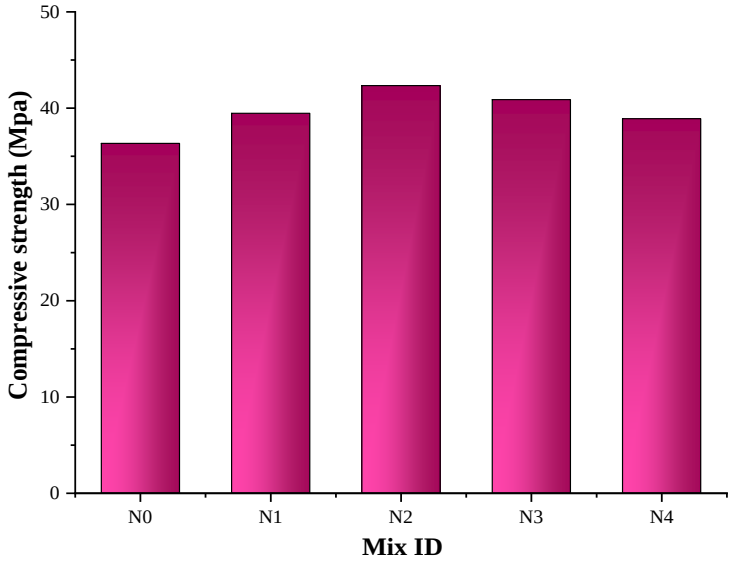

Fig. 2. Compressive strength

4.2. Splitting Tensile Strength Test

Following a 28-day curing period, the concrete's splitting tensile strength test results were acquired. The findings are shown in Figure 3 for specimens N0, N1, N2, N3, and N4. Concrete performance is impacted by NS, SF, and Bacillus subtilis, as shown by the splitting tensile strength tests for mixes N0, N1, N2, N3, and N4. The control mix N0, with a tensile strength of 4.2 N/mm^2, acts as the reference point, demonstrating the lowest strength.

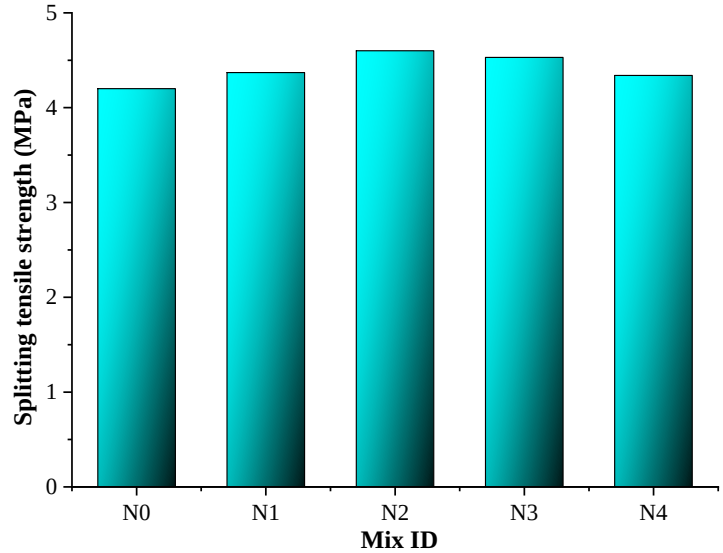

Fig. 3. Splitting tensile strength

The incorporation of 1% NS in mix N1 results in a tensile strength increase to 4.37 N/mm^2, reflecting a 4.05% enhancement due to improved microstructural densification and the crack-

bridging properties of the SF. The formulation containing N2 achieves a maximum tensile strength of 4.6 N/mm^2, indicating an 8.69% enhancement compared to N0. The enhanced performance results from the synergistic interactions of NS, which refines the concrete matrix; SF, which enhances crack resistance; and Bacillus subtilis, which facilitates biomineralization through calcium carbonate ($CaCO_3$) production, thereby sealing microcracks and increasing material density. Exceeding this threshold of NS content leads to a reduction in tensile strength. The N3 mix, which includes 3% NS, demonstrates a tensile strength of 4.53 N/mm^2, indicating a 7.86% increase; nonetheless, it is still inferior to N2, possibly due to particle agglomeration at higher NS concentrations. The N4 mix, which includes 4% NS, decreases to 4.34 N/mm^2, indicating a 3.33% increase, likely attributed to microstructural inconsistencies and insufficient dispersion of the additional NS. The results suggest that a 2% NS concentration is optimal for enhancing tensile strength, as increased concentrations result in diminishing returns[42]. The integration of NS, SF, and B. Subtilis enhances tensile strength, with mix N2 exhibiting the most effective and balanced performance.

4.3. Flexural Strength Test

After a 28-day curing period, the concrete specimens' flexural strength was evaluated. Figure 4 presents the test findings for samples N0, N1, N2, N3, and N4. Since the N0, without NS, has the lowest flexural strength, adding NS significantly increases the concrete's ability to withstand bending pressures. At 6.34 N/mm^2, N2, which has 2% NS, has the maximum flexural strength and is 12.61% better than N0. The observed increase may be ascribed to NS's capacity to improve particle packing, optimize the microstructure of concrete, and promote the production of calcium silicate hydrate (C-S-H), all of which strengthen the binding within the matrix. Mixes N3 and N4 exhibit enhanced performance compared to N0; however, their flexural strength values are marginally lower than those of N2. This suggests that elevated concentrations of NS may lead to particle aggregation or enhanced brittleness, which could impede efficient stress transfer within the matrix [43]. The findings suggest that a 2% NS dosage and 1% SF in bacterial concrete are optimal for maximizing flexural strength, achieving an effective balance between strength and durability. This highlights the importance of optimizing mix designs to attain enhanced performance in concrete applications.

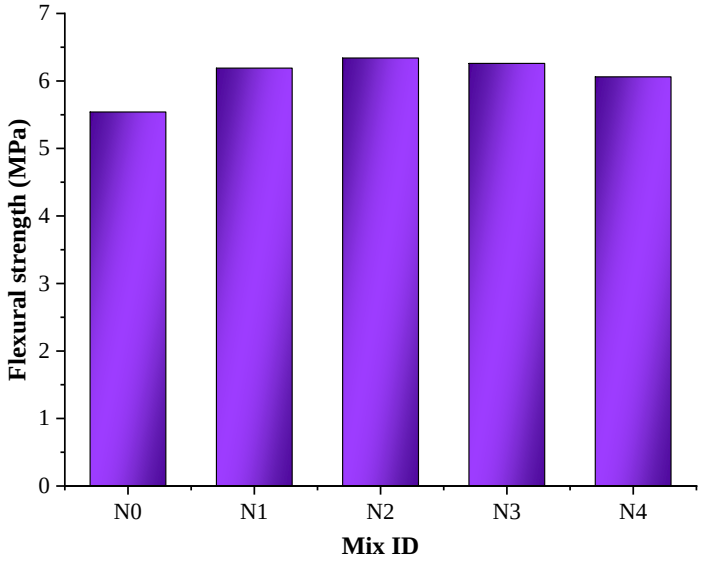

Fig. 4. Flexural strength

4.4. Impact Strength Test

A comparison between the initial and terminal fracture loads for mixes N0, N1, N2, N3, and N4 as determined by impact strength tests is shown in Figure 5. The assessment measured the number of jolts required to achieve the final fracture and to create the first visible crack, and the findings were recorded for every combination. For N0, N1, N2, N3, and N4, the corresponding first crack jolts were 16, 19, 25, 20, and 18. Crack values were 20, 24, 29, 23, and 19 at the end. Findings

reveal that using NS instead of cement greatly increases concrete's impact strength, with N2 doing the best. The fact that N2 was found to increase both initial and ultimate fracture loads suggests that NS helps to densify the matrix and improves its resistance to crack propagation. The incorporation of SF in bacterial concrete enhances impact strength. The incorporation of extended, continuous fibres improves the cohesion of concrete, allowing it to endure greater impact loads prior to cracking. The incorporation of fibre reinforcing enhances the material's toughness and ductility [44]. The findings demonstrate that N1, N3, and N4 outperform N0, with N2 showing the most substantial enhancement. This indicates that the integration of 2% NS, SF, and bacterial activity produces the most effective synergy for improving impact resistance in concrete.

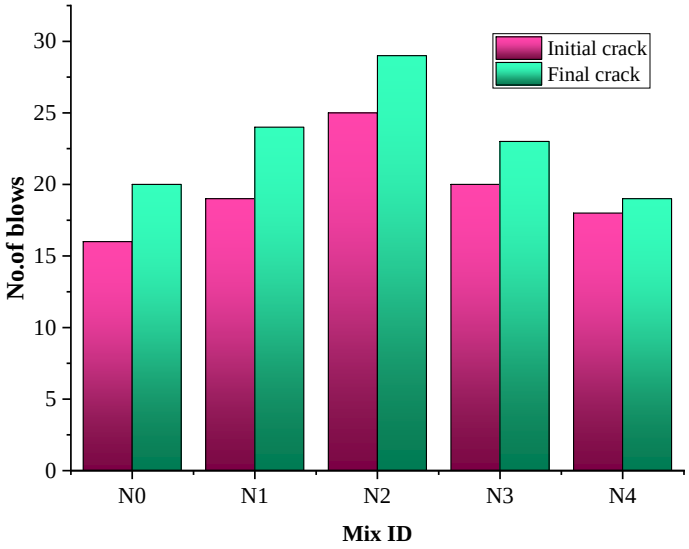

Fig. 5. Impact strength

4.5. Bond Strength Test

In Figure 6, the bond strengths of concrete mixes N0, N1, N2, N3, and N4 are shown. Concrete bond strength was measured using cubes of 150 x 150 x 150 mm^3, to which High Yield Strength Deformed (HYSD) bars were inserted during pouring. Because steel bar adhesion to the concrete matrix is crucial to maintaining structural integrity and facilitating effective load transfer in reinforced concrete, it is investigated in this study. 1.98, 2.0, 2.5, 2.3, and 2.19 N/mm^2 were the reported bond strength values for mixes N0, N1, N2, N3, and N4, respectively.

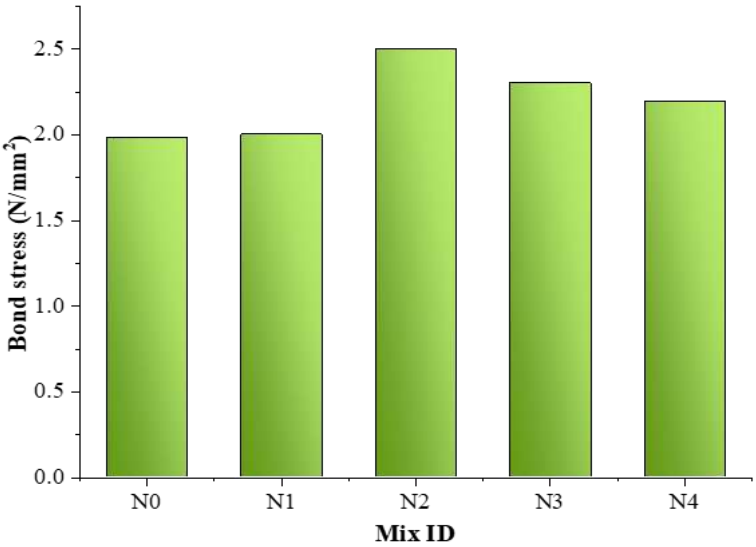

Fig. 6. Bond strength

The lowest bond strength, 1.98 N/mm^2, was shown by the control mix (N0), which was used as a benchmark. Thanks to the bacterial concrete formulation's optimal inclusion of N2 and 1% SF, mix

N2 obtained the greatest bond strength of 2.5 N/mm^2. By filling voids and increasing matrix density, NS improves the microstructure of the concrete and is primarily responsible for the notable increase in bond strength. The use of SF enhances the mechanical interlock between concrete and steel reinforcement because of its ability to bridge cracks. Bacterial agents strengthen the connection between steel bars by forming calcium carbonate deposits around them. In comparison to N0, mixes N3 and N4 demonstrated enhanced binding strength; nonetheless, their values were somewhat less than those of N2. Accordingly, 2% NS and 1% SF seem to provide the best results, while greater doses may cause problems such agglomeration or poor particle dispersion. Based on the results, N2 is the best combination for reinforcing concrete buildings because the combined impacts of NS, SF, and bacterial activity greatly increase the bond strength.

4.6. Scanning Electron Microscope (SEM) with Energy dispersive X-ray spectroscopy (EDS)

The 28-day crushed strength specimen yielded the optimal concrete mix (N2) SEM picture, which is shown in Figure 7. The photograph obtained from the Scanning Electron Microscope (SEM) using electron backscattering shows the concrete sample's microstructure, highlighting its surface shape and hydrated grains. The optimal concrete formulation includes calcium hydroxide, also called portlandite (CH), which is essential to the hydration process, as well as calcium silicate hydrate (C-S-H) particles, which increase strength. Picture 7. (a) shows circular slices at a 200 µm scale, showing the presence of calcium carbonate ($CaCO_3$) precipitation linked to CH and the ideal mix (N2). Furthermore, the optimized mixture displays monosulfo aluminate phases that resemble prismatic needles. At a 20 µm scale, Figure 7(b) shows the ideal composition, highlighting durability and strength. Due to the consumption of CH, the N2 mix displays a fibrous structure of secondary C-S-H. When portlandite is combined with amorphous NS, a secondary C-S-H gel is created [40]. C-S-H gel, CH, and many aluminate and ferrite phases work in concert to raise the density of the cement matrix, which is reflected in the presence of hydrated grains. The addition of a 2% NS matrix to concrete enhances its strength and durability due to its uniform shape.

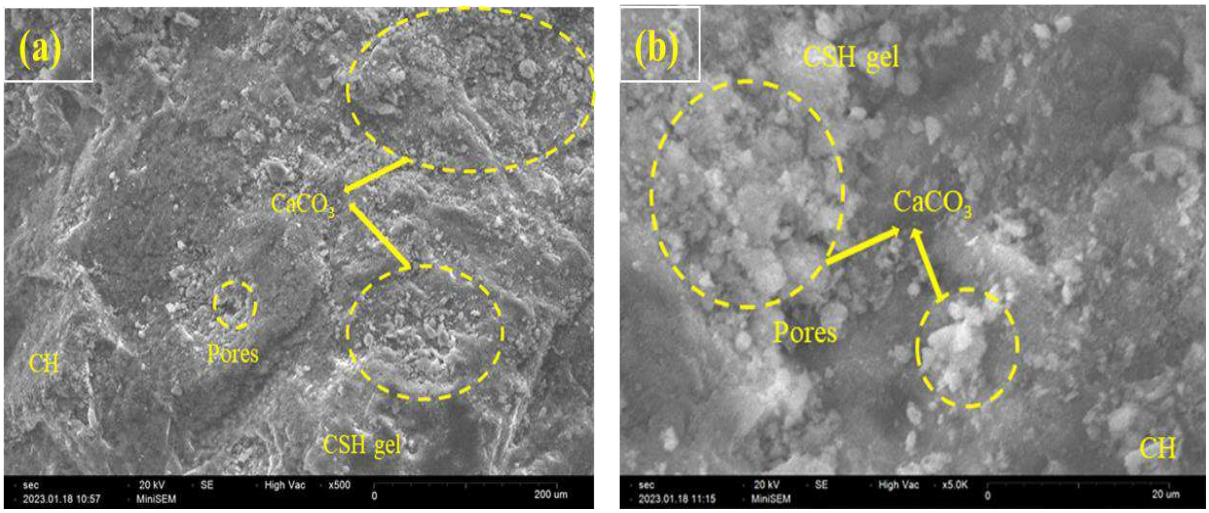

Fig. 7. SEM image of the optimized mix (N2) (a) under 200 µm and (b) under 20 µm

Energy Dispersive X-ray spectroscopy (EDS) is utilized to analyze the structure and composition of magnetic nanoparticles and immobilized enzymes. Figure 8 illustrates the EDS of the optimized mix (N2). EDS testing was conducted on the optimized mixture (N2) to identify the peaks of chemical elements present in the sample and to verify the formation of calcite. The primary elemental components present in concrete mixes include Calcium (Ca), Oxygen (O), Carbon (C), and Silicon dioxide (Si). The EDS results demonstrate that the precipitate is composed of C, Ca, and O atoms, thus confirming its identification as calcium carbonate. The peaks of Silicon (Si) and Oxygen (O) signify the presence of NS in the concrete. The results demonstrate that the optimized mix (N2) displayed calcium peaks, with more significant peaks noted after the incorporation of bacterial spores, which additionally augmented the levels of NS and SF in conjunction with increased

bacterial content. The incorporation of 2% NS and 1% SF into bacterial concrete resulted in elevated concentrations of Oxygen (O), Calcium (Ca), and Carbon (C).

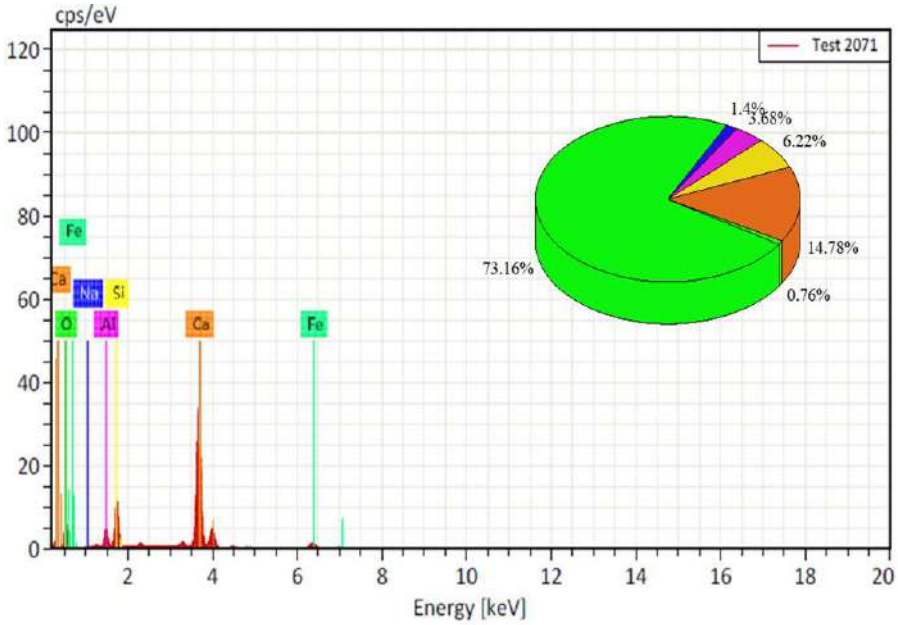

Fig. 8. Element's verification of the optimized mix (N2)

5. Conclusion

This investigation thoroughly examined the effects of Nano Silica (NS) and Steel Fiber (SF) reinforcement in bacterial concrete, emphasizing improvements in mechanical strength and microstructural characteristics. The results highlight the critical contribution of NS to enhancing the structural performance of concrete.

- The addition of NS improved the load-bearing capability by increasing the compressive strength by 14.17% as compared to the control mix.
- Moreover, the bacterial concrete enhanced with NS and SF demonstrated 8.69% enhanced splitting tensile strength, reflecting a higher resistance to tensile stresses.
- The flexural strength of the N2 mix (which included NS) was 12% higher than that of N0, suggesting better performance in bending situations. In order to strengthen the adhesion between the cementitious matrix and aggregates, the combination of NS and SF greatly increased impact and bond strength.
- Compressive, tensile, flexural, impact, and bond strength were significantly improved after a 28-day curing period using the optimal formulation, which included 2% NS, 1% SF, and 10% bacterial solution.
- By confirming the formation of calcium silicate hydrate (C-S-H) gel and a notable increase in calcium carbonate ($CaCO_3$) in NS and SF-modified concrete, the SEM investigation helped to plug cracks and improve the overall densification of the concrete matrix.
- The presence of calcium (Ca), oxygen (O), and carbon (C) in the optimum mix (N2) suggests the creation of calcium carbonate ($CaCO_3$). Concrete containing nanosilica (NS) was verified by the detection of silicon (Si) and oxygen (O). The composition and microstructural integrity of the concrete were improved by the addition of 2% NS and 1% SF, which led to higher levels of Ca, O, and C.
- NS's incorporation greatly increased mechanical strength while also improving sustainability and cost-effectiveness by lowering the carbon footprint associated with the manufacture of concrete.

The combination of NS and SF in bacterial concrete offers a practical and effective method for enhancing mechanical properties and durability, highlighting its promise for high-performance and sustainable construction materials.

References

[1] Makul N. Advanced smart concrete-A review of current progress, benefits and challenges. J Clean Prod. 2020;274:122899. https://doi.org/10.1016/j.jclepro.2020.122899

[2] Vishwakarma V, Uthaman S. Environmental impact of sustainable green concrete. In: Smart Nanoconcretes and Cement-Based Materials. Elsevier; 2020. p. 241-55. https://doi.org/10.1016/B978-0-12-817854-6.00009-X

[3] Zamora-Castro SA, et al. Sustainable development of concrete through aggregates and innovative materials: A review. Appl Sci. 2021;11(2):629. https://doi.org/10.3390/app11020629

[4] Miller SA. Supplementary cementitious materials to mitigate greenhouse gas emissions from concrete: can there be too much of a good thing? J Clean Prod. 2018;178:587-98. https://doi.org/10.1016/j.jclepro.2018.01.008

[5] Akhtar A, Sarmah AK. Construction and demolition waste generation and properties of recycled aggregate concrete: A global perspective. J Clean Prod. 2018;186:262-81. https://doi.org/10.1016/j.jclepro.2018.03.085

[6] Silva RV, De Brito J, Dhir RK. Properties and composition of recycled aggregates from construction and demolition waste suitable for concrete production. Constr Build Mater. 2014;65:201-17. https://doi.org/10.1016/j.conbuildmat.2014.04.117

[7] Askar MK, Al-Kamaki Y, Ferhadi R, Majeed HK. Cracks in concrete structures causes and treatments: A review. J Duhok Univ. 2023;26(2):148-65. https://doi.org/10.26682/csjuod.2023.26.2.16

[8] Kan L, Dai L, Kong N, Peng B, Wang F. Experimental study on tensile behaviors of cracked ultra-high performance concrete under freezing and thawing. Constr Build Mater. 2024;411:134187. https://doi.org/10.1016/j.conbuildmat.2023.134187

[9] Rajadesingu S, et al. Exploring the potential of bacterial concrete: A sustainable solution for remediation of crack and durability enhancement--A critical review. Constr Build Mater. 2024;439:137238. https://doi.org/10.1016/j.conbuildmat.2024.137238

[10] Luhar S, Luhar I, Shaikh FUA. A review on the performance evaluation of autonomous self-healing bacterial concrete: mechanisms, strength, durability, and microstructural properties. J Compos Sci. 2022;6(1):23. https://doi.org/10.3390/jcs6010023

[11] Gupta S, Dai Pang S, Kua HW. Autonomous healing in concrete by bio-based healing agents--A review. Constr Build Mater. 2017;146:419-28. https://doi.org/10.1016/j.conbuildmat.2017.04.111

[12] Jonkers HM, Thijssen A, Muyzer G, Copuroglu O, Schlangen E. Application of bacteria as self-healing agent for the development of sustainable concrete. Ecol Eng. 2010;36(2):230-5. https://doi.org/10.1016/j.ecoleng.2008.12.036

[13] Tayebani B, Mostofinejad D. Penetrability, corrosion potential, and electrical resistivity of bacterial concrete. J Mater Civ Eng. 2019;31(3):4019002. https://doi.org/10.1061/(ASCE)MT.1943-5533.0002618

[14] Gao M, et al. Immobilized bacteria with pH-response hydrogel for self-healing of concrete. J Environ Manage. 2020;261:110225. https://doi.org/10.1016/j.jenvman.2020.110225

[15] Castanier S, Le Métayer-Levrel G, Perthuisot J-P. Bacterial roles in the precipitation of carbonate minerals. In: Microbial sediments. Springer; 2000. p. 32-9. https://doi.org/10.1007/978-3-662-04036-2_5

[16] Siddique R, et al. Properties of bacterial rice husk ash concrete. Constr Build Mater. 2016;121:112-9. https://doi.org/10.1016/j.conbuildmat.2016.05.146

[17] Andalib R, et al. Optimum concentration of Bacillus megaterium for strengthening structural concrete. Constr Build Mater. 2016;118:180-93. https://doi.org/10.1016/j.conbuildmat.2016.04.142

[18] Sun X, Miao L, Wu L, Chen R. Improvement of bio-cementation at low temperature based on Bacillus megaterium. Appl Microbiol Biotechnol. 2019;103:7191-202. https://doi.org/10.1007/s00253-019-09986-7

[19] Wang J, Dewanckele J, Cnudde V, Van Vlierberghe S, Verstraete W, De Belie N. X-ray computed tomography proof of bacterial-based self-healing in concrete. Cem Concr Compos. 2014;53:289-304. https://doi.org/10.1016/j.cemconcomp.2014.07.014

[20] Chahal N, Siddique R, Rajor A. Influence of bacteria on the compressive strength, water absorption and rapid chloride permeability of fly ash concrete. Constr Build Mater. 2012;28(1):351-6. https://doi.org/10.1016/j.conbuildmat.2011.07.042

[21] Chen H-J, Peng C-F, Tang C-W, Chen Y-T. Self-healing concrete by biological substrate. Materials (Basel). 2019;12(24):4099. https://doi.org/10.3390/ma12244099

[22] De Muynck W, Debrouwer D, De Belie N, Verstraete W. Bacterial carbonate precipitation improves the durability of cementitious materials. Cem Concr Res. 2008;38(7):1005-14. https://doi.org/10.1016/j.cemconres.2008.03.005

[23] Shilar FA, Ganachari SV, Patil VB. A comprehensive review on the strength, durability, and microstructural analysis of bacterial concrete. In: Structures. 2024. p. 107078. https://doi.org/10.1016/j.istruc.2024.107078
[24] Huseien GF. A review on concrete composites modified with nanoparticles. J Compos Sci. 2023;7(2):67. https://doi.org/10.3390/jcs7020067
[25] Adebanjo AU, et al. Effect of nanosized titanium dioxide and zinc oxide as antimicrobial agents on early compressive strength of high-performance concrete. In: E3S Web of Conferences. 2024. p. 3003.
[26] Ahmad J, Zhou Z. Waste marble based self compacting concrete reinforced with steel fiber exposed to aggressive environment. J Build Eng. 2024;81:108142. https://doi.org/10.1016/j.jobe.2023.108142
[27] Jain R, Lee L. Fiber reinforced polymer (FRP) composites for infrastructure applications: focusing on innovation, technology implementation and sustainability. Springer; 2012. https://doi.org/10.1007/978-94-007-2357-3
[28] Silva G, et al. Optimization of a reinforced geopolymer composite using natural fibers and construction wastes. Constr Build Mater. 2020;258:119697. https://doi.org/10.1016/j.conbuildmat.2020.119697
[29] Niu Y, et al. Investigation of fatigue crack propagation behavior in steel fiber-reinforced ultra-high-performance concrete (UHPC) under cyclic flexural loading. Compos Struct. 2022;282:115126. https://doi.org/10.1016/j.compstruct.2021.115126
[30] Achal V, Mukherjee A, Reddy MS. Microbial concrete: way to enhance the durability of building structures. J Mater Civ Eng. 2011;23(6):730-4. https://doi.org/10.1061/(ASCE)MT.1943-5533.0000159
[31] Balam NH, Mostofinejad D, Eftekhar M. Effects of bacterial remediation on compressive strength, water absorption, and chloride permeability of lightweight aggregate concrete. Constr Build Mater. 2017;145:107-16. https://doi.org/10.1016/j.conbuildmat.2017.04.003
[32] Jonkers HM, Schlangen E. Self-healing of cracked concrete: A bacterial approach. In: Proceedings of the 6th international conference on fracture mechanics of concrete and concrete structures. 2007. p. 1821-6.
[33] Althoey F, et al. Physical, strength, durability and microstructural analysis of self-healing concrete: A systematic review. Case Stud Constr Mater. 2023;18:e01730. https://doi.org/10.1016/j.cscm.2022.e01730
[34] Damodaran P, Nagarajan M, Thangasamy L. Assessing the durability, mechanical, and microstructural properties of nanosilica-enhanced coconut shell concrete: A sustainable approach. J Environ Nanotechnol. 2024;13(3):237-45. https://doi.org/10.13074/jent.2024.09.243845
[35] Ali OAI, et al. Enhancing concrete performance through microbial intervention: a comprehensive experimental study. Eng Res J. 2024;183(4):85-106.
[36] Tanimola JO, Efe S. Predicting compressive strength of nano-silica enhanced concrete using machine techniques. Available SSRN 4963162.
[37] Shakir QM, Alghazali AF. Sustainable precast composite deep beams including concrete with partial replacement (50%) of recycled coarse aggregate. J Build Pathol Rehabil. 2024;9(2):140. https://doi.org/10.1007/s41024-024-00493-5
[38] Shakir QM, Alghazali AF. Innovative friendly-environmental hybrid model of precast reinforced concrete deep beams based on curved hybridization. Innov Infrastruct Solut. 2024;9(12):463. https://doi.org/10.1007/s41062-024-01664-6
[39] Shakir QM, et al. New model of eco-friendly hybrid deep beams with wastes of crushed concrete. J Teknol. 2023;85(6):145-54. https://doi.org/10.11113/jurnalteknologi.v85.20431
[40] Manigandan N, Ponmalar V. M100 concrete probing on quinary cementitious matrix incorporated with industrial ferrochrome slag sand. Constr Build Mater. 2024;420:135478. https://doi.org/10.1016/j.conbuildmat.2024.135478
[41] Nanthini M, Ganesan R, Jaganathan V. Studies on alkaline activator, manufacturing method and mechanical properties of geopolymer concrete for sustainable environment-A review. J Environ Nanotechnol. 2024 Sep;13(3):52-72. https://doi.org/10.13074/jent.2024.09.242753
[42] Nanthini M, Ganesan R, Jaganathan V. Experimental investigation of the durability of ambient-cured metakaolin-based geopolymer concrete in different sustainable environmental conditions. J Environ Nanotechnol. 2024 Sep;13(3):73-81. https://doi.org/10.13074/jent.2024.09.242754
[43] Nanthini M, Ganesan R, Jaganathan V. Incorporation of nanoalumina in potassium feldspar-based phosphoric acid activated geopolymer composites: A sustainable approach. J Environ Nanotechnol. 2024 Sep;13(3):89-98. https://doi.org/10.13074/jent.2024.09.243840
[44] Nanthini M, Ganesan R, Xavier JR. Experimental and theoretical investigation of the influence of graphene oxide/nanozirconia on the mechanical and durability properties of geopolymer concrete. Polym Bull. 2024 Dec. https://doi.org/10.1007/s00289-024-05607-0
[45] Manigandan N, Ponmalar V. Ferrochrome slag and manufactured sand as fine aggregate replacement in concrete and mortar-a brief review. Indian J Sci Technol. 2020;13:2657-67. https://doi.org/10.17485/IJST/v13i26.526

Research on Engineering Structures & Materials
www.jresm.org

Research Article

Impact of recycled concrete powders on the behavior of high-performance concrete in fresh and hardened states

Safia Mebarek Haddad [*,a], Mebarek Belaoura [b]

Laboratoire des Travaux publics, ingénierie de Transport, environnement, Ecole Nationale supérieure des travaux publics-Francis Jeanson, Kouba, Algiers, Algeria

Article Info

Article History:

Received 20 Nov 2024

Accepted 21 Mar 2025

Keywords:

Concrete demolition powders;
Concrete sample scraps powders;
Cement substitute;
High-performance concrete;
Mechanical properties;
Porosity

Abstract

The substantial volume of construction and demolition waste (CDW) generated annually poses a significant environmental challenge, necessitating innovative solutions for waste management and resource conservation. Recycled concrete powder (RCP) is a primary by-product of the reclamation process of CDW. This study investigates the potential of using RCP as a cement substitute in high-performance concrete (HPC), evaluating its effect on both fresh and hardened properties. Concrete mixtures were prepared by replacing cement with Concrete Demolition Powders (CDP) and Concrete Sample Scraps Powders (CSSP) at substitution rates of 10%, 15%, and 20%. The slump test was used to assess workability, while density, compressive strength, flexural strength, and porosity were measured at curing ages of 7, 28, and 90 days. The control mix was designed to achieve a targeted compressive strength of 80 MPa at 28 days. Results show that increasing the RCP substitution rate leads to a progressive reduction in workability. Both fresh and hardened density also decrease with the substitution rate, though this reduction remains relatively limited (< 2%), regardless of the type of powder or substitution rate. Compared to the control mix, compressive strength decreased by 3.85% to 11.5%, depending on the rate and type of powder used. The addition of RCP also reduced flexural strength and increased porosity. Despite these effects, concrete mixtures with RCP maintain the mechanical properties of HPC, supporting their potential as a cement substitute. This approach helps reduce cement consumption and promotes the valorization of construction waste.

© 2025 MIM Research Group. All rights reserved.

1. Introduction

During The process of rapid urbanization is leading to a significant increase in the amount of construction and demolition (C&D) waste generated worldwide. This waste not only occupies valuable land resources but also contributes to the depletion of already limited landfill space. C&D waste amounts will be at a high level in the next decades [1]. Annual reports suggest that the total amount of C&D waste generated worldwide exceeds 10 billion tons, of which the United States produces about 700 million tons and the European Union more than 800 million tons [2]. In Algeria, the annual production of construction and demolition waste represented about 13 million ton in 2020 [3]. The construction sector is not only considered the main source of waste, but also the primary cause of environmental pollution [4]. The environmental impacts of C&D waste have become a worldwide issue [5]. This generation of waste has a significant impact on the environment, including the depletion of landfills, the emission of carbon and greenhouse gases, substantial waste of raw materials, and elevated project costs [6].

*Corresponding author: s.mebarekhaddad@enstp.edu.dz
[a]orcid.org/0009-0006-8692-4248; [b]orcid.org/0000-0002-1974-6801
DOI: http://dx.doi.org/10.17515/resm2025-540ma1120rs

Compared to recycling, landfilling remains the predominant method for managing construction and demolition (C&D) waste in many regions of the world, accounting for around 35% of such waste disposed of in landfills worldwide [7]. However, from a sustainability perspective, it is imperative to reduce, recycle and reuse this waste [8]. Recycling is increasingly seen as a viable option, particularly when it can significantly reduce the overall environmental impact throughout the life cycle of recycled products.

Numerous studies indicate that it is possible to use recycled concrete aggregates (RCA) in concrete, rather than just as road gravel, as an alternative approach. Recycled aggregates can be considered as another type of normal aggregate, suitable for construction in accordance with national and international specifications, when properly processed and classified [9]. On the other hand, the incorporation of recycled concrete aggregates could potentially exert adverse effects on the properties of concrete. Many studies have shown that the compressive strength of concrete incorporating recycled aggregates is often 5% to 40% lower than that of concrete made with natural aggregates [10], also a decrease in workability of fresh concert [11]. The presence of RCA significantly impacts the majority of durability indicators [12]. Numerous researchers have studied the incorporation of recycled concrete aggregates fine (RCAF) into mortars and concrete as a sand [13]. The results show a reduction in concrete properties when recycled sand is used, both in the fresh and hardened state [14,15]. In practice, the use of recycled sand in concrete mix design is strongly discouraged [10]. Nevertheless, given that recycled sand can make up as much as 50% of total recycled aggregates [16], it is essential to conduct research into other potential ways of optimizing the use of recycled sand. Instead of using fine RCA to replace natural sand, they will be considered as mineral additive to substitute cement after an additional crushing and screening process. The aim is to produce a powder with a maximum diameter of less than 80 μm, called RCP (Recycled Concrete Powders).

On the other hand, the production of Portland cement (PC) is responsible for around 7 to 8% of global greenhouse gas emissions [17,18] making it one of the most environmentally damaging materials in the construction industry [19]. Replacing Portland Cement (PC) with supplementary cementitious materials (SCMs) has emerged as a practical choice for several reasons. From an economic perspective, it offers advantages such as the availability of locally sourced materials and the possibility of large-scale production. Additionally, it offers significant environmental benefits, including the reuse of waste and substantial reductions in CO2 emissions. From a technical point of view, composite materials have been extensively studied for their long-term durability and suitability for use in construction, which contributes to their attractiveness as a substitute for PC [20]. From this point of view, PCR appears to be a viable option for use as SCM, as a waste product with wide local and global availability to encourage ecological recycling [21].

Previous studies have investigated the effect of thermal treatment on RCP and have shown that it has the potential to improve the characteristics of RCP. This improvement could allow higher levels of PC to RCP substitution. Xu et al found that thermal treatment of RCP has significant effect on material rehydration [22]. LV's results indicate that when the content of recycled concrete powder is less than 30%, its effect on cement strength is equivalent to that of fly ash. However, this influence becomes more significant after heat treatment [23]. However, heat treatment of these fines is difficult to achieve in ordinary building materials companies [24]. The active effect of RCF is therefore not investigated further in this study.

Florea et al. demonstrated in their study that recycled concrete fines, can be used as a substitute for up to 20% of the cement without a significant loss of strength, even without undergoing thermal treatment [25]. According to Ma and Wang, class C20 concrete can be prepared with the incorporation of 20% recycled concrete fines, as the results show little effect on rheological properties and mechanical strength [24]. Overall research shows a decrease in mechanical properties when using recycled concrete powder (RCP). The study by Zhao et al. demonstrated a progressive reduction in compressive strength with increasing cement replacement by RCP, decreasing from 65.96 MPa for the control mix to 45.64 MPa at a 40% replacement rate [26]. This trend continues as the percentage of RCP used to replace PC increases [27–31]. Also, the employed RP has a significant influence on the water transport and porosity. Huixia[32] reported that the

porosity increases as RP incorporates. The majority of publications on PCR come from China, with 69.83% of studies, which is significantly higher than the second and third countries, Portugal 7.77% and Spain 6.80% [20]. In comparison, Algeria has had limited participation in scientific research in this field.

This study presents the results of laboratory studies on the properties of high-performance concrete (HPC) prepared with recycled concrete powders (RCP) of the same particle size as fillers (< 80 μm). These recycled concrete powders were obtained from two types of waste: the first from construction and demolition waste found in landfills, and the second from scraps concrete samples obtained in the laboratory. The aim of the study was to analyze the effect of replacing cement by varying proportions of recycled concrete powder, i.e., 10%, 15% and 20%, into high-performance concrete. Then, the experimental program was designed to evaluate both the rheological behavior and mechanical properties of the concrete by analyzing workability, density, compressive and flexural strength and porosity. This study contributes to the application of recycled concrete powders in the formulation of high-performance concrete, particularly in Algeria, where there is an immediate demand for sustainable construction practices and where scientific research in this field is still very limited.

2. Materials and methods

2.1 Materials

The studied fines were sourced from two distinct materials, both derived from concrete. The first source consists of mixed construction and demolition (C&D) waste aggregates, obtained by crushing waste from various construction sites and building materials. This C&D waste was collected from the technical landfill platform in Algiers (GECTAL) (Fig. 1). The second source comprises concrete sample scraps provided by the LCTP Algiers laboratory (Fig. 2). These scraps were obtained by fragmenting cylindrical concrete specimens (Ø16 × 32 cm) using a compression process. Both materials were processed using a ball mill to obtain fine particles below 80 μm (Fig. 3). The feasibility of using recycled concrete powder (RCP) from C&D waste is considered more practical than RCP derived from concrete sample scraps due to its greater availability.

The cement used in this study is a Portland cement of type CEM II 42.5N, produced by the GICA company at the Meftah factory in Algeria. The chemical and physical properties of the cement and both recycled powders, Concrete Demolition Powders (CDP) and Concrete Sample Scraps Powders (CSSP), are presented in Tables 1 and 2, respectively.

Fig. 1. Construction and demolition from GECTAL (Algiers)

Fig. 2. Scraps of concrete samples

(a) (b)

Fig. 3. (a) Concrete Demolition Powders, and (b) Concrete Sample Scraps Powders

The coarse aggregates used were crushed limestone gravels supplied by the GICA quarry in Algiers. Two fractions of gravel were used in this study: 3/8 gravel and 8/15 gravel. Additionally, two types of sand were used in this study: dune sand (rolled) sourced from the BOUSAÂDA region and crushed sand from the GICA quarry. The main characteristics and granulometric curve of these gravels are shown on Table 3 and Fig.4, respectively. The admixture used VISCOCRETE-775 FLOW, is a super plasticizer supplied by SIKA (Algiers - Algeria) company. Table 4 summarizes the main characteristics of the admixture. The mixing water used for concrete production was potable tap water.

Table1. Chemical compositions of the utilized binders

Binder	Composition (%)						
	SiO_2	Al_2O_3	Fe_2O_3	CaO	MgO	SO_3	Na_2O
Cement	14,37	4,28	3,67	70,61	1,6	3.47	1.2
CDP	10,2	1,83	1,81	82,65	1,7	0,66	0,39
CSSP	12,33	2,89	3,1	70,12	2,67	0,86	0,42

Table2. Physical properties of the utilized binders

Procedure	EN 1097-6[33]	EN 196-6[34]
Binder	Density (g/cm^3)	Specific area (cm^2/g)
Cement	3.19	4300
CDP	2.65	5440
CSSP	2.71	5430

Table3. Physical and mechanical properties of aggregates

Material	gravels 3/8	gravels 8/15	Crushed sand	Dune sand	Procedure
Specific Gravity	2.65	2.64	2.64	2.53	EN 1097-6[33]
Water absorption(%)	1.65	1.41	1.78	0.95	EN 1097-6[33]
Los Angeles(%)	22.5	22.3	---	---	EN 1097-2[35]
Micro Deval(%)	25.65	27.9	---	---	EN 1097-1[36]
Sand equivalent (%)	---	---	71.43	84.3	EN 933-8[37]
Finesse module(%)	---	---	3.36	0.66	EN 933-1[38]

Table 4. Properties of the chemical admixture

Density	1.1 ± 0.02
pH Value	4.7 ± 1.0
Total Chloride Ion Content	≤ 0.1%
Sodium Oxide Equivalent	≤ 3,5%
Solid content	31%

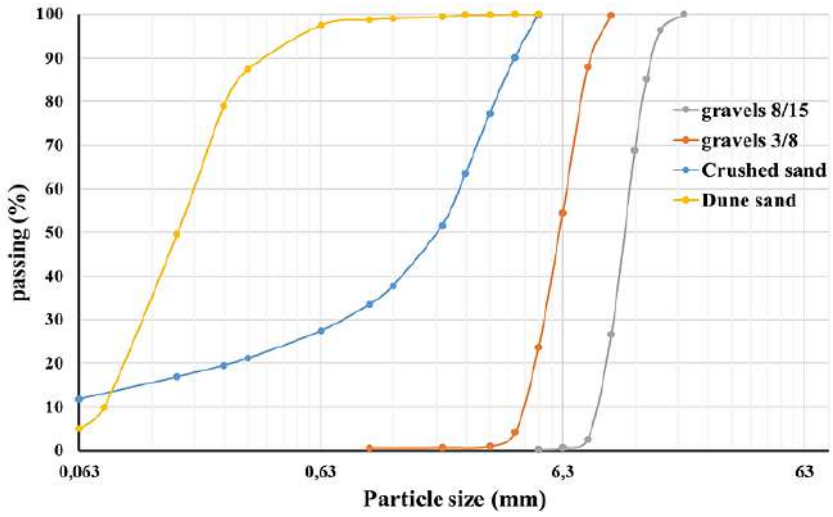

Fig. 4. The granulometric curve of gravels, crushed sand and Dune sand

2.2. Methods

2.2.1. Preparation Method

Table 5 presents the mix proportions of concrete containing recycled powders at various substitution rates. The concrete mixtures were designed following the University of Sherbrooke method, developed by Pierre-Claude Aïtcin [39]. A total of seven concrete mixes were prepared, maintaining a constant binder content (cement + recycled powder) of 450 kg/m^3 while varying the replacement level of cement by recycled concrete powders. The mix designs are as follow:

- Reference mix (C.REF): A control concrete served as the baseline for comparison.
- Concrete with Concrete Demolition Powders (C.CDP): Cement replacement at 10%, 15%, and 20%.
- Concrete with Concrete Sample Scraps Powders (C.CSSP): Cement replacement at 10%, 15%, and 20%.

Table 5. Mix proportion of HPC incorporating RPs (kg/m^3).

Material	C.REF	10 CDP	15 CDP	20 CDP	10 CSSP	15 CSSP	20 CSSP
Gravels 8/15	738.5	738.5	738.5	738.5	738.5	738.5	738.5
Gravels 3/8	316.5	316.5	316.5	316.5	316.5	316.5	316.5
Crushed sand	566.72	566.72	566.72	566.72	566.72	566.72	566.72
Dune sand	242.88	242.88	242.88	242.88	242.88	242.88	242.88
Cement	450	405	382.5	360	405	382.5	360
CDP	0	45	67.5	90	0	0	0
CSSP	0	0	0	0	45	67.5	90
Water	144.3	144.3	144.3	144.3	144.3	144.3	144.3
Superplasticizer	9.24	9.24	9.24	9.24	9.24	9.24	9.24
W/B	0.32	0.32	0.32	0.32	0.32	0.32	0.32

For all mixtures, the water-to-binder (W/B) ratio was maintained at 0.32, and the superplasticizer dosage (VISCOCRETE-775 FLOW) was fixed at 0.7%. The mixing process was conducted using a laboratory mixer. Initially, aggregates, cement, and recycled powders were dry-mixed for one minute. Water and superplasticizer were then introduced and mixing continued for an additional five minutes. The fresh concrete was cast into standardized cube and prism molds and compacted using a vibrating table. After 24 hours, the specimens were demolded and cured in water at 23°C until the designated testing ages.

2.2.2 Test Methods

Each test used a set of three specimens to ensure the accuracy of the results. The workability was measured by the Abrams slump cone test according to EN 12350-2[40]. The measurement of the density is done on cubic specimens (150 × 150 × 150 mm) according to the standard EN 12350-6[41]. The compressive and flexural strengths tests were performed at the ages of 7, 28 and 90 days, the compressive tests were performed on three test cubes (150 × 150 × 150 mm) according to EN 12390-3[42] and the tensile–flexural tests on three prisms (70 × 70 × 280 mm) according to EN 12390-5[43]. The evaluation of the total porosity was based on the measurement of the water absorption and the determination of the dry density according to ASTM C 642[44]. To obtain the latter, the samples were dried at 105°C and then their dimensions and weights were measured.

3. Results and Discussion

3.1. Workability

Fig. 5(a) and 5(b) present the workability of concretes with an increasing substitution rate. As shown, the incorporation of RCP led to a decrease in workability. The reference concrete is a plastic concrete with a workability of 21 cm. The workability of mixes containing CDP was approximately 5 to 12% lower than that of the reference concrete. For example, with a replacement rate of 10%, the workability becomes 20 cm, and 19 cm with a replacement rate of 15%. The same observation applies to the results obtained for the CSSP. A reduction of 6% was obtained at a substitution rate of 10%, while at 15% and 20% substitution, the reduction was 9.5% and 13%, respectively. The results indicate that concrete mixtures incorporating CDP and CSSP share similar trends in workability reduction, within the substitution range of up to 20%. When comparing concretes mixtures with CDP and CSSP, both exhibit a reduction in workability, though with slightly different variations. At a 10% substitution rate, the workability decreases by 5% for CDP and 6% for CSSP. At a 15% substitution rate, the reduction is approximately 9% for CDP and 9.5% for CSSP. These differences can be attributed to the porous microstructure and water absorption capacity of each powder.

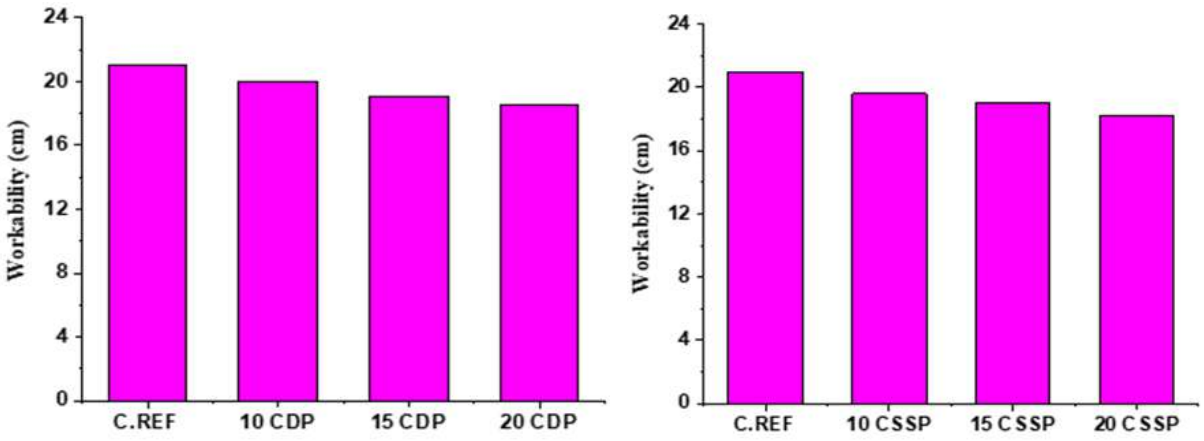

(a) (b)

Fig. 5. Workability of concretes containing various RCPs (a)CDP and (b)CSSP

RCPs exhibit significant water absorption, as confirmed by the study of Zhenhua et al. [45], which found that all recycled powders (RPs) used in their research show irregular shapes and rough

surfaces, with fine particles agglomerated on larger ones. This characteristic may be the main reason for the higher water demand of RPs compared to cement. Furthermore, these recycled powders, having undergone prior hydration, result in the formation of hydrated phases such as C-S-H gel and interconnected porous microstructures [27]. These interconnected pores increase the capacity of the powders to retain water and reduce the availability of free water in the mixture. Previous studies, notably that of Kim et al. [46], confirm that increasing the replacement rate of recycled powders systematically reduces the workability of mixtures due to their absorption and irregular microstructure. Furthermore, the results obtained in this study are consistent with the findings of [28, 47], which observed similar trends, particularly at higher replacement rates.

3.2 Density

The density in both fresh and hardened states for all studied mixes (Fig.6) decreased with increasing contents of recycled concrete powders.

In the fresh state, the density of the reference concrete (C.REF) is the highest, with a value of 2504 kg/m^3, indicating that without the addition of recycled concrete powders, the base mix is relatively dense. When concrete demolition powders (CDP) are introduced, the fresh density of the concrete gradually decreases as the substitution rate increases. For example, with a 10% substitution of CDP, the density is 2485 kg/m^3, and it drops to 2482 kg/m^3 at a 20% substitution rate, a reduction of 0.88% compared to C.REF. Similarly, mixes containing concrete sample scraps powders (CSSP) show a reduction in density. At 10 CSSP, the density reaches 2465 kg/m^3, a reduction of 1.56% compared to the reference concrete, and this decrease continues, reaching 2462 kg/m^3 at a 20% substitution rate. The decrease in fresh state density is explained by the intrinsically lower density of recycled powders compared to cement [48]. These powders, derived from the demolition or crushing of concrete, contain more porous and less dense particles, which affects the overall density of the mix. Furthermore, increasing the substitution rate amplifies this effect as the proportion of less dense material increases in the total mixture.

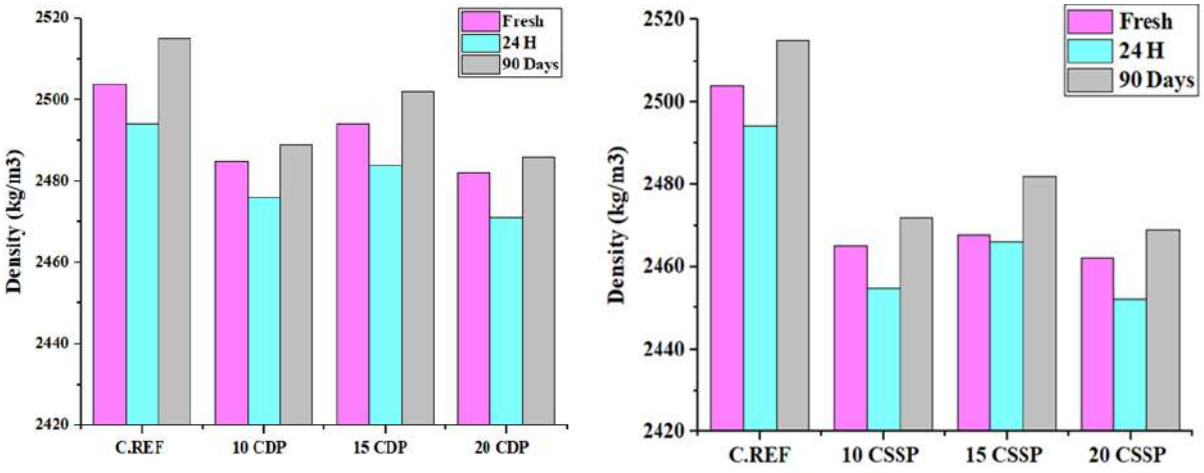

Fig. 6. Density of concretes containing various RCPs (a)CDP and (b)CSSP

In the hardened state (after 90 days), the reference concrete shows a density of 2515 kg/m^3, slightly higher than in the fresh state due to the ongoing process of hydration, which gradually densifies the material. In contrast, for mixtures containing CDP, the hardened density remains lower than that of the reference concrete. For example, with 10CDP, the density represents a decrease of about 1.04%, while at 20% substitution, it shows a reduction of approximately 1.15%. This decrease is attributable to the porous microstructure of the recycled powders, which limits densification through hydration. Mixtures containing CSSP also show a reduced density after curing, with a 1.7% decrease at a 10% substitution rate and a density of 2469 kg/m^3 at a 20% rate. The observed reduction is primarily attributed to the porous structure of the recycled powders, which hinders the densification of the material. Since the powders derived from recycled concrete have already undergone a hydration reaction during their initial life cycle, their potential to

produce new hydration products is significantly reduced. Furthermore, these porous particles lead to the formation of low-density zones within the cementitious matrix, compromising the microstructural compactness of the concrete after setting and hardening. These results indicate that the use of recycled powders leads to a predictable decrease in density due to their porous microstructure and low reactivity. However, this reduction remains relatively limited (< 2%), regardless of the type of powder or the substitution rate, indicating that these materials can be incorporated without significant impact in applications where a slightly reduced density is acceptable.

3.3 Compressive and Flexural Strength

The results of compressive strength and flexural strength are presented in Fig.7 and Fig.8 respectively. The evaluation was carried out after 7, 28, and 90 days of curing. The results indicate that both compressive and flexural strength decrease with increasing substitution rates of recycled concrete powders, whether using concrete demolition powders (CDP) or concrete sample scraps powders (CSSP). After 28 days, the highest compressive and flexural strengths were recorded for the reference concrete at 80 MPa and 15 MPa, respectively, while the compressive and flexural strengths of mixtures with RCP ranged from 75 MPa to 70 MPa and from 14 MPa to 13 MPa depending on the substitution rate and the type of recycled concrete powder.

At 28 days, for mixtures containing CDPs, compressive strength decreased by 6.14% and 11.5% compared to the reference concrete for mixtures with 10CDP and 20CDP, respectively. This trend continued at 90 days, although the overall compressive strength increased with curing time. For instance, with a 10 CDP substitution, compressive strength at 90 days was 4.75% lower than that of the reference concrete, while at 20%, the reduction reached 14.5%. For mixes with concrete sample scraps powders (CSSP), a similar trend was observed. At 28 days, incorporating 10 CSSP reduced compressive strength by 3.85%, and with 20 CSSP, the decrease reached 11.2%. At 90 days, the mixture with 10 CSSP displayed only a 2.23% reduction in strength compared to the reference concrete, while the 20% substitution rate led to a 14.5% decrease.

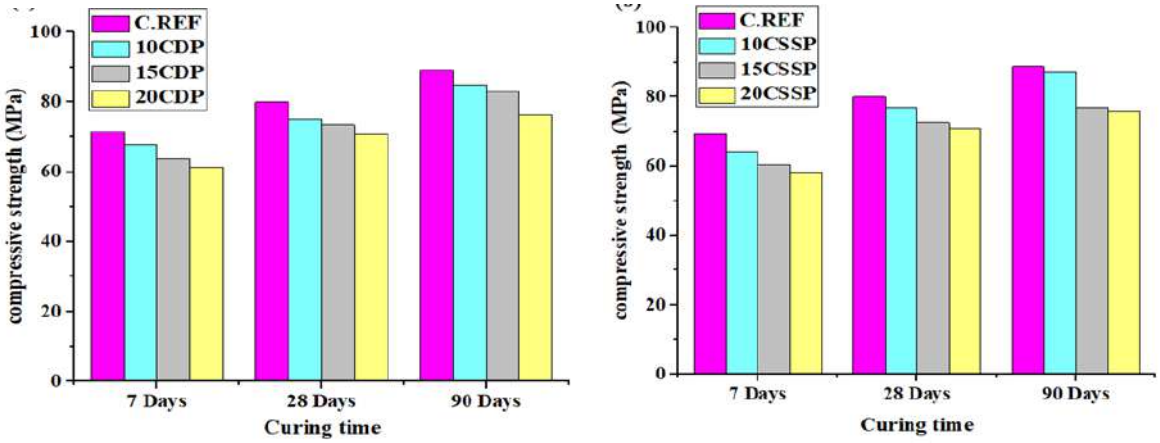

(a) (b)

Fig. 7. Compressive strength of concretes containing various RCPs (a)CDP and (b)CSSP

The incorporation of recycled concrete powders also reduced flexural strength. This finding has been confirmed by various studies demonstrating that the substitution of cement with recycled concrete powders decreases flexural strength [49, 50]. The results show a similar trend to that observed in compressive strength. For example, at 28 days, mixtures containing 10 CDP and 20CDP had a flexural strength 9.27% and 14.3% lower than the reference concrete, respectively. At 90 days, the decrease on the flexural strength was 10.26% and 19% for mixtures with 10CDP and 20CDP, respectively. For mixtures containing CSSP, flexural strength reductions were also observed. At 90 days, flexural strength losses reached 4.6% for 10CSSP and 10.3% for 20 CSSP.

Overall, compressive and flexural strengths of concretes containing CDP and CSSP showed a linear decrease as the substitution rate of recycled concrete powder increased. However, at lower

substitution rates (≤10%), the negative impact of CSSP on strength is less pronounced than that of CDP. However, at higher substitution rates (≥15%), the beneficial effect of CSSP becomes insufficient to compensate for the reduction in reactive phases, leading to a strength decrease similar to that observed with CDP.

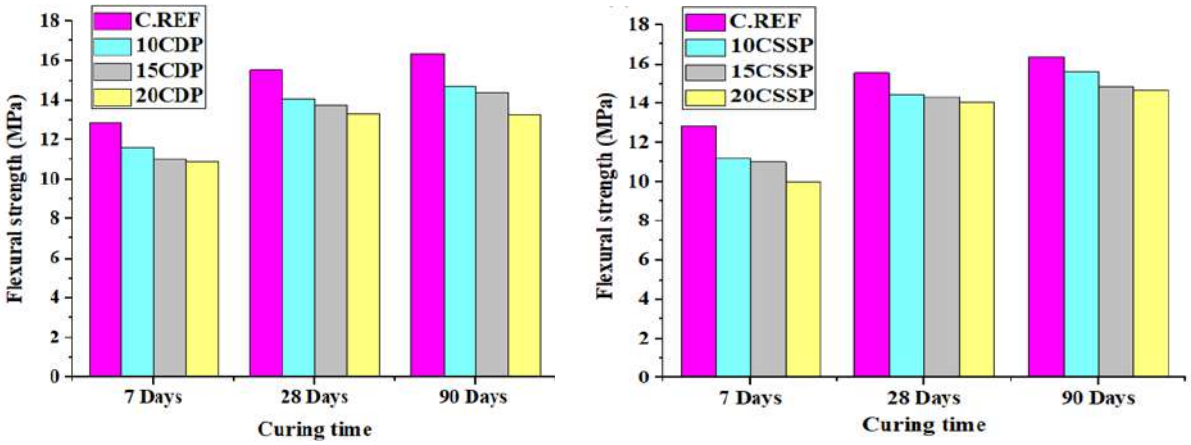

(a) (b)

Fig. 8. Flexural strength of concretes containing various RCPs (a)CDP and (b)CSSP

The compressive and flexural strength of concrete prepared with powders is always lower than that of the reference concrete, decreasing with increasing substitution rate, regardless of the curing time. This decrease in mechanical strength (compressive and flexural strength) is due to the reduction in the main reactive phases, C2S and C3S, as well as the low reactivity of fine particles compared to cement, which has reduced the content of new hydration products in the mixture [20] which are responsible for binding and developing mechanical strength. Moon et al. [51] also explained that the decrease in strength is due to the inert components present in the recycled powders, leading to a decrease in the formation of new hydration products and strength as the recycled powders are incorporated. These results are consistent with previous studies [52, 53].

3.4 Porosity

Fig.9 compares the results of porosity levels in concrete mixes under different conditions of substitution ratio and curing time. For the reference concrete (C.REF), porosity decreases significantly with curing time, dropping from 9.07% at 7 days to 7.97% at 90 days. This reduction can be attributed to the continuous hydration process, which densifies the cement matrix by gradually filling the pores. For mixtures containing CDP, the porosity is higher than that of the reference concrete and increases with the substitution rate. At 28 days, the porosity of REF is 9.07%, while mixtures with 10%, 15%, and 20% CDP show porosity levels of 9.17%, 9.37%, and 9.43%, respectively. At 90 days, although there is a slight reduction in porosity due to ongoing hydration, mixtures containing CDP maintain higher porosity levels than the reference concrete.

For CSSP, porosity follows a similar trend. For example, at 28 days, a mix with 10CSSP exhibits a porosity of 9.41%. At 90 days, porosity also decreases in mixes with CSSP, reaching, for instance, 9% for 10 CSSP and 9.14% for 20 CSSP, which remains higher than the porosity of the reference concrete. At the same substitution rates, both types of recycled powders increase the porosity compared to the reference concrete. For example, at 28 days, a mixture with 10% CSSP shows a porosity of 9.41%, while a mixture with 10% CDP shows a porosity of 9.17%. This slight difference indicates that CSSP have a slightly more pronounced influence on increasing porosity than CDP.

For both types of recycled powders, increasing the substitution rate leads to an increase in porosity. This is explained by the use of recycled concrete powders, which reduce the amount of new hydration products in cementitious composites. Additionally, as recycled powders are incorporated, the pore size of cementitious materials increases, resulting in a porous structure [54]. Regardless of the substitution rate, prolonged curing leads to a reduction in porosity in all mixtures. This observation is explained by the continuous hydration process of the recycled concrete in the

mixture. Consequently, even if the substitution rate of recycled concrete powder remains constant, porosity decreases as curing time increases due to the continuous hydration phenomenon.

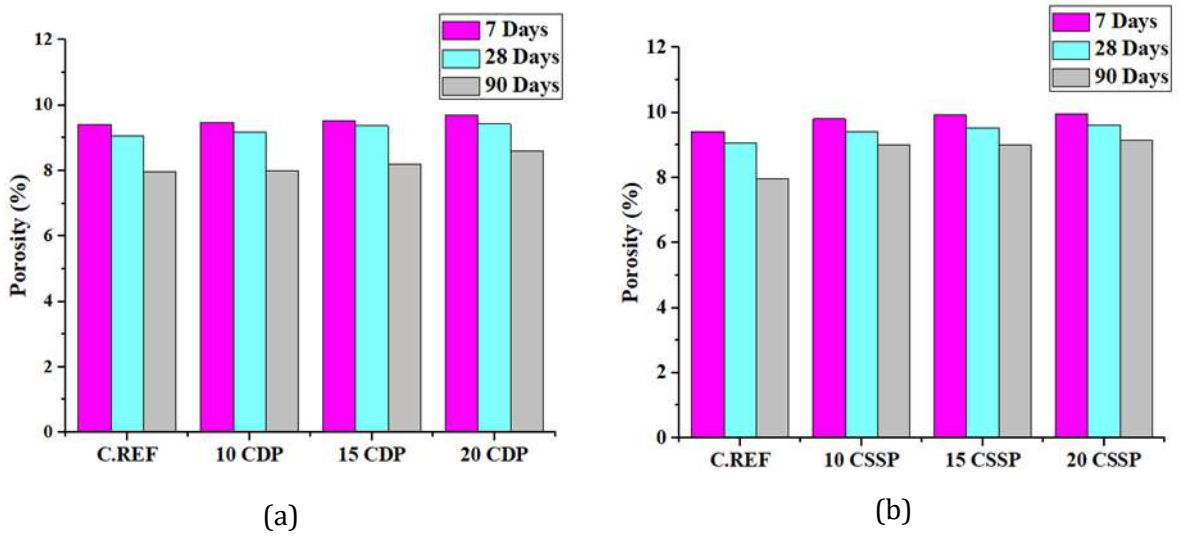

Fig. 9. Porosity of concretes containing various RCPs (a)CDP and (b)CSSP

4. Conclusion

This research represents an experimental approach aimed at substituting cement with recycled concrete powders in high-performance concrete mixtures. This study contributes to the research and application of recycled powders while supporting environmental preservation and sustainable development in Algeria. The main conclusions can be drawn as follows:

- The use of powder reduces workability by 5%–12% in mixes with demolition concrete powder and by 6%–13% in mixes containing concrete sample scraps powder, both relative to reference concrete. This reduction is due to the high absorption and irregular microstructure of the recycled powders. Furthermore, as the rate of substitution increases, the reduction in workability becomes more pronounced, showing a direct correlation between the proportion of recycled powders added and the reduced workability of the concrete mixtures.
- Recycled powder decreases the density, especially when the substitution rate of the powder is 20%. The decrease in density is primarily caused by the lower density of recycled powders compared to cement and the reduced formation of hydration products due to the lower cement content. However, the variation remains minimal, with changes of less than 2% compared to the reference concrete, regardless of the type of powders or the substitution rate.
- At 28 days, the compressive strength of the mixture containing 10% concrete demolition powders (CDP) decreased by 6.14%, while the mixture containing 20CDP showed an 11% reduction compared to the reference concrete. As the substitution rate increased, the strength loss became more significant. Similar results were observed in mixes incorporating concrete sample scraps powders (CSSP). This decrease is due to the decrease in the formation of new hydration products in cementitious materials, which affects overall strength development of the concrete.
- The incorporation of recycled concrete powders also resulted in a decrease in flexural strength, with trends similar to those observed for compressive strength. For example, at 28 days, the flexural strength of mixes containing 10% CDP and 20% CDP was 9.27% and 14.3% lower, respectively, then that of the reference concrete.
- The study of the porosity of concrete mixtures shows that the incorporation of recycled concrete powders increases this effect in newly prepared concretes. This increase in porosity is linked to the reduced formation of new hydration products in the mixture, which results in a more porous structure.

The results indicate that although there are slight reductions in some mechanical properties and rheological behavior, these changes remain within acceptable limits and do not significantly affect the overall performance of the concrete. This suggests that recycled concrete powders could be used as a substitute for traditional cement, helping to reduce the environmental impact of cement production and promoting the principles of the circular economy in the construction industry.

References

[1] Tang Q, Ma Z, Wu H, Wang W. The utilization of eco-friendly recycled powder from concrete and brick waste in new concrete: A critical review. Cem Concr Compos 2020;114:103807. https://doi.org/10.1016/j.cemconcomp.2020.103807

[2] Wu H, Zuo J, Zillante G, Wang J, Yuan H. Status quo and future directions of construction and demolition waste research: A critical review. J Clean Prod 2019;240:118163. https://doi.org/10.1016/j.jclepro.2019.118163

[3] Report on the State of Waste Management in Algeria. Natl Waste Agency n.d.

[4] Menegaki M, Damigos D. A review on current situation and challenges of construction and demolition waste management. Curr Opin Green Sustain Chem 2018;13:8-15. https://doi.org/10.1016/j.cogsc.2018.02.010

[5] Wang J, Wu H, Duan H, Zillante G, Zuo J, Yuan H. Combining life cycle assessment and Building Information Modelling to account for carbon emission of building demolition waste: A case study. J Clean Prod 2018;172:3154-66. https://doi.org/10.1016/j.jclepro.2017.11.087

[6] Akanbi LA, Oyedele LO, Akinade OO, Ajayi AO, Delgado MD, Bilal M, et al. Salvaging building materials in a circular economy: A BIM-based whole-life performance estimator. Resour Conserv Recycl 2018;129:175-86. https://doi.org/10.1016/j.resconrec.2017.10.026

[7] Kabirifar K, Mojtahedi M, Wang C, Tam VW. Construction and demolition waste management contributing factors coupled with reduce, reuse, and recycle strategies for effective waste management: A review. J Clean Prod 2020;263:121265. https://doi.org/10.1016/j.jclepro.2020.121265

[8] Sormunen P, Kärki T. Recycled construction and demolition waste as a possible source of materials for composite manufacturing. J Build Eng 2019;24:100742. https://doi.org/10.1016/j.jobe.2019.100742

[9] Silva R, De Brito J, Dhir R. Properties and composition of recycled aggregates from construction and demolition waste suitable for concrete production. Constr Build Mater 2014;65:201-17. https://doi.org/10.1016/j.conbuildmat.2014.04.117

[10] PN-RECYBETON R. RECYclage complet des BETONs 2011.

[11] Topcu IB, Şengel S. Properties of concretes produced with waste concrete aggregate. Cem Concr Res 2004;34:1307-12. https://doi.org/10.1016/j.cemconres.2003.12.019

[12] Katz A. Properties of concrete made with recycled aggregate from partially hydrated old concrete. Cem Concr Res 2003;33:703-11. https://doi.org/10.1016/S0008-8846(02)01033-5

[13] Nedeljković M, Visser J, Šavija B, Valcke S, Schlangen E. Use of fine recycled concrete aggregates in concrete: A critical review. J Build Eng 2021;38:102196. https://doi.org/10.1016/j.jobe.2021.102196

[14] Zhao Z, Remond S, Damidot D, Xu W. Influence of fine recycled concrete aggregates on the properties of mortars. Constr Build Mater 2015;81:179-86. https://doi.org/10.1016/j.conbuildmat.2015.02.037

[15] Neno C, Brito J de, Veiga R. Using fine recycled concrete aggregate for mortar production. Mater Res 2014;17:168-77. https://doi.org/10.1590/S1516-14392013005000164

[16] Nguyen VN. Valorisation de fines et granulats issus de bétons recyclés comme matériaux cimentaires: Enhancement of fine and aggregate issued from recycled concrete as cementitious materials 2016.

[17] Miller SA, Horvath A, Monteiro PJ. Readily implementable techniques can cut annual CO2 emissions from the production of concrete by over 20%. Environ Res Lett 2016;11:074029. https://doi.org/10.1088/1748-9326/11/7/074029

[18] Pavlů T, Kočí V, Hajek P. Environmental assessment of two use cycles of recycled aggregate concrete. Sustainability 2019;11:6185. https://doi.org/10.3390/su11216185

[19] Nwankwo CO, Bamigboye GO, Davies IE, Michaels TA. High volume Portland cement replacement: A review. Constr Build Mater 2020;260:120445. https://doi.org/10.1016/j.conbuildmat.2020.120445

[20] Rocha JHA, Toledo Filho RD. The utilization of recycled concrete powder as supplementary cementitious material in cement-based materials: A systematic literature review. J Build Eng 2023:107319. https://doi.org/10.1016/j.jobe.2023.107319

[21] Zhang H, Xiao J, Tang Y, Duan Z, Poon C. Long-term shrinkage and mechanical properties of fully recycled aggregate concrete: Testing and modelling. Cem Concr Compos 2022;130:104527. https://doi.org/10.1016/j.cemconcomp.2022.104527

[22] Xu J, Kang A, Wu Z, Gong Y, Xiao P. The effect of mechanical-thermal synergistic activation on the mechanical properties and microstructure of recycled powder geopolymer. J Clean Prod 2021;327:129477. https://doi.org/10.1016/j.jclepro.2021.129477

[23] Lv X, Wang L, Chen X, Li Q. Experimental study on the activity of concrete recycled powder. J Qingdao Technol Univ 2009;30:137-9.
[24] Ma X, Wang Z. Effect of ground waste concrete powder on cement properties. Adv Mater Sci Eng 2013;2013. https://doi.org/10.1155/2013/918294
[25] Florea M, Ning Z, Brouwers H. Activation of liberated concrete fines and their application in mortars. Constr Build Mater 2014;50:1-12. https://doi.org/10.1016/j.conbuildmat.2013.09.012
[26] S. Zhao, Y. Li, X. Kang, et Y. Fan, « Experimental Study on Frost Resistance of Recycled Fine Powder Concrete », Ind Constr, vol. 50, no 96, p. 112-118, 2020.
[27] Kim J, Jang H. Closed-loop recycling of C&D waste: Mechanical properties of concrete with the repeatedly recycled C&D powder as partial cement replacement. J Clean Prod 2022;343:130977. https://doi.org/10.1016/j.jclepro.2022.130977
[28] Li S, Gao J, Li Q, Zhao X. Investigation of using recycled powder from the preparation of recycled aggregate as a supplementary cementitious material. Constr Build Mater 2021;267:120976. https://doi.org/10.1016/j.conbuildmat.2020.120976
[29] Xiao J, Ma Z, Sui T, Akbarnezhad A, Duan Z. Mechanical properties of concrete mixed with recycled powder produced from construction and demolition waste. J Clean Prod 2018;188:720-31. https://doi.org/10.1016/j.jclepro.2018.03.277
[30] Chen X, Li Y, Bai H, Ma L. Utilization of Recycled Concrete Powder in Cement Composite: Strength, Microstructure and Hydration Characteristics. J Renew Mater 2021;9:2189-208. https://doi.org/10.32604/jrm.2021.015394
[31] Cantero B, Bravo M, De Brito J, Sáez Del Bosque IF, Medina C. Thermal Performance of Concrete with Recycled Concrete Powder as Partial Cement Replacement and Recycled CDW Aggregate. Appl Sci 2020;10:4540. https://doi.org/10.3390/app10134540
[32] H. Wu, D. Yang, J. Xu, C. Liang, et Z. Ma, « Water transport and resistance improvement for the cementitious composites with eco-friendly powder from various concrete wastes », Constr. Build. Mater., vol. 290, p. 123247, 2021. https://doi.org/10.1016/j.conbuildmat.2021.123247
[33] EN 1097-6:2022 - Tests for mechanical and physical properties of aggregates - Part 6: Determination of particle density and water absorption n.d.
[34] EN 196-6:2018 - Methods of testing cement - Part 6: Determination of fineness n.d.
[35] EN 1097-2:2010 - Tests for mechanical and physical properties of aggregates - Part 2: Methods for the determination of resistance to fragmentation n.d.
[36] EN 1097-1:2023 - Tests for mechanical and physical properties of aggregates - Part 1: Determination of the resistance to wear (micro-Deval) n.d.
[37] EN 933-8:2012 - Tests for geometrical properties of aggregates - Part 8: Assessment of fines - Sand equivalent test n.d.
[38] EN 933-1:2012 - Tests for geometrical properties of aggregates - Part 1: Determination of particle size distribution - Sieving method n.d.
[39] Aïtcin P-C. Bétons haute performance. 2001.
[40] EN 12350-2:2019 - Testing fresh concrete - Part 2: Slump test n.d.
[41] EN 12350-6:2019 - Testing fresh concrete - Part 6: Density n.d.
[42] EN 12390-3:2019 - Testing hardened concrete - Part 3: Compressive strength of test specimens n.d.
[43] EN 12390-5:2019 - Testing hardened concrete - Part 5: Flexural strength of test specimens n.d.
[44] C09 Committee. Test Method for Density, Absorption, and Voids in Hardened Concrete n.d.
[45] Z. Duan, S. Hou, J. Xiao, et B. Li, « Study on the essential properties of recycled powders from construction and demolition waste », J. Clean. Prod., vol. 253, p. 119865, 2020. https://doi.org/10.1016/j.jclepro.2019.119865
[46] Kim J, Nciri N, Sicakova A, Kim N. Characteristics of waste concrete powders from multi-recycled coarse aggregate concrete and their effects as cement replacements. Constr Build Mater 2023;398:132525. https://doi.org/10.1016/j.conbuildmat.2023.132525
[47] Wu H, Liang C, Xiao J, Xu J, Ma Z. Early-age behaviour and mechanical properties of cement-based materials with various types and fineness of recycled powder. Struct Concr 2022;23:1253-72. https://doi.org/10.1002/suco.202000834
[48] Cantero B, Bravo M, De Brito J, Sáez Del Bosque IF, Medina C. Mechanical behaviour of structural concrete with ground recycled concrete cement and mixed recycled aggregate. J Clean Prod 2020;275:122913. https://doi.org/10.1016/j.jclepro.2020.122913
[49] P. Zhang, L. Gu, Q. Wang, et X. Chen, « Study on the Method of Stimulating the Activity of Regenerated Micropowder », China Concr Cem Prod, vol. 2, p. 90-93, 2019.
[50] Y. Ma, « Experimental study on proper-ties of recycled micro powder concrete mixed with construction waste », China Concr Cem Prod, vol. 3, p. 88-90, 2016.
[51] Moon D-J, Moon H-Y, Kim Y-B. Fundamental Properties of Mortar Containing Waste Concrete Powder. Geosystem Eng 2005;8:95-100. https://doi.org/10.1080/12269328.2005.10541243

[52] Liu X, Liu L, Lyu K, Li T, Zhao P, Liu R, et al. Enhanced early hydration and mechanical properties of cement-based materials with recycled concrete powder modified by nano-silica. J Build Eng 2022;50:104175. https://doi.org/10.1016/j.jobe.2022.104175
[53] Wu H, Yang D, Ma Z. Micro-structure, mechanical and transport properties of cementitious materials with high-volume waste concrete powder and thermal modification. Constr Build Mater 2021;313:125477. https://doi.org/10.1016/j.conbuildmat.2021.125477
[54] Wu H, Liang C, Wang C, Ma Z. Properties of green mortar blended with waste concrete-brick powder at various components, replacement ratios and particle sizes. Constr Build Mater 2022;342:128050. https://doi.org/10.1016/j.conbuildmat.2022.128050

Blank Page

Research on Engineering Structures & Materials
www.jresm.org
MIM Research Group

Research Article

Influence of samarium oxide mixing on the structural and optical properties of tin oxide thin films prepared by pulsed laser deposition

Noor Sadie Saleh [a], Jamal M. Rzaij [*,b]

Department of Physics, College of Science, University of Anbar, Ramadi, Iraq

Article Info

Article History:

Received 06 Dec 2024

Accepted 15 Apr 2025

Keywords:

Sn;
Structural and optical properties;
Rare–earth elements;
Optoelectronic applications

Abstract

Due to the growing demand for optoelectronic applications, it is imperative to investigate the properties of thin films and identify the most suitable ones for use in optical detectors, gas sensors, and solar cells. In a novel investigation, this work analyses the impact of samarium oxide (Sm_2O_3) mixing at varying weight ratios (5, 7, and 9 wt.%) on the structural, morphological, and optical properties of tin oxide (Sn) films deposited by pulsed laser deposition (PLD). XRD analysis confirmed the crystallization of a polycrystalline structure of SnO_2 and SnO phases (SnOx). The crystallite size decreased from 13.1 nm to 7.2 nm with samarium content up to 7 wt.% and then increased to 11.3 nm at 9 wt.%. Top-view field emission scanning electron microscopy (FE-SEM) images revealed a broad particle size distribution that fluctuated with the Sm_2O_3 mixing ratio, exhibiting an average diameter of 44.53–35 nm. The incorporation of Sm_2O_3 elevated the film thickness to 629 nm at the maximum ratio. Atomic emissions of Sn, Sm, and O elements were identified using Energy-dispersive X-ray spectroscopy (EDX), and elemental mapping verified the homogeneous distribution of Sm into the SnOx film's surface. UV-visible transmittance spectra showed decreased transmittance from 80% to 63% at a higher Sm_2O_3 mixing ratio. In contrast, photoluminescence (PL) spectra exhibited a red emission peak shift, which reduced the optical bandgap from 3.4 eV to 3.15 eV. The results indicate that Sm_2O_3-mixed SnOx thin films exhibit adjustable characteristics appropriate for optoelectronic and catalytic applications.

© 2025 MIM Research Group. All rights reserved.

1. Introduction

Transparent conducting oxides (TCO) are outstanding semiconductors with high electrical conductivity and a wide transmittance in the visible spectrum. The applications of TCO materials are widely used in research and technology due to their distinctive qualities. Deep studies on the wide optical band gap of semiconducting metal oxides, such as Ti, ZnO, GaN, In2O3, and Sn, have been conducted over the past few decades and are still highly active materials being studied recently. Because of its greater stability in ambient circumstances, stability at high temperatures, mechanical hardness, and chemically inert properties. Sn is one of the most widely used materials among the available TCOs [1,2].

Among transparent conducting oxides, tin dioxide is an n-type semiconductor with a negative majority of charge carriers (n-type) and a tetragonal crystal structure. Due to its broadband gap (about 3.6 eV), it is a promising option for optoelectronic applications such as gas sensors, light-emitting diodes (LEDs), phototransistors, and solar cell window layers [3].

*Corresponding author: sc.jam72al@uoanbar.edu.iq
[a]orcid.org/0009-0003-1954-514X; [b]orcid.org/0000-0003-2287-3083
DOI: http://dx.doi.org/10.17515/resm2025-566ma1206rs

Pure Sn thin films have limited use in many optoelectronic device applications because of their low carrier density and mobility. The electrical conductivity and optical transmittance of Sn are typically caused by oxygen vacancies in the crystal lattice [4]. Several suggestions have been investigated for doping tin oxide with metal ions, such as Sm [5], Eu [6], and Gd [1], or semiconductor oxides, such as Sn:CdO [7], CdS: Sn [8], and ZnO: Sn [9], to enhance its physical and chemical characteristics for employment in the applications mentioned earlier. Previous researchers have employed various deposition techniques, including magnetron sputtering [10], Sol-gel [11], hydrothermal route [12], and spray pyrolysis [2], to develop thin tin oxide coatings in nanosized structures. Thin films of Sn were prepared by Emeka Charles et al. [13] using metalorganic precursors on glass substrates at different annealing temperatures. The synthetic results showed that the films deposited at an annealing temperature of 500 °C were polycrystalline with a tetragonal structure, while those deposited at 250 °C were random. The surface morphology results confirmed the presence of nanometer-sized particles, which increased with rising annealing temperature. The absorption spectra showed that the energy gap decreased with increasing annealing temperature, while the deposited films' transmittance reached its peak (83.2%) at a wavelength around 350 nm. The conclusions confirmed that the Ti films show promising properties at annealing temperatures around 500 °C.

Thin films of Sn doped with Sm_2O_3 at different weight percentages were deposited by Ahmadnia-Feyzabad et al. using a chloride solution combustion calcined at 400 °C in the air for gas sensor applications [14]. The diffraction index of the polycrystalline samples is indexed to the tetragonal rutile structure of Sn, and no peak corresponds to Sm_2O_3. When the wt.% of Sm_2O_3 reached its maximum, the size of the particles increased from less than 100 nm to more than 300 nm. Sm_2O_3 alters the reaction mechanism, reduces the crystallite sizes of nanoparticles, raises the concentration of oxygen vacancies, and modifies the catalytic activity of the Sn sensing characteristics. Singkammo et al. [15] used flame spray pyrolysis to create Sn thin films doped with 0.1-2 wt% Sm_2O_3 nanoparticles. The study concentrated on Sm_2O_3's catalytic properties and their effects on C2H4O sensing features. XRD investigation revealed a highly sharp peak of the tetragonal Sn structure with an average crystallite size of 10 nm. The top-view SEM images of Sm-doped Sn nanoparticles show agglomerated nanoparticles with particle sizes of less than 50 nm. The gas sensing results indicated that the incorporation of Sm_2O_3 enhanced the sensitivity of the Sn thin film by approximately sixfold relative to the as-deposited sample.

Researchers in most of the above studies reported the Sn deposition using chemical deposition methods. One drawback of chemical deposition methods is that they involve high deposition temperatures. In contrast, physical methods can develop thin films of high homogeneity and purity at comparatively low temperatures. Moreover, compared to physical techniques, chemical procedures are more expensive and complicated and can be connected with hazards. An important physical method for depositing different metals, oxides, sulfates, and nitrides is pulsed laser deposition (PLD) [16]. The basic principle of PLD is the interaction of a high-energy laser beam with the target material inside a vacuum chamber to develop a plasma plume driving the ablated material toward the deposition substrate. The technique yields high-purity thin films while preserving the stoichiometry material, enabling precise control over the thickness of the formed films at a relatively rapid deposition rate. However, PLD can suffer from particulate contamination and limited area uniformity, and expensive laser systems and vacuum chambers are required. The discrete nature of target material delivery in PLD results in a plasma plume with energetic species, such as ions, atoms, and molecules, that deposit on the substrate [17–20].

The rare-earth elements are interesting dopants due to their unique electronic and optical properties. Rare-earth doping/mixing can improve semiconductor oxides' structural, optical, and electrical characteristics by introducing additional charge carriers, which is beneficial for numerous applications. They can also enhance reactivity by creating more active sites on their surface for gas sensing or catalysis applications [21]. Additionally, rare-earth elements can modify the optical properties of Sn by introducing new energy levels within its band gap, enhancing optoelectronic and sensing features [22,23]. The incorporation of rare-earth elements, such as samarium atoms, into catalyst materials results in a reduction in crystal size, an increase in surface area, and exceptional stability in chemical reactions [24]. Furthermore, the occupied Sm, a

substitutional site of Sn in the crystal lattice of Sn, demonstrates donor-like characteristics, whereas oxygen vacancies function as acceptors [25]. This study investigated the impact of mixing samarium oxide at varying weight ratios on the structural, morphological, and optical characteristics of tin oxide films deposited via the pulsed laser deposition technique.

2. Experimental

2.1 Substrate Cleaning

The prepared films were deposited on soda lime glass substrates measuring 2.5×2.5 cm to investigate their optical properties after they were washed with distilled water and detergent solution. They were subsequently cleaned ultrasonically in ethanol for fifteen minutes and finally dried with a dryer. Moreover, silicon wafers measuring 1.5×1.5 cm were used to examine the deposited films' structural characteristics and surface morphology. The silicon wafers were cleansed using a Hydrofluoric acid (HF) solution diluted with water at a 1:5 ratio, subsequently rinsed with distilled water to eliminate residual acid, then immersed in an ethanol bath for fifteen minutes and dried with a dryer.

2.2 Materials and Methods

A Q-switching pulsed ND-YAG laser system (Smart Pico, Deka, Italy) with double wavelengths of 1064 nm and 532 nm was used to deposit unmixed and Sm_2O_3 mixed-Sn thin films at varying weight percentages (5, 7, and 9 wt.%) on n-type silicon substrates. The deposition chamber comprises a holder supporting a rotating base (35 rpm), upon which the target is affixed to avoid fast etching and uniform ablation of the target. The substrate holder is positioned approximately 4 cm vertically above the substrate holder. A tin oxide target, measuring 0.5 cm in thickness and 3 cm in diameter, was formed using 5 gm of Sn powder utilizing a hydraulic press at about 118 kPa for 24 hours to enhance atomic cohesion within the compressed target disc. This increased its stability and density, improving the deposited film's quality. The resulting target was condensed by annealing at 550 °C for 2 hours in air. The SnO_2 target was selectively ablated at room temperature (~28 °C) using an Nd-YAG laser with a wavelength of 1064 nm, pulse energy of 700 mJ, pulse frequency of 6 Hz, pulse duration of 9 nanoseconds, a focal spot area of 12.56 mm^2, an energy density of 55.73 mJ/mm^2 per laser pulse, and a total of 700 pulses. Fig. 1 illustrates the schematic diagram of the pulsed laser deposition system.

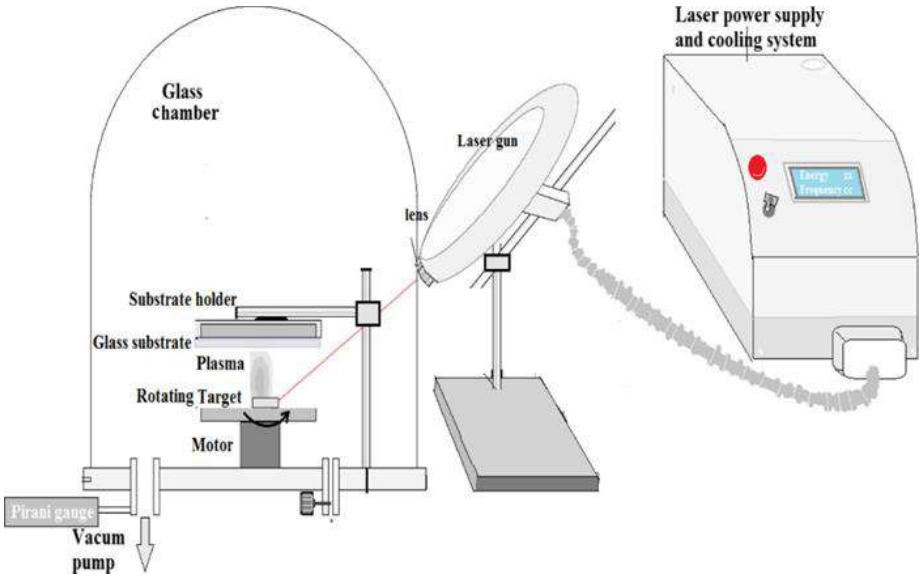

Fig. 1. Schematic diagram of pulsed laser deposition system

The impulse and coupling coefficient at varying pressures depend on the target's ablation and plasma characteristics, which are affected by the laser wavelength. As the wavelength of the laser decreases, there is a corresponding increase in both the depth of the crater and the bulk of the ablated material. Under atmospheric pressure, the plasma plume tends to disperse, whereas its

length continuously extends in low-pressure conditions. This leads to a plasma comprising more ablated particles exhibiting increased velocities, enhancing both the impulse and coupling coefficients [26]. Thus, in this work, the deposition chamber was evacuated to 20 Pa, and a laser pulse with a wavelength of 1064 nm was used to achieve more uniform thin film coatings and decrease the mean free path of the ablated particles. Finally, the deposited films were annealed at 500°C in air for 2 hours. To obtain SnO_2 targets mixed with Sm_2O_3, the previous procedure was repeated with 5, 7, and 9 wt.% Sm_2O_3 mixed. SnO_2 and Sm_2O_3 powders were purchased from Aldrich Chem., USA, with a high purity of 99.98%.

2.3 Thin Film Characterization

A Dandong Haoyuan DX-2700B XRD with a Cu-Kα source was employed at ambient temperature to examine crystalline structures. A diffraction angle (2θ) range of 10° to 80° with an X-ray wavelength of 1.54056 Å. The surface morphology of SnO_2 thin films was examined using a Field Emission Scanning Electron Microscope (FE-SEM, MIRA3 diffractometer (TESCAN)) equipped with energy-dispersive X-ray Spectroscopy. The optical properties of the developed thin films were investigated by depositing them on glass substrates and detecting the optical absorption spectra. Spectral measurements were conducted with a dual-beam UV-Vis spectrometer manufactured in England, with a 200 to 900 nm spectral range. The Photoluminescence (PL) analysis was performed utilizing the FluoroMate FS-2 spectrometer manufactured by Scinco, Korea. The excitation wavelength was 290 nm at room temperature, and the detection range ranged from 300 to 600 nm.

3. Results and Discussions

3.1 X-ray Diffraction

Fig. 2 shows the as-deposited and SnO_x XRD patterns mixed with Sm_2O_3 at different concentrations (5, 7, and 9 wt.%) of thin films by pulsed laser deposition technique. Polycrystalline structure of mixed phases of the dominant orthorhombic SnO with tetragonal SnO_2 structure according to standard PDF cards 000-55-0837 and 010–75-9495, respectively. The matching result was obtained by Nikiforov et al. using the molecular beam epitaxy deposition method [27].

The XRD pattern verified the crystallization of the polycrystalline structure of SnO_2 and SnO phases, which agrees with the previous studies [28,29]. Given that the fabricated films were produced using laser ablation in a vacuum environment, a significant concentration of oxygen vacancies will be expected. When atoms of the target material are ablated in a vacuum to be deposited on the substrate at room temperature, the diffusion length of similar atoms on the substrate's surface is small, inhibiting the movement of the ablated atoms. The restricted mobility of similar atoms supports the formation of polycrystalline structure films instead of a single crystalline structure [30]. Moreover, the enrichment of Sn on the target surface due to interaction with the plasma plume considerably elevates the Sn concentration in the films, enhancing its stoichiometric content in the SnO_2 structure [31]. The substitution of Sn by Sm causes nearest-neighboured oxygen vacancies, causing an increase in the crystallinity of the as-deposited SnO_2 compared with the SnO_2 mixed samples [32].

A crucial crystallographic characteristic is the crystallite size (D), determined using Scherrer's formula (Eq (1)) [33], which corresponds to the dominant diffraction peaks of the SnO and SnO_2 phases.

$$D = k\lambda/\beta\ cos\theta \tag{1}$$

where λ represents the X-ray wavelength, θ denotes the diffraction angle in radians, and k signifies the Scherrer correction factor (k=0.89).

Table 1 lists the diffraction angles (2θ), Full width at half maximum (β), interplanar distance (d_{hkl}), crystallite size (D), and the stress ($\boldsymbol{\varepsilon}$) of the deposited films. It illustrates a reduction in crystallite size from 13.1 nm to 7.2 nm with the increment of samarium content up to 7 at wt.%, followed by an increase to 11.3 nm when the samarium oxide content attains 9 wt.%. However, the effect of

samarium oxide mixing effectively decreased the deposited films' crystal size. The reduction in crystal size can be attributed to the incorporation of samarium oxide in the tin oxide lattice. The crystal deformation caused by the incorporation of samarium in the tin oxide lattice can be determined by calculating the stress (Eq (2)) [34], which corresponds to the stress related to the diffraction peak width.

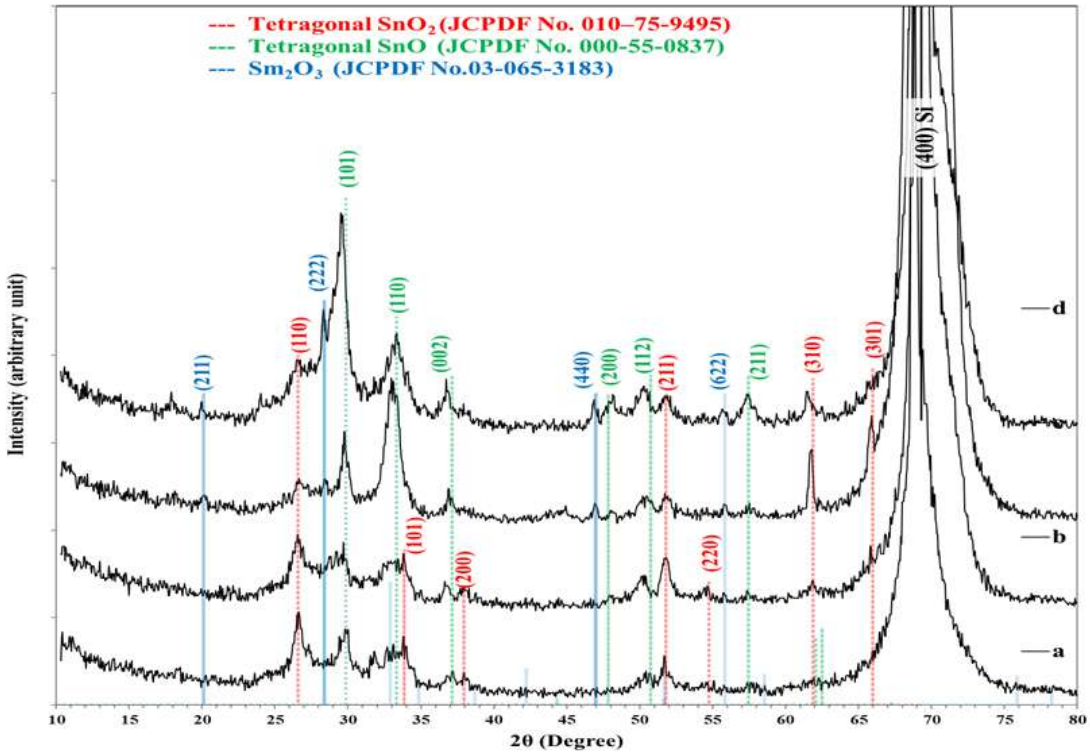

Fig. 2. XRD patterns of (a) the as-deposited SnO_2, (b) 5 wt.% Sm_2O_3 mixed-SnO_x, (c) 7 wt.% Sm_2O_3 mixed-SnO_x, and (d) 9% Sm_2O_3 mixed-SnO_x

$$\varepsilon\ (\%) = \beta/4\ tan\theta \tag{2}$$

The stress induced by samarium within the tin oxide lattice inhibits the development of tin oxide crystals and limits the movement of grain boundaries, as illustrated in Table 1. Singkammo *et al.* [15] reported a comparable outcome. In optoelectronic applications, reduced nano-sized crystal dimensions provide an increased surface area for the interaction with target gas molecules and/or incident light, enhancing the interaction with gas and/or optical detectors and markedly improving their responsiveness [35].

Table 1. Diffraction angle and crystallite size corresponding to the dominant diffraction peak at various Sm_2O_3 concentrations

Sm_2O_3%	2θ (Deg.)	β (Deg.)	β (rad)	d_{hkl} (Å)	D (nm)	(hkl)	Phase	ε(%)
0	26.5835	0.651	0.0114	3.3504	13.1	(110)	SnO_2	1.20
5	26.5492	0.7881	0.0138	3.3547	10.8	(110)	SnO_2	1.46
7	32.9907	1.1992	0.0209	2.7129	7.2	(110)	SnO	1.77
9	29.5672	0.758	0.0132	3.0188	11.3	(101)	SnO	1.25

The examination of the structural characteristics of the deposited films confirmed that an increase in Sm_2O_3 wt.% resulted in a slight shift of the diffraction peaks towards lower diffraction angles, signifying an increase in the crystal lattice constants, as illustrated in Table 2. The lattice constants of the prepared films were calculated based on the dominant diffraction peak of each diffraction

pattern. The increased value of the lattice constants is ascribed to the larger atomic radius of samarium (185 pm) relative to that of tin (145 pm). An identical investigation has been reported by Shaikh *et al*. [36].

Table 2. Lattice parameters of SnO_2 and SnO at various Sm_2O_3 wt.% contents.

Sm_2O_3 wt.%	SnO_2		SnO	
	a (Å)	c (Å)	a (Å)	c (Å)
0	4.72281	3.18377	3.80041	4.83804
5	4.72629	3.18432	3.80648	4.86839
7	4.72826	3.18551	3.81613	4.87713
9	4.73326	3.18639	3.81677	4.89031

3.2 Surface Morphology Analysis

Fig. 3a presents the top view of FE-SEM images at two magnifications, along with a histogram illustrating the particle size distribution of SnO_x as it is deposited and mixed with Sm_2O_3 thin films. The SnO_x thin films have a broad surface interlaced with randomly distributed spherical nanoparticles. The histogram depicts a diverse particle size distribution ranging from 10 nm to 200 nm, with a mean diameter of 44.53 nm and a standard deviation of 27.1 nm; the analysis was determined by ImageJ software. The incorporation of Sm_2O_3 into SnO_x at varying wt.% considerably impacts particle diameter and distribution, hence changing the characteristics of the samples. As shown in Fig. 3b, the average particle diameter decreased to 25.74 nm at a 5 wt.% Sm_2O_3 mixing ratio, with a standard deviation of 11.0 nm. The Sm_2O_3 addition reduced the size distribution to between 10 and 45 nm, in contrast to the as-deposited SnO_x sample, indicating a homogeneous particle size distribution. At a 7 wt.% Sm_2O_3 mixing ratio (Fig. 3c), the average particle diameter increased to 26.4 nm, with a standard deviation of 15 nm. However, the average particle diameter increased to 35.2 nm, with a standard deviation of 17.8 nm, indicating a broader size distribution when the Sm_2O_3 mixing ratio reached 9 wt.% (Fig. 3d).

The incorporation of Sm_2O_3 reduced the particle diameter, resulting in deposited surfaces with an enhanced surface area-to-volume ratio; smaller particles augment this ratio, thus improving the film's reactivity, adsorption capacity, or catalytic efficiency. These alterations are substantial in applications such as coatings, sensors, or electronic devices, where particle size directly influences performance [37,38]. Adding samarium oxide also controls grain development, resulting in a reduced, more homogenous structure that improves mechanical characteristics. The narrow, homogenous distribution raises the threshold electric field to enhance variable varistors' non-linear electrical characteristics. Moreover, the films' high surface-to-volume ratio enhances oxidation and reduction reactions when used as gas sensors [35,39].

Cross-sectional scanning electron microscope images (Fig. 4a-d) indicated that the thickness of the SnO/SnO_2 thin films increased from 376 nm to 629 nm with increasing Sm_2O_3 content; the analysis was determined by ImageJ software. Film thickness increase can be explained by including Sm in the SnO_x lattice, which is attributed to the ionic/atomic diameter disparity between tin and samarium. This discrepancy increased interatomic distance inside the crystal lattice, enhancing lattice parameters, confirmed by structural analysis results, and, ultimately, a thicker deposited layer [40–42]. This is demonstrated in Fig. (4-d), which indicates that the film incorporating 9 wt.% samarium oxide, the maximum mixing ratio, exhibited the highest thickness.

Fig. 5 shows the variation in the thickness as a function of the Sm_2O_3 wt.% thin films with the standard deviation value. Adding Sm_2O_3 to SnO/SnO_2 films can be crucial in controlling their thickness. This control over thickness is essential for various applications, such as gas sensors, catalysis, and optoelectronic devices, where specific film thicknesses are required for optimal performance.

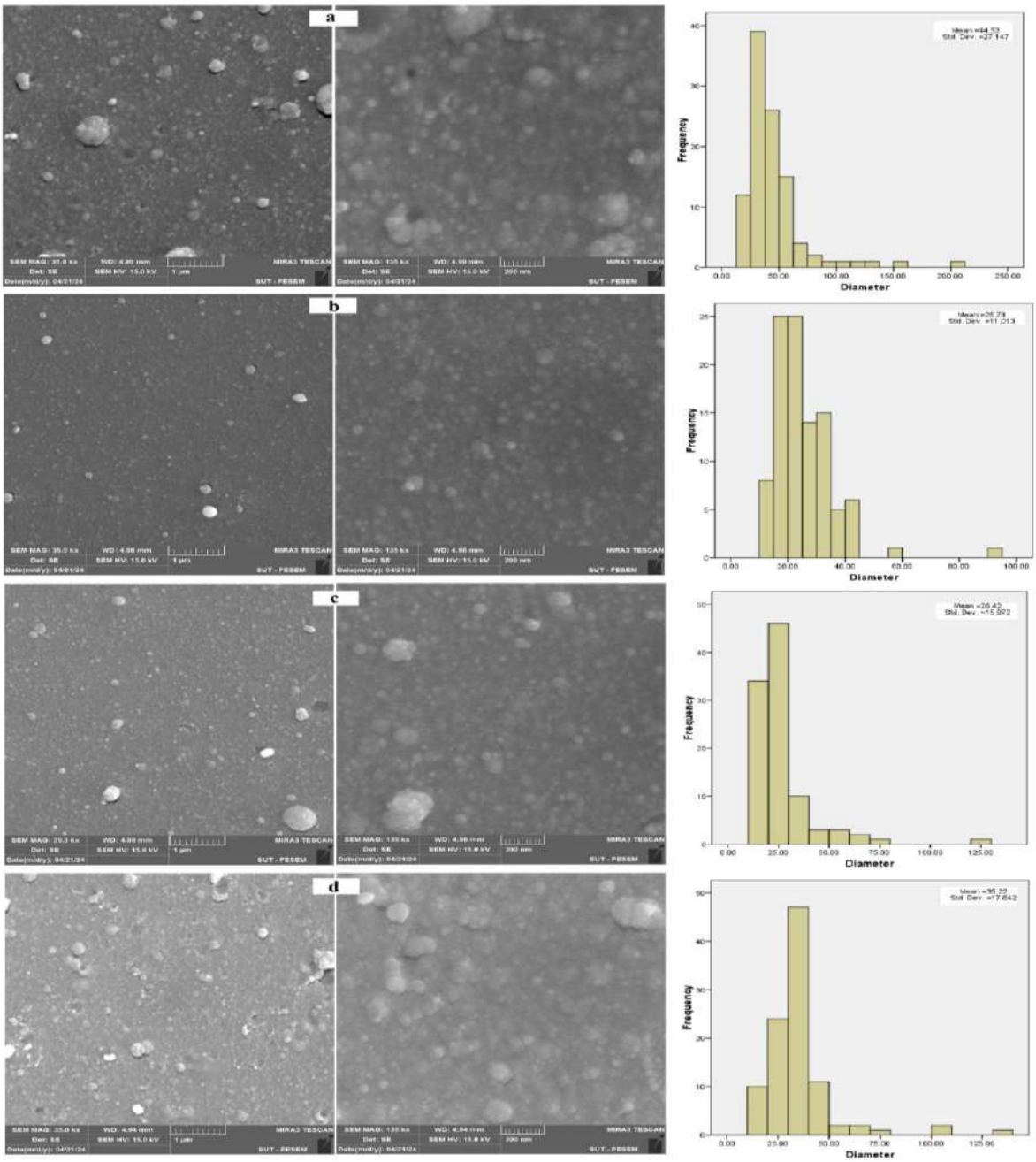

Fig. 3. Top-view FE-SEM images and particle diameter distribution (a) the as-deposited SnO_x, (b) 5 wt.% Sm_2O_3 mixed-SnO_x, (c) 7 wt.% Sm_2O_3 mixed-SnO_x, and (d) 9% Sm_2O_3 mixed-SnO_x

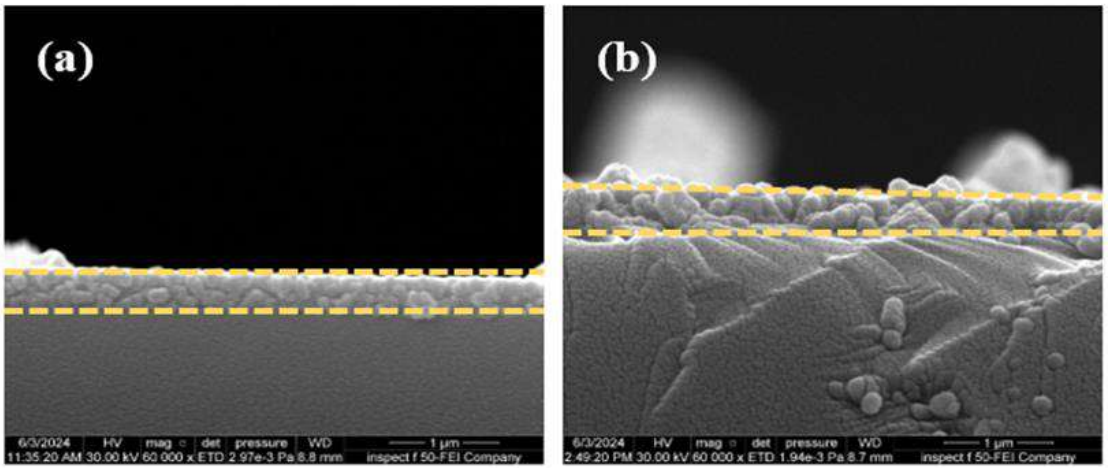

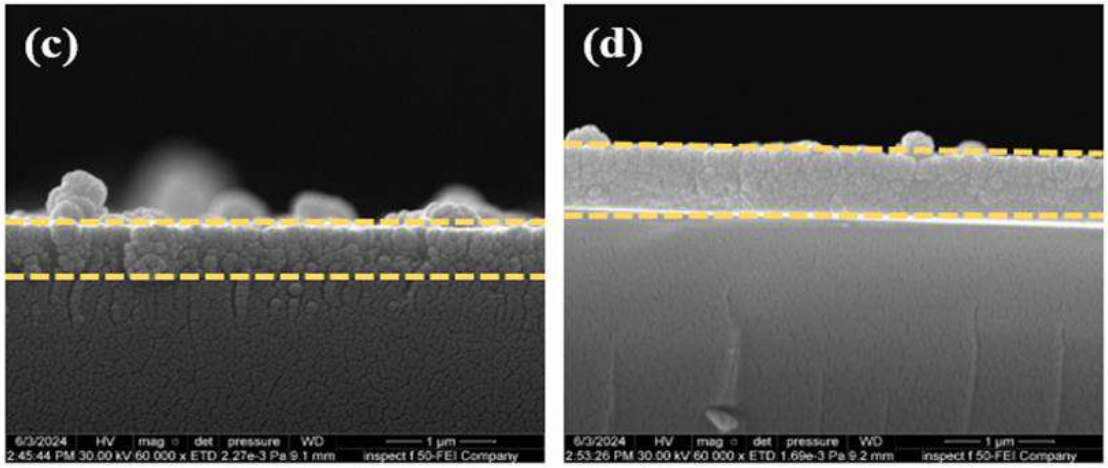

Fig. 4. Cross-sectional FE-SEM images of (a) the as-deposited SnO_x, (b) 5 wt.% Sm_2O_3 mixed-SnO_x, (c) 7 wt.% Sm_2O_3 mixed-SnO_x, and (d) 9% Sm_2O_3 mixed-SnO_x

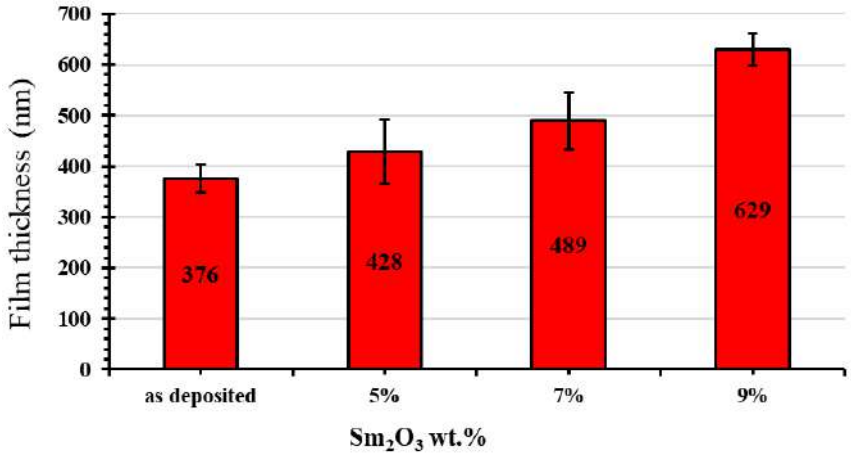

Fig. 5. Thickness variation of SnO_x as a function of the Sm_2O_3 wt.% thin films (The bar represents the standard deviation)

3.3 EDS Spectra Analysis

EDS spectra of the as-deposited SnO/SnO_2 and Sm_2O_3-mixed SnO/SnO_2 thin films at various mixing ratios are illustrated in Fig. 6(a-d). Atomic emissions of Sn, Sm, and O elements were detected. A significant peak at 1.7 keV, corresponding to Si emission from the Si substrate, was also observed. Additionally, an Au emission peak was present due to the prior deposition of a gold layer onto the samples as a preparatory step for SEM testing.

Table 3. Elemental analysis of Sm_2O_3 mixed-SnO_x at various mixing ratios

Sample	Element	Wt%	Atomic %
SnOx	O	28.27	74.21
	Sn	71.73	25.79
5% Sm_2O_3	O	29.69	75.9
	Sn	68.61	23.64
	Sm	1.7	0.46
7% Sm_2O_3	O	21.99	67.8
	Sn	75.55	31.4
	Sm	2.45	0.81
9% Sm_2O_3	O	22.89	69.02
	Sn	72.95	29.65
	Sm	4.15	1.33

These two peaks were neglected when determining element ratios. The decreased intensity of the O emission peak with increasing Sm_2O_3 content indicates a reduced incorporation of O atoms within the lattice, as listed in Table 3. Furthermore, the incorporation of Sm_2O_3 resulted in the development of Sm emission peaks, which correlated with a rise in the weight percentage of the film's components associated with Sm_2O_3 content. The EDS map shown next to the spectra, corresponding to Sn, O, and Sm atoms, indicates the uniform distribution of film surface elements and confirms the incorporation of Sm into the SnO_x matrix.

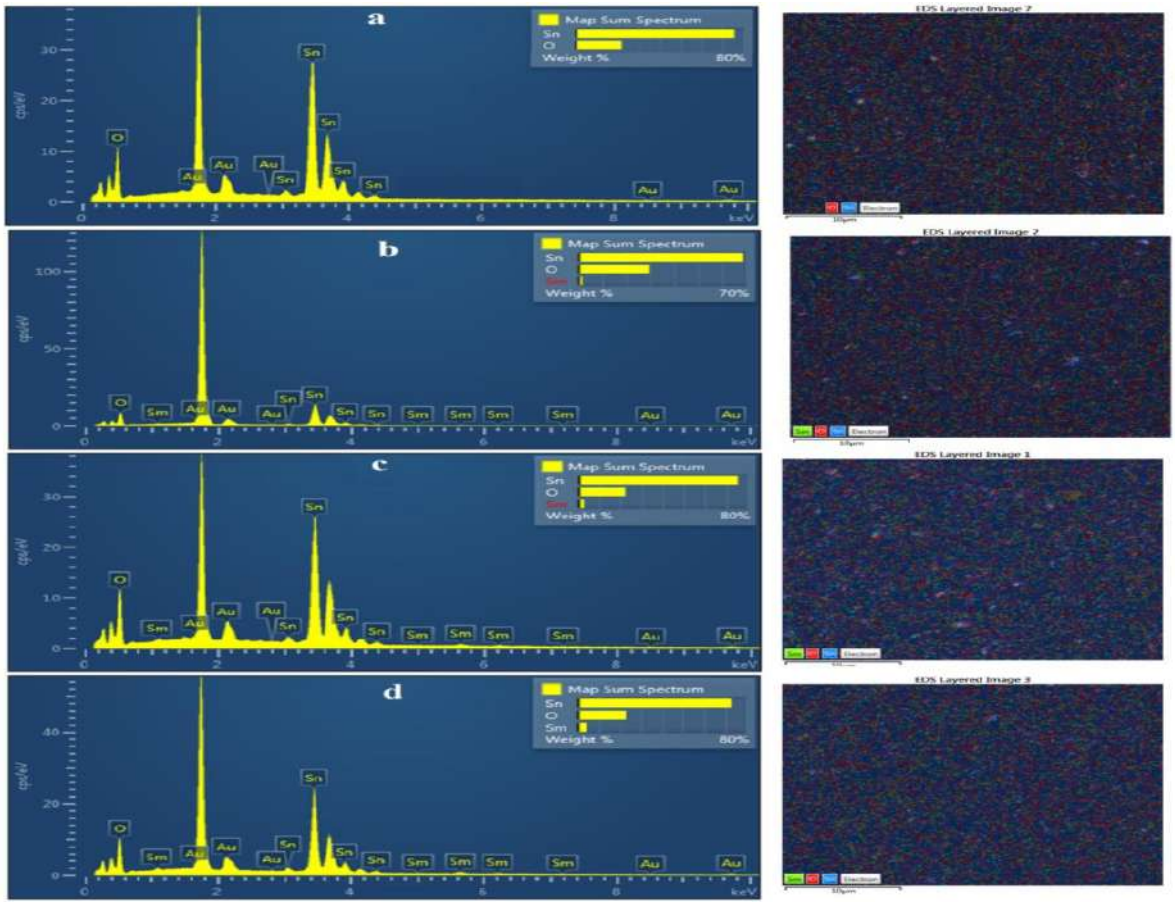

Fig. 6. EDX analysis of (a) the as-deposited SnO_x, (b) 5 wt.% Sm_2O_3 mixed-SnO_x, (c) 7 wt.% Sm_2O_3 mixed-SnO_x, and (d) 9% Sm_2O_3 mixed-SnO_x

3.4 Optical Properties

The transmittance spectrum analysis findings of the as-deposited and SnO_x-mixed Sm_2O_3 thin films are presented in Fig. 7. The average transmittance of the deposited films was determined within the wavelength ranging from 380 nm to 800 nm. The transmittance was determined to be 80%, 72%, 67%, and 63% for the as-deposited SnO_x thin films mixed with 5 wt.%, 7 wt.%, and 9 wt.% Sm_2O_3, respectively. The reduction in transmittance may be ascribed to incorporating samarium into the tin oxide crystals. The samarium atom contributes an extra electron, increasing the concentration of free electrons, enhancing the photon absorption of free carriers, and reducing the optical transmittance of the tin oxide films. Nion *et al.* observed the same behavior when magnesium oxide films were doped with aluminum. [43].

Fig. 7 additionally illustrates periodic fluctuations in the recorded transmittance spectrum. The fluctuation periodicity increased with increasing Sm_2O_3 content, indicating an increasing the film thickness [44]. The fluctuations in the transmittance spectrum result from interference effects on smooth surfaces. Smooth film surfaces reduce scattering and random light refraction, improving interference patterns; Sinha and Ramadan *et al.* recorded the same periodic fluctuations in the transmittance spectrum [45,46].

It is also noted that the optical absorption edge shifted towards longer wavelengths (redshift) with increasing samarium content, indicating a decrease in the optical energy gap [47], as shown in the energy gap results. The shift in the optical absorption edge is ascribed to the structural alterations of the synthesized films, where enhanced crystallinity leads to a shifting of the absorption edge towards longer wavelengths, which decreases extended to localized state transitions caused by the band tails formed by the defects (Sm_2O_3 content within the SnO_x lattice) [48].

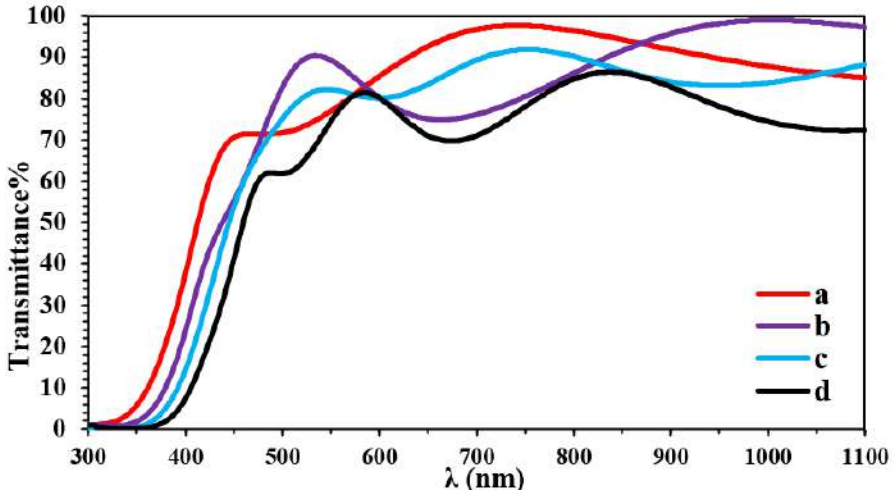

Fig. 7. Optical transmittance spectra of (a) as deposited-SnO_x and SnO_x mixed with (b) 5 wt.% (c) 7 wt.%, and (d) 9 wt.% of Sm_2O_3 thin films

The optical bandgap (Eg^{opt}) was determined using the Tauc relation, Eq (3), as depicted in Fig. 8, which demonstrates that the optical energy gap reduced from 3.4 eV to 3.15 eV with the rise of Sm_2O_3 content in the target to 9 wt.%. Numerous authors have explained the phenomenon of the reduction in the energy gap associated with an increase in particle size, which is further evidenced by a red shift in the absorption edge, as depicted in the optical transmittance spectrum (Fig. 7). This behavior is attributed to bulk defects from incorporating samarium oxide within the tin oxide matrix. These defects have been reported to have reversibly influenced the characteristics of molecular orbitals associated with the conduction band, thereby creating deep electron energy traps and resulting in a reduced energy gap [49–51].

$$\alpha h\upsilon = B(h\upsilon - E_g)^r \tag{3}$$

where $h\upsilon$ is the energy of the absorbed photon, B is a material-dependent constant and r is the exponential coefficient that varies with the type of transitions.

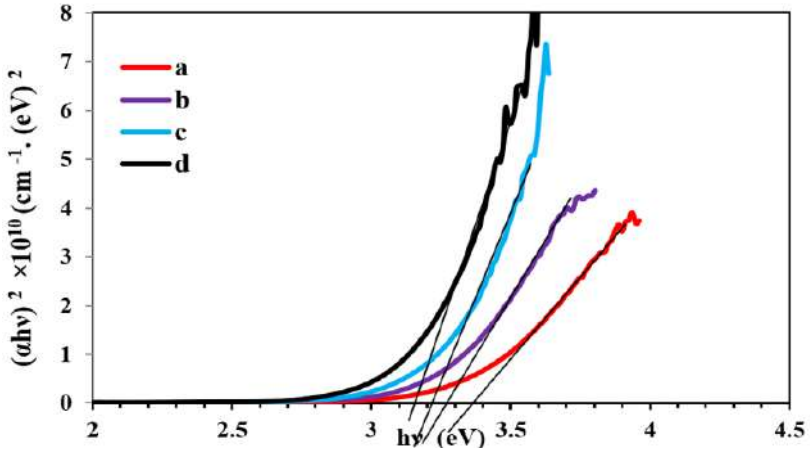

Fig. 8. Tauc-Plot of (a) as deposited-SnO_x and Sm_2O_3-mixed SnO_x at (b) 5 wt.% (c) 7 wt.%, and (d) 9 wt.%

Fig. 9 highlights the investigation's findings regarding average optical transmittance, optical energy gap, and the thickness of the developed films as a function of samarium oxide contents. The maximum content of samarium oxide (9 wt.%) reduced the optical transmittance of the as-deposited tin oxide films by roughly 21%. Reducing optical transmittance can enhance various applications, including protective glasses, solar cells, light filters, optical insulating materials, and light-shielding coatings in surgical and industrial settings. Compared to tin oxide films, samarium oxide contents reduce the energy gap, allowing the deposited films to be used as optical windows in solar cell applications, which allows a wider spectrum of light transmission. Additionally, compared to the as-deposited tin oxide, manufactured coatings can improve the sensitivity and efficiency of optical detectors by enhancing light transmission over a wider wavelength range. The developed films may also increase surface activity and chemical interaction, improving sensor responses against gases [41,52].

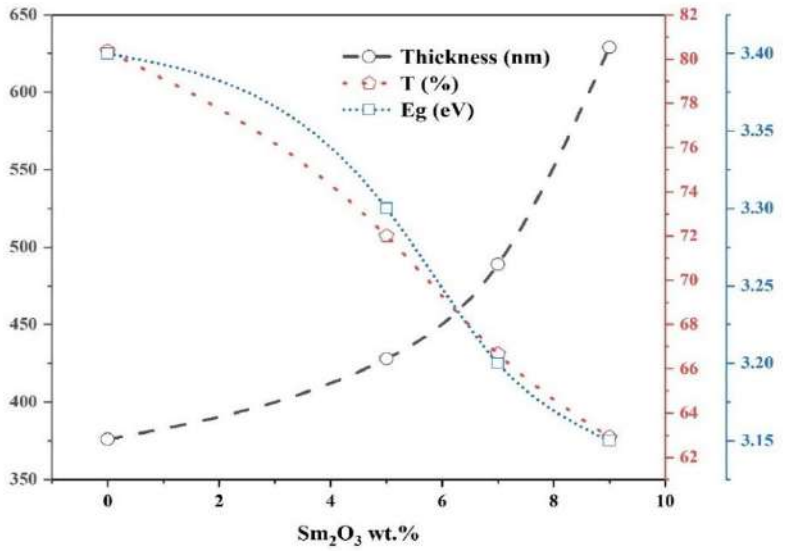

Fig. 9. Variation of optical transmittance, optical energy gap, and the thickness of the developed films as a function of samarium oxide contents

3.4 Photoluminescence results

Fig. 10 presents the photoluminescence spectra of the SnO_x and Sm_2O_3-mixed SnO_x at various wt.% thin films at room temperature, covering the wavelength range of 320 to 560 nm and utilizing an excitation wavelength of λ_{exc}=290 nm. A broad peak was observed in all samples at approximately 361 nm (3.43 eV), attributed to band-to-band transitions [53]. Incorporating the Sm_2O_3 to 9 wt.% caused a red shift in the emission peak up to 387 nm, indicating a reduction in the energy bandgap to 3.2 eV, as listed in Table 4.

Table 4. λ_{max}, Intensity, and corresponding PL emission of SnO_x and SnO_x mixed with Sm_2O_3 at various wt.% concentrations

Sample	λmax (nm)	Intensity (a.u)	Energy (eV)
SnOx	361	10.65	3.43
5 wt.% Sm_2O_3	371	9.55	3.34
7 wt. % Sm_2O_3	382	8.15	3.25
9 wt. % Sm_2O_3	387	6.84	3.2

The energy bandgap values derived from the photoluminescence spectra closely align with those determined using the Tauc relation, showing a decrease from 3.4 eV to 3.15 eV with increasing Sm_2O_3 content. The reduction in emission peak intensity suggests an increase in lattice defects with increasing Sm_2O_3 wt.% [54].

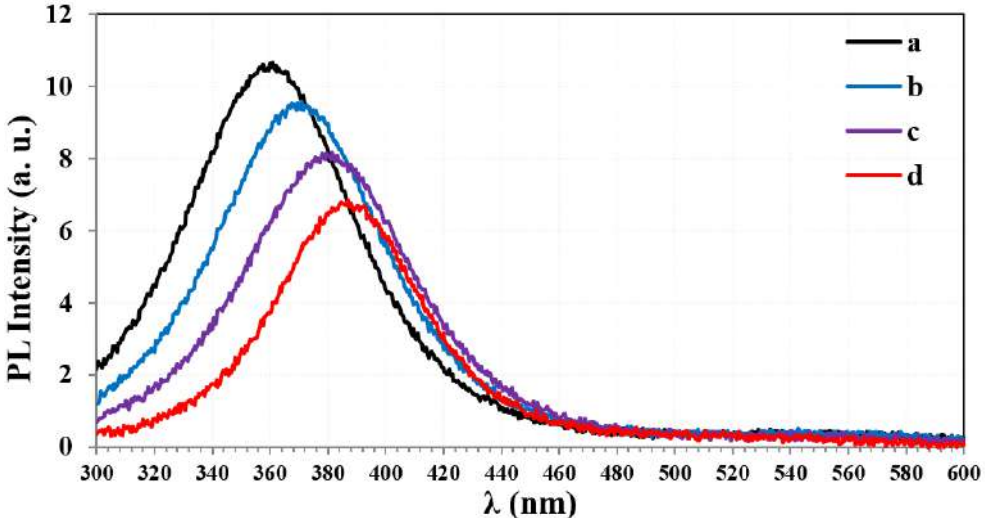

Fig. 10. PL of (a) as-deposited SnOx and Sm_2O_3-mixed SnO_x at (b) 5 wt.% (c) 7 wt.%, and (d) 9 wt.% thin films.

4. Conclusions

In this work, the pulsed laser deposition technique was successfully used to analyze the structural, morphological, and optical characteristics of SnO_x thin films mixed with various weight ratios of samarium oxide. The study demonstrates that Sm_2O_3 mixing significantly influences the structural, morphological, and optical properties of SnO_x thin films. Incorporating samarium oxide improved the crystallization of a polycrystalline structure and reduced the crystal size of tin oxide films. Polycrystalline phases greatly impact electronic applications by improving materials' electrical and thermal performance and supporting the creation of innovative materials with enhanced properties, such as gas sensors and photodetector features.

The morphological analysis revealed an extensive tin oxide thin film surface coated with almost spherical nanoparticles that are randomly distributed, exhibiting a uniform particle size distribution. Adding samarium oxide controls the surface area to volume ratio by reducing the diameters of tin oxide thin film particles, forming a more homogeneous microstructure that improves mechanical properties studies and gas sensor redox reactions. The thickness of the SnO_x thin films increased from 376 nm to 629 nm with the increasing samarium oxide mixing ratio, attributable to the incorporation of Samarium into the SnO_x lattice. This expands the interatomic distance of the SnO_x crystal lattice, enhances lattice parameters, and eventually results in a thicker deposition layer. The maximum content of samarium oxide (9 wt.%) reduced the optical transmittance of the as-deposited tin oxide films by roughly 21%. Reducing optical transmittance can enhance various applications, including protective glasses, solar cells, light filters, optical insulating materials, and light-shielding coatings in surgical and industrial settings. Moreover, reduced energy gap coatings transmit more light across a wider wavelength range for solar cell optical windows, boosting optical detector sensitivity and efficiency. These tunable properties make samarium oxide-mixed SnO_x thin films promising candidates for optoelectronic applications requiring specific optical and surface characteristics.

References

[1] S. P, J. RM, K. DAK, P.S. SK, S. P, L. A. Physical Properties of Rare Earth Metal (Gd3+) Doped SnO2 Thin Films Prepared by Simplified Spray Pyrolysis Technique Using Nebulizer. Optik, 2019; 194: 162887. https://doi.org/10.1016/j.ijleo.2019.05.093

[2] Rzaij JM, Abbas QA, Khalaf AM. Investigating the Structural, Topographical, Morphological and Optical Effects of AgO on Sprayed SnO2 Thin Films. Bulletin of Materials Science, 2023; 46(4): 200. https://doi.org/10.1007/s12034-023-03040-z

[3] Orhan Z, Daş E, Bozkurt G. Microemulsion Synthesis of SnO2 Nanoparticles and Their Integration in Au/n-Si/Al Device Structure. Journal of Materials Science: Materials in Electronics, 2025; 36(2): 158. https://doi.org/10.1007/s10854-025-14242-y

[4] Villamagua L, Stashans A, Lee P, Liu Y, Liu C, Carini M. Change in the Electrical Conductivity of SnO 2 Crystal from n -Type to p -Type Conductivity. CHEMICAL PHYSICS, 2015; 452: 71-77. https://doi.org/10.1016/j.chemphys.2015.03.002
[5] Akkera HS, Kumar Y, Kumar MD, Reddy GS, Kumar BR, Pasha UM, Bitla Y, Ganesh V. Structural, Electrical, and Optical Properties of Rare-Earth Sm3+ Doped SnO2 Transparent Conducting Oxide Thin Films for Optoelectronic Device Applications: Synthesized by the Spin Coating Method. Optical Materials, 2022; 133: 112993. https://doi.org/10.1016/j.optmat.2022.112993
[6] Morais EA de, Scalvi LVA, Cavalheiro AA, Tabata A, Oliveira JBB. Rare Earth Centers Properties and Electron Trapping in SnO2 Thin Films Produced by Sol-Gel Route. Journal of Non-Crystalline Solids, 2008; 354(42-44): 4840-4845. https://doi.org/10.1016/j.jnoncrysol.2008.04.029
[7] Suhail MH. Preparation and Characterization of Mixed SnO2:CdO Thin Films as Gas Sensor. Iraqi Journal of Physics, 2019; 15(33): 28-39. https://doi.org/10.30723/ijp.v15i33.137
[8] Sao AK, Sharma A, Verma M, Tomar M, Chowdhuri A. Development of CdS-SnO2 Hybrid Nanocomposite Thin Films for Trace Level Detection of NO2 Gas. Sensors and Actuators B: Chemical, 2023; 393: 134198. https://doi.org/10.1016/j.snb.2023.134198
[9] Al-Jumaili HS, Jasim MN. Preparation and Characterization of ZnO: SnO2 Nanocomposite Thin Films on Porous Silicon as H2S Gas Sensor. Journal of Ovonic Research, 2019; 15(1): 81-87.
[10] Abuelwafa AA, El-sadek MSA, Elnobi S, Soga T. Effect of Transparent Conducting Substrates on the Structure and Optical Properties of Tin (II) Oxide (SnO) Thin Films: Comparative Study. Ceramics International, 2021; 47(10): 13510-13518. https://doi.org/10.1016/j.ceramint.2021.01.209
[11] Kadhim MA, Ramadhan AA, Al-Gburi MOS. Effect of PEG Addition on an SnO2 Gas Sensor Fabricated Using Spin Coating. Karbala International Journal of Modern Science, 2021; 7(1). https://doi.org/10.33640/2405-609X.2486
[12] Meng D, Liu D, Wang G, Shen Y, San X, Li M, Meng F. Low-Temperature Formaldehyde Gas Sensors Based on NiO-SnO2 Heterojunction Microflowers Assembled by Thin Porous Nanosheets. Sensors and Actuators B: Chemical, 2018; 273: 418-428. https://doi.org/10.1016/j.snb.2018.06.030
[13] Nwanna EC, Imoisili PE, Jen T-C. Synthesis and Characterization of SnO2 Thin Films Using Metalorganic Precursors. Journal of King Saud University - Science, 2022; 34(5): 102123. https://doi.org/10.1016/j.jksus.2022.102123
[14] Ahmadnia-Feyzabad S, Mortazavi Y, Khodadadi AA, Hemmati S. Sm2O3 Doped-SnO2 Nanoparticles, Very Selective and Sensitive to Volatile Organic Compounds. Sensors and Actuators B: Chemical, 2013; 181: 910-918. https://doi.org/10.1016/j.snb.2013.02.101
[15] Singkammo S, Wisitsoraat A, Tuantranont A, Phanichphant S, Yodsri V, Liewhiran C. Catalytic Roles of Sm2O3 Dopants on Ethylene Oxide Sensing Mechanisms of Flame-Made SnO2 Nanoparticles. Applied Surface Science, 2018; 454: 30-45. https://doi.org/10.1016/j.apsusc.2018.05.146
[16] Enad AM, Rzaij JM. Investigate the Structural , Morphological , and Topographical Characteristics of CuO Thin Films Utilizing a Pulsed Laser Deposition Method. Journal of Theoretical and Applied Physics, 2024; 18(AICIS'23): 1-8.
[17] Conde Garrido JM, Silveyra JM. A Review of Typical PLD Arrangements: Challenges, Awareness, and Solutions. Optics and Lasers in Engineering, 2023; 168: 107677. https://doi.org/10.1016/j.optlaseng.2023.107677
[18] Devitsky O V., Kravtsov AA. Effect of Thermal Annealing on the Structural Evolution of Thin Ceramic YAG: Ce Films Grown by Pulsed Laser Deposition. Ceramics International, 2024. https://doi.org/10.1016/j.ceramint.2024.12.047
[19] Pashchenko AS, Devitsky O V., Lunina ML, Danilina EM, Pashchenko OS, Ber B, Sakharov VI. Epitaxial Growth of GaInAsBi Thin Films on Si (001) Substrate Using Pulsed Laser Deposition. Vacuum, 2024; 227: 113372. https://doi.org/10.1016/j.vacuum.2024.113372
[20] Lorenz M, Hochmuth H, von Wenckstern H, Grundmann M. Flexible Hardware Concept of Pulsed Laser Deposition for Large Areas and Combinatorial Composition Spreads. Review of Scientific Instruments, 2023; 94(8). https://doi.org/10.1063/5.0142085
[21] Xu H, Li J, Li P, Shi J, Gao X. Effect of Rare Earth Doping on Electronic and Gas-Sensing Properties of SnO2 Nanostructures. Journal of Alloys and Compounds, 2022; 909: 164687. https://doi.org/10.1016/j.jallcom.2022.164687
[22] Mohammed Enad A, Rzaij JM. Synthesis of CuO Thin Film Incorporated with Nanostructured Nd 2 O 3 Deposited by Pulsed Laser Deposition for Ammonia Sensing Applications. Nano, 2024. https://doi.org/10.1142/S1793292024501133
[23] Madkhali O. A Review of Novel Methods to Improve the Optical and Electrical Properties of N-Type and p-Type Sulphides and Oxides: Leading the Frontiers of Semiconductor Technology. Physica Scripta, 2024; 99: 022004. https://doi.org/10.1088/1402-4896/ad1e44

[24] Tepamatr P, Laosiripojana N, Sesuk T, Charojrochkul S. Effect of Samarium and Praseodymium Addition on Water Gas Shift Performance of Co/CeO2 Catalysts. Journal of Rare Earths, 2020; 38(11): 1201-1206. https://doi.org/10.1016/j.jre.2019.12.003
[25] Kumar A, Kumar N, Chitkara M, Dhillon G. Physicochemical Investigations of Structurally Enriched Sm3+ Substituted SnO2 Nanocrystals. Journal of Materials Science: Materials in Electronics, 2022; 33(8): 5283-5296. https://doi.org/10.1007/s10854-022-07716-w
[26] Xu Y, Yang L, Li J, Zhou D, Li Q, Shi W, Jin Y. Effect of Laser Wavelength on Ablation Propulsion and Plasma Characteristics with Acrylonitrile Butadiene Styrene Target. Journal of Physics D: Applied Physics, 2024; 57(44): 445201. https://doi.org/10.1088/1361-6463/ad6877
[27] Nikiforov A, Timofeev V, Mashanov V, Azarov I, Loshkarev I, Volodin V, Gulyaev D, Chetyrin I, Korolkov I. Formation of SnO and SnO2 Phases during the Annealing of SnO(x) Films Obtained by Molecular Beam Epitaxy. Applied Surface Science, 2020; 512: 145735. https://doi.org/10.1016/j.apsusc.2020.145735
[28] Ding X, Fang F, Jiang J. Electrical and Optical Properties of N-Doped SnO 2 Thin Films Prepared by Magnetron Sputtering. Surface and Coatings Technology, 2013; 231: 67-70. https://doi.org/10.1016/j.surfcoat.2012.03.060
[29] Ebrahimiasl S, Yunus WMZW, Kassim A, Zainal Z. Synthesis of Nanocrystalline SnOx (x = 1-2) Thin Film Using a Chemical Bath Deposition Method with Improved Deposition Time, Temperature and PH. Sensors, 2011; 11(10): 9207-9216. https://doi.org/10.3390/s111009207
[30] Singh LP, Luwang MN, Srivastava SK. Luminescence and Photocatalytic Studies of Sm 3+ Ion Doped SnO 2 Nanoparticles. New J. Chem., 2014; 38(1): 115-121. https://doi.org/10.1039/C3NJ00759F
[31] Anthopoulos TD, Mclachlan MA. Exploring and Controlling Intrinsic Defect Formation in SnO2 Thin Films. Journal of Materials Chemistry C, 2016; 4: 758-765. https://doi.org/10.1039/C5TC03520A
[32] Cao E, Zhang Y, Hao W, Peng H, Sun L, Hu J. Applied Surface Science Room Temperature Ferromagnetism in Sm-Doped SnO 2 PLD Film. Applied Surface Science, 2013; 282: 376-383. https://doi.org/10.1016/j.apsusc.2013.05.139
[33] E. WB. X-Ray Diffraction. New York: Dover Publications 1990;
[34] Heryanto, Abdullah B, Tahir D, Mahdalia. Quantitative Analysis of X-Ray Diffraction Spectra for Determine Structural Properties and Deformation Energy of Al, Cu and Si. Journal of Physics: Conference Series, 2019; 1317(1): 012052. https://doi.org/10.1088/1742-6596/1317/1/012052
[35] Shawki OS, Rzaij JM. Effect of Fe2O3 Upper Layer on Structural, Morphological, and Photoluminescence Characteristics of TiO2 Thin Film Prepared by Chemical Spray Pyrolysis. In:. 1st Diyala Int. Conf. Pure Appl. Sci. Iraq: AIP Conference Proceedings 2023; 020009. https://doi.org/10.1063/5.0112172
[36] T.O. O, K.O. A, S.O. O. Estimation Of The Atomic Radii Of Periodic Elements Using Support Vector Machine. International Journal of Advanced Information Science and Technology, 2014; 28(28): 39-49. https://doi.org/10.15693/IJAISTAUG001/001
[37] Sen P, Bhattacharya P, Mukherjee G, Ganguly J, Marik B, Thapliyal D, Verma S, Verros GD, Chauhan MS, Arya RK. Advancements in Doping Strategies for Enhanced Photocatalysts and Adsorbents in Environmental Remediation. Technologies, 2023; 11(5): 144. https://doi.org/10.3390/technologies11050144
[38] Baig N, Kammakakam I, Falath W. Nanomaterials: A Review of Synthesis Methods, Properties, Recent Progress, and Challenges. Materials Advances, 2021; 2(6): 1821-1871. https://doi.org/10.1039/D0MA00807A
[39] Modhi MK, Rzaij JM. Synthesis and Characterization Study of CuO Thin Film and CuO-CeO2 Nanostructured Composite Using Chemical Spray Pyrolysis. In:. AL-KADHUM 2ND Int. Conf. Mod. Appl. Inf. Commun. Technol. Baghdad, Iraq: AIP Conference Proceedings 2023; 030066. https://doi.org/10.1063/5.0120468
[40] Li L, Zhou C, Yu D, Zheng Y, Du Y, Ma L, Zhao J, Rao G. Effect of Film Thickness on the Microstructure and Dielectric and Ferroelectric Properties of (Bi0.5Na0.5)0.94Ba0.06TiO3 Films by Pulsed Laser Deposition. Journal of Electronic Materials, 2023; 52(5): 3488-3498. https://doi.org/10.1007/s11664-023-10321-0
[41] Ibraheam AS, Rzaij JM, Arshad MKM. Influence of Magnesium Content on the Structural, Optical, and Electrical Properties of Cu2(Zn1-XMgx)SnS4 Nanostructured Quaternary Thin Film Synthesized Using the Sol-Gel Method. Journal of Electronic Materials, 2023; 52(1): 414-421. https://doi.org/10.1007/s11664-022-10002-4
[42] Nix WD. Mechanical Properties of Thin Films. Metallurgical Transactions A, 1989; 20(11): 2217-2245. https://doi.org/10.1007/BF02666659
[43] Golam Mortuza Nion M, Humayan Kabir M, Mona MA, Jahidul Haque M, Shahariar N, Hafiz M, Rahman MS. Effect of Al Doping on Morphology and Optical Properties of Spray Pyrolized MgO Thin Films. Results in Materials, 2021; 12: 100235. https://doi.org/10.1016/j.rinma.2021.100235
[44] Chowdhury FR, Choudhury S, Hasan F, Begum T. Optical Properties of Undoped and Indium-Doped Tin Oxide Thin Films. Journal of Bangladesh Academy of Sciences, 2011; 35(1): 99-111. https://doi.org/10.3329/jbas.v35i1.7975

[45] Ramadan R, Abdelhady K, Manso-Silván M, Torres-Costa V, Martín-Palma RJ. Microwave Plasma and Rapid Thermal Processing of Indium-Tin Oxide Thin Films for Enhancing Their Performance as Transparent Electrodes. Journal of Photonics for Energy, 2019; 9(03): 1. https://doi.org/10.1117/1.JPE.9.034001
[46] K. Sinha S. Tunable Structural, Optical And Electrical Properties Of Annealed ZnO-SnO2 Composite Thin Films Deposited By Pulsed Laser Deposition. Advanced Materials Letters, 2016; 7(4): 319-324. https://doi.org/10.5185/amlett.2016.6155
[47] Tawfeeq HA, Rzaij JM. Effect of Thickness on the Structural and Optical Properties of Cadmium Oxide Thin Films Deposited by Thermal Vacuum Evaporation Technique. In:. Recent Trends Adv. Artif. Intell. Internet Things. Springer International Publishing 2024; 582-591. https://doi.org/10.1007/978-3-031-70924-1_44
[48] Buchholz DB, Proffit DE, Wisser MD, Mason TO, Chang RPH. Electrical and Band-Gap Properties of Amorphous Zinc-Indium-Tin Oxide Thin Films. Progress in Natural Science: Materials International, 2012; 22(1): 1-6. https://doi.org/10.1016/j.pnsc.2011.12.001
[49] ŞİMŞEK T, CEYLAN A, AŞKIN GŞ, ÖZCAN Ş. Band Gap Engineering of ZnO Nanocrystallites Prepared via Ball-Milling. Politeknik Dergisi, 2022; 25(1): 89-94. https://doi.org/10.2339/politeknik.647702
[50] LIN H, HUANG C, LI W, NI C, SHAH S, TSENG Y. Size Dependency of Nanocrystalline TiO2 on Its Optical Property and Photocatalytic Reactivity Exemplified by 2-Chlorophenol. Applied Catalysis B: Environmental, 2006; 68(1-2): 1-11. https://doi.org/10.1016/j.apcatb.2006.07.018
[51] Brus L. Electronic Wave Functions in Semiconductor Clusters: Experiment and Theory. The Journal of Physical Chemistry, 1986; 90(12): 2555-2560. https://doi.org/10.1021/j100403a003
[52] Tawfeeq HA, Rzaij JM. The Effect of Nb2O5 and Pdo Nanostructures Coating on the Structural and Morphological Properties of CdO Thin Films. In:. 4TH Int. Conf. PURE Sci. ICPS2023. Baghdad, Iraq: 2024; 050011. https://doi.org/10.1063/5.0196260
[53] Li N, Fan Y, Shi Y, Xiang Q, Wang X, Xu J. A Low Temperature Formaldehyde Gas Sensor Based on Hierarchical SnO/SnO2 Nano-Flowers Assembled from Ultrathin Nanosheets: Synthesis, Sensing Performance and Mechanism. Sensors and Actuators, B: Chemical, 2019; 294(January): 106-115. https://doi.org/10.1016/j.snb.2019.04.061
[54] Rzaij JM. A Novel Room-Temperature Nitrogen Dioxide Gas Sensor Based on Silver-Doped Cerium Oxide Thin Film. Sensors and Actuators A: Physical, 2023; 363: 114748. https://doi.org/10.1016/j.sna.2023.114748

Blank Page

Research on Engineering Structures & Materials
www.jresm.org
Research Group

Research Article

Effects of web openings on axial compression in cold-formed steel lipped channel columns

P. Sangeetha [*,a]

Department of Civil Engineering, Sri Sivasubramaniya Nadar College of Engineering, Chennai-603 110, Tamil Nadu, India

Article Info

Article History:

Received 14 Dec 2024

Accepted 21 Mar 2025

Keywords:

Lipped channel columns;
Web holes;
Axial compression;
Stress distribution;
Local buckling;
Finite element analysis

Abstract

Cold-formed steel (CFS) is widely used in commercial construction due to its structural efficiency, achieved through cold-bending processes, and its adaptability to various prefabricated geometries. However, the introduction of web openings, commonly incorporated for practical purposes such as service integration, can significantly influence the structural performance of CFS columns under axial compression. This study investigates the experimental and analytical behavior of CFS lipped channel columns with web holes, focusing on the effects of hole shape (circular and rectangular) and the number of holes (0, 1, 2, and 3) positioned at equal intervals along the column length. All specimens, fabricated from 2 mm thick channel sections, were subjected to axial compression to evaluate their load-deflection and load-strain responses. The results reveal that web holes affect the load-carrying capacity, with circular holes demonstrating superior performance compared to rectangular ones. Local inward buckling of the web and outward buckling of the flanges were prominent near the web hole regions, particularly for rectangular holes. Finite Element Analysis (FEA) models showed excellent agreement with experimental results, with deviations of less than 4%, validating their predictive accuracy. A comparative evaluation of design codes, including AISI, BS 5950, and Eurocode, highlighted that BS 5950 closely aligns with experimental findings, attributed to its detailed consideration of local buckling effects and conservative safety factors. This study provides valuable insights into the structural behavior of CFS columns with web holes, offering guidance for their design and application.

© 2025 MIM Research Group. All rights reserved.

1. Introduction

Cold-formed steel (CFS) has gained widespread popularity in the construction industry due to its high strength-to-weight ratio, ease of fabrication, and versatility in structural applications [1]. Unlike hot-rolled steel, CFS members are manufactured by bending thin steel sheets at room temperature, allowing for a broad range of cross-sectional shapes and geometries. These properties make CFS an ideal choice for modern construction practices, particularly in lightweight and prefabricated structures. In practical applications, CFS members are often designed with web holes to accommodate services such as electrical conduits, plumbing pipes, or HVAC systems. However, these modifications can significantly influence the structural performance of the members, particularly when subjected to axial compression. Web holes introduce stress concentrations, reduce cross-sectional area, and alter the buckling behavior of the member, making it essential to understand and quantify their effects on structural performance.

The incorporation of web holes into CFS members allows for the integration of services such as electrical and plumbing systems, enhancing their functional adaptability. However, the presence of

*Corresponding author: sangeethap@ssn.edu.in
[a]orcid.org/0000-0002-7630-011X
DOI: http://dx.doi.org/10.17515/resm2025-577me1214rs

perforations significantly impacts their load-carrying capacity and structural behavior under various loading conditions [2-4]. Previous studies have extensively investigated the effects of perforations on the buckling and post-buckling behavior of CFS members. Crisan et al. [5] conducted numerical simulations to complement experimental findings, providing valuable insights into the structural performance of perforated sections. Similarly, Moen and Schafer [6] introduced the Direct Strength Method (DSM) for designing CFS columns with holes, demonstrating its efficacy in predicting failure loads accurately. The influence of different hole shapes and arrangements on the axial capacity of CFS columns has also been explored, highlighting the critical role of geometric parameters in structural stability [7,8].

Experimental investigations by Tekcham Singh and Singh [9] revealed that perforated tubular stub columns exhibit reduced stiffness and load-carrying capacity compared to solid sections, emphasizing the need for design optimizations to mitigate these drawbacks. Pham et al. [10] further analyzed high-strength CFS channel sections with rectangular and slotted openings, reporting a significant impact of hole geometry on shear and compressive performance. The effects of perforations in CFS channel sections, with and without lips, have been investigated, focusing on failure modes, ultimate strength, and elastic stiffness [11]. Additional studies [12,13] have analyzed the behavior of perforated CFS beams, identifying the critical impact of hole geometry and spacing on the structural response. Reviews of the influence of web holes on CFS columns and beams [14–16] emphasize the need for a detailed investigation of perforation effects under axial compression. A majority of prior works have focused on elliptical web openings, highlighting outcomes from both experimental and analytical investigations. However, comprehensive studies comparing variations in hole shape (e.g., circular and rectangular) and the number of holes in CFS columns under axial compression remain limited.

This study addresses this gap by investigating the structural behavior of CFS-lipped channel columns with web holes under axial compression through both experimental and analytical methods. The key parameters considered include the shape (circular and rectangular) and number of web holes (0, 1, 2, and 3) positioned at equal intervals along the column length. The load-deflection and load-strain characteristics of the columns are analyzed to evaluate the influence of these parameters on the overall performance. Finite element modeling is employed to simulate the experimental conditions, and the results are validated against experimental data.

1.1 Novelty and Significance

This study provides a unique contribution by systematically analyzing the effects of web hole geometry and number on the axial performance of CFS lipped channel columns. Unlike previous works that primarily focus on elliptical holes or isolated cases, this research offers a broader understanding of how circular and rectangular holes influence load-carrying capacity, stiffness, and failure modes. The findings contribute to the development of optimized design guidelines for perforated CFS members, ensuring enhanced structural performance and safety in practical applications.

2. Materials and Methods

2.1 Specimen Details

The cold-formed steel-lipped channel section was selected from the IS 811-1987 [17] 120 x 50 x 15 x 2 mm with pre-punched web holes were tested to failure under compressive loading to find ultimate load, axial compression and strain. The ultimate load-carrying capacity is the maximum load that the column can sustain before failure. The columns were fabricated using CR4-grade steel conforming to IS 513:2008. The circular and rectangular holes were made along the web at the middle, 1/3rd and 1/4th height of the specimen with center-to-center spacing of 267 mm. The details of the specimen are depicted in Figure 1(a &b). The specifications of all the column specimens are listed in Table 1. The overall length of the specimen was 800 mm. The boundary conditions for the experimental setup simulated hinged supports at both ends of the column. The specimens without web holes were also tested for failure and acted as control specimens for comparison.

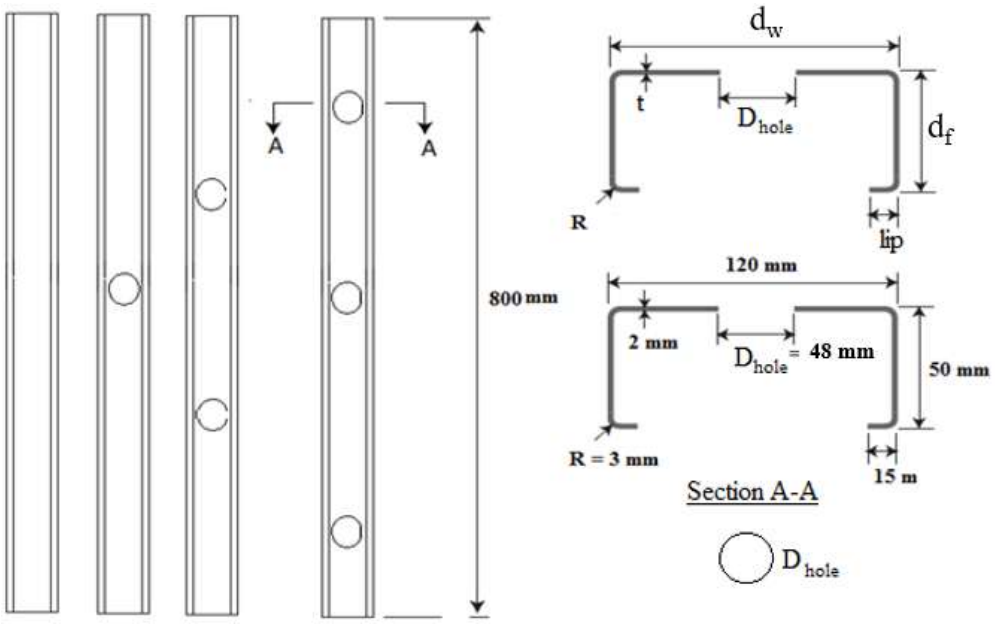

(a)

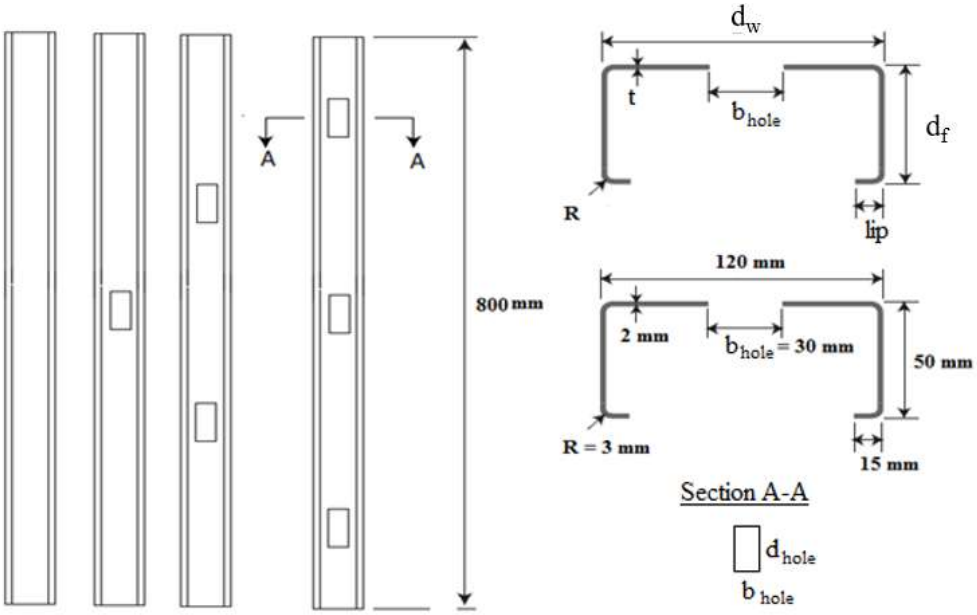

(b)

Fig. 1. Specimen dimensions (a) CFST Columns with circular web holes and (b) CFST Columns with rectangular web holes

Table 1. Specification of the specimen

Specimen	L	b_f	d_w	t	R	Lip	Type of Hole	Number of Hole	b_{hole}	d_{hole}	D_{hole}
	[mm]								[mm]		
CFSC-0H	800	50	120	2	3	15	-	-	-	-	-
CFSC-1RH	801	50	120	2	3	15	Rectangular	1	30	60	-
CFSC-2RH	802	50	120	2	3	15	Rectangular	2	30	60	-
CFSC-3RH	800	50	120	2	3	15	Rectangular	3	30	60	-
CFSC-1CH	799	50	120	2	3	15	Circular	1	-	-	30
CFSC-2CH	801	50	120	2	3	15	Circular	2	-	-	30
CFSC-3CH	802	50	120	2	3	15	Circular	3	-	-	30

2.2 Description of the Test

A coupon test was performed for three specimens of standard size as per ASTM E8[18] under a tensile testing machine to know the mechanical properties of the cold-formed steel section. Figure 2 shows the coupon test specimen before and after testing. After testing the stress-strain curve was plotted and it is shown in Figure 3. The yield stress and Young's modulus of materials were found as 245 N/mm^2 and 1.95 x 10^5 N/mm^2 respectively from the stress-strain plot (Fig. 3). All the specimens were fabricated with pre-punched web holes and were shown in Figure. 4. Each specimen was pasted with one 20 mm stain gauge at the mid-height of the specimen to measure the strain along the direction of the application of axial load. The test set-up was employed with a dial gauge with the least count of 0.01 mm to measure the axial compression of the CFS channel section with web holes. Figure. 5 shows that specimen CFSC-2CH was under universal testing machine of capacity 600 kN. and load is applied at the uniform rate of 5kN/mm on the top of the CFS lipped channel section.

Fig. 2. Tensile test on CFS Coupon specimen

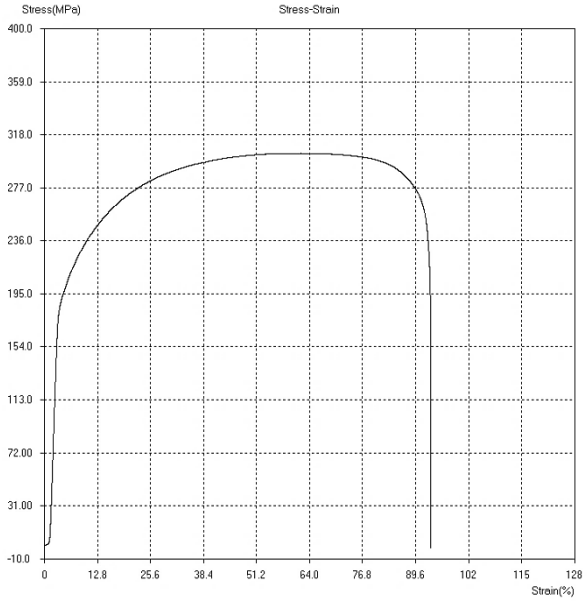

Fig. 3. Stress-strain behaviour of the cold-formed steel

Fig. 4. CFS Column specimens before testing

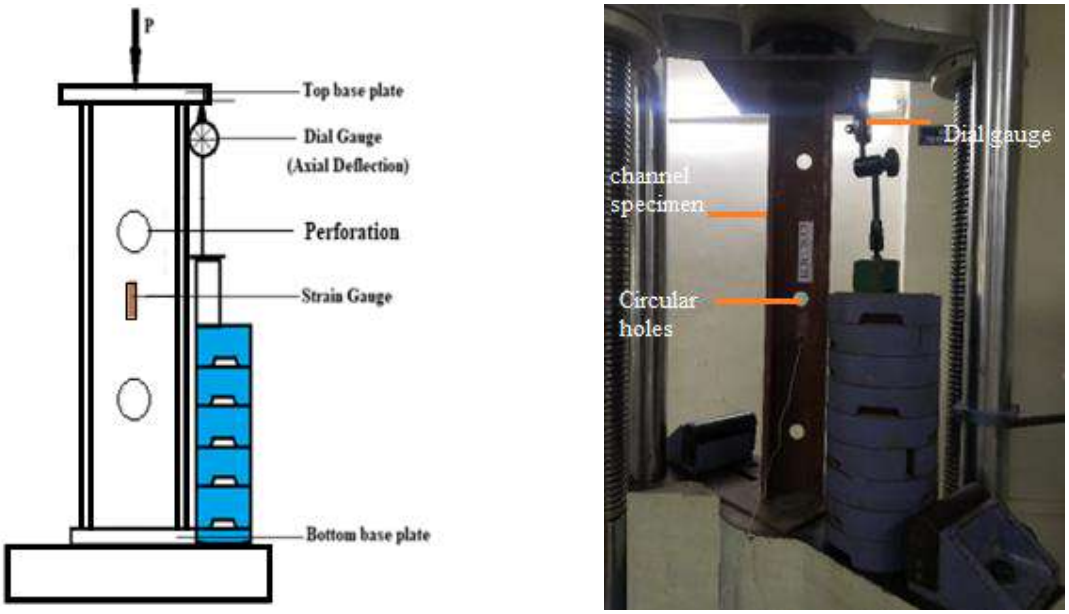

Fig. 5. Experimental set-up

3. Numerical Study

Finite Element Analysis (FEA) using ANSYS [19] was conducted to simulate the behavior of cold-formed steel (CFS) lipped channel columns with web holes under axial compression, aiming to replicate experimental conditions and evaluate structural performance. The SHELL 181 element was employed for meshing, offering a balance between computational efficiency and accuracy in capturing membrane and bending effects. A uniform mesh with an element size of 15 mm × 15 mm was applied. Fig. 6 shows the mesh model of the CFS columns with web holes. Material properties were defined using a bilinear stress-strain curve to represent elastic and plastic behavior, incorporating isotropic hardening to account for strain hardening. The elastic modulus was set at 1.95 GPa, Poisson's ratio at 0.3, yield strength at 245 MPa, and ultimate tensile strength at 298 MPa, based on tensile coupon tests for consistency with experimental conditions. Table 2 gives the material properties for FEA.

Table 2. Material properties for FEA

Details	Elastic Modulus E [GPa]	Poisson's Ratio γ	Yield Strength σ_y [Mpa]	Ultimate Tensile Strength σ_u [Mpa]	Strain Hardening Modulus E_t [Gpa]	Plastic Strain ε_p
Values	195	0.3	245	298	1.5	0.12

To simulate realistic imperfections, the first buckling mode shape was scaled to a maximum amplitude of L/1000, where L is the column length, representing manufacturing defects and initial geometric imperfections. A damage model using a von Mises stress failure criterion was included to predict localized yielding and plastic deformation, capturing the onset of local inward buckling in the web and outward buckling in the flanges. Boundary conditions were applied to replicate the experimental setup, with all translational degrees of freedom (Ux, Uy, Uz) restrained at the top and bottom ends and partial rotational restraint to simulate fixed supports. Axial compression was applied incrementally at the column's top using displacement control to ensure stability during analysis.

The analysis accounted for geometric and material nonlinearities using the Newton-Raphson iterative method, with convergence criteria based on displacement and residual force tolerances set at 1×10^{-3}. The FEA results, including load-deflection and load-strain responses, showed excellent agreement with experimental data, with deviations of less than 4%, validating the model's accuracy. The validated model was then utilized for a parametric study to evaluate the influence of web hole geometry (circular and rectangular) and configurations (0, 1, 2, and 3 holes) on load-carrying capacity, stiffness, and failure modes. This robust methodology bridges experimental and analytical approaches, offering valuable insights into the structural behavior of perforated CFS columns and contributing to the development of efficient design guidelines.

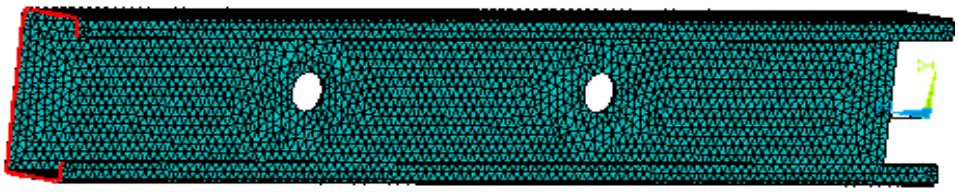

Fig. 6. Finite element mesh model of the CFS column (CFSC-2CH)

4. Result and Discussion

4.1 Load-Axial Compression Behavior

Figure. 7 (a & b) shows the load–axial compression curve of the CFS columns with circular and rectangular web holes respectively. The stiffness of the CFS column with circular holes is stiffer than the columns with rectangular holes. In the elastic range, axial compression is minimal and increases linearly with load. As the load exceeds the elastic limit, localized buckling or plastic deformation around the holes leads to a non-linear increase in axial compression. Columns with circular holes generally show a more uniform and gradual increase in compression, while rectangular holes cause more abrupt compression due to the higher stress concentrations at the hole corners. The local inward buckling along the web and local outward buckling along the flange at the places of web holes was observed in all the CFS columns both from experimental and analytical studies. This has occurred due to stress concentrations around the holes, which reduce the column's effective stiffness.

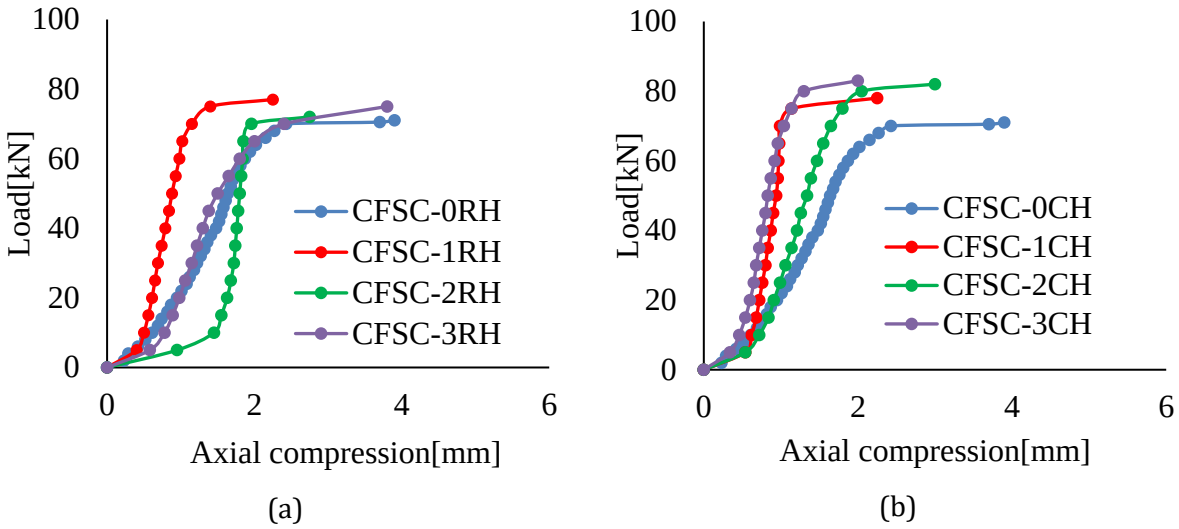

Fig. 7. Load-Axial compression curve of the CFST columns (a) Columns with rectangular web holes and (b)Columns with circular web holes

4.2 Load-Micro Strain Behavior

The load versus axial strain curve was plotted for CFS lipped channel columns with rectangular and circular holes using the measured strain from the mid-height of the column with the help of a 20 mm strain gauge. The stain values are recorded in the 5-channel strain indicator. Figure 8(a &b) shows the load versus micro strain plot for CFS columns with rectangular and circular holes. From fig. 8, it was observed that the load-micro strain behavior of cold-formed steel columns reflects the material's response to stress and deformation under increasing load, with notable differences based on the geometry and number of web holes. For circular holes, the strain distribution is more uniform, resulting in a smoother transition from elastic to plastic behavior and delayed strain localization. In contrast, rectangular holes exhibit sharp strain peaks due to stress concentrations at the corners, leading to earlier yielding and non-linear behavior.

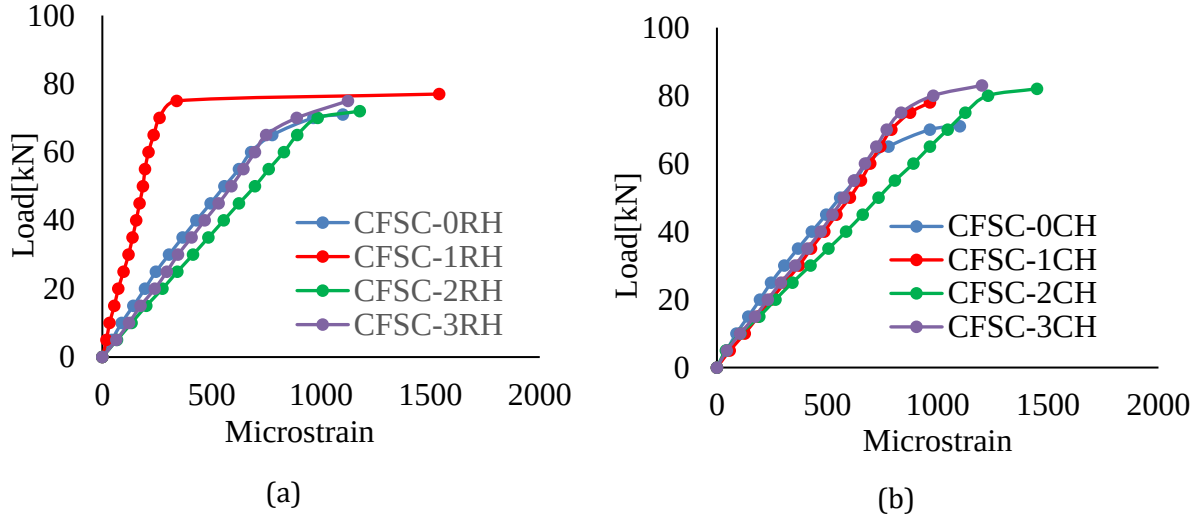

Fig. 8. Load-Micro strain curves of the CFS columns (a) Rectangular web hole and (b) Circular web hole

4.3 Effect of Holes in Lipped Channel Column

The load-carrying capacities of cold-formed steel columns with web holes demonstrate a consistent improvement over those without holes. Among the specimens with rectangular holes, CFSC-1RH (1 rectangular hole) showed an 8.45% increase in capacity, while CFSC-2RH (2 rectangular holes) and CFSC-3RH (3 rectangular holes) exhibited increases of 2.82% and 5.63%, respectively. Columns

with circular holes performed even better, with CFSC-1CH (1 circular hole) achieving a 9.86% increase, CFSC-2CH (2 circular holes) achieving 15.49%, and CFSC-3CH (3 circular holes) achieving the highest improvement at 18.31%. These findings indicate that circular holes contribute more significantly to enhancing the load-carrying capacity compared to rectangular holes, and the increase in the number of holes further improves structural performance, with CFSC-3CH emerging as the most efficient configuration. The average percentage increase in the ultimate load-carrying capacity was 10 % for rectangular and circular slotted-lipped channel columns as compared with columns without web holes. The change in the shape of the web holes from rectangular to circular increases the load-carrying capacity by 2%, 14% and 11% for one, two and three holes respectively. This may be due to redistributing stresses and influencing buckling patterns. The presence of multiple circular holes may cause stress redistribution along the web, reducing the concentration of stresses in a single region. This redistribution can lead to better utilization of the material, improving the structural performance under axial loading. Figure 9 shows the variation in the load-carrying capacity between lipped channel sections with and without web holes.

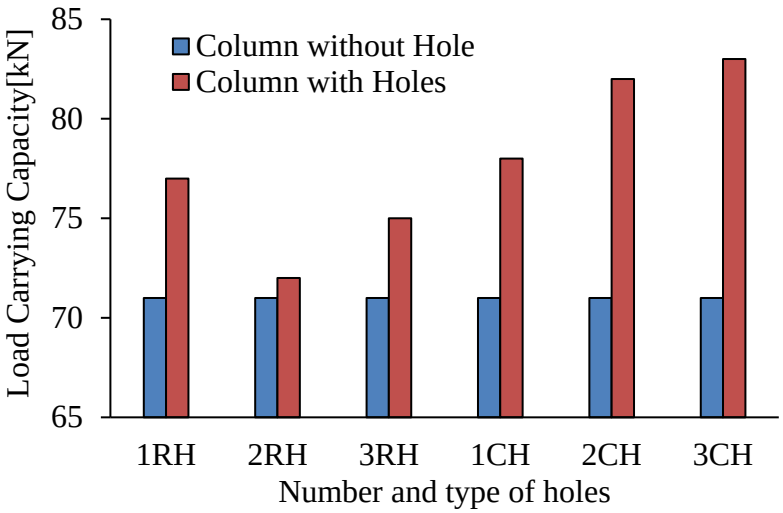

Fig. 9. Comparison between the load-carrying capacity of the slotted CFS columns

4.4 Failure Mode of CFS Column with Web Holes

Figure 10 shows the failure modes of the specimens. The typical failure mode observed was local buckling of the web near the top end of the columns along with inward torsional buckling at the location of web holes. The presence of web holes reduces the web plate transverse stiffness and thus deformation in the web and flange around the hole was more in the columns. These failures were observed on the first web hole from the top of the column as the load was applied at the top. The percentage increase in the load-carrying capacity of CFS columns with circular openings was 12.5 % as compared to rectangular web holes. The reduction in the load-carrying capacity of CFSC-1RH, CFSC-2RH and CFSC-3RH may be due to the weaker axis of the rectangular holes. Thus, the presence of web holes influences the distortional buckling shape and buckling loads.

From the Figure 10, it is also clear that rectangular web holes in the CFS-lipped channel section tend to cause more significant structural performance degradation due to their sharp corners and higher stress concentrations. This leads to earlier yielding and localized buckling, which collectively lower the load-carrying capacity and stability of the column. On the other hand, circular holes distribute stresses more evenly, mitigating some of the adverse effects and generally leading to better performance in terms of structural integrity and resistance to failure.

Figure. 11 shows the deformed plot along the z-axis (axial direction) obtained from the analysis of the CFS columns using ANSYS. From the plot, it was observed that variation in the color shows the intensity of the stress along the axial direction. It was also observed at the location of web holes; the intensity of stress is higher. It shows that dissipation of the stress and energy takes place through the web holes.

Fig. 10. Failure of the perforated CFS columns

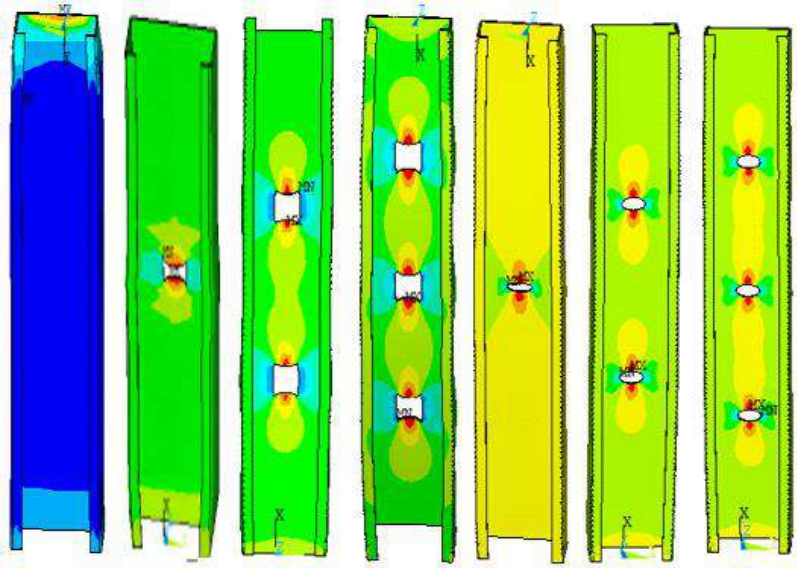

Fig. 11. Stress plot of the CFS columns with and without web holes

Fig. 12 shows the load-axial compression behavior for cold-formed steel columns with web holes (rectangular and circular) between experimental (solid lines) and finite element analysis (FEA) results (dashed lines). The FEA and experimental results show similar trends, validating the FEA model. However, FEA slightly overestimates the ultimate load and underestimates failure displacement, with deviations being more pronounced for rectangular holes due to stress concentrations at sharp corners. Circular holes exhibit better agreement between experimental and FEA results, indicating their superior performance in minimizing stress concentrations. Overall, FEA reliably predicts the behavior of columns with web holes under axial compression.

The ultimate loads of the cold-formed steel channel columns with web holes were calculated using the codal provisions of AISI-2022[20], BS5950[21] and ENV 1993[22]. The correlation between the calculated and experimental values was made and listed in Table 3. From Table 3, it was observed the predicted value using BS 5950 was close to experimental results because the effective width approach in BS 5950 accounts for local buckling effects, which are prominent in cold-formed steel sections. This approach could closely reflect the actual load-carrying behavior of the tested specimens, especially if local buckling dominated failure. The mean and standard deviation were in

the range of 1.016– 1.054 and 0.007 - 0.006 respectively for all the CFS columns with web holes between the predicted and measured values.

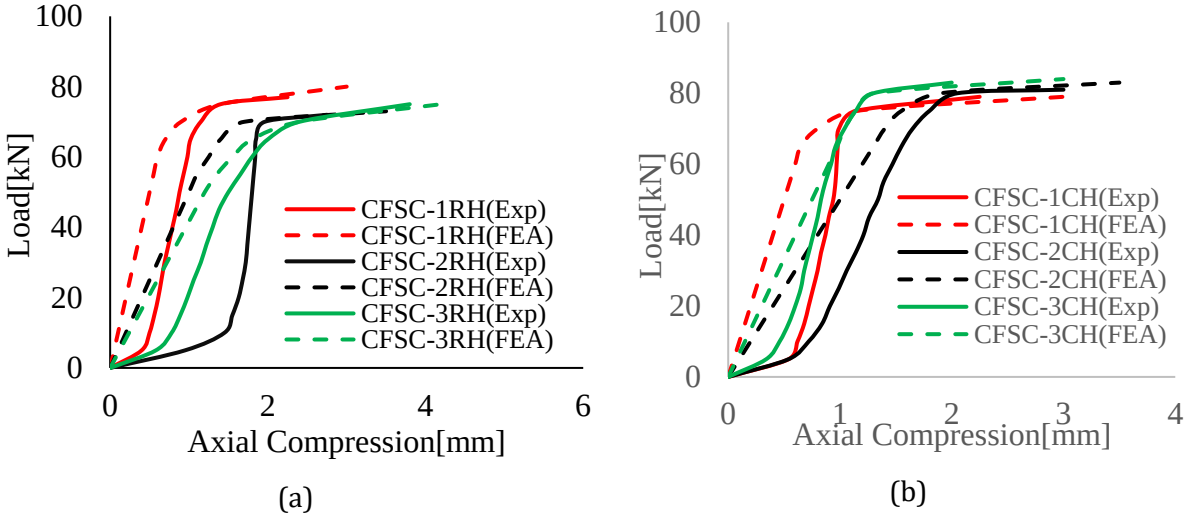

Fig. 12. Comparison between the load- axial compression between Experimental and FEA results

Table 3. Comparison of FEA results and design code calculation with experimental results

Specimen	Maximum load carrying capacity[kN]					Maximum load ratio			
	Test P_{Exp}	FEA P_{FEA}	AISI P_{cre}	BS 5950 $P_{c'}$	Eurocode $N_{h,Rd}$	P_{FEA} / P_{Exp}	P_{cre} / P_{Exp}	$P_{c'}$/ P_{Exp}	$N_{h,Rd}$ / P_{Exp}
CFSC-0H	71.02	72.51	74.25	71.85	75.24	1.021	1.045	1.012	1.059
CFSC-1RH	77.42	78.35	80.24	77.12	81.25	1.012	1.036	0.996	1.049
CFSC-2RH	72.56	73.01	75.62	73.25	77.26	1.006	1.042	1.010	1.065
CFSC-3RH	75.40	76.21	78.14	75.89	79.25	1.011	1.036	1.006	1.051
CFSC-1CH	78.26	79.56	81.05	79.05	82.25	1.017	1.036	1.010	1.051
CFSC-2CH	82.05	84.01	85.45	82.75	86.02	1.024	1.041	1.009	1.048
CFSC-3CH	83.32	85.21	86.12	82.45	87.52	1.023	1.034	0.990	1.050
Mean, X						1.016	1.039	1.005	1.054
Standard Deviation, S						0.007	0.004	0.008	0.006
Coefficient of Variation, COV						0.007	0.004	0.008	0.006

The study emphasizes that the increase in load-carrying capacity of lipped-channel sections with web openings is a result of the combined effects of stress redistribution, interaction between section components, and optimized material utilization. The experimental and FEA results highlight these effects, which may not be fully captured by simplified design code calculations.

5. Conclusions

This study investigated the structural behavior of cold-formed steel (CFS) lipped channel columns with web holes under axial compression using experimental tests and finite element analysis (FEA). The findings reveal the significant influence of hole geometry and number on the load-carrying capacity and failure modes of the columns.

- Columns with web holes exhibited enhanced load-carrying capacities compared to those without holes. Among the tested configurations, CFSC-3CH (3 circular holes) demonstrated the highest increase in load-carrying capacity, achieving an 18.31% improvement over the column without holes.

- Circular holes proved to be more effective than rectangular holes in reducing stress concentrations and improving structural performance. For example, CFSC-2CH showed a 15.49% increase, whereas CFSC-2RH showed only a 2.82% increase in capacity.
- The presence of web holes altered the failure modes of the columns. Local inward buckling of the web and outward buckling of the flanges were more prominent in specimens with rectangular holes, whereas columns with circular holes exhibited more uniform stress distribution and better structural efficiency.
- Finite element analysis results showed excellent agreement with experimental findings, with deviations in ultimate load capacities being less than 4%, validating the accuracy of the FEA model.
- Among the design codes considered, BS 5950 predictions were closest to experimental results, likely due to its consideration of local buckling effects and conservative safety factors.
- The presence of CFS-lipped columns with circular web holes increases the ultimate load-carrying capacity by 10 % when compared to the columns without slotted holes. Rectangular web holes reduced the load-carrying capacity by 10% compared to circular web holes of the same area.
- CFS-lipped channel columns with rectangular holes primarily fail due to localized buckling and crack initiation at the sharp corners, driven by high-stress concentrations. In contrast, columns with circular holes exhibit a more uniform stress distribution, resulting in localized buckling around the hole without crack propagation.
- The load-carrying capacity of all the columns with web holes was also calculated based on the various codal provisions and the coefficient of variation between the calculated and measured experimental values ranged between 0.004 to 0.009.

Future research could explore the behavior of CFS columns with alternative hole shapes (e.g., elliptical or triangular) and varying hole sizes to assess their influence on structural performance. Additionally, parametric studies on different column lengths, end-support conditions, and loading types could provide more comprehensive insights for practical applications. Advanced numerical techniques and optimization algorithms can also be employed to design web hole configurations that maximize structural efficiency while ensuring safety.

Acknowledgement

The authors would like to thank the management of Sri Sivasubramaniya Nadar College of Engineering for the facilities to complete this research work.

List of Notations

CFSC	Cold-formed steel column	d_w	Web depth of the channel section
RH	Rectangular hole	t	thickness of the channel section
CH	Circular Hole	R	Corner radius of the channel section
FEA	Finite Element Analysis	b_{hole}	breadth of the rectangular web hole
L	Length of the column	d_{hole}	depth of the rectangular web hole
b_f	Flange width of the channel section	D_{hole}	Diameter of the circular hole

References

[1] Yao X. Experiment and design method on cold-formed thin-walled steel lipped channel columns with slotted web holes under axial compression. Open Civ Eng J. 2017;11:244-57. https://doi.org/10.2174/1874149501711010244

[2] Kulatunga MP, Macdonald M, Rhodes J, Harrison DK. Load capacity of cold-formed column members of lipped channel cross-section with perforations subjected to compression loading-part I: FE simulation and test results. Thin-Walled Struct. 2014;80:1-12. https://doi.org/10.1016/j.tws.2014.02.017

[3] M.P.Kulatunga & M.Macdonald, Investigation of cold-formed steel structural members with perforations of different arrangements subjected to compression loading, Thin-Walled Structure, 67, 2013: pp. 78-87. https://doi.org/10.1016/j.tws.2013.02.014

[4] Kulatunga MP, Macdonald M. Investigation of cold-formed steel structural members with perforations of different arrangements subjected to compression loading. Thin-Walled Struct. 2013;67:78-87. https://doi.org/10.1016/j.tws.2013.02.014
[5] Crisan A, Ungureanu V, Dubina D. Behaviour of cold-formed steel perforated sections in compression Part 1-experimental investigations. Thin-Walled Struct. 2012;61:86-96. https://doi.org/10.1016/j.tws.2012.07.016
[6] Crisan A, Ungureanu V, Dubina D. Behaviour of cold-formed steel perforated sections in compression Part 2-numerical investigations and design considerations. Thin-Walled Struct. 2012;61:97-105. https://doi.org/10.1016/j.tws.2012.07.013
[7] Moen C, Schafer B. Direct strength method for design of cold-formed steel columns with holes. J Struct Eng. 2011;137(5):559-70. https://doi.org/10.1061/(ASCE)ST.1943-541X.0000310
[8] Sangeetha P, Dhinagaran M, Gobinaath AS, Saravana Kumar RS, Jeevan Raj AD. Performance assessment of the perforated CFS unlipped and lipped channel section under compression. Lect Notes Civ Eng. 2022;179:265-77. https://doi.org/10.1007/978-981-16-5041-3_20
[9] Sangeetha P, Revathi SM, Sudhakar V, Swarnavarshini S, Sweatha S. Behaviour of cold-formed steel hollow beam with perforation under flexural loading. Mater Today Proc. 2021;38(5):3103-9. https://doi.org/10.1016/j.matpr.2020.09.492
[10] Singh TG, Singh KD. Experimental investigation on performance of perforated cold-formed steel tubular stub columns. Thin-Walled Struct. 2019;131:107-21. https://doi.org/10.1016/j.tws.2018.06.042
[11] Pham DK, Pham CH, Pham SH, Hancock GJ. Experimental investigation of high strength cold-formed channel sections in shear with rectangular and slotted web openings. J Constr Steel Res. 2020;165:105889. https://doi.org/10.1016/j.jcsr.2019.105889
[12] Muftah F, Sani MSHM, Kamal MMM. Flexural strength behaviour of bolted built-up cold-formed steel beam with outstand and extended stiffener. Int J Steel Struct. 2019;19(3):719-32. https://doi.org/10.1007/s13296-018-0157-0
[13] Ghannam M. Bending moment capacity of cold-formed steel built-up beams. Int J Steel Struct. 2019;19(2):660-71. https://doi.org/10.1007/s13296-018-0155-2
[14] Živaljević V, Jovanović Đ, Kovačević D, Džolev I. The influence of web holes on the behaviour of cold-formed steel members: a review. Buildings. 2022;12(8):1-33. https://doi.org/10.3390/buildings12081091
[15] Yao Z, Rasmussen KJR. Perforated cold-formed steel members in compression. I: parametric studies. J Struct Eng. 2017;134(5):1-15. https://doi.org/10.1061/(ASCE)ST.1943-541X.0001635
[16] Moen CD, Schafer BW. Experiments on cold-formed steel columns with holes. Thin-Walled Struct. 2008;46:1164-82. https://doi.org/10.1016/j.tws.2008.01.021
[17] Casafont M, Pastor MM, Roure F, Pekoz T. An experimental investigation of distortional buckling of steel storage rack columns. Thin-Walled Struct. 2011;49:933-46. https://doi.org/10.1016/j.tws.2011.03.016
[18] Bureau of Indian Standards. Specification for cold formed light gauge structural steel sections. IS 811-1987. New Delhi; 1987.
[19] ASTM International. Standard test methods for tension testing of metallic materials. ASTM E8-2016. West Conshohocken, PA; 2016.
[20] ANSYS. ANSYS Mechanical APDL Structural Analysis Guide: ANSYS Release 21.0. USA; 2021.
[21] American Iron and Steel Institute. North American cold-formed steel specification for the design of cold-formed steel structural member. AISI-2012; 2012.
[22] British Standards Institution. British standards for structural use of steel work in buildings - Part 5: Code of practice for design of cold formed thin gauge sections. BS5950-1998; 1998.
[23] Eurocode 3. Design of steel structures; Part 1.3: General rules - Supplementary rules for cold formed thin gauge members and sheeting. ENV 1993-1-3:2006; 2009.

Research on Engineering Structures & Materials
www.jresm.org
Research Group

Research Article

Mechanical and durability studies on different grades of concrete using cinder aggregates

Shahazadi Begum [*,1,a], Shaik Yajdani [2,b]

[1]*Dept. of Civil Eng., Baba Institute of Technology and Sciences Visakhapatnam, India*
[2]*Dept. of Civil Eng., Andhra University College of Engineering Visakhapatnam India*

Article Info

Article History:

Received 06 Oct 2024
Accepted 09 Apr 2025

Keywords:

M-Sand; cinder; Mechanical performance; Water absorption; Rapid chloride permeability test

Abstract

Effective waste management in the steel industry is crucial for sustainability. With rising construction costs and the depletion of natural resources, integrating industrial by-products into construction has become increasingly important. Cinder, a significant by-product of steel manufacturing, forms when molten steel separates from impurities in the furnace. This study investigates the impact of cinder on the mechanical performance of concrete, focusing on compressive strength, split tensile strength, and flexural strength after 7 and 28 days of curing, along with microstructural analysis using SEM and XRD. The research explores replacing coarse aggregate with cinder in varying proportions from 0% to 80% in 10% increments to assess its feasibility for sustainable concrete production. The test results indicate that the target compressive strength is achieved with 70%, 50%, and 40% cinder aggregate replacement in M20, M30, and M40 concrete grades, attaining 27.56 MPa, 38.67 MPa, and 49.77 MPa, respectively. Additionally, durability tests, including water absorption and RCPT, were conducted. The charge passed in M20, M30, and M40 concrete with 70%, 50%, and 40% cinder aggregate was 3550.35, 2231.22, and 1936.65 coulombs, classifying them under moderate to low permeability categories, indicating its potentiality to be used in the concrete.

© 2025 MIM Research Group. All rights reserved.

1. Introduction

The rapid growth of industrialization and urbanization has accelerated the depletion of natural resources, creating significant challenges for their sustainable availability in the future. Furthermore, waste generated by manufacturing industries and construction activities consumes valuable land, reducing its utility and property value. The construction sector faces dual challenges: the scarcity of natural resources and the efficient disposal of industrial and construction waste. Adopting alternative resources to replace conventional ones is a promising step toward sustainability. Using these alternatives not only preserves natural resources for future generations but also enables the production of greener concrete. Advances in modern construction materials have facilitated the development of durable and lightweight options, significantly contributing to reducing structural weight. This progress has led to the creation of lightweight aggregate concrete (LWC). Lightweight aggregates can originate from natural rock materials, manufactured products, or industrial by-products. These aggregates are commonly used in bulk fillers for lightweight concrete, precast structural products, and road surfacing materials. Lightweight concrete is particularly advantageous for producing precast components, as its reduced weight allows for transporting larger quantities at a time. Additionally, lightweight concrete (LWC) enables the design of longer spans and more efficient bridge structures [1]. A key goal in LWC development is further reducing its density without compromising strength or increasing production costs. This is often achieved by substituting traditional aggregates with lightweight natural, agricultural, or

*Corresponding author: drshahazadibegum23@bitsvizag.com
[a]orcid.org/0009-0001-7908-5021; [b]orcid.org/0009-0008-0035-7313
DOI: http://dx.doi.org/10.17515/resm2025-475me1006rs

synthetic materials [2]. The physical properties of the coarse aggregate can significantly affect the fresh and hardened properties of the concrete [3]. This weight reduction enhances longevity and reduces the maintenance requirements of superstructures. Historically, aggregates like cinder and pumice have been employed as substitutes for conventional aggregates in lightweight concrete [4]. Yang and Huang demonstrated that the compressive strength of concrete is mainly affected by the properties and volume fraction of aggregate [5]. Lydon pointed out that for some lightweight aggregates, the compressive strength depends on the type of aggregate and increases with an increase in density [6].

Cinder, a lightweight aggregate derived as a by-product of steel and iron manufacturing, offers unique properties that influence its application in construction. Generally coarse and highly porous, with a 100% crushed face, the mineral structure of cinder contributes to its lightweight nature. This makes it ideal for various building applications, including partition wall blocks, screeding, and plastering on flat roofs. The amount of cinder waste developed in India is quite significant for use as an aggregate in concrete [7]. The high air content of aggregate provides effective sound absorption, soundproofing, and thermal insulation. With a linear coefficient of thermal expansion of approximately 3.8×10^{-6}/°C, cinder-based concrete exhibits low thermal conductivity, which makes it suitable for lightweight concrete (LWC) applications due to its reduced density, which reduces dead load, accelerating construction progress., and lowers maintenance costs [8]. Lightweight, with better insulation and high strength, lightweight concrete increases construction efficiency and reduces the foundation's strength [9]. However, developing high-strength, lightweight concrete structures is challenging, especially with increased stress and possible environmental effects that can damage and compromise the structure's integrity. Lightweight aggregates, including fly ash, are essential as bulk aggregates in various concrete applications [10], [11]. Recent studies have investigated the effect of aggregate size on the mechanical properties of lightweight concrete containing fly ash. By examining different sizes of aggregates and the composition of mineral aggregates, these studies aim to optimize the compressive and tensile strength and well strength of LWC. Proper mix design for such concretes is complex due to high water absorption and the porous nature of lightweight aggregates. Achieving the perfect combination means a lot of experimentation and tweaking. However, appropriate equations can simplify the mixing process and improve the composite design [12]. In their investigation, Hanuman Sai Gupta [8] used cinder aggregate and cinder powder to replace the coarse and fine aggregates. It was observed that the cinder powder didn't significantly impact the strength properties of concrete. However, the design target strength was attained with 40% cinder aggregates as a replacement.

Dandu Chinna Narasimhudu [13] studied lightweight concrete by replacing cement with fly ash, silica fumes, and coarse aggregate with cinder. The study concluded that 5% silica fumes and 20% fly ash with up to 60% cinder showed satisfactory results. Dr. V. Bhaskar Desai and Mr. A. Sathyam [14] studied the behavior of lightweight concrete by replacing natural aggregate with cinder aggregate in proportions such as 0,25,50,75 and 100 by volume. A total of 105 specimens were cast to evaluate their performance. It was concluded that an increase reduced concrete's mechanical behavior in the cinder aggregate proportion. However, the target mean strength of concrete was achieved with 75% cinder aggregate content.

N. Sivalinga Rao et al. [15] demonstrated the importance of trial mixes in lightweight concrete, highlighting the lack of precise water absorption and moisture content data. Their research indicated that replacing 60% of regular aggregate with cinder by volume and substituting 10% of the cement weight with silica fume could achieve the desired strength for M20 concrete. They found that using 40% cinder and 60% natural aggregates with 10% silica fume replacement for cement was the optimal combination. They also observed a slight increase in strength and other properties with extended curing periods. The unit weight of the cinder concrete ranged from 1980 kg/m^3 to 2000 kg/m^3 depending on the amount of cinder used, although the density decreased after prolonged curing.

Rathish Kumar P et al. [16] assessed concrete's strength and Sorptivity characteristics using cinder-based lightweight aggregates. They started by optimizing the aggregate size and evaluating the

mechanical properties of medium-grade concretes with different aggregate sizes. Their findings revealed that the best mechanical properties for 20 MPa lightweight concrete were achieved with 12.5 mm aggregates and a 30% fly ash replacement. Conversely, for 30 MPa concrete, 10 mm aggregates with a 30% fly ash replacement improved the properties.

Sanjana et al. [17] studied the performance of concrete using cinders and fly ash granules as a substitute for coarse and fine aggregates on M20-grade concrete. It was observed that the performance of concrete in compression and tension was reduced by 35% and 15% with 100% cinder aggregate. They also concluded that cinder can be used as an aggregate replacement for up to 60% of the conventional aggregate. H. Z. Cui et al. [18] investigated the impact of lightweight aggregates (LWA) on the mechanical properties and brittleness of lightweight aggregate concrete (LWAC). The research introduces a new "Shape Index" to quantify aggregate shape characteristics and evaluates its influence on concrete performance. Experimental results show that LWA volume fraction significantly affects compressive strength and elastic modulus, with higher LWA content leading to increased brittleness. LWAC is more brittle than normal-weight concrete (NWC) for similar strengths. Additionally, fracture energy analysis confirms that NWC exhibits better toughness. The findings emphasize the importance of LWA properties in LWAC design.

1.1 Research Significance

Incorporating cinder aggregates in concrete holds significant research value regarding sustainability, economic benefits, and structural performance. This study contributes to the growing demand for eco-friendly construction materials by utilizing cinder, a by-product of steel manufacturing, as a partial replacement for natural coarse aggregates. The present study focused on using the cinder aggregates and manufactured sand in combination in which the proportions of the cinder aggregates varied from 0-80% with 10% intervals in different grades of concrete, such as M20, M30, and M40.

2. Materials

2.1 Binding Material

The entire research utilized Ordinary Portland Cement of 43 grade as a binding material manufactured by Sagar cement, conforming to IS: 8112-2013[19], having a specific gravity of 3.13 with 2% fineness.

2.2 Fine Aggregate

Manufactured sand (M-Sand) was fully utilized to replace natural river sand as a fine aggregate, classified under Zone-II as per IS: 383-2016 [20]. The specific gravity was 2.66, and the water absorption rate was 1.32%. The grading curve for the m-sand is illustrated in (Fig. 1).

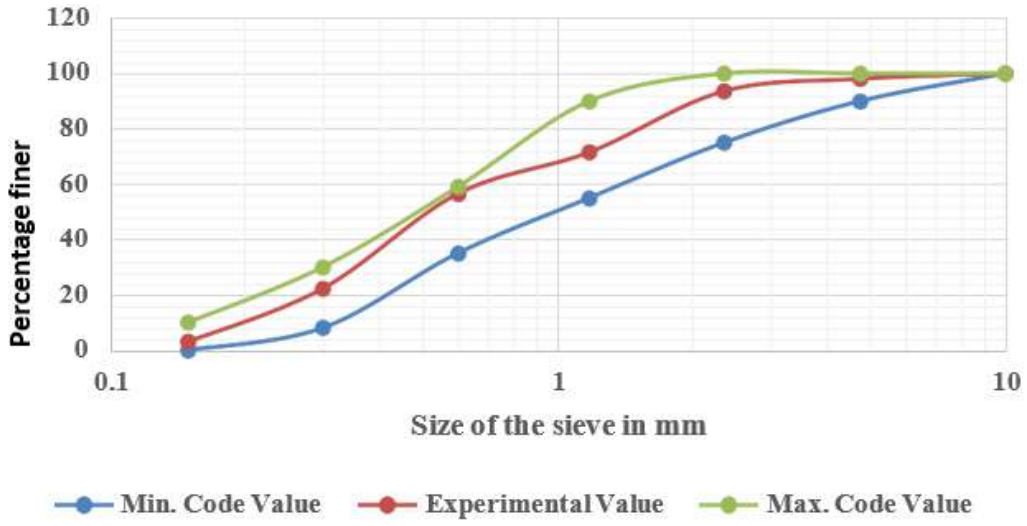

Fig. 1. Grading curve of M-Sand

2.3 Natural Coarse Aggregates and Cinders

The natural coarse aggregates (NCA) used in the study were obtained from the local area and had nominal sizes of 20 mm and 10 mm. Cinder partially replaced the coarse aggregates, as seen in (Fig. 2). The EDAX analysis of the cinder aggregate is presented in (Fig. 3) and Table 1. The cinders used were derived from small, porous volcanic rocks and are commonly utilized in lightweight concrete applications due to their lightweight and porous nature. The high porosity of cinder aggregates contributes to reduced density, and using high percentages of cinder aggregate could amplify the challenges related to strength reduction. Cinder aggregate have low density, high porosity, availability and cost- effectiveness, compatibility with cement, and sustainability. The specific gravity of the cinder aggregate was measured to be 1.95, and the grading curve is depicted in (Fig. 4).

Fig. 2. Cinder aggregate

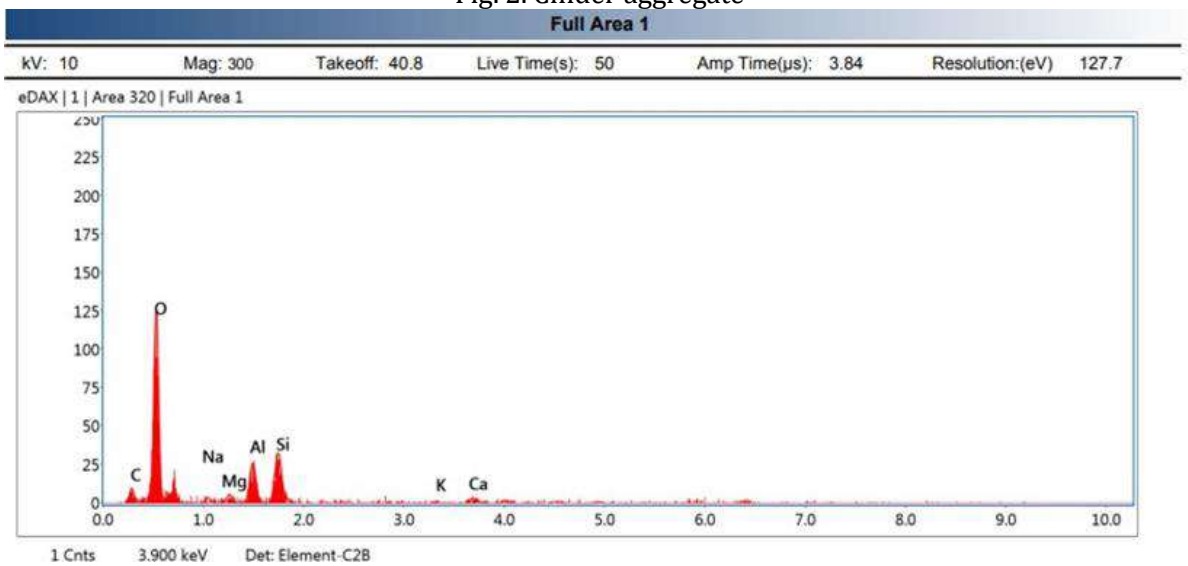

Fig. 3. EDAX analysis of cinder aggregate

The EDAX analysis spectrum shown in the above figure provides a qualitative and quantitative analysis of the elemental composition of the cinder aggregate used in the concrete mix. The peaks represent different elements in the cinder, such as Si, Al, Ca, etc., contributing to its mineralogical properties—the high silica and alumina content support pozzolanic activity, improving the concrete matrix's strength and density. Calcium content enhances hydration, contributing to better bonding in the interfacial transition zone (ITZ). The porous structure and lightweight oxides (e.g., silica and alumina) ensure a significant reduction in density, which is crucial for lightweight concrete applications. Stable oxides such as Fe_2O_3, SiO_2, and Al_2O_3 enhance resistance to chemical attacks and environmental degradation. The high oxygen and silica content correlate with cinder aggregates' excellent thermal insulation properties.

Table 1. EDAX analysis of cinder aggregate

Element	C	O	Na	Mg	Al	Si	K	Ca	Ti
Weight (%)	0.32	47.49	2.16	2.47	11.95	16.69	3.05	8.52	7.35

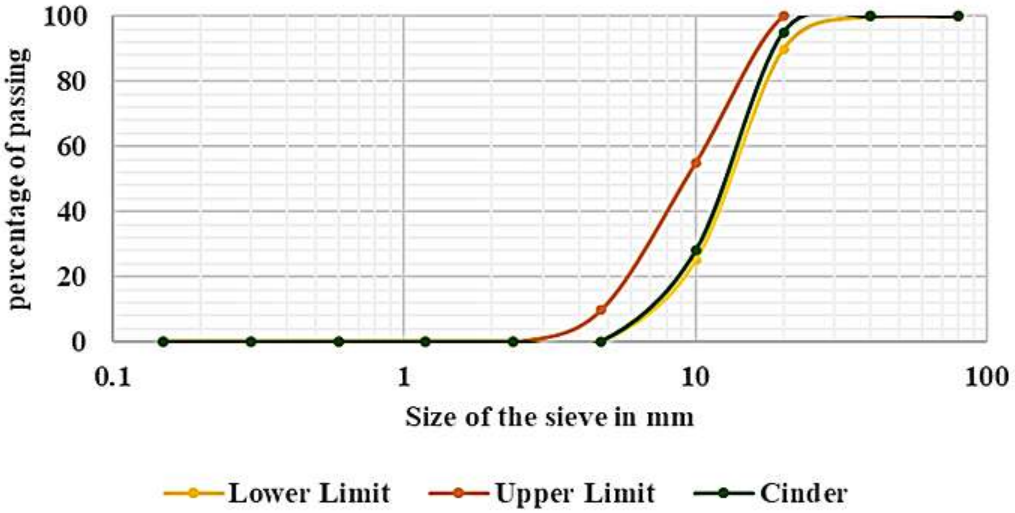

Fig. 4. Grading curve of coarse aggregate

3. Mix Proportion and Designation

The mix design was conducted according to the guidelines specified in IS:10262-2019 [21]. The target strengths were 26.6 MPa, 38.25 MPa, and 48.25 MPa for M20, M30 and M40 respectively. Tables 2 and 3 provide the details of mix notations and proportions, while Table 4 outlines the number of specimens cast. In total, 22 different mixes were evaluated in this study. Among these, three were conventional mixtures using 100% Natural Coarse Aggregate (NCA). NCA was partially replaced with a cinder in the remaining mixes, with replacement levels of 0% to 80% for M20, 0% to 60% for M30, and 0% to 50% for M40 concrete grades.

Table 2. Notations of the mixes

Series	Notation	Abbreviation
M20	M20C0	M20 grade concrete with 0% cinder aggregate
	M20C10	M20 grade concrete with 10% cinder aggregate
	M20C20	M20 grade concrete with 20% cinder aggregate
	M20C30	M20 grade concrete with 30% cinder aggregate
	M20C40	M20 grade concrete with 40% cinder aggregate
	M20C50	M20 grade concrete with 50% cinder aggregate
	M20C60	M20 grade concrete with 60% cinder aggregate
	M20C70	M20 grade concrete with 70% cinder aggregate
	M20C80	M20 grade concrete with 80% cinder aggregate
M30	M30C0	M30 grade concrete with 0% cinder aggregate
	M30C10	M30 grade concrete with 10% cinder aggregate
	M30C20	M30 grade concrete with 20% cinder aggregate
	M30C30	M30 grade concrete with 30% cinder aggregate
	M30C40	M30 grade concrete with 40% cinder aggregate
	M30C50	M30 grade concrete with 50% cinder aggregate
	M30C60	M30 grade concrete with 60% cinder aggregate
M40	M40C0	M40 grade concrete with 0% cinder aggregate
	M40C10	M40 grade concrete with 10% cinder aggregate
	M40C20	M40 grade concrete with 20% cinder aggregate
	M40C30	M40 grade concrete with 30% cinder aggregate
	M40C40	M40 grade concrete with 40% cinder aggregate
	M40C50	M40 grade concrete with 50% cinder aggregate

Table 3. Proportions of the mixes for 1m3 of concrete

Series	Mix Id	Cement (kg/m^3)	Water	Fine aggregate (kg/m^3)	20 mm aggregate (kg/m^3)	10 mm aggregate (kg/m^3)	Cinder aggregate (kg/m^3)
M20	M20C0	320	144	740.12	793.07	528.720	0
	M20C10	320	144	740.12	713.767	475.844	132.179
	M20C20	320	144	740.12	634.459	422.973	264.358
	M20C30	320	144	740.12	555.152	370.101	396.537
	M20C40	320	144	740.12	475.844	317.230	528.716
	M20C50	320	144	740.12	396.480	264.358	660.838
	M20C60	320	144	740.12	317.230	211.486	793.074
	M20C70	320	144	740.12	237.922	158.615	925.253
	M20C80	320	144	740.12	158.615	105.743	1057.43
M30	M30C0	400	176	679.44	734.340	489.550	0
	M30C10	400	176	679.44	694.566	440.595	122.389
	M30C20	400	176	679.44	587.472	391.640	244.778
	M30C30	400	176	679.44	514.038	342.685	367.167
	M30C40	400	176	679.44	440.604	293.730	489.556
	M30C50	400	176	679.44	367.167	244.778	611.945
	M30C60	400	176	679.44	293.736	195.820	734.334
M40	M40C0	435	166	655.58	746.340	497.560	0
	M40C10	435	166	655.58	671.706	447.804	124.390
	M40C20	435	166	655.58	597.072	398.048	248.780
	M40C30	435	166	655.58	522.438	348.292	373.170
	M40C40	435	166	655.58	447.804	298.536	497.560
	M40C50	435	166	655.58	373.170	248.780	621.950

Table 4. Details of the specimen cast

Property	Shape of the specimen	Size of the specimen (mm)	Code	Testing age (days)	Number of specimens M20	M30	M40
Slump	-	-	IS:1199-2018(PartII)	Fresh concrete	-	-	-
Compressive strength	Cube	150x150x150	IS: 516-1999	7,28	54	42	36
Split tensile strength	Cylinder	150 x 300	IS: 5816-1999	7,28	54	42	36
Flexural strength	Prism	500 x 100 x100	IS: 516-1999	7,28	54	42	36
Density	Cube	150 x 150 x150	IS: 6441-1997 (Part– I)	28	Performed on the cubes used for finding compressive strength		
Water absorption	Cube	150 x 150 x150	IS: 6441-1997 (Part-II)	28	6	6	6
RCPT	Cylinder	100 mm Ø with 50 mm thickness	ASTM C 1202-12	28	6	6	6
Sorptivity	Disc	100 mm Ø with 50 mm thickness	ASTM C 1585-04	28	6	6	6

4. Results and Discussion

4.1 Workability

The workability of concrete refers to how easily freshly mixed concrete can be placed, compacted, and finished without the components separating. It measures how well concrete can be handled and worked into the desired shape and location while maintaining uniformity and consistency. The current study evaluates the workability of the concrete by performing a slump cone test on all grades of concrete as per IS: 1199-2018 [22]. In all the concrete grades, it has been observed that when the cinder's content increased, a slump reduction was observed due to the cinder's rough surface texture and highly porous nature. The variation in the slump of the concrete is illustrated in (Fig. 5).

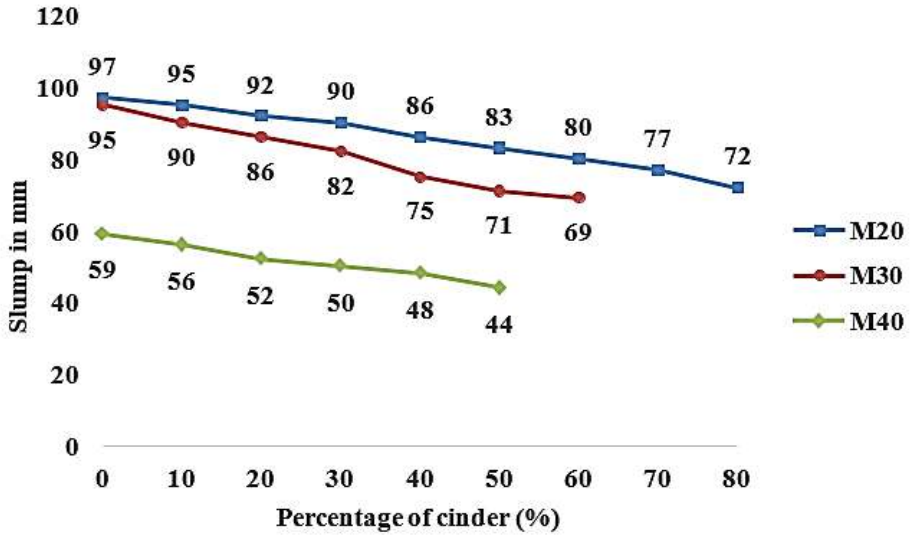

Fig. 5. Variation of slump in concrete

4.2 Density

The concrete density was examined using cube specimens for all mixes after completing the curing period as per the Indian code IS: 6441-1997 [23]. The density of concrete exhibited a declining nature with an increase in the level of cinder aggregate. Similar behavior in decreasing density is observed in work carried out by Chinmay Sahoo et al. [24]. This decrease is likely due to the lightweight nature of the cinder aggregates. Specifically, the density decreased from 2675 kg/m^3 to 2059 kg/m^3 for M20, from 2527 kg/m^3 to 2068 kg/m^3 for M30, and from 2705 kg/m^3 to 2092 kg/m^3 for M40 grades of concrete. The variation in concrete density is shown in (Fig. 6).

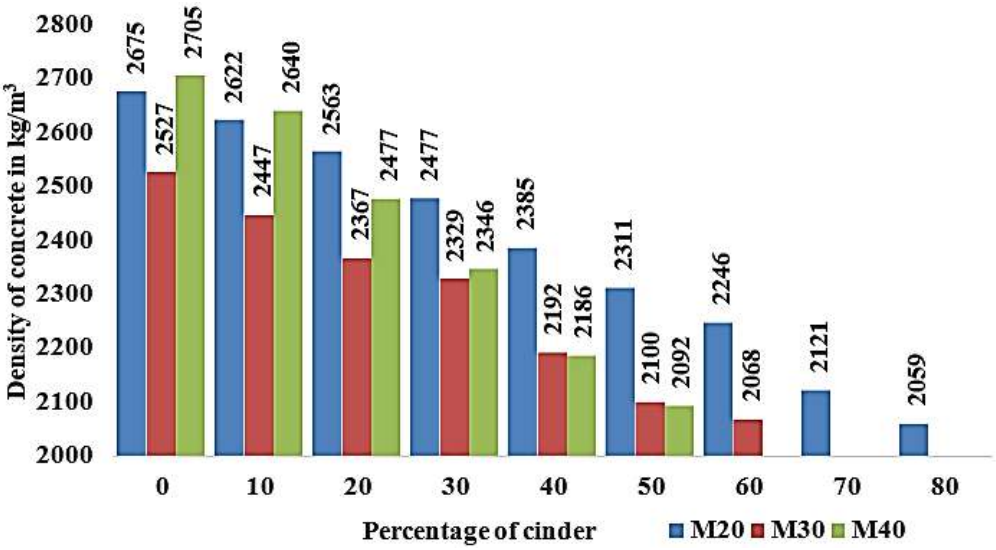

Fig. 6. Variation of the density of concrete

4.3 Compressive Strength

For all the mixes specified in Table 3, the compression test is performed after completing the 7 and 28-day curing period as per IS: 516-1999 [25]. Table 5 presents the mechanical performance of concrete for all mixes. From Table 5, the compressive strength decreased as the replacement level of cinder aggregate increased. A similar declining pattern of the test outcomes in compressive strength is observed in the work carried out by Anil Kumar Agarwal et al. [26].

Table 5. Mechanical performance results on M20, M30 and M40 concrete grades

Mix Id	Compressive strength(N/mm²)			Split tensile strength (N/mm²)			Flexural strength (N/mm²)		
	7 days	28 days	% of decrease	7 days	28 days	% of decrease	7 days	28 days	% of decrease
M20C0	24.44	31.11	0	2.54	3.11	0	5.12	5.21	0
M20C10	23.56	30.67	1.41	2.47	2.97	4.50	5.07	5.14	1.34
M20C20	22.67	30.36	2.41	2.38	2.94	5.47	4.96	5.07	2.69
M20C30	21.78	30	3.57	2.33	2.87	7.72	4.85	4.99	4.22
M20C40	20	29.78	4.28	2.26	2.83	9.00	4.7	4.77	8.45
M20C50	16.89	28.89	7.14	2.12	2.66	14.47	4.47	4.63	11.13
M20C60	16	28	10.00	2.06	2.63	15.43	4.19	4.41	15.36
M20C70	15.56	27.56	11.41	2.04	2.54	18.33	4.04	4.26	18.23
M20C80	14.67	24.89	19.99	1.87	2.47	20.58	3.45	3.49	33.01
M30C0	23.56	42.67	0	2.54	4.1	0	7.56	7.8	0
M30C10	22.67	40.89	4.17	2.47	3.9	4.88	7.1	7.4	5.13
M30C20	22.22	40	6.26	2.26	3.88	5.37	6.75	7.1	8.97
M30C30	21.78	39.56	7.29	2.12	3.68	10.24	6.62	6.7	14.10
M30C40	20.89	39.11	8.34	2.06	3.58	12.68	6.57	6.3	19.23
M30C50	20.44	38.67	9.37	2.04	3.47	15.37	6.38	6	23.08
M30C60	18.67	36.44	14.60	1.87	3.22	21.46	5.67	5.9	24.36
M40C0	51.56	54.67	0	3.32	3.58	0	7.75	8.73	0
M40C10	51.48	53.68	1.81	3.25	3.4	5.03	7.16	8.25	5.50
M40C20	43.55	51.56	5.69	3.12	3.25	9.22	7	7.6	12.94
M40C30	42.67	50.67	7.32	2.97	3.12	12.85	6.94	7.43	14.89
M40C40	40.87	49.77	8.96	2.83	3.11	13.13	6.87	6.67	23.60
M40C50	36.44	44.87	17.93	2.63	2.93	18.16	5.93	6.13	29.78

Due to the porous nature of the aggregate, it increases porosity, and due to the lower density of cinder aggregate, it produces concrete having lower density, which correlates with lower compressive strength because the material has more voids and less solid mass to resist compressive forces. The compressive strength of mix M20C0 after 28 days was found to be 31.11 MPa. However, for M20C80, which contains 80% cinder aggregates, the compressive strength decreased to 24.89 MPa. The decrease percentage was 19.99% for concrete, with 80% cinder aggregates in M20 concrete. The rate of decrease in strength is shown in Figure 7 for M20 concrete. The compressive strength of mix M30C0 after 28 days was found to be 42.67 MPa. However, for M30C60, which contains 60% cinder aggregates, the compressive strength decreased to 36.44 MPa. The decrease percentage was 14.60% for concrete, with 60% cinder aggregates in M30 concrete. The rate of decrease in strength is shown in Figure 8 for M30 concrete. The compressive strength of mix M40C0 after 28 days was found to be 51.56 MPa. However, for M40C50, which contains 50% cinder aggregates, the compressive strength decreased to 44.87 MPa. The decrease percentage was 17.93% for concrete, with 50% cinder aggregates in M40 concrete. The rate of decrease in strength is shown in Figure 9 for M40 concrete. However, it must be noted that the target strength can be achieved even with a 70% replacement of cinder aggregates in M20-grade concrete. Regarding the M30 and M40 grades of concrete, the target strength can be achieved even with 50% and 40% replacement levels of cinder aggregates, respectively.

4.4 Split Tensile Strength

As concrete is weaker in tension than compressive strength, this test helps understand how concrete will behave under tensile stresses. Knowledge of tensile strength helps predict concrete cracking behavior. The specimens are tested after 7 and 28 days of curing, following the procedure detailed in IS-5816-1999[27]. Like the compressive strength, the split tensile strength decreased as the cinder aggregate replacement increased. The test results are mentioned in Table 5. The strength of the M20C0 mix was 3.11 MPa after 28 days. However, for M20C80, it decreased to 2.47 MPa, marking a 20.58% reduction in strength with 80% cinder aggregates. This decrease is depicted in Figure 7. In the M30C0 mix, the strength was 4.1 MPa after 28. M30C60's strength dropped to 3.22 MPa, resulting in a 21.46% decrease with 60% cinder aggregates. Figure 8 illustrates this reduction. After 28 days, the strength of the M40C0 mix was 3.58 MPa. This strength fell to 2.93 MPa for M40C50, a decrease of 18.16% with 50% cinder aggregates. The reduction is shown in Figure 9. The decrease in concrete performance is attributed to the characteristics of cinder aggregate, which is highly porous. This porosity increases micro-cracking within the concrete matrix when under tensile stress. The split tensile strength of concrete also relies on the strength of the aggregates. Given that cinder aggregates are weaker than conventional aggregates, the split tensile strength of cinder aggregate concrete may be lower.

4.5 Flexural Strength

The flexural strength of concrete significantly affects its structural performance. The flexural behavior is evaluated after 7 and 28 days of curing, following the guidelines of IS- 516-1959 [25]. The test results are listed in Table 5. The flexural strength of the M20C0 mix was 5.21 MPa after 28 days of curing. However, M20C80 decreased to 3.49 MPa, indicating a 33.01% reduction in strength with 80% cinder aggregates. This decrease can be seen in (Fig. 7). In the M30C0 mix, the flexural strength was 7.8 MPa after 28 days. M30C60's strength dropped to 5.9 MPa, resulting in a 24.36% decrease with 60% cinder aggregates. (Fig. 8) illustrates this reduction. After 28 days, the flexural strength of the M40C0 mix was 8.73 MPa. This strength fell to 6.13 MPa for M40C50, a decrease of 29.78% with 50% cinder aggregates. The reduction can be seen in (Fig. 9). The negative performance is due to the light weight of the cinder, which produces lightweight concrete that exhibits different stress distribution and deformation characteristics under load.

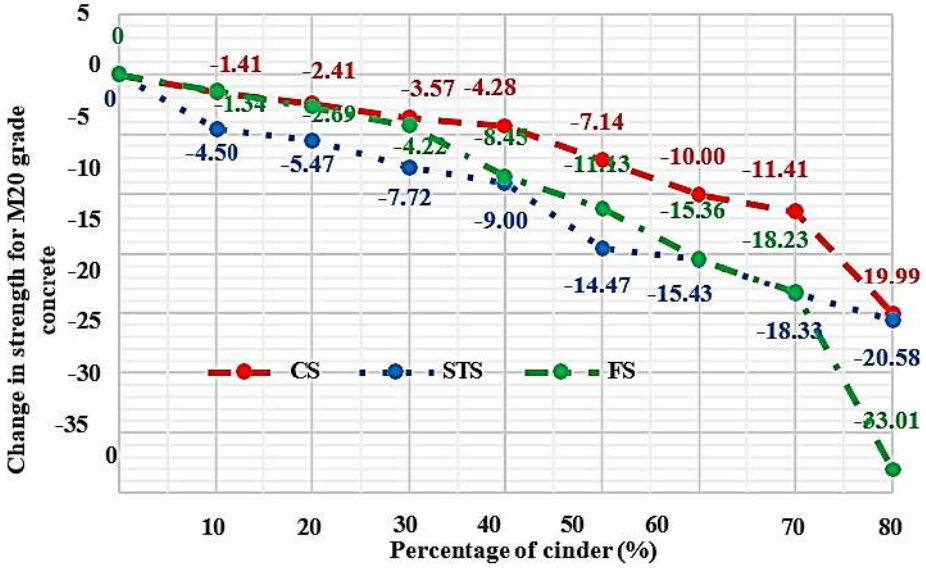

Fig. 7. Change in strength for M20 grade concrete

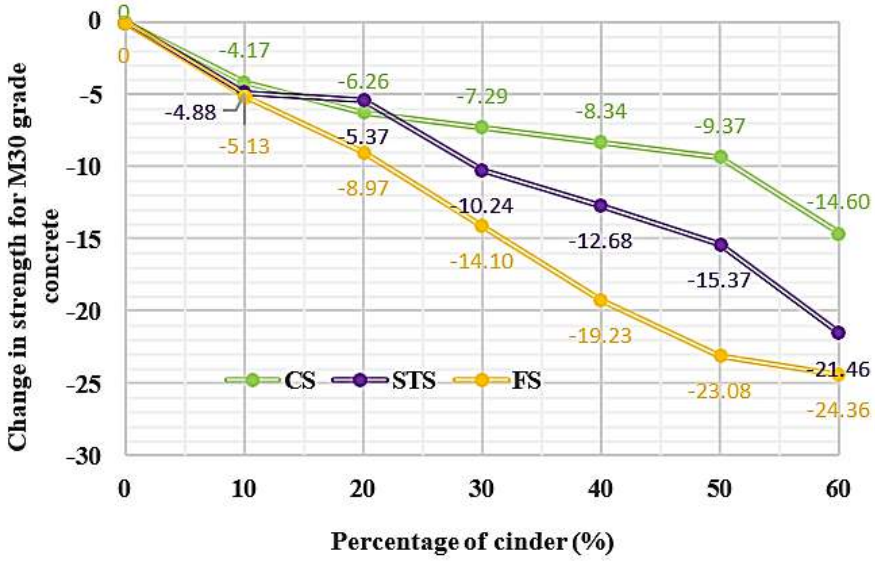

Fig. 8. Change in strength for M30 grade concrete

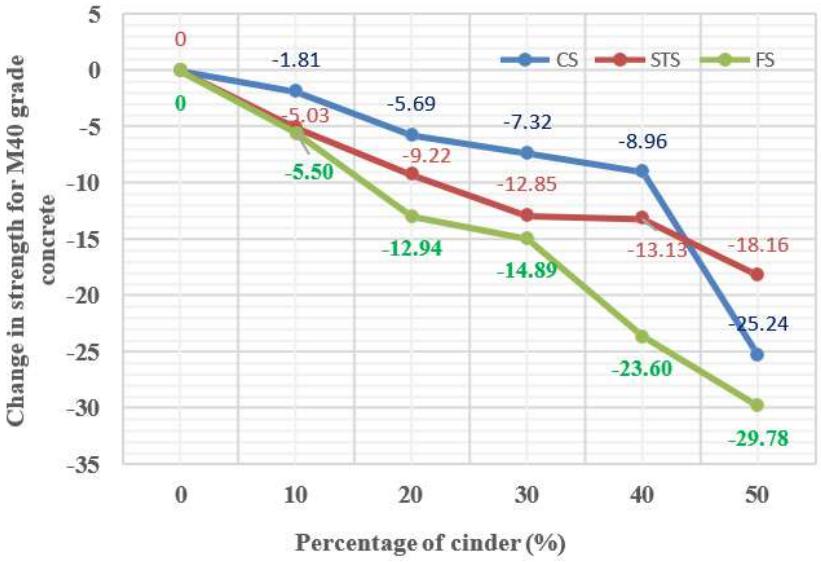

Fig. 9. Change in strength for M40 grade concrete

4.6. Correlation Among the Mechanical Properties of Concrete

The R^2 values were found to be 0.8809, 0.8685, and 0.8801, which indicates a strong correlation for the M20, M30, and M40 grades of concrete, respectively, between the compressive strength and hardened density of concrete, and is illustrated in (Fig. 10). The R^2 values were 0.8664, 0.9481, and 0.8846 for the M20, M30, and M40 concrete grades, suggesting a strong correlation between compressive and split tensile strength, as shown in (Fig. 11). For the relationship between compressive strength and flexural strength, shown in (Fig. 12), the R^2 values were found to be 0.9925 for M20 concrete, 0.9163 for M30 concrete, and 0.8075 for M40 concrete, indicating a robust correlation.

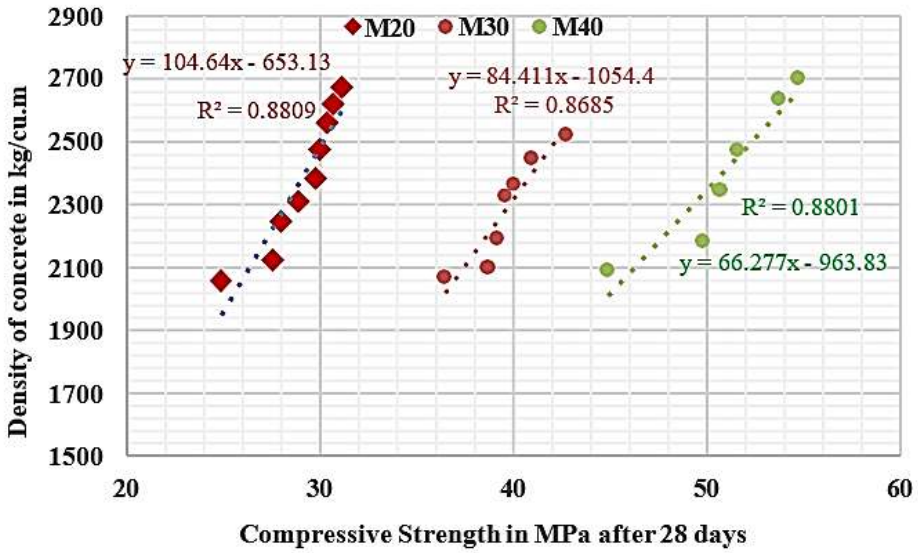

Fig. 10. Linear regression between compressive strength and density on all mixes

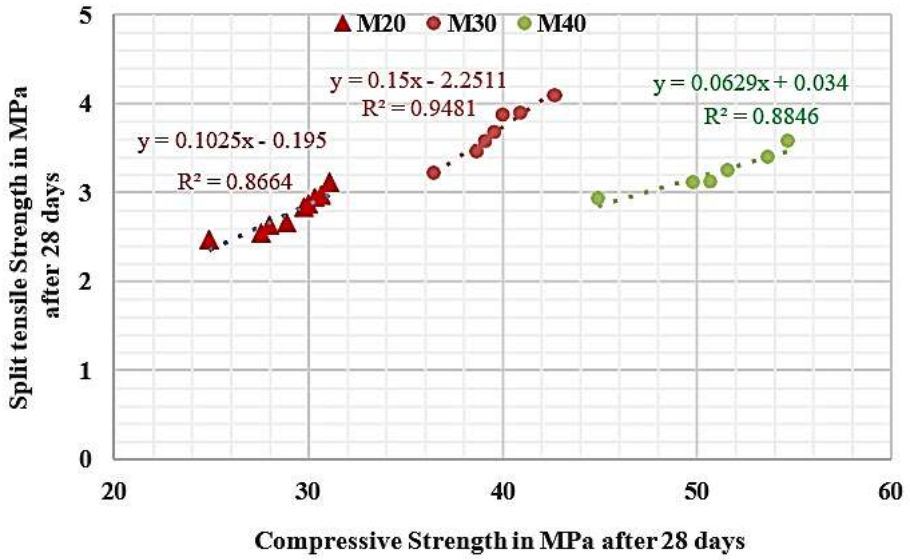

Fig. 11. Linear regression between compressive strength and split tensile strength on all mixes

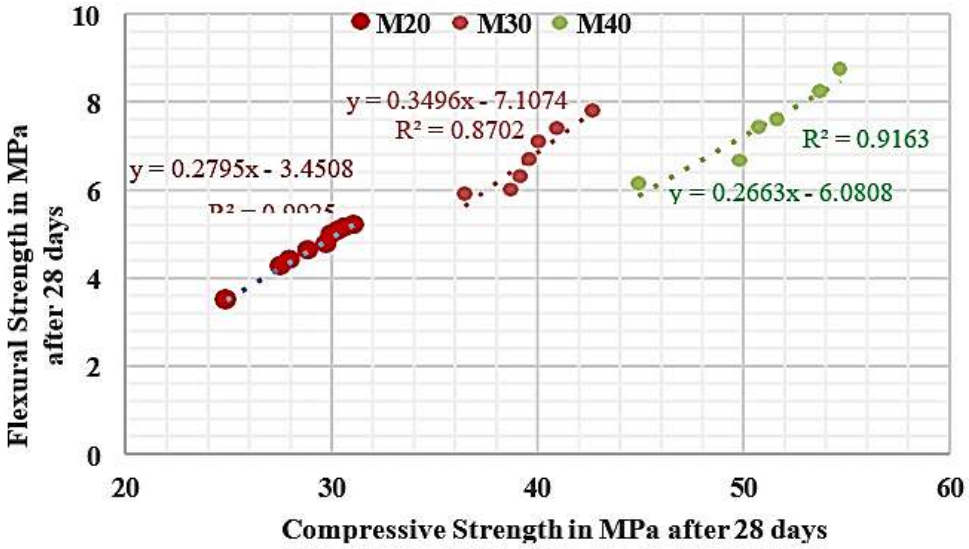

Fig. 12. Linear regression between compressive strength and flexural strength on all mixes

4.7 Water Absorption

By predicting the potential performance and long-term maintenance needs of concrete structures, the water absorption test helps ensure their longevity and reliability. This test is conducted on 150 mm cube specimens by ASTM C-642 [28]. It is applied to both conventional mixes and those with the maximum replacement of cinder aggregate.

Fig. 13. Specimens subjected to water curing

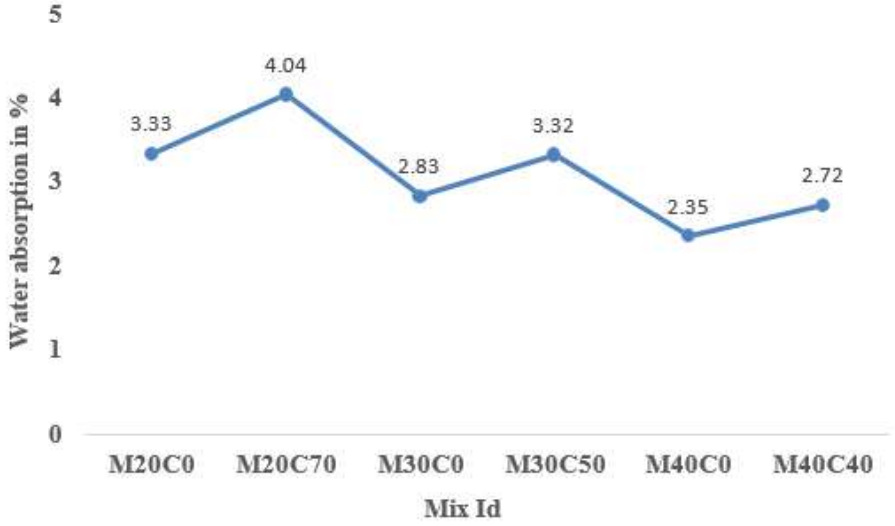

Fig. 14. Water absorption

The samples tested have undergone 28 days of curing. (Fig. 13). shows the specimens immersed in water required for water absorption. (Fig. 14). shows that water absorption decreased with higher concrete grades and increased with higher levels of cinder aggregate. Cinder aggregates typically have a higher degree of porosity and high-water absorption than traditional aggregates, which results in more water being absorbed. The variation in the test results is presented in (Fig. 14).

4.8 Rapid Chloride Penetration Test

The Rapid Chloride Permeability Test (RCPT) is a crucial durability test used to assess the resistance of concrete to the penetration of chloride ions.

Table 6. Test results of RCPT

Mix Id	Charge passed in coulombs	Permeability	ASTM C-642
M20C0	1868.85	Low	High permeability: > 4000 coulombs Moderate permeability: 2000 to 4000 coulombs Low permeability: 1000 to 2000 coulombs Very low permeability: 100 to 1000 coulombs Negligible permeability: < 100 coulombs
M20C70	3550.35	Moderate	
M30C0	1664.85	Low	
M30C50	2231.22	Moderate	
M40C0	1500.33	Low	
M40C40	1936.65	Low	

The test involves cylindrical specimens in line with ASTM C-642 [28]. Table 6 shows that the charge passed increased with an increase in the replacement level of cinder aggregate. The high porosity of the cinder aggregate allows a large amount of chloride ions to pass through. The weaker interfacial transition zone between the cinder aggregates and the cement paste also creates a more porous pathway for chloride ions. For reference, the test setup is illustrated in (Fig. 15), and the outcomes are presented in Table 6.

Fig. 15. RCPT test setup

5. Conclusions

- Replacing natural river sand with manufactured sand can help reduce environmental impacts, preserving natural resources and the economy.
- The use of cinder aggregates not only helps conserve natural resources but also supports the broader goals of sustainable construction.
- The test outcomes of the workability by slump have shown that the ease of work with the cinder aggregates reduced with an increase in the proportion of the cinder aggregate in concrete in all the grades.
- The test results indicated that higher-grade concrete exhibited greater density values. However, as the proportion of cinder aggregate increased, the overall density of the concrete showed a decreasing trend.
- The strength of concrete in compression is 27.56 MPa, 38.67 MPa, and 49.77 MPa for M20C70, M30C50, and M40C40 mixes, which is more than the target strength.
- From the mechanical performance outcomes, it can be concluded that the lower the grade of concrete, the higher the replacement level of cinder aggregate can be used.
- The experimental results indicate that in M20 grade concrete, the desired strength is attained even when 70% of natural coarse aggregates are substituted with cinder aggregates. For M30 and M40 grades of concrete, the corresponding percentages are 50% and 40%.
- At higher dosages of cinder aggregates particularly in the higher grades of concrete, the performance of concrete exhibited a poorer performance.
- The regression analysis shows a strong correlation between compressive strength and hardened density, split tensile strength, and flexural strength.
- The results of the RCPT test indicate that as the concrete grade increases, the charge passed in coulombs decreases, showing high resistance to chloride ion penetration.
- The test results for water absorption show that concrete with cinder aggregates has increased water absorption due to the porous nature of the aggregate. The more cinder aggregate present, the higher the water absorption.
- As cinder aggregates have low specific gravity, they can be used for lightweight concrete applications.

- Cinder aggregates may be more suitable for applications where high strength and low permeability are less critical, such as in non-structural elements or buildings in low-exposure environments.

References

[1] Ramu B, Prasad BBCO, Kumar KS. Cost comparison of light weight aggregate concrete by using cinder. Int J Sci Eng Technol Res. 2015;4(53):11473-9. Available from: www.ijsetr.com
[2] Uma SG, Lakshmi SM, Hemalatha G. Study on lightweight concrete using steel cinders. Mater Today Proc. 2020;46:3813-6. https://doi.org/10.1016/j.matpr.2021.02.039
[3] Baudouin M, et al. Influence of aggregate characteristics on workability of superworkable concrete. Mater Struct. 2015:1-13.
[4] Chengula DH. The use of blended cinder aggregates for concrete mixes. Int J Sci Basic Appl Res. 2022;61(1):44-61.
[5] Yang CC, Huang R. A two-phase model for predicting the compressive strength of concrete. Cem Concr Res. 1996;26:1567-77. https://doi.org/10.1016/0008-8846(96)00137-8
[6] Lydon FD. Concrete mix design. 2nd ed. London: Applied Science Publishers; 1982.
[7] Nataraja MC, Das L. Feasibility study for the production of non-structural lightweight concrete using characterized cinder and GGBS. Indian J Eng Mater Sci. 2011;18:361-9.
[8] Hanuman E, Gupta S, Kumar VG. Investigations on properties of light weight cinder aggregate concrete. 2015. Available from: www.ijerd.com
[9] Kumar R, Rao K. A study on the effect of size of aggregate on the strength and sorptivity characteristics of cinder based light weight concrete. Res J Eng Sci. 2012;1(6):27-35. Available from: www.isca.in
[10] Veeresh B, Prasad BBCO, Kumar KS. Light weight aggregate concrete by using cinder. 2015. Available from: www.ijsetr.com
[11] Sadhana K, Suguna K, Raghunath PN. Experimental study on properties of cinder aggregate lightweight concrete with fiber reinforcement. Mater Express. 2024;14(6):877-83. https://doi.org/10.1166/mex.2024.2701
[12] Abdullahi M, Al-Mattarneh HMA, Mohammed BS, Sadiku S. M-file for mix design of structural lightweight concrete using developed models. J Eng Sci Technol. 2011;6(4):520-31.
[13] Narasimhudu DC, Sri Chandana P. A study on properties of light weight cinder aggregate concrete with silica fume and fly ash as admixtures. IJMETMR. 2015;2(10).
[14] Desai VB, Sathyam A. Some studies on strength properties of light weight cinder aggregate concrete. Int J Sci Res Publ. 2014;4(2). Available from: www.ijsrp.org
[15] Rao NS, Desai VB. Structural properties of silica fume modified light weight aggregate (cinder) concrete. IOSR J Mech Civ Eng. 2016;16(053):36-40. https://doi.org/10.9790/1684-16053013640
[16] Kumar R, Rao K. A study on the effect of size of aggregate on the strength and sorptivity characteristics of cinder based light weight concrete. Res J Eng Sci. 2012;1(6):27-35. Available from: www.isca.in
[17] Sanjana M, Mahesh Babu V, Manjunatha L. Performance of lightweight concrete replacing coarse and fine aggregates with cinder and fly ash. J Sci Eng Manag. 2019;7(2):6-14.
[18] Cui HZ, Lo TY, Memon SA, Xu W. Effect of lightweight aggregates on the mechanical properties and brittleness of lightweight aggregate concrete. Constr Build Mater. 2012;35:149-58. https://doi.org/10.1016/j.conbuildmat.2012.02.053
[19] Bureau of Indian Standards. IS 8112 (1989): Specification for 43 grade ordinary Portland cement. New Delhi: BIS; 1989.
[20] Bureau of Indian Standards. IS 383: 1970 Specification for coarse and fine aggregates from natural sources for concrete. Indian Standards. 1970:1-24.
[21] Indian Standard. Concrete mix proportioning - guidelines. 2019. Available from: www.standardsbis.in
[22] Bureau of Indian Standards. IS 1199-2018: Methods of sampling and analysis of concrete. New Delhi: BIS; 2018.
[23] Bureau of Indian Standards. IS 6441-1 (1972): Methods of test for autoclaved cellular concrete products. Part I: Determination of unit weight or bulk density and moisture content. New Delhi: BIS; 1972.
[24] Sahoo C, Sahoo SK, Das M, Mishra SP. Lightweight aggregate concrete: strength analysis. Curr J Appl Sci Technol. 2022:32-41. https://doi.org/10.9734/cjast/2022/v41i3131811
[25] Bureau of Indian Standards. IS 516: Method of tests for strength of concrete. New Delhi: BIS; 1959:1-30.
[26] Agrawal AK, Singh AK. Experimental study of light weight concrete by replacing fine aggregates and coarse aggregates by cinder aggregates. Int J Eng Sci Comput. 2020 Apr.
[27] Bureau of Indian Standards. IS 5816-1999: Indian standard splitting tensile strength of concrete - method of test. New Delhi: BIS; 1999:1-14.
[28] ASTM. ASTM C642-97: Standard test method for density, absorption, and voids in hardened concrete. ASTM International; 1997.

Research on Engineering Structures & Materials
www.jresm.org
Research Group

Research Article

Characterizing rheological properties and rutting risk of VG30 and PMB 40 binders with warm mix additives

Bindhu Bernard [1,a], Kavitha Madhu [*,2,b]

[1]*Department of Civil Engineering, College of Engineering Trivandrum, 695016, APJ Abdul Kalam Technological University, Kerala, India*
[2]*Department of Civil Engineering, TKM College of Engineering, Kollam 691005, Kerala, India*

Article Info

Article History:

Received 06 Oct 2024
Accepted 08 Apr 2025

Keywords:

Warm mix additives;
Rheological properties;
Rutting potential;
Short term ageing;
Temperature susceptibility;
Fourier transform infra-red

Abstract

In hot mix constructions, the paving and compaction processes must be carried out at temperatures ranging from 130°C to 150°C. Due to this, many countries restrict the paving activities to the summer months. However, the high temperatures lead to increased fuel consumption and significant environmental pollution. The emission of CO_2, a major greenhouse gas, poses a serious environmental concern. In response to rising environmental awareness and increasing energy costs, alternative paving materials have been developed that require lower operating temperatures not compromising to the performance. Warm Mix Asphalt (WMA) technology has emerged as a sustainable solution. The WMA technology allows the bituminous mixes to produce at comparatively lower mixing and laying temperatures and thus reducing the emission of greenhouse gases. The study aims at preparing mixes with two types of base binders along with warm mix additives in which six types of binders were prepared and studied the viscosity characteristics. Based on these, optimum additive content was determined. Fourier Transform Infra-Red (FTIR) tests were done to assess the variation in chemistry by the inclusion of organic and chemical warm mix additives in VG30 and PMB40 binders. Modulus values and phase angle data were determined using Dynamic Shear Rheometer (DSR) for all the binders along with the short-term aged binders and assessed the rutting potential. The rutting parameter was determined from the data obtained on the DSR and based on its relationship with temperature, VG30 and PMB40 with organic warm mix additive gave better results. Multiple Stress Creep Recovery (MSCR) tests were done to assess the rutting potential.

© 2025 MIM Research Group. All rights reserved.

1. Introduction

Hot Mix Asphalt (HMA) construction is contributing to increased fuel consumption and environmental pollution in the pavement construction sector. The high temperatures required for mixing and compacting hot mix asphalt contribute to significant CO_2 emissions, which pose serious environmental concerns. However, incorporating a 1% organic warm mix additive into the base binder can reduce heat energy consumption by 2.8% and CO_2 emissions by 3.0% [1]. Increased environmental awareness and rising energy costs have driven the development of alternative paving materials that require lower operating temperatures while maintaining performance comparable to Hot Mix Asphalt (HMA). Warm mix asphalt (WMA) technology has emerged as a sustainable solution in this context [2]. This technology reduces the temperatures at which the asphalt is mixed and laid by incorporating warm mix additives into the binder prior to mixing [3]. WMA technology lowers mixing and laying temperatures significantly, resulting in reduced fuel consumption and cost, and minimizing risks [4].

*Corresponding author: kavithamadhu@tkmce.ac.in
[a]orcid.org/0000-0002-7652-077X; [b]orcid.org/0000-0002-0253-1230
DOI: http://dx.doi.org/10.17515/resm2025-478ma1006rs

Research has shown that adding warm mix additives can lower production temperatures by over 10°C, according to the equi-viscous concept [5]. Although increasing the amount of organic warm mix additive reduces mixing and compaction temperatures, it also decreases resistance to fatigue.

Organic additives are effective in reducing viscosity and improving workability at low temperatures; also, environmentally friendly by reducing energy consumption; but having limited effect on long-term aging resistance and rutting performance. Chemical additives effective at improving binder durability over time but subjected to higher cost and complexity compared to organic additives. Foaming additives are excellent for reducing mixing temperature, leading to energy savings and lower emissions; environmentally sustainable, but may not provide significant long-term improvements in aging resistance or rutting resistance and the performance can vary depending on binder type. Experimental studies indicate that using a low viscosity binder with 1.6% organic warm mix additive can alleviate fatigue issues [6,7].

Among different WMA additives—organic, chemical, and foaming—organic warm mix additives have been found to produce the least emissions and energy consumption [8]. The optimal temperature for mixing and placing asphalt should be determined [9,10]. For improved pavement performance, polymer-modified bitumen is commonly used [11]. Evaluations of polymer-modified bitumen with organic warm mix additives, using Dynamic Shear Rheometer (DSR), showed that 3% organic warm mix additive with polymer-modified bitumen yielded the best results [12,13].

Studies comparing the rheological properties of polymer-modified bitumen with warm mix additives against short-term aged binders revealed that wax modification had a greater impact on aging [14]. Short-term performance assessments of plant-mixed warm stone mastic asphalt with chemical warm mix additives showed that pavements could be opened to traffic earlier compared to conventional mixes due to lower compaction temperatures [15]. The addition of organic WMA additives has been found to mitigate the effects of aging more effectively than chemical WMA additives [16]. Analysis of binder samples before and after aging, using conventional and DSR tests, indicated that modified binders exhibited greater property variations than base binders [17]. The influence of aging on the rheological properties and temperature susceptibility of three binder samples was analysed, with a focus on maltene content and residue viscoelastic response [18]. Penetration index values were used to assess binder response to temperature changes [19]. Evaluations of complex modulus and phase angle values in DSR showed that complex modulus is more sensitive to preheating variations than phase angle values [20].

The rheological properties of binders modified with various dosages of organic warm mix additives were analysed at different temperatures using DSR. The rutting factor decreased with increasing temperature and increased with higher additive dosage [21]. The Surface Free Energy method was used to find the rutting and fatigue resistance of nano clay modified binder and the study was conducted with four different types of aggregates. The fatigue performance was evaluated using Linear Amplitude Sweep test. The analyses of the data showed that addition of nano clay enhances the fatigue life of binder. Enhanced resistance to rutting and fatigue was observed with the addition of nanomaterials [22]. Chemical and rheological analyses of binders from two sources showed that one exhibited better aging performance based on its chemical composition [23]. FTIR spectra comparisons between base and modified binders revealed additional peaks in the modified binders [24]. FTIR was used to characterize both unmodified and modified binders [25]. Rubber-modified asphalt showed significant performance improvements at high temperatures, as evidenced by MSCR tests and statistical analysis, with a decrease in residual strain upon modification [26].

Remisova, E. and Holy, M. (2017) studied the changes of properties of bitumen binders by additives application. To improve the qualitative properties, four types of additives were added with the base binders and the effects of additives on penetration, softening point and viscosity were studied as per European standards. The addition of some additives changed the PI values significantly and moved the binders to less temperature susceptible, resulting an enhancement in their resilience and adaptability to varying climatic conditions. These findings provide a comparative study for understanding the modifications and highlighting the potential of additives to improve binder performance in diverse environmental scenarios [36]. Mokhtari and Nejad studied the rheological properties of binders modified with wax and SBS modified in which penetration, penetration index,

softening point and ductility were measured. Also, the rate at which the consistency of the binder changes, that is temperature susceptibility was assessed based on the penetration index values [2]. Sengoz and Isikyakar evaluated the properties and microstructure of polymer modified bitumen. The results indicated that the properties and morphology are dependent on the polymer modification, which improved the conventional properties such as penetration, softening point and penetration index values. The increase in softening point values were favorable since bitumen with higher softening point values may be less susceptible to permanent deformation [38].

The literature reveals a gap in detailed comparative studies on the viscosity and rheological properties of VG30 and PMB40 binders with organic and chemical warm mix additives across various dosages. Additionally, there is insufficient exploration of how these additives interact with different binder types, particularly regarding their long-term aging and rutting potential. The primary objective of this study is to compare the viscosity and rheological properties of VG30 and PMB40 binders with the incorporation of organic and chemical warm mix additives. FTIR spectra were analyzed for binder samples with various additive dosages. Rheological properties were assessed using Dynamic Shear Rheometer data for both unaged and short-term aged samples, modified with these additives and subjected to the Rolling Thin Film Oven Test. Additionally, rutting potential was evaluated through the MSCR test.

The study aims at preparing mixes with two types of base binders, VG30 and PMB40 along with organic and chemical warm mix additives in which six types of binders were prepared and studied the viscosity characteristics. Based on these, optimum additive content was determined. FTIR tests were done to assess the variation in chemistry by the inclusion of organic and chemical warm mix additives in the base binders. The rutting parameter was determined from the rheological data obtained on the DSR and MSCR tests were done to assess the rutting potential. So the study aims at assessing the properties of base binders along with organic and chemical warm mix additives and making a comparison between them.

2. Methodology

2.1 Materials and Components

VG30 and PMB40 serve as base binders for this study, with both organic and chemical warm mix additives used. The organic warm mix additive is incorporated into the base binder once it reaches pouring consistency, while the chemical warm mix additive is blended using a Cowls' blade mechanical shaker (Fig. 1(a)). Organic warm mix additives are added in concentrations ranging from 1% to 4%, while chemical warm mix additives are used at 0.1% for unmodified binders and 0.125% for modified binders, according to manufacturer recommendations. VG30 (V) is combined with organic warm mix additives at 1% (VS1), 2% (VS2), 3% (VS3), 4% (VS4), VS with optimum organic additive, and with chemical warm mix additive (VZ). Similarly, PMB40 (P) is mixed with organic warm mix additives at 1% (PS1), 2% (PS2), 3% (PS3), 4% (PS4), PS with optimum organic additive, and with chemical warm mix additive (PZ).

The conceptual framework guiding the choice and dosage of organic and chemical warm mix additives was based on their influence on binder properties and mixture performance. Organic additives were selected for their ability to reduce the viscosity of bitumen through internal lubrication mechanisms, while chemical additives were chosen for their surfactant properties that improve coating and workability at lower temperatures. Dosages were determined through preliminary trials, aligning with manufacturer recommendations and optimized based on their compatibility with the binder and aggregate properties. These additives were assessed to ensure they met the desired performance criteria, such as reduced mixing and compaction temperatures without compromising the mechanical properties of the mix. Also, the additives must meet the specifications which may vary due to the traffic conditions and environmental factors. The maximum binder content was determined using the proposed mixes prepared with the addition of warm mix additives, following the Marshall method of mix design.

The DSR is a key rheological test that measures the viscoelastic properties of asphalt binders at different temperatures and loading conditions. It helps to assess the binder's ability to resist deformation under low and high temperatures in which the complex shear modulus (G)* and phase

angle (δ) of the binder is calculated which are the critical parameters for evaluating rutting resistance. The MSCR test is a crucial tool for evaluating the rutting resistance and viscoelastic properties of binders under simulated traffic loading conditions which provides additional insights into the high-temperature behavior of binders, complementing the DSR test. The MSCR test subjects the binder to stress application and recovery cycles at high temperatures, simulating the effects of repeated traffic loading. This allows the measurement of the non-recoverable creep compliance (Jnr), which quantifies the binder's susceptibility to permanent deformation. The Jnr value measures the degree of permanent deformation after multiple loading cycles in which a lower Jnr indicates better rutting resistance. DSR primarily measures the stiffness and elasticity of the binder, while the MSCR test focuses on the deformation characteristics of the binder under repeated traffic loading.

FTIR spectroscopy is a tool for characterizing functional groups and chemical bonds in materials, making it an ideal method for analyzing the chemical changes in binders, especially when modified with warm mix additives. The basic reason for using FTIR can be such that it provides detailed information about the chemical structure of the binder and also can detect the minor changes in the functional groups that may be induced by the additives.

2.2 Experimental Setup

VG30 and PMB40, used as base binders, are tested to determine physical properties such as specific gravity, penetration, softening point, ductility, and viscosity. The physical properties of binders modified with organic and chemical warm mix additives are also evaluated. The effects of these modifications are analyzed using FTIR spectra. Viscosity is measured with a Brookfield Viscometer, short-term aging is assessed using the Rolling Thin Film Oven Test, complex modulus and phase angle are obtained from a DSR (Fig. 1(b)), and rutting potential is evaluated through the MSCR test.

(a)

(b)

Fig. 1(a). Cowls' blade mechanical shaker and (b) Dynamic Shear Rheometer (DSR)

3. Results and Discussions

3.1 Physical Properties of Binders

Physical properties of VG30 and VG30 modified with organic and chemical warm mix additives; and PMB40 and PMB40 modified with organic and chemical warm mix additives are given in Table1.

Table1. Physical properties of binders

Bitumen	Penetration, 1/10 of a mm	Softening point, °C	Ductility, cm	Elastic recovery, %	Specific Gravity	Penetration Index
V	58	51	83	63	1.01	-0.61
VS1	55	56.5	>75	64	1.01	0.54

VS2	45	66	>75	68	1.01	1.88
VS3	35	70	>75	69	1.02	1.95
VS4	33	71	>75	68	1.02	1.97
VZ	41	71	>75	68	1.02	2.49
P	56	61.5	>75	71	1.02	1.62
PS1	55	63	>75	68	1.02	1.86
PS2	53	64	>75	71	1.02	1.94
PS3	51	73	>75	70	1.01	3.36
PZ	46	75	>75	68	1.01	3.39

3.2 Temperature Susceptibility Based on Penetration Index Values

The basic characterization of the binders was performed through penetration tests at 25°C and softening point tests. Temperature susceptibility was evaluated by calculating the penetration index (PI) values, which assess how the binder's properties change with temperature. PI values for all binder samples were determined following the methodology outlined in the Shell Bitumen Handbook [27] as described in Eq (1):

$$PI = \frac{1952 - 500 * log(Pen25) - 20 * SP}{50 * log(Pen25) - SP - 120} \quad (1)$$

Where, Pen25 is the penetration at 25°C and SP is the softening point temperature. Penetration and softening point values of binders modified with varying dosages of organic warm mix additives are given in Fig. 2(a).

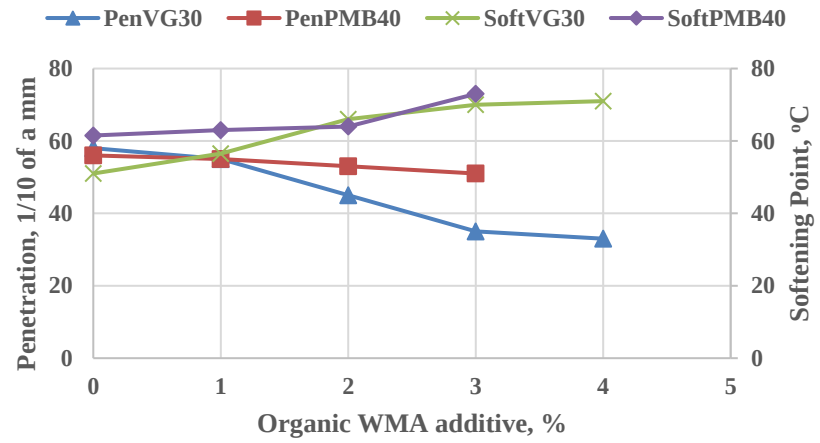

(a)

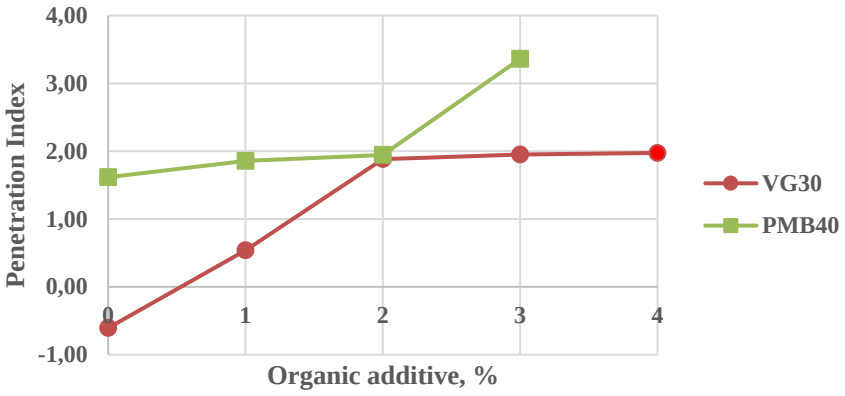

(b)

Fig. 2. (a) Penetration and softening point values of binders modified with varying dosages of organic warm mix additive, (b) Penetration index values of binders modified with organic warm mix additive

For VG30, increasing the dosage of organic warm mix additives from 0% to 4% results in a 43% decrease in penetration values, while the reduction with chemical warm mix additives is 29%. For PMB40, increasing the dosage of organic warm mix additives from 0% to 3% leads to a 9% decrease in penetration values, whereas the reduction with chemical warm mix additives is 18%. This reduction in penetration values may be attributed to the binder hardening caused by the addition of warm mix additives at intermediate temperatures. Regarding the softening point, for VG30, increasing the organic warm mix additive dosage from 0% to 4% results in a 39% increase, with a similar 39% increase observed when using chemical warm mix additives. For PMB40, increasing the organic warm mix additive dosage from 0% to 3% leads to a 19% increase in the softening point, while the increment with chemical warm mix additives is 22%. The increase in softening point values may be due to binder hardening caused by the warm mix additives at higher temperatures. This hardening could potentially enhance rutting resistance. The penetration index (PI) values for the base binders and those modified with warm mix additives are presented in Fig. 2(b). For paving bitumen, the penetration index (PI) values should fall between -2 and +2. A lower PI indicates that the binder's consistency changes more rapidly with temperature fluctuations, demonstrating greater temperature sensitivity. For VG30, when modified with organic warm mix additives, the PI values remain within this range, but with chemical warm mix additives, the PI values slightly increase. For PMB40, the PI values remain within the range when modified with up to 2% organic warm mix additive, but increase slightly with 3% organic warm mix additive and chemical warm mix additives. Consequently, the temperature susceptibility of all mixes, except those with chemical warm mix additives, is improved. VG30 and PMB40 with chemical warm mix additives, and PMB40 with 3% organic warm mix additive, show higher temperature susceptibility compared to other binders.

3.3 Viscosity Analysis Using Brookfield Viscometer

Viscosity tests were performed using a Brookfield viscometer, which assesses dynamic viscosity through a rotating spindle. The mixing and compacting temperatures for both the base binders and those modified with warm mix additives were determined according to the equi-viscous concept. The results are summarized in Table 2.

Table 2. Mixing and compacting temperatures for VG30 & PMB40 with warm mix additives

Binder	Mixing Temperature, °C	Compacting Temperature, °C
V	155-160	145-150
VS1	150-155	140-145
VS2	137-142	133-138
VS3	135-140	130-135
VZ	135-140	125-130
P	165-170	155-160
PS1	160-165	150-155
PS2	145-150	130-135
PS3	140-145	133-138
PZ	140-145	128-132

The addition of organic warm mix additives lowers the mixing and compaction temperatures for all samples. For VG30, a 1% organic warm mix additive reduces the mixing temperature by 3.2% compared to the base binder, while 2-4% reduces it by 10%. The corresponding reductions in compaction temperatures are 3.4% and 7%, respectively. In contrast, the addition of a chemical additive lowers the mixing temperature by 16% and the compaction temperature by 17%. For PMB40, a 1% organic warm mix additive reduces the mixing temperature by 3% compared to the base binder, with 2-4% reducing it by 12%. The corresponding reductions in compaction temperatures are 3.2% and 11%, respectively. The chemical additive reduces the mixing temperature by 15% and the compaction temperature by 16%.

Dynamic viscosity measurements from the Brookfield viscometer for all binder types with organic and chemical warm mix additives are shown in Fig. 3. Both types of additives significantly reduce

the mixing temperatures of the binders. The desired viscosity for proper mixing is 0.17 ± 0.02 Pa·s. Compared to the base binders; viscosity decreases considerably with increasing temperature due to the addition of warm mix additives.

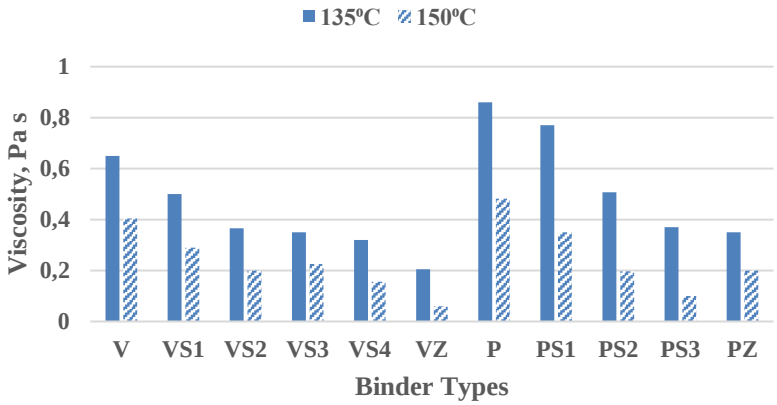

Fig. 3. Viscosity data for the binders

3.4 FTIR Analysis of Binder Modifications with Warm Mix Additives

The spectroscopic technique utilizes infrared light to study the interaction between radiation in the infrared region and molecules. Infrared radiation is absorbed by the sample, causing bonds to stretch, a process known as vibrational transition, which can be identified from the spectrum. The infrared spectrum is recorded by passing a beam of infrared light through the sample. Absorption occurs when the frequency of the infrared light matches the vibrational frequency of a bond or group of bonds. The transmitted light is analyzed to determine how much energy was absorbed at each frequency (or wavelength). Adding warm mix additives can alter the chemistry and rheology of binders, and FTIR is used to identify the functional groups. FTIR spectra for VG30 and PMB40 modified with 1%, 2%, and 3% organic and chemical warm mix additives are shown in Fig. 4(a) and Fig. 4(b).

For PMB40, the peak values in the range of 3000 to 3500 cm^{-1} also correspond to the strong O-H stretching bonds of carboxylic acids. The percentage absorption for PMB40 mixed with 2% organic warm mix additive is higher compared to the base binder. The broad peak in the range of 2850 to 2920 cm^{-1} reflects the C-H stretch of alkanes, indicating a higher saturate content in PMB40 binders with 2% organic warm mix additive.

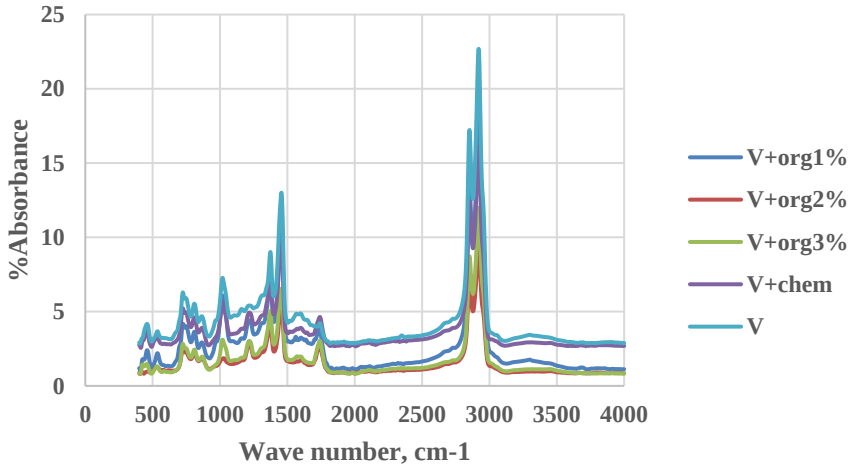

(a)

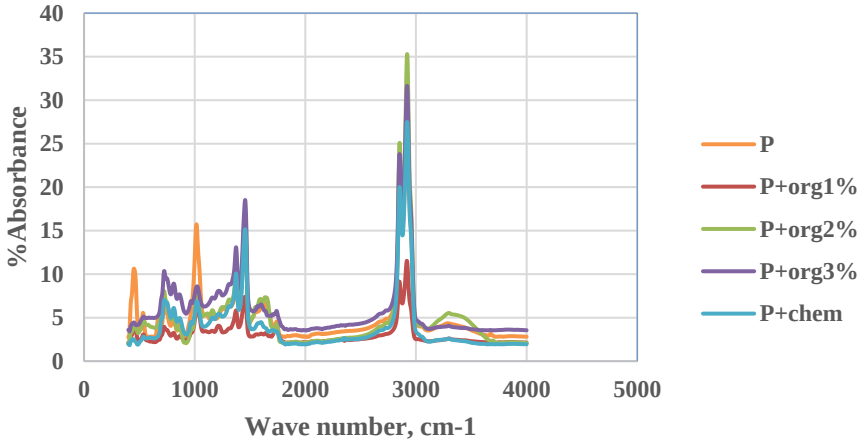

(b)

Fig. 4. (a) FTIR spectra of VG30 with varying % of organic WMA additive and chemical WMA additive and (b) FTIR spectra of PMB40 with varying % of organic WMA additive and chemical WMA additive

The reduction in viscosity at lower temperatures may be attributed to this increased saturate content. The peak at 1650 cm^{-1} denotes the C=C stretch of alkenes, with PMB40 mixed with 2% organic warm mix additive showing higher absorption compared to the base binder. The peak at 1456 cm^{-1}, representing the bending of CH_2 and CH_3, shows higher absorption for PMB40 mixed with 2% and 3% organic warm mix additives, indicating more aromatic compounds or asphaltenes. Similarly, the peak at 1378 cm^{-1} shows increased absorption for PMB40 with 2% and 3% organic warm mix additives compared to the base binder. The peak at 1230 cm^{-1} represents the C-O bond in carboxylic acids, with higher absorption observed for PMB40 mixed with 2% and 3% organic warm mix additives. The optimum content of organic warm mix additive was determined to be 2% based on the equi-viscous concept and FTIR analysis, which is also confirmed by temperature susceptibility studies based on PI values.

3.5 Comparative Analysis of Rutting Factor Using DSR

Total resistance to deformation can be measured by complex modulus, G*. Complex modulus and phase angle data will give an idea about how the material behave under traffic conditions at specified temperature. The test was conducted at 10rad/sec. An increase in the value of $G^*/\sin\partial$ indicates better rutting potential than in the case of base binders for various strain levels. A drastic increase such as 4 to 7 times in rutting factor is observed in VG30 modified with organic warm mix additives. Also, an increase of 2 times in rutting factor is observed in VG30 modified with chemical warm mix additives. An increase in trend is also observed in rutting factor in PMB40 modified with organic warm mix additives but a slightly decreasing trend is observed in PMB40 modified with chemical warm mix additives. Both the base binders modified with organic warm mix additives are showing more rutting potential as compared to the other mixes.

Variation of rutting factor with different strain values at 60°C for the unaged and aged binders are given in Fig. 5(a) and Fig. 5(b) respectively. After the binders are aged by RTFOT method, the base binder VG30 and PMB40 mixed with organic warm mix additive are showing good results to rutting potential. Aged PMB40 and aged VG30 with organic warm mix additive are showing similar results. Both the base binders mixed with chemical warm mix additive are showing least results in the form of rutting potential after ageing. At 60°C, $G^*/\sin\partial$ should be greater than 1.0kPa and for all the samples the values are more than that. Also, for the aged specimens, the value should be more than 2.2kPa [28].

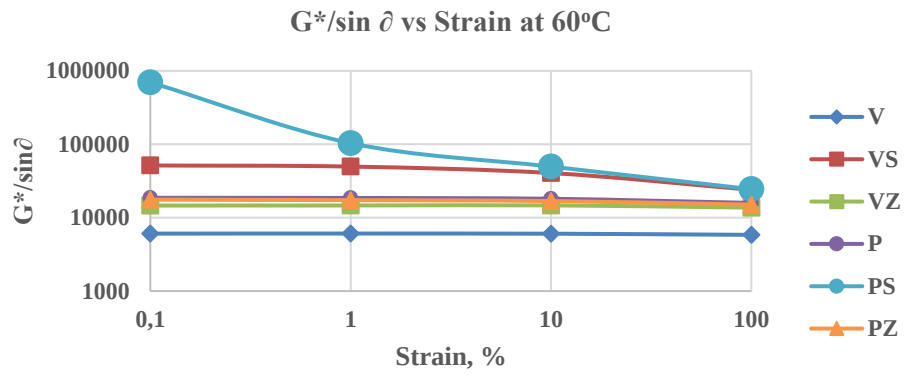

(a)

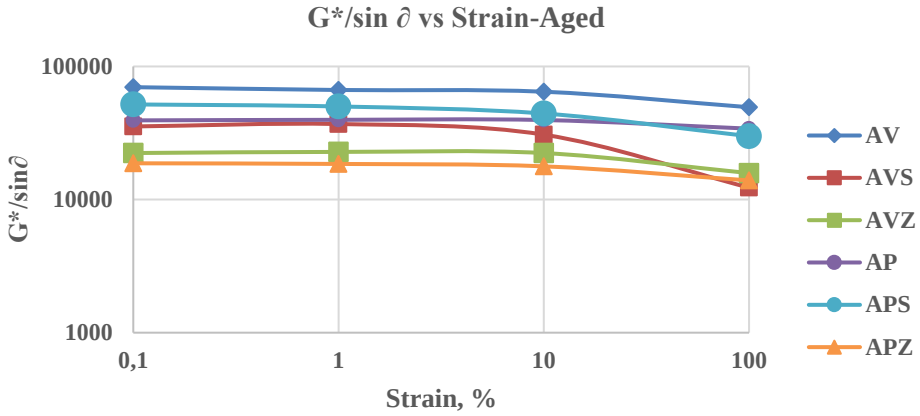

(b)

Fig. 5. (a) Variation of rutting factor for the unaged binders and (b) Variation of rutting factor for the aged binders

3.6 Variation of Rutting Parameter with Temperature

Variation of rutting factor at high temperatures for the base binders and for the base binders modified with warm mix additives are shown in Fig. 6(a); and for the RTFOT samples are shown in Fig. 6(b). For all the samples, the rutting factor is more than the standard value of 2.2kPa after RTFO test method. Increasing trend of rutting factor indicates improvement in rutting potential in the case of PMB40 and VG30 & PMB40 modified with organic warm mix additives.

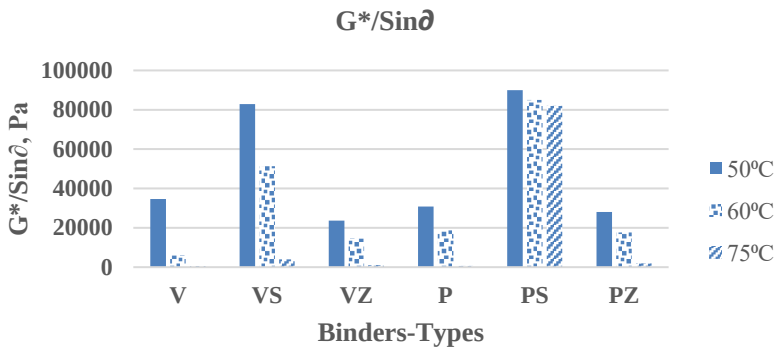

(a)

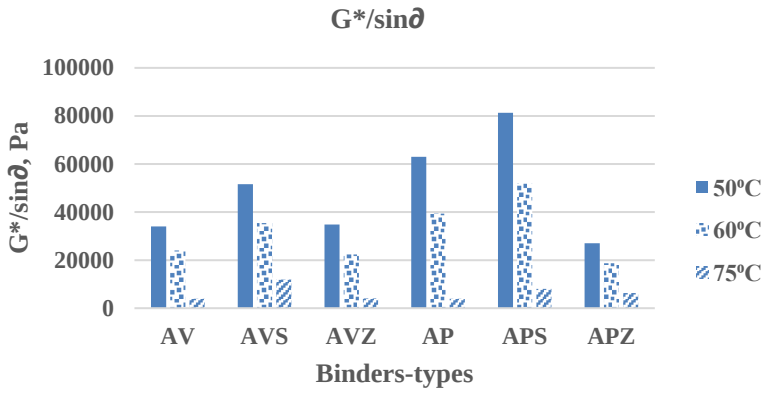

(b)

Fig. 6. (a) Variation of rutting factor at high temperatures and (b) Variation of rutting factor at high temperatures for RTFOT samples

The increase in rutting factor in VG30 with organic and chemical warm mix additives as compared to the base binder are 51% and 2.2% respectively. The change in rutting factor in PMB40 with organic and chemical warm mix additives as compared to the base binder are 29% and -57% respectively. Also, the rutting potential is decreasing at the increase of temperature. There is no improvement in rutting potential as compared to the other binders can be seen in PMB40 modified with chemical warm mix additive.

3.7 Influence of RTFOT Ageing on Binder Temperature Susceptibility

In dynamic mechanical analysis, the temperature susceptibility of binders may be calculated by measuring storage and loss moduli and complex modulus at different temperatures [29] as per the Eq (2):

$$G^*TS = (\text{loglog}G1^* - \text{loglog}G2^*)/(\log T2 - \log T1) \quad (2)$$

where, G_1^* is the complex modulus at T_1, G_2^* is the complex modulus at T_2, and T_1 & T_2 temperature in Kelvin. Also, G*TS is the temperature susceptibility due to complex modulus.

Ageing of binders can be evaluated by calculating ageing index, which is obtained by taking the ratio of the rheological parameter of the aged binder to that of the unaged binder. Table 3 compares the values of the temperature susceptibility obtained using the complex modulus values at 50°C and 60°C; and also, the ageing index values.

Table 3. Temperature susceptibility in terms of complex modulus; and ageing index values

	G*TS 50°C to 60°C		Ageing Index	
Binder	Before RTFOT	After RTFOT	At 50°C	At 60°C
V	5.90	1.87	1.87	3.58
VS	1.53	1.09	0.59	0.70
VZ	1.66	1.52	1.39	1.43
P	1.64	1.51	2.11	2.12
PS	0.60	1.38	0.29	0.23
PZ	1.40	1.27	0.96	1.00

Base binder VG30 is less temperature susceptible compared to the other binder combinations. From 50°C and 60°C, the aged specimens also have not much reduction in temperature susceptibility and this may be due to the increased values of complex modulus after ageing by RTFOT method. At 60°C, for the base binders VG30 and PMB40 and VG30 with chemical warm mix

additive, high value of the ageing index is showing which indicates high degree of binder hardening. Also, the same trend is seen in the case of 50°C.

3.8 MSCR Test for Assessing the Rutting Potential

The MSCR test in binders uses the concept of creep and recovery to evaluate the potential for permanent deformation. After the one second load is removed, the sample is allowed to recover for 9 seconds for the low and high stress levels of 0.1kPa and 3.2kPa respectively. Sometimes the G*/sin∂ data obtained does not exactly serve the ability of some polymer modified binders to resist rutting as low levels of stress and strain are used in the test procedure. But in MSCR test, higher levels of stress and strain are applied to the binder which represents the actual condition of the pavement. Non recoverable creep compliance (Jnr) values from MSCR test for all the binder samples for the stress levels of 0.1kPa and 3.2kPa are given in Fig. 7.

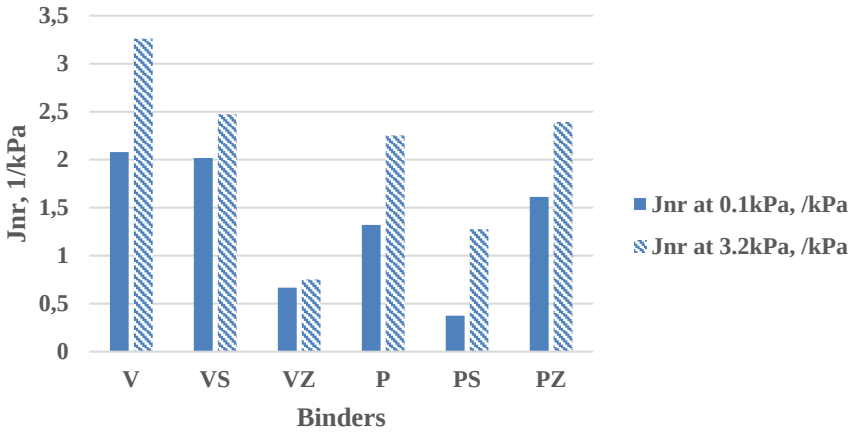

Fig. 7. Variation of Non recoverable creep compliance values (Jnr) for the binders

The influence of additives on rutting resistance was evaluated through non-recoverable creep compliance (Jnr) values under repeated load testing at different stress levels. Based on the Jnr values, for standard traffic loading, the base binders VG30 and PMB40; and VG30 with organic additive and PMB40 with chemical additive gave better rutting potential. For heavy traffic loading, VG30 with chemical additive and PMB40 with organic additive gave better rutting potential. At lower stress level, the non-recoverable creep compliance values under repeated load for the binder samples of VG30, VG30 with organic additive, PMB40 and PMB40 with chemical additive are higher as compared to the samples of VG30 with chemical additive and PMB40 with organic additive. The same trend is observed at higher stress level also for the same samples under repeated load. The difference between the values at the lower and higher stress levels for the same sample is low in VG30 with chemical additive indicating its superior performance and suitability for applications involving heavy traffic loading. This behavior underscores the ability of chemical additives to enhance binder stiffness and improve rutting resistance across varying stress conditions.

4. Conclusions

The study demonstrates that the addition of organic and chemical warm mix additives to VG30 and PMB40 binders significantly impacts their physical and performance characteristics. Notably, VG30 and PMB40 show substantial reductions in penetration values when mixed with these additives, with the most pronounced effects observed at 2-3% organic additive content. This results in similar trends in softening point values, indicating that both types of warm mix additives increase the binder's resistance to temperature variations. This reduction in penetration values may be attributed to the binder hardening caused by the addition of warm mix additives. As PI indicates binder's ability to change with temperature fluctuations, the results of the samples with organic warm mix additives showed better temperature susceptibility properties as compared to the chemical additives. Increasing the organic warm mix additive dosage from 0% to 4% results in a 39% increase, with a similar 39% increase observed when using chemical warm mix additives. For

PMB40, increasing the organic warm mix additive dosage from 0% to 3% leads to a 19% increase in the softening point, while the increment with chemical warm mix additives is 22%.

The equi-viscous concept applied to viscosity studies reveals that both organic and chemical warm mix additives lower the mixing and compacting temperatures of the binders. This adjustment in temperature contributes to improved rutting potential as measured by the G*/sinδ parameter, except for PMB40 with chemical warm mix additive, which does not meet the standard specifications at 60°C. VG30 and PMB40 binders, particularly with organic additives, show enhanced rutting performance for both unaged and aged samples, comparing with the rutting performance of the samples with the chemical additives. Studies using DSR revealed a drastic increase such as 4 to 7 times in rutting factor in VG30 modified with organic warm mix additives. Also, an increase of 2 times in rutting factor is observed in VG30 modified with chemical warm mix additives. An increase in trend is also observed in rutting factor in PMB40 modified with organic warm mix additives but a slightly decreasing trend is observed in PMB40 modified with chemical warm mix additives. Both the base binders modified with organic warm mix additives are showing more rutting potential as compared to the other mixes.

After the binders are aged by RTFOT method, the base binder VG30 and PMB40 mixed with organic warm mix additive are showing good results to rutting potential.

In the FTIR analysis, the peak values in the range of 3000 to 3500 cm^{-1} represent the strong O-H stretching bonds associated with carboxylic acids. The percentage absorption of both the binders mixed with organic and chemical warm mix additives is higher compared to the base binders. A broad peak in the range of 2850 to 3000 cm^{-1} corresponds to the C-H stretch of alkanes, which are long-chain hydrocarbons. Among VG30 binders, those with 2% and 3% organic warm mix additives show higher saturate content. The reduction in viscosity at lower temperatures for VG30 with 2% organic warm mix additive may be due to the increased saturates content.

Ageing assessments using the ageing index indicate a higher degree of binder hardening at 50°C and 60°C for VG30, PMB40, and VG30 with chemical warm mix additives. The MSCR test results highlight that VG30 and PMB40 base binders, along with VG30 with organic additives and PMB40 with chemical additives, exhibit better rutting potential under standard traffic loading conditions. For heavy traffic loading, VG30 with chemical additives and PMB40 with organic additives provide superior rutting resistance.

In the laboratory, temperatures during mixing and compaction were measured manually, which differs from field practices where automated temperature controllers and monitoring systems are typically employed to ensure consistent thermal conditions. While the manual method provided adequate control for experimental purposes, it may not fully replicate the precision achievable in actual field scenarios. To address this limitation, future studies could incorporate advanced temperature control systems during mixing and compaction to better simulate real-world conditions and improve the reliability of lab-to-field performance correlations. Predicting the exact temperature in the mixing plant is challenging, but the development of a suitable temperature control system could be achieved by adopting an interdisciplinary approach in collaboration with researchers from other fields, which could greatly benefit the Transportation Engineering sector. As the additives used in this study are present in very small quantities, determining their precise environmental impact is complex. Additionally, the long-term effects of these additives on environmental balance could be explored in future research, including any cumulative impacts that might emerge over time. Future research could build on these findings by focusing on real-world testing at mixing plants, conducting life cycle assessments of additives, and exploring their long-term environmental consequences. Such studies would provide a more comprehensive understanding of the sustainability and practical implications of using warm mix additives in bituminous binders.

Acknowledgement

The study is completed with the help of transportation divisions of College of Engineering Trivandrum and National Institute of Technology, Calicut; and also thankful to the staff, PG students and research scholars.

References

[1] Hamzah MO, Jamshidi A, Shahadan Z. Evaluation of the potential of Sasobit® to reduce required heat energy and CO_2 emission in the asphalt industry. J Clean Prod. 2010;18(18):1859-65. https://doi.org/10.1016/j.jclepro.2010.08.002

[2] Mokhtari A, Nejad FM. Comparative study on performance of wax modified and typical SMA mixtures. J Mater Civ Eng. 2013;25(3):419-27. https://doi.org/10.1061/(ASCE)MT.1943-5533.0000584

[3] Kristjansdottir O. Warm mix asphalt for cold weather paving [Master's thesis]. University of Washington; 2006.

[4] Kristjansdottir O, Muench ST, Michael L, Burke G. Assessing potential for warm mix asphalt technology adoption. Transp Res Rec. 2007;(2040):91-9. https://doi.org/10.3141/2040-10

[5] Wagh VP, Saboo N, Gupta A. Using tribological approach to assess production temperatures of asphalt binders. Constr Build Mater. 2024;419:135513. https://doi.org/10.1016/j.conbuildmat.2024.135513

[6] Jamshidi A, Hamzah MO, Aman MY. Effects of Sasobit content on the rheological characteristics of unaged and aged asphalt binders at high and intermediate temperatures. Mater Res. 2012;15(4):628-38. https://doi.org/10.1590/S1516-14392012005000083

[7] Abd DM, Ahmed TM, Ahmed TY. Characterization of rutting resistance of warm modified asphalt mixtures tested in a Dynamic Shear Rheometer. J Mech Behav Mater. 2023;32:20220277. https://doi.org/10.1515/jmbm-2022-0277

[8] Sukhija M, Saboo N, Pani A. Economical and environmental aspects of warm mix asphalt mixtures: a comparative analysis. Transp Res D Transp Environ. 2022;109:103355. https://doi.org/10.1016/j.trd.2022.103355

[9] Yildirim Y, Ideker J, Hazlett DPE. Evaluation of viscosity values for mixing and compaction temperatures. J Mater Civ Eng. 2006;18:545-53. https://doi.org/10.1061/(ASCE)0899-1561(2006)18:4(545)

[10] Silva HMRD, Oliveira JRM, Ferreira CIG, Pereira PAA. Assessment of the performance of warm mix asphalts in road pavements. Int J Pavement Res Technol. 2010;3(3):119-27.

[11] Yildirim Y. Polymer modified asphalt binders. Constr Build Mater. 2007;21:66-72. https://doi.org/10.1016/j.conbuildmat.2005.07.007

[12] Airey GD. Rheological evaluation of ethylene vinyl acetate polymer modified bitumens. Constr Build Mater. 2002;16:473-87. https://doi.org/10.1016/S0950-0618(02)00103-4

[13] Kok BV, Akpolat M. Effects of using Sasobit and the SBS on the engineering properties of bitumen and stone mastic asphalt. J Mater Civ Eng. 2015;27(10):04015006. https://doi.org/10.1061/(ASCE)MT.1943-5533.0001255

[14] Iwanski M, Cholewinska M, Mazurek G. Viscoelastic properties of PMB in warm mix asphalt technology in terms of ageing. Procedia Eng. 2017;172:401-8. https://doi.org/10.1016/j.proeng.2017.02.007

[15] Al-Khadi IL, Leng Z, Baek J, Wang H, Doyen M, Gillen SL. Short term performance of plant-mixed warm stone mastic asphalt. Transp Res Rec. 2012;(2306):86-94. https://doi.org/10.3141/2306-10

[16] Oner J, Sengoz B, Rija SF, Topal A. Investigation of the rheological properties of elastomeric polymer modified bitumen using warm mix asphalt additives. Road Mater Pavement Des. 2017;18(5):1049-66. https://doi.org/10.1080/14680629.2016.1206484

[17] Miro R, Martinez AH, Navarro FM, Gamez MCR. Effect of ageing and temperature on the fatigue behaviour of bitumens. Mater Des. 2015;86:129-37. https://doi.org/10.1016/j.matdes.2015.07.076

[18] Mastrofini D, Scarsella M. The application of rheology to the evaluation of bitumen ageing. Fuel. 2000;79:1005-15. https://doi.org/10.1016/S0016-2361(99)00244-6

[19] Fazaeli H, Amini AA, Nejad FM, Behbehani H. Rheological properties of bitumen modified with a combination of FT paraffin wax and other additives. J Civ Eng Manag. 2016;22(2):135-45. https://doi.org/10.3846/13923730.2014.897977

[20] Sheidaei M, Gudmarsson A, Langfjell M. Effect of various Dynamic Shear Rheometer testing methods on the measured rheological properties of bitumen. Materials. 2023;16:2745. https://doi.org/10.3390/ma16072745

[21] Zhang J, Liu G, Pei G. Effect of WMA additive on the rheological properties of asphalt binder and high temperature performance grade. Adv Mater Sci Eng. 2015. https://doi.org/10.1155/2015/467891

[22] Ashish PK, Singh D, Bohm S. Evaluation of rutting, fatigue and moisture damage performance nanoclay modified asphalt binder. Constr Build Mater. 2016;113:341-50. https://doi.org/10.1016/j.conbuildmat.2016.03.057

[23] Mischalica P, Kazatchkov IB, Stastna J, Zanzotto L. Relationship between chemical and rheological properties of two asphalts of different origins. Fuel. 2008;87:3247-53. https://doi.org/10.1016/j.fuel.2008.05.021

[24] Olabemiwo OM, Esan AO, Abediran GO. The performance of Agbabu natural bitumen modified with polyphosphoric acid through fundamental and Fourier transform infrared investigations. Case Stud Constr Mater. 2016;5:39-45. https://doi.org/10.1016/j.cscm.2016.06.003

[25] Murana AA, Ochepo J, Yerima MA, Ejike IK. Properties of HMA containing high density polyethylene modified with reclaimed asphalt. Jordan J Civ Eng. 2024;18(3):389-404. https://doi.org/10.14525/JJCE.v18i3.03
[26] Lei Z, Chao X, Fei G, Shuai LT, Qiu TY. Using DSR and MSCR tests to characterize high temperature performance of different rubber modified asphalt. Constr Build Mater. 2016;127:466-74. https://doi.org/10.1016/j.conbuildmat.2016.10.010
[27] Whiteoak D. Shell Bitumen Handbook. London: Shell Bitumen UK; 1990.
[28] Indian Roads Congress. IRC: SP: 53-2010 Guidelines on use of modified bitumen in road construction. New Delhi: IRC; 2010.
[29] Lu X, Isacsson U. Chemical and rheological evaluation of ageing properties of SBS polymer modified bitumens. Fuel. 1998;77(9-10):961-72. https://doi.org/10.1016/S0016-2361(97)00283-4
[30] ASTM. ASTM D5-97 Standard test method for penetration of bituminous materials. 1998 Annual Book of ASTM Standards, Vol. 04.03. Philadelphia: ASTM; 1998.
[31] ASTM. ASTM D7405-20 Standard test method for MSCR of asphalt binder using a DSR. West Conshohocken, PA: ASTM; 2020.
[32] Bureau of Indian Standards. IS 15462: Polymer and Rubber Modified Bitumen - Specification. New Delhi: BIS.
[33] Bureau of Indian Standards. IS 73-2013: Paving Bitumen - Specification. New Delhi: BIS.
[34] ASTM. ASTM D1559-76 Standard method of test for resistance to plastic flow of bituminous mixtures using Marshall apparatus. West Conshohocken, PA: ASTM; 1976.
[35] ASTM. ASTM D2493: Standard viscosity charts for asphalts. West Conshohocken, PA: ASTM.
[36] Remisova E, Holy M. Changes of properties of bitumen binders by additives application. Mater Sci Eng. 2017;245. https://doi.org/10.1088/1757-899X/245/3/032003
[37] Madhu K, Raj JA, Shibu N, Viswa G. Assessing recycled asphalt pavement: Impact of waste cooking oil and waste engine oil as rejuvenators on mechanical properties. Res Eng Struct Mater. 2024.
[38] Sengoz B, Isikyakar G. Evaluation of the properties and microstructure of SBS and EVA polymer modified bitumen. Constr Build Mater. 2008;22:1897-905. https://doi.org/10.1016/j.conbuildmat.2007.07.013

Research on Engineering Structures & Materials
www.jresm.org
Research Group

Research Article

A study on flexural behaviour and strengthening of fibre reinforced concrete beams using microorganisms

Sasikumar Palanisamy [*,1,a], Subitha Thirupathi [2,b]

[1]*Department of Civil Engineering, K.Ramakrishnan College of Technology, Trichy – 621112, India*
[2]*Dept. of Civil Eng., Avinashilingam Institute for Home Science and Higher Education for Women, Avinashilingam University, Tamil Nadu-641043, India*

Article Info

Article History:

Received 08 Jan 2025
Accepted 31 Mar 2025

Keywords:

Bacterial concrete;
Finite element model;
Crack pattern;
Steel fibre;
Peak ductility;
Stiffness

Abstract

This study used microorganisms to investigate the flexural behavior of reinforced concrete beams with a cross-section of 150mm x 180mm and a length of 1500mm. The research focuses on the effects of these microorganisms on the mechanical properties and flexural behavior of the concrete. The study specifically investigated the mechanical properties of concrete by incorporating different ranges of Steel Fibers (SF): 0.2%, 0.4%, 0.6%, 0.8%, and 1.0%. Additionally, the research examined the flexural behavior of the RC beams, with incorporation of Bacillus Subtilis bacteria concentrations of 1%, 2% and 3% for both the control and optimum mix. Six concrete mixtures were designed with SF at the following percentages: 0.2%, 0.4%, 0.6%, 0.8%, and 1.0%. The study utilized M40-grade concrete. Bacillus Subtilis bacteria were incorporated into the concrete by the weight of the cement during the casting process. The specimens took on different shapes, such as cubes, cylinders, and prisms. The concrete specimens were cast and tested after 7, 14, and 28 days of curing. According to the experimental results, the optimal SF content was 0.8%. Finite Element Model (FEM) was developed using ANSYS to analyze the RC beams. The FEM approach proved helpful in predicting the experimental outcomes. Adding 0.8% of steel fibre and 2% microorganisms enhanced the compressive strength by 4.20% compared to the control sample. Similarly, the flexural behavior of the RC beams was increased by 19.98% and 24.40% compared to the conventional specimens. This study aims to provide the potential benefits of using microorganisms in concrete technology.

© 2025 MIM Research Group. All rights reserved.

1. Introduction

Generally, concrete, while strong in compression, tends to be weak in tension. Fibres have been added to address this issue and enhance its overall performance. One standard method involves incorporating steel fibres of various geometries into the concrete mix. These steel fibres act as reinforcements, improving the materials tensile strength and ductility. Closed Steel Fibres (CSF) tend to improve the strength properties of the concrete. Unlike traditional open fibres, CSFs are designed to prevent fibre pull-out during tension, allowing for better utilization of their tensile capacity. The workability of fibre-reinforced concrete decreased with increasing steel fibre content. The mechanical properties were increased by 46% and 36% for tensile and flexural strength [1]. The effect of Recycled Steel Fibres (RSF) on concrete mechanical properties. Notably, RSF had a negligible impact on durability but significantly enhanced mechanical properties. These findings highlight the potential of RSF as a sustainable reinforcement option for concrete structures [2]. The effects of varying SF content and length on concrete strength properties. Parameters studied included slump, pore structure, CS, STS, flexural toughness, and impact resistance. The study provides valuable insights into optimizing steel fibre reinforcement in concrete [3]. The

*Corresponding author: sasikumarp.civil@krct.ac.in
[a]orcid.org/0000-0002-9674-5319; [b]orcid.org/0000-0002-1646-1237
DOI: http://dx.doi.org/10.17515/resm2025-616me0108rs

comparative studies of steel and hybrid fibre-reinforced concrete: While compressive strength showed slight effects, the hybridization increased the mechanical properties of the concrete by adding mixed fibres. Overall, fibre-reinforced concrete exhibited improved strengths with fibre reinforcement [4].

Fibre-reinforced concrete (FRC) is a composite material that integrates the advantages of conventional concrete with the enhanced strength and durability embedded fibres provide. Steel fibres, in particular, play a crucial role in enhancing the mechanical properties of concrete. Steel fibres act as tiny reinforcements within the concrete matrix, effectively bridging cracks and improving tensile strength. Including steel fibres significantly enhances the concrete ability to withstand tensile forces, making it more resistant to cracking and structural failure. Steel fibres improve ductility, allowing the concrete to absorb more energy during deformation. Steel fibres reduce crack widths and prevent crack propagation [5]. The mechanical performances of concretes and RC beams increased using steel fibres. Steel fibre RC concrete flexural strengths have increased significantly [6]. The addition of SF to concrete can substantially enhance its performance. Steel fibre-reinforced has gained popularity due to several advantages, including hindrance in macro crack propagation, prevention of micro-crack growth to macroscopic levels, improved ductility and residual strength after the first crack formation and high toughness [7]. Combining steel and polypropylene fibres offers a promising approach to enhancing concrete structure's strength, durability, and high-temperature performance [8,9]. Adding steel fibres improves the mechanical properties of concrete. SF enhanced the concrete's ability to withstand impact loads, making it more resistant to sudden forces. SFRC exhibits improved toughness, preventing brittle failure and enhancing durability. Including steel fibres enhances flexural strength, which is crucial for resisting bending stresses. SFRC shows increased tensile strength, reducing the risk of cracking and improving overall performance. Steel fibres contribute to ductility, allowing the concrete to deform plastically before failure. Moreover, SFRC resists cracking and spalling, making it suitable for various construction applications. Researchers continue to explore optimal fibre content and geometry to maximize these benefits [10].

The main disadvantages of concrete include low tensile strength when subjected to external loads and the formation of micro-cracks, which can lead to structural corrosion. Nowadays, concrete structures are protected from micro-cracks and corrosion by using Bacillus subtilis bacteria in the concrete [11–15]. Bacillus Subtilis bacteria make cement mortar more hydrated, which makes it safe to use and improves concrete performance [16–18]. The microorganisms fill the existing gaps in the concrete, so they propagate to increase the strength properties of the concrete, such as CS, STS and FS [19–22]. Bio concrete, which incorporates microorganisms, aims to enhance the strength properties of traditional concrete. This research contributes valuable insights into sustainable construction materials. The microorganisms actively fill existing voids within the concrete matrix. This process contributes to the enhancement of overall strength. Using concrete reduces the environmental footprint associated with traditional concrete production. Using microorganisms promotes sustainability and contributes to environmental protection [23]. Self-healing properties are at the core of this novel construction material, promising longevity and reduced maintenance costs. Bioengineered concrete incorporates microorganisms that actively repair cracks and fissures. These tiny agents play a crucial role in maintaining structural integrity over time. By promoting self-healing, bioengineered concrete contributes to environmental conservation. Reduced need for repairs translates to less material consumption and waste. The study emphasizes the long-term durability of bioengineered concrete. It withstands ecological stressors, making it an attractive choice for sustainable infrastructure. Bioengineered concrete represents a paradigm shift in construction practices. Its self-healing capabilities align with sustainability principles, making it a promising solution for resilient and eco-conscious infrastructure [24].

Soft computing methods, especially Artificial Neural Networks (ANN) and Gene Expression Programming (GEP), present considerable benefits in assessing the flexural strength of T-shaped concrete beams reinforced with FRP. These approaches yield more precise and dependable predictions than conventional empirical models, establishing them as essential resources in structural engineering [25]. Bacterial bio composite concrete presents a sustainable and efficient

approach to improving concrete structures' strength and self-repairing properties, especially in environments exposed to soil. Incorporating bacteria like Bacillus flexus and Bacillus paramycoides has demonstrated considerable promise in enhancing the durability and lifespan of concrete, positioning it as a noteworthy advancement in civil engineering [26]. Wavelet transform methods, especially for modal excitation responses, provide a reliable and precise approach to identifying damage in reinforced concrete beams. Their capability to identify localized irregularities and variations in modal characteristics renders wavelet transform an essential instrument in structural health monitoring [27]. Using effective microorganism solutions in sustainable self-curing concrete presents a valuable approach to improving the durability and functionality of concrete structures.

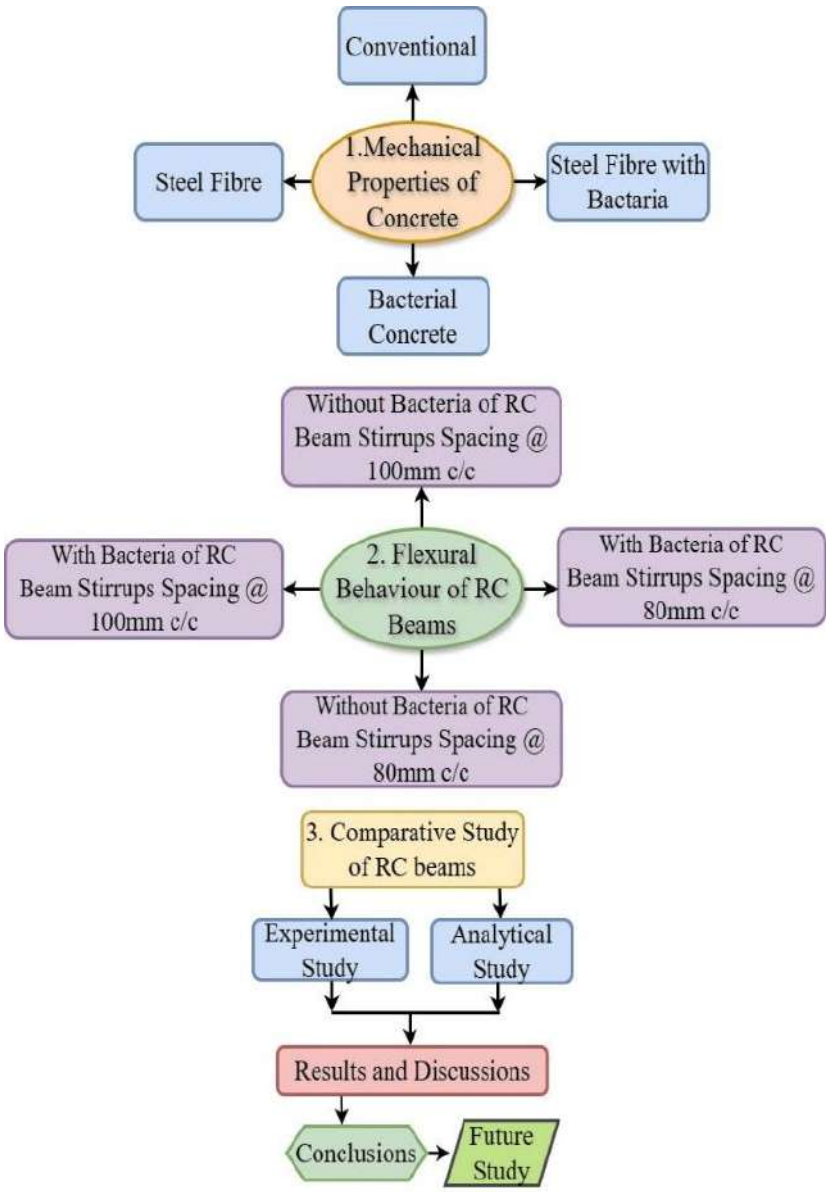

Fig. 1. Graphical abstract for this study

This innovative concrete reduces sorptivity, drying shrinkage, and expansion while enhancing microstructure and strength, marking notable progress in sustainable construction materials [28,29]. Soft computing methods, especially Genetic Programming (GEP) and ANN, present considerable benefits in assessing the load-carrying capacity of reinforced concrete beam-column joints. These approaches yield more precise and dependable predictions than conventional empirical models, establishing them as essential resources in structural engineering [30,31].

Concrete is widely used in construction due to its versatility and applications. Combining different types of fibres within a concrete mixture has been shown to enhance the strength properties of

cementitious materials by monitoring crack initiation and propagation. In this study, we focus on the impact of integrating steel fibres ranging from 0.2% to 1% on the mechanical properties of concrete. Steel fibres play a crucial role in enhancing the strength and performance of concrete. The research continues to explore the optimal fibre content of 0.8% and the microorganism dosages of 1%, 2%, and 3%. The optimum steel fibre and microorganisms' content was 0.8% and 2%, respectively. This optimum mix is recommended for the flexural behavior of the RC beams investigation with various shear reinforcement spacing. The research underscores the potential of bio-concrete as an eco-friendly alternative. Further exploration and implementation of bio concrete in real-world construction projects are recommended. The significance of this study lies in its exploration of self-healing concrete, which addresses one of the major challenges in concrete structures: cracking. Cracks in concrete can arise from various factors, such as plastic shrinkage, drying shrinkage, thermal contraction, and structural loads. These cracks compromise the structural integrity and reduce the longevity of concrete structures by allowing external agents to penetrate and cause further damage. The graphical abstract gives details of the present study, as shown in (Fig. 1).

2. Research Methodology

The present study investigated steel fibre-reinforced concrete (SFRC) beams by adding steel fibres and microorganisms in various percentages. The research methodology of this study includes the collection of materials, mix design of concrete, preparation of the specimens, casting of the specimens, testing (mechanical properties and flexural behavior), experimental analysis, finite element analysis, and data analysis.

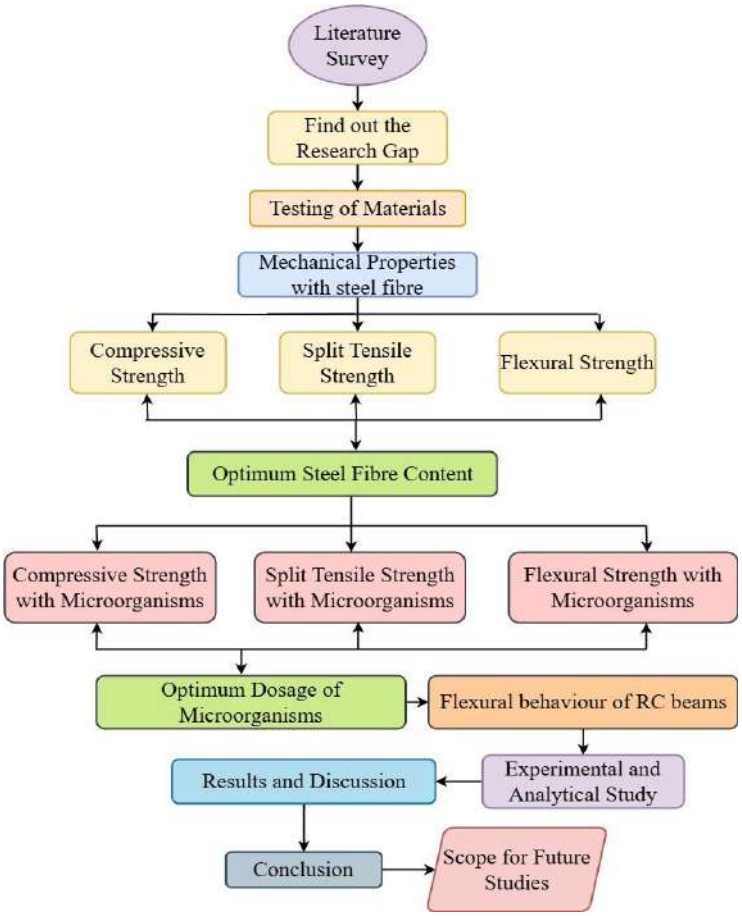

Fig. 2. Flow chart for the research methodology

The experimental results were compared to the FEM predictions. The addition of 0.8% steel fiber and 2% microorganisms showed an enhancement in compressive strength by 4.20% and the flexural behavior of RC beams by 19.98% and 24.40% compared to conventional specimens. This

research methodology provides a comprehensive approach to investigating the effects of steel fibers and Bacillus Subtilis bacteria on self-healing concrete's mechanical properties and flexural behavior. The operating conditions of structures, such as moisture level, temperature, pH level, exposure to chemicals, structural load, maintenance, and monitoring, can significantly impact the effectiveness of bacterial hardening in concrete. The long-term effectiveness of bacterial hardening in concrete can be influenced by various factors, including the operating conditions of the structures and the impact of negative temperatures. A detailed investigation of the present study in different phases and the research methodology is shown in (Fig. 2).

3. Experimental Study

3.1. Materials

The study used 53-grade Ordinary Portland Cement (OPC), which conforms to IS 12269-1987 [32]. The fine aggregate was collected from the local market and adheres to grading zone II as specified in IS 383 – 2016 [33]. Natural crushed rocks were employed for the coarse aggregate, and the angular coarse aggregate also adheres to IS 383 – 2016 [33]. This study used a water-reducing or chemical admixture (Conplast SP430) to reduce the water content and increase the strength properties of the concrete. The initial tests were conducted, and the physical properties of the cement, fine aggregate, coarse aggregate and superplasticizer are provided in Table 1.

Table 1. Physical properties of cement

Properties	Test values			
	CE	FA	CA	SP
Specific gravity (g/cm^3)	3.14	2.65	2.69	1.08
Final setting time (min)	258	-	-	-
Initial setting time (min)	36	-	-	-
Fineness modulus (%)	3.56	-	-	-
Consistency (%)	34.15	-	-	-
Water absorption (%)	-	1.68	0.62	-
Fineness modulus (%)	-	2.94	6.28	-
Crushing values (%)	-		9.74	-
Impact value (%)	-		10.16	-

Note: CE- Cement; FA – Fine aggregate; CA – Coarse aggregate; SP – Superplasticizer

Bacillus subtilis microorganisms were cultivated in the laboratory, enhancing concrete's mechanical properties and reinforcing the concrete beam's flexural behaviour. Bacillus subtilis was added to the concrete mix based on the weight of the cement. Adding bacteria to concrete under production conditions involves a few key steps to ensure the bacteria remain viable and effective. Incorporated the bacterial suspension into the concrete mix during the mixing process and also ensured the bacteria were evenly distributed throughout the mix. Introducing bacterial additives into concrete can lead to significant changes in its structure and the hydration conditions of clinker minerals. Bacteria such as Bacillus Subtilis can precipitate calcium carbonate (CaCO3) within the concrete matrix. This process fills the pores and cracks, enhancing the density and reducing the permeability of the concrete. Incorporating bacterial additives can significantly enhance the concrete structure, leading to improved mechanical properties and durability.

Table 2. Physical properties of steel fibre

Properties	Test values
Diameter (mm)	0.72
Length (mm)	50
Aspect ratio (L/D)	69.45
Tensile strength (MPa)	1100
Modulus of elasticity (MPa)	204
Unit weight (kg/m^3)	7850

The hydration conditions of clinker minerals are also optimized, resulting in a more stable and resilient concrete matrix. Additionally, steel fibres were procured from the Chennai fibre region, and their physical properties are detailed in Table 2. The percentages of steel fibres and microorganisms were added to the concrete mix concerning the weight of the cement in the concrete mix, and the materials are shown in (Fig. 3).

(a)

(b)

(c)

Fig. 3. Materials of the study(a) Steel fibre, (b) Concrete mix, and (c)Bacillus subtilis

3.2 Mix Design

According to IS 10262 - 2019 [34], the mix design used M40-grade concrete with a concentrated w/c of 0.40. The mix proportions ratio in this study is 1:1.57:2.84. A total of six mix proportions were designed: M40-SF0, M40-SF0.2, M40-SF0.4, M40-SF0.6, M40-SF0.8, and M40-SF1.0 is reported in Table 3. SFs were added to the concrete mix based on the weight of the cement. These SF were incorporated at various percentages (0.2%, 0.4%, 0.6%, 0.8%, and 1.0%). After the mix design, the material quantities were calculated: cement 416 kg/m^3, fine aggregate 654 kg/m^3, coarse aggregate 1182 kg/m^3, water content 147 kg/m^3 and a w/c of 0.40. The mechanical properties, including CS, STS and FS, were examined after curing periods of seven, fourteen, and twenty-eight days. One hundred sixty-two samples were cast and tested for these properties: 54 for CS, 54 for STS, and 54 for FS.

Table 3. Materials required for concrete 1M^3 in kg/m^3

Mix ID	CE	FA	CA	Water	SP	W/C	SF (%)
M40-SF0	416	654	1182	147	2.08	0.4	0
M40-SF0.2	416	654	1182	147	2.08	0.4	0.2
M40-SF0.4	416	654	1182	147	2.08	0.4	0.4
M40-SF0.6	416	654	1182	147	2.08	0.4	0.6
M40-SF0.8	416	654	1182	147	2.08	0.4	0.8
M40-SF1.0	416	654	1182	147	2.08	0.4	1.0

3.3 Mechanical Properties of Concrete

3.3.1 Compressive, Split Tensile and Flexural Strength of Concrete

The mechanical properties of Steel Fibre-Reinforced Concrete (SFRC), including CS and FS are examined as per IS 516 - 516 [35], and STS, are evaluated according to IS 5816 - 1999 [36]. The steel moulds used for testing have the following dimensions: compressive strength mould: 150 mm x 150 mm x 150 mm, split tensile strength mould: 150 mm diameter x 300 mm height and flexural strength mould: 150 mm x 150 mm x 750 mm. The waste oil is applied to the interior faces to prevent concrete adhesion to the steel moulds.

Fig. 4. Compressive strength test

Fig. 5. Split tensile strength test

The concrete mix is prepared using a machine mix and poured into the steel moulds in three layers, compacting each layer twenty-five times. Excess concrete is then removed with a trowel. The steel moulds are placed at room temperature for 24 hours. After demolding, the samples are cured in a water tank. The CS and STS tests are conducted using a Compressive Testing Machine (CTM) with a capacity of 3000 kN, as shown in (Figs. 4 and 5). Similarly, the FS of SFRC is evaluated using a Universal Testing Machine (UTM) with a capacity of 400 kN under two-point loading, illustrated in (Fig. 6). The calculated CS, STS, and FS values follow the recommended equations from IS 516 - 1959 [35,36].

Fig. 6. Flexural strength test

3.3.2 Optimum Steel Fibre and Dosage of Microorganisms Content

Based on the experimental test results, the optimum SF content was examined by 0.8%, listed in Table 4. The microorganisms' content (0%, 1%, 2%, and 3%) was added by the weight of the cement to the optimum content mix M40-SF0.8, which is reported in Table 5. The Bacillus Subtilis bacteria are added to the concrete with the required quantity of water while pouring the concrete

casting. Three mix proportions were designed, and it's recommended that the reinforced concrete beams be cast. The optimal steel fibre content and dosage of microorganisms were found to be 0.8% and 2%, respectively. The optimum mixes performed better than the other concrete mixes, as presented in Table 6. Beyond the optimum mix, the bond behavior between aggregates and cement paste becomes inadequate, reducing strength.

Table 4. Mechanical properties of the SFRC at various ages

Mix ID	Mechanical properties at 28 days (MPa)									Increased strength (%)		
	CS			STS			FS			CS	STS	FS
	7	14	28	7	14	28	7	14	28	28	28	28
M40-PF0	30.53	42.16	46.78	3.08	4.28	4.68	3.92	5.42	5.98	-	-	-
M40-PF0.2	31.42	43.48	48.25	3.46	4.68	5.12	4.36	5.98	6.58	3.14	9.40	21.40
M40-PF0.4	33.08	45.98	51.06	3.62	5.12	5.64	4.98	6.87	7.62	9.15	20.51	40.59
M40-PF0.6	33.89	46.87	52.18	4.17	5.72	6.32	5.27	7.38	8.17	11.54	35.04	50.74
M40-PF0.8	35.52	49.43	54.87	4.53	6.28	6.89	5.86	8.02	8.96	17.29	47.22	65.31
M40-PF1.0	34.64	47.92	53.16	4.25	5.34	6.27	5.34	7.43	8.42	13.64	33.97	55.35

Table 5. Mechanical properties of the SFR bacterial concrete at various ages

Mix ID	Mechanical properties at 28 days (MPa)									Increased strength (%)		
	CS			STS			FS			CS	STS	FS
	7	14	28	7	14	28	7	14	28	28	28	28
M40-SF0.8	35.62	49.42	54.87	4.52	6.28	6.89	5.74	7.93	8.79	-	-	-
M40-SF0.8-B1	36.24	50.12	55.64	4.68	6.46	7.12	5.98	8.26	9.14	1.40	3.34	4.70
M40-SF0.8-B2	37.24	51.38	57.18	5.18	7.12	7.84	6.76	9.28	10.28	4.21	13.79	17.75
M40-SF0.8-B3	36.72	50.82	56.42	4.92	6.53	7.38	6.21	8.74	9.68	2.82	7.11	10.88

Table 6. Optimum steel fibre, microorganisms' content and CS of concrete at 28 days

Mix ID	Bacteria content (%)	Optimum steel fibre (%)	CS (MPa)
M40-SF0.8-B0	0	0.8	54.87
M40-SF0.8-B1	1	0.8	55.64
M40-SF0.8-B2	2	0.8	57.18
M40-SF0.8-B3	3	0.8	56.42

4. Experimental Study on RC Beams

4.1. Fabrication and Experimental Setup of the RC beams

In this study, RC beams were cast with a cross-section of 150 mm x 180 mm and a length of 1500 mm, and the fabrication of the RC beam is shown in (Fig. 7). The RC beam was designed according to IS 456 – 2000 [37]. Two 10 mm diameter and two 8 mm diameter deformed steel bars were provided for tension and compression reinforcement. Shear reinforcement was uniformly placed at 100 mm and 80 mm c/c throughout the length. Four RC beams were cast and tested under four-point loading, with various shear reinforcement spacing of 100 mm and 80 mm, respectively. Geometric details of the specimens are reported in Table 7. The RC beams were fabricated in two proportions: M40-SF0.8-B0 and M40-SF0.8-B2%. The reinforcement was cut to 1450 mm, and shear reinforcement was placed at 100 mm and 80 mm c/c.

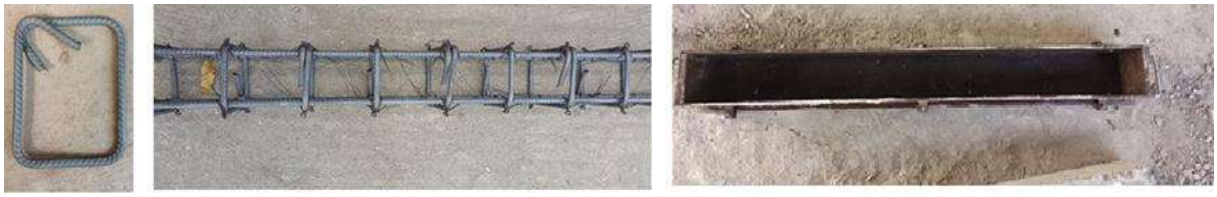

(a) (b)

(c) (d)

Fig. 7. Fabrication of the RC beams (a) Cross-section and longitudinal reinforcement details, (b) Steel mould, (c) Steel mould with reinforcement cage, and (d) Casting RC beams

The compression, tension, and shear reinforcement were bonded with steel wire. The steel mould for the RC beam is cleaned, and waste oil is applied to serve as a lubricant. Once the reinforcement steel cage is aligned correctly within the mould, machine-mixed concrete is poured into it. The concrete is thoroughly compacted using a vibrator machine to prevent the formation of honeycomb structures. After compaction, the concrete is levelled and left at room temperature for 24 hours. The following day, the steel mould is carefully removed from the RC beam without causing any damage. After a curing period of 28 days, the RC beams are removed from the curing tank, and their outer surfaces are cleaned. Additionally, the beams are white-washed and marked with a grid.

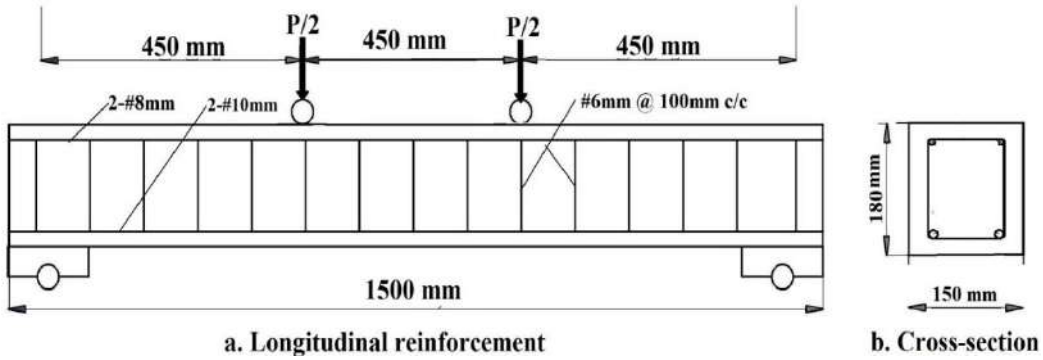

Fig. 8. Loading positions, cross-section and longitudinal reinforcement details of the RC beam

Each specimen is placed on a 50T capacity loading frame, with deflection meters positioned at marked locations. The graphical representation and experimental setup of the RC beam are shown in (Fig. 8). loading is gradually applied to the RC beams until they fail, and axial load and deflection are recorded at initial cracks, ultimate load, and failure load. The loading rate for all specimens is maintained at 0.5 mm/minute. This facilitates a more consistent stress distribution throughout the beam, which is essential for analyzing the material's flexural behavior. Four-point loading is commonly employed in flexural testing to accurately assess the beam's flexural strength and stiffness, as illustrated in (Fig. 9).

Fig. 9. Experimental setup of RC beam

Table 7. Geometric properties of the RC beams

Specimen ID	Details of Specimen (mm)			Reinforcement		Shear reinforcement
	B	D	L	Bottom	Top	
M40-SF0.8-B0	150	180	1500	2#10mm	2#8mm	#6mm @ 100mm c/c
M40-SF0.8-B0	150	180	1500	2#10mm	2#8mm	#6mm @ 80mm c/c
M40-SF0.8-B2	150	180	1500	2#10mm	2#8mm	#6mm @ 100mm c/c
M40-SF0.8-B2	150	180	1500	2#10mm	2#8mm	#6mm @ 80mm c/c

5. Analytical Study

5.1. Finite Element Model

The Finite Element Model (FEM) was developed using ANSYS software. The experimental test results were compared and examined against the analytical results. The 3D model was created, and the FEM analysis was conducted on the RC beam with various mesh sizes (fine, medium, and coarse). Based on the sensitivity analysis, the coarse mesh size yielded better results and saved time than the remaining mesh sizes. The finite element model helps predict experimental test results and correlates highly with experimental data. The 3D model of the RC structure developed in ANSYS software is shown in (Fig. 10). The meshing of the 3D model and the loading arrangement of the RC beam are illustrated in (Fig. 11 and 12).

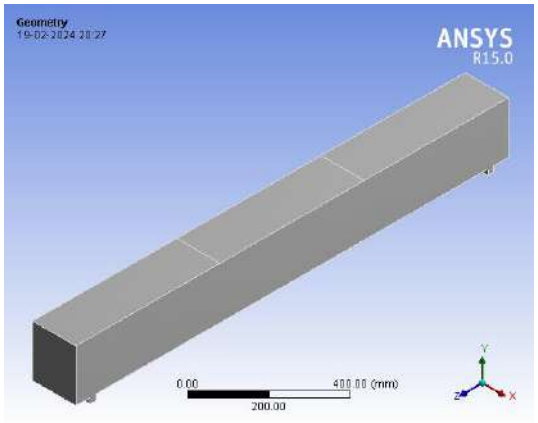

Fig. 10. D model of RC beam

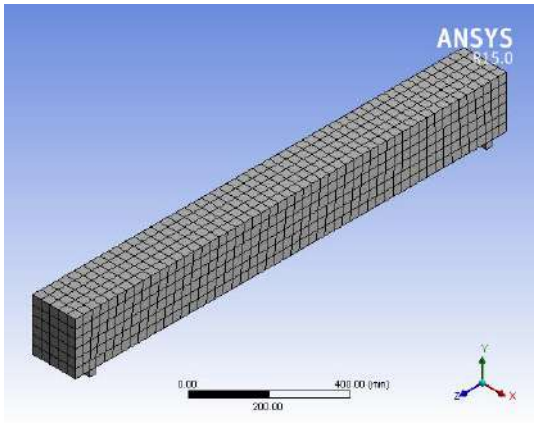

Fig. 11. Meshing of RC beam

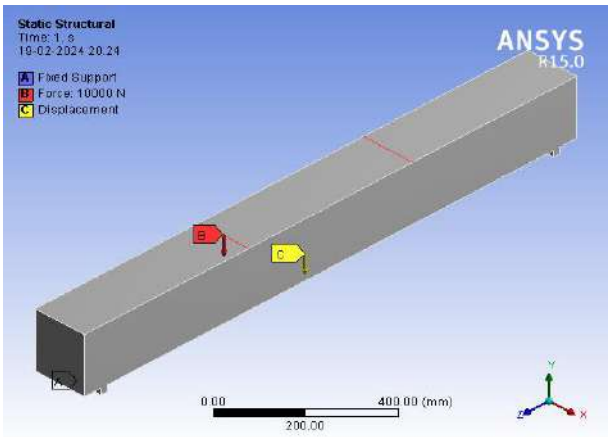

Fig. 12. Load and support arrangement of RC beam

5.2. Boundary Condition of RC beam

The boundary condition of the RC beam was considered as one end being roller support, and the other is supported for the analysis in ANSYS. The roller support restricts movement in the x and z directions while allowing movement in the y direction where the load is applied. Similarly, in the

simple support condition, the beam's y direction is also restrained to prevent the free rotation of the RC beam.

6. Results and Discussion

6.1. Steel Fibres and Microorganisms Influence in CS of Concrete

The CS of steel fibre-reinforced concrete was examined at seven, fourteen, and twenty-eight days, respectively, as depicted in (Fig. 13). The CS of the concrete is enhanced with the addition of SF by 3.14%, 9.15%, 11.54%, 17.29%, and 13.64% for M40-SF0.2, M40-SF0.4, M40-SF0.6, M40-SF0.8, and M40-SF1, compared to the conventional concrete mix M40-SF0. Based on the experimental study, the optimum SF content is 0.8%. Additionally, the CS of the concrete was studied with the optimum SF content of 0.8%. Furthermore, microorganisms (at concentrations of 0%, 1%, 2%, and 3%) were added to the optimum SF content of 0.8%, resulting in mixes such as M40-SF0.8-B1, M40-SF0.8-B2, and M40-SF0.8-B3.

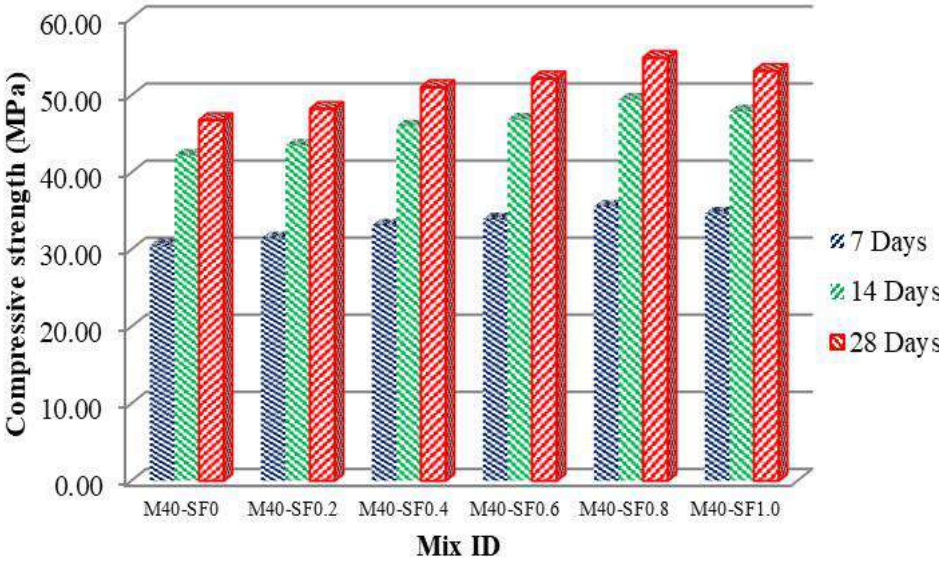

Fig. 13. Compressive strength of SFC at various ages

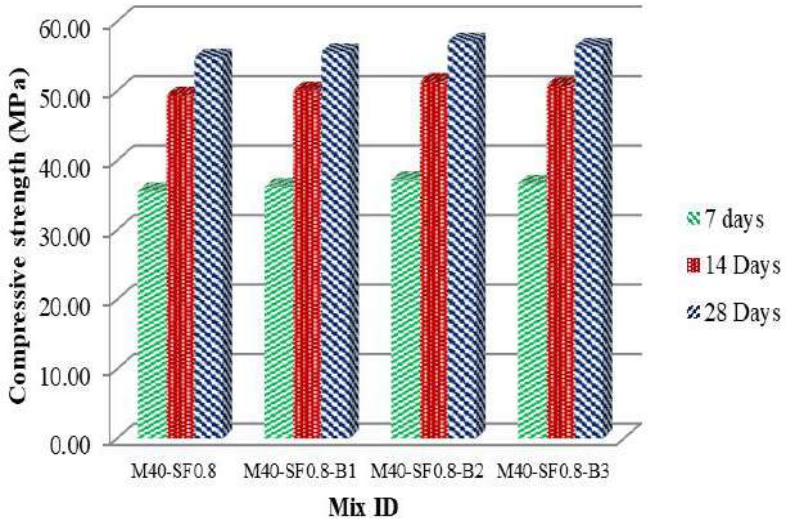

Fig. 14. CS of SFC with microorganisms at various ages

The strength properties of the concrete also increased by 1.40%, 4.21%, and 2.82% compared to the control mix M40-SF0.8-B0, as presented in (Fig. 14). The experimental study achieved the optimum strength properties with 17.29% enhancement for M40-SF0.8 and 4.21% enhancement for M40-SF0.8-B2. The CS of the SFRC was increased by with the addition of microorganism's

content by 2%. The microorganisms fill the existing voids, which is the reason the strength properties of the concrete have been increased.

6.2. Steel Fibres and Microorganisms Influence the STS Of Concrete

The strength properties of the concrete, precisely the split tensile strength, were evaluated using various steel fibre ranges (0%, 0.2%, 0.4%, 0.6%, 0.8%, and 1%) and microorganisms (0%, 1%, 2%, and 3%) at different ages 7, 14 &28 days, respectively. In the first portion of the study, the STS properties of the concrete increased by 9.40%, 20.51%, 35.04%, 47.22%, and 33.97% for mixes M40-SF0.2, M40-SF0.4, M40-SF0.6, M40-SF0.8, and M40-SF1, compared to the conventional concrete mix M40-SF0 as depicted in (Fig. 15). Adding steel fibre enhanced split tensile strength properties, with the optimum content identified as 0.8% steel fibre compared to the other mixtures. In the second part, microorganisms were incorporated at concentrations of 0%, 1%, 2%, and 3% into the optimal fibre content of 0.8%.

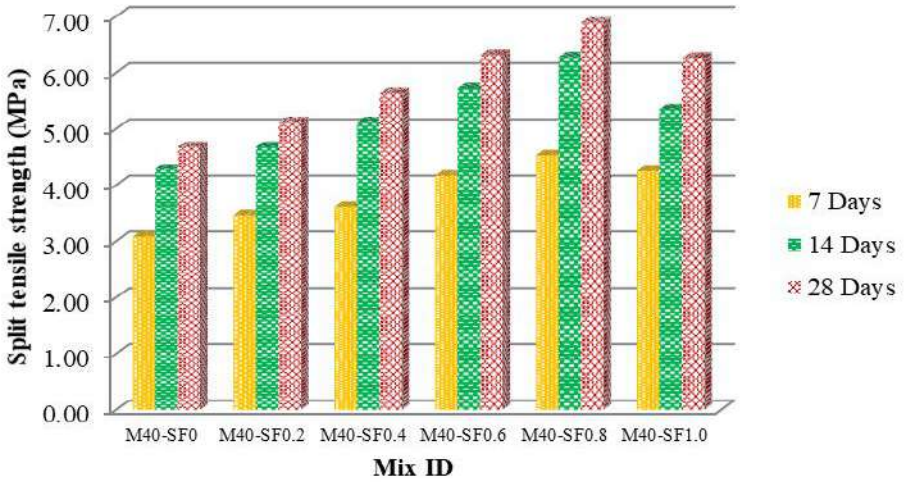

Fig. 15. Split tensile strength of steel fibre concrete at various ages

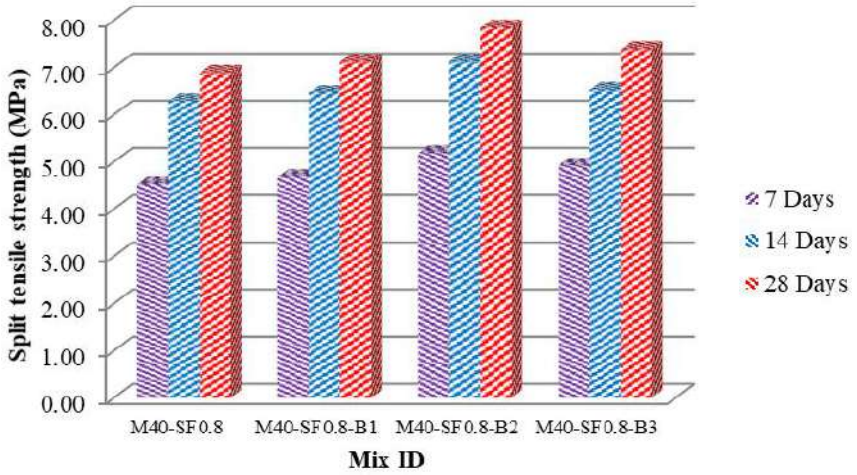

Fig. 16. STS of steel fibre concrete with microorganisms at various ages

The mechanical properties of concrete were enhanced by adding SF and microorganisms for M40-SF0.8-B1, M40-SF0.8-B2, and M40-SF0.8-B3. Notably, the strength properties of the concrete exhibited improvements of 3.34%, 13.79%, and 7.11% when compared to the control mix M40-SF0.8-B0, as illustrated in (Fig. 16). Based on the experimental study, the STS increased by adding 2% microorganisms' content to the optimum steel fibre content of 0.8%. It is clearly shown that the STS of concrete mix M40-SF0.8-B2 exceeds that of the M40-SF0.8 concrete mix. The 0.8% steel fibre and 2% microorganisms content improved the split tensile strength. The steel fibre interconnects with the cement paste and aggregates, while the microorganisms fill the existing voids [38]. Overall,

the mechanical properties of the split tensile strength were enhanced by using steel fibre and microorganisms.

6.3. Steel Fibres and Microorganisms Influence the FS of Concrete

Similarly, the FS of the concrete was determined using steel fibre and microorganisms at the ages of 7, 14 &28 days, respectively. (Fig. 17) depicts the effect of SFs on concrete's flexural behavior at those ages.

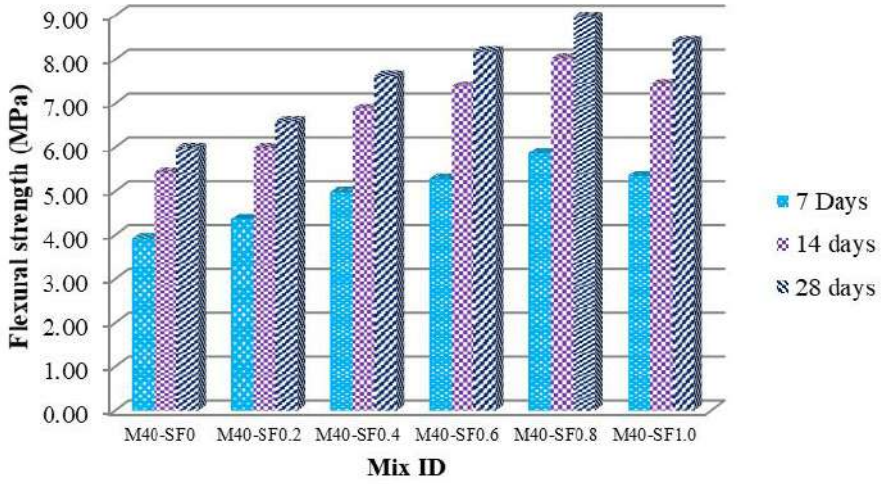

Fig. 17. Flexural strength of steel fibre concrete at various ages

The flexural strength increased by 21.40%, 40.59%, 50.74%, 65.31%, and 55.35%, with the addition of steel fibre in the range from 0.2% to 1%. The optimum flexural strength concrete mix was found to be M40-SF0.8. Additionally, the flexural strength increased when incorporating microorganisms (at 1%, 2%, and 3%). According to the experimental test results, the FS of the concrete improved by 4.70%, 17.70%, and 10.88% for M40-SF0.8-B1, M40-SF0.8-B2, and M40-SF0.8-B3, as shown in (Fig. 18). The experimental study observed that the FS of the concrete increased with the addition of 0.8% steel fibre and 2% microorganisms. The recommended combination for further investigation of RC beams is 0.8% fibre content and 2% microorganisms.

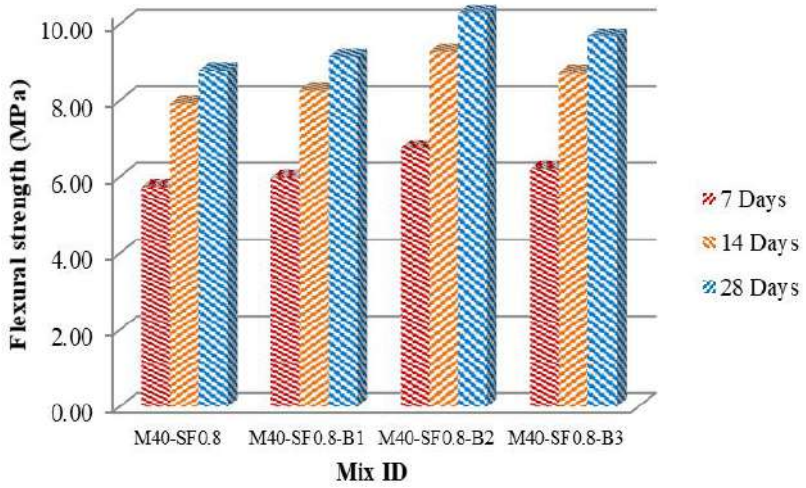

Fig. 18. FS of steel fibre concrete with microorganisms at various ages

6.4. Flexural Behavior of RC Beams

This study investigated the flexural behavior of RC beams by combining steel fibres and microorganisms. They cast and tested four RC beams after a 28-day curing period, varying the shear-reinforced spacings to 100 mm and 80 mm. Incorporating SF and microorganisms led to improved mechanical properties and enhanced flexural behavior in the RC beam. The study's main

objective was to investigate parameters such as axial load versus deflection, failure mode, peak ductility, stiffness, and energy absorption. In past studies, bacteria such as Bacillus Subtilis, Bacillus Sphaericus, and Sporosarcina Pasteurii have been frequently used for self-healing concrete. The current study also uses Bacillus Subtilis, aligning with established research. Compressive strength studies have shown varying levels of improvement, typically ranging from 5% to 15%. The previous study reported a 10% increase in compressive strength by incorporating Bacillus Subtilis [23]. Improvements in flexural strength have also been reported, ranging from 10% to 20%. Another study found a 12% increase in flexural strength with bacteria-induced self-healing [39]. The current study reports an enhancement in compressive strength by 4.20%, incorporating 0.8% steel fiber and 2% microorganisms. This improvement is slightly lower than some previous studies but still demonstrates a significant positive impact [40]. Additionally, the study found an increase in the flexural behavior of RC beams by 19.98% and 24.40% compared to conventional specimens. This is higher than the improvements reported in earlier studies, indicating a notable enhancement in flexural properties [41].

6.5. Axial Load-Deflection Responses of RC Beams

A total of four reinforced concrete beams with dimensions 150mm x 180mm x 1500mm (labelled M40-SF0.8-B0-S100, M40-SF0.8-B0-S80, M40-SF0.8-B1-S100 and M40-SF0.8-B1-S80) were cast and tested after a curing period of 28 days. Axial load versus deflection was recorded, including the initial crack load, ultimate load, and failure load for all reinforced concrete beams, as reported in Table 8. The flexural behavior of the reinforced concrete beams was studied under axial loading, gradually increasing the axial load until the specimen failed. The initial crack loads were 94 kN, 116 kN, 103 kN, and 126 kN. The ultimate loads were 187.32 kN, 224.75 kN, 206.17 kN, and 256.48 kN. The failure loads were 183 kN, 217 kN, 201 kN, and 252 kN for the M40-SF0.8-B0-S100, M40-SF0.8-B0-S80, M40-SF0.8-B1-S100, and M40-SF0.8-B1-S80 reinforced concrete beams, respectively. The flexural behavior of the reinforced concrete beam axial load increased by 19.98% when reducing the shear reinforcement spacing for M40-SF0.8-B0-S80 reinforced concrete specimens, compared to the M40-SF0.8-B0-S100 RC specimens. Similarly, the axial load's flexural behavior showed a 24.40% increase when reducing the shear reinforcement spacing for M40-SF0.8-B2-S80 RC specimens compared to the M40-SF0.8-B2-S100 RC specimens. Based on experimental observations, flexural behavior performance is enhanced by incorporating steel fibres and microorganisms into reinforced concrete beams. The axial load versus deflection response of the M40-SF0.8-B0-S100, M40-SF0.8-B0-S80, M40-SF0.8-B1-S100, and M40-SF0.8-B1-S80 reinforced concrete beams are shown in (Fig. 19).

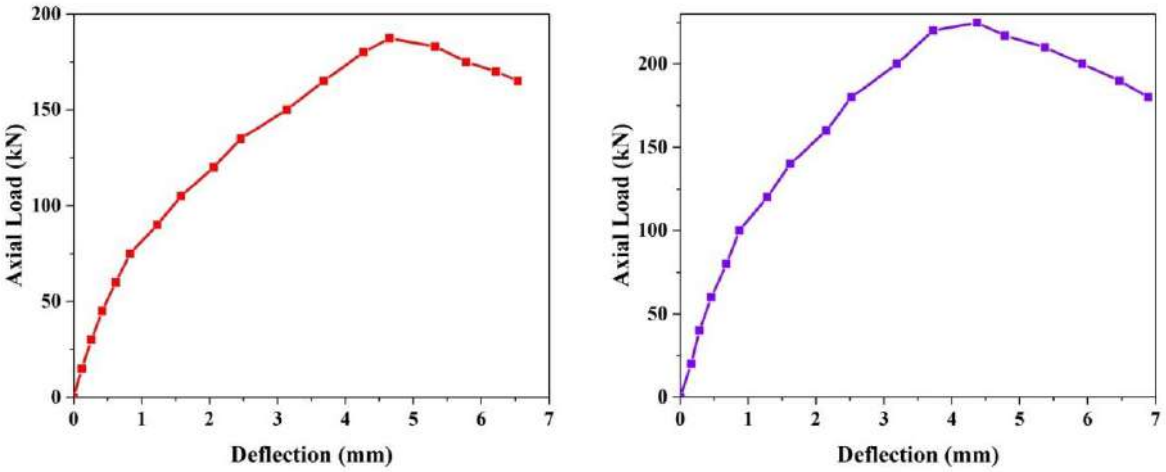

(a) (b)

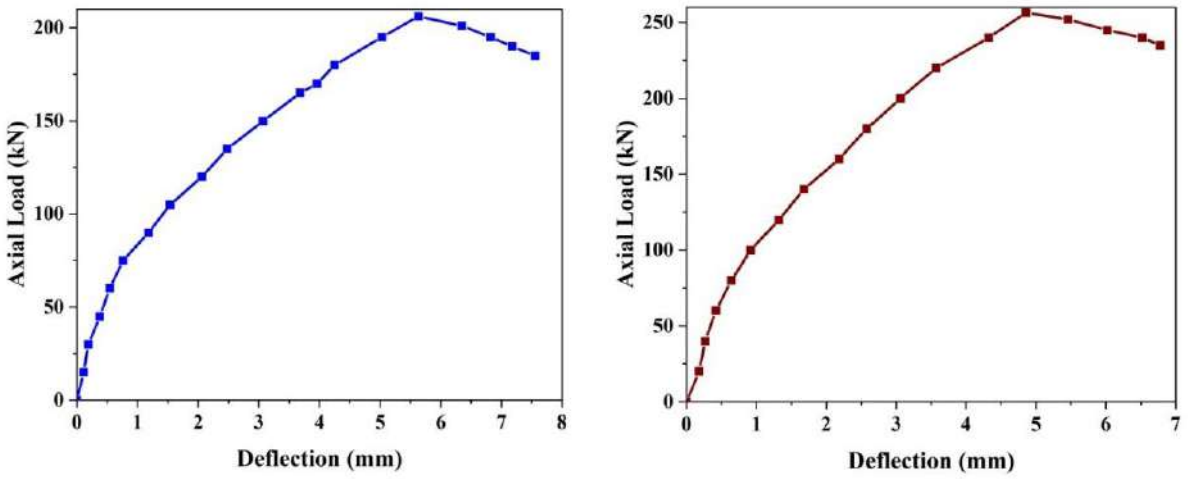

(c) (d)

Fig. 19. Axial load-deflection response from an experimental study (a) M40-SF0.8-B0-S100, (b) M40-SF0.8-B0-S80, (c) M40-SF0.8-B2-S100, and (d) M40-SF0.8-B2-S80

Table 8. Experimental results for RC beam with steel fibre and microorganisms

Specimen ID	Experimental load (kN)			Ultimate deflection (mm)
	Initial cracks	Ultimate	Failure	
M40-SF0.8-B0-S100	94	187.32	183	4.65
M40-SF0.8-B0-S80	116	224.75	217	4.37
M40-SF0.8-B2-S100	103	206.17	201	5.63
M40-SF0.8-B2-S80	128	256.48	252	4.86

6.6. Mode of Failure of the RC Beams

The flexural behaviour of the RC beams was tested, and all RC beams commonly exhibited flexural failure and fibre pull-out. Axial load was applied to the RC beams, forming initial cracks at loads of 94 kN, 116 kN, 103 kN, and 126 kN. The load was incrementally increased to the ultimate load, reaching values of 187.32 kN, 224.75 kN, 206.17 kN, and 256.48 kN. During this process, the cracks propagated throughout the specimens. Subsequently, the RC beams failed as further load was applied, with failure loads of 183 kN, 217 kN, 201 kN, and 252 kN. The ductility index increased when the shear reinforcement spacing was reduced from 100mm to 80mm by ductility factors of 3.52, 3.70, 3.43, and 3.80. Similarly, the stiffness also increased, with values of 40.28 kN/mm, 51.43 kN/mm, 36.62 kN/mm, and 52.77 kN/mm for the M40-SF0.8-B0-S100, M40-SF0.8-B0-S80, M40-SF0.8-B1-S100, and M40-SF0.8-B1-S80 RC beams, respectively is reported in Table 9. Adding steel fibres and microorganisms enhanced the FS of the RC beams. (Fig. 20) depicts the mode of failure of the RC beams. The mechanism of action for bacteria in self-healing concrete involves a fascinating process that helps repair cracks and enhance the longevity of concrete structures [42].

Table 9. Experimental results for RC beam with steel fibre and microorganisms

Specimen ID	Experimental test results				Ductility	Stiffness (kN/mm)	Failure mode
	Initial load(kN)	Deflection (mm)	Ultimate load(kN)	Deflection (mm)			
M40-SF0.8-B0-S100	94	1.32	187.32	4.65	3.52	40.28	FF+FP
M40-SF0.8-B0-S80	116	1.18	224.75	4.37	3.70	51.43	FF+FP
M40-SF0.8-B2-S100	103	1.64	206.17	5.63	3.43	36.62	FF+FP
M40-SF0.8-B2-S80	128	1.28	256.48	4.86	3.80	52.77	FF+FP

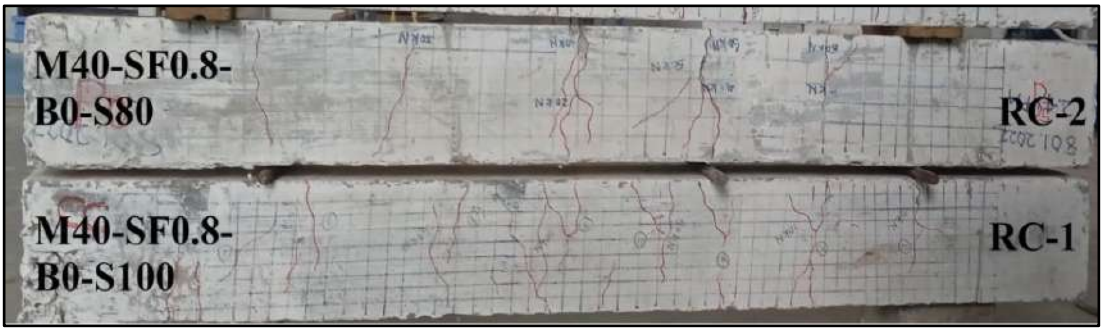

(a)

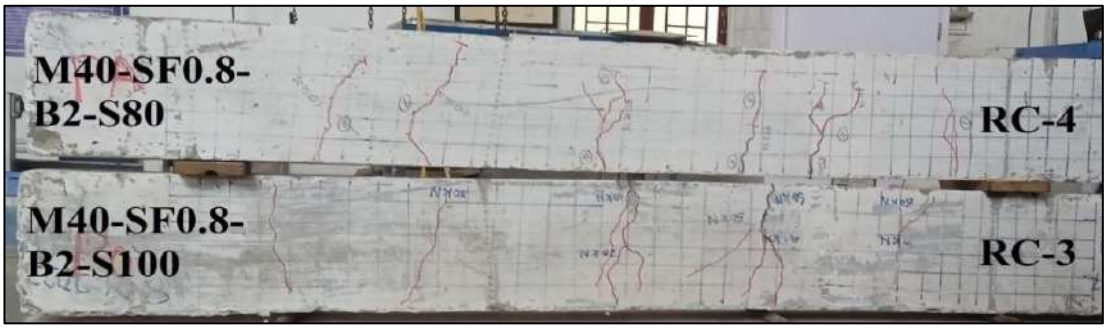

(b)

Fig. 20. Tested RC beams (a) M40-SF0.8-B0-S100 and M40-SF0.8-B0-S80 and (b) M40-SF0.8-B2-S100 and M40-SF0.8-B2-S80

6.7. Comparison of Experimental and Analytical Study

The experimental test results were compared to the analytical results regarding flexural behavior. (Fig. 21) illustrates the axial load-deflection curves for both analytical and experimental responses. Up to 70% of the load, the axial load versus deflection curve exhibits linear behavior [40]. After that, the RC beams reach to elastic to plastic behavior. The experimental ultimate load for the RC beams was 187.32 kN, 224.75 kN, 206 kN, and 256.54 kN, respectively. The corresponding experimental deflection values were 4.65 mm, 4.37 mm, 5.63 mm, and 4.68 mm. Similarly, the ultimate load and deflection from the analytical results were compared to the experimental results. The mean, standard deviations, and coefficient of variation were 0.99, 0.04, and 0.45 for the ultimate load and 0.99, 0.007, and 0.69 for the deflection. These results are reported in Table 10. The finite element analysis deflection of the RC beams (M40-SF0.8-B0-S100, M40-SF0.8-B0-S80, M40-SF0.8-B1-S100, and M40-SF0.8-B1-S80) is presented in (Fig. 22).

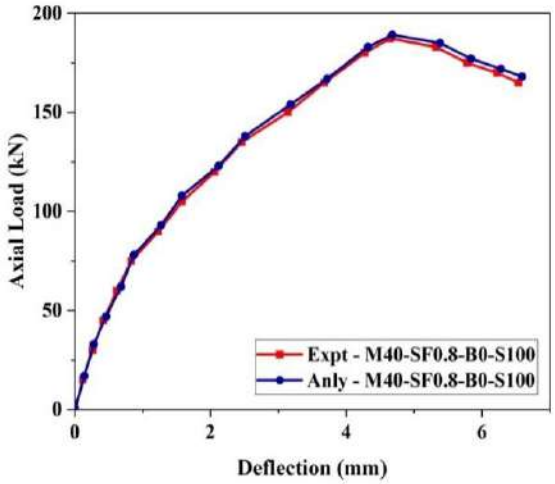

(a)

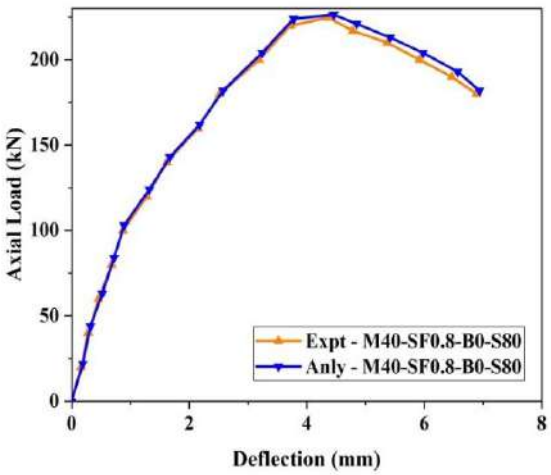

(b)

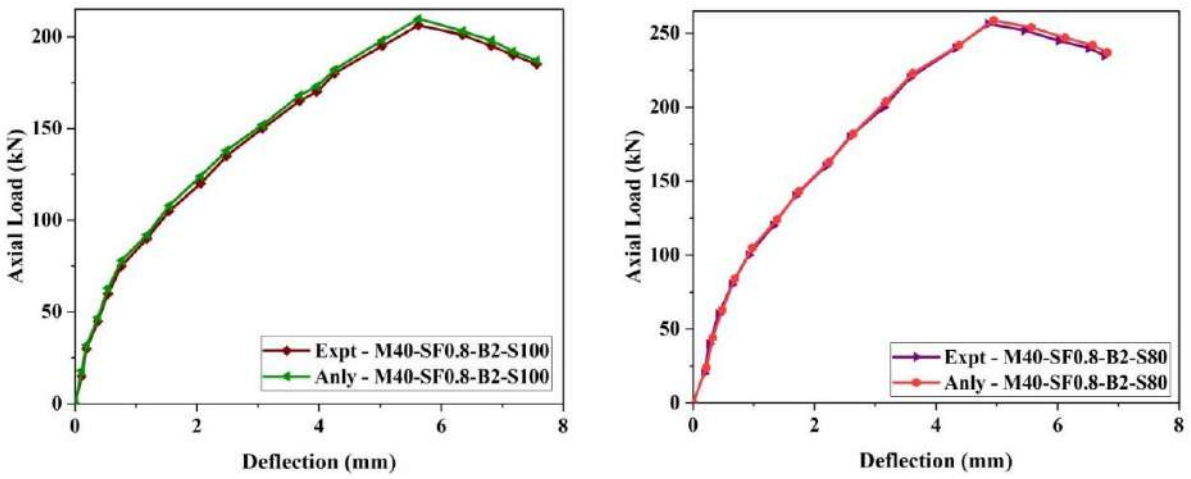

(c) (d)

Fig. 21. Comparison of the experimental and analytical axial load-deflection response of all RC beams (a) M40-SF0.8-B0-S100, (b) M40-SF0.8-B0-S80, (c) M40-SF0.8-B2-S100, and (d) M40-SF0.8-B2-S80

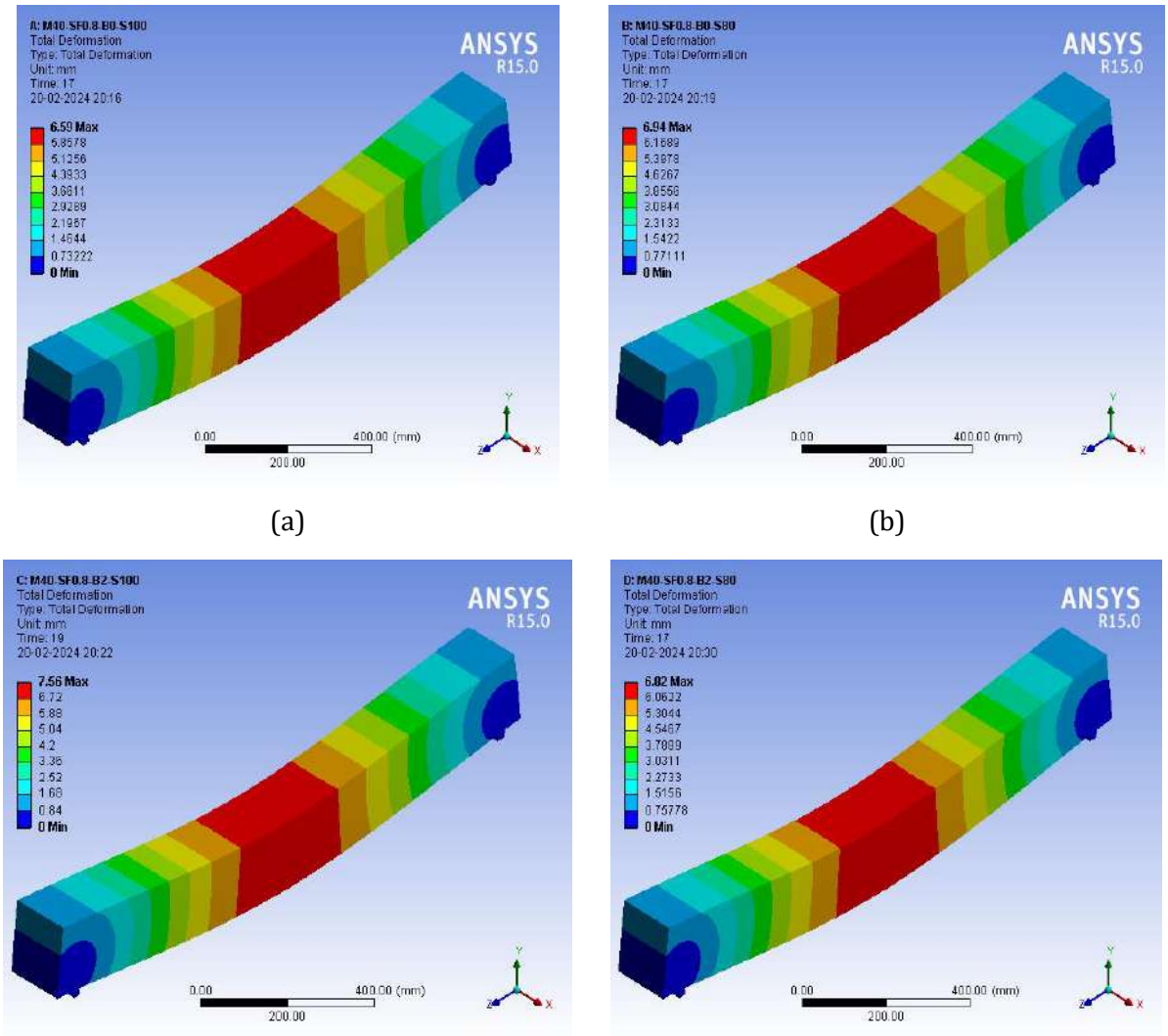

(a) (b)

(c) (d)

Fig. 22. Axial load-deflection response from the analytical study (a) M40-SF0.8-B0-S100, (b) M40-SF0.8-B0-S80, (c) M40-SF0.8-B2-S100, and (d) M40-SF0.8-B2-S80

Table 10. Comparative study between the experimental and analytical results

	Experimental values at the ultimate point		Analytical values at the ultimate point		P_{Expt} / P_{Anly}	
	Load (kN)	Deflection (mm)	Load (kN)	Deflection (mm)	Load	Deflection
M40-SF0.8-B0-S100	187.32	4.65	189.16	4.68	0.99	0.99
M40-SF0.8-B0-S80	224.75	4.37	226.38	4.46	0.99	0.98
M40-SF0.8-B2-S100	206.17	5.63	209.74	5.68	0.98	0.99
M40-SF0.8-B2-S80	256.54	4.86	258.67	4.95	0.99	0.98
		Mean			0.99	0.99
		SD			0.004	0.007
		CV (%)			0.45	0.69

7. Conclusions

This study introduces a novel approach to enhancing concrete structures mechanical properties and flexural behavior by incorporating self-healing properties using microorganisms, specifically Bacillus Subtilis bacteria and steel fibers. By exploring the synergistic effects of steel fibers and Bacillus Subtilis bacteria on the mechanical properties of self-healing concrete, this study contributes to the advancement of concrete technology and offers new possibilities for constructing more resilient and sustainable structures. The present study investigated the experimental and analytical study on the flexural behavior of RC beams with the addition of various percentages of steel fibre (0%, 0.2%, 0.4%, 0.6%, 0.8%, and 1%) and microorganisms (0%, 1%, 2% and 3%). The experimental and analytical test results led to the following conclusions:

The strength properties of steel fibre concrete (CS, STS and FS) were studied with percentages ranging from 0%, 0.2%, 0.4%, 0.6%, 0.8%, and 1% at ages seven, fourteen, and twenty-eight days. According to the experimental study, the optimum SF content was 0.8%. Compared to the conventional concrete mix, the CS, STS and FS improved by 17.29%, 47.22% and 65.21%, respectively. The optimum SF content of 0.8% (in the concrete mix) was investigated by adding microorganisms at 0%, 1%, 2% and 3%.

The mechanical properties of steel fibre concrete were enhanced by adding microorganisms. The optimum dosage of microorganisms was found to be 2%. Compared to the conventional concrete mix, the CS, STS, and FS increased by 4.21%, 13.79% and 17.75%, respectively. Based on the experimental test results, the optimum SF and microorganism content were 0.8% and 2%, respectively. This optimum mix was recommended for studying the flexural behavior of RC beams.

Four RC beams (namely, M40-SF0.8-B0-S100, M40-SF0.8-B0-S80, M40-SF0.8-B1-S100, and M40-SF0.8-B1-S80) were studied with various shear reinforcement spacing of 100mm and 80mm. The axial load increased by 19.98% for M40-SF0.8-B0-S100 and 24.40% for M40-SF0.8-B1-S100, compared to M40-SF0.8-B0-S80 and M40-SF0.8-B1-S80 RC beams.

The modes of failure commonly observed in all RC beams are flexural failure and fibre pull-out. Adding steel fibre and microorganisms enhances the strength properties related to the flexural behavior of the RC beams. The ductility index and stiffness of the RC beams increased by 3.70 and 51.43 kN/m with the addition of steel fibres and microorganisms. Furthermore, the ductility index and stiffness were enhanced by 3.80 and 52.77 kN/m when shear reinforcement spacing was reduced from 100 mm to 80 mm. The experimental and analytical axial load versus deflection curves exhibit similar behavior. When comparing the experimental and analytical load and deflection, the mean, standard deviations, and coefficient of variation were 0.99, 0.04, and 0.45 for the ultimate load and 0.99, 0.007, and 0.69 for the deflection.

Finite element models were developed for RC beams, and the analytical study results were compared to the experimental test results. The finite element model helps predict the experimental test results, and the analytical results were highly correlated with the empirical findings.

8. Recommendation for the Future Studies

The present research examined the mechanical properties of concrete and the flexural behavior of RC beams with the incorporation of steel fiber and bacteria. Future studies can focus on implementing the current project in the actual field and comparing the experimental results with field test outcomes.

Acknowledgement

The authors gratefully acknowledge the Kumaraguru College of Technology for providing all the required facilities to accomplish this study.

List of Abbreviations

ANN	- Artificial neural networks
CA	- Coarse aggregate
CE	- Cement
CS	- Compressive strength
CSF	- Closed steel fibres
CTM	- Compressive testing machine
CV	- Coefficient of variation
RC	- Reinforced concrete
SD	- Standard deviation
SP	- Superplasticizer
FA	- Fine aggregate
FEM	- Finite element model
FRC	- Fibre-reinforced concrete
FS	- Flexural strength
GF	- Steel fibre
IS	- Indian standard
OPC	- Ordinary Portland cement
RSF	- Recycled steel fibres
SFRC	- Steel fibre-reinforced concrete

References

[1] Ali. B, Raza. S. S, Hussain. I, Iqbal. M. Influence of different fibres on mechanical and durability performance of concrete with silica fume. Structural Concrete, 2021;22(1):318-333. https://doi.org/10.1002/suco.201900422

[2] Dvorkin. L, Konkol, J, Marchuk. V, Huts. A. Efficient, Fine-Grained Fly Ash Concrete Based on Metal and Basalt Fibers. Materials. 3023;16(11):3969. https://doi.org/10.3390/ma16113969

[3] Zhou. R. Z, Jin. Y. Study on mechanical properties of concrete with different steel fibre content. The International Journal of Multiphysics. 2021;15(1):87-99. https://doi.org/10.21152/1750-9548.15.1.87

[4] Varma. S. M. S, Raju. P. M. Mechanical properties of hybrid polypropylene-steel fibre-reinforced concrete composite. In IOP Conference Series: Materials Science and Engineering. 2021;1025(1):012022. https://doi.org/10.1088/1757-899X/1025/1/012022

[5] Adlparvar. M. R, Esmaeili. M, Taghavi Parsa. M. H. Strength properties of fibre reinforced concrete including steel fibres. World Journal of Engineering, 2024;21(1):194-202. https://doi.org/10.1108/WJE-12-2021-0680

[6] Gu. Z, Wang. J, Gao. D, Zhao. J. Effects of steel fibres on the flexural behavior of recycled concrete beam: Testing and analysis. Journal of Building Engineering. 2024:108718. https://doi.org/10.1016/j.jobe.2024.108718

[7] Anas. M, Khan. M, Bilal. H, Jadoon. S, Khan. M. N. Fiber reinforced concrete: a review. Engineering Proceedings. 2022;22(1):3. https://doi.org/10.3390/engproc2022022003

[8] Zhang. T, Pan. D. Mechanical properties of steel-polypropylene hybrid fibre reinforced concrete in building structure: steel-polypropylene hybrid fibre reinforced concrete in building structure. Stavební obzor-Civil Engineering Journal. 2021;30(2). https://doi.org/10.14311/CEJ.2021.02.0037

[9] Mansour. W, Fayed. S. Flexural rigidity and ductility of RC beams reinforced with steel and recycled plastic fibres. Steel and Composite Structures, An International Journal. 2021;41(3):317-334.

[10] Kaplan. G, Bayraktar. O. Y, Gholampour. A, Gencel. O, Koksal. F, Ozbakkaloglu. T. Mechanical and durability properties of steel fibre-reinforced concrete containing coarse recycled concrete aggregate. Structural Concrete. 2021;22(5):2791-2812. https://doi.org/10.1002/suco.202100028

[11] Rohini. I, Padmapriya. R. Properties of bacterial copper slag concrete. Buildings. 2023;13(2):290. https://doi.org/10.3390/buildings13020290

[12] Khan. F, Kachchhap. A, Kumar. P, Soan. K. Self-healing concrete or bio-concrete to repair cracks. Advances in Applied Mathematics Science. 2022;21:5397–5403.

[13] Shobana. K, Thenmozhi. R. Experimental investigation of self-repairing bio concrete in self- compacting concrete. Materials Express. 2022;12:705–712. https://doi.org/10.1166/mex.2022.2197

[14] Chetty. K, Garbe. U, Wang. Z, Zhang. S, McCarthy. T, Hai. F. Bioconcrete based on sulfate-reducing bacteria granules: cultivation, mechanical properties, and self-healing performance. Journal of Sustainable Cement-Based Materials. 2022;11:1–12. https://doi.org/10.1080/21650373.2022.2153389
[15] Bhina. M. R, Wibowo. A. H, Liu. K. Y, Khan. W, Sali. M. Microbes in bioconcrete technology: exploring the fundamentals and state-of-the-art findings for advancing civil engineering. Journal of the Chinese Institute of Engineers. 2023;46(7):726-736. https://doi.org/10.1080/02533839.2023.2238789
[16] Maurya. K. K, Rawat. A, Shanker. R. Health monitoring of bacterial concrete structure under dynamic loading using electro-mechanical impedance technique: a numerical approach. Environmental Science and Pollution Research. 2023;30(10):25382-25401. https://doi.org/10.1007/s11356-022-21949-6
[17] Sundravel. K. V, Jagatheeshwaran. S, Dineshkumar. P, Parthasarathi. C. Experimental investigation on strength and durability of self-healing concrete using bacteria. Materials Today: Proceedings. 2023. https://doi.org/10.1016/j.matpr.2023.04.652
[18] Maurya. K. K, Rawat. A, Shanker. R. Review on bacteria based cementitious matrix for sustainable building construction. In F-EIR Conference on Environment Concerns and its Remediation. 2021:1-17. https://doi.org/10.1007/978-3-030-96202-9_1
[19] Priyom. S. N, Islam. M. M, Shumi. W. The Utilization of Bacillus Subtilis Bacteria to Improve the Mechanical Properties of Concrete. In Journal of the Civil Engineering Forum. 2021;7(1):97-108.
[20] Pal. S, Mohanty. I, Panda. I. Self-healing conventional concrete using bacteria. In Recent Developments in Sustainable Infrastructure: Select Proceedings of ICRDSI 2019. 2021:441-451. https://doi.org/10.1007/978-981-15-4577-1_36
[21] Shukla. A, Gupta. N, Dixit. S, Ivanovich Vatin. N, Gupta. M, Saxena. K. K, Prakash. C. Effects of various pseudo-monas bacteria concentrations on the strength and durability characteristics of concrete. Buildings. 2022;12(7): 993. https://doi.org/10.3390/buildings12070993
[22] Chekravarty. D. S. V. S. M. R. K, Mallika. A, Sravana. P, Rao. S. Durability studies of concrete added with nanosilica. I-Manager's Journal on Structural Engineering. 2021;10(4).
[23] Devinta. A, Zulaika. E. Viability and Production Calcifying Bacterial Endospore on Sand-Cement Carrier. Journal Ilmiah Biologi Eksperimen Dan Keanekaragaman Hayati (J-BEKH). 2021;8(1):8-13.
[24] Zhang. L. V, Nehdi. M. L, Suleiman. A. R, Allaf. M. M, Gan. M, Marani. A., Tuya. M. Crack self-healing in bio-green concrete. Composites Part B: Engineering 2021;227:109397. https://doi.org/10.1016/j.compositesb.2021.109397
[25] Eidgahee. D. R, Soleymani. A, Hasani. H, Kontoni. D. P. N, Jahangir. H. Flexural capacity estimation of FRP reinforced T-shaped concrete beams via soft computing techniques. Computers and Concrete, 2023;32(1):1-13. https://doi.org/10.12989/cac.2023.32.1.001
[26] Rajesh. A, Sumathi. A. Strength and self-healing behavior of bacteria biocomposite concrete in soil exposure condition. In Structures. 2024;59:105673. https://doi.org/10.1016/j.istruc.2023.105673
[27] Soleymani. A, Jahangir. H, Rashidi. M, Mojtahedi. F. F, Bahrami. M, Javanmardi. A. Damage identification in reinforced concrete beams using wavelet transform of modal excitation responses. Buildings. 2023;13(8):1955. https://doi.org/10.3390/buildings13081955
[28] Huseien. G. F, Memon. R. P, Baghban. M. H, Faridmehr. I, Wong. L. S. Effective microorganism solution-imbued sustainable self-curing concrete: Evaluation of sorptivity, drying shrinkage and expansion. Case Studies in Construction Materials. 2024; 20: e03255. https://doi.org/10.1016/j.cscm.2024.e03255
[29] Eidgahee. D. R, Soleymani. A, Jahangir. H, Nikpay. M, Arora; H. C, Kumar, A. Estimating the load carrying capacity of reinforced concrete beam-column joints via soft computing techniques. In Artificial Intelligence Applications for Sustainable Construction. 2024:367-387. Woodhead Publishing. https://doi.org/10.1016/B978-0-443-13191-2.00014-6
[30] Shukla. A, Gupta. N, Singh. K. R, Bajaj., P. K. V, Ayalew. F. Performance evaluation of bio concrete by cluster and regression analysis for environment protection. Computer Intelligence and Neuroscience. 2022;4411876. https://doi.org/10.1155/2022/4411876
[31] Zhang. J, Deng. J, He. Y, Wu. J, Simões. M. F, Liu. B, Li. Y, Zhang. S, Antunes. A. A review of biomineralization in healing concrete: Mechanism, biodiversity, and application. Science of The Total Environment. 2024:170445. https://doi.org/10.1016/j.scitotenv.2024.170445
[32] IS 12269:1987. Specification for 53 grade ordinary Portland cement.
[33] IS 383:1970. Specification for Coarse and Fine Aggregates From Natural Sources for Concrete.
[34] IS 10262:2019. Recommended guidelines for concrete mix design.
[35] IS 516:1959. Method of Tests for Strength of Concrete.
[36] IS 5816:1999. Indian standard Splitting tensile strength of concrete- method of test.
[37] IS 456:2000. Plain Concrete and Reinforced.
[38] Rama Rao. P, Chaitanya. M. Experimental investigation on mechanical and durability properties of basalt fibre-reinforced concrete. In Recent Advancements in Civil Engineering: Select Proceedings of ACE 2020. 2022;172: 329-339. https://doi.org/10.1007/978-981-16-4396-5_30

[39] Pani. A. K, Sahoo. K. K. Study on mechanical properties of steel fibre concrete. In Recent Developments in Sustainable Infrastructure: Select Proceedings of ICRDSI 2019. 2021:499-505. https://doi.org/10.1007/978-981-15-4577-1_41
[40] Naser. N, Naser. F. H, Hameed Naser Almamoori. F. Hussien. L. M. Experimental and FEM Analyses of RC Beams with Radius Corner Arch at Bottom Tension Face. Journal of Rehabilitation in Civil Engineering. 2024;12(2): 26-40. https://doi.org/10.22075/JRCE.2023.30269.1828
[41] Sasikumar. P, Govindh. M. A, Subitha. T, Ananthakumar. A. A study on the flexural behaviour and self-healing of fibre reinforced bacterial concrete beams. Asian Journal of Civil Engineering. 2024;25(6):1-13. https://doi.org/10.1007/s42107-024-01201-x
[42] Subitha/ T, Manju/ R, Sasikumar. P. Sustainable and strength-enhanced concrete using microbial consortia. Revista de la Construction. 2024;23(2):403-12. https://doi.org/10.7764/RDLC.23.2.403

Blank Page

Research on Engineering Structures & Materials
www.jresm.org
Research Group

Research Article

Mechanical and fractography behavior of nano and micro boron carbide particles reinforced Al2014 alloy composites for aerospace applications

K C Vishwanath [1,a], Nagabhushana N [2,b], Bharath V [3,c], Virupaxi Auradi [4,d], Rajendra P [5,e], Madeva Nagaral [6,f], Manjunath Vatnalmath [4,g], Mohammed Kareemullah [7,h], Nagaraj Namdev [8,i], Abhishek Bhattacherjee [9,j], Balaraj V [10,k]

[1]*Dept. of Robotics and Automation, Rajarajeswari College of Eng., Bangalore, Karnataka, India*
[2]*Dept. of Mechanical Eng., New Horizon College of Engineering, Bangalore, Karnataka, India*
[3]*Dept. of Mechanical Eng., RNS Institute of Technology, Bengalru, Karnataka, India*
[4]*Dept. of Mechanical Eng., Siddaganga Institute of Technology, Tumakuru, Karnataka, India*
[5]*Dept. of Mechanical Eng. Ramaiah Institute of Technology, Bangalore, India*
[6]*Aircraft Research and Design Centre, Hindustan Aeronautics Limited, Bangalore, Karnataka, India*
[7]*Dept. of Mechanical Eng., Graphic Era (Deemed to be University), Dehradun, Uttarakhand & Centre of Research Impact & Outcome, Chitkara University, Rajpura, Punjab*
[8]*Dept. of Mechanical Eng., APS Polytechnic, Bangalore, Karnataka, India*
[9]*Dept. of Computer Science Eng., Lovely Professional University, Punjab, India*
[10]*Dept. of Mechanical Eng., Rao Bahadur Y. Mahabaleshwarappa Engineering College, Ballari, Karnataka, India*

Article Info

Article History:

Received 29 Dec 2024
Accepted 05 May 2025

Keywords:

Al2014 alloy;
Nano and micro B4C;
Microstructure;
Density;
Mechanical behavior;
Tensile fractography

Abstract

Nano- and micro particle-reinforced aluminum matrix composites are promising materials for the aerospace and automotive industries. These composites exhibit high strength and specific modulus with low density. In this study, the authors looked into how adding boron carbide (B4C) in nano and micron sizes altered the mechanical properties of Al2014 alloy composites. Using a novel two-stage casting method, composites of Al2014 alloy were synthesized with 3 and 6 wt.% of B4C, respectively, using particles with sizes of 200 nm and 25 microns. Microstructural analysis using SEM and EDS was performed on Al2014 alloy with nano- and micron-sized B4C composites. Additionally, studies of density, mechanical properties, and fractography were conducted to understand the impact of particle size on the behavior of the Al2014 alloy. Elemental presence was verified by EDS spectra, and microstructural analysis of the Al2014 alloy showed a regular distribution of particles. A minor reduction in elongation occurred, accompanied by enhancements in all other mechanical parameters with the addition of nano- and micron-sized B4C. Moreover, in comparison to micron-sized particle-reinforced composites, the Al2014 alloy containing 3 and 6 wt.% of 200 nm B4C exhibited markedly superior hardness, ultimate strength, yield strength, and compressive strength.

© 2025 MIM Research Group. All rights reserved.

*Corresponding author: vsauradi@gmail.com
[a]orcid.org/0000-0003-0191-7403 ; [b]orcid.org/0000-0002-1375-9791; [c]orcid.org/0000-0001-6765-4728; [d]orcid.org/0000-0001-6549-6340; [e]orcid-org/0000-0001-9054-0972; [f]orcid.org/0000-0002-8248-7603; [g]orcid.org/0000-0003-3138-9453; [h]orcid.org/0000-0001-8914-3603; [i]orcid.org/0000-0003-4097-9631; [j]orcid.org/0000-0002-3494-0880; [k]orcid.org/0009-0001-9094-3410
DOI: http://dx.doi.org/10.17515/resm2025-601me1229rs

1. Introduction

During For aircraft, automotive, civil development, and current gadget applications, high-quality, rigid materials are needed [1, 2]. This enabled composite material enhancement. Composite materials are macroscopic combinations of two or more materials having a comprehensible interface [3-5]. Composites are employed for many uses due to their mechanical, thermal, tribological, and other properties [5-8]. Modern materials seek towards property parity for a specific application. It is proposed that aluminum metal matrix composites (AMCs) replace monolithic general materials in a variety of applications [9, 10], including ferrous and nonferrous alloys and titanium (Ti) alloys. When designing systems for widespread implementation, AMCs are utilized as alternatives to conventional materials; therefore, the entire system must be updated in order to achieve weight and volume reductions [11]. Particle-reinforced aluminum matrix composites (PAMCs) incorporate ceramics in the form of oxides, carbides, or borides, including Al_2O_3, TiB_2, TiO_2, SiC, TiC, and B_4C, among others [12-15]. When compared to the unenhanced matrix, particle-reinforced metal composites demonstrate enhanced performance in terms of wear resistance, structural efficiency, and regulation of physical parameters including density and coefficient of thermal extension (CTE). These improvements ultimately lead to more effective implementation of design concepts [16]. PAMCs are attractive due to the aforementioned characteristics and the inexpensiveness of fortifications. In addition, extensive interfacial reactions, microstructural heterogeneity, fiber-to-fibre contact, and fibre degradation that are typical of MMCs can be circumvented. When comparing PAMCs to un-strengthened materials, isotropic properties such as increased strength and rigidity are observed. Al2014 is an alloy of moderate strength and low density. The alloy is fortified with B_4C particles measuring nanometers and micrometers in size in order to augment its oxidizing traits.

The specifications of MMC components are critical for their effective production, functionality, and characteristics. Considerable attention is devoted to the structure and behavior of the interface region in the fundamental study of MMCs. Numerous investigations employed powder metallurgy (PM), liquid state [17, 18], and semisolid state methodologies to fabricate a variety of Al alloy composites through the incorporation of SiC, Al_2O_3, B_4C, and graphite particles [19, 20]. Spray co-deposition, stir casting, squeeze casting, and liquid metal infiltration are a few of the innovative fabrication techniques that were utilized to create MMC materials [21, 22]. Stir casting, alternatively referred to as the vortex technique, is the most straightforward and economical among these methods due to its capacity to manufacture components with a high degree of flexibility and near-net shape at a minimal expense.

Moreover, the reinforcement's dimensions and configuration significantly impact the enhancement of the characteristics exhibited by metal matrix composites. Furthermore, ancillary operations such as rolling, forming, and extrusion contribute to the enhancement of the grain through refinement. Despite the fact that numerous Al alloys have been utilized as matrix ingredients, the literature review indicates that aluminum alloys continue to be the preferred option due to the aforementioned factors. Fork hinges, bulkheads, wing root connections, and mounting brackets are a few of the numerous aerospace applications for Al2014 alloy. The incorporation of B_4C particles at the nano-scale and micro-scale into Al2014 alloy can significantly enhance its strength, a critical attribute in aerospace applications where weight is invariably restrictive. In numerous applications, the condensed cross-sectional area of these high-tech metal composites provides an alternative material option. By decreasing the cross-sectional area of the component, its weight can be decreased, leading to improved efficiency [23].

Al-boron carbide composites play a significant role in advanced industrial applications where the demand for lightweight materials is increasing. Based on the aforementioned discoveries, Al2014 alloys containing B_4C composites measuring 200 nanometers and 25 microns in size were fabricated at weight percentages of variable 3 and 6 wt.%. Hardness, ultimate yield, ductility, and compressive strengths of Al2014 alloy were compared to those of nano and micro composite materials. In the present work, an attempt has been made to develop 3 and 6 wt.% of nano and micro boron carbide particles reinforced Al2014 alloy composites. To overcome the challenges about wettability and having proper distribution of nano and micro particles during development

of metal composites using metal and ceramic reinforcements, a novel two stage stir casting method was adopted in the present study.

2. Experimental Details

2.1 Matrix and Reinforcement Materials

The stir casting method was used to create nano- and micro-metal composites containing 3 and 6 weight percent of B_4C particles, respectively. As can be seen in Fig. 1 (a-b), an Al2014 alloy was used as the main material, and B_4C particles in two different sizes (200 nm and 25 m) were added as reinforcements. The elements and proportions that make up Al2014 are listed in Table 1.

Table 1. Chemistry of Al2014 alloy by weight %

Zn	Mg	Si	Fe	Cu	Ti	Mn	Cr	Al
0.19	0.64	0.72	0.20	4.50	0.06	0.83	0.01	Balance

The synthesis of Al2014 alloys containing B_4C composites containing 3% by weight of 200 nanometer particles was accomplished via liquid metallurgy. For liquefaction, a specific quantity of Al2014 compound ingots is inserted in the furnace. Aluminum alloys have a melting point of 660 °C. The temperature at which the substance liquefied was raised to 750 degrees Celsius. The liquid is subsequently degassed using solid hexachloroethane (C_2Cl_6) [24] for three minutes. In order to generate a vortex, the liquid metal is mixed using a Zr-coated impeller made of tempered steel. At 300 revolutions per minute, the impeller will be plunged to a depth of sixty percent of the liquid metal's height as seen from the exterior of the liquefy.

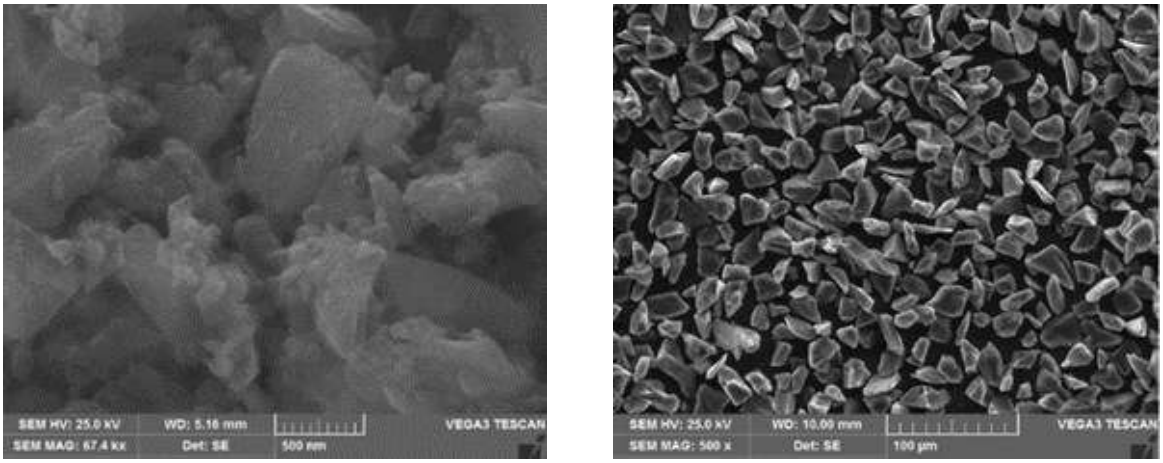

(a) (b)

Fig. 1. SEM micro-photographs of (a) 200 nano-meter (b) 25-micron sized B_4C particles

Additionally, 3% by weight of B_4C particulates were heated to 500°C in a heater prior to introduction into the vortex. Until the interface communications between the support particles and the network reach a state of equilibrium, stirring will continue. Subsequently, the Al2014 - 3 weight percent B_4C composite is shaped into a durable cast iron object measuring 120 mm in length and 15 mm in diameter. In a comparable fashion, composites were produced that were reinforced with B_4C particles, including nanocomposite at 6% by weight and 25 micron-sized composites at 3% and 6% by weight. Furthermore, based on the microstructural analysis, mechanical properties were assessed in accordance with ASTM standards. In the present research composites were produced by a novel two stage casting method, in this process the particles are included in the molten metal two times rather than including at a time. This helps in improving the wettability between the matrix and particles by avoiding agglomeration.

The cast specimen is subjected to microstructural analysis using a TESCAN VEGA 3 LMU instrument (Czech Republic) to determine the uniform distribution of reinforcing particles within the Al2014

alloy. The structures of Al2014 alloy and Al2014-reinforced composites containing 3% and 6% B_4C by weight are visualized via micrographs. The microstructure specimen has the following dimensions: 15 mm in diameter and 5 mm in height. Specimen surface polishing is performed with grain papers of 240, 600, and 800. Distilled water is used to remove any residual dirt or contaminants from the samples following the polishing process. Keller's reagent [25] is used to etch the specimens, imparting a unique and discernible surface.

Fig. 2. Al-Boron Carbide composites

Fig. 3. Tensile test specimen

The densities of Al2014 alloy and B_4C composite were measured. Density estimations were calculated using the conventional weight process and the law of mixture and then compared to experimental densities. To perform the hardness test, the specimen must be machined in compliance with ASTM standard E10 [26]. A Brinell hardness tester is used to assess the material's hardness (Krystal Industries, Ichalkaranji). After polishing, the specimen's surface is as good as new. A 5 mm ball indenter loaded with 250 kg creates a depression.

Tensile specimens assessed according to ASTM standard E8 [27, 28] evaluate Al2014 alloy and Al2014 with varied nano and micro B_4C composite percentages. Tensile strength, Al2014 alloy-reinforced composite behavior under unidirectional tension, and uniform distribution were assessed using an Instron computer-measured tensile machine. Total length is 104 mm, gauge length is 45 mm, and gauge diameter is 9 mm. Tensile testing evaluates composites and cast alloys under stress. The standard compression strength test is ASTM E9 [29]. Figure 3 shows the tensile specimen.

3. Results and Discussion

3.1 Microstructural Characterization

Figure 4 (a) shows the as-cast Al2014 alloy microstructure without B_4C particles. Scanning Electron Microscope (SEM) images 4b and 4c shows Al2014 alloys with 6% 200 nm B_4C and 6% 25-micron B_4C particles reinforced composites. The grain boundaries in Al2014 are clean and easily visible. If the micrograph shows a smooth, pore-free surface, casting is a suitable method for producing composites. These images show a clear and consistent dispersal of particles. The micrographs all show that the B_4C particles are firmly adhered to the Al2014 alloy. The enhanced properties of composites made from the Al2014 alloy benefit from this strong bonding. The distribution of particles plays an important role on the properties metal composites.

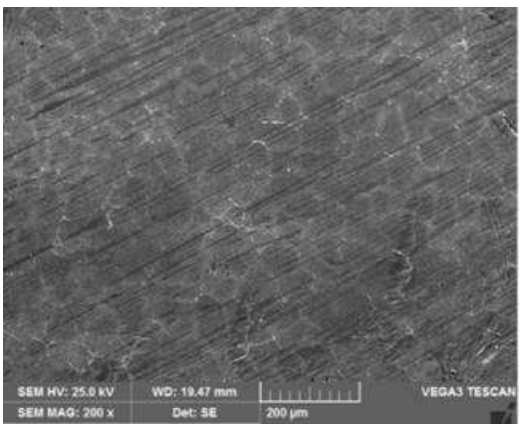

(a)

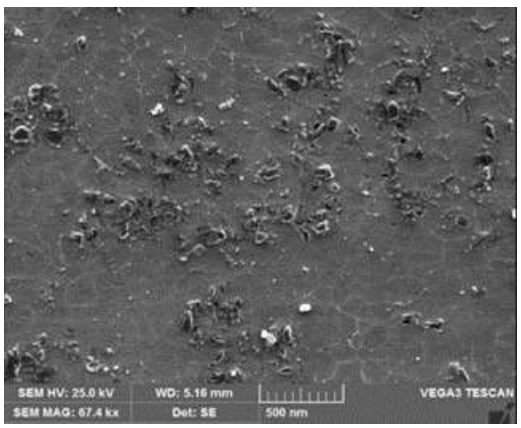

(b)

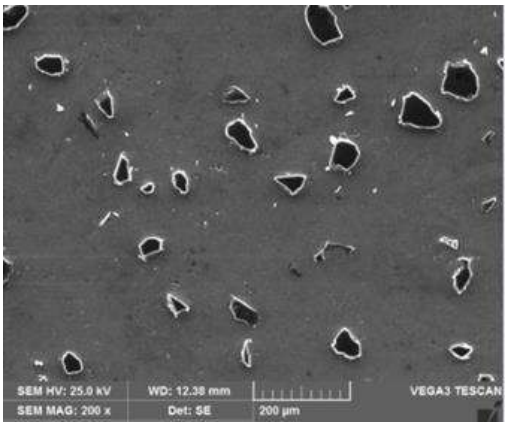

(c)

Fig. 4. (a-c) SEM of (a) Al2014 metal (b) Al2014-6 wt.% of 200 nm B_4C (c) Al2014-6 wt.% of 25 micron B_4C composites

The distribution helps in load transfer from the matrix to the particles, thus particles act as a barrier for the material deformation and reduces the strain development. Fig. 5 shows energy dispersal spectra for pure Al2014 and Al2014 doped with 6 wt. % 200 nm B_4C. (a, b). Fig. 5 (a) shows the principal Al and Cu alloying elements in aluminum 2XXX series alloys. In Fig. 5 (b), boron (B) and carbon (C) atoms appear alongside the Al peaks, showing B_4C in the produced Al2014 alloy with B_4C composites.

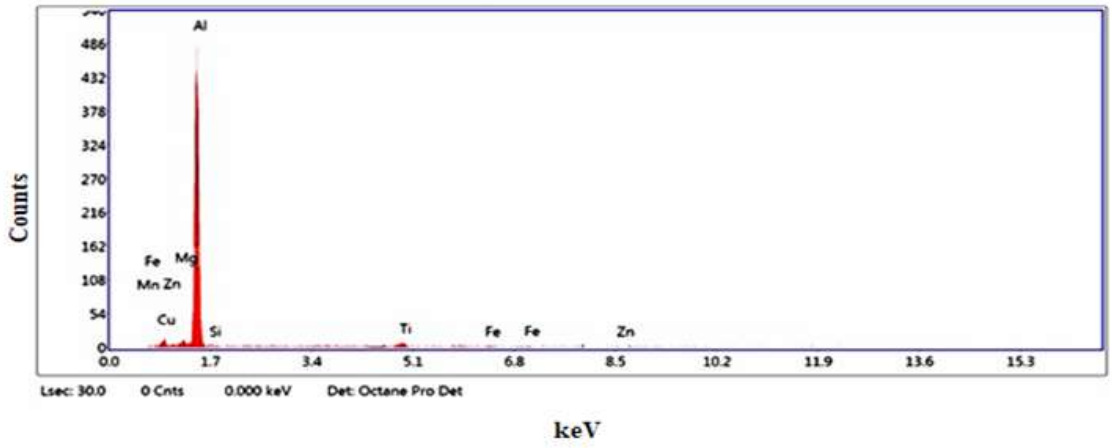

(a)

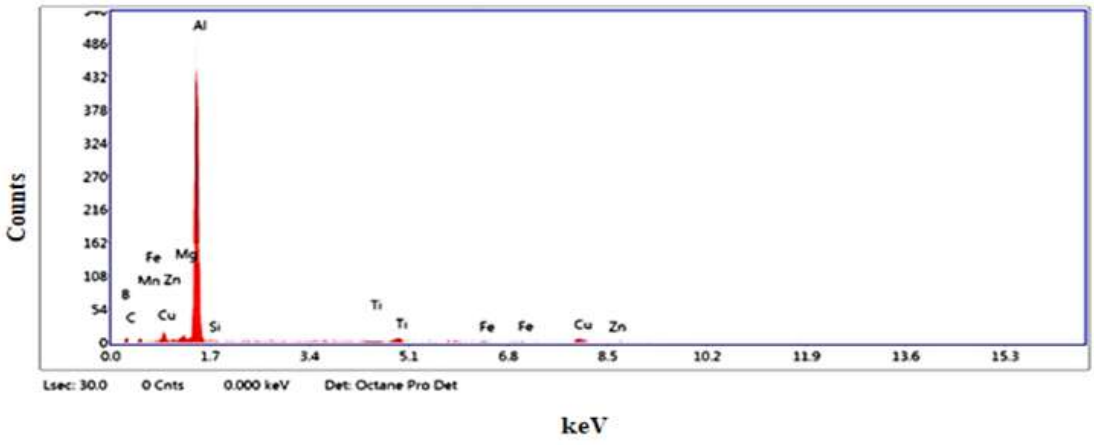

(b)

Fig. 5. (a-b) EDS of (a) Al2014 (b) Al2014-6 wt. % of 200 nm B_4C composite

3.2 Density Measurements

Fig. 6 compares predicted and experimental densities of Al2014 and Al2014 with 3–6% 200 nanometer and 25-micron B_4C composites. Figure 6 illustrates that as weight percentages increase and boron carbide particle sizes decrease, the curve for both theoretical and experimental density of the composites decreases linearly. B_4C particles are lighter than Al2014 alloy, reducing composite density. In contemporary investigations, particle size decreases increase densities, which are closer to theoretical values. This may indicate good composite castings. Al2014 and Al22014 with 6% by weight of 200 nm and 25-micron B_4C composites have experimental densities of 2.692 and 2.682 g/cm^3, respectively.

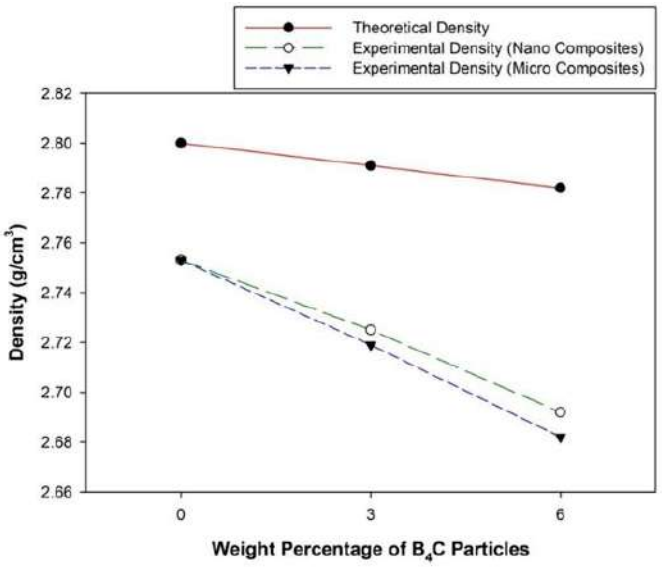

Fig. 6. Comparison of densities of Al2014 alloy with nano and micro B_4C composites

3.3 Hardness Measurements

In this study, Brinell hardness of Al2014 with micro and nano B_4C at 3 and 6 wt.% were studied. Each sample has three trials, and Fig. 7 shows the average values. Fig. 7 shows that composite hardness increases linearly with B4C concentration. BHN is 63.89 for a conventional Al2014 alloy, but 85.62 and 81.49 for alloys with 6 wt. % 200 nm and 25-micron B4C reinforced composites.

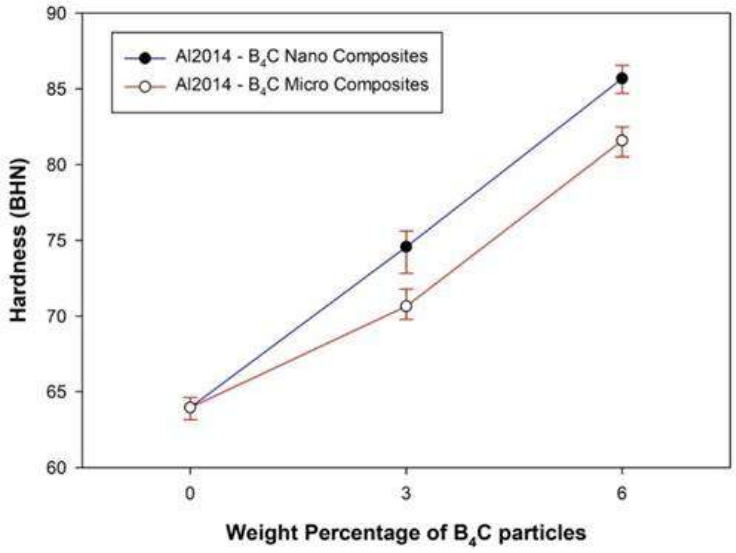

Fig. 7. Comparison of hardness of Al2014 alloy with nano and micro B_4C composites

Hardness of composites increases by 34% and 27.5% at 200 nm and 25 µm, respectively. As B_4C composites shrink, hardness increases, with the Al2014 alloy with 6% 200 nm composites improving the most. B_4C makes Al2014 matrix harder. Strengthening particles distribute alumina particles throughout the matrix, making it stronger and stiff. Milling down the particle size increases the reinforced composite's hardness (Fig. 7). Many factors contribute to this toughness. Most notably, 200 nm particles have a greater interface than 25-micron reinforced particles, increasing toughness. Smaller particles have a higher surface area than 25-micron particles in a composite. There are different perspectives on this situation. Smaller particles reinforced composites interact better than 25-micron ones. Compared to bigger particles, smaller particles provide more surface area in the composite they reinforce.

3.4 Tensile Properties

Tensile tests on the base Al2014 alloy and Al2014 reinforced with B_4C composites of 3 and 6 weight percent, respectively, with 200 nm and 25-micron B_4C particles, assess UTS, YS, and elongation as a percentage. Fig. 8 indicates that Al2014 alloy composite UTS increases linearly with B_4C content by decreasing particle sizes. The graph clearly indicates that hard B_4C particles reinforce the Al2014 matrix, increasing UTS. The UTS for pure Al2014 alloy is 205.97 MPa, however with 6 wt. % of 200 nm and 25-micron B4C reinforced composites, it rises to 267.65 and 258.33 MPa. The UTS of composites improved by 200 nm nano composites is 29.94%, whereas 25 µm improves it by 25.42%. UTS are maximum in Al2014 alloy doped with 6% 200 nm B_4C composites. Reinforcing particles boost a base alloy's tensile strength, making it more stress-resistant. Since B_4C particles are stiffer than Al2014 matrix, they first experience a lot of stress. The reinforcement's geometric limitations improve composite work hardening when B_4C particles are added to the matrix alloy [30, 31]. Orwan effect, where dislocations interact with non-shear-able B_4C, increases B_4C reinforced composite strength. As revealed by hardness data, particle addition gradually strengthens, therefore expected tensile strength increases should be represented as weight percentages [32].

Fig. 9 shows how increasing the weight percent of B_4C and decreasing the particle sizes leads to a linear increase in the YS of the Al2014 alloy composites. The graph shows that YS is enhanced in the Al2014 matrix following reinforcement with hard B_4C particles. A standard Al2014 alloy has a YS of 167.93 MPa, while the same alloy with 6 wt.% of 200 nm and 25-micron sized B_4C reinforced composites has YS values of 227.71 MPa and 219.10 MPa. Composites with particles of 200 nm and 25 µm show a 35.73 percent and 30.47 percent increase in yield strength, respectively. Al2014 alloy containing 6 wt. % of 200 nm sized B_4C composites shows the highest YS.

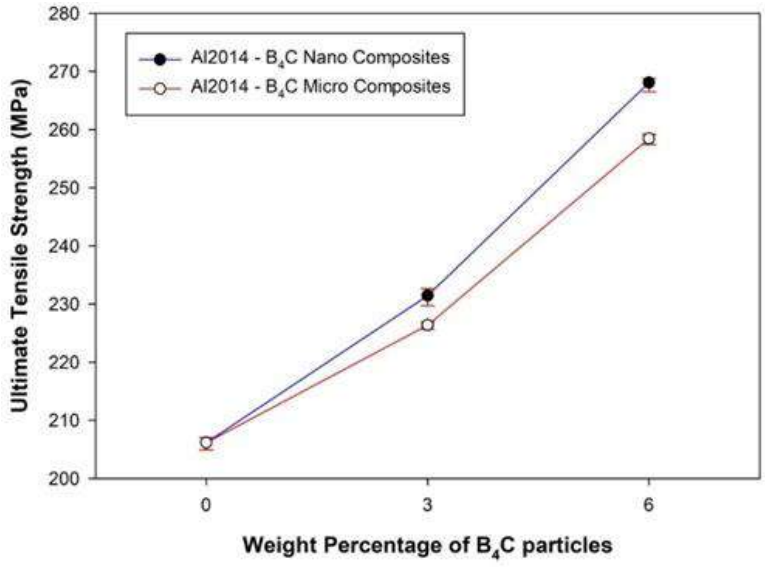

Fig. 8. Al2014 alloy ultimate strength vs nano and micro B_4C composites

Figures 8 and 9 illustrate the ultimate tensile strength (UTS) and yield strength (YS) of composites containing 3 and 6 wt.% B_4C, as well as the influence of particle size on these properties. Figures 8 and 9 illustrate that an increase in B_4C weight percentage results in a reduction of composite particle size, while enhancing ultimate tensile strength (UTS) and yield strength (YS). Composites with diverse compositions and 25 µm variable particles demonstrated that the composite containing Al2014 with 6 wt.% B_4C particles of 200 nanometer size had the highest tensile strength. A molecular-level elucidation of the matrix and the robust cohesion of particles. It seems that minuscule particles are closely associated with the matrix. Fig. 10 shows that composites with more B_4C by weight had better elongation throughout particle sizes. The graph demonstrates that the composite's elongation falls linearly as B_4C weight increases compared to the cast Al2014 matrix. The inclusion of hard particles in the soft matrix reduces the ductility and makes the materials as brittle. This brittle behavior of materials is not good for industrial applications, however with increased strength and ductility up to 9% are suitable for industrial applications.

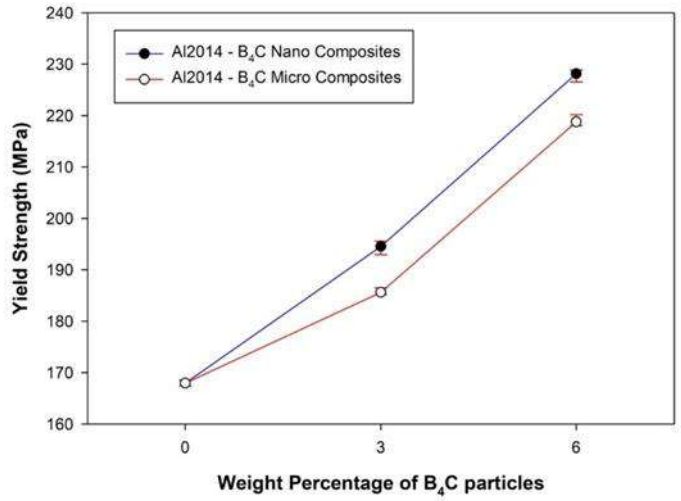

Fig.9. Al2014 alloy yield strength vs. nano and micro B_4C composites

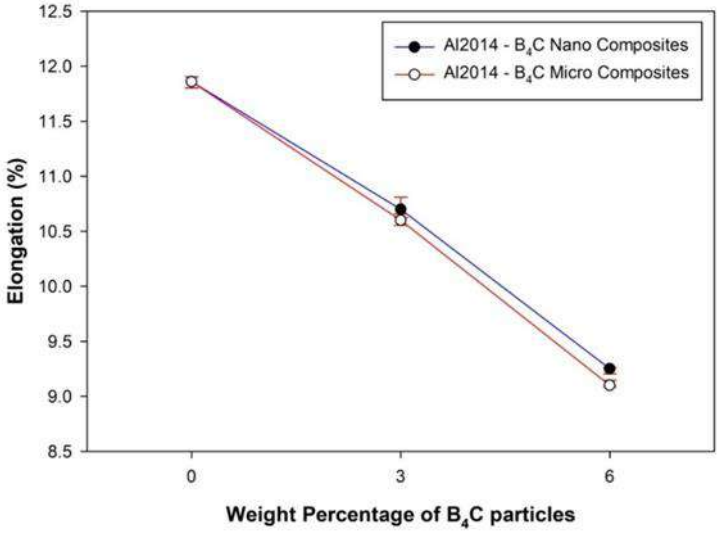

Fig. 10. Comparison of ductility of Al2014 with B_4C composites

3.5 Compression Strength

Al2014 alloys with 3 and 6 weight percent B_4C reinforcement and 200- to 25-micron particles are tested for compression strength. Fig. 11 shows that Al2014 alloy composite compressive strength rises linearly with B_4C wt.% at decreasing particle sizes. The graph shows that hard B_4C particles boost compression strengths in an Al2014 matrix. Al2014 alloy with 6 wt.% 200 nm and 25-micron B_4C reinforced composites has compression strengths of 775.04 MPa and 730.64 MPa, respectively,

while its strength is 568.26 MPa. Nano and micro particles increase composite compressive strength by 36.38 and 28.57 percent. Compression strength is highest in Al2014 alloy doped with 6 wt.% nano B_4C composites. A composite composed of fine particles has superior compression strength compared to one with intermediate particle sizes or an unreinforced alloy. The augmentation of particle quantity and the reduction of inter-particle spacing at varying weight percentages of B_4C, when particle size is significant, may elucidate this phenomenon [35]. With more particles blocking dislocations, hardening is faster and compression plastic deformation is reduced [36].

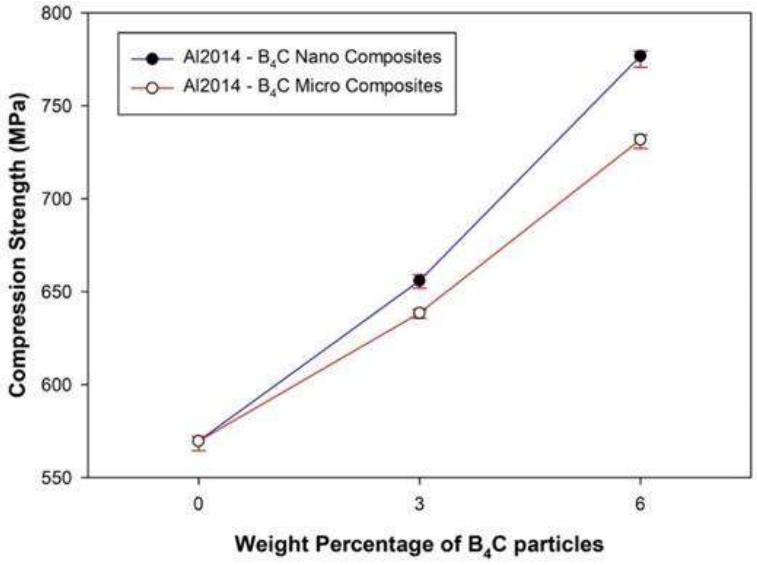

Fig.11. Al2014 alloy compressive strength vs. nano and micro B_4C composites

3.6 Tensile Fractography

Tensile fracture studies were done to elucidate the alterations in the composite's fracture behavior following reinforcement with B_4C particles. The fractures in Fig. 12 (a) of the Al2014 are larger and more homogeneous, indicating its malleability. The fracture of a composite containing 6 wt.% B_4C nano-composites of 200 nm and 25-micron sizes is depicted in Fig. 12 (b, c). The presence of minor ductile dimples in the matrix alloy indicates that minimal plastic deformation has transpired following the incorporation of B_4C particles. Additionally, particle de-cohesion between the Al and particle was evident in scanning electron micrographs of the fracture surfaces of 200 nm B_4C composites. The incorporation of hard particles into the Al matrix converts the ductile mode fracture to the brittle mode. Further, this brittle fracture is more in the case of micron sized particles reinforced composites compared to the nano sized particles.

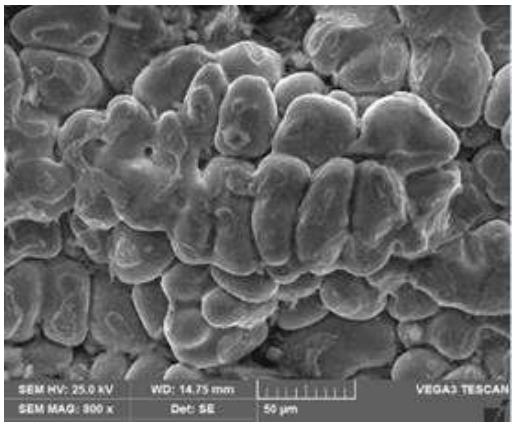

(a)

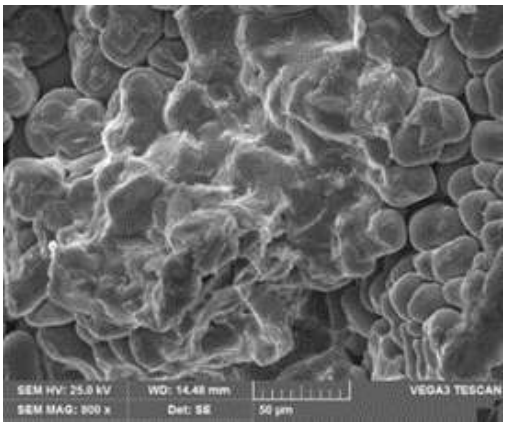

(b)

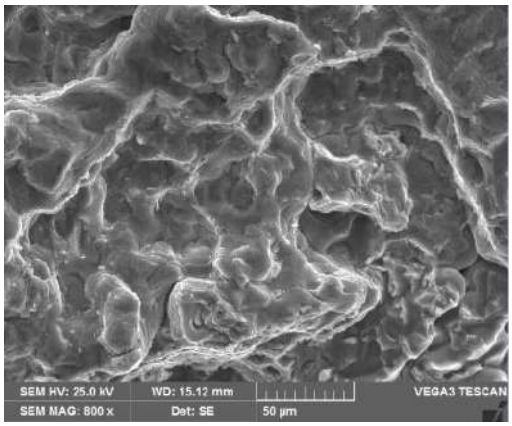

Fig. 12. Tensile fractured surfaces (a) Al2014 alloy (b) Al2014 – 6 wt. % of 200 nm B_4C (c) Al2014 – 6 wt. % of 25 micron B_4C composites

4. Conclusions

The current study has resulted in the following conclusions:

- The Al2014 alloy, incorporating nano and micron-sized B_4C particles in metal matrix composite at 3 and 6 wt. percent, was effectively produced using the stir casting method.
- The SEM micrographs demonstrate that the B_4C particles are evenly distributed throughout the Al2014 alloy. The EDS analysis revealed the presence of B_4C particles in engineered composites.
- UTS, YS, and compression strength, as well as hardness, have all increased in B_4C reinforced composites, while ductility has decreased slightly.
- The hardness, tensile, and compressive behaviors of Al2014 alloy reinforced with 200 nm B_4C nanoparticles were significantly superior to those of 25-micron B_4C reinforced composites.
- Fractographic analysis of surfaces using a SEM demonstrated the distinct fracture mechanisms of the base Al2014 alloy and its resultant composites.
- A composite made from Al2014 with 6% nano B_4C particles exhibited 29.9% and 35.7% increases in ultimate and yield strengths, respectively, compared to the original Al2014 alloy. Thus, these composites can reduce weight and cross-sectional area in the manufacture of aeronautical components.

References

[1] Suresh S, Moorthi NSV, Vettivel SC, Selvakumar N, Jinu GR. Effect of graphite addition on mechanical behavior of Al6061-TiB2 hybrid composites using acoustic emission. Mater Sci Eng A. 2014;612:16-27. https://doi.org/10.1016/j.msea.2014.06.024

[2] Kumar NGS, Shivashankar GS, Basavarajappa S, Suresh R. Some studies on mechanical and machining characteristics of Al2219/n-B4C/MoS2 nano hybrid metal matrix composites. Measurement. 2017;107:1-11. https://doi.org/10.1016/j.measurement.2017.05.003

[3] Krishna UB, Vasudeva B, Auradi V, Nagaral M. Effect of percentage variation on wear behaviour of tungsten carbide and cobalt reinforced Al7075 matrix composites synthesized by melt stirring method. J Bio Tribo-Corros. 2021;7(3):1-8. https://doi.org/10.1007/s40735-021-00528-1

[4] Kumar GBV, Chowdary GV, Vamsi MS, Reddy KJ, Nagaral M, Naresh K. Effects of addition of titanium diboride and graphite particulate reinforcements on physical, mechanical and tribological properties of Al6061 alloy based hybrid metal matrix composites. Adv Mater Process Technol. 2021:1-18. https://doi.org/10.1080/2374068X.2021.1904370

[5] Zheng R, Chen J, Zhang Y, Ameyama K, Ma C. Fabrication and characterization of hybrid structured Al alloy matrix composites reinforced by high volume fraction of B4C particles. Mater Sci Eng A. 2014;601:20-8. https://doi.org/10.1016/j.msea.2014.02.032

[6] Bharath V, Auradi V, Nagaral M, Boppana SB. Experimental investigations on mechanical and wear behaviour of 2014Al-Al2O3 composites. J Bio Tribo-Corros. 2020;6(2):1-10. https://doi.org/10.1007/s40735-020-00341-2

[7] Sekar K, Allesu K, Joseph MA. Effect of heat treatment in tribological properties of A356 aluminium alloy reinforced with Al2O3 nano particles by combination effect of stir and squeeze casting method. Appl Mech Mater. 2014;592-594:968-71. https://doi.org/10.4028/www.scientific.net/AMM.592-594.968
[8] Umanath K, Selvamani ST, Palanikumar K, Raphael T, Prashanth K. Effect of sliding distance on dry sliding wear behavior of Al6061-SiC-Al2O3 hybrid composite. In: Proc Int Conf Adv Mech Eng. 2013. p. 749-75. https://doi.org/10.1016/j.compositesb.2013.04.051
[9] Ramchandra M, Abhishek A, Siddeshwar P, Bharathi V. Hardness and wear resistance of ZrO2 nanoparticle reinforced Al nanocomposites produced by powder metallurgy. Procedia Mater Sci. 2015;10:212-9. https://doi.org/10.1016/j.mspro.2015.06.043
[10] Nagaral M, Kalgudi S, Auradi V, Kori SA. Mechanical characterization of ceramic nano B4C-Al2618 alloy composites synthesized by semi solid state processing. Trans Indian Ceram Soc. 2018;77(3):1-4. https://doi.org/10.1080/0371750X.2018.1506363
[11] Dhanalakshmi P, Mohansundararaju N, Venkatkrishnan PG. Preparation and mechanical characterization of stir cast hybrid Al7075-Al2O3-B4C metal matrix composites. Appl Mech Mater. 2014;592-594:705-10. https://doi.org/10.4028/www.scientific.net/AMM.592-594.705
[12] Devnani GL, Sinha S. Effect of nano fillers on the properties of natural fiber reinforced polymer composites. Mater Today Proc. 2019;18(3):647-54. https://doi.org/10.1016/j.matpr.2019.06.460
[13] Narimani M, Lotfi B, Sadeghian Z. Evaluation of the microstructure and wear behavior of AA6063-B4C/TiB2 mono and hybrid composite layers produced by friction stir processing. Surf Coat Technol. 2016;285:1-10. https://doi.org/10.1016/j.surfcoat.2015.11.015
[14] Pakdel A, Witecka A, Rydzek G, Awang Shri DN, Nicolosi V. A comprehensive analysis of extrusion behavior, microstructural evolution and mechanical properties of 6063 Al-B4C composites produced by semisolid stir casting. Mater Sci Eng A. 2018;721:28-37. https://doi.org/10.1016/j.msea.2018.02.080
[15] Murthy IN, Rao DV, Rao JB. Microstructure and mechanical properties of aluminium fly ash nano composites made by ultrasonic method. Mater Des. 2012;35:55-65. https://doi.org/10.1016/j.matdes.2011.10.019
[16] Shashidhar S, Kumar PV, Shivananda HK, Nagaral M. Processing, microstructure, density and compression behavior of nano B4C particulates reinforced Al2219 alloy composites. Int J Adv Technol Eng Explor. 2018;5(46):350-5. https://doi.org/10.19101/IJATEE.2018.546015
[17] El-Kady O, Fathy A. Effect of SiC particle on the physical and mechanical properties of extruded Al matrix composites. Mater Des. 2014;54:348-53. https://doi.org/10.1016/j.matdes.2013.08.049
[18] Ramnath BV, Elanchezhian C, Jaivignesh M, Rajesh S, Parswajinan C, Ghias ASA. Evaluation of mechanical properties of aluminium alloy-alumina-boron carbide metal matrix composites. Mater Des. 2014:332-8. https://doi.org/10.1016/j.matdes.2014.01.068
[19] Matti S, Shivakumar BP, Shashidhar S, Nagaral M. Dry sliding wear behavior of mica, fly ash and red mud particles reinforced Al7075 alloy hybrid metal matrix composites. Indian J Sci Technol. 2021;14(4):310-8. https://doi.org/10.17485/IJST/v14i4.2081
[20] Ali Z, Muthuraman V, Rathnakumar P, Gurusamy P, Nagaral M. Studies on mechanical properties of 3 wt% of 40 and 90 µm size B4C particulates reinforced A356 alloy composites. Mater Today Proc. 2022;52:494-9. https://doi.org/10.1016/j.matpr.2021.09.260
[21] Kumar R, Deshpande RG, Gopinath B, Harti J, Nagaral M, Auradi V. Mechanical fractography and worn surface analysis of nanographite and ZrO2-reinforced Al7075 alloy aerospace metal composites. J Fail Anal Prev. 2021;21:525-36. https://doi.org/10.1007/s11668-020-01092-5
[22] Bharath V, Ajawan SS, Nagaral M, Auradi V, Kori SA. Characterization and mechanical properties of 2014 aluminum alloy reinforced with Al2O3p composite produced by two-stage stir casting route. J Inst Eng India Ser C. 2019;100:277-82. https://doi.org/10.1007/s40032-018-0442-x
[23] Prasad GP, Chittappa HC, Nagaral M, Auradi V. Influence of B4C reinforcement particles with varying sizes on the tensile failure and fractography of LM29 alloy composites. J Fail Anal Prev. 2020;20(6):2078-86. https://doi.org/10.1007/s11668-020-01021-6
[24] Nagaraj N, Mahendra KV, Nagaral M. Microstructure and evaluation of mechanical properties of Al-7Si-fly ash composites. Mater Today Proc. 2018;5(1):3109-16. https://doi.org/10.1016/j.matpr.2018.01.116
[25] Dama K, Prashanth L, Nagaral M, Mathapati R, Hanumantharayagouda MB. Microstructure and mechanical behavior of B4C particulates reinforced ZA27 alloy composites. Mater Today Proc. 2017;4(8):7546-53. https://doi.org/10.1016/j.matpr.2017.07.086
[26] Hanumantharayappa AKB, Prasanna C, Ragavendra CC, Beekam CS, Boluvar LS, Nagaral M, et al. Synthesis and mechanical characterization of Si3N4 reinforced copper-tin matrix composites. J Mech Behav Mater. 2021;30(1):199-206. https://doi.org/10.1515/jmbm-2021-0020
[27] Kumar HSV, Kempaiah UN, Nagaral M, Auradi V. Impact, tensile and fatigue failure analysis of boron carbide particles reinforced Al-Mg-Si (Al6061) alloy composites. J Fail Anal Prev. 2021;21(6):2177-89. https://doi.org/10.1007/s11668-021-01265-w

[28] Nagaraj N, Mahendra KV, Nagaral M. Investigations on mechanical behaviour of micro graphite particulates reinforced Al-7Si alloy composites. IOP Conf Ser Mater Sci Eng. 2018;310(1):012131. https://doi.org/10.1088/1757-899X/310/1/012131
[29] Venkataraman V, Nagaral M. Mechanical characterization and wear behavior of aerospace alloy AA2124 and micro B4C reinforced metal composites. J Met Mater Miner. 2020;30(4):97-105. https://doi.org/10.55713/jmmm.v30i4.641
[30] Murthy BV, Auradi V, Nagaral M, Vatnalmath M, Namdev N, Anjinappa C, et al. Al2014-alumina aerospace composites: particle size impacts on microstructure, mechanical, fractography, and wear characteristics. ACS Omega. 2023;8(14):13444-55. https://doi.org/10.1021/acsomega.3c01163
[31] Kumar HSV, Revanna K, Kumar N, Sathyanarayana N, Madeva N, Manjunath GA, et al. Impact of silicon carbide particles weight percentage on the microstructure, mechanical behaviour, and fractography of Al2014 alloy composites. 2022;Article ID: 2839150. https://doi.org/10.1155/2022/2839150
[32] Bharath V, Ashita DH, Auradi V, Nagaral M. Influence of variable particle size reinforcement on mechanical and wear properties of alumina reinforced 2014Al alloy particulate composite. FME Trans. 2020;48(4):968-78. https://doi.org/10.5937/fme2004968B
[33] Basavaraja P, Nagaral M, Auradi V, Vidyashankar. Evaluation of mechanical properties of Al2219-SiC-Graphite reinforced hybrid composites. Int J Appl Eng Res. 2015;10(9):9300-3.
[34] Boppana SB, Dayanand S, Murthy BV, Nagaral M, Telagu A, Kumar V, et al. Development and mechanical characterisation of Al6061-Al2O3-graphene hybrid metal matrix composites. J Compos Sci. 2021;5(6):155. https://doi.org/10.3390/jcs5060155
[35] Fazil N, Venkataramana V, Nagaral M, Auradi V. Synthesis and mechanical characterization of micro B4C particulates reinforced AA2124 alloy composites. Int J Eng Technol UAE. 2018;7(2.23):225-9. https://doi.org/10.14419/ijet.v7i2.23.11954
[36] Manjunatha TH, Basavaraj Y, Nagaral M, Venkataramana V, Harti JI. Investigations on mechanical behavior of Al7075-nano B4C composites. IOP Conf Ser Mater Sci Eng. 2018;376(1):012091. https://doi.org/10.1088/1757-899X/376/1/012091

Research on Engineering Structures & Materials
www.jresm.org
Research Group

Research Article

Durability and microstructure of ternary binder geopolymer concrete: A comprehensive study

Rayana Harika [1,a], Panugalla Rama Rao [1,b], Sankar Boomibalan [2,c], Arunkumar Kadarkarai [*,2,d], Rameshkumar Deivasigamani [2,e]

[1]*Dept. of Civil Eng., VNR Vignana Jyothi Institute of Engineering and Technology, Hyderabad, India*
[2]*Dept. of Civil Eng., Mangalam College of Engineering, Kottayam, India*

Article Info

Article History:

Received 02 Feb 2025

Accepted 05 May 2025

Keywords:

Geopolymer concrete;
Ternary binder;
Nano silica;
Sulfate resistance;
Sorptivity;
Microstructural analysis

Abstract

Geopolymer concrete (GPC) is emerging as a promising, eco-friendly alternative to traditional cement concrete due to its lower carbon footprint and enhanced durability. A key challenge with geopolymer concrete is its dependence on heat activation at varying temperatures, which restricts its practical applications. In this study, the impact of various molarities of NaOH (2 to 10 M) on the sorptivity, sulfate attack resistance, and microstructure of geopolymer concrete (GPC) made with ternary binders is investigated. Ternary binders of Fly Ash, GGBS, and Nano silica are utilized in the proportion of 49:48:3 for all the molarities. Concurrently, Plain Cement Concrete (PCC) of equivalent grade is assessed for comparative analysis. The study found that GPC with a 10 molar concentration exhibits less weight loss and strength degradation, at 1.24% and 12.26%, respectively, when immersed in a sulfate solution. The sorptivity test reveals that GPC with 10M had the lowest water absorption, measuring only 0.14mm compared to the other mixes. The formation of (N-A-S-H) was observed in all samples, indicating a compact and dense microstructure of the geopolymer matrix. This study finds an alternate binder to traditional cement concrete with lower molar concentration, that can exhibit better performance in durability characters.

© 2025 MIM Research Group. All rights reserved.

1. Introduction

Concrete production poses environmental challenges, primarily due to the significant carbon emissions generated during cement manufacturing [1]. To address these challenges, ongoing research and development efforts are exploring sustainable alternatives, such as geopolymers and recycled concrete, to mitigate the environmental impact of concrete production and promote eco-conscious construction practices [2]. Geopolymer concrete (GPC) stands out as a symbol of innovation and advancement in the building industry amid the growing emphasis on environmental responsibility. Geopolymer concrete (GPC) transforms conventional building methods by adopting the principles of sustainable development and the circular economy, utilizing industrial byproducts such as fly ash and GBBS [3]. These alternative materials sourced from industries help reduce industrial waste and minimize carbon footprints. The transformative geo-polymerization process imbues these materials with remarkable properties, endowing the resulting concrete with exceptional strength and durability [4]. In contrast to traditional concrete, geopolymer isolation is a unique chemical process that occurs in geopolymer concrete (GPC) [5]. During this process, alkaline activators react with alumina and silica-rich materials such as fly ash and GBBS, initiating polycondensation reactions [6,7]. These reactions lead to the formation of a three-dimensional network, known as the geopolymer gel, which is the primary reason for

*Corresponding author: arunapcivil@gmail.com
[a]orcid.org/0000-0001-7785-6243; [b]orcid.org/0000-0001-8911-567X; [c]orcid.org/0000-0002-2572-2689;
[d]orcid.org/0000-0002-5745-6864; [e]orcid.org/0000-0002-2314-9524
DOI: http://dx.doi.org/10.17515/resm2025-657me0202rs

enhancing the structural integrity of the concrete [8,9]. Meanwhile, geopolymer concrete (GPC) exhibits exceptional mechanical properties and also resilience to harmful environmental conditions. The combination of different precursors helps refine the geopolymer matrix, resulting in an enhanced performance. GGBS enhances early strength gain, while fly ash contributes to long-term strength development [10–12]. However, the pores present in the binary geopolymer blends lead to a reduction in the efficiency of geopolymer concrete (GPC) in harsh ecological conditions [13,14]. Hence, including ternary binders in geopolymer formulations optimizes mechanical properties, workability, and durability while promoting sustainability. This makes them a superior choice for modern construction applications, ensuring long-term performance and environmental benefits.

The incorporation of nanoparticles in GPC has sparked considerable interest in recent studies due to their prospective advantages in augmenting mechanical properties and overall durability. Researchers are keenly studying the distinctive features of these nanoparticles to maximize the efficiency and longevity of geopolymer concrete structures [3]. This novel subject has the potential to revolutionize the construction industry by utilizing nanoparticles in geopolymer concrete (GPC), which can help fill pores and create a compact geopolymer structure. Meanwhile, geopolymer concrete exhibits greater strength at 60°C than at 80°C, despite the slower polymerization process. However, curing it at ambient temperatures (27°C ± 2°C) remains a challenge, with limited literature on the use of geopolymers for this purpose [3]. The addition of nano-silica as a binder in conventional and geopolymer concrete (GPC) provides a compact and dense mixture, which enhances strength and resistance to adverse environmental conditions [15]. Nano silica is a material composed of 95 percent SiO2. Due to its smaller size of less than 1 μm, it occupies a larger surface area, which helps it fill the nanopores. Due to its pozzolanic nature, the NS is involved in accelerating the formation of geopolymer gels and portlandite in the geopolymer concrete (GPC), which can promote strength development by its compactness [16].

In geopolymer, a high alkaline medium is required as a monomer for the dissolution of oxides (such as SiO_2, Al_2O_3, and CaO) present in the precursors. The molarity and type of activators have a significant influence on geopolymers, which are renowned for their exceptional durability and sustainability advantages. Changes in NaOH molarity provide geopolymer concrete (GPC) mixes a complex layer that influences key properties, including workability, setting time, and, most crucially, durability [17,10]. Adjusting the concentration of NaOH allows for targeted modifications to be made to the geopolymer formulation. The study conducted by [16] examines the performance of GPC at various molarities of NaOH and different curing temperatures. It demonstrates that the compressive strength increases with increasing molarity and curing temperature. The study concluded that samples made with 16M yield better performance in terms of strength. However, higher concentration leads to inefficient strength development in later ages. The GPCs made with 12 M NaOH concentration had the greatest strength. Increased concentrations of NaOH inhibited the polycondensation by accelerating the dissolving of silica and alumina. The resistance of GPC in an acidic environment increases with the molarity of the sodium hydroxide (NaOH) solution [18]. The results of GPC specimens after immersion in sulfuric acid showed a weight loss of 2.03% and a strength loss of 1.81%, respectively, indicating a better performance of GPC samples in acidic conditions. According to [19], the production of crystalline phases within the aluminosilicate network determines the stability of geopolymer materials in acidic environments. This indicates that more crystalline phases lead to better stability in hostile environments. The alkalinity of the binder itself serves as the foundation for the concept of acidic attack [20]. The primary cause of acid damage is an interaction between acidic and alkaline components within the binder network. The primary reason why alkali-activated material is more durable than an OPC binder is due to its low Calcium concentration. Heat-cured geopolymer concrete test specimens exhibit surface degradation, and after one year of exposure, a mass loss of approximately 3% occurs due to a sulfuric acid solution. FESEM and EDX investigations revealed that the performance improvement was attributed to the formation of crystalline structures. The better performance was due to the promotion of high NASH gel products [21]. It confirms that the concentration of alkaline liquids plays a vital role in the performance of GPC. Additionally, the pores in any type of concrete should be a more significant concern in terms of its performance [22].

Hence, there is a need to fill the pores, and this study incorporates nanomaterials to reduce the pores available in GPC and investigate the quantity of alkaline medium in the activation process and durability of geopolymer concrete (GPC). Therefore, nano silica has been used as a replacement binder with a fixed weight of 2%. This study also investigates the durability and microstructural behavior of geopolymer concrete (GPC) as the molarity of NaOH is varied.

2. Materials and Methods

The materials used in this study included FA, GGBS, nano-silica, alkaline activators, fine and coarse aggregates, and admixtures. This research involves the casting process, curing, and evaluation of samples according to standard procedures.

2.1. Materials

2.1.1 Fly Ash

Fly ash is a fine powder composed primarily of spherical, glassy particles generated as a byproduct of coal combustion in power plants. The primary constituents of fly ash are silica, alumina, and iron oxide. Due to its pozzolanic properties, fly ash can react with lime to form cementitious compounds. According to IS 3812 (Part I) [23], the current investigation utilized Class F Fly Ash. Fly ash with a specific gravity of 2.1 is used.

2.1.2. GGBS

A by-product of iron production, it is cementitious in nature. GGBS is a waste by-product of the steel industry, and its principal components are CaO, SiO_2, Al_2O_3, and MgO. In the present study, the GGBS manufactured by the JSW Cements Company is utilized. GGBS has a specific gravity of 2.4.

2.1.3 Nano Silica

The main component of nano-silica is silicon dioxide (SiO_2), which can be either crystalline or amorphous. The nanoparticles of silica utilized in this study are 17 nm in size. In polymer compounds, nano silica is used as a filler to enhance mechanical and durability performance.

2.1.4 Fine Aggregate

This project utilized sand from a nearby location with a specific gravity of 2.55 and a Zone II classification, as per IS 383-1970 [24].

2.1.5 Coarse Aggregate

In this investigation, locally obtainable aggregate having a specific gravity of 2.60 was utilized.

2.1.6 Alkaline Solutions

Sodium hydroxide and sodium silicate were used as alkaline activating solutions in the current research work. The resulting fluids react with fly ash and other cementitious materials rich in silica and alumina. Before use, NaOH pellets must be dissolved in water at the required concentration. The sodium hydroxide used has concentrations of 2, 4, 6, 8, and 10 M. After combining the sodium hydroxide and water glass solution, it was allowed to settle for one day. The ratio of NaOH to Na_2SiO_3 is 1:2.5 [25]. The sodium silicate solution contains SiO_2-33.92% and Na_2O-16.33%. The NaOH pellets used for making NaOH solution in each molarity of (GPC) mix for a total of 100 percent is, i.e., for 2M – 8.1%, 4M – 15.1%, 6M – 21%, 8M – 26.23%, 10M – 30.37% and the remaining percentage is diluted with water.

2.1.7 Admixture

Conplast SP 430, a water-reducing additive, is used to improve workability.

2.2. Methodology

The current study utilized GPC mix proportions from earlier studies [23–25] to define the GPC composition. Materials are originally sourced and then quantified in batches. The aggregates were initially added to the pan mixer, followed by batched FA, GGBS, and Nano silica, and the mixture

was then vigorously mixed. The additive and alkaline mixtures are then added and blended with the ingredients in the mixer. The mixing process was repeated until an evenly distributed and homogenous mixture was obtained. The test items used were cube specimens measuring 150 mm for acid attack and 100 mm for sorptivity. The cast specimens were removed from the mold and left to cure for 28 days at ambient temperature. Table 1 shows the mix proportion of GPC and PCC mix. As per ASTM C1898-20 [26], the acid attack test was performed in the concrete cubes of size 150 mm^3. For conducting the sorptivity test, 100 mm cubes, as mentioned by Liu et. al [27], are cast, demoulded after 24 hours, and placed for ambient curing, the temperature ranging between 27^{0}C to 30^{0}C, and the test was performed as per ASTM C1585-04 [28] standards.

Table 1. The details of the mix proportions are given in this table for 1 m^3 of concrete.

Mix	Binder (kg/m^3)	Fine aggregate (kg/m^3)	Coarse aggregate (kg/m^3)	NaOH (kg/m^3)	Na_2SiO_3 (kg/m^3)	Water (kg/m^3)	SP (kg/m^3)
Fly ash + GGBS + NS	443	656	1264	44.2	110.8	-	8.86
PCC	368	707	1136	-	-	186	-

3. Results and discussions

3.1. Durability

3.1.1 Sulfate Attack

Table 2 presents the weight loss and strength loss resulting from the immersion of specimens in acids. The graph in Fig. 1 compares the percentage weight loss for the various concrete compositions listed in Table 2. According to the figure and table above, PCC mix cubes lost 8.22% of their weight after 28 days of immersion in 5% H_2SO_4. When compared to other mixes, the PCC mix sheds more weight. The GPC-10M mix sheds less weight, i.e., 1.24%, than all other mixes. The percentage of weight loss of GPC-8M and GPC-10M are comparably near to each other.

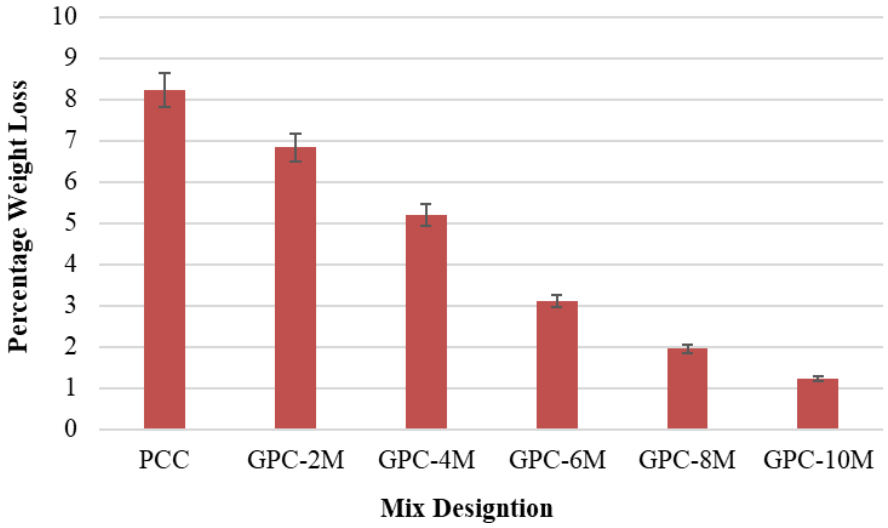

Fig. 1. Percentage weight loss of different concrete mixes.

The graph in Fig. 2 compares the percentage loss in compressive strength for the various concrete combinations listed in Table 2. The image and table above show that PCC mix cubes lose 26.81% of their compressive strength after 28 days of immersion in 5% H_2SO_4 and lose 54% of their strength compared to GPC-10M. PCC mix loses greater compressive strength when compared to other mixtures. The GPC-10M mix loses less compressive strength, i.e., 12.26%, than all other mixes.

Table 2. Percentage Loss in weight and Strength of Specimens after Immersed in H_2SO_4 Solution for 28 days

Mix Designation	Initial weight in kg	Final weight in kg	Percentage weight loss	Initial compressive strength in MPa	Final compressive strength in MPa	Percentage Loss in strength
PCC	8.16	7.48	8.22	48.52	35.49	26.81
GPC-2M	8.17	7.60	6.84	27.13	20.28	25.22
GPC-4M	8.17	7.74	5.21	34.49	26.35	23.60
GPC-6M	8.18	7.92	3.12	39.12	31.44	19.58
GPC-8M	8.18	8.01	1.96	44.71	38.08	14.82
GPC-10M	8.18	8.07	1.24	50.30	44.13	12.26

This demonstrates that increasing the molarity of NaOH in GPC mixes, as well as adding Nano Silica, improved resistance to sulfate attack. As a result, GPC concrete has demonstrated superior resistance to sulfate attack than PCC mix. The positive effect of nano-silica on pozzolanic activity led to the development of Si-Al bonds, which increases the strength of the binder paste. The nanoparticles of nano silica increased the packing capacity of the geopolymer matrix by filling the pores of the binder paste, lowering acid permeability in concrete specimens while modestly boosting durability. GPC varies from PCC such that it has very little calcium content, making it more resistant to acid assaults. Its aluminosilicate gel, formed during geo-polymerization, forms a solid, impermeable structure that serves as a barrier to acidic chemicals.

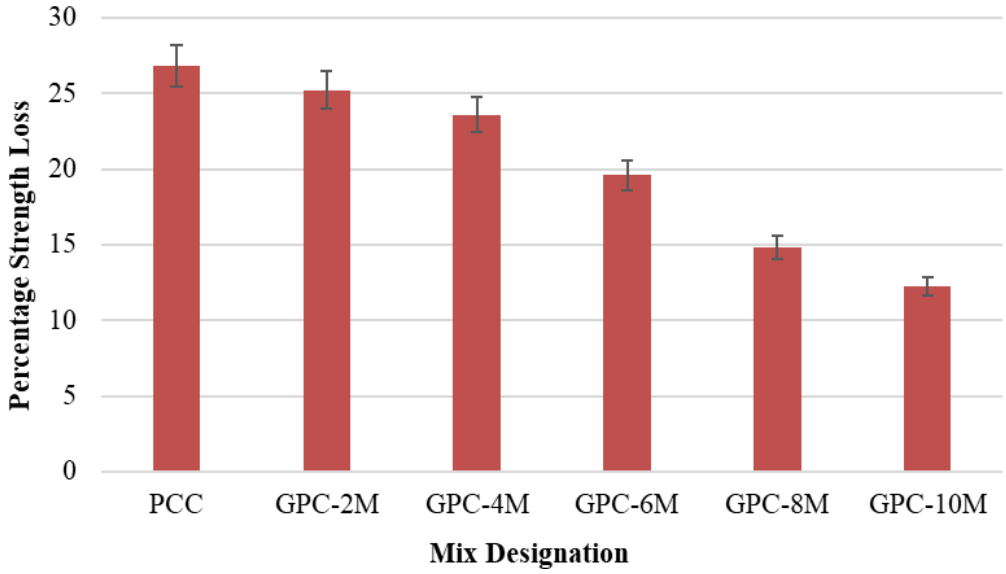

Fig. 2. Percentage strength loss of different concrete mixes.

The decreased porosity of GPC reduces acid intrusion, reducing possible chemical reactions and increasing overall durability. PCC samples primarily consist of calcium silicate compounds, when exposed to sulfuric acid, these compounds can undergo chemical reactions leading to the formation of gypsum (calcium sulfate) and other soluble compounds. This results in the degradation of the PCC matrix and the weakening of the concrete. When more NaOH is used, it helps break down the raw materials more effectively, which leads to the formation of a strong and well-connected aluminosilicate network, also known as N-A-S-H gel. This network plays a key role in protecting the concrete. It creates a dense, tightly packed structure that makes it harder for harmful sulphate ions to get inside. Because the material has fewer pores and pathways, there's less chance for sulfates to react with the concrete and cause damage like cracking or expansion.

3.1.2 Sorptivity

The absorption values of the sorptivity test on a 100 mm cube specimen at various time intervals are shown in Table 3. The absorption results of the sorptivity test are shown in Table 3 and Fig. 3. It can be seen that the incorporation of Nano Silica resulted in less absorption than that of the PCC mix. At 28 days, compared to the other mixes, the GPC-2M mix has a higher absorption value (i.e., 0.38mm). The water absorption of the GPC-2M mix is 80.95% more than the PCC mix at 28 days. The GPC-10M mix has absorbed less water than the other mixes.

Table 3. Absorption values for different concrete mixes with respect to time.

Time	Absorption (I) Values in mm					
	PCC	GPC-2M	GPC-4M	GPC-6M	GPC-8M	GPC-10M
0 Minutes	0	0	0	0	0	0
30 Minutes	0.03	0.08	0.05	0.03	0.04	0.03
60 Minutes	0.05	0.13	0.09	0.05	0.05	0.03
2 Hours	0.07	0.17	0.14	0.08	0.06	0.05
4 Hours	0.10	0.21	0.18	0.12	0.08	0.07
6 Hours	0.12	0.26	0.22	0.15	0.10	0.08
1 Day	0.14	0.29	0.25	0.18	0.13	0.10
3 Days	0.16	0.32	0.27	0.21	0.15	0.11
7 Days	0.19	0.34	0.29	0.23	0.16	0.12
14 Days	0.20	0.36	0.30	0.25	0.18	0.13
28 Days	0.21	0.38	0.31	0.26	0.19	0.14

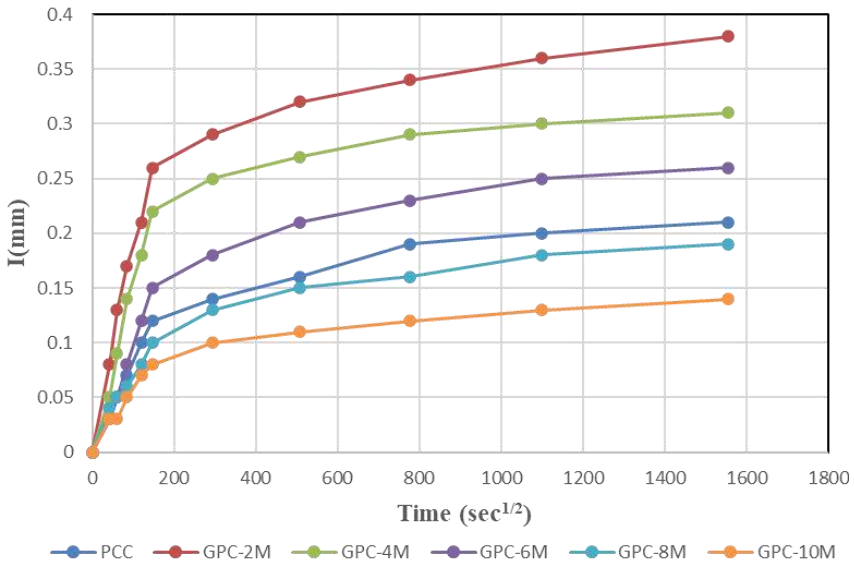

Fig. 3. Variation of water absorption values of different concrete mixes with time

The graph shows that the absorption values for all mixes increased with time. It states that the capacity of water to penetrate the concrete cube rises with the time it is immersed in water. GPC-10M has the lowest absorption value (0.14 mm) after 28 days, whereas PCC has the highest value (0.21mm). However, the mixes GPC-6M and GPC-8M also have lower absorption values than the PCC mix at 28 days. The results show that sorptivity decreases as the NaOH molarity increases. This means the concrete absorbs less water when more NaOH is used. The reason behind this is that higher NaOH concentration helps break down the raw materials more effectively, which leads to better formation of a binding gel called N-A-S-H. This gel fills the spaces inside the concrete, making it denser and less porous. As a result, the concrete becomes more resistant to water absorption. From the experimental results, it was found that Geopolymer concrete at higher molarities has lower porosity than PCC concrete mix. The probable reason for this effect is that the geo-polymerization method forms a three-dimensional network of aluminosilicate gel, resulting in

a more compact and less porous structure. This decreased porosity slows the water flow through the concrete, making it more resistant to water penetration.

3.2. Microstructure Analysis of Concrete

3.2.1 Field Emission Scanning Electron Microscopy (FESEM)

FESEM (Field Emission Scanning Electron Microscopy) is a useful method for investigating the microstructure and surface morphology of various materials, including concrete. FESEM scans a sample's surface with a high-energy electron beam, producing a different signal like secondary electrons, backscattered electrons, and distinctive X-rays. These signals help analyze surface characteristics at a microscopic level, providing insights into the material's composition and structural integrity.

For FESEM analysis, core concrete samples were collected to reflect the relevant region and then split into smaller pieces. These components were ensured to fit on SEM stubs. The surface was prepared for examination by removing any impurities or loose debris using compressed air or a mild solvent. It was ensured that the surface was free of any impurities that might interfere with imaging or analysis. The samples were carefully dried to prevent artifacts during analysis. This allowed for the analysis of the cement paste structure, including the detection of hydration products, voids, and the distribution of different components such as calcium hydroxide, calcium silicate hydrate, and un-hydrated cement particles. These parameters are crucial for evaluating the concrete strength, porosity, and durability variations over a period of time.

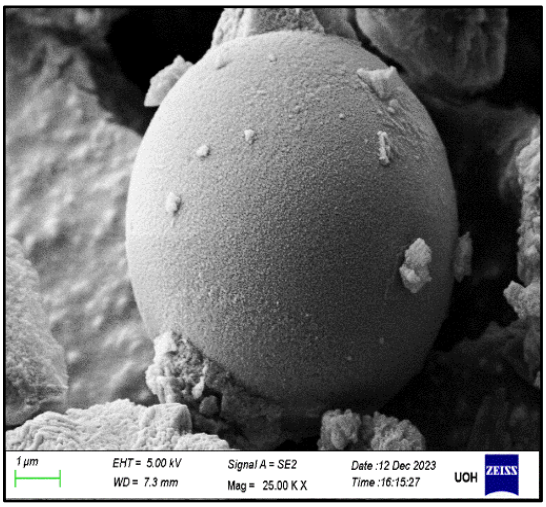

Fig. 4. FESEM image of Flyash

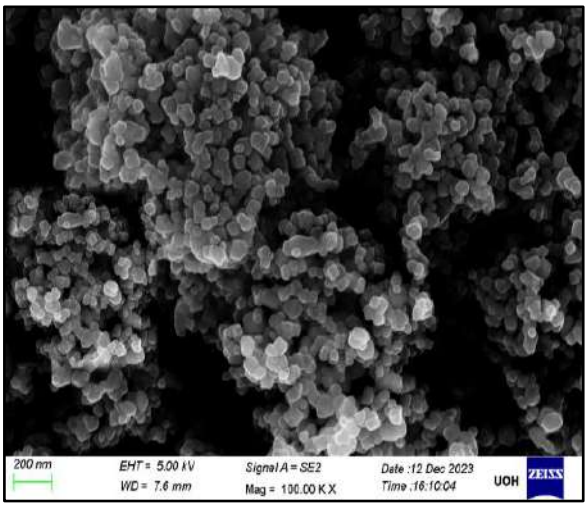

Fig. 5. FESEM image of Nanosilica

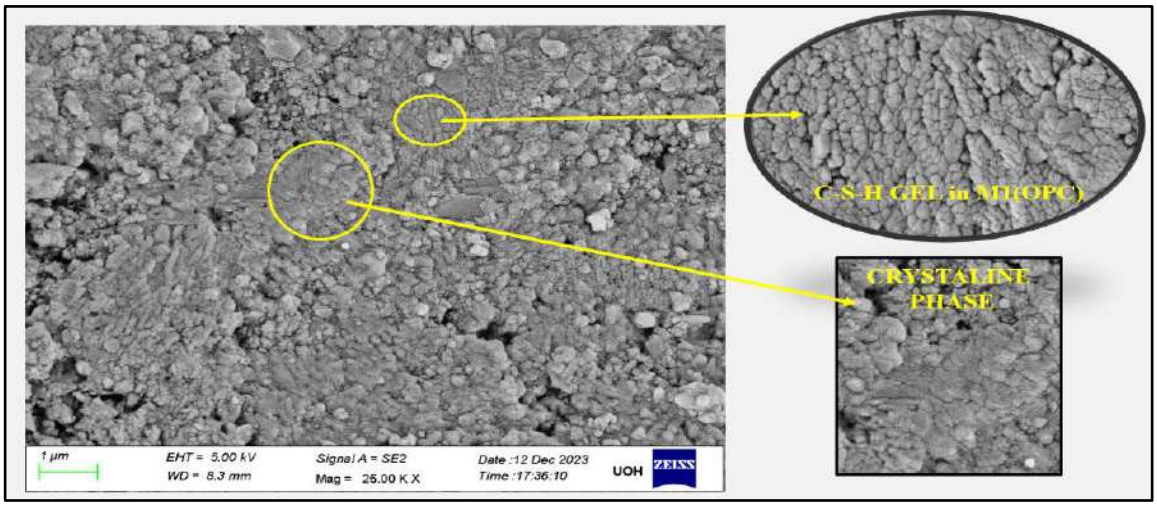

Fig. 6. FESEM image of PCC mix

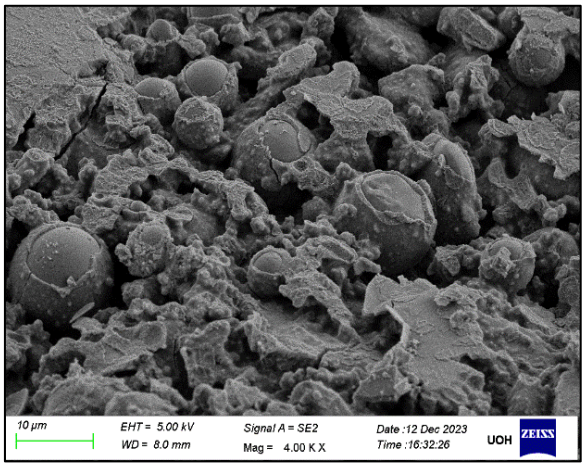

Fig. 7. FESEM image of GPC-2M mix

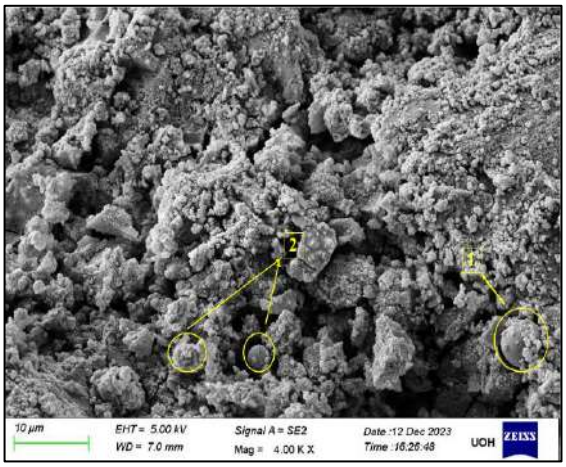

Fig. 8. FESEM image of GPC-4M mix

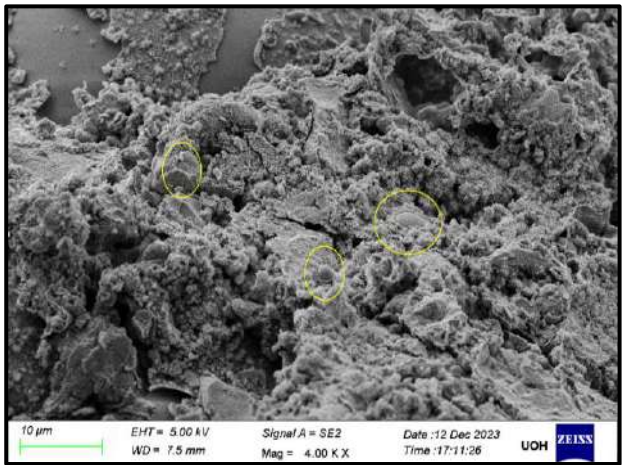

Fig. 9. FESEM image of GPC-6M mix

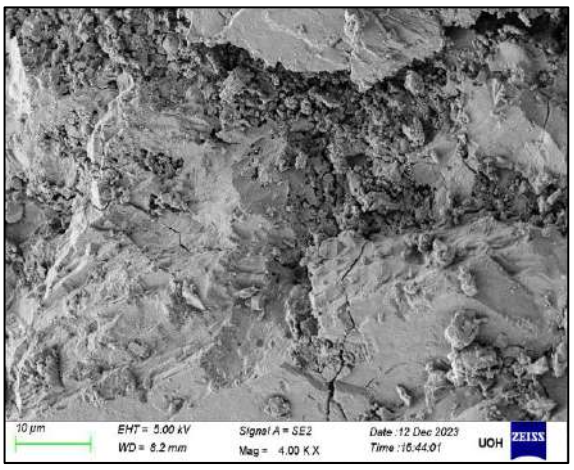

Fig. 10. FESEM image of GPC-8M mix

Fig. 4 and 5 show the FESEM image of fly ash and Nano silica particles. Lower alkali concentrations result in insufficient breakdown of Si and Al ions, leading to the formation of few Si- Al bonds, resulting in less N-A-S-H gel formation and more unreacted particles, which leads to less amorphous phase formation. The presence of unreacted fly ash particles is more significant in the low molar concentration samples, and large voids are observed in Figures 6-8. These samples have exhibited quicker crack development and less compressive strength. Samples with a low NaOH molarity are less dense because of their loose matrix. A high cross-sectional area of components is observed from Fig. 12 at 4M concentration because of less production of N-A-S-H gel, which is caused by more unreacted particles.

In contrast, at higher alkali concentrations, the disintegration of Si and Al ions is adequate. The formation of Si-Al bonds results in more N-A-S-H gel formation, and more particles are reacted and mixed. High-molarity solutions accelerated the geo-polymerization process. The presence of unreacted fly ash particles is low, and small voids are observed in high-molarity samples (Fig.11 and 13). Samples with a high NaOH molarity are denser because of their compact matrix. The zone encircling the unreacted particles seems compact despite the fact that few microfractures were identified in the region from Fig. 9 & 10. The interlocking morphology of the hydrated gel with the remaining unreacted particles leads to dense microstructure and decreased crack propagation in Fig 11. Further, the presence of increased molarity promoted the crystalline phase formation in GPC 8M 10M, resulting in a dense matrix. As depicted in Fig. 12 and 13, the reduced cross-sectional area of components in higher molarities has significantly improved geo-polymerization. Additionally, the presence of Nano Silica in the Pozzolanic activity caused the formation of Si-Al bonds and raised the density of the binder paste by filling the pores, all of which resulted in marginally better mechanical and durability qualities. These structural refinements contribute to superior mechanical and durability in geopolymer concrete.

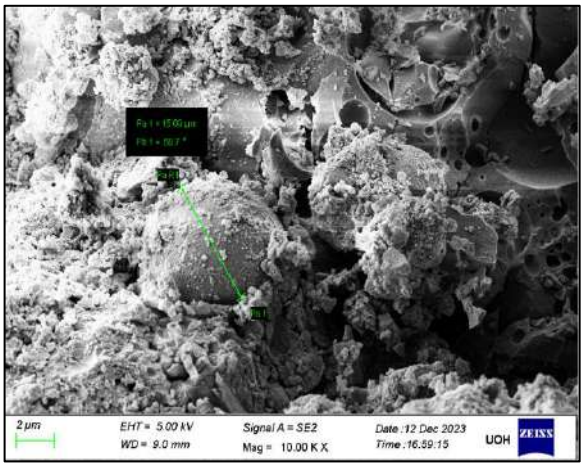

Fig. 11. FESEM image of GPC-10M mix

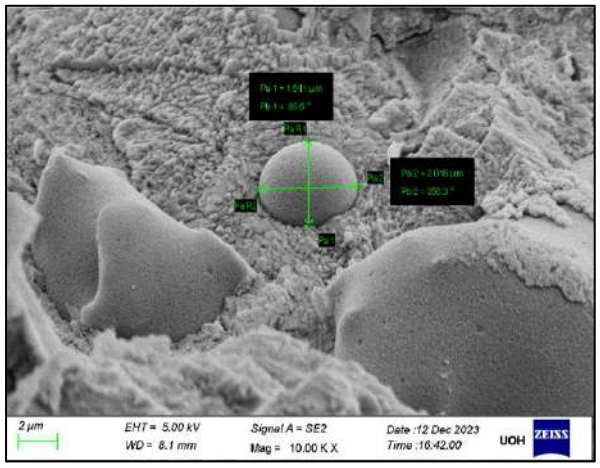

Fig. 12 FESEM image of flyash particle of GPC-4M mix

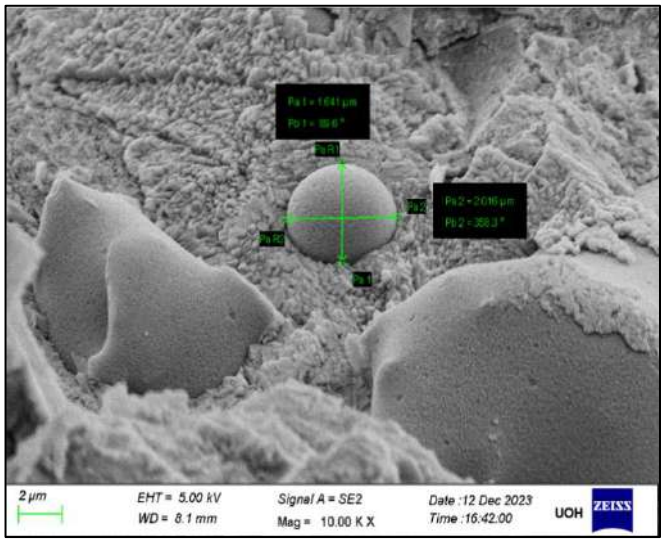

Fig. 13 FESEM image of fly ash particle of GPC-10M mix

3.2.1 Field Emission Scanning Electron Microscopy (FESEM)

Elemental analysis of various components inside the concrete may be performed using energy-dispersive X-ray spectroscopy (EDX) in conjunction with FESEM. This helps to determine the presence and distribution of distinct elements, which is essential for understanding concrete composition and probable sources of degradation. Configure the EDS system to gather data. Ensure that the detector is calibrated and aligned appropriately. After that, diagram the components on the concrete surface and designate specific regions or characteristics for in-depth elemental investigation. Obtain X-ray spectra from different concrete surface regions of interest. Analyze the spectra to determine their elemental composition.

Higher NaOH molarity suppressed calcium dissolution, resulting in lesser hydration products in GPC 10M from Table 4. The steady rise in GPC sample strength with increased activator concentrations is mostly due to the greater disintegration of aluminosilicate resources. The presence of magnesium in GPC offers chemical stability or so-called interatomic connections in the matrix through the creation of various linkages such as Si-O-Mg, Si-O-Al, Ca-O-Si, and Si-O-Si. From the above EDX compositions shown in Fig 15-16, it can observe that with an increase in molarity, there will be more reactions between particles and more gel formation, such as N-A-S-H and C-A-S-H gel which directly indicates the decrease in weight percent of Na in higher molarities from table 6. In lower molarities, because of fewer reactions, there will be more unreacted particles and more water content, and the gel formed will be less viscous, indicating an increase in the weight percent of Na in lower molarities from Table 4.

Table 4. Elements presents in various mixes

Element	Weight%		
	PCC	GPC-2M	GPC-10M
O K	41.25	55.04	46.14
Ca K	33.37	17.97	26.92
Si K	12.29	13.43	6.51
Al K	3.89	6.26	8.12
Na K	0.98	4.29	1.95
Mg K	0.00	1.52	0.64

Higher concentrations of oxygen, silicon, and aluminum have been found in GPC 10M samples from Table 6, confirming the production of aluminum silicate gels. In contrast, the PCC's EDX spectra from Table 4 show relatively high amounts of calcium and silica. These high calcium concentrations, along with the presence of oxygen, silicon, and aluminum, resulted in the development of extra calcium silicate (C-S-H) and calcium aluminosilicate (C-A-S-H). The development of these additional outcomes led to more compact & denser microstructures in PCC samples.

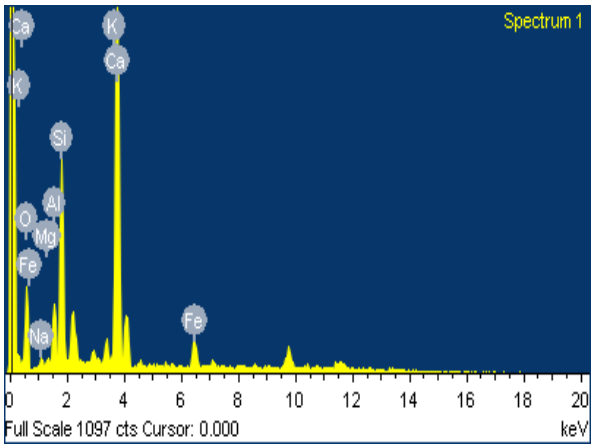

Fig. 14. EDX of PCC mix

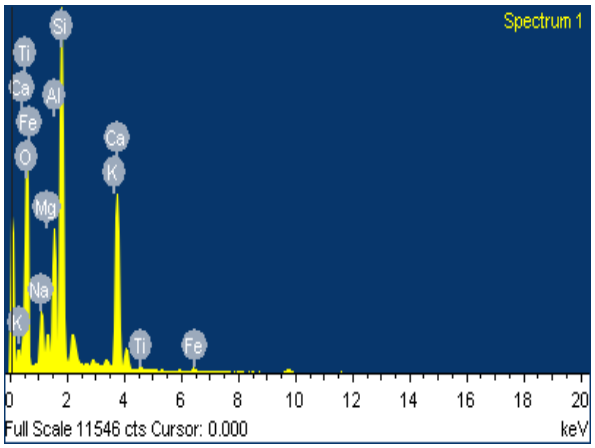

Fig. 15. EDX of GPC-2M mix

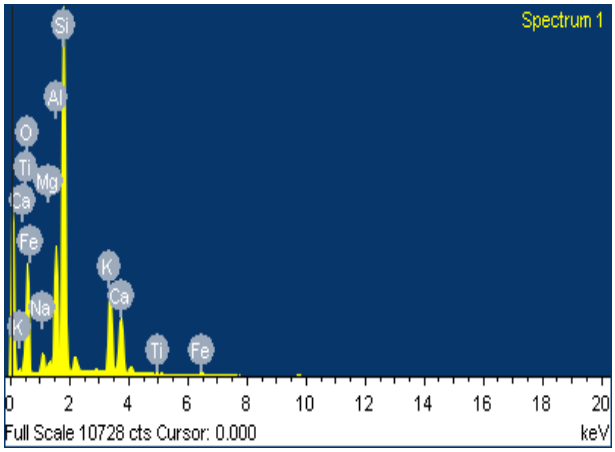

Fig. 16. EDX of GPC-10M mix

4. Conclusions

From the investigation of the effect of NaOH molarity on the various properties of geopolymer concrete (GPC) made with ternary binders, the study concludes that,

- Geopolymer concrete with Nano-silica increased the dissolution rate of Si and Si–Al phases, which strongly affects the polymerization rate. The presence of Nano-silica in the

geopolymer mixture is the key factor in enhancing the polymerization process for its amorphous property and the high specific surface area.

- PCC mix loses greater compressive strength when compared to other mixes. The PCC mix loses 26.81%, and GPC-10M loses 12.26% of its compressive strength after 28 days of immersion in 5% H2SO4 solution.
- The GPC-2M has a higher absorption value of 0.38 mm when compared to the GPC-10M mix, i.e., 0.14 mm, which has absorbed less water in comparison to the other mixes.
- Geopolymer concrete samples at higher molarities are composed of aluminosilicate materials and contain less calcium content and fewer pores when compared with PCC, has undergone a geo-polymerization process forming a three-dimensional network composed of Si-O-Al bonds, which are more resistant to the corrosive effects of sulfuric acid.
- In PCC, it primarily consists of calcium silicate compounds, when exposed to sulfuric acid, these compounds can undergo chemical reactions leading to the formation of gypsum (calcium sulfate) and other soluble compounds. This results in the degradation of the PCC matrix and the weakening of the concrete.
- From FESEM, it can understand that the high cross-sectional area of fly ash components is evidenced at low solution molarity because more unreacted particles, more pores, and less N-A-S-H gel formation led to a less dense matrix.
- Increasing NaOH molarity in the N-A-S-H phase reduced the cross-sectional area of fly ash components and led to the strength development of GPCS.
- EDX spectra confirmed the enhanced dissolution of silicate with an increase in alkali concentration, which indicates the formation of more N-A-S-H gel, and enhanced dissolution of calcium at the Conventional PCC mix, which indicates the formation of more C-S-H gel.
- From the above EDX compositions, at higher alkaline concentrations, due to more polymerization, the weight percent of Na is less, and at lower alkaline concentrations, the weight percent of Na is more.
- In real-world construction, GPC could help build longer-lasting structures with lower maintenance which can provide a sustainable solution by using industrial waste materials.

5. Future Study

This study will be extended to investigate the effect of ternary blend GPC on other durability properties at long-term durations. The authors are also focusing on investigating other microstructural studies, such as FTIR, to understand the effect of nano silica incorporation in the ternary blend.

References

[1] Andrew RM. Global CO2 emissions from cement production, 1928-2018. Earth Syst Sci Data 2019;11:1675–710.

[2] Mikulčić H, Klemeš JJ, Vujanović M, Urbaniec K, Duić N. Reducing greenhouse gasses emissions by fostering the deployment of alternative raw materials and energy sources in the cleaner cement manufacturing process. J Clean Prod 2016;136:119–32. https://doi.org/10.1016/j.jclepro.2016.04.145

[3] Adak D, Sarkar M, Mandal S. Structural performance of nano-silica modified fly-ash based geopolymer concrete. Constr Build Mater 2017;135:430–9. https://doi.org/10.1016/j.conbuildmat.2016.12.111

[4] Adak D, Sarkar M, Mandal S. Effect of nano-silica on strength and durability of fly ash based geopolymer mortar. Constr Build Mater 2014;70:453–9. https://doi.org/10.1016/j.conbuildmat.2014.07.093

[5] Arunkumar K, Muthukannan M, Kumar AS, Ganesh AC, Devi RK. Invention of sustainable geopolymer concrete made with low calcium waste wood ash. World J Eng 2021. https://doi.org/10.1108/WJE-03-2021-0162

[6] Zhang P, Wang K, Wang J, Guo J, Ling Y. Macroscopic and microscopic analyses on mechanical performance of metakaolin/fly ash based geopolymer mortar. J Clean Prod 2021;294:126193. https://doi.org/10.1016/j.jclepro.2021.126193

[7] Arunkumar K, Muthukannan M, Suresh Kumar A, Ganesh AC, Devi RK. Hybrid fibre reinforced eco-friendly geopolymer concrete made with waste wood ash: A mechanical characterization study. Eng Appl Sci Res 2022;49:235–47. https://doi.org/10.14456/easr.2022.26

[8] Hajimohammadi A, Ngo T, Vongsvivut J. Interfacial chemistry of a fly ash geopolymer and aggregates. J Clean Prod 2019;231:980–9. https://doi.org/10.1016/j.jclepro.2019.05.249
[9] Kadarkarai Arunkumar, Muthiah Muthukannan, Arunachalam Sureh Kumar ACG. Mechanical characterisation of waste wood ash-based green geopolymer concrete incorporated with waste rubber and polypropylene fibre. Int J Environ Waste Manag n.d.;XX:(Accepted)
[10] Arunkumar K, Muthukannan M, Suresh Kumar A, Ganesh AC, Devi RK. Production of Eco-Friendly Geopolymer Concrete by using Waste Wood Ash for a Sustainable Environment. Pollution 2021;7:993–1006. https://doi.org/10.22059/POLL.2021.320857.1039
[11] Arunkumar K, Sureshkumar A, Ganesh AC, Parthiban L, Premkumar V. Optimization of hybrid fibre reinforced geopolymer concrete using hardened and durability properties. Res Eng Struct Mater 2023;9:113–30. https://doi.org/10.17515/resm2022.450ma0620
[12] ArunKumar K, Muthukannan M, Raja Abinaya R, Suresh Kumar A. Structural Behaviour of Green Geopolymer Concrete Beams and Columns Made with Waste Wood Ash a Partial Substitution Binder. Mater Sci Forum 2022;1048:333–44. https://doi.org/10.4028/www.scientific.net/MSF.1048.333
[13] Kabir SMA, Alengaram UJ, Jumaat MZ, Yusoff S, Sharmin A, Bashar II. Performance evaluation and some durability characteristics of environmental friendly palm oil clinker based geopolymer concrete. J Clean Prod 2017;161:477–92. https://doi.org/10.1016/j.jclepro.2017.05.002
[14] Arunkumar K, Muthukannan M, Suresh Kumar A, Ganesh AC, Devi RK. Incorporation of Waste Wood Ash and Polypropylene Fibre on the Production of Sustainable GPC. Lect. Notes Civ. Eng., vol. Recent Adv, 2023, p. 693–707. https://doi.org/10.1007/978-981-19-4040-8
[15] Ahmed HU, Mohammed AS, Faraj RH, Qaidi SMA, Mohammed AA. Compressive strength of geopolymer concrete modified with nano-silica: Experimental and modeling investigations. Case Stud Constr Mater 2022;16:e01036. https://doi.org/10.1016/J.CSCM.2022.E01036
[16] Jindal BB, Sharma R. The effect of nanomaterials on properties of geopolymers derived from industrial by-products: A state-of-the-art review. Constr Build Mater 2020;252:119028. https://doi.org/10.1016/j.conbuildmat.2020.119028
[17] Xiao R, Ma Y, Jiang X, Zhang M, Zhang Y, Wang Y, et al. Strength, microstructure, efflorescence behavior and environmental impacts of waste glass geopolymers cured at ambient temperature. J Clean Prod 2020;252:119610 (12 pages). https://doi.org/10.1016/j.jclepro.2019.119610
[18] Veronie J, Sreevidya V. Experimental investigation and comparison on structural behaviour of Ferro-Geopolymer concrete and mortar cubes with conventional cubes. Mater Today Proc 2020;21:531–6. https://doi.org/10.1016/j.matpr.2019.06.693
[19] Bakharev T. Geopolymeric materials prepared using Class F fly ash and elevated temperature curing. Cem Concr Res 2005;35:1224–32. https://doi.org/10.1016/j.cemconres.2004.06.031
[20] Chiranjeevi K, Abraham M, Rath B, Praveenkumar TR. Enhancing the properties of geopolymer concrete using nano-silica and microstructure assessment: a sustainable approach. Sci Rep 2023;13:17302. https://doi.org/10.1038/s41598-023-44491-y
[21] Zidi Z, Ltifi M, Zafar I. Characterization of Nano-Silica Local Metakaolin Based-Geopolymer: Microstructure and Mechanical Properties. Open J Civ Eng 2020;10:143–61. https://doi.org/10.4236/ojce.2020.102013
[22] Yip CK, Lukey GC, Van Deventer JSJ. The coexistence of geopolymeric gel and calcium silicate hydrate at the early stage of alkaline activation. Cem Concr Res 2005;35:1688–97. https://doi.org/10.1016/j.cemconres.2004.10.042
[23] IS:3812 (Part-1). Pulverized fuel ash — specification. Part 1: For use as Pozzolana in cement, Cement Mortar and Concrete (Second Revision). Bur Indian Stand New Delhi, India 2013:1–14.
[24] IS 383: 1970 Specification for Coarse and Fine Aggregates From Natural Sources for Concrete. Bur Indian Stand 1970:1–24.
[25] Arunkumar., Muthukannan M, Suresh kumar A, Chithambar Ganesh A. Mitigation of waste rubber tire and waste wood ash by the production of rubberized low calcium waste wood ash based geopolymer concrete and influence of waste rubber fibre in setting properties and mechanical behavior. Environ Res 2021;194:110661. https://doi.org/10.1016/J.ENVRES.2020.110661
[26] ASTM-C1898-20. Standard Test Methods for Determining the Chemical Resistance of Concrete Products to Acid Attack 2015;i:1–4. https://doi.org/10.1520/D1898-20.1
[27] Liu J, Xing F, Dong B, Ma H, Pan D. Study on water sorptivity of the surface layer of concrete. Mater Struct 2014;47:1941–51. https://doi.org/10.1617/s11527-013-0162-x
[28] ASTM C1585-13. Standard Test Method for Measurement of Rate of Absorption of Water by Hydraulic Cement Concretes. ASTM Int 2013;41:1–6.

Research on Engineering Structures & Materials
www.jresm.org
MIM Research Group

Research Article

Compressive strength prediction of ecofriendly recycled aggregate concrete: A machine learning approach

Vidhya Ramesh [1,a], Gajalakshmi Pandulu [*,1,b], Nisha Khanam [1,c], Oh Chai Lian [2,d]

[1]*Department of Civil Engineering, B. S. Abdur Rahman Crescent Institute of Science & Technology, Chennai - 600 048, Tamil Nadu, India*
[2]*School of Civil Engineering, College of Engineering, Universiti Teknologi MARA, 40450, Shah Alam Selangor, Malaysia*

Article Info

Article History:

Received 12 Dec 2024
Accepted 15 Apr 2025

Keywords:

Soft-computing techniques;
ANN model;
Compressive strength;
Eco-friendly concrete;
Recycled coarse aggregate;
Treated textile wastewater

Abstract

Soft computing techniques, particularly Artificial Intelligence (AI), have become pivotal technologies with transformative potential across various industries worldwide. Among these, Artificial Neural Networks (ANNs) are particularly effective in addressing intricate issues that are beyond the capabilities of conventional methods. In the construction industry, increasing emphasis on sustainability and environmental responsibility has spurred extensive research into innovative materials and methods that enhance the durability of structures while minimizing their environmental footprint. This study is conducted in two phases. Phase I involves the development of an ANN-based soft computing model designed to predict the compressive strength of eco-friendly concrete. In order to train, test, and validate the model, a comprehensive database of experimental data on eco-friendly concrete is compiled. Phase II focuses on validating the ANN model by comparing its predictions with experimental compressive strength data for eco-friendly concrete incorporating recycled aggregate concrete (RAC) and treated textile wastewater (TTW). The model's potential is a dependable instrument for promoting sustainable construction practices which is underscored by the strong correlation between the experimental and ANN-predicted values, as illustrated by the validation results.

© 2025 MIM Research Group. All rights reserved.

1. Introduction

Prediction of the concrete compressive strength using soft-computing techniques has become a pivotal research frontier, fueled by the urgent need to optimize material use, minimize environmental impact, and elevate structural performance. To tackle this challenge, a variety of sophisticated modeling techniques have been employed, including artificial neural networks (ANNs), ensemble algorithms, and statistical methods [2,5,6,15,19]. These models strive to decode the complex interplay between input parameters such as mix proportions [1], curing conditions [2,5], aggregate characteristics [2,5], and mechanical performance [2,5].

In particular, ANNs stand out for their novel methodology that replicates the intricate workings of the human brain. Artificial Neural Networks (ANNs), which process information similarly to biological neural networks, are made up of interconnected nodes or "neurons" grouped into layers. After processing input using an activation function, each neuron in an ANN relays the outcome to neurons in later layers.

*Corresponding author: gajalakshmi@crescent.education
[a]orcid.org/0009-0002-4678-4202; [b]orcid.org/0000-0003-0583-4621; [c]orcid.org/0000-0001-7725-4234; [d]orcid.org/0000-0002-9474-8276
DOI: http://dx.doi.org/10.17515/resm2025-595me1212rs

Several research studies have utilized ANN to develop and assess complex structures, including transmission lines, double-layer grids, and large-scale space frameworks. Hosein Naderpour et al [2] emphasized the importance of developing accurate prediction models for environmentally friendly concrete to meet sustainability goals and regulatory requirements. These studies have consistently demonstrated the superior speed of counter-propagation over back-propagation, as evidenced by the works of Kaveh and Iranmanesh [3], and Kaveh A and Servati [4]. Recent advancements in deep learning have further refined these methodologies. For instance, Khademi et al [5] introduced a neural network model for accurately predicting the compressive strength of concrete. The use of the ANN model on the MATLAB platform has proven to be an efficient tool for predicting the compressive strength of recycled aggregate concrete. In a similar vein, Duan et al. [6] investigated the use of recurrent neural networks (RNN) for modeling time-series data related to concrete curing, effectively forecasting properties such as strength development over time, as noted by Tanhadoust et al. [7]. Furthermore, graph neural networks (GNN) have been utilized to optimize concrete mixtures by analyzing the relationships between various ingredients and their effects on concrete properties, as demonstrated by Chen et al. [8]. These advancements underscore the increasing significance of neural networks in revolutionizing concrete design and analysis.

Recent advancements in predictive modeling have significantly contributed to the refinement and validation of concrete compressive strength prediction models. Many research works focused on learning the intricate relationships between different ingredients used in concrete mixes and their influence on concrete properties, such as compressive strength. For instance, Chopra et al [9] identified that the Levenberg Marquardt (LM) algorithm, when combined with a tan-sigmoid activation function, provides the most accurate predictions for concrete compressive strength. Numerous studies have explored the behavior of Recycled Aggregate Concrete (RAC) incorporating various types of wastewaters, evaluating the viability of using wastewater in concrete production as a sustainable construction practice. Researchers such as Ali Raza et al [10], Asadollahfardi, Mahdavi [11] and Meena, Luhar [12] have reported promising results in similar research.

Despite the utilization of various cutting-edge deep learning techniques for forecasting the compressive strength of concrete, there exists a discernible gap in the development of ANN models specifically tailored for eco-friendly concrete particularly RAC incorporating treated textile wastewater. This research endeavor aims to address this gap by precisely constructing an advanced ANN model to accurately anticipate the compressive strength of sustainable concrete utilizing treated textile wastewater (TTW). The proposed model undergoes comprehensive training, rigorous testing, and meticulous validation using an extensive database compiled from relevant literature. Furthermore, the predicted results were meticulously compared against real-time experimental data to confirm its precision, reliability, and practical application.

2. Methods

2.1. Development of Database: Phase 1

Based on literature reviews, there are several studies were reported examining the compressive strength of eco-friendly concrete using different types of wastewaters. A state-of-the-art database consisting of different mixtures of eco-friendly concrete (RAC concrete) specimens made using different wastewater, was developed based on identified literatures [17 - 39] and compiled as a dataset.

Table 1. Statistical Data of Input Parameters

Parameters	C	FA	NCA	RCA	MA	TTW
	(kg/m3)					
Min	300	400	396.16	0	0	185
Max	541.75	638	1088	594.24	54.17	209
Mean	487.45	620.9	769.35	292.17	40.24	203.33
SD	37.06	26.15	255.98	220.61	23.52	7.81
COV	0.076	0.042	0.332	0.755	0.584	0.038

The selected dataset consists of samples which were cured in PW rather than wastewater and only few dataset samples were cured in treated wastewater. The crucial parameters included in the database are the weight of Cement (C), Fine Aggregate (FA), Natural Coarse Aggregate (NCA), Recycled Coarse Aggregate (RCA), Mineral Additives (MA), treated textile wastewater (TTW) and their Compressive Strength (CS). The histogram of distribution of the statistical data was illustrated in Fig. 1. The statistical data of those input and output parameters were summarized in Table 1 and Table 2.

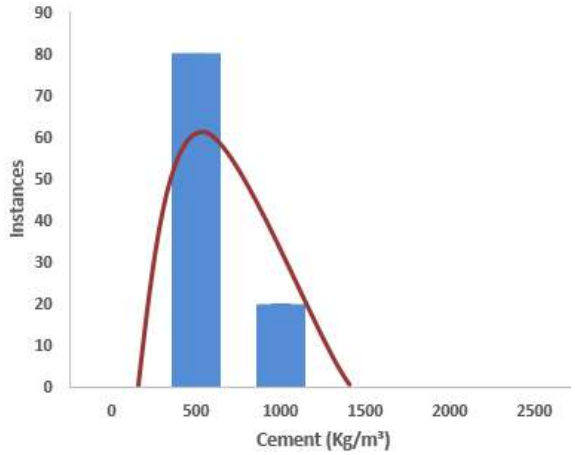

(a)

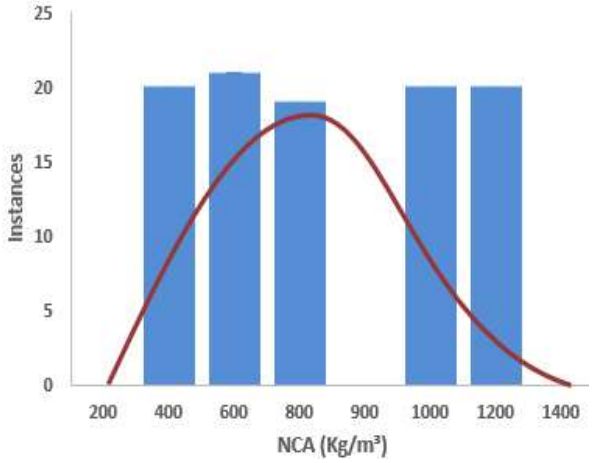

(b)

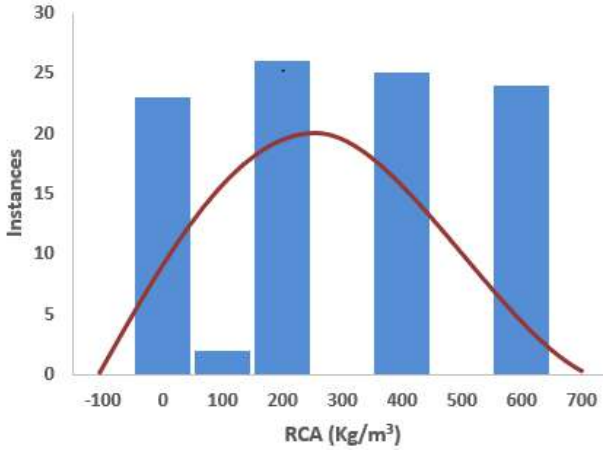

(c)

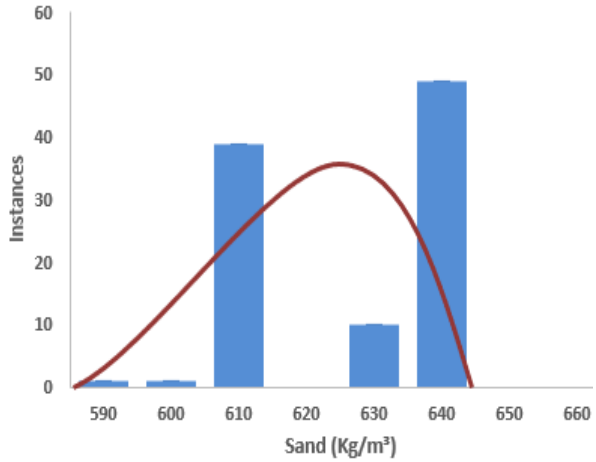

(d)

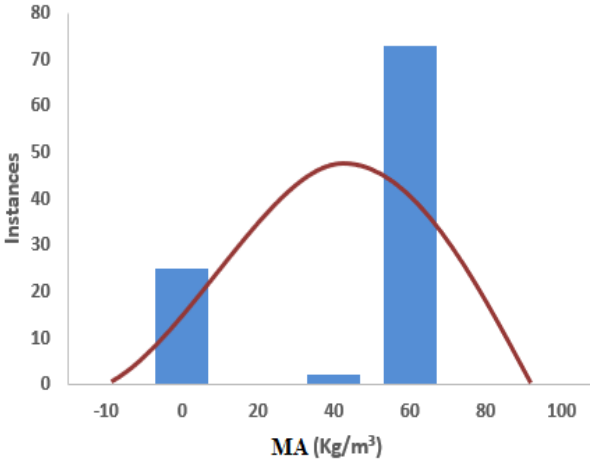

(e)

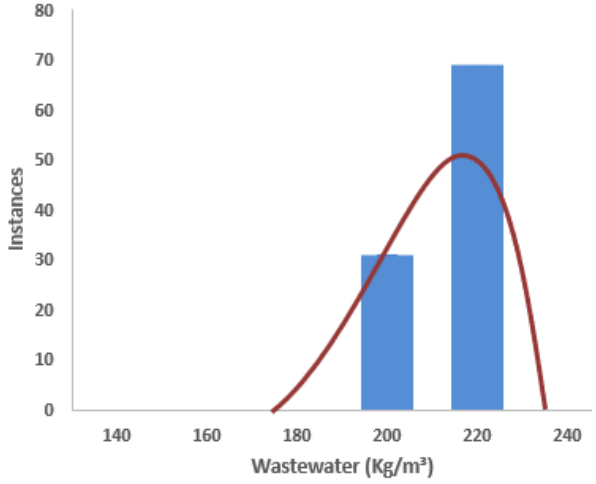

(f)

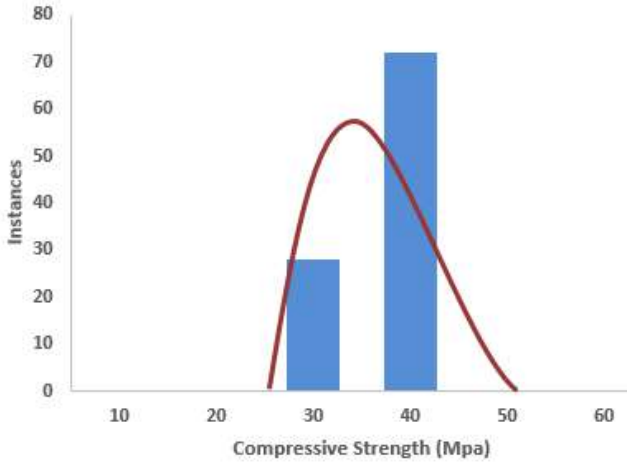

(g)

Fig. 1. Histogram of distribution of the statistical data (a) Quantity of Cement , (b) Quantity of Normal Coarse Aggregate , (c) Quantity of Recycled Coarse Aggregate , (d) Quantity of Sand , (e) Quantity of MA , (f) Quantity of Wastewater , and (g) Compressive Strength

Table 2. Statistical Data of Output Parameters

Parameters	Compressive Strength (MPa)
Min	29.58
Max	35.71
Mean	32.07
SD	2.18
COV	0.068

2.2 ANN Modelling

The research aims to employ advanced ANN methodologies to develop a sophisticated model capable of accurately predicting the compressive strength of eco-friendly concrete. This involves utilizing *MATLAB R2021a* [53], which is a prominent tool in the field of soft computing. This section explains the modeling process involving the use of a comprehensive set of experimental datasets [17-39] to thorough exploration of the relationship between various factors and the compressive strength of eco-friendly concrete.

2.2.1 ANN and It's Architecture

As detailed by Knight [13], these networks consist of interconnected nodes arranged in distinct layers namely input, hidden, and output layers, as shown in Fig.2. ANN's process input data through a network of weighted connections and activation functions to generate predictions or classifications [13]. The essential components of an ANN model include the input, hidden, and output layer, as well as weights and biases [13]. During the training phase, the weights and biases are adjusted through iterative processes to minimize prediction errors, refining the network's accuracy and performance [13]. Moreover, ANNs are versatile tools used for tasks such as regression, classification, and pattern recognition in various domains, such as image recognition and financial forecasting. To achieve more accurate results and reduce errors, increasing the number of epochs is recommended, as suggested by Prasad *et al* [14].

2.2.2 Input, output, and elements of ANN

The study involves the use of input parameters such as cement, fine aggregate, coarse aggregate (natural and recycled aggregate), mineral additive, and treated textile wastewater. It specifically focuses on evaluating the compressive strength of concrete specimens as output parameter. Within the neural network, the raw inputs received from the domain are directly channeled to the hidden

layer, which serves as the core interpretative component. The output layer resulting in the generation of the final target value is achieved by carefully processing these variables. Importantly, this final output closely mirrors the data obtained by the hidden layer, thus demonstrating the intricate processing mechanisms within the network.

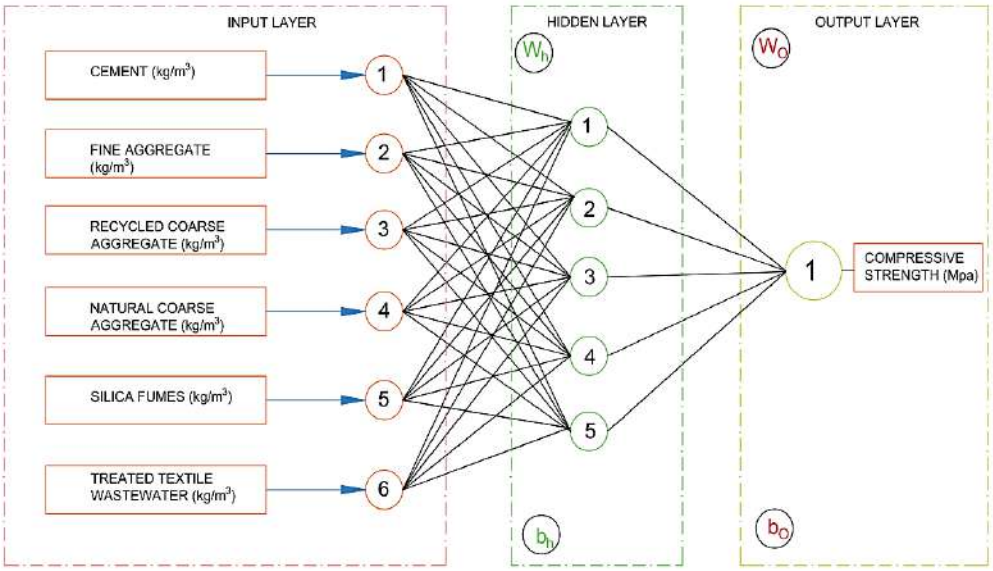

Fig. 2. Neural network structure

2.2.3 Development of the ANN Model

To effectively implement an ANN model for anticipating the compressive strength of concrete, it is essential to have a deep understanding of the internal characteristics that significantly influence the process. These internal parameters encompass a range of crucial elements, including data preprocessing and presentation, the determination of initial synaptic weights, the selection of an appropriate learning rate, the configuration of the number of hidden layers, the specification of the number of neurons in each hidden layer, the choice of activation functions for both hidden and output layers, and the careful consideration of the number of training epochs. These factors collectively contribute to developing a robust feed-forward back-propagation network structure and training process, as highlighted by Sharma *et al* [15].

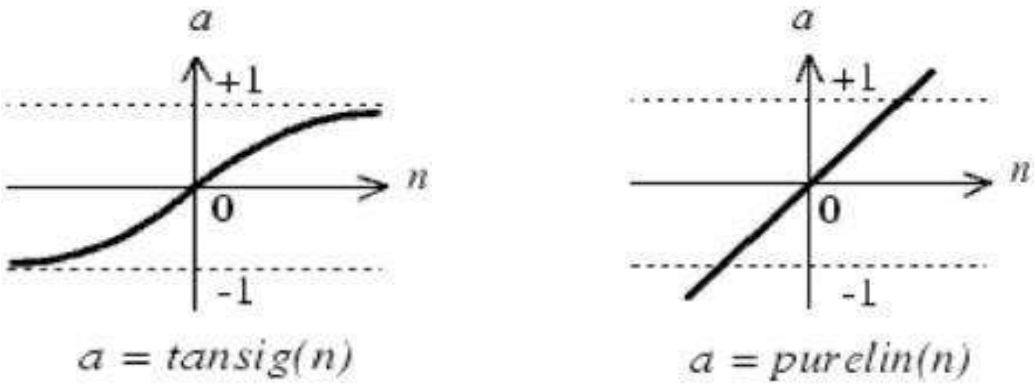

(a) (b)

Fig. 3. Activation Functions (a) Tansigmoid function[51] and (b) Purelin function[51]

In a study by Chopraa *et al* [9], the Levenberg–Marquardt (LM) algorithm [52] was utilized to train a network for predicting concrete strength. The LM algorithm, known for its accuracy and speed, combines the Gauss-Newton and Gradient descent methods for curve fitting, making it a superior choice compared to other algorithms. This technique is widely used to tackle complex multidimensional problems by leveraging the favorable characteristics of multiple algorithms. Notably, the LM algorithm incorporates the neural neighborhood concept, thereby enhancing optimization performance and effectively addressing time and memory constraints. Even in

scenarios where initial assumptions are uncertain, this method demonstrates proficiency in handling systems with numerous uncertain model parameters, yielding optimal solutions.

The dataset was split into training, validation, and testing subsets following the default 70-15-15% split. The Tansigmoid function as presented in Fig.3a. used as the hidden layer activation function, generates data values within the interval [-1, +1]. Furthermore, Fig.3b. provides a visual representation of the weights and biases of both layers, while the activation function of purelin is used for the output layer, a linear transfer function that preserves the input [51]. Detailed design parameters for the suggested ANN model are provided in Table 3 and Fig.4. for a comprehensive understanding [51].

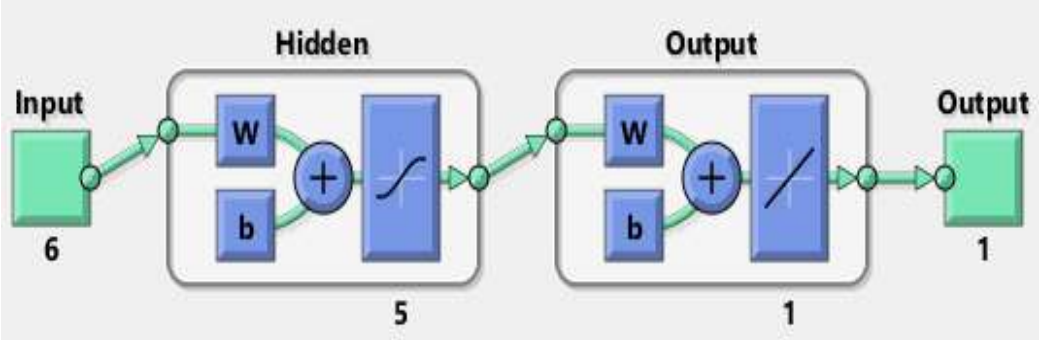

Fig. 4. Architecture Model[51]

Table 3. ANN model design parameters

MATLAB tool	Nftool
Network type	Levenberg–Marquardt
Training function	Trainscg
Data division	Dividerand
Performance analysis	Mean Squared Error (MSE)
Hidden layers	1
Hidden neurons	5
Number of epochs	14
Maximum fail	6
Minimum gradient	1.00 x e-05

2.2.4 Training, Validation, and Testing of ANN model for the specimens cured in TTW

In this extensive and detailed research study, a thorough approach was taken to allocate 70% of the complete dataset for the training of the ANN model. Additionally, 15% of the data was set aside for rigorous testing, while another 15% was dedicated to comprehensive model validation. The training phase was carefully monitored and concluded after approximately 14 epochs for predicting the compressive strength of RAC specimens cured in TTW and after an extensive 23 epochs for RAC specimens cured in Potable Water (PW). Throughout the study, the accuracy of the ANN structure was carefully evaluated using the "Mean Squared Error" (MSE) criterion, offering valuable insights into the complex relationships within the training, testing, and validation data [51].

The performance of the developed ANN model was diligently monitored throughout the training, testing, and validation process [51]. Detailed results are depicted in Fig.5. offering valuable insights into the consistent decrease in error as the number of training epochs progresses. It should be noted that as the network begins to overfit the training data, the validation error may start to increase. According to the default configuration, training ends when a validation error increases six times in a row, and the epoch with the lowest validation error yields the best performance. Furthermore, the highest validation performance is observed at epoch 14 for samples cured in TTW, with a validation performance of 1.00×10^{-5}, and at epoch 23 for samples cured in potable water PW, with a validation performance of 1.00×10^{-3}.

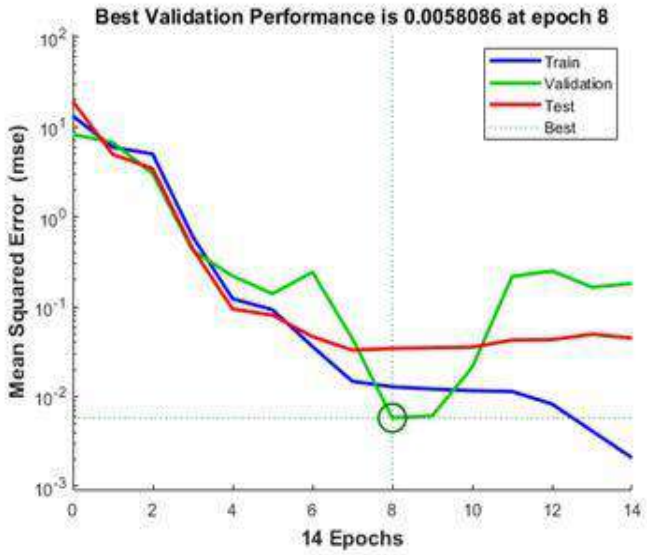

(a)

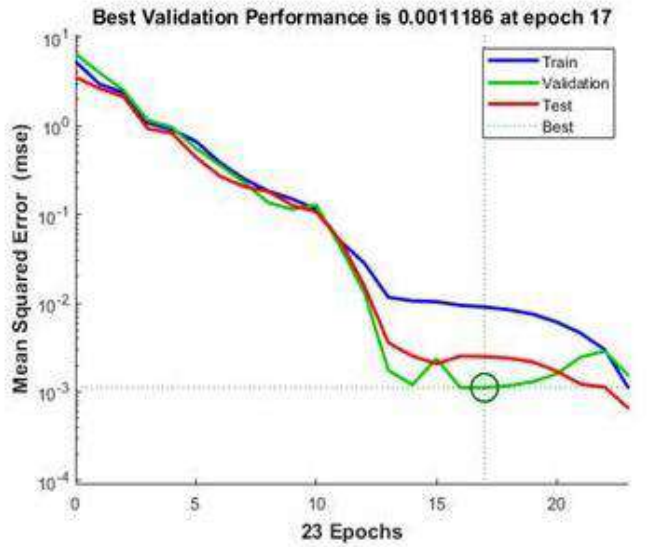

(b)

Fig. 5. (a) Validation performance slot of samples cured in TTW and (b) Validation performance slot of samples cured in PW

The graph demonstrating validation performance utilizes a logarithmic scale to showcase the dynamic trends of mean square error across all datasets. It is crucial to note that the validation and test MSE should mirror the training MSE, which should exhibit a consistent decrease. This pattern signifies an optimal training process. Additionally, the training state plot provides a comprehensive overview of various training statistics, as illustrated in Fig.6. During the training of an ANN model, the gradient assumes a logarithmic value to optimize parameters through iterative updates based on back propagation gradients of the loss function. The specific values 0.31484 and 0.119911 play a critical role in ensuring the model converges towards minimal loss for samples cured in TTW and PW, respectively.

Validation curves play a pivotal role in monitoring model performance and generalization. While the training curve highlights the model's fit to the training data, the validation curve assesses its ability to generalize to unseen data. Any disparities between these two curves can serve as indicators of potential over fitting, prompting the need for adjustments such as regularization or modifications to the architecture of the model. It is imperative to continuously monitor both curves throughout the training process to ensure effective model learning and to mitigate the risk of over fitting.

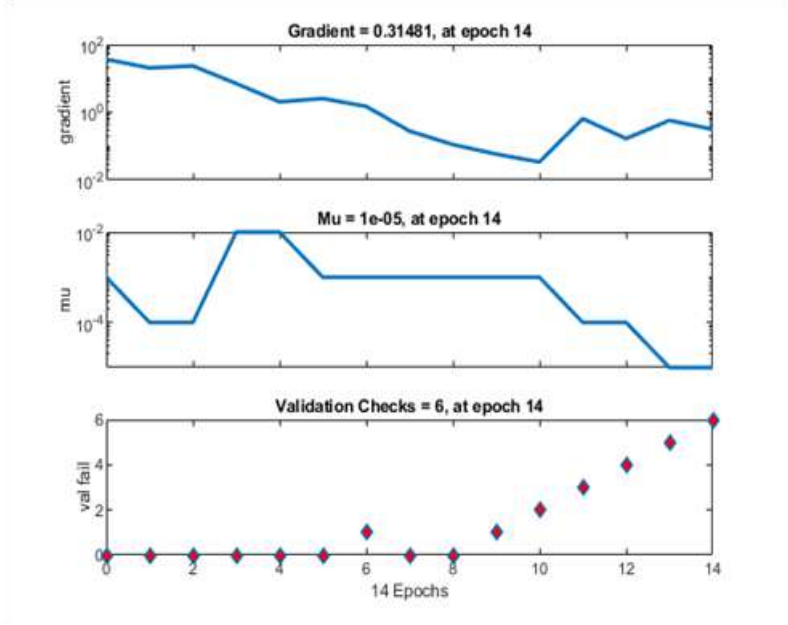

(a)

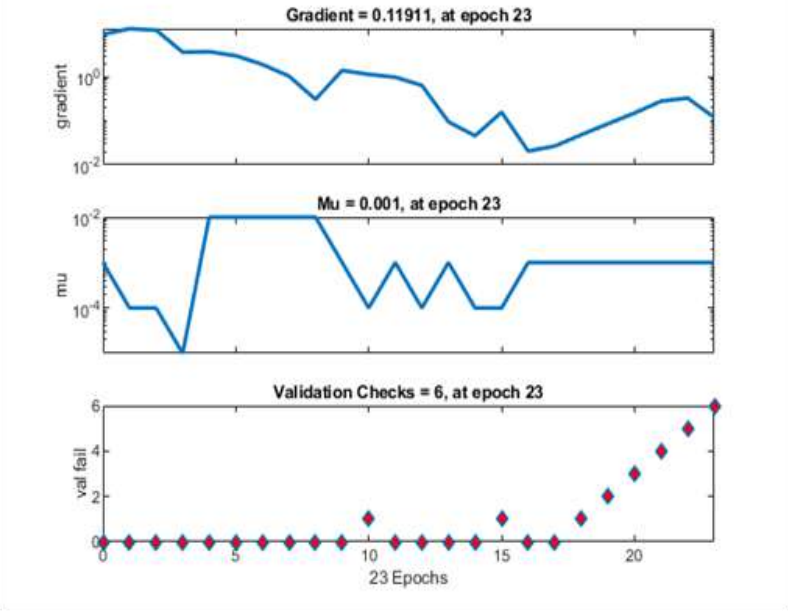

(b)

Fig. 6. (a) Training state plots for samples cured in TTW and (b) Training state plots for samples cured in PW

Fig.7 display regression plots that provide a detailed analysis of the performance of the model across different stages, including training, validation, testing, and the overall process. These plots offer a visual representation of the behavior and effectiveness of the model. Furthermore, the Regression (R) values for samples cured in TTW and PW are presented for each stage of the process. The values obtained during training, validation, and testing are as follows: 0.99873, 0.99902, 0.99678, and 0.99904, 0.99999, and 0.99983 respectively. These values offer insights into the performance of the model and its capability to predict outcomes for samples cured in different environments. The optimal regression for the overall process of samples cured in TTW and PW is represented by 0.99842 and 0.99927, highlighting strong performance across the training, validation, and testing phases for the proposed ANN model.

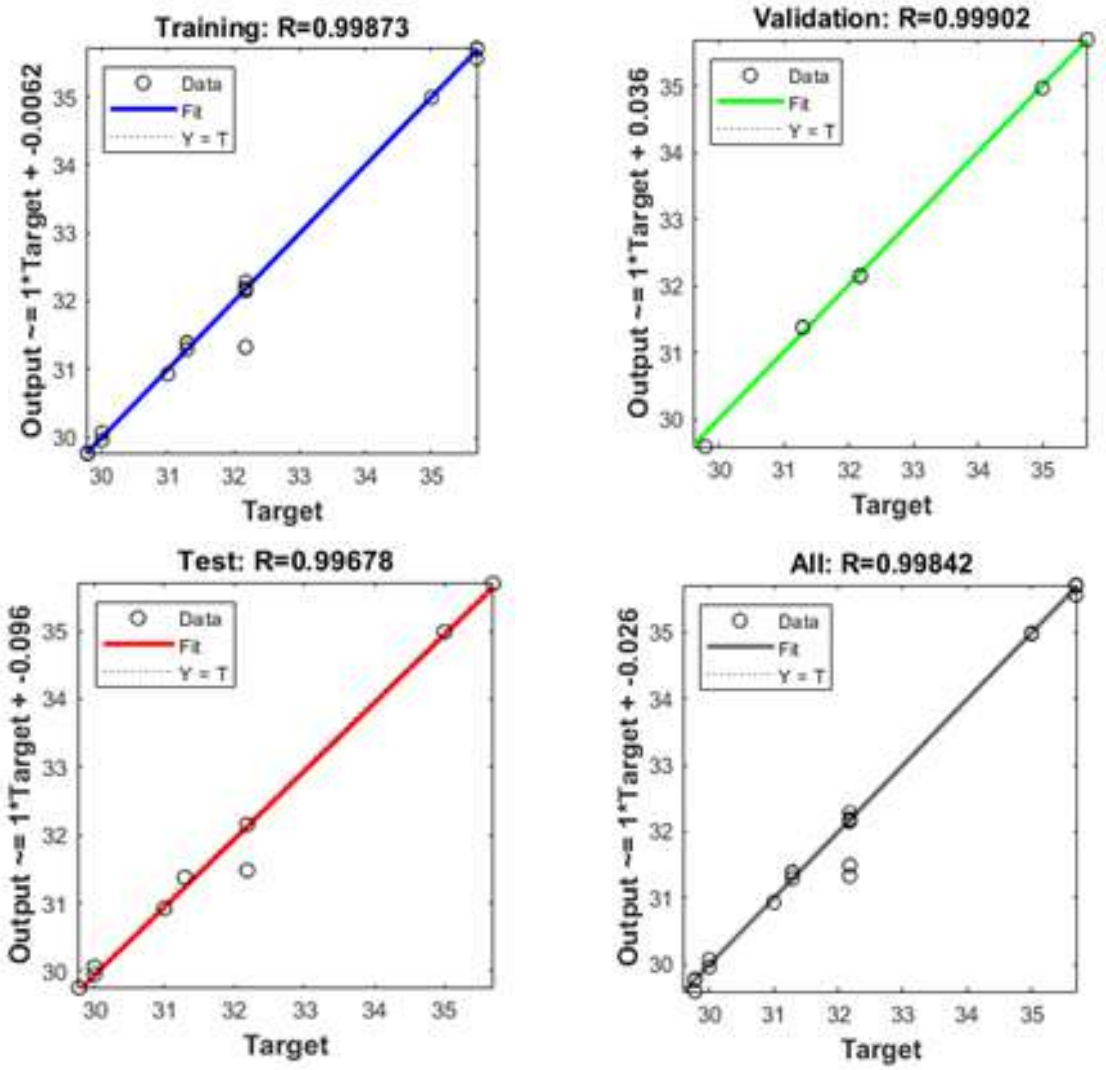
Training: R=0.99873
Data
Fit
Y = T
Output ~= 1*Target + -0.0062
Target
Validation: R=0.99902
Output ~= 1*Target + 0.036
Test: R=0.99678
Output ~= 1*Target + -0.096
All: R=0.99842
Output ~= 1*Target + -0.026

(a)

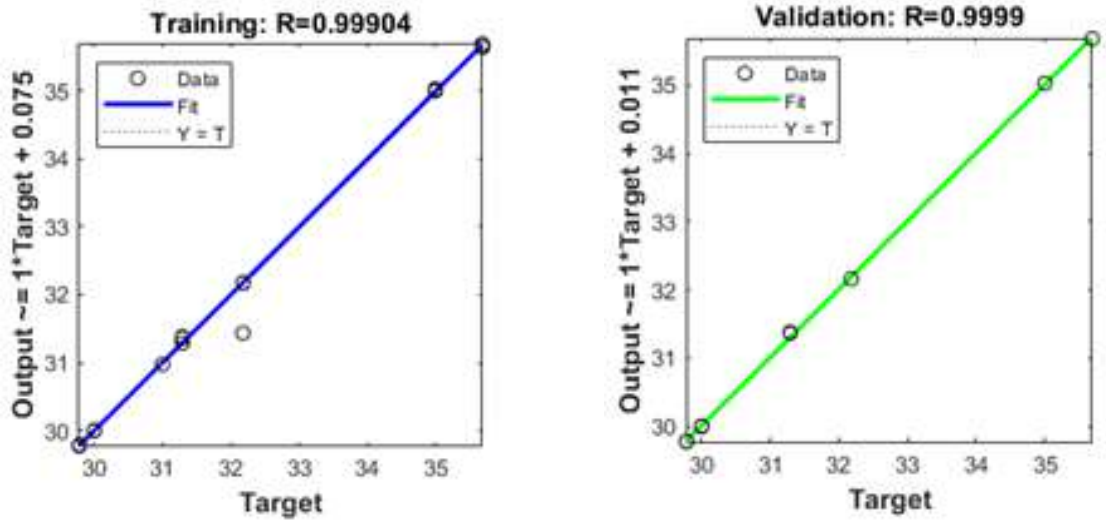
Training: R=0.99904
Data
Fit
Y = T
Output ~= 1*Target + 0.075
Target
Validation: R=0.9999
Output ~= 1*Target + 0.011

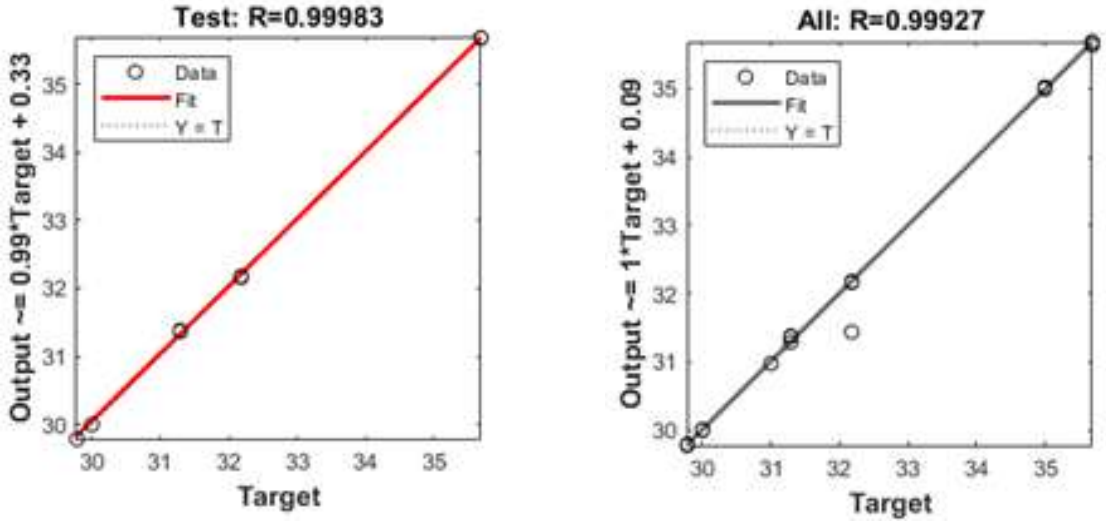

(b)

Fig. 7. (a) Regression plots of the model of samples cured in TTW and (b) Regression plots of the model of samples cured in PW

3. Experimental Program –Phase II

In the experimental program, two sets of eco-friendly concrete specimens were cast. The first set underwent curing in PW, while the second set was cured in TTW. The eco-friendly concrete comprising cement, fly ash, m-sand, RCA, NCA, silica fumes as mineral additives, and 100% of treated TTW for mixing. The experimental results of compressive strength were validated against the developed ANN model.

3.1 Material

In this research, Grade 53 ordinary Portland cement with partial substitution of fly ash was utilized as a binding material, ensuring compliance with the requirements stipulated in IS 4031:1988 [40, 41, 42] and IS 3812:2013 [43], respectively. M-sand was chosen as the fine aggregate, meeting the specifications outlined in IS 383:1970 [44], and its particle size distribution curve lies between the upper and lower limit lines across most of the particle sizes, indicating that it mostly meets the specified grading limits. For finer particles (around 150–300 microns), the M-sand curve closely follows the lower limit, suggesting that it has fewer fines compared to the maximum permissible limit. For coarser particles (around 1.18 mm to 4.75 mm), the M-sand curve is closer to the upper limit. A comprehensive presentation of the properties of cement, fly ash, sand, Normal Coarse aggregate and Recycled Coarse aggregate is provided in Table 4.

Table 4. Properties of cement, fly ash and fine aggregate

Materials	Properties	Values
OPC 53 Grade	Specific gravity	3.12
	Standard consistency (%)	33
	Initial setting time	45 mins
	Final setting time	540 mins
Flyash (Class F)	Specific gravity	2.2
	Fineness modulus	33%
Fine aggregate	Specific gravity	2.5

	Grading zone	Zone II
	Water absorption	1%
NCA	Specific gravity	3.12
	Water absorption	0.933%
	Bulk density	1532 Kg/m^3
RCA	Specific gravity	2.4
	Water absorption	6.5%
	Bulk density	14.35kN/m^3

The M-sand distribution curve indicating a higher percentage of coarser particles within the acceptable range. Particle Distribution curve for Normal Coarse Aggregate shows a gradual increase in percentage passing as particle size increases. There is a rapid rise between 11 mm and 21 mm, after which nearly 100% of particles pass through the sieve at around 21-31 mm sizes. Particle Distribution curve for Recycled Coarse Aggregate follows a similar trend but shows a steeper increase between 11 mm and 21 mm, reaching near 100% passing at 21 mm, slightly earlier than the Normal Coarse Aggregate. During the casting process, TTW was entirely replaced with PW. The fabric wash water from the textile industry, having undergone treatment and repurposing for gardening and equipment washing, was utilized as the TTW for the study.

Table 5. Various features of TTW and PW

S. No.	Parameters	PW	TTW	IS 456:2000 [46] and IS 3025:1986 [47]
1.	pH value	7.0	7.8	6.5 – 8.5
2.	TSS (mg/l)	31	22	2000
3.	TDS (mg/l)	896	383	500
4.	Turbidity (NTU)	0.39	0.92	1
5.	DO (mg/l)	5.2	4	NA
6.	BOD5 (mg/l)	1.3	9.0	30
7.	COD (mg/l)	304	302	250
8.	Electrical Conductivity (µs/cm)	-	5340	500
9.	Hardness (mg/l)	360	510	200
10.	Alkalinity (mg/l)	82	336	600
11.	Bicarbonate (mg/l)	333	410	600
12.	Fluoride (mg/l)	0.4	0.39	1.5
13	Chloride (mg/l)	12	1086	2000 for PCC 500 for RCC
14.	Sulphate (mg/l)	7	515	400
15.	Nitrate (mg/l)	1.4	14	45
16.	Iron (mg/l)	0.23	0.08	0.3

The chemical properties of the TTW were thoroughly examined in the environmental laboratory, and the results were documented in Table 5, by IS 10500:2012 [45]. Subsequent comparison with the permissible limits of IS standards confirmed the suitability of the treated water for the experimental study, and it was consequently employed for casting and curing an environmentally

friendly concrete specimen. In line with existing literature, silica fumes were incorporated as a mineral admixture with RCA to enhance the strength of the environmentally friendly concrete. Silica fumes, a by-product of silicon metals and ferrosilicon alloy production in the silicon industry, comprise fine particles with a high surface area and significant silicon dioxide (SiO_2) content, as per IS 15388: 2003 [48].

3.2 Casting and Testing of Specimens

The study conducted by J G Gonz´alez *et al* [16] involved immersing the RCA in potable water for 10 minutes to reduce water absorption and prepare it for use in concrete. The design mix proportion was determined according to IS 10262:2009 [49] standards. The results of the slump test ranged from 85mm to 100mm.

Fig. 8. RAC Specimens

Table 6. RAC MIX ID and its Constituents

Mix ID	Cement	Flyash	Fine Aggregate	NCA	RCA	Silica Fumes	TWW
				(kg/m^3)			
CCP	270.875	270.875	607	990.4	0	0	207.7
CCW	270.875	270.875	607	990.4	0	0	207.7
RAC1P	243.787	243.787	607	792.32	198.08	54.175	207.7
RAC1W	243.787	243.787	607	792.32	198.08	54.175	207.7
RAC2P	243.787	243.787	607	594.24	396.16	54.175	207.7
RAC2W	243.787	243.787	607	594.24	396.16	54.175	207.7
RAC3P	243.787	243.787	607	396.16	594.24	54.175	207.7
RAC3W	243.787	243.787	607	396.16	594.24	54.175	207.7

Note: CCP – Control Concrete cured in Potable water, CCW – Control Concrete cured in treated textile waste water,RAC1P – 20% RAC replaced with NCA and cured with Potable water,RAC1W – 20% RAC replaced with NCA and cured with treated textile waste water, RAC2P – 40% RAC replaced with NCA and cured with Potable water, RAC2W – 40% RAC replaced with NCA and cured with treated textile wastewater, RAC3P – 60% RAC replaced with NCA and cured with Potable water, RAC3W – 60% RAC replaced with NCA and cured with treated textile wastewater.

Two sets of RAC mixtures, cured using potable water (PW) and treated textile wastewater (TTW), were prepared. Each set included three mixes with recycled coarse aggregate (RCA) replacing

natural coarse aggregate at proportions of 20%, 40%, and 60%. A total of 72 cubes, each measuring 150 mm × 150 mm × 150 mm, were cast to evaluate compressive strength at 7, 14, and 28 days as per IS 516:1959 [50]. This comprehensive approach allowed for a thorough examination of the impact of water absorption reduction and specific mix proportions on the compressive strength of the recycled aggregate concrete. The ingredients and quantities used for each RAC MIX ID are detailed in Table 6. These casted specimens shown in Fig.8. were separated into two sets, one set of specimens were allowed to cure in PW and the other were cured in TTW to understand the implication of behavior of concrete during curing process.

4. Results and Discussions

4.1 ANN - based Formulation

4.1.1 Samples Cured in Potable Water

Based on the detailed analysis presented in the previous section, the proposed ANN model has been shown to effectively and accurately anticipate the compressive strength of eco-friendly concrete. This advanced ANN model can generate a precise empirical formula, which greatly simplifies its practical application in design and offers an innovative solution to the complexities associated with traditional analytical methods. By harnessing the intricate interplay of activation functions and parameters such as weights and biases within the ANN model, a specific and detailed formulation for the compressive strength is derived. The predicted value of the compressive strength (CS), as determined by the ANN model, is intricately linked to the various parameters under consideration and is represented by expression (1) specifically for samples that have been subjected to curing in PW.

$$\rho_u\,(MPa) = -(b_0 + (tan\,h \sum W_h\,x_i + b_h)W_0) - 348.75 \quad (1)$$

Where the number of neurons in the hidden layer (n) is set to 5, the weights (w) and bias (b) of the output layer are represented as 1x1 matrices. The weights (W) and bias (B) of the hidden layer are denoted by 6x6 and 6x1 matrices, respectively. The inputs (X) are represented by a 6x1 matrix. Additionally, the value 348.75 is employed as a neutralizer to effectively counter any noise present in the ANN.

$$[\mathrm{W_h}]_{5\times6} = \begin{bmatrix} 0.6065 & 0.2309 & 0.0234 & 0.6075 & -1.3349 & -1.3517 \\ -1.0391 & -0.7746 & -2.1904 & 2.5389 & 0.3958 & 0.9694 \\ 0.7759 & -1.3490 & 0.1045 & -0.9377 & 1.3261 & 2.0367 \\ -0.0002 & -0.0002 & -0.0009 & 0.0129 & -4.3768 & 1.3441 \\ 0.1657 & -1.0465 & 0.1127 & 0.6578 & 0.6596 & 0.9430 \end{bmatrix}$$

$$[\mathrm{x}]_{6\times1} = \begin{bmatrix} \text{Cement + Flyash} \\ \text{Fine aggregate} \\ \text{RCA} \\ \text{NCA} \\ \text{Silica fumes} \\ \text{TTW} \end{bmatrix} \quad [\mathrm{b_h}]_{5\times1} = \begin{bmatrix} 1.8662 \\ -1.2166 \\ 0.4105 \\ -1.0964 \\ -1.7336 \end{bmatrix} \quad [\mathrm{W_0}]_{5\times1} = \begin{bmatrix} -0.01525 \\ -0.00213 \\ 0.37487 \\ -1.04540 \\ -0.01580 \end{bmatrix}$$

4.1.2 Samples Cured in Treated Textile Wastewater

The target value of the compressive strength (CS), as determined by the ANN model, is a function of the considered parameters and is represented by the expression (2) for samples cured in TTW,

$$\rho_u\,(MPa) = \left(b_0 + \left(tan\,h \sum W_h\,x_i + b_h\right)W_0\right) \quad (2)$$

Where n = 5 (hidden layer neuron); W_0 , $b_0 = -0.1667$ are the weights $_{(1x1)}$ and bias of the output layer; W_h , b_h are the weights $_{(6x6)}$ and bias $_{(6x1)}$ of the hidden layer; x_i are the inputs $_{(6x1)}$ parameter.

$$[W_h]_{6\times6} = \begin{bmatrix} -0.0620 & -0.7718 & 0.8316 & 1.5093 & -1.7292 & -0.8507 \\ 0.4212 & -0.7762 & -0.9105 & 0.0660 & -1.3110 & -0.4138 \\ -0.0294 & -0.9722 & -1.0591 & 1.5184 & -0.2028 & 0.2582 \\ 0.7906 & -0.8036 & 0.6063 & -0.7657 & -0.7199 & 0.9828 \\ -0.5707 & -0.5181 & -0.1744 & -0.5804 & -1.2708 & -0.3845 \end{bmatrix}$$

$$[x]_{6\times1} = \begin{bmatrix} \text{Cement + Flyash} \\ \text{Fine aggregate} \\ \text{RCA} \\ \text{NCA} \\ \text{Silica fumes} \\ \text{TTW} \end{bmatrix} \quad [b_h]_{5\times1} = \begin{bmatrix} 1.4364 \\ -0.1516 \\ -0.7011 \\ 1.0285 \\ -1.9512 \end{bmatrix} \quad [W_0]_{5\times1} = \begin{bmatrix} -0.4890 \\ -0.4587 \\ 0.8756 \\ -0.50475 \\ -0.1121 \end{bmatrix}$$

4.2 Real-Time Experimental Values

The discussion describes about the comparison of 2 sets of concrete samples, focusing on the effects of curing methods and use of recycled aggregate concrete (RAC). The first set consists of conventional concrete samples made using natural aggregate cured in PW and samples made using different proportions of RAC cured in PW which is described in the graphical representation of Fig. 9a. The second set of samples consists of concrete made using natural aggregate cured in TTW and samples made using different proportions of RAC cured in TTW which is described in the graphical representation of Fig. 9b.

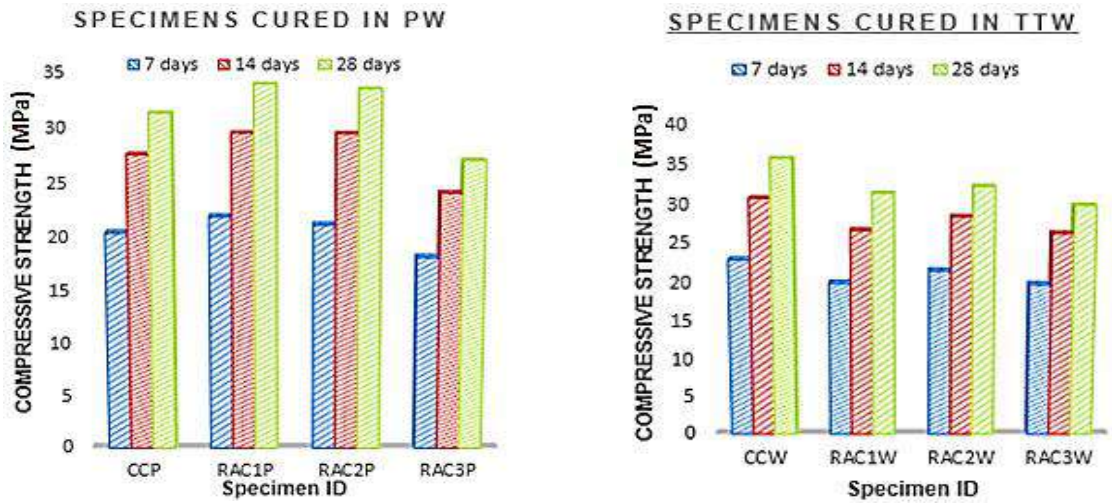

(a) (b)

Fig. 9. (a) CS of Specimens cured in PW and (b) CS of Specimens cured in TTW

According to the experimental results illustrated in the graphs, the conventional concrete specimen cured in PW exhibit a 13% higher compressive strength than the conventional concrete specimen cured in TTW. This finding suggests that curing concrete in PW results in better strength development than those cured in TTW. Similarly, for the RAC samples, a comparison between different curing conditions reveals the following results:

- RAC1P samples (60% of RAC with 40% natural aggregate proportion) when cured in PW show a 9% increase in compressive strength compared to the RAC1W samples cured in TTW.
- RAC2P samples (40% of RAC with 60% natural aggregate proportion RAC with 2% natural aggregate proportion) cured in PW demonstrate a 4% strength gain over the RAC2W samples cured in TTW.
- On the other hand, RAC3W samples (20% of RAC with 80% natural aggregate proportion RAC) cured in TTW show a 10% increase in strength compared to the RAC3P samples cured in PW.

The RAC3W mix cured in TTW yields the highest strength among all samples. Hence to achieve the greater strength of an ecofriendly concrete made using TTW, the RAC3W mix proportion of materials can be recommended for optimal performance.

This study and its findings were based on tests conducted on the concrete samples at the age of 28 days, which is the standard curing time to obtain the higher compressive strength of concrete. Furthermore, the study extends by comparing the experimental results with the ANN model predicted values which is described below.

4.3 Comparison Between Compressive Strength Of Experimental Vs ANN Predicted Values

Further to the extensive study, the ANN model was developed and undergone rigorous analysis and validation through a real-time experimental study using concrete specimens. The extensive research findings indicated that the model exhibited a remarkably low percentage error of less than 1%, offering compelling evidence of its exceptional precision in accurately projecting the compressive strength of environmentally sustainable concrete. These findings are detailed in Table 7, and as a proof Fig.10 visually presents the model's high R^2 value of 0.9974, further emphasizing its reliability.

Table 7. Comparison on CS of Experimental Vs ANN

Specimen Label	CS of the specimens cured in PW (MPa)		Percentage Error (%)
	Experimental	Predicted	
CCP	31.38	31.4	0.09
CCW	35.69	35.62	0.19
RAC1P	34	34.33	0.97
RAC1W	31.29	31.18	0.35
RAC2P	33.56	33.69	0.38
RAC2W	32.18	32.22	0.12
RAC3P	27.07	27.11	0.15
RAC3W	29.78	29.69	0.3

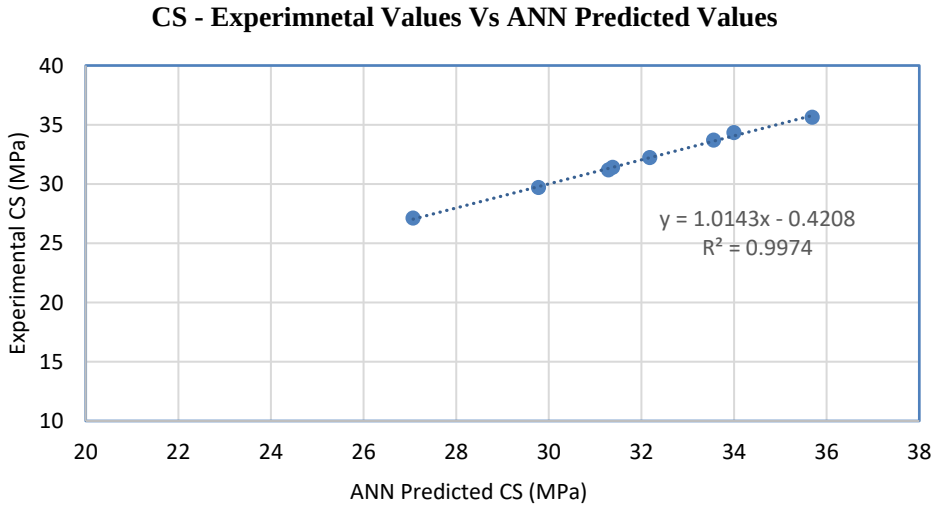

Fig. 10. Linear regression curve

5. Conclusions

The primary objective of the study was to diligently design and constructs an advanced ANN model tailored specifically for accurately predicting the compressive strength of eco-friendly concrete. The development process involved a comprehensive exploration and evaluation of various training algorithms to optimize the network's performance. Additionally, the empirical examination

encompassed a meticulous and in-depth analysis of a wide array of architectural parameters, including but not limited to the number of hidden neurons, learning rate, activation functions, performance goal, and epochs. This thorough analysis aimed to fine-tune the neural network to ensure superior predictive capabilities and overall model performance.

- The use of treated textile water in RAC provides an alternative solution for water conservation in concrete production, aligning with sustainable construction practices.
- After conducting numerous trials, it was observed that the ANN model with 6 neurons in the hidden layer exhibited exceptional performance, yielding a remarkable regression value of R = 0.91635 as compared to the experimental results.
- The proposed empirical equation not only provides a reliable method for calculating the compressive strength of eco-friendly concrete but also showcases a strong alignment with current and real-time testing results.
- Furthermore, the validation of the developed model was exactly carried out through real-time experimental studies involving RAC specimens, thereby revealing a negligible percentage error of less than 1%. This underscores the model's high accuracy in predicting concrete compressive strength, with minimal margin for errors.
- The linear regression value for the experimental versus predicted compressive strength was determined to be 0.9974, highlighting the exceptional accuracy of the model's predictions in comparison to the experimental values. This serves as a testament to the commendable performance and reliability of the developed model.

However, the proposed model does have limitations, notably its applicability restricted to recycled aggregate concrete cube specimens. Based on the analysis of the results, it is determined that the implementation of the ANN approach exhibits substantial promise for accurately predicting the compressive strength of eco-friendly concrete, indicating its potential to revolutionize the field of concrete strength prediction. Future endeavors should focus on extending similar models to encompass the complete mechanical properties of RAC beams and columns with different cross-sections. Attention must be given to optimizing design parameters, considering the computational intensity of these neural network models.

References

[1] Mollah MYA, Hossain MK. Modeling of concrete mix design using neural networks. Computers and Concrete, An International Journal. 2013;11(6):559-72.
[2] Naderpour H, Rafiean AH, Fakharian P. Compressive strength prediction of environmentally friendly concrete using artificial neural networks. Journal of Building Engineering. 2018;16:213-9. https://doi.org/10.1016/j.jobe.2018.01.007
[3] Kaveh A, Iranmanesh A. Comparative study of backpropagation and improved counterpropagation neural nets in structural analysis and optimization. International Journal of Space Structures. 1998;13(4):177-85. https://doi.org/10.1177/026635119801300401
[4] Kaveh A, Servati H. Design of double layer grids using backpropagation neural networks. Computers & Structures. 2001;79(17):1561-8. https://doi.org/10.1016/S0045-7949(01)00034-7
[5] Khademi F, Jamal SM, Deshpande N, Londhe S. Predicting strength of recycled aggregate concrete using artificial neural network, adaptive neuro-fuzzy inference system and multiple linear regression. International Journal of Sustainable Built Environment. 2016;5(2):355-69. https://doi.org/10.1016/j.ijsbe.2016.09.003
[6] Duan ZH, Kou SC, Poon CS. Prediction of compressive strength of recycled aggregate concrete using artificial neural networks. Construction and Building Materials. 2013;40:1200-6. https://doi.org/10.1016/j.conbuildmat.2012.04.063
[7] Tanhadoust A, Yang TY, Dabbaghi F, Chai HK, Mohseni M, Emadi SB, et al. Predicting stress-strain behavior of normal weight and lightweight aggregate concrete exposed to high temperature using LSTM recurrent neural network. Construction and Building Materials. 2023;362:129703. https://doi.org/10.1016/j.conbuildmat.2022.129703
[8] Chen F, Xu W, Wen Q, Zhang G, Xu L, Fan D, et al. Advancing concrete mix proportion through hybrid intelligence: A multi-objective optimization approach. Materials. 2023;16(19):6448. https://doi.org/10.3390/ma16196448
[9] Chopra P, Sharma RK, Kumar M. Artificial neural networks for the prediction of compressive strength of concrete. International Journal of Applied Science and Engineering. 2015;3(3):187-204.

[10] Raza A, Rafique U, Haq F. Mechanical and durability behavior of recycled aggregate concrete made with different kinds of wastewater. Journal of Building Engineering. 2021;34:101950. https://doi.org/10.1016/j.jobe.2020.101950
[11] Asadollahfardi G, Mahdavi AR. The feasibility of using treated industrial wastewater to produce concrete. Structural Concrete. 2019;20(1):123-32. https://doi.org/10.1002/suco.201700255
[12] Meena K, Luhar S. Effect of wastewater on properties of concrete. Journal of Building Engineering. 2019;21:106-12. https://doi.org/10.1016/j.jobe.2018.10.003
[13] Knight K. Connectionist ideas and algorithms. Communications of the Association for Computing Machinery. 1990;33(11):58-74. https://doi.org/10.1145/92755.92764
[14] Prasad BR, Eskandari H, Reddy BV. Prediction of compressive strength of SCC and HPC with high volume fly ash using ANN. Construction and Building Materials. 2009;23(1):117-28. https://doi.org/10.1016/j.conbuildmat.2008.01.014
[15] Sharma AK, Sharma RK, Kasana HS. Prediction of first lactation 305-day milk yield in Karan Fries dairy cattle using ANN modeling. Applied Soft Computing. 2007;7(3):1112-20. https://doi.org/10.1016/j.asoc.2006.07.002
[16] González JG, Robles DR, Valdés AJ, Morán del Pozo JM, Romero MIG. Influence of moisture states of recycled coarse aggregates on the slump test. Advanced Materials Research. 2013;42:379-83. https://doi.org/10.4028/www.scientific.net/AMR.742.379
[17] Çakır Ö. Experimental analysis of properties of recycled coarse aggregate (RCA) concrete with mineral additives. Construction and Building Materials. 2014;68:17-25. https://doi.org/10.1016/j.conbuildmat.2014.06.032
[18] Borger J, Carrasquillo RL, Fowler DW. Use of recycled wash water and returned plastic concrete in the production of fresh concrete. Advanced Cement-Based Materials. 1994;1(6):267-74. https://doi.org/10.1016/1065-7355(94)90035-3
[19] Chithra S, Kumar SS, Chinnaraju K, Ashmita FA. A comparative study on the compressive strength prediction models for high performance concrete containing nano silica and copper slag using regression analysis and artificial neural networks. Construction and Building Materials. 2016;114:528-35. https://doi.org/10.1016/j.conbuildmat.2016.03.214
[20] Hwang K, Noguchi T, Tomosawa F. Prediction model of compressive strength development of fly-ash concrete. Cement and Concrete Research. 2004;34(12):2269-76. https://doi.org/10.1016/j.cemconres.2004.04.009
[21] Yan S, Sagoe-Crentsil K, Shapiro G. Properties of cement mortar incorporating de-inking wastewater from waste paper recycling. Construction and Building Materials. 2012;29:51-5. https://doi.org/10.1016/j.conbuildmat.2011.09.012
[22] Nirmalkumar K, Sivakumar V. Corrosion studies on concrete using treated and untreated textile effluent and impact of corrosion inhibitor. Journal of Sustainable Development. 2008;1(3):68-72. https://doi.org/10.5539/jsd.v1n3p68
[23] Padmini AK, Ramamurthy K, Mathews MS. Influence of parent concrete on the properties of recycled aggregate concrete. Construction and Building Materials. 2009;23(2):829-36. https://doi.org/10.1016/j.conbuildmat.2008.03.006
[24] Behnood A, Golafshani EM. Predicting the compressive strength of silica fume concrete using hybrid artificial neural network with multi-objective grey wolves. Journal of Cleaner Production. 2018;202:54-64. https://doi.org/10.1016/j.jclepro.2018.08.065
[25] Charalampakis AE, Papanikolaou VK. Machine learning design of R/C columns. Engineering Structures. 2021;226:111412. https://doi.org/10.1016/j.engstruct.2020.111412
[26] Kaveh A, Gholipour Y, Rahami H. Optimal design of transmission towers using genetic algorithm and neural networks. International Journal of Space Structures. 2008;23(1):1-19.https://doi.org/10.1260/026635108785342073
[27] Heidari A, Hashempour M, Tavakoli D. Using of backpropagation neural network in estimation of compressive strength of waste concrete. Journal of Soft Computing in Civil Engineering. 2017;1(1):54-64.
[28] Asadollahfardi G, Delnavaz M, Rashnoiee V, Ghonabadi N. Use of treated domestic wastewater before chlorination to produce and cure concrete. Construction and Building Materials. 2016;105:253-61. https://doi.org/10.1016/j.conbuildmat.2015.12.039
[29] Elchalakani M, Elgaali E. Sustainable concrete made of construction and demolition wastes using recycled wastewater in the UAE. Journal of Advanced Concrete Technology. 2012;10(3):110-25. https://doi.org/10.3151/jact.10.110
[30] Ahmed S, Alhoubi Y, Elmesalami N, Yehia S, Abed F. Effect of recycled aggregates and treated wastewater on concrete subjected to different exposure conditions. Construction and Building Materials. 2021;266:120930. https://doi.org/10.1016/j.conbuildmat.2020.120930

[31] Raza A, Ali B, Haq FU, Awais M, Jameel MS. Influence of fly ash, glass fibers and wastewater on production of recycled aggregate concrete. Materiales de Construcción. 2021;1(343):e253. https://doi.org/10.3989/mc.2021.15120
[32] Raza A, Shah SAR, Kazmi SNH, Ali RQ, Akhtar H, Fakhar S, et al. Performance evaluation of concrete developed using various types of wastewaters: A step towards sustainability. Construction and Building Materials. 2020;262:120608. https://doi.org/10.1016/j.conbuildmat.2020.120608
[33] Gómez-Soberón JM. Porosity of recycled concrete with substitution of recycled concrete aggregate: An experimental study. Cement and Concrete Research. 2002;32(8):1301-11. https://doi.org/10.1016/S0008-8846(02)00795-0
[34] Yang KH, Chung HS, Ashour A. Influence of type and replacement level of recycled aggregates on concrete properties. 2008.
[35] Matias D, De Brito J, Rosa A, Pedro D. Mechanical properties of concrete produced with recycled coarse aggregates-Influence of the use of superplasticizers. Construction and Building Materials. 2013;44:101-9. https://doi.org/10.1016/j.conbuildmat.2013.03.011
[36] de Almeida MEP, Tonetti AL. Eco-friendly concrete: Combining treated wastewater and recycled aggregates. Water Science & Technology. 2024;90(3):807-23. https://doi.org/10.2166/wst.2024.253
[37] Ramadevi K, Chitra R. Concrete using recycled aggregates. International Journal of Civil Engineering and Technology. 2017;8(9):413-9.
[38] Elsayed KMNI, Guico GBF, Rustum R. Concrete behavior using recycled wastewater. GEOMATE Journal. 2023;25(110):192-9. https://doi.org/10.21660/2023.110.s8647
[39] Sheen YN, Wang HY, Juang YP, Le DH. Assessment on the engineering properties of ready-mixed concrete using recycled aggregates. Construction and Building Materials. 2013;45:298-305. https://doi.org/10.1016/j.conbuildmat.2013.03.072
[40] Bureau of Indian Standards. IS 4031(Part 11):1988 Methods of physical test for hydraulic cement. Part 11: Determination of density.
[41] Bureau of Indian Standards. IS 4031(Part 4):1988 Methods of physical test for hydraulic cement. Part 4: Determination of consistency of standard cement paste.
[42] Bureau of Indian Standards. IS 4031(Part 5):1988 Methods of physical test for hydraulic cement. Part 5: Determination of initial and final setting times.
[43] Bureau of Indian Standards. IS 3812(Part 1):2013 Pulverized fuel ash - Specification. Part 1: For use as pozzolana in cement, cement mortar and concrete.
[44] Bureau of Indian Standards. IS 383:1987 Specification for coarse and fine aggregates from natural sources for concrete.
[45] Bureau of Indian Standards. IS 10500:2012 Drinking water - Specifications.
[46] Bureau of Indian Standards. IS 456:2000 Plain and reinforced concrete - Code of practice.
[47] Bureau of Indian Standards. IS 3025(Part 1-22):1986 Methods of sampling and test for water and wastewater.
[48] Bureau of Indian Standards. IS 15388:2003 Silica fume - Specification.
[49] Bureau of Indian Standards. IS 10262:2019 Concrete mix proportioning - Guidelines.
[50] Bureau of Indian Standards. IS 516:1959 Methods of test for strength of concrete.
[51] Veerapandian V, Pandulu G, Jayaseelan R, Mohammed Asif MY. Simplified deep-learning approach for estimating the ultimate axial load of circular composite columns. Asian Journal of Civil Engineering. 2023.
[52] Levenberg K. A method for the solution of certain nonlinear problems in least squares. Quarterly of Applied Mathematics. 1944;2(2):164-8. https://doi.org/10.1090/qam/10666
[53] MathWorks. MATLAB R2021a [Computer software]. MathWorks; 2021. https://www.mathworks.com/products/matlab.html

Research on Engineering Structures & Materials
www.jresm.org

Research Article

Compressive and tensile strength of fly ash based lightweight geopolymer concrete with variation of Na_2SiO_3 and NaOH using expanded polystyrene

Rifkah [1,a], Saloma [*,2,b], Siti Aisyah Nurjannah [2,c]

[1]*Engineering Science, Doctoral Program, Faculty of Engineering, Universitas Sriwijaya, Indonesia*
[2]*Department of Civil Engineering, Faculty of Engineering, Universitas Sriwijaya, Indonesia*

Article Info

Article History:

Received 08 Mar 2025

Accepted 07 June 2025

Keywords:

Lightweight geopolymer concrete;
Fly ash;
Expanded polystyrene;
Fresh material properties;
Compressive strength;
Tensile strength

Abstract

Conventional concrete production contributes significantly to global CO2 emissions, encouraging a sustainable alternative material. Geopolymer concrete, exceptionally lightweight geopolymer concrete (LWGC), an innovative approach, offers a promising solution by utilizing industrial by-products like fly ash while reducing environmental impact. However, optimizing alkali activator ratios remains a critical challenge in developing LWGC with adequate mechanical properties for structural applications. This study investigates the effect of varying sodium silicate (Na_2SiO_3) to sodium hydroxide (NaOH) ratios on the properties of LWGC synthesized from fly ash and expanded polystyrene (EPS). Three different Na_2SiO_3/NaOH ratios (1.5, 2.0, and 2.5) were examined to evaluate their effects on fresh and hardened concrete properties. Fresh concrete properties were assessed through setting time and slump flow tests, while hardened concrete was evaluated for density, compressive strength, and splitting tensile strength at 14, and 28 days. Results demonstrated that increasing the Na_2SiO_3/NaOH ratio decreased workability but enhanced mechanical properties, with the 2.5 ratio achieving the highest 28-day compressive strength (22.85 MPa) and splitting tensile strength (1.43 MPa). All LWGC variations exhibited densities between 1080-1250 kg/m^3, qualifying them as lightweight concrete according to ASTM C125 standards. Polynomial regression analysis revealed a non-linear positive correlation between activator ratio and mechanical strength development. This research demonstrates that fly ash-based LWGC with EPS aggregate can be effectively engineered by optimizing the alkali activator ratio, providing sustainable construction materials with mechanical properties suitable for structural applications while contributing to circular economy principles through waste utilization properties.

© 2025 MIM Research Group. All rights reserved.

1. Introduction

The production of Portland cement contributes significantly to global CO_2 emissions, accounting for approximately 7-8% of anthropogenic CO_2 releases [1]. Conventional concrete, a remarkable building material composite, comprises 12% cement, 8% water, and 80% aggregate. Annually, global production includes 1.6 billion tons of cement, nearly 10 billion tons of sand and rock, plus 1 billion tons of water. With total consumption reaching 12.6 billion tons of raw materials yearly, the concrete industry stands as the world's largest consumer of natural resources[2]. Cement, one of the most widely utilized materials for construction, plays a crucial role as the primary binder in

*Corresponding author: salomaunsri@gmail.com
[a]orcid.org/0009-0003-4182-900X; [b]orcid.org/0000-0003-4302-0282; [c]orcid.org/0000-0003-3058-592X
DOI: http://dx.doi.org/10.17515/resm2025-734me0308rs

concrete [3]. However, developing sustainable construction materials has become a critical focus in recent years due to the increasing demand for friendly and high-performance building materials [4]. Geopolymer concrete has emerged as a promising alternative to traditional Portland cement-based concrete. Concrete technology innovation was also developed so that concrete has a lighter specific gravity because standard concrete has a reasonably high weight and reduces the dead load of concrete in buildings [5,6]. Lightweight concrete (LW) has a lighter specific gravity than conventional concrete [7,8]. LW is a suitable replacement for normal concrete, especially in applications prioritizing weight reduction and insulation [9].

Among the sustainable concrete innovations, Geopolymer concrete (GC) is primarily composed of industrial by-products such as fly ash and offers several advantages, including lower carbon emissions, enhanced durability, and better chemical resistance [10]. Geopolymers, formed by polymerizing organic and inorganic materials, can be made from recycled silica-rich sources [11]. Fly ash, a waste product from coal-fired power plants is a pozzolanic material that reacts with alkali activators to form a binding matrix in geopolymer systems. Commonly classified as waste, fly ash is a material generated by burning or combustion. These industrial by-products mitigate the environmental impact of waste disposal and reduce the carbon footprint associated with cement production [12,13,14]. As a sustainable and composite material activated by alkaline substances, geopolymer concrete (GC) offers the construction industry a valuable tool for reducing carbon footprint by providing lower-carbon alternatives to traditional cement [15]. When combined with appropriate alkaline activators, typically sodium silicate (Na_2SiO_3) and sodium hydroxide (NaOH), fly ash can form strong cementitious materials through geo-polymerization reactions.

The combination of lightweight concrete and geopolymer concrete has led to the development of lightweight geopolymer concrete (LWGC), representing an advancement in sustainable material design. Expanded Polystyrene (EPS), known for its ultra-lightweight properties and excellent thermal insulation characteristics, has been used as a lightweight concrete aggregate [16]. EPS offers reduced density, improved workability, and enhanced thermal performance. It also presents a sustainable solution for EPS disposal, addressing environmental concerns [17]. However, EPS incorporation offers benefits such as reduced density, improved workability, and enhanced thermal performance while presenting a sustainable solution for EPS disposal.

Geopolymers with a combination of lightweight concrete have been limitedly investigated (18). Previous studies have investigated various aspects of fly ash-based geopolymer concrete and lightweight concrete separately. LWGC presents a promising solution for creating environmentally friendly concrete that combines the advantages of lightweight materials with enhanced performance. Its reduced mass helps address structural load issues, thereby lessening the strain on building foundations while maintaining durability and strength [19]. Studies have shown that incorporating EPS can reduce density and improve thermal insulation but may affect mechanical properties and durability, a study [20] show the result in tha density range 1321-1912 kg/m3.

The optimization of the Na_2SiO_3/NaOH ratio in lightweight geopolymer concrete remains a critical area requiring further investigation, particularly regarding the combined effects of activator ratio variation and EPS incorporation. This study investigates the influence of various Na_2SiO_3/NaOH ratios on the compressive and tensile strength of fly ash-based lightweight geopolymer concrete containing expanded polystyrene with fresh material properties. The research aims to optimize the alkaline activator composition to achieve desirable mechanical properties while maintaining the lightweight characteristics of the concrete. The findings will contribute to developing sustainable construction materials that combine reduced environmental impact, lightweight properties, and adequate structural performance.

1.1. Research Significance

More studies exploring various material properties in LWGC have been investigated and published. However, the potential of LWGC using EPS as lightweight aggregate, particularly regarding its mechanical properties and mix design optimization, has not yet been thoroughly investigated and requires further research. This study aimed to acknowledge and evaluate the LWGC using EPS, focusing on mechanical, compressive, and tensile strength properties. The research concerns

construction issues and uses fly ash as the primary material in geopolymer concrete, one alternative to traditional Portland cement and a way to reduce emissions.

The study investigated optimizing alkaline activator ratios, Na_2SiO_3, and NaOH variation from 1.5, 2.0, and 2.5 to optimize the polymerization process. This study also determines the optimal balance between alkali activator ratios for enhanced mechanical properties, targeting compressive strength above 17 Mpa and split tensile strength exceeding 1.5 Mpa for structural applications. It also includes detailed mechanical property analysis to mix design parameters and concrete performance.

This study's unique factor is its focus on incorporating Expanded Polystyrene (EPS) as a lightweight aggregate of 25% by concrete volume. The justification of 25% is based on concrete trial as substitution of fine aggregate and related study The analysis of particle size influence was performed using a substitution level of 25%, carefully selected to facilitate clear observation of the interactive dynamics between sand and plastic components [21]. EPS provides an innovative solution to reduce concrete density while maintaining structural integrity through mixed proportions and curing conditions [22]. This study fills a knowledge gap in lightweight applications and supports the management of EPS recycling waste.

LWGC offers potential cost reduction in construction through waste materials and enables significant material behavior, which leads to more efficient structural design and application in elements. This research also provides a structure for future sustainable construction material research. An investigation of concrete mechanical properties, integrated with the reuse of waste materials, provides a structure to improve LWGC. Future research may optimize lightweight geopolymer concrete formulations, particularly in long-term durability, thermal resistance, and microstructural analysis.

2. Materials and Methods

The production of LWGC is shown in Fig. 1. Production begins with fly ash as a precursor mixed with sand and EPS. The alkali activator is Sodium Hydroxide, and Sodium Silicate is added in variation ratios of 1.5, 2.0, and 2.5. All materials are mixed through the LWGC mix design and cured in an oven at 60^{0}C for 24 hours to produce LWGC.

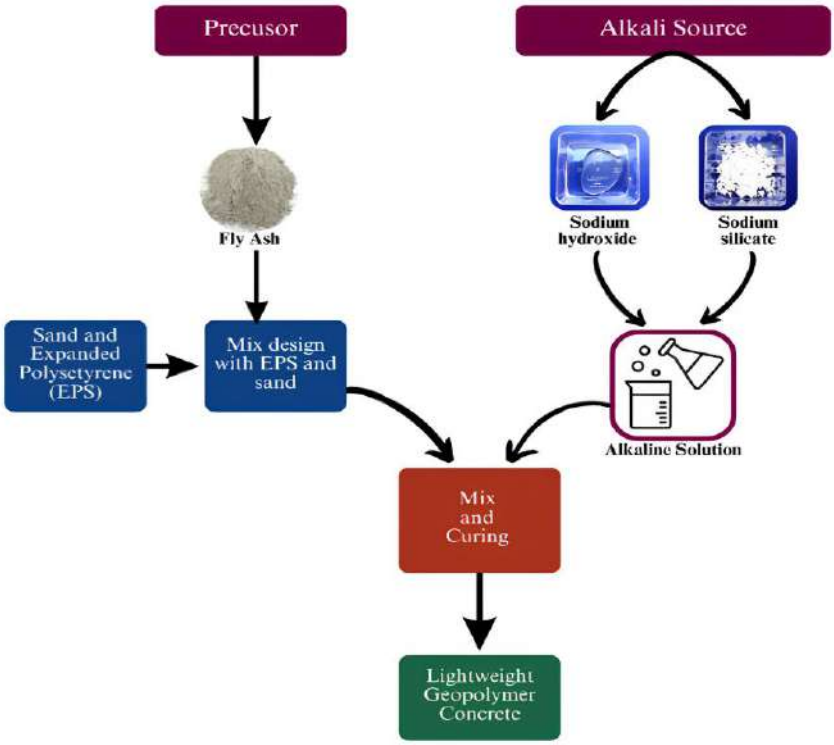

Fig. 1. An overview lightweight geopolymer concrete productions

2.1. Fly Ash

The fly ash utilized in this research was sourced from Pupuk Sriwidjaja Palembang Company and subjected to analysis using XRF (X-ray fluorescence), XRD (X-ray diffraction), and SEM (Scanning Electron Microscopy) techniques to know the class and characteristic [14]. Fly ash, also called pulverized fuel ash, is a by-product of thermal power plants composed of fine particles. Fly ash's properties will change depending on the source and composition of coal [13]. Fly ash is the main solid waste from coal combustion in power stations [23]. Table 1 presents the chemical composition (XRF) of the fly ash, while Figures 2 and 3 show the results of SEM and XRD, respectively.

Scanning Electron Microscopy (SEM), an electron microscope technique that creates images by scanning a sample's surface with a focused electron beam, was used to examine the fly ash [24]. As the electron beam interacts with the sample, emitted or reflected electrons are detected, amplified, and displayed as shades of gray on a monitor, thus forming the image [14]. As shown in Fig. 3 (3000x magnification), the SEM revealed that most fly ash particles exhibit a spherical morphology, facilitating their rapid reaction with other components during geopolymer mixture production. The particle size distribution is broad, ranging from approximately 0.3 µm to over 5 µm in diameter, as estimated from the 10 µm scale bar.

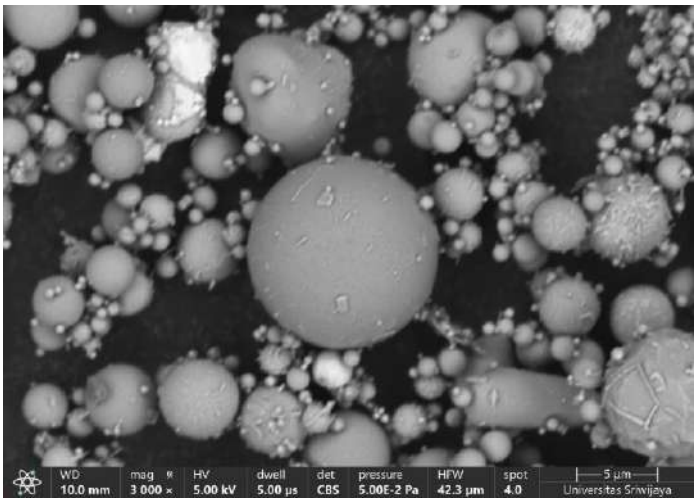

Fig. 2. SEM of fly ash

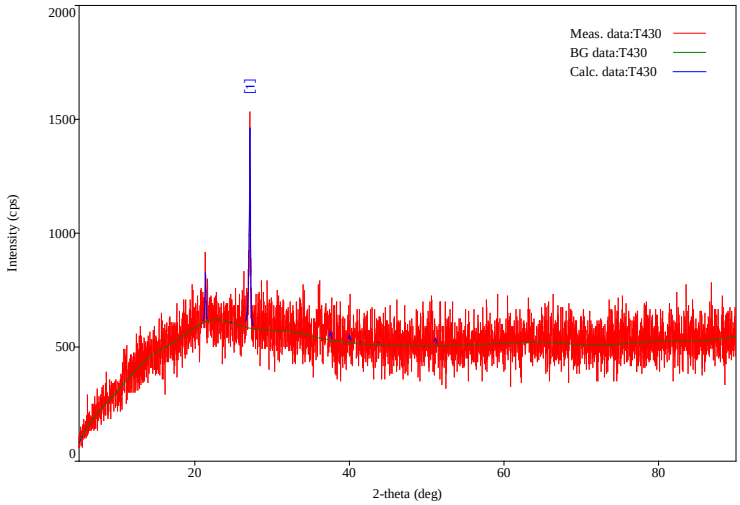

Fig. 3. XRD of fly ash

Table 1. XRF (chemical composition) fly ash

Component	% in mass
SiO_2	50,531 ± 0,180%
Al_2O_3	22,944 ± 0,142%
Fe_2O_3	11,298 ± 0,041%
CaO	4,927 ± 0,027%
Na_2O	4,472 ± 0,268%
MgO	1,853 ± 0,088%
SO_3	1,526 ± 0,022%
K_2O	1,369 ± 0,020%
TiO_2	0,837 ± 0,011%
P_2O_5	0,174 ± 0,020%
Mn_3O_4	0,070 ± 0,004%

X-ray fluorescence (XRF) analysis is attempted to identify the chemical composition of fly ash. The material process works by exposing to high-energy X-rays and measuring the characteristic secondary X-rays emitted by the elements present, enabling both qualitative and quantitative elemental analysis [25]. According to the ASTM 618 standard [26], fly ash can be classified as type F because it contains $SiO_2 + Al_2O_3 + Fe_2O_3 \geq 70\%$ and low CaO content (typically <10%).

X-ray diffraction (XRD) analysis was conducted on the fly ash to assess its crystalline content, as a high degree of crystallinity can hinder its reactivity in material casting processes. XRD aims to determine the crystal system, lattice parameters, atomic arrangement, structure type, orientation, and grain size [27]. The XRD analysis, as illustrated in Fig. 3, reveals a broad, amorphous hump with a relatively small, sharp peak at approximately 27.12° with an intensity of 1486.56 cps. The relatively low intensity of the crystalline peak demonstrates that the fly ash used in this study possesses a predominantly amorphous structure, which is favourable for geopolymerization. These microstructural characteristics directly influence mechanical performance through multiple mechanisms: the spherical morphology enhances workability and improves compaction; the varied particle sizes create an efficient packing effect that increases matrix density; and the high reactive silica and alumina content participates in pozzolanic reactions with cement hydration products to form additional C-S-H gel that fills capillary pores. As a result, concrete incorporating this fly ash exhibits improved mechanical properties, including enhanced compressive strength development (particularly long-term) and better resistance to aggressive agents, demonstrating the apparent correlation between the observed microstructure and enhanced mechanical performance in cementitious systems.

2.2. Alkali Activator

Sodium hydroxide (NaOH) and sodium silicate (Na_2SiO_3) were used as alkali activators [28]. The activator consists of NaOH and silica, where silica acts as a strong acid that reacts with the strong base. Na_2SiO_3 speeds up the polymerization process. Simultaneously, NaOH 14M interacts with the Si and Al in the fly ash, forming strong polymer bonds. This combination is used to prepare the alkaline activator [29].

2.3. Fine Aggregate

Tanjung Raja sand, ranging from 4.75 mm to 0.075 mm in size, was used as fine aggregates for the investigation. The sand was used in saturated surface dry (SSD) conditions, where internal pores are water-filled, but the surface is dry [30]. The fine aggregate's fine modulus is 2.545, within the recommended range (usually 2.3-3.1) for good fine aggregate [31]. Based on the standard color test with an organic plate, the samples are in color number two. These results indicate that fine aggregates have relatively low organic content and will not interfere with the cement hydration process or concrete strength [32]. These fine aggregates can be used in concrete construction without the need for additional processing [33].

2.4. Expanded Polystyrene

Expanded polystyrene (EPS) is a versatile material widely used in various industries, including construction, packaging, and aquaculture. Despite its utility, EPS poses significant environmental and health challenges due to its persistence and potential toxicity. This response explores the multifaceted aspects of EPS, including its environmental impact, applications, and recycling methods. The EPS size used in this study was ranging 3-4 mm.

EPS is valued for its low thermal conductivity and cost-effectiveness in construction as an insulation material. Innovations such as EPS-alumina aerogel composites enhance its fire resistance and mechanical properties, making it suitable for practical applications [34]. Due to its recyclability, expanded polystyrene (EPS) is a common choice as the insulation core in structural insulated panels. This rigid and tough polymeric foam features a closed-cell structure [35].

2.5. Admixture

Admixture is a material other than water, aggregate, and hydraulic cement mixed with concrete or mortar added before or during mixing. Admixtures modify the properties and characteristics of concrete, for example, to improve its workability or for other purposes, namely, energy savings [36]. The admixture used in this study is a superplasticizer type F. It helps the workability of the LWGC mixture and accelerates the binding time [37].

2.6. Design Mix Proportion and Experimental Methodology

This study investigates fresh material properties, compressive strength, and tensile strength of LWGC using EPS. The materials used in this study are Fly ash as a primary binder, fine aggregate, EPS as Lightweight aggregate replacement, and alkali activator consisting of a combination of sodium silicate (Na_2SiO_3) and sodium hydroxide ($NaOH$). The target density of LWGC developed on less than. The alkali activator to binder ratio was maintained at 0.3 for all mixtures. Three different $Na_2SiO_3/NaOH$ ratios were investigated: 1.5, 2.0, and 2.5. The solution was prepared 24 hours before being mixed with pellets in distilled water to a 14 M concentration. EPS beads were used to replace 25% of the total concrete volume target. The LWGC concrete mixtures shown in Table 2LWGC are characterized by their compressive strength (CS) and Split Tensile Strength (STS), which are prepared at 14 days and 28 days. CS and STS were tested on a compression testing machine (CTM). The specimen was cast like a $50mm \times 50mm \times 50mm$ cube or a $150\,mm \times 300\,mm$ length cylinder.

Table 2. LWGC concrete mixtures for $1m^3$ volume of concrete

Materials	Specimen Shape	Specimen size (mm)	Number of Specimens
	LWGC_1.5	LWGC_2.0	LWGC_2.5
Fly Ash (kg)	692	692	692
Fine Aggregate (kg)	540	540	540
EPS	10.8	10.8	10.8
AA/B	0.3	0.3	0.3
Ratio AA	1.5	2.0	2.5
Alkali Activator (AA) (Kg)	207.6	207.6	207.6
Mol NaOH (M)	14	14	14
Superplasticizer (kg)	14.5	14.5	14.5

This study investigates fresh material properties, compressive strength, and tensile strength of LWGC using EPS. The materials used in this study are Fly ash as a primary binder, fine aggregate, EPS as Lightweight aggregate replacement, and alkali activator consisting of a combination of sodium silicate (Na_2SiO_3) and sodium hydroxide ($NaOH$). The target density of LWGC developed on less than 1800 kg/m^3. The alkali activator to binder ratio was maintained at 0.3 for all mixtures. Three different $Na_2SiO_3/NaOH$ ratios were investigated are 1.5, 2.0, and 2.5. $NaOH$ The solution was prepared 24 hours before being mixed with NaOH pellets in distilled water to a 14 M concentration. EPS beads were used to replace 25% of the total concrete volume. Fig. 4

shows the mixing process of LWGC. The LWGC concrete mixtures for $1m^3$ volume of concrete shown in Table 2.

Fig. 4. Mixing process of LWGC

2.7. Proportions of Test Specimens

LWGC is characterized by its compressive strength (CS) and Split Tensile Strength (STS), which are prepared at 7 days and 28 days. CS and STS were tested on a compression testing machine (CTM). The specimen was cast like a $50mm \times 50mm \times 50mm$ cube or a $150\ mm\ \times 300\ mm$ length cylinder. The number of specimens and tests is shown in Table 3.

Table 3. The number of specimens and tests

Mix Design	Specimen Shape	Specimen size (mm)	Number of Specimens	Purpose
LWGC_1.5	Cube	50 × 50 × 50	6	Compressive Strength (CS)
LWGC_1.5	Cylinder	150 × 300	6	Split Tensile Strength (STS)
LWGC_2.0	Cube	50 × 50 × 50	6	Compressive Strength (CS)
LWGC_2.0	Cylinder	150 × 300	6	Split Tensile Strength (STS)
LWGC_2.5	Cube	50 × 50 × 50	6	Compressive Strength (CS)
LWGC_2.5	Cylinder	150 × 300	6	Split Tensile Strength (STS)

2.8. Process of Casting and Curing

The mold used for this casting is steel cubic $50mm \times 50mm \times 50mm$ dimensions for compressive strength and cylindrical molds of $150\ mm\ \times 300\ mm$ height for splitting tensile strength testing. All molds used are thoroughly cleaned and coated with oil to facilitate easy demolding. Sodium hydroxide 14 M concentration was prepared 24 hours before mixing with sodium silicate.

First, Weigh the lightweight geopolymer concrete material according to the mix design. Then, Dissolve the solid with distilled water according to the planned molarity of 14 M. Then, mix the solutions until they are evenly distributed according to the planned ratio to become an alkali activator solution. Put fly ash and fine aggregate into the mixer at gear speed 1 for 3 minutes with the addition of superplasticizer little by little until evenly mixed. After that, Mix the alkali activator solution into the mixer, then stir with gear 2 for 3 minutes. Mix the weighed EPS (Expanded Polystyrene) into the mixer, then stir with gear 1 for about 2 minutes until everything is evenly distributed. Fig. 5 show many LWGC's specimen after casting.

Test the fresh concrete properties, such as slump flow and setting time testing. Then, put the test object into a $150\ mm\ \times 300\ mm$ cylinder mold and a $50mm \times 50mm$ cube mold. After the concrete object is molded for 24 hours, the mold is opened. Then, the specimens are cured in an

oven at 60^{0}c for 24 hours are shown in Fig. 6. After initial curing in an oven at 60°C for 24 hours, the specimens were transferred to a room with controlled relative humidity of 65±5% at room temperature (23±2°C) until the designated testing age. This process is important to ensure that the geo-polymerization process continues in a controlled manner, preventing overly rapid drying that could cause micro-cracking.

Fig. 5. Many LWGC's specimens

Fig. 6. Curing in oven LWGC's specimen

3. Result and Discussion

3.1. Setting Time

From the research results, the time setting is shown in Fig. 7. The graph compares the initial time (initial time) and the final time (final time) for three LWGC variations, namely LWGC_1.5, LWGC_2.0, and LWGC_2.5.

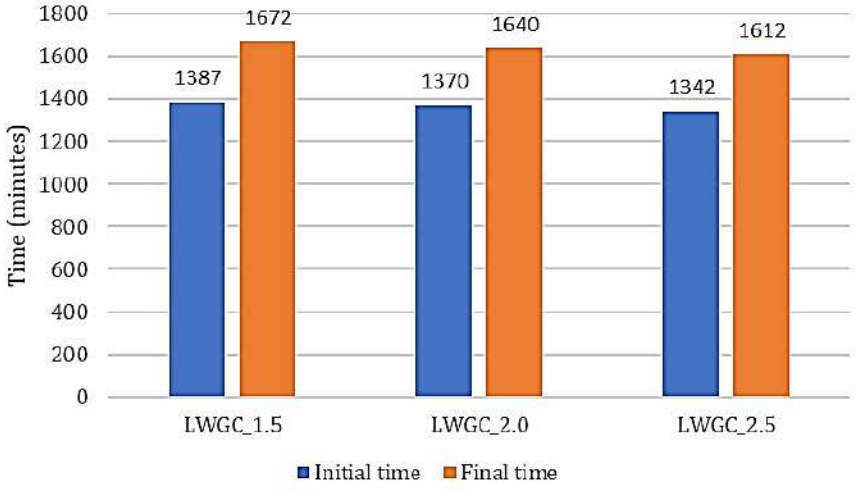

Fig. 7. Setting time LWGC

Time is measured in minutes. The third variation shows a consistent pattern where the initial time ranges from around 1200 minutes and the Final time ranges from around 1500 minutes. The difference between initial and final times is relatively the same for all variations. These results show that the Na_2SiO_3/NaOH ratio has no significant effect. However, LWGC_1.5 takes longer than other variations. This is because the higher proportion of NaOH in the mixture affects the reaction kinetics, so it has a more intensive geo-polymerization reaction [38].

3.2. Slump Flow Test

The workability of the LWGC mixture was measured using slump flow testing by ASTM C1611. The results of the slump flow test for the three mixture variations are shown in Figure 8. The highest slump flow value was obtained in LWGC_1.5 of 22.78 cm, while LWGC_2.0 and LWGC_2.5 reached 21.5 cm and 20.40 cm, respectively. There is a tendency for the slump flow value to decrease with the increase in the Na_2SiO_3/NaOH ratio in the mixture. This decrease in workability can be attributed to the characteristics of sodium silicate (Na_2SiO_3), which has a higher viscosity than sodium hydroxide (NaOH). When the proportion of Na_2SiO_3/ increases in the mixture, the viscosity of the geopolymer paste also increases, resulting in a decrease in the flowability of the mixture. However, all mixture variations still show adequate levels of workability for the casting and compaction process of LWGC with EPS aggregates. The difference in slump value occurs due to different geo-polymerization reactions where different Na_2SiO_3/NaOH ratios affect the rate of aluminosilicate gel formation and polymerization process [37]. The mixture with a lower Na_2SiO_3/NaOH ratio (LWGC_1.5) has a higher NaOH concentration, contributing to increased workability due to the more fluid nature of NaOH.

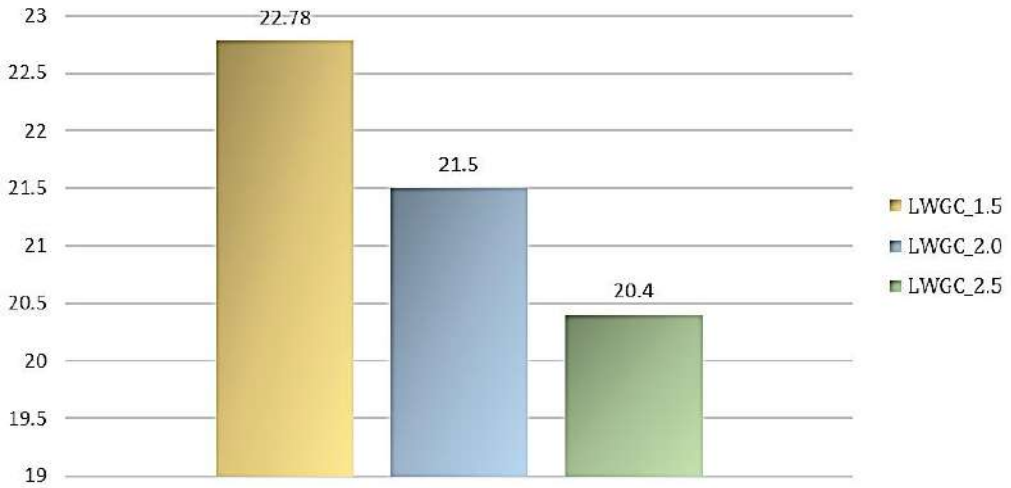

Fig. 8. Slump flow LWGC

3.3. Density

Density testing was conducted to evaluate the effect of Na_2SiO_3/NaOH ratio variations on the specific gravity of LWGC. The density test results presented in Figure 9 show an increase in density values along with an increase in the Na_2SiO_3/NaOH ratio. LWGC_1.5 has the lowest density of 1080 kg/m^3, while LWGC_2.0 and LWGC_2.5 each reached 1217.07 kg/m^3 and 1249.87 kg/m^3. This density increase is related to forming a denser geopolymer matrix structure at a higher Na_2SiO_3/NaOH ratio. Sodium silicate (Na_2SiO_3) plays an important role in forming aluminosilicate gel and the polymerization process, where increasing its proportion produces a more compact structure. Despite the variation in density, all mixtures still meet the criteria for lightweight concrete [31], which requires a maximum specific gravity of 1900 kg/m^3. Using EPS aggregates as a substitute for conventional aggregates contributes significantly to achieving the target specific gravity of lightweight concrete. At the same time, variations in the Na_2SiO_3/NaOH ratio have a more subtle effect on the final density of LWGC [34].

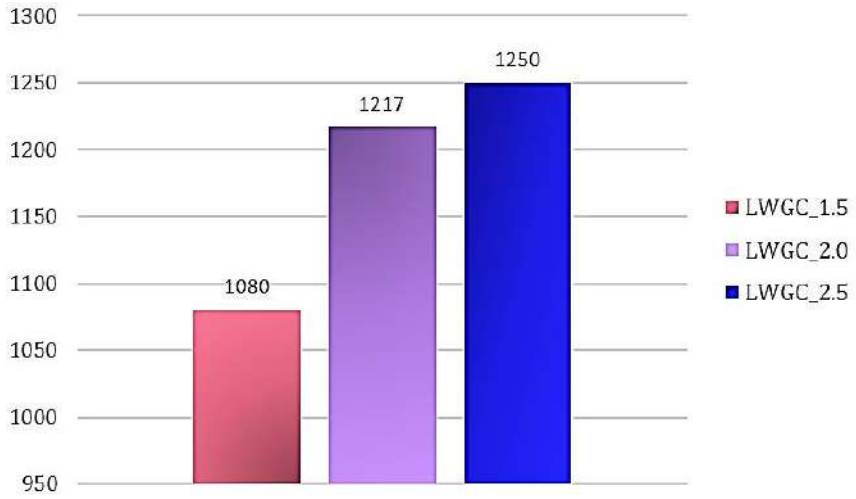

Fig. 9. Density of LWGC

3.4. Compressive Strength

The compressive strength of LWGC was tested at 14 and 28 days to evaluate the effect of varying the Na_2SiO_3/NaOH ratio on the development of concrete compressive strength. As shown in Fig. 10, there is a consistent increase in compressive strength along with the increase in the Na_2SiO_3/NaOH ratio and the age of the concrete. In the 14-day test, LWGC_1.5 achieved a compressive strength of 15.52 MPa, LWGC_2.0 was 17.46 MPa, and LWGC_2.5 obtained the highest value of 21.02 MPa. A similar pattern was seen in the 28-day test with an increase in compressive strength to 16.87 MPa, 18.98 MPa, and 22.85 MPa for LWGC_1.5, LWGC_2.0, and LWGC_2.5, respectively. This increase in compressive strength occurs due to the role of sodium silicate (Na_2SiO_3) in forming the geopolymer structure. Higher Na_2SiO_3/NaOH ratios resulted in a denser geopolymer matrix and a more regular microscopic structure, contributing to the increase in compressive strength. In addition, increasing the concrete age from 14 to 28 days provided more time for the geo-polymerization process, increasing compressive strength by about 10-15% across all mix variations. Despite using EPS aggregates with relatively low strength, the test results showed that LWGC could still achieve adequate compressive strength for lightweight structural applications. LWGC_2.5 showed the best performance with a compressive strength of 22.85 MPa at 28 days, indicating that higher Na_2SiO_3/NaOH ratios resulted in more optimal geopolymer matrix bonding [39].

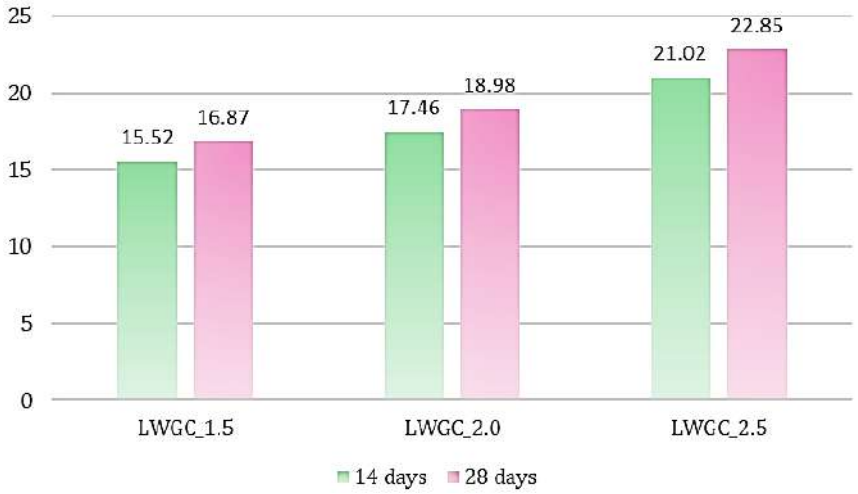

Fig. 10. Compressive strength

3.5. Split Tensile Strength

Splitting tensile strength was tested on cylindrical specimens at 28 days. The results of the splitting tensile strength test are shown in Figure 11. The splitting tensile strength values vary depending on the molarity, and $Na_2SiO_3/NaOH$ ratio used in the mixture. LWGC_1.5 showed the lowest splitting tensile strength, which was 1.23 MPa. Increasing the Alkali activator ratio to LWGC_2.0 resulted in a higher splitting tensile strength of 1.31 MPa. The highest splitting tensile strength was achieved by LWGC_2.5, reaching 1.43 MPa. These results indicate that increasing the molarity and NaOH generally increases the splitting tensile strength of fly ash-based lightweight geopolymer concrete. Higher molarity likely causes a more efficient geo-polymerization process, resulting in a denser and stronger matrix, improving the tensile performance of concrete. The increase in splitting tensile strength, along with increasing variations in alkali activator, indicates the important role of alkali activation in developing the mechanical properties of this lightweight geopolymer concrete [40].

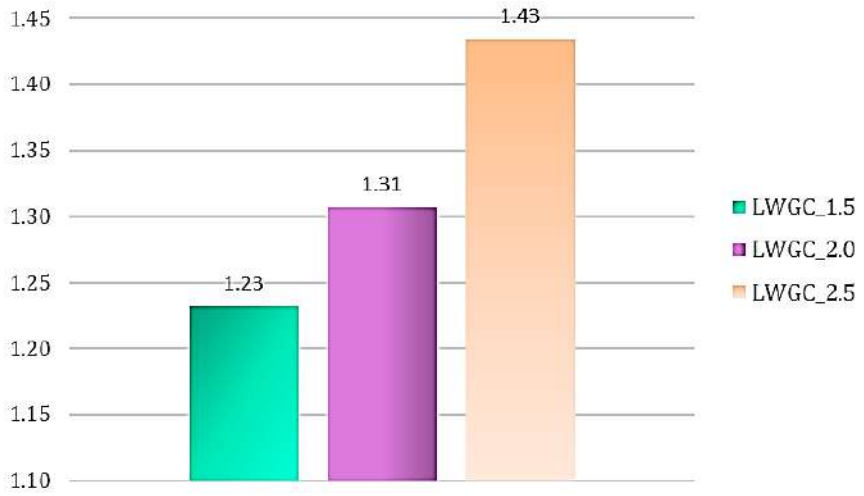

Fig. 11. Split Tensile strength

3.6. Effect of $Na_2SiO_3/NaOH$ Ratio

The results in fig. 12 showed a significant relationship between the alkali activator ratio ($Na_2SiO_3/NaOH$) and the mechanical strength of geopolymer concrete. Based on second-degree polynomial regression analysis, a powerful correlation was obtained between the activator ratio and both compressive strength and splitting tensile strength, indicated by the R^2 value of 1 for both parameters (R^2 = 1 for compressive strength and R^2 = 1 for splitting tensile strength). The compressive strength of geopolymer concrete increased polynomially with increasing activator ratio, following the equation $y = 3.5181x^2 - 8.0961x + 21.098$. The curve pattern indicates that within the tested activator ratio range (1.5 to 2.5), the compressive strength experiences an accelerating rate of increase as the activator ratio increases. The resulting compressive strength varied from 16.87 MPa to 22.85 MPa in this activator ratio range. Correspondingly, the splitting tensile strength also increased polynomially, as the equation $y = 0.1041x^2 - 0.2143x + 1.319$. Although the increase is more moderate than the compressive strength, the polynomial curve reveals that the splitting tensile strength increases at higher activator ratios. The splitting tensile strength values ranged from 1.23 MPa to 1.43 MPa across the tested ratio range.

The polynomial growth trend in both parameters indicates that the geo-polymerization reaction is optimal within the studied activator ratio range and suggests a non-linear effect of the activator ratio on mechanical strength. This may be attributed to the complexity of the geo-polymerization reaction involving the formation of aluminosilicate networks influenced by alkali activator concentration. This polynomial model provides a more comprehensive understanding of material behavior than a simple linear model, with the perfect R^2 value (R^2 = 1) demonstrating that this model is highly accurate in predicting the mechanical strength of geopolymer concrete across various alkali activator ratios. The activator ratio 2.5 gave the best results for both strength

parameters, and the absence of an optimum point indicates the potential for further strength increases at higher ratios. This strong correlation also indicates the reliability of the mix design in producing consistent strength, with a ratio of increase in compressive strength to splitting tensile strength [39].

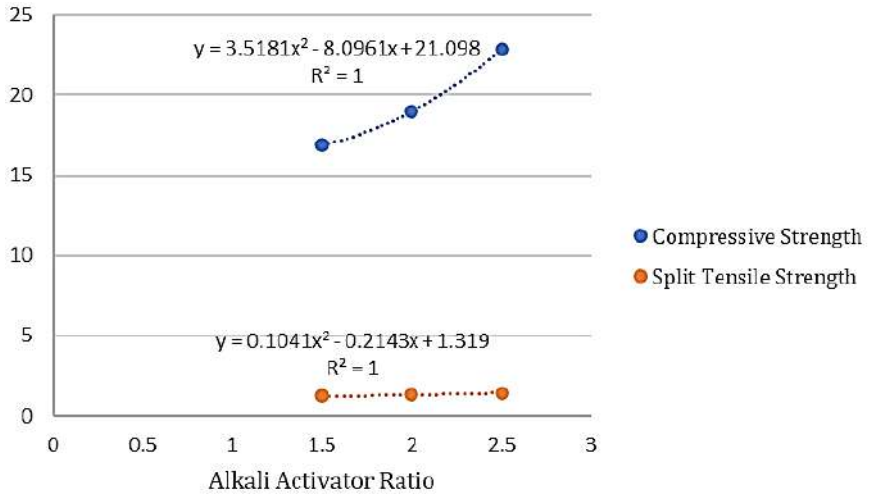

Fig. 12. Effect of Na_2SiO_3/NaOH Ratio

3.7. Future Research

After the research, LWGC has good mechanical properties of compressive and tensile strength and has the potential to be developed. Adding EPS as a lightweight aggregate, replacing ordinary aggregate, and variations in alkali activators provide significant improvements in properties. However, to maximize the potential of this material, several areas of further research can be explored. Future research can focus on further optimization of the mixture composition to improve mechanical performance and durability by further exploring different Na_2SiO_3/NaOH ratios to find the most effective combination in promoting the geo-polymerization reaction and the effect of EPS size variations. Investigating rupture strength for prisms and mechanical testing for 90 days can for next studies. To better understand the underlying mechanisms of lightweight geopolymer concrete behavior, microstructural characterization with techniques such as SEM/EDX and its durability testing are essential. Further research can focus on developing customized mix designs for specific structural applications, such as wall panels, deep beams, building blocks, or precast elements.

4. Conclusions

From the experimental study on the mechanical behavior of LWGC in terms of compressive strength, tensile strength, and fresh material properties using three different alkali activators in concrete, respectively. The following conclusions are drawn:

- The variation in the Na_2SiO_3/NaOH ratio affects the physical and mechanical properties of fly ash-based LWGC with EPS aggregate. LWGC_2.5 shows the best mechanical strength performance, LWGC_2.5, with the highest sodium silicate proportion, exhibits superior mechanical strength characteristics due to the formation of more compact and well-developed alumina-silicate gel networks. While LWGC_1.5 has the highest workability, its higher NaOH concentration, demonstrates superior workability characteristics as the higher alkalinity facilitates faster initial dissolution of fly ash particles, creating a more fluid mixture initially.
- The setting time does not show significant differences between variations, but LWGC_1.5 requires a longer setting time because the higher NaOH concentration results in a more intensive geo-polymerization reaction.

- The slump flow value decreases as the Na_2SiO_3/NaOH ratio increases, with the highest value of 22.78 cm in LWGC_1.5 and the lowest of 20.40 cm in LWGC_2.5. This is due to the higher viscosity of Na_2SiO_3 compared to NaOH.
- The density of LWGC increases with the increase in the Na_2SiO_3/NaOH ratio, ranging from 1080 to 1250 kg/m^3. All variations meet the requirements of lightweight concrete according to ASTMC.125
- The compressive strength of LWGC increases with the increase in the Na_2SiO_3/NaOH ratio and the age of the concrete. At 28 days, LWGC_2.5 achieved the highest compressive strength, 22.85 MPa, followed by LWGC_2.0 (18.98 MPa) and LWGC_1.5 (16.87 MPa).
- The splitting tensile strength at the age of 28 days showed a similar pattern to the compressive strength, where LWGC_2.5 reached the highest value of 1.43 MPa, while LWGC_2.0 and LWGC_1.5 reached 1.31 MPa and 1.23 MPa, respectively.
- The polynomial regression models with perfect R^2 values of 1 for both compressive and splitting tensile strength demonstrate that the mechanical properties of geopolymer concrete increase non-linearly with increasing alkali activator ratio within the tested range (1.5 to 2.5)
- The LWGC has good mechanical behavior and provides sustainable construction materials.
- The implementation of Lightweight Geopolymer Concrete (LWGC) in actual construction projects offers significant advantages, particularly in reducing dead loads on structures

Acknowledgement

The authors acknowledge that this study is supported by all authors are grateful to the financial support of the Ministry of Education, Culture, Research, and Technology of the Republic of Indonesia via HIBAH PMDSU 2024 under contract number 090/E5/PG.02.00.PL/2031 and derivative contract number 0017.005/UN9/SB1.LP2M.PT/2024 as an additional output. In addition, all authors express appreciation to Universitas Sriwijaya for support this study and Thanks to PT. Pupuk Sriwidjaja for providing fly ash.

References

[1] Amran M, Makul N, Fediuk R, Lee YH, Vatin NI, Lee YY, Mohammed K. Global carbon recoverability experiences from the cement industry. Case Studies in Construction Materials, 2022; 17:e01439. https://doi.org/10.1016/j.cscm.2022.e01439

[2] Arun BR, Srishaila JM, Md Khalid S, Veerabhadrappa A, Kavyashree K, Tanu HM. Prediction of machine learning application in the development of novel sustainable self-compacting geopolymer concrete. Research on Engineering Structures & Materials, 2024; 1-22. http://dx.doi.org/10.17515/resm2024.354ma0716rs

[3] Kaptan K, Cunha S, Aguiar J. A Review: Construction and Demolition Waste as a Novel Source for CO2 Reduction in Portland Cement Production for Concrete. Sustainability (Switzerland), 2024; 16:585. https://doi.org/10.3390/su16020585

[4] Abera YA. Sustainable building materials: A comprehensive study on eco-friendly alternatives for construction. Composites and Advanced Materials, 2024; 33:1-17. https://doi.org/10.1177/26349833241255957

[5] Federowicz K, Techman M, Sanytsky M. Modification of lightweight aggregate concretes with silica nanoparticles-a review. Materials, 2021;14:15. https://doi.org/10.3390/ma14154242

[6] Mohamed AM, Tayeh BA, Majeed SS, Aisheh YIA, Salih MNA. Ultra-light foamed concrete mechanical properties and thermal insulation perspective: A comprehensive review. Journal of CO2 Utilization, 2024; 83: 102827. https://doi.org/10.1016/j.jcou.2024.102827

[7] Agrawal Y, Gupta T, Sharma R, Panwar NL, Siddique S. A comprehensive review on the performance of structural lightweight aggregate concrete for sustainable construction. Construction materials, 2021; 1: 39-62. https://doi.org/10.3390/constrmater1010003

[8] Hasan M, Saidi T, Afifuddin M. Mechanical properties and absorption of lightweight concrete using lightweight aggregate from diatomaceous earth. Construction and Building Materials, 2021; 277: 122324. https://doi.org/10.1016/j.conbuildmat.2021.122324

[9] Kumar R, Srivastava A, Lakhani R. Industrial wastes-cum-strength enhancing additives incorporated lightweight aggregate concrete (Lwac) for energy efficient building: A comprehensive review. Sustainability (Switzerland, 2024; 14: 331. https://doi.org/10.3390/su14010331

[10] Luhar I, Luhar S. A Comprehensive Review on Fly Ash-Based Geopolymer. Journal of Composites Science, 2022; 6:1-59. https://doi.org/10.3390/jcs6080219

[11] Saloma, Hanafiah, Elysandi DO, Meykan DG. Effect of Na2SiO3/NaOH on mechanical properties and microstructure of geopolymer mortar using fly ash and rice husk ash as precursor. AIP Conference Proceedings, 1903: 050013-1-050013-11, 2017. https://doi.org/10.1063/1.5011552
[12] Okoye FN, Durgaprasad J, Singh NB. Effect of silica fume on the mechanical properties of fly ash based-geopolymer concrete. Ceramic International, 2016; 42: 3000-3006. https://doi.org/10.1016/j.ceramint.2015.10.084
[13] Madirisha M, Dada OR, Ikotun BD. Chemical fundamentals of geopolymers in sustainable construction. Materials Today Sustainability, 2024; 27: 100842. https://doi.org/10.1016/j.mtsust.2024.100842
[14] Adhitya B, Saggaf A, Saloma. Manufacture of Geopolymer Artificial Aggregates by Pelletization and Crushing Processes. Civil Engineering and Architecture, 2023; 11 (1): 13-21. https://doi.org/10.13189/cea.2023.110102
[15] Sbahieh S, McKay G, Al-Ghamdi SG. Comprehensive Analysis of Geopolymer Materials: Properties, Environmental Impacts, and Applications. Materials, 2023; 16: 7363. https://doi.org/10.3390/ma16237363
[16] Kioupis D, Skaropoulou A, Tsivilis S, Kakali G. Properties and durability performance of lightweight fly ash based geopolymer composites incorporating expanded polystyrene and expanded perlite. Ceramics, 2022; 5: 821-836. https://doi.org/10.3390/ceramics5040060
[17] Maghfouri M. Alimohammadi V, Gupta R. Saberian M, Azarsa P, Hashemi M, Asadi I, Roychand R. Drying shrinkage properties of expanded polystyrene (EPS) lightweight aggregate concrete: A review. Case Studies in Construction Materials, 2022; 16: e00919. https://doi.org/10.1016/j.cscm.2022.e00919
[18] Mukkala P, Venkatesh C, Habibunnisa S. Evaluation of mix ratios of light weight concrete using geopolymer as binder. Materials Today: Proceedings, 2022; 52:2053-2056. https://doi.org/10.1016/j.matpr.2021.12.140
[19] Mostafa SA, Agwa IS, Elboshy B, Zeyad AM, Hassan AMS. The effect of lightweight geopolymer concrete containing air agent on building envelope performance and internal thermal comfort. Case Studies in Construction Materials, 2024; 20: e03365. https://doi.org/10.1016/j.cscm.2024.e03365
[20] Wei J, Yang Q, Jiang Q, Li X, Liu S, Li K, Wang Q. Mechanical properties of basalt fiber reinforced ambient-cured lightweight expanded polystyrene geopolymer concrete. Journal of Building engineering, 2023; 80: 108072. https://doi.org/10.1016/j.jobe.2023.108072
[21] Olsen K, Ulus H, Head MH, Advani SG. Effect of particle size and replacement ratio on mechanical performance of cementitious mortar containing ground recycled acrylonitrile butadiene styrene (GRABS) waste plastics. Composite, 2025; 289: 111914. https://doi.org/10.1016/j.compositesb.2024.111914
[22] Al-Lami MS, Abdul-Majeed Al-saadi E. The relationships between compressive strength and density of polystyrene lightweight concrete and their component ratios. Journal of Applied Engineering Science, 2021; 19: 175-185. https://doi.org/10.5937/jaes0-27471
[23] Kavipriya S, Deepanraj CG, Dinesh S, Prakhash N, Lingeshwaran N, Ramkumar S. Flexural strength of Lightweight geopolymer concrete using sisal fibers. Materials Today: Proceedings, 2021; 47: 5503-5507. https://doi.org/10.1016/j.matpr.2021.08.135
[24] Alterary SS, Marei NH. Fly ash properties, characterization, and applications: A review. Journal of King Saud University - Science, 2021; 33: 101536. https://doi.org/10.1016/j.jksus.2021.101536
[25] Tian X, Zhao L. Determination of concentrations of Sr and Ba in coal and coal combustion by-products: A comparison between results by ICP-MS and XRF techniques. Talanta, 2024; 266: 124919. https://doi.org/10.1016/j.talanta.2023.124919
[26] ASTM C 618.Standard Specification for Coal Fly Ash and Raw or Calcined Natural Pozzolan for Use in Concrete. In ASTM International, West Conshohocken, PA, USA, 2014; pp.1-5.
[27] Luo Y, Klima KM, Brouwers H J H, Yu Q. Effects of ladle slag on Class F fly ash geopolymer: Reaction mechanism and high temperature behavior. Cement and Concrete Composites, 2022; 129: 104468. https://doi.org/10.1016/j.cemconcomp.2022.104468
[28] Saloma, Usman AP, Hanafiah, Ramadhanty CV. The Durability of Lightweight Geopolymer Concrete (LGC) on Chloride Resistance. Civil Engineering and Architecture, 2022; 10: 1881-1890. https://doi.org/10.13189/cea.2022.100514
[29] Hui-Teng N, Cheng-Yong H, Yun-Ming L, Abdullah M M A B, Ern Hun K, Razi H M, Yong-Sing N. Formulation, mechanical properties and phase analysis of fly ash geopolymer with ladle furnace slag replacement. Journal of Material Research and Technology, 2021; 12: 1212-1226. https://doi.org/10.1016/j.jmrt.2021.03.065
[30] Liyew G, Mesfin WM, Park S, Kim, HK. Alternative determination of saturated-surface-dry condition for aggregates using centrifugal compaction with alcohol-cement paste. Materials and Structures/Materiaux et Constructions, 2023; 56: 77. https://doi.org/10.1617/s11527-023-02169-x
[31] ASTM C33/C33M-13. Standard specification for concrete aggregates. In ASTM International, West Conshohocken, PA, USA, 2003.

[32] ASTM C40-04. Standard Test Method for Organic Impurities in Fine Aggregates for Concrete. In ASTM International, West Conshohocken, PA, USA, 2009.
[33] Priyono BRCP. Pengujian material agregat Halus Pabrik Precast Margorejo Yogyakarta. Jurnal Menara, 2024; 12:2.
[34] Hasyim S, Nurjannah SA, Usman AP, Putra FS, Hashim MFA. The durability of lightweight concrete against 5% hydrochloric acid solution with various size of expanded polystyrene. AIP Conference Proceedings, 2347, 020227, 2021. https://doi.org/10.1063/5.0051716
[35] Ankesh, Jaikant, Sanjeev G. Properties of Expanded Polystyrene (EPS) and Its Environmental Effect. Department of Mechanical Engineering. Advances and Applications in Mathematical Sciences, 2021; 20(10):2151-2162.
[36] ASTM C.125. Standard Definition of Terminology Relating to Concrete and Concrete Agregates. 1995;61.
[37] Singh B, Singh SB, Barai SV, Ojha PN, Kumar R. Mechanical properties and fracture behavior of concrete made with sintered fly ash lightweight coarse aggregate and electric arc furnace slag as fine aggregate. Research on Engineering Structures & Materials, 2024; 1-22. http://dx.doi.org/10.17515/resm2024.396me0814rs
[38] Siyal AA, Radin Mohamed RMS, Shamsuddin R, Ridzuan MB. A comprehensive review of synthesis kinetics and formation mechanism of geopolymers. RSC Advances, 2024; 14: 446-462. https://doi.org/10.1039/D3RA06205H
[39] Kumar Verma N, Chakradhara Rao M, Kumar S. Effect of molarity of NaOH and alkalinity ratio on compressive strength of geo-polymer concrete. Materials Today: Proceedings, 64: 940-947, 2022. https://doi.org/10.1016/j.matpr.2022.03.687
[40] Radhi Taha A, Abbas Al-Attar A, Mohammed Ahmed H. the Effect of Different Design Ratios on the Compressive Strength of Geopolymer Concrete: a Parametric Study Using the Taguchi Method. NTU Journal of Engineering and Technology, 2023; 2(4): 1-11. https://doi.org/10.56286/ntujet.v2i4.682

Blank Page

Research on Engineering Structures & Materials
www.jresm.org
MIM Research Group

Research Article

Properties of sustainable concrete incorporating cold-bonded lightweight aggregate manufactured from expired cement, biopolymer, and various waste

Ghazwan F. Khudhair [*,a] , Waleed A. Abbas [b]

Civil Engineering Department, University of Technology, Iraq

Article Info

Article History:

Received 27 Mar 2025

Accepted 16 June 2025

Keywords:

Sustainable concrete;
Cold-bonded lightweight aggregate;
Expired cement;
Waste;
Compressive strength;
Splitting;
Flexural

Abstract

This investigation aims to evaluate the performance of sustainable concrete incorporating artificial coarse aggregate in both its fresh and hard states. The dry reference aggregate mixture, containing 90% fly ash and 10% expired cement, was pelletized utilizing cold-bonded technology. Nine distinct types of aggregates were produced alongside a reference aggregate and subsequently categorized into three groups according to the curing method after a duration of 28 days. This was achieved using the same technique and a water quantity of 20–22% by weight after adding 0.5%, 0.75%, and 1% by weight for each starch, alginate, and tire waste. The reference aggregate categories containing 1% starch (RSS1, ROS1) and 0.75% tire waste (RWR0.75), subjected to self-curing, oven curing, and water curing, represent the optimal formulations of cold-bonded aggregates identified through physical and mechanical testing. Six varieties of sustainable concrete were made by increasing the amount of synthetic coarse aggregate used from 50% to 100%. The water-to-cement ratio stayed at 0.4, and the cement content was kept at 400 kg/m^3. When 50% and 100% of the ROS1 class aggregate were replaced, the density of fresh and hard concrete dropped to its lowest levels, with rates of 7.95%, 16.27%, 10.69%, and 17.63%, respectively. ROS1 aggregate concrete presents exceptional performance across sustainable concrete classifications regarding mechanical characteristics, including compressive strength, splitting, flexural strength, and modulus of elasticity at a 100% replacement rate and an age of 28 days, with decreases of 28.47%, 27.42%, 18.11%, and 36.65% relative to ordinary concrete. Although a good assessment of sustainable concrete styles is according to water absorption test values, normal concrete continues to yield superior outcomes.

© 2025 MIM Research Group. All rights reserved.

1. Introduction

Concrete is the most extensively employed material in the global building industry [1, 2]. The primary constituents of concrete are cement, natural sand, coarse aggregate, and water. It is essential to acknowledge that aggregates, such as sand and gravel, constitute a significant amount, around 70–80%, of the overall volume of concrete [3]. The substantial demand for large amounts of aggregates not only exhausts limited natural resources but also creates considerable environmental sustainability issues [4]. Consequently, there is an immediate necessity to discover alternate choices to either substitute or reduce the use of these aggregates [5]. Moreover, cement that is unused or incorrectly stored will expire if not utilized during the advised storage period and could be classified as waste material [6, 7]. While the production of one ton of cement generates approximately 900 kg of carbon dioxide, which accounts for roughly 5-7% of global CO_2 emissions [8]. As a result, the construction sector has had considerable hurdles for a long time in developing sustainable and environmentally acceptable structures. The density of conventional concrete

*Corresponding author: bce.22.35@grad.uotechnology.edu.iq
[a]orcid.org/0009-0009-1464-0432; [b]orcid.org/0000-0001-8287-2782
DOI: http://dx.doi.org/10.17515/resm2025-790ma0327rs

ranges from 2200 to 2600 kg/m^3 [9]. Lightweight concrete (LWC) often possesses densities ranging from 1400 to 1900 kg/m^3, attributable to the presence of Pores in the lightweight aggregate (LWA). It is characterized by an enhanced strength-to-weight ratio, an appropriate coefficient of thermal expansion, superior strain capacity, and exceptional insulating properties. The implementation of LWC can yield substantial cost reductions by decreasing the dead load of the structure and minimizing the cross-sectional area of steel-reinforced columns, slabs, beams, and foundations [10–12].

Artificial aggregates are typically produced using two methods: cement-based granulation (cold-bonding) and high-temperature burning (sintering)[13, 14]. A significant disadvantage of the sintering process is its elevated energy consumption during granulation. This technique involves the formation of pellets at temperatures up to 1200 °C [15, 16], while the manufacture of aggregates in restricted quantities and high density constitutes a primary obstacle to the extensive industrial implementation of cold bonding technology [5, 13]. In the cold-bonding method, by-products like fly ash, and waste material transform into a water-resistant substance with initially low compressive strength, which increases based on the curing technique and duration [17]. Cold-bonded aggregate offers a viable approach for the advancement of sustainably sourced aggregate manufacturing, providing a solution that conserves valuable natural resources besides transforming waste materials into profitable, environmentally beneficial products [18, 19]. This technique takes into account production parameters including rotation speed, pelletizer angle, pillarization period, and moisture content [20]. Manikandan and Ramamurthy [21] found that low angles and velocities restrict aggregate granule collisions, resulting in a diminutive, ineffective aggregate. Numerous researches have investigated the impact of binder types on lightweight aggregate cold bonding. Gomathi and Sivakumar [22] conducted a comparison of lime- and cement-bound fly ash aggregates. Cement aggregates exhibited a 37% superior crushing strength, a 34% increased dry bulk density, and a 50% reduced water absorption compared to lime aggregates. Studies [23] and [24] show that adding new elements to the reference mix for fly ash aggregate can change its characteristics and enhance some of its attributes. The aggregate particles are influenced by the curing methods employed, analogous to their impact on concrete [15, 25, 26]. The inclusion of cold bonding aggregate (CBA) has been shown to influence the fresh density of concrete, which is associated with the densities of its components. Tang and Brouwers [27] discovered that replacing normal aggregate NA with CBA at change levels of 30% and 60% by volume results in a reduction of fresh density of NAC by approximately 5% and 8%, respectively, while the fresh density of CBAC was identified to be 17% lower than that of NAC [28]. Gesoglu et al. [29] noted that the compressive strength of concrete diminishes when the volume proportion of fabricated cold-bonded fly ash aggregate increases. Joseph with Ramamurthy [30] indicated that synthetic lightweight cold-bonded fly ash aggregate is effective in producing concrete with strengths reaching 52 MPa. The replacement of lightweight fly ash aggregates for normal weight aggregates in concrete led to decreased mechanical characteristics. The study via Kockal and Ozturan [17] indicates that utilizing fly ash aggregate as a complete replacement for normal weight coarse aggregate resulted in a notable reduction in compressive strength and splitting tensile strength, decreasing from 62.9 MPa and 5.1 MPa to 42.3 MPa and 3.7 MPa, correspondingly. Gesoğlu et al. [31] reported analogous findings, demonstrating that the compressive strength and splitting tensile strength of fly ash aggregate concrete diminished from 40.1 and 3.22 MPa to 29.1 and 2.58 MPa, respectively, as the percentage of cold-bonded FA aggregate in concrete with a water-to-cement proportion of 0.35 rose from 30% to 60% of the total aggregate volume in the mixture. Tires provide environmental hazards due to their composition, rendering them highly durable, non-biodegradable, a fire risk, and a breeding ground for rodents and vermin [32]. Hence, much prior research has concentrated on incorporating tire waste into concrete to address several environmental problems related to the accumulation of this waste [33–37]. This study introduces a fresh approach for eco-friendly building systems by producing and assessing the characteristics of sustainable concrete that incorporates replacement ratios of 50-100% of natural coarse aggregate with optimum artificial coarse aggregate created through the cold bonding technique, utilizing a reference mix made from waste materials, including expired cement and used tires.

2. Experimental Program

The practical aspect of this research consists of two parts. The initial stage involved the manufacture of ten types of semi-lightweight coarse aggregates using the cold bonded technique. In the second stage, normal-weight concrete and six varieties of semi-lightweight sustainable concrete were produced by replacing different amounts of natural coarse aggregates with the optimal kind of artificial coarse aggregates.

2.1 Materials

2.1.1 Portland Cement (PC), Expired Cement (EC), Fly Ash (FA)

Portland Cement type CEMI 42.5R, compliant with BS EN 197-1-2011 [38], was employed in the production of normal and sustainable concrete. The expired cement (EC) utilized as a binding agent in the manufacture of coarse aggregate was sourced from cement bags that had been held in the laboratory for almost three months over the expiration date under improper storage circumstances. As shown in Figure 1a, a part of the cement powder has transformed into a semi-solid clumping product and requires re-crushing.

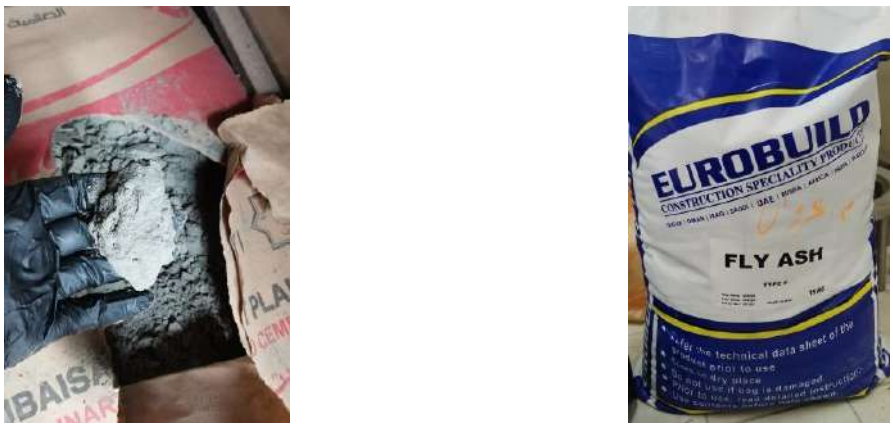

(a) (b)

Fig. 1. Materials (a) expired cement, (b) fly ash

The Portland cement comprises four primary mineral phases: C3S, C2S, C3A, and C4AF, each possessing distinct properties and specific formation temperatures [39]. The percentage of the four minerals may be computed using the values from table 1 and the Bogue's equations [40] , table 2 presents the conclusive findings about the mass loss proportion between normal cement and expired cement [41, 42]. In the reference mix for artificial aggregate, EC was combined with type F fly ash (Figure 1b) meeting ASTM C618 [43] from EUROBUILD company. Table 1 presents the Properties of PC, EC, and FA.

Table 1. Properties for OPC, EC, FA

Ingredients (%)	Normal Cement OPC	Expired cement EC	Fly ash FA
CaO	62.55	59.92	5.1
Al_2O_3	5.3	4.43	27.7
Fe_2O_3	4.02	3.52	8.44
SiO_2	20.23	20.05	49.66
SO_3	2.27	2.1	0.34
Na_2O	0.21	0.33	0.38
MgO	2.83	2.63	2.65
K_2O	0.91	0.99	3.36
Specific gravity	3.14	3.14	2.1
Loss on ignition	1.01	2.17	3.7

Table 2. Main components of PC, EC

Mass Ratio %	C_3S	C_2S	C_3A	C_4AF
PC	52.98	18.31	7.25	12.22
EC	50.7	19.51	5.79	10.6

2.1.2 Natural Aggregate

Natural sand from the second zone was utilized as fine natural aggregate with a maximum size of 4.75 mm, while crushed gravel functioned as conventional coarse aggregate. Table 2 presents the gradation and characteristics of each kind.

Table 3. Sieve analysis and features of natural aggregates

Fine Aggregate		
Size of Sieve (mm)	Accumulative passing %	Limitations of ASTM C 33[44]
4.75	98	95-100
2.36	92	80-100
1.18	84	50-85
0.6	43	25-60
0.3	23	12-40
0.15	4	0-10
Fineness Modulus	2.56	---
Specific Gravity	2.64	---
Absorption %	2.94	---
Coarse Aggregate		
Size of Sieve (mm)	Accumulative passing %	Limitations of ASTM C 33[44]
19	100	100
12.5	97	90-100
10	65	40-70
4.75	8	0-15
2.36	3	0-5
1.18	1	---
0.6	0	---
0.3	0	---
Fineness Modulus	5.26	---
Specific Gravity	2.68	---
Absorption %	0.61	---
Density (kg/m^3)	1678	---

2.1.3 Tire Waste (R), Starch (S), Alginate (A)

To obtain different types of artificial coarse aggregates, three weight percentages (0.5%, 0.75%, and 1%) of tire waste, starch, and alginate were separately added to the reference mixture. Tire waste granules were collected from the Diwaniyah Tire Factory, with sizes ranging from 0.3 to 0.85 mm. Given the presence of carbon in the microstructure of tire waste granules, which is a soft material impacting aggregate strength, these waste materials were exclusively analyzed using X-ray diffraction (XRD) to more precisely evaluate the effect of tire waste aggregates on the properties of semi-lightweight sustainable concrete. Figure 2 displays test findings revealing carbon levels of up to 75%, oxygen levels of around 17%, and other components ranging from 0.2% to 3%. In this study, both starch and alginate serve as natural biopolymer admixtures. Starch was sourced from local shops, while normal-setting alginate, which dental applications employ as an irreversible hydrocolloid impression substance, demonstrates elastic qualities, obtained from Zhermack Tropicalgin. The widespread consumption of irreversible hydrocolloid surpasses that of any other impression substance [45]. Table 4 presents the chemical characteristics of the substances, whereas. Table 5 delineates their physical characteristics.

Table 4. Chemical characteristics

Chemical Elements	Concentration (ppm)		Percentages
	Starch (S)	Alginate(A)	Tire waste (R)
Iron (Fe)	9.5	---	0.4
Manganese (Mn)	9.6	---	---
Chromium (Cr)	8.4	---	---
Phosphor (P)	45.2	63	---
Sulfur (S)	< 2	906	2.0
Chlorine (CI)	0.3	---	---
Sodium (Na)	< 640	<2100	---
Magnesium (Mg)	< 100	<350	0.2
Aluminum (Al)	< 18	<84	0.6
Silicon (Si)	55.4	17597	0.6
Titanium (Ti)	< 1.5	2431	---
Vanadium (V)	9.5	23.2	---
Calcium (Ca)	45.7	26482	0.4
Potassium (K)	86	---	---
Zink (Zn)	---	---	2.8
Oxygen (O)	---	---	17.2
Carbon (C)	---	---	75.8

Table 5. Physical characteristics

Characteristics	Particle size	Appearance	Density (kg/m^3)	Color
Starch	85.82 nm	Fin Powder	1498	White
Alginate	117.74 nm	Fin Powder	1412	Orang
Tire waste	0.3-0.85 mm	Powder	586	Black

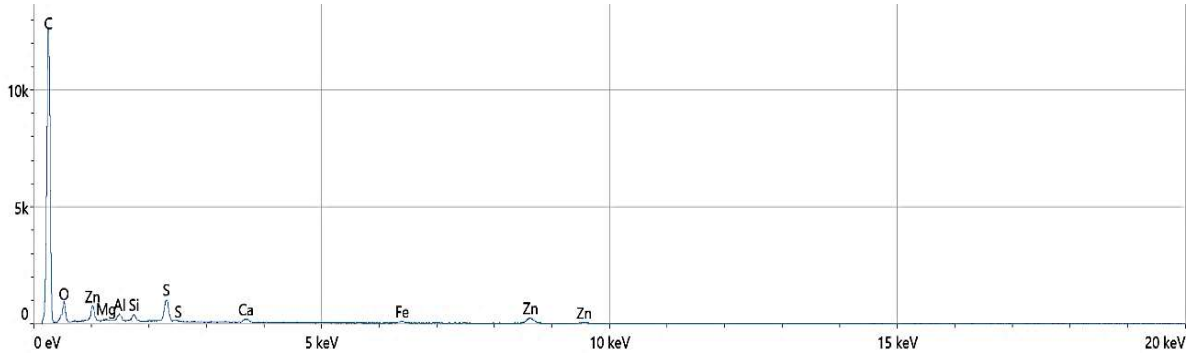

Fig. 2. XRD image for tire waste elements

(a) (b) (c)

Fig, 3. Materials (a) Tire waste, 8b) Starch, (c) Alginate

2.1.4 Superplasticizer

Sika's ViscoCrete-5930 superplasticizer have been choosing for enhancing the workability of concrete and achieve the desired consistency. A third-generation superplasticizer for concrete and mortar, according to the standards for superplasticizers delineated in ASTM C-494 Classes G and F [46], plus BS EN 934 Part 2: 2001[47]. Table 6 offers the characteristics of the superplasticizer [48].

Table 6. Properties of superplasticizer*

Properties	Result [48] *
Dosage	0.8-2 % by weight of cement
Density	1.095 kg/ litter (ASTM C 494) [46]
Storage	5-35° C
Toxicity	Non-toxic
packaging	5-20-200 kg
Appearance	Turbid liquid
Life	12 months from production

* Data from Production Company

2.2 Production of Cold-Bonded Fly Ash Coarse Aggregate

The practical part of this research starts with the creation of synthetic semi-lightweight coarse aggregate at room temperature. This is done using a pelletizing machine and a cold bonding technique for the dry mixture components. The pelletizing apparatus comprises a drum with a depth of 350 mm, a diameter of 850 mm, an operating angle of 90 degrees, and a rotational speed of up to 45 rpm like seen in the figure 4. Through previous investigations [23, 25, 49, 50] and several trials, the optimal operational parameters of the machine were established, including speed, inclination angle, and water amount. The dry reference mixture, including 90% fly ash and 10% expired cement, is poured in the container and blended at a rotational speed of 4 to 6 rpm to attain homogeneity. The device's water pumps release water in three successive batches, maintaining a water-to-mixture ratio of 20% to 22% by weight. After the initial 10 minutes, freshly spherical pellets start formation.

Table 7. Sieve analysis of lightweight coarse aggregate (LWCA)

Sieve size (mm)	LWCA	%Passing - ASTM C330
19	100	100
12.5	96	90-100
9.5	57	40-80
4.75	10	0-20
2.36	2	0-10

The agglomeration process extends for an extra 10 minutes to guarantee the grains attain the requisite size and enough hardness for handling. Upon completion of the pelletizing process, the resultant aggregate is held in sealed plastic bags for 24 hours at a temperature of 20 degrees Celsius, with a permissible variation of ±2 degrees, and a humidity level of 70% [51]. Executed three separate curing methods on 10 aggregate classes during a 28-day period: self-curing, water-curing, and oven-curing at a temperature of 64°C. Oven curing elevates the specific gravity and bulk density of lightweight coarse aggregate from 1.85 and 976 kg/m^3 for water-cured aggregate and from 1.87 and 984 kg/m^3 for self-cured aggregate to 1.92 and 1012 kg/m^3, respectively. The heat-curing regimes result in enhanced hydration dynamics, which provide a denser structure [52], while the LWCA pellets disintegrate owing to water curing [49]. Furthermore, oven curing achieved the maximum crushing strength values of the aggregate at 9.24 MPa, reflecting an increase of 0.32% relative to the self-cured aggregate and 5.84% compared to the water-cured aggregate. Subsequently, a sieve analysis was performed in accordance with ASTM C330 [53]. According to the criteria stated in BS-812-110-1990[54], the crushing strength of the particle for ALWA was assessed using the California Bearing Ratio (CBR). Employing ASTM C127[55] to ascertain the

specific gravity of the lightweight aggregate in a saturated surface dry condition and its water absorption capacity.

(a) (b) (c) (d)

Fig. 4. Steps for manufacturing artificial coarse aggregate via the cold bonding technique (a) Pelletizer disc, (b) Dry powder, (c) Homogeneity of ingredients, (d) Formation of pellets

2.2.1 Scanning Electron Microscopy Test (SEM)

Figures 5 a, b, and c present S.E.M. analysis of aggregate particles roughly 1 cm in size for the optimum categories of the produced aggregate (RSS1, ROS1, RWR0.75). Photographs taken with a scanning electron microscope show the interior structure and illustrate the development of various pore patterns. The primary distinction among ideal aggregation types is in the pores, which may be circular, unconnected, and irregular, or linked and longitudinal. The oven-cured granules demonstrate enhanced homogeneity in their exterior matrix and a more robust structure due to improvements in the hydration dynamics, in contrast to the water-treated granules, which experienced degradation in their external matrix and an enlargement of pore size. The self-cured aggregate particles exhibit a surface and microscopic structure of moderate solidity. Microstructure investigations suggest that a closed structure formed from the interaction between the components of the additional substance and calcium hydroxide (portlandite) in the reference mix may account for the diminished water absorption ratio of the optimal lightweight aggregates ROS1.

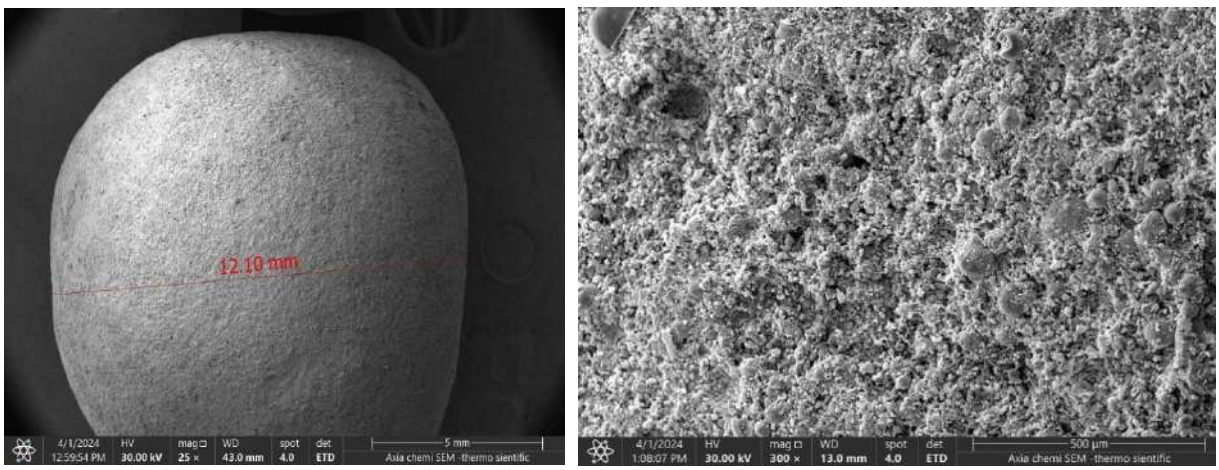

(a)

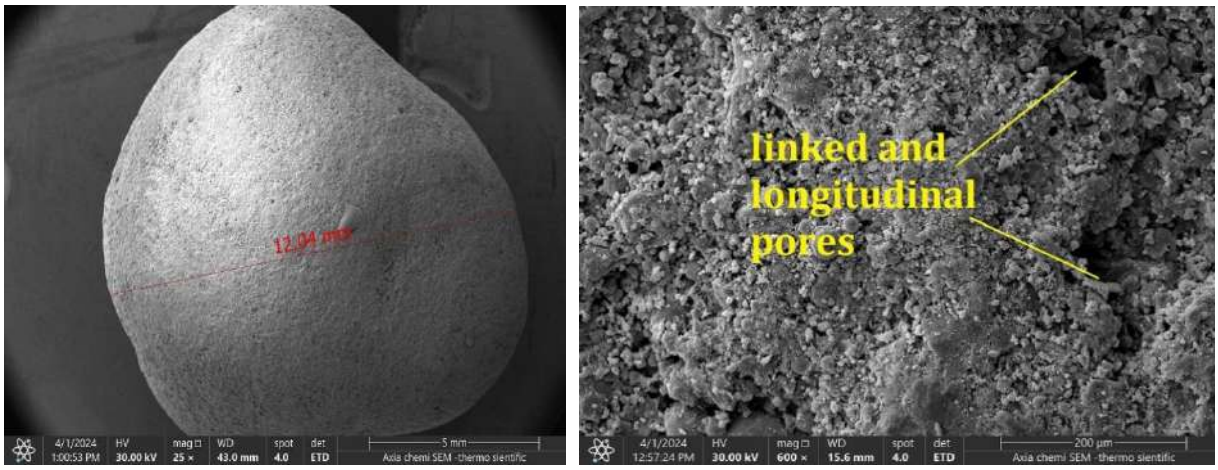

(b)

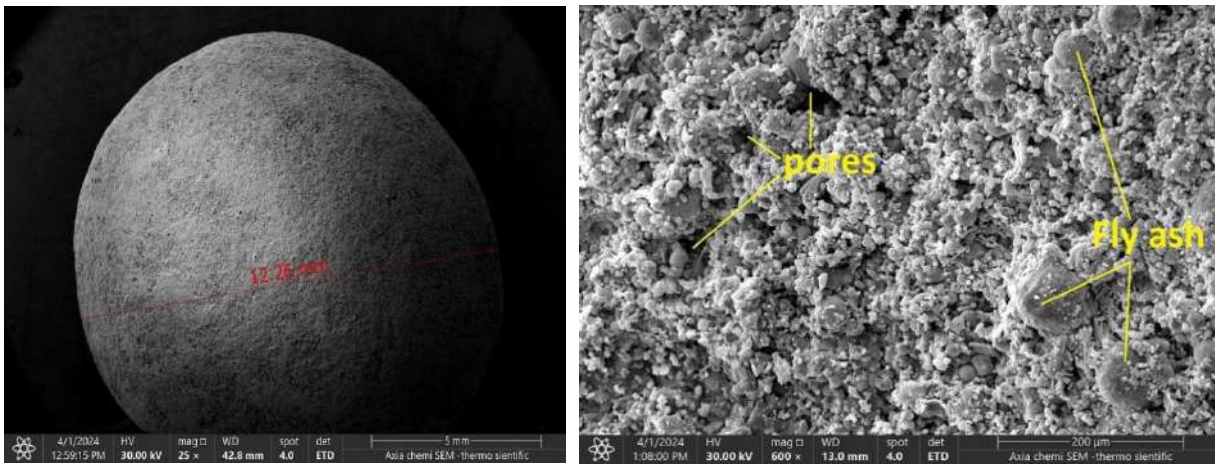

(c)

Fig. 5. SEM analysis (a) Oven-Cured Aggregate with 1% Starch (ROS1), (b) Water-Cured Aggregate with 0.75% Tire waste (RWR0.75) and (c) Self-Cured Aggregate with 1% Starch (RSS1)

3. Mix Proportions of Concrete

This section covers the experimental program's strategy for creating semi-lightweight sustainable concrete using the best types of coarse aggregates (RWR0.75, RSS1, ROS1) that the study's initial phase produced and identified. To assess the influence of this aggregate type, a reference concrete was formulated containing 100% natural aggregate (NA), 400 kg /m^3 cement quantity, and a ratio of water to cement W/C 0.4. Additionally, a sustainable concrete was made by substituting the natural coarse aggregate (NCA) with synthetic lightweight coarse aggregate (LWCA) at volumetric proportions of 50% and 100%, respectively, while maintaining the weights of the other components of the concrete mix constant. To achieve a 120 mm slump in conventional concrete and a 75 mm slump in sustainable concrete while ensuring modified workability, the dose of superplasticizer was tailored for each concrete mix [56]. The adjustment is primarily due to the spherical morphology of lightweight coarse aggregate (LWCA), in contrast to the angular characteristics of normal coarse aggregate (NCA), which required an extra superplasticizer dose [57–59]. This work employed an electric rotary mixer with a capacity of 1 cubic meter, as depicted in figure 6. Artificial coarse aggregate particles must reach a state of saturation and a dry surface (SSD) before manufacturing, as their ability to absorb significant amounts of water negatively affects the concrete [41, 60]. Consequently, the weights of the aggregates utilized in the generated mixtures were altered according to the absorption rate of each type, attaining the saturated surface

dry (SSD) condition [40]. The document ACI 211.2-98 [61] outlines protocols for formulating concrete mixes. The ratio of concrete components for one cubic meter is presented in table 8.

Table 8. Details mix proportions for concrete kg/m^3

Mixes designation*	Cement kg/m^3	NFA kg/m^3	NCA kg/m^3	LWCA kg/m^3	W/C ratio	Super plasticizers%	Slump mm
NWC	400	656	1024	0	0.4	1.3	120
50RSS1C	400	656	512	350.88	0.4	1.005	75
100RSS1C	400	656	0	701.76	0.4	0.946	75
50RWR0.75C	400	656	512	357.12	0.4	1.107	75
100RWR0.75C	400	656	0	714.24	0.4	0.964	75
50ROS1C	400	656	512	362.17	0.4	0.982	75
100ROS1C	400	656	0	724.34	0.4	0.642	75

*Note: W/C : water-to-cement ratio; NWC : normal weight concrete; NFA : natural fine aggregate; NCA : natural coarse aggregate; LWCA : lightweight coarse aggregate; RSS1 : self-cured aggregate with 1% starch; ROS1 : oven-cured aggregate with 1% starch; RWR0.75 : water-cured aggregate with 0.75% tire waste; RSS1C, ROS1C, and RWR0.75C represent sustainable concrete incorporating 50% and 100% lightweight coarse aggregate.

(a) (b) (c) (d)

Fig. 6. Concrete production process (a) Artificial aggregate immersed in water, 8b) Electric blender 1m^3, 8c) Slump checking, (d) Concrete pouring

4. Methodology for Sample Preparation and Testing

Conforming with BS EN 12390-3 [62] determined the compressive strength using a 100 x 100 x 100 mm test cube. The test was performed on three specimens at 7, 28, and 60 days of age, employing a 2000 KN compression apparatus with a loading rate of 15 N/mm per minute, Prior to that, Ultrasonic Pulse Velocity of these samples are examined in line with ASTM C597 [63]. The mean of three results for each test age is extracted through inputting the readings of each sample into Equations 1 and 2.

$$f_{cu} = \frac{P}{A} \quad (1)$$

where, f_{cu}: The compressive strength MPa, P: Load failure (N), A: Cross-section area (mm²).

$$\mathcal{V} = \frac{L}{T} \tag{2}$$

where, V: Ultrasonic pulse speed meter/second, L: path length (m), T: pulse transit period (sec).

As per ASTM C642-13 [64], this study checks the density of concrete and the absorption ratio at different curing ages by heating samples in an oven at 110 ± 5 degrees Celsius for 24 hours. Once the specimens reached room temperature, recorded their weight (A). Later returned them to the water tanks. Following an additional 24 hours, documented the samples' weight in water (C) and allow them to air dry at room temperature until they reach a saturated and surface-dry condition, after which measured their weight (B). The splitting tensile strength was calculated on three cylindrical samples, each measuring 100 × 200 mm, in line to the specified testing age [65]. Slender plywood bearing strips are employed to evenly distribute the tension exerted across the cylinder's length when put inside the test machine. Equation 3 is applied to ascertain the outcomes figure 7.

$$f_t = \frac{2p}{\pi L d} \tag{3}$$

where, f_t: splitting tensile strength MPa, P: Maximum apple load (N), L: Length of specimen (mm), d: Diameter of specimen (mm).

Prism-shaped models measuring 100 mm by 100 mm by 400 mm are utilized to examine flexural strength corresponding with ASTM C78[66] the formula 4 serves to determine the values that can symbolize the rupture modulus. Figure 7 depicts the sample and the device used.

$$f_r = \frac{p \times l}{b \times d^2} \tag{4}$$

where, f_r: flexural strength MPa, p: Maximum load (N), L, b, d: Length, Width, Depth, of specimen.

The final findings of the Static Modulus of Elasticity test reflect the average values obtained from three cylinders measuring 100 by 300 mm at ages of 28 and 60 days, which meet with ASTM C469 [67]. The equation 5 was utilized to ascertain the ratio of stress to strain and the ratio of longitudinal strain to lateral strain of hardened concrete under specified curing conditions.

$$E_c = \frac{S_2 - S_1}{\varepsilon_2 - 0.00005} \times 10^{-3} \tag{5}$$

where, E_c: Elastic modulus GPa, S_1: Stress correlated with longitudinal strain of 0.000050 MPa, S_2: Stress equivalent to 40% of the ultimate load MPa, ε_2: Longitudinal strain induced by stress S2.

(a) (b) (c) (d)

Fig. 7. Concrete specimens and examination devices: (a) Oven, (b) Splitting, (c) Flexural, (d) Modules of elasticity

5. Findings and Discussion

5.1 Density

Table 9 illustrates the disparity in fresh density results between conventional concrete and sustainable concrete, with the latter's density consistently diminishing as the ratio of natural coarse aggregate replaced by artificial lightweight coarse aggregate increases, owing to the porous characteristics of the lightweight aggregate particles [68]. The density values vary from 2427 kg/m^3 to 2032 kg/m^3. These results align with [18, 56, 69], specific gravity, and bulk density of each aggregate type selected. The change in specific gravity of the components in the concrete mixes results in differing dry density values. As illustrated in Figure 8, the values rise as the concrete matures because of ongoing hydration, gel formation, and enhancements in the properties of the interfacial transition zone. Nonetheless, their performance declines when manufactured coarse aggregate exceeds 50% as a substitute for natural coarse aggregate [70].

Table 9. Density mixes of concrete

Mix Designation	weights of Cubes for Concrete Mixtures(kg)	Fresh Concrete Density kg/m^3
NWC	11.26	2427
50RWR0.75	11.09	2254
100RWR0.75	10.91	2078
50RSS1	11.13	2293
100RSS1	10.92	2081
50ROS1	11.07	2234
100ROS1	10.87	2032

Conventional concrete exhibits superior performance due to the elevated specific gravity of the natural coarse aggregate and its low porosity [18]. The densities of concrete incorporating 50% and 100% ROS1 aggregate diminished at the most significant rates (10.99%, 10.69%, 10.78%, and 17.56%, 17.63%, 17.66%), respectively, relative to conventional concrete during the designated testing dates. This was due to a decrease in the overall specific gravity and density of the aggregate particles. Even though RSS1 aggregate concrete's dry density values keep going down compared to normal concrete, it performs better than ROS1 and RWR 0.75 aggregate concrete because the aggregate particles have a higher specific gravity and density. The test results demonstrated that the dry density of the semi-lightweight sustainable concrete corresponds with prior research findings [71].

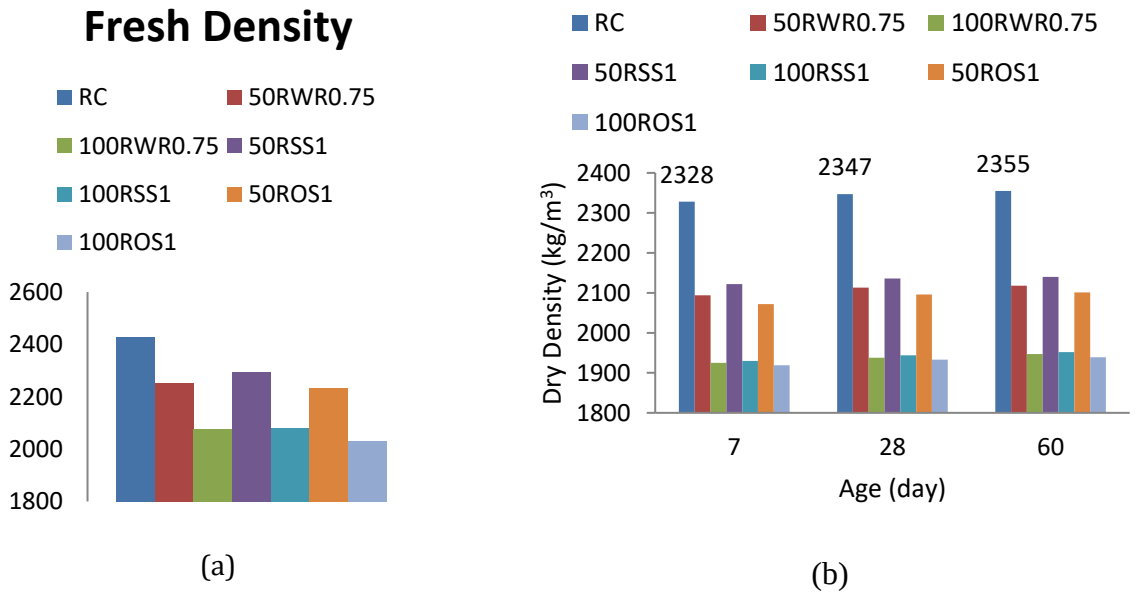

Fig. 8. Density: (a)Fresh density, (b) Dry density

5.2 Ultrasonic Pulse Velocity (UPV)

The results of this test improve as both normal and sustainable concrete mature due to ongoing hydration and the evolution of hydration products that enhance structural integrity. However, the velocity of ultrasonic pulse transmission in the standard concrete model is superior to that in the sustainable concrete, owing to its higher density and more effective filling of pores with hydration products [41, 71]. The test assesses the quality of the concrete, the uniformity of its internal components, and the impact of voids by measuring the pulse propagation velocity between the two sides of the sample. Figure 9 demonstrates a reduction in pulse transmission velocity as the proportion of natural coarse aggregate substituted with lightweight artificial aggregate escalates from 50% to 100%. The drop attains its minimum in concrete containing 100% ROS1 type aggregate 3625, 3628, and 3629 m/s, demonstrating reduction rates of 21.09%, 21.79%, and 25.80% relative to conventional concrete 4594, 4639, and 4891 m/s at 7, 28, and 60 days, respectively, attributable to the low bulk density of ALWA [72]. However, it is still classified as good concrete in accordance with ASTM C597[73]. In contrast, the concrete incorporating 50% RSS1 class aggregate had the highest pulse arrival velocity, 4111, and 4112 reaching a maximum of 4115 meters per second at 60 days, and is classified as excellent concrete. Figure 9 depicts that all concrete mixtures generated in this investigation are classified from good to excellent according to ASTM C 597-02 specifications [73].

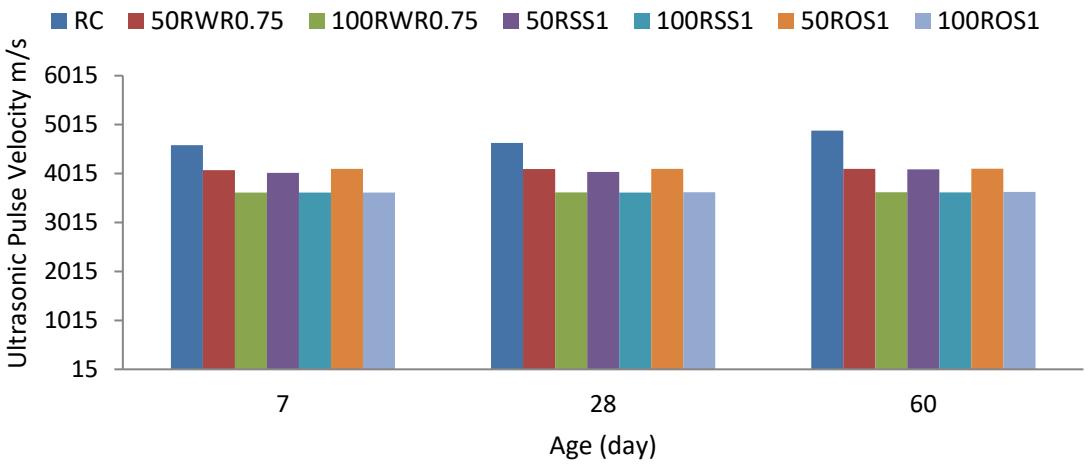

Fig. 9. Ultrasonic Pulse Velocity Results

5.3 Compressive Strength

The compressive strength of concrete indicates its quality and reflects its other characteristics. Figure 10 displays a drop in concrete strength when the ratio of natural coarse aggregate substituted with artificial coarse aggregate rises, due to the disparity in strength between the two aggregate types [71, 74]. Conversely, regardless of the replacement ratios, prolonged water curing improves the strength of the concrete due to the ongoing hydration process. This process results in the formation of additional materials, such as calcium silicate hydrate (C-S-H), which in turn enhances the internal structure's integrity [18, 41]. This investigation used a reference concrete that included natural aggregate, which exhibited compressive strengths of 39.7, 49.35, and 57 MPa at the designated testing ages, and sustainable concrete, with 50% and 100% replacement for ideal cold-bonded lightweight aggregate categories. Evaluations were conducted at 7, 28, and 60 days of curing. The type two concrete results were between 31.5 and 45.7 MPa, which is in line with the ASTM C330 [53] and ACI 318 [75] standards for structural lightweight concrete, which say that the concrete must have a minimum 28-day compressive strength of 17.2 MPa. Employing a 50% and 100% replacement ratio of aggregate class RWR0.75, the strength of semi-lightweight sustainable concrete diminishes to its lowest of 35.4, 38, 40.9 ,31.5, 33.25, and 35 MPa, demonstrating a decline rate of 10.83%, 22.99%, 28.24%, 20.65%, 32.62%, and 38.59% in a 7, 28, and 60-day test, respectively. The reduced solidity of the aggregate particles containing rubber negatively affects

the overall strength of the concrete [76]. The concrete aggregate type RSS1 comes with average values of 36.6, 38.45, 41.77, 33.1, 34.14, and 36.28, respectively, as illustrated in figure 10. During this test, concrete made with aggregate ROS1 did better than other sustainable concrete mixes. This is because heat curing processes influence aggregate particles, which leads to the highest crushing strength [25, 52, 71]. The findings align with [56, 77].

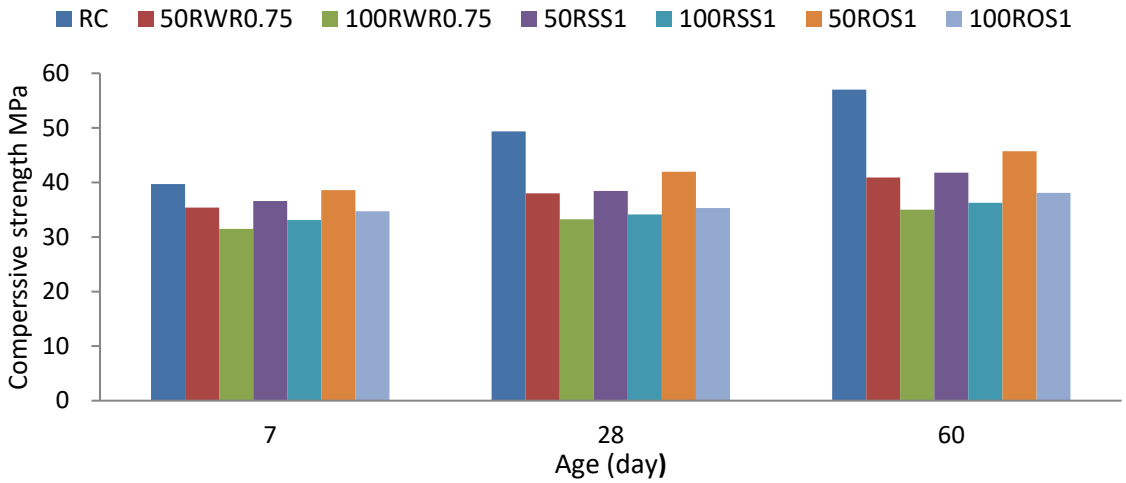

Fig. 10. Compression strength at 7, 28, and 60 day

5.4 Splitting Tensile Strength

The partially or complete substitution of natural coarse aggregate with synthetic lightweight coarse aggregate diminishes the splitting tensile force of concrete at testing ages of 7, 28, and 60 days [68]. This results from the low tensile strength of the ALWA particles and the existence of empty voids in their structure, which cause failure along paths aligned with these pores [18]. Figure 11 display test results that vary from 3.4 to 4.3 MPa for standard concrete and from 1.6 to 4.1 MPa for sustainable concrete. An examination of various semi-lightweight concrete types at 50% and 100% replacement levels indicates that ROS1 aggregate concrete has the highest splitting tensile strength, with lowering rates of 17.64%, 5.71%, and 4.65%, as well as 25.85%, 27.42%, and 38.37%, respectively, in comparison with natural aggregate concrete. On the other hand, concrete involving coarse aggregate type RWR0.75 gives the lowest results at all specified testing dates. This is due to the inherent fragility of the industrial aggregate [78, 79].

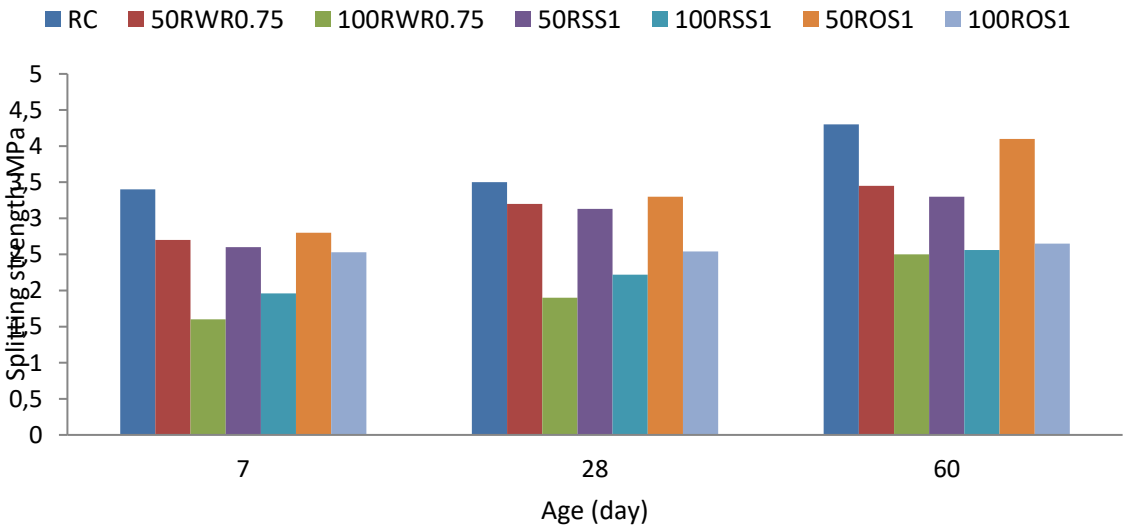

Fig. 11. Splitting tensile strength

5.5 Flexural Strength

This attribute enhances over time in normal and sustainable concrete owing to advancements in the curing and hydration processes [80]. The flexural strength of regular concrete is higher than that of sustainable concrete at all testing ages and replacement ratios, as shown in figure 12. This is mostly because natural coarse aggregate is stronger [20, 68]. Normal concrete had test results ranging from 5.5 to 8.5 MPa, while sustainable concrete had results ranging from 2.92 to 7.92 MPa after the required curing times. Compared to the other types of concrete that used coarse industrial aggregate, ROS1 aggregate concrete did better at 7 and 28 days, reaching a peak 7.92 MPa after 60 days with a 50% replacement, attributable to the strength of the aggregate [18]. As illustrated in figure 12, RSS1 aggregate concrete demonstrates average performance. Conversely, the RWR0.75 aggregate concrete exhibits weaker performance relative to conventional concrete, with decreasing rates (12, 25.76, 27.05) at 50% replacement and 46.9, 62.24, and 60.23 at 100% replacement, owing to the negative effect of rubber on the strength of aggregate grains [76].

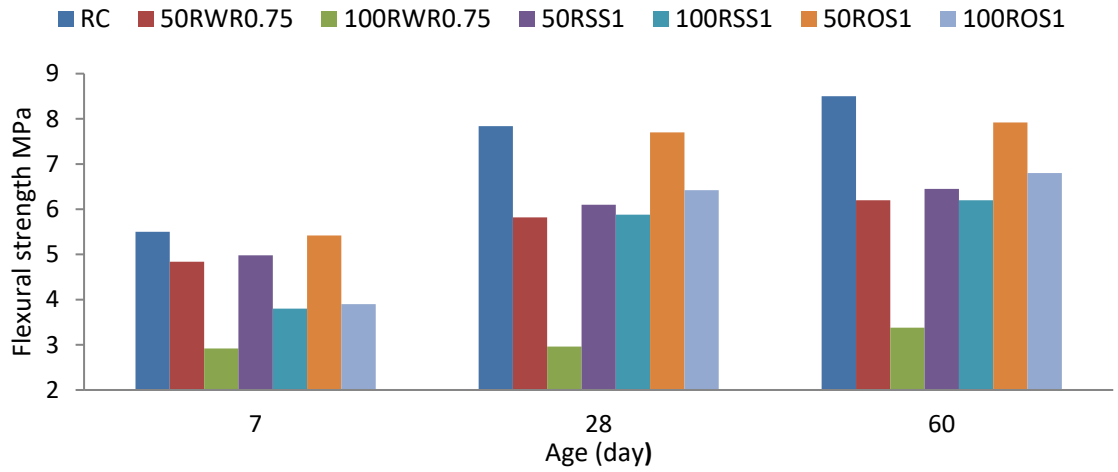

Fig. 12. Flexural strength

5.6 Modulus of Elastic (E_c)

Properties of the aggregate (strength, structural composition, amount used) affect the modulus of elasticity of concrete [29], with these values varying according to changes in concrete compressive strength (goes up or down) [18]. Figure 13 exhibit that the modulus of elasticity values to all category's concrete get stronger over time [68], which ranges from 27.57 GPa at 7 days to 33.54 GPa at 60 days for normal concrete.

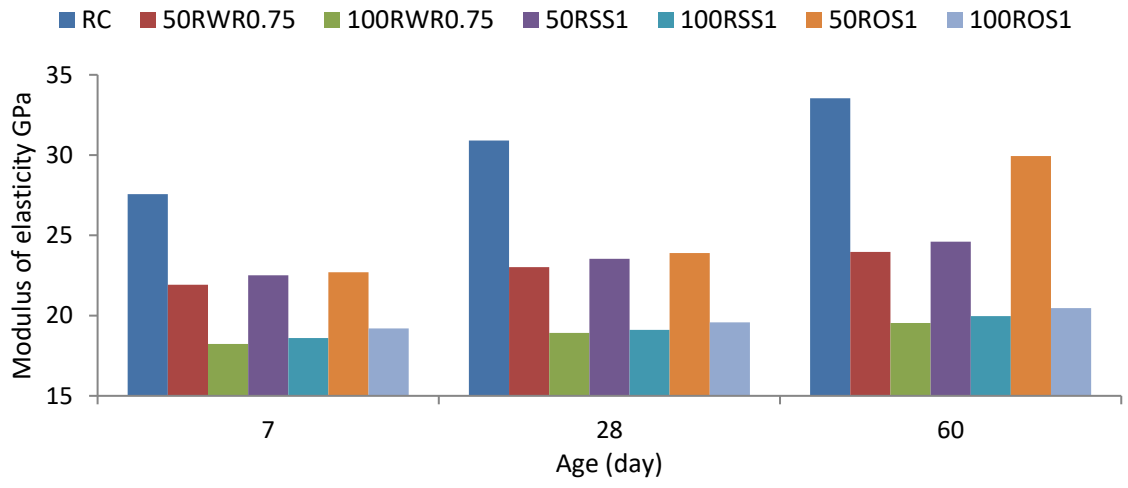

Fig. 13. Modulus of Elastic

In contrast, the modulus of elasticity for sustainable concrete differs from a minimum of 18.23 GPa at 7 days to a maximum of 29.94 GPa after 60 days of curing, attributable to the superior strength and less porous structural composition of natural coarse aggregate compared to artificial coarse lightweight aggregate [81]. Figure 13 demonstrates that the modulus of elasticity declines when the lightweight aggregate (LWA) replacement percentage increases from 50% to 100% [18, 82]. For example, among similar types, concrete employing coarse aggregate of type ROS1 works the best, while the incorporation of 50%, 100% RWR0.75 aggregate results in a decline in the concrete's elastic modulus by 20.49%, 25.52%, 28.53%, and 33.87%, 38.79%, 41.74% after 7, 28, and 60 days, respectively, in comparison to concrete made with natural aggregate. The RSS1 aggregate concrete possesses average values.

5.7 Water Absorption

Porosity significantly affects the properties of concrete regarding water absorption, as it creates channels for water infiltration and movement inside its structural matrix, hence augmenting the amount of absorbed water. Figure 14 demonstrates a decline in these ratios as curing age advances for concrete mixtures, due to the continuous hydration process and the formation of additional calcium silicate gel, which reduces pore size and their connectivity [72], while simultaneously improving the strength of the interfacial transition zone. In standard concrete, water is absorbed mainly by the cement paste; however, in sustainable concrete (semi-lightweight), it is absorbed by both the cement paste and the coarse artificial aggregate due to its porous properties. As a result, sustainable concrete displays a higher absorption of water than conventional concrete [83, 84]. The test values ranged from 4.6 to 3.2 for standard concrete and from 10.24 to 5.22 for sustainable concrete across planning age categories. The concrete with ROS1 type aggregate at a 50% ratio exhibited notable performance at 7 and 28 days, approaching optimal conditions after 60 days with a 38.69% increase relative to conventional concrete, aligned with improvements in aggregate particle characteristics [10]. At the identical replacement percentage, the concrete incorporating RWR0.75% aggregate exhibited an elevation in absorption values, attributable to the heightened absorption of the aggregate assessed in the initial part of the investigation. The elevated water absorption rate of the RSS1 type aggregate led to a corresponding rise in the concrete absorption rate, achieving the maximum values, with increases of 44.24%, 55.34%, and 58.81% relative to standard concrete. The amount of water permeating the concrete is associated with the presence of pores; hence, figure 14 depicts its increase when the substitute ratios of natural coarse aggregate with lightweight artificial coarse aggregate change from 50% to 100%, in accordance with research findings [41, 85]. Except for the test result for the 7-day-old concrete made of 100% RSS1 class aggregate, the sustainable concrete mixes developed in this study are very good, as shown by the fact that they didn't absorb more than 10% [9].

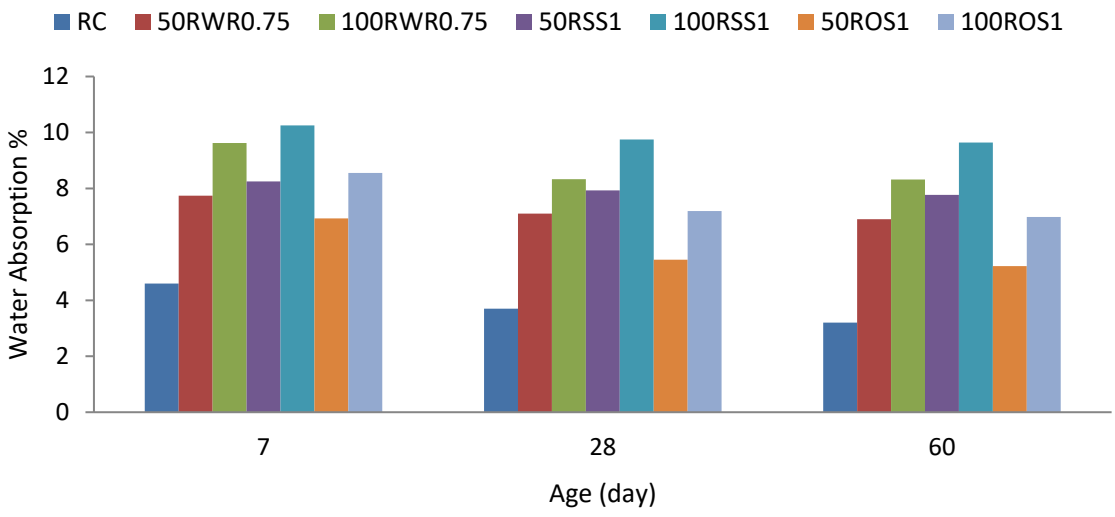

Fig. 14. Water absorption

6. Conclusion

The findings of the experimental program in the present research yield the following conclusions:

- Conventional concrete has superior performance compared to concrete with an equivalent blend of natural and artificial coarse aggregates. The latter performs better than concrete that completely employs synthetic coarse aggregate.
- In the Ultrasonic Pulse Velocity test, normal concrete attained findings categorizing it as excellent, whereas the assessment of sustainable concrete varied from excellent at 50% replacement ratios to good at 100% replacement ratios.
- The compressive strength of concrete generally diminishes while the growing substitution of natural coarse aggregate with artificial coarse aggregate. Owing to the influence of aggregate particle strength on this property, RWR0.75 aggregate concrete exhibits the lowest values among the various types of produced aggregates at 28 days, with reduction rates of 22.99% and 32.62% relative to normal concrete. Concurrently, ROS1 aggregate concrete demonstrates better results, with decline rates of 14.99% and 28.47%, respectively.
- As the fraction of ROS1 aggregate usage increases from 50% to 100%, the rates of fresh density reduction in sustainable concrete rise from 7.95% to 16.27% in comparison to normal concrete. The documented outcomes for this aggregate type are the lowest in comparison to RSS1 and RWR0.75 aggregates.
- Semi-lightweight sustainable concrete that uses manufactured coarse aggregate doesn't need as much superplasticizer as regular concrete that uses natural coarse aggregate. The decrease becomes more evident when the ratio of artificial aggregates used instead of natural aggregates increases.
- Achieving a replacement rate of 100%, ROS1 aggregate effectively diminished the dry density of sustainable concrete, registering the lowest values with a decline rate of 10.69% and 17.66% at 28 and 60 days, respectively.
- The superior quality of the natural aggregate supplied enhances the performance of normal concrete in tests of splitting, flexural, and elasticity. The results of these examinations decline with the use of coarse industrial aggregate, proportional to the quantities employed. This investigation revealed that the sustainable concrete ROS1-type aggregate exhibited positive findings, with reductions of 27.42%, 18.11%, and 36.56%, respectively, after 28 days.
- Despite the reduction in water absorption rate with the aging of concrete, normal concrete maintains lower results compared to sustainable concrete. The absorption rate of the aggregate influences this attribute. The concrete incorporating ROS 1 aggregate at 50% and 100% yields good results, with increases of 32.11% and 48.35%, respectively, at a 28-day testing period.

Reference

[1] Tenza-Abril AJ, Compañ-Rosique P, Satorre-Cuerda R, et al. Smartphone Application for Determining the Segregation Index of Lightweight Aggregate Concrete. Sustainability 2021; 13: 12564. https://doi.org/10.3390/su132212564

[2] Kabay N, Mert M, Miyan N, et al. Pumice as Precursor in Geopolymer Paste and Mortar. J Civ Eng Constr 2021; 10: 225-236. https://doi.org/10.32732/jcec.2021.10.4.225

[3] Almeshal I, Tayeh BA, Alyousef R, et al. Use of recycled plastic as fine aggregate in cementitious composites: A review. Constr Build Mater 2020; 253: 119146. https://doi.org/10.1016/j.conbuildmat.2020.119146

[4] Hamada HM, Alattar AA, Yahaya FM, et al. Mechanical properties of semi-lightweight concrete containing nano-palm oil clinker powder. Phys Chem Earth, Parts A/B/C 2021; 121: 102977. https://doi.org/10.1016/j.pce.2021.102977

[5] Özkan H, Kabay N, Miyan N. Properties of Cold-Bonded and Sintered Aggregate Using Washing Aggregate Sludge and Their Incorporation in Concrete: A Promising Material. Sustain; 14. Epub ahead of print 2022. https://doi.org/10.3390/su14074205

[6] Ibrahim H, Abbas W. Fresh Properties of Self-Consolidating Expired Cement-Fly Ash Cold Bonded Lightweight Aggregate Concrete with Different Mineral Admixtures. Eng Technol J 2023; 41: 734-744. https://doi.org/10.30684/etj.2023.139260.1424

[7] Meddah A, Chikouche MA, Yahia M, et al. The Efficiency of Recycling Expired Cement Waste in Cement Manufacturing: a Sustainable Construction Material. Circ Econ Sustain 2022; 2: 1213-1224. https://doi.org/10.1007/s43615-022-00161-1
[8] Bordy A, Younsi A, Aggoun S, et al. Cement substitution by a recycled cement paste fine: Role of the residual anhydrous clinker. Constr Build Mater 2017; 132: 1-8. https://doi.org/10.1016/j.conbuildmat.2016.11.080
[9] A. M. Neville. Properties of concrete Fifth. 2009.
[10] Abbas ML, Abbas WA. Influence of Novel Cold Bonded Attapulgite Lightweight Aggregate on the Performance Properties of Lightweight Aggregate Concrete. University of Technology, 2023.
[11] Ibrahim MA, Atmaca N, Abdullah AA, et al. Mechanical properties of concrete produced by light cement-based aggregates. Sustainability 2022; 14: 15991. https://doi.org/10.3390/su142315991
[12] Kumar R, Srivastava A, Lakhani R. Industrial wastes-cum-strength enhancing additives incorporated lightweight aggregate concrete (LWAC) for energy efficient building: A comprehensive review. Sustainability 2021; 14: 331. https://doi.org/10.3390/su14010331
[13] Güneyisi E, Gesoğlu M, Pürsünlü Ö, et al. Durability aspect of concretes composed of cold bonded and sintered fly ash lightweight aggregates. Compos Part B Eng 2013; 53: 258-266. https://doi.org/10.1016/j.compositesb.2013.04.070
[14] Cioffi R, Colangelo F, Montagnaro F, et al. Manufacture of artificial aggregate using MSWI bottom ash. Waste Manag 2011; 31: 281-288. https://doi.org/10.1016/j.wasman.2010.05.020
[15] Mohamad Ibrahim N, Ismail KN, Che Amat R, et al. Properties of cold-bonded lightweight artificial aggregate containing bottom ash with different curing regime. E3S Web Conf; 34. Epub ahead of print 2018. https://doi.org/10.1051/e3sconf/20183401038
[16] Rosicki Ł, Narloch P. Studies on the ageing of cement stabilized rammed earth material in different exposure conditions. Materials (Basel) 2022; 15: 1090. https://doi.org/10.3390/ma15031090
[17] Kockal NU, Ozturan T. Effects of lightweight fly ash aggregate properties on the behavior of lightweight concretes. J Hazard Mater 2010; 179: 954-965. https://doi.org/10.1016/j.jhazmat.2010.03.098
[18] Abbas ML, Abbas WA, Güneyisi E. Shrinkage and thermo-mechanical properties of concretes incorporated with different substitutions of natural aggregates by cold bonded calcined attapulgite lightweight aggregates. J Build Eng 2023; 79: 107921. https://doi.org/10.1016/j.jobe.2023.107921
[19] Thomas J, Harilal B. Sustainability evaluation of cold-bonded aggregates made from waste materials. J Clean Prod 2019; 237: 117788. https://doi.org/10.1016/j.jclepro.2019.117788
[20] Ibrahim MA, Atmaca N. Cold bonded and low temperature sintered artificial aggregate production by using waste materials. Period Polytech Civ Eng 2023; 67: 112-122. https://doi.org/10.3311/PPci.20885
[21] Manikandan R, Ramamurthy K. Swelling characteristic of bentonite on pelletization and properties of fly ash aggregates. J Mater Civ Eng 2009; 21: 578-586. https://doi.org/10.1061/(ASCE)0899-1561(2009)21:10(578)
[22] A. Sivakumar. Pelletized fly ash lightweight aggregate concrete: A promising material. J Civ Eng Constr Technol 2012; 3: 42-48. https://doi.org/10.5897/JBD11.088
[23] Sabr HA, Abbas WA. Influence of fiber types on the properties of the artificial cold-bonded lightweight aggregates. Open Eng 2024; 14: 20220498. https://doi.org/10.1515/eng-2022-0498
[24] Yıldırım H, Özturan T. Impact resistance of concrete produced with plain and reinforced cold-bonded fly ash aggregates. J Build Eng 2021; 42: 102875. https://doi.org/10.1016/j.jobe.2021.102875
[25] Ibrahim HA, Abbas WA. Production of Cold-Bonding Pelletized Artificial Expired Cement-Fly Ash Lightweight Aggregates with Various Curing Regime. Tikrit J Eng Sci 2024; 31: 184-197. https://doi.org/10.25130/tjes.31.2.18
[26] Manikandan R, Ramamurthy K. Effect of curing method on characteristics of cold bonded fly ash aggregates. Cem Concr Compos 2008; 30: 848-853. https://doi.org/10.1016/j.cemconcomp.2008.06.006
[27] Tang P, Brouwers HJH. The durability and environmental properties of self-compacting concrete incorporating cold bonded lightweight aggregates produced from combined industrial solid wastes. Constr Build Mater 2018; 167: 271-285. https://doi.org/10.1016/j.conbuildmat.2018.02.035
[28] Tajra F, Abd Elrahman M, Chung S-Y, et al. Performance assessment of core-shell structured lightweight aggregate produced by cold bonding pelletization process. Constr Build Mater 2018; 179: 220-231. https://doi.org/10.1016/j.conbuildmat.2018.05.237
[29] Gu E, Turan O. Shrinkage cracking of lightweight concrete made with cold-bonded fly ash aggregates. 2004; 34: 1121-1130. https://doi.org/10.1016/j.cemconres.2003.11.024
[30] Joseph G, Ramamurthy K. Autogenous curing of cold-bonded fly-ash-aggregate concrete. J Mater Civ Eng 2011; 23: 393-401. https://doi.org/10.1061/(ASCE)MT.1943-5533.0000177
[31] Gesoğlu M, Özturan T, Güneyisi E. Effects of fly ash properties on characteristics of cold-bonded fly ash lightweight aggregates. Constr Build Mater 2007; 21: 1869-1878. https://doi.org/10.1016/j.conbuildmat.2006.05.038

[32] Di Mundo R, Petrella A, Notarnicola M. Surface and bulk hydrophobic cement composites by tyre rubber addition. Constr Build Mater 2018; 172: 176-184. https://doi.org/10.1016/j.conbuildmat.2018.03.233
[33] Ahmad J, Zhou Z, Majdi A, et al. Overview of Concrete Performance Made with Waste Rubber Tires: A Step toward Sustainable Concrete. Materials (Basel) 2022; 15: 5518. https://doi.org/10.3390/ma15165518
[34] Asutkar P, Shinde SB, Patel R. Study on the behaviour of rubber aggregates concrete beams using analytical approach. Eng Sci Technol an Int J 2017; 20: 151-159. https://doi.org/10.1016/j.jestch.2016.07.007
[35] Roychand R, Gravina RJ, Zhuge Y, et al. A comprehensive review on the mechanical properties of waste tire rubber concrete. Constr Build Mater 2020; 237: 117651. https://doi.org/10.1016/j.conbuildmat.2019.117651
[36] Salam N, Khalil WI. The Effect of Scrap Tires Recycled Steel Fibers on Some Hardened Properties of Green SCC. Eng Technol J 2022; 40: 810-818. https://doi.org/10.30684/etj.2022.132605.1133
[37] Motloq RF, Khalil WI, Dawood ET. Some Properties of Sustainable Concrete with Rubber Waste Aggregate. Eng Technol J 2023; 41: 1337-1345. https://doi.org/10.30684/etj.2023.140271.1458
[38] BS EN 197-1:2011. Cement - Composition, specifications and conformity criteria for common cements.
[39] Al-Jiboory YM, Al-hazaa SH. Assessment of Altawseea Ordinary Portland Cement Northern Iraq: Mineralogy, Microstructure, and Hydration. Iraqi Geol J 2022; 200-210. https://doi.org/10.46717/igj.55.2C.15ms-2022-08-28
[40] Neville AM, Brooks JJ. Concrete Technology, 2nd Editio. Edinburgh, Engl Pearson Educ Ltd.
[41] Ibrahim HA, Abbas WA. An experimental investigation of sustainable self-compacting concrete with expired cement cold bonded fly ash lightweight aggregate on strength and permeability. In: AIP Conference Proceedings. AIP Publishing, 2024. Epub ahead of print 2024. https://doi.org/10.1063/5.0237179
[42] Yu Y, Ge Y, Liu P. Recycling of expired cement and aged supplementary cementitious materials based on close packing theory and space filling effect. J Clean Prod; 239. Epub ahead of print 2019. https://doi.org/10.1016/j.jclepro.2019.118064
[43] ASTM C618. Standard Specification for Coal Fly Ash and Raw or Calcined Natural Pozzolan for Use, Annu. B. ASTM Stand., (C), (2010) 3-6. 1-3.
[44] ASTM C33/C33M-18. Standard specification for concrete aggregates. Philadelphia, PA Am Soc Test Mater. Epub ahead of print 2003.
[45] Mohesson HM, Abbas WA. Effect of Biopolymer Alginate on some properties of concrete. J Eng 2020; 26: 121-131. https://doi.org/10.31026/j.eng.2020.06.10
[46] ASTM C494/C494M-17. Standard specification for chemical admixtures for concrete. Astm C494 2005; 1-10.
[47] BS EN 934-2:2001. Admixtures for concrete, mortar and grout - Part 2: Concrete admixtures - Definitions, requirements, conformity, marking and labelling. BSI Stand Publ 2003; 3-36.
[48] Performance H, Concrete S. Sika ViscoCrete ® -5930. 2015; 4-5.
[49] Abbas ML, Abbas WA. Cold-bonded lightweight synthetic aggregate involving high reactive attapulgite at different curing conditions. Eng Technol J 2023; 41: 1-14. https://doi.org/10.30684/etj.2023.139775.1442
[50] Lin J, Mo KH, Goh Y, et al. Potential of municipal woody biomass waste ash in the production of cold-bonded lightweight aggregates. J Build Eng 2023; 63: 105392. https://doi.org/10.1016/j.jobe.2022.105392
[51] Abbas WA, Abbas ML. Physico-durability aspects of partial substitution via pelletized fly ash lightweight nano-silica concrete. Res Eng Struct Mater 2023; 9: 475-491.
[52] İpek S, Mermerdaş K. Experimental & computational study on fly ash and kaolin based synthetic lightweight aggregate. Comput Concr An Int J 2020; 26: 327-342.
[53] ASTM C330. Standard Specification for Lightweight Aggregates for Structural Concrete. ASTM Int 2009; 552: 4.
[54] BS 812-110:1990. Testing aggregates - Methods for determination of aggregate crushing value (ACV). BS 812; 110.
[55] ASTM C127-15. Standard Test Method for Density, Relative Density (Specific Gravity), and Absorption of Coarse Aggregate. ASTM Stand B 2013; 1-6.
[56] Sabr HA, Abbas WA. Study the Influence of Curing Methods on Fiber- Reinforced Cold-Bonded Artificial Lightweight Aggregate and Its Effect on Lightweight Concrete Properties. University of Technology, 2023.
[57] Reddy MVS, Nataraja MC, Sindhu K. Performance of Light Weight Concrete using Fly Ash Pellets as Coarse Aggregate Replacement. 2016; 9: 95-104.
[58] González-Corrochano B, Alonso-Azcárate J, Rodas M, et al. Microstructure and mineralogy of lightweight aggregates manufactured from mining and industrial wastes. Constr Build Mater 2011; 25: 3591-3602. https://doi.org/10.1016/j.conbuildmat.2011.03.053

[59] Bai Y, Ibrahim R, Basheer PAM. Properties of lightweight concrete manufactured with fly ash, furnace bottom ash, and lytag. In: International workshop on sustainable development and concrete technology. Center for Transportation Research and Education, Iowa State University, 2004, pp. 77-88.
[60] Güneyisi E, Gesoğlu M, Booya E. Fresh properties of self-compacting cold bonded fly ash lightweight aggregate concrete with different mineral admixtures. Mater Struct 2012; 45: 1849-1859. https://doi.org/10.1617/s11527-012-9874-6
[61] ACI 211.2-98. Standard Practice for Selecting Proportions for Structural Lightweight Concrete. Am Concr Inst 1998; 1-18.
[62] BS EN 12390-3:2019. Testing hardened concrete-Part 3: Compressive strength of test specimens. BSI Stand Publ.
[63] ASTM C597-22. Standard test method for pulse velocity through concrete. ASTM Stand C597-16, ASTM Int West Conshohocken. Epub ahead of print 2016.
[64] ASTM C642-21. Standard test method for density, absorption, and voids in hardened concrete. ASTM, ASTM Int. Epub ahead of print 2013.
[65] ASTM C496-96. Test Method for Splitting Tensile Strength of Cylindrical Concrete Specimens. ASTM International 1996; 1: 5-7.
[66] ASTM C78/C78M-21. Standard Test Method for Flexural Strength of Concrete (Using Simple Beam with Third-Point Loading). ASTM Int 2010; 1: 5-7.
[67] ASTM C469. Standard Test Method for Static Modulus of Elasticity and Poisson's Ratio of Concrete in Compression. ASTM Stand 2014; 04: 1-5.
[68] Ibrahim HA, Abbas WA. Synergistic Effects of Composite Expired Cement Fly Ash Cold-bonding Aggregates and Mineral Admixtures on Mechanical and Drying Shrinkage Performance of Sustainable Self-compacted Concrete. Int J Eng 2024; 37: 2276-2287. https://doi.org/10.5829/IJE.2024.37.11B.13
[69] Ibrahim H, Abbas W. Behavior of Self-Compacted Lightweight Concrete Containing Cold Bonded Aggregate. University of Technology, 2024.
[70] Mehta PK, Monteiro P. Concrete: microstructure, properties, and materials. Epub ahead of print 2006.
[71] Bui LA, Hwang C, Chen C, et al. Manufacture and performance of cold bonded lightweight aggregate using alkaline activators for high performance concrete. Constr Build Mater 2012; 35: 1056-1062. https://doi.org/10.1016/j.conbuildmat.2012.04.032
[72] Wu W, Wang R, Zhu C, et al. The effect of fly ash and silica fume on mechanical properties and durability of coral aggregate concrete. Constr Build Mater 2018; 185: 69-78. https://doi.org/10.1016/j.conbuildmat.2018.06.097
[73] ASTM C 597-02. Standard test Method For Pulse Velocity Through Concrete. United States Am Soc Test Mater 2003; 04: 3-6.
[74] Güneyisi E, Gesoglu M, Azez OA, et al. Physico-mechanical properties of self-compacting concrete containing treated cold-bonded fly ash lightweight aggregates and SiO2 nano-particles. Constr Build Mater 2015; 101: 1142-1153. https://doi.org/10.1016/j.conbuildmat.2015.10.117
[75] ACI. 318-19 Building Code Requirements for Structural Concrete and Commentary. 2019. Epub ahead of print 2019.
[76] Lakhiar MT, Kong SY, Bai Y, et al. Thermal and mechanical properties of concrete incorporating silica fume and waste rubber powder. Polymers (Basel) 2022; 14: 4858. https://doi.org/10.3390/polym14224858
[77] Tajra F, Abd Elrahman M, Stephan D. An experimental study of using core-shell structured lightweight aggregate in producing lightweight concrete. In: International Conference on Sustainable, Environmental Friendly Construction Materials, ICSEFCM. 2018, pp. 35-40.
[78] Samadar Salim. Fracture and Permeability Properties of Artificial Fly Ash and Slag aggregate Concretes at Different Water-to-Cement Ratios. J Mater Sci Technol Res 2020; 7: 11-29. https://doi.org/10.31875/2410-4701.2020.07.02
[79] Atmaca N, Abbas ML, Atmaca A. Effects of nano-silica on the gas permeability, durability and mechanical properties of high-strength lightweight concrete. Constr Build Mater 2017; 147: 17-26. https://doi.org/10.1016/j.conbuildmat.2017.04.156
[80] Mermerdaş K, İpek S, Algın Z, et al. Combined effects of microsilica, steel fibre and artificial lightweight aggregate on the shrinkage and mechanical performance of high strength cementitious composite. Constr Build Mater 2020; 262: 120048. https://doi.org/10.1016/j.conbuildmat.2020.120048
[81] Hatami F, Amiri M. Experimental study of mechanical properties and durability of green concrete containing slag, waste rubber powder and recycled aggregate with artificial neural network. Clean Mater 2022; 5: 100112. https://doi.org/10.1016/j.clema.2022.100112
[82] ACI 213 R. Guide for Structural Lightweight-Aggregate Concrete. Concrete 2014; 0-39.
[83] Salim S. Fracture and permeability properties of artificial fly ash and slag aggregate concretes at different water-to-cement ratios. J Mater Sci Technol Res 2020; 7: 11-29. https://doi.org/10.31875/2410-4701.2020.07.02

[84] Tajra F, Abd Elrahman M, Stephan D. The production and properties of cold-bonded aggregate and its applications in concrete: A review. Constr Build Mater 2019; 225: 29-43. https://doi.org/10.1016/j.conbuildmat.2019.07.219

[85] Wu B, Ye G. Development of porosity of cement paste blended with supplementary cementitious materials after carbonation. Constr Build Mater 2017; 145: 52-61. https://doi.org/10.1016/j.conbuildmat.2017.03.176

Research on Engineering Structures & Materials
www.jresm.org
Research Group

Research Article

Experimental study on energy-saving effect of alternate temperature system with cold storage unit

Leilei Zhu [a], Jiren Li [b], Houlei Zhang [*,c]

School of Energy and Power Engineering, Nanjing University of Science and Technology, Nanjing, P R China

Article Info

Article History:

Received 11 Apr 2025

Accepted 13 June 2025

Keywords:

Alternate temperature;
Cold storage;
Energy-saving

Abstract

Alternate temperature systems with variable cooling load are commonly found in many applications, such as environmental tests. In this paper, we incorporate an ice-cold storage unit (i.e., a new design degree of freedom) into an alternate temperature system, and present an experimental study on the energy-saving effect of the design with cold storage. The cold storage energy comes from a part of the refrigerant bypass loss. Two lab-scale prototypes were developed and the work consumption of the system with cold storage was compared to that without cold storage. The experiment shows that the incorporation of the cold storage unit significantly reduces the energy consumption. Under the specified nominal design conditions, the compressor consumes 5.32 kWh/period energy for the design without cold storage, while it consumes only 3.77 kWh/period energy for the design with cold storage due to less compressor operating time. Compared with the design without cold storage, the energy consumption reduction ratio (α) of the design with cold storage reaches approximately 24.7%. When the heat capacity of the load increases, e.g., from 6.84 kJ/°C to 20.66 kJ/°C, the energy-saving effect of the design with cold storage becomes weaker, e.g., α decreasing from 24.7% to 20.8% accordingly. For extremely low heat generation in the load, the energy-saving effect of the design with cold storage diminishes. The effects of the fan's operating frequency and the cold-water temperature are also analyzed. Further design improvement is suggested. This work emphasizes the value of the incorporation of cold storage (i.e., adding more design degrees of freedom) for alternate temperature systems which reduces the heat transfer difference and the entropy generation.

© 2025 MIM Research Group. All rights reserved.

1. Introduction

Alternate temperature systems with strict temperature variation processes are widely used in reliability tests of electronic instruments with internal heat generation [1-4]. Figure 1 shows a typical alternate temperature process that comprises four stages, which is commonly applied in environmental test chambers [5]. Usually, the high temperature T_H is higher than the ambient temperature T_0, and the low temperature T_L is below T_0. In this paper, T_L is assumed less than T_{CS0} (0°C, the melting point of ice). In this case both heating and cooling are necessary. Since the duration of the rising temperature stage (i.e., Stage II) and the falling temperature stage (i.e., Stage IV) is much shorter than that of the two constant temperature stages (i.e., Stage I and Stage III), the cooling rate is highly imbalanced within one cycle. This imbalance in cooling rate demand requires the maximum capacity in Stage IV, which determines the size of the refrigeration device (or the compressor). In Stages other than Stage IV, the refrigeration device operates under part-load conditions with low energy efficiency.

*Corresponding author: houlei_zhang@aliyun.com
[a]orcid.org/0009-0001-3972-1134; [b]orcid.org/0009-0006-9858-3102; [c]orcid.org/0000-0002-8980-5416
DOI: http://dx.doi.org/10.17515/resm2025-814st0411rs

The most widely used cooling method is based on vapor compression refrigeration, either single-stage or multi-stage systems [6,7]. To meet the cooling rate demand accurately, constant-speed vapor compression (CSVC) with refrigerant bypass adjustment offers a cost-effective solution in terms of equipment investment but comes with significant bypass energy losses. Both single- and multi-compressor designs incorporating refrigerant bypass adjustment are used in practice [8]. A more expensive variable-speed vapor compressor can improve energy efficiency under part-load conditions, but it does not fully eliminate the part-load issue [9, 10]. Beyond these methods, cold storage technology provides an alternative solution to address the imbalance between cooling supply and demand.

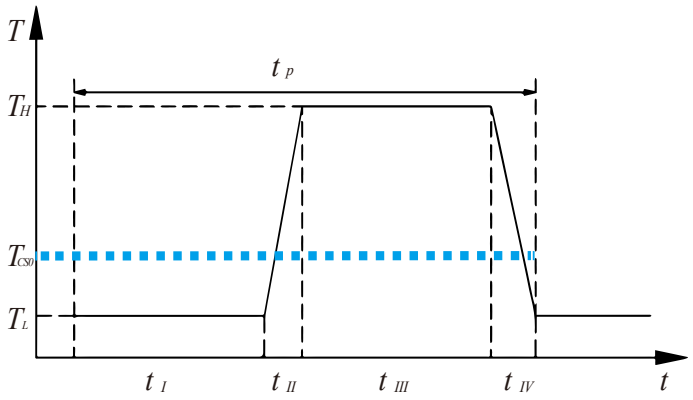

Fig. 1. Alternate temperature process [5]

In building air conditioning systems, cold storage has been employed for many years to reduce peak-hour utility consumption [11-14], and single-phase materials or phase change materials (PCMs) are commonly used to minimize temperature fluctuations and enhance energy efficiency. Recently, Rahgozar et al. [15] analyzed the economic feasibility of ice storage systems for office buildings. They highlight that the payback period is highly sensitive to climate conditions, storage strategies, and other factors. Conti et al. [16] presented a design method for heat storage-based heat pump system in building services to reduce partial-load losses. The electricity consumption may be reduced by up to 45% in a typical test case. Zhu et al. [17] proposed a model predictive control (MPC) strategy of a hybrid cooling system with a cold-water storage system in a data center, which can be regarded as a generalized form of a building with substantial internal heat generation. Their study optimized the cold storage tank volume, achieving a significant reduction in total annual energy consumption across multiple operational modes. Zhao et al. [18] developed a method coupled with multi-objective optimization and MPC for ice-storage air conditioning systems in building applications, showing that their optimization approach led to greater energy savings compared to storage-priority control. Lin et al. [19] employed a model-based control strategy utilizing deep learning to enhance chiller energy efficiency by leveraging the inherent cold storage capacity of cooling systems. Their test results indicated that this control strategy can reduce energy consumption during the nighttime and at the end of working hours markedly. References [17-19] underscore the importance of operational control and optimization when integrating cold storage technology.

PCMs-based cold storage has been also incorporated into refrigerators (including domestic appliances and cold-chain containers, etc.) to improve energy efficiency and product quality. For instance, Azzouz et al. [20, 21] showed a shorter compressor ON-time ratio and therefore a higher *COP* for domestic refrigerators with PCM cold storage. Marques et al. [22] recorded 19% energy-saving potential for domestic refrigerators with cold storage. Khan et al. [23] tested the performance improvement of a household refrigerator with PCM. The COP is improved around 20-27%, depending on the types of PCM and thermal load. Marques et al. [24] investigated the design and operation of a thermal storage refrigerator. The effects of the compressor capacity and the PCM in the refrigerator were evaluated. The results showed that the integration of a well-designed PCM slab can reduce the compressor operating time. Liu et al. [25] reported a significant reduction in both energy consumption and compressor ON-time ratio for an air-cooled domestic refrigerator

with PCMs in both cooling and freezing chambers. Ezan et al. [26] studied the effect of a PCM slab inside a vertical beverage cooler numerically and showed that the PCM integration reduces the compressor ON-time. Cheng et al. [27] discussed three thermal storage designs in domestic refrigerators, i.e., heat storage condenser, cold storage evaporator and dual energy storage, and showed that dual energy storage achieves the highest energy savings. Joybari et al. [28] reviewed the research on domestic refrigerators with cold storage. In Ref. [29], Liao et al. used a mixed salt solution as the cold storage PCM and studied the cold storage performance of the phase change cold storage module for refrigerated containers. They defined two new performance indicators, i.e., the cold storage coefficient and the cold storage efficiency. The effects of the structure layout and the unit power on the phase change cold storage were discussed and proper (or optimal) parameters were recommended. Gao et al. [30] studied the application of a direct current refrigerator with a phase-change cold storage and mini-electrical storage. The results demonstrated the most energy-efficient and cost-effective On-Off mode. Besides the research and development in building air conditioning systems and refrigerators, very recently, Zhang et al. [31] reviewed the studies and applications of PCMs for cold storage in China. Ouaouja et al. [32] conducted a comprehensive review of PCMs for cold storage applications for multiple perspectives, such as energy efficiency, temperature stabilization, and product quality, etc. In particular, new biomass-based PCMs were evaluated in detail.

The above-mentioned studies involve various analytical/research tools. In addition, other analytical tools have also been employed to investigate cold storage and its applications. The Constructal law, a physical law proposed by Bejan in 1996 [33, 34], provided a new thinking method in helping improving performance of thermal systems, including multi-scale design (considering space, time or other parameters) and entropy generation minimization design of cold storage-based processes [35-38]. Radcenco et al. [35] analyzed the intermittent operation of a defrosting refrigerator and presented the optimal on/off frequency by using thermodynamic optimization method (entropy generation minimization). Zamfifirescu and Bejan [36] applied constructal law to a tree-shaped network (a multi-scale design structure) for cold storage, and the design with the maximization of ice production per unit volume was obtained. Using entropy generation minimization as the optimization objective, Bi et al. [37] studied the charging and discharging processes in a gas-hydrate cold storage system. The optimal control strategy for the cold storage system was determined. Very recently, Tavakoli et al. [38] investigated the effects of internal sinusoidal fins and phase change materials on a thermal storage system by performing entropy generation analysis. The design that minimized entropy generation was identified.

In our previous work, inspired by constructal law and entropy generation minimization thoughts, we formulated a multi-source cooling design of alternate temperature systems [5], which incorporates multiple cold storage temperatures and one evaporating temperature to match the source temperature and demand temperature. Such design incorporates more degrees of freedom to improve the system's performance. Theoretically, it was shown that the design with cold storage can simultaneously reduce energy consumption and the size of the refrigeration device. In Ref. [39], an alternate temperature test chamber with ice cold storage (a special case of the multi-source cooling design in Ref. [5]) was studied through numerical modeling. In this context, each cold storage temperature adds one degree of freedom to the design compared to a system without cold storage. When cold water from the cold storage unit is used in Stage III (cf. Fig. 1), the compressor ON-time decreases and then the energy consumption is reduced. Both Refs. [5] and [39] are based on theoretical analysis with certain simplifying assumptions. In this paper, we present an experimental study on the energy-saving effect of a real alternate temperature system (i.e., an environmental test chamber with periodically varying temperature) with ice cold storage unit. The results are also compared with those of a system without cold storage.

2. Experimental Setup

2.1. Prototype development

Two prototypes were developed: Prototype A, representing the conventional design without cold storage and Prototype B, featuring the improved design with cold storage. The working principles

of Prototypes A and B are shown in Fig. 2a and Fig. 2b respectively. The abbreviations in Fig. 2 are listed in Nomenclature. In Fig. 2a, a refrigerant bypass through the valve V is used to regulate the cooling capacity which leads to significant energy loss [5, 39]. In Stage I of Fig. 2b, the compressor operates to maintain the temperature of the chamber and store cold energy in the cold storage tank (CST) (V1, V2: open; V: open or closed) simultaneously. In Stage II of Fig. 2b, the compressor may either run or stop, depending on the load of the object (OBJ). In Stage III of Fig. 2b, CST supplies cooling capacity to the chamber through the coolant heat exchanger (CHE) (V3: open), allowing the compressor to remain off. In Stage IV of Fig. 2b, the compressor resumes operation to provide cooling capacity to drop the temperature in the chamber according to the temperature demand. A comparison between the two prototypes shows that Prototype B has a shorter compressor operating time than Prototype A (seen in Section 3.3), leading to reduced energy consumption. It is also feasible to discharge cold storage energy from CST to the chamber in the high temperature parts of Stages II and IV. But, usually t_{III} is typically much longer than t_{II} or t_{IV}, the energy-saving effect in Stage III is dominant. In this research, the cold storage energy was exclusively discharged and applied only in Stage III.

From Fig. 1, we know that the cooling rate demand (i.e., the cooling load) is different from that for normal air conditioning applications and refrigerators, e.g., the strict periodic temperature change (including fast temperature rising and falling stages) and the significant cooling load imbalance. For the systems in Fig. 2, the refrigerant bypass adjustment is used for cooling capacity control due to its cost-effective equipment investment. The cold storage energy in Fig. 2b comes from a part of the refrigerant bypass loss in Stage I. In this design, some previously "wasted" cold energy is recovered and therefore the compressor operating time is reduced, e.g., in Stage III. The experimental work based on the above key points is new, which was not explored in the studies reviewed before.

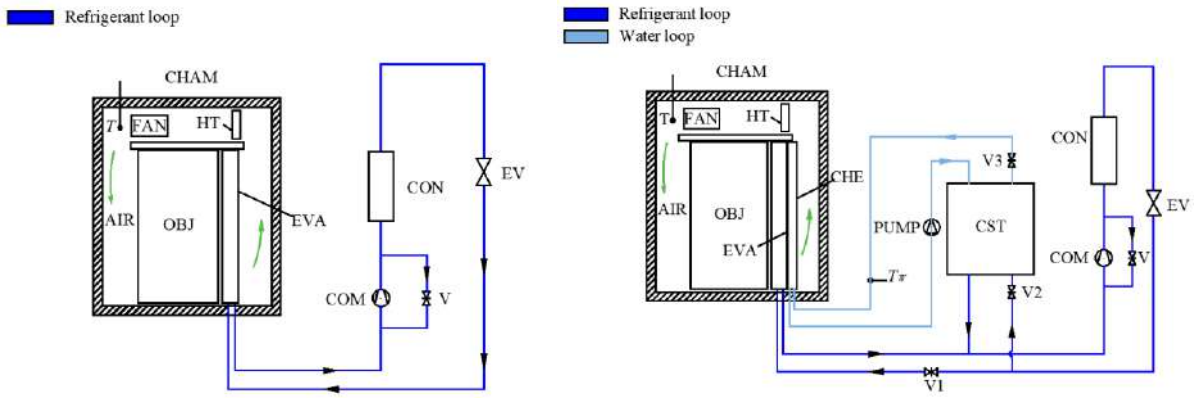

Fig. 2. Working principle: (a) prototype A; (b) prototype B

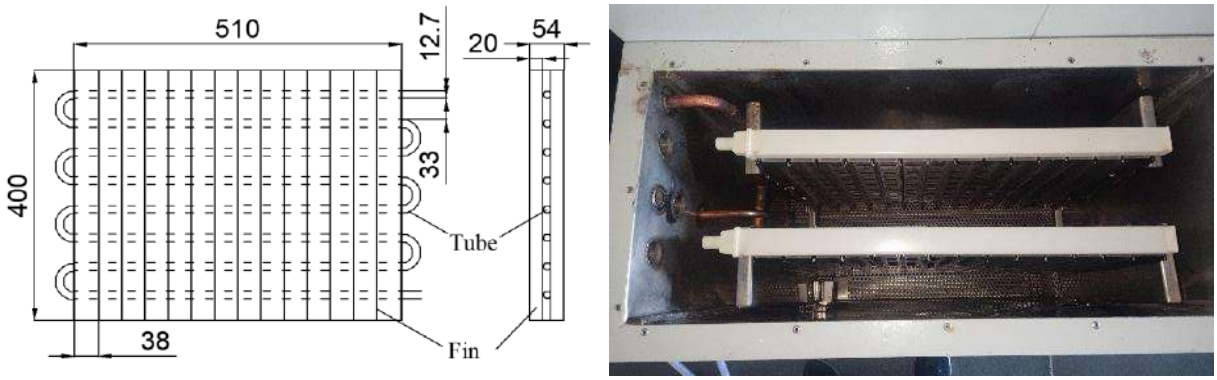

Fig. 3. Cold storage unit: (a) Dimensions (mm); (b) Photo of cold storage unit

(a) (b)

Fig. 4. Photo of prototypes: (a) Prototype A; (b) Prototype B

Two fin-and-tube ice-generating heat exchangers (IHEs) are installed in CST of Prototype B. The dimensions of an IHE are provided in Fig. 3a and its photo is shown in Fig. 3b. Photos of Prototypes A and B are presented in Fig. 4a and Fig. 4b respectively. The design parameters used for Prototypes A and B are summarized in Table 1.

Table 1. Design parameters of Prototypes A and B

Design parameters	Value
The size of OBJ in Prototypes A and B (Width×Height×Depth)	600 mm×850 mm×500 mm
The volume of the test space	225 L
The external dimension of Prototype (Width×Height×Depth)	800 mm×1970 mm×1360 mm (Prototypes A) 800 mm×1970 mm×1960 mm (Prototypes B)
The total weight of Prototype	300 kg (Prototypes A) 360 kg (Prototypes B)
Operating temperature range	-30℃~100℃
Temperature fluctuation	≤±1℃
Temperature deviation	≤±2℃
Temperature uniformity	≤2℃

2.2. Data Measurement and Analysis

To evaluate the energy-saving performance of Prototype B, the energy consumption reduction ratio and the compressor work reduction ratio are defined respectively as follows [5, 39].

$$\alpha = \frac{W_{t,A} - W_{t,B}}{W_{t,A}} \tag{1}$$

$$\beta = \frac{W_{c,A} - W_{c,B}}{W_{c,A}} \tag{2}$$

The total energy consumption W_t includes a few terms [40]:

$$W_t = W_c + W_h + W_f + W_p + W_e \tag{3}$$

where W_c, W_h, W_f and W_p represent the energy consumption of the compressor, the heater, the fan and the pump, respectively. W_e refers to all other energy consumption, except that consumed by

the compressor, heater, fan and pump. For instance, W_e includes the energy consumption due to air leakage between the inside and the outside of the chamber, the heating energy that is used to remove frost on the surfaces of the inside walls of the chamber, and so on. This will be further discussed in the next section. By measuring W_t, W_c, W_h, W_f and W_p, W_e is calculated using Eq. (3). For Prototype A, W_p = 0 since there is no water pump.

For both Prototypes A and B, the characteristic temperature (T) and the air velocity (v) in the chamber in front of OBJ are measured by a resistance temperature sensor (PT100) and an anemometer (Fluke 925 propeller flowmeter). For Prototype B, the water temperature is measured by K-type thermocouples. The water flow rate circulating between CST and CHE is measured by a vortex flowmeter. All data are acquired continuously and input into a computer for further analysis. The sensors used in the experiment are listed in Table 2.

Table 2. List of sensors

Sensor	Range	Accuracy
PT100	-50℃~+200℃	±0.5℃
K-type thermocouple	-40℃~+375℃	±1℃
Fluke 925 propeller flowmeter	0.4 m/s~25 m/s	±0.5 m/s
Electric power measurement YD2037Y-F	0 kW~6 kW	±0.02 kW
Vortex flowmeter KLWGY-DC-D6-W	0~0.6 m^3/h	±0.05 m^3/h

The uncertainty analysis is conducted following the methodology described by Moffat [41]. The absolute uncertainty associated with W_i ($\delta(W_i)$) is 0.02kW at the 95% confidence level. The total energy consumption relative uncertainties ($u(W_t)$) are calculated using Eq. (4), while the relative uncertainties of α and β ($u(\alpha)$, $u(\beta)$) are derived from Eqs. (5) and (6) respectively. Under the specified nominal design conditions, i.e., T_H = 70℃, T_L = -5℃, T_w = 2℃, f = 50 Hz, Q = 1 kW and C = 6.84 kJ/℃, the relative uncertainties of $W_{t,A}$, $W_{t,B}$, α and β are 0.75%, 1.11%, 4.08% and 0.95%, respectively. From the viewpoint of engineering applications, the uncertainties are acceptable.

$$u(W_t) = \frac{\sqrt{(\frac{\partial W_t}{\partial W_c}\delta W_c)^2 + (\frac{\partial W_t}{\partial W_h}\delta W_h)^2 + (\frac{\partial W_t}{\partial W_f}\delta W_f)^2 + (\frac{\partial W_t}{\partial W_p}\delta W_p)^2 + (\frac{\partial W_t}{\partial W_e}\delta W_e)^2}}{W_t} \tag{4}$$

$$u(\alpha) = \frac{1}{\alpha}\sqrt{(\frac{\partial \alpha}{\partial W_{t,A}}\delta W_{t,A})^2 + (\frac{\partial \alpha}{\partial W_{t,B}}\delta W_{t,B})^2} \tag{5}$$

$$u(\beta) = \frac{1}{\beta}\sqrt{(\frac{\partial \beta}{\partial W_{c,A}}\delta W_{c,A})^2 + (\frac{\partial \beta}{\partial W_{c,B}}\delta W_{c,B})^2} \tag{6}$$

3. Results and Discussion

3.1. Nominal Design Conditions

First, we set the nominal design conditions as follows: T_H = 70℃, T_L = -5℃, T_w = 2℃, f = 50 Hz, Q = 1 kW and C = 6.84 kJ/℃. Among these parameters, T_H and T_L do not change in the experiment. Figures 5 and 6 show two examples of the temperature curves of Prototype A (the design without cold storage) and Prototype B (the design with cold storage) respectively for the nominal design conditions. The difference of the ambient conditions of the two tests is negligible. The two time-dependent temperature curves show negligible difference that means the two prototypes fulfill the same design requirement. It should be noted that at the end part of Stage IV, the temperature profile is not strictly linear, which does not affect the energy efficiency evaluation due to its very short time. This non-linearity can be reduced or eliminated in real products, although linear temperature dropping in Stage IV is not always necessary. Here the temperature control accuracy (i.e., the temperature fluctuation) is set as ±1℃, and slight temperature fluctuations are observed.

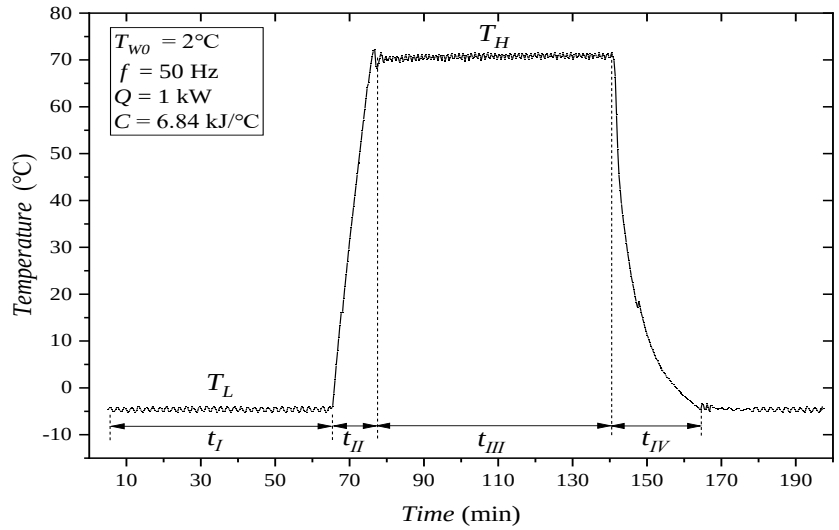

Fig. 5. Temperature curve of Prototype A under reference design conditions

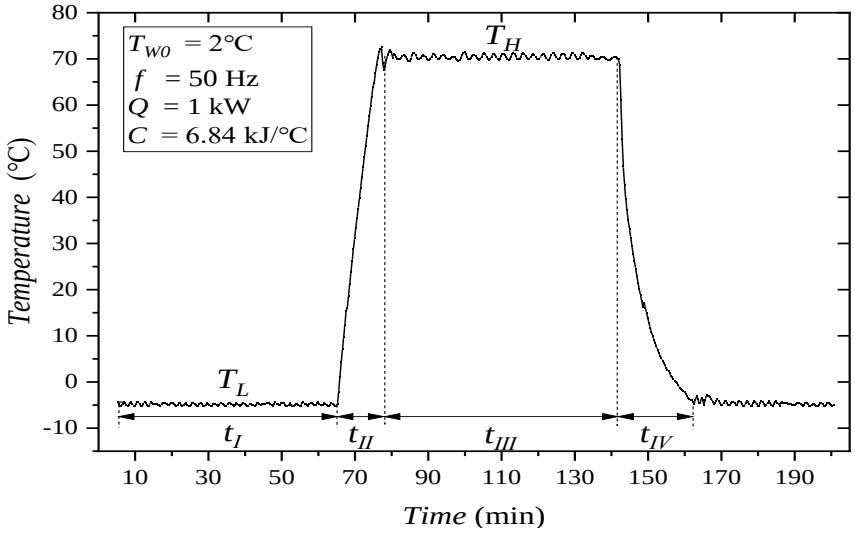

Fig. 6. Temperature curve of Prototype B under reference design conditions

For Prototype B, cold water from CST is used to cool the chamber in Stage III. The dynamic water temperature and flow rate are shown in Fig. 7, where T_w is the temperature at the inlet of CHE, and T_{w0} is the initial value of T_w. In Stage I and Stage II where the water pump does not run (i.e., $\dot{m}_w = 0$), T_w is lower (~ 2°C) and changes very little. In Stage III where the water pump runs to provide cooling to the chamber through CHE, T_w becomes higher. The flow rate in Stage III varies significantly because a large pump is used in building the prototype. In real product design, this can be optimized. The variation of T_w shows that the melting velocity of the ice in CST is slow which cannot maintain a constant water temperature. Heat transfer enhancement (e.g., using well-designed ice-side fins) in the ice melting process can help solve this problem, which will be studied in the future work.

Figure 8 shows the energy consumption distribution of the two prototypes under the nominal design conditions. In Stages III, as the compressor for Prototype B does not run, the energy saving is significant, and in this stage, W_t for Prototype B is much less than that for Prototype A. This is the main reason that the cold storage-based design saves energy overall the entire period. In Stage I, the energy consumption of the two prototypes is nearly the same. In Stage II, Prototype B consumes slightly less energy than Prototype A. In Stage IV, due to the cooling effect of cold water that is not fully discharged from CHE when the temperature starts to drop, Prototype B consumes less energy than Prototype A.

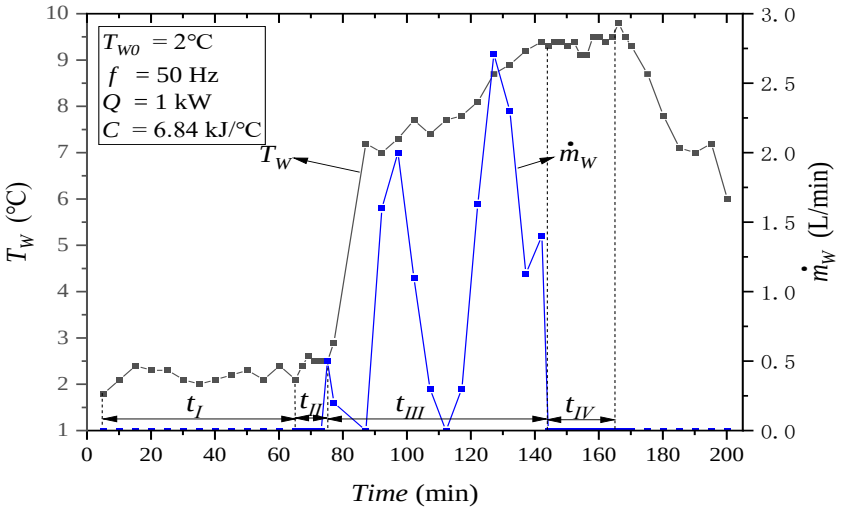

Fig. 7. Water temperature and flow rate of Prototype B under the nominal design conditions

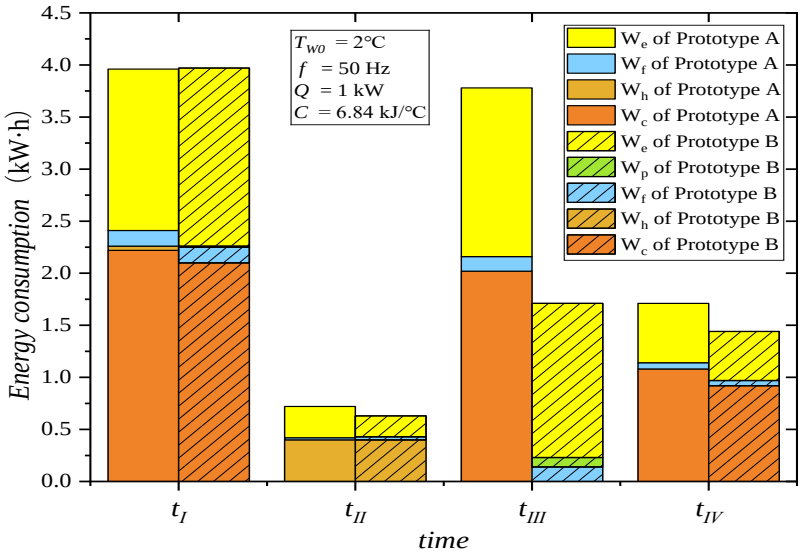

Fig. 8. Energy consumption distribution of Prototypes A and B under nominal design conditions

In one period, for Prototype A, W_c, W_h, W_f and W_e are 5.32 kWh, 0.44 kWh, 0.37 kWh and 4.04 kWh, respectively. Among the four terms, W_c (52.3% of the total) and W_e (39.7% of the total) are dominant, and W_h and W_f are much less. Here W_e includes the energy consumption due to air leakage, the heating energy for defrosting of the inner surfaces of the chamber and preventing condensation near the chamber door sealing zones, and the energy consumption for measurement and control system. In the test procedure, humid air circulates in the chamber and frost emerges on the inner surfaces of the chamber when its temperature drops below 0°C. Electrical heaters attached to the surfaces run to remove the frost. Such frosting and defrosting processes occur periodically. It is possible to use dry air in the chamber as the circulating fluid which is not the focus of this work. Apparently, frosting and defrosting processes do not affect evaluating the goodness of the cold storage-based design. The importance of W_e is a reminder that the present prototypes (A and B) are not ideal, and there exists considerable improvement space.

In one period, for Prototype B, W_c, W_h, W_f, W_p and W_e are 3.02 kWh, 0.40 kWh, 0.37 kWh, 0.10 kWh and 3.77 kWh, respectively. W_c and W_e are still dominant. By comparing the two prototypes, we see that W_h and W_e have a small gap. The energy consumption W_f is the same for the two prototypes which means that the incorporation of CHE does not increase the fan's work. For Prototype B, the energy consumption of the water pump W_p is much less than W_c, so it is negligible in the energy consumption analysis. The key difference between Prototype A and Prototype B lies in W_c. Based

on Fig. 8, the energy consumption reduction ratio (α) and the compressor work reduction ratio (β) are 24.7% and 43.2%, respectively. The improvement in energy efficiency of Prototype B is significant. This result confirms our previous theoretical design [39].

3.2. Effects of Operating Conditions

Under the nominal design conditions in Section 3.1 (e.g., Fig. 8), the load heat capacity C = 6.84 kJ/°C. Figures 9 and 10 show the energy consumption distribution for the load heat capacity C = 13.75 kJ/°C and 20.66 kJ/°C respectively. Combined with Fig. 8, we see that in Stage IV (i.e., the temperature dropping process), with the increase of C, both W_c and W_t increase for both Prototype A and Prototype B. In fact, a larger heat capacity in the chamber is always detrimental to the temperature dropping process as more cold energy is needed. Stage III determines the energy-saving effect of Prototype B which does not change with C significantly. Considering the above two points (the features in Stage IV and III), we know that α and β may decrease with the increase of C according to Eqs. (1) and (2). The test results of the effects of C are summarized in Fig. 11, which reveals that in the specified range cold storage-based design is more attractive for smaller load heat capacities.

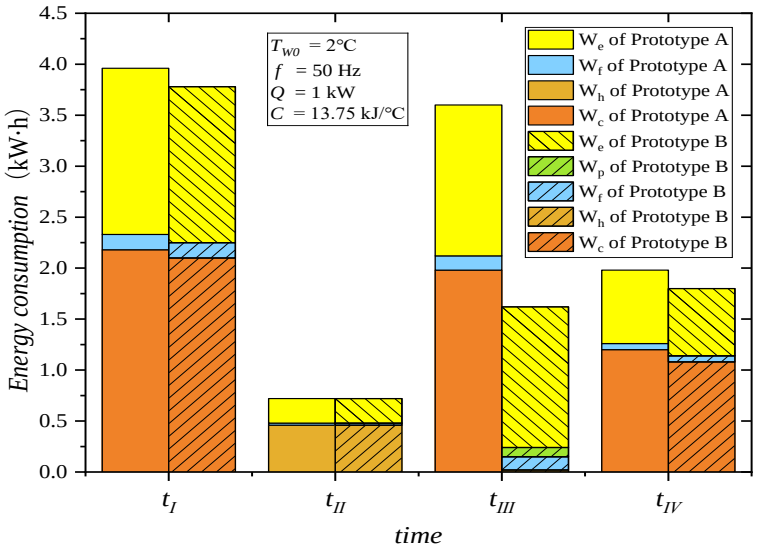

Fig. 9. Energy consumption distribution with C = 13.75 kJ/°C

Another important parameter of the load is its internal heat generation Q. Usually the test is performed under the nominal design conditions (1 kW in this paper), but sometimes Q may be very small or even zero (non-working state of the load). Figure 12 shows the energy consumption distribution for the heat generation in the load Q = 0.2 kW.

According to Fig. 12, W_c and W_t are 3.39 kWh and 5.93 kWh for Prototype A, and 2.24 kWh and 5.04 kWh for Prototype B. Here α = 15.0% and β = 33.9% which indicate a lower energy-saving performance than that with Q = 1 kW. Actually, due to very small Q (= 0.2 kW) and the cold storage effect in the insulation material, the compressor does not have to run for the overall t_{III} for Prototype A. It is recorded in the test that only 25 min compressor operating time is needed in Stage III for Prototype A, much less than t_{III} for Q = 1 kW (Seen in Fig. 5). Here, less compressor operating time of Prototype A leads to lower α and β according to Eqs. (1) and (2). The observation in Fig. 12 tells us that the cold storage effect in the insulation material (or the size of the chamber) is related to the energy-saving effect of the cold storage-based design, which needs more research. In Section 3.1, the fan runs with frequency f = 50 Hz. Through inverter control, the frequency f or the circulating air flow rate in the chamber can be adjusted.

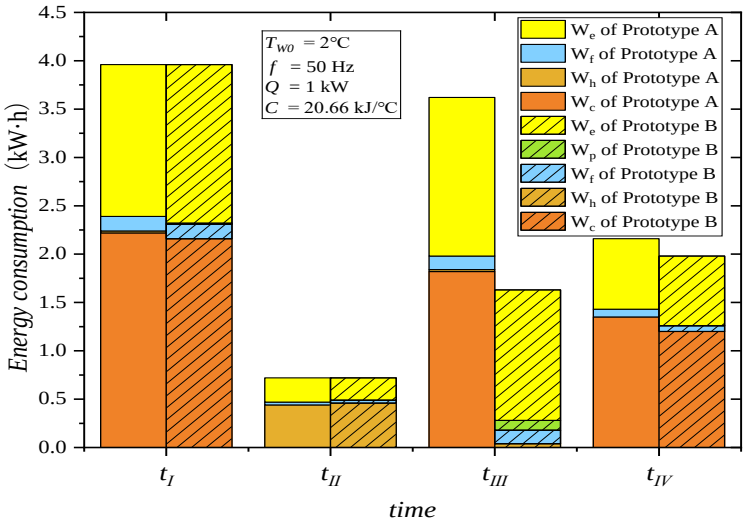

Fig. 10. Energy consumption distribution with C = 20.66 kJ/°C

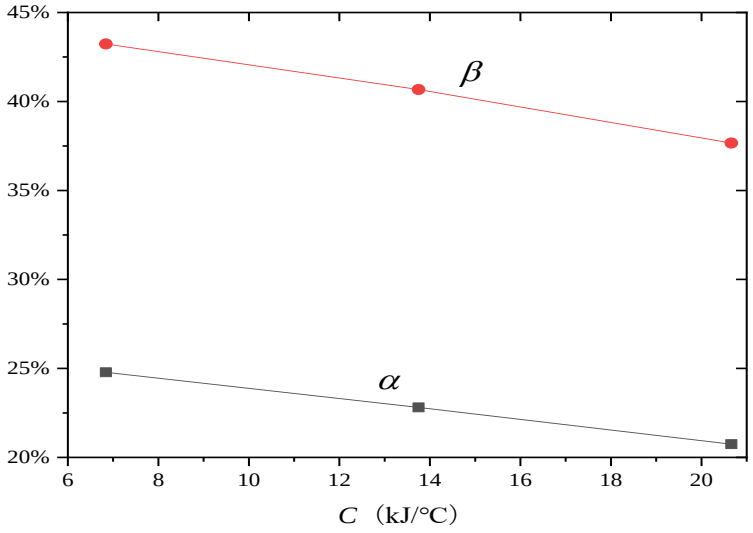

Fig. 11. Effects of C on α and β

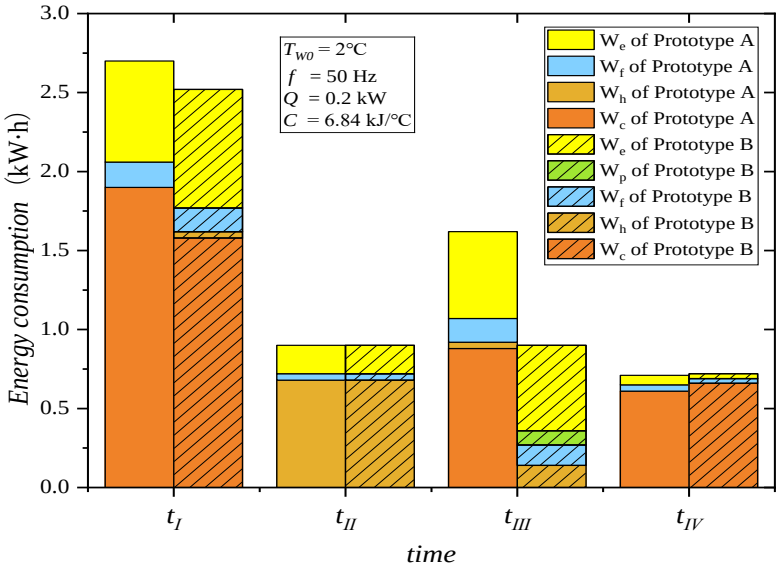

Fig. 12. Energy consumption distribution with Q = 0.2 kW

Figure 13 shows the energy consumption distribution for f = 30 Hz. With the decrease of f from 50 Hz to 30 Hz, W_f reduces from 0.37 kWh to 0.26 kWh. Here, when f = 30 Hz, W_c and W_t are 5.29 kWh and 9.63 kWh for Prototype A, and 3.10 kWh and 7.38 kWh for Prototype B. Both α (= 23.4%) and β (= 41.4%) are slightly lower than that with f = 50 Hz. We know that f affects not only W_f but also the heat transfer coefficients of CHE and EVA. The values of α and β are the final results of these effects. It should be noted that the conclusion is only suitable for the present designs and cannot be extended to the conditions with very low fan frequency. In fact, when f is very low, the heat transfer areas of EVA and CHE may not be sufficient, and the heat transfer between OBJ and the air will become worse too. The optimal air flow rate (corresponding to f) is not the work of the present paper, but should be considered in real designs.

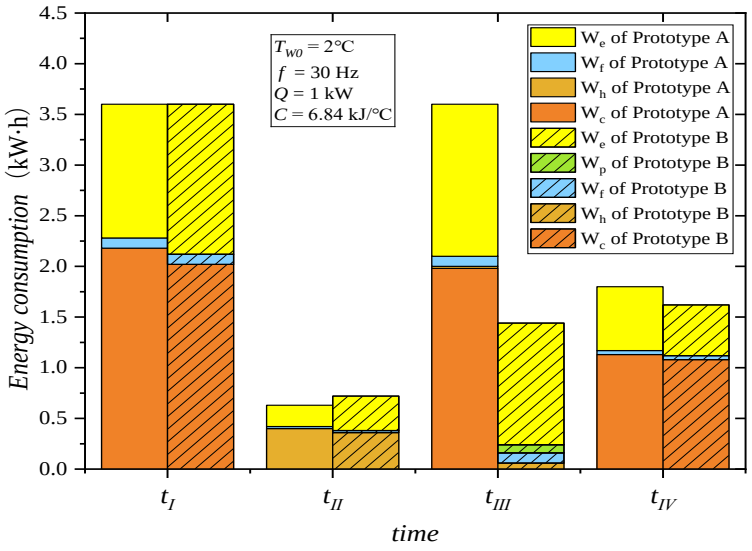

Fig. 13. Energy consumption distribution with f = 30 Hz

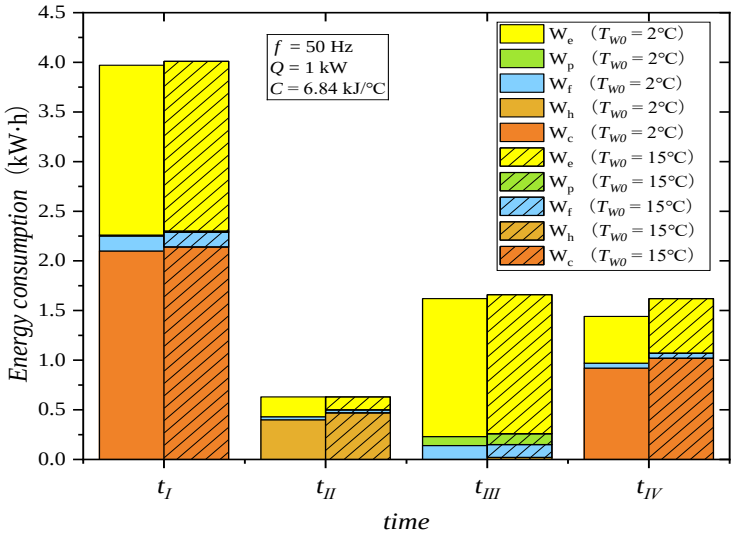

Fig. 14. Energy consumption distribution for Prototype B with T_{w0} = 15°C

We have shown (in Fig. 7) that T_w may change in Stage III because for the present Prototype B we did not consider sufficient heat transfer enhancement in CST that may realize constant water temperature. The initial water temperature T_{w0} in Section 3.1 is 2°C. For Prototype B, by rising T_{w0} to 15°C, we performed similar test as in Section 3.1 under the nominal design conditions except different T_{w0}. The energy consumption distribution for T_{w0} = 15°C for Prototype B is shown in Fig. 14. In this case, W_c and W_t rise to 3.16 kWh and 7.92 kWh, slightly higher than that for T_{w0} = 2°C. This observation tells that variable T_{w0} does not affect the energy consumption significantly and constant T_w in CST design is not mandatory. Based on Fig. 14, α and β are 22.2% and 40.6%, also

slightly lower than that under nominal design condition (with T_{w0} = 2°C). It should be noted that higher T_{w0} means less heat transfer temperature difference in CHE, but we can still adjust the water flow rate to fulfill the design requirements for the present prototype (Prototype B).

3.3. Further Technical Discussion

In the above sections, we measured the energy-saving effect of the cold storage-based designs. Because ice and water are used as the cold storage substance and the coolant in CHE respectively, the stored cold energy cannot be utilized in Stage I or the part of Stage IV with $T < T_w$. Therefore, the present cold storage-based design (Prototype B) cannot reduce the size of the compressor or the refrigeration device. If low temperature substances ($T < T_L$) to store cold energy are employed, the energy efficiency can be improved and the size of the compressor can be reduced simultaneously. Besides, we may further adopt two cold storage temperatures, for instance, one with coolant temperature T_{CS1} between T_H and T_L ($T_L < T_{CS1} < T_H$), another with coolant temperature T_{CS2} ($T_{CS2} < T_L$), schematically shown in Fig. 15. The coolant with T_{CS2} is used to burden a part of the cooling capacity demand in Stage IV, therefore the size of the compressor can be reduced. The above design with two cold storage temperatures also decreases the average temperature difference between the supply and the demand (or the entropy generation induced by heat transfer), besides it also increases the average coefficient of performance of the refrigeration device. More analysis is available in Ref. [5].

Additionally, even only one cold storage temperature with coolant temperature $T_w > 0$°C provides the possibility in reducing the size of the compressor. For instance, the cold water from CST can be used to sub cool the refrigerant at the outlet of the condenser and increase the cooling capacity supply. If the cooling capacity demand is specified, we can therefore reduce the size of the compressor.

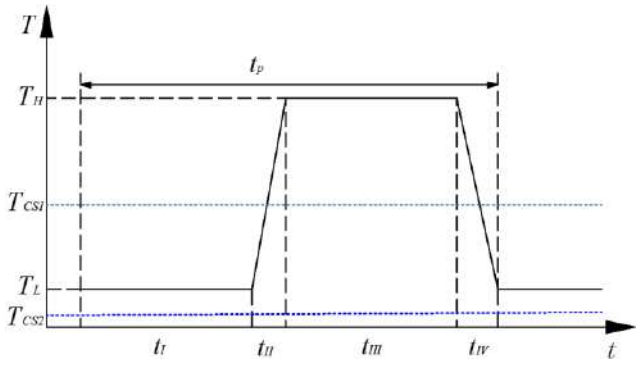

Fig. 15. The scheme of two cold storage temperatures

It is reminded that Fig. 15 shows the scheme of the two-scale design, i.e., the design with two coolant temperatures (T_{CS1} and T_{CS2}) or cold storage temperature. In Fig. 1, $T_L < T_{CS0}$ = 0°C (the melting temperature of ice), where T_{CS0} represents the merely cold storage temperature (the one-scale design) in the experimental system in Section 2.

In Section 1, we mentioned that some studies showed that the incorporation of cold storage reduces the compressor operating time and therefore decreases the energy consumption. These studies mainly focused on normal air conditioning systems and refrigerators. The cooling load feature and the supply method of the cold storage energy in this paper are different from that in the literature, so it is difficult to compare them directly. In our previous theoretical analysis in Ref. [39], typical α value is higher than 30%. But it is reminded that in Ref. [39], W_e is not considered, which is shown to be significant in this paper. Besides, the geometries of the prototypes used in this paper are not the same due to the consideration of manufacture and cost. Therefore, it is not proper to compare the experimental data (e.g., α) with the simulation results in Ref. [39] quantitatively. Nevertheless, it is clear that the experimental results in this paper are in agreement with the theoretical design in Ref. [39] qualitatively.

3.4. Brief Economic Analysis

One important application of the systems in Fig. 2 is the reliability test of electronic and electrical devices, which usually needs long-time operation. As a case study, the lab-scale prototypes A and B in this paper consume 10.17 kWh/period and 7.66 kWh/period electricity respectively (cf. Section 3.1) under the specified nominal design conditions. In one year's, continuous operation (8760 h), compared with Prototype A, the energy-saving of Prototype B is around 8245 kWh.

On the other side, the investment of Prototype B is increased, including the cold storage tank, the coolant heat exchanger, the pump, more sensors, etc. In addition, the operation and maintenance are more complicated. For instance, when the temperature in the chamber is lower than 0°C (e.g., in Stage I), the water (i.e., the coolant) in the coolant heat exchanger should be discharged completely to avoid possible freezing damage. For the lab-scale Prototype B, the additional investment is limited [40]. For large-scale industrial applications, both the profit in energy-saving and the additional investment are significant. The trade-off depends on many factors, like users' demand, manufacturing level, electricity price, among others, which are beyond the scope of this paper.

4. Conclusions

In this work we developed two alternate temperature system prototypes with or without cold storage unit and presented the energy-saving effect of the cold storage-based design based on experimental results. The cold storage energy comes from a part of the refrigerant bypass loss. Under the specified nominal design conditions, the compressor consumes 5.32 kWh/period energy for the design without cold storage, while it consumes only 3.77 kWh/period energy for the design with cold storage due to less compressor operating time. Compared with the design without cold storage, the energy consumption reduction ratio (α) of the design with cold storage reaches approximately 24.7%. When the heat capacity of the load increases, e.g., from 6.84 kJ/°C to 20.66 kJ/°C, the energy-saving effect of the design with cold storage becomes weaker, e.g., α decreasing from 24.7% to 20.8% accordingly. For extremely low heat generation in the load, the energy-saving effect of the design with cold storage diminishes. The fan's operating frequency and the cold-water temperature, which are important for the design of the heat exchangers of the prototypes, affect the energy consumption reduction ratio slightly for the specified conditions.

It should be acknowledged that the present prototypes are preliminary, i.e., not fully optimized. There is great space for improvement, e.g., in reducing W_e. The important point is that the incorporation of one or more cold storage temperatures offer new design degrees of freedom which increases the possibility of evolving design toward better performance or less entropy generation (e.g., due to the heat transfer between the coolant and the air). If the size reduction of the compressor is not considered, e.g., Prototype B in this work, cold storage also implies higher investment and more complicated control, so trade-off is always necessary in real product development. If the size of compressor is reduced as analyzed in Section 3.3, the investment may not increase. More product development and test are worthy.

Nomenclature

C	heat capacity [JK^{-1}]
f	fan's operating frequency [Hz]
$\dot{m}_w$	water flow rate [$Lmin^{-1}$, m^3h^{-1}]
Q	heat transfer rate [W, kW]
T	temperature [°C, K]
t	time [s]
T_0	ambient temperature [°C, K]
u	relative uncertainty
W	energy consumption or work [J, kJ, MJ]

Greek symbols

α	energy consumption reduction ratio
β	compressor work reduction ratio
δ	absolute uncertainty

Subscripts

0	initial
I, II, III, IV	Stages I, II, III, IV
A, B	Prototype A, B
c	compressor
CS0, CS1, CS2	cold storage temperature 0,1, 2
e	other energy consumption
f	fan
H	high
h	heater
L	low
p	pump
t	total
w	water

Abbreviations

CHAM	the chamber
CHE	the coolant heat exchanger
COM	the compressor
CON	the condenser
CST	the cold storage tank
EV	the expansion valve
EVA	the evaporator
FAN	the fan
HT	the heater
IHE	the ice-generating heat exchanger
OBJ	the object
V, V1, V2,V3	valves in Fig. 2

References

[1] Garimella SV, Fleischer AS, Murthy JY, Keshavarzi A, Prasher R, Patel C, Bhavnani SH, Venkatasubramanian R, Mahajan R, Joshi Y, Sammakia B, Myers BA, Chorosinski L, Baelmans M, Sathyamurthy P, Raad PE. Thermal Challenges in Next-Generation Electronic Systems. IEEE Transactions on Components and Packaging Technologies, 2008;31(4):801-15. https://doi.org/10.1109/TCAPT.2008.2001197

[2] Steinberg DS. Preventing Thermal Cycling and Vibration Failures in Electronic Equipment. Wiley, 2001, ISBN 978-0-471-35729-2.

[3] Yang S, Bryant A, Mawby P, Xiang D, Ran L, Tavner P. An Industry-Based Survey of Reliability in Power Electronic Converters. IEEE Transactions on Industry Applications, 2011;47(3):1441-51. https://doi.org/10.1109/TIA.2011.2124436

[4] Chen X, Zhang C, Wang Y, Tan Y. Accelerated Life Testing Technology and Applications. National Defence Industry Press, Beijing, China, 2013.

[5] Zhang H, Zhou R, Lorente S, Ginestet S. Thermodynamic design of cold storage-based alternate temperature systems. Applied Thermal Engineering, 2018;144:736-46. https://doi.org/10.1016/j.applthermaleng.2018.08.099

[6] Selimli S, Recebli S, Görken M. Evaluation the effects of used refrigerants R134a and R600a in cooling systems on the system performance. Journal of Engineering and Natural Sciences, 2014; Sigma 32: 290-295.

[7] Patiluna DNG, Donasco EAA, Hernandez NM, Mamalias JBA, Viña RR. Energy and exergy analysis of a two-stage cascade vapor compression refrigeration system with modified system configuration. International Journal of Refrigeration, 2025;169:33-54. https://doi.org/10.1016/j.ijrefrig.2024.10.013

[8] Widell KN, Eikevik T. Reducing power consumption in multi-compressor refrigeration systems. International Journal of Refrigeration, 2010;33(1):88-94. https://doi.org/10.1016/j.ijrefrig.2009.08.006

[9] Qureshi TQ, Tassou SA. Variable-speed capacity control in refrigeration systems. Applied Thermal Engineering, 1996;16(2):103-13. https://doi.org/10.1016/1359-4311(95)00051-E

[10] Li W. Simplified steady-state modeling for variable speed compressor. Applied Thermal Engineering, 2013;50(1):318-26. https://doi.org/10.1016/j.applthermaleng.2012.08.041
[11] Li G, Hwang Y, Radermacher R. Review of cold storage materials for air conditioning application. International Journal of Refrigeration, 2012;35(8):2053-77. https://doi.org/10.1016/j.ijrefrig.2012.06.003
[12] Zhai XQ, Wang XL, Wang T, Wang RZ. A review on phase change cold storage in air-conditioning system: Materials and applications. Renewable and Sustainable Energy Reviews, 2013;22:108-20. https://doi.org/10.1016/j.rser.2013.02.013
[13] Kalnæs SE, Jelle BP. Phase change materials and products for building applications: A state-of-the-art review and future research opportunities. Energy and Buildings, 2015;94:150-76. https://doi.org/10.1016/j.enbuild.2015.02.023
[14] Souayfane F, Fardoun F, Biwole P-H. Phase change materials (PCM) for cooling applications in buildings: A review. Energy and Buildings, 2016;129:396-431. https://doi.org/10.1016/j.enbuild.2016.04.006
[15] Rahgozar S, Dehghan M, Pourrajabian A, Haghgou H. Economic feasibility of ice storage systems for office building applications: A climate sensitivity analysis. Journal of Energy Storage, 2022; 45:103712. https://doi.org/10.1016/j.est.2021.103712
[16] Conti P, Franco A, Bartoli C, Testi D. A design methodology for thermal storages in heat pump systems to reduce partial-load losses. Applied Thermal Engineering, 2022;215:118971. https://doi.org/10.1016/j.applthermaleng.2022.118971
[17] Zhu Y, Zhang Q, Zeng L, Wang J, Zou S. An advanced control strategy of hybrid cooling system with cold water storage system in data center. Energy, 2024;291:130304. https://doi.org/10.1016/j.energy.2024.130304
[18] Zhao J, Liu D, Yuan X, Wang P. Model predictive control for the ice-storage air-conditioning system coupled with multi-objective optimization. Applied Thermal Engineering, 2024;243:122595. https://doi.org/10.1016/j.applthermaleng.2024.122595
[19] Lin X, Shan K, Wang S. Model predictive control of large chiller plants for enhanced energy efficiency utilizing inherent cold storage of cooling systems. Journal of Energy Storage, 2025;113:115697. https://doi.org/10.1016/j.est.2025.115697
[20] Azzouz K, Leducq D, Gobin D. Performance enhancement of a household refrigerator by addition of latent heat storage. International Journal of Refrigeration, 2008;31:892-901. https://doi.org/10.1016/j.ijrefrig.2007.09.007
[21] Azzouz K, Leducq D, Gobin D. Enhancing the performance of household refrigerators with latent heat storage: An experimental investigation. International Journal of Refrigeration, 2009;32(7):1634-44. https://doi.org/10.1016/j.ijrefrig.2009.03.012
[22] Marques AC, Davies GF, Evans JA, Maidment GG, Wood ID. Theoretical modelling and experimental investigation of a thermal energy storage refrigerator. Energy, 2013;55:457-65. https://doi.org/10.1016/j.energy.2013.03.091
[23] Khan MIH, Afroz HMM. Effect of phase change material on performance of a household refrigerator. Asian Journal of Applied Sciences, 2013;6(2):56-67. https://doi.org/10.3923/ajaps.2013.56.67
[24] Marques AC, Davies GF, Maidment GG, Evans JA, Wood ID. Novel design and performance enhancement of domestic refrigerators with thermal storage. Applied Thermal Engineering, 2014;63:511-519. https://doi.org/10.1016/j.applthermaleng.2013.11.043
[25] Liu Z, Zhao D, Wang Q, Chi Y, Zhang L. Performance study on air-cooled household refrigerator with cold storage phase change materials. International Journal of Refrigeration, 2017;79:130-42. https://doi.org/10.1016/j.ijrefrig.2017.04.009
[26] Ezan MA, Ozcan Doganay E, Yavuz FE, Tavman IH. A numerical study on the usage of phase change material (PCM) to prolong compressor off period in a beverage cooler. Energy Conversion and Management, 2017;142:95-106. https://doi.org/10.1016/j.enconman.2017.03.032
[27] Cheng W, Ding M, Yuan X, Han B. Analysis of energy saving performance for household refrigerator with thermal storage of condenser and evaporator. Energy Conversion and Management, 2017;132:180-8. https://doi.org/10.1016/j.enconman.2016.11.029
[28] Joybari M, Haghighat F, Moffat J, Sra P. Heat and cold storage using phase change materials in domestic refrigeration systems: The state-of-the-art review. Energy and Buildings, 2015;106:111-24. https://doi.org/10.1016/j.enbuild.2015.06.016
[29] Liao Z, Zhuang C, Huang G, Pu H, Zhang H, Li S, Zhang X, Cheng L, Gan F. Optimization research on phase change cold storage module for refrigerated containers. Journal of Energy Storage, 2024;82:110506. https://doi.org/10.1016/j.est.2024.110506
[30] Gao L, Xu S, Yu G, Ma G, Chang Y, Li S. Application study of direct current refrigerator combining phase-change cold storage and mini-electrical storage. Energy, 2025;320:135308. https://doi.org/10.1016/j.energy.2025.135308

[31] Zhang L, Xia X, Lv Y, Wang F, Cheng C, Shen S, Yang L, Dong H, Zhao J, Song Y. Fundamental studies and emerging applications of phase change materials for cold storage in China. Journal of Energy Storage, 2023;72:108279. https://doi.org/10.1016/j.est.2023.108279
[32] Ouaouja Z, Ousegui A, Toublanc C, Rouaud O, Havet M. Phase Change Materials for Cold Thermal Energy Storage applications: A critical review of conventional materials and the potential of bio-based alternatives. Journal of Energy Storage, 2025;110:115339. https://doi.org/10.1016/j.est.2025.115339
[33] Bejan A. Constructal-theory network of conducting paths for cooling a heat generating volume. International Journal of Heat and Mass Transfer, 1997;40(4):799-816. https://doi.org/10.1016/0017-9310(96)00175-5
[34] Bejan A, Lorente S. Design with Constructal Theory. Wiley, 2008, ISBN 978-0-471-99816-7. https://doi.org/10.1002/9780470432709
[35] Radcenco V, Vargas JVC, Bejan A, Lim JS. Two design aspects of defrosting refrigerators. International Journal of Refrigeration, 1995;18(2):76-86. https://doi.org/10.1016/0140-7007(94)00003-G
[36] Zamfirescu C, Bejan A. Tree-shaped structures for cold storage. International Journal of Refrigeration, 2005;28(2):231-41. https://doi.org/10.1016/j.ijrefrig.2004.08.010
[37] Bi Y, Guo T, Zhang L, Chen L, Sun F. Entropy generation minimization for charging and discharging processes in a gas-hydrate cool storage system. Applied Energy, 2010;87(4):1149-57. https://doi.org/10.1016/j.apenergy.2009.07.020
[38] Tavakoli A, Farzaneh-Gord M, Ebrahimi-Moghadam A. Using internal sinusoidal fins and phase change material for performance enhancement of thermal energy storage systems: Heat transfer and entropy generation analyses. Renewable Energy, 2023;205:222-37. https://doi.org/10.1016/j.renene.2023.01.074
[39] Zhou R, Tu P, Zhang H. Performance improvement of alternate temperature systems with ice storage-based internal water loop. Energy and Buildings, 2019;204:109521. https://doi.org/10.1016/j.enbuild.2019.109521
[40] Zhu L. Study on performance optimization of high and low temperature test chambers (Thesis, in Chinese). Nanjing University of Science and Technology, China, 2021.
[41] Moffat RJ. Describing the uncertainties in experimental results. Experimental Thermal and Fluid Science. 1988;1(1):3-17. https://doi.org/10.1016/0894-1777(88)90043-X

Research on Engineering Structures & Materials
www.jresm.org
MIM Research Group

Research Article

In-situ investigation of earthen building materials in the Ksour of the Ziban region, Algeria: A comparative study between Chetma and Lichana

Amdjed Islam Dali [*,1,2,a], Sami Zerari [2,b], David Gandreau [1,c]

[1]*CRATerre, École Nationale Supérieure d'Architecture de Grenoble, France*
[2] *LACOMOFA Laboratory, Department of Architecture, Faculty of Architecture and Urbanism, Civil Engineering, and Hydraulics, University of Biskra, Biskra, Algeria*

Article Info

Article History:

Received 11 Jan 2025

Accepted 04 June 2025

Keywords:

State of conservation;
Building materials;
Earthen materials;
In-situ tests;
Ksar of Chetma,
Ksar of Lichana;
Algeria

Abstract

Earth is one of the primary building materials utilized in the Saharan region of Algeria. This study seeks to characterise, diagnose, and compare the earthen materials employed in constructing two (2) ksour in southern Algeria: the ksar of Chetma and the ksar of Lichana in the Ziban region. The research methodology combined in-situ observations, analysis of traditional construction techniques, and applying three (3) fundamental tests developed by CRAterre in 1979 and 1989: sedimentation in a bottle, the cigar test, and the pellet test. The investigation into the conservation state of the ksour of Lichana and Chetma revealed their highly precarious condition. Furthermore, the tests revealed that the earth used for construction at the two sites shows similarities, with the earth from Chetma containing slightly more clay than that from Lichana. This difference is more apparent in the composition of the mud bricks (40x20x10 cm), as those from Chetma incorporate a natural fibre, wheat straw. In contrast, the bricks from Lichana do not contain straw, resulting in distinct properties. In addition, the investigation into the conservation state of the ksour of Lichana and Chetma revealed their highly precarious condition. The article's findings contribute to the characterisation of the mud bricks, offering valuable insights for documentation purposes and informing future conservation and restoration efforts requiring compatible construction materials.

© 2025 MIM Research Group. All rights reserved.

1. Introduction

Architecture has long been a profound expression of cultural and social values, often described as humanity's "great book" [1]. Indeed, earthen architecture is one of the most vital and original expressions of the human ability to shape the environment by making the most of local resources (Fig. 1). It encompasses various creations, from simple houses, granaries, palaces, and religious buildings to urban centers, cultural landscapes, and archaeological sites. Earthen architecture plays a crucial role in revealing local identities, and its construction techniques are enduring and often linked to genuine artistic expression. It is attracting growing interest because it can be used to make a significant contribution to social and cultural development while respecting the environment and promoting sustainable development [2–8].

The study of earthen architecture gained scholarly interest in the 20th century, beginning with Le Corbusier's *Les Constructions Murondins* [10], advocating for local materials like rammed earth amid post-WWII shortages. This marked a shift towards organic aesthetics in modern architecture. In 1945, Hassan Fathy's project in Gourna (Luxor), later published as *Gourna: A Tale of Two Villages* [11], became a seminal work in sustainable and community-oriented architecture. It revived

*Corresponding author: emdjed@gmail.com
[a]orcid.org/0000-0003-4316-3056; [b]orcid.org/0000-0003-1894-0108; [c]orcid.org/0009-0005-7164-9717
DOI: http://dx.doi.org/10.17515/resm2025-621ma0111rs

Nubian mud-brick techniques to address housing needs through climate-responsive and low-cost solutions.

In the 1950s, CSTB published Le béton de terre in France, as reported by Guillaud H, et al [12], detailing the technical properties and applications of earthen concrete. In Senegal, Dreyfus released *Manuel de Construction en Terre Stabilisée en Afrique Occidentale Française* [13]. The United Nations, translated by SMUH in 1974, issued *Le béton de terre stabilisée*, which further advocated stabilised earth as a sustainable construction alternative.

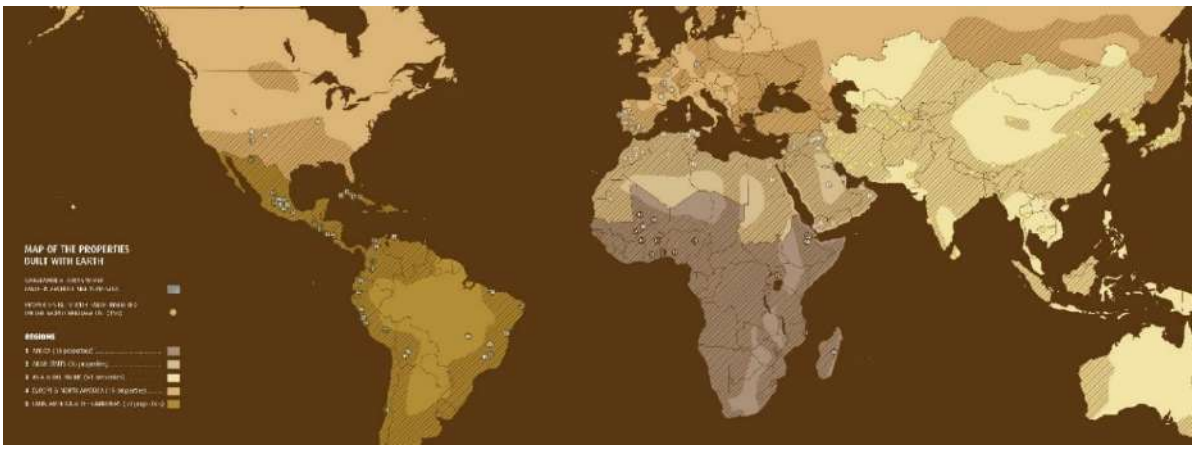

Fig. 1. Distribution of Earthen Architecture Around the World [9]

Notable publications followed: *Archi de terre* by Bardou & Arzoumanian [14], CRAterre's *Construction en terre* [15], and the *Traité de construction en terre* [16], all of which documented techniques like mud brick, cob, and rammed earth, promoting sustainability and heritage conservation. CRAterre, founded in 1979, has since led global education and research in earthen architecture, notably through its DSA postgraduate program launched in 1984.

In North Africa, French colonisation sparked early documentation of local techniques. Texier [17] researched Constantine and the Ziban region, while Cauvet [18] analyzed the symbolic and architectural importance of marabouts in Maghreb. The mapmaker Didier [19] also contributed to promoting earthen architecture through detailed drawings of Algerian sites, such as the ksar Tamacine in the Oued Righ region (Southeastern Algeria).

During the colonial period, major earthen projects like the Sahara Hotel in Biskra city and the Hospital of Adrar by Michel Luyckx were built [20]. However, post-independence Algeria witnessed a decline in the use of earth in construction, as modern materials and techniques gained prominence, often at the expense of local know-how and traditions.

Algeria, located in the north of Africa, has a long strip of land, naturally divided into three zones: The Tell, the high plateau, and the Sahara. The Sahara occupies 80-85% of Algeria's total surface area, occupying a large part of the country [21]. The Sahara's climate is marked by extreme heat, especially in summer, when temperatures often exceed 45°C and significant diurnal temperature variations occur. Rainfall is scarce, and evaporation rates are high due to intense solar radiation and low humidity. In addition, the Saharan regions of Algeria experience strong winds, leading to sandstorms, and despite the heat, winter nights can be very cold. These harsh conditions have shaped the sparse vegetation and traditional architecture, which is adapted to mitigate the effects of the intense climate.

In the Saharan regions of Algeria, urbanization manifests in the form of ksour (plural of ksar), which are the product of a continuous process reflecting the ingenuity of Saharan societies in planning, building, and sustaining themselves in an arid environment [21–27] These ksours are densely packed traditional dwellings with an inward-facing design. They are constructed using locally sourced materials such as earth, stone, and palm wood and are often encircled by fortified walls.

Earth has long been a cornerstone in constructing vernacular architecture in Algeria, especially in the arid and semi-arid regions where other materials like wood and stone are scarce. The techniques used, such as rammed earth, cob, and mud brick (sun-dried mud bricks), have been refined over centuries and passed down through generations to create functional structures perfectly adapted to these regions' harsh climatic conditions.

The use of earth in vernacular architecture is shaped by specific requirements related to its composition and application, ensuring resilience to the extreme temperatures and occasional heavy rains characteristic of Algeria's desert and semi-desert regions. These principles are exemplified in the Ziban region (plural of Zab) in southeastern Algeria, particularly in the ksour of Lichana and Chetma, located in the northern Zab (Zab Dahraoui) and eastern Zab (Zab Chergui), respectively. Builders in these areas possess deep knowledge of local earth properties, enabling them to create durable structures well-suited to the harsh climate. Earth's natural ability to regulate temperature enhances the suitability of these buildings, providing cool interiors in the Ziban's hot, dry environment.

Significant research has examined the ksour of the Ziban, focusing on the thermal performance and climate adaptability of traditional architecture [28,29]. These studies highlighted how centuries of refinement have led to effective architectural strategies for managing extreme temperatures. However, despite this focus, there is a notable lack of detailed analysis regarding the composition and preparation of the building materials, primarily mud brick. While this material is valued for its thermal mass properties and durability, deeper insight into its characterization and preparation techniques are essential for preserving traditional practices and advancing sustainable construction.

This study aims to address this gap by characterizing, diagnosing, and comparing the earthen materials (mud bricks) used in constructing two ksour in southeastern Algeria: the ksar of Chetma and the ksar of Lichana in the Ziban region. It focuses on documenting the ancestral techniques and know-how, as well as material properties integral to their construction.

2. Brief Overview of Ksour as Generators of Oasis Environments

The ksour (plural of ksar) represents a type of human settlement widely distributed across the Sahara, with numerous examples in southern Algeria, southern Morocco, Libya, southern Tunisia, Mauritania, and Mali [22,23,25,30–32]. Romey [33] distinguished the ksar from the medina based on their economic and social functions rather than appearance. Public buildings like mosques serve religious and social purposes, while public squares host meetings and markets. The medina's architecture is characterized by two-level houses with decorated façades. However, Zerari [21], considers geographical location the main criterion for distinguishing between the medina and the ksar. The latter is generally located in arid and semi-arid regions. The author also highlighted several points of similarity: the centrality around a sacred building, the hierarchization of space (from public to private), and the strategies for fortification.

Undoubtedly, the ksar is an architectural model with the fascinating characteristic of being disseminated at different periods (likely since antiquity, as indicated by structures dated to the early first millennium BCE in Libya's Fezzan region) and enabling the construction of similar habitation modes adapted to desert environments. The origins of this type of settlement lie not only in the long-distance trade between the peoples of the Maghreb and Bilad Al-Sudan but also in the connections between Africa and the Mashreq and between Africa and Europe. Additionally, during the medieval period, the spread of Islam and the diffusion of Ibadism, one of the forms of Kharijism, played a role in forming the ksour. These settlements also reflect the interaction between sedentary and nomadic lifestyles, initially belonging to a semi-sedentary model and later becoming entirely sedentary. The ksour is often built on elevated ground, such as a rocky promontory, and typically near an Oued (water source). The morphology of the terrain on which the ksour are constructed, along with their immediate environment (such as a palm grove, erg, depression, or rocky plateau), determine the construction materials used, their overall shape, and the internal distribution of their spaces, which are most frequently arranged in a radio concentric or grid pattern [30].

Urbanization in the Ziban, as in other Saharan regions, took the form of ksour shaped by geographical, religious, historical, and economic factors. The ksour were often named after a sedentary community, a notable landmark, a revered figure, or the geomorphological features of the settlement site [34].

An “oasis” is a fertile area in a desert where water is available from springs or wells, enabling vegetation and often supporting human settlement. This water availability allows for the growth of plants, which can range from grasses and shrubs to trees and crops. Oases have historically been crucial for trade routes and settlements in arid regions, providing essential resources for survival and agriculture [35]. An oasis typically comprises three primary components: water sources, ksar, and palm groves. These elements work in harmony to create a sustainable living environment in arid regions [22,23,25,35–37].

3. Methodology and Data Collection

This article adopted a comparative approach, encompassing historical studies and architectural analysis to reveal detailed construction techniques. Additionally, in situ observations and examinations were conducted to assess the state of conservation and photographically document the building system. Moreover, the investigation concluded in-situ tests of the mud bricks used to construct each of the two studied ksour, Lichana and Chetma. To this end, a representative sampling [38,39] was set up to reflect the characteristics and overall composition of the mud bricks observed in the studied ksour. Accordingly, three (03) samples of mud bricks were selected and learned from the ksar of Lichana (S1; S2; S3), and Ksar of Chetma (S’1; S’2; S’3) to cover the predominant material’s characteristic. In this study, one representative sample from each ksar (S1 and S’2) was selected for presentation, as it effectively captures the key properties shared with the two remaining samples (S2; S3 and S’2; S’3).

The samples (S1 and S’2) for the said tests were prepared from mud bricks taken from specific locations in the two ksour and were finely crushed before testing. The protocol for these tests was based on CRAterre’s earliest and most recent work [15,16] and adapted by the authors (Fig. 2). These tests are:

- Sedimentation in a bottle: This test allows researchers to observe the different components of earth used in construction (sand, silt, and clay) and to compare their regularity in different samples. However, this test cannot provide information on the grain size proportions due to the more or less inflated character of grains such as clay. The test is done in 4 steps: 1) in a transparent bottle, fill 1/4 with earth and 3/4 with water; 2) shake vigorously; 3) leave to stand for at least 24 hours until the water is clean; 4) note the proportions of the different constituents: gravel and sand at the bottom, silt, and clay at the top.
- Cigar test: The “cigar” test allows us to identify a primary understanding of the cohesion of the earth. The test is done in 4 steps: 1) Eliminate particles larger than 5 mm from the sample; 2) Prepare the sample in the plastic state and let it rest. Thus, the clay has time to react with the water; 3) Make a cigar 3 cm thick and gently push it into the void; 4) Measure the length of the cigar (L): if L<5 cm, the earth is sandy; and if L>20 cm, the earth is of clay nature. Repeat the test three (3) times consecutively for accuracy.
- Pellet test: Like the cigar test, the pellet test is used to determine the cohesion of the earth and to check if the amount of clay in the earth is appropriate for making mud bricks. The test is done in 4 steps: 1) Remove the gravels from the sample and prepare the earth to achieve a plastic state; 2) Mould three pellets using a piece of PVC tube or similar; 3) After drying, observe any shrinkage phenomena; 4) Evaluate the resistance of the earth by breaking and crushing between the thumb and the index finger.

At the end of these tests, qualitative and quantitative information was provided, enabling a reasonably detailed classification of the earth used to construct two ksour. In addition to these tests, the soil texture triangle was used to classify the earth and determine the earth’s texture typology. Indeed, there are 12 earth textural classes. This triangle is used so that terms like “clay” or “loam” always have the same meaning.

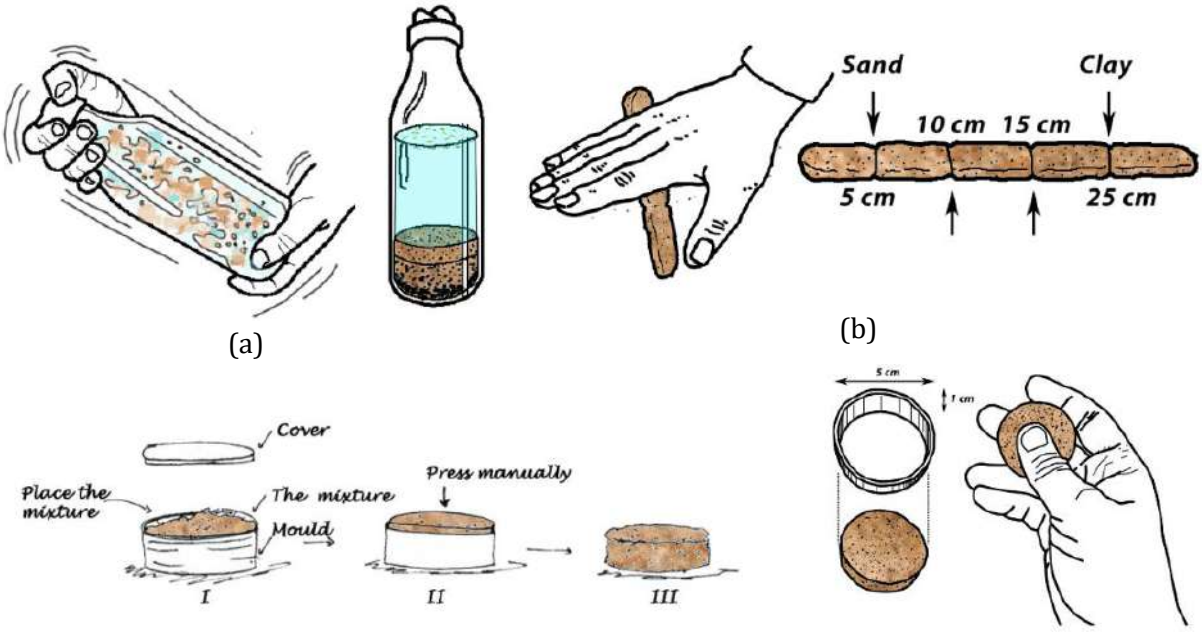

Fig. 2. Schematisation of the protocol of the three tests: (a) Sedimentation in bottle test; (b) Cigar test; (c) Pellet test. Developed by authors, 2024

Each texture corresponds to specific percentages of sand, silt, or clay (Fig. 3). The soil texture triangle is not an inherent part of the sedimentation test, but is an essential tool for interpreting the results. After performing the sedimentation test, record the proportions of sand, silt, and clay. These proportions are then plotted on the soil texture triangle to determine the sample's classification. Based on this position, the earth texture class, such as sandy loam or silty clay, can be identified using the standard classifications provided by the triangle. Finally, the findings should be documented, and recommendations should be made based on the soil texture analysis. At the end of these tests, qualitative and quantitative information was provided, enabling a reasonably detailed classification of the earth used to construct two ksour.

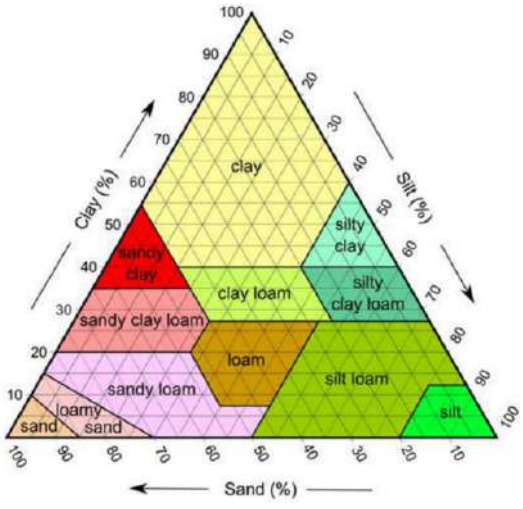

Fig. 3. Soil Texture Triangle [40]

4. Presentation of The Context of The Study: The Ziban Region

The Ziban region is located in southeastern Algeria. According to Cataldo [41], this region is divided into three distinct zones: Northern Zab, Southern Zab, and Eastern Zab. Each regroups a set of sub-regions represented by ksourian establishments (or oasis-cities). Largeau [42], considered Biskra

an independent central Zab.

The Ziban is crossed by two main Oueds: The Oued Biskra (also known as Oued Sidi Zerzzour) and the Oued Djedai, which impacted the development and distribution of these ksourian establishments. However, each ksar has its particular shape. The common feature of all these ksours is their integration into the palm groves, which gave them a distinctive oasis landscape [43].

Algeria periodically experiences episodes of floods, which manifest catastrophically, posing a constraint on activities, hindering economic and social development, and creating a housing crisis [44]. The Ziban region, located in the Algerian lower Sahara at the hyper-arid zone's northern limit, faces water and wind. The risk of flooding is not specific to Saharan cities, but it is often underestimated due to its rarity. However, the characteristics of the Sahara lead to a distinction between risks related to Oueds (river flooding) and those related to closed depressions [45].

In the second half of the 20th century, the Ziban and surrounding areas underwent one of the most significant natural disasters in the region's modern history. In 1969, heavy rainfall caused catastrophic flooding, affecting urban and rural areas. Indeed, the rains caused oueds to overflow, inundating vast portions of Biskra and its surroundings. The floodwaters caused widespread damage to houses, infrastructure, and agricultural lands, notably the palm groves essential to the region's economy. In addition, many people were displaced, and there were reports of casualties, though the exact figures vary. The flooding disrupted daily life, leaving communities isolated and needing emergency assistance. The 1969 flooding spurred discussions on water management and the construction of better infrastructure to mitigate the risk of future flooding in Biskra.

The case studies focus on two ksour: the ksar of Lichana and Chetma, located respectively in northern Zeb (Zab Dahraoui) and eastern Zab (Zab Chergui) (Fig. 4). These ksour were selected for several reasons. Firstly, the authors have in-depth knowledge of these sites, having been involved in research, academic, professional, and participatory/volunteer projects since 2013. Multidisciplinary teams, including architects, engineers, archaeologists, and craftsmen specializing in heritage conservation, have conducted extensive studies and interventions in these ksour, providing valuable data for this research. Secondly, the ksar of Chetma and Lichana were chosen for their heritage significance and potential to contribute to local development in the Ziban region.

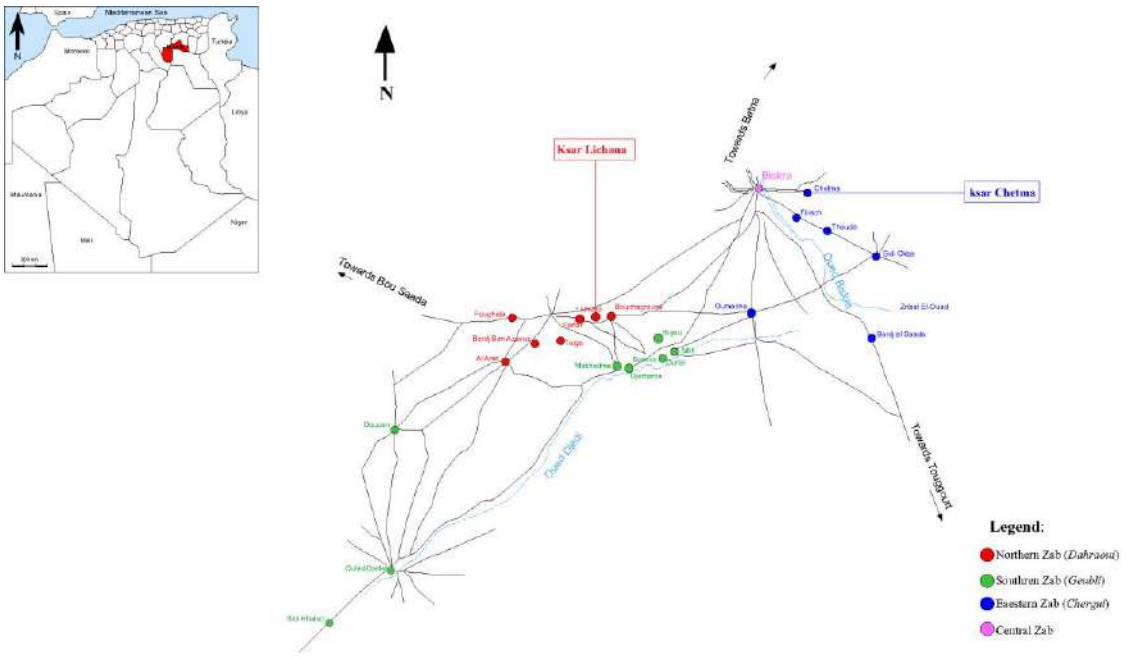

Fig. 4. Map showing the location of the ksar Lichena and Chetma. Developed by authors, based on [46]

The ksar of Lichana and Chetma exhibit similarities: they are prime examples of earthen architecture, reflecting the ingenious use of locally available materials. The architecture of these two ksour integrates environmental adaptability, such as thick walls for insulation and compact layouts to reduce exposure to heat and sandstorms [47]. Their construction primarily employs earth and palm wood, which are abundant in the region and have historically been central to vernacular building practices (Fig. 5).

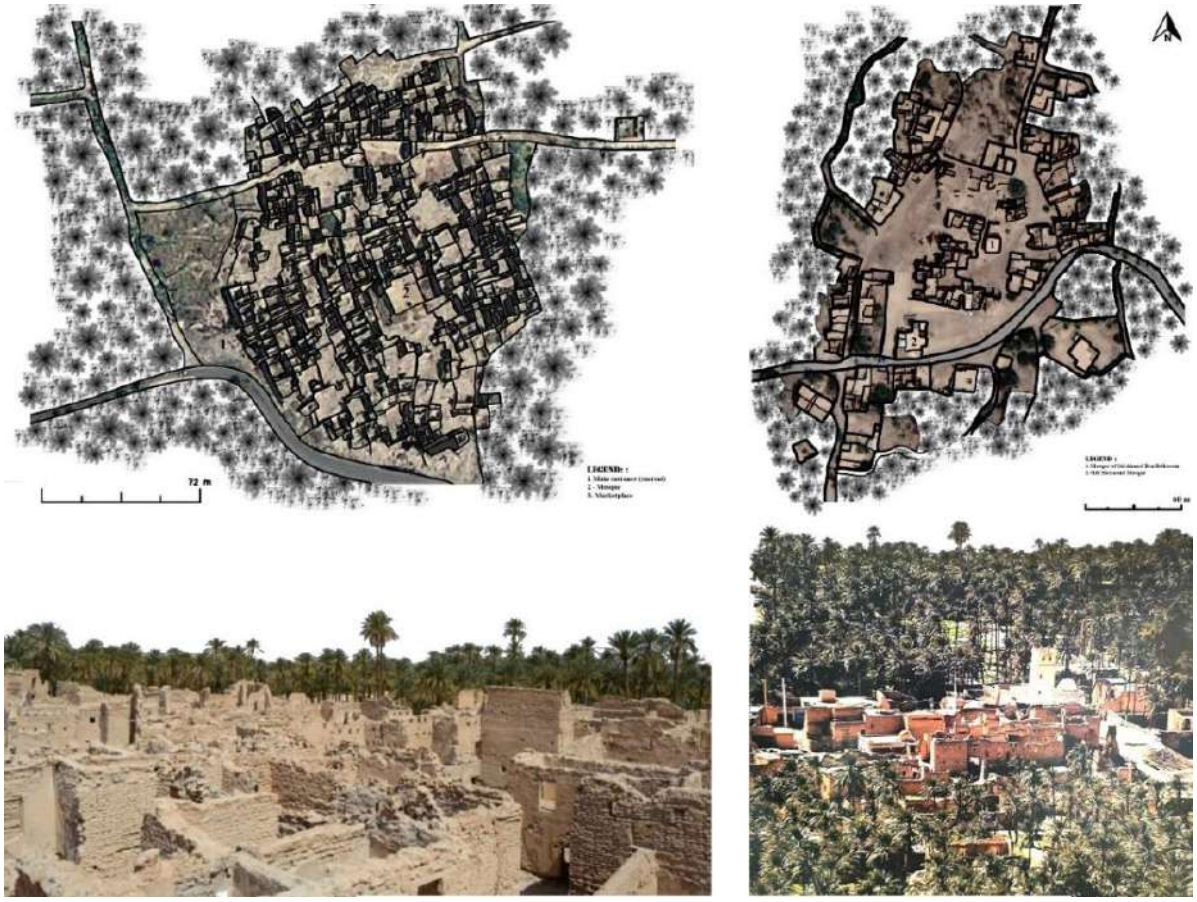

(a) (b)

Fig. 5. Views of the two ksour: (a) the ksar of Lichana; (b) the ksar of Chetma. Elaborated by authors, based on Google Earth, 2024, and CAPTerre [48]

In the ksar of Lichana and Chetma, the load-bearing walls were built in an English bonding pattern (in French: *Appareillage debout*) and coated on both the outside and inside with an earth-based plaster, giving the walls a harsh texture (Fig. 6 and Fig. 8). In addition, the mud bricks used are rectangular with dimensions of 40x20x10 cm. However, it is possible to find mud bricks 36 or 37 cm long. Palm trunks are utilised for vertical and horizontal structural elements like pillars, beams, and joists (Fig. 7 and Fig. 9).

In the studied ksour, the load-bearing walls rest on foundations laid in the form of trenches filled with large river stones brought from oueds. Certain walls have a stone base to prevent capillary rise. Building materials of Roman origin, such as stone blocks and columns, were sometimes reused in vernacular architecture. These walls are in a better state of conservation than walls without a stone base. As confirmed by Zerari, Pace, and Sriti [34], the reuse of building materials is a common practice in the Ziban region, particularly in areas close to the Limes line.

The mosque of Lichana features a distinctive building element: its roof was constructed using IPN joists (I-beams) filled with fired hollow bricks, a building technique that reflects French colonial influences (Fig. 7), as stated by Dali and Belakehal [20]. However, the locals have managed to preserve the authenticity of the two ksour, as no significant changes in construction techniques or new materials have been observed. This resilience is primarily attributed to *Touisa*, an ancestral

practice of community mutual aid in Algeria [49]. It involves members of the same family or tribe taking turns to carry out collective tasks. Particularly widespread in the southern Saharan regions, *Touisa* has played a crucial role in the construction and maintenance of buildings, ensuring the continuity of traditional practices and know-how across generations.

The ksar Lichana is in an alarming state of conservation, with most buildings either fully or partially in ruin. During our visit, the first noticeable feature was the widespread debris. Many remaining walls show significant erosion and extensive plaster detachment, exposing the underlying mud brickwork on nearly all surfaces. Rising damp due to capillary action is a prevalent issue in the ksar, attributed to the water-retentive nature of the earth used in construction, which promotes the upward movement of moisture.

Like many of the ksour in the Ziban, the decline of the ksar of Chetma began after the floods of 1969, which forced its inhabitants to relocate to the new city of Chetma, just a few kilometres away. The Ksar has also been transformed following a poorly executed conservation intervention two decades ago, during which many houses around the mosque were razed, further impacting its integrity. Today, the ksar stands largely abandoned, with many homes in ruins or completely collapsed. Its current state of conservation is marked by severe pathologies, including erosion, rising damp, top wall erosion, extensive plaster detachment, structural deformation, and damage to wooden beams. This situation closely mirrors the condition of the Lichana ksar, emphasising the urgent need for conservation efforts to protect this invaluable cultural and historical heritage before it disappears entirely.

(a)

(b)

Fig. 6. Views of the wall systems in the ksar of Lichana: (a) load-bearing walls (base, wall, and top); (b) construction systems of the base of load-bearing walls (with and without stone footing). Photos by authors, 2024

(a)

(b)

Fig. 7. Views of the roof structures in the ksar of Lichana: palm wood post-and-beam; b) IPN joists of the mosque. Photos by authors, 2024

(a)

(b)

Fig. 8. Views of the wall systems in the ksar of Chetma: a) load-bearing walls (base, wall, crowning, and surface); b) construction systems of the base of load-bearing walls. Photos by authors, 2024

Fig. 9. Views of the roof structures in the ksar of Chetma: palm wood post-and-beam. Photos by authors, 2024

5. Nature of the Earth Used in The Ksar of Lichana and Chetma

Field tests were carried out on two samples: one taken from the ksar of Lichana (S1), specifically a piece of mud brick that was retrieved from a ruined house near the western gate of the ksar. Despite the deterioration of its original structure, the piece of brick appeared in relatively good condition, making it a viable specimen for detailed earth analysis (Table 1). The second sample (S'1), concerning the ksar of Chetma, was taken from a ruined property between the two mosques of the

ksar. According to the local people's oral history, the brick-making earth originated from Ouldja, north of the ksar, and was transported by donkeys. The mud bricks appeared in relatively good condition, making them viable specimens for detailed earth analysis (

Table 2 and

Table 3).

Table 1. Collection and preparation of mud brick samples (S1 and S'1) for testing. Elaborated by authors, 2024

Ksar	Source of the mud-brick	Samples	
		Mud brick samples	Crushed mud brick
Lichana			
Chetma			

Table 2. Stages and explanation of the results of the three in-situ tests performed on the sample (S1) from Lichana. Elaborated by authors, 2024

Tests	Observation and interpretation	Tests' illustrations
Sedimentation in bottle	This earth comprises grains of different sizes (clay 13%, silt 22%, and sand 65%). The test indicates a sandy earth with probably some clay and silt.	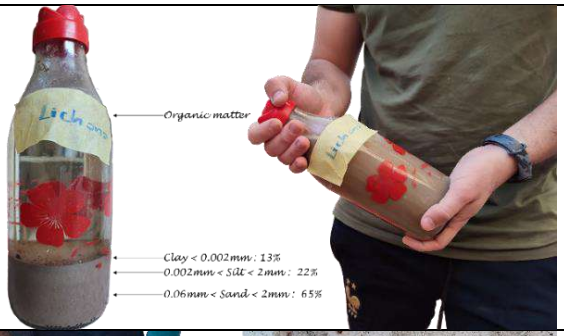
Cigar test	The cigar is cut to an average length of 11.73 cm, indicating a significant level of earth cohesiveness.	

Pellet test	No shrinkage was observed, and the breakage required little force and was easy to reduce to powder. This indicates sandy earth.	
Soil Texture Triangle	The earth is a balanced mixture of sand (65%), silt (22%), and clay (13%), which means it is a sandy loam earth.	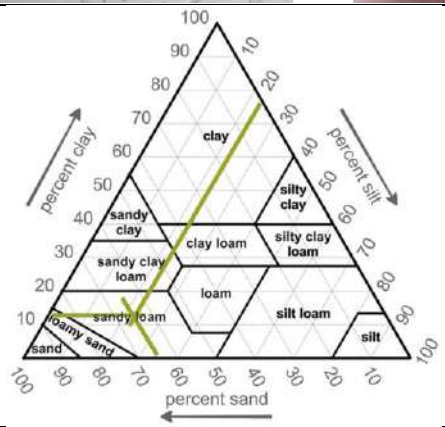

Table 3. Stages and explanation of the results of the three in-situ tests performed on the sample (S'1) from the ksar of Chetma. Elaborated by authors, 2024

Tests	Observation and interpretation	Tests' illustrations
Sedimentation in bottle	This earth is a mixture of different grains (16% clay, 18% silt, and 66% sand). The test conducted indicates that it is sandy in nature.	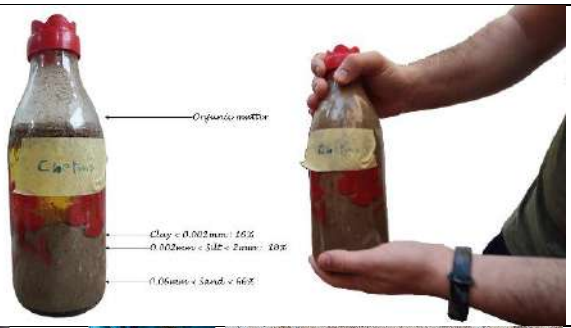
Cigar test	The cigar is cut to an average length of 13.67 cm. This earth is more cohesive than the first sample from Lichana.	
Pellet test	The shrinkage of the pallet was greater than 1 mm. Breaking it required significant force, and the sample was not very friable. This demonstrates the excellent cohesion of the clay in the earth.	

Soil Texture Triangle	The earth is a sandy loam, a mixture of sand (66%), silt (18%), and clay (16%).	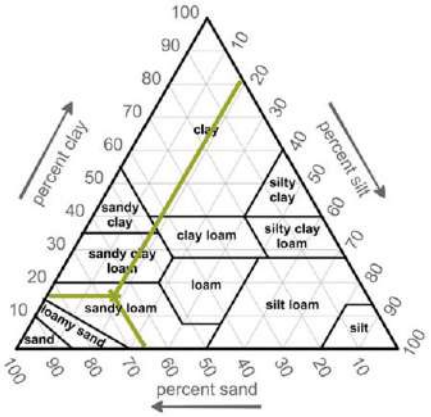

The conservation of the mud bricks' integrity suggests that it can provide valuable insights into the composition and quality of the building materials historically used in the said ksour, shedding light on the construction techniques and material resilience employed in traditional Saharan architecture. The mud bricks used in both ksour are uniform in size, measuring 40x20x10 cm. Although the earth in both locations is similarly classified as sandy loam, their composition has notable differences. The earth in Ksar Lichana exhibits good cohesion due to its clay content. However, the earth in Ksar of Chetma demonstrates even greater cohesion, attributed to adding wheat straw, a component absents in Lichana's mud brick sample. This difference highlights a variation in material choice and construction techniques between the two ksour.

Adding wheat straw to the mud paste reduces shrinkage and improves the tensile strength of mud bricks, while strengthening the resistance of mud plasters to rain-induced erosion [50,51]. In mud materials, straw is used in mud brick masonry and other techniques, such as cob construction [52], where it primarily enhances performance by bridging microcracks, which prevents crack propagation [53]. This crack-bridging effect increases the material's ductility and toughness, helping to maintain its integrity under stress and significantly improving its overall mechanical properties. In Algeria, wheat straw is one of the most commonly used vegetable fibres in mud materials [54,55], due to its abundance and availability in the region.

6. Synthesis

The structures of the two studied ksour are remarkably similar in design (Fig. 10). Both utilise a construction system centred on load-bearing walls made of mud bricks measuring 40x20x10 cm. Particular walls stand on a stone base up to 60 cm high to protect them against rising damp. Mud bricks are sun-dried bricks made from earth, mixed manually, and containing a blend of clay, silt, sand, aggregate, and sometimes natural fibres like the ones of Chetma that contain the wheat straw. Floors are crafted from palm tree trunks, overlaid with palm rib branches (*jerides*), and finished with a layer of raw earth. Foundations consist of trenches filled with large river stones brought from the oueds. In both studied ksour, certain buildings rest on large cut stone bases, stone columns, and other architectural elements, potentially of Roman origin.

Since mud brick is the primary building material in both the ksar of Lichana and Chetma, it is essential to note that it is fragile and highly susceptible to water damage (Fig. 10). Indeed, rainwater, rising damp, and even splashing water can cause major problems, such as erosion at the top and the base of walls and plaster detachment, which threaten the structure's stability. In addition, wind erosion can affect the conservation of earthen buildings, particularly the protruding elements and the exterior plaster. To mitigate these risks, earthen buildings require adequate protection at both the base and the top of walls; the exterior skin of walls, including mud plaster, also needs regular maintenance. In the said ksour, stone bases, sometimes as high as 60 cm, were used by locals to protect mud brick walls from rising damp. However, in cases where no stone base was used, and the mud brick walls were in direct contact with the ground, these structures were more susceptible to moisture damage.

The walls were coated with a thick layer of mud plaster, often applied in multiple layers, specifically designed to shield the walls and their tops from erosion caused by rainwater. Locals regularly repaired the plaster after each rainy season to maintain its protective properties. This regular maintenance was crucial for preventing water damage and preserving the structural integrity of the building. Similarly, the layers of mud on the floor required regular maintenance, with new layers of mud added on top of existing layers, particularly after the rainy season. While this process helped preserve the floors, the cumulative weight of the layers increased the load on the structure. Over time, the additional weight could strain the beams, leading to bending or deformation. Furthermore, the lack of roof maintenance could result in rainwater stagnation, causing water infiltration that leads to rotting of the palm wood.

The preservation of earthen structures is critically dependent on regular maintenance to prevent deterioration and ensure their longevity. This challenge is particularly pronounced in the ksour of Lichana and Chetma, where the departure of the local population has significantly disrupted the upkeep of these buildings. Following the exodus of the inhabitants, the responsibility for maintaining the structures was neglected, leading to the gradual erosion of the ancestral know-how essential for their care. As a result, this expertise, passed down from generation to generation, has been lost. The absence of such knowledge within contemporary local communities has accelerated the decay of these culturally and historically significant structures.

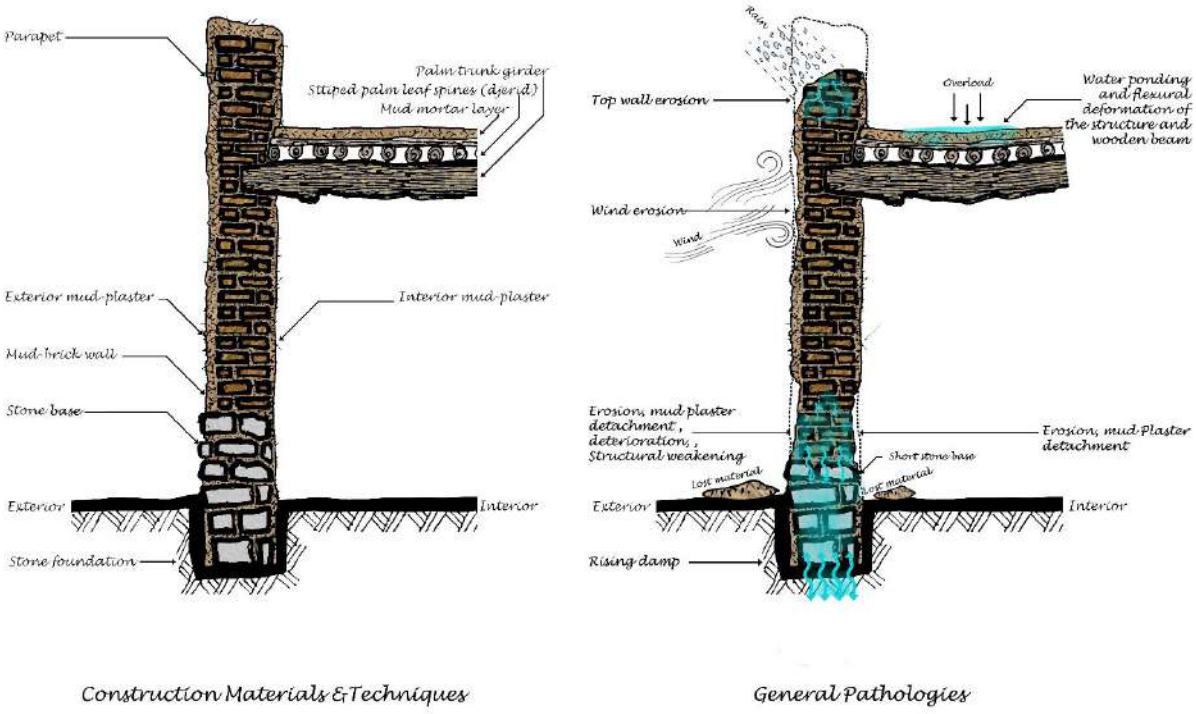

Fig. 10. Construction details and general pathologies in the ksar of Lichana and Chetma. Elaborated by authors, 2024

Knowing the earth's condition directly on-site is not just a technical step; it plays a central role in shaping how conservation work should be approached. In Chetma, where the earth is richer in clay and the mud is mixed with straw, preserving the traditional technique of adding organic fibres becomes essential. It helps control shrinkage and improves the strength of repairs, staying true to how the original builders worked. In contrast, at Lichana, where the earth shows lower clay content and less use of straw, conservation efforts must focus more on protecting surfaces from erosion, without introducing materials or methods that were not originally there. Respecting these small but essential differences ensures that preservation strategies stay faithful to the spirit of the vernacular architecture while helping these fragile structures endure over time. Moreover, any new mud materials produced for conservation efforts must be compatible with the traditional ones identified and characterised in this study, ensuring material coherence and long-term preservation

success. Specifically, in conserving the two ksour, sandy loam earth should be used as a base material; however, for the ksar of Chetma, the mixture should include wheat straw fibres to replicate the original technique, while for Lichana, a sandy loam without added straw would be more appropriate.

7. Conclusions

This article analyzed the use of earthen materials in the construction of two ksour located in the Ziban region of south-eastern Algeria: the ksar of Lichana and the ksar of Chetma. Based on a comparative approach, the study combines historical research and architectural analysis with in situ tests (sedimentation in a bottle, the cigar test, and the pellet test) on the mud bricks used in constructing these two ksour. In addition, field observations and visual examinations were carried out to assess the state of conservation of the structures, together with photographic documentation of the construction techniques observed.

The tests, sedimentation in a bottle, the cigar test, and the pellet test revealed that, although the composition of the mud bricks used in the construction of the two ksour is broadly similar, specific differences were identified, reflecting the natural variability of the raw earth, even in geographically close locations. The mud brick from Chetma contains more clay content and exhibits a greater shrinkage rate. However, incorporating straw fibres into the bricks' composition mitigates this issue, enhancing their quality and performance. These analyses have enabled the mud bricks from each ksar to be identified and characterized, providing essential data for documentation and informing future conservation efforts that require compatible building materials. It is reasonable to assume that the earth produced mud bricks, mortar, and plaster often originates from the same local source. This is mainly due to practical considerations such as ease of access, cost-effectiveness, and traditional building knowledge. As these materials derive from the same soil, they are likely to share similar physical and mechanical characteristics, such as clay content and shrinkage behavior. However, variations in preparation methods or adding specific additives can lead to distinct differences between the properties of bricks, mortar, and plaster.

The investigation into the conservation state of the ksar of Lichana and Chetma highlights their critical condition. Currently abandoned and neglected, these structures face significant conservation issues. Many buildings have partially or entirely collapsed, leaving much of the architectural heritage in ruins.

In situ investigation and analysis are fundamental to the conservation of heritage sites. Before any intervention project, a thorough preparatory study focusing on the characterization of building materials is essential. The methodology employed in this study serves as a valuable framework, highlighting the importance of systematic analysis in understanding the properties of materials. In-situ testing of mud bricks plays a vital role, particularly in contexts where laboratory analyses are unavailable, impractical, or constrained by logistical limitations. Although laboratory testing provides more precise measurements and comprehensive data, in-situ methods are essential for obtaining direct, real-time assessments of material conditions in their actual environmental context. These field evaluations offer critical insights into the current state and performance of the materials, thereby informing appropriate conservation strategies.

Acknowledgement

The authors would like to express their sincere gratitude to Ms. Rachida Aboudil Dali and Mr. Aomar Dali for their invaluable support, assistance, and insightful comments throughout this research.

References

[1] Hugo V. Notre-Dame de Paris. Paris: Charles Gosselin Libraire; 1831.
[2] Azizi-Bondarabadi H, Haji Sadeghi N. Local seismic culture in Iranian vernacular architecture: evidence from Yazd earthen architecture. Built Heritage 2022;6. https://doi.org/10.1186/s43238-022-00051-3
[3] Parracha JL, Lima J, Freire MT, Ferreira M, Faria P. Vernacular earthen buildings from Leiria, Portugal - Architectural survey towards their conservation and retrofitting. Journal of Building Engineering 2021;35. https://doi.org/10.1016/j.jobe.2020.102115

[4] Tomasi J, Barada J. The technical and the social: challenges in the conservation of earthen vernacular architecture in a changing world (Jujuy, Argentina). Built Heritage 2021;5. https://doi.org/10.1186/s43238-021-00034-w
[5] Dali AI, Belakehal A. Style architectural des monuments de l'époque coloniale : cas de l'Hôtel du Sahara à Biskra, Algérie. In: Conservation and promotion of architectural and landscape heritage of the Mediterranean coastal sites. Milano: Franco Angeli; 2019. page 154-67.
[6] Porada K. Earthen Forms in Landscape Architecture-from Geoglyphs to Contemporary Urban Parks. 2018; https://www.researchgate.net/publication/340127001
[7] Gandreau D, Delboy L. Inventory of earthen architecture [Internet]. Unesco; 2012 [cited 2025 Feb 17]. http://catalogue.bnf.fr/ark:/12148/cb316787287
[8] Metallaoui MA, Dali AI. Sustainable Building Materials in the Architecture of Saudi Arabian Oases: Past and Present Examining AlUla. 2025. page 441-51. https://doi.org/10.1007/978-981-97-8588-9_42
[9] UNESCO, WHC-CRATerre. World Heritage. Inventory of earthen architecture [Internet]. Grenoble: 2012 [cited 2024 Nov 9]. https://whc.unesco.org/document/116577
[10] Le Corbusier. Les Constructions "Murondins." Paris: Étienne Chiron; 1942.
[11] Fathy H. Gourna : A tale of two villages. Cairo: Ministry of Culture; 1969.
[12] Guillaud H, Doat P, Rollet P, Houben H, Garnier P, Fontaine L, et al. Technologie de construction et architecture de terre. Proposition de directions prioritaires de recherche pour la République de Corée : Rapport final (Volume 1/2) [Internet]. 2022. https://hal.science/hal-03716122v1
[13] Dreyfus J. Manuel de construction en terre stabilisée en Afrique Occidentale Française. Rufisque: Impr. du Gouvernement général; 1954.
[14] Bardou P, Arzoumanian V. Archi de terre. 1978;103.
[15] Doat P, Hays A, Houben H, Matuk S, Vitoux F. Construire en terre . Paris: Édition Alternative et Parallèles; 1979.
[16] Houben H, Guillaud H. Traité de construction en terre. Marseille : Édition Parenthèses; 1989.
[17] Texier C. Exploration de la province de Constantine et des Zibans. Revue Archéologique [Internet] 1848 [cited 2024 Nov 9];5:129-35. http://www.jstor.com/stable/41745678
[18] Cauvet C. Les marabouts : petits monument funéraire et votifs du nord de l'Afrique. Revue africaine : journal des travaux de la Société historique algérienne [Internet] 1923 [cited 2024 Nov 9];274-329. https://gallica.bnf.fr/ark:/12148/bpt6k57297525
[19] Didier G. Souvenirs d'Algérie : de 1877 à 1882. Bibliothèque nationale de France, département Cartes et plans; 1882.
[20] Dali AI, Belakehal A. Hotel Architecture in the French Colonization Era. The Case of Biskra City, Algeria. Prostor [Internet] 2023 [cited 2024 Oct 31];31:154-67. https://doi.org/10.31522/p.31.2(66).2
[21] Zerari S. Contribution à la caractérisation morphologique et architecturale du patrimoine religieux musulman en Algérie. Cas des mosquées du Bas-Sahara. 2021;
[22] Melouka N. Stratification entre Ville Coloniale et le Ksar Traditionnel de Ouargla. 2024;
[23] Dali AI. Matériaux et techniques de construction des hôtels de Biskra : Entre influences locales et expérimentations coloniales. 2023;
[24] Zerari S, Sriti L, Mensouri K. Dégradation du patrimoine ksourien du sud algérien. Cas du tissu résidentiel des Ziban (Biskra). Al-Sabîl : Revue d'Histoire, d'Archéologie et d'Architecture Maghrébines [Internet] 2019;7. https://www.researchgate.net/publication/349120388
[25] Dali A. Étude et revalorisation du patrimoine architectural de terre, cas des ksour dans le sud algérien . 2001;
[26] Zine A. Les ksour. L'espace Ksourien ou la mémoire en risque de péremption. Habitat Tradition Modernité. HTM 1994;2:17-21.
[27] Marouf N. Lecture de l'espace oasien. Sindbad; 1980.
[28] Boumerzoug A. L'apport référentiel de l'habitat vernaculaire pour assister la production d'une architecture contemporaine localement située et climatiquement performante : l'exemple des ksour des Ziban. 2023;
[29] Boumerzoug A, Rais M, Sriti L. Thermal analysis of the vernacular architecture in the Ziban, Algeria. Pollack Periodica 2022;17:123-8. https://doi.org/10.1556/606.2022.00648
[30] Chekhab-Abudaya M. Les Villes Du Sahara : l'exemple des Qsûr (Algérie). In: Histoire du Maghreb médiéval - XIe-XVe siècle. Malakoff (Hauts-de-Seine): Armand Colin; 2021. page 239-42. https://doi.org/10.3917/arco.bures.2021.01.0239
[31] Moukhenachi S. Evolution Urbaine Des ksour : Permanences Et Mutations. Cas De Timimoun. 1997.
[32] Guide Michelin. Maroc 1972. In: Medina et Ksours, une culture millénaire. Grenoble: Association les 2Rives; 1991.
[33] Romey A. Les Sa'īd 'Aṭbā de N'Goussa: Histoire et état actuel de leur nomadisme. Paris: L'Harmattan; 1983.

[34] Zerari S, Pace V, Sriti L. Towards an Understanding of the Local Interpretations of the Arab Mosque Model in the Saharan Regions. Re-exploration of the Ziban in South-Eastern Algeria. ArcHistoR 2023;19:96-129.
[35] Barker G. Oasis. In: The Oxford Companion to Archaeology. Oxford: Oxford University Press; 2012.
[36] Ben Charif H, Belakehal A, Zerari S. Earthen Architecture in Southern Algeria: An Assessment of Social Values and the Impact of Industrial Building Practices. Open Archaeology [Internet] 2023 [cited 2024 Oct 31];9. https://doi.org/10.1515/opar-2022-0324
[37] Jouve P. Les oasis du Maghreb, des agro-écosystèmes de plus en plus menacés. Comment renforcer leur durabilité ? Courrier de l'environnement de l'INRA [Internet] 2012 [cited 2024 Oct 31];62:113-22. https://hal.science/hal-01222196/file/C62-Jouve-04-02-13.pdf
[38] De Singly F. L'enquête et ses méthodes: le questionnaire. Paris: 1992.
[39] Ghiglione R, Matalon B. Les Enquêtes sociologiques. Théories et Pratiques. Paris: 1978.
[40] Bhandari BP, Dhakal S. A multidisciplinary approach of landslide characterization: A case of the Siwalik zone of Nepal Himalaya. Journal of Asian Earth Sciences: X 2021;5:100061. https://doi.org/10.1016/j.jaesx.2021.100061
[41] Cataldo H. Biskra et les Ziban. Montpellier: SupExam; 1988.
[42] Largeau LV. Le Sahara algérien, les déserts de l'Erg. Paris: Hachette; 1881.
[43] Zerari S, Cirafici A, Sriti L. Issues in the Expression of Local Identity in the Saharan Regions of Algeria: In Search of References to Vernacular Architecture. Conservation Science in Cultural Heritage 2022;22:181-206.
[44] Lahlah S. Les inondations en Algérie. In: », Actes des Journées Techniques/ Risques Naturels : Inondation, Prévision, Protection. Batna: 2004; 43-57.
[45] Côte M. La ville et le désert. Le Bas-Sahara algérien. Paris: Karthala; 2005.
[46] Zerari S, Sriti L, Pace V. Morphological Diversity Of Ancient Minarets Architecture In The Ziban Region (Algeria): The Question Of Form, Style And Character. METU Journal of the Faculty of Architecture [Internet] 2020 [cited 2024 Nov 9];37:127-52. https://doi.org/10.4305/METU.JFA.2020.2.6
[47] Alkama D, Tacherift A. Essai d'analyse typo-morphologique des noyaux urbains traditionnels dans la region des ziban. Courrier du Savoir [Internet] 2001 [cited 2024 Oct 31];1:81-8. https://revues.univ-biskra.dz/index.php/cds/article/view/195
[48] Terki Y. De Terre et d'Argile. Catalogue de l'exposition dédiée aux architectures de terre dans le monde. Alger: Les presses de l'imprimerie En Nakhla; 2013.
[49] Aboudil R, Dali A. Civil participation in the restoration of the ancient nucleus of the M'cid mosque in Biskra, Algeria. In: LiMeS Project. Life between Mediterranean and Sahara. Padova: Padova University Press; 2024. page 141-8.
[50] Facey W. Dir'iyyah and the First Saudi State. London: Stacey International; 1997.
[51] Alnowaiser M ibn AA. Khasais al-Turath al-Omranie fie al-Mamlaka al-Arabiah al-Saudia (Characteristics of Urban Tradition of Saudi Arabia). Riyadh: Darat Al-Malek Abdul Aziz; 1999.
[52] Manel N, Abdellah F. Raw Earth Architecture, an Adaptation Lesson in Distress. The Case of Khanguet Sidi Nadji ksar, Biskra, Algeria. International Journal of Innovative Studies in Sociology and Humanities 2022;7:60-76. https://doi.org/10.20431/2456-4931.0706007
[53] Xie L, Chen Z, Hu X, Cai W. Effect of straw and starch on mechanical performance of mud mortar for rubble masonry. Journal of Building Engineering 2025;104:112268. https://doi.org/10.1016/j.jobe.2025.112268
[54] Baiche B, Osmani M, Walliman N, Ogden R. Earth construction in Algeria between tradition and modernity. Proceedings of the Institution of Civil Engineers - Construction Materials 2017;170:16-28. https://doi.org/10.1680/jcoma.15.00048
[55] Kassou Y, Alkama D, Bouzaher S. Earthen Architectural Heritage in the Gourara Region of Algeria: Building Typology, Materials, and Techniques. Heritage 2024;7:3821-50. https://doi.org/10.3390/heritage7070181

Research on Engineering Structures & Materials
www.jresm.org
Research Group

Research Article

Detection of defects in steel oil and gas operating pipelines using a neural network, based on the results of optical diagnostics

Shcherban Pavel Sergeyevich [*,1,a], Potapov Boris Vasilievich [2,3,b], Karagadyan Artur Nairievich [1,4 c]

[1]*Baltic Federal University of Immanuel Kant, BSC "Institute of high technologies", Kaliningrad, Russia*
[2]*RTU MIREA Institute of Information Technology*
[3]*Russian State Agrarian University - Moscow Timiryzev Agricultural Academy*
[4]*JSC VNIIST, Moscow, Russia*

Article Info

Article History:

Received 01 Feb 2025

Accepted 15 June 2025

Keywords:

Metal pipes;
Optical control;
Neural network;
Surface diagnostics;
Pipe defects

Abstract

In today's world, steel pipelines are an essential part of the infrastructure for various industries, such as oil and gas, energy, and industry. However, their flaws can lead to major accidents, resource loss, and environmental hazards. Therefore, it is crucial to identify defects early on and accurately determine them to ensure the safe and efficient operation of pipeline transportation systems. During research, a technique was developed for automatically detecting and classifying defects in steel oil and gas pipelines using neural networks. This method processes image data from an in-line inspection system. The initial data for this analysis comes from optical inspections of oil and gas pipelines. The study involved developing and testing a method that can detect defects in oil pipelines automatically with significant accuracy using data from optical examinations. Optical examination can be performed using both specialized endoscopic equipment and a crawler robot. The processing of diagnostic results using a neural network and data library can be done on an external medium or integrated into a diagnostic system for in-line monitoring. Testing of the pipe defect recognition method during optical inspection of the inner pipe surface demonstrated good results for detecting corrosion and erosion defects (response rates of 67% and 68%, respectively, with mAP values of up to 49% and 65%). Crack-type defects were identified with lower accuracy (response rate of 57%, mAP up to 42%).

© 2025 MIM Research Group. All rights reserved.

1. Introduction

The existing methods of inline diagnostics of steel pipelines include the use of ultrasonic, eddy current, and magnetic flaw detectors. The use of this devices allows us to determine the type of defect and its geometric parameters with high accuracy. However, in steel pipes with small diameters, such as those used in oil and gas fields systems with diameters less than 250 millimeters, it can be challenging to perform these types of diagnostic procedures due to the lack of specialized equipment and technical tools [1].

For pipes of this type, an optical examination of the inner surface is a simpler and more natural method, according to which one can judge the integrity and reliability of the pipes. The length of these pipes can be considerable, amounting to several kilometers, significantly complicating the processing of photographic and video data obtained during the examination. This process requires

*Corresponding author: ursa-maior@yandex.ru
[a]orcid.org/0000-0001-5106-7852; [b]orcid.org/0000-0002-9635-3809; [c]orcid.org/0000-0002-8427-8362
DOI: http://dx.doi.org/10.17515/resm2025-650st0201rs

a lot of time, but an increase in processing speed and data quality can be achieved through the use of a specialized neural network. Optical control methods in conjunction with neural networks for processing and detection of emergency situations and defects, are developing extremely actively and are used in various industrial and transport sectors [2]. The efficiency, detection speed, and accuracy of neural networks in identifying individual defects and emergency situations are steadily improving.

In recent scientific works [3], there has been an increase in the use of various machine learning methods for diagnosing oil and gas pipes and identifying internal defects. In that regard, the most interesting studies are [4,5], which conduct a deep analysis of the applied use of various machine learning algorithms and establish the possibility of detecting and segmenting defects in oil and gas pipelines in the optical range (in particular, corrosion and crack defects). In addition, research [6,7] has significant potential, where corrosion and erosion datasets are formed and defects of this type in pipelines are determined.

Researchers are developing and testing various algorithms [8, 9], which forms a representative array of information on their effectiveness for solving specific production problems. This confirms that the use of computer vision methods will soon find a direct response in the methodological foundations of diagnostics of oil and gas equipment in general and determining pipe defects in particular. The development of a general methodology and further adoption of the corresponding standard at the national and international level are expected. Obviously, this will happen based on the results of testing various algorithms, taking into account their effectiveness and accuracy of detection and segmentation of defects. It is also likely that the most effective approaches will be determined for various control methods (optical, ultrasonic, eddy current, radiographic).

The aim of this research was to develop a neural network capable of processing and segmenting defects with high accuracy, including bulges, corrosion, cracks, and erosion, in oil and gas steel pipes during optical examination. The distinctive features of this study from any previously published works in scientific periodicals is that to form a dataset of pipes with defects, JSC All-Union Scientific Research Institute for the Construction and Operation of Pipelines and Fuel and Energy Complex Facilities (VNIIST) used video and photo materials from optical inspection of field oil and gas pipelines collected by the institute in the period of 1980-2020s (the institute itself was founded in the USSR in 1948). In addition, based on the dataset, a specialized YOLO (You Only Look Once) neural network was trained to recognize specific defects in oil and gas equipment. (The main abbreviations are presented in Appendix 1.).

During the research, we analyzed the most critical types of defects and created a dataset for each one (based on internal surveys of steel pipes, used in oil and gas field transportation systems). For each type of defect, the dataset contained at least 100 images. Then, we trained a neural network to segment images of bulges, corrosion, cracks, and erosion in steel pipes using the results of optical examination. Based on this neural network, the software was developed. The results of the study will lead to the creation of an improved methodological apparatus and software solutions for robotic means of conducting diagnostic examination of pipeline systems. This is an important part of the technical condition monitoring system, which is necessary for a long-term and safe operation of objects.

The remainder of this paper is organized as follows: the section “In-line diagnostics and the main types of defects in steel pipelines” provides an overview of approaches for gathering of optical data from the inner pipe surfaces. Section “The formation of a neural network and the creation of a library of defects” outlines dataset construction and preprocessing. Also, it contains information about the selection and architecture of neural network to be used with the data. In section “Training a neural network to detect pipe defects and analyzing the results” we provide both visual and quantitative results. These include images of recognized defects and metric plots—to evaluate the model’s performance. We conclude the paper in section “Conclusions” where we summarize the obtained information and outline future researches.

2. In-Line Diagnostics and The Main Types of Defects in Steel Pipelines

The formation of a database of defects was based on images obtained from inspections of oil and gas systems transporting borehole products. These images were collected through endoscopic examinations of the systems or using a crawler robot (see Figure 1). All sites where optical data was collected were made from steel pipes. Among the most common defects in the received information package are bulges, corrosion, cracks, and erosion. This is generally due to a wide range of conditions (physical and chemical processes) that change and predetermine these defects' occurrence. Such violations lead to a significant decrease in the reliability and strength characteristics of the pipe system, resulting in the pipes ceasing to fulfill their main transport function [10].

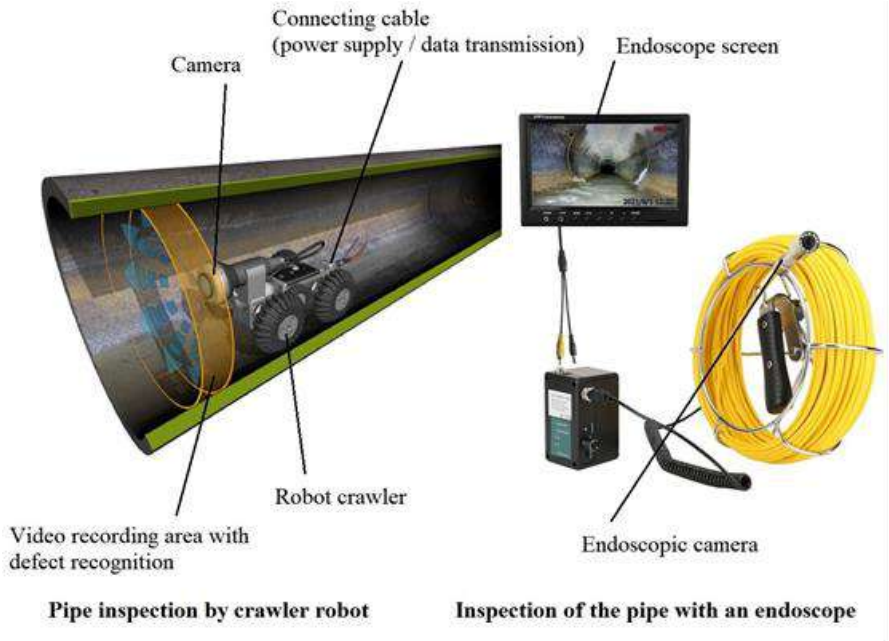

Fig. 1. Examples of a crawler and an in-tube endoscope for optical examination of pipes

The issue of the frequency of frame capture of the inner surface of the pipes is crucial for ongoing research. Therefore, it seems reasonable to split the video stream into frames at a frequency of 20 frames per second for optical diagnostics. Based on the speed of movement of a self-propelled robotic platform or endoscope moving in a straight line, this frequency is the minimum necessary. When diagnostic equipment moves at a speed of 1 cm per second, this frame rate allows us to capture damages up to 0.5 mm in size. If smaller defects need to be captured, the frame rate needs to be increased. The recorded video stream needs to be processed and analyzed frame by frame. After that, the results of processing are analyzed and combined every 20 consecutive frames. This process allows us to identify the most damaged areas, their approximate location, size, geometric shape, and color distribution.

To create an accurate image of the pipe's surface, a wide-angle camera and illuminator system should be used. They should be fixed in such a way that the entire pipe falls within the camera's field of view. Then, the part of the frame around the perimeter of the pipe that is in focus is selected, forming a ring. The center of this ring is the optical center of the lens [11]. This process results in an annular panoramic image of the pipe. Next, either direct processing of the video data can be done, or each individual frame can be preprocessed to reduce geometric distortion. Geometric distortions can occur due to the lens's distortion. These distortions cause straight lines in the image to bend, creating a "barrel" effect that reduces distance from the optical center. However, the part of the image that corresponds to the plane of the optical axis remains undistorted.

No additional image preprocessing unit has been developed in the software that was created to eliminate distortion effects. Instead, a direct assessment of defects observed in the optics was carried out without scanning images. This approach has a slightly lower accuracy in general,

particularly with respect to minor defects such as pitting and hairlines. However, it is also less resource-intensive and significantly faster.

There are numerous different types of defects on the inner surface of steel pipes, and their systematics and specific features are reflected in various regulatory documents. These include ISO 11971:2020 Steel and iron castings — Visual testing of surface quality, ISO 3183:2019 Petroleum and natural gas industries — Steel pipe for pipeline transportation systems; ISO 11960:2020 Petroleum and natural gas industries — Steel pipes for use as casing or tubing for wells; ISO 7005-1:2011 Part 1: Steel flanges for industrial and general service piping systems.

In their research, the authors [12,13] and [14] rely on international regulatory documents and the classification of defects. It should be noted that national or industry classifiers can also be used, where the characteristics of defects can be presented in more detail. National classifiers can be linked to pipe manufacturers and manufacturers of equipment used in diagnostics. Among Russian regulatory documents, the taxonomy of in-pipe defects is most fully presented in GOST R 59496-2021 Welded steel pipes. Welded joint defects. Terms and definitions and in the current OST 14-82-82 "Industry quality management system for ferrous metallurgy products. Departmental quality control of products. Seamless rolled steel pipes. Surface defects. Terms and definitions". Unfortunately, at the moment, various scientific works on the detection of defects in steel pipes using neural network technologies do not cover all types of defects (regardless of their classification). This is often due to the lack of a representative and high-quality sample of defects for use in neural network training [15]. The defects can be divided into three categories: pipe geometry defects, pipe wall defects, and welded joint defects (Figure 2).

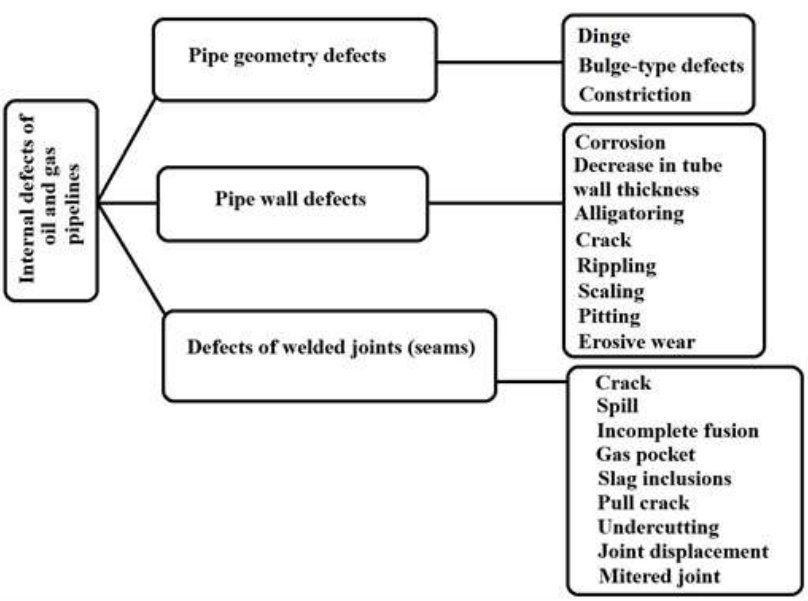

Fig. 2. Main categories of defect types in steel pipelines

Due to the lack of frame-by-frame pre-processing in this study, geometric distortions were not eliminated and images obtained from the side surface of the crawler or endoscope were not processed (only images from the front camera were used). As a result, some potential defects at pipe connections may have been missed. To solve this problem, it is necessary to consider the issue of distortions or, even better, conduct panoramic or side-by-side shooting. In such a case, defect detection will be maximized within the optical range [16].

In this regard, as part of the ongoing research, it was decided not to consider defects in pipe connections separately (since either a different type of survey or additional data preprocessing is required), but to limit ourselves to determining defects in the inner surface of the pipe body. The most common defects affecting the strength of the inner surface of the steel pipe body are the following: bulges, corrosion, cracks and erosion. Potholes and delaminations are relatively common, but there were no defects of these types in the available set of photo and video data used for the study. Let's take a closer look at the defects analyzed in the study.

The bulge is a local, gentle deflection of the pipe wall, with possible thinning in some areas. It indicates a local loss of strength and bearing capacity of the pipe, as well as a violation of the geometric shape. This may be caused by cyclic loads. Bulges can be convex or concave, and their presence leads to a change in the flow rate of liquid, which increases the impact of the transported material on the pipe walls in that area. It should be noted that the number of bulges is relatively small in the data set. This defect is rare and difficult to detect visually from inside the pipe. For steel pipes, the most common type of defect is corrosion. Corrosion can be of various types, such as rivulet, pitting, and solid. The generated data library takes into account all these types of corrosion damage to pipes. In general, corrosion refers to the spontaneous chemical interaction of metal with its environment, resulting in a change in its composition and properties. This process occurs without the need for external energy input. The corrosion process involves the chemical reaction between the metal and the medium.

Therefore, if a metal structure loses its bearing capacity due to exposure to a dry hydrocarbon gas stream containing abrasive particles, this is not considered as corrosion-related damage. If aggressive components such as moisture, hydrogen sulfide and carbon dioxide are present in the gas and the destruction occurs as a result of the chemical interaction between the pipe metal and these components, then we can talk about corrosion damage to the metal. The consequence of corrosion is always a change in the properties of the metal (chemical and mechanical), and as a result, a change in the operational characteristics of the pipeline. However, a pipe affected by corrosion may continue to function without failure for a certain period of time.

Cracks are a common type of defect in metal pipes. They can occur either longitudinally or annularly, and can be found in the base metal or at a welded joint. Our database takes into account all these possibilities. It should be noted that cracks are often caused by stress concentrators, such as non-welds, sinks, or other defects in the pipe or weld. Additionally, pressure drops in the pipe can also lead to cracks. Both of these factors can contribute to the formation of a crack in a pipe. The last type of defect in steel pipes that we will consider is erosion. This is a gradual loss of material from the pipe wall caused by the flow of liquid and particles that are transported through it. The impact of these particles on the wall and the resulting cavitation effects lead to local deterioration of the inner surface of the pipe.

A number of scientific studies, such as [17] and [18], have also conducted optical diagnostics of pipes using crawler robots, successfully detecting defects using machine learning techniques. Other studies obtained positive results by acquiring and processing magneto metric and acoustic data using neural networks [19]. The algorithms and neural networks applied demonstrated relatively high accuracy in detecting defects such as corrosion and cracks (about 69–75%), which is considered a good result for field studies, given the low quality of the initial data and limited statistical samples. Of course, the results obtained so far cannot be compared to those obtained by using machine learning on diagnostic samples in a laboratory setting. This is especially true for experiments on individual metal plates with defects. When learning occurs on such samples (cleaned of contaminants) under direct illumination, as well as on a flat, rather than a concave surface, the results of defect recognition can be extremely high.

For example, in [20], the proposed GAN-based augmentation scheme significantly improves the performance of CNN for classifying surface defects. The classically augmented CNN yields sensitivity and specificity of 90.28% and 98.06%, respectively. In contrast, the synthetically augmented CNN yields better results with sensitivity and specificity of 95.33% and 99.16%, respectively. Unfortunately, it is extremely difficult to obtain similar results in sensitivity and specificity in the field; this is probably not due to the quality of the proposed algorithms, but rather to a large number of external factors. Despite these factors, researchers are making quite successful attempts to increase the performance of a neural network and increase the accuracy of detecting various types of deviations, defects and objects [21]. However, the issue of testing the results obtained on a large volume of field data and the applicability of the developed algorithms and networks for solving specific diagnostic problems remain the subject of further research. A separate problem which is highlighted by a number of works such as [22] and [23], is the binding of a pipeline defect to a specific point along the route. It is important to not only determine the

presence or absence of a defect, but also to indicate the problem area. In steel pipes, due to the possibility of using them as signal amplifiers, such a problem is not as severe [24]. But it represents a certain challenge for the detection and localization of defects in polymer reinforced and plastic pipes [25].

During the standard in-tube optical inspection, the flaw detector records all observed pipe defects, determining their geometric parameters and referring them to the picket along the route. In this case, binding was carried out to a specific frame that was received. At the same time, no selection of acceptable or unacceptable defects was made. All potential defects were recorded in the processed frame. Determining acceptable and unacceptable defects for a specific type of pipe requires creating an additional add-on in the software. To do this, it will first be necessary to determine the geometric parameters of the defect (information on frame size, focal length, illumination, etc., will need to be provided to the neural network) as well as information on acceptable defect sizes for this pipe type (a defect library linked to regulatory and technical documentation requirements must be created).

In general, this suggests the need for a three-stage development of an in-tube optical diagnostic system that uses neural networks to recognize defects [26]. At the first stage, the neural network would be trained to recognize defects from a live video feed (based on the results of this study). At the second stage, either a system would be developed to combat distortion (by creating a scan of the frame) or the neural network would be refined to recognize defects when shooting from side cameras (taking into account connection defects). Finally, at the third stage, a representative library would be assembled containing data on the geometric parameters of defects and their acceptability for pipes of different types and brands. This would allow for secondary processing of diagnostic results, not only to mark defective zones but also to determine the acceptability or unacceptability of a defect. Next, let's move on to solving the main goal of this research: recognizing defects in steel pipes from live video footage.

3. The Formation of a Neural Network and The Creation of a Library of Defects

As part of the study, a library of images containing a total of 500 images was used. These images of steel pipes were captured through in-line photography of different types of oil and gas steel pipes. This library served as the foundation for the development of a learning neural network. During the creation of this system, advanced techniques from the field of artificial intelligence, specifically machine learning, were employed.

So, the YOLO neural network was used as a basis. This network makes it possible to achieve high accuracy and speed in detecting defects in pipelines. The YOLO system, developed by Joseph Redmon and others, considers object detection as a regression task on spatially separated bounding boxes and associated class probabilities. It examines the entire image during testing, so its predictions are based on the global context of the image. The YOLO algorithm uses a convolutional neural network, which is a deep learning algorithm that takes an input image and assigns importance (studied weights and offsets) to aspects or objects in the image, distinguishing one from the other. Compared to other algorithms, images require much less preprocessing with this method.

Figure 3 shows the architecture of the YOLO network. The basic idea is to reduce the feature dimensionality using convolutional layers alternating with 1x1 convolutions that compress features from preceding layers. YOLOv8 consists of several key components. Backbone - this is the core part of the model designed to extract features from the input image. YOLOv8 uses a new Backbone architecture designed to improve the efficiency and accuracy of the model. Neck -this section connects the Backbone to the Head and is responsible for aggregating and passing on the extracted features. YOLOv8 uses structures such as Spatial Pyramid Pooling - Fast (SPPF) and Path Aggregation Network (PANet), which improve the model's ability to handle contextual information and different scales of objects. Head (output part) - this component is responsible for predicting the coordinates of bounding boxes, object classes, and assessing the confidence in detection. YOLOv8 uses a new Anchor-Free head, which simplifies the prediction process and improves the accuracy of the model.

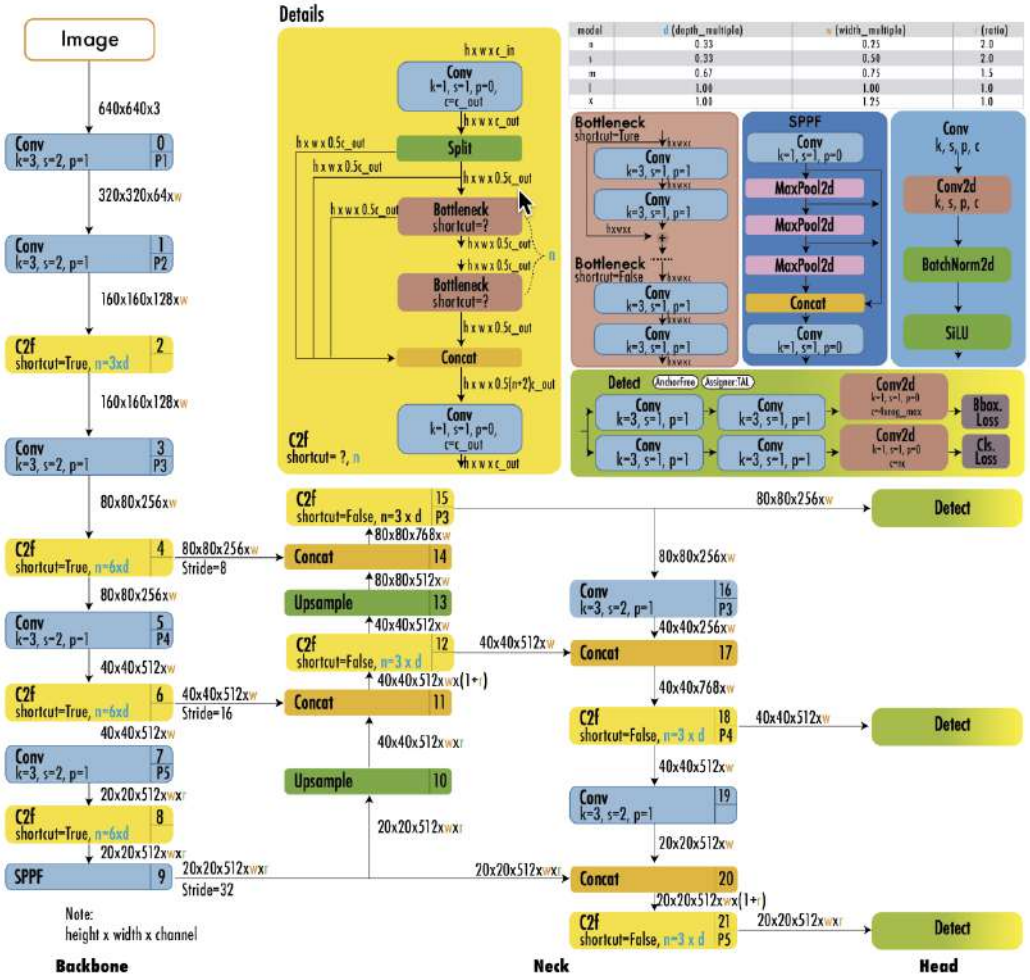

Fig. 3. Architecture of a convolutional neural network. The top right part of the diagram shows the model parameters: depth_multiple – model depth multiplier (0.33, 0.5, 0.75, 1.0, 1.25). Width_multiple – model width multiplier, ratio – scaling factors

Important improvements in YOLOv8 include the Anchor-Free approach. It involves abandoning the use of pre-defined anchor boxes, allowing the model to be more flexible and accurate in detecting objects of different sizes and shapes. A new loss function is also used, which contributes to more stable and efficient model training. An improved backbone network is also used. The updated Backbone improves the efficiency of feature extraction, which contributes to increased detection accuracy. The input image fed to the network has the size: 640×640×3 (RGB image with three channels). It is fed to convolutional layers (Conv), which reduce the dimensionality and extract features. The network processes this image through a series of convolutional layers, each of which performs a convolution using different kernel sizes. Convolutional layers reduce the dimensionality of the image and increase the number of channels. C2f (Cross Stage Partial with Fusion) is used - an improved version of Cross Stage Partial (CSP) blocks, responsible for efficient feature extraction and SPPF (Spatial Pyramid Pooling - Fast) – a layer that uses multiple levels of MaxPool2d to improve the model's perception of different scales of objects, allowing the model to focus on the most significant features [27].

YOLO convolutional layers are alternated with 1x1 convolutions, which help to reduce the number of features between main convolutional layers, thus reducing the computational load and increasing the efficiency of the model. MaxPooling layers with a 2x2 kernel and a stride of 2 are also used to reduce the image size, halving its width and height at each stage. This helps to preserve important features while reducing the image's size. The convolutional layers are followed by two fully connected layers. The first fully connected layer contains 4096 neurons, and the second contains 30 output neurons, which are responsible for predicting the coordinates of bounding

boxes and object classes. These layers complete the image processing and form the final predictions.

Three outputs (P3, P4, P5) are responsible for detecting objects at different scales: P3 (80×80) – for small objects, P4 (40×40) – for medium objects, P5 (20×20) – for large objects. The network uses Conv2d convolutional layers to predict Bounding Box, Class, Objectness Score.

During the training process, visualization was performed to monitor the effectiveness of the training. The learning rate is a very sensitive parameter. With a very high learning rate, the error curve will have an unacceptable shape. With a low learning rate, the error will decrease very slowly even after a large number of epochs. With a high learning rate, the error initially decreases quickly but then becomes stuck in a local minimum, preventing the network from achieving good accuracy. When the learning rate is appropriately chosen, the error smoothly decreases to a minimal value.

Thanks to YOLO, it is now possible to quickly and accurately detect the location and type of defects, which is essential for a swift response to potential security risks. However, a significant amount of labeled data was required to train the neural network. Initially, the process of labeling defects in images was done manually. Later on, the Label Studio tool was utilized. With its assistance, it became feasible to swiftly create annotations for pictures of faulty pipes, which served as the foundation for training the neural network.

One of the key benefits of using YOLOv8 is its built-in optimized architecture, which greatly simplifies the process of training and deploying a model. Unlike alternative frameworks such as Detectron2 or MMDetection, which require explicit definition of neural network layers and training parameters, YOLOv8 offers a ready-made, well-tested architecture that provides a balance between accuracy and speed. The Ultralytics library provides a convenient API that allows us to run training, validation, and inference in just a few lines of code, reducing the complexity of development and making it accessible even to users with minimal experience in machine learning. In addition, YOLOv8 includes automatic hyperparameter tuning, built-in data augmentation functions, and computational optimization, making it an ideal choice for object detection tasks (Figure 4).

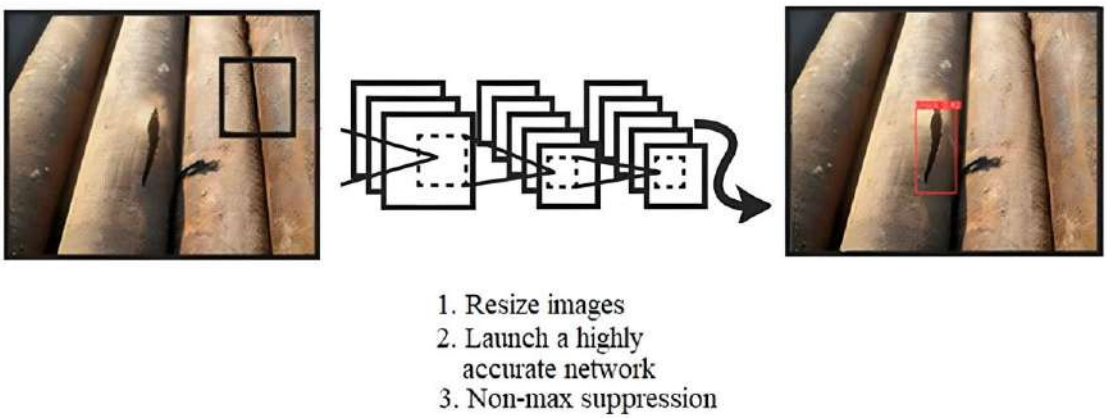

Fig. 4. YOLO object detection and convolutional neural network

Another advantage of YOLOv8 is its high speed, achieved thanks to its single-stage architecture, which is critical when analyzing large amounts of data in real time. Using pre-trained weights and built-in methods for fine-tuning allows the model to be adapted to various datasets with minimal computational resources. These features make YOLOv8 the most effective solution for object detection, especially in conditions where ease of integration, performance, and detection quality are important.

In this work, "YOLOv8" was used – the latest version of this model. Data preparation for training the YOLOv8n object detection model includes several stages. The first stage of data preparation is to collect and organize a set of images on which various objects are marked. The data is organized in a hierarchical folder structure, where each subfolder corresponds to a specific class of objects. All images are stored in a folder named "images". In the second stage, annotation tools such as "Label studio" are used to create annotation files in YOLO format. These files, usually with the

extension ".txt", are saved in the "labels" folder and contain information about the coordinates of the defect boundaries (x, y, width, height) on each image. The third stage involves dividing the dataset into three parts: training (train), validation (valid) and test (test). The ratio between these parts is usually 70% for the training set, 15% for the validation set and 15% for the test set [28]. The structure of the prepared dataset is shown in Figure 5.

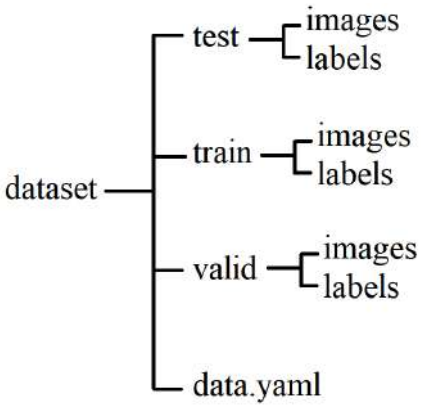

Fig. 5. Folder structure

At the fourth stage, the configuration file is created. The YAML configuration file plays a key role in configuring and managing the parameters of the YOLOv8n model. This file, usually with the extension ".yaml", contains detailed information about the structure of the model, as well as about the training parameters and data. Next, the model object is created. This file contains the weights of a model that has been pre-trained on a large dataset such as COCO, which allows you to use this model as a starting point for further training. The final step is to train the model.

4. Training a Neural Network to Detect Pipe Defects and Analyzing the Results

The training of the YOLO neural network was performed using the ultralytics library. To begin, the YOLO class was imported from the library using the code 'from ultralytics import YOLO'. This allowed us to utilize YOLO's features in our research. Then, an instance of the YOLO class was created with the pre-trained YOLOv8x model stored in the file 'yolov8x.pt'. The line of code used was 'model = YOLO("yolov8x.pt")'. After this, we proceeded to train the model (see Figure 6).

Starting the process of training the model using the 'train' method, we specified the path to the training data file, the number of training epochs, the image size, and the batch size. For example, the line of code: results = model.train('external_defects/crack/data.yaml', 250, 640, 16) starts training the model on the data from the 'external_defects/crack/data.yaml' file for 250 epochs, with an image size of 640 pixels and a batch size of 16. The results of the training are stored in the 'results' variable. This allows us to analyze and evaluate the performance of the model. Thus, based on the generated training and learning algorithms, all 500 images were processed. At the same time, groups of human-recognized images were previously formed with reference to defects of a specific type. Let's further explore the process of training a neural network and see its results.

During each iteration of training, the YOLO model processes images from the training dataset using a neural network. The images are analyzed and classified by the network, and features are extracted to determine the presence of objects. After analyzing the images, the model compares its predictions with actual image labels to calculate losses. These losses show how different the predictions are from the true values. The error is then propagated backwards through the network, where the weights and parameters are adjusted to minimize the error and improve predictions. This process is repeated multiple times during each epoch of training. An epoch ends when all weights in the network have been updated based on data from the training set. It is important to note that after each training iteration, the model's performance is evaluated on a separate validation dataset in order to monitor the learning process and prevent overfitting. Training stops when a certain stopping criterion is met, such as reaching a certain level of accuracy or completing a predetermined number of iterations.

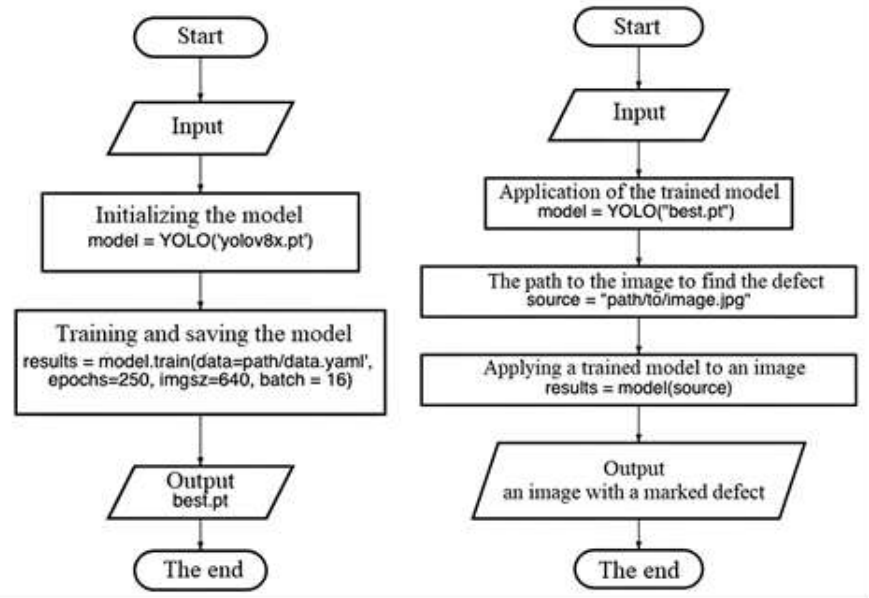

Fig. 6. Neural network training and learning algorithms

The model is trained using Python and the Ultralytics YOLOv8 library. The dataset is pre-labeled in the YOLO format, which includes object annotations in the form of bounding box coordinates and corresponding classes. We use data augmentation strategies to improve the model's robustness to various shooting conditions. The training code is provided in Appendix 2. During the training, hyperparameters such as the number of epochs, input image size, and mini-batch size were varied to optimize the detection quality. Using a GPU allowed us to speed up the training process and improve the convergence rate of the model. After training, the model is evaluated on a test dataset, where its accuracy (mAP) and defect detection completeness are analyzed. As a result of training the YOLOv8 model on a specialized dataset containing images of defects in steel oil and gas pipes, key metrics characterizing the detection accuracy and prediction quality were obtained. The training was carried out for 250 epochs, and the final learning rate was 0.00003584, which indicates gradual convergence of the model. The mean square error (MSE) on the training set was 1.7973, and on the validation set - 2.3834. Such values indicate the presence of a certain gap between the training and validation samples, which may indicate slight overfitting of the model. The regression error, coinciding with the MSE, confirms the stability of the model in predicting the coordinates of the bounding boxes of objects. The prediction accuracy was assessed using the mAP (Mean Average Precision) metric. The average mAP50 value, which measures the accuracy of object detection with a 50% intersection over Union (IoU) tolerance, was 0.2076, and the more stringent mAP50-95 metric, which takes into account different IoU thresholds, was 0.0988. This indicates that the model has potential for improvement, especially in terms of defect localization accuracy. The total error of the model, calculated as 1 - mAP50-95, was 0.9012, which indicates the need for further optimization of the parameters or an increase in the amount of training data. In addition, the precision and recall metrics were calculated. The average precision value was 0.3325, which means that 33.25% of the predicted objects actually correspond to real defects. However, the recall is 0.3036, which indicates that the model detects only about 30.36% of all defects present in the data. Such a gap between precision and recall indicates a tendency for the model to miss defects, which may be due to insufficient information content of the dataset or the complex structure of the detected objects.

Speaking about the results obtained, we will consistently focus on the various types of defects detected on the inner surface of the steel pipe. For example, the detection of bulge-type defects in pipes turned out to be insufficiently accurate. This was due, firstly, to the small number of available photographs containing defects of this type, which limited the number of examples on which the model could learn. Secondly, the quality of these photos turned out to be insufficient and this, in turn, could make it difficult for the neural network to recognize defects. Factors such as poor lighting, noise, distortion or blurring could have affected this. To improve the results of the study,

it is necessary to pay attention to the process of taking images and take measures to improve the quality and quantity of photographs with a bug type defect (Figure 7).

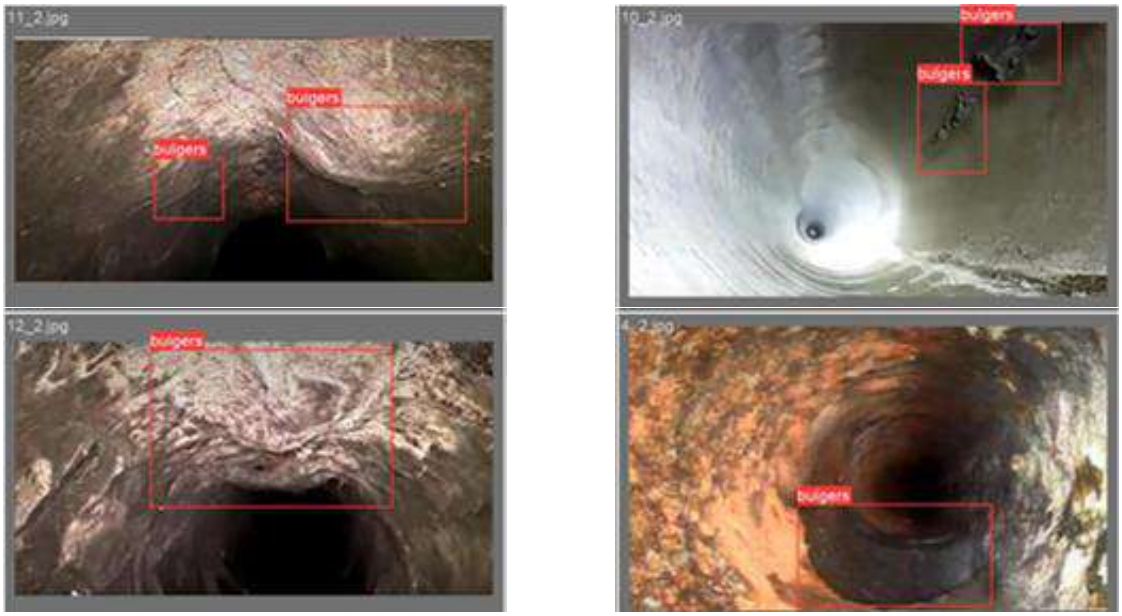

Fig. 7. An example of training a neural network to recognize a bulge-type defects

The overall performance of YOLOv8 in the proposed data set for the bulge defect is illustrated by graphs of accuracy, average accuracy, response and errors for the models in Figure 8. As can be seen from the graphs, the model reaches no more than 48% accuracy, and up to 85% response. According to mAP, very low indicators are obtained, which indicates a weak detection of this type of defects during training.

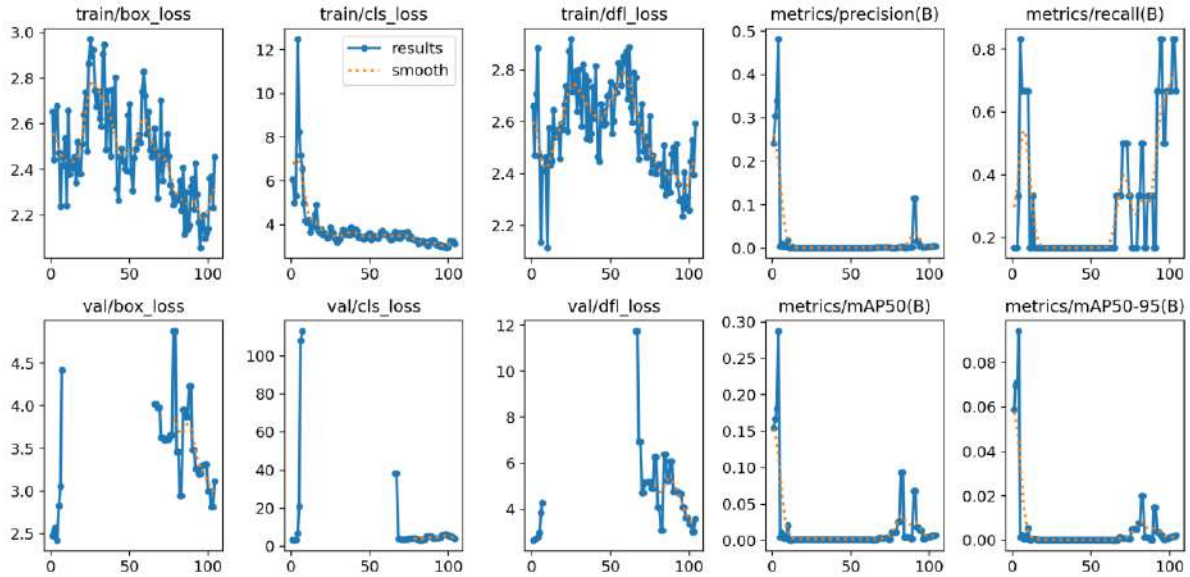

Fig. 8. The loss function and metrics of the YOLOv8 model in determining Bulge-type defects in steel pipes. The first line shows the learning curves for loss of regression in the block, loss of class, accuracy, and response. The second line shows the validation curves for block regression loss, class loss, average accuracy: 50 and average accuracy: 50:95

The results of training a neural network to detect a corrosion defect turned out to be significantly better than for a bulge defect. In general, a neural network can perform rather effective segmentation of defects of this type inside steel pipes. At the same time, the network made it possible to determine both areal corrosion, as well as pitting and stream corrosion. The learning outcomes are shown in Figure 9. In terms of training efficiency, it can be noted that sorting losses

decreased from about 2.5 to 1.0. Classification losses showed good convergence from 5.0 to 1.0. Distribution Focal Loss (DFL) decreased from 2.5 to about 1.5. Accuracy reaches about 0.6, and recall time stabilizes at about 0.4. In terms of validation metrics, Val/box_loss stabilizes at 2.6-2.7, which is higher than in the erosion model, and Val/cls_loss drops to almost zero after early spikes. The final mAP50 is about 0.45, and mAP50-95 is about 0.15.

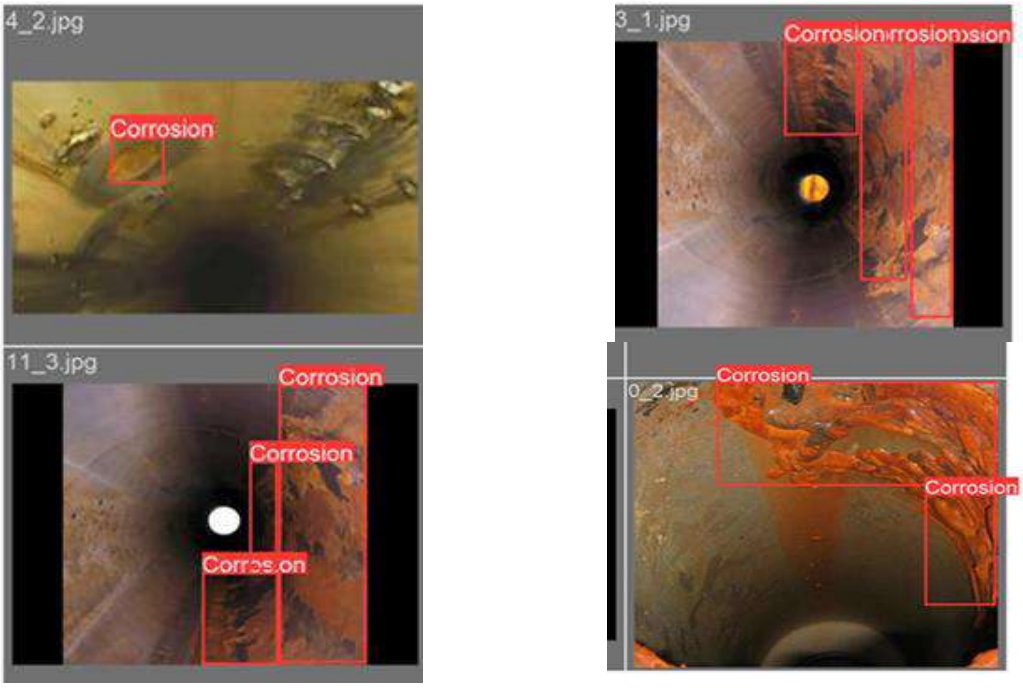

Fig. 9. An example of training a neural network to recognize a bulge-type defects

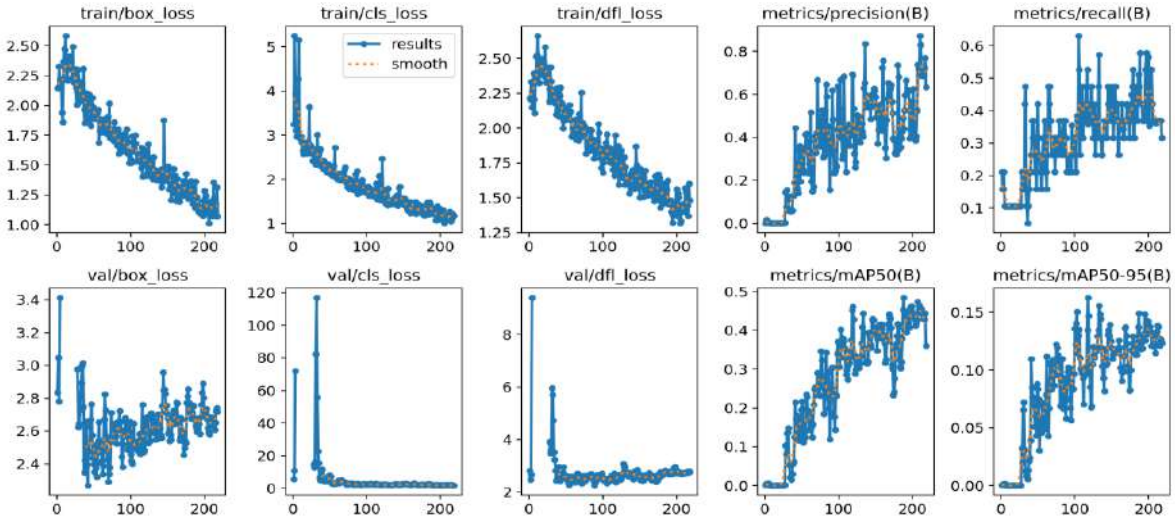

Fig. 10. The loss function and metrics of the YOLOv8 model in determining corrosion defects in steel pipes. The first line shows the learning curves for loss of regression in the block, loss of class, accuracy, and response. The second line shows the validation curves for block regression loss, class loss, average accuracy: 50 and average accuracy: 50:95

Overall, the results show a relatively high selectivity for the images. The corrosion defect is segmented much more accurately than the bulge defect. Compared to the accuracy of recognition and the results of the learning process for the bulge defect, the corrosion defect is segmented more accurately. This can be seen from the clearer trends in the charts with a smaller spread of individual values. Similarly, the performance indicators for YOLOv8 on the corrosion defect are summarized in a series of graphs (Figure 10). In this case, the accuracy of the model is higher, reaching 88%, while the response is lower compared to the previous type of defect but still reaches 67%. Overall, this gives a good result, with an average precision of 49% according to the mAP metric. For a crack-

type defect, very good image segmentation results were also obtained (Figure 11). At the same time, the neural network made it possible to identify both longitudinal and transverse cracks of various types, and to isolate a grid of cracks. With an increase in the size of the Dataset, segmentation accuracy is expected to increase. Summary data of the loss function and metrics for the YOLOv8 model on the crack defect is shown in Figure 12. The model achieves an accuracy of up to 98% with a response rate of up to 57%, but the heterogeneity in prediction and response results in a relatively low mean average precision (mAP) of around 42%. This may be due to the need for more training data. It should be noted that for the full implementation of the results in real conditions, it is necessary to unify the illumination of the survey areas, expand the database and increase the amount of data for training the neural network.

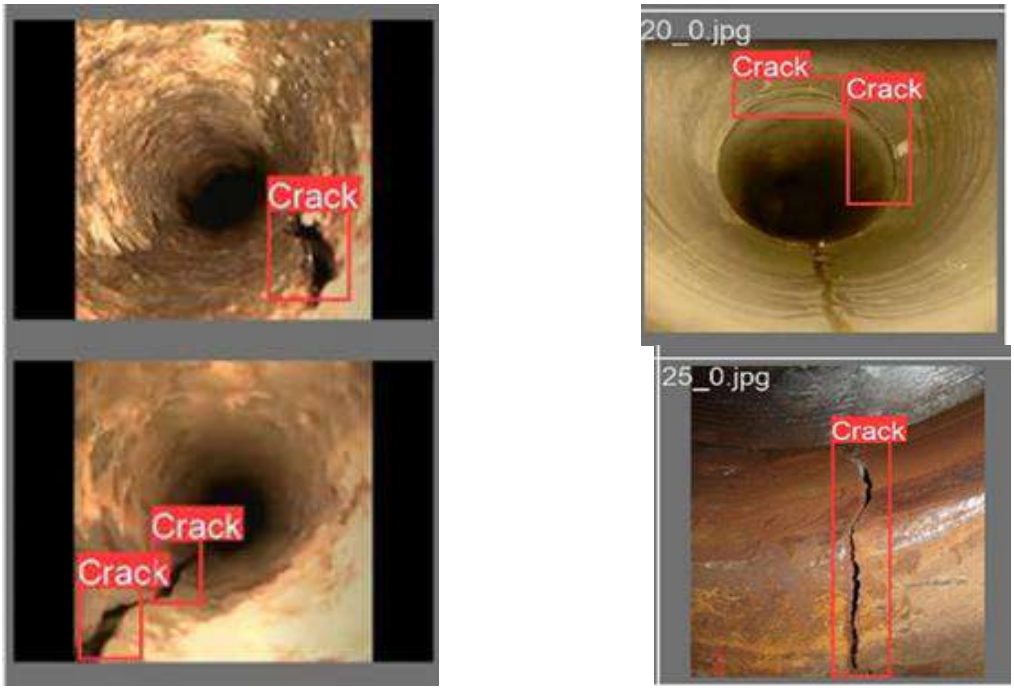

Fig. 11. Example of training a neural network to recognize a crack-type defect

For crack segmentation, the box loss (train/box_loss) shows a steady decrease from about 2.5 to 1.0 over 250 epochs, indicating good bounding box prediction convergence. The classification loss (train/cls_loss) has significantly decreased from about 5.0 to less than 1.0. The DFL loss (train/dfl_loss) shows a similar decreasing trend from 2.5 to 1.2. The precision and recall metrics show an increasing trend, with precision reaching about 0.5 and recall about 0.4 by the end of training. Analyzing the validation metrics, we note that for the crack dataset, the validation loss shows an initial spike followed by stabilization. The Val/cls_loss and val/dfl_loss metrics decrease sharply at the beginning of training. The mAP50 metrics steadily increase to about 0.35, and the mAP50-95 metrics gradually improve to about 0.2. A neural network to recognize an erosion type defect is presented (Figure 13). The results of the erosion defect analysis are summarized in a series of graphs (Figure 14). In this case, the model's accuracy is high, reaching 87%. This is an improvement compared to the previous type of defect, with a response of 68%. This makes erosion the most accurately detected defect, based on the mAP metric. The value reached 65%, which is the best result among all the considered defects. Looking at the training metrics for erosion, we see that the loss has decreased from 2.5 to about 0.5, which shows better convergence than the crack model. The classification loss has decreased from 5.0 to about 0.5, and the accuracy has reached higher values (about 0.7) compared to the crack model. The recall has improved to about 0.5. The validation metrics show more stable loss curves after the initial jumps. Importantly, the final val/box_loss has a lower value (about 2.4) compared to the crack model. The Val/cls_loss value stabilizes at a level close to zero. We also note the higher mAP50 (about 0.5) and mAP50-95 (0.25) values compared to the crack model.

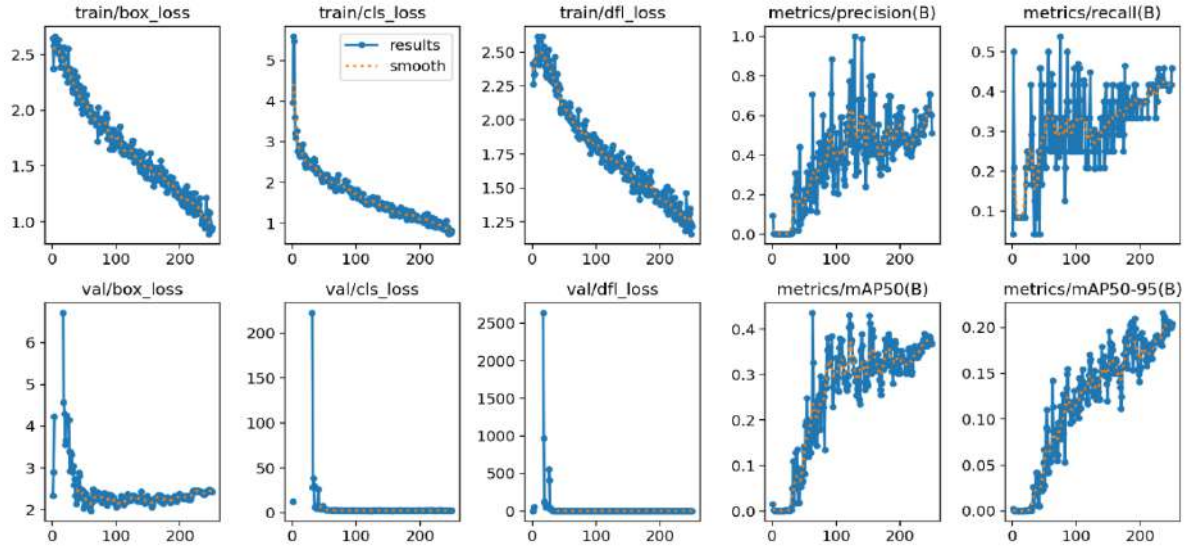

Fig. 12. The loss function and metrics of the YOLOv8 model in determining crack-type defects in steel pipes. The first line shows the learning curves for loss of regression in the block, loss of class, accuracy, and response. The second line shows the validation curves for block regression loss, class loss, average accuracy: 50 and average accuracy: 50:95

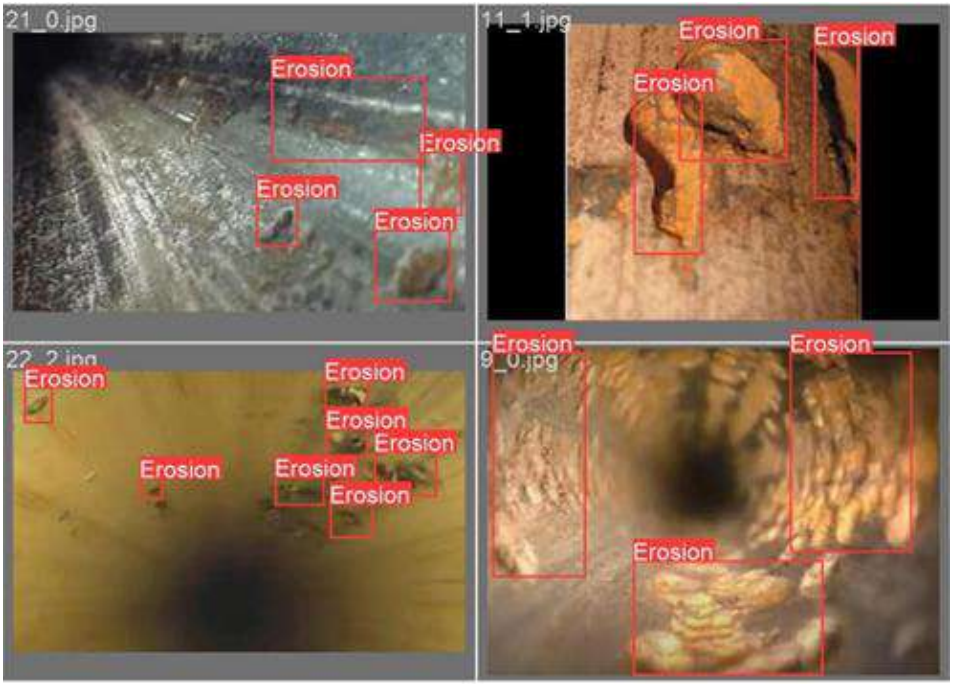

Fig. 13. Training a neural network to recognize an erosion type defect

The results obtained (Figures 8, 10, 12, and 14) indicate that, overall, neural networks are able to solve the tasks they are assigned. However, it is necessary to improve their accuracy and selectivity. It should be noted that the limited number of training data available negatively affects the model's performance [29]. Insufficient training examples make the model less capable of generalizing, which can result in low accuracy in defect recognition. Additionally, the quality of training data is also crucial [30]. Low-resolution or poorly lit photos of defects can make it difficult for the model to recognize them correctly. Based on the training results, we note that the erosion model demonstrates the best overall performance with the lowest final loss and the highest precision/recall and mapping scores. The crack detection model appears to be the most challenging due to its relatively high final loss values and low mAP scores. The corrosion model occupies an intermediate position between the other two models.

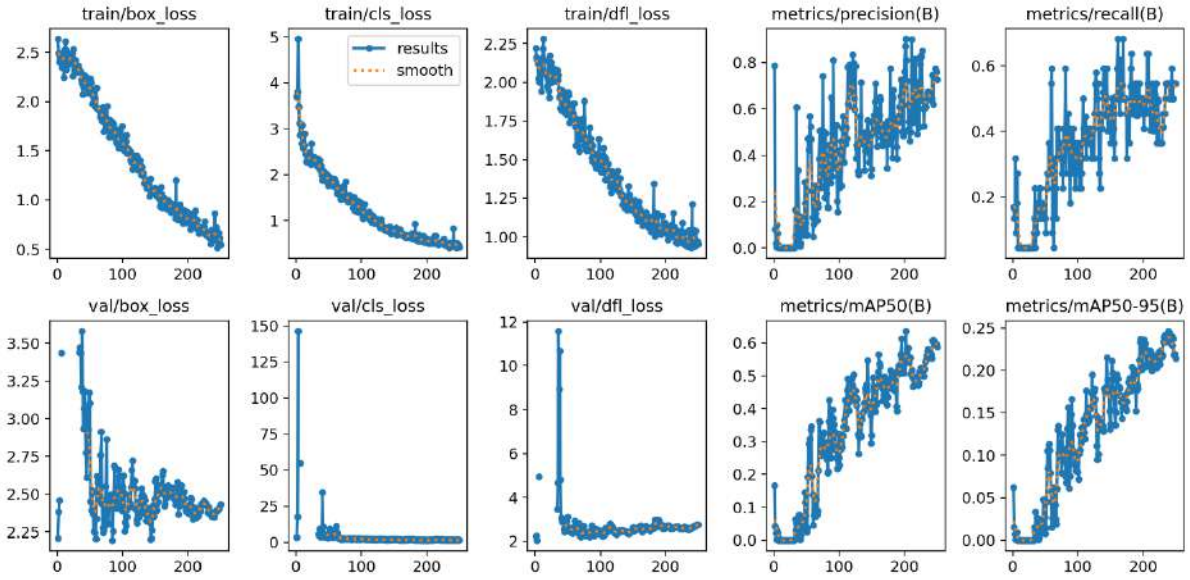

Fig. 14. The loss function and metrics of the YOLOv8 model in determining erosion-type defects in steel pipes. The first line shows the learning curves for loss of regression in the block, loss of class, accuracy, and response. The second line shows the validation curves for block regression loss, class loss, average accuracy: 50 and average accuracy: 50:95

Table 1. Results of training the neural network to recognize in-pipe defects in steel oil and gas pipelines that are under operation.

Type of defect	Precision	Recall	F1-metrics	mAP50	mAP50-95	Box Loss (train)	Box Loss (val)	Cls Loss (train)	Cls Loss (val)
Bulge	~0.0174	~0.30	0.032	~0.0068	~0.002	~2.46	~3.11	~3.1	~3.9
Crack	~0.50	~0.40	0.444	~0.35	~0.20	~1.0	~2.4	~0.8	~3.0
Erosion	~0.70	~0.50	0.583	~0.50	~0.25	~0.6	~2.4	~0.5	~2.0
Corrosion	~0.60	~0.40	0.480	~0.45	~0.15	~1.0	~2.7	~1.0	~2.5

All models display the expected training pattern: an initial high loss that decreases over time and evaluation scores that improve as training progresses. Performance metrics for the YOLO models include intersection over union (IoU), mAP, precision and recall, and F1 score. Summarize the results obtained for all types of defects in a single table (Table 1). As a result, a neural network was created that allows detecting and segmenting in-tube defects of the body surface in steel oil and gas pipelines that are under operation in the optical range. Based on this development, it will be possible to analyze both endoscopic examination data of steel pipes and probe-based examination data. Various defects are determined with different accuracy (the worst for buckles, the best for corrosion and erosion).

It is important to note that most of the results of neural network training for defect recognition presented in scientific periodicals are based not on data obtained from real operating conditions of technical systems, but on pre-prepared samples in a laboratory. Of course, the results, given in Table 1, indicate a relatively low selectivity of defects by the neural network. At the same time, they are based not on artificial and prepared laboratory pipe samples, but on photo and video materials obtained in operated field oil and gas pipelines. Contamination of pipe walls, difficult shooting conditions affected the quality of the dataset, which significantly increased the complexity of the images. With an increase in the sample size, and re-training of the neural network on a wider base, as well as using other types of neural networks in the future, it may be possible to obtain higher accuracy and precision in defect detection.

5. Conclusions

The conducted research establishes both the methodological framework and software basis for automating the in-line optical diagnostic process, with the potential to significantly reduce the cost of defect detection in steel pipes used in the oil and gas industry. The proposed solutions are applicable to optical inspection systems employing endoscopic equipment and robotic crawlers. The core of the approach is the application of convolutional neural networks (CNNs), specifically the YOLOv8 architecture, selected for its high detection speed and accuracy. From an applied perspective, the developed system has some selectivity in detecting defects on the inner surface of steel pipes in the optical spectrum.

The detection of the Bulge defect yielded the poorest performance among all defect types evaluated. Based on the current stage of research, it can be concluded that the neural network model is not yet capable of reliably identifying this defect in in-pipe optical diagnostics of operational oil and gas pipelines. These results indicate that the model fails to both accurately distinguish bulges from other image features and to localize them when detected. The model demonstrates moderate performance in crack recognition, with a precision of ~0.50 and recall of ~0.40, indicating a tendency toward false positives and a limited capacity to capture all relevant defects. The F1 score (~0.444) reflects a fair trade-off between precision and recall, suggesting foundational learning but insufficient reliability for deployment in safety-critical environments. Localization performance, as measured by mAP@50 (~0.35) and mAP@50–95 (~0.20), highlights challenges in accurately bounding crack regions, particularly under stricter IoU thresholds.

Moderately good results were obtained in erosion defect detection, with notable strengths in classification accuracy during training but clear limitations in generalization and precise localization. A precision of approximately 0.70 indicates high specificity, suggesting that the model effectively minimizes false positives. However, the recall of ~0.50 reveals a substantial proportion of missed erosion instances, limiting its reliability in scenarios where defect omission carries safety implications. The F1 score (~0.583) reflects a balanced, though not optimal, trade-off between precision and recall. Localization performance, as shown by mAP@50 (~0.50) and mAP@50–95 (~0.25), indicates acceptable detection under relaxed conditions but a drop in accuracy when stricter spatial alignment is required.

In case of corrosion recognition, the model exhibits partial effectiveness. The precision score of 0.60, indicates a moderate ability to correctly identify corrosion instances while maintaining a low false positive rate. However, the recall remains limited at ~0.40, reflecting the model's tendency to miss a significant proportion of true corrosion cases. The F1 score of ~0.48 highlights an imbalance between sensitivity and specificity. Localization performance under relaxed conditions is moderate (mAP@50 ≈ 0.45), but it declines sharply under stricter criteria (mAP@50–95 ≈ 0.15). For crack, erosion and corrosion defects detection, the difference between training and validation losses suggests possible overfitting. This point to the dataset being imbalanced. Field conditions and the limited number of images (at least 100 images per defect type) may cause such issues. We expect to obtain better results with the model as our dataset grows.

The lower detection rates observed for certain types of defects can be attributed to their complex geometries, uneven illumination, and the absence of side-view imaging, and the limited amount of images. The primary limitations affecting the deployment of the developed methodological and software framework include the small physical size of the target defects, the sensitivity of detection performance to specific lighting configurations, the necessity of pre-inspection pipe cleaning to prepare the surface for analysis, and the current incompleteness of the defect dataset. The latter underscores the need to expand the database to encompass a broader range of defect types commonly encountered in oil and gas pipelines. From a methodological perspective, the findings of this study have led to the identification of several promising avenues for further development, which could significantly enhance the performance and applicability of the proposed neural network model for defect recognition in steel pipelines. To improve the accuracy and robustness of defect detection, future work should focus on expanding the image dataset and add the ability to recognize new defect types.

A key future task involves the development of a unified and scalable database of permissible defect thresholds tailored to various steel pipe diameters and wall thicknesses. This database should be integrated with software capable of recalculating defect dimensions based on imaging parameters and standardized pipe geometries. Importantly, this system must align with current regulatory and technical standards governing the production and operation of oil and gas pipelines. Although the current neural network model demonstrates relatively modest accuracy, its potential remains high due to its training on real-world data obtained from operational oil and gas systems—data that is inherently unstructured and noisy, and thus more representative of field conditions than data obtained in controlled laboratory settings. This alignment with practical operating environments gives the model significant value and relevance for industrial application. To further advance this work, additional research should explore the incorporation of alternative video acquisition techniques, such as multi-angle or 3D imaging, which could improve detection coverage and spatial resolution. Finally, future investigations should aim to extend defect recognition capabilities beyond the pipe surface to include welding joints, which are critical areas of structural vulnerability.

Appendix 1. Table of abbreviations

YOLO	You Only Look Once
ConvNet/CNN	Convolutional Neural Network
mAP	Mean Average Precision
C2f	Cross Stage Partial with Fusion
SPPF	Spatial Pyramid Pooling - Fast
PANet	Path Aggregation Network
train	training
valid	validation
yaml	file type
ultralytics	YOLO Libraries
ISO	International standard organization
GOST	Russian State Standard
OST	Report (Industrial) Russian Standard

Appendix 2. Training code

```
from ultralytics import YOLO

# Loading a pre-trained model YOLOv8

model = YOLO("yolov8n.pt")

# Training on a custom dataset

results = model.train(data="dataset.yaml", epochs=50, imgsz=640, batch=16, device="cuda")

# Saving the trained model

model.save("yolov8_defects.pt")
```

References

[1] Kazeminasab S, Sadeghi N, Janfaza V, Razavi M, Ziyadidegan S, Banks MK. Localization, mapping, navigation, and inspection methods in in-pipe robots: A review. IEEE Access. 2021;9:162035-58. https://doi.org/10.1109/ACCESS.2021.3130233

[2] Sharkawy A-N, Ma'arif A, Furizal, Sekhar R, Shah P. A comprehensive pattern recognition neural network for collision classification using force sensor signals. Robotics. 2023;12:124. https://doi.org/10.3390/robotics12050124

[3] Al-Sabaeei AM, et al. Prediction of oil and gas pipeline failures through machine learning approaches: A systematic review. Energy Rep. 2023;10:1313-38. https://doi.org/10.1016/j.egyr.2023.08.009

[4] Malashin I, et al. Deep learning approach for pitting corrosion detection in gas pipelines. Sensors. 2024;24(11):3563. https://doi.org/10.3390/s24113563

[5] Hussain M, et al. Review of prediction of stress corrosion cracking in gas pi pelines using machine learning. Machines. 2024;12(1):42. https://doi.org/10.3390/machines12010042
[6] Chen J, Cao L, Song G. Detection of the pipeline elbow erosion by percussion and deep learning. Mech Syst Signal Process. 2023;200:110546. https://doi.org/10.1016/j.ymssp.2023.110546
[7] Liu L. Machine learning-driven corrosion detection and classification in pipelines. [dissertation]. University of Wales Trinity Saint David; 2024.
[8] Yuan J, et al. A classification and quantitative assessment method for internal and external surface defects in pipelines based on ASTC-Net. Adv Eng Inform. 2024;61:102492. https://doi.org/10.1016/j.aei.2024.102492
[9] Chen K, et al. An automatic defect detection system for petrochemical pipelines based on cycle-GAN and YOLOv5. Sensors. 2022;22(20):7907. https://doi.org/10.3390/s22207907
[10] Kammoun M, Kammoun A, Abid M. Leak detection methods in water distribution networks: A comparative survey on artificial intelligence applications. J Pipeline Syst Eng Pract. 2022;13(3). https://doi.org/10.1061/(ASCE)PS.1949-1204.0000646
[11] Zhu YK, et al. A review of optical NDT technologies. Sensors. 2011;11(8):7773-7798. https://doi.org/10.3390/s110807773
[12] Seghier MEAB, Höche D, Zheludkevich M. Prediction of the internal corrosion rate for oil and gas pipeline: Implementation of ensemble learning techniques. J Nat Gas Sci Eng. 2022;99:104425. https://doi.org/10.1016/j.jngse.2022.104425
[13] Hussain M, et al. Application of machine learning approaches to prediction of corrosion defects in energy pipelines. Adv Corros Model. 2024;127-166. https://doi.org/10.1007/978-3-031-60358-7_7
[14] Lyu F, et al. Application research of ultrasonic-guided wave technology in pipeline corrosion defect detection: A review. Coatings. 2024;14(3):358. https://doi.org/10.3390/coatings14030358
[15] Silva Motta R. Artificial neural networks for the rapid detection of defects. 2024.
[16] Petushkov G., Sigov A. Analysis and selection of the structure of a multiprocessor computing system according to the performance criterion. Russian Technological Journal. 2024;12(6):20-25. https://doi.org/10.32362/2500-316X-2024-12-6-20-25
[17] Zholtayev D, et al. Smart pipe inspection robot with in-chassis motor actuation design and integrated AI-powered defect detection system. IEEE Access. 2024. https://doi.org/10.1109/ACCESS.2024.3450502
[18] Fu Q, et al. Pipeline defect detection system based on crawling robots. In: Third International Conference on Electronic Information Engineering, Big Data, and Computer Technology (EIBDCT 2024); 2024. SPIE. p. 988-994. https://doi.org/10.1117/12.3031224
[19] Jain S, et al. Synthetic data augmentation for surface defect detection and classification using deep learning. J Intell Manuf. 2022;1-14.
[20] Liu Y, Bao Y. Review on automated condition assessment of pipelines with machine learning. Adv Eng Inform. 2022;53:101687. https://doi.org/10.1016/j.aei.2022.101687
[21] Sharkawy A-N. The effect of increasing hidden layers on the performance of the deep neural network: Modelling, investigation, and evaluation. Res Eng Struct Mater. 2024. http://dx.doi.org/10.17515/resm2024.442st0909tn
[22] Sampath S, et al. An innovative approach towards defect detection and localization in gas pipelines using integrated in-line inspection methods. J Nat Gas Sci Eng. 2021;90:103933. https://doi.org/10.1016/j.jngse.2021.103933
[23] Parlak BO, Yavasoglu HA. A comprehensive analysis of in-line inspection tools and technologies for steel oil and gas pipelines. Sustainability. 2023;15(3):2783. https://doi.org/10.3390/su15032783
[24] Hansen P, Alismail H, Rander P, Browning B. Visual mapping for natural gas pipe inspection. Int J Rob Res. 2015;34(4-5):532-558. https://doi.org/10.1177/0278364914550133
[25] Guo R, Tao Z. A study of neural network for surface characteristics in-process optical measurement. Optik. 2013;124(17):2821-2824. https://doi.org/10.1016/j.ijleo.2012.08.063
[26] Rizzo P, et al. Defect classification in pipes by neural networks using multiple guided ultrasonic wave features extracted after wavelet processing. 2005;294-303. https://doi.org/10.1115/1.1990213
[27] Datta S, Sarkar S. A review on different pipeline fault detection methods. J Loss Prev Process Ind. 2016;41:97-106. https://doi.org/10.1016/j.jlp.2016.03.010
[28] Mittal N, Vaidya A, Kapoor S. Object detection and classification using Yolo. Int J Sci Res Eng Trends. 2019;5(2).
[29] Kamenskiy A., Akaeva T., Grebenshchikova D. Digital three-stage recursive-separable image processing filter with variable sizes of scanning multielement aperture. Russian Technological Journal. 2024;12(6):48-58. https://doi.org/10.32362/2500-316X-2024-12-6-48-58
[30] Shcherban P, Sokolov A, Abu Hamdi R. Study of failure statistics of cavitators in the fuel oil facilities through the application of regression and cluster analysis. Proc Eng Sci. 2023;5(1):39-48. https://doi.org/10.24874/PES05.01.004

Research on Engineering Structures & Materials
www.jresm.org
Research Group

Research Article

Flexural behavior of GFRP rebars and steel rebars with polypropylene fibers and fly ash-based concrete

Vudata Harsha Sai [*,1,a], Lingeshwaran N [1,b], P. K. Prasanna [2,c], George Fernandez Raj A [3,d], P. Jayanthi [4,e]

[1]*Department of Civil Engineering, Koneru Lakshmaiah Education Foundation (Deemed to be University), Guntur, Vaddeswaram, India*
[2]*Department of Civil Engineering, Siddhartha Academy of Higher Education (Deemed to be University), Vijayawada, Andhra Pradesh, India*
[3]*Department of Civil Engineering, Aditya University, Surampalem, India*
[4]*Department of Civil Engineering, V.R.S. College of Engineering and technology, Arasur, Villupuram, Tamilnadu, India*

Article Info

Article History:

Received 14 Feb 2025

Accepted 26 May 2025

Keywords:

Glass fiber reinforced polymer rebars;
Fiber reinforced concrete;
Corrosion resistance;
Flexural performance

Abstract

Alternative materials are required since steel reinforcement in concrete constructions is prone to rust, which creates durability issues. This study investigates the feasibility of replacing steel reinforcement in concrete applications with glass fiber-reinforced polymer (GFRP) rebars. The experimental work used M30 grade concrete with two mix designs: fiber-reinforced concrete (FA+PP), which replaces cement with 20% fly ash, and nominal concrete (NC), which uses 1% polypropylene fiber. Both mixes met M30 standards, FA+PP showed higher strength. Four steel or GFRP reinforced concrete beams sized as 1500 mm × 230 mm×300 mm underwent flexural loading tests. The period for NC beam curing amounted to 28 days but FA+PP beams received 56 days of treatment before testing. The experimental results demonstrated that steel-reinforced beams made with FA+PP produced the highest resistance against loading force alongside minimal beam movement yet FA+PP beams using GFRP bars displayed an average strength level together with continuous flexural deflection. Structural specimens reinforced using steel demonstrated superior results than specimens made of GFRP and NC materials during load-bearing examination. GFRP rebars demonstrate value as steel reinforcement replacement because they provide corrosion protection and structural strength according to this research finding.

© 2025 MIM Research Group. All rights reserved.

1.Introduction

Construction project design requirements and service life depend directly on the behavior of concrete-reinforced beams during flexure. Traditional steel reinforcement serves as a standard building material due to its combination of strength attributes together with ductility properties since decades. The usage of fiber-reinforced polymer (FRP) rebars [1] as construction alternatives materialized because engineers wanted to overcome material sustainability issues along with corrosion protection limitations. The scientific community adopted GFRP rebars as steel replacements [2] because they provide lightweight material strength while exhibiting high durability against corrosion. Structural concrete performances improve when fly ash serves as cementitious material and incorporates polypropylene fibers into it. This paper examines steel

*Corresponding author: 2301020001@kluniversity.in
[a]orcid.org/0000-0001-8720-2515; [b]orcid.org/0000-0003-2998-7315; [c]orcid.org/0000-0002-3345-3992; [d]orcid.org/0009-0007-3785-6696; [e]orcid.org/0009-0009-5259-094X
DOI: http://dx.doi.org/10.17515/resm2025-686me0214rs

rebar flexural behavior studies and GFRP-reinforced concrete beam research while analyzing the improvement effects of fly ash and polypropylene fibers on concrete material properties. [3-7].

The construction industry uses steel rebars as its standard reinforcement material because engineers understand their behavior and they have high strength for bending actions. Industrial applications of steel reinforcement experience corrosion that generates both structural deterioration and expenses for maintenance (ACI 440.1R-15, 2015) [8]. The corrosion-resistant nature of GFRP rebars makes them the optimal choice for structures located in salty water or bridge conditions based on research presented in references [9-11]. Consequently, researchers have looked for alternative means of steel reinforcement since there is rising demand for sustainable construction practices. High tensile strength to weight ratio and non-conducting properties have emerged which advantageous over other rebars like corrosion resistance and marine environment. However, despite their structural behavior which is different from steel, their evaluation must be discussed systematically.

The flexural behavior of concrete beams which use steel in combination with GFRP has been measured through experimental studies. Service load deflections from beams reinforced with GFRP yielded elevations over steel-reinforced beams according to Benmokrane et al. [1]. The results of Zhang et al. [12] support observations about GFRP-reinforced beams which display decreased stiffness because of their elastic modulus but maintain acceptable load-load capacity. GFRP reinforcement shows its main disadvantage through its characteristic brittleness which leads to sudden failure. GFRP rebar is also known as Pseudo ductile material. GFRP shows a different failure behavior by breaking instantly through fiber rupture instead of yielding like steel does before failure occurs. Seamless ductility enhancement of GFRP-reinforced beams occurs with optimized reinforcement ratios combined with steel reinforcement according to El-Gamal et al. [13].

Concrete builders extensively use polypropylene fibers because they enhance tensile strength and provide impact resistance together with crack control capability. The study conducted by Alhozaimy et al. [14] proved that concrete becomes less brittle after adding polypropylene fibers through their role as microcrack bridge elements that slow down the spread of cracks. Fiber reinforcement enables concrete to absorb more energy along with improving its toughness because of which it exhibits greater resilience to impact and cyclic loading [15-16]. The flexural properties of concrete beams under examination by Sivakumar and Santhanam [17] depended on the polypropylene fiber volume percentage. The researchers discovered that adding 1% fibers resulted in the maximum toughness enhancement while maintaining workability at optimal levels. The research of Karthik et al. [19] revealed that concrete beams became tougher and developed better ductility upon addition of polypropylene fibers while maintaining quality workability metrics.

Research conducted by Nili and Afroughsabet [20] demonstrates that fiber-reinforced concrete maintains increased strength after the load peak and this feature enhances the structural behavior of GFRP-reinforced members. Workability problems and unreliable fiber distribution may occur because of high fiber content so mix design requires proper proportioning. Fly ash serves as a frequently employed supplementary cementitious material to replace Portland cement in concrete because it stems from coal burning operations. Fly ash delivers numerous advantages to concrete through improved durability as well as better workability combined with lower heat of hydration and stronger long-term strength according to Mehta and Monteiro [21-22]. According to Thomas and Matthews [23] replacing 20-30% of cement with fly ash produces maximum strengths in both compressive and flexural tests on concrete. According to Malhotra [24], fly ash improves both sulfate resistance and lowers permeability, allowing it to function effectively in oceanic and corrosive environments. The sustainable benefits of fly ash arise from its ability to decrease cement production emissions during manufacturing.

The use of polypropylene fibers with fly ash-based concrete produces combined advantages. Chidambaram et al. [25] showed that polypropylene fibers make up for the strength decline caused by fly ash in early concrete development and fly ash extends concrete lifetime expectancy. The simultaneous use of fly ash together with fiber reinforcement offers a practical approach to strengthen concrete durability as well as its mechanical elements. Research investigates the use of GFRP rebars in flexural areas next to steel stirrups in shear regions to maximize advantages from

each reinforcement type. The implementation of steel stirrups in GFRP-reinforced beams demonstrated according to Ali et al. [26] that steel stirrups enhance shear resistance and stop sudden structural failures. This combined approach provides excellent shear reinforcement through steel bars and extends GFRP's corrosion-resistant properties within flexural areas. According to Nanni et al. [27] a beam benefits from its combined GFRP longitudinal reinforcement and steel stirrups because these elements establish an efficient load redistribution system which improves structural performance. Hybrid reinforcement methods find practical use in aggressive settings because they address primary concerns regarding corrosion resistance. Also, partial substitution of cement with industrial by product such as fly ash did not only reduce the carbon footprint but also has some advantages of mechanical property and long-term durability. Under flexural loading, crack resistance, improved toughness and energy absorption have been contributed by the inclusion of polypropylene fibers. Thus, combining these materials offers a synergistic method towards sustainable and durable concrete components with good structural stiffness.

Research on GFRP reinforcement, polypropylene fibers and fly ash extends throughout concrete beams flexural performance but combined implementation still lacks significant investigation. Current research exists separately as steel vs. GFRP reinforcement investigations or studies on fiber-reinforced concrete without assessing multiple components together within one structural framework. Strengthening infrastructure durability requires studies of multifactor effects between GFRP rebars and polypropylene fibers and fly ash-based concrete for flexural strength assessment since infrastructure demands will continue to grow. The present research gap receives resolution through comprehensive laboratory testing of concrete beams containing these materials. The researched information about load-deflection behavior alongside failure mechanisms and cracking patterns generated new understanding to develop improved structural systems which resist corrosion. Through systematic research both present standards can improve, and scientists gain essential data for deploying hybrid reinforcement systems under various environmental conditions for long-term performance.

1.1 Purpose and Objectives of the Study

This study is primarily concerned with experimental evaluation of flexural performance of concrete beams with Glass fiber reinforced polymer (GFRP) rebars as opposed to conventional steel rebars. For the purpose of improving the sustainability and mechanical properties of concrete, a hybrid mix of 20% fly ash as partial cement replacement and 1% polypropylene fibers by volume was employed.

The study seeks to achieve the following specific objectives.

- An investigation on the effects of replacing steel rebars with GFRP rebars as an alternative choice in reduced strength reinforced concrete beams under flexural load was conducted.
- It is necessary to evaluate mechanical performance of the normal as well as fiber reinforced concrete with GFRP and steel reinforcements (load vs. deflection).
- A systematic assessment of GFRP rebars viability as a structural concrete application with industrial by products (fly ash) and synthetic fibers (polypropylene) from a sustainability as well as strength improvement perspective.

This study helps to build the body of knowledge about advanced composite reinforcement for eco efficient systems by addressing the combined effects of the various modifiers as well as alternative reinforcement.

2. Experimental Program

2.1. Materials And Properties of Materials

The materials used in the experimental program are characterized to illustrate the following instances.

2.1.1 GFRP Rebar and Steel Rebar

The steel bars used in the longitudinal and stirrup bars for the beam were 10mm FE 550 for top longitudinal reinforcement and 12mm steel bars for bottom longitudinal reinforcement and 8mm steel bars for the stirrup bars respectively. GFRP Rebars of 12mm were used as top and bottom longitudinal reinforcement and 8mm steel bars are used as shear reinforcement. The test results of the GFRP and FE 550 steel bars in terms of mechanical properties are shown in Table 1. It should be also stated that the mechanical performance specifications for the steel and GFRP bars were offered by the material supplier.

Fig. 1. GFRP rebar and steel rebar

Table 1. Rebar properties

Rebar Type	Tensile Strength (MPa)	Elastic Modulus (GPa)	Ultimate Strain (%)	Shear Strength (MPa)	Density (g/cm^3)	Poisson's Ratio	Thermal Expansion (μm/m°C)
12mmϕ GFRP	920	46.59	3.5	72.55	2.06	0.28	35
12mmϕ STEEL	550	200	13	460	7.85	0.3	13

2.1.2 Cement

The IS 269:2015 [28] compliance is achieved through using OPC 53 grade cement of good quality and locally available material.

2.1.3 Fly Ash

Industries that produce fly ash byproducts leave behind ashes, rich in alumina, silica and ferric oxide, when coal is heated at high temperatures in thermal power plants. Fly ash (FA) is used in the concrete to improve workability, to reduce heat of hydration and is resistant to extremely chemical attacks. The class F type Fly ash is used as binder material replacing 20% cement in the experiment.

Table 2. Properties of Binding Materials

Material	Specific gravity	Standard consistency (%)	Initial setting time (Minutes)	Final setting time (Minutes)	Bulk density (kg/m^3)
Cement	3.14	32	40 min	10 hours 600	1440
Fly Ash	2.2	30	55 min	12 hours 720	1100

2.1.4 Coarse Aggregate

The size of the coarse aggregate employed for casting, as specified in IS 383:1970, varies between 20 mm with a specific gravity of 2.74 [29]. We use the mixture which contains 100% of 20 mm in weight. Table 3 displays the results of the preliminary test.

2.1.5 Fine Aggregate

Fine aggregates were used from uncrushed, locally occurring local river sand ~~having a maximum~~ passing through sieve size of 4.75 mm, ~~a~~ fineness modulus of 3.35 and a specific gravity of 2.65 need to be attained as per IS 383:1970. Table 3 displays the results of the preliminary test.

Table 3. Properties of aggregates

Material	Density (kg/m^3)	Water Absoprtion (%)	Fineness modulus	Max Dia (mm)	Zone	Specific gravity
Fine Aggregate	3.14	2.1	3.23	-	II	2.67
Coarse Aggregate	2.2	0.43	3.18	20	-	2.89

2.1.6 Tap Water

Mixing and curing was done with Ordinary Potable tap water.

2.1.7 Super Plasticizer

A high range water reducing agent (water reducers) with specific gravity of 1.11, having a chemical admixture complying to IS: 9103:1999 [30] was used; this water reducer was used as HYPERFLUID R200 for the purpose of increasing the workability as well as the strength of concrete. Specifications of superplasticizer are shown in Table.4

Table 4. Properties of super plasticizer

S.no	Parameter	Specifications
1	Appearance	Yellowish brown liquid
2	Base material	Poly carboxylic ether
3	Specific gravity	1.11
4	Ph	6.7
5	Solid content	41
6	Chloride content	Nil

2.1.8 Polypropylene Fiber

Polypropylene fibers are added to the concrete mixtures in order to improve some of the key performance parameters. The most important of their properties is to help enhance impact resistance, mitigate plastic shrinkage cracking and improve long term durability of the concrete matrix. No, these discontinuous, uniformly dispersed fibers are not to be significant on the compressive strength, but they are greatly beneficial to post cracking behavior by increasing toughness, energy absorption, and crack bridging capacity.

Table 5. Specifications of polypropylene fiber

S.no	Parameter	Specifications
1	Length	20mm
2	Diameter	19-40 micron
3	Aspect ratio	215-1250
4	Specific gravity	0.91
5	Melting point	162°C
6	Ignition point	360°C
7	Thermal conductivity	Low
8	Alkali resistance	Low

Fig. 2. Polypropylene fiber

The structural integrity of this fiber reinforced concrete is enhanced due to the presence of this reinforcement fiberization mechanism, therefore polypropylene fibers can be used as an additive in the performance oriented and durable concrete applications.

2.1.7 Mix Design

Concrete mix design was performed by using IS 456-2000 [32] and IS 10262-2019 [31]. ~~The~~ M30 concrete grade is mixed, and the weight ratio is determined. A water reducing agent (superplasticizer) is utilized and this is given in Table 6. 20% of Fly Ash has been replaced in cement for FA+PP mix. Nomenclature for concrete mix designs is given as NC – Nominal Concrete, FA+PP – Fly Ash + Polypropylene Fiber Concrete

Table 6. Material proportions for concrete

Mix ID	Cement	Fly Ash	Water	Fine Aggregates	Coarse Aggregates	Chemical Admixture	Fiber
NC	352	-	158	704.98	1213.96	1.056	-
FA+PP	280.88	70.22	158	695.76	1198.08	1.4	9

Material Proportions given in the above table are calculated for Kg/m³

3. Experimental Program

3.1. Materials And Material Properties

Conventional size cube specimens (0.15 m × 0.15 m × 0.15 m) are cast for every curing phase. After mixing two concrete recipes, the cubes are stored for curing. With Compressive Testing Machine (CTM) dried specimens are placed for the curing of 7, 14, 28 & 56 days. Fig. shows the samples being tested and prepared. IS 516[33] recommends the normal loading rate at which the concrete compressive strength is tested at a rate of 14 MPa per minute for cubes.

Fig. 3. Compressive strength test setup

3.2. Flexural Studies of RC Beams

Four reinforced concrete beams were cast and tested to investigate the load vs. deflection behavior in this study. All the beams were sized 1500 mm×230 mm×300 mm. Based on the concrete mix and testing conditions, the beams were placed into two groups:

- Nominal Concrete (NC):

M30 Nominal Concrete (NC), which RC beams were reinforced with GFRP and steel rebars that are allowed to cure for 28 days, was used to cast two RC beams.

- Replaced Concrete (FA+PPF):

M30 concrete was used to cast two beams, with Fly Ash replacing 20% of the cement and 1% of polypropylene fibers. Reinforcement was given by GFRP and steel rebars, which were allowed to cure for 56 days.

Table 7. Specification of Beam Types and Identification Codes

Specification	Beam ID
Beam with GFRP as internal reinforcement for NC	NC-G
Beam with STEEL as internal reinforcement for NC	NC-S
Beam with GFRP as internal reinforcement for FA+PPF	FA+PPF-G
Beam with STEEL as internal reinforcement for FA+PPF	FA+PPF-S

3.3. Reinforcement Details

- Each beam was reinforced as follows:

The beams reinforcing details included for shear resistance, 8 mm diameter stirrups are used as transverse reinforcement, To effectively resist tensile stresses induced under flexure loading 12 mm diameter rebars are used as bottom longitudinal reinforcement, and to provide necessary compression and enhance ductility and crack control capacity under the reversed or negative moment zones steel bars with 10 mm diameter rebars are used as top longitudinal reinforcement..

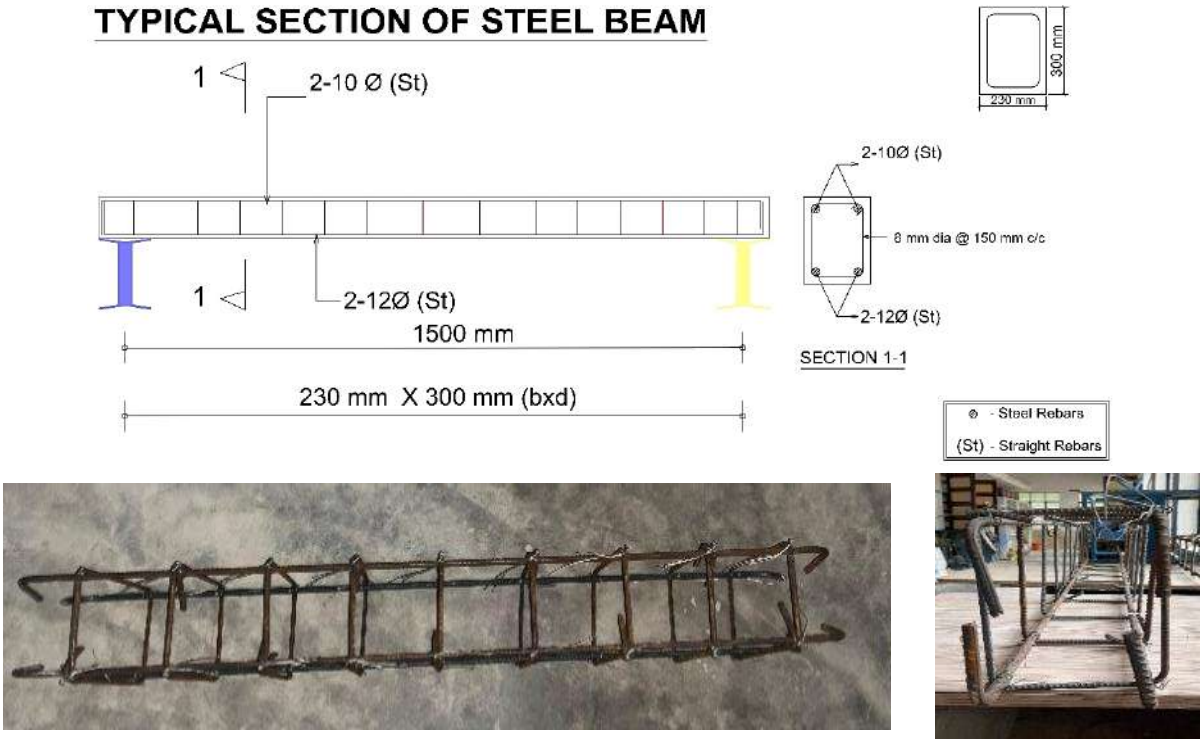

Fig. 4. Reinforcement detail of Steel beam

The structural performance under service and ultimate conditions was balanced through a strategic design of this reinforcement configuration. For the alternative reinforcement setup to structure, 12 mm diameter GFRP rebars were used symmetrically for both the top and bottom longitudinal reinforcement to create balanced flexural capacity at the bottom. Top of the beam specimens and strength to improve the tensile strength and control deflection under service loads, strategically embedded at the center of the two bottom longitudinal reinforcement layers, a single 12 mm diameter steel rebar was used, while 8 mm diameter mild steel rebars were used as transverse support in the form of stirrups to provide shear resistance that was uniformly distributed along the span to confine the concrete core and prevent the diagonal tension failureIn this hybrid reinforcement approach, a low modulus of elasticity of GFRP is compensated with steel reinforcement in order to release the structural stiffness, while using the corrosion resistance and high tensile strength-to-weight ratio of GFRP bars.

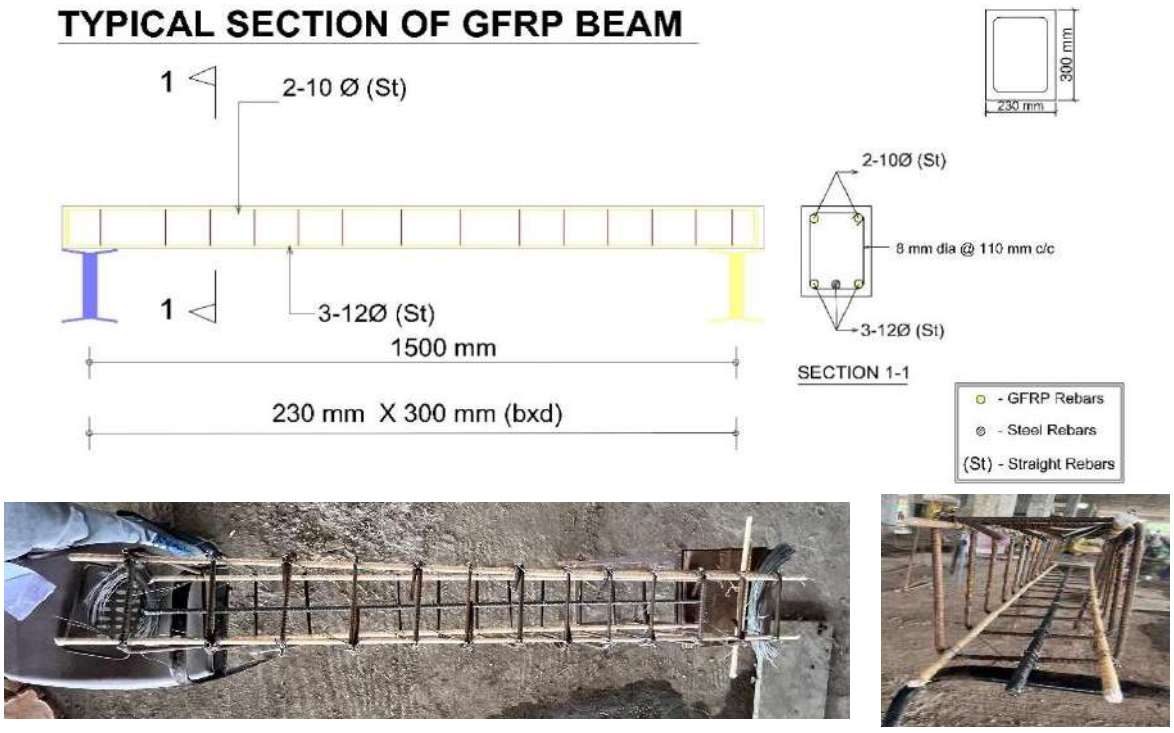

Fig. 5. Reinforcement detail of GFRP beam

3.4. Reinforcement Preparation

Rigid steel plates were fabricated to make the beam molds with dimensional stability and to prevent slurry leakage during casting. The inner surfaces were then coated uniformly with a coating release agent to promote smooth demolding before placement of concrete. Three successive layers of concrete mix, placed with the aid of a mechanical mixer to ensure homogeneity, were made. The compaction of each layer was also ensured by thoroughly compacting the entrapped air and ensuring proper consolidation using a mechanical vibrator. The beams were set up for 24 hours and carefully demolded after which membrane curing was done using moist gunny bags in order to maintain adequate surface hydration and attain optimum strength development.

(a) (b)

(c) (d)

Fig. 6. Step-by-step casting procedure of reinforced concrete beam specimens (a) preparation of mold (b) placement of reinforcement (c) wet concrete in mold and (d) membrane curing

3.5. Testing Procedure of Beam

A loading frame with a two-point loading mechanism was used to characterize all four beams: NC-S, NC-G, FA+PP-S, and FA+PP-G. The supports and loading points had equal distance between them because the load was distributed symmetrically. To evaluate the flexural behavior of the beams, the load vs. deflection data was recorded at regular intervals after loading until failure. The characterization of the effect of reinforcement type (GFRP vs. steel), fly ash replacement (20%), and polypropylene fiber (1%) on the structural performance of the beam was made by this testing procedure. These findings deepen understanding of the influence of fiber reinforcement and additional cementitious materials on failure characteristics, stiffness, and flexural capacity.

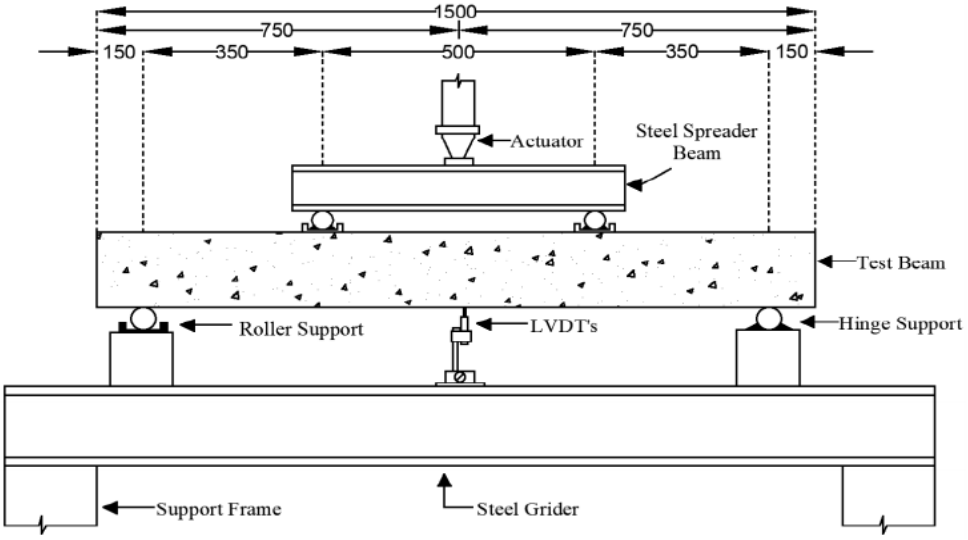

Fig. 7. Sketch of experimental setup

4. Results and Discussions

4.1. Compressive Strength

Specific trends in the development of the compressive strength were observed for the Normal Concrete (NC) mix and the Fly Ash with Polypropylene Fiber (FA+PP) modified concrete mix as they result from dissimilar hydration and pozzolanic reaction kinetics. The compressive strength at an early age for the NC mix was measured to be 18.22 MPa at 7 days, 24.19 MPa at 14 days, and 40.65 MPa at 28 days. Mildly continuous improvement of strength was noted, again achieving 44.85 MPa at 56 days which increased by 10.34% from 28 to 56 days, implying conventional hydration maturity. On the contrary, FA+PP mix showed relatively lower early age strengths of 16.18 MPa and 22.55 MPa at age 7 and 14 respectively, which are around 11.2 % and 6.8 % lower than the NC mix at the same ages. But beyond 28 days, there was a marked shift in the development of strength. The compressive strength of the FA+PP mix at 28 days was 30.28 MPa (25.5% lower than the NC mix at the same age), however the strength gain accelerated fast from 28 days to 56 days resulting in a compressive strength of 54.28 MPa at 56 days. 78.5% higher than 28 days strength and, still relatively, far beyond the NC mix by about 21% at 56 days.

Table 8. Compressive strength test results for NM and FA+PP mixes at different curing ages

Days	Nominal Concrete (NC)	FA+PP
7	18.22	16.18
14	24.19	22.55
28	40.65	30.28
56	44.85	54.28

Results show that the results are characteristic in fly ash-based systems because the pozzolanic reaction is slow and becomes more accentuated beyond 28 days of curing time. In addition, the long-term strength was likely for the one with polypropylene fibers since it enhanced crack-bridging capacity and microstructural integrity. FA+PP mix shows improved 56-day performance over the other mixes, which demonstrates its potential for use in structural applications focusing around higher final strength gain, long term durability and utilization of material over its service life where early age strength is less important.

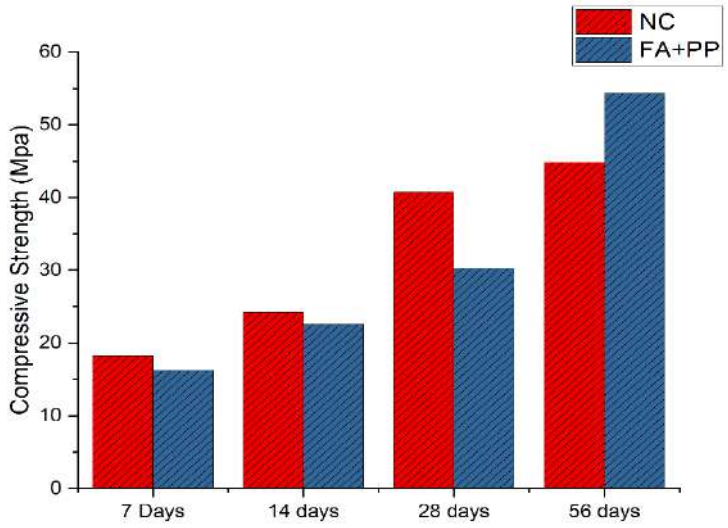

Fig. 8. Compressive strength of NC and FA+PPF concrete mixes

In Table 9, there is a comprehensive statistical analysis regarding compressive strength data of the Normal Mix (NM) and the Fly Ash with Polypropylene Fiber (FA+PP) mix at 7, 14, 28 and 56 days of curing. Average compressive strength, standard deviation, and coefficient of variation (COV) analysis is also carried out which collectively analyzes the reliability and homogeneity of the results. COVs for NM mix were low and varied from 0.99 to 2.19% among all ages, reminding us of consistent performance of this mix. The COV of FA+PP was slightly higher in the early age of up to 2.80% but this decreased dramatically to 0.38% at 56 days. This reduction in variability over time brought about by ongoing pozzolanic reactions and polypropylene fibers indicates that the FA+PP can have reliable long term structural performance.

Table 9. Statistical analysis of compressive strength for NM mixes at different curing ages for Normal Mix (NM)

Age (days)	Average (MPa)	Standard Deviation (MPa)	Coefficient of Variation (%)
7	18.22	0.18	0.99%
14	24.19	0.41	1.70%
28	40.83	0.41	1.01%
56	44.17	0.97	2.19%

Table 10. Statistical analysis of compressive strength for FA+PP mixes at different curing ages for Polypropylene + Fly Ash Mix (FA+PP)

Age (days)	Average (MPa)	Standard Deviation (MPa)	Coefficient of Variation (%)
7	16.17	0.41	2.54%
14	22.83	0.64	2.80%
28	30.30	0.76	2.51%
56	54.97	0.21	0.38%

4.2. Flexural Studies of RC Beams (Load vs Deflection)

4.2.1 Load vs. Deflection Behavior of Beams

These analyses include the load vs. deflection behavior of four different configurations: FA+PP-S (Fly Ash + Polypropylene Fiber with Steel Rebars), FA+PP-G (Fly Ash + Polypropylene Fiber with GFRP Rebars), NC-S (Nominal Concrete with Steel Rebars), and NC-G (Nominal Concrete with GFRP Rebars). This work compares and presents the structural performance of these beams under flexural loading. While the FA+PP-S beam without steel reinforcement, fly ash, and polypropylene fiber only yielded a peak load of 20.5 kN at a corresponding failure deflection of 16 mm, the FA+PP-S beam with reinforcement reached the peak load of 305.6 kN at a deflection of 27.35 mm. In the first phase, the load-deflection relation was linear, displaying elastic behavior, and at high deflections, the beam remained structure intact, showing good ductility and crack resistances. On the other hand, the beam identified FA+PP-G which was reinforced GFRP rebars reached a peak load of 279.9 kN at deflection of 21.47 mm. The overall load-deflection response of FA+PP-S was a relatively less deflection compared to FA+PP-S, indicating a more brittle behavior experienced under GFRP reinforcement. While its first stiffness was lower than that of its steel-reinforced counterpart, the overall stiffness attained showed proper strength to load.

The NC-S beam, which is made of nominal concrete and reinforced with steel rebars, achieved a maximum load of 216 kN at a deflection of 15.38 mm. The main reason this beam behaved similarly to FA+PP-S but had a lower load capacity was because it lacked fly ash and polypropylene fibers, which increase strength and resistance to cracking. The steel reinforcement's adequate ductility allowed the beam to support heavier loads before failing. The NC-G beam demonstrated a maximum load of 215.7 kN at a deflection of 15.25 mm when strengthened with GFRP rebars and free of fly ash or fibers. Because GFRP rebars are more brittle and often show higher deflections before failure, this beam demonstrated less ductility than its steel-reinforced equivalent. When compared to steel reinforcement, the final deflection values indicate that GFRP reinforcement influences the failure process but does not significantly change peak load capacity.

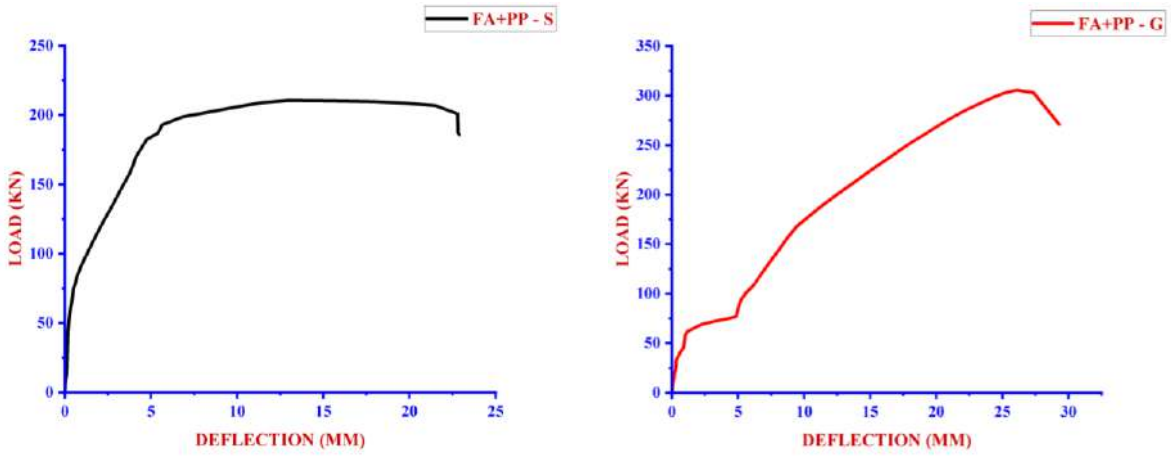

(a) (b)

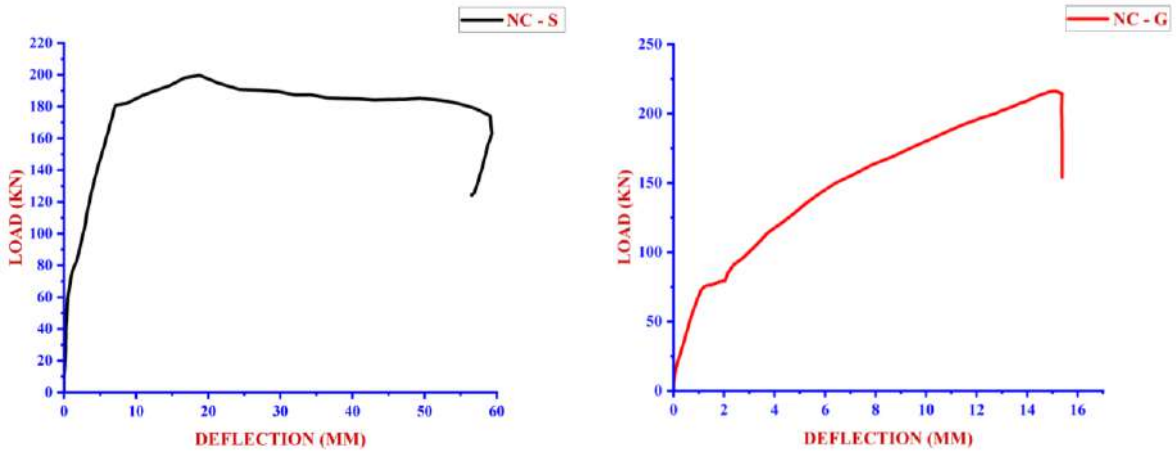

(c) (d)

Fig. 9. Load vs. Deflection Graphs (a) FA+PP – S beam (b) FA+PP - G beam (c) NC – S beam and (d) NC-G beam

When the four beam configurations were evaluated, the FA+PP-S specimen exhibited the highest ultimate load-bearing capacity, followed sequentially by FA+PP-G, NC-S, and NC-G. Despite steel-reinforced beams (FA+PP-S and NC-S) displaying greater initial stiffness, the deflection responses differed significantly, with GFRP-reinforced beams (FA+PP-G and NC-G) experiencing larger mid-span deflections due to the lower modulus of elasticity and increased flexibility of GFRP rebars. The incorporation of fly ash and polypropylene fibers in FA+PP-S and FA+PP-G enhanced overall structural efficiency, with notable improvements in both load capacity and deflection control, resulting in superior crack resistance and post-cracking behavior compared to their nominal concrete counterparts. Additionally, the results indicate FA+PP-S to be the most load bearing and ductile beam. Furthermore, FA+PP-G offers a nice alternative with comparable performance and lower corrosion risks with reinforcement provided by steel. Its performance was poorer than that of the fiber inclusion or the fly ash inclusion on nominal concrete beams, steel and GFRP rebar. Finally, it is established in this study that GFRP can replace concrete based structural steels with the cautions of brittleness nature and higher deflections.

Table 11. Ultimate load and deflection characteristics of tested beams

Mix ID	Load (KN)	Deflection (mm)
NC-G	199.7	18.8
NC-S	216.1	15.1
FA+PP-S	210.5	12.97
FA+PP-G	305.6	26.07

4.3. Comparison of Load vs. Deflection Behavior of Beams

4.3.1 Comparison of NC and FA+PP Beams

The load vs. deflection behavior of the NC-S and NC-G beams was then analyzed and substantial difference were noted. Notably, NC-S beams have higher initial stiffness given the fact that steel has a higher modulus of elasticity than concrete, while NC-G beams show a more rapid increase in deflection. The peak load before failure being NC-S of 199.7 KN and NC-G of 216 KN, thus showing higher load capacity. At the maximum deflection, NC-S exhibits 57.28 mm while NC-G has 15.38 mm; this implies a better flexural stiffness. The NC-S beams exhibited plastic failure prior to failure, whereas the NC-G showed brittle failure after peak load. For ductility dependent applications GFRP's potential as viable alternative to steel reinforcement is strengthened by results showing higher load and lower deflection but must be considered for its brittleness. It is shown that GFRP rebars can serve as a sustainable, durable alternative to carbon in the fabrication of concrete structures.

Comparison was made in deflection and load behavior of FA+PP-S (fly ash + polypropylene fiber reinforced with steel reinforcement) and FA+PP-G (fly ash + polypropylene fiber reinforced with GFRP reinforcement) beams. In both cases, the deflection increased with the load, and FA+PP-S reached 29.3 mm at the maximum 270.7 KN, while FA+PP-GFRP achieved 29.3 mm at same load. Steel reinforced beams could hold more loads earlier than GFRP beams, which were also demised at the same peak (302.4 KN). FA+PP-S beams had 5.61 mm, 19.04 mm deflection at 100 KN and 200 KN respectively, and FA+PP-GFRP beams had 6.17 mm, 19.64 mm deflection at 100 KN and 200 KN respectively. Although its deflection is like the peak load, GFRP beams present advantages such as corrosion resistance, thus becoming a viable alternative for the construction in sustainable terms. The FA+PP-G beams exhibit slightly higher deflections than FA+PP-S at intermediate load levels. For instance:

- FA+PP-S deflected 5.61 mm at 100 kN, which is 0.56 mm more than FA+PP-G deflected.
- FA+PP-S and FA+PP-G were respectively 19.04 and 19.64 mm upon 200 kN.
- FA+PP-G beams deflected marginally higher but failed to crack before they displayed better stress redistribution and crack resistance, which was attributed to the fibers being polypropylene.

In addition, while both FA+PP-S and FA+PP-G delayed the propagation of crack and had greater energy absorption compared to the NC mixes, a brittle failure of FA+PP-G remained. Nevertheless, the introduction of fibers helped enhancing post peak behavior and cracked bridging, as well as load redistribution, alleviating for intrinsic brittleness of GFRP reinforced systems.

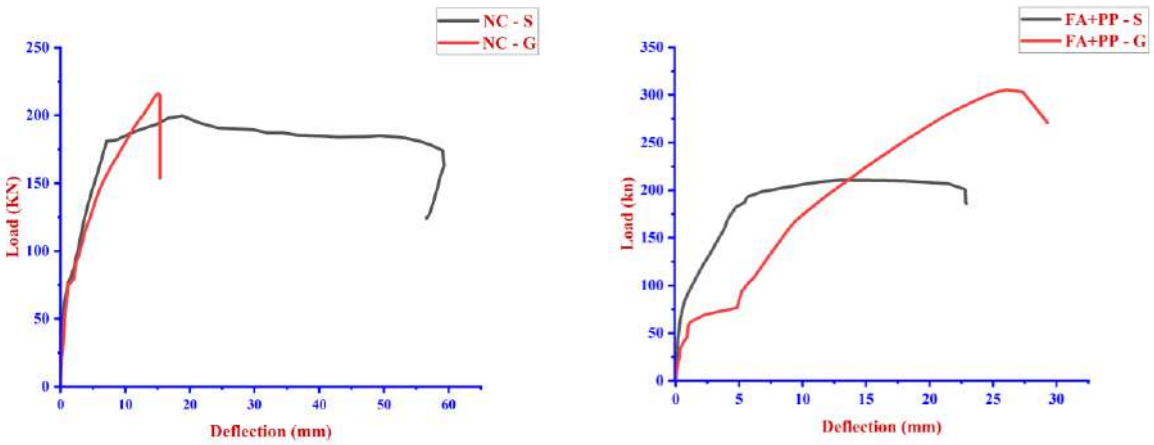

(a) (b)

Fig. 10. Comparison of load vs. deflection graph for (a) NC and (b)FA+PP Beams

4.3.2 Comparison of Steel and GFRP Beams

FA+PP-S (Fly Ash + Polypropylene Fiber and Steel Reinforced) NC-S (Nominal Concrete and Steel Reinforced) beams were analyzed for the load vs. deflection behavior. At applied load, both the beam types experienced an initial increase in deflection, until FA+PP-S beam deflected less sharply than the NC-S beams. Maximum load experienced by the FA+PP-S was 210.5 kN with a maximum displacement of 22.79 mm and by the NC-S was 210.3 kN with a maximum displacement of 57.28 mm at failure. The flexural stiffness of the NC-S beams in NC-S beams was lower as deflection increased more rapidly at higher loads and yielded at a higher value of deflection. Both beam types had stable loading post peak but NC-S deflected and experienced more plastic deformation before failure. It is concluded that both beam types have the same load carrying capacity, but FA+PP-S beams have better deflection control leading to better flexural performance and better overall structural behavior.

The FA+PP-G (Fly Ash + Polypropylene Fiber + GFRP reinforcement) and NC-G (Nominal concrete + GFRP reinforcement) beams were analyzed on basis of load versus deflection behavior. There was a less abrupt increase in deflection of FA+PP-G beams under applied load as compared to NC-G beams. The highest load occurring at the peak was 302.4 kN for FA+PP-G, while NC-G beamed out

at 216 kN and 15.38 mm at deflection. Deflection gradually increased on increasing load for FA+PP-G beams, which exhibits more flexible response prior to failure, and deflection becomes constant after the maximum load for NC-G beams. The deflection capacity of FA+PP-G beams was found to be greater than that of NC-G beams and its load carrying capacity is also higher. Therefore, FA+PP-G beams shows better ductility than NC-G beams. Therefore, these results suggest the application of FA+PP-G beams as an alternative to GFRP beams in concrete structures in terms of load capacity and flexural performance. Nevertheless, their higher deflections should be considered in design.

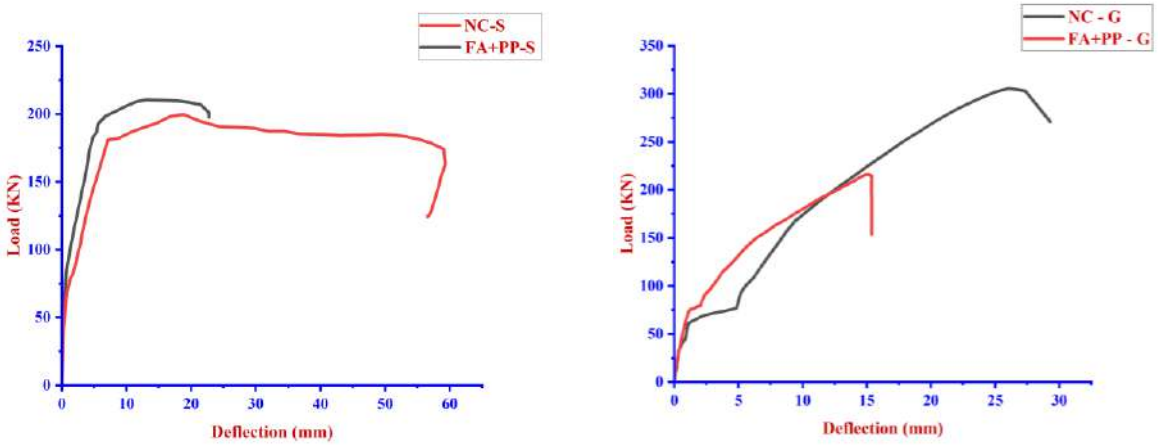

(a) (b)

Fig. 11. Comparison of load vs. deflection graph for (a) steel and (b) GFRP beams

4.4. Crack Behavior

Reinforced concrete beams remain structurally and serviceably strong only if the crack formation and propagation in them can be inhibited. Four beam types were evaluated in the study, the FA+PP-S (fly ash + polypropylene fiber + steel rebars), FA+PP-G (fly ash + polypropylene fiber + GFRP rebars), NC-S (nominal concrete + steel rebars) and NC-G (nominal concrete + GFRP rebars). Visible cracks appeared at lower load levels in NC-S and NC-G beams than by FA+PP-S and FA+PP-G beams.' The delay of the onset of cracks by polypropylene fibers present in the FA+PP beams was due to the fibers' success in distribution of stress. Steel rebars reinforced beams (NC-S and FA+PP-S) especially had better crack control from the ductility of the steel that provides energy dissipation before failure. Both toughness and crack widening resistance were improved in the FA+PP-S beam. Reinforced with GFRP rebars, the NC-G and FA+PP-G beams showed wider cracks than their counterparts with steel rebars. GFRPs lower modulus of elasticity explains it: it allows greater deformations before failure.

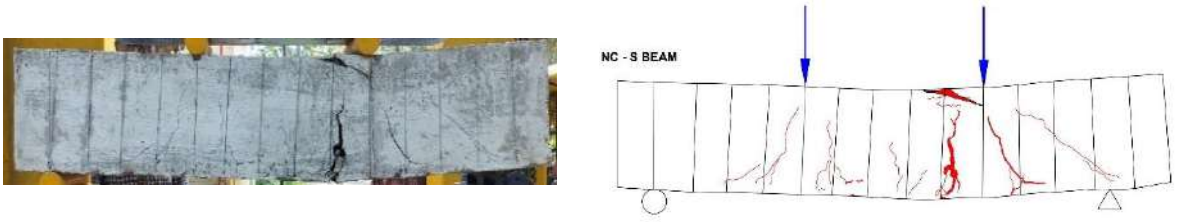

(a)

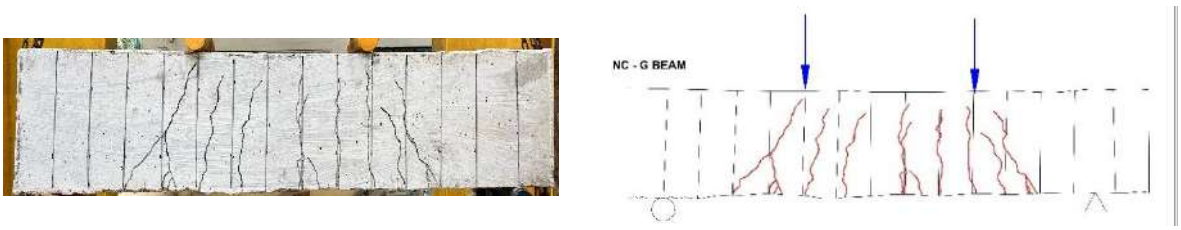

(b)

(c)

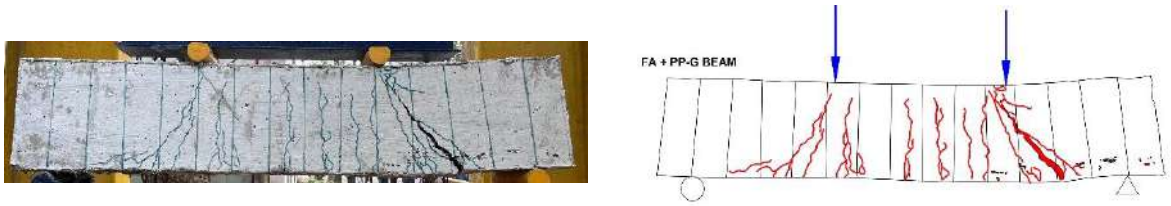

(d)

Fig. 12. Crack pattern of RC beams (a) NC- S Beam (b) NC – G Beam (c) FA+PP – S Beam (d) FA+PP – G Beam

Nevertheless, fly ash+ polypropylene fibers (FA+PP G) beams had better crack control because of the synergistic effect of polypropylene fibers and fly ash. The ductile failure modes of the NC-S and FA+PP-S beams experience gradual crack widening and plastic deformations before ultimate failure. On the other hand, NC-G and FA+PP-G beams had more brittle failure characteristics with sudden crack propagation to induce failure. However, in FA+PP-G beams, the presence of fibers bridging offered an effect that enhanced post crack load resistance. As a result, the crack resistance and durability of the steel as well as GFRP reinforced FA+PP mixes with fly ash and polypropylene fibers was enhanced over the control FA+PP mixer to improve its suitability for structural applications where high crack control is required.

5. Conclusions

The effect of fiber and fly ash using this experimental study was to evaluate the mechanical performance as well as durability of reinforced concrete. Compressive strength, flexural response, crack behavior, and corrosion resistance of the concrete were examined on incorporating 20 percent fly ash as cement replacement and 1 percent polypropylene fibers by volume in a study. According to the experimental findings, these can be inferred.

- The addition of 1% polypropylene fibers and 20% fly ash increases the long term compressive strength, FA+PP mixes attained 54.98 MPa at 56 days but exceeded the nominal mix as the pozzolanic reaction and matrix densification are delayed. High load bearing capacity (305.6 kN) was observed in FA+PP-S beams and FA+PP-G beams performed well in complying with the strength (279.9 kN), thereby proving the synergy between fibers and fly ash in reinforced concrete systems.
- Steel reinforced beams were ductile and GFRP reinforced beams were brittle. The failure mode for FA+PP-G beams is improved with incorporation of polypropylene fibers as they delay the crack propagation and improve the post crack stability. They also showed improvement in both energy dissipation capacity and deformation capacity by virtue of fiber inclusion in GFRP reinforced beams, especially FA+PP-G.
- Crack propagation was well controlled by the polypropylene fibers. This suggests that FA+PP-G beams had reduced crack width and FA+PP-S beams had fine, closely spaced cracks, both of which represent improved crack resistance from fiber bridging. Fly ash use saves cement demand, lower CO_2 emissions and fosters sustainable construction. FA + PP-G systems are corrosion free with the help of GFRP rebars that provide risk free solutions for harsh corrosive environments like coastal and marine structures.
- Coring, combining fly ash and polypropylene fibers with the GFRP reinforcement thus produces a corrosion resistant, mechanically efficient, durable composite system and

justifies a role as a candidate for infrastructure systems that may be required for long term resilience in aggressive exposure.

- Further research works can study the effect of different fiber types (e.g., basalt, carbon, steel, or hybrid fibers) on performance of the mechanical and durability of fly ash concrete and determine quite design optimum fiber reinforcement strategies for various applications. Examine how the total fiber content changes past 1% to establish the amount of fiber which optimizes workability, strength, and crack resistance in fiber reinforced fly ash concrete. Study the interaction between fly ash and other supplementary cementitious materials, silica fume, metakaolin, or slag to improve early age and long-term performance.

References

[1] Benmokrane B, Chaallal O, Masmoudi R. Glass fibre reinforced plastic (GFRP) rebars for concrete structures. Constr Build Mater. 1995;9(6):353-64. https://doi.org/10.1016/0950-0618(95)00048-8

[2] Jabbar SA, Farid SBH. Replacement of steel rebars by GFRP rebars in the concrete structures. Karbala Int J Mod Sci. 2018;4(2):216-27. https://doi.org/10.1016/j.kijoms.2018.02.002

[3] Issa MS, Metwally IM, Elzeiny SM. Influence of fibers on flexural behavior and ductility of concrete beams reinforced with GFRP rebars. Eng Struct. 2011;33(5):1754-63. https://doi.org/10.1016/j.engstruct.2011.02.014

[4] Pour AK, Shirkhani A, Zeng JJ, Zhuge Y, Farsangi EN. Experimental investigation of GFRP-RC beams with Polypropylene fibers and waste granite recycled aggregate. Structures. 2023;1021-34. https://doi.org/10.1016/j.istruc.2023.02.068

[5] de Sá FRG, Silva FA, Cardoso DCT. Tensile and flexural performance of concrete members reinforced with polypropylene fibers and GFRP bars. Compos Struct. 2020;253:112784. https://doi.org/10.1016/j.compstruct.2020.112784

[6] Orouji M, Najaf E. Effect of GFRP rebars and polypropylene fibers on flexural strength in high-performance concrete beams with glass powder and microsilica. Case Stud Constr Mater. 2023;18:e01769. https://doi.org/10.1016/j.cscm.2022.e01769

[7] Rahman Md M, Rahman MM. Characterization and predictive modeling of thermally aged glass fiber reinforced plastic composites. Res. Eng. Struct. Mater., 2024; 10(1): 305-330.. http://dx.doi.org/10.17515/resm2023.24me0609rs

[8] Higgins IC. Impact of changes in the design methodology between the American Concrete Institute's draft code provisions for GFRP-reinforced concrete and the ACI 440.1 R-15 guide for the design and construction of structural concrete reinforced with FRP bars [master's thesis]. Chester (PA): Widener University; 2020.

[9] Emparanza AR, Kampmann R, De Caso F, Morales C, Nanni A. Durability assessment of GFRP rebars in marine environments. Constr Build Mater. 2022;329:127028. https://doi.org/10.1016/j.conbuildmat.2022.127028

[10] Stankiewicz B. Composite GFRP deck for bridge structures. Procedia Eng. 2012;40:423-7. https://doi.org/10.1016/j.proeng.2012.07.119

[11] Mai G, Xiong Z, Zhu H, Zhou L, Zhou H, Li L. Durability of GFRP bars embedded in seawater sea sand concrete in marine environments. Constr Build Mater. 2025;458:139488. https://doi.org/10.1016/j.conbuildmat.2024.139488

[12] Sun L, Wei M, Zhang N. Experimental study on the behavior of GFRP reinforced concrete columns under eccentric axial load. Constr Build Mater. 2017;152:214-25. https://doi.org/10.1016/j.conbuildmat.2017.06.159

[13] El-Gamal S, Al-Fahdi AM, Meddah M, Al-Saidy A, Sohel KMA. Flexural behavior of FRP bars after being exposed to elevated temperatures. J Eng Res [TJER]. 2021;18(1):12-9. https://doi.org/10.53540/tjer.vol18iss1pp12-19

[14] Alhozaimy AM, Soroushian P, Mirza F. Mechanical properties of polypropylene fiber reinforced concrete and the effects of pozzolanic materials. Cem Concr Compos. 1996;18(2):85-92. https://doi.org/10.1016/0958-9465(95)00003-8

[15] Emamjomeh H, Behfarnia K, Raji A, Almohammad-Albakkar M. Influence of PVA and PP fibers addition on the durability and mechanical properties of engineered cementitious composites blended with silica fume and zeolite. Res Eng Struct Mater. 2023;9(2):457-73.

[16] Sarıkaya H, Susurluk G. Effect of polypropylene fiber addition on thermal and mechanical properties of concrete. Res Eng Struct Mater. 2019;5(1):1-12.

[17] Sivakumar A, Santhanam M. Mechanical properties of high strength concrete reinforced with metallic and non-metallic fibres. Cem Concr Compos. 2007;29(8):603-8. https://doi.org/10.1016/j.cemconcomp.2007.03.006

[18] Sarikaya H, Susurluk G. Effect of polypropylene fiber addition on thermal and mechanical properties of concrete. Res. Eng. Struct. Mat., 2019; 5(1): 1-12. http://dx.doi.org/10.17515/resm2018.72ma1109
[19] Karthik AS, Gorabal SV. Effect of Polypropylene (PP)/Glass fibers on the Mechanical behaviour of Epoxy composites with Al_2O_3 and $Mg(OH)_2$ fillers. IJFRD, 2020 May; 1(1): 1-8. https://doi.org/10.46625/IJFRD.2020.1101
[20] Nili M, Afroughsabet V. The effects of silica fume and polypropylene fibers on the impact resistance and mechanical properties of concrete. Constr Build Mater. 2010;24(6):927-33. https://doi.org/10.1016/j.conbuildmat.2009.11.025
[21] Celik K, Meral C, Mancio M, Mehta PK, Monteiro PJM. A comparative study of self-consolidating concretes incorporating high-volume natural pozzolan or high-volume fly ash. Constr Build Mater. 2014;67:14-9. https://doi.org/10.1016/j.conbuildmat.2013.11.065
[22] Shinde P, Patankar S, Sayyad A. Investigation on effects of fineness of flyash and alkaline ratio on mechanical properties of geopolymer concrete. Res Eng Struct Mater. 2017 May.
[23] Thomas MDA, Matthews JD. Carbonation of fly ash concrete. Mag Concr Res. 1992;44(160):217-28. https://doi.org/10.1680/macr.1992.44.160.217
[24] Malhotra VM, Valimbe PS, Wright MA. Effects of fly ash and bottom ash on the frictional behavior of composites. Fuel. 2002;81(2):235-44. https://doi.org/10.1016/S0016-2361(01)00126-0
[25] Bharti R, Chidambaram RS, Kwatra N. Influence of fiber reinforced concrete on plastic behavior on exterior beam column joint under cyclic loading. Procedia Eng. 2017;173:1122-9. https://doi.org/10.1016/j.proeng.2016.12.077
[26] Raza A, Ali B, Nawaz MA, Ahmed I. Structural performance of FRP-RC compression members wrapped with FRP composites. Structures. 2020;1693-709. https://doi.org/10.1016/j.istruc.2020.07.071
[27] Nanni A, De Luca A, Zadeh H. Reinforced concrete with FRP bars. In: Reinforced concrete with FRP bars. London: CRC Press; 2014. p. b16669. https://doi.org/10.1201/b16669
[28] Indian Standards. IS:269 - Indian Standard Ordinary Portland Cement - Specification. 2015.
[29] Bureau of Indian Standards. Specification for Coarse and Fine Aggregates From Natural Sources for Concrete (IS: 383 - 1970). Indian Stand. 1970;1-24.
[30] IS 9103. Specification for Concrete Admixtures. Bur Indian Stand. Dehli. 1999;1-22.
[31] Bureau of Indian Standards. IS 10262:2019 - Concrete Mix Proportioning - Guidelines. Bur Indian Stand. 2019;Second Rev(January):1-40.
[32] IS 456. Plain Concrete and Reinforced. Bur Indian Stand. Dehli. 2000;4:1-114.
[33] IS 516. Method of Tests for Strength of Concrete. Bur Indian Stand. 1959;1-30.

Blank Page

Research on Engineering Structures & Materials
www.jresm.org

Research Article

Effect of areca catechu fiber and superplasticizer interaction on the optimization of concrete compressive strength using the Box-Behnken design statistical approach

Teuku Farizal [*,1,a], Teuku Budi Aulia [2,b], Dian Febrianti [1,c], Roni Agusmaniza [1,d], Muhammad Arrie Rafshanjani Amin [1,e]

[1]*Department of Civil Engineering, Teuku Umar University, Meulaboh, Indonesia*
[2]*Department of Civil Engineering, Syiah Kuala University, Banda Aceh, Indonesia*

Article Info

Article History:

Received 01 Mar 2025

Accepted 26 June 2025

Keywords:

High-performance concrete;
Areca nut fiber;
Superplasticizer;
Compressive strength;
Box-Behnken design

Abstract

The use of natural fiber BSKP (Areca Nut Fiber) as a sustainable reinforcement in concrete is promising due to its mechanical properties and biodegradability. However, the hygroscopic nature of BSKP increases the viscosity of the concrete mixture, which affects workability and homogeneity. To overcome this, superplasticizer (SP) is used as a chemical admixture to improve fluidity without altering the water-to-cement ratio, thus supporting cement hydration and strength development. This study investigates the effect of varying BSKP concentrations combined with a fixed SP dosage on compressive strength using Box-Behnken Design within the Response Surface Methodology to optimize the mix. Experiments used BSKP at 2.0, 2.5, and 3.0% by cement weight with a fixed SP dosage of 2.1%. Compressive strength was tested at 7- and 28-days following ASTM C39. The BBD method within Response Surface Methodology (RSM) optimized material proportions. Results showed 2.0% BSKP + 2.1% SP achieved optimal performance with 26.445 MPa at 28 days and a desirability score of 0.542. Increasing BSKP to 3.0% reduced strength to 22.379 MPa due to impaired cement hydration. Statistical analysis confirmed SP's significant effect (coefficient = 6.4884, $p < 0.01$). Model validation indicated high predictive reliability (Adjusted $R^2 = 0.8953$, Predicted $R^2 = 0.8665$). In conclusion, the combination of 2.0% BSKP and 2.1% SP effectively enhances compressive strength while maintaining workability. The Box-Behnken Design within the RSM framework proved useful in optimizing material proportions. These findings support the development of durable, eco-friendly natural fiber-reinforced concrete and offer practical guidance for sustainable concrete formulation.

© 2025 MIM Research Group. All rights reserved.

1. Introduction

Concrete is the primary material in the construction industry, continuously evolving to enhance its mechanical performance, sustainability, and efficiency [1-3]. As the demand for High-Performance Concrete (HPC) increases, various approaches have been developed to improve its mechanical strength and durability against environmental factors [4-6]. One of the most promising innovations in sustainable concrete development is the incorporation of natural fibers as supplementary materials, which has been shown to enhance toughness, reduce plastic shrinkage, and improve resistance to microcracking [7-12].

Natural fibers like coconut, bamboo, and ramie fibers, have also been studied in concrete as they can increase the tensile strength, cohesion between materials, and limit the formation of

*Corresponding author: teukufarizal@utu.ac.id
[a]orcid.org/0000-0002-8163-4958; [b]orcid.org/0000-0003-1807-1088; [c]orcid.org/orcid.org/0000-0003-4905-0255; [d]orcid.org/0009-0006-1813-6960; [e]orcid.org/0009-0004-1449-7406
DOI: http://dx.doi.org/10.17515/resm2025-714me0301rs

microcracks [13-17]. Areca catechu (areca nut) fiber, is one of the natural fibers with high tensile strength, is affordable and more sustainable than synthetic fibers that have potential to run four times strong constructional practice in concrete [2,18,19]. Nonetheless, the high-water absorption tendency of areca nut fiber is a significant challenge because it increases viscosity and reduces the workability of concrete [20-24].

Findings by [25,26] have shown that addition of natural fibers reduces workability, making it difficult to mix and cast the mixtures, and that can influence homogeneity of the mixture and thus strength of concrete. Superplasticizers, chemical admixtures that improve the plasticity and flowability of the cement paste while maintaining hydration levels [27-30], have thus been widely used to mitigate this issue. Superplasticizers aid in a wetting of the cement particles, allowing for a more homogenous material, with greater compressive strengths achieved without losing workability [31-34]. There have been limited studies on the interaction between areca nut fiber and superplasticizers and their effect on enhancing concrete performance [35-39].

Several studies have been conducted on fiber-reinforced concrete, but very few relate to the interaction between areca nut fiber and superplasticizers and their influence on the mechanical properties of concrete. The studies mentioned so far were prior research on natural fibers added to concrete, detailed in Table below, which did not investigate workability and compressive strength simultaneously when superplasticizers were mixed with natural fibers [22,40-42]. Furthermore, the previous research on natural fibers in concrete is more qualitative with a great degree of trial-and-error optimization of the fiber and admixture dosage, which is inefficient [43-46].

Thus, there is a need for a more systematic approach to optimize natural fiber-reinforced concrete mixtures and improve the efficiency of research in this field. A possible approach is the Box-Behnken Design (BBD), a micro-vox of Response Surface Methodology (RSM). The advantage of BBD is that it allows you to explore relationships between numerous variables with fewer experimental trials than would be required in standard experimentations, which results in a more efficient way of identifying which combinations of materials work best [1,2,21,47]. It is commonly used for combinatorial optimization problem research in the case of concrete specimens, where the goal is to test the best performance of concrete with various combinations of supplementary materials, natural fibers, and superplasticizers [32,48-51]. However, till date the research on optimizing the areca nut fiber-based concrete using BBD is mostly unexplored [51].

At the laboratory scale, the study uses main materials involving Type I Portland cement, fine aggregate (uniformly graded sand), and coarse aggregate (graded gravel) that are well mixed and uniformly distributed in the concrete matrix [52,53]. In order not to contaminate the cement hydration reaction, the water injected into the concrete mixture is in accordance with [54] standards [19]. The effect of its inclusion on properties of concrete is studied by adding it in different percentages of 2.0, 2.5 and 3.0% v/s cement weight, while maintaining a fixed dosage of superplasticizer (2.1% of cement wt) to improve workability without compromising compressive strength [28]. Compressive strength tests are also carried out at 7 and 28 days for strength variation over time [21,48].

The present study was conducted to investigate the effect of interaction between areca nut fiber and superplasticizers on the compressive strength of concrete and to optimize their proportions through BBD approach. The study also aims to conduct a comparative study between areca nut fiber-reinforced concrete and plain concrete to highlight the performance of this material as an authentic component for structural applications [41,55,56]. This research novelty focuses on the systematic exploration of the behavior of the areca nut fiber on the superplasticizers, which has been rarely reported in existing literature [6,40,57].

It is assumed that the findings would contribute to filling research gaps in the field and would help in opening up new avenues for natural fiber-reinforced concrete technology, particularly as applying areca nut fiber in structural applications has yet to be fully explored. These discoveries not only provide scientific basis for further studies, but also may act as natural solutions for the construction industry to design more effective, longer lasting, and eco-friendlier concrete building materials [5,8,26,58].

2. Materials and Methods

2.1 Materials

The materials that were used in this study are cement, fine aggregate, coarse aggregate, water, Areca catechu fiber, and superplasticizer. The materials were chosen according to well-known quality indicators so as to obtain homogeneity and uniformity in the concrete mixture.

2.1.1 Cement

Commercially available Type I Portland Cement, in accordance with [59], was used in this study. The versatile nature and good early and final strength load ensured the use of this type of cement. Cement is the main binder in the concrete mixture and takes part in hydration reactions that lead to the generation of compressive strength.

Fig. 1. Type I Portland Cement used in the concrete mixture

2.1.2 Fine and Coarse Aggregates

Fine aggregate: it comprises natural sand having a uniform gradation that satisfies [60] requirements to promote even particle distribution and facilitate convenient workability. The function of sand is to fill the voids in between the coarse aggregates to promote the high-density matrix as much as possible. It is used to develop the bond or link between the cement paste and the aggregate particles. Two types of sands used included fine sand and coarse sand. The former is characterized by smaller-sized particles and improves the cohesion of the major four constituents. Cohesion would help to prevent segregation and promote uniformity across the newly constructed matrix, ensuring the proper function. The latter has bigger and enhances the stability of the combination. Shrinkage is minimized to avoid excessiveness across the construction. Appropriate particle size distribution and grading are employed to optimize the workability of the concrete mix, while controlling bleeding to maintain mixture stability and achieve an ideal proportioning of constituents.

Fig. 2. Fine sand (left) and coarse sand (right) used in the concrete mix

The coarse aggregate used is crushed gravel with a uniform size distribution that also meets [60] specifications. Fine aggregate is provided by a park sand plant, while a gravel pit supplies coarse aggregate, which is becoming increasingly important in providing structural strength, lowering

shrinkage and enhancing the mechanical performance of the mix. No new ideas just fancy wording in this phrasing of the degree of angularity of the selected gravel resulting in increased interlocking and bond strength in the concrete matrix. Properly graded aggregate of small enough size provides a compact mass with minimal voids for efficient load transfer, in turn increasing the overall durability of the concrete structure. This study used an upper limit of 20 mm for the maximum aggregate size following the guidelines prescribed for structural concrete [60].

Fig. 3. Coarse aggregate (gravel) used in the concrete mixture

2.1.3 Water

Comply with the [54] standard for mixing water, free from harmful substances such as chloride or sulfate, which could interfere with cement hydration. Good quality mixing water is crucial for preserving the bond between cement and aggregates and to obtain the best mechanical properties of hardened concrete.

2.1.4 Areca Catechu Fiber

Fiber was obtained from dried areca nut husks (Areca catechu) and was mechanically processed for separating the natural fibers. The pre-treatment process for the fibers before mixing them with the concrete includes washing to remove uncleanness and drying to reduce moisture content. The length of fiber used in this study was 30–50 mm depending on what has been recommended in the prior literature regarding the application of natural fibers in concrete [20], [23]. The fiber percentage was taken as 2.0, 2.5, and 3.0% of weight of cement. These variations were chosen because previous studies showed that natural fibers could help increase the crack resistance of concrete but excessive fiber will have a negative effect on mixture homogeneity, hindering the cement hydration process [7], [9].

Fig. 4. Areca catechu fiber after processing, cut into lengths of 30–50 mm before being used in the concrete mixture

2.1.5 Superplasticizer

The superplasticizer employed in this research is a polycarboxylate-based admixture with a constant dosage of 2.1% by weight of cement. Superplasticizers are used to enhance the workability of the concrete, allowing a decrease of viscosity at the same time as no increase of water is added to the mixture. The application of its most significant alkaloids aims to reduce the adverse effects of Areca catechu fiber in increasing water consumption as well as in decreasing the flowability of the mixture [28], [31].

Fig. 5. Superplasticizer admixture used to improve the workability of fiber-reinforced concrete

2.2 Experimental Design

This research utilized statistical Box-Behnken Design (BBD) under Response Surface Methodology (RSM); for the interaction study of Areca fiber and Superplasticizer for Concrete Compressive strength [1]. Here, corresponds to experimental design for three main factors affecting compressive strength: areca fiber percentage (A), superplasticizer percentage (B) and curing age (C). To evaluate the effect of the fiber dosage on mechanical properties of the concrete, the A variable (fiber content), was set to the values 2%, 2.5% and 3% according to the mass of cement (see Table 3). The B variable reflects the amount of superplasticizer, which was defined as 2.1% of the cement mass, according to previous studies indicating the usefulness of admixtures in workability improvement and compressive strength [3]. As for the curing age C variable, it was based on 7 and 28 days, just to see how compressive strength evolves through time due to cement hydration. The Box-Behnken Design (BBD) method was used to evaluate these three variables, which can explore interaction (interdependent) effects with fewer trials than traditional methods [1].

2.3 Concrete Preparation and Testing

2.3.1 Mixing and Casting of Concrete

The dry mixing method of preparing the concrete was used, with the fine aggregate, coarse aggregate, and cement mixed first until a complete homogeneous mix was obtained. After that, water and superplasticizer were added according to the designed proportions, and then areca fiber. To ensure the uniform distribution of the optical fibers in the concrete matrix [3], the mixing was performed for 5 min by use of a laboratory concrete mixer.

Fig. 6. Concrete mixing process incorporating Areca catechu fiber before casting in cylindrical molds

The concrete specimens were cast in cylindrical molds with dimensions of 150 mm diameter and 300 mm height, in accordance with [61] standards for compressive strength testing. The casting process followed the procedures specified in [61], including proper compaction using a mechanical vibrator to ensure uniform density and minimize entrapped air voids. These procedures align with the requirements outlined in Tables 1 and 2 of [61], which standardize specimen preparation to ensure reliable and reproducible compressive strength results.

2.3.2 Curing of Concrete

Concrete specimens were kept in the Ambient environment for demolding for 24 h and then placed inside the water-curing tank until the test age. Hydration continues under controlled moisture conditions, so this curing method enables the concrete to achieve ultimate strength [4].

Fig. 7. Curing of concrete specimens in a water tank to maintain hydration and ensure optimal strength development

2.3.3 Compressive Strength Test

Compressive strength test was carried out using Universal Testing Machine (UTM) as per [62] standard. The concrete specimens were prepared and cured in accordance with [61] standards prior to compressive strength testing, which was conducted using a Universal Testing Machine (UTM) as per [62]. Each mix variation was tested for three specimens to give a representative average value for the two tests performed at 7 and 28 days respectively.

Fig. 8. Compressive strength testing of concrete cylinders using a Universal Testing Machine (UTM) as per [62] standards

The objectives of this study are to acknowledge the effects of Areca catechu fiber on the properties of concrete, specifically regarding the effect superplasticizer may have on the composition of the mixture through the Box-Behnken Design (BBD). It is anticipated that the conclusion of this research will help for the creation of energy-efficient, fiber-reinforced sustainable concrete bases.

3. Results and Discussion

3.1 Experimental Results

3.1.1 Effect of Areca Catechu Fiber and Superplasticizer on Concrete Compressive Strength

Compressive strength testing was conducted at 7 and 28 days to evaluate the effect of Areca Catechu Fiber (BSKP) and superplasticizer (SP) on concrete strength. Various BSKP contents and SP dosages were used to determine their impact on the mechanical performance of the concrete. The results of the compressive strength tests from different mixtures are presented in Table 1.

Table 1. Compressive strength test results

Specimen Name	Testing Age	Specimen Weight	Cylinder Area	Cylinder Volume	Load (P)		fc= P/A	Average
	(days)	(kg)	(mm^2)	(mm^3)	kN	N	(Mpa)	(Mpa)
BN. I	7	12.14	17671.46	5301437.60	243.164	243164	13.7603	14.084
BN. II		12.12	17671.46	5301437.60	248.980	248980	14.0894	
BN. III		11.98	17671.46	5301437.60	254.488	254488	14.4011	
BSKP 2% + SP 2,1%. I	7	11.52	17671.46	5301437.60	343.336	343336	19.4288	19.729
BSKP 2% + SP 2,1%. II		11.60	17671.46	5301437.60	350.276	350276	19.8216	
BSKP 2% + SP 2,1%. III		11.70	17671.46	5301437.60	352.308	352308	19.9366	
BSKP 2,5% + SP 2,1%. I	7	11.36	17671.46	5301437.60	340.916	340916	19.2919	19.341
BSKP 2,5% + SP 2,1%. II		11.37	17671.46	5301437.60	341.196	341196	19.3077	
BSKP 2,5% + SP 2,1%. III		11.38	17671.46	5301437.60	343.224	343224	19.4225	
BSKP 3% + SP2,1%. I	7	11.52	17671.46	5301437.60	325.224	325224	18.4039	18.384
BSKP 3% + SP2,1%. II		11.48	17671.46	5301437.60	320.180	320180	18.1185	
BSKP 3% + SP2,1%. III		11.66	17671.46	5301437.60	329.236	329236	18.6309	
BSP 2,1%. I	7	12.08	17671.46	5301437.60	424.256	424256	24.0080	24.106
BSP 2,1%. II		12.04	17671.46	5301437.60	427.564	427564	24.1952	
BSP 2,1%. III		12.14	17671.46	5301437.60	426.152	426152	24.1153	
BN. I	28	11,77	17671.46	5301437.60	354.492	354492	20.0601	20.500
BN. II		11,78	17671.46	5301437.60	364.356	364356	20.6183	
BN. III		11,74	17671.46	5301437.60	367.960	367960	20.8223	
BSKP 2% + SP 2,1%. I	28	11,26	17671.46	5301437.60	446.240	446240	25.2520	25.242
BSKP 2% + SP 2,1%. II		11,27	17671.46	5301437.60	448.984	448984	25.4073	
BSKP 2% + SP 2,1%. III		11,44	17671.46	5301437.60	442.976	442976	25.0673	
BSKP 2,5% + SP 2,1%. I	28	11,52	17671.46	5301437.60	406.508	406508	23.0036	22.960
BSKP 2,5% + SP 2,1%. II		11,56	17671.46	5301437.60	401.236	401236	22.7053	
BSKP 2,5% + SP 2,1%. III		11,58	17671.46	5301437.60	409.448	409448	23.1700	
BSKP 3% + SP2,1%. I	28	11,25	17671.46	5301437.60	398.836	398836	22.5695	22.379
BSKP 3% + SP2,1%. II		11,24	17671.46	5301437.60	396.960	396960	22.4633	

Specimen Name	Testing Age	Specimen Weight	Cylinder Area	Cylinder Volume	Load (P)		fc= P/A	Average
	(days)	(kg)	(mm^2)	(mm^3)	kN	N	(Mpa)	(Mpa)
BSKP 3% + SP2,1%. III		11,28	17671.46	5301437.60	390.620	390620	22.1046	
BSP 2,1%. I		11,94	17671.46	5301437.60	653.952	653952	37.0061	
BSP 2,1%. II	28	12,04	17671.46	5301437.60	656.764	656764	37.1652	37.003
BSP 2,1%. III		11,74	17671.46	5301437.60	650.992	650992	36.8386	

It was noticed that the compressive strength has increased remarkably at 7 and 28 days for all specimens. At 7 days, the average compressive strength of normal concrete (BN) was 14.084 MPa, that increased to 20.500 MPa at 28 days, which corresponds to an increase of 45% due to continuous hydration of cement. The use of added materials improved the compression strength. [9] As a comparison, BSKP 2% + SP 2.1% concrete reached a 7-day average compressive strength of 19.729 MPa and a compressive strength of 25.242 MPa at 28 days-an obvious indicator of how effective their admixture was at improving strength development. Increasing BSKP dosage to 3% decreased the strength as compared to 2% dosage with average compressive strength of 18.384 MPa at 7 days and 22.379 MPa at 28 days. This indicates that there is an optimal level of BSKP dosage, beyond which too much may be detrimental to strength gains. The average compressive strength of concrete containing BSP 2.1% was the best at 24.106 MPa at 7 days and 28 days was 37.003 MPa. The obtained values are greater than normal concrete and all BSKP variations, indicating that BSP is more effective than BSKP in enhancing compressive strength. These results highlight the need for a further investigation for selecting the dose and material of supplementary material to ensure the best performance of concrete. When it came to the best at improving compressive strength was the dosage application of BSP 2.1% while the dosages of BSKP must be optimized further to avoid strength deterioration due to overdoses.

3.1.2 Analysis of the Effect of Areca Fiber Concrete (BSKP) and Superplasticizer on Concrete Mechanical Performance: Comparison with Additional Literature

This study concludes that the addition of Areca Fiber Concrete (BSKP) and superplasticizer (SP) to the concrete greatly impacts the strength of concrete compressive strength, but the results will depend largely on the amount of these materials used. Experimental Results show BSKP 2% + SP 2.1% give the most strength improvement, while compressive strength drops when increasing BSKP to 3% as viscosity increases and workability decreases. Also, excess amounts hinder cement hydration, causing non-homogeneous distribution within the concrete.

Table 2. Comparison of experimental results and literature

Aspect	Experimental Findings	Findings from Additional Literature
Effect of BSKP on Compressive Strength	BSKP 2% + SP 2.1% increased compressive strength by 39.9% (7 days) and 23.5% (28 days).	Areca fiber enhances internal cohesion and crack resistance [7], [9].
Optimal BSKP Dosage	BSKP 3% led to a reduction in compressive strength (18.384 MPa - 7 days, 22.379 MPa - 28 days).	Excessive fiber content increases viscosity and reduces workability [20], [23].
Role of SP in Workability	SP improves cement dispersion, resulting in better workability and compressive strength.	Superplasticizer reduces water demand and prevents segregation [28], [31].
Interaction of BSKP & SP	BSKP 2% + SP 2.1% was found to be the optimal combination.	Studies on the interaction of areca fiber and SP remain limited [35], [38].
Comparison with Conventional Concrete	BSP 2.1% achieved the highest compressive strength (37.003 MPa - 28 days, +80.6% vs. normal concrete).	Optimized fiber-admixture combinations significantly enhance HPC performance [32], [34].

The kind and amount of fiber can determine whether the fiber is effective since it induces a substantial increase in bonding strength [7], [9], similarly as found in this work and supported by others where natural fibers were shown to reduce the volume of microcracks, enhancing material cohesion, ultimately improve its compressive strength, [42] confirming their positive effect on BSKP concrete at a dosage of 2%. Nevertheless, the addition of BSKP at 3% would reduce the compressive strength due to higher viscosity and lower homogeneity, as supported by the previous findings of the adverse impact of a large amount of high water-absorbing fibers on cement hydration. Superplasticizer (SP) based materials promote enhanced workability, optimal cement dispersion, and segregation control, leading to the formation of concrete with improved compressive strength. The confirmed optimum combination was BSKP 2% + SP 2.1% that showed a 39.9% increase in strength at 7 days and 23.5% increase in strength at 28 days in comparison with control concrete. On the other hand, BSKP was shown to increase only 71.45%, while BSP 2.1% was 80.60% compared to normal concrete at 28 days, indicating that BSP proves to be more efficient than BSKP in improving structural concrete performance.

This study applies the Box-Behnken Design (BBD) response surface methodology (RSM) to systematically optimize the proportions of Areca fiber and superplasticizer for enhancing concrete compressive strength. The BBD approach, widely utilized in concrete research, offers an efficient experimental framework to explore multifactor interactions and reduce the number of required trials, as supported by previous studies [1,2,21,32,48-50]. Integrating BBD in this research strengthens the reliability and robustness of the optimization process, thereby enriching the contribution to sustainable HPC development. Moreover, while the compressive strength values obtained may appear moderate relative to traditional HPC benchmarks, it is critical to recognize that HPC performance encompasses multifaceted criteria beyond compressive strength alone, including durability, toughness, crack resistance, and workability. The synergistic effect of natural fibers and superplasticizers in this study aligns with this comprehensive HPC paradigm. Consequently, the findings are consistent with the evolving understanding of HPC as a multifunctional material system, emphasizing sustainability and practical workability alongside mechanical strength. This holistic perspective, reinforced by systematic optimization using BBD, validates the applicability of optimized fiber-admixture combinations in producing eco-friendly, high-performance concrete.

3.2 Statistical Analysis

3.2.1 Analysis of the Interaction between Areca Fiber and Superplasticizer

This study analyzes three main factors affecting concrete compressive strength. Factor 1 (Areca Fiber Concrete, BSKP) refers to the percentage of areca fiber (0%, 2.0%, 2.5%, 3.0%), which enhances crack resistance but may reduce cement homogeneity at higher doses. Factor 2 (Superplasticizer, SP) represents the superplasticizer content (0% and 2.1%), which reduces the water-cement ratio and optimizes hydration. Factor 3 (Concrete Age) is the testing period (7 and 28 days) to evaluate strength development due to the hydration process.

Table 3. Design (actual)

Std	Run	Factor 1	Factor 2	Factor 3	Response 1
		A: Areca Nut Fiber Variation with Superplasticizer	B: Superplasticizer	C: Testing Age	Compressive Strength
		%	%	day	MPa
16	2	0	2.1	7	24.008
20	3	0	0	7	13.7603
21	5	0	0	7	14.4011
9	8	0	2.1	7	24.1952
22	9	0	0	28	20.0601
7	13	0	0	7	14.0894
23	14	0	0	28	20.6183
18	19	0	2.1	7	24.1153

Std	Run	Factor 1	Factor 2	Factor 3	Response 1
		A: Areca Nut Fiber Variation with Superplasticizer	B: Superplasticizer	C: Testing Age	Compressive Strength
		%	%	day	MPa
17	21	0	2.1	28	37.1652
25	23	0	2.1	28	36.8386
29	25	0	0	28	20.8223
15	29	0	2.1	28	37.0061
24	1	2	2.1	7	19.9366
26	4	2	2.1	28	25.252
28	6	2	2.1	28	25.4073
1	7	2	2.1	28	25.0673
3	17	2	2.1	7	19.4288
5	22	2	2.1	7	19.8216
13	11	2.5	2.1	28	23.0036
30	12	2.5	2.1	7	19.2919
10	15	2.5	2.1	7	19.3077
19	16	2.5	2.1	28	22.7053
11	18	2.5	2.1	28	23.17
14	20	2.5	2.1	7	19.4225
4	10	3	2.1	7	18.6309
8	24	3	2.1	28	22.1046
27	26	3	2.1	28	22.5695
6	27	3	2.1	7	18.4039
12	28	3	2.1	28	22.4633
2	30	3	2.1	7	18.1185

3.2.2 Fit Summary

Statistical analysis shows that the linear model has a p-value of 1.75×10^{-13}, an Adjusted R^2 of 0.895, and a Predicted R^2 of 0.866, making it the recommended choice. The 2FI model has an Adjusted R^2 of 0.985 and a Predicted R^2 of 0.983 but suffers from aliasing. While the 2FI model fits better statistically, the linear model is simpler and free from aliasing, making it more reliable for predicting compressive strength.

Table 4. Response 1: compressive strength

Source	Sequential p-value	Lack of Fit p-value	Adjusted R^2	Predicted R^2	
Linear	< 0.0001	< 0.0001	0.8953	0.8665	Suggested
2FI	< 0.0001	< 0.0001	0.9854	0.9830	Aliased

Table 5. Results of the Sequential Model Sum of Squares [Type I]

Source	Sum of Squares	df	Mean Square	F-value	p-value	
Mean vs Total	15016.33	1	15016.33			
Linear vs Mean	898.00	3	299.33	83.69	< 0.0001	Suggested
2FI vs Linear	81.01	2	40.51	81.16	< 0.0001	Aliased
Residual	11.98	24	0.4991			
Total	16007.31	30	533.58			

The linear model shows a sum of squares of 897.997, an F-value of 83.69, and a p-value of 1.75×10^{-13}, indicating high statistical significance. The 2FI model has a p-value of 2.09×10^{-11} but suffers from aliasing, which may hinder interpretation. Therefore, the linear model is recommended due to its stability and aliasing-free nature, making it more reliable for compressive strength analysis.

Table 6. Results of the lack of conformity test

Source	Sum of Squares	df	Mean Square	F-value	p-value	
Linear	91.83	6	15.31	264.11	< 0.0001	Suggested
2FI	10.82	4	2.70	46.67	< 0.0001	Aliased
Pure Error	1.16	20	0.0580			

The linear model demonstrates high significance but has a lack-of-fit that should be considered. The 2FI model has a lower lack-of-fit but suffers from aliasing. Therefore, the linear model remains recommended, with caution in result interpretation. The 2FI model has a higher Adjusted R^2 (0.985) and Predicted R^2 (0.983) compared to the linear model (Adjusted R^2 0.895, Predicted R^2 0.866), along with a lower standard deviation. However, the 2FI model suffers from aliasing, which may affect parameter interpretation. The 2FI model is statistically superior, but aliasing effects should be carefully considered.

Table 7. Model summary statistics

Model	Std. Dev.	Adjusted R^2	Predicted R^2	Press	Information
Linear	1.891	0.895	0.866	132.323	Recommended, but less than optimal
2FI	0.706	0.985	0.983	16.858	Aliased, better performance but needs attention

3.2.3. ANOVA Analysis for Linear Model on Compressive Strength

Analysis of variance (ANOVA) was performed to evaluate the effect of Areca Nut fiber variation, superplasticizer usage, and curing age on compressive strength. The results indicate that the model is statistically significant ($F = 83.69$, $p = 1.748 \times 10^{-13}$), with all three factors significantly influencing the response. However, the Lack of Fit is also significant ($F = 264.11$, $p = 5.837 \times 10^{-18}$), suggesting a discrepancy between the model and the actual data. The Areca Nut fiber variation, superplasticizer usage, and curing age significantly influence the compressive strength. The significant Lack of Fit indicates that the model may not fully align with the observed data.

Table 8. ANOVA for linear model

Source of Variation	SS	df	MS	F-value	p-value	Interpretation
Model	897.9965	3	299.3322	83.6933	1.748×10^{-13}	Significant
A - Areca Nut Fiber Variation with Superplasticizer	388.6576	1	388.6576	108.669	8.859×10^{-11}	
B - Superplasticizer	524.1400	1	524.1400	146.550	3.450×10^{-12}	
C - Curing Age	315.7199	1	315.7199	88.2753	7.641×10^{-10}	
Residual	92.9900	26	3.5765			
Lack of Fit	91.8309	6	15.3052	264.106	5.837×10^{-18}	Significant
Pure Error	1.1590	20	0.05795			
Total Correlation	990.9865	29				

3.2.4. Model Fit Statistics.

The model fit evaluation indicates good predictive performance. The coefficient of determination (R^2) = 0.9062 shows that 90.62% of the response variability is explained by the model. The Adjusted R^2 = 0.8953 and Predicted R^2 = 0.8665 differ by less than 0.2, indicating strong predictive capability. The Adequate Precision = 28.187, well above the minimum threshold of 4, confirms a strong signal for reliable predictions. The high R^2 values and Adequate Precision suggest that the model is reliable and effective for exploring and optimizing the design space.

Table 9. Model fit statistics

Statistic	Value	Interpretation
Standard Deviation	1.8912	Measures model error
Mean	22.3728	Average response value
Coefficient of Variation (C.V. %)	8.4530	Relative measure of data dispersion
R^2 (Coefficient of Determination)	0.9062	Model explains 90.62% of response variability
Adjusted R^2	0.8953	Adjusted for predictor count
Predicted R^2	0.8665	Close agreement with Adjusted R^2, indicating good predictive accuracy
Adequate Precision	28.1870	Signal-to-noise ratio, confirming model suitability for prediction

3.2.5. Model Comparison Statistics.

The model comparison evaluation indicates that PRESS = 132.323 represents the model's prediction error. -2 Log Likelihood = 119.075 assesses model fit, where lower values indicate a better-fitting model. BIC = 132.680 and AICc = 128.675 balance model fit and complexity, with lower values suggesting a more optimal model. These values assist in selecting the best model by balancing goodness of fit and complexity.

Table 10. Model comparison statistics

Statistic	Value	Interpretation
PRESS	132.323	Prediction error; lower is better
-2 Log Likelihood	119.075	Model fit; lower is better
BIC	132.680	Balances model fit and complexity; lower is better
AICc	128.675	Corrected Akaike Information Criterion for small sample sizes

3.2.6. Coefficients in Terms of Coded Factors.

Regression analysis shows that Superplasticizer (B) has the highest positive impact on the response (coefficient = 6.4884), while Areca Nut Fiber Variation with Superplasticizer (A) has a negative effect (-1.7668). Testing Age (C) also contributes positively (3.2441). The Variance Inflation Factor (VIF) ≤ 1.542 indicates no significant multicollinearity issues among factors. These results indicate that Superplasticizer has the most significant positive effect on the response, while Areca Nut Fiber Variation with Superplasticizer negatively affects it.

Table 11. Coefficients in Terms of Coded Factors

Factor	Coefficient Estimate	df	Standard Error	95% CI Low	95% CI High	VIF
Intercept	14.9461	1	0.6832	13.5417	16.3505	-
A - Areca Nut Fiber Variation with Superplasticizer	-1.7668	1	0.1695	-2.1152	-1.4185	1.542
B - Superplasticizer	6.4884	1	0.5360	5.3867	7.5901	1.542
C - Testing Age	3.2441	1	0.3453	2.5343	3.9538	1.000

3.2.7. Final Equation in Terms of Actual Factors.

The final equation is used to predict compressive strength based on factor values in their original units:

$$Compressive\ Strength = 11.8851 - 3.5337(A) + 6.1794(B) + 0.3089(C) \quad (1)$$

Where, A = Areca Nut Fiber Variation with Superplasticizer; B = Superplasticizer; C = Testing Age

Superplasticizer has the highest positive contribution to compressive strength, while Areca Nut Fiber Variation with Superplasticizer has a negative impact. Testing Age has a small but positive effect. This equation is for prediction purposes only and should not be used to determine the relative impact of each factor.

3.2.8. Data Analysis Results

The analysis indicates that some data points have high residuals, suggesting potential outliers or significant influence on the model. Run 2, 8, 21, 23, and 29 have notable Cook's Distance and DFFITS values, meaning these data points may strongly affect the model's performance. Further evaluation is needed to determine whether the model should be adjusted or if these points require special handling. These results indicate that some data points have a strong influence on the model, requiring further investigation.

Table 12. Data Analysis Results

Run Order	Actual Value	Predicted Value	Residual	Leverage	Internally Studentized Residuals	Externally Studentized Residuals	Cook's Distance	DFFITS	Standard Order
1	19.94	19.96	-0.02	0.076	-0.011	-0.011	0.000003	-0.0032	24
2	24.01	27.02	-3.02	0.188	-1.770	-1.851	0.1813	-0.8905	16
3	13.76	14.05	-0.29	0.200	-0.170	-0.167	0.0018	-0.0834	20
4	25.25	26.45	-1.19	0.076	-0.656	-0.649	0.0088	-0.1855	26
5	14.40	14.05	0.35	0.200	0.209	0.205	0.0027	0.1025	21
6	25.41	26.45	-1.04	0.076	-0.571	-0.563	0.0067	-0.1610	28
7	25.07	26.45	-1.38	0.076	-0.758	-0.752	0.0117	-0.2148	1
8	24.20	27.02	-2.83	0.188	-1.660	-1.722	0.1595	-0.8284	9
9	20.06	20.54	-0.48	0.200	-0.281	-0.276	0.0049	-0.1381	22
10	18.63	16.42	2.21	0.116	1.241	1.255	0.0504	0.4538	4
11	23.00	24.68	-1.67	0.088	-0.927	-0.925	0.0206	-0.2864	13
12	19.29	18.19	1.10	0.088	0.610	0.602	0.0089	0.1865	30
13	14.09	14.05	0.04	0.200	0.025	0.024	0.00004	0.0120	7
14	20.62	20.54	0.08	0.200	0.049	0.048	0.0001	0.0239	23
15	19.31	18.19	1.12	0.088	0.618	0.611	0.0092	0.1893	10
16	22.71	24.68	-1.97	0.088	-1.092	-1.097	0.0286	-0.3397	19
17	19.43	19.96	-0.53	0.076	-0.291	-0.285	0.0017	-0.0816	3
18	23.17	24.68	-1.51	0.088	-0.835	-0.830	0.0167	-0.2571	11
19	24.12	27.02	-2.91	0.188	-1.707	-1.777	0.1686	-0.8547	18
20	19.42	18.19	1.23	0.088	0.682	0.675	0.0112	0.2090	14
21	37.17	33.51	3.65	0.188	2.143	2.316	0.2658	1.1143	17
22	19.82	19.96	-0.14	0.076	-0.075	-0.073	0.0001	-0.0209	5
23	36.84	33.51	3.33	0.188	1.952	2.071	0.2204	0.9965	25
24	22.10	22.91	-0.81	0.116	-0.454	-0.447	0.0067	-0.1616	8
25	20.82	20.54	0.29	0.200	0.169	0.166	0.0018	0.0830	29
26	22.57	22.91	-0.34	0.116	-0.192	-0.189	0.0012	-0.0683	27
27	18.40	16.42	1.98	0.116	1.114	1.119	0.0405	0.4046	6
28	22.46	22.91	-0.45	0.116	-0.252	-0.248	0.0021	-0.0895	12
29	37.01	33.51	3.49	0.188	2.050	2.195	0.2431	1.0561	15
30	18.12	16.42	1.69	0.116	0.953	0.951	0.0297	0.3440	2

The normal plot of residuals is used to assess the normality assumption of the regression model residuals. In this plot, the residual data points closely follow the diagonal reference line, indicating that the residuals approximate a normal distribution. This is an important assumption for the validity of linear regression models. Meeting this assumption implies that the regression model is appropriate and the statistical analysis results can be reliably interpreted.

The Residuals vs. Predicted plot is used to assess the homoscedasticity (constant variance) assumption of the regression model. In this plot, the residuals are randomly scattered around zero without any discernible pattern, indicating that the residual variance is consistent across all predicted values. This suggests that the model fits the data well and that the homoscedasticity assumption is satisfied, supporting the reliability of the regression analysis.

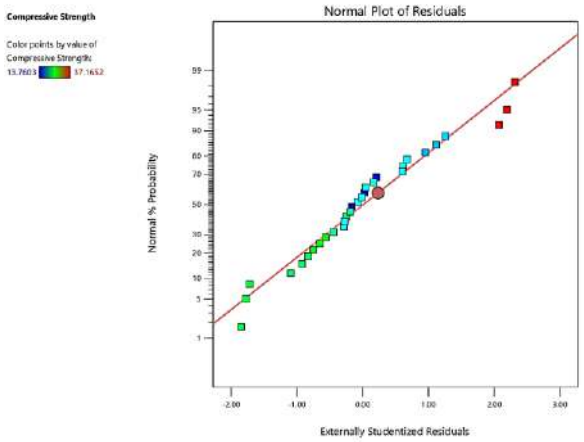

Fig. 9. Normal Plot of Residuals

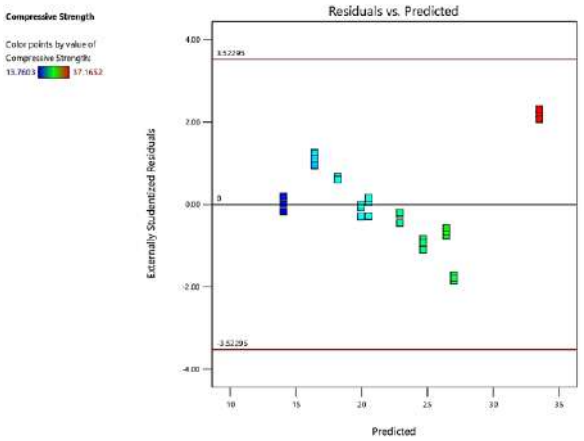

Fig. 10. Residuals vs. Predicted

The Residuals vs. Run plot is used to examine the pattern of residuals across the sequence of experimental runs. A random scatter of residuals without any systematic pattern indicates that there is no autocorrelation or run order effect influencing the data. This confirms the independence of residuals and supports the validity and stability of the regression model throughout the experimental runs.

The Cook's Distance plot is used to identify data points with a disproportionately large influence on the regression model. Data points with high Cook's Distance values indicate a significant impact on parameter estimates and overall model fit. In this plot, points approaching or exceeding the threshold are flagged for further examination to ensure the stability and reliability of the regression analysis. The absence of extreme Cook's Distance values suggests no outliers unduly dominate the model results.

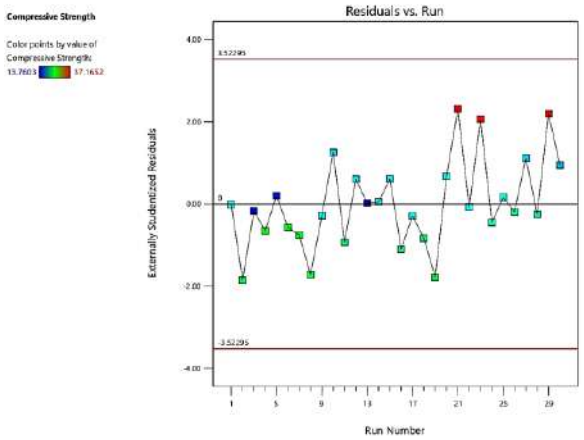

Fig. 11. Residuals vs. Run

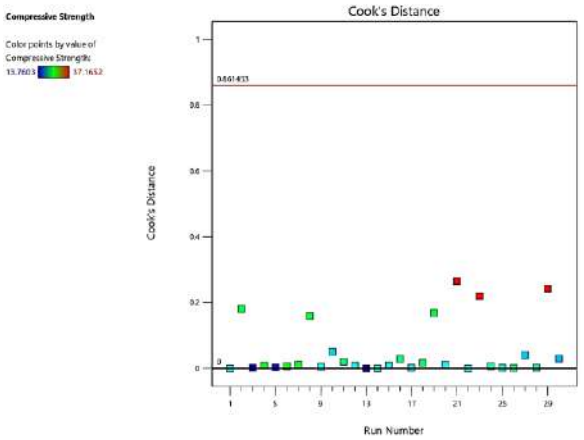

Fig. 12. Cook's Distance

The Box-Cox plot is utilized to identify the optimal power transformation that stabilizes variance and improves the normality of residuals in the regression model. This transformation aids in satisfying the assumptions of homoscedasticity and normality, which are essential for valid statistical inference. The plot displays the range of lambda (λ) values within the confidence interval, indicating acceptable transformation values. A lambda value close to 1 suggests no transformation is necessary, whereas values differing from 1 indicate that data transformation is required to enhance model validity.

The Predicted vs. Actual plot is used to evaluate the accuracy of the regression model in predicting concrete compressive strength based on experimental data. Data points closely clustered around the diagonal line indicate a strong agreement between predicted and actual measured values, demonstrating the model's robust predictive capability. Minor deviations from the diagonal

represent minimal prediction errors, confirming the model's reliability in estimating concrete performance across different variable combinations. This plot reinforces the validity and robustness of the statistical model employed in this study.

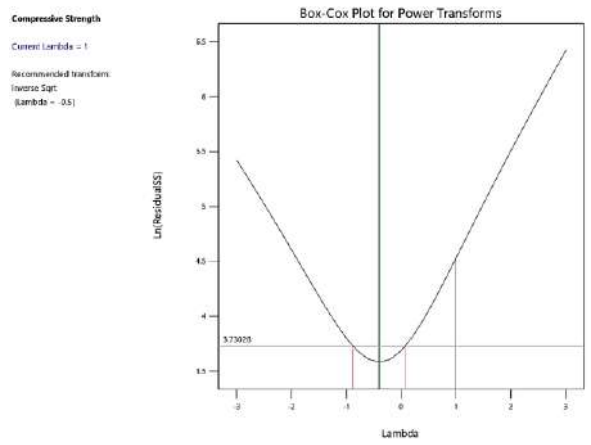

Fig. 13. Box-Cox Plot for Power Transforms

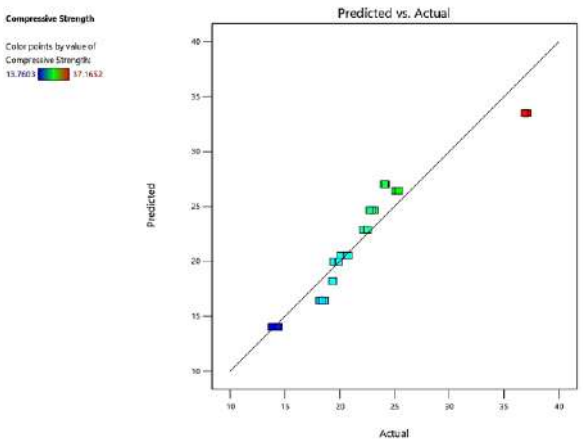

Fig. 14. Predicted vs. Actual

This plot illustrates the residuals from the regression model against variations in Areca Nut Fiber dosage combined with a fixed percentage of superplasticizer. The random scatter of residuals without any clear pattern indicates that the model consistently explains the variability of the data across the tested fiber dosage range. The absence of systematic trends confirms that the assumptions of linearity and homoscedasticity are met for this factor, supporting the validity of the regression analysis in predicting concrete compressive strength with varying fiber content.

The Leverage vs. Run plot is used to identify data points that have a significant influence on the regression model. High leverage values indicate observations that are outliers in terms of predictor variables and have a strong impact on the estimation of model parameters. In this plot, no data points exhibit extremely high leverage, suggesting that there are no observations disproportionately influencing the model. This supports the stability and reliability of the regression analysis results.

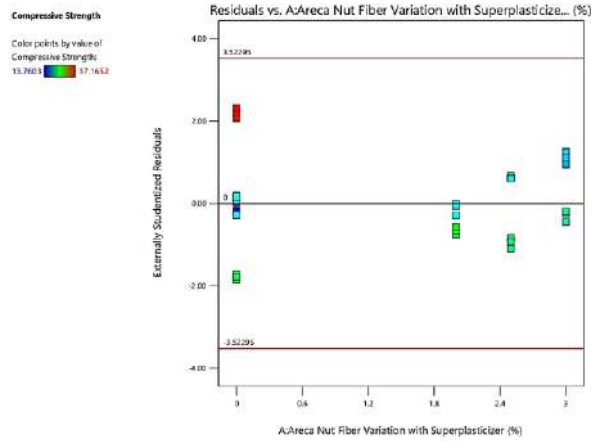

Fig. 15. Residuals vs. A: Areca Nut Fiber Variation with Superplasticizer (%)

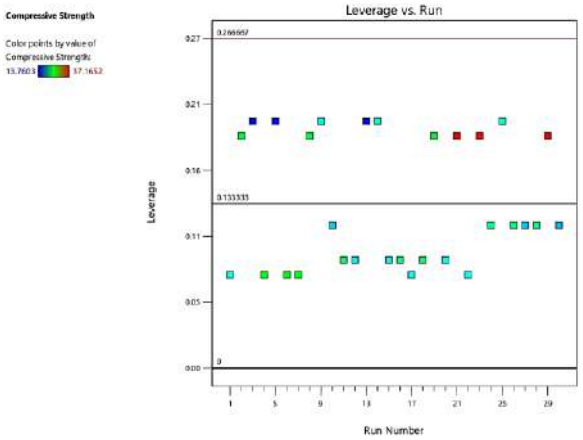

Fig. 16. Leverage vs. Run

The DFFITS vs. Run plot is used to detect observations that have a significant influence on the regression model's predictions. DFFITS measures the impact of removing each data point on the fitted model values. Data points with large absolute DFFITS values exceeding a critical threshold are considered influential and may disproportionately affect the model estimates. In this plot, no data points exceed this threshold, indicating that no individual observation unduly influences the model, thereby reinforcing the robustness and reliability of the regression analysis.

The DFBETAS for Intercept vs. Run plot assesses the influence of individual data points on the estimated intercept of the regression model. DFBETAS measures the change in the intercept coefficient when each data point is excluded. Points with large absolute DFBETAS values indicate observations that have a strong impact on the intercept estimation. In this plot, no points exceed the typical threshold, suggesting that no single observation unduly affects the intercept, supporting the stability and robustness of the regression model.

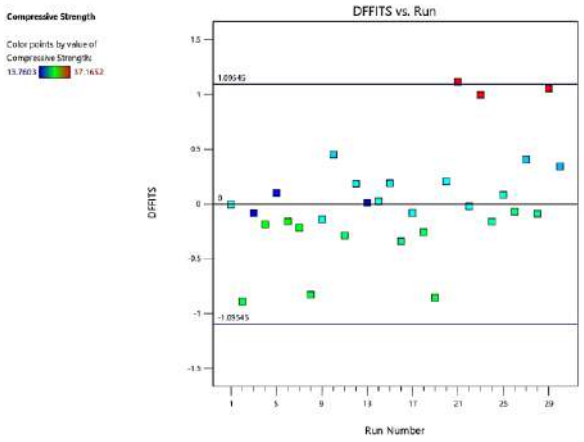

Fig. 17. DFFITS vs. Run

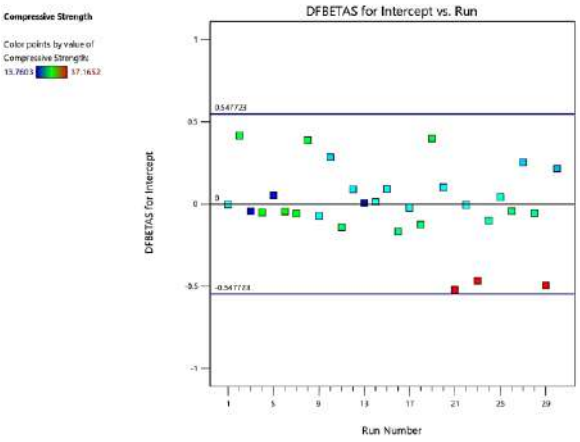

Fig. 18. DFBETAS for Intercept vs. Run

The perturbation plot illustrates the sensitivity of the response variable—in this case, compressive strength—to small changes in each factor while holding other factors constant at a reference point. Steeper slopes on the plot indicate greater sensitivity, highlighting which variables have the most significant effect on the response. This information guides the optimization of mixture proportions by identifying key influential factors.

The one factor plot illustrates the individual effect of each variable on the response, compressive strength, by varying one factor at a time while holding other factors constant. This plot helps in understanding the direct influence of each factor independently, revealing trends such as linearity or non-linearity in the response. It is a useful tool for identifying the optimal range and levels of factors to enhance compressive strength.

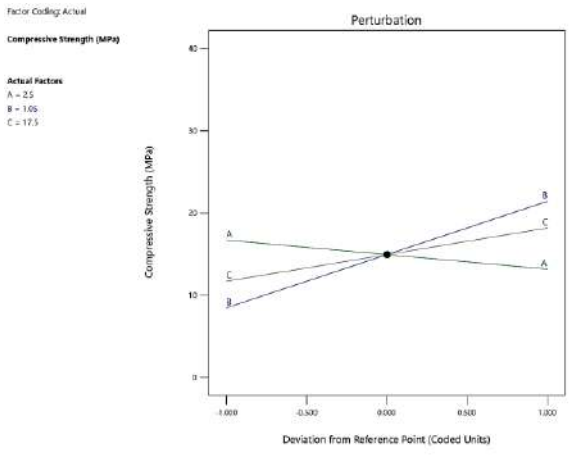

Fig. 19. Perturbation

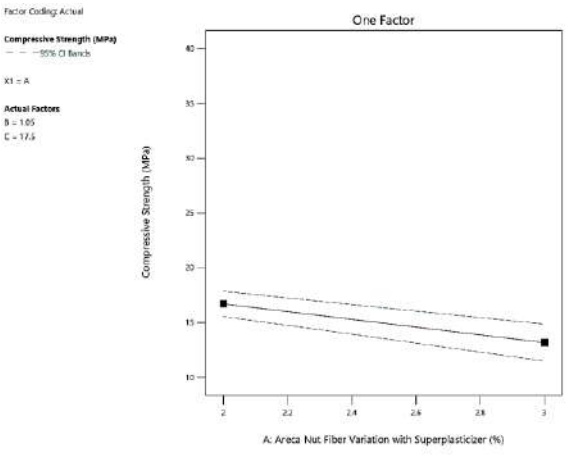

Fig. 20. One Factor

The analysis examines the effects of Factors A, B, and C on Compressive Strength (MPa: 13.7603 to 37.1652), validated by 95% Confidence Intervals (CI). Factor A (0% to 2.5%) shows a negative correlation, reducing compressive strength. Factor B (0.8% to 1.2%) and Factor C (7 to 28 days) exhibit positive correlations, increasing strength. All factors significantly impact compressive strength, with B and C enhancing strength and A reducing it. The 95% CI bands confirm statistical reliability.

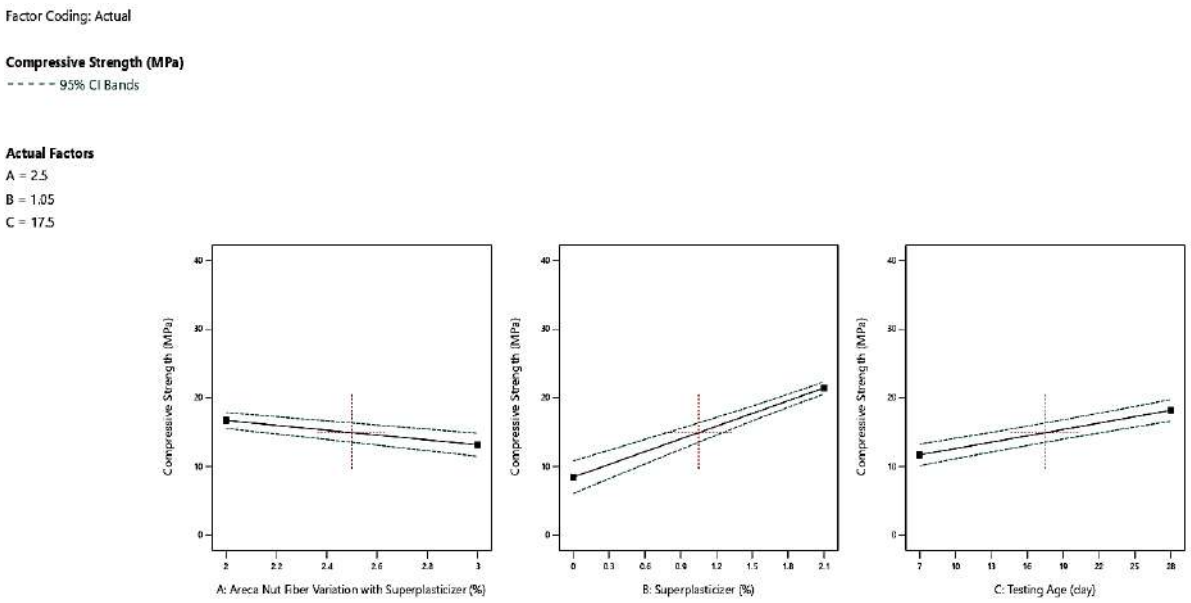

Fig. 21. All Factor

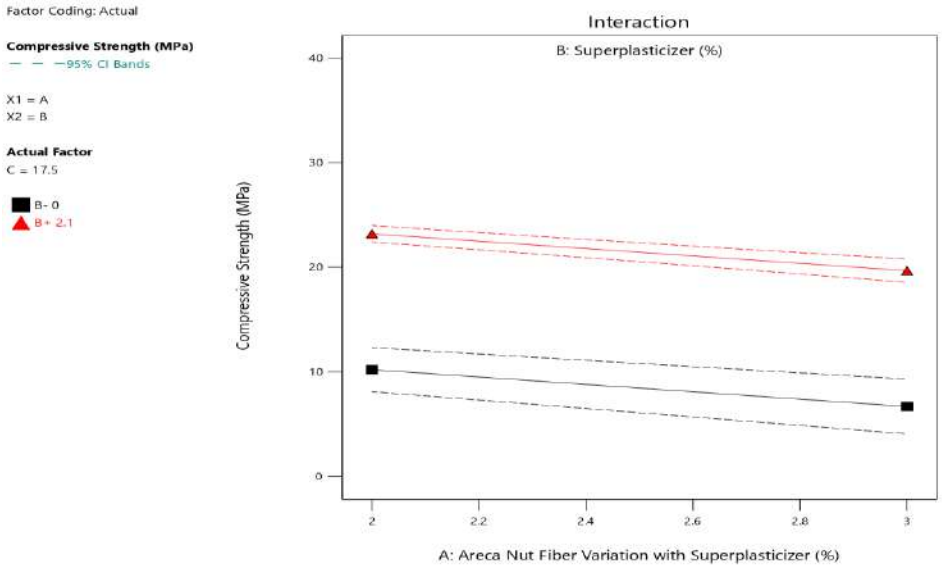

Fig. 22. Interaction

The Interaction Plot examines the effect of Factor A (Areca Nut Fiber Variation: 2.0% to 3.0%) and Factor B (Superplasticizer: 0.0 and 2.1%) on Compressive Strength (MPa: 13.7603 to 37.1652), with Factor C (Testing Age) fixed at 17.5. When B = 0.0, compressive strength decreases as A increases. At B = 2.1, compressive strength remains higher at increased A levels. The 95% Confidence Interval (CI) overlap suggests an interaction effect, with A's influence stronger at B = 2.1.

The 3D Surface Plot illustrates the relationship between Areca Nut Fiber Variation (A: 2.0% to 3.0%), Superplasticizer (B: 0.0% to 2.1%), and Compressive Strength (MPa: 10 to 20), with Testing Age (C) fixed at 17.5. The plot shows a positive correlation, where increasing A and B leads to higher compressive strength, as indicated by the upward slope and color gradient (blue to green).

In the experiment, 94 solutions were analyzed based on Desirability values, which assess factor suitability for maximizing compressive strength. The optimal solution (Desirability = 0.542) achieved 26.445 MPa with a standard error of 0.520, using 2.0% Areca Nut Fiber, 2.1% Superplasticizer, and 28-day Testing Age.

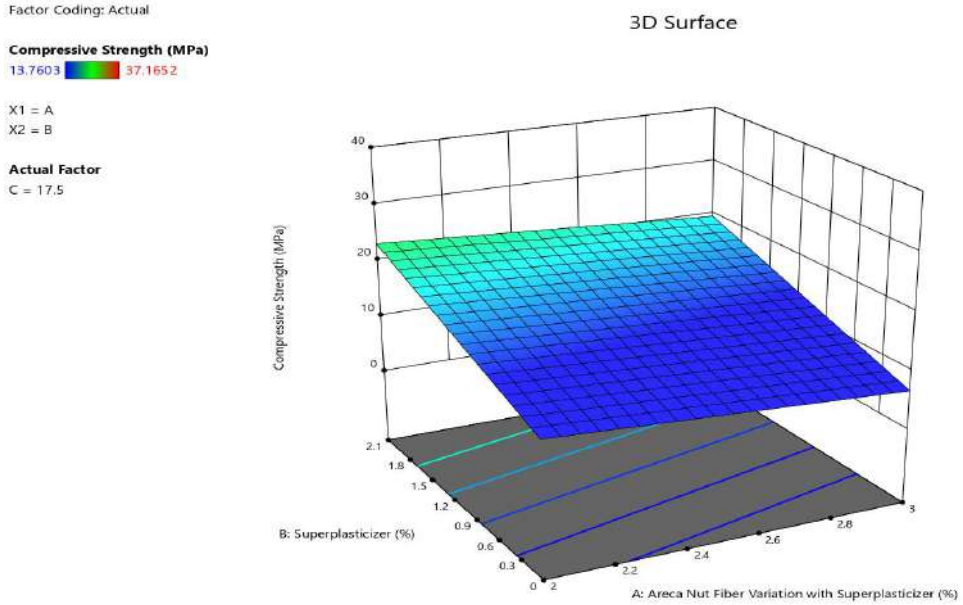

Fig. 23. 3D Surface Plot illustrates

Table 13. Experimental results for the 94 solutions tested, showing the Desirability values and factors used

Number	Areca Nut Fiber Variation with Superplasticizer	Superplasticizer	Testing Age	Compressive Strength (MPa)	StdErr (Compressive Strength)	Desirability	Remarks
1	2.000	2.100	28	26.445	0.520	0.542	Optimal solution, highest Desirability
2	2.007	2.100	28	26.415	0.520	0.541	
3	2.016	2.100	28	26.389	0.520	0.540	
4	2.022	2.100	28	26.367	0.520	0.539	
5	2.031	2.100	28	26.326	0.520	0.537	
6	2.026	2.092	28	26.304	0.520	0.536	
7	2.037	2.100	28	26.295	0.520	0.536	
8	2.031	2.091	28	26.281	0.520	0.535	
9	2.057	2.100	28	26.242	0.522	0.533	
10	2.045	2.085	28	26.196	0.520	0.531	
11	2.076	2.100	28	26.139	0.520	0.529	
12	2.055	2.081	28	26.132	0.520	0.529	
13	2.088	2.100	28	26.089	0.520	0.527	
14	2.101	2.100	28	26.035	0.520	0.524	
15	2.073	2.071	28	26.012	0.520	0.523	
16	2.078	2.068	28	25.970	0.520	0.522	
17	2.119	2.100	28	25.955	0.520	0.521	
18	2.099	2.070	28	25.911	0.521	0.519	
19	2.088	2.061	28	25.896	0.520	0.518	
20	2.092	2.058	28	25.863	0.520	0.517	
21	2.166	2.100	28	25.857	0.527	0.517	
22	2.186	2.100	28	25.788	0.529	0.514	
23	2.150	2.076	28	25.765	0.524	0.513	
24	2.165	2.098	28	25.746	0.520	0.512	
25	2.171	2.100	28	25.726	0.520	0.511	
26	2.175	2.100	28	25.708	0.520	0.510	
27	2.236	2.100	28	25.612	0.532	0.506	
28	2.242	2.100	28	25.592	0.533	0.506	
29	2.127	2.020	28	25.503	0.520	0.502	
30	2.272	2.100	28	25.450	0.536	0.499	
31	2.292	2.100	28	25.415	0.537	0.498	
32	2.135	1.988	28	25.400	0.520	0.497	
33	2.305	2.100	28	25.368	0.538	0.496	
34	2.315	2.100	28	25.331	0.539	0.494	
35	2.320	2.100	28	25.314	0.539	0.493	
36	2.326	2.100	28	25.292	0.540	0.493	

Number	Areca Nut Fiber Variation with Superplasticizer	Superplasticizer	Testing Age	Compressive Strength (MPa)	StdErr (Compressive Strength)	Desirability	Remarks
37	2.296	2.075	28	25.243	0.536	0.491	
38	2.147	1.987	28	25.220	0.520	0.490	
39	2.358	2.100	28	25.166	0.543	0.487	
40	2.388	2.100	28	25.074	0.546	0.483	
41	2.376	2.100	28	25.042	0.540	0.482	
42	2.404	2.100	28	25.020	0.548	0.481	
43	2.159	1.959	28	25.009	0.520	0.481	
44	2.466	2.100	28	24.800	0.555	0.472	
45	2.481	2.100	28	24.747	0.557	0.469	
46	2.428	2.100	28	24.445	0.520	0.456	
47	2.134	1.849	28	24.423	0.520	0.456	
48	2.433	2.100	28	24.413	0.520	0.455	
49	2.440	2.100	28	24.377	0.520	0.454	
50	2.432	2.084	28	24.328	0.520	0.451	

The optimal solution, achieving the highest Desirability value (0.542), is found in Solution Number 1. This combination-Areca Nut Fiber Variation (2%), Superplasticizer (2.1%), and Testing Age (28 days)-yields the highest compressive strength (26.445 MPa). These results suggest that this specific factor combination optimally enhances material performance.

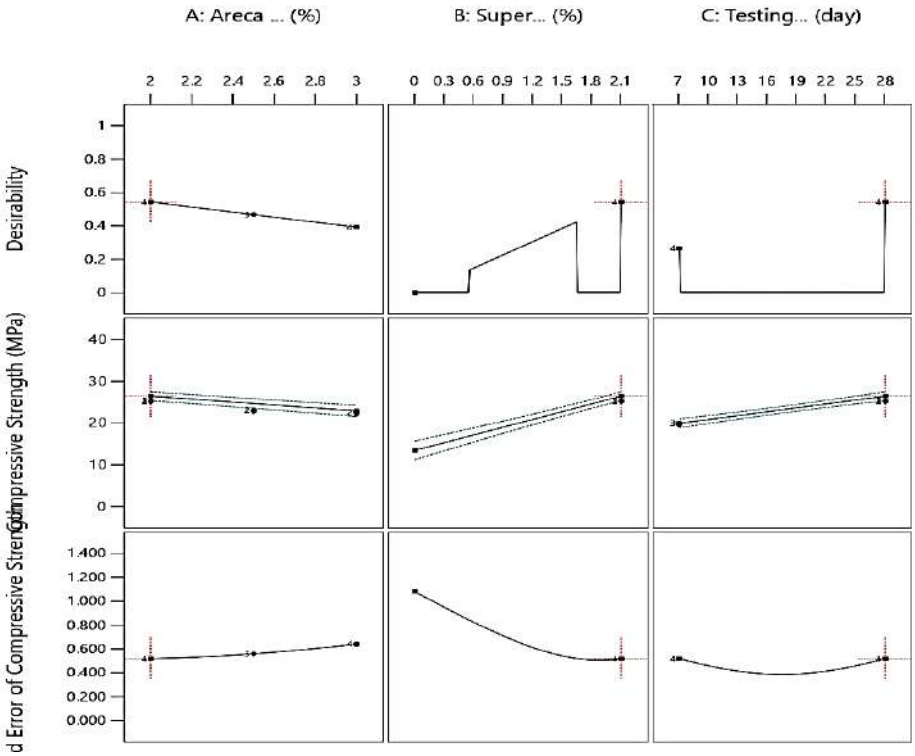

Fig. 24. Graph all factor

The graph examines the effect of Areca Nut Fiber (0%–2.5%), Superplasticizer (0.8%–2.1%), and Testing Age (7–28 days) on Desirability and Compressive Strength Error (0.1–1.5 MPa). Desirability increases with Areca and Superplasticizer, though inconsistently. Compressive Strength declines initially, then stabilizes. Error fluctuations suggest measurement uncertainty, requiring further analysis to improve reliability.

The 3D Surface Plot visualizes desirability for optimizing Compressive Strength, based on Areca Nut Fiber Variation (A: 2%–3%) and Superplasticizer (B: 0%–2.1%), with Testing Age (C) fixed at 28 days. The Z-axis represents Desirability (0 to 1), transitioning from blue (low) to green (high). Green regions indicate optimal factor combinations, while blue regions reflect suboptimal conditions. Red design points mark experimental settings. This plot helps identify the best A and B combinations for improved material performance.

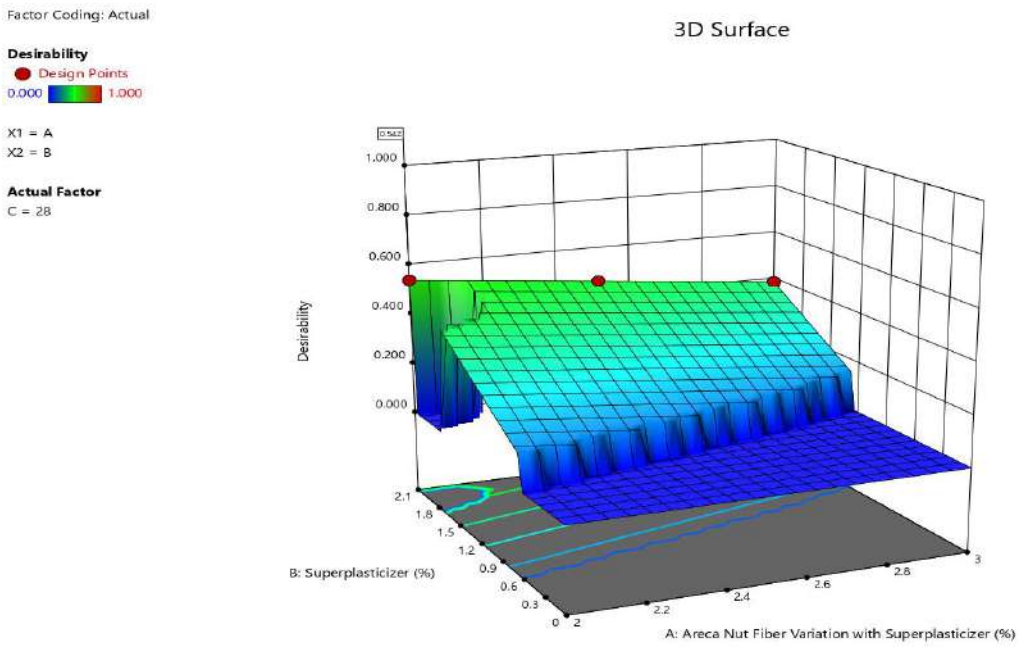

Fig. 25. 3D Surface Plot visualizes desirability

4. Conclusions

This study demonstrates that the incorporation of Superplasticizer (SP) and Areca Nut Fiber (BSKP) significantly improves the compressive strength of concrete. The optimal mixture, consisting of 2.0% BSKP and 2.1% SP, achieved a compressive strength of 26.445 MPa at 28 days. Increasing BSKP content to 3.0% resulted in a strength reduction to 22.379 MPa, attributed to increased mixture viscosity adversely affecting cement hydration and homogeneity. Meanwhile, BSP at 2.1% exhibited the highest compressive strength of 37.003 MPa, representing an 80.6% improvement over conventional concrete. Optimization via the Box-Behnken Design (BBD) identified effective dosage ranges for BSKP and SP at 1.8%–2.2% and 1.9%–2.3%, respectively, producing desirability values ≥ 0.55 and compressive strengths between 27.5 and 28.0 MPa.

The findings hold significant implications for sustainable development and innovation in construction materials. Utilizing renewable Areca catechu fiber as a reinforcing agent not only enhances mechanical performance but also reduces reliance on synthetic fibers, thereby mitigating environmental impacts. This approach valorizes agricultural waste into value-added construction materials, supporting resource efficiency and circular economy principles. The observed improvements in compressive strength and workability enable broader application across structural elements, potentially extending service life and lowering maintenance costs. Accordingly, this technology aligns with sustainable development goals by reducing the ecological footprint of construction and fostering local economic empowerment through sustainable material sourcing.

Nonetheless, several limitations should be acknowledged. Comprehensive durability assessments, including water absorption, permeability, and chemical resistance tests, were not conducted, restricting evaluation of long-term material performance. The fixed superplasticizer dosage (2.1%) limited exploration of dose-response relationships and formulation optimization. While the employed linear statistical model provided stability and interpretability, it may inadequately capture complex nonlinear interactions among factors. Additionally, the experimental scope was confined to laboratory-scale investigations, necessitating field-scale validation and long-term performance monitoring to confirm practical applicability and durability under real-world conditions. Therefore, future research should prioritize comprehensive durability testing to assess long-term resilience against environmental and chemical degradation. Expanding the range of superplasticizer dosages will facilitate a deeper understanding of dose effects and interactions with natural fibers. The development and application of advanced statistical models, including nonlinear

and interaction-based approaches, will improve predictive accuracy and mechanistic insight. Moreover, field trials incorporating extended performance monitoring are critical to validate laboratory findings and establish reliability for sustainable natural fiber-reinforced concrete in construction practice.

In summary, this study contributes substantially to the advancement of eco-friendly, high-performance concrete materials reinforced with natural fibers, while charting a clear path for ongoing research and innovation to support efficient and sustainable construction in the future.

References

[1] Montgomery EJ, Vannier CN. Of Spirit, Slave and Sea. 2017.
[2] Hasan R, et al. Eco-friendly self-consolidating concrete production with reinforcing jute fiber. J Build Eng. 2023;63:105519. https://doi.org/10.1016/j.jobe.2022.105519
[3] Zhang L, Zhao J, Fan C, Wang Z. Effect of surface shape and content of steel fiber on mechanical properties of concrete. Adv Civ Eng. 2020;2020:1-11. https://doi.org/10.1155/2020/8834507
[4] Ahmed A. Potential of utilizing coir, straw, and recycled PET fibres as sustainable & economical alternative in fibre reinforced concrete. Res Dev Mater Sci. 2022;16(5). https://doi.org/10.31031/RDMS.2022.16.000899
[5] Herrera-Sosa ES, Martínez-Barrera G, Barrera-Díaz C, Cruz-Zaragoza E. Waste tire particles and gamma radiation as modifiers of the mechanical properties of concrete. Adv Mater Sci Eng. 2014;2014:1-7. https://doi.org/10.1155/2014/327856
[6] Jalal A, Shafiq N, Nikbakht E, Kumar R, Zahid M. Mechanical properties of hybrid basalt-polyvinyl alcohol (PVA) fiber reinforced concrete. Key Eng Mater. 2017;744:3-7. https://doi.org/10.4028/www.scientific.net/KEM.744.3
[7] Acosta-Calderon S, Gordillo-Silva P, García-Troncoso N, Bompa DV, Flores-Rada J. Comparative evaluation of sisal and polypropylene fiber reinforced concrete properties. Fibers. 2022;10(4):31. https://doi.org/10.3390/fib10040031
[8] Fauzan F. The effects of steel fibers extracted from waste tyre on concrete containing palm oil fuel ash. Int J Geomate. 2018;14(44). https://doi.org/10.21660/2018.44.3563
[9] Gupta D, et al. Novel naturally derived whey protein isolate and aragonite biocomposite hydrogels have potential for bone regeneration. Mater Des. 2020;188:108408. https://doi.org/10.1016/j.matdes.2019.108408
[10] Rather AH. Utilisation of coir fiber as reinforcement in M20 concrete mix. Int J Multidiscip Res. 2024;6(4). https://doi.org/10.36948/ijfmr.2024.v06i04.25509
[11] Johnson J, Eswari S, Saravanan R. Influence of hybrid basalt fibre with varied length on the mechanical properties of normal and high strength concrete. Res Eng Struct Mater. 2025;11(2):679-96. http://dx.doi.org/10.17515/resm2024.239me0413rs
[12] Balcioglu HE. An investigation on the mechanical strength, impact resistance and hardness of SiC filled natural jute fiber reinforced. Res Eng Struct Mater. 2019;5(3):213-31. http://dx.doi.org/10.17515/resm2019.131me0529
[13] Bennehalli B, Sampathkumar D, Punyamurth R, Venkateshappa SC. Effect of esterification on moisture absorption of single areca fiber. Int J Agric Sci. 2012;4(4):227-9. https://doi.org/10.9735/0975-3710.4.4.227-229
[14] Ghanem H, Ramadan R, Khatib J, Elkordi A. Volume stability and mechanical properties of cement paste containing natural fibers from Phragmites-Australis plant at elevated temperature. Buildings. 2024;14(4):1170. https://doi.org/10.3390/buildings14041170
[15] Li J, Wang Y, Wang X, Wu D. Crystalline characteristics, mechanical properties, thermal degradation kinetics and hydration behavior of biodegradable fibers melt-spun from polyoxymethylene/poly(l-lactic acid) blends. Polymers. 2019;11(11):1753. https://doi.org/10.3390/polym11111753
[16] Okeola AA, Abuodha S, Mwero J. Experimental investigation of the physical and mechanical properties of sisal fiber-reinforced concrete. Fibers. 2018;6(3):53. https://doi.org/10.3390/fib6030053
[17] Rashid KT, Mansour K, Abid MF, Ali SM, Abed KN. Synthesis of dimethyl carbonate for enhancement of gasoline performance. J King Saud Univ Eng Sci. 2019;31(2):171-7. https://doi.org/10.1016/j.jksues.2018.11.006
[18] Kadhem AA, Al-Yousefi HA, Jabal QA. Effects of using corn cover fibers on some mechanical properties of concrete. Key Eng Mater. 2021;895:41-9. https://doi.org/10.4028/www.scientific.net/KEM.895.41
[19] Rajkumar R, Arumugam CAK, Palanisamy S, Ayrılmış N. Mechanical properties of epoxy composites reinforced with areca catechu fibers containing silicon carbide. Bioresources. 2024;19(2):2353-70. https://doi.org/10.15376/biores.19.2.2353-2370

[20] Hamda M, Guergah C, Benmarce A, Khechekhouche A, Siqueira AMO, Campos JCC. Effects of polypropylene and date palm fiber reinforcements on high performance concrete at elevated temperatures and their impact on spalling phenomena. J Eng Exact Sci. 2023;9(12):17717. https://doi.org/10.18540/jcecvl9iss12pp17717
[21] Madjene F, Assassi M, Chokri I, Enteghar T, Lebik H. Optimization of photocatalytic degradation of rhodamine B using Box-Behnken experimental design: mineralization and mechanism. Water Environ Res. 2020;93(1):112-22. https://doi.org/10.1002/wer.1360
[22] Moasas AM, et al. Bibliographic trends in mineral fiber-reinforced concrete: a scientometric analysis. Front Mater. 2022;9. https://doi.org/10.3389/fmats.2022.1100276
[23] Rajkohila A, Prakash Chandar S, Ravichandran PT. Influence of natural fiber derived from agricultural waste on durability and micro-morphological analysis of high-strength concrete. Buildings. 2023;13(7). https://doi.org/10.3390/buildings13071667
[24] Saxena T, Chawla VK. Evaluation of mechanical properties for banana-carbon fiber reinforced nano-clay epoxy composite using analytical modeling and simulation. Res Eng Struct Mater. 2022;8(4):773-98. https://doi.org/10.17515/resm2022.403me0219
[25] Simedru AF, Cadar O, Becze A, Simedru D. Restructuring the basic design of several accelerator-based concrete mixes by integrating superplasticizers. Materials. 2024;17(22):5582. https://doi.org/10.3390/ma17225582
[26] Mishutin AV, Chintea L. The effect of modified additives on strength and frost resistance in fibrous concrete of rigid road pavements. Bull Odessa State Acad Civ Eng Archit. 2020;(80):68-74. https://doi.org/10.31650/2415-377X-2020-80-68-74
[27] Li ZK, Peng JH. Influence of polycarboxylate superplasticizer on cement hydration products. Appl Mech Mater. 2014;638-640:1354-9. https://doi.org/10.4028/www.scientific.net/AMM.638-640.1354
[28] Qi C, Huang B, Wu M, Wang K, Yang S, Li G. Concrete strength prediction using different machine learning processes: effect of slag, fly ash and superplasticizer. Materials. 2022;15(15):5369. https://doi.org/10.3390/ma15155369
[29] Wang LY, et al. Synthesis and performance of polycarboxylate superplasticizers with hydrophobic side chains. Appl Mech Mater. 2013;357-360:1124-9. https://doi.org/10.4028/www.scientific.net/AMM.357-360.1124
[30] Zhang N, Ji M, Pan T, Sun C. Application of Box-Behnken design in optimization of allelopathic effects of Potamogeton pectinatus against Microcystis aeruginosa. Trans Tianjin Univ. 2014;20(5):344-9. https://doi.org/10.1007/s12209-014-2205-y
[31] Alsadey S, Omran A. Effect of superplasticizers to enhance the properties of concrete. Design, Construction, Maintenance. 2022;2:84-91. https://doi.org/10.37394/232022.2022.2.13
[32] Attah IC, Etim RK, Alaneme GU, Bassey O. Optimization of mechanical properties of rice husk ash concrete using Scheffe's theory. SN Appl Sci. 2020;2(5). https://doi.org/10.1007/s42452-020-2727-y
[33] Kazanskaya L, Smirnova O. Influence of mixture composition on fresh concrete workability for ballastless track slabs. E3S Web Conf. 2020;157:06022. https://doi.org/10.1051/e3sconf/202015706022
[34] Kutluay S, Baytar O, Şahin Ö, Arran A. Optimization of process conditions for adsorption of methylene blue on formaldehyde-modified peanut shells using Box-Behnken experimental design and response surface methodology. Eur J Technic. 2020;131-42. https://doi.org/10.36222/ejt.649205
[35] Chkheiwer AH. Estimation of compressive strength of the concrete containing superplasticizers. Kufa J Eng. 2017;8(1):1-15. https://doi.org/10.30572/2018/KJE/811190
[36] Chowdari GK, Krishna Prasad DVV. Mechanical characterization of areca fiber and coconut shell powder reinforced hybrid composites. Mater Sci Forum. 2021;1034:61-71. https://doi.org/10.4028/www.scientific.net/MSF.1034.61
[37] Pakolpakçıl A, Kılıç A, Draczyński Z. Optimization of the centrifugal spinning parameters to prepare poly(butylene succinate) nanofibers mats for aerosol filter applications. Nanomaterials. 2023;13(24):3150. https://doi.org/10.3390/nano13243150
[38] Ren B, Wang J, Zhou Z, Du P, Zhang X. Regulation of the composition of metakaolin-based geopolymer: Effect of zeolite crystal seeds. Case Stud Constr Mater. 2023;19:e02421. https://doi.org/10.1016/j.cscm.2023.e02421
[39] Attari A, Lallotra B. Enhancing concrete mechanical properties using nano-silica, calcined clay, and glass fibers optimized by response surface methodology. Res Eng Struct Mater. 2025. http://dx.doi.org/10.17515/resm2025-492me1018rs
[40] Eddhie J. Strength development of high-performance concrete using nanosilica. Int J Technol. 2017;8(4):728. https://doi.org/10.14716/ijtech.v8i4.9485
[41] Reddy GVR, Deopura BL, Joshi M. Dry-jet-wet spun polyurethane fibers. I. Optimization of the spinning parameters. J Appl Polym Sci. 2010;118(4):2291-303. https://doi.org/10.1002/app.31373

[42] Sahib MMM, Salim SR. Influence of fiber hybridization on strength and toughness of RC beams. Civ Eng J. 2022;8(3):549-66. https://doi.org/10.28991/CEJ-2022-08-03-010
[43] Miniappan PK, et al. Exploring the mechanical, tribological, and morphological characteristics of areca fiber epoxy composites reinforced with various fillers for multifaceted applications. Front Mater. 2023;10. https://doi.org/10.3389/fmats.2023.1185215
[44] Pasma SA, Daik R, Maskat MY, Hassan O. Application of Box-Behnken design in optimization of glucose production from oil palm empty fruit bunch cellulose. Int J Polym Sci. 2013;2013:1-8. https://doi.org/10.1155/2013/104502
[45] Sadegh-Zadeh SA, et al. Machine learning modelling for compressive strength prediction of superplasticizer-based concrete. Infrastructures. 2023;8(2):21. https://doi.org/10.3390/infrastructures8020021
[46] Poonam, Singh VP. Response surface methodology use in optimization of concrete properties using blast furnace slag aggregate and recycled concrete sand. Res Eng Struct Mater. 2024;10(1):111-33.
[47] Selvam K, Balakrishnan S, Selvankumar T. Optimization of low-cost biosurfactant produced by Bacillus subtilis SASCBT01 and their environmental remediation potential. Lett Appl Microbiol. 2020;72(1):74-81. https://doi.org/10.1111/lam.13394
[48] Mohammad SF, Feng Y, Yang G. Optimization of cell culture and cell disruption processes to enhance the production of thermophilic cellulase FnCel5A in E. coli using response surface methodology. PLoS One. 2019;14(1):e0210595. https://doi.org/10.1371/journal.pone.0210595
[49] Venkateshappa SC, Jayadevappa SY, Puttiah PKW. Mechanical behavior of areca fiber reinforced epoxy composites. Adv Polym Technol. 2011;31(4):319-30. https://doi.org/10.1002/adv.20255
[50] Widodo S, Satyarno I, Tudjono S. Effects of hybrid polypropylene-steel fiber addition on some hardened properties of lightweight concrete with pumice breccia aggregate. ISRN Civ Eng. 2012;2012:1-8. https://doi.org/10.5402/2012/475751
[51] Efa DA, Gutema EM, Lemu HG, Gopal M. Friction stir-welding of AZ31B Mg and 6061-T6 Al alloys optimization using Box-Behnken design (BBD) and artificial neural network (ANN). Res Eng Struct Mater. 2024;10(1):413-30. http://dx.doi.org/10.17515/resm2023.50ma0703rs
[52] Kim JH, et al. Mechanical properties and sulfate resistance of high volume fly ash cement mortars with air-cooled slag as fine aggregate and polypropylene fibers. Materials. 2019;12(3):469. https://doi.org/10.3390/ma12030469
[53] Wang J, Yuan W, Feng R, Guo J, Dang X. Dynamic performances of ultra-high-performance fiber-reinforced concrete-strengthened concrete columns subjected to blast impacts. Adv Struct Eng. 2020;23(14):3009-23. https://doi.org/10.1177/1369433220924797
[54] ASTM C1602. Specification for mixing water used in the production of hydraulic cement concrete. 2022.
[55] Leite AM, Castro ALd. Influence of the cementitious matrix on the behavior of fiber reinforced concrete. Rev IBRACON Estrut Mater. 2020;13(3):543-62. https://doi.org/10.1590/s1983-41952020000300006
[56] Raj RR, et al. Investigation of weight fraction and alkaline treatment on Catechu linnaeus/Hibiscus cannabinus/Sansevieria ehrenbergii plant fibers-reinforced epoxy hybrid composites. Adv Mater Sci Eng. 2022;2022:1-9. https://doi.org/10.1155/2022/4861346
[57] Zhu H, Wu X, Zhang Y, Li H. Fast setting and high early strength alkali-activated fly ash synthetized with pre-polymerized suspension combined with ultrafine fly ash at ambient temperature. Case Stud Constr Mater. 2024;20:e02939. https://doi.org/10.1016/j.cscm.2024.e02939
[58] Hasgül U, Türker K, Birol T, Yavaş A. Flexural behavior of ultra-high-performance fiber reinforced concrete beams with low and high reinforcement ratios. Struct Concr. 2018;19(6):1577-90. https://doi.org/10.1002/suco.201700089
[59] Badan Standardisasi Nasional. SNI 2049-2015 - Semen Portland. 2015 [cited 2025 Jun 27]. Available from: http://sispk.bsn.go.id/SNI/DetailSNI/14305
[60] ASTM C33. Specification for concrete aggregates. 2023.
[61] ASTM C192/C192M-24. Practice for making and curing concrete test specimens in the laboratory. 2024.
[62] ASTM C39. Test method for compressive strength of cylindrical concrete specimens. 2023.

Blank Page

Research on Engineering Structures & Materials
www.jresm.org
Research Group

Research Article

Development of sustainable high performance self-compacting concrete incorporating natural and waste pozzolanic materials

Ruwaida Kareem Khoman [*,a], Haider M. Owaid [b]

Civil Engineering Department, College of Engineering, University of Babylon, Babylon, Iraq

Article Info

Article History:

Received 20 May 2025

Accepted 26 June 2025

Keywords:

Calcined kaolin clay;
Waste marble powder;
Sustainable high-performance self-compacting concrete;
Natural pozzolanic;
Waste pozzolanic;
Ground granulated blast furnace slag

Abstract

High-Performance Concrete (HPC) satisfies specific requirements (such as high strength and permeability, enhanced durability, and low shrinkage) and uniformity standards that exceed those of conventional concrete. Self-Compacting Concrete (SCC) is placed by its weight, as it is sufficiently flowable to navigate through densely reinforced areas and prevent aggregate segregation. To minimize cement usage and the associated CO2 emissions from its production, two blending systems were developed: binary and ternary, including (OPC+CKC, OPC+WMP, OPC+GGBS, OPC+CKC+WMP, and OPC+CKC+GGBS). This study examined and compared the fresh-state properties (slump flow (D (mm), L-box, and segregation resistance tests), mechanical-state properties (unit weight and compressive strength), microstructural characteristics (Scanning Electron Microscopy (SEM)) and durability properties (water absorption and chloride and sulfate resistance) of high-performance self-consolidating concrete (HPSCC) against a reference mix (M0). All HPSCC mixes satisfied EFNARC criteria, with no bleeding or segregation. The optimal ternary mix (70% OPC, 10% CKC, 20% GGBS) achieved a compressive strength of 85.2 MPa at 90 days, lowest water absorption (2.74%), and significant improvement (25.24% and 25.94%) in durability (weight loss) under chloride and sulfate exposure, respectively. SEM analysis confirmed enhanced microstructural density and reduced calcium hydroxide formation. These results highlight the potential of CKC, WMP, and GGBS as effective supplementary materials for producing eco-efficient, durable high-performance self-compacting concrete.

© 2025 MIM Research Group. All rights reserved.

1. Introduction

Self-Compacting Concrete (SCC) is a highly flowable concrete that consolidates under its own weight without external vibration, filling complex formwork and dense reinforcement while maintaining homogeneity [1]. High-Performance Concrete (HPC) enhances durability and mechanical strength through optimized mix design and curing, offering superior workability and resistance to segregation compared to conventional concrete. Both SCC and HPC are increasingly favored for demanding construction applications due to these engineered advantages [2,3]. Advancements in concrete technology have led to the development of a novel class of concrete known as High-Performance Self-Compacting Concrete (HPSCC)—a material that combines the superior properties of Self-Compacting Concrete (SCC) and High-Performance Concrete (HPC). HPSCC is characterized by its ability to flow under its own weight without the need for vibration, while also delivering exceptional compressive strength and durability. Unlike conventional concrete, HPSCC typically incorporates a higher cement content, superplasticizers, and highly reactive mineral admixtures such as silica fume. This unique composition enables the concrete to completely fill intricate formworks with congested reinforcement, ensuring self-leveling and

*Corresponding author: ruwaida.jabbar.engh354@student.uobabylon.edu.iq
[a] orcid.org/0009-0003-1600-1526; [b]orcid.org/0000-0001-7252-5875
DOI: http://dx.doi.org/10.17515/resm2025-912ma0520rs

homogeneous placement. As a result, HPSCC offers enhanced mechanical performance and long-term durability, making it ideal for demanding structural applications [4,5]. The increasing demand for cement in high-performance self-compacting concrete (HPSCC) necessitates the exploration of alternative materials to reduce cement consumption and enhance sustainability in construction. The use of alternative cementitious materials such as silica fume, ground granulated blast furnace slag, fly ash, metakaolin, limestone powder, and marble powder is highlighted as a means to develop eco-efficient concrete. These materials contribute to a significant reduction in the carbon footprint associated with traditional concrete production, aligning with global efforts to promote environmentally friendly construction practices [6-9].

Metakaolin is an environmentally friendly pozzolanic material produced by calcining kaolin clay at temperatures between 650 and 900 °C. This thermal activation process is notable for producing minimal carbon dioxide emissions, thereby positioning metakaolin as a sustainable alternative in concrete applications. Kavitha et al. [10] emphasized the benefits of incorporating metakaolin (MK) with ordinary Portland cement (OPC) in self-compacting concrete (SCC), particularly in efforts to reduce CO_2 emissions. Furthermore, studies by Melo and Carneiro [11] and Ghoddousi and Saadabadi [12] have demonstrated that metakaolin improves the viscosity of concrete mixtures and significantly enhances early-age strength due to its high pozzolanic reactivity. These properties make metakaolin both an environmentally responsible and technically effective additive in advanced concrete formulations. Ground Granulated Blast Furnace Slag (GGBS) is an industrial by-product resulting from the iron and steel manufacturing process. GGBS is an effective supplementary cementitious material that improves concrete properties. It slows the setting time, minimizes heat generation during hydration, and enhances resistance to sulfate and chloride attacks, making it particularly suitable for marine environments [1,13].

The marble industry has witnessed a significant increase in waste generation over recent decades, largely due to the alkaline nature of marble and its associated production processes. This waste, commonly produced as fine marble powder, poses environmental and health risks when improperly managed. However, the reuse of marble waste in concrete presents a promising sustainable strategy to mitigate its environmental impact [14,15]. Studies such as that by Tennich et al. [16] have shown that incorporating marble waste into self-compacting concrete (SCC) can improve fresh properties by reducing plastic shrinkage. Additionally, the high calcium content in marble dust (MD) contributes to enhanced strength development in hardened SCC [17]. A recent investigation by Djeddou et al. [18] explored the valorization of three local Algerian waste materials—marble powder (MP), ground granulated blast furnace slag (GGBS), and glass fibre-reinforced plastic waste (GFRPW)—as mineral additives in SCC. This study offers valuable insights into optimizing the use of MP, GGBS, and GFRPW in SCC, thereby promoting more sustainable and cost-effective concrete production.

In general, binary and ternary concrete mixes—those that combine two or three cementitious materials—offer significant advantages over mixes containing only Portland cement or blended cement. By using two types of supplementary cementitious materials (SCMs) in a ternary blend, the combined properties of each component can be synergistically optimized. This approach can enhance key performance aspects of concrete, such as early and late-age strength, workability, durability, and cost-effectiveness. Water absorption, which is directly related to a concrete's resistance to water penetration, plays a crucial role in various deterioration mechanisms. Like other engineering properties, concrete's water absorption is strongly influenced by its porosity, which governs the microstructure. Therefore, the absorption capacity depends on the quantity and distribution of pores of different sizes. As porosity decreases, water absorption also tends to reduce. It has been reported that the rate of water absorption in self-compacting high-performance concrete (SCHPC) typically ranges between 3% and 6% [19]. Sulfate ions, which may originate from soil, groundwater, or seawater, are often present alongside other ions such as sodium, potassium, magnesium, and calcium. The impact of sulfates on concrete durability depends on both the chemical form of the sulfate and the environmental conditions to which the concrete is exposed. Sulfate attack compromises durability by reacting with the cement matrix, leaching out calcium ions and replacing them with magnesium or sodium ions. This substitution leads to the formation of expansive sulfate compounds, increasing internal stress and causing microcracking within the

concrete [20].The incorporation of pozzolanic materials such as ground granulated blast furnace slag (GGBS), fly ash (FA), metakaolin (MK), and silica fume (SF) as partial replacements for cement has proven effective in enhancing resistance to sulfate attack [21,22]. The impact of chloride on concrete durability, however, remains a debated topic. Gruber et al. [23] studied the effect of high-reactivity metakaolin (HRM) on chloride diffusion in concrete over 365 days. Their findings indicated that increasing HRM content reduced the diffusion coefficients, particularly with longer exposure durations and lower water-to-binder (w/b) ratios. Additionally, the partial replacement of cement with GGBS has shown promise in enhancing concrete's resistance to chloride penetration [24]. Chandru et al. [25] investigated ternary blends of SCC with crushed stone and induction furnace slag, demonstrating that such systems can significantly enhance durability while maintaining workability and compressive strength. Vivek [26] developed self-compacting concrete (SCC) using a ternary blend system. The fresh property test results—including slump flow, T500 time, V-funnel, L-box, and U-box tests—met the criteria established by EFNARC guidelines. However, it was observed that higher levels of cement replacement using metakaolin (MK) and ground granulated blast furnace slag (GGBS) led to a reduction in filling ability and passing ability in the ternary SCC mixes. The optimal performance was achieved when 30% GGBS was blended with either 5% or 15% MK, resulting in improved strength characteristics. Similarly, Chavan et al [27] demonstrated that multi-blended M70-grade concrete incorporating supplementary cementitious materials (SCMs) not only enhances durability but also provides economic advantages by reducing overall life cycle costs. These findings offer valuable insights for engineers and decision-makers seeking to design durable, cost-effective, and sustainable concrete structures.

This study aims to investigate the fresh, mechanical, and durability properties of High-Performance Self-Compacting Concrete (HPSCC) incorporating alternative supplementary cementitious materials such as calcined kaolin clay (CKC), ground granulated blast furnace slag (GGBS), and waste marble powder (WMP). The research also seeks to compare the performance of these mixes with conventional Self-Compacting Concrete (SCC) to evaluate the effectiveness of these materials in enhancing overall concrete performance, reducing cement consumption, and achieving environmental and economic benefits through lower CO_2 emissions and improved structural durability.

2. Materials and Experimental Procedure

This study introduces a novel approach by integrating locally available pozzolanic materials—CKC, WMP, and GGBS—into ternary blends to develop sustainable HPSCC. Unlike previous studies focusing on limited combinations, this work explores the synergistic effects of these materials, particularly ternary mixes such as 10% CKC + 10% WMP and 10% CKC + 20% GGBS, which showed superior strength, durability, and microstructural performance. By maintaining a constant water-to-binder ratio and assessing a broad range of properties, the study provides a holistic evaluation, contributing to the advancement of durable, eco-efficient concrete for modern infrastructure. The flowchart (Fig. 1) outlines the five major stages: preparation of materials, mix design, mixing and casting, fresh tests, and hardened & durability tests.

2.1. Materials

Ordinary Portland Cement (OPC-CEM I) produced by Lafarge, complies with the Iraqi Standard IQS 5 [28] was used. It has a specific gravity of 3.12 and a specific surface area (SSA) of 358 m^2/kg, indicating its quality and suitability for construction applications. The production of Calcined Kaolin Clay (CKC) in this study utilized Iraqi kaolin clay sourced from the Dewekhla region in the Al Ramadi desert. The raw clay was first ground and then thermally activated by calcination in a furnace at approximately 800 °C for two hours, with a controlled heating rate of 5 °C/min. After calcination, the material was allowed to cool gradually to room temperature over a period of 24 hours. This method of thermal treatment is consistent with the procedures reported by Khoman and Owaid [29]. Following calcination, the CKC was further processed using the air blast grinding technique to enhance its fineness, resulting in a high-quality pozzolanic material. Chemical analysis revealed that the combined content of the major oxides—SiO_2, Al_2O_3, and Fe_2O_3—exceeded 70%, thereby meeting the requirements of ASTM C618 [30] for Class N natural pozzolans. Additionally,

the specific gravity of CKC was determined to be 2.6, and its specific surface area (SSA) was measured at 1640 m^2/kg, indicating its suitability as a supplementary cementitious material in construction applications.

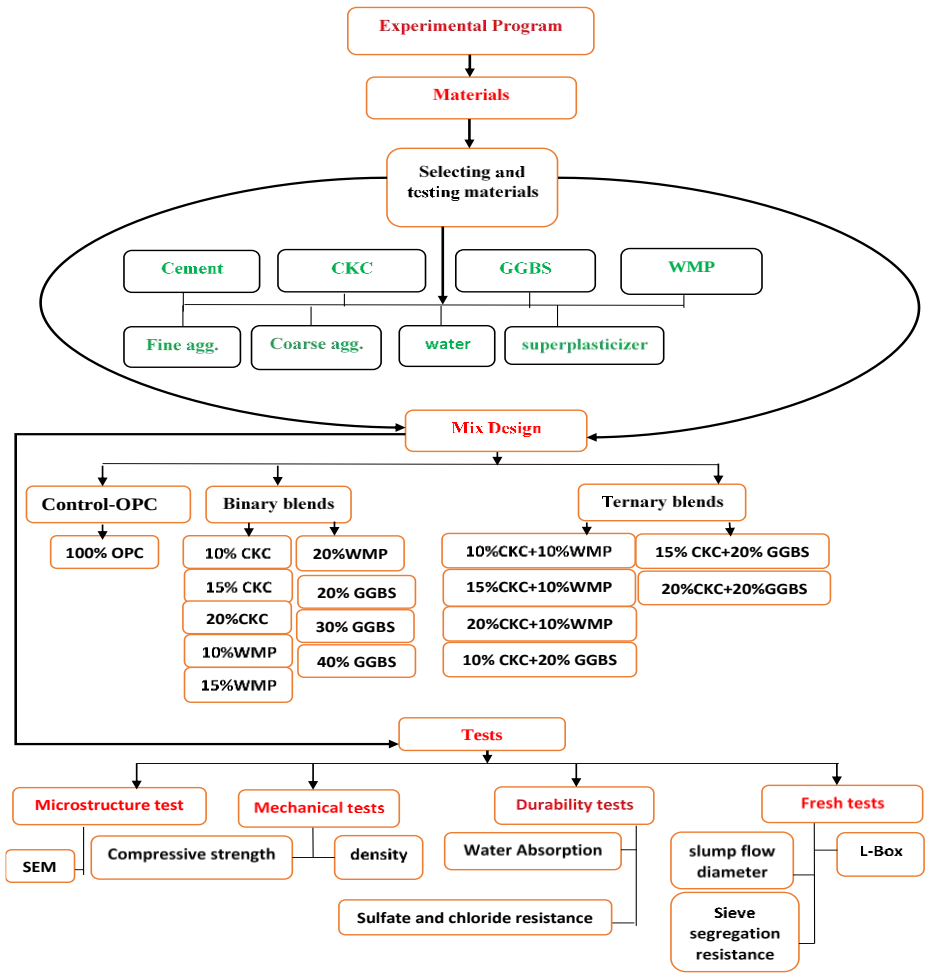

Fig. 1. Flowchart of the experimental procedure

Waste Marble Powder (WMP) sourced from marble masonry operations in Al-Hilla, Iraq. Collected as sludge during the marble cutting process, the WMP is dried before analysis. The findings reveal that WMP contains 85.62% calcium oxide, indicating potential use as a cement substitute due to its cementitious properties. Additionally, the specific gravity of WMP is measured at 2.68, which is slightly lower than that of OPC, while its specific surface area is found to be 569 m^2/kg. Ground granulated blast furnace slag (GGBS) is recognized for its environmental benefits as a by-product in construction. It requires less energy and generates considerably lower carbon dioxide emissions compared to traditional Portland cement [31]. The GGBS studied adheres to ASTM C989 [32] standards, is characterized as a fine white powder, and serves as a partial replacement for cement. With a specific gravity of 2.9 and a specific surface area of 418 m^2/kg, GGBS demonstrates a lower density and higher surface area than OPC, enhancing its utility in sustainable building practices.

The critical factors influencing the production of high-performance self-compacting concrete, specifically the fine aggregate's quantity, grading, and particle shape. The fine aggregate analyzed is local sand from the Al-Ukhaidher region, which satisfies the third grading zone criteria and complies with Iraqi standards IQS 45 [33], having a fineness modulus of 2.52. The coarse aggregate used is crushed and washed gravel from the Al-Nabai'i area, with a maximum size of 10 mm, also meeting relevant Iraqi specifications. SikaViscocrete-180GS is a superplasticizer admixture formulated from polycarboxylic ether, designed specifically for the ready-mix concrete industry. This admixture is based on polycarboxylic ether and is an economical high-range water reducer

that enhances early and final strength while maintaining workability. SikaViscocrete-180GS meets the requirements of ASTM C494[34] Type F&G based on dosage.

2.2. Mix Proportions

Table 1 presents the mix proportions of the developed HPSCC mixes in kg/m^3, with a constant w/b ratio of 0.33 and total binder content of 530 kg/m^3. Table 2 compares the actual values of key parameters with EFNARC recommendations [35] to validate compliance. The concrete mixtures were developed using two blending systems—binary and ternary—executed in two distinct phases to evaluate their performance and effectiveness. In the first phase, a control mix was prepared using only ordinary Portland cement (OPC). Subsequently, binary blend systems were developed by partially replacing OPC with 10%, 15%, and 20% of calcined kaolin clay (CKC); 10%, 15%, and 20% of waste marble powder (WMP); and 20%, 30%, and 40% of ground granulated blast furnace slag (GGBS) by mass.

Table 1. Mix proportions of HPSCCs

Mix Num.	Mix Notation	*W/B*	Quantities of ingredients (kg/m3)						
			OPC	CKC	WMP	GGBS	FA	CA	SP
M0	Control-OPC	0.33	530	-	-	-	872	887	10.6
M1	10%CKC	0.33	477	53	-	-	872	887	10.6
M2	15%CKC	0.33	450.5	79.5	-	-	872	887	10.6
M3	20%CKC	0.33	424	106	-	-	872	887	10.6
M4	10%WMP	0.33	477	-	53	-	872	887	10.6
M5	15%WMP	0.33	450.5	-	79.5	-	872	887	10.6
M6	20%WMP	0.33	424	-	106	-	872	887	10.6
M7	20%GGBS	0.33	424	-	-	106	872	887	10.6
M8	30%GGBS	0.33	371	-	-	159	872	887	10.6
M9	40%GGBS	0.33	318	-	-	212	872	887	10.6
M10	10%CKC+ 10%WMP	0.33	424	53	53	-	872	887	10.6
M11	15%CKC+ 10%WMP	0.33	397.5	79.5	53	-	872	887	10.6
M12	20%CKC+ 10%WMP	0.33	371	106	53	-	872	887	10.6
M13	10%CKC+ 20%GGBS	0.33	371	53	-	106	872	887	10.6
M14	15%CKC+ 20%GGBS	0.33	344.5	79.5	-	106	872	887	10.6
M15	20% CKC+ 20%GGBS	0.33	318	106	-	106	872	887	10.6

Table 2. Comparison with EFNARC recommendations [35]

Constituent	Typical range by mass (kg/m3)	Values Used in Study	Compliance
Water	150-210	174.9	✓ Compliant
Binder Content	380 – 600 kg/m^3	530 kg/m^3	✓ Compliant
Coarse Aggregate	750-1000	887	✓ Compliant
Fine Aggregate	48 – 55% of total aggregate weight.	49.6%	✓ Compliant

In the second phase, ternary blend systems were formulated using two combinations: OPC + CKC + WMP and OPC + CKC + GGBS. In the first combination, CKC was used at replacement levels of 10%, 15%, and 20%, each combined with a fixed 10% of WMP. In the second combination, CKC was used at 10%, 15%, and 20% replacement levels, each combined with a fixed 20% of GGBS. All replacements were made by mass as partial substitutes for OPC.

2.3. Preparation of Specimen

The process of concrete mixing was conducted within a laboratory setting, adhering to a stringent temperature regulation of 25±2°C, utilizing a horizontal drum mixer apparatus. Subsequent to the mixing process, the freshly prepared concrete was transferred into standardized cube molds, each measuring 100 mm on all sides. In order to facilitate adequate curing, the specimens were enveloped in nylon sheeting and retained in the casting room for a duration of 24 hours prior to their demolding. Following the demolding procedure (Fig.2), the specimens were immersed in a water basin for additional testing at ambient temperature at specified ages.

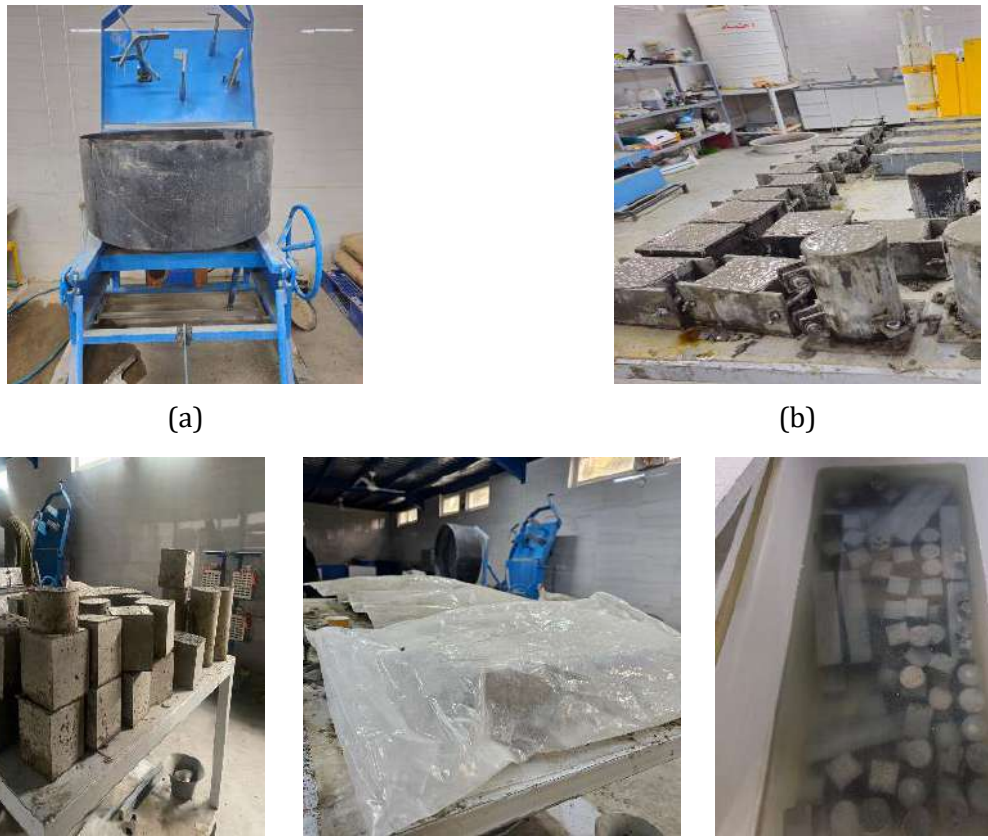

(a) (b) (c) (d) (e)

Fig. 2. (a) Mixing (b-d) casting process and (e) curing of test specimens for HPSCC

2.4. Testing Methods

2.4.1 Fresh Tests

Fresh properties of HPSCC are critical for its performance in construction. According to EFNARC [35], three main properties need evaluation: passing ability, segregation resistance, and filling ability. However, no single test can assess all these characteristics at once. The study utilizes the slump flow measurements to evaluate filling ability Fig. 3(a), sieve segregation resistance for segregation assessment Fig. 3(b), and L-box test for passing ability Fig. 3(c), providing a comprehensive understanding of HPSCC's fresh properties.

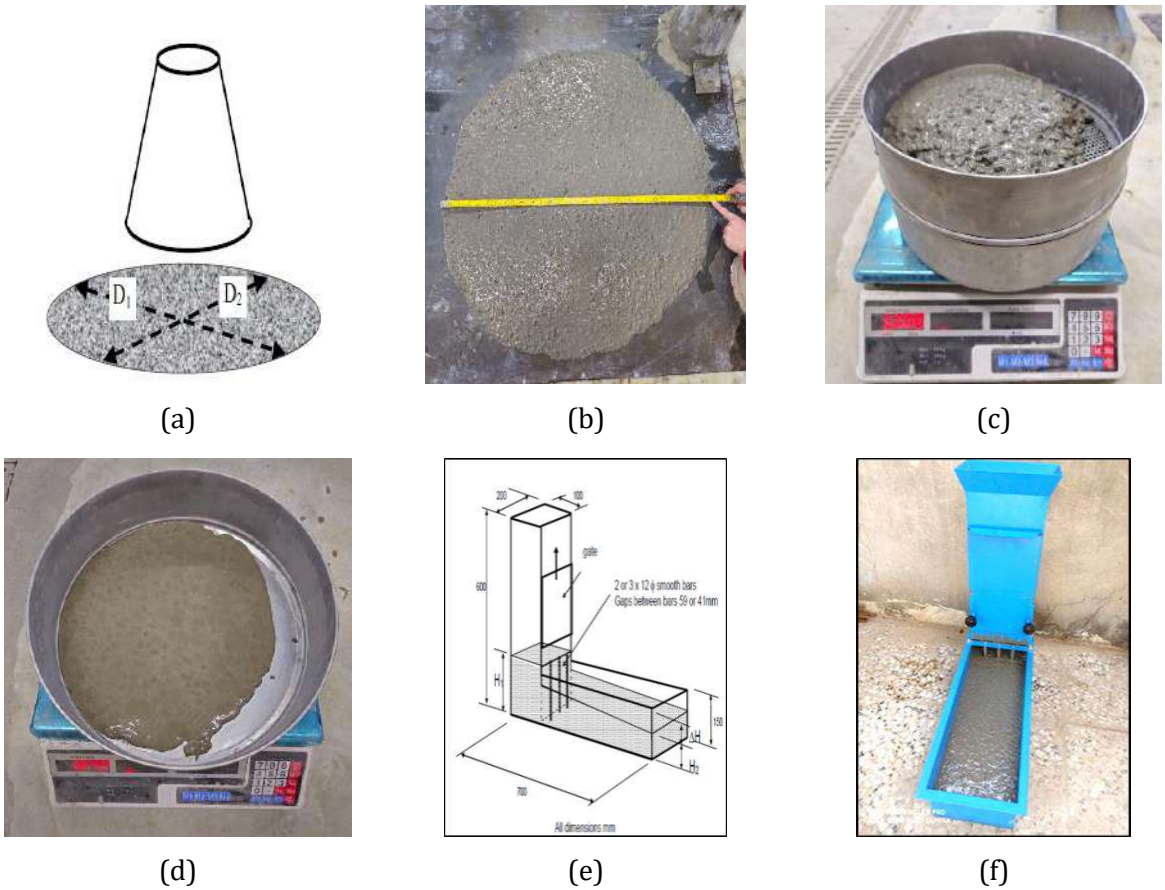

Fig. 3. (a-b) Slump (c-d) sieve segregation resistance and (e-f) L-box tests for HPSCC

2.4.2 Mechanical Tests

Essential tests for hardened concrete in this study included density measurement, scanning electron microscopy (SEM), and compressive strength evaluation. The density of the concrete was measured in kg/m^3 in accordance with BS 1881: Part 114 [36]. It was determined by calculating the mass-to-volume ratio of standard cube specimens (100 × 100 × 100 mm) prior to compression testing at curing ages of 7 and 28 days.

Fig. 4. Compressive strength test

The compressive strength test was conducted to assess the mechanical performance and structural integrity of the concrete. All procedures followed BS 1881: Part 116 [37], using 100 mm cubic specimens. For each mix, the average compressive strength was calculated based on the results of three specimens tested at 7, 28, and 90 days of curing. A compression testing machine with a capacity of 1900 kN was used to apply load until failure occurred. The compressive strength was

then computed by dividing the maximum applied load by the cross-sectional area of the specimen (see Fig. 4).

The microstructure of HPSCC specimens containing blended pozzolanic materials was examined using scanning electron microscopy (SEM). SEM analysis was performed on selected mixes (M1, M4, M7, M10, and M13) that exhibited optimal compressive strength at 28 days, and the results were compared with the reference mix (M0), in accordance with ASTM C1723 [38]. Concrete cube cores were sectioned using a precision saw to obtain specimens measuring 10 × 10 × 10 mm. The SEM examination was conducted using a high-resolution setup with an accelerating voltage of 20 kV (HV: 20 kV) at various magnifications to capture detailed surface morphology and microstructural features.

2.4.3 Durability Tests

The water absorption test was carried out in accordance with ASTM C642 [39] to evaluate the volume of voids in hardened concrete and assess the concrete's resistance to water penetration. The test was conducted on all mixtures at 28 and 90 days (following initial 28-day curing).
Cube specimens measuring 100 × 100 × 100 mm were first oven-dried at 110 ± 5 °C for a minimum of 24 hours until a constant mass was achieved (dry mass A). The specimens were then immersed in tap water for at least 48 hours. Saturation was considered reached when two consecutive mass measurements taken 24 hours apart showed either constant mass or a mass increase of less than 0.5% of the higher value. After immersion, the surface of each specimen was quickly wiped with a damp cloth, and the saturated surface-dry mass (B) was recorded immediately. The percentage of water absorption (WA) was then calculated using the following equation Eq (1):

$$WA\ (\%) = [(B - A) / A] \times 100 \quad (1)$$

Where, WA: Water absorption, A: Oven-dried mass, B: Saturated surface-dry mass.

This test allowed the determination of the total volume of permeable pores in the concrete, providing a key indicator of its durability performance. Sulfate and chloride ions are among the most aggressive agents affecting the durability of concrete structures. In this study, durability assessment was conducted in two stages.In the first stage, concrete cube specimens (100 × 100 × 100 mm) were submerged separately in 5% sodium sulfate (Na_2SO_4) and 5% sodium chloride (NaCl) solutions for 90 and 180 days, following an initial 28-day period of water curing. As per ASTM C1012 [40], each liter of solution was prepared by dissolving 50 grams of either NaCl or Na_2SO_4 in 900 mL of water, and then diluting with distilled or deionized water to reach a total volume of 1.0 L. The solutions were prepared one day in advance, stored at a controlled temperature of 23 ± 2 °C, and renewed monthly throughout the exposure period.In the second stage, the weight change of the HPSCC specimens was monitored at various ages. After 28 days of moist curing, the initial weight of each specimen was recorded as the reference weight (W_0). The specimens were then exposed to NaCl and Na_2SO_4 solutions separately and reweighed after 90 and 180 days of exposure (denoted as W_i). The cumulative weight change was calculated using the following equation Eq (2):

$$Weight\ Change\ (\%) = [(W_i - W_0) / W_0] \times 100 \quad (2)$$

Where, W_i: Weight after 90 and 180 days of exposure to NaCl and Na_2SO_4 solutions separately, W_0: Reference weight.

3. Results and Discussion

3.1. Fresh Properties, Results and Discussion

In self-compacting concrete (SCC), powder content plays a crucial role in determining flowability and stability. According to EFNARC [35], the total powder content, including cement and supplementary cementitious materials (SCMs), should generally exceed 380 kg/m^3 to ensure sufficient cohesiveness and viscosity. In this study, the powder content was maintained at 530 kg/m^3 across all mixes, aligning with these recommendations. One of the key parameters

influencing the fresh behavior of HPSCC is the particle size distribution of the powder materials. Fine particles, especially those smaller than 125 microns, contribute significantly to the mix's rheological properties. These ultrafine particles fill voids between larger aggregates, leading to improved particle packing density. As a result, internal friction is reduced, enhancing the mixture's flowability. Materials such as Calcined Kaolin Clay (CKC), Waste Marble Powder (WMP), and Ground Granulated Blast Furnace Slag (GGBS) used in this study contained a substantial proportion of particles below 125 μm. For example, CKC, with a specific surface area of 1640 m^2/kg, provided high fineness and reactivity, thereby increasing the mixture's cohesiveness and reducing the risk of segregation. WMP, with its smooth morphology and fine particle structure, acted as a filler that enhanced deformability and helped in achieving high slump flow values. Similarly, the finely ground particles of GGBS contributed to improved lubrication within the paste matrix, facilitating better flow. However, an excessive amount of ultrafine powder can increase water demand and reduce flow [41]. In this study all HPSCC mixtures achieved slump flow diameters ranging from 740 to 845 mm (Fig. 5), corresponding to the SF3 classification according to EFNARC guidelines, with the exception of binary mixtures containing 20% CKC, which fell under the SF2 category.

Consequently, all mixtures were deemed to possess satisfactory consistency and workability from a filling perspective. For the reference mixture (M0), comprising only of ordinary Portland cement (OPC), the slump flow diameter was recorded at 800 mm, whereas the slump flow diameters for mixtures M1, M2, and M3 were 780 mm, 765 mm, and 740 mm, respectively (the minimum flow diameter). It was observed that the inclusion of 10%, 15%, and 20% CKC resulted in a reduction of the flow diameter by 2.5%, 4.37%, and 7.5%, respectively. Notwithstanding the dosage of superplasticizer (SP) being maintained at 2%, the flow diameter experienced a decrement due to the incorporation of CKC. The decline in filling capacity signifies that the addition of up to 20% CKC adversely impacts the consistency of the concrete. This may attribute to CKC's particles size which is can be categorised as an ultra-fine and pozzolanic reactivity produced the internal friction among the grains increased. Therefore, this friction causes a loss of fluidity (deformability) [41,42]. For the mixtures incorporating WMP, M4, M5, and M6, the slump flow diameters were recorded at 805 mm, 810 mm, and 825 mm, respectively. It was observed that in comparison to M0, the increase of the replacement levels of WMP enhances flowability (deformability). This improvement was manifested in the M4, M5, and M6 mixtures, which demonstrated increases in flowability of 0.63%, 1.25%, and 3.13% relative to M0, respectively. This modest enhancement can be primarily attributed to the fine particle size of the marble powder, which facilitates more efficient particle packing and marginally diminishes internal friction within the mixture [43,44].

For the mixtures incorporating Ground Granulated Blast Furnace Slag (GGBS), the formulations M7, M8, and M9 attained slump flow diameters of 820 mm, 835 mm, and 845 mm, respectively, thereby signifying enhanced flow diameters. It was noted that, in contrast to M0, augmenting the levels of GGBS replacement significantly improves flowability (deformability). This enhancement was evident in the M7, M8, and M9 mixtures, which exhibited increases in flowability of 2.5%, 4.37%, and 5.62% in relation to M0, respectively. The fine particles of GGBS serve to occupy the voids present between the aggregate sand and cement, thereby facilitating an improved flow of the concrete mixture, as a reduced quantity of water is necessitated for lubrication, consequently leading to an elevated slump value [45]. Regarding the ternary mixtures (M10, M11, M12, M14, and M15), it was documented that the slump diameter values diminished by 0.63%, 2.5%, 4.37%, 1.87%, and 3.13%, respectively, when compared to M0. Conversely, for M13, the slump flow diameter attained 800 mm, which exhibits equivalent flowability to that of M0, thus preserving the workability of the concrete. In comparison with binary blends inclusive of CKC, the slump diameter value of the ternary blend demonstrated an increase. The prospective utilization of the combinations of CKC + WMP and CKC + GGBS as partial cement replacements within a ternary blending framework yielded satisfactory fresh properties of High-Performance Self-Compacting Concrete (HPSCC). The incorporation of GGBS in the HPSCC mixtures improved the fresh properties and effectively mitigated the reduction in workability associated with the use of CKC. Additionally, the inclusion of WMP in ternary blends further enhanced the workability of HPSCC. These findings

reinforce the significant influence of supplementary cementitious materials on the rheological behavior of cementitious systems[46,47].

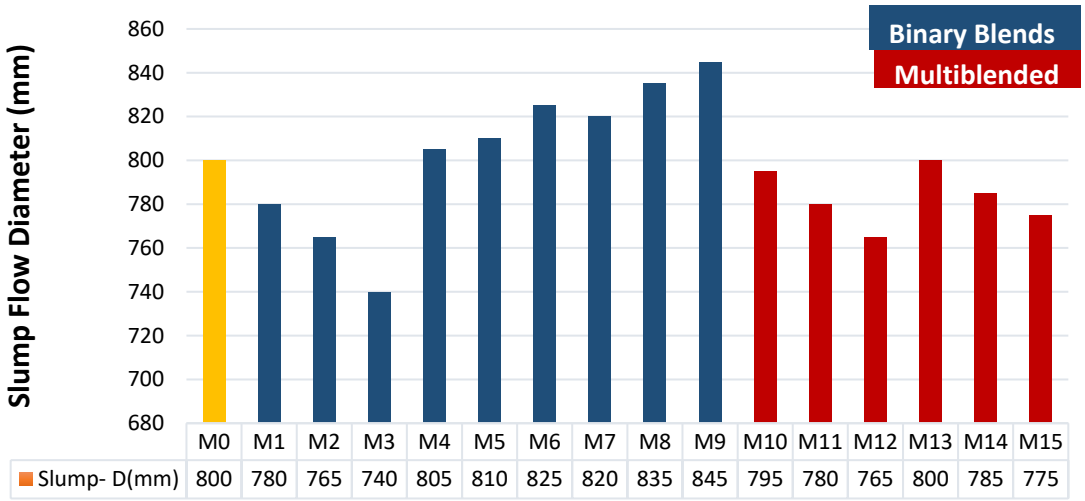

Fig. 5. Slump flow diameter results of HPSCCs

The elevated passing ability (PA) value signifies an enhanced capacity for the concrete mixture to facilitate the flow of materials. The PA values recorded range from 0.874 to 0.996(Fig.6), classifying the mixtures within the second category (PA2) as delineated by the standards established by EFNARC [35]. No evidence of segregation or blockage was detected in any of the concrete mixtures analyzed. The PA values determined for mixtures M0, M1, M2, and M3 were 0.948, 0.936, 0.912, and 0.874, respectively. The observed decline in PA is attributed to the incorporation of calcined kaolin clay (CKC), which may adversely affect the passing ability of the mix. It is evident that the integration of CKC results in a diminished passing ability due to a concomitant reduction in fluidity. This phenomenon may be explained by the geometric configuration of the long, hexagonal plates of CKC, which may create impediments within the fresh mixture and augment the frictional forces among the constituent particles. Furthermore, the fine particulate nature of CKC, characterized by a markedly increased surface area capable of water absorption, results in a reduction of free water availability, thereby impairing the flow capability [48]. The passing ability of the mixtures M4, M5, and M6 was determined to be 0.962, 0.976, and 0.980, respectively, demonstrating that the flow as measured by the L-box test improved concomitantly with increasing percentages of waste material powder (WMP). An increase in WMP content correlates with enhanced workability in high-performance self-consolidating concrete (HPSCC), as it increases the free water quantity available to bolster the filling capacity of the concrete matrix. Moreover, the volume of paste relative to the aggregate content is elevated, which effectively diminishes the frictional interactions among the aggregate particles [49].The passing ability of concrete mixtures M7, M8, and M9, which were found to have passing ability scores of 0.984, 0.991, and 0.996, respectively. The results indicate a correlation between the percentage of GGBS in the mixtures and their passing ability, with higher GGBS percentages leading to improved flow characteristics. This enhancement is likely due to the particle size of GGBS, which reduces internal friction, thus improving the fluidity and passability of the mixtures, as noted by [1].

However, for the ternary blend mixes (M10, M13, and M14), the passing ability increased by 0.32%, 1.37%, and 3.90% compared to M0. It is noted that the passing ability of (M11, M12, and M15) decreased by 1.05%, 3.59%, and 2.22% in comparison with M0. In comparison with binary blends containing CKC, the passing ability of the ternary blend mixtures was enhanced. The potential use of the combinations CKC + WMP and CKC + GGBS as partial cement replacements resulted in satisfactory fresh properties of HPSCC. The enhancement in the passing ability of concrete mixtures is attributed to the particle size of GGBS, which reduces internal friction and enhances fluidity.

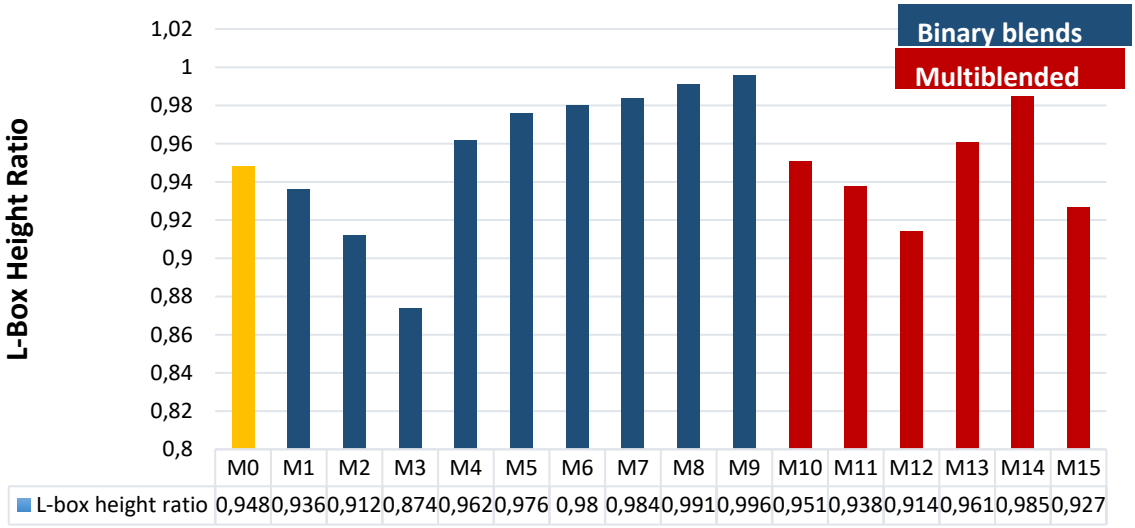

Fig. 6. L-box height ratio results of HPSCCs

The inclusion of WMP further improves the workability of HPSCC by increasing the free water content, thus enhancing filling ability and reducing friction among aggregate particles [1,49). The segregation ratio exhibited a range spanning from 9.7% to 14.6% (SR2 class) (Fig.7). Analyzing the segregation data allows for the inference that all High-Performance Self- Compacting Concrete (HPSCC) samples possess commendable quality and demonstrate acceptable segregation resistance as per EFNARC [35]. The segregation ratio (SR) values recorded for mixtures M1, M2, and M3 were determined to be 11.3, 10.8, and 9.7, correspondingly. It is evident that the binary mixtures (10% CKC, 15% CKC, and 20% CKC) exhibit superior segregation resistance compared to the control mixture (M0), as the segregation percentage diminishes with an increased proportion of partial replacement. The observed percentage reductions were approximately 7.38%, 11.48%, and 20.49% for the aforementioned binary mixtures, respectively, thereby indicating enhanced resistance to segregation. The ultrafine particles derived from CKC displayed a high level of reactivity, which facilitated hydration and augmented the viscosity of the mixture [41,42].

As the percentages of Waste Marble Powder (WMP) increased (M4, M5, and M6), the segregation ratios escalated by 4.92%, 7.74%, and 9.02%. The elevation of WMP content resulted in a less cohesive concrete mixture, yielding a higher slump flow while concomitantly lowering the flow time. A reduction in cohesiveness leads to an increased separation of mortar, consequently yielding a higher segregation ratio, which indicates that viscosity diminishes with the augmentation of the marble powder ratio [50]. It noted that, the GGBS replacement level increases, the segregation ratio also rises significantly, with the highest increase observed at 40%. Specifically, the segregation ratios increased by 12.3%, 14.75%, and 19.67% for 20%, 30%, and 40% GGBS replacements, respectively, compared to a control mix. Increasing the replacement levels of GGBS up to 40% gives a higher flowability and lower viscosity of concrete, thus resulting in a higher value of segregation ratio [6,51]. Whereas, ternary blend mixes (M10, M11, M12, M14, and M15) have a higher segregation resistance compared with control mix (M0). That is, the segregation ratio decreased by 1.63%, 4.09%,7.38%,0.82%, and 5.74%, respectively in comparison to (M0). But the segregation ratio for (M13) increased by 4.09 % in comparison to (M0). This is a result of the synergistic effect of the reasons explained above; no segregation or blocking phenomena were experimental in the mixes during the test execution [6,41] and [50,51].

Overall, the mixtures exhibit good workability, consistency, and stability, with GGBS and WMP effectively compensating for fluidity reductions caused by CKC. The significant correlation between slump flow diameter and segregation ratio in High- Performance Self-Consolidating Concrete (HPSCC) mixes were shown in Fig 8., with a correlation coefficient of 0.9529. This strong linear relationship suggests that measuring the slump flow can effectively indicate the segregation resistance of HPSCCs, highlighting the importance of slump flow in evaluating the performance of these concrete mixes.

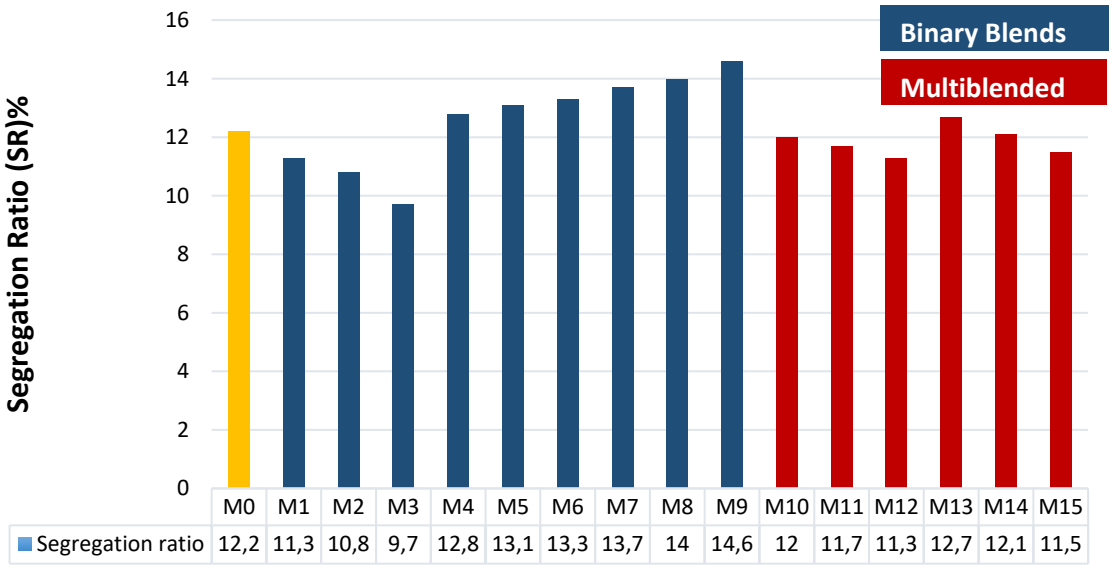

Fig. 7. Segregation ratio results of HPSCCs

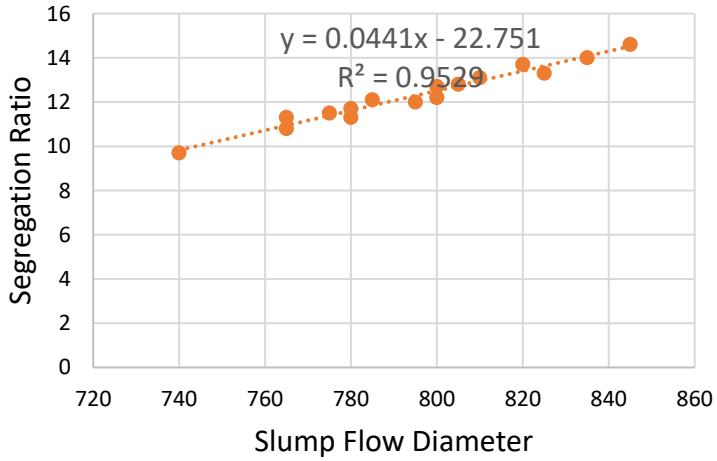

Fig. 8. Relationship between slump flow diameter and segregation ratio of HPSCCs

3.2. Mechanical Properties – Results and Discussion

The self-weight of any structure is completely dependent on the unit weight of the ingredient materials. The HPSCC mixtures density decreased as the pozzolan percentage (CKC, WMP, and GGBS) replacement increased (Fig. 9). The density of all HPSCC mixes increased with curing age. The observed percentage reductions in the density of HPSCCs (M1-M15) were (0.77, 1.06, 1.42, 0.45, 0.77, 1.38, 0.28, 0.61, 1.22, 1.26, 1.47, 1.75, 1.10, 1.34, and 1.59) % at the 28-day respectively, in compared to the control mixture (M0). A further decline in density was noted in ternary mixtures, with the most significant reduction recorded in mixture M12, which comprised 20% CKC and 10% WMP. This phenomenon can be rationalized by the observation that the specific gravity of the pozzolanic materials is lower than that of cement, resulting in a diminished mass per unit volume [50,52]. Therefore, CKC, WMP, and GGBS can be utilized in mortar or concrete as lighter alternatives to cement. The findings are promising in reducing the self-weight of structures on soils with poor bearing capacity to some extent.

The experimental outcomes regarding the compressive strength of the specimens, as depicted in Fig.10, suggest that all concrete formulations generated within the scope of this investigation exhibit high-performance characteristics, with the strength at 28 days varying from 63.7 to approximately 79.2 MPa, and the strength at 90 days ranging from 69.7 to 85.2 MPa. Collectively,

the findings elucidate that all high-performance self-compacting concrete (HPSCC) mixtures exhibit a gradual enhancement in compressive strength corresponding with the extended duration of curing. This increment in compressive strength of the specimens is ascribed to the persistent hydration process that engenders novel hydration products within the concrete matrix. The compressive strength of binary blends incorporating CKC (M1, M2, and M3) increased by 10.25%, 7.32%, and 2.26%, respectively, in relation to the control mix (M0) at the 90-day mark.

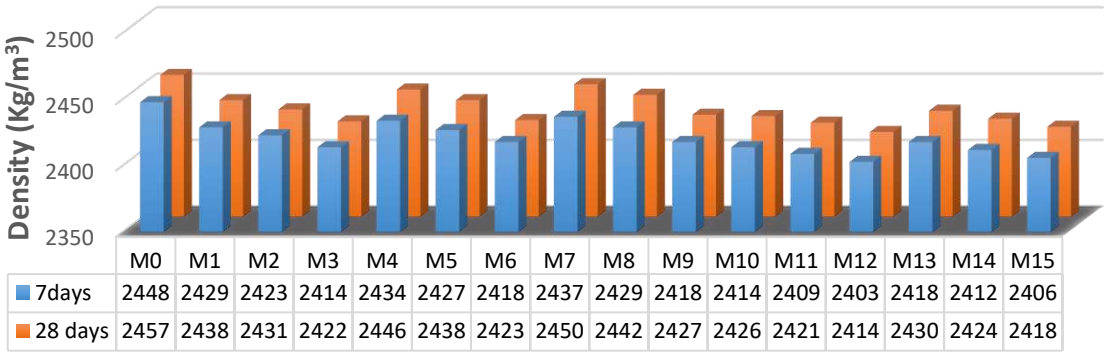

	M0	M1	M2	M3	M4	M5	M6	M7	M8	M9	M10	M11	M12	M13	M14	M15
7days	2448	2429	2423	2414	2434	2427	2418	2437	2429	2418	2414	2409	2403	2418	2412	2406
28 days	2457	2438	2431	2422	2446	2438	2423	2450	2442	2427	2426	2421	2414	2430	2424	2418

Fig. 9. Density results of HPSCCs

It is significant to note that the compressive strength was maximized in the formulation incorporating 10% CKC (M1), achieving a strength of 82.8 MPa at 90 days. This enhancement can be primarily attributed to the finer particle size of CKC, which augments its reactivity with $Ca(OH)_2$, thereby facilitating the formation of additional calcium silicate hydrate (C–S–H) and(C-A-H), subsequently, superior compressive strength. The reduced particle size of CKC further contributes to this gain in strength [53,54]. However, an increase in CKC content to 15% and 20% precipitates a decline in compressive strength in comparison to the 10% substitution level. This reduction can be elucidated by the clinker dilution effect, which emerges when a portion of the cement is supplanted by CKC. In CKC concrete, the filler effect, the pozzolanic interaction between CKC and calcium hydroxide, and the synergistic influence of mineral admixtures serve to mitigate the dilution effect [53,55]. Concerning binary blends utilizing WMP, mixtures M4 and M5 exhibited compressive strength enhancements of 5.73% and 1.99%, respectively, whereas mixture M6 encountered reductions of 7.19% and 6.66% at 90 days when assessed against the control mix (M0). The data clearly show that the 10% replacement of WMP yields the highest compressive strength of 79.4 at 90 days.

The study investigates the impact of fine particles from WMP on concrete strength, demonstrating a notable improvement in compressive strength due to the filling of micro-pores in the concrete matrix [47]. Increasing the WMP content to 15% and 20% leads to a decline in strength, showing that optimal benefits are realized at or below the 10% mark. In binary blends with GGBS, 20% GGBS blend exhibited the highest compressive strength, reaching 80.3. The chemical reactions between GGBS and calcium hydroxide lead to the formation of additional C-S-H gel compounds, improving overall strength [26,56]. Various ternary mixes demonstrated increased compressive strength at 90 days, with mix M13 exhibiting the highest strength of 85.2 MPa. Conversely, mix M15 experienced a slight decrease in strength. The incorporation of pozzolanic materials, specifically 20% Ground Granulated Blast Furnace Slag (GGBS) and fine particles of calcined Kaolinite Clay (CKC), contributes to strength improvement in high-performance self-compacting concrete.

GGBS serves as a filler, increasing packing density and chemically reacting with calcium hydroxide to form additional crystalline C-S-H gel, which enhances the cohesive transition zone and overall compressive strength (26,46). CKC further aids in sealing micro-pores, thereby enhancing the concrete's durability and strength. It highlights that the combination of CKC and WMP yields higher compressive strength compared to when they are used separately. However, specific mixes,

particularly those with 20% CKC and varying percentages of WMP or GGBS, exhibit a reduction in strength, attributed to limited calcium hydroxide availability and slower GGBS reactivity. Increased CKC proportions may also negatively impact strength due to greater surface area [13,47, 51].

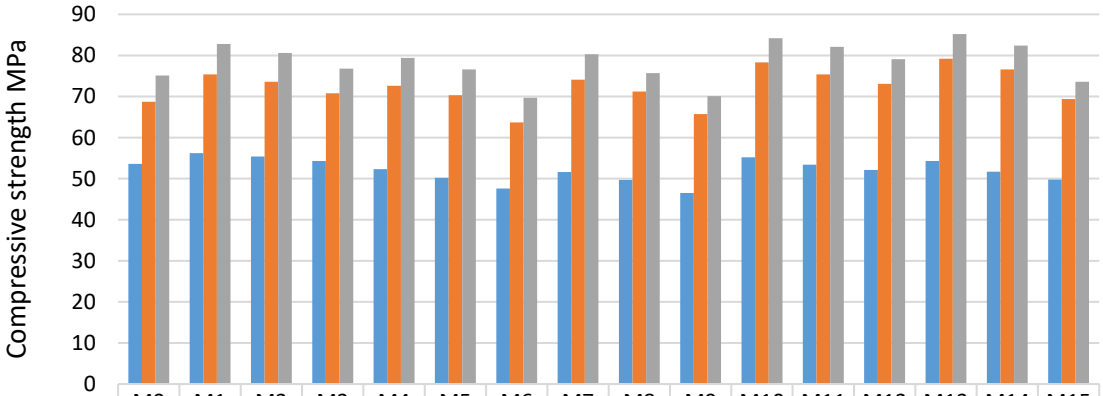

	M0	M1	M2	M3	M4	M5	M6	M7	M8	M9	M10	M11	M12	M13	M14	M15
7 days	53,6	56,2	55,4	54,3	52,3	50,2	47,6	51,6	49,7	46,5	55,2	53,4	52,1	54,3	51,7	49,8
28 days	68,7	75,4	73,6	70,8	72,6	70,3	63,7	74,1	71,2	65,7	78,3	75,4	73,1	79,2	76,6	69,4
90 days	75,1	82,8	80,6	76,8	79,4	76,6	69,7	80,3	75,7	70,1	84,2	82,1	79,1	85,2	82,4	73,6

Fig. 10. Development of compressive strength in HPSCCs

Figure 11 displays the SEM results for concrete mixes M1, M4, M7, M10, and M13, compared to a reference mix (M0), were analyzed to assess their mechanical performance at ambient temperature. These mixes were chosen for their optimal compressive strength after 28 days of curing. The control mix exhibited key hydrated products such as portlandite, ettringite crystals, and C-S-H plates. Notably, the mix with a 10% CKC replacement showed enhanced compressive strength and active pozzolanic reactions, characterized by increased C- S-H and decreased calcium hydroxide, leading to improved cement microstructure. Studies confirm that replacing cement with calcined clay leads to a finer pore network and increased matrix compactness, contributing to enhanced mechanical properties.

Cement-based paste specimens with replaced calcined kaolin clay exhibit a denser and more refined pore structure, which aligns with observed improvements in compressive strength [57]. Similarly, mixes containing marble powder also develop a denser and less porous microstructure compared to conventional cement pastes. The microstructural features of concrete pastes that include amorphous calcium silicate hydrate (C-S-H) and ettringite, which promote complete hydration and efficient void filling. The use of supplementary materials such as GGBS is highlighted for its role in minimizing the size and quantity of calcium hydroxide crystals in the ITZ. This results in a denser ITZ microstructure, enhancing the overall strength and durability of concrete mixes when optimized with calcined clay or GGBS alongside Portland cement [58,59].

Yuksel [60] noted that the microstructure of concrete containing Ground Granulated Blast- furnace Slag (GGBS) is distinct from that of traditional Portland Cement (PC) concrete, primarily due to the unique chemical reactions involving GGBS. The formation of calcium silicate hydrate (C-S-H) compounds is crucial for improving the durability and longevity of concrete, as supported by the findings of [61,62]. Generally, the absence of cracks in the concrete signifies effective mixing and strong bonding among the constituent materials. The ITZ, which develops where different components meet, can be minimized through better mixing and uniform distribution, thereby enhancing the material's integrity. Ternary blends containing 10% CKC and 10% WMP, or 10% CKC and 20% GGBS, demonstrate strong bonding with the cement matrix, as evidenced by the absence of visible cracks. The ITZ, formed by the interaction of various chemical components, is distinctly observed and contributes positively to the concrete strength. This enhancement is attributed to the high reactivity of CKC, whose fine particles react with calcium hydroxide to generate additional C-S-H, further densifying the microstructure. Moreover, the fine particles of WMP and CKC assist in

sealing micro-pores, decreasing porosity and improving the binding properties of the mix through chemical hydration reactions [54].

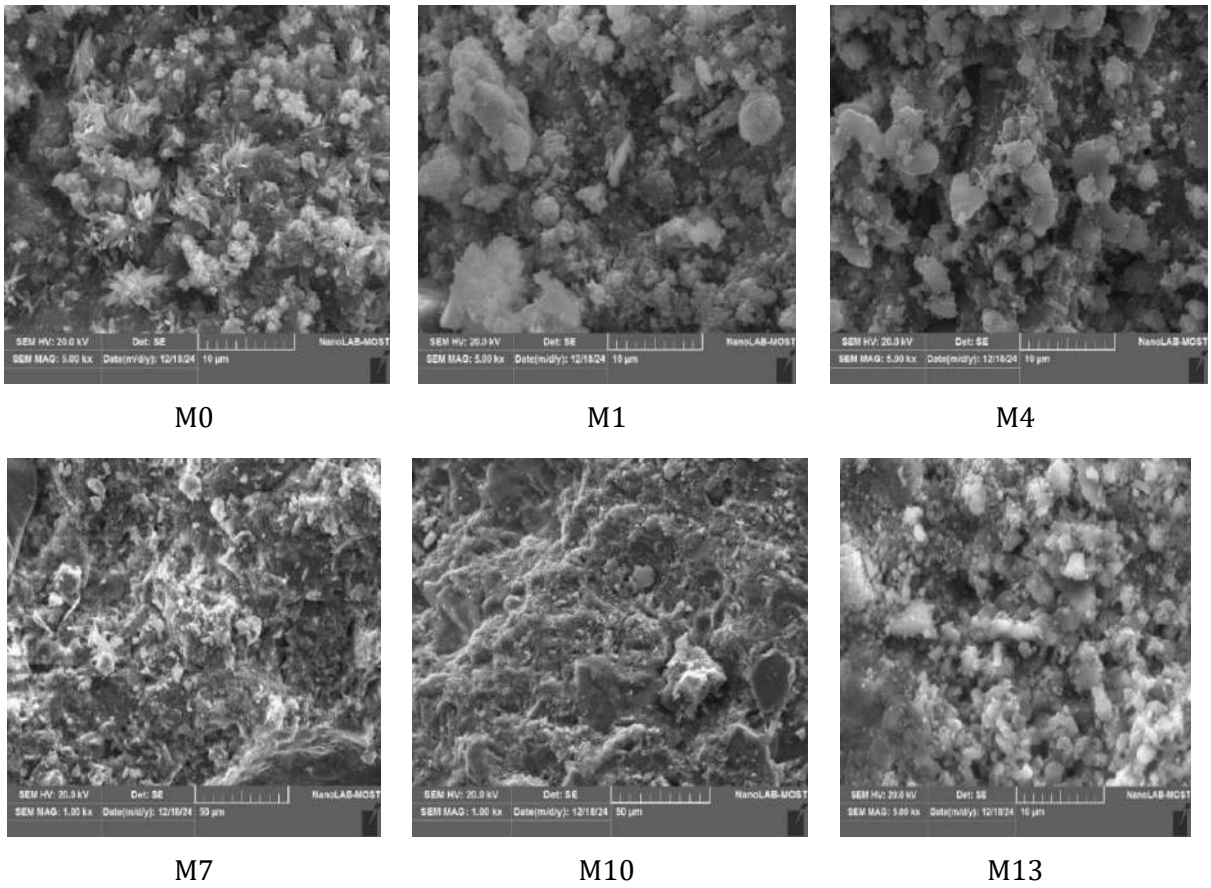

M0 M1 M4

M7 M10 M13

Fig. 11. Scanning Electron Microscopy (SEM) results of HPSCCs

3.3. Durability Properties – Results and Discussion

Water absorption (WA) determines the amount of water absorbed under specified conditions, which indicates the degree of porosity in a material. The characteristics of concrete absorption indirectly represent the porosity.

The average test results for the water absorption of binary blends, and ternary mixes of HPSCCs at 28 and 90 days are illustrated in Fig 12. It could be noted that the water absorption values declined with an increase in the curing period for all blended HPSCCs. This is due to the reduction of pore volume with hydration products. The water absorption of high-quality concrete (high- strength concrete or high-performance concrete) is generally less than 5% [63]. The absorption for binary, and ternary mixes was in the range of 3.04–3.65%, at 28 days, and 2.74–3.34% at 90 days, respectively. So, all HPSCCs could be categorized as “high quality”.

Introducing calcined kaolin clay (CKC) in M1 at 10% led to a clear improvement in water absorption, dropping the value to 2.82%, which corresponds to an 9% reduction relative to the control mix (M0) at age 90 days. This improvement is attributed to the pozzolanic reaction between the amorphous silica and alumina of CKC and calcium hydroxide, forming additional C–S–H gel that refines the pore structure. However, increasing the CKC content to 20% (M3, 3.04%) resulted in a gradual loss of efficiency, with reductions of only 1.93%, respectively at age 90 days. Mixes incorporating waste marble powder (WMP) showed variable behavior. At 10% replacement (M4), the absorption decreased to 2.94%, representing a 5.16% improvement. Ground granulated blast furnace slag (GGBS) at 20% (M7) reduced water absorption to 2.91%, yielding a 6.13% improvement at age 90 days. Due to filling ability of GGBS, this slag can reduce porosity in concrete and reduce water absorption. As the replacement increased to 40% (M9, 3.32%), the absorption increased again. GGBS contributes to long-term strength and durability through the latent

hydraulic reaction; however, it is known to have low early-age reactivity.The combination of CKC and WMP in M10 (10% each) significantly enhanced performance, reducing absorption to 2.77%, equivalent to a 10.65% reduction at age 90 days. Similarly, mixes with CKC and GGBS displayed favorable behavior: M13 (10% CKC + 20% GGBS) reached 2.74%, achieving the highest reduction (11.61%) in water absorption comparing to control mix(M0). The strong performance of these ternary mixes is due to the synergistic action of fast-reacting CKC and slow-reacting or filler-type SCMs, which enhance early hydration and pore refinement [26,47,64].

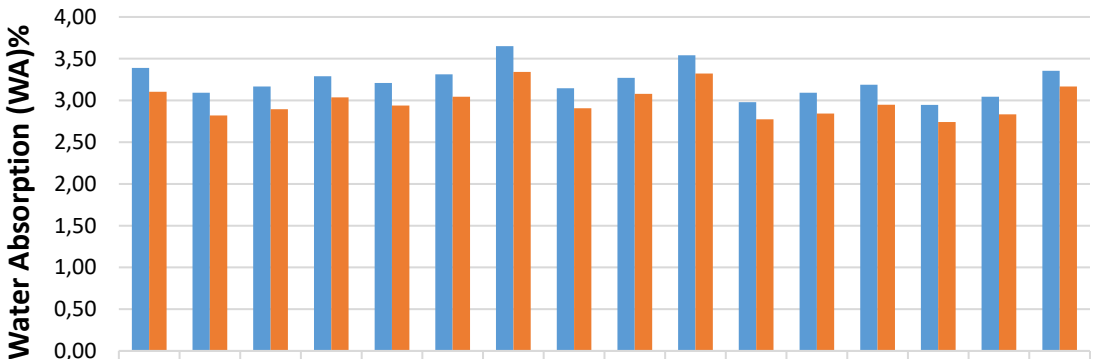

	M0	M1	M2	M3	M4	M5	M6	M7	M8	M9	M10	M11	M12	M13	M14	M15
28 days	3,39	3,09	3,17	3,29	3,21	3,31	3,65	3,15	3,27	3,54	2,98	3,09	3,19	2,95	3,04	3,36
90 days	3,10	2,82	2,90	3,04	2,94	3,04	3,34	2,91	3,08	3,32	2,77	2,84	2,95	2,74	2,83	3,17

Fig. 12. Water absorption results for binary blends and ternary mixes of HPSCCs

Fig. 13-14 shows the average weight loss of HPSCCs incorporating calcined kaolin clay (CKC), Waste Marble Powder (WMP), and Ground Granulated Blast Furnace Slag (GGBS) in binary, and ternary blend systems, that exposed to solutions of NaCl, and Na_2SO_4, over periods of 90 and 180 days (after 28 days of curing in water). At both 90 and 180 days, the relative weight loss values of the mixes under NaCl exposure indicate a generally milder form of degradation compared to sulfate salts. Mixes containing CKC (M1–M3) exhibited significant improvement, particularly M1, which recorded 23.88% improvement compared to M0 weight loss at 180 days. This indicates that the incorporation of 10% CKC enhanced the internal microstructure by densification through pozzolanic reactions, reducing ingress and crystallization pressure from NaCl [65]. Mixes with WMP (M4–M6) achieved moderate improvement (around 16.13–9.54%), which can be attributed primarily to the filler effect of marble powder, enhancing particle packing but lacking chemical interaction [66]. Meanwhile, GGBS-based mixes (M7–M9) performed similarly to CKC, particularly M7 (23.41% at 180d), due to GGBS's latent hydraulic properties and its ability to reduce portlandite content [67]. Combination of CKC and WMP (M10–M12) showed moderate reduction in weight loss, with M10 achieving 24.54%improvment compared to the control at 180 days. Also combining CKC with GGBS (M13–M15) showed effective reduction in weight loss, with M13 achieving 25.24%improvment compared to the control at 180 days.

Under Na_2SO_4 exposure, the degradation mechanisms intensified due to the chemical reactivity of sulfate ions with aluminate phases in cement, forming expansive ettringite and gypsum. CKC mixes (M1–M3) displayed reduced weight loss ranging from 24.98–14.56% compared to M0 at 90 days, with M1 (24.98% at 90d) showing the best performance. CKC's pozzolanic reaction reduces C_3A reactivity by forming additional C-S-H and C-A-H, thus mitigating ettringite formation (41). WMP mixes (M4–M6) showed slightly inferior performance (17.36–10.89%), confirming their limited chemical action. GGBS mixes (M7– M9) achieved better performance than WMP with 24.54-13.59% improvement than control mix, due to the ability of GGBS to bind Ca^{2+} and lower the availability of calcium hydroxide for gypsum formation [67]. Among the ternary mixes, M13 stood out. M13 showed 25.94%improvment in weight loss at 180 days, compared to control mix (M0), the lowest of all, underscoring the role of combined material functions: CKC's pozzolanic reactivity, and GGBS's chemical stabilization.

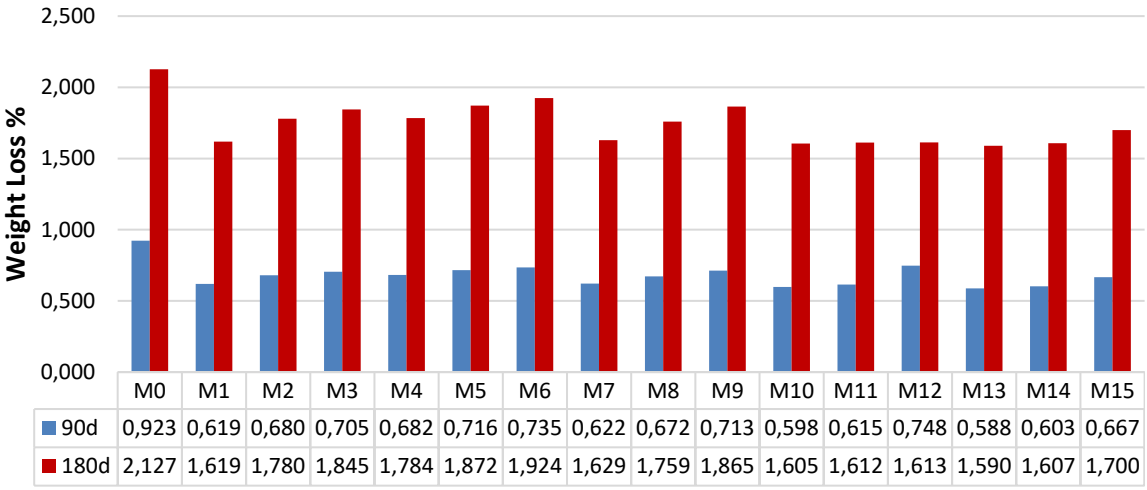

	M0	M1	M2	M3	M4	M5	M6	M7	M8	M9	M10	M11	M12	M13	M14	M15
90d	0,923	0,619	0,680	0,705	0,682	0,716	0,735	0,622	0,672	0,713	0,598	0,615	0,748	0,588	0,603	0,667
180d	2,127	1,619	1,780	1,845	1,784	1,872	1,924	1,629	1,759	1,865	1,605	1,612	1,613	1,590	1,607	1,700

Fig. 13. Weight change results for binary blends and ternary mixes of HPSCCs under chloride (NaCl) exposure at various ages

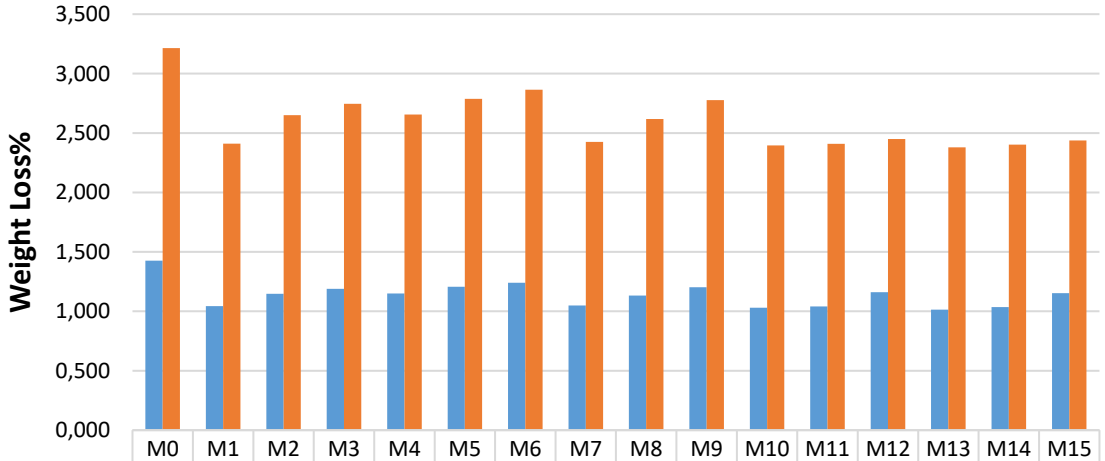

	M0	M1	M2	M3	M4	M5	M6	M7	M8	M9	M10	M11	M12	M13	M14	M15
90 days	1,426	1,044	1,147	1,189	1,150	1,207	1,240	1,049	1,133	1,202	1,030	1,041	1,161	1,014	1,035	1,153
180 days	3,214	2,411	2,650	2,746	2,656	2,788	2,864	2,425	2,618	2,777	2,395	2,409	2,450	2,380	2,403	2,438

Fig. 14. Weight change results for binary blends and ternary mixes of HPSCCs under sulfate (Na2SO4) exposure at various ages

4. Conclusions

This study presents a comprehensive experimental investigation into the design and performance evaluation of Sustainable High-Performance Self-Compacting Concrete (HPSCC) through the incorporation of locally available natural and industrial pozzolanic materials—Calcined Kaolin Clay (CKC), Waste Marble Powder (WMP), and Ground Granulated Blast Furnace Slag (GGBS). The concrete mixtures were developed in both binary and ternary blending systems with the primary objective of enhancing workability, mechanical strength, and durability while minimizing the environmental footprint associated with Ordinary Portland Cement (OPC) usage.

- Slump flow diameters ranged from 740 mm to 845 mm, placing most mixtures within the SF3 class. However, binary mixtures containing 20% CKC were categorized as SF2 due to slightly reduced flowability.
- Passing ability values (L-box ratios) ranged between 0.874 and 0.996, meeting the criteria for PA2 classification with no evidence of blocking or segregation. Segregation resistance

was satisfactory for all mixes, with segregation ratios ranging from 9.7% to 14.6%, which falls within SR2 classification.

- The addition of GGBS and WMP improved flow characteristics and reduced viscosity due to their fine particle size and smooth morphology. In contrast, higher CKC contents slightly reduced flowability, attributed to its high surface area and internal friction. Nonetheless, ternary systems effectively balanced these effects, maintaining high performance in fresh-state behavior.
- Binary blends achieved peak performance at 10% CKC (M1, 82.8 MPa), 10% WMP (M4, 79.4 MPa), and 20% GGBS (M7, 80.3 MPa).
- Ternary blend M13 (10% CKC + 20% GGBS) exhibited the highest compressive strength: 85.2 MPa at 90 days, representing a 13.3% improvement over the control mix. The increase in strength is attributed to the synergistic pozzolanic activity between CKC and GGBS. CKC actively reacts with calcium hydroxide to form additional calcium silicate hydrate (C–S–H), while GGBS contributes to later-age strength through its latent hydraulic properties and refinement of the microstructure.
- Water Absorption: All mixes exhibited absorption values below 5%, classifying them as high-quality concrete. The lowest absorption was observed in M13 (2.74%), achieving the highest reduction (11.61%) compared to reference mix, followed closely by M10 and M1. This indicates improved pore structure due to pozzolanic reactions and filler effects.
- Resistance to Chloride (NaCl): M13 showed 25.24% (highest improvement) in weight loss compared to the control mix at 180 days.M10 also demonstrated significant resistance, reducing degradation by 24.54% at 180d.
- Resistance to Sulfate (Na_2SO_4):M13 again exhibited the best performance, with a 25.94%improvment in weight loss at 180 days, confirming the beneficial synergy of CKC and GGBS.M10 followed closely with comparable improvements (25.48%).
- At both 90 and 180 days, the relative weight loss values of the mixes under NaCl exposure indicate a generally milder form of degradation compared to sulfate salts. These results validate that the ternary blends not only improve strength but also significantly enhance long-term chemical durability under aggressive environments.
- Uniform distribution of hydration products, especially in mixes M1, M7, M10, and M13 with reduced calcium hydroxide ($Ca(OH)_2$) content. Denser and more refined microstructure. Enhanced Interfacial Transition Zone (ITZ) with minimal micro cracks The most compact and homogenous microstructure was observed in M13, confirming the link between microstructural densification and superior mechanical and durability outcomes.

References

[1] Dadsetan S, Bai J. Mechanical and microstructural properties of self-compacting concrete blended with metakaolin, ground granulated blast-furnace slag and fly ash. Constr Build Mater. 2017;146:658–667. https://doi.org/10.1016/j.conbuildmat.2017.04.158

[2] Zhutovsky S, Kovler K. Influence of water to cement ratio on the efficiency of internal curing of high-performance concrete. Constr Build Mater. 2017;144:311–316. https://doi.org/10.1016/j.conbuildmat.2017.03.203

[3] Afroughsabet V, Biolzi L, Ozbakkaloglu T. Influence of double hooked-end steel fibers and slag on mechanical and durability properties of high performance recycled aggregate concrete. Compos Struct. 2017;181:273–284. https://doi.org/10.1016/j.compstruct.2017.08.086

[4] Dybeł P, Wałach D, Ostrowski K. The top-bar effect in specimens with a single casting point at one edge in high-performance self-compacting concrete. J Adv Concr Technol. 2018;16(7):282–292. https://doi.org/10.3151/jact.16.282

[5] Megid WA, Khayat KH. Effect of concrete rheological properties on quality of formed surfaces cast with self-consolidating concrete and superworkable concrete. Cem Concr Compos. 2018;93:75–84. https://doi.org/10.1016/j.cemconcomp.2018.06.016

[6] Özbay E, Erdemir M, Durmuş Hİ. Utilization and efficiency of ground granulated blast furnace slag on concrete properties – A review. Constr Build Mater. 2016;105:423–434. https://doi.org/10.1016/j.conbuildmat.2015.12.153

[7] Vivek SS, Dhinakaran G. Durability characteristics of binary blend high strength SCC. Constr Build Mater. 2017;146:1–8. https://doi.org/10.1016/j.conbuildmat.2017.04.063

[8] Mohan A, Mini KM. Strength and durability studies of SCC incorporating silica fume and ultra fine GGBS. Constr Build Mater. 2018;171:919–928. https://doi.org/10.1016/j.conbuildmat.2018.03.186
[9] Mohammed MK, Al-Hadithi AI, Mohammed MH. Production and optimization of eco-efficient self compacting concrete SCC with limestone and PET. Constr Build Mater. 2019;197:734–746. https://doi.org/10.1016/j.conbuildmat.2018.11.189
[10] Kavitha OR, Shanthi VM, Arulraj GP, Sivakumar VR. Microstructural studies on eco-friendly and durable self-compacting concrete blended with metakaolin. Appl Clay Sci. 2016;124:143–149. https://doi.org/10.1016/j.clay.2016.02.011
[11] Melo KA, Carneiro AM. Effect of metakaolin's fineness and content in self-consolidating concrete. Constr Build Mater. 2010;24(8):1529–1535. https://doi.org/10.1016/j.conbuildmat.2010.02.002
[12] Ghoddousi P, Saadabadi LA. Study on hydration products by electrical resistivity for self- compacting concrete with silica fume and metakaolin. Constr Build Mater. 2017;154:219–228. https://doi.org/10.1016/j.conbuildmat.2017.07.178
[13] Altoubat S, Badran D, Junaid MT, Leblouba M. Restrained shrinkage behavior of self-compacting concrete containing ground-granulated blast-furnace slag. Constr Build Mater. 2016;129:98–105. https://doi.org/10.1016/j.conbuildmat.2016.10.115
[14] Bhuva P, Patel A, George E, Bhatt D. Development of self-compacting concrete using different range of cement content. In: Nat Conf Recent Trends Eng Technol; 2011.
[15] Elyamany HE, Abd Elmoaty M, Mohamed B. Effect of filler types on physical, mechanical and microstructure of self-compacting concrete and flow-able concrete. Alex Eng J. 2014;53(2):295 307. https://doi.org/10.1016/j.aej.2014.03.010
[16] Tennich M, Ouezdou MB, Kallel A. Thermal effect of marble and tile fillers on self-compacting concrete behavior in the fresh state and at early age. J Build Eng. 2018;20:1–7. https://doi.org/10.1016/j.jobe.2018.06.015
[17] Suprakash AS, Karthiyaini S, Shanmugasundaram M. Future and scope for development of calcium and silica rich supplementary blends on properties of self-compacting concrete – A comparative review. J Mater Res Technol. 2021;15:5662–5681. https://doi.org/10.1016/j.jmrt.2021.11.026
[18] Djeddou M, Amieur M, Chaid R, Mesbah HA. Development of eco-friendly self-compacting concrete using marble powder, blast furnace slag and glass fibre-reinforced plastic waste: Application of mixture design approach. Res. Eng. Struct. Mater., 2025; 11(1): 113-138. http://dx.doi.org/10.17515/resm2024.178ma0208rs
http://dx.doi.org/10.17515/resm2024.178ma0208rs
[19] De Schutter G, Audenaert K, Boel V, Vandewalle L, Dupont D, Heirman G, et al. Transport properties in self-compacting concrete and relation with durability. In: Proc 3rd Int RILEM Symp; 2003. p. 799–807.
[20] Neville AM. Properties of Concrete. 4th ed. Essex: Pearson Education Ltd; 2005.
[21] Sarathy RV, Dhinakaran G. Strength and durability characteristics of GGBFS based HPC. Asian journal of applied sciences. 2014 Apr;7(4):224-31. http://dx.doi.org/10.3923/ajaps.2014.224.231
[22] Al-Dulaijan AU, Maslehuddin MZ, Sharif MM, Shameem AM, Ibrahim MM. Sulfate resistance of plain and blended cements exposed to varying concentrations of sodium sulfate. Cem Concr Compos. 2003;25:429–437. http://dx.doi.org/10.1016/S0958-9465(02)00083-5
[23] Gruber KA, Ramlochan T, Boddy A, Hooton RD, Thomas MDA. Increasing concrete durability with high-reactivity metakaolin. Cem Concr Res. 2001;23(6):479–484. https://doi.org/10.1016/S0958-9465(00)00097-4
[24] Binici H, Huseyin T, Mehmet MK. The effect of fineness on the properties of the blended cements incorporating ground granulated blast furnace slag and ground basaltic pumice. Constr Build Mater. 2007;21(5):1122–1128. http://dx.doi.org/10.1016/j.conbuildmat.2005.11.005
[25] Chandru P, Karthikeyan J, Sahu AK, Sharma K, Natarajan C. Some durability characteristics of ternary blended SCC containing crushed stone and induction furnace slag as coarse aggregate. Constr Build Mater. 2021;270:121483. http://dx.doi.org/10.1016/j.conbuildmat.2020.120953
[26] Vivek SS. Performance of ternary blend SCC with ground granulated blast furnace slag and metakaolin. Mater Today Proc. 2022;49:1337–1344. https://doi.org/10.1016/j.matpr.2021.09.204
[27] Chavan AD., Rattan VK, Patil YS. Impact of supplementary cementitious materials on life cycle cost of high-strength concrete in coastal environments. Res. Eng. Struct. Mater., 2025; 11(2): 465-480. http://dx.doi.org/10.17515/resm2024.232st0404rs
[28] Iraqi Standard Specification. Portland Cement. IQS No. 5; 2019.
[29] Khoman RK, Owaid HM. Influence of nanoparticles additions on fresh properties and compressive strength of sustainable self-compacting high performance concrete containing calcined pozzolanic materials. Int J Mech Eng. 2022;7(1):870–874.
[30] ASTM C618. Standard specification for coal fly ash and raw or calcined natural pozzolan for use in concrete. ASTM Int; 2019.

[31] Rajini B, Rao AN. Mechanical properties of geopolymer concrete with fly ash and GGBS as source materials. Int J Innov Res Sci Eng Technol. 2014;3(9):15944–15953. http://dx.doi.org/10.15680/IJIRSET.2014.0309023
[32] ASTM C989. Standard specification for ground granulated blast-furnace slag for use in concrete and mortars. ASTM Int; 2022.
[33] Iraqi Specification IQS No. 45. Aggregates. Central Org Standardization and Quality Control; 1984.
[34] ASTM C494. Standard specification for chemical admixtures for concrete. ASTM Int; 2017.
[35] EFNARC. The European guidelines for self-compacting concrete: Specification, production and use. UK: Association House; 2005.
[36] BS 1881-114. Method for determination of density of hardened concrete. BSI; 1983.
[37] BS 1881-116. Method for determination of compressive strength of concrete cubes. BSI; 1983.
[38] ASTM C1723. Standard guide for examination of hardened concrete using SEM. ASTM Int; 2022.
[39] ASTM C642. Standard test method for density, absorption, and voids in hardened concrete. ASTM Int; 2021.
[40] ASTM C1012. Standard test method for length change of hydraulic-cement mortars exposed to a sulfate solution. ASTM Int; 2013.
[41] Thankam GL, Renganathan NT. Ideal supplementary cementing material – Metakaolin: A review. Int Rev Appl Sci Eng. 2020. https://doi.org/10.1556/1848.2020.00008
[42] Al Menhosh A, Wang Y, Augusthus-Nelson L. Long-term durability properties of concrete modified with metakaolin and polymer admixture. Constr Build Mater. 2018;172:41–51. https://doi.org/10.1016/j.conbuildmat.2018.03.215
[43] Hilal N, Sor NH, Hadzima-Nyarko M, Radu D, Tawfik TA. The influence of nanosunflower ash and nanowalnut shell ash on sustainable lightweight self-compacting concrete characteristics. Sci Rep. 2024;14(1):9450. https://doi.org/10.1038/s41598-024-60096-5
[44] Amin M, Hadzima-Nyarko M, Agwa IS, et al. A review on the effect of marble powder on properties of self-compacting concrete. Adv Sci Technol. 2024;152:61–72. https://doi.org/10.4028/p- gw4vSr
[45] Yuksel I, Genç A. Properties of concrete containing nonground ash and slag as fine aggregate. ACI Mater J. 2007;104(4):397.
[46] Al-Oran AAA, Safiee NA, Nasir NAM. Fresh and hardened properties of self-compacting concrete using metakaolin and GGBS as cement replacement. Eur J Environ Civ Eng. 2022;26(1):379–392. https://doi.org/10.1080/19648189.2019.1663268
[47] Bheel N, Benjeddou O, Almujibah HR, et al. Effect of calcined clay and marble dust powder as cementitious material on the mechanical properties and embodied carbon of high strength concrete by using RSM-based modelling. Heliyon. 2023;9(4):e14709. https://doi.org/10.1016/j.heliyon.2023.e14709
[48] Fahad DK, Owaid HM. Study on the effects on self-compacting concrete using waste marble powder and high volume calcined kaolin clay. Salud Ciencia Tecnol Ser Conf. 2024;3:836. http://dx.doi.org/10.56294/sctconf2024836
[49] Sharobim K, Hassan HM, Ragheb S. Durability improvement of self compacting recycled aggregate concrete using marble powder. Port Said Eng Res J. 2017;21(2):68–77. https://doi.org/10.21608/pserj.2017.33292
[50] Fahad DK, Owaid HM. Enhancing mechanical properties of self-compacting concrete through the utilization of pozzolanic materials and waste products. Ann Chim Sci Matér. 2024;48(1):114. https://doi.org/10.18280/acsm.480114
[51] Yamuna P, Krishna AH. Experimental investigation of strength characteristics on micro level properties of self-compaction concrete using lime stone powder & GGBS. Int J Sci Res Sci Technol. 2017;3(1):418–423.
[52] Ahmad J, Kontoleon KJ, Majdi A, et al. A comprehensive review on the ground granulated blast furnace slag (GGBS) in concrete production. Sustainability. 2022;14(14):8783. https://doi.org/10.3390/su14148783
[53] Dinakar P, Sahoo PK, Sriram G. Effect of metakaolin content on the properties of high strength concrete. Int J Concr Struct Mater. 2013;7:215–223. https://doi.org/10.1007/s40069-013-0045-0
[54] Al-Hashem MN, Amin MN, Ajwad A, et al. Mechanical and durability evaluation of metakaolin as cement replacement material in concrete. Materials. 2022;15(22):7868. https://doi.org/10.3390/ma15227868
[55] Parande AK, Babu BR, Karthik MA, Kumaar KD, Palaniswamy N. Study on strength and corrosion performance for steel embedded in metakaolin blended concrete/mortar. Constr Build Mater. 2008;22(3):127–134. https://doi.org/10.1016/j.conbuildmat.2006.10.003
[56] Saranya P, Nagarajan P, Shashikala AP. Eco-friendly GGBS concrete: a state-of-the-art review. IOP Conf Ser Mater Sci Eng. 2018;330(1):012057. https://doi.org/10.1088/1757- 899X/330/1/012057
[57] Abbasi Dezfouli A. Experimental investigation into the metakaolin used in concrete. J Civ Eng Mater Appl. 2021;5(2):67–80. https://doi.org/10.22034/jcema.2020.253922.1041

[58] Alyousef R, Benjeddou O, Khadimallah MA, et al. Study of the effects of marble powder amount on the self-compacting concretes properties by microstructure analysis. Adv Civ Eng. 2018;2018:6018613. https://doi.org/10.1155/2018/6018613
[59] Khan MA, Khan B, Shahzada K, et al. Conversion of waste marble powder into a binding material. Civ Eng J. 2020;6(3):431–445. http://dx.doi.org/10.28991/cej-2020-03091481
[60] Yuksel I. Blast-furnace slag. In: Waste and Supplementary Cementitious Materials in Concrete. Woodhead Publishing; 2018. p. 361–415. https://doi.org/10.1016/B978-0-08-102156-9.00012-2
[61] Khmiri A, Chaabouni M, Samet B. Chemical behaviour of ground waste glass when used as partial cement replacement in mortars. Constr Build Mater. 2013;44:74–80. https://doi.org/10.1016/j.conbuildmat.2013.02.040
[62] Kim J, Yi C, Zi G. Waste glass sludge as a partial cement replacement in mortar. Constr Build Mater. 2015;75:242–246. https://doi.org/10.1016/j.conbuildmat.2014.11.007
[63] Kosmatka SH, Kerkhoff B, Panarese WC. Design and Control of Concrete Mixtures. 14th ed. Skokie, IL: Portland Cement Association; 2002.
[64] Moghadam AS, Omidinasab F, Goodarzi SM. Characterization of concrete containing RCA and GGBFS: Mechanical, microstructural and environmental properties. Constr Build Mater. 2021;289:123134. https://doi.org/10.1016/j.conbuildmat.2021.123134
[65] Badogiannis E, Aggeli E, Papadakis VG, Tsivilis S. Evaluation of chloride-penetration resistance of metakaolin concrete by means of a diffusion–binding model and of the k-value concept. Cem Concr Compos. 2015;63:1–7. http://dx.doi.org/10.1016/j.cemconcomp.2015.07.012
[66] Ulubeyli GC, Bilir T, Artir R. Durability properties of concrete produced by marble waste as aggregate or mineral additives. Procedia Eng. 2016;161:543–548. http://dx.doi.org/10.1016/j.proeng.2016.08.689
[67] Chen W, Wu M, Liang Y. Effect of SF and GGBS on pore structure and transport properties of concrete. Materials. 2024;17(6):1365. http://dx.doi.org/10.3390/ma17061365

Blank Page

Research on Engineering Structures & Materials
www.jresm.org
MIM Research Group

Research Article

Solar energy-driven heat treatment of concrete and mortar in desert environments: A case study of Bechar region, Algeria

Tidjar Boudjemaa [*1,2,a], Khelafi Hamid [3,b], Bella Nabil [1,c], Bennaceur Saïd [4,d], Lammari Khelifa [5,e], Benabdelfattah Mohamed [3,f], Hadj Djelloul Nasser Dine [1,g], Slimani Abdeldjalil [2,h], Dahbi Abdeldjalil [2,3,i]

[1]*FIMAS Laboratory, University of Tahri Mohammed, Bechar B.P 417, Bechar, 08000, Algeria*
[2]*Unité de Recherche en Energies Renouvelables en Milieu Saharien, URERMS, Centre de Développement des Energies Renouvelables, CDER, 01000, Adrar, Algeria*
[3]*Faculty of sciences and technologies, University of Adrar. Laboratory of Sustainable Development and Computer Science (LDDI), University of Adrar, Ahmed Draïa, RN6, 01000 Adrar, Algeria*
[4]*Laboratory for the Development of Renewable Energies and their Applications in Saharan Areas (LDREAS), Faculty of Exact Sciences, TAHRI Mohammed University, BP 417 Béchar, Algeria*
[5]*Faculty of Exact Sciences. Energy Laboratory in Arid Zones (ENERGARID). University of Béchar, TAHRI Mohammed, Algeria*

Article Info

Article History:

Received 07 Feb 2025
Accepted 17 June 2025

Keywords:

Early-age strength;
Concrete mass loss;
Total shrinkage;
Endogenous shrinkage;
Solar energy treatment;
Energy consumption

Abstract

This study investigates the effectiveness of solar energy-based heat treatment for concrete and mortar as a sustainable alternative to conventional curing methods. The approach aims to enhance early-age strength while reducing energy consumption, lowering production costs, and minimizing environmental impact. The acceleration of concrete and mortar hardening contributes to early-age strength development, which is beneficial for the prefabricated construction industry. Two treatment cycles were conducted: The first was: A 10 hours cycle in a solar dryer (SD) and an oven, reaching a maximum temperature of 55°C, with an average relative humidity of 60%. The second was: A 12 hours cycle in a solar greenhouse (SG), achieving 60°C with 50% relative humidity. The results of the tests were compared with those of the control specimens, hardened in at 25°C, 50% of relative humidity. The heat treatment significantly enhanced early-age strength development. On day one, mortar flexural strengths in SD, oven, and SG reached 25%, 25%, and 18%, respectively, of 28 days control specimen strength. However, treatment conditions did not significantly affect flexural strength at 120 days, with treated specimens exhibiting strengths comparable to control specimens. Moreover, these treatments lower concrete production costs while reducing CO_2 emissions by approximately 214.6 g/m^3, underscoring their positive environmental impact.

© 2025 MIM Research Group. All rights reserved.

1. Introduction

Currently, the technological development that is happening in the world has led to a trend toward the use of renewable energy due to global warming gas emissions from conventional energy production [1]. Renewable energies are promising alternatives and without contributing to global warming gas emissions [2], their use is very important in various applications, providing a solution to growing energy consumption, while improving energy stability and sustainability [3].

*Corresponding author: boudjtidjar@yahoo.fr
[a]orcid.org/0000-0002-9915-4610; [b]orcid.org/0000-0002-3617-0437; [c]orcid.org/0000-0003-3586-8304; [d]orcid.org/0000-0001-7230-5792; [e]orcid.org/0000-0003-0679-5425; [f]orcid.org/0000-0003-4504-4560; [g]orcid.org/0000-0003-3296-7112; [h]orcid.org/0000-0002-8983-1702; [i]orcid.org/0000-0003-3630-6688
DOI: http://dx.doi.org/10.17515/resm2025-680en0207rs

Solar energy, earth's most abundant and perpetual resource, can be directly harnessed from solar radiation. The earth's surface receives approximately 100000 TW of solar energy annually [4]. Algeria's desert regions rank among the world's highest solar-exposed areas, averaging 10 hours of daily irradiation [5] and 2500–4000 hours annually [6]. This makes solar energy an efficient, sustainable solution for southern Algeria. Among these applications, heat treatment of cement products serves as a notable example [7], which also reduces energy costs in developing economies [8,9] .

Heat treatment accelerates cementitious materials hardening to achieve high early-age strength [10,11]. However, this treatment can negatively impact the long-term properties of the cement materials [12]. The durability of heat-treated cementitious materials is influenced by many factors, including the method of treatment [13].

A single heat treatment cycle suffices to achieve high demolding resistance in the short-term [14], final strength is typically attained during storage [15]. Heat treatment aims to accelerate early-age strength development through elevated temperatures. The American Concrete Institute (ACI) [16] and Zeyad et al. [17] recommend steam curing as the standard method, which typically follows a four-stage cycle:

- Preheating period: The temperature is maintained at or slightly above ambient levels for up to 4 hours [18].
- Heating period: The rate of temperature increase is substantially constant from 13 °C to 30 °C per hour [19,20].
- Isothermal period: The temperature is kept constant, Erdogˇdu et al. [21] and Türkel et al. [22] recommend the optimal temperatures treatment range from 60°C to 80°C.
- Cooling period: The temperature of the treated element returns to ambient temperature.

Several researchers Naas et al. [23] and Hanif et al. [24] have adopted the practice of using cooling rates equivalent to the rate of temperature increase during the heating period. Famy et al. [25] preferred the cooling speed to be slower than the heating speed. The sudden drop in temperature leads to cracks, which can compromise concrete strength. However, other researchers Yazici et al. [26] and Liu et al. [27] have adopted a cooling phase practice for a shorter period of the heating phase.

Rapid reheating of concrete above 70°C accelerates cement hydration, leading to late ettringite formation and potential sulfate attack [28]. While elevated temperatures enhance early-age strength through rapid CSH (calcium silicate hydrate) gel formation [29] and increased hydration product density [30], they may compromise long-term durability [31]. Notably, solar-powered heat treatment of concrete is more energy-efficient [32].

The adoption of solar energy for concrete heat treatment presents significant economic and environmental advantages. Conventional methods rely on carbon-intensive processes, exacerbating CO_2 emissions, whereas renewable energy integration aligns with sustainable development goals by reducing both emissions and production costs. Solar-treated concrete demonstrates improved mechanical performance, minimizing long-term strength deficiencies observed in traditional heat curing. For instance, Benammar et al. [33] reported a 77% strength increase at 28 days compared to control specimens. Despite these benefits, no comprehensive study has yet evaluated renewable energy-based heat treatment for its triple advantage: Simultaneous strength enhancement, emission reduction, and cost efficiency. Therefore, this paper reviews the potential of concrete and mortar heat treatment by solar energy as a technology capable of:

- Early-age strength development for industrial applications (prefabricated concrete [34]).
- Operational cost savings through reduced energy demand.
- CO_2 emission mitigation.

In this study, the effect of the treatment method on the mechanical properties of concrete has been studied as well as its environmental impact. Solar heat treatment of concrete and mortar is expected to achieve the desired goal of improving strength, contributing to environmental sustainability, and reducing carbon dioxide emissions.

2. Materials and Methods

This section outlines the materials used, temperature analysis in SD, oven, and SG, test methods, concrete and mortar mix design, specimen preparation, and testing procedures.

2.1. Materials and Characterization

2.1.1 Cement

This study used CEM II/A-L 42.5 N cement for mortar and concrete mixtures. Table 1 presents its chemical composition, while Tables 2 and 3 show its mechanical and physical, respectively.

Table 1. Chemical composition of cement (%)

Cement	SO_3	SiO_2	Al_2O_3	Fe_2O_3	CaO	MgO	K_2O	Na_2O	Cl
CEM II/A-L 42.5 N	1.59	18.86	4.51	2.56	65.20	2.33	0.64	0.33	0.005

Table 2. Mechanical characteristics of cement

Cement	2 days	7 days	28 days
CEM II/A-L 42.5 N	Compression (MPa)	Compression (MPa)	Compression (MPa)
	17.4	36.9	45.7

Table 3. Physical characteristics of cement

	Cement CEM II/A-L 42.5 N
Consistency (%)	31
Expansion (mm)	1
Absolute density (g/cm^3)	3.10
Apparent density (g/cm^3)	0.95
Fineness (cm^2/g)	3750

2.1.2 Sand and Gravel

used rounded sand from Oued Ksiksou banks, with an apparent density of 1580 kg/m^3, specific density of 2600 kg/m^3, and fineness modulus 1.95, for all mortar and concrete mixtures. Locally produced crushed stones from Bechar region served as aggregates for concrete. Gravel 1 has an apparent density of 1430 kg/m^3 and specific density of 2620 kg/m^3, while gravel 2 has an apparent density of 1440 kg/m^3 and specific density of 2610 kg/m^3. The particle size curves of sand and gravel are given in Fig. 1.

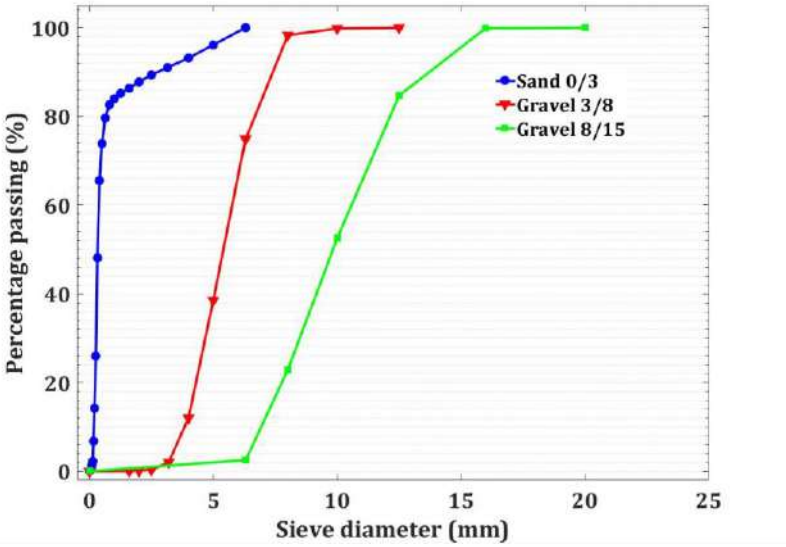

Fig. 1. The particle size distribution of sand and gravel

2.2. Mortar and Concrete Mix

The concrete mix comprised (0/3 mm) sand, (3/8 mm) gravel 1, and (8/15 mm) gravel 2. The desired workability is characterized by a subsidence to the cone of Abrams A=6.5 cm (plastic concrete). For the concrete formulation, we chose the Dreux-Gorisse method. This method makes it possible to determine the optimal quantities of the various components (sand, cement, gravel, water), based on particle size analysis [35]. The concrete formulation obtained is characterized by a water/cement ratio of 0.55, a sand percentage of 30%, gravel (3/8 mm) 34%, and gravel (8/15 mm) 36%. Mortar mixture proportions follow the EN 196-1 standard while maintaining the concrete's 0.55 W/C ratio to preserve the same cement matrix. The compositions of the concrete and mortar are presented in Table 4.

Table 4. Composition of concrete and mortar

Components	Water (kg/m^3)	Cement (kg/m^3)	W/C	Sand (kg/m^3)	Gravel 3/8 (kg/m^3)	Gravel 8/15 (kg/m^3)
Concrete	192.5	350	0.55	631.8	721.5	764
Mortar	247.5	450	0.55	1350	/	/

2.3. Heat Treatment Arrangement

A research team from the Laboratory of Energy in Arid Zones (ENERGARID) locally manufactured both SD and SG.

2.3.1 Sustainable Heat Treatment Systems

Operating partially through indirect solar energy via forced thermal convection, SD can also be powered entirely or partially by electricity. This dual capability allows it to function year-round, even in winter. However, SG, relies entirely on solar energy, limiting its nighttime use. Both models were constructed locally using raw materials purchased from ordinary markets in the Bechar region.

Fig. 2. The arrangement of the specimens. (a) in SD (b) in the greenhouse

Two systems were used for specimen drying. The first system, a SD, operates as an indirect thin-layer dryer using partial solar energy with forced convection (see Fig. 2a). This dryer also functions as an electric oven by covering the collector glass, blocking air inlet and outlet, and activating the electrical resistances in the heating unit. The second system is a fully solar-powered greenhouse (see Fig. 2b). We measured temperatures and humidity with a combined temperature-humidity sensor.

2.3.2 Specimens Preparation

We prepared the concrete and mortar at room temperature using the following procedure: Dry-mixed the aggregates and cement for one minute and 30 seconds to achieve homogeneity. Added two-thirds of the water and mixed for 2 minutes. Incorporated the remaining water and continued

mixing for 5 minutes (4 minutes for mortar). After mixing, we poured concrete into cubic molds (100 mm × 100 mm × 100 mm) and mortar into prismatic molds (40 mm × 40 mm × 160 mm). Each mold was filled in two layers and compacted on a vibrating table.

2.3.3 Solar Heat Treatment Cycles and Processing Protocol

Immediately after casting, all molds were covered with a plastic film, and the specimens were then subjected to heat treatment using solar energy. The placement of specimens in both SG and SD is illustrated in Fig. 3. Humidity is supplied in both systems by the air humidifier, as shown in Fig. 3b. The specimens were exposed to three different drying practical cycles the first and second in SD and oven for 10 hours, and the third for 12 hours in the SG, as shown in Fig. 4.

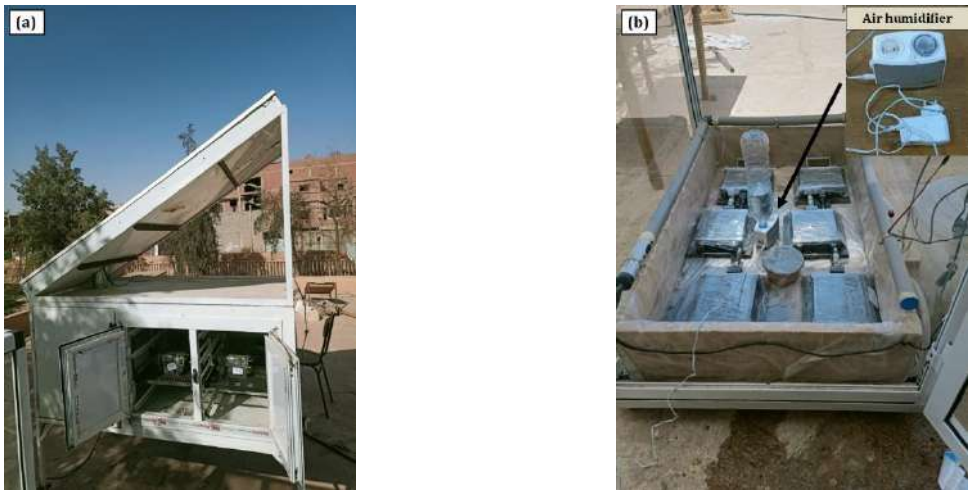

Fig. 3. Heat treatment system (solar radiation drying): (a) SD, (b) SG

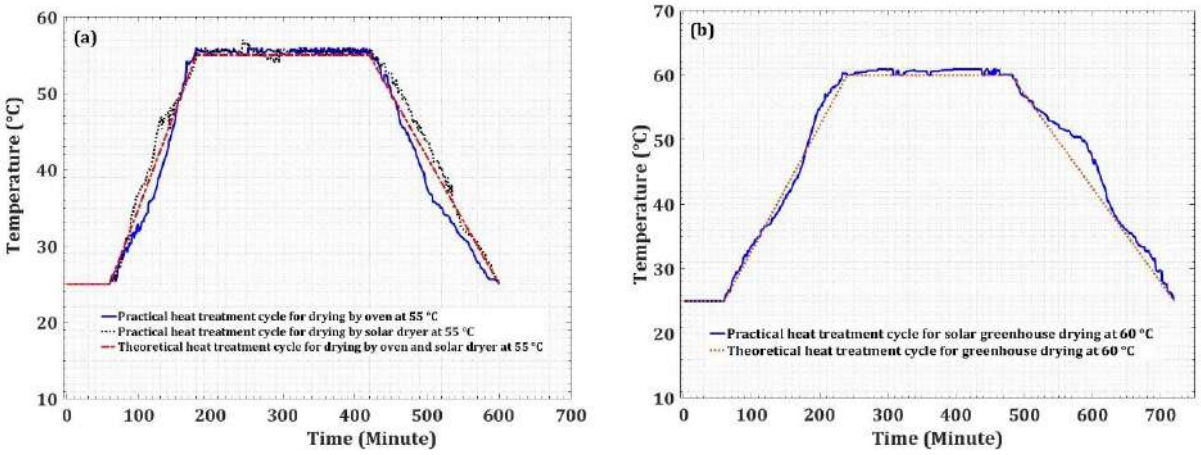

Fig. 4. Practical and theoretical heat treatment cycles for drying by (a) SD and oven; (b) SG

The processing cycle includes four phases:

- Preheating: Temperature remains constant at 25°C for one hour across all cycles.
- Heating: Temperature increases at 15°C/h for 2 hours in the first and second cycles, and at 11.6°C/h for 3 hours in the third cycle.
- Isothermal phase: Temperature maintains at 55°C for 4 hours in the first and second cycles, and at 60°C for 4 hours in the third cycle.
- Cooling: Temperature decreases to ambient levels at 15°C/h for 3 hours in the first and second cycles, and at 8.75°C/h for 4 hours in the third cycle.

2.4. Experimental investigation

We conducted an experimental program to study how different drying methods influence evaluation indicators, energy saving, and economic impact. We compared results with control specimens across three drying cycles: Oven, SD and SG.

2.4.1 Compressive Strength

The compressive strength test on concrete (100 mm × 100 mm × 100 mm) cubic specimens was conducted using a 300 KN capacity press, a continuous and regular load was applied at a constant rate of 1 mm/min until fracture. The maximum fracture force of the specimen was recorded (KN), with three specimens tested for each concrete mixture.

2.4.2 Flexural Strength

We determined flexural strength using (40 mm × 40 mm × 160 mm) prismatic specimens according to EN 196-1. The maximum (KN) at specimen fracture was recorded on the display screen. Data for each mortar represent average values from three tests.

2.4.3 Mass Loss Investigation

We measured mortar mass loss Pm(t) at the end of each cycle period, after demolding, and continuing through 120 days. The mass m(t) was measured by electronic balance with a relative uncertainty of ±0.2 g. We calculated specimen mass loss as follows:

$$Pm(t) = \frac{m(t) - m_0}{m_0} \quad (1)$$

Where, m_0: Mass of mould after pouring mortar before demolding or the mass of the specimen after demolding, m(t): Mass of the mould at the late of each cycle period before release or the mass of the specimen after t days after release. The mass loss value retained is the average of three measurements on (40 mm × 40 mm × 160 mm) test specimens.

2.4.4 Shrinkage Investigation Endogenous and Total

We conducted shrinkage tests on (40 mm × 40 mm × 160 mm) prismatic specimens. After treatment cycle and demolding, endogenous shrinkage specimens were covered with three layers: A first layer of cellophane plastic film and two additional layers of aluminum foil. This process is necessary to prevent external exchange and evaporation (see Fig. 5a). For shrinkage measurement, specimens (40 mm × 40 mm × 160 mm) were prepared following the standard NF P 15-433. These measurements were carried out using a linear variation comparator to determine the length change of the specimens (see Fig. 5b). Final reported shrinkage values represent averages from three specimens.

(a) (b)

Fig. 5. Shrinkage specimens and measurement device. (a) Endogenous shrinkage specimens; (b) Shrinkage measurement device

2.4.5 Energy Consumption

Energy consumed during the treatment cycle is measured using a wattmeter located in the control box mounted on the back face of the drying chamber, as shown in Fig. 6.

Fig. 6. Calculation of energy consumed

3. Results and Interpretations

3.1. Compressive Strength

The compressive strength test was carried out on cubic specimens (100 mm × 100 mm × 100 mm) immediately after the drying cycles up to 120 days.

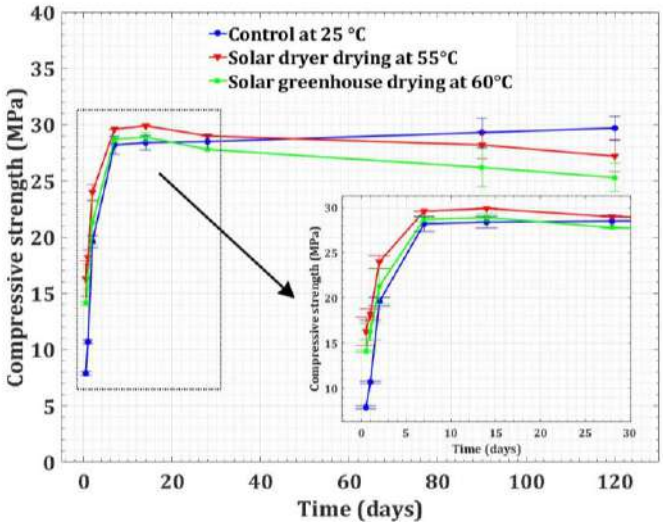

Fig. 7. Influence of the heat treatment method by solar energy on the development of compressive strength

3.1.1 Early-age Compressive Strength

As shown in Fig. 7, the control concrete exhibited a low compressive strength of 7.9 MPa after 12 hours of storage in the laboratory at 25°C, which was lower than the target strength of 10 MPa. In contrast, the SD and SG concretes exceeded 10 MPa, reaching 14.1 MPa and 16.3 MPa, respectively, after treatment. By the second day, their compressive strengths increased to 24 MPa for SD and 21.3 MPa for SG, representing 99.8% and 99.7%, respectively, of the 28 days strength of the control specimen. This improvement was attributed to the elevated temperature during both the final heating and isothermal phases, which accelerated hydration. This process promoted rapid formation of CSH [36], leading to increased material density [37,38] and, consequently, enhanced early-age compressive strength.

3.1.2 Medium-term Compressive Strength

The compressive strength of SG and SD treated specimens decreased after 28 days compared to the control specimens. This reduction was primarily attributable to less uniform distribution of hydration products in the paste, caused by initial rapid hydration [39]. These results align with findings from Benammar et al. [33], Emmanue et al. [40], and Benouadah et al. [41]. Additionally, concrete specimens treated in SD and SG showed a 1 MPa decrease in compressive strength at 28 days compared to 14 days. Moreover, at 28 and 90 days, their compressive strengths were slightly lower than those of the control specimens.

3.1.3 Long-Term Compressive Strength

At 120 days, SD and SG treated concrete reached a compressive strength of 27.2 MPa and 25.3 MPa, respectively, representing 99.92% and 99.85% of the control concrete strength. Furthermore, as expected, the increased humidity in SD during treatment yielded slightly greater long-term compressive strength compared to that of SG. This confirms Nabil et al. [42] conclusion that humidity enhances strength development during heating. In addition, both treated specimens exhibited slight strength reductions in the long-term. This phenomenon was attributed primarily to solar radiation exposure and elevated temperatures during the initial hardening phase. These conditions have accelerated the cement hydration process in the presence of free water within the concrete mixture, which is consistent with the conclusions of Mehdizadeh et al. [43].

3.2. Flexural Strength

The flexural strength tests were carried out on prismatic mortar specimens of dimensions (40 mm × 40 mm × 160 mm), using three specimens per test immediately after heating cycles at ages 12 hours, 1, 2, 7, 14, 28, 90, and 120 days. Fig. 8 illustrates the influence of method and temperature of heat treatment on the specimens treated by solar energy and the control specimens with respect to the development of flexural strength.

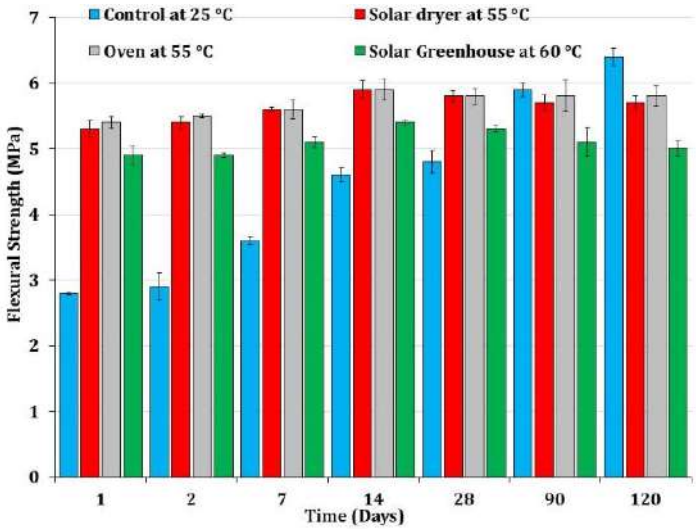

Fig. 8. Influence of the heat treatment method by solar energy on the development of flexural strength

3.2.1 Early-age Flexural Strength

The flexural strength results correlated closely with compressive strength development under all treatment conditions. The dryer and oven treated specimens demonstrated remarkably similar strength behavior, which was attributed to their identical treatment cycles. Testing confirmed that greenhouse, dryer, and oven treatments significantly improved early-age flexural strength development. At 24 hours, dryer and oven treated specimens achieved the highest flexural strengths 5.3 MPa, 5.4 MPa, respectively. This improvement results from air condensation (the greenhouse effect) and elevated temperatures, which accelerated cement hydration and produced greater early-age strength compared to control specimens and SG treated specimens.

3.2.2 Medium and Long-Term Flexural Strength

While the control specimens showed continued flexural strength gain, heat-treated specimens exhibited strength reduction after 14 days. This behavior was primarily attributed to rapid initial hydration, which resulted in less compact microstructural formation of hydration products [44].

3.3. Mass Loss

Fig. 9 shows mortar mass loss over time under different temperatures and heating methods. The mass loss trends of the different mortars are similar; it increases rapidly during the treatment cycle and tends to stabilize as the hardening age progresses.

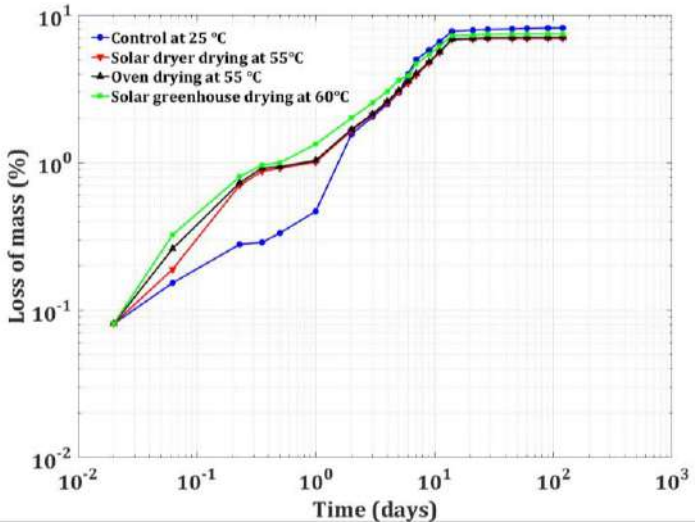

Fig. 9. Mass loss for the specimens treated and the control mortar

3.3.1 Initial Mass Loss

Oven, SD, and SG treated mortars showed the highest mass losses 0.92%, 0.94%, and 1% after 12 hours, respectively, while the control mortar lost only 0.33%. Parrott [45] and Jiang et al. [46] have demonstrated that free water evaporation causes mass loss. Studies have confirmed that higher initial free water content leads to greater mass loss [47]. After six days, control specimens demonstrated greater mass loss than treated specimens, as the latter had already lost significant water during treatment. SD, oven, and SG treated specimens showed more rapid initial mass loss and reached equilibrium faster than control specimens.

3.3.2 Stability of Mass Loss

Mass loss of the heat-treated specimens stabilized by day 14, reaching values of 6.81%, 6.84%, and 7.25%, respectively. However, the control specimen achieved mass loss stability later, at day 21, with 7.89%. This stabilization occurs when CSH gels form, filling pores and reducing water evaporation at later ages, which confirms the long-term flexural and compressive strength results.

3.4. Total Shrinkage of Mortar

3.4.1 First Phase: Increase of Total Shrinkage

Fig. 10 shows that on the first day, shrinkage values reached 154, 159, 173, and 81 μm/m for SD, oven, greenhouse treated, and control mortars, respectively. The SG treated specimen exhibited the highest shrinkage, which was attributable to elevated hardening temperatures combined with low relative humidity.

Following the rapid development phase, shrinkage values progressively increased to final measurements of 1009, 1027, 1081, and 579 μm/m for the respective specimens. All heat-treated mortars demonstrated continued shrinkage growth with age, with significantly more rapid development compared to the control specimen, which showed more gradual shrinkage progression. During the initial 60 days period for dryer and oven treated specimens and the first

35 days for SG specimens, total shrinkage showed comparable and significant deformation. These values were slightly higher than those measured in control specimens at 70 days.

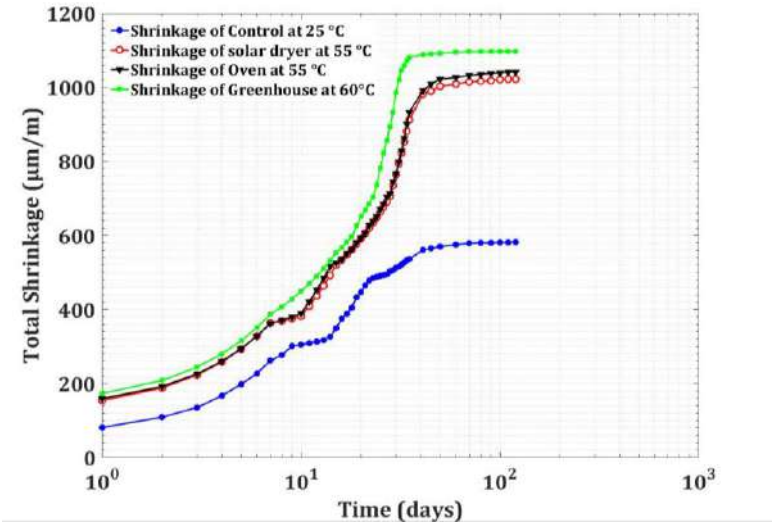

Fig. 10. Total shrinkage evolution for the specimens treated and the control mortar

Elevated hardening temperatures significantly increased shrinkage, this finding is consistent with the results of Bouziadi et al. [48], where higher temperatures accelerate hydration but create irregular CSH distribution, increasing early-age porosity and shrinkage [49,50]. This explains the rapid short-term shrinkage development in heat-treated specimens.

3.4.2 Second Phase: Stability of Total Shrinkage

In this phase, shrinkage tends to stabilize. After the initial setting and hardening phase, total specimen shrinkage reaches stability due to rapid water loss caused by high temperatures during treatment.

3.5. Endogenous Shrinkage of Mortar

Fig. 11 demonstrated rapid early-age endogenous shrinkage development across all mortar specimens, resulting from auto-desiccation of the cementitious matrix during hydration and hardening. The heat-treated specimens exhibited gradually decreasing shrinkage until day 21, while the control specimen showed continued reduction until day 35.

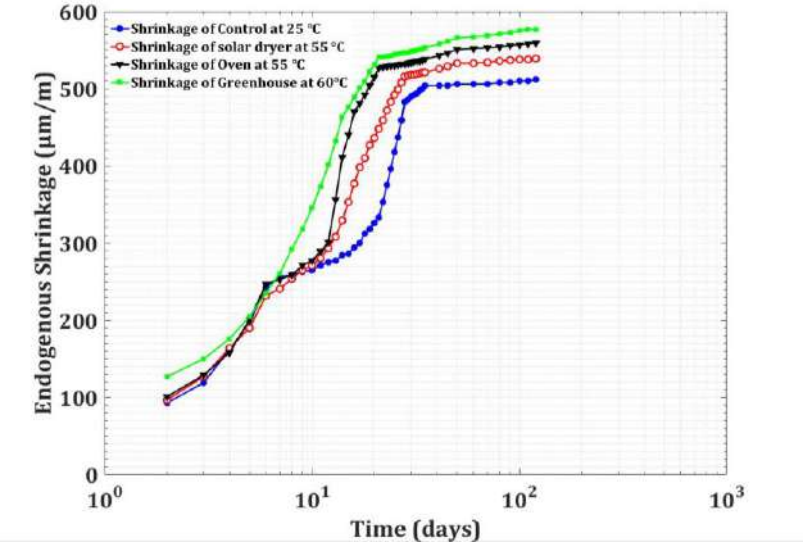

Fig. 11. Endogenous shrinkage evolution for the specimens treated and the control mortar

By 120 days, endogenous shrinkage values converged to 539 µm/m (SD), 559 µm/m (oven), 577 µm/m (SG), and 512 µm/m (control), despite differing treatment conditions.

3.6. Economic and Environmental Feasibility of the Study

3.6.1 Energy Consumption

Table 5 compares the energy consumption (E_c) during specimen treatment cycles between the partially electricity-powered SD and the oven using traditional heat treatment methods. Both specimens exceeded the desired compressive strength after the first day. The SD specimen, using renewable energy, achieved 16.3 MPa, surpassing the electric-powered oven specimen's value of 14.3 MPa. Furthermore, the oven consumed 0.79 kWh/m^3 of electrical energy, while the SD specimen, consumed 0.21 kWh/m^3.

Table 5. Electrical energy consumed

Heat treatment method	Renewable energy	Traditional method (electric power)
Energy consumed during the cycle (KWh)	0.35	1.36
Mass of specimens (Kg)	1.70	1.72
Energy to dry 1 m3 (KWh/m3)	0.21	0.79
Compressive strength after 24 hours (MPa)	16.3	14.3

As shown in Fig. 12, conventional heat treatment methods exhibited substantially higher energy requirements than renewable alternatives. The oven's energy consumption (0.79 kWh/m^3) was 3.8 times greater than SD, representing an estimated energy savings of 0.58 kWh/m^3 through solar drying. These energy savings contribute to reduced CO_2 emissions. According to the Intergovernmental Panel on Climate Change (IPCC) [51], producing 1 kWh of energy contributes to the emission of 370 g of CO_2. Consequently, using SD saves approximately 214.6 g of CO_2 emissions per 1 m^3 of concrete.

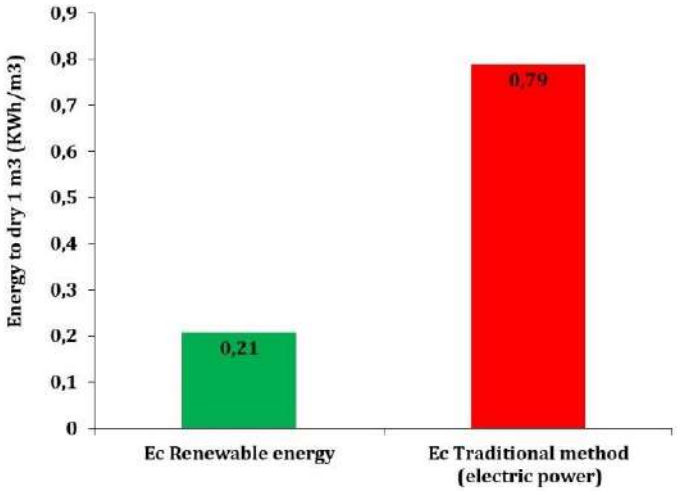

Fig. 12. Energy consumed by heat treatment

3.6.2 Environmental and Economic Impact

To evaluate environmental impact through CO_2 emissions and economic effectiveness, we conducted a financial analysis comparing conventional and renewable energy-based heating methods for mortar mixes. We applied the C_p indicator developed by Ma et al. [52]. The cost-efficiency and environmental impact C_p is calculated according to the following Eq (2):

$$C_p = \frac{Cost}{f_{c28}} \tag{2}$$

Where, Cost: Total material cost per cubic meter, f_{c28}: 28 days compressive strength. The costs of local raw materials in Algeria were taken from previous research by Benammar et al. [53], these values are detailed in Table 6.

Table 6. Cost of raw materials

Materials	Sand	Cement	Water	Energy	Heating
Real study Cost ($/kg) [53]	0.029	0.12	0.00372	($/kwh)	0.28

Fig. 13 shows the calculated C_p values for mortars treated with renewable energy versus electric energy. The C_p values of electrically treated mortar significantly exceed those of renewable energy treated mortar. The C_p values of conventionally treated mortar were approximately 4.4 times greater than those treated with renewable energy. This difference stems from the higher electricity costs compared to renewable energy sources, contributing to the increase C_p in electrically treated mortar.

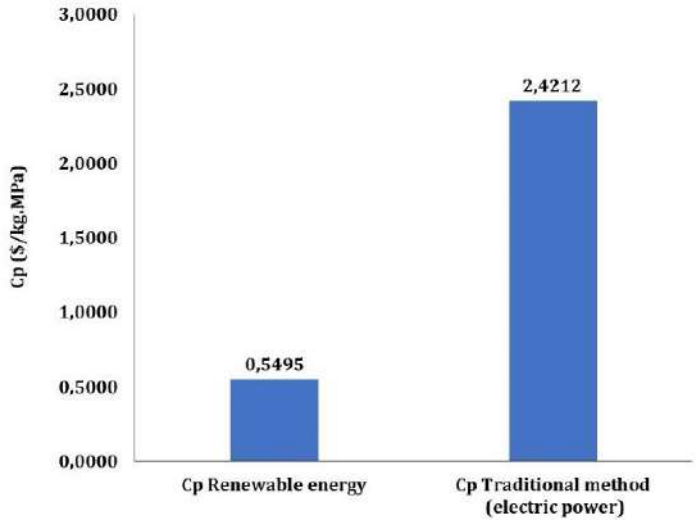

Fig. 13. The cost-efficiency and environmental impact

4. Effectiveness of the Study in the Global Context

This research demonstrates significant potential for global application, particularly in regions with abundant solar energy. The findings support solar heat treatment as a viable, cost-effective alternative to conventional treatment methods. Furthermore, our study supports previous similar research by Aruova et al. [54] and Sarkisov et al. [55] from other regions of the world, concluding that solar thermal treatment enhances early-age strength, provides an environmentally friendly approach, and offers cost-efficiency compared to traditional treatment methods.

The method's simplicity and scalability make it especially suitable for prefabricated construction in developing countries, where energy costs pose challenges. Additionally, its congruence with sustainable construction practices enhances its relevance worldwide, contributing to international efforts to reduce the environmental impact of concrete production. Further validation in diverse industrial settings could strengthen its global applicability. However, the study provides a strong foundation for adopting solar heat treatment as a practical, eco-friendly solution in the construction sector.

5. Conclusion

This study demonstrated the viability of solar heat treatment as a sustainable method for enhancing the early-age strength of concrete and mortar without compromising long-term performance. The results confirmed that this approach not only reduces production costs and energy consumption but also significantly lowers CO_2 emissions, supporting its potential for large-scale adoption in precast construction.

An experimental procedure evaluated the effect of the method of heat treatment of concrete and mortar by solar energy on the strength. Additionally, other properties such as mass loss, total

shrinkage, and endogenous shrinkage were studied. The results achieved were compared to control specimens.

Energy from SD, oven and SG accelerated hydration of cement paste, resulting in:

- Early-age strength enhancement: Treated specimens achieved rapid strength development, reaching 99.8% in SD and 99.7% in SG of 28 days control strength within two days. Notably, early-age rapid strength gain did not influence long-term strength.
- Mass loss: Heat-treated exhibited high mass loss compared to control specimens, mainly attributed to the evaporation of free water during treatment.
- Total shrinkage: Early-age shrinkage was similar between treated and control specimens. However, long-term shrinkage diverged, with treated specimens exhibiting higher values.
- Endogenous shrinkage: Consistency appeared between treated and control specimens in the short and long-term. However, the control specimens consistently exhibited higher endogenous shrinkage values than treated specimens.

Based on these results, the following conclusions can be drawn:

- The abundance of solar radiation in areas with the highest solar radiation in the world should be exploited in the concrete industry, which would allow savings in the industrial sector.
- Miniature models of SD and SG, represent a preliminary step toward developing of drying chambers for cement-based materials such as bricks, curbs, and decorative elements. This innovation benefits the economy by reducing energy consumption costs and contributes to environmental protection by lowering CO_2.
- Heat treatment by solar energy accelerates and increases the strengths of concrete and mortar in the short-term, without negatively affecting their long-term strengths.
- SD and oven yielded similar results, this similarity stems from comparable treatment cycles and the maximum temperature of the isothermal period at 55°C, these results are slightly higher than those in SG, where higher temperatures (60°C) and lower humidity reduced performance slightly.
- The utilization of solar energy, particularly through SD, reduced energy consumption by approximately 3.8 times for treating 1 m^3 of concrete, which has resulted in a reduction in carbon dioxide emissions, thus ensuring environmental preservation. Furthermore, the cost-effectiveness of heat treatment using renewable energy enhances environmental effectiveness by a factor of 4.4.

These results prove that treatment with renewable energies is a promising viable alternative to conventional heat treatment, enabling rapid strength gain while maintaining mechanical properties. This approach deserves consideration for implementation in construction applications, where rapid strength gain at an early-age is critical, particularly in geographic areas characterized by abundant solar radiation.

References

[1] Bahadori A, Nwaoha C. A review on solar energy utilisation in Australia. Renewable and Sustainable Energy Reviews 2013;18:1–5. https://doi.org/10.1016/j.rser.2012.10.003.
[2] Tsoutsos T, Frantzeskaki N, Gekas V. Environmental impacts from the solar energy technologies. Energy Policy 2005;33:289–96. https://doi.org/10.1016/S0301-4215(03)00241-6.
[3] Madlool NA, Saidur R, Hossain MS, Rahim NA. A critical review on energy use and savings in the cement industries. Renewable and Sustainable Energy Reviews 2011;15:2042–60. https://doi.org/10.1016/J.RSER.2011.01.005.
[4] Bhutto AW, Bazmi AA, Zahedi G. Greener energy: Issues and challenges for Pakistan-Solar energy prospective. Renewable and Sustainable Energy Reviews 2012;16:2762–80. https://doi.org/10.1016/j.rser.2012.02.043.
[5] Gairaa K, Khellaf A, Benkacilai S, Guermoui M. Solar radiation measurements in Algeria: case of Ghardaïa station as member of the enerMENA meteorological network. Energy Procedia 2017;141:50–4. https://doi.org/10.1016/j.egypro.2017.11.010.
[6] Boukar M, Harmim A. Performance evaluation of a one-sided vertical solar still tested in the Desert of Algeria. Desalination 2005;183:113–26. https://doi.org/10.1016/j.desal.2005.02.045.

[7] Pirasteh G, Saidur R, Rahman SMA, Rahim NA. A review on development of solar drying applications. Renewable and Sustainable Energy Reviews 2014;31:133–48. https://doi.org/10.1016/J.RSER.2013.11.052.
[8] Mahn D, Best R, Wang C, Abiona O. What drives solar energy adoption in developing countries? Evidence from household surveys across countries. Energy Econ 2024;138:107815. https://doi.org/10.1016/j.eneco.2024.107815.
[9] Opoku R, Adjei EA, Ahadzie DK, Agyarko KA. Energy efficiency, solar energy and cost saving opportunities in public tertiary institutions in developing countries: The case of KNUST, Ghana. Alexandria Engineering Journal 2020;59:417–28. https://doi.org/10.1016/j.aej.2020.01.011.
[10] Bella IA, Asroun A, Bella N. Effect of Curing Temperature on Mortar Based on Sustainable Concrete Material's and Poly-Carboxylate Superplasticizer. Journal of Civil Engineering and Architecture 2014;8:66. https://doi.org/10.17265/1934-7359/2014.01.008.
[11] Shi J, Liu B, He Z, Wu X, Tan J, Chen J, et al. Properties evolution of high-early-strength cement paste and interfacial transition zone during steam curing process. Constr Build Mater 2020;252:119095. https://doi.org/10.1016/j.conbuildmat.2020.119095.
[12] Gonzalez-Corominas A, Etxeberria M, Poon CS. Influence of steam curing on the pore structures and mechanical properties of fly-ash high performance concrete prepared with recycled aggregates. Cem Concr Compos 2016;71:77–84. https://doi.org/10.1016/j.cemconcomp.2016.05.010.
[13] Ranz J, Aparicio S, Fuente J V., Anaya JJ, Hernández MG. Monitoring of the curing process in precast concrete slabs: An experimental study. Constr Build Mater 2016;122:406–16. https://doi.org/10.1016/j.conbuildmat.2016.06.041.
[14] Baoju L, Youjun X, Shiqiong Z, Jian L. Some factors affecting early compressive strength of steam-curing concrete with ultrafine fly ash. Cem Concr Res 2001;31:1455–8. https://doi.org/10.1016/S0008-8846(01)00559-2.
[15] He Z, Liu J, Zhu K. Influence of mineral admixtures on the short and long-term performance of steam-cured concrete. Energy Procedia 2011;16:836–41. https://doi.org/10.1016/j.egypro.2012.01.134.
[16] Committee ACI. Cementitious Materials for Concrete. ACI Education Bulletin E3-13 ACI Committee E-701(2013) ACI Education Bulletin E3-13 Cementitious Materials for Concrete Recuperado 2013;15:950–5.
[17] Zeyad AM, Tayeh BA, Adesina A, de Azevedo ARG, Amin M, Hadzima-Nyarko M, et al. Review on effect of steam curing on behavior of concrete. Cleaner Materials 2022;3:100042. https://doi.org/10.1016/j.clema.2022.100042.
[18] Etxeberria M. The suitability of concrete using recycled aggregates (RAs) for high-performance concrete. Elsevier Ltd.; 2020. https://doi.org/10.1016/B978-0-12-819055-5.00013-9.
[19] Yang J, Hu H, He X, Su Y, Wang Y, Tan H, et al. Effect of steam curing on compressive strength and microstructure of high volume ultrafine fly ash cement mortar. Constr Build Mater 2021;266:120894. https://doi.org/10.1016/j.conbuildmat.2020.120894.
[20] Bi L, Long G, Ma C, Xie Y. Experimental investigation on the influence of phase change materials on properties and pore structure of steam-cured mortar. Archives of Civil and Mechanical Engineering 2021;21:1–10. https://doi.org/10.1007/s43452-020-00170-7.
[21] Erdoğdu S, Kurbetci S. Optimum heat treatment cycle for cements of different type and composition. Cem Concr Res 1998;28:1595–604. https://doi.org/10.1016/S0008-8846(98)00134-3.
[22] Türkel S, Alabas V. The effect of excessive steam curing on Portland composite cement concrete. Cem Concr Res 2005;35:405–11. https://doi.org/10.1016/j.cemconres.2004.07.038.
[23] Naas A, Taha-Hocine D, Salim G, Michèle Q. Combined effect of powdered dune sand and steam-curing using solar energy on concrete characteristics. Constr Build Mater 2022;322. https://doi.org/10.1016/j.conbuildmat.2022.126474.
[24] Hanif A, Kim Y, Usman M, Park C. Optimization of steam-curing regime for recycled aggregate concrete incorporating high early strength cement-a parametric study. Materials 2018;11. https://doi.org/10.3390/ma11122487.
[25] Famy C, Scrivener KL, Atkinson A, Brough AR. Influence of the storage conditions on the dimensional changes of heat-cured mortars. Cem Concr Res 2001;31:795–803. https://doi.org/10.1016/S0008-8846(01)00480-X.
[26] Yazici H, Aydin S, Yiğiter H, Baradan B. Effect of steam curing on class C high-volume fly ash concrete mixtures. Cem Concr Res 2005;35:1122–7. https://doi.org/10.1016/j.cemconres.2004.08.011.
[27] Liu B, Xie Y, Li J. Influence of steam curing on the compressive strength of concrete containing supplementary cementing materials. Cem Concr Res 2005;35:994–8. https://doi.org/10.1016/j.cemconres.2004.05.044.
[28] Amine Y, Leklou N, Amiri O. Effect of supplementary cementitious materials (scm) on delayed ettringite formation in heat-cured concretes. Energy Procedia 2017;139:565–70. https://doi.org/10.1016/j.egypro.2017.11.254.

[29] Li W, Fan Y, Hong J, Shi Y, Yang D, Wang P. Investigation on the early proceeding of cement hydration containing dispersed nano Calcium Silicate Hydrated (CSH) seeds. Constr Build Mater 2024;425:136039. https://doi.org/10.1016/j.conbuildmat.2024.136039.
[30] Shi J, Liu B, Zhou F, Shen S, Guo A, Xie Y. Effect of steam curing regimes on temperature and humidity gradient, permeability and microstructure of concrete. Constr Build Mater 2021;281:122562. https://doi.org/10.1016/j.conbuildmat.2021.122562.
[31] Ramezanianpour AA, Khazali MH, Vosoughi P. Effect of steam curing cycles on strength and durability of SCC: A case study in precast concrete. Constr Build Mater 2013;49:807–13. https://doi.org/10.1016/j.conbuildmat.2013.08.040.
[32] Yu K, Jia M, Yang Y, Liu Y. A clean strategy of concrete curing in cold climate: Solar thermal energy storage based on phase change material. Appl Energy 2023;331:120375. https://doi.org/10.1016/j.apenergy.2022.120375.
[33] Benammar B, Mezghiche B, Guettala S. Influence of atmospheric steam curing by solar energy on the compressive and flexural strength of concretes. Constr Build Mater 2013;49:511–8. https://doi.org/10.1016/j.conbuildmat.2013.08.085.
[34] Sebaibi N, Boutouil M. Reducing energy consumption of prefabricated building elements and lowering the environmental impact of concrete. Eng Struct 2020;213:110594. https://doi.org/10.1016/j.engstruct.2020.110594.
[35] Hamza C, Bouchra S, Mostapha B, Mohamed B. Formulation of ordinary concrete using the dreux-gorisse method. Procedia Structural Integrity 2020;28:430–9. https://doi.org/10.1016/j.prostr.2020.10.050.
[36] He J, Long G, Ma K, Xie Y. Comprehensive study on the hydration kinetics, mechanical properties and autogenous shrinkage of cement pastes during steam curing. Cem Concr Res 2023;174:107310. https://doi.org/10.1016/j.cemconres.2023.107310.
[37] Balaji T, Jeyashree TM, R KRP, J BS. Effect of elevated temperature on concrete incorporating zeolite , silica fume and fly ash as replacement for cement 2024;x:1–14. https://doi.org/10.17515/resm2024.267ma0506rs.
[38] Gallucci E, Zhang X, Scrivener KL. Effect of temperature on the microstructure of calcium silicate hydrate (C-S-H). Cem Concr Res 2013;53:185–95. https://doi.org/10.1016/j.cemconres.2013.06.008.
[39] John E, Lothenbach B. Cement hydration mechanisms through time – a review. J Mater Sci 2023;58:9805–33. https://doi.org/10.1007/s10853-023-08651-9.
[40] Emmanuel AC, Krishnan S, Bishnoi S. Influence of curing temperature on hydration and microstructural development of ordinary Portland cement. Constr Build Mater 2022;329:127070. https://doi.org/10.1016/j.conbuildmat.2022.127070.
[41] Benouadah A, Merbouh M, Nabil B, Benammar A. Effect of Self-Curing Admixture and Sand Type on the Mechanical and Microstructural Properties of Concrete in Hot Climate Conditions. Annales de Chimie. Science des Materiaux, vol. 48, International Information and Engineering Technology Association (IIETA); 2024, p. 85. https://doi.org/10.18280/acsm.480110.
[42] Nabil B, Aissa A, Aguida BI. Use of a new approach (design of experiments method) to study different procedures to avoid plastic shrinkage cracking of concrete in hot climates. Journal of Advanced Concrete Technology 2011;9:149–57. https://doi.org/10.3151/jact.9.149.
[43] Mehdizadeh H, Jia X, Mo KH, Ling T-C. Effect of water-to-cement ratio induced hydration on the accelerated carbonation of cement pastes. Environmental Pollution 2021;280:116914. https://doi.org/10.1016/j.envpol.2021.116914.
[44] Bogner A, Link J, Baum M, Mahlbacher M, Gil-Diaz T, Lützenkirchen J, et al. Early hydration and microstructure formation of Portland cement paste studied by oscillation rheology, isothermal calorimetry, 1H NMR relaxometry, conductance and SAXS. Cem Concr Res 2020;130:105977. https://doi.org/10.1016/j.cemconres.2020.105977.
[45] Parrott LJ. Basic creep, drying creep and shrinkage of a mature cement paste after a heat cycle. Cem Concr Res 1977;7:597–604. https://doi.org/10.1016/0008-8846(77)90121-1.
[46] Jiang C, Jin C, Wang Y, Yan S, Chen D. Effect of heat curing treatment on the drying shrinkage behavior and microstructure characteristics of mortar incorporating different content ground granulated blast-furnace slag. Constr Build Mater 2018;186:379–87. https://doi.org/10.1016/j.conbuildmat.2018.07.079.
[47] Rebai K, Bella IA, Bella N, Seghir A. Contribution to the modeling of the short-term behavior of cured concrete in hot weather. Advances in Concrete Construction 2025;19:163–72. https://doi.org/10.12989/acc.2025.19.3.163.
[48] Bouziadi F, Boulekbache B, Hamrat M. The effects of fibres on the shrinkage of high-strength concrete under various curing temperatures. Constr Build Mater 2016;114:40–8. https://doi.org/10.1016/j.conbuildmat.2016.03.164.
[49] Jennings HM, Thomas JJ, Gevrenov JS, Constantinides G, Ulm FJ. A multi-technique investigation of the nanoporosity of cement paste. Cem Concr Res 2007;37:329–36. https://doi.org/10.1016/j.cemconres.2006.03.021

[50] Toledo Filho RD, Ghavami K, Sanjuán MA, England GL. Free, restrained and drying shrinkage of cement mortar composites reinforced with vegetable fibres. Cem Concr Compos 2005;27:537–46. https://doi.org/10.1016/j.cemconcomp.2004.09.005.
[51] Intergovernmental Panel on Climate Change. Technology-specific Cost and Performance Parameters. Climate Change 2014: Mitigation of Climate Change 2015:1329–56. https://doi.org/10.1017/cbo9781107415416.025.
[52] Ma C, Long G, Shi Y, Xie Y. Preparation of cleaner one-part geopolymer by investigating different types of commercial sodium metasilicate in China. J Clean Prod 2018;201:636–47. https://doi.org/10.1016/j.jclepro.2018.08.060.
[53] Benammar A, Noui A, Benouadah A, Maafi N, Kessal O, Dridi M, et al. Enhancing sustainability and performance in alkali-activated mortars with recycled rubber aggregates subjected to varied curing methods. Research on Engineering Structures and Materials 2024. https://doi.org/10.17515/resm2024.192ma0226rs.
[54] Aruova L, Shashpan Z h., Utkelbaeva A, Alibekov N. Solar Energy for Foam Concrete Production Technology in Modern Conditions. J Mech Eng Res Dev 2018;41. https://doi.org/10.26480/jmerd.02.2018.49.55.
[55] Sarkisov DA, Zhadanovskii B V, Sinenko SA, Esenov MK. Prospects for the use of solar energy to accelerate the hardening of concrete in the construction of monolithic structures in Russia. E3S Web of Conferences, vol. 284, EDP Sciences; 2021, p. 6001.

Research on Engineering Structures & Materials
www.jresm.org

Research Article

Initial setting time of cement using sugarcane juice as an admixture

Sudhir Sharma [*,a], Pushpendra Kumar Sharma [b]

School of Civil Engineering, Lovely Professional University, Phagwara, Punjab, India

Article Info

Article History:

Received 14 Feb 2025

Accepted 26 June 2025

Keywords:

Cement;
Hydration;
Initial setting time of cement;
Chemical admixtures;
Sugarcane juice

Abstract

Concrete is a widely used material in construction projects globally, valued for its durability and strength. Comprised of cement, sand, aggregate, and water, the addition of admixtures further enhances its properties. Cement plays a pivotal role in the hardening of concrete through a chemical process known as hydration, which occurs upon mixing with water. To tailor the setting process according to specific project requirements or environmental conditions, chemical admixtures such as retarders or accelerators are incorporated. These additives are instrumental in extending or shortening the initial setting time of cement, ensuring optimal performance. While chemical admixtures are commonly employed to improve concrete characteristics in modern construction practices, they have environmental and health implications. The study examined the effect of sugarcane juice as an organic admixture on cement's initial setting time. By analyzing sugarcane juice proportions ranging from 0% to 28% of the cement's weight. The initial setting times were precisely measured with the Vicat apparatus. All results were benchmarked. The percentages included are 5%, 10%, 15%, 20%, 25%, and 28%. All results were compared to a 0% sugarcane juice baseline. The cement's initial setting time notably decreased from 140 to 75 minutes with 5% sugarcane juice added. Progressive additions of 10%, 15%, 20%, and 25% sugarcane juice steadily reduced the initial setting time. At 28% with only sugarcane juice as the admixture, the initial setting time decreased significantly to 23 minutes. The research indicated that higher proportions of sugarcane juice speed up hydration, significantly reducing the cement's initial setting time.

© 2025 MIM Research Group. All rights reserved.

1. Introduction

Concrete is an essential construction material utilized in the majority of construction activities (1). When water is added to the cement and aggregate blend, the cement initiates a reaction with the water. Under typical weather conditions, this combination solidifies and strengthens over time, resulting in concrete. Once the mixture is placed in formwork and permitted to cure, it transforms into a durable mass akin to stone. The chemical interaction between cement and water is responsible for the solidification process of this blend (2). The characteristics that determine the strength of solidifying concrete are closely tied to the microscopic structure of cement material. As a result, the formation of structures can be connected to the alterations in material characteristics that happen during the process of hardening (3).

Construction activities require strict adherence to parameters and procedures in order to achieve the desired quality outcomes. One critical factor to consider is temperature, as it significantly impacts the performance of concrete. In hot weather conditions where temperatures exceed 100°F, the hydration process of cement is accelerated, leading to faster setting times. While concrete may

*Corresponding author: nl.sudhir@gmail.com
[a]orcid.org/0009-0002-5147-1809; [b]orcid.org/0000-0002-6621-6862
DOI: http://dx.doi.org/10.17515/resm2025-685ma0214rs
Res. Eng. Struct. Mat. Vol. 11 Iss. 6 (2025) 3149-3166

exhibit early strength development in such conditions, it is important to note that significant strength can be compromised in the long term.

Furthermore, hot weather conditions can give rise to plastic shrinkage due to rapid water evaporation from the concrete surface. Tensile stresses may be formed as a result of this within the material, ultimately leading to cracking. To mitigate these risks and ensure the longevity and durability of concrete structures, it is essential to follow precise procedures and take appropriate measures to address the challenges posed by hot weather conditions. By carefully monitoring and adjusting construction practices in high temperatures, the quality and integrity of concrete can be effectively maintained (4,5). The heat created during the concrete's shrinkage and expansion after hardening creates tensions that eventually result in tiny cracks within the concrete structure. This phenomenon is problematic when building big concrete structural elements like bridges, dams, and piers, as well as when concreting structures in hot regions in general (6,7). Similarly, concreting in cold weather can have negative effects. The volume of concrete increases as water sets in its plastic state, impacting chemical reactions. Without sufficient water, the concrete setting and hardening process are delayed, leading to the formation of numerous pores. Ultimately, this results in concrete with lower strength (4,8). The difficulties experienced when working with concrete in cold weather are caused by the negative effects of frost on recently poured concrete. When the wet concrete becomes frozen, the water used in the mixing process transforms into ice, leading to an expansion in the concrete's volume. The lack of water for chemical reactions results in a delay in the concrete's curing and solidification. The cold temperature poses challenges for the concrete's curing and hardening process, as well as the risk of freezing and thawing during the initial stages. As a result of this process, ice needles begin to form inside the concrete, which then leads to the creation of cavities when the ice melts. These cavities significantly weaken the structural integrity of the concrete and result in a significant decrease in strength. In extreme conditions, the cold temperatures can make the concrete completely useless, causing it to become weak and easily breakable. Nonetheless, if the concrete has already hardened before freezing temperatures set in, it will not cause significant structural damage to the concrete. Once the concrete has solidified properly, any water that was used in the mixing process will have either evaporated or been consumed during hydration. There will be minimal excess water in the concrete structure to freeze as the capillary voids will have contracted due to the formation of cement gel (9).

Hence, chemical admixtures are utilized to uphold the prescribed standards (10). With the exception of cement, aggregates, and water, the additional material employed in the production of concrete is commonly referred to as an admixture (11). Admixtures play a crucial role in shaping the characteristics of concrete beyond the traditional components of cement, aggregates, and water. These supplementary materials are incorporated either during or just before the concrete mixing process to tailor its properties to specific construction requirements. Admixtures are instrumental in enhancing attributes like workability while effectively addressing challenges posed by extreme temperatures (12).

Concrete possesses multiple advantageous qualities that make it a highly favorable material for construction purposes, including its binding capabilities, strength, and durability. However, its utility across diverse weather conditions in its natural state is limited due to varying setting times. To address this challenge, the use of retarders and accelerators as admixtures becomes imperative in hot and cold weather scenarios to prolong or hasten the initial setting time, respectively. This strategic application ensures optimal performance and efficiency of concrete in a range of environmental conditions (13).

Retarders and accelerators can change the way hydration occurs (14). Admixtures that effectively improve the hydration process and prolong setting times are commonly referred to as retarders (10). A retarder is a substance that delays the hardening process of cement paste, and consequently, the hardening process of cement-based materials like concrete or mortar (15). Retarders are additive ingredients that delay the concrete’s initial setting time, giving concrete operations extra time, and can be utilized to slow down the rate of hydration, heat generation, and strength development. By preventing cement from reacting with water, retarding admixtures reduce the rate of hydration (16).

Under normal weather conditions, adding water to cement causes it to set and harden. However, in certain countries, hot weather conditions can lead to challenges in the concreting process. Hot winds, low humidity, and high temperatures can accelerate the evaporation of moisture from recently laid concrete. This quick evaporation can result in early setting of the concrete, limiting the time available for proper concreting processes. Research has shown that when the temperature of cement mortar rises between 27.80°C and 45.50°C, with a water-cement ratio of 0.6, both the initial and final setting times are significantly reduced to approximately half. In such adverse weather conditions, it becomes crucial to allow for sufficient time for the proper mixing, transporting, and placing of concrete. To address these challenges, the use of retarding admixtures is recommended. By incorporating these admixtures into the concrete mix, construction projects can maintain the required workability and achieve the desired results (17,18). Accelerators are indeed a crucial type of admixture in construction projects. Their primary function is to modify the hydration process's mechanism and kinetics, resulting in accelerated setting times (19,20). An accelerator is a substance that, when mixed with grout, concrete, or mortar, speeds up the hydraulic cement hydration process, cuts down the setting time, or hastens the hardening and strengthening process (15).

It is important to acknowledge the significant role those chemical admixtures play in enhancing concrete properties, such as retarders and accelerators. However, it is evident that these additives have negative implications for the environment, primarily due to leaching. The exposure of chemical admixtures during demolition or the use of debris containing them as gravel can contribute to environmental harm. Furthermore, environmental pollution can occur during the production, storage, transportation, and usage of concrete with chemical admixtures. Given the water-soluble nature of these additives, leaching poses a significant risk to environmental health. The cost implications of utilizing synthetic admixtures also contribute to the overall disadvantages associated with their usage. In light of these limitations, there is a rising curiosity about investigating alternate bio-based admixtures that are able to effectively enhance concrete properties without causing harm to the environment. This shift towards bio-admixtures not only aligns with sustainability goals but also presents an opportunity to reduce costs compared to synthetic options. As the construction industry continues to prioritize environmental considerations, the investigation and adoption of bio-based admixtures represent a promising pathway towards sustainable concrete solutions (21- 27). When using high-performance concrete, admixture costs can sometimes exceed those of cement. Therefore, research and the development of organic admixtures are essential to the advancement of concrete technology. This underscores the importance of focusing on the development of organic admixtures over cement enhancements (28). Therefore, the creation of environmentally friendly concrete will be aided by the discovery of substitute admixtures. Globally, scientists and researchers working with concrete are working to create non-chemical admixtures that are regarded as environmentally friendly and sustainable construction materials. Green or natural admixtures can be a realistic alternative and support green building because of their abundance and simple manufacturing process. Animal products, fruit, and herpes are combined to produce these concoctions. Natural admixtures and biopolymers produced through biotechnological processes are commonly called "bio-admixtures." It appears that employing natural admixtures made from plant or fruit extracts is a reasonable choice, despite the lack of research on the topic. Studies conducted on old buildings indicate that plant extract and lime were employed in construction (29). Hence, the incorporation of natural admixtures proves advantageous for improving the characteristics of both fresh and hardened concrete. Due to their environmentally friendly nature and cost-effectiveness, natural admixtures are deemed superior to chemical alternatives (30).

The history of the use of admixtures closely parallels that of concrete and mortar. Dating back to around 3000 BC in India, various types of natural admixtures, such as molasses, fruit juices, bananas, olive oil, milk products, and others, were commonly employed. These natural admixtures were integrated into lime mortar for a variety of purposes, including accelerators like starch, fig juice, and soured milk, plasticizers such as sugar, mineral oils, and olive oils, as well as glycerol, pine resin, protein, and reducing agents like bee wax (31,32). In ancient times, herbs used as admixtures in lime mortars (29). Jaggery is a natural product, making it environmentally friendly.

Its excellent binding qualities have led to its longstanding use in construction works in India and China for centuries (23). In ancient times, jaggery was a prevalent admixture (33). In Thirrsur, Kerala, India, the ancient Vadakkunnathan temple was renovated using jaggery, powdered shells, and various kinds of nine plants. A palm leaf manuscript found at the Padmanabhapuram Palace identified the various plaster mixture compositions used in the repair work at Fort Vettimurichakotta, East Fort, West Fort, Pazhavangadi, Puthen Street, Virakupurakkotta, and Sreevaraham in India. Palm jaggery was mixed with a variety of fruits, herbs, and a particular type of cactus, and the concoction was left to ferment for a period of fifteen days. This mixture was mixed with lime to make the plaster (29). For a very long time, the construction of the Channel between England and France used molasses(sugar), as a retardant (34). Molasses can be used as a retarder, water reducer, and grinding aid in construction materials. Molasses is a common admixture used in China in cement and concrete to reduce and retard water and also serves as a grinding aid (35).

2. Materials

2.1 Cement

When a material undergoes a chemical reaction with water and solidifies into a hard mass, it is commonly known as cement. Cement is essentially the capability of a substance to form strong bonds with other materials through a series of chemical reactions (36-38).

When calcareous (such as limestone) and argillaceous (such as clay) raw materials are subjected to high temperatures of 1400–1450 °C, clinker nodules form due to partial fusion. A specific percentage of calcium sulphate is blended with the clinker, and after finely grinding this mixture, cement is produced. Calcium sulphate, commonly referred to as gypsum, has a vital function in controlling the cement's setting process (38-40). The raw materials required for the production of cement include lime, silica, alumina, and iron oxide.

Table 1. Portland cement's approximate composition limits

Oxide	Content Percentage
CaO(Lime)	60-67
SiO_2(Silica)	17-25
Al_2O_3 (Alumina)	3-8
Fe_2O_3(Iron oxide)	0.5-6
MgO (Magnesia)	0.1-4
Alkalis	0.2-1.3
SO_3(Sulphur trioxide)	1-3

Throughout the kiln's heating process, various compounds present in the mixture react with each other, leading to the formation of a series of complex products. Among these products, four compounds are recognized as the primary constituents of Portland cement (enumerated in Table 2 along with their shortened symbols). The chemical symbols for these compounds are abbreviated for convenience in cement chemistry. For instance, CaO is represented as C, SiO_2 as S, Al_2O_3 as A, and Fe_2O_3 as F. Furthermore, in the context of hydrated cement, water (H_2O) is symbolized by the letter H.

Table 2. Portland cement's primary ingredients

Name of Compound	Oxide composition	Abbreviation
Tricalcium silicate	$3CaOSiO_2$	C3S
Dicalcium silicate	$2CaOSiO_2$	C2S
Tricalcium aluminate	$3CaOAl_2O_3$	C3A
Tetracalcium aluminoferrite	$4CaOAl_2O_3$ Fe_2O_3	C4AF

Once hydrated, Portland cement's strength is mostly determined by the silicates, specifically C3S and C2S. These compounds have a substantial effect on the cement's overall strength and durability. On the other hand, C3A is considered undesirable in Portland cement as it provides minimal to no contribution to the strength characteristics of the cement (38). Tricalcium silicate

(C3S or alite) is recognized as the primary compound in Portland cement, constituting 50-70% of its composition. Additionally, the percentages of dicalcium silicate (C2S or belite), tricalcium aluminate (C3A or aluminate), and tetracalcium aluminoferrite (C4AF or ferrite) in Portland cement typically range from 15-30%, 5-10%, and 5-15%, respectively (39).

2.1.1 Hydration of Cement

When water is mixed with anhydrous cement or its components, the resultant reaction leads to a series of chemical changes known as hydration (39). Hydration is a fundamental chemical process involving the interaction between anhydrous compounds and water molecules, leading to the formation of hydrated compounds with distinctive properties. This reaction not only induces superfluidity in the resultant compounds but also triggers mechanical, physical, and chemical changes (41). Concrete hardens through hydration, an exothermic event involving cement and water (16). When cement and water are mixed, numerous chemical reactions occur, initiating the transformation of a workable cement paste into a durable, solid structure. This conversion process is driven by the hydration reactions between ordinary Portland cement and water molecules, resulting in the formation of various components. The complexity of this process is influenced by the initial composition of the clinker, which in turn is affected by the alterations within the cement matrices. The intricate nature of these reactions underscores the intricacy involved in the solidification of cement through hydration (42).

Hydration kinetics is usually divided into three separate stages. In the beginning, there is an initial induction period followed by a nucleation and growth stage, and finally a diffusion-controlled phase. During the diffusion-controlled phase, which lasts around 48 hours after mixing, despite being early in the hydration process, it significantly affects the hydration kinetics (43). hydration, the silicates and aluminates found in Portland cement undergo a chemical reaction with water, as a result of which a solid mass form. The hydration of silicates results in the production of calcium silicate hydrate (C-S-H) and $Ca(oH)_2$ (38).

The hydration process of ordinary Portland cement is thoroughly documented, detailing the composition of its clinker which comprises four main phases: C2S and C3S (calcium silicates), C3A (calcium aluminate), and C4AF (ferrite). The addition of calcium sulphate helps regulate the setting process of ordinary Portland cement by acting on these phases. Early hydration primarily stems from C3S and C3A, whereas the slower hydration of C2S plays a more critical role in determining the cement's later properties (44).

The chemical reactions of cement during the hydration process closely resemble those of its individual calcium silicate phases, including C3S (alite) and β-C2S (the dominant form of belite). When these phases react with water independently, they generate comparable final products, which include calcium hydroxide and calcium silicate hydrates (commonly referred to as CSH gel). The primary composition of CSH gel is typically 3CaO·2SiO2·3H2O, although there may be variations in lime: silica ratios. Given that C3S and C2S make up around 75% of Portland cement, their hydration reactions are crucial in the overall cement hydration process. Although both silicates need a comparable quantity of water for hydration in terms of weight, C3S creates three times more Ca(OH)2 than C2S. Although most cements have low levels of C3A, the way it behaves and interacts structurally with other cement phases is of great interest. When tricalcium aluminate hydrate, likely when mixed with other solid substances, produces a dark, prism-like substance in between. Typically, this substance is found as flat plates encircled by calcium silicate hydrates. When C3A reacts with water independently, it triggers a fierce reaction that causes a rapid setting and the release of significant heat, making the cement difficult to work with. The equation C3A + 6H2O = C3AH6 (tricalcium aluminate hydrate) represents a quick response. In order to avoid this unwanted situation, gypsum (CaSO4.2H2O) is added to the cement clinker. This additional ingredient encourages the creation of ettringite, which regulates the setting process of the cement. The resulting chemical process can be summarized as: C3A + 3CaSO4.2H2O + 26H = C3A3CaSO4.32H2O (also known as ettringite) (45).

The hydration of cement is a complex and multifaceted process involving many chemical and physical interactions at a microscopic level. In essence, when the unhydrated cement and the mixture's free water combine, it results in the creation of different hydrates. Portland cement is

made up of important minerals like calcium silicates (C3S and C2S), calcium aluminates (C3A), and calcium aluminoferrites (C4AF). When mixed with water, it produces different hydrates such as calcium silicate hydrate (CSH), calcium hydroxide (CH), ettringite (Aft), and monosulfate (Afm). A thorough grasp of the mechanisms underlying hydration is still elusive, despite a century and more of research on the subject. It is clear that the various components' reaction rates differ greatly from one another. As such, the computer modeling of the complex interactions in a hydrating poly-mineral and poly-size mechanism is extremely intricate and requires the take-in of physical, chemical, stereological, and granular parameters. Because of these intricacies, it is crucial to move from studying the different compounds' hydration to studying the clinker hydration phenomenon. This means that the problem must be explained in terms of the entire hydration process. In conclusion, the hydration process of cement involves a complex interaction of different elements, necessitating a comprehensive approach to fully understand its complexities (46).For the purpose of comprehensively understanding the cement's hydration process, it is essential to examine the four primary clinker phases: alite, belite, aluminate, and ferrite. Simplistically, the following can be used to represent how cement hydrates:

- Clinker phases + water → Hydrated phase + energy
  (High in energy with no water) (low energy contains water) (heat of hydration) (47)

The hydration process in Portland cement is a key aspect in understanding its setting and hardening characteristics. Initially, When Portland cement's silicates react with water, calcium hydroxide $Ca(OH)_2$, often referred to as portlandite, and calcium silicate hydrate (C-S-H) are created. The following is a representation of this reaction:

- Silicates + water → C-S-H + portlandite

Additionally, the aluminates in Portland cement react with gypsum (calcium sulfate) in the presence of water to form ettringite. This reaction can be depicted as

- Aluminate (C3A) + calcium sulfate + water → ettringite (39).

Tricalcium aluminate's two primary hydration products are ettringite (AFt) and monosulfoaluminate (AFm(MS)). Gypsum promotes ettrigite production, and in a system that contains a low calcium carbonate content, monosulfoaluminate is the typical AFm phase (48).

The solidification and firming process of tricalcium silicate (alite) is similar to that of Portland cement. This process is affected by both the ratio of water to cement and the particle size distribution. As a result, gel-like calcium-silicate-hydrate (C-S-H) and calcium hydroxide (CH) are formed. Ettringite and monosulfate are produced during the process of cement hydration. Ettringite is a compound with a columnar structure made up of calcium sulfo-aluminate hydrates ($3CaO{\cdot}Al2O3{\cdot}3CaSO4{\cdot}32H2O$) and is known as an AFt-phase. In contrast, monosulfate is a type of AFm-phase compound that has a layered structure and is made up of ($3CaO{\cdot}Al2O3{\cdot}CaSO4{\cdot}12H2O$). In the beginning stages of Portland cement's hydration process, Ettringite, which is the main component of AFt, is created (39). In the absence of calcium sulphate, C3A reacts rather quickly. Unlike alite, C3A does not show a noticeable slow reaction time, leading to an almost instantaneous setting. Poorly crystallized aluminum hydroxide, or AFm3, phases are formed upon initial hydration; these phases are commonly recognized as C_2AH_8 and C_4AH_{13}(39,49,50,51).

The process of cement hydration involves a complex chemical reaction that progresses through several distinct stages. The cement's hydration can be broken down into four main stages. Initially, the silicates and aluminates present in Portland cement engage in a reaction with water, resulting in the formation of a durable solid mass. Specifically, the hydration process in Portland cement is kickstarted by the interaction between silicates and aluminates with water. Aluminates, when there is water present, also undergo a reaction with gypsum (calcium sulphate) to produce ettringites, further contributing to the overall hydration process.

Stage 1:

- $C3A + 3CaSO_4 + 32H_2O \rightarrow 3CaO.Al_2O_3.3CaSO_4.32H_2O$
  (Trisulphate or ettringite)

Furthermore, the combination of silicates with water forms calcium hydroxide, which is also called portlandite Ca(OH), and calcium silicate hydrate. The main source of strength in Portland cement comes from C3S, also known as alite, which is the primary component in cement. When Alite comes into contact with water, it rapidly undergoes a reaction. The external ions of alite start to break down, releasing silicate and hydroxyl ions. Therefore, the negative charge of ions such as hydroxyl and silicate anions balance out the positive charge of Ca+ ions. As alite dissolves quickly, the liquid phase becomes saturated before surface ions have a chance to permeate through. Due to this process of hydration, the formation of CSH, also known as tobermorite, occurs. Dicalcium silicates (C2S or belite) exhibit a similar hydration process to that of alite, but their reaction occurs at a slower pace. Tricalcium silicate (alite) behaves like Portland cement in terms of setting and hardening, with its properties being influenced by the water-to-cement ratio and particle size distribution. As a result, Calcium hydroxide (CH) and C-S-H (having a gel-like consistency) are formed. The process of adding water to cement leads to the creation of ettringite, which is a type of crystalline calcium sulfo-aluminate hydrate ($3CaO.Al_2O_3.3CaSO_4.32H_2O$, an AFt-phase) with a column structure, and monosulfate, which is another type of calcium sulfo-aluminate hydrate ($3CaO.Al_2O_3.CaSO_4.12H_2O$, an AFm-phase) with a lamellar structure. In the early stages of the hydration of Portland cement, ettringite, the most significant phase of the AFt, is formed.

Stage 2:

- $2C3S + 6H_2O \rightarrow 3CaO.2SiO_2.3H_2O + 3Ca(OH)_2$
  (Calcium silicate hydrate or C-S-H) (portlandite)

- $2C2S + 4H_2O \rightarrow 3CaO.2SiO_2.3H_2O + Ca(OH)_2$
  (Calcium silicate hydrate or C-S-H) (portlandite)

Stage 3:

- $C3A + Ca(OH)_2 + 12H_2O \rightarrow 4CaO.Al_2O_3.13H_2O$
- $C3AF + 4Ca(OH)_2 + 22H_2O \rightarrow 4CaO.Al_2O_3.13H_2O + 4CaO.Fe_2O_3.13H_2O$

Stage 4:

- $2C3A + 3CaO.Al_2O_3.3CaSO_4.32H_2O + 4H_2O \rightarrow 3CaO.Al_2O_3.CaSO_4.12H_2O$
  (ettringite) (monosulfate)

Ettringite plays a significant role in the early stages of the hydration of cement, serving as the initial precipitation product. Its formation is facilitated by the interaction of calcium aluminates with gypsum in the presence of water. This process effectively impedes the setting of cement. Subsequently, the reaction between calcium trisulfate and calcium disulfate with water gives rise to calcium silicate hydrate and calcium hydroxide (portlandite). Notably, calcium silicate hydrate stands out as the predominant product of cement hydration, accounting for 60-65% of the resulting solid mass (38,39,52-55). During the initial hydration of cement, a crucial phase in AFT is the formation of ettringite (39).

2.1.2 Setting of Cement

When water is added to the cement, it creates a paste that gradually becomes stiff, resulting in the paste beginning to harden (56). Setting is the process by which cement stiffens without a significant increase in compressive strength, and typically takes place within a few hours (39). Anhydrous cement particles are dispersed, while setting refers to the process where these scattered particles come together to form a strong, connected system. Typically, this process of change is achieved through a chemical interaction that occurs when water is mixed with the cement, initiating hydration - a reaction between the cement particles and water (57).

2.1.3 Initial Setting Time of Cement

Setting time is the amount of time that concrete takes to harden after water is mixed with the cement-aggregate mixture (16). The initial time for setting is a crucial factor when working with materials containing cement. The initial time of the setting process controls the timing of the

transportation schedule, the pouring and finishing of the concrete, and the consolidation of the concrete (58,59,60). The amount of time cement takes to set is incredibly important when it comes to placing concrete and conducting quality checks during the process. The duration in which the concrete sets dictate every step of the process, from mixing and transportation, to placement and finishing (61). The unhydrated cement particles dissolve in water upon the addition of water. In the first few hours, very little chemical activity is seen. During this initial phase, referred to as the induction period, hydration products lack a percolating structure, which causes concrete to behave in a roughly plastic manner with better workability. As a result, the material that is based on cement has minimal stiffness and strength, which are frequently viewed as unimportant. The products of hydration resulting from various cement particles begin to interact as the induction period comes to an end, causing the initial setting to occur. During this initial period, a cluster of hydration products begins to form, leading to the development of stiffness and strength. At this point, the material that is based on cement becomes stiff and difficult to work with (3).

The pure C3A rapidly undergoes a violent reaction with water. Therefore, the cement paste quickly becomes stiff, a process known as flash setting. Gypsum is included in the cement to avoid the occurrence of this sudden flash setting. If gypsum is absent in the cement, the tricalcium aluminate (C3A) will react very quickly, as demonstrated.

$$3Cao.\ Al_2O_3+6H2O\rightarrow 3Cao.\ Al_2O_3.6H_2O \quad (47) \qquad (1)$$

This fast-hardening property, while important for specific uses, may be inconvenient in the construction of concrete, where the concrete must be workable for a sufficient amount of time before it permanently hardens. Therefore, calcium sulfate is frequently added to cement mixes in order to regulate the aluminate phase's reaction. Gypsum (CaSO4•2H2O) is the most commonly utilized type of calcium sulfate added, but natural gypsum sources also often contain anhydrite (CaSO4). The presence of the hemihydrate form (CaSO4•0.5H2O) may occur when gypsum partially dehydrates during the grinding process. When calcium sulfate is present, it results in a notable change in the reaction behavior of C3A. Understanding and regulating these chemical reactions is essential for ensuring the effectiveness and standard of cement applications, especially in the context of producing concrete (62). Likewise, it quickly responds when exposed to calcium hydroxide, which is produced during the hydration of calcium silicates.

$$3Cao.\ Al_2O_3+\ Ca(oH)_2+12H_2O\rightarrow 4Cao.\ Al_2O_3.13H_2O \qquad (2)$$

Both reactions mentioned above showcase the rapid hardening of Portland cement paste. Therefore, the calcium sulphate in the form of gypsum is added to the clinker in the grinding mill. The gypsum helps slow down the setting of cement paste, while the calcium aluminate reacts with gypsum when mixed with water to create ettringite.

$$3Cao.\ Al_2O_3+\ 3(CaSO_4\ .2H_2O)+26H_2O\rightarrow 3Cao.\ Al_2O_3.\ 3CaSO_4.32H_2O \qquad (3)$$

Calcium Aluminate Gypsum Water Trisulphate or ettringite

In reactions 1 and 2 mentioned earlier, the creation of calcium aluminate hydrate occurs rapidly, causing the cement paste to gain some strength at its initial set. The interaction between calcium aluminate and calcium sulfate, specifically gypsum, leads to the formation of ettringites. During the initial phase of the hydration process, ettringites coat the cement particles and create a thin layer on them. This film allows the particles to slide freely, causing the cement paste to stay in a plastic state (47)**.** The inclusion of calcium ions and sulphate ions in cement paste helps regulate the flow properties of any system containing cement. The creation of ettringite is significant in determining the flow properties of cement paste. The addition of the sulphate phase is equally important to the dosage of sulphate in controlling the setting of cement. In order to form ettringite, a large quantity of Ca^{2+} ions are required as alkali sulphate cannot promote the formation of ettringite since it only provides SO_4^{2-} ions (63). Gypsum leads to the creation of an ettringite coating over the cement particles, serving to delay the rapid setting process (52). The incorporation of gypsum into Portland cement serves to prolong its setting time until a certain threshold is attained, characterized by a

plateau effect. Subsequent additions of gypsum beyond this critical point exhibit minimal impact on the setting time of the cement (64). A significant correlation was observed between the production of ettringite and the rheology of cement paste. The development of ettringite seems to be positively correlated with the reduction in cement paste workability. As the cement paste's ettringite content increased, so did the impact of the additional increased ettringite on the workability of the paste. The water-to-solid ratio of the cement paste changes when low-density ettringite forms (65). Fast reaction takes place at the beginning, followed by a swift reduction in speed within a short period. Ettringite is the primary hydrated phase that is produced during the initial stages of the reaction. Following the swift phase of reaction, there is a subsequent period characterized by decreased heat generation, the duration of which is determined by the concentration of calcium sulphate within the system. After the depletion of the introduced calcium sulphate, there is a swift acceleration in the reaction rate, leading to the formation of calcium monosulfoaluminate as the predominant product stage. In cement systems, the slow reaction of C3A must continue for an extended period of time following the peak rate of alite in order to achieve the appropriate setting and hardening. The primary concern with regard to the hydration process of C3A with calcium sulphate is focused on the unexpected delay in the initial reaction. Three possible reasons exist for the observed event:

- The reaction may be impeded by the existence of the product phase ettringite as it forms a diffusion barrier on the surfaces of C3A.
- Other phases, like AFm, may also hinder the reaction in a similar way.
- The presence of certain solute species released during the dissolution of calcium sulphate may directly inhibit the reaction (39,66,67).

2.2 Use of Chemical Admixtures to Regulate the Initial Setting Time

In the beginning stages of cement hydration, there is a quick sequence of reactions between C3S and water that begins as soon as the cement is mixed with water. During this stage, there is a notable exothermic reaction, with the heat generated from the wetting process and the dissolving of C3S being key factors. Thorough chemical examinations of the solution stages have given compelling proof that C3S dissolves completely and quickly at the beginning of wetting. As the reaction continues, the pace of response decreases because a thin but continuous layer of a metastable phase called C-S-H(m), which is calcium silicate hydrate, forms quickly. This layer serves to protect the surface by preventing water from entering and stopping the release of ions from the surface. It is suggested that by the conclusion of the initial response time, this thin layer will reach a state of equilibrium with the solution. In unretarded and unannealed alite and C3S systems, the time of the delay is when the pace of hydration reaches its lowest point following the initial response, before the rapid formation of products of hydration begins. A distinct induction period is only noticeable when the chemical retarders are used or when the materials are annealed. This postponement is primarily due to a slow reaction caused by one of the mechanisms mentioned before, until it reaches a critical point, which then accelerates the nucleation and growth processes (68). The kinetics of cement hydration are significantly influenced by concrete admixtures, particularly in the early stages of inactivity. The adjustments of the intermolecular forces between ion species in the aqueous solution within the concrete appear to be the primary influence of these admixtures. Repulsive forces predominate during the solvation stage, whereas attractive forces do so during the crystallization stage. As the hydration advances, these bound force transitions result in two volumetric changes. Concrete admixture’s impact on cement reactions can be clearly observed through experiments conducted with an immersion weighing system. Accelerators cause instant shrinkage tendencies, while retarder agents cause volume expansion. A Le Chatelier-like theoretical model involving a solvation-crystallization sequence is found to be a suitable model to describe the hydration kinetics. Volume expansion happens when repulsive forces are in charge, preventing the development of strength. The dormant phase is determined by how long the swelling process takes. When volume shrinkage is visible, the hardening and strength-building process begins (69).

An essential part of the process of creating concrete is the admixture. The way an admixture reacts to cement paste influences both the paste's fluidity and the cement's stiffness (7). The admixture is

important to the process of making concrete as a key ingredient. Not only does the admixture-cement paste interaction affect the cement paste's flow characteristics, but it also influences the rigidity of the cement itself (28). An admixture is an ingredient included in a concrete mix to alter or enhance the characteristics of the concrete when it is freshly poured or once it has hardened (7). Chemical additives are primarily utilized to regulate the setting time, hardening time, and flow characteristics of concrete (70). The setting time can be adjusted to speed up or slow down by using the right admixtures (12). Chemical additives manage the flow properties of newly mixed concrete. Retarders and accelerators can alter the process of cement hydration (71). The quantity of admixture applied can affect how quickly cement hydrates. Some admixtures can be used as water reducers to delay the hydration of cement; this depends on the mixing ratio (72). Concrete's workability and rheological qualities are crucial; hence admixtures are typically added to the mixture to enhance these qualities. When these admixtures are applied to concrete in the recommended dose, the concrete's characteristics typically change (73). The rheological characteristic is crucial for concrete. The interaction between the admixture and cement can lead to abrupt alterations in the flow of concrete and result in varying levels of stiffness, depending on the specific combination of admixture and cement used (28,74,75,76,77).

Admixtures play an important part in the concrete production process. The characteristics of admixtures play a vital part in deciding their suitability for various applications. Table 3 displays the different types of chemical admixtures and the properties of their particles (78).

Table 3. Chemical admixtures types

Chemical admixtures	Function
Superplasticizer	To decrease the amount of water needed by 15% to 20% without compromising the workability, resulting in a strong and compact concrete
Accelerator	In cold weather concreting, accelerator is added to concrete to decrease the time it takes for the concrete to set, enabling the forms to be removed sooner
Retarder	Slowing down the hydration of cement helps to prolong the setting time, making retarders a preferred option for concreting in hot environments
Water reducing admixture	In order to attain a specific amount of workable consistency in concrete with a low water-cement ratio for a desired strength, thereby reducing the amount of cement needed
Air entraining admixture	Incorporating tiny air bubbles into concrete serves as rollers that enhance its workability. This is particularly beneficial in cold climates, as the air bubbles act as a cushion to prevent damage from expanding water during freeze-thaw cycles.

2.3 Use of Sugarcane Juice and Its Products as Admixtures

Sugarcane is a significant crop. It is grown in tropical and subtropical regions around the globe. India ranks as the second-biggest producer of this crop following Brazil. The composition of sugarcane juice includes 75 to 85% water, 0.3 to 3% reducing sugar, and 10 to 21% nonreducing sugar (79,80).

The process of tricalcium silicate (alite) setting and hardening is similar to that of Portland cement, and it is influenced by the water-to-cement ratio and particle size distribution. This leads to the formation of C-S-H (gel-like) and calcium hydroxide (CH). In the process of cement hydration, ettringite and mono sulfate are formed. Ettringite is a crystalline calcium sulfo-aluminate hydrate with a column structure ($3CaO{\cdot}Al_2O_3{\cdot}3CaSO_4{\cdot}32H_2O$, AFt-phase), and mono sulfate is a calcium sulfo-aluminate hydrate with a lamellar structure ($3CaO{\cdot}Al_2O_3{\cdot}CaSO_4{\cdot}12H_2O$, AFm-phase). During the initial hydration process of Portland cement, Ettringite is the most critical phase within the AFt mineral (39).

The microstructure of C-S-H undergoes changes when sucrose is added, impacting the formation process (81). Admixtures used to modify the characteristics of concrete include sugar and jaggery. The principal justification for the addition of jaggery and sugar as admixtures is that, as they are introduced, their adsorption creates a thin coating on top of the cement particles, delaying the hydration process. Calcium hydroxide formation will be inhibited by the generation of calcium ions, which will improve their solubility. This has led to an improvement in concrete's setting characteristics (73). By including sucrose in the cement paste, the setting process of the cement is initiated, leading to either accelerated or delayed setting based on the production of Aft (82). The number of admixtures that cause delays in setting time is crucial. In simpler terms, the extent of delay or acceleration depends on the quantity of the admixture used. Additives such as sucrose, glucose, and other substances. because of retardation and additives such as organic compounds, inorganic salts, etc. because it speeds up the cement's hydration process. Substances like triethanolamine and triisopropanolamine can speed up the process when used in small amounts (83). The slowing down of cement hydration is influenced by the amount of admixture used. The hydration of cement may be delayed by adding certain admixtures that act as water reducers, depending on how they are mixed (72). A strong relationship was found between the formation of ettringite and the flow characteristics of cement paste. The decreased workability of cement paste was directly linked to the increased production of ettringite. As the amount of ettringite in the cement paste increased, the impact of the additional ettringite on the workability of the paste also increased. The water-to-solid ratio of the cement paste shifts as low-density ettrigite is produced (65).

The large quantity of AFt was produced by adding varying amounts of sucrose solution to Portland cement. The addition of a high amount of sucrose solution to cement sped up the hydration process, thus causing the cement to set faster (84). Ettringite development in cement-based materials can be linked to both helpful and detrimental activities (48). When a small amount of sucrose, specifically 0.045% of the weight of the cement, is included, it leads to a decrease in the consistencies of Ca^{2+} and OH^- ions, resulting in the formation of highly soluble Ettringite (Aft). Hence, the AFT is formed as a gel-like substance that coats the clinker particle surface, causing sucrose to function as a retarding agent. Increasing the sucrose content to 0.24% negatively affects the C2S and C3S hydration, as the consistency of Ca^{2+} and OH^- speeds up the setting process, causing Aft to act more effectively. and the AFt acts like a needle to construct a network of hydration products and quicken the setting procedure. C2S and C3S are unable to produce enough C-S-H, which hinders the development of strength (85). Having more molasses will result in extending the duration of the induction phase. The aluminate phase's dissolution can be accelerated with a small quantity of sugarcane molasses, whereas too much may increase the formation and growth of AFt in the initial stages. The addition of 1.0% molasses accelerates the formation of AFt during the hydration of C3A and ferrite. Nevertheless, the addition of 1.0% molasses to cement paste significantly inhibits the secondary hydration of C3A and Ferrite, while also delaying the hydration of C3S (86).

The use of sugar as an additive significantly affects the cement's times for both initial and final setting. The addition of a small quantity of sugar caused a significant increase in the setting times of the cement. The addition of approximately 0.05% sugar caused the initial and final setting times of the cement to reach their highest levels. When sugar content exceeded 0.05%, the setting times started to decrease. It was found that the initial setting time of the cement decreased by a smaller amount when the sugar content was above 0.1% compared to when the sugar content was zero (87). It was discovered in the research that adding different types of sugar like granular, caster, or brown in amounts of 0.5%, 1.5%, or 0.5% can slow down the setting process of cement. Nevertheless, when included in proportions of 2.5% and 5%, all of these sugars functioned as a cement accelerator. The cement's final setting time was found to increase when sugar was added up to a certain ratio, specifically the optimal 1.5%, but decrease when added in higher amounts. The initial setting time of cement was decreased and extended by adding sugar of any kind (88).

It was found that adding up to 0.2% sugar to the cement paste caused a longer initial setting time compared to adding no sugar, and that adding up to 0.15% sugar resulted in a longer final setting time. With no sugar added, the initial and final settings took place at 120 and 349 minutes,

respectively. The cement hardened in 174 minutes with the addition of 0.2% sugar, compared to 112 minutes with 0.15% sugar. The final settings took place at 491, 316, and 294 minutes by adding 0.15%, 0.2%, and 0.25% sugar, respectively (89).

3. Methodology

The sugarcane juice utilized for this study was procured from a facility located near the laboratory in Uttar Pradesh, India, which is equipped with a machine specifically designed for the extraction of sugarcane juice. The ambient laboratory temperature during the testing phase was maintained at a controlled range of [23-27°C], ensuring consistent conditions for all experimental procedures. This controlled environment is critical for minimizing variability in the results and enhancing the reliability of the data obtained. All procedures adhered to established protocols to ensure the integrity of the sugarcane juice and the accuracy of the testing outcomes. Tests were conducted using cement paste without any sugarcane juice added, as well as with various ratios of sugarcane juice to the weight of the cement.

3.1 Consistency of Cement

3.1.1 Sample Preparation

Initially, a sample consisting of 400 grams of cement is prepared. Sugarcane juice is then added at varying percentages of 0%, 5%, 10%, 15%, 20%, 25%, and 28% by weight of the cement sample. The remaining water is used to adjust the consistency of the paste. For instance, when adding 5% sugarcane juice to the cement, 20 grams of sugarcane juice are incorporated, and the consistency is adjusted using water. Interestingly, with the addition of 28% sugarcane juice, no additional water is needed, indicating that the paste consists solely of sugarcane juice.

The prepared cement pastes samples undergo testing using the Vicat apparatus in accordance with IS 4031-4 standard. This involves placing the samples in a mould and positioning them under the Vicat apparatus's plunger. The percentage of combined water and sugarcane juice is carefully noted when the plunger penetrates 5 to 7 mm from the bottom of the sample within five minutes after the addition of water and sugarcane juice to the cement.

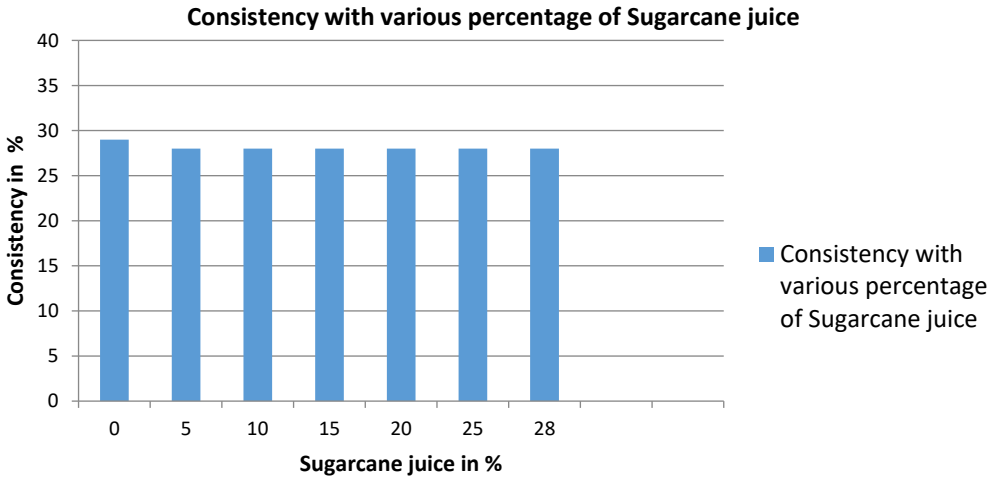

Fig. 1. Consistency with various percentage of Sugarcane juice

Table 4. Consistency with various percentage of Sugarcane juice

Percentage of Sugarcane juice (in %)	0	5	10	15	20	25	28
Consistency (in %)	29	28	28	28	28	28	28

3.2 Initial Setting Time of Cement

3.2.1 Sample Preparation

First, 400 grams of cement is taken and different amounts of sugarcane juice are added at percentages ranging from 0% to 28% by weight of the cement (0%, 5%, 10%, 15%, 20%, 25%, and 28%). Then, 85% of the normal consistency of cement, along with water and the specified percentage of sugarcane juice, are added to the mixture. The cement paste sample is prepared and tested using the Vicat apparatus in accordance with IS 4031-5. That is to say, the samples that have been prepared are placed in the mold and positioned under the needle of the Vicat apparatus. The time it takes for the needle to penetrate 5.0 ± 0.5 mm from the bottom of the sample is then recorded.

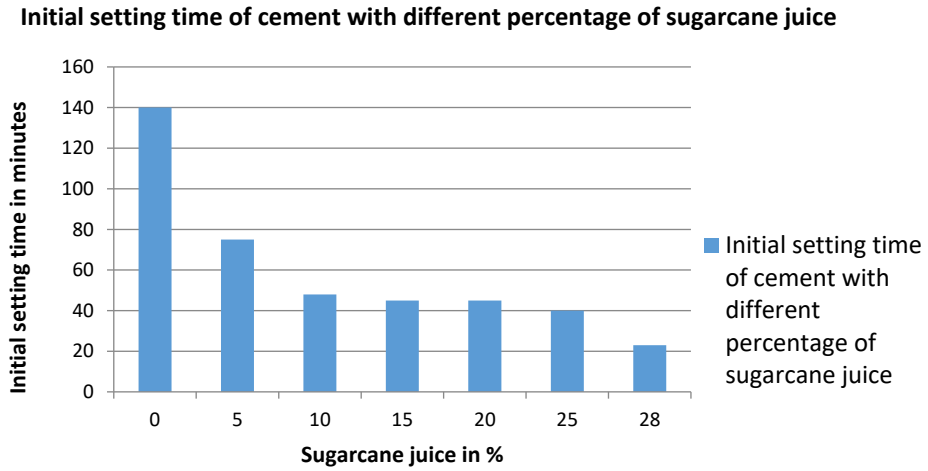

Fig. 2. Initial setting time of cement with different percentage of sugarcane juice

Table 5. Initial setting time of cement with different percentage of sugarcane juice

Percentage of Sugarcane juice (in %)	0	5	10	15	20	25	28
Initial setting time (in min.)	140	75	48	45	45	40	23

4. Results and Discussion

During the investigation, it was discovered that adding various amounts of sugarcane juice (5%, 10%, 15%, 20%, 25%, and 28%) did not significantly change the consistency of the cement paste compared to when no sugarcane juice was added. Overall, adding sugarcane juice to cement paste can considerably reduce its penetration depth or setting time. The initial setting time of cement paste decreased by 46%, 66%, 68%, 68%, 71%, and 84% when sugarcane juice was added in percentages of 5, 10, 15, 20, 25, and 28%, respectively. These findings indicate that adding larger quantities of sugarcane juice speeds up the setting process of the cement paste. If the hydration process of cement speeds up (causing the cement paste to harden rapidly), the time it takes for the cement to initially set decreases significantly. Therefore, the needle penetrates the Vicat's apparatus less when compared to the control cement paste (without sugarcane juice).

Prior research has also mentioned a decrease in setting time as a common trend. S.C.Paul and colleagues examined that the adding sugarcane juice to the cement paste caused a notable decrease in the time it took for the mixture to set. Experimentation revealed that adding higher amounts of sugarcane juice to the cement paste led to even faster setting times when compared to the standard cement paste without any sugarcane juice added. More precisely, the addition of sugarcane juice at 2, 5, 10, and 20% by weight of cement resulted in a decrease in the initial setting time of the cement by 33, 57, 70, and 90% respectively, in comparison to the regular cement paste. These results clearly show that sugarcane juice is a powerful catalyst, expediting the hardening of cement (90). The

setting time was noticeably affected by the small amount of sugar added. The setting time peaked when sugar was added to 0.05% of the weight of the cement. Nevertheless, adding more sugar caused the setting time to decrease. More precisely, the addition of 0.1% sugar caused a further decrease in setting time compared to cement paste without sugar (87). In the study, it was observed that both the initial and final setting times of the cement increased as the proportions of sugar were raised. However, these setting times reached their peak when the sugar proportion was at 0.05%. Subsequently, with sugar proportions exceeding 0.08%, both setting times began to decrease. Notably, the setting time of the cement exhibited a significant drop starting from a sugar proportion of 0.2%. Furthermore, the cement's initial setting time was discovered to be only a few minutes when mixed with sugar at levels ranging from 0.8% to 1.0%(91).

5. Conclusion

Research findings from multiple scholars highlight an enduring pattern of incorporating sugarcane-derived products, including jaggery, molasses, and sugar, as additive components in the formulation of construction materials. This tradition has its origins rooted in ancient history and has managed to retain its significance, playing an important role in various modern-day applications. The results derived from these studies emphasize the substantial influence that sugarcane juice and its related by-products exert on the chemical and physical processes involved in the hydration of cement.

This specific investigation involved conducting experimental research to thoroughly evaluate and analyze the impact of incorporating sugarcane juice as an admixture in cement mixtures, aiming to understand its influence on the properties and performance of the cement formulations. The findings of this study indicate that the addition of varying percentages of sugarcane juice does not significantly affect the consistency of cement paste. Specifically, when no sugarcane juice was added (0% concentration), the consistency was measured at 29%. This value remained relatively stable with the incorporation of sugarcane juice, with consistency measurements recorded at 28% for 5%, 10%, 20%, and 25% concentrations, as well as for a 28% concentration of sugarcane juice.

However, the results unequivocally demonstrate that the inclusion of sugarcane juice in the cement mixture significantly reduces the duration required for the initial setting process of the cement. This finding suggests that while the consistency remains largely unchanged, the setting time is notably influenced by the presence of sugarcane juice, which could have practical implications for construction practices and the use of cementitious materials. In particular, as the proportion of sugarcane juice in the mixture rises, there is a significant decrease observed in the initial setting times of the cement paste, indicating a faster onset of the setting process. The data reveal a significant reduction in the initial setting times of cement paste when sugarcane juice is added in varying proportions. Specifically, incorporating sugarcane juice at concentrations of 5%, 10%, 15%, 20%, 25%, and 28% resulted in decreases of 46%, 66%, 68%, 68%, 71%, and 84%, respectively, compared to the initial setting time of the control cement paste that contained no sugarcane juice.

The results highlight the significant role played by sugarcane juice in expediting the hydration process of cement, with its effectiveness becoming increasingly pronounced when used in higher concentrations. This research holds substantial importance as it paves the way for the advancement and innovation of construction materials that prioritize both efficiency in performance and sustainability in environmental impact.

6. Acknowledgement

I would like to express my sincere gratitude to Mr. Prashant Kumar (Material Engineer, Highways and Bridges projects, India) for his support. I am especially thankful to Mr. Pankaj Tiwari (Material Engineer, Highways and Bridges projects, India) and Mr. Manoj Sharma (Material Engineer, Highways and Bridges projects, India) for their efforts in arranging the necessary equipment and personnel in their respective labs for my experiments. I extend my heartfelt appreciation to Mr. Shivam Kumar (Highways and Bridges projects, India), whose assistance as a technician was invaluable during my experiments. With the collective support of all, I was able to conduct my research work with ease and efficiency. Thank you all for your contributions.

References

[1] Memon RA, Memon FA. Experimental study on the effect of sugarcane juice as an admixture on fresh and hardened properties of concrete. Int Res J Mod Eng Technol Sci. 2022;4(5):e-ISSN:2582-5208.
[2] Otunyo AW, Koate I. Sugar cane juice as a retarding admixture in concrete production. Glob J Eng Res. 2015;14:17-23. https://doi.org/10.4314/gjer.v14i1.3
[3] De Schutter G. Influence of hydration reaction on engineering properties of hardening concrete. Mater Struct. 2002;35:447-52. https://doi.org/10.1007/BF02483131
[4] Neville AM, Brooks JJ. Concrete technology. New Delhi: Dorling Kindersley; 2006.
[5] Usman ND, Idusuyi FO, Ojo EB, Simon BM. The use of sawdust and palm kernel shell as substitute for fine and coarse aggregates in concrete construction in developing countries. J Chem Mech Eng Pract. 2012;2(3):51-62.
[6] Neville AM. Properties of concrete. 5th ed. Harlow, UK: Trans-Atlantic Publications; 2012.
[7] Li Z. Advanced concrete technology. New York, NY: John Wiley & Sons; 2011.
[8] Usman ND, Adebitan EO, Kwari JK, Gyang JB. Determination of engineering properties of locust bean waste and wild vine use in construction in Nigeria. In: SABS Conf; 2013 Oct 10-12; Nairobi, Kenya. Jomo Kenyatta Univ Agric Technol.
[9] Naqash JA, Bhat ZB, Malik MI, Ahmad S, Kumar D. Effect of accelerating admixture on properties of concrete. IOSR J Eng. 2014;4(3):48-55. https://doi.org/10.9790/3021-04314855
[10] Lea F. The chemistry of cement and concrete. 3rd ed. London, UK: Edward Arnold; 1988.
[11] Maheswari AU, Harshavardhan R, Tejas JS, Chandradeep K, Monisha SK, Padal S, et al. Utilization of sugarcane bagasse as retarder in concrete. Int J Innov Res Technol. 2021;8(3):ISSN:2349-6002.
[12] Shah DS, Shah PM, Pitroda JK. Chemical admixtures: A major role in modern concrete materials and technologies. In: Natl Conf Trends Challenges Civ Eng. 2014. ISBN:978-81-929339-0-0.
[13] Kawade A, Kamthe I, Khemalapure AB. Experimental study of effect of sugar on properties of concrete. J Struct Transp Stud. 2017;2(1).
[14] Mohamed AK, Weckwerth SA, Mishra RK, Heinz H, Flatt RJ. Molecular modeling of chemical admixtures; opportunities and challenges. Cem Concr Res. 2022;156:106783. https://doi.org/10.1016/j.cemconres.2022.106783
[15] Bureau of Indian Standards. IS 9103 (1999): Specification for concrete admixtures. New Delhi: BIS; 1999.
[16] Eloge MO, Abuodha SO, Winja MMO. The effect of sisal juice extract admixture on compressive and flexural strength of cement concrete. Eng Technol Appl Sci Res. 2021;11(2):7041-6. https://doi.org/10.48084/etasr.4030
[17] Dheenadhayalan M, Suvetha G, Monica D, Shenoi PS, Dhanasekaran R. Effect of sugarcane juice in concrete by partial replacement of water, recycled coarse aggregate and silica fume in fine aggregate. Int J Intell Res. 2016;7:ISSN:0976-9859.
[18] Khan B, Baradan B. The effect of sugar on setting-time of various types of cements. Q Sci Vis. 2002;8:71-8.
[19] Prudencio LR. Accelerating admixtures for shotcrete. Cem Concr Compos. 1998;20:213-9. https://doi.org/10.1016/S0958-9465(98)80007-3
[20] Salvador RP, Cavalaro SHP, Segura I, de Figueiredo AD, Perez J. Early age hydration of cement pastes with different types of accelerating admixtures for sprayed concrete. Cem Concr Compos. 2016;ISSN:0950-0618. https://doi.org/10.1016/j.conbuildmat.2016.02.101
[21] Faqe H, Dabbagh H, Mohammed A. Natural admixture as alternative for chemical admixture in concrete technology: a review. J Duhok Univ. 2020;23(2):301-8. https://doi.org/10.26682/csjuod.2020.23.2.24
[22] Patel GK, Deo SV. Effect of natural organic materials as admixture on properties of concrete. Indian J Sci Technol. 2016;9(37). https://doi.org/10.17485/ijst/2016/v9i37/93541
[23] Dandotiya A, Parihar RS, Jha AK. An investigational properties of concrete using jaggery. Int J Trend Sci Res Dev. 2022;6(5). Available from: www.ijtsrd.com
[24] Togero A. Leaching of hazardous substances from additives and admixtures in concrete. Environ Eng Sci. 2006;23(1):102-16. https://doi.org/10.1089/ees.2006.23.102
[25] Abdulrahman AS, Mohammad I. Green plant extract as a passivation promoting inhibitor for reinforced concrete. Int J Eng Sci Technol. 2011;3(8):6484-90.
[26] Chandra S, Eklund L, Villarreal RR. Use of cactus in mortars and concrete. Cem Concr Res. 1998;28(1):41-51. https://doi.org/10.1016/S0008-8846(97)00254-8
[27] Dwivedi VN, Das SS, Singh NB, Rai S, Gajbhiye NS. Portland cement hydration in the presence of admixtures black gram pulse and superplasticizer. Mater Res. 2008;11(4):427-31. https://doi.org/10.1590/S1516-14392008000400008
[28] Hanehara S, Yamada K. Interaction between cement and chemical admixture from the point of cement hydration, absorption behaviour of admixture, and paste rheology. Cem Concr Res. 1999;29:1159-65. https://doi.org/10.1016/S0008-8846(99)00004-6

[29] Thirumalini P, Sekar SK. Review on herb used as admixture in lime mortar used in ancient structures. Indian J Appl Sci. 2013;3(8):295-8. https://doi.org/10.15373/2249555X/AUG2013/93
[30] Mahmood HF, Dabbagh H, Mohammed AA. Comparative study on using chemical and natural admixtures (grape and mulberry extracts) for concrete. Case Stud Constr Mater. 2021;15:e00699. https://doi.org/10.1016/j.cscm.2021.e00699
[31] Chandra S. Architecture and ancient building materials in India. New Delhi: Tech Books International; 2003.
[32] Kurdowski W. Cement and concrete chemistry. Dordrecht: Springer; 2014. ISBN: 978-94-007-7944-0.
[33] Michelle S. Did our church builders use egg white as mortar ingredients? The bimolecular reason behind collecting mortar samples from historical sites. Proc Soc Philipp Archaeol. 2009;7. Available from: https://www.academia.edu
[34] Neville AM. Properties of concrete. Vol. 4. London: Longman; 1995.
[35] Olbrich H. The molasses. Berlin: Biotechnologie-Kempe GmbH; 2006.
[36] Paul SC, Van Rooyen AS, Van Zijl GP, Petrik LF. Properties of cement-based composites using nanoparticles: a comprehensive review. Constr Build Mater. 2018;189:1019-34. https://doi.org/10.1016/j.conbuildmat.2018.09.062
[37] Bahhou A, Taha Y, Khessaimi YE, Hakkou R, Tagnit-Hamou A, Benzaazoua M. Using calcined marls as non-common supplementary cementitious materials-a critical review. Minerals. 2021;11(5):517. https://doi.org/10.3390/min11050517
[38] Neville AM, Brooks JJ. Concrete technology. Malaysia: Prentice Hall; 2010. ISBN: 978-0-273-73219-8.
[39] Taylor HFW. The chemistry of cements. 2nd ed. New York: Thomas Telford Services Ltd; 1997.
[40] Singh NB, Chaturvedi S, Rai S. Chemistry of Portland cement. J Indian Chem Soc. 2003;80:319-25.
[41] Whittaker M, Dubina E, Plank J, Black L. The effects of prehydration on cement performance. In: Proc 30th Cement and Concrete Science Conf; 2010 Sep 13-15; Birmingham, UK.
[42] Lavagna L, Nistico R. An insight into the chemistry of cement-a review. Appl Sci. 2023;13:203. https://doi.org/10.3390/app13010203
[43] Bishnoi S, Scrivener KL. Studying nucleation and growth kinetics of alite hydration using μic. Cem Concr Res. 2009;39:849-60. https://doi.org/10.1016/j.cemconres.2009.07.004
[44] Taylor HFW. Cement chemistry. London: Academic Press, Harcourt Brace Jovanovich Publishers; 1990.
[45] Potgieter JH, Kaspar H. Hydration of cement. S Afr Tydskr Chem. 1999;52(4).
[46] Van Breugel K. Numerical simulations and microstructural development in hardening cement-based material. Heron. 1992;37(3):1-61.
[47] Labahn O, Amerongen CV (translator), Kohlhaas C (editor). Cement engineers handbook. 4th Engl. ed. Wiesbaden, Berlin: Bauverlag; 1983.
[48] Honorio T, Guerra P, Bourdot A. Molecular simulation of the structure and elastic properties of ettringite and monosulfoaluminate. Cem Concr Res. 2020;135:106126. https://doi.org/10.1016/j.cemconres.2020.106126
[49] Corstanje WA, Stein HN, Stevels JM. Hydration reactions in pastes C3S + C3A + CaSO4·2H2O at 25 °C. Cem Concr Res. 1973;3:791-806. https://doi.org/10.1016/0008-8846(73)90012-4
[50] Corstanje WA, Stein HN, Stevels JM. Hydration reactions in pastes C3S + C3A + CaSO4·2H2O at 25 °C III. Cem Concr Res. 1974;4:417-31. https://doi.org/10.1016/0008-8846(74)90107-0
[51] Breval E. C3A hydration. Cem Concr Res. 1976;6:129-38. https://doi.org/10.1016/0008-8846(76)90057-0
[52] Cocke DL, Mollah MYA. The chemistry and leaching mechanisms of hazardous substances in cementitious solidification/stabilization systems. In: Spence RD, editor. Chemistry and microstructure of solidified waste forms. Boca Raton, FL: Lewis Publishers; 1993. p. 187-241.
[53] Collepardi M. A state-of-the-art review on delayed ettringite attack on concrete. Cem Concr Compos. 2003;25(4-5):401-7. https://doi.org/10.1016/S0958-9465(02)00080-X
[54] Batic OR, Milanesi CA, Maiza PJ, Marfil SA. Secondary ettringite formation in concrete subjected to different curing conditions. Cem Concr Res. 2000;30:1407-12. https://doi.org/10.1016/S0008-8846(00)00343-4
[55] Wang L, Yang HQ, Zhou SH, Chen E, Tang SW. Hydration, mechanical property and C-S-H structure of early-strength low-heat cement-based materials. Mater Lett. 2018;217:151-4. https://doi.org/10.1016/j.matlet.2018.01.077
[56] Baradan B. Construction materials - II. 5th ed. Izmir: Dokuz Eylul University, Technical Faculty Publication Section; 1998.
[57] Jiang SP, Mutin JC, Nonat A. Studies on mechanism and physico-chemical parameters at the origin of cement setting. Cem Concr Res. 1995;25(4):779-89. https://doi.org/10.1016/0008-8846(95)00068-N
[58] Lee HK, Lee KM, Kim YH, Yim H, Bae DB. Ultrasonic in-situ monitoring of setting process of high-performance concrete. Cem Concr Res. 2004;34:631-40. https://doi.org/10.1016/j.cemconres.2003.10.012

[59] Zheng JJ, Zhang J, Scherer GW. Prediction of the degree of hydration at initial setting time of cement paste with particle agglomeration. Cem Concr Res. 2012;42:1280-5. https://doi.org/10.1016/j.cemconres.2012.05.020
[60] Aydin AC, Gül R. Influence of volcanic originated natural materials as additives on the setting time and some mechanical properties of concrete. Constr Build Mater. 2007;21:1277-81. https://doi.org/10.1016/j.conbuildmat.2006.02.011
[61] Pessiki SP, Carino NJ. Setting time and strength of concrete using the impact-echo method. ACI Mater J. 1988;85:389-99. https://doi.org/10.14359/2312
[62] Minard H, Garrault S, Regnaud L, Nonat A. Mechanisms and parameters controlling the tricalcium aluminate reactivity in the presence of gypsum. Cem Concr Res. 2007;37:1418-26. https://doi.org/10.1016/j.cemconres.2007.06.001
[63] Prince IW, Espagne M, Aitcin PC. Cement and Concrete Research. 2003;33(5):635-41. https://doi.org/10.1016/S0008-8846(02)01042-6
[64] Lea F. The chemistry of cement and concrete. 4th ed. London: Edward Arnold; 2006.
[65] Jakob C, Jansen D, Ukrainczyk N, Koenders E, Pott U, Stephan D, Neubauer J. Relating Ettringite Formation and Rheological Changes during the Initial Cement Hydration: A Comparative Study Applying XRD Analysis, Rheological Measurements and Modeling. Materials. 2019;12:2957. https://doi.org/10.3390/ma12182957
[66] Gaidis JM, Gartner EM. Hydration mechanisms, II. In: Skalny J, Mindess S, editors. Materials Science of Concrete, Vol. 2. Westerville (OH): American Ceramic Society; 1989. p. 9-39.
[67] Tenoutasse N. The hydration mechanism of C3A and C3S in the presence of calcium chloride and calcium sulphate. In: Proc 5th Int Symp on the Chemistry of Cement. Tokyo: The Cement Association of Japan; 1968. p. 372-8.
[68] Bullard JW, Jennings HM, Livingston RA, Nonat A, Scherer GW, Schweitzer JS, et al. Mechanisms of cement hydration. Cem Concr Res. 2011;41:1208-23. https://doi.org/10.1016/j.cemconres.2010.09.011
[69] Paulini P. Reaction mechanisms of concrete admixtures. Cem Concr Res. 1990;20:910-8. https://doi.org/10.1016/0008-8846(90)90053-Z
[70] Sakai E, Ishida A, Ohta A. New trends in the development of chemical admixtures in Japan. J Adv Concr Technol. 2006;4(2):211-23. https://doi.org/10.3151/jact.4.211
[71] Nkinamubanzi PC, Mantellato S, Flatt RJ. Superplasticizers in practice. In: Aïtcin PC, Flatt RJ, editors. Science and Technology of Concrete Admixtures. Amsterdam: Elsevier; 2016. p. 353-78. https://doi.org/10.1016/B978-0-08-100693-1.00016-3
[72] Marchon D, Flatt RJ. Mechanisms of cement hydration. In: Aïtcin PC, Flatt RJ, editors. Science and Technology of Concrete Admixtures. Amsterdam: Elsevier; 2016. p. 129-46. https://doi.org/10.1016/B978-0-08-100693-1.00008-4
[73] Kumar AVP, Venkatesh B, Prasad BBCO. Effect of sugar, jaggery & sugar cane ash on properties of concrete. Int J Sci Eng Technol Res. 2015;4(51).
[74] Nocun-Wczelik W, Trybalska B. Effect of admixtures on the rate of hydration and microstructure of cement paste. Cem Wapno Beton. 2007;6:284-9.
[75] Du L, Folliard KJ. Mechanisms of air entrainment in concrete. Cem Concr Res. 2005;35:1463-71. https://doi.org/10.1016/j.cemconres.2004.07.026
[76] Yang Q, Zhu P, Wu X, et al. Properties of concrete with a new type of saponin air-entraining agent. Cem Concr Res. 2000;30:1313-7. https://doi.org/10.1016/S0008-8846(00)00340-9
[77] Mohamed AK, Weckwerth SA, Mishra RK, Heinz H, Flatt RJ. Molecular modeling of chemical admixtures: Opportunities and challenges. Cem Concr Res. 2022;156:106783. https://doi.org/10.1016/j.cemconres.2022.106783
[78] Patel V, Shah N. A survey of high performance concrete developments in civil engineering field. Open J Civ Eng. 2013;3:69-79. https://doi.org/10.4236/ojce.2013.32007
[79] Phanikumar HK. Sugarcane juice powder by spray drying technique. Sci Tech Enterpreneur. Bengaluru: National Research Development Corporation; 2011.
[80] Swaminathan V. Food science chemistry & experimental foods. Bangalore: The Bangalore Printing & Publishing Co. Ltd.; 1995.
[81] Maria C, Garci J, Jennings H. New insights into the effects of sucrose on the hydration and microstructure of cement pastes. Cem Concr Res. 2002;32(3):393-9. https://doi.org/10.1016/S0008-8846(01)00689-5
[82] Wu J, Wang P. Mechanism of regulation set of sucrose in Portland cement. J Chin Ceram Soc. 1998;26(2):164-70.
[83] Gartner E, Myers D. Influence of tertiary alkanolamines on portland cement hydration. J Am Ceram Soc. 1993;76:1521-30. https://doi.org/10.1111/j.1151-2916.1993.tb03934.x
[84] Wang P. Formation of hydration on C3A mineral and Portland clinker with and without sucrose. J Shangh Inst Build Mater. 1994;7(2):107-17.

[85] Li Z, Song W, Liu Q, Cao L, Xu Z. Influence of sucrose on hydration process of Portland cement. Key Eng Mater. 2014;599:46-51. https://doi.org/10.4028/www.scientific.net/KEM.599.46
[86] Li W, Ma S, Zhang S, Sun X. Physical and chemical studies on cement containing sugarcane molasses. J Therm Anal Calorim. 2014;118:83-91. https://doi.org/10.1007/s10973-014-3947-4
[87] Ahmad S, Lawan A, Al-Osta M. Effect of sugar dosage on setting time, microstructure and strength of Type I and Type V Portland cements. Case Stud Constr Mater. 2020;13:e00364. https://doi.org/10.1016/j.cscm.2020.e00364
[88] Al Khafaji ZS, Ruddock F. Study the retardant effect of using different sugar's types on setting time and temperature of cement paste. Int J Civ Eng Technol. 2018;9:519-30.
[89] Kawade A, Kamthe I, Khemalapure AB. Experimental study of effect of sugar on properties of concrete. J Struct Transp Stud. 2017;2(1).
[90] Paul SC, Babafemi AJ, Miah MJ, Basit MA, Hasan NMS, Kong SY. Role of sugarcane juice as a natural admixture on setting time and hardened properties of cementitious materials. Infrastructures. 2022;7:145. https://doi.org/10.3390/infrastructures7100145
[91] Abalaka AE. Comparative effects of cassava starch and simple sugar in cement mortar and concrete. ATBU J Environ Technol. 2011;4(1).

Research on Engineering Structures & Materials
www.jresm.org
MIM Research Group

Research Article

Improved PGA and PGV estimation in soft soils for earthquake engineering applications

Aicha Rouabeh [*,1,a], Issam Aouari [1,b], Baizid Benahmed [2,c], Mehmet Palanci [3,d]

[1]*Department of Civil Engineering, Faculty of Applied Sciences, University of Bouira, Bouira, Algeria*
[2]*Development Laboratory in Mechanics and Materials, Ziane Achour University, Djelfa, Algeria*
[3]*Department of Civil Engineering, Istanbul Arel University, Istanbul, Turkiye*

Article Info

Article History:

Received 29 Apr 2025

Accepted 23 June 2025

Keywords:

Peak ground acceleration;
Peak ground velocity;
Soft soils;
Seismic attenuation;
NGA-West2;
Engineering strong motion

Abstract

Soil characteristics play a pivotal role in seismic risk assessment and earthquake-resistant design, with softer soils exhibiting significant ground motion amplification that elevates structural vulnerability. Construction on soft soil sites presents engineering challenges, as seismic wave propagation significantly alters signal characteristics between the source and the site. This study focuses on two critical engineering parameters—Peak Ground Acceleration (PGA) and Peak Ground Velocity (PGV)—developing site-specific predictive models for soft soil conditions (V_{s30} = 180–360 m/s). Utilizing 4,328 records from the PEER NGA-West2 database and 2,462 records from the Engineering Strong Motion (ESM) database, we derive magnitude- and distance-dependent attenuation relationships through nonlinear regression analysis. The models incorporate key variables: moment magnitude (M_w), epicentral distance ($EpiD$), and shear-wave velocity (V_{s30}). The PGA model exhibits accelerated attenuation at short distances compared to conventional models (e.g., Boore et al. 1993), while converging with Campbell (1981) at larger distances. For PGV, the formulation effectively captures intermediate-frequency amplification, addressing systematic underprediction by Joyner & Boore (1988) and overprediction by volcanic-region models (e.g., Tusa & Langer 2016). These advancements provide engineers with optimized tools for soft soil seismic design, directly addressing liquefaction risks, resonance effects, and structural performance.

© 2025 MIM Research Group. All rights reserved.

1. Introduction

Earthquakes pose a severe threat to regions near tectonic plate boundaries, where strong seismic activity can devastate buildings and infrastructure, leading to catastrophic collapses and substantial human and economic losses. The 2023 Kahramanmaraş earthquake exemplifies this vulnerability, with over 38,000 collapsed buildings, 55,000 fatalities, and widespread urban destruction—most of which occurred in soft soil zones [1].

Soft soils, characterized by fine-grained composition, high moisture content, and low shear strength, present critical challenges for geotechnical and structural engineering. These soils are prevalent in coastal seismic hotspots, including Indonesia, the Philippines, Mexico, India, and China. Under static conditions, structures on soft soils often undergo differential settlements, while during earthquakes, they experience amplified ground motion due to two key phenomena:

- Amplification of seismic waves: Soft soils can increase peak acceleration by 1.5–3.5 and extend shaking duration [2,3].

*Corresponding author: a.rouabeh@univ-bouira.dz
[a]orcid.org/0009-0004-8485-523X; [b]orcid.org/0000-0001-6920-4608; [c]orcid.org/0000-0003-4924-0059; [d]orcid.org/0000-0002-9223-5629
DOI: http://dx.doi.org/10.17515/resm2025-857ea0429rs

- Frequency filtering: High-frequency waves attenuate, while low frequencies amplify, lengthening the predominant period of ground motion [2]. This shift can resonate with flexible structures (e.g., high-rises, bridges), exacerbating damage.

Soft soils filter high-frequency seismic waves while amplifying longer-period motions, increasing the dominant period of ground shaking transmitted to structures. This effect can lead to seismic subsidence and reduced earthquake resistance, particularly during large earthquakes [3]. This effect increases stress on buildings and infrastructure, making them more vulnerable to damage. Structures designed without considering this amplification may experience unexpected forces, leading to failure.

Soft ground conditions pose significant geotechnical challenges, particularly for structures built on weak or filled-up soil [4], [5]. Soft soils tend to trap and amplify seismic waves, leading to prolonged shaking durations compared to firmer ground [6]. This effect is especially detrimental to high-rise buildings, bridges, and other flexible structures with longer natural vibration periods. To mitigate these risks, seismic isolation has been explored as a viable solution for buildings founded on soft soil, as demonstrated in a case study of a reinforced concrete (RC) building in Shanghai [7]. Nonlinear time-history analyses of base-isolated RC buildings on soft soil further highlight the complexities involved in seismic design under such conditions [8]. Moreover, nonlinear site response analyses often predict significant shear strain (3–10%) for soft soil sites, resulting in large deformations that can introduce unusual characteristics in surface ground motions [9]. These factors emphasize the need for advanced engineering solutions to enhance structural resilience in seismic-prone regions with soft soil foundations.

In their 2024 book [10], Kramer and Stewart comprehensively summarized key seismic parameters (also termed seismic indicators) and discussed their applications in ground motion analysis. These parameters are widely acknowledged as critical indicators of seismic damage potential. The most widely used parameters include Peak Ground Acceleration (PGA), Peak Ground Velocity (PGV), and Peak Ground Displacement (PGD), alongside the PGV/PGA ratio. Additional significant measures encompass root-mean-square (RMS) values of acceleration, velocity, and displacement; Arias Intensity (Ia); Cumulative Absolute Velocity (CAV); and the Predominant Period (Tp).

Horizontal accelerations are widely employed in seismic design to characterize ground motions, owing to their direct correlation with inertial forces. Indeed, Peak Ground Acceleration (PGA) is particularly critical, as it governs the largest dynamic forces in many structures. PGA serves as a fundamental parameter for the Global Earthquake Seismic Hazard Map [11], which depicts the geographic distribution of PGA values corresponding to a 10% probability of exceedance within 50 years. Additionally, PGA is a key metric for regional seismic risk assessment [12,13].

The peak horizontal velocity (PGV) is another useful parameter for characterization of ground motion amplitude. Since the velocity is less sensitive to the higher-frequency components of the ground motion, the PGV is more likely than the PGA to characterize ground motion amplitude accurately at intermediate frequencies [14]. For structures or facilities that are sensitive to loading in this intermediate-frequency range (e.g., tall or flexible buildings, bridges, etc.). Additionally, Peak Ground Velocity (PGV) sometimes employed for risk map evaluation [15]. PGV plays a role in evaluating soil-structure interaction by determining how seismic waves affect soft soil sites and how the ground motion transfers to structures. It helps predict soil liquefaction potential, which can cause foundation instability. Engineers use PGV as an intensity measure for evaluating structural damage, particularly in non-structural components, which can influence retrofitting decisions [16]. Higher PGV values indicate greater deformation potential, serving as a critical metric for estimating structural and geotechnical damage during earthquakes. This relationship is particularly significant in the design and assessment of pipelines and underground structures, where velocity-based loading governs stability and failure mechanisms [17,18].

Previous studies on predicting earthquake amplitude (PGA) for engineering applications have predominantly neglected the critical role of ground conditions in structural response. As highlighted in prior research, structures situated on soft soil sites exhibit pronounced soil-structure interaction effects, which manifest through four principal mechanisms: (1) modification

of input ground vibrations, (2) alteration of system vibration characteristics, (3) dissipation of radiant energy, and (4) material damping energy. To account for these factors and enhance the reliability of computational evaluations, this study develops a predictive model for Peak Ground Acceleration (PGA) and Peak Ground Velocity (PGV) that explicitly incorporates soft soil conditions.

The primary objective of this study is to develop a novel predictive relationship for Peak Ground Acceleration (PGA) and Peak Ground Velocity (PGV) specifically tailored for soft soil sites, with direct applications in structural engineering design and analysis. To achieve this, we employ advanced statistical methods, particularly nonlinear regression techniques, to establish robust and accurate predictive models for these critical seismic parameters under soft soil conditions.

2. Materials and Methods

The study methodology comprised three main phases: data collection, parameter calculation, and model development. Ground motion records were systematically extracted from two authoritative databases - the Pacific Earthquake Engineering Research Center (PEER NGA-West2) [19] and Engineering Strong-Motion (ESM) [20] - with selection criteria requiring moment magnitude (M_w), epicentral distance ($EpiD$), and soil classification data, specifically targeting soft soil conditions (V_{s30} = 180-360 m/s). This yielded 8,790 quality-controlled records from 875 global earthquakes (324 PEER, and 551 ESM). For consistent orientation-independent intensity measures, PGA and PGV were derived using the Rotated Geometric Mean (RotD50) approach, which calculates the median geometric mean across all possible component rotations (0°-180°). Nonlinear regression techniques were then employed to develop predictive models incorporating M_w, $EpiD$, and V_{s30} as primary variables, with particular attention to capturing soft soil amplification characteristics that existing models often misrepresent. The rigorous methodology ensures reliable attenuation relationships specifically optimized for seismic hazard assessment in soft soil regions. The adopted methodology is presented in the flowchart of Fig. 1.

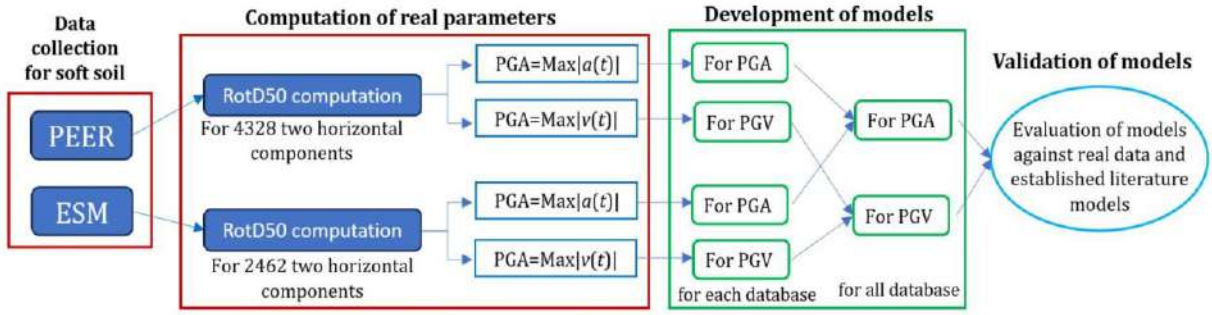

Fig. 1. Flowchart of the adopted methodology

2.1. PGA and PGV Definition

The PGA of a seismic motion component is simply the largest (absolute) value of the acceleration a(t) obtained from the accelerogram. The maximum PGA can be obtained by making the vector sum of two orthogonal components.

$$PGA = Max(|a(t)|) \tag{1}$$

Since velocity, $v(t)$, is the integral of acceleration, a(t), it can be computed as a function of time using numerical integration methods such as the trapezoidal rule. The PGV is defined as the absolute maximum value of $v(t)$.

$$v(t) = \int a(t)dt \;\; hence \; PGV = Max\;(|v(t)|) \tag{2}$$

Fig. 2 compares two different recording stations: Gilroy Array #1, located on a rock site, and Gilroy Array #3, located on a soft soil site, during the Loma Prieta earthquake (magnitude 6.9) on October 17, 1989. From Fig. 2, we observe that at a station located on a rock site (V_{s30} =1428.14 m/sec) at a distance of 9.64 km, the peak acceleration (PGA = 0.485g) and peak velocity (PGV = 32.451 m/sec)

are lower than those recorded at a station on soft soil (V_{s30} = 349.85 m/sec) at a distance of 12.82 km, where PGA = 0.559g and PGV = 36.306 m/sec. These observations confirm the importance of distinguishing between predictive PGA and PGV models for different soil.

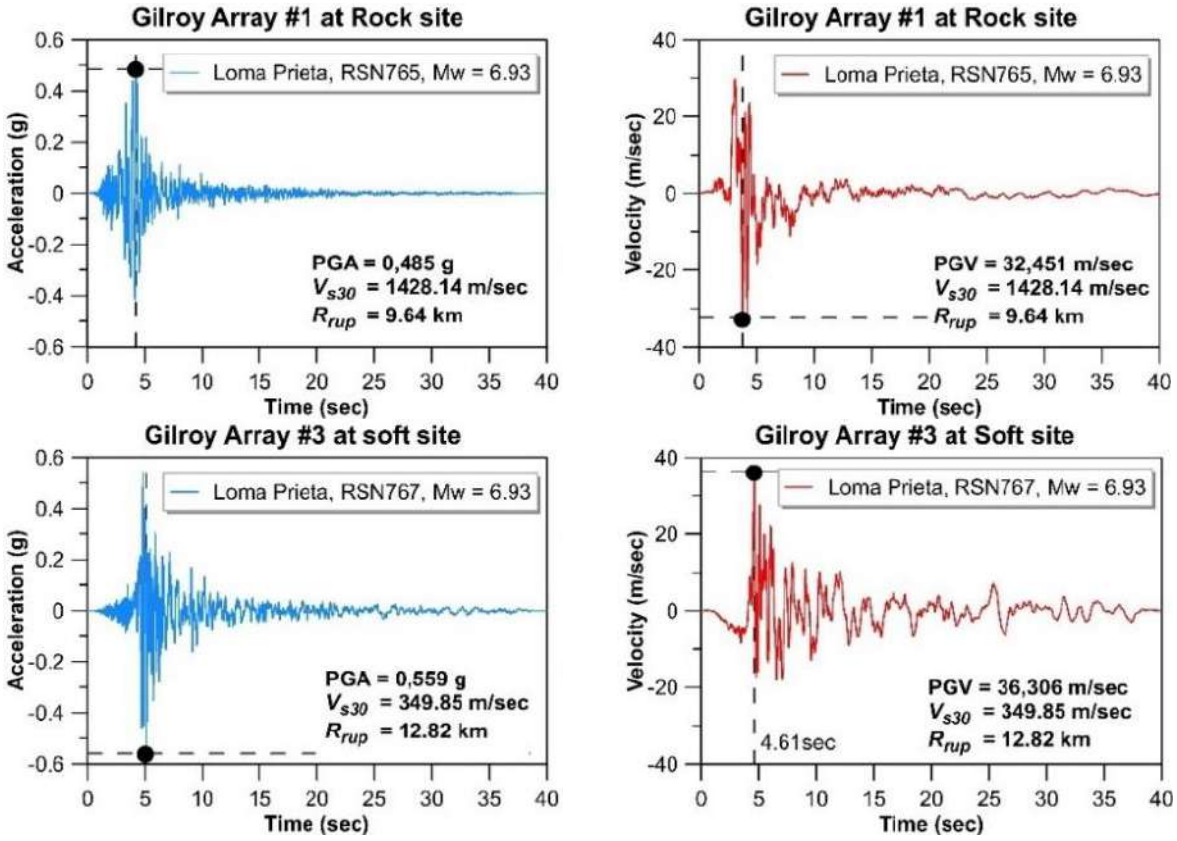

Fig. 2. Acceleration and velocity recordings of the 1989 Loma Prieta earthquake (M_w = 6.93) at two stations: Gilroy Array #1 (rock site) and Gilroy Array #3 (soft soil site)

2.2. Strong Motion Database

This study compiled 6,790 strong-motion records (4,328 from PEER NGA-West2 and 2,462 from ESM) specifically from soft soil sites, defined by shear-wave velocity (V_{s30}) values of 180-360 m/s in accordance with international seismic design standards. The Pacific Earthquake Engineering Research Center's PEER database provided globally distributed records, while the Engineering Strong-Motion (ESM) database contributed European-Mediterranean and Middle Eastern events, ensuring broad geographic representation. All selected records included complete data for moment magnitude (M_w), epicentral distance (*EpiD*), and processed acceleration time histories. The V_{s30} range served as the primary classification parameter, aligning with international seismic design codes (e.g., Eurocode 8, ASCE 7-22). Table 1 summarizes the V_{s30} ranges adopted by major codes and this study's classification thresholds.

Table 1. Soft soil sites class with various codes

Code	Range of V_{s30} (m/s)	Site Classification	Reference
IBC (2006)	180 - 360	D, Stiff and Soft	[21]
NEHRP (2001)	180 - 360	D, Dense to medium soils	[22]
Eurocode 8 (2004)	180 - 360	C, Deep, medium dense or stiff	[23]
UBC (1997)	183 - 366	D, Stiff and Soft	[24]
RPA2024 (2024)	180 - 360	S3, Soft Soil	[25]

Fig. 3 presents the distribution of strong-motion records assembled from the PEER and ESM databases as a function of epicentral distance *EpiD* (a) and shear-wave velocity V_{s30} (b), both plotted against M_w.

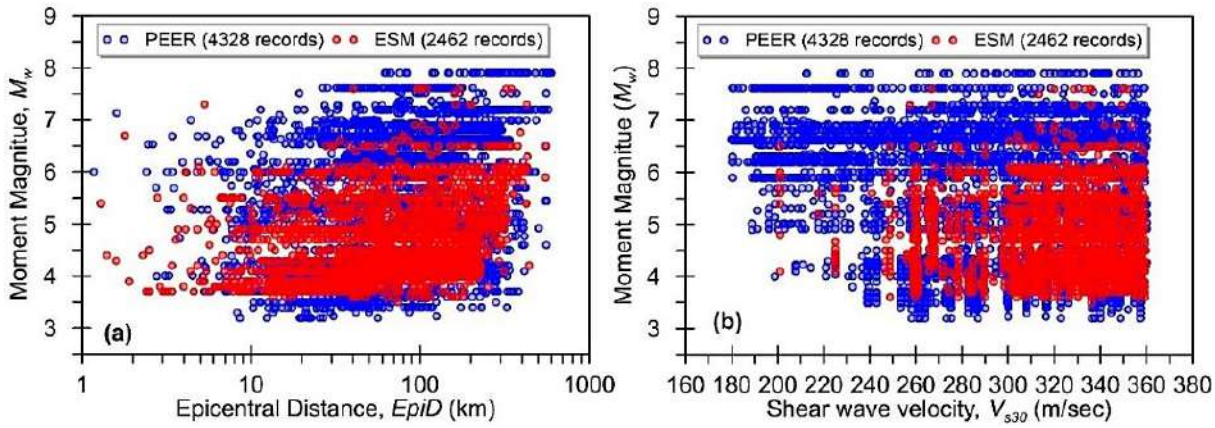

Fig. 3. Distribution of ground-motion records used in the analysis from the PEER (Pacific Earthquake Engineering Research Center) and ESM (Engineering Strong-Motion) databases. (a) Moment magnitude M_w versus epicentral distance (*EpiD*), and (b) Moment magnitude M_w versus average shear-wave velocity in the top 30 meters (V_{s30})

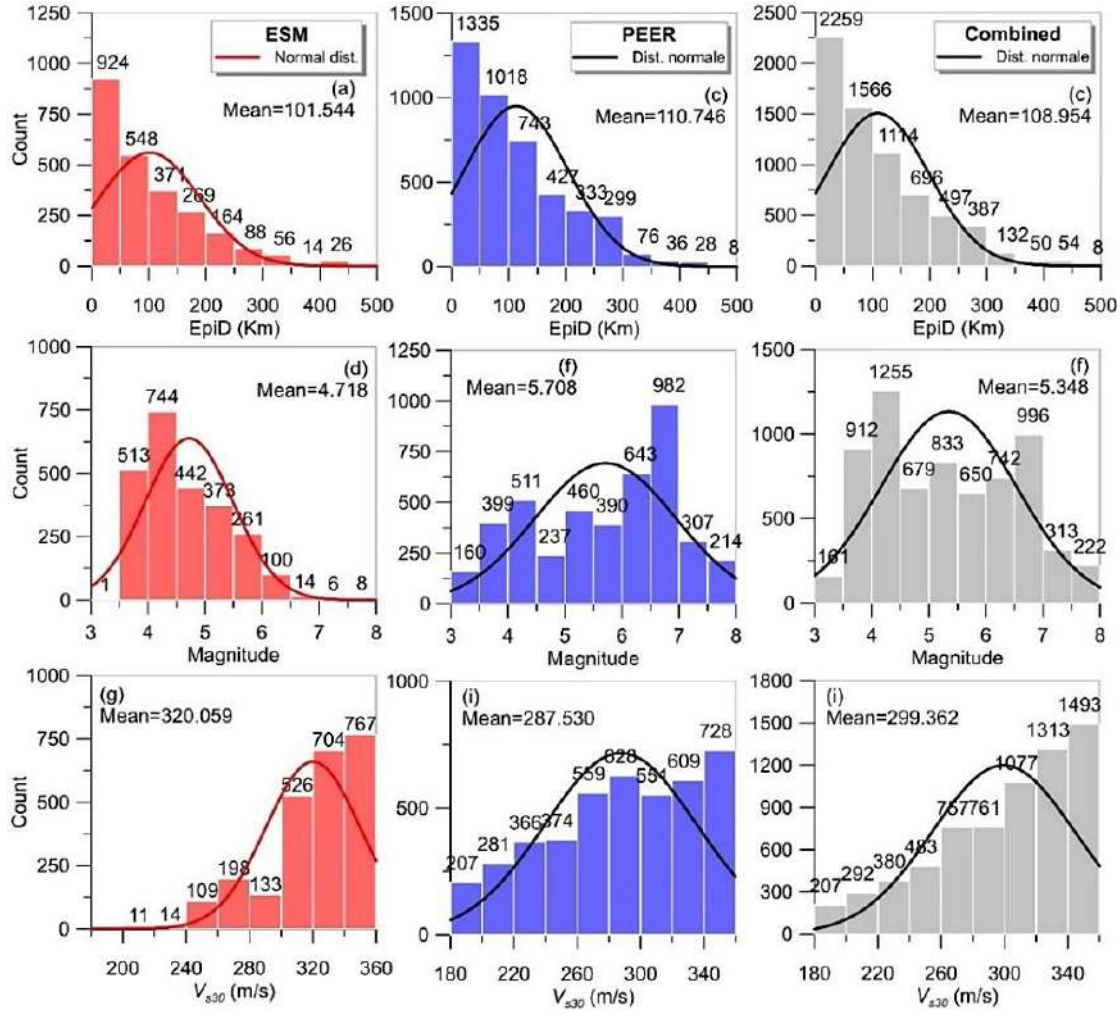

Fig. 4. Distribution of seismic parameters for ground motion records on soft soil sites from the ESM and PEER NGA-West2 databases. Histograms show the distributions of (a–c) epicentral distance (*EpiD*), (d–f) moment magnitude (M_w), and (g–a) average shear-wave velocity in the upper 30 meters (V_{s30})

In panel (a), the PEER database (blue circles) covers a broader range of magnitudes and distances, particularly capturing a significant number of large-magnitude events (M_w > 6) at a wide range of distances (up to several hundred kilometers). The ESM database (red circles), while also spanning

a wide distance range, includes a higher density of records for moderate magnitudes ($M_w \approx 4 - 6$) and distances below 100 km, reflecting its strong regional focus, particularly in Europe. Panel (b) shows the distribution of moment magnitudes against V_{s30}, where the PEER dataset generally exhibits a higher shear-wave velocity range (soft soil sites), while the ESM records cluster around lower V_{s30} values, indicative of softer site conditions. The PEER records extend into very high V_{s30} values (> 350 m/s), whereas the ESM records are more concentrated between 200 and 320 m/s. Overall, the combination of the two datasets ensures a diverse and representative coverage of seismic events, distances, and site conditions, essential for the robust development and validation of ground-motion prediction models.

Fig. 4 illustrates the distribution of key seismic parameters—epicentral distance (*EpiD*), moment magnitude (M_w), and average shear-wave velocity in the upper 30 meters (V_{s30})—for ground motion records on soft soil sites from the ESM and PEER NGA-West2 databases. Subplots (a), (d), and (g) represent the ESM dataset, (b), (e), and (h) represent the PEER dataset, while (c), (f), and (I) show the combined distribution from both sources. Each histogram is overlaid with a fitted normal distribution curve, and the mean values are indicated for reference.

The distributions reveal key differences between the two datasets. The PEER records tend to have slightly larger epicentral distances (mean ≈ 110.7 km) and magnitudes (mean ≈ 5.71) compared to the ESM records (mean *EpiD* ≈ 101.5 km, mean $M_w \approx 4.72$), suggesting broader regional and seismic event coverage. In contrast, the ESM dataset is characterized by higher average V_{s30} values (mean ≈ 320.1 m/s), indicating generally stiffer soft soil site classifications. The combined dataset reflects a balanced integration of both sources, enhancing the representativeness of the seismic input for ground motion analysis on soft soil sites.

3. Results and Discussions

Fig. 5 illustrates the computed Peak Ground Acceleration (PGA, in g) and Peak Ground Velocity (PGV, in cm/s) as functions of moment magnitude (M_w), epicentral distance (*EpiD*), and the average shear-wave velocity in the upper 30 meters (V_{s30}). The analysis is based on ground-motion records from the European Strong-Motion (ESM) and PEER NGA-West2 databases, following the methodology outlined in Section 2.1.

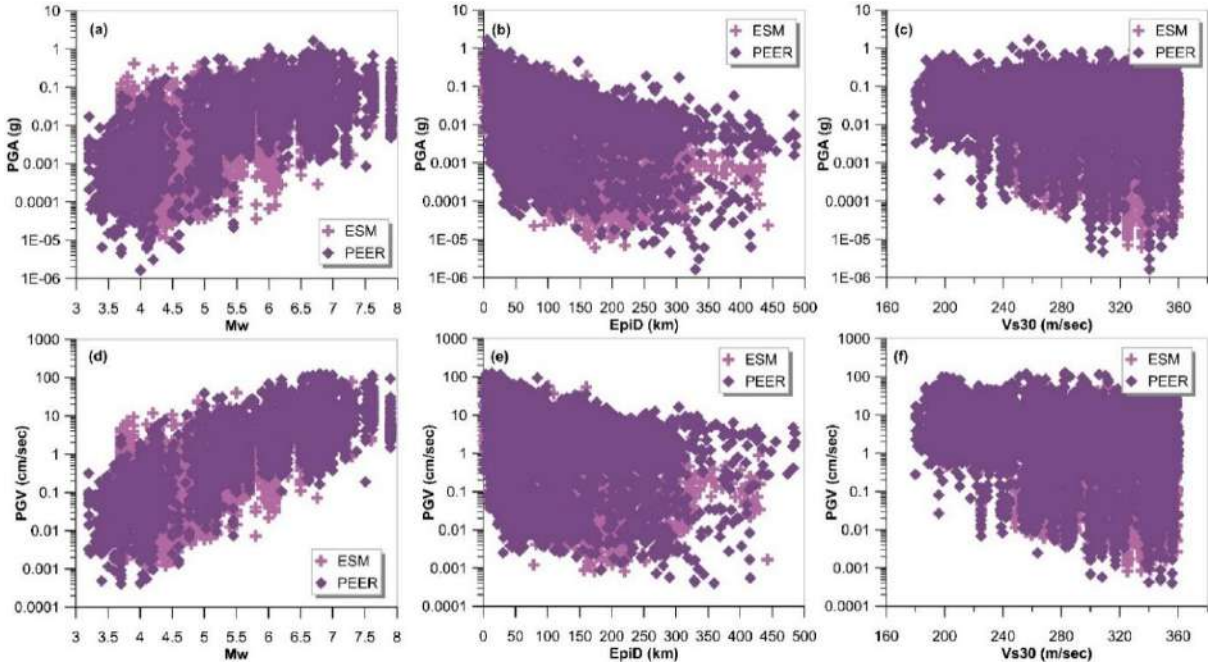

Fig. 5. Peak Ground Acceleration (PGA) and Peak Ground Velocity (PGV) plotted against: (a and d) moment magnitude (M_w), (b and e) epicentral distance (*EpiD*), and (c and f) average shear-wave velocity in the upper 30 meters (V_{s30})

Subplots (a) and (d) demonstrate a well-defined positive correlation between both PGA and PGV and moment magnitude (M_w), confirming the expected relationship where larger earthquakes produce stronger ground motions. The majority of the data cluster between M_w 4.5 and 6.5, with the PEER NGA-West2 dataset notably extending the coverage to higher magnitudes and more extreme PGV values, thereby enriching the analysis of high-energy events. Subplots (b) and (e) depict the characteristic attenuation of ground motion with increasing epicentral distance, a phenomenon driven by geometric spreading and anelastic attenuation. The consistent trends observed across both the ESM and PEER datasets validate the reliability of the combined dataset for analyzing distance-dependent ground motion behavior. In subplots (c) and (f), PGA and PGV exhibit more scattered and less pronounced correlations with V_{s30}, underscoring the complex influence of local site conditions. While higher V_{s30} values (typically indicative of stiffer rock sites) generally correspond to reduced amplification, the variability in the data highlights the significant role of other site-specific factors, such as basin effects and nonlinear soil response.

Collectively, these observations align well with established ground motion principles. The synergistic use of the ESM and PEER datasets strengthens the analysis by providing complementary coverage across different magnitude ranges and distances, thereby enhancing the robustness and generalizability of the findings.

3.1. Prediction Models

To develop a reliable prediction model for PGA and PGV on soft soil sites, a functional form was adopted based on the general model proposed by Kramer (1996) [10]. This formulation links key parameters influencing ground motion, such as moment magnitude (M_w), epicentral distance ($EpiD$), and site conditions characterized by the average shear wave velocity over the top 30 meters (V_{s30}). The chosen functional form closely reflects the physical mechanisms of ground motion generation and propagation, minimizing reliance on purely empirical adjustments. Following the log-normal distribution assumption for ground motion parameters, regression analyses were performed on the logarithmic values of PGA and PGV. This approach ensures a robust predictive model that accurately incorporates the effects of magnitude scaling, source distance attenuation, and site amplification, aligning with best practices established in seismic hazard analysis.

3.2. PGA Model for Soft Soil

Predictive relationships for parameters that decrease with distance—such as peak acceleration and peak velocity—are often referred to as attenuation relationships. Douglas (2019) [26] has summarized over 450 attenuation relationships for predicting PGA. Each model is best suited to conditions similar to those of the databases from which it was derived. Eq. (3) is commonly used to describe PGA attenuation [27–31]. In this study, we adopt this formula to represent PGA attenuation in soft soil sites. Typically, the constant b is positive and relates to seismic energy attenuation, while the constant c is negative, representing the effect of distance attenuation.

$$log(PGA) = a + b(M_w - 6) + c(M_w - 6)^2 + d \times log(R) + e(R) \quad (3)$$

In Eq. (3), *a, b, c, d*, and *e* are regression coefficients; PGA is the predicted peak ground acceleration expressed in units of g (where 1 g = 9.80665 m/s^2 = 980.665 cm/s^2); M denotes the source energy, represented by the moment magnitude M_w; R is the hypocentral distance to the recording site (in kilometers); and log refers to the base-10 logarithm. Table 2 presents the regression coefficients for the ESM and PEER databases individually, derived using nonlinear multiple regression analysis based on the Nonlinear Least Squares algorithm. Table 3 provides the corresponding model coefficients for the combined dataset, including their associated confidence intervals, using the same functional form as Eq. (3).

Table 2. Coefficients of the proposed PGA prediction model for PEER and ESM datasets

Coefficients	*a*	*B*	*c*	*d*	*e*	R^2	RMSE
PEER	0.6525	0.5704	-0.101600	-1.052	-0.002018	0.8663	0.3402
ESM	0.9484	0.6613	0.009506	-1.394	-0.001616	0.7632	0.4402
All data	0.8400	0.6349	-0.056670	-1.211	-0.001906	0.8354	0.3962

Table 3. Coefficients of the proposed PGA prediction model for combined dataset.

Coefficients	*A*	*b*	*c*	*d*	*e*
Combined database	0.8400	0.6349	-0.05667	-1.211	-0.001906
Confidence interval	0.7733; 0.9066	0.6232; 0.6466	-0.06407; -0.04927	-1.255; -1.167	-0.002112; -0.0017

Fig. 6 presents both the prediction surfaces and residual distributions for PGA models developed using three datasets: All (combined), PEER, and ESM. In subplots (a)–(c), the predicted Log(PGA) surfaces illustrate a consistent physical trend across all datasets: ground motions increase with magnitude and decrease with epicentral distance, reflecting attenuation effects. The scatter points show the actual data used for model fitting, and the surfaces indicate good alignment between observed and predicted values.

Subplots (d)–(f) visualize the residuals—differences between observed and predicted Log(PGA) values—for each dataset. In these plots a positive residual indicates under-prediction by the model and a negative residual indicates over-prediction by the model. In all three cases, the residuals are generally centered around zero with no evident systematic bias, indicating satisfactory model performance. However, the residual spread differs slightly among datasets: the PEER and ESM datasets (e, f) exhibit more compact residuals, potentially due to more homogeneous data characteristics or smaller sample sizes. In contrast, the All dataset (d) shows greater variability, likely due to combining data from diverse sources. These visualizations collectively validate the predictive strength of the developed models while also highlighting areas of potential refinement, especially for broader datasets.

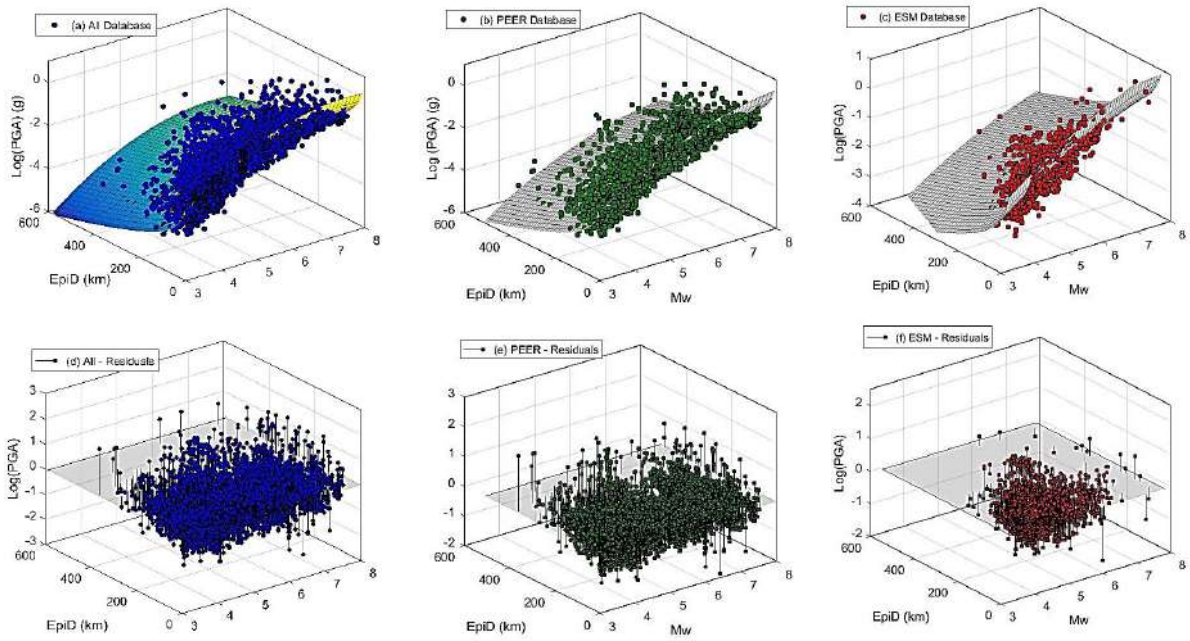

Fig. 6. (a–c) Three-dimensional views of the predicted PGA models for the All, PEER, and ESM datasets, respectively, as a function of *EpiD* and M_w. The surfaces represent the model fit to the observed data. (d–f) Corresponding residual plots for each dataset. Residuals are plotted in the same 3D space to evaluate the model's performance across magnitude and distance ranges

3.3. Assessment of the Proposed PGA Model

To assess whether the PGA model presented above, based on the employed data, accounts for behavior primarily influenced by M_w and *EpiD*, we have plotted the predicted PGA as a function of both parameters in the following figures. Fig. 7 presents the variation of Peak Ground Acceleration (PGA) as a function of epicentral distance (*EpiD*) for different earthquake magnitudes (M_w = 3.5, 4.5, 5.5, 6.5, and 7.5) in soft soil conditions. In all subplots, PGA decreases as the epicentral distance

increases, which is expected due to energy dissipation over distance. Higher magnitude earthquakes (M_w = 6.5, 7.5) show higher PGA values, especially at short distances.

The PEER and combined models seem to align closely, indicating that the PEER dataset follows the overall trend well. The ESM dataset (blue dashed line) generally predicts higher PGA values compared to PEER, particularly at shorter distances. For smaller magnitudes (M_w = 4.5, 5.5), differences between the models are relatively minor. For larger magnitudes (M_w = 6.5, 7.5), the divergence between ESM and PEER predictions becomes more noticeable, with ESM systematically predicting higher PGA.

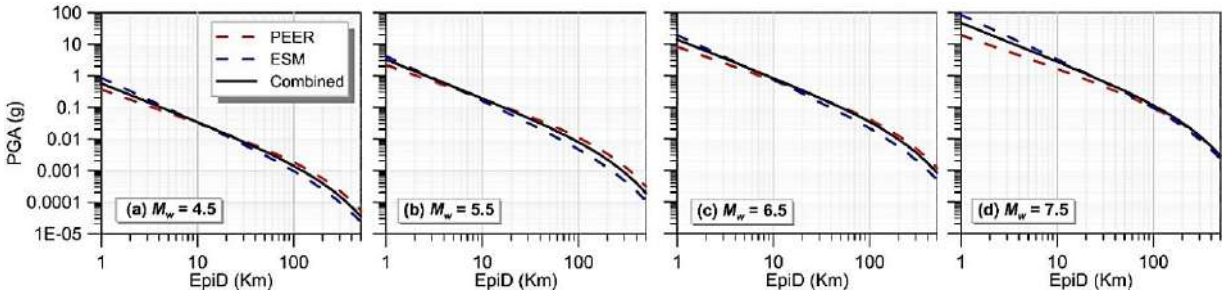

Fig. 7. Variation of PGA as a function of *EpiD* for different earthquake magnitudes (M_w = 3.5, 4.5, 5.5, 6.5, and 7.5) in soft soil conditions. The black continuous line represents the developed predictive model using the combined datasets

The Fig. 8 illustrates the variation of predicted Peak Ground Acceleration (PGA) with moment magnitude (M_w) for four source-to-site epicentral distances (*EpiD* = 10 km, 50 km, 100 km, and 150 km), based on empirical ground motion models calibrated using three datasets: the PEER and ESM strong-motion databases, and their combined compilation.

For all distance intervals, PGA increases systematically with M_w, consistent with source scaling behavior observed in empirical ground motion studies. A pronounced attenuation trend is evident with increasing epicentral distance, reflecting both geometric spreading and anelastic damping effects in crustal propagation paths. The ESM-derived model consistently yields higher PGA estimates across the magnitude range, particularly in the near field (e.g., *EpiD* = 10 km), potentially due to regional differences in site amplification, crustal attenuation, and event selection criteria.

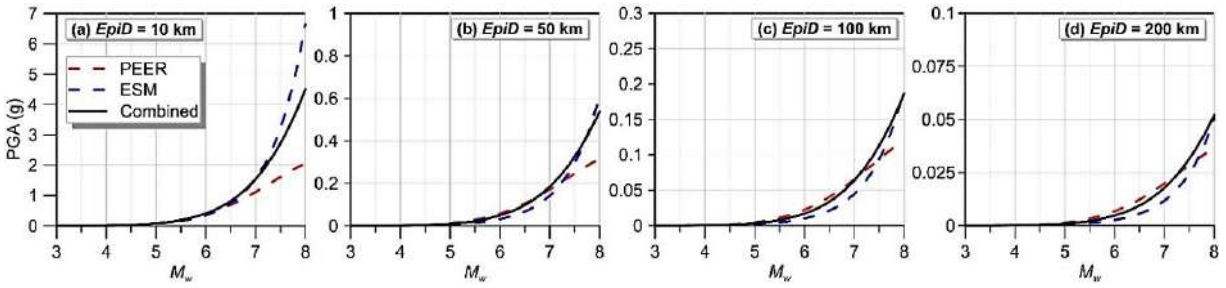

Fig. 8. Predicted Peak Ground Acceleration (PGA) as a function of moment magnitude (M_w) for four epicentral distances: (a) 10 km, (b) 50 km, (c) 100 km, and (d) 200 km. Ground motion prediction models were developed using the PEER (red dashed line) and ESM (blue dashed line) strong-motion databases, along with their combined dataset (black solid line)

In contrast, the PEER-based model predicts lower PGA values, particularly at shorter distances. The combined dataset generates intermediate predictions, capturing characteristics from both regions and offering a more generalized model. The reduced spread between models at greater distances suggests that far-field motions are less sensitive to localized site and source-region effects.

The ESM-based model yields higher PGA values, particularly in the near field, which may reflect stronger site amplification effects and regional attenuation characteristics. The PEER-based model provides lower estimates, while the combined model exhibits intermediate behavior, suggesting a balanced integration of source and path effects from both datasets. The convergence of predictions at larger distances indicates reduced sensitivity to local site and regional source characteristics in

the far field. The ESM dataset generally predicts higher PGA values, especially at shorter distances, whereas the PEER dataset aligns more closely with the overall model. At greater distances, the differences between models diminish, highlighting the dominant effect of attenuation on seismic ground motion.

A second comparison is conducted using actual data from each database. Fig. 9 presents Peak Ground Acceleration (PGA) values from the PEER dataset (blue triangles) and the ESM dataset (red triangles), alongside model-predicted PGA curves for different epicentral distances (Fig. 9a) and earthquake magnitudes (Fig. 9b) in soft soil conditions.

The proposed model accurately predicts PGA variations with both magnitude and distance, demonstrating strong alignment with observed values from the PEER dataset. As expected, shorter distances and higher magnitudes correspond to greater PGA values, while attenuation effects become more prominent at larger distances.

For the ESM dataset, the model effectively captures the overall trend of PGA variation. However, some recorded values exceed predictions, highlighting the complexity of seismic ground motion behavior in soft soil conditions and the potential influence of site-specific factors. Despite this variability, the model provides a reliable representation of attenuation trends and magnitude-dependent PGA variations.

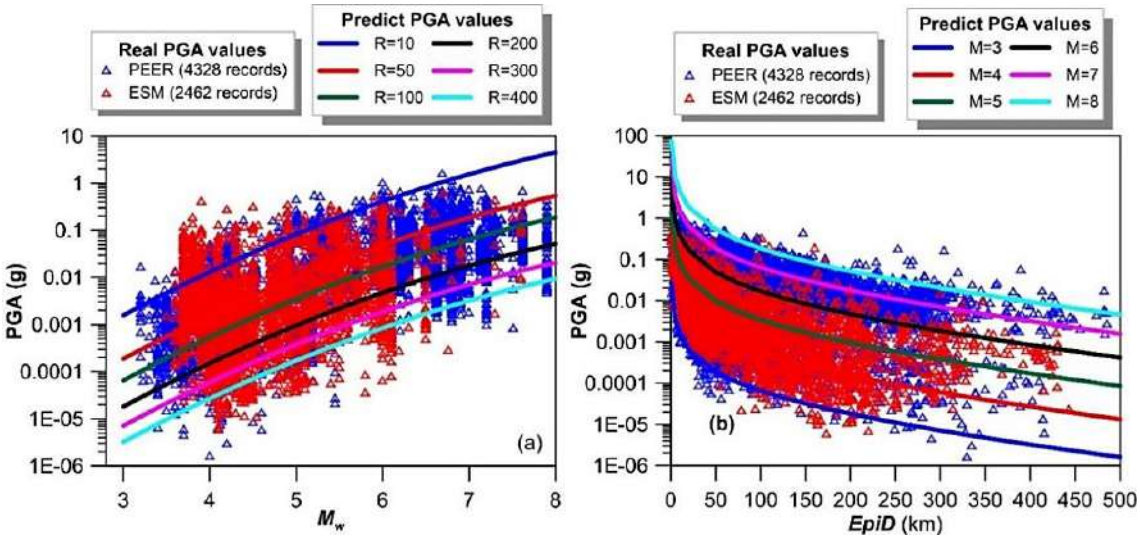

Fig. 9. Comparison of observed and predicted PGA values from the PEER (blue triangles) and ESM (red triangles) datasets. (a) PGA as a function of M_w for different *EpiD* and (b) PGA as a function of *EpiD* for different M_w

As the final validation, we conducted a comprehensive benchmarking analysis against established ground motion prediction equations (GMPEs) from the literature. Douglas (2017) [26] systematically reviewed over 450 PGA attenuation relationships, the majority of which employ regression-derived coefficients. For this comparative study, we selected representative models that: (1) incorporate site classification parameters, (2) demonstrate robust performance in previous validation studies, and (3) are widely adopted in engineering practice. This comparative framework enables rigorous evaluation of our soft soil-specific PGA model's predictive capabilities relative to conventional approaches.

In 1981, Campbell [32] developed an attenuation relationship using global data to estimate the average PGA at sites located within 50 km of the fault rupture during earthquakes with magnitudes ranging from 5.0 to 7.7. This model, represented by Eq. 1 in Table 4, was considered state-of-the-art at the time. Subsequently, Youngs et al. (1988) [33] used strong-motion records from rock sites during 60 earthquakes, along with numerical simulations for events with $M_w < 8$, to develop an attenuation relationship specific to subduction zones. Their proposed formula is given by Eq. 2 in Table 4.

In 1993, Boore et al. [28] introduced a more advanced model incorporating multiple terms. Their model was based on data from earthquakes with magnitudes ranging from 5.0 to 7.7 in western North America at distances of less than 100 km from the surface projection of the fault. The corresponding formula is presented in Eq. 3 in Table 4.

The next proposed comparison model is given by Akkar et al. (2014) [34], who introduced a new generation of ground-motion models derived from pan-European databases. Their formula, representing the latest advancements in ground-motion modeling, is provided in Eq. 4 in Table 4.

Another prediction model called as Campbell and Bozorgnia (2014) for the horizontal components of PGA and PGV, developed by the Pacific Earthquake Engineering Research Center (NGA-West2) team, was used for comparison with the established models [35]. This model, applicable for periods ranging from 0.01 to 10 s (Eq. 5 in Table 4), employs a complex functional form with nine terms. These terms account for various factors, including earthquake magnitude scaling, geometric attenuation, faulting style, hanging-wall effects, shallow site response, basin effects, hypocentral depth, rupture dip, and apparent anelastic attenuation

More recently, Zuccolo et al. (2017) [36] developed a model using data from 61 stations located on Eurocode 8 class B sites ($360 \leq V_{s30} < 800$ m/s), primarily from 33 stations within the Irpinia Seismic Network, supplemented by data from other networks. Although data were originally collected from sites of different classes, 93% of the accelerograms were from class B sites.

The final chosen model for comparison is given by Shiuly (2018) [37] proposed a global attenuation relationship for estimating PGA at rock sites, making it applicable to any region worldwide. He developed four relationships using multiple regression and an additional model based on Genetic Programming. The model is given by Eq. 7 in Table 4.

Table 4. Selected PGA models for comparison with the proposed model

N	Prediction Model	Ref.
(1)	$\ln(PGA)_g = -4.141 + 0.868M - 1.09\ln(R + 0.0606e^{0.7M})$	[32]
(2)	$\ln(PGA)_g = 19.16 + 1.045M_w - 4.738\ln(R + 205.5e^{0.0968M_w}) + 0.54Z_t$	[33]
(3)	$\log(PGA)_g = -0.038 + 0.216(M_w - 6) - 0.77\log(R) + 0.158G_B + 0.254G_C, with\ R = \sqrt{d^2 + 5.48^2}$	[28]
(4)	$\ln(PGA)_g = \ln[PGA_{REF}(M_w, R, SoF)] + \ln[S(V_{s30}, PGA_{REF})]$	[34]
(5)	$\ln(\mathrm{PGA}) = f_{mag} + f_{dis} + f_{flt} + f_{hang} + f_{site} + f_{sed} + f_{hyp} + f_{dip} + f_{atn}$	[35]
(6)	$\log(PGA)_{m/sec^2} = -2.1575 + 0.8359M - 1.969log\ (R)$	[36]
(7)	$\log(PGA) = 0.3646 + 0.4215(M - 6) - 0.01869(M - 6)^2 - 0.9707\log(R) - 0.0008(R)$	[37]

Where M is the magnitude and R is the closest distance to the fault rupture in kilometers. Zt is the focal depth, which takes a value of 0 for convergent events and 3 for divergent events. d is the closest distance to the surface projection of the fault in kilometers, and: GB = {0 for site class A, 1 for class B, and 0 for class C}, GC = {0 for site class A, 0 for class B, and 1 for class C}. Note that in all proposed relationship, PGA is expressed in terms of the decimal logarithm rather than the natural logarithm. Site classes are defined based on the average shear wave velocity in the top 30 meters of depth.

Fig. 10 systematically compares the performance of our proposed ground motion attenuation model (solid black line) against seven established prediction models (Table 4) across four characteristic earthquake magnitudes: (a) M_w = 4.5, (b) M_w = 5.5, (c) M_w = 6.5, and (d) M_w = 7.5. This comparative analysis spans the full range of engineering interest, from minor to major seismic events, evaluating model behavior through peak ground acceleration (PGA) attenuation curves plotted against epicentral distance.

The comparative analysis between proposed PGA model for soft soils (V_{S30} = 180–360 m/s) and seven established attenuation relationships (Fig. 10) reveals critical insights about ground motion prediction in vulnerable soil conditions:

For moderate-magnitude earthquakes (M_w 5.5–6.5), the proposed model aligns closely with Akkar et al. (2014) at intermediate distances (50–200 km). However, it diverges significantly from rock-

site model (Campbell 1981; Shiuly 2018) and Campbell and Bozorgnia (2014) model, which systematically underpredict PGA by 30–50% due to their neglect of soil amplification effects. This discrepancy is particularly pronounced in the 0.1–1.0 g range, where soft soil amplification is most critical for structural design. The results confirm that magnitude significantly influences PGA prediction accuracy in soft soils, with conventional models failing to capture the nonlinear response of these vulnerable sites.

The proposed model exhibits distinct distance attenuation behavior compared to existing relationships. At short distances (<100 km), it shows faster PGA attenuation than Boore et al. (1993) and Youngs et al. (1988), reflecting the enhanced energy dissipation typical of soft soils. Beyond 300 km, the predictions converge with Campbell (1981), validating the model's far-field behavior. This dual-phase attenuation pattern—rapid decay near the source followed by stable far-field trends—highlights the importance of distance-dependent terms tailored to soft soil mechanics, which are absent in most conventional models.

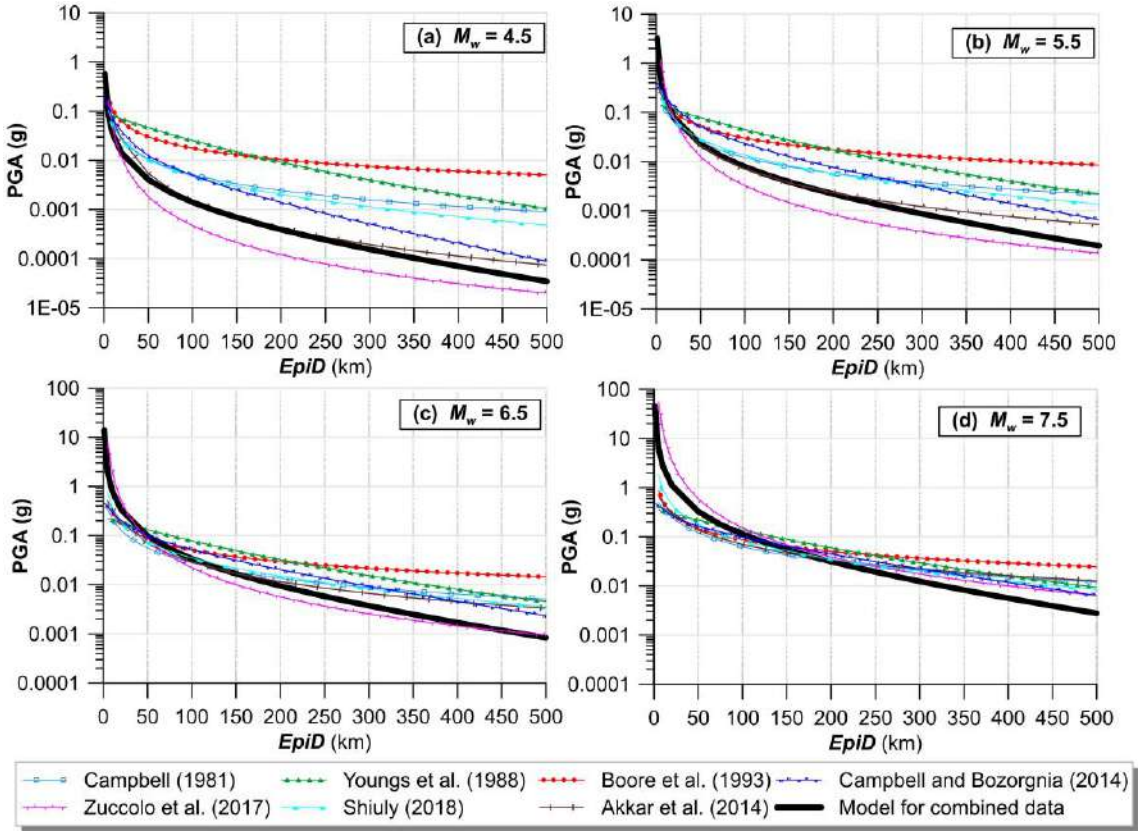

Fig. 10. Variation of PGA with epicentral distance for magnitudes M_w = 4.5, 5.5, 6.5, and 7.5, based on the proposed relationships for comparison

Rock-site models (Shiuly 2018; Zuccolo et al. 2017) consistently underpredict PGA across all magnitudes and distances, failing to capture the amplification peak observed at 50–150 km in soft soils. These models disregard key mechanisms such as impedance contrast and nonlinear soil behavior, leading to unsafe underestimations of ground motion. Their poor performance underscores the necessity of site-specific formulations for accurate hazard assessment in soft soil regions, particularly for infrastructure design where PGA thresholds are critical.

Region-specific models like Boore et al. (1993) (Western North America) and Akkar et al. (2014) (Europe) exhibit erratic behavior outside their calibration ranges, especially for $M_w \geq 7.5$. Their reliance on localized datasets introduces biases when applied to other tectonic settings or soil conditions. For instance, Boore et al. overpredicts PGA at intermediate distances in soft soils, while Akkar et al. shows inconsistent magnitude scaling. These limitations emphasize the need for globally representative data, as incorporated in the present model through the combined PEER and ESM databases.

The largest discrepancies between models occur in the 0.1–1.0 g PGA range, which is most relevant for seismic design. Existing models may underpredict PGA by up to 40% for $M_w \geq 6.5$, potentially leading to nonconservative designs. Our results demonstrate that soft soil amplification cannot be approximated using generic correction factors—a practice common in current standards. Instead, dedicated attenuation relationships, like the one proposed here, are essential to ensure safety and resilience in vulnerable regions.

The proposed model outperforms references by explicitly accounting for soft soil physics (V_{s30} 180–360 m/s) and combining global datasets (PEER + ESM). Its robust performance across magnitudes and distances stems from: (1) nonlinear soil response terms, (2) dual-phase attenuation formulation, and (3) calibration against modern strong-motion records. This advancement eliminates the need for ad-hoc corrections, providing a unified framework for PGA prediction in soft soils.

3.4. PGV Model for Soft Soil

Building upon the attenuation model developed by Joyner and Boore (1988) [38], we developed a PGV prediction model tailored for soft soil conditions. The model is expressed by the following equation:

$$log(PGV)_{[cm/sec]} = a + b(M_w - 6) + c(M_w - 6)^2 + d \times log\left(\sqrt{EpiD^2 + e^2}\right) \quad (4)$$

Where PGV denotes the peak ground velocity, and *EpiD* represents the epicentral distance (in kilometers). The model coefficients (*a, b, c, d, e*) were determined through nonlinear regression analysis and are summarized in Table 4 for each sub-dataset individually, and in Table 5 for the combined dataset. Each coefficient plays a distinct role in shaping the attenuation behavior of ground motion:

- Coefficient a represents a constant term that primarily influences the overall amplitude of the PGV. It sets the baseline level of the ground motion prediction across all distances and magnitudes.
- Coefficient b quantifies the influence of earthquake magnitude on PGV. A positive value, as observed in all datasets, indicates a direct correlation between magnitude and PGV, consistent with physical expectations.
- Coefficient c introduces a nonlinear adjustment—typically associated with a quadratic or higher-order magnitude term—allowing for finer calibration of the model, particularly at extreme magnitude values.
- Coefficient d governs the attenuation rate of PGV with respect to epicentral distance. The negative values observed across all datasets reflect the expected decay of ground motion intensity with increasing distance from the earthquake source.
- Coefficient e serves as an additional constant or intercept term, potentially accounting for site-specific effects or regional baseline shifts in PGV values.

Model performance was evaluated using the coefficient of determination (R^2) and the root mean square error (RMSE). The results show a strong model fit for the PEER database (R^2 = 0.9065, RMSE = 0.3154), indicating excellent predictive capability. The ESM database also yielded satisfactory results (R^2 = 0.8107, RMSE = 0.3783), albeit with slightly higher variability. The model calibrated on the combined dataset achieved a balanced performance (R^2 = 0.8862, RMSE = 0.3553), demonstrating its robustness across diverse records. The coefficient intervals provided in Table 6 represent the estimated 95% confidence bounds, highlighting the statistical reliability of the regression parameters.

Table 5. Coefficients of the proposed PGV prediction model given in Eq. (4) for PEER and ESM database

Coefficients	a	b	c	d	e	R2	RMSE
PEER	3.184	0.723	-0.09806	-0.7181	-11.97	0.9065	0.3154
ESM	3.062	0.8597	0.02912	-0.7620	-4.703	0.8107	0.3783

Table 6. Coefficients of the proposed PGV prediction model given in Eq. (4) for combined database

Coefficients	a	b	c	d	e	R2	RMSE
All data	3.147	0.7826	-0.05475	-0.738	-7.369	0.8862	0.3553
interval	3.084; 3.21	0.772; 0.7932	-0.06147; -0.04802	-0.7531; -0.7229	-8.51; -6.228		

Fig. 11 presents three-dimensional regression surfaces of the proposed PGV prediction model (Eq. 4), applied to different datasets: the combined dataset (Fig. 11a), the PEER database (Fig. 11b), and the ESM database (Fig. 11c). The plots illustrate the relationship between epicentral distance (*EpiD*), earthquake magnitude (M_w), and the logarithm of peak ground velocity (Log(PGV)). Each plot overlays the fitted regression surface onto the observed data points, enabling visual assessment of model performance across the parameter space.

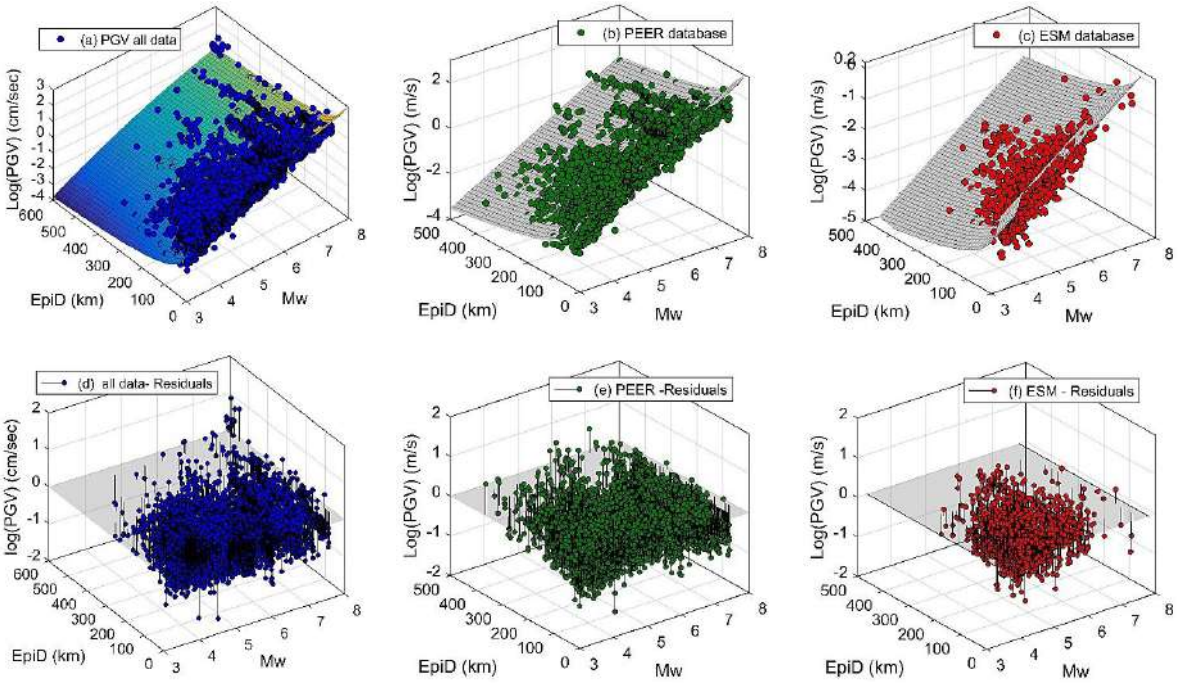

Fig. 11. (a–c) 3D views of the predicted PGV models for the All, PEER, and ESM datasets, respectively, as a function of *EpiD* and M_w. (d–f) Corresponding residual plots for each dataset

Fig. 11a demonstrates the model's fit to the entire dataset, showing a generally good agreement between observed and predicted values. The regression surface effectively captures the expected trend of increasing PGV with higher magnitudes and decreasing PGV with increasing epicentral distance. Fig. 11b focuses on the PEER dataset, which exhibits a dense and well-distributed set of observations. The regression surface closely aligns with the data, indicating strong model performance, consistent with the high R^2 value (0.9065) and low RMSE (0.3154) reported in Table 4. Fig. 11c displays the model performance for the ESM dataset, which shows a more dispersed pattern. While the general trend is captured, a slightly greater scatter around the regression surface is observed, which corresponds with the comparatively lower R^2 (0.8107) and higher RMSE (0.3783).

To further evaluate model accuracy, the bottom row of Fig. 11 (Figs. 11d-f) presents the residual distributions, defined as the difference between the observed and predicted Log(PGV) values. Fig. 11d shows the residuals for the combined dataset. The residuals are generally centered around zero, with no significant bias across the ranges of M_w or *EpiD*, indicating an overall balanced model. Fig. 10e displays residuals for the PEER dataset. The residuals are tightly clustered with minimal dispersion, further validating the high predictive quality of the model for this dataset. Fig. 11f presents residuals for the ESM dataset. Although the residuals remain centered near zero, a slightly broader spread is evident, especially at lower magnitudes, reflecting the higher variability in this

subset. Overall, the 3D regression surfaces and residual plots confirm that the proposed model reliably captures the attenuation trends of PGV for soft soil sites across different datasets, with particularly strong performance for the PEER records. The consistency in residual distributions supports the statistical robustness of the model across varying magnitudes and distances.

3.5. Assessment of the Proposed PGV Model

Fig. 12 presents the empirical prediction and observed data of Peak Ground Velocity (PGV) as functions of epicentral distance (*EpiD*) and moment magnitude (M_w), using ground motion records from the ESM (2462 records) and PEER (4328 records) databases. In subplot (a), PGV is plotted against *EpiD* for a range of fixed M_w values (3.5 to 8.0). The scatter points show the observed PGV values from both datasets, while the solid lines represent model predictions for the specified magnitudes. As expected, PGV shows a clear attenuation trend with increasing distance, and higher magnitudes produce significantly larger PGV values across all distances. In subplot (b), PGV is plotted against M_w for fixed epicentral distances (ranging from 10 km to 600 km). Here, PGV increases consistently with M_w, and the rate of increase is steeper at shorter distances. Model prediction curves closely follow the central tendency of the data, validating the model's ability to capture the magnitude-distance scaling relationship. The comparison highlights good agreement between the ESM and PEER datasets, reinforcing the robustness of the derived regression model across diverse regional data sources.

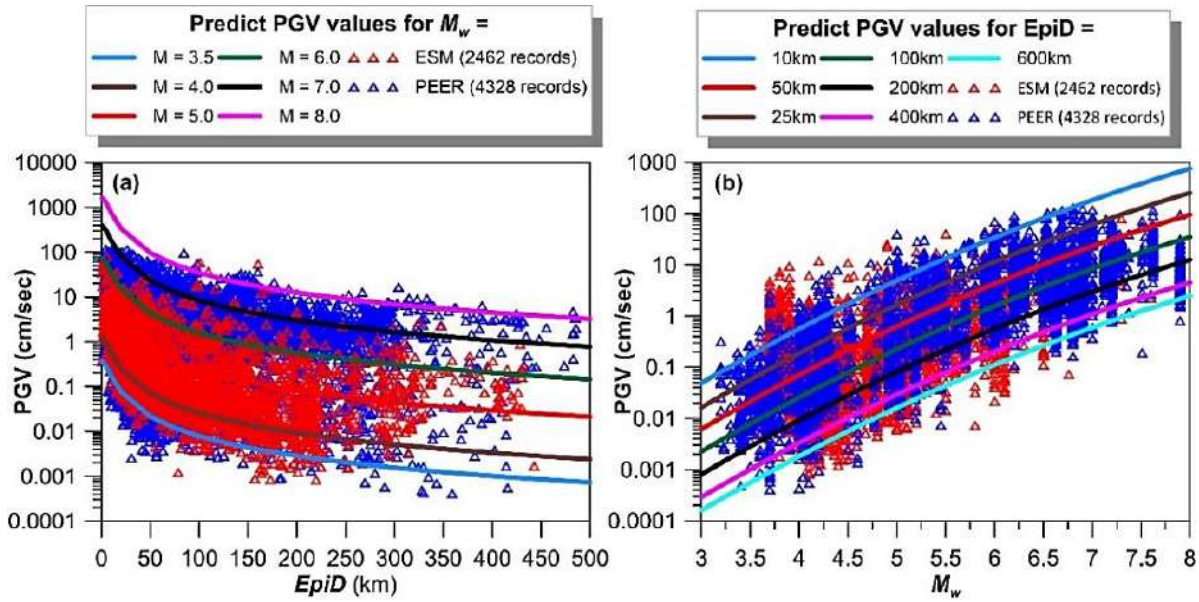

Fig. 12. Comparison of predicted and observed PGV values from the ESM (red triangles) and PEER (blue triangles) databases. (a) PGV versus *EpiD* for fixed M_w (3.5 to 8.0); (b) PGV versus M_w for fixed *EpiD* (10 km to 600 km). Solid lines represent regression model predictions

A second comparison is conducted using empirical models previously proposed in the literature. The first model, developed by Joyner and Boore (1988) [38], is presented in Equation (1) of Table 7. This attenuation relationship was derived from strong-motion recordings of earthquakes with moment magnitudes ranging from 5.0 to 7.7. However, it does not account for local site conditions, which may limit its applicability across diverse geological settings. The second comparison model, proposed by Massa et al. (2007) [39], was specifically developed for Central–Northern Italy, using a dataset of 2,126 ground-motion records. Their model incorporates site classification based on Eurocode 8, distinguishing between three categories: Class A (rock), Class B (stiff soil), and Class C (soft soil). The site condition parameter, S, is set to 1 for stiff or soft soil, and 0 otherwise. Additionally, the prediction model of Campbell and Bozorgnia (2014) [35], previously presented in Section 3.3, was utilized for comparison for the horizontal components of PGV. It should be noted that this model operates within specific parameter boundaries: moment magnitudes ranging from 3.3 to 8.5 for strike-slip faults, 8.0 for reverse faults, and 7.5 for normal faults; source-to-site distances limited to 300 km; shear wave velocities (V_{s30}) between 150-1500 m/s; and hypocentral

depths spanning 0-20 km [35]. A fourth comparison model was introduced by Akkar et al. (2014) [34], who developed a new generation of ground-motion prediction equations (GMPEs) based on a comprehensive pan-European strong-motion database. This model incorporates recent advancements in ground-motion modeling and is expressed in Eq. (4) of Table 1.

Finally, the model proposed by Tusa and Langer (2016) [40], based on an extensive dataset of seismic events from Mount Etna, Italy, was included. Their study considered 1,158 shallow and 1,957 deep events recorded across 91 stations, covering a magnitude range from 0.5 to 4.8 and epicentral distances up to 100 km. Their model accounts for both geological and volcanic site classifications, providing valuable insights for seismic hazard assessment in volcanic regions.

Table 7. Selected PGV models for comparison with the proposed model.

N	Prediction Model	Ref.
(1)	$\log(PGV)_{cm/s} = 2.09 + 0.49(M-6) - \log(R) - 0.002R + 0.17, with\ R = \sqrt{r_0{}^2 + 16}$	[38]
(2)	$\log(PGV)_{cm/s} = -4.197 + 0.856(M) - 1.727\log(R) + 0.178S$	[39]
(3)	$\ln(\mathrm{PGV}) = f_{mag} + f_{dis} + f_{flt} + f_{hang} + f_{site} + f_{sed} + f_{hyp} + f_{dip} + f_{atn}$	[35]
(4)	$\ln(PGV)_{cm/sec} = \ln[PGV_{REF}(M_w, R, SoF)] + \ln[S(V_{s30}, PGV_{REF})]$	[34]
(5)	$\ln(PGV)_{cm/sec} = -1.412 + 0.085M + 0.094M^2 + [-1.67 + 0.171(M-3.6)]\log\left(\sqrt{R_{ep}{}^2 + 3.056^2}\right) + 0.003\left(\sqrt{R_{ep}{}^2 + 3.056^2} - 1\right)$	[40]

Where M is the moment magnitude, and r_0 is the shortest distance (in kilometers) between the site and the vertical projection of the seismic fault rupture. *Rep* is the epicentral distance (km). S = 0 for Rock Site and 1 for Soil Site.

Fig. 13 presents a comparative analysis between the proposed PGV prediction model for soft soil sites and several established models from the literature given in Table 7. The comparison of PGV values is performed for four representative moment magnitudes: M_w = 4.5, 5.5, 6.5, and 7.5 against epicentral distance (*EpiD*) up to 400 km.

The Joyner & Boore (1988) model, while foundational for ground motion prediction, exhibits significant underestimation of PGV for soft soil sites across all magnitudes (Fig. 13). This discrepancy is most pronounced for $M_w \geq 5.5$, where the model underpredicts PGV by 40–60% at distances <100 km. The deviation stems from the model's lack of site-specific terms (e.g., V_{s30}), rendering it unsuitable for soft soil applications. These results underscore a critical gap in early attenuation relationships: their inability to account for soil amplification effects, which are particularly severe in loose, saturated deposits. Consequently, using such models for seismic hazard assessment in soft soil regions may lead to nonconservative designs, increasing vulnerability to infrastructure damage.

The Campbell and Bozorgnia (2014) and Akkar et al. (2014) models show region-dependent biases when applied to soft soils. Despite its comprehensive framework, Campbell and Bozorgnia (2014) overpredicts PGV for moderate magnitudes (M_w = 4.5–5.5), but aligns better for $M_w \geq 6.5$, likely due to its calibration with California-specific basin effects. Conversely, Akkar et al. (2014) performs well for M_w = 5.5–6.5 but diverges at M_w = 7.5, reflecting limitations of its pan-European dataset. Both models struggle with very soft soils (V_{s30} < 250 m/s), as their functional forms prioritize broader applicability over localized nonlinear effects. This highlights a key challenge in ground motion modeling: balancing regional generality with site-specific accuracy, particularly for high-risk soft soil zones.

Tusa & Langer (2016)'s model, developed for volcanic environments ($M_w \leq 4.8$, $EpiD \leq 100$ km), performs poorly in this comparison (Fig. 13). Its predictions deviate substantially for $M_w \geq 5.5$ and distances >100 km, as it neglects crustal earthquake dynamics and deep soil amplification. This mismatch emphasizes the dangers of adopting region-specific models outside their intended context, particularly when assessing soft soil response to larger, non-volcanic events. Engineers

working in tectonic settings with mixed seismicity (e.g., Japan, Central America) should avoid such models unless volcanic hazards dominate.

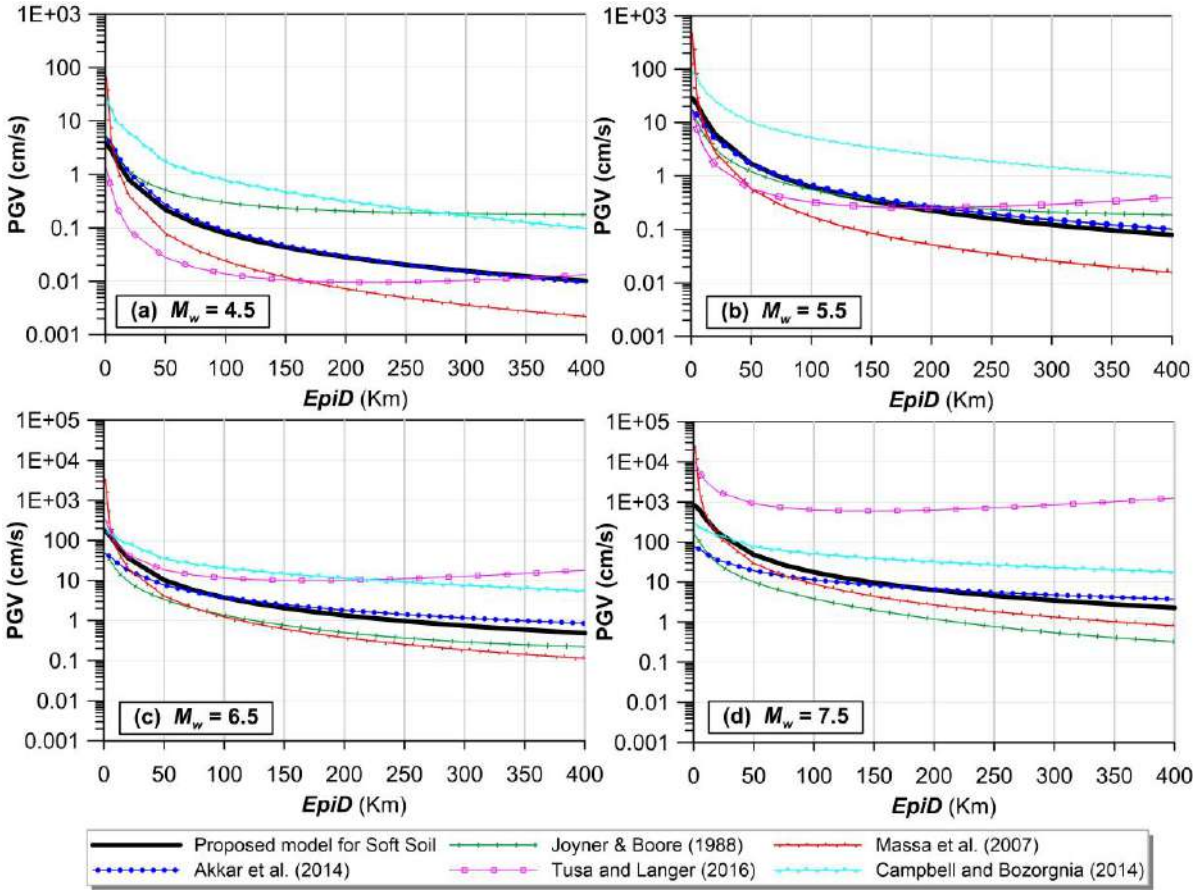

Fig. 13. Comparison of the proposed PGV prediction model for soft soil sites (black line) with established models from the literature: Joyner & Boore (1988), NGA-West2 (2014), Akkar et al. (2014), Massa et al. (2007), and Tusa & Langer (2016). PGV is plotted as a function of *EpiD* for four different M_w: (a) 4.5, (b) 5.5, (c) 6.5, and (d) 7.5

The proposed model shows superior agreement with observed PGV trends across all magnitudes and distances (Fig. 13), particularly in the 20–300 km range most critical for infrastructure design. Its enhanced accuracy derives from three key innovations: (1) explicit V_{s30}-dependence (180–360 m/s) to capture nonlinear soil behavior, (2) calibration with global datasets (PEER + ESM) to minimize regional biases, and (3) physics-based attenuation terms that account for dual-phase decay (rapid near-field vs. stable far-field shaking) in soft soils. Notably, for M_w = 7.5 events, the model predicts PGV values 20–30% higher than Campbell and Bozorgnia (2014) at 50–150 km distances, accurately reflecting empirical observations of prolonged shaking in soft basins. This improvement has direct implications for assessing liquefaction risk and designing long-period structures, where PGV serves as a critical demand parameter.

This comprehensive evaluation demonstrates that conventional ground motion models—whether rock-site-based (e.g., Joyner & Boore 1988), regionally constrained (e.g., Akkar et al. 2014), or volcanically calibrated (Tusa & Langer 2016)—exhibit systematic limitations in predicting PGV for soft soil conditions. The proposed model overcomes these shortcomings through its physics-based formulation incorporating V_{s30}-dependent nonlinearity (180-360 m/s), global dataset integration (PEER+ESM), and dual-phase attenuation behavior. Quantitative comparisons reveal its superior performance, particularly for critical scenarios (M_w ≥6.5, *EpiD* = 50-300 km), where it resolves 20-50% underprediction by existing models. These findings underscore the necessity of adopting site-specific attenuation relationships in seismic design codes, particularly for vulnerable soft soil regions where conventional approaches may compromise structural safety through unconservative predictions. The model's validated accuracy across magnitudes (4.5-7.5) and

distances (0-500 km) provides engineers with a robust tool for realistic hazard assessment in high-risk environments.

4. Conclusion

This study presents the development of a predictive model for Peak Ground Acceleration (PGA) and Peak Ground Velocity (PGV) in soft soil conditions, emphasizing the significant role of soft soil in amplifying seismic waves and increasing structural vulnerability during earthquakes.

The predictive model, based on nonlinear regression analysis, integrates key predictor variables, including moment magnitude (M_w), epicentral distance ($EpiD$), and average shear wave velocity over the top 30 meters (V_{s30}). Analyzing an extensive dataset of over 6790 ground motion records from 875 earthquakes (sourced from the PEER and ESM databases), the study underscores the importance of site classification, particularly shear wave velocity (V_{s30}), in assessing ground motion characteristics.

Key Conclusions:

- The proposed models effectively capture the influence of earthquake magnitude and epicentral distance on seismic ground motion in soft soil conditions, showing strong agreement with observed data from the PEER and ESM datasets.
- For PGA, the model accurately describes attenuation trends and magnitude-dependent variations. While the ESM dataset predicts slightly higher PGA values, especially at short distances, the model aligns well with established attenuation relationships (e.g., Campbell, 1981; Youngs et al., 1988; Boore et al., 1993). The findings highlight the importance of site-specific datasets for seismic hazard assessments in soft soil environments, given the faster attenuation observed at short distances.
- Fig. 10 demonstrates that soft soil response exhibits strong dependencies on both earthquake magnitude (M_w) and source-to-site distance ($EpiD$), necessitating specialized modeling approaches. Traditional models developed for rock sites or limited regional conditions are inadequate for these high-risk areas, highlighting the urgent need to adopt soil-specific attenuation relationships in seismic codes and hazard assessments. The proposed model addresses this gap, providing reliable predictions for critical engineering applications.
- For PGV, results confirm that earthquake magnitude has a stronger influence than distance, with PGV values increasing significantly as magnitude grows. The proposed model predicts higher PGV values at short distances than the widely used Joyner and Boore (1988) model, emphasizing the role of local soil amplification effects.
- Overall, the findings validate the reliability of the proposed models for seismic hazard analysis in soft soil regions. Comparisons with existing models reinforce the necessity of site-specific ground motion prediction equations (GMPEs) for accurate seismic risk assessments, particularly in areas where soft soil conditions amplify seismic waves.

To further enhance the accuracy and applicability of these predictive models, future research should:

- Incorporate additional geotechnical parameters for improved ground motion prediction.
- Develop refined earthquake-resistant design strategies, ultimately enhancing structural resilience in seismically active areas with soft soil conditions.
- Expand the database to include V_{s30} < 180 m/s (very soft soils).
- Incorporate basin depth effects, which may further modulate long-period motions.

The ground motion prediction equations (GMPEs) developed in this study provide a critical foundation for site-specific seismic hazard assessment in soft soils. However, to fully leverage these results for engineering applications, future research should investigate the role of soil-structure interaction (SSI) in modulating the seismic response of structures subjected to the predicted PGA and PGV. Such work would enhance the practical utility of these GMPEs by bridging the gap between ground motion prediction and performance-based seismic design, particularly for infrastructure in soft-soil regions.

Acknowledgement

The contributions of the PEER and ESM working group are acknowledged to provide earthquake database of this study.

References

[1] Vuran E, Serhatoğlu C, Timurağaoğlu MÖ, Smyrou E, Bal İE, Livaoğlu R. Damage observations of RC buildings from 2023 Kahramanmaraş earthquake sequence and discussion on the seismic code regulations. Bull Earthq Eng 2025;23:1153–82. https://doi.org/10.1007/s10518-023-01843-3
[2] Yao X, Wu B. Progress in Seismic Isolation Technology Research in Soft Soil Sites: A Review. Buildings 2024;14:3198. https://doi.org/10.3390/buildings14103198
[3] Shi F, Lin Z, Li Q, Ozbulut OE, He Z, Zhou Y. Design, manufacturing, and testing of a hybrid self-centering brace for seismic resilience of buildings. Earthq Eng Struct Dyn 2023;52:1381–402. https://doi.org/10.1002/eqe.3821
[4] Gue SS, Gue CS. Geotechnical Challenges On Soft Ground. J Civ Eng Sci Technol 2022;13:84–96. https://doi.org/10.33736/jcest.4760.2022.
[5] Roy M. Foundation on Soft and Filled-Up Soil. Geotech. Found. Eng. Pract. Ind. Proj., Singapore: Springer Nature Singapore; 2024, p. 93–103. https://doi.org/10.1007/978-981-99-7906-6_6
[6] Aouari I, Benahmed B, Palanci M, Aidaoui L. Empirical Model for the Prediction of Ground Motion Duration on Soft Soils. Indian Geotech J 2024;54:421–40. https://doi.org/10.1007/s40098-023-00778-5
[7] Almansa FL, Weng D, Li T, Alfarah B. Suitability of Seismic Isolation for Buildings Founded on Soft Soil. Case Study of a RC Building in Shanghai. Buildings 2020;10:241. https://doi.org/10.3390/buildings10120241
[8] Dagen W, Li T, López-Almansa F. Nonlinear Time-History Analysis of A Base-Isolated RC Building in Shanghai Founded on Soft Soil. 16th World Conf. Earthq. Eng., Santiago Chile: 2017, p. 2634.
[9] Griffiths SC, Cox BR, Rathje EM. Challenges associated with site response analyses for soft soils subjected to high-intensity input ground motions. Soil Dyn Earthq Eng 2016;85:1–10. https://doi.org/10.1016/j.soildyn.2016.03.008
[10] Kramer SL, Stewart JP. Geotechnical Earthquake Engineering. 2nd Editio. Boca Raton: CRC Press; 2024. https://doi.org/10.1201/9781003512011
[11] Giardini, D., Grünthal, G., Shedlock, K. M. and Zhang P. No TitleThe GSHAP Global Seismic Hazard Map. In: Academic Press A, editor. Int. Handb. Earthq. Eng. Seismol. Internatio, Amsterdam: 2003, p. 1233–9.
[12] Chasanah U, Handoyo E, Rahmawati NN, Musfiana M. Mapping Risk Level Based on Peak Ground Acceleration (PGA) and Earthquake Intensity Using Multievent Earthquake Data in Malang Regency, East Java, Indonesia. J ILMU Fis | Univ ANDALAS 2022;14:64–72. https://doi.org/10.25077/jif.14.1.64-72.2022
[13] Basid A, Rusli R, Purwandari P. Mapping The Risk Level of Earthquake Damage in Central Java Based on Data From PGA, PD and HDI. J Pendidik Fis Dan Keilmuan 2022;7:130. https://doi.org/10.25273/jpfk.v7i2.12078
[14] Akkar S, Özen Ö. Effect of peak ground velocity on deformation demands for SDOF systems. Earthq Eng Struct Dyn 2005;34:1551–71. https://doi.org/10.1002/eqe.492
[15] Hunter JA, Motazedian D, Crow HL, Brooks GR, Miller RD, Pugin AJ-M, et al. Near-Surface Shear-Wave Velocity Measurements for Soft-Soil Earthquake-Hazard Assessment: Some Canadian Mapping Examples. Adv. Near-surface Seismol. Ground-penetrating Radar, Society of Exploration Geophysicists, American Geophysical Union, Environmental and Engineering Geophysical Society; 2010, p. 339–59. https://doi.org/10.1190/1.9781560802259.ch21
[16] FEMA P-58. Seismic Performance Assessment of Buildings. Federal Em. 2018.
[17] KAWASHIMA K, UNJOH S. The Damage of Highway Bridges in The 1995 Hyogo-Ken Nanbu Earthquake and Its Impact on Japanese Seismic Design. J Earthq Eng 1997;1:505–41. https://doi.org/10.1080/13632469708962376
[18] Course S. Seismic Design of Buried Pipelines. University at Buffalo, State University of New York: 2012.
[19] Timothy D. Ancheta, Robert B. Darragh, Jonathan P. Stewart, Emel Seyhan, Walter J. Silva, Brian S.J. Chiou, Katie E. Wooddell, Robert W. Graves, Albert R. Kottke, David M. Boore, Tadahiro Kishida and JLD. PEER NGA-West2 Database. 2013.
[20] Luzi L, Lanzano G, Felicetta C, D'Amico MC, Russo E, Sgobba S, et al. Engineering Strong Motion Database (ESM), version 2.0 2020. https://doi.org/10.13127/ESM.2.
[21] Council IC, International Code Council. International Building Code. 5th ed. ICC; 2006.
[22] BSSC. 2000 NEHRP recommended provisions for seismic regulations for new buildings and other structures. FEMA-368 Part 1 Dev Fed Emerg Manag Agency, Washington, DC 2001.

[23] Eurocode-8. Eurocode 8: Design of structures for earthquake resistance - Part 1 : General rules, seismic actions and rules for buildings. Brussels, Belgium: European Committee for Standardization; 2004.
[24] UBC. Uniform Building Code. California, USA: International Conference of Building Officials; 1997.
[25] RPA. Régles Parasismiques Algériennes RPA 2024. Algeria: 2024.
[26] Douglas J. Ground motion prediction equations 1964-2018. vol. 69. 75 Montrose Street, Glasgow, United Kingdom: 2019. https://doi.org/10.1111/j.1651-2227.1980.tb07069.x
[27] Abrahamson NA, Silva WJ. Empirical Response Spectral Attenuation Relations for Shallow Crustal Earthquakes. Seismol Res Lett 1997;68:94–127. https://doi.org/10.1785/gssrl.68.1.94
[28] Boore DM, Joyner WB, Fumal TE. Equations for Estimating Horizontal Response Spectra and Peak Acceleration from Western North American Earthquakes: A Summary of Recent Work. Seismol Res Lett 1997;68:128–53. https://doi.org/10.1785/gssrl.68.1.128
[29] Campbell KW. Empirical Near-Source Attenuation Relationships for Horizontal and Vertical Components of Peak Ground Acceleration, Peak Ground Velocity, and Pseudo-Absolute Acceleration Response Spectra. Seismol Res Lett 1997;68:154–79. https://doi.org/10.1785/gssrl.68.1.154
[30] Chiou B-J, Youngs RR. An NGA Model for the Average Horizontal Component of Peak Ground Motion and Response Spectra. Earthq Spectra 2008;24:173–215. https://doi.org/10.1193/1.2894832
[31] Campbell KW. Updated Near-Source Ground-Motion (Attenuation) Relations for the Horizontal and Vertical Components of Peak Ground Acceleration and Acceleration Response Spectra. Bull Seismol Soc Am 2004;94:2417. https://doi.org/10.1785/0120040147
[32] Campbell K. Near-source attenuation of peak horizontal acceleration. Bull Seismol Soc Am 1981;71:2039–70.
[33] Youngs RR, Day SM, Stevens JL. Near field ground motions on rock for large subduction earthquakes. Earthq. Eng. Soil Dyn. II, vol. ASCE, 1988, p. 445–62
[34] Akkar S, Sandıkkaya MA, Bommer JJ. Empirical ground-motion models for point- and extended-source crustal earthquake scenarios in Europe and the Middle East. Bull Earthq Eng 2014;12:359–87. https://doi.org/10.1007/s10518-013-9461-4
[35] Campbell KW, Bozorgnia Y. NGA-West2 Campbell-Bozorgnia Ground Motion Model for the Horizontal Components of PGA , PGV , Response Spectra for Periods Ranging from 0.01 to 10 sec. Berkeley: 2013.
[36] Zuccolo E, Bozzoni F, Lai CG. Regional Low-Magnitude GMPE to Estimate Spectral Accelerations for Earthquake Early Warning Applications in Southern Italy. Seismol Res Lett 2017;88:61–71. https://doi.org/10.1785/0220160038
[37] Shiuly A. Global Attenuation Relationship for Estimating Peak Ground Acceleration. J Geol Soc India 2018;92:54–8. https://doi.org/10.1007/s12594-018-0952-4
[38] Joyner WB, Boore DM. Measurement, characterization, and prediction of strong ground motion. Earthq. Eng. Soil Dyn. II, Proc. Am. Soc. Civ. Eng. Geotech. Eng. Div. Spec. Conf., June 27–30, 1988, Park City, Utah, 1988, p. 43–102.
[39] Massa M, Marzorati S, D'Alema E, Di Giacomo D, Augliera P. Site Classification Assessment for Estimating Empirical Attenuation Relationships for Central-Northern Italy Earthquakes. J Earthq Eng 2007;11:943–67. https://doi.org/10.1080/13632460701232675
[40] Tusa G, Langer H. Prediction of ground motion parameters for the volcanic area of Mount Etna. J Seismol 2016;20:1–42. https://doi.org/10.1007/s10950-015-9508-x

Research on Engineering Structures & Materials
www.jresm.org
Research Group

Research Article

Buckling resistance of layered reinforced concrete columns: Experimental evaluation of normal and lightweight thermo-stone aggregate configurations

Hammad D. Merie [1,a], Diyar N. Qader [*,1,b], Baraa T. Kamel [1,c], Muyasser Mohammed Jomaa [2,d]

[1]*Civil Engineering Department, University of Kirkuk, Kirkuk, Iraq*
[2]*Civil Department, Engineering College, Tikrit University, Tikrit, Iraq*

Article Info

Article History:

Received 28 Mar 2025
Accepted 02 July 2025

Keywords:

Buckling resistance;
Layered RC columns;
Normal concrete;
Lightweight concrete;
Thermo-stone

Abstract

Reinforced concrete (RC) columns are the vital part of building structures and play an important role in the stability and safety of the entire building under axial compression load. In this study, the buckling performance of layered RC columns made of NC, LWC and containing thermo-stone aggregate replacements was studied experimentally. Eighteen square and circular RC columns with different layer arrangements—LNN, LNL, and NNL—were tested under axial loading. Results showed that the NNL and LNN geometry performed better than the fully LWC columns in terms of axial compression and buckling. More precisely, square NNL columns with 25% thermo-stone replacement can attain an axial load capacity of 339.13kN, that represents a value 21.6% larger than the same fully LWC column (278.85kN). Similarly, layered circular columns with 50% thermo-stone replacement (CR-7 and CR-8) recorded 290.5–290.8kN, compared to 245.9kN for the fully LWC counterpart (CR-6). Deflections ranged from 3.75 mm in NC columns to 5.23 mm in layered LWC columns. Square columns consistently exhibited higher buckling resistance than circular ones due to their greater moment of inertia. The findings highlight that strategically placing NC in the middle and upper layers enhances structural performance while maintaining weight reduction.

© 2025 MIM Research Group. All rights reserved.

1. Introduction

In reinforced concrete (RC) buildings, columns are important and indispensable components that deliver and provide support to the structure by withstanding axial and lateral forces. Hence, these columns are responsible for the structural response and to effectively support dominantly loads, the columns must possess good strength, durability, and ductility [1, 2]. Different reasons include the collapsing of structures and other human error factors, but the primary factor is mostly overloading and uncalculated or unconsidered additional weight put on the structures, and poor column design that is associated with poor knowledge of the properties of these columns. Particularly in tall or thin constructions where instability might result in catastrophic failure, the buckling behavior of these columns is a serious problem [3, 4].

Recently, layered columns have been used in many buildings and on a wide range as one of the new applications for lightweight columns with a high strength-to-weight ratio column, which incorporates multiple layers of concrete or reinforcement with different characteristics, have drawn interest due to their capacity to increase load-bearing capacity, ductility, and resistance to buckling [5, 6]. The behavior of these structures largely depends on the properties of concrete in each layer in addition to the type of their connection between layers. For layered columns, the

*Corresponding author: diyar.nasih@uokirkuk.edu.iq
[a]orcid.org/0000-0002-6871-8823; [b]orcid.org/0000-0003-3842-1313; [c]orcid.org/0009-0004-2300-9064; [d]orcid.org/0000-0002-0721-8200
DOI: http://dx.doi.org/10.17515/resm2025-792me0328rs

interaction between different layers of concrete and reinforcement introduces additional complexity. If the layers have different stiffnesses, strengths, and ductility, the buckling mode and critical load will also change. Moreover, it is impossible to completely ensure conformity between inter-layers, leading to inter-layer slip. If slip is sufficiently large, it has a profound effect on the mechanical behavior of the composite system. Consequentially, inter-layer slides have to be considered for the so-called partial interaction analysis of composite structures [7, 8].

In recent years, an approach to use a dual concrete column, also known as layered concrete column, has become widely studied to optimize the benefits of high-performed resistances and the physical characteristics of concrete. The authors of [9] studied the buckling behavior of layered composite columns with partial interaction between layers. Their study emphasized the challenges posed by the difference in stiffness and strength of the layers, affecting the buckling critical load and failure mode. This interlayer slip impacts the mechanical behavior of the composite system, and therefore they proposed a theoretical model taking this into account. This work highlighted the importance of inclusion of partial interaction in the response of such members. Numerical study of the buckling of axial loaded two-layer columns using finite difference method was performed by [10]. They discovered that the level of adhesion between laminates has a significant impact on the buckling strength of the column. with increasing interlayer bond defect, the slip of column will easily take place on the interlayer, which leads to decreasing of buckling resistance. These investigations show that despite the benefits of using layered columns to increase strength and decrease mass, their performance in buckling is complex should be further investigated especially with respect to material properties and layer stacks.

Lightweight concrete (LWC) has been widely used in construction for its ability to reduce the overall weight of a structure. However, the reduced stiffness of LWC compared to normal concrete (NC) raises concerns about its performance in load-bearing members. The authors of [11] conducted a review of fiber-reinforced polymer (FRP) RC columns, highlighting the potential for LWC to improve structural performance when combined with exterior FRP wraps. Their study found that LWC columns with FRP reinforcement exhibited up to 30% higher buckling resistance compared to conventional RC columns, suggesting that LWC can be a viable option when combined with appropriate reinforcement. However, there is a substantial body of literature that analyzes composite beams and beam-columns both analytically and numerically, for example, [12-19].

In continuation to the above investigations, recent studies have significantly increased our knowledge on lightweight and layered concrete columns under axial and buckling loads. The authors of [20] studied the behavior of the slender LWC-NC columns with lightweight aggregates in combination with steel confinement, showing that confined LWC-NC columns increase load capacity and ductility – observations that are pertinent to our layer-up LWC-NC configurations. In [21], the authors studied the seismic response of LWC columns under different axial forces and they found that the addition of extra transverse reinforcement is crucial for maintaining ductility, and this verifies the structural philosophy of our thermo-stone-based LWC cores. Moreover, the authors of [22] investigated the compressive axial performance of lightweight aggregate concrete (LWAC) columns confined by transverse steel confining reinforcement. They concluded that transverse confinement was effective in not only improving the compressive strength but also the ductility, because of experimental results. The work demonstrates the significant effect of steel confinement on increasing strength and deformation capacity of the LWAC for structural use. Finally, the authors of [23] investigated buckling of axially compressed, fully-encased composite columns constructed with high strength concrete (approximately 80 MPa) and ISMB 100 steel sections. Three unreinforced columns having different cross sections were tested under axial loading. It was found that larger cross sections and denser shear reinforcement enhance the buckling capacity. EC4 yielded more accurate estimates than AISC 360–10 when compared with test results. The results of tests were simulated by finite element analysis with ANSYS codes, and ANOVA demonstrated that EC4 was the most reliable model to predict the buckling resistance.

The current research addresses a gap in the understanding of the buckling behavior of layered RC columns, where limited studies have explored the influence of layering normal and LWC on structural performance, particularly under axial loading conditions. While previous research has

focused on composite and lightweight columns, the specific buckling resistance of columns with various concrete layer arrangements remains underexplored. Therefore, this study aims to experimentally investigate the structural behavior of layered RC columns, utilizing normal and LWC (with different replacement ratios of thermo-stone aggregate) in varying arrangements. The research seeks to determine how these configurations impact buckling resistance, deflection, and overall structural performance.

1.1. Research Significance

This study aims to conduct an experimental investigation on the effect of different parameters on the structural behavior of layered columns combining NC and LWC, which parameters include the shape of these columns, the arrangement of layers, and the type of LWC that was manufactured by replacing different proportions of thermo-stone instead of aggregate. Thus, obtaining concrete columns with light weights that can bear external loads without any loss of their structural properties. Fig. 1 illustrates the research methodology flowchart for the current experimental investigation.

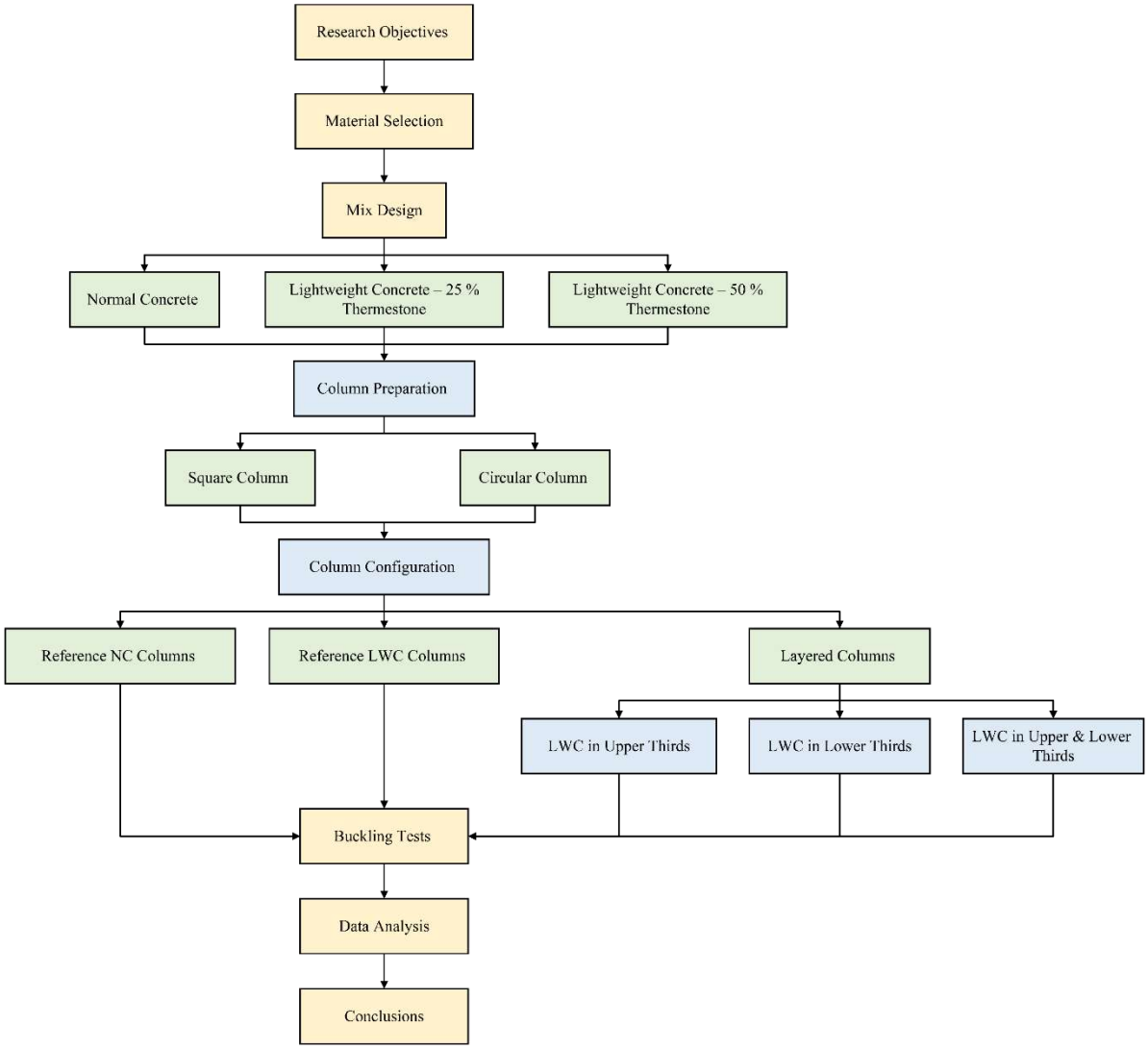

Fig. 1. Methodology flowchart for the present study

2. Experimental Program

The purpose of this experimental program is to investigate the behavior of intermediate reinforced concrete columns with square and circular cross-sections, constructed using both NC and LWC. The study includes layered configurations incorporating two thermo-stone replacement ratios for gravel (25% and 50%), as well as non-layered reference specimens for comparison. A detailed

explanation of the materials used, the technique employed, and the results obtained may be found below.

2.1. Materials and Properties

2.1.1 Cement

According to Iraqi Standard (IQS) No. 5 [24], the main binding ingredient in each concrete mixture was ordinary Portland cement (OPC) type-I. Tables 1 and 2, respectively, outline the chemical and physical characteristics of the utilized cement in this study.

Table 1. Chemical characteristics of the employed cement

Properties	Composition content (%)	IQS Standard, No. 5 [24]
Oxide composition		
Alumina, Al_2O_3	4.92	
Silica, SiO_2	21.82	
Ferric Oxide, Fe_2O_3	2.98	
Lime, CaO	61.01	
Sulphatic Anhydride, SO_3	2.2	Max. 2.5
Magnesia, MgO	2.21	Max. 5
Compound composition		
C_3A	4.2	
C_2S	21.7	
C_3S	50.64	
C_4AF	7.071	
Free Lime	1.41	
Loss on ignition	1.23	Max. 4
Lime Saturation Factor (L.S.F)	0.92	0.66-1.02
Insoluble residue	0.42	1.5% max

Table 2. Physical characteristics of the utilized cement

Properties	Test result	IQS Standard, No. 5 [24]
Initial setting time, min	2hr 35 min	≥45
Final setting time, min	3hr 25 min	≤600
Specific surface area (Blaine method), m^2/kg	346	230 m^2/kg min
Compressive strength (MPa)		
at 3 days	18.32	≥ 10.0
at7 days	27.83	23 MPa min
at 28 days	35	≥ 32.5

2.1.2 Fine Aggregate

The sand employed in this investigation had maximum size of the aggregate is 4.75 mm with round-shape particles, for each mixture, dry amounts of sand were utilized. The grading of the sand was conformed to the Iraqi Standard (IQS) No. 45 [25].

2.1.3 Coarse Aggregate

Coarse aggregate, commonly found in nature as gravel, can be obtained through quarry blasting, manual crushing, or mechanical crushers. Before being used in concrete production, it must be thoroughly cleaned. Its angularity and strength influence the properties of the concrete in various ways. The gravel employed in this investigation is a river gravel with a maximum size of 12.5 mm

and graded between 4.75 to 12.5 mm. It was found to conform to the Iraqi standard specifications No. 45 [25]. The gravel had a specific gravity of 2.66, and absorbed water at a rate of 0.76% as listed in Table 3.

Table 3. Characteristics of coarse aggregate employed in the current study

Properties	Specifications	Test results	Limits of specification
Specific gravity	ASTM C127 [26]	2.66	-
Absorption, %	ASTM C127 [26]	0.76%	-
Dry loose unit weight, kg/m^3	ASTM C29/C29M [27]	1341	-
Sulfate content (as SO_3), %	IQS No. 45 [25]	0.027	0.1 max

2.1.4 Water

Drinking clean water was utilized for mixing and curing the concrete samples.

2.1.5 Reinforcing Steel

A deformed reinforcing steel with nominal diameters of 10 mm (for longitudinal bars) and 6 mm (for stirrups) was used in this study. Where a reinforcing steel with a diameter of 6 mm was used in the stirrups and the reinforcing steel with a diameter of 10 mm in the longitudinal reinforcement of the specimen. The results of the laboratory test shown in Table 4 according to the reinforcing steel diameter.

Table 4. Properties of rebars

Diameter (mm)	Yield strength (MPa)		Ultimate strength (MPa)	
6	-	-	140.7	148.02
	-		147.8	
	-		155.55	
10	518.51	545.93	673.83	689.94
	568.27		713.26	
	550.99		682.75	

2.1.6 Lightweight Aggregate (Thermo-stone)

Thermo-stone is a type of block made from cellular concrete (autoclaved aerated concrete). In the original blocks it is used as an alternative over bricks in multi-story buildings to lessen the overall weight of the building and to provide thermal comfort within it. Thermo-stone is a blend of hydrated lime, sand, cement, water, and aluminum powder. The mixing process incorporates aluminum powder into the mixture, producing a gas-bubble structure in the concrete. It is happening because of a chemical reaction between aluminum powder, silica and hydrated lime. The concrete block is cured under high pressure stain at a set period of time after the primary placing. Waste from this concrete block can also be recycled to make a lightweight aggregate.

In this experimental investigation, the impact of utilizing lightweight aggregate, ranging in size from 4.75 to 12.5 mm, sourced from LWC blocks as coarse aggregate has been examined. The aggregate was obtained by crushing LWC blocks, brought from thermo-stone factory in Kirkuk city, into a similar grading to that of the natural aggregate (12.5 mm), and was used in the saturated surface dry (SSD) condition. This was then utilized to replace the coarse aggregate only with 25% and 50% as a volumetric replacing ratio. The replacement is volumetric for lightness weight of thermo-stone aggregate. Fig. 2 shows the stages of crushing thermo-stone. Table 5 lists the physical properties of thermo-stone.

Fig. 2. Stages of crushing thermo-stone

Table 5. Properties of thermo-stone aggregate

Properties	Specifications	Test results	Limits of specification
Specific gravity	ASTM C127 [26]	1.08	-
Absorption, %	ASTM C127 [26]	44.3%	-
Dry loose unit weight, kg/m^3	ASTM C29/C29M [27]	355	-
Sulfate content (as SO_3), %	IQS NO. 45 [25]	0.31	1 max

2.2. Sample Preparation and Mix Proportions

The standard compression cubes (0.15 x 0.15 x 0 .15) m and standard compression cylinders (0.15 x 0.3) m were used for testing the compressive strength of concrete. Then, the influence of using LWC on the physical properties of concrete was studied to obtain a suitable standard mixture to achieve the specifications mentioned previously. Table 6 shows the mixing ratios of the three concrete mixtures and the physical properties of each mixture with compressive strength for each mixture with a curing period of 28 days.

Table 6. Details of concrete mixtures

Trial mix	Mix type	Cement (kg/m^3)	Gravel (kg/m^3)	Sand (kg/m^3)	Water (kg/m^3)	Thermo-stone kg/m^3	Superplasticizer L/100kg (cement)
1	NC	410	1035	723	179	0	0
2	LWC (25%)	410	776.5	723	198.3	54.31	1
3	LWC (50%)	410	517.62	723	205	105.62	1.1

2.2.1 Types of Specimens

In this research, two types of RC columns—square (0.15 x 0.15 m) and circular (0.15 m diameter), each measuring 0.75 m in length—were constructed using different configurations of NC and LWC with thermo-stone replacement. Table 7 provides the details for RC column specimens. The reinforcement details included 4 Ø10 longitudinal bars and Ø6 stirrups spaced at 150 mm (see Figs. 3, 4, and 5). The purpose was to assess how these variations influenced the columns' structural performance and buckling resistance. NC was used as the reference material, while LWC involved replacing either 25% or 50% of the gravel with thermo-stone aggregate to reduce the overall

weight of the columns. In addition to fully NC or LWC columns, layered configurations were introduced, where the columns were divided into three layers along their length.

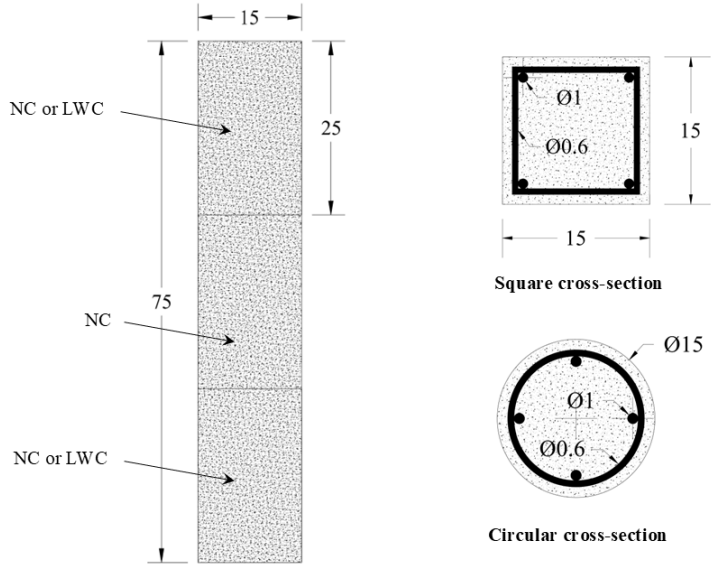

Fig. 3. Layered RC column configurations (all dimensions are in cm)

Fig. 4. Reinforcing steel cages of square and circular columns

Fig. 5. Square and circular steel molds

A total of 18 RC columns were tested, split equally into 9 square and 9 circular columns (Fig. 6), each with different concrete layer configurations. These configurations included: LNN (lower third LWC, middle third NC, upper third NC), LNL (lower third LWC, middle third NC, upper third LWC), and NNL (lower third NC, middle third NC, upper third LWC). The same layering schemes were applied to both square and circular columns to examine how the arrangement of the concrete layers influenced their buckling behavior under axial loading. The arrangement of concrete layers was modified in the upper and lower layers, while the middle layer was kept as NC to ensure strength in that region, which experiences the greatest deflection and, therefore, requires the highest strength. In the naming scheme, the first and second letters indicate the type of column, with SQ representing a square column and CR representing a circular column. The mechanical properties of fresh and hardened concrete are listed in Table 8. The RC columns were tested under axial compression using universal testing machine as shown in Fig. 7. A schematic representation of the test setup utilized in this study is illustrated in Fig. 8.

Table 7. Details of specimens

Specimen		Details of layers		
Square	Circular	Lower layer	Middle layer	Upper layer
Reference specimens (NC)				
SQ-1	CR-1	NC		
Reference specimens (LWC) (25% replacing ratio)				
SQ-2	CR-2	LWC (25%)		
Layered specimens				
SQ-3	CR-3	NC	NC	LWC (25%)
SQ-4	CR-4	LWC (25%)	NC	NC
SQ-5	CR-5	LWC (25%)	NC	LWC (25%)
Reference specimens (LWC) (50% replacing ratio)				
SQ-6	CR-6	LWC (50%)		
Layered specimens				
SQ-7	CR-7	NC	NC	LWC (50%)
SQ-8	CR-8	LWC (50%)	NC	NC
SQ-9	CR-9	LWC (50%)	NC	LWC (50%)

Fig. 6. Total RC column specimens

Table 8. Properties of concrete mixtures

Trial mix	Mix type	Density (kg/m^3)	Compressive strength, f'_c (MPa)	W/C	Slump (mm)
1	NC	2364	32.7	0.436	7
2	LWC (25%)	2279.55	22.4	0.482	9
3	LWC (50%)	2201.62	23.7	0.507	8

Fig. 7. RC column specimen inside the universal testing machine

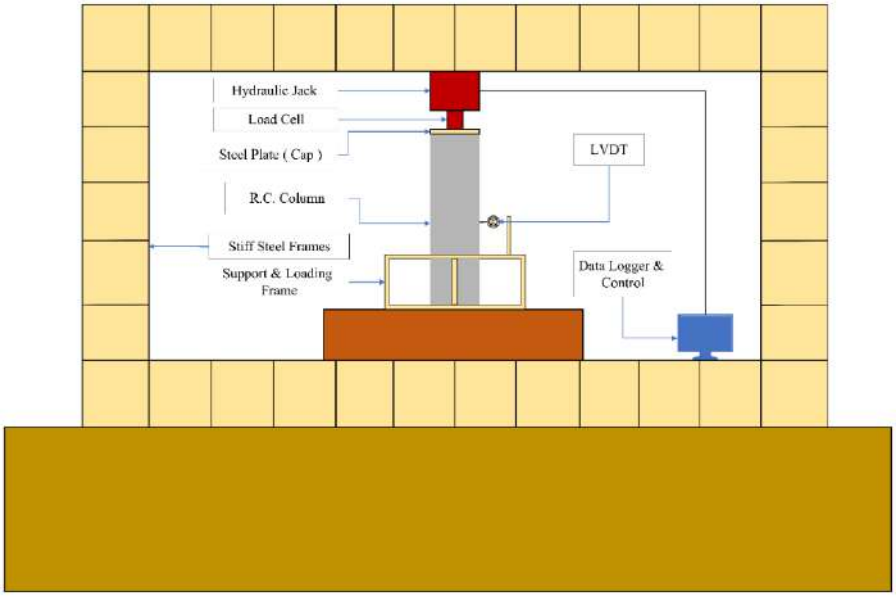

Fig. 8. An illustration of the experiment test setup used in the current study

3. Results and Discussion

This section provides a detailed analysis of the experimental results obtained from the study, comparing the performance of various layered concrete columns with different combinations of NC and LWC. The results for both square and circular column specimens are discussed, focusing on their buckling behavior, deflection characteristics, and overall structural performance.

3.1. NC Columns (Reference Specimens)

The reference specimens in this study consisted of NC columns, which provided a baseline for analyzing the buckling behavior of layered RC columns. The reference specimens used NC mixes with a compressive strength of 32.7 MPa (the density was 2364 kg/m^3), providing the necessary stiffness and mass to prevent buckling when subjected to axial loads. The major failure modes identified in the columns subjected to axial compression loading were lateral deflection followed by concrete crushing. This typical failure mode for slender columns under axial load resulted in deflection that was most pronounced in the middle third of the column height. Table 9 summarizes the properties of the specimens, including their geometry, reinforcement details, and material properties, which are essential for understanding the behavior of the reference specimens. While Table 10 provides a comparison of the results for the reference specimens, showing the critical buckling loads and deflection values.

Figs. 9 and 10 show the calculated axial load versus deflection behavior of the square and circular columns, respectively. The square column (Fig. 9) demonstrates a higher critical buckling load with lower deflection, indicating greater stiffness and resistance to buckling due to its higher moment of inertia. Its deflection curve rises gradually, reflecting slower progression toward failure. In contrast, the circular column (Fig. 10) shows a lower critical buckling load and higher deflection, indicating greater flexibility and faster approach to buckling. This comparison highlights that square column provide better buckling resistance, while circular columns exhibit more deflection under similar loading conditions.

Table 9. Properties of the square and circular column specimens

Type of specimen	Specimen code	f'_c for each layer (MPa)			$f'_{c,avg}$ (MPa)	A_g (mm^2)	A_s (mm^2)	f_y (MPa)
		Upper	Middle	Lower				
Square								
Reference (NC)	SQ-1	32.7	32.7	32.7	32.7	22500	314	545.93
Reference (LWC) with 25% thermo-stone	SQ-2	22.4	22.4	22.4	22.4	22500	314	545.93
Layered with 25% thermo-stone	SQ-3	22.4	32.7	32.7	32.7	22500	314	545.93
	SQ-4	32.7	32.7	22.4	25.83	22500	314	545.93
	SQ-5	22.4	32.7	22.4	25.83	22500	314	545.93
Reference (LWC) with 50% thermo-stone	SQ-6	23.7	23.7	23.7	23.7	22500	314	545.93
Layered with 50% thermo-stone	SQ-7	23.7	32.7	32.7	32.7	22500	314	545.93
	SQ-8	32.7	32.7	23.7	26.7	22500	314	545.93
	SQ-9	23.7	32.7	23.7	26.7	22500	314	545.93
Circular								
Reference (NC)	CR-1	32.7	32.7	32.7	32.7	17662.5	314	545.93
Reference (LWC) with 25% thermo-stone	CR-2	22.4	22.4	22.4	22.4	17662.5	314	545.93
Layered with 25% thermo-stone	CR-3	22.4	32.7	32.7	32.7	17662.5	314	545.93
	CR-4	32.7	32.7	22.4	25.83	17662.5	314	545.93
	CR-5	22.4	32.7	22.4	25.83	17662.5	314	545.93
Reference (LWC) with 50% thermo-stone	CR-6	23.7	23.7	23.7	23.7	17662.5	314	545.93
Layered with 50% thermo-stone	CR-7	23.7	32.7	32.7	32.7	17662.5	314	545.93
	CR-8	32.7	32.7	23.7	26.7	17662.5	314	545.93
	CR-9	23.7	32.7	23.7	26.7	17662.5	314	545.93

Table 10. Results of RC column specimens

Type of specimen	Specimen code	Axial load (kN)	Deflection (mm)	I (mm^4)	E_{avg} (MPa)
		Square			
Reference (NC)	SQ-1	374.98	3.75	42187500	21214
Reference (LWC) with 25% thermo-stone	SQ-2	278.85	4.2	42187500	14251
Layered with 25% thermo-stone	SQ-3	339.13	5.09	42187500	18893
	SQ-4	342.56	5.14	42187500	18893
	SQ-5	307.29	4.61	42187500	16572
Reference (LWC) with 50% thermo-stone	SQ-6	289.75	4.35	42187500	12312
Layered with 50% thermo-stone	SQ-7	346.06	5.19	42187500	18246.67
	SQ-8	347.21	5.21	42187500	18246.67
	SQ-9	318.85	4.78	42187500	15279.33
		Circular			
Reference (NC)	CR-1	313.42	4.07	24837891	21214
Reference (LWC) with 25% thermo-stone	CR-2	238.93	4.3	24837891	14251
Layered with 25% thermo-stone	CR-3	284.9	5.17	24837891	18893
	CR-4	287.44	5.18	24837891	18893
	CR-5	262.9	4.73	24837891	16572
Reference (LWC) with 50% thermo-stone	CR-6	245.92	4.43	24837891	12312
Layered with 50% thermo-stone	CR-7	290.51	5.23	24837891	18246.67
	CR-8	290.83	5.23	24837891	18246.67
	CR-9	267.82	4.82	24837891	15279.33

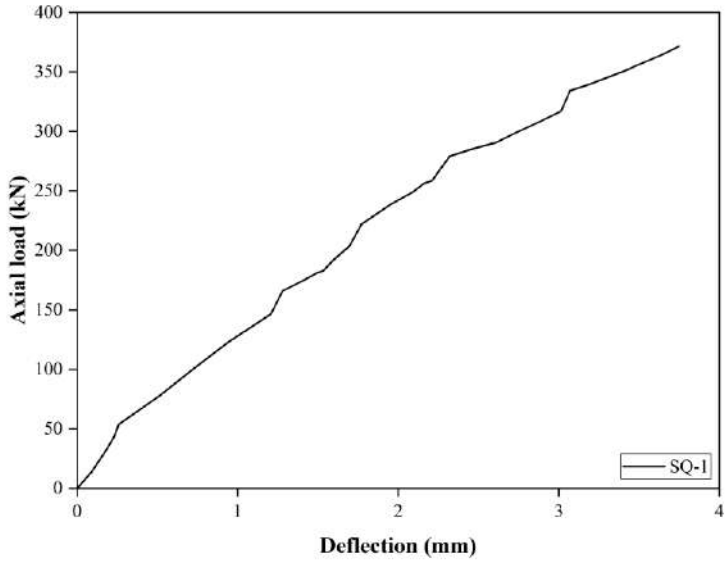

Fig. 9. Load versus deflection response for the reference square column (SQ-1)

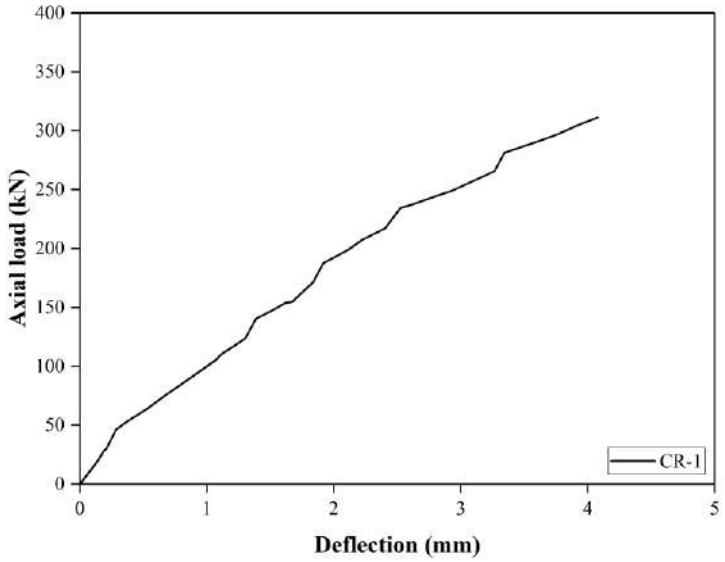

Fig. 10. Load versus deflection response for the reference circular column (CR-1)

3.2. Performance of Layered Columns: NC and LWC Configurations

The performance of layered reinforced concrete columns integrating NC and LWC was examined to determine their buckling resistance, axial load capacity, and deflection characteristics. Figs. 11 to 22 present the comparative analysis of load versus deflection behavior for square and circular column specimens with different configurations of NC and LWC. These configurations include fully NC columns, fully LWC columns with 25% and 50% replacement of thermo-stone aggregate, and layered specimens arranged in LNN, LNL, and NNL sequences.

The results indicate that fully NC columns exhibited the highest buckling resistance, as demonstrated in Figs. 10 and 11, where the NC circular column (CR-1) and NC square column (SQ-1) had significantly higher axial load capacities compared to their respective LWC counterparts (CR-2 and SQ-2). However, when LWC was used in a layered arrangement, such as the NNL configuration (CR-3 and SQ-3), an improvement in load-bearing capacity was observed compared to fully LWC columns. This suggests that placing NC in the middle and upper layers provides additional stiffness, enhancing the overall stability of the column.

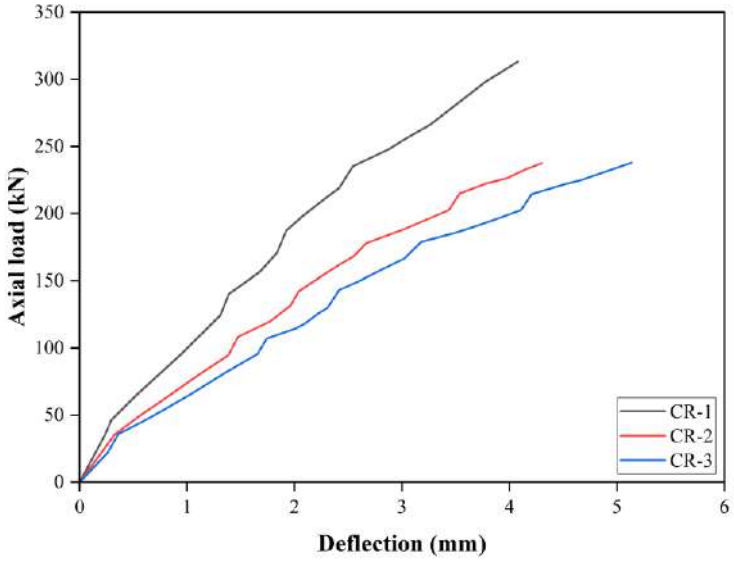

Fig. 11. Load versus deflection response between circular column NC (CR-1) and both LWC (CR-2) and layered NNL (CR-3) circular columns with 25% replacement ratio

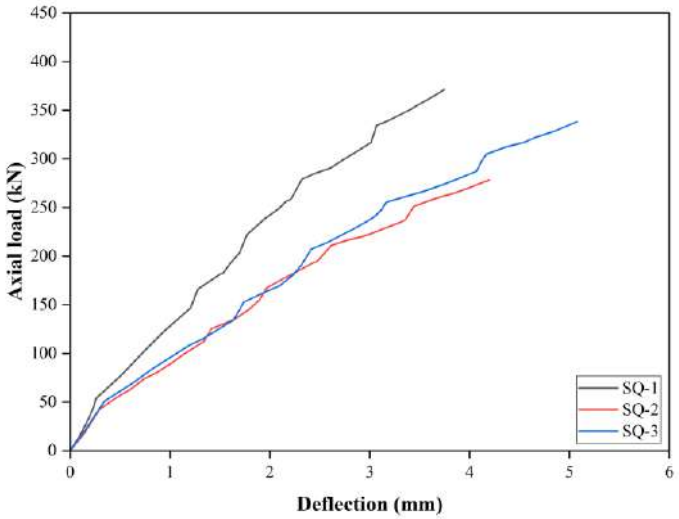

Fig. 12. Load versus deflection response between circular column NC (SQ-1) and both LWC (SQ-2) and layered NNL (SQ-3) square columns with 25% replacement ratio

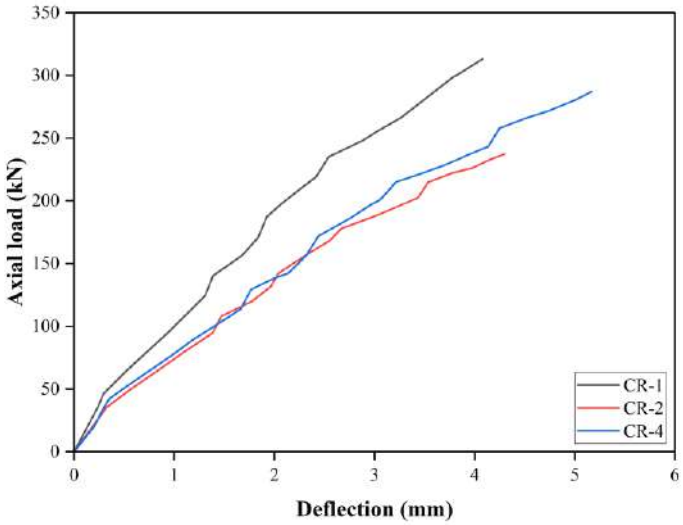

Fig. 13. Load versus deflection response between circular column NC (CR-1) and both LWC (CR-2) and layered LNN (CR-4) circular columns with 25% replacement ratio

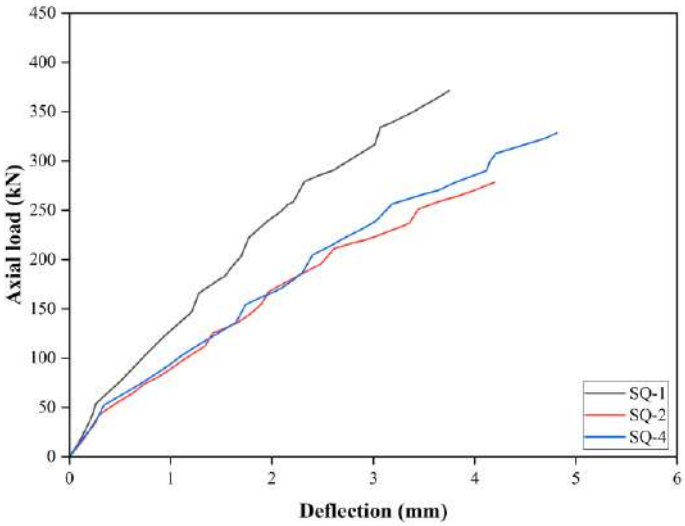

Fig. 14. Load versus deflection response between circular column NC (SQ-1) and both LWC (SQ-2) and layered LNN (SQ-4) square columns with 25% replacement ratio

Further insights into the effect of layering are shown in Figs. 12 and 13, where the LNN arrangement (CR-4 and SQ-4) is compared with fully NC and fully LWC columns. The LNN configuration, where the lower third consists of LWC, demonstrated a slight reduction in axial capacity compared to NC columns, but it significantly outperformed fully LWC columns. This trend was consistent in both circular and square columns, emphasizing the strategic advantage of maintaining NC in critical regions where maximum bending and deflection occur.

Figs. 14 and 15 illustrate the response of LNL-configured columns (CR-5 and SQ-5) in comparison to NC and LWC columns. The LNL arrangement, which incorporates LWC in both the lower and upper thirds while keeping NC in the middle, resulted in lower axial load resistance than the NNL and LNN configurations. This is attributed to the reduced stiffness in the upper and lower sections, which are essential for resisting lateral deflections under axial compression. These results suggest that the inclusion of NC in the middle layer contributes significantly to enhanced stability.

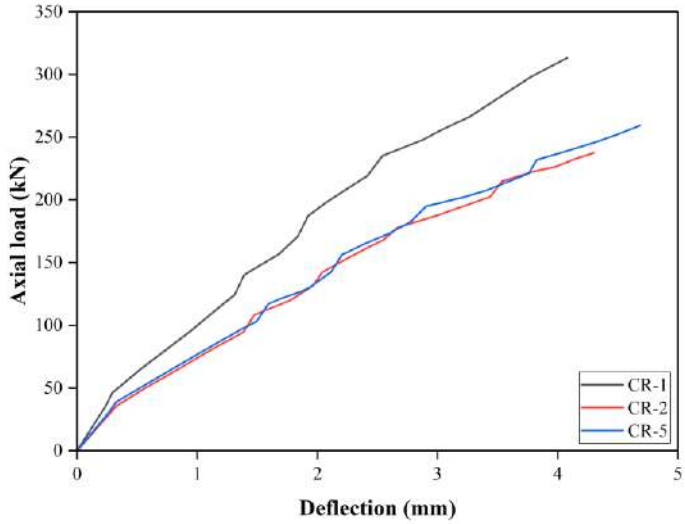

Fig. 15. Load versus deflection response between circular column NC (CR-1) and both LWC (CR-2) and layered LNL (CR-5) circular columns with 25% replacement ratio

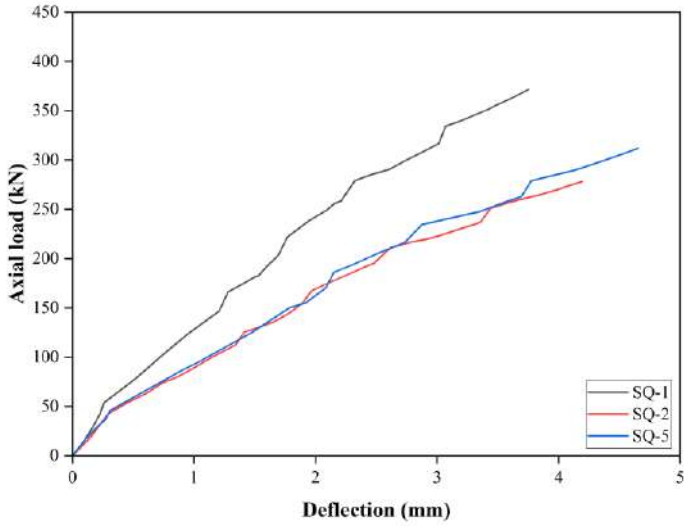

Fig. 16. Load versus deflection response between circular column NC (SQ-1) and both LWC (SQ-2) and layered LNL (SQ-5) square columns with 25% replacement ratio

A similar trend was observed for columns with 50% thermo-stone replacement, as illustrated in Figs. 16 to 21. The NC reference columns (CR-1 and SQ-1) consistently displayed superior load resistance, while the fully LWC columns with 50% replacement (CR-6 and SQ-6) exhibited reduced structural performance due to the lower stiffness of LWC. Layered specimens (CR-7, SQ-7, CR-8, SQ-8, CR-9, and SQ-9) demonstrated varying degrees of improvement over fully LWC columns, with

the NNL and LNN configurations (Figs. 16-19) showing the highest performance among layered arrangements. In contrast, the LNL configuration (Figs. 20 and 21) displayed the lowest buckling resistance among the layered specimens, reinforcing the observation that LWC placement in both upper and lower thirds compromise overall stability.

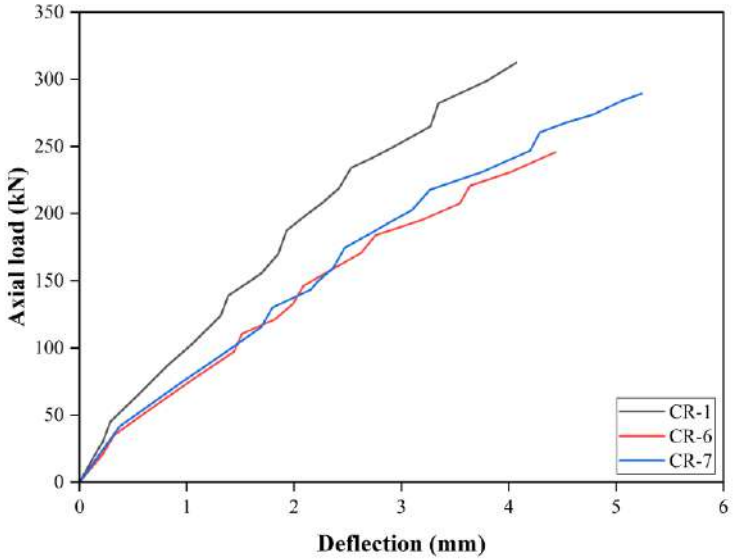

Fig. 17. Load versus deflection response between circular column NC (CR-1) and both LWC (CR-6) and layered NNL (CR-7) circular columns with 50% replacement ratio

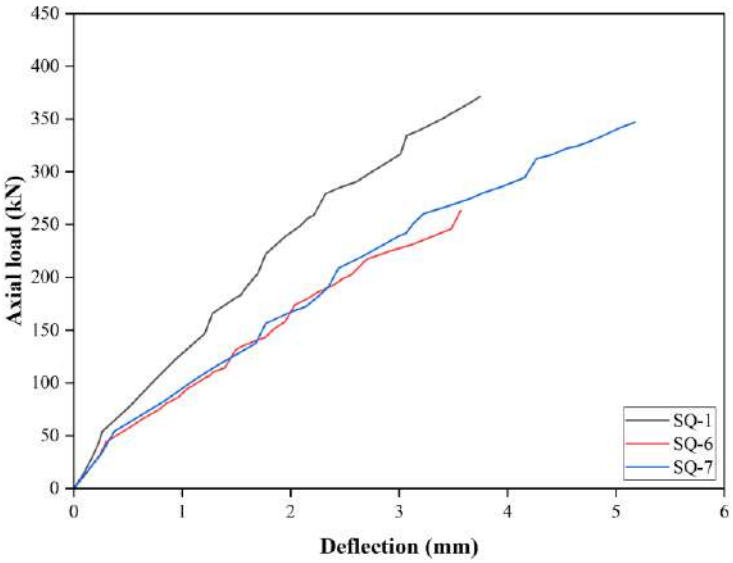

Fig. 18. Load versus deflection response between circular column NC (SQ-1) and both LWC (SQ-6) and layered NNL (SQ-7) square columns with 50% replacement ratio

The observed failure modes and structural behavior of the tested columns suggest that the internal interaction between different concrete layers plays a critical role in the buckling performance. In particular, the interface between NC and LWC in layered configurations influenced the stress distribution and deformation shape during loading. Columns with NC placed in the middle or upper segments (NNL and LNN) showed delayed initiation of lateral deflection, indicating that the stiffer NC core resisted deformation more effectively, while the adjacent LWC layers allowed for controlled flexibility. This synergy contributed to improved stability and higher buckling loads. Conversely, in LNL configurations, where LWC was used in both end regions, early buckling initiation was observed due to insufficient stiffness at the zones most susceptible to compression and tension during buckling. Furthermore, the difference in stiffness and density between NC and LWC caused differential strain behavior across the column height, which influenced the mode and location of failure. Square columns exhibited more uniform crack patterns, while circular ones

showed localized buckling near the mid-height. These outcomes confirm that the interaction of layer configuration, material stiffness, and column geometry collectively govern the buckling response and failure mechanisms.

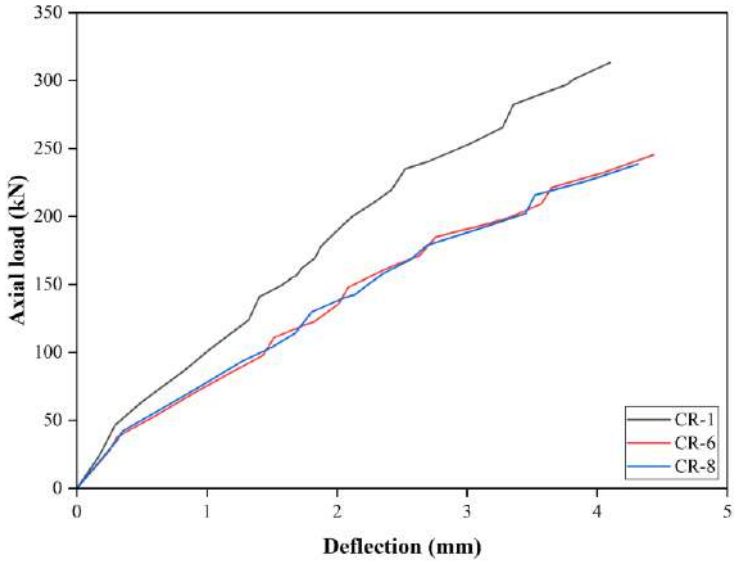

Fig. 19. Load versus deflection response between circular column NC (CR-1) and both LWC (CR-6) and layered LNN (CR-8) circular columns with 50% replacement ratio

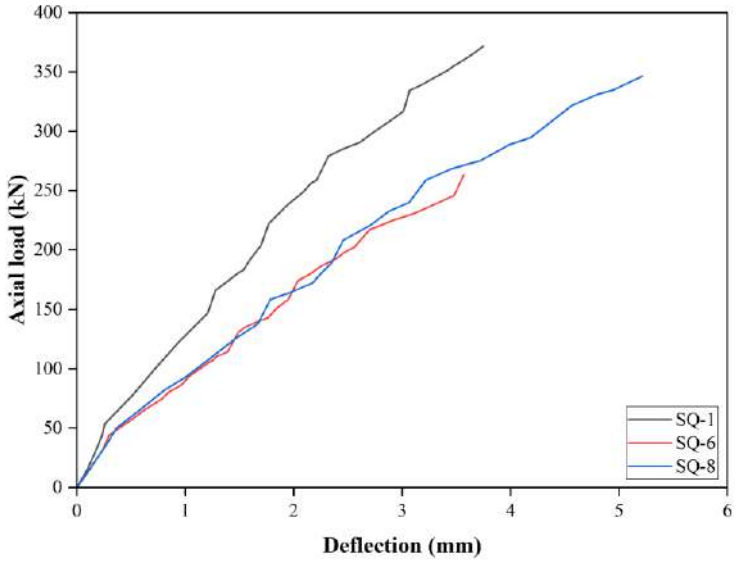

Fig. 20. Load versus deflection response between circular column NC (SQ-1) and both LWC (SQ-6) and layered LNN (SQ-8) square columns with 50% replacement ratio

According to the experimental findings, the NNL and LNN configurations demonstrated better buckling resistance than the LNL configuration. The performance benefit comes from the placement of NC in between the middle and upper sections of the part, which lends it increased stiffness and limits deflection. At all of these tested shapes, square columns showed a superior buckling resistance than circular columns. This was attributed to a higher moment of inertia leading to better stiffness response and less deflection with the same axial loading conditions. Thus, layered concrete configurations incorporating NC in critical regions can enhance stability, while square columns provide improved structural performance.

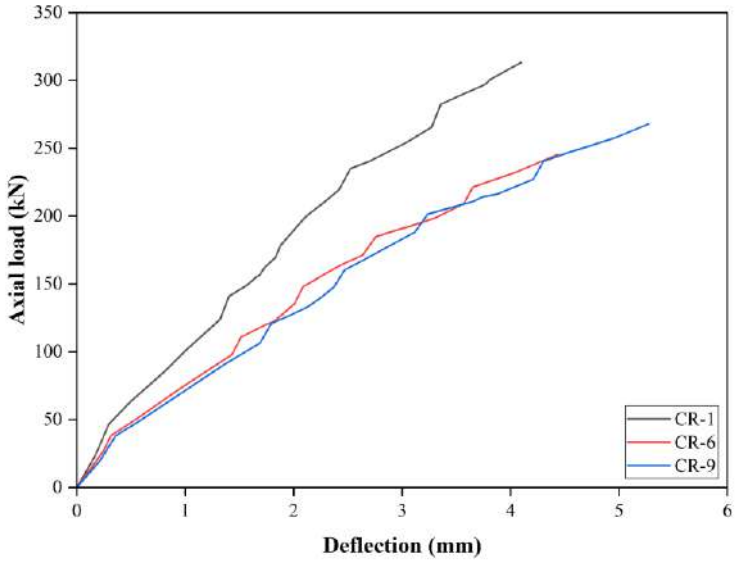

Fig. 21. Load versus deflection response between circular column NC (CR-1) and both LWC (CR-6) and layered LNL (CR-9) circular columns with 50% replacement ratio

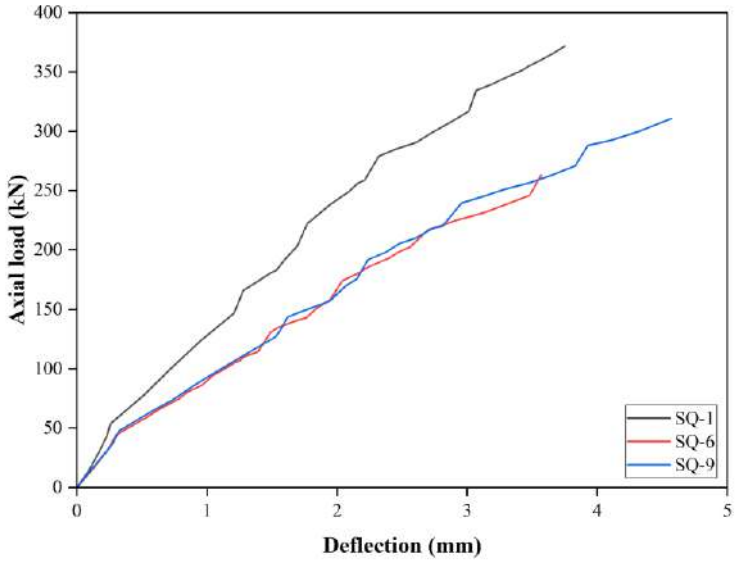

Fig. 22. Load versus deflection response between circular column NC (SQ-1) and both LWC (SQ-6) and layered LNL (SQ-9) square columns with 50% replacement ratio

The enhanced performance of the NNL and LNN configurations can be explained by the strategic placement of high-stiffness NC in the middle and/or upper zones of the columns—regions experiencing maximum compressive stress during buckling. This layered design limited lateral deflections and postponed instability onset, yielding axial load capacities up to 21% higher than fully LWC counterparts. These findings are consistent with prior studies on partial interaction and composite systems [9, 13], where stiffness contrast and bonding effectiveness between layers played a key role in structural response. Similarly, the findings align with [22], who showed that transverse reinforcement improves ductility in LWC columns; however, our results suggest that layer configuration alone can offer notable improvements even without additional confinement. Additionally, square columns exhibited higher buckling resistance than circular ones, attributed to their larger moment of inertia, aligning with classical Euler buckling theory. However, the inclusion of LWC in both top and bottom layers (LNL configuration) reduced performance, highlighting the necessity of maintaining stiffer material in tension and compression zones for buckling-critical elements.

4. Conclusions

This experimental investigation evaluated the buckling resistance of layered reinforced concrete (RC) columns constructed with combinations of normal concrete (NC) and lightweight concrete (LWC) incorporating thermo-stone aggregate. A total of 18 square and circular RC columns were tested under axial loads to assess the influence of shape, concrete layering sequence, and aggregate replacement ratio on structural behavior.

The results clearly indicate that the configuration and material composition of the layers have a significant effect on the buckling performance of RC columns. Among the various configurations, the NNL and LNN layered arrangements demonstrated the highest buckling resistance. These configurations strategically positioned the higher-stiffness NC in the middle and/or upper portions of the column, regions most vulnerable to high compressive stress and deflection. As a result, these designs enhanced overall column stability, delayed the onset of lateral buckling, and increased the ultimate axial load capacity. Notably, square NNL columns with 25% thermo-stone replacement attained axial loads up to 21.6% higher than their fully LWC counterparts, which confirms the mechanical advantage of layering concrete with appropriate stiffness profiles.

Furthermore, square columns consistently outperformed circular ones across all configurations, a trend attributed to their greater moment of inertia, which results in higher stiffness and lower lateral deflection. The study also revealed that a 25% replacement of natural aggregate with thermo-stone in LWC offered a good compromise between weight reduction and strength, while the 50% replacement ratio led to reduced performance due to lower stiffness and greater deflection.

In summary, the study confirms that layering RC columns with NC in critical regions can effectively enhance structural performance and buckling resistance without significantly increasing the overall weight. This makes such designs highly suitable for mid- and high-rise structures. Future research should explore the effects of interlayer bond quality, fatigue behavior, temperature cycling, and seismic response to further validate the practical application of layered concrete columns.

Acknowledgement

The authors extend their gratitude to the Civil Engineering Department Laboratory at the College of Engineering, Tikrit University, for its support and approval in conducting and testing the RC column specimens.

References

[1] Hasan AT, Mashrei MA, Makki JS. Behavior of Circular Reinforced Concrete Columns Strengthened by Different Techniques Subjected to Axial Loading. Civil And Environmental Engineering. 2024;20(1):319-31. https://doi.org/10.2478/cee-2024-0025

[2] Ali NK, Salahaldin AI, Hamza AJ. Impact Analysis of Reinforced Concrete Columns with Side Openings Subjected to Eccentric Axial Loads. Journal of Engineering. 2015;21(02):1-19. https://doi.org/10.31026/j.eng.2015.02.01

[3] Olivova K, Bilcik J. Strengthening of concrete columns with CFRP. Slovak Journal of Civil Engineering. 2009;1:1-9.

[4] Qader DN, Merie HD, Abdulhaleem KN. Impact of Incorporating Plastic Fibers, Walnut Shells, and Tire Rubber Fibers on the Mechanical Properties of Concrete. Electronic Journal of Structural Engineering. 2025;25(1):19-24. https://doi.org/10.56748/ejse.24738

[5] Bai Y-L, Dai J-G, Teng J, editors. Experimental study on the buckling behavior of reinforcing bars in FRP-confined RC columns. Proc, 15th World Conf on Earthquake Engineering; 2012.

[6] Yue C, Isleem HF, Qader DN, Mahmoudian A, Weiming T, JANGIR P, et al., editors. Utilization finite element and machine learning methods to investigation the axial compressive behavior of elliptical FRP-confined concrete columns. Structures; 2024: Elsevier. https://doi.org/10.1016/j.istruc.2024.107681

[7] Kryžanowski A, Schnabl S, Turk G, Planinc I. Exact slip-buckling analysis of two-layer composite columns. International Journal of Solids and Structures. 2009;46(14-15):2929-38. https://doi.org/10.1016/j.ijsolstr.2009.03.020

[8] Wang Y, Elmeligy MA, Isleem HF, Hamed AY, Qader DN, Sharaf M, et al. Modeling of concrete-filled PVC tube columns confined with CFRP strips under uniaxial eccentric compression: machine learning and

finite element approaches. Journal of Big Data. 2025;12(1):34. https://doi.org/10.1186/s40537-024-01058-6
[9] Atashipour SR, Challamel N, Girhammar UA. On buckling of layered composite heavy columns-Effect of interlayer bonding imperfection. International Journal of Solids and Structures. 2023;260:112030. https://doi.org/10.1016/j.ijsolstr.2022.112030
[10] Rzhanitsyn A, Davydova E. The stability of a composite bar under the action of a longitudinal force varying along the length. Soviet Applied Mechanics. 1968;4(1):46-9. https://doi.org/10.1007/BF00920324
[11] Hosseini M, Jian B, Li H, Yang D, Wang Z, Feng Z, et al. A Review of Fibre Reinforced Polymer (FRP) reinforced concrete composite column members modelling and analysis techniques. Journal of Renewable Materials. 2022;10(12):3243-62. https://doi.org/10.32604/jrm.2022.022171
[12] Ranzi G, Bradford M, Uy B. A general method of analysis of composite beams with partial interaction. Steel and composite structures. 2003;3(3):169-84. https://doi.org/10.12989/scs.2003.3.3.169
[13] Čas B, Saje M, Planinc I. Buckling of layered wood columns. Advances in Engineering Software. 2007;38(8-9):586-97. https://doi.org/10.1016/j.advengsoft.2006.08.021
[14] Ayoub A. A force-based model for composite steel-concrete beams with partial interaction. Journal of Constructional Steel Research. 2005;61(3):387-414. https://doi.org/10.1016/j.jcsr.2004.08.004
[15] Gara F, Ranzi G, Leoni G. Displacement-based formulations for composite beams with longitudinal slip and vertical uplift. International journal for numerical methods in engineering. 2006;65(8):1197-220. https://doi.org/10.1002/nme.1484
[16] Dall'Asta A, Zona A. Comparison and validation of displacement and mixed elements for the non-linear analysis of continuous composite beams. Computers & structures. 2004;82(23-26):2117-30. https://doi.org/10.1016/j.compstruc.2004.04.009
[17] Schnabl S, Saje M, Turk G, Planinc I. Analytical solution of two-layer beam taking into account interlayer slip and shear deformation. Journal of structural engineering. 2007;133(6):886-94. https://doi.org/10.1061/(ASCE)0733-9445(2007)133:6(886)
[18] Schnabl S, Saje M, Turk G, Planinc I. Locking-free two-layer Timoshenko beam element with interlayer slip. Finite Elements in Analysis and Design. 2007;43(9):705-14. https://doi.org/10.1016/j.finel.2007.03.002
[19] Leon RT, Viest IM, editors. Theories of incomplete interaction in composite beams. Composite construction in steel and concrete III; 1996: ASCE.
[20] Wang J, Hu P, Liu Y, Qian Z, Hu C, Zhang H. Axial compressive behavior of the PEC slender columns with lightweight aggregate concrete. Journal of Constructional Steel Research. 2023;211:108206. https://doi.org/10.1016/j.jcsr.2023.108206
[21] Jung Y-B, Mun J-H, Yang K-H, Im C-R. Seismic performance of lightweight aggregate concrete columns subjected to different axial loads. Structural Engineering and Mechanics, An Int'l Journal. 2023;88(2):169-78.
[22] Wu T, Wei H, Zhang Y, Liu X. Axial compressive behavior of lightweight aggregate concrete columns confined with transverse steel reinforcement. Advances in Mechanical Engineering. 2018;10(3):1687814018766632. https://doi.org/10.1177/1687814018766632
[23] Sasikumar P. A comparative study between buckling behaviour and statistical analysis of axially loaded fully encased composite columns made with high strength concrete. Revista de la construcción. 2023;22(3):694-706. https://doi.org/10.7764/RDLC.22.3.694
[24] IQS(No.5). Characteristics of Ordinary Portland Cement. 1984.
[25] IQS(No.45). Iraqi Specifications for Aggregates of Natural Resources used for Concrete and Construction. 1984.
[26] ASTM-C127. Standard Test Method for Relative Density (Specific Gravity) and Absorption of Coarse Aggregate. 2015.
[27] ASTM-C29/C29M. Standard Test Method for Bulk Density ("Unit Weight") and Voids in Aggregate. 2023.

Blank Page

Research on Engineering Structures & Materials
www.jresm.org
Research Group

Research Article

Prediction and performance enhancement of R600a refrigerator adopting machine learning algorithms

A. Senthilkumar *,a

Department of Mechanical Engineering, Saveetha Engineering College, Thandalam, Chennai-602 105, Tamil Nadu, India

Article Info

Article History:

Received 26 Feb 2025

Accepted 17 June 2025

Keywords:

Refrigeration;
Hybrid nano lubricants;
Machine learning;
Prediction

Abstract

Enhancing the energy efficiency of domestic refrigeration systems is vital due to their significant role in global electricity consumption. The low environmental impact of R600a makes it stand out among eco-friendly refrigerants. Recent developments in hybrid nanomaterials and nano lubricants potential to enhance system performance. The machine learning (ML) algorithms are emerging as effective tools for accurate, data-driven predictions in complex thermodynamic systems. The present research employs machine learning techniques to estimate the performance of a vapor compression refrigeration system based on the R600a and enhanced with CuO/SiO_2 hybrid nano lubricants. Experimental data were collected under various operating conditions, including different nano lubricant concentrations (0–0.6 g/L) and refrigerant mass charges (50–70 g). Three ML models—Linear Regression, Artificial Neural Network (ANN), and Support Vector Machine (SVM) were developed. The dataset was partitioned into 70% training, 15% validation and 15% testing sets. Models were evaluated using performance metrics such as Root Mean Square Error (RMSE), Mean Absolute Error (MAE), Mean Squared Error (MSE) and the coefficient of determination (R^2). The Quadratic SVM model demonstrated the highest prediction accuracy with an R^2 of 0.970196 and a low MAE of 0.055486, outperforming both ANN and Linear Regression models. The study confirms that integrating hybrid nano lubricants with intelligent ML models significantly enhances the Coefficient of Performance (COP) prediction capability and provides a reliable approach for optimizing energy efficiency in refrigeration systems.

© 2025 MIM Research Group. All rights reserved.

1. Introduction

Energy conservation is essential in vapor compression refrigeration systems, especially with their extensive use in commercial, residential, and industrial applications. Improving energy efficiency leads to better cooling performance, enhanced system operation and lower energy consumption. The refrigeration sector is responsible for 20% of global energy consumption [1] with traditional refrigeration systems consuming more energy. HCFC and HFC systems, known for their higher global warming potential and energy demands are being replaced by HC refrigerants that consume less energy and have a smaller global warming impact. The energy conservation problems identified in conventional systems are clarified by the subsequent studies which contributes for a energy efficient system. The study involved dispersing SiO_2 nanoparticles in four refrigerants, with the R1234ze/SiO_2 mixture resulting in a 59.58 kW reduction in energy consumption and a significant increase in COP [2]. Incorporating TiO_2 at a 0.1% mass fraction into the HFC134a/POE system resulted in the lowest recorded energy consumption, reducing it by 26.1% [3]. POE oil mixed with CuO and MWCNTs at volume ratios of 0.5%, 1% and 2% was theoretically analyzed with R152a and R134a refrigerants. The R152a nano refrigerant containing MWCNTs

*Corresponding author: senthilmahathi@gmail.com
[a]orcid.org/0000-0001-9662-670X
DOI: http://dx.doi.org/10.17515/resm2025-710ml0226rs

demonstrated a COP enhancement of 27.63% over standard R152a [4]. Compared to R290+1234yf, the R290+R600 nano refrigerant achieved the highest COP increase of 15.41% when CuO nanoparticles were used, with the evaporator temperature maintained at -5°C [5]. According to past research, adding various nano refrigerants to a vapor compression refrigeration system can improve thermal conductivity. However, if nanoparticle concentration is too high, it may increase viscosity, causing greater compressor work and a decrease in COP. Additionally, challenges like agglomeration and stability of nanoparticles may impact the system's long-term performance, potentially reducing refrigerator efficiency. No notable increase in COP or refrigeration effect is observed with reduced compressor energy consumption [6]. The incorporation of nanoparticles into traditional refrigeration lubricants to create nano lubricants has proven to be an effective strategy for enhancing the performance and energy efficiency of Vapor Compression Refrigeration (VCR) systems.

This advancement not only improves lubrication but also leads to lower energy consumption and a longer lifespan for essential system components [7].The nano lubricant prepared by dispersing graphene at 0.2 g/L concentration resulted in a peak COP of 3.2.The system's efficiency improved due to lower power consumption and higher cooling capacity [8].It is evident that replacing conventional POE oil with TiO_2-based nano lubricant boosts the refrigerating effect, lowers compressor power consumption by 27%, and increases system COP by about 29%.[9].Integrating graphene nano lubricant with R600a led to a higher COP, as it improved cooling capacity by 5.2% to 14.2% and decreased energy usage by 8.8% to 26.4% [10].

When 50 g of R600a was blended through 0.4 g/L of multi-walled CNTs nano lubricant, energy consumption dropped between 25.9% and 13.7% for R600a quantities ranging from 50 g to 70 g, in contrast to a system with clean lubricant. Moreover, the COP of the MWCNT system improved from 2.1 to 2.9 compared to a conventional refrigerator [11]. The use of TiO_2 in an R600a refrigerator yielded the highest COP of 2.8, whereas the R134a system reached a maximum of 1.9. Additional experiments with Al_2O_3 and SiO_2 produced COP values of 2.4 and 2.7, respectively. Among all variations, the TiO_2-enhanced system exhibited the lowest energy consumption, cutting it by 23.3% compared to other combinations and the R134a system [12]. The combination of 0.2 g/L of graphene and 50 g of LPG resulted in the highest COP of 3.4. It also reduced compressor power consumption to 82.1 kJ/kg and enhanced the cooling effect by 279.1 kJ/kg, outperforming other nano lubricant mixtures and refrigerants [13]. Using nano lubricants with 0.5% diamond nanoparticles enhanced the R32 refrigerator cooling capability by 2.4%. In addition, nano lubricants with 0.1% and 0.5% diamond mass fractions produced the highest COP elevation of 2.6% and 3.2% [14].A COP of 2.76 and a 27.36% decrease in power usage were noted when 200 g of R134 refrigerant was combined with 500 ppm of amine-treated graphene quantum dots in a polyalkylene glycol-based nanosuspension [15].The coefficient of performance in the R134a refrigerator improved by 28.4% through the use of a polyol ester oil-based nano lubricant containing 0.1 vol% multiwalled carbon nanotubes. [16]. A 4% rise in COP was observed for the 0.1% diamond mass concentration, and an 8% increase was noted when using 0.5% [17].The system's energy consumption was lowest at 62.80 W when using 60g of R600a refrigerant with 0.2 g/L of TiO2, while the highest COP value of 4.20 was achieved with the same 60g R600a charge and 0.2 g/L concentration of nano lubricant [18].

In ice cream production unit ammonia cascade system was used and the COP value resulted by this system was lower than single stage ammonia system [19]. Machine learning models can estimate COP, power consumption, refrigerant flow rate and cooling capacity under various operating conditions. By replacing intricate thermodynamic equations, these models enable real-time optimization with minimal computational effort. The R290 refrigerant performed better by attaining a 23.77% higher COP, but the R600a refrigerant reduced compressor power utilization by an average of 33.44%. Additionally, R290 provided an 82.55% increase in cooling capacity and an increase in second-law efficiency of 20.99% over R600a. SVM method resulted in highest accuracy by predicting all parameters with the least error. It outperformed other machine learning techniques in forecasting performance indicators, making it the most effective prediction model [20]. CPSO-TSA model resulted in 84.4% accuracy during training and achieved strong

performance with a low MAE of 0.16. It further exhibited reliable results with an RMSE of 0.39 and a kappa statistic of 0.69 [21].

A data-driven approach that harnesses modern deep learning methods to construct component models while upholding physical conservation constraints in system simulations are explored. [22]. The control parameters using PI and PID leads to enhance the energy efficiency ratio (EER) in refrigeration systems. EER increased by 21% to 32% with the PI and PID models, and by 28% with the factory-set PI control. [23]. The evaluation of the SLFN model is conducted on actual experimental data and compared with models trained with radial basis function neural networks (RBF), support vector regression (SVR), and back propagation (BP). The findings indicate that in regard to prediction accuracy and durability to input errors, the SLFN model performs best [24]. The latest theories and applications of computational intelligence (CI) techniques in the optimization of refrigeration systems are explored. Genetic algorithms (GA) and their variations are particularly prevalent, especially in multi-objective optimization and the use of CI methods in refrigeration system optimization has significantly increased [25]. In industrial vapor compression refrigeration systems, a new technique for identifying refrigerant leaks has been presented. Two feature sets are used to assess the performance of several regression models in order to identify the most successful one, utilizing certain metrics and a model comparison technique [26]. The ANN model estimated the mass flow rate with an average error of 0.79% when trained using both steady-state and transient datasets. Only steady-state data were used to train the model, which led to a little greater inaccuracy of 0.81%. It was found that the average prediction error of the embedded system was 1.22% [27].

The ANN model developed to estimate performance indicators such as power consumption, refrigeration effect and COP utilizes feedback-backpropagation and the Levenberg-Marquardt training algorithm. With an R^2 value of 0.989, the model showed a strong correlation with a multiple regression model, highlighting that ANN provides a more accurate method than MRA for predicting the performance of home refrigeration systems [28].

In smaller refrigeration system the ANN model has been applied. With a power consumption error of 0.05 and negligible relative errors for cooling capacity and coefficient of performance, the models were evaluated using cross-validation. The results revealed that R450A consumed approximately 10% less electricity compared to R134a and R513A [29].

The application of machine learning (ML) in vapor compression refrigeration systems has introduced advanced methods for performance prediction and optimization. By processing real-time data, ML models can predict significant parameters including COP, energy usage and cooling efficiency under dynamic operating conditions. Adding CuO/SiO_2 hybrid nano lubricants to an R600a refrigeration system improves the system's thermal properties. The optimized nano lubricants combination facilitates higher COP and reduced energy consumption. Applying and comparing multiple ML models (SVM, ANN, Linear Regression) under real experimental conditions. A novel finding is the superiority of Quadratic SVM, which achieved the lowest Mean Absolute Error and highest R^2 among all models.

2. Experimental Setup and Methodology

The system comprises a compressor, an expansion valve, an evaporator and a condenser. The actual setup of the R600a refrigeration system used for the experiment is shown in [Fig. 1]. Hermetic compressor capacity of 100 W compatible with R600a and air-cooled finned type condenser are employed in this test rig. In 50 L evaporator copper pipes are wounded as coil and kept in stainless steel tank insulated with polyurethane foam. Capillary tubes of diameters ranging from 0.50 to 0.80 mm and length 0.6 to 0.9 m are used as expansion devices. Dial type two pressure gauges are used one is for suction and another for discharge ranges from 0 to 250 Kg/cm^2. Over load and over current protectors are fixed for safety control in compressors. RTD PT100 type digital temperature sensors are used. The panel comprises of voltmeter, ammeter and wattmeter. It is also provided with drier and shut off valve. A single phase 220V- AC power supply is used for operation.

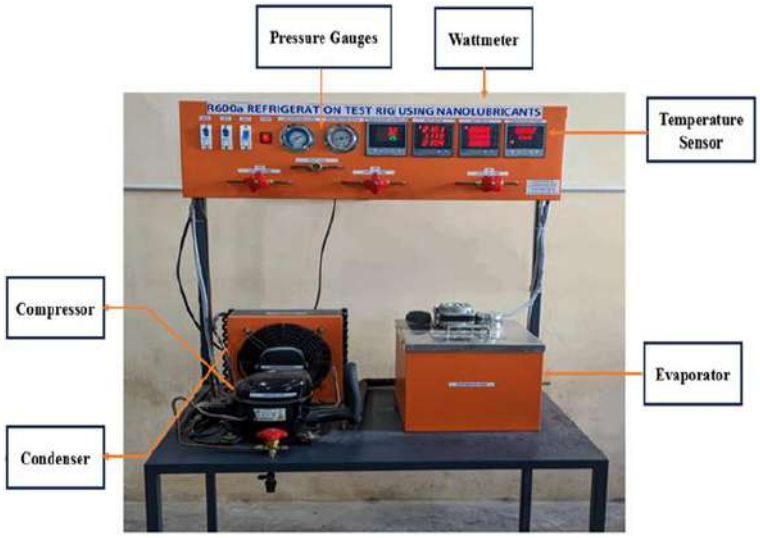

Fig. 1. Experimental setup

The experimental setup, data collection, feature engineering, model training, assessment and comparison of machine learning techniques are discussed in this section. Hybrid nano lubricants consisting of CuO and SiO_2 nanoparticles were prepared in specific concentrations (0–0.6 g/L) and mixed with standard lubricant. Experiments were conducted under controlled ambient temperatures (29–35 °C) with varied refrigerant mass charges (50–70 g). During each test enthalpy values at key points (compressor inlet/outlet, evaporator inlet/outlet) were recorded. The subsequent equations were used to assess the refrigerator's performance. To estimate the cooling capacity of the R600a refrigerator,

$$Qevap = \dot{m}(h4 - h1) \quad (1)$$

Where, Qevap— Cooling capacity of evaporator, expressed in kW; ṁ — R600a mass flow rate, in kg/s

h1— Compressor inlet enthalpy value; h4— Evaporator outlet enthalpy value; The compressor's energy consumption is indicated by;

$$WC = \dot{m}(h_2 - h_1) \quad (2)$$

Where, Wc-Input power of the compressor in kW; ṁ-R600a mass flow rate, in kg/s; h_1- Compressor inlet enthalpy value; h_2-Compressor outlet enthalpy value. The R600a COP is estimated by;

$$COP = \frac{Q_{evap}}{wc} \quad (3)$$

Equation (1) is used to determine the initial cooling capacity of the refrigerator, as well as the refrigerant mass flow rate and enthalpy values at the compressor inlet and evaporator outlet. The compressor work is then derived using experimental enthalpy data at the compressor inlet and outlet, in combination with the refrigerant mass flow rate. Finally, Eqs. (2) and (3) are employed to calculate the COP.

2.1 Nanoparticle Dispersion Method

The hybrid nano lubricants (CuO/SiO_2) were prepared by dispersing the required mass of each nanoparticle into a base mineral oil using an ultrasonic bath (40 kHz, 100 W) for 60 minutes to ensure uniform distribution and prevent agglomeration. A small amount of surfactant (Span-80, 0.05% by volume) was added to improve colloidal stability without affecting thermophysical properties.

2.2 Concentration Measurement and Stability

The concentration of nanolubricants (0.0 to 0.6 g/L) was controlled by accurately weighing the nanoparticles using an analytical balance with 0.0001 g precision and dissolving them into 100 mL of lubricant. Stability was verified by visual observation over a 48-hour period and by using a UV-Vis spectrophotometer, ensuring minimal sedimentation prior to use in the refrigeration system. No additional filtration was performed to preserve the experimental nature of the real-world application.

2.3 Ambient Temperature Control:

Experiments were conducted in a thermally insulated room where ambient temperature was maintained between 29°C and 35°C using digital thermostats and ceiling insulation. Temperature variations were continuously monitored using calibrated RTD PT100 sensors. All measurements were logged to confirm that fluctuations remained within ±1°C during each test cycle.

2.4 Data Collection

2.4.1 Number of Trials

For each test configuration (defined by a unique combination of refrigerant mass charge and nano lubricant concentration), the experiment was repeated three times to ensure consistency and statistical reliability. The reported values represent the mean of these three trials, and deviations were found to be within an acceptable range of ±2%.

2.4.2 Time Intervals for Measurements

All measurements were recorded at one-minute intervals using a digital data logging system. The following parameters were logged continuously:

- Evaporator and condenser temperatures
- Compressor power consumption
- Suction and discharge pressures
- Ambient temperature

This high-frequency data acquisition ensured accurate tracking of transient and steady-state behavior.

2.4.3 Criteria for Steady-State Conditions

Steady-state was defined as the point at which:

- Temperature readings at the evaporator outlet and condenser outlet varied by less than ±0.2°C over a 10-minute period.
- Compressor power draw remained within ±3 W variation during the same window.
- No cycling or sharp fluctuations were observed in system pressure. Data were only considered valid for analysis and model training if collected during these steady-state conditions. Transient start-up and shutdown data were excluded to ensure the integrity of the input features and output variables used in the machine learning models.

The dataset was randomly partitioned into three subsets: 70% for training, 15% for validation and 15% for testing, ensuring that each subset represented the variability in the data and supported robust model development and evaluation. The split was performed using a stratified random sampling method to ensure that each subset represents the variability in nano lubricant concentrations and refrigerant mass charges. In this study, Linear Regression, Artificial Neural Networks (ANN) and Support Vector Machines (SVM) were employed as machine learning models, each chosen for their distinct advantages in predictive modeling of thermodynamic system performance. All machine learning models underwent hyperparameter tuning using a grid search approach, with validation conducted on a dedicated validation set to ensure effective parameter selection and reduce the possibility of overfitting. Model performance was rigorously evaluated using standard regression metrics, namely Root Mean Square Error (RMSE), Mean Absolute Error (MAE), Mean Squared Error (MSE) and the Coefficient of Determination (R^2). These evaluation

criteria facilitated a detailed assessment of each model's prediction accuracy, consistency and generalization capability.

3. Machine Learning Methods

Machine learning is a branch of artificial intelligence that leverages mathematical models to facilitate classification, regression, decision-making, and predictive analysis. Support Vector Machines were developed a predictive model for energy consumption, achieving high accuracy with minimal computational effort [30].Artificial Neural Networks were applied to predict system efficiency, showing that ANN-based models outperformed conventional regression techniques [31].Random forest model produced outstanding results and provided significant results for diagnosing diabetes and prediction of risk [32].Random Forest model implemented to estimate refrigeration system efficiency based on operational data. Their study indicated that RF-based models could capture nonlinear patterns more effectively than traditional thermodynamic equations [33]. The machine learning structure for predicting performance is illustrated in [Fig.2].

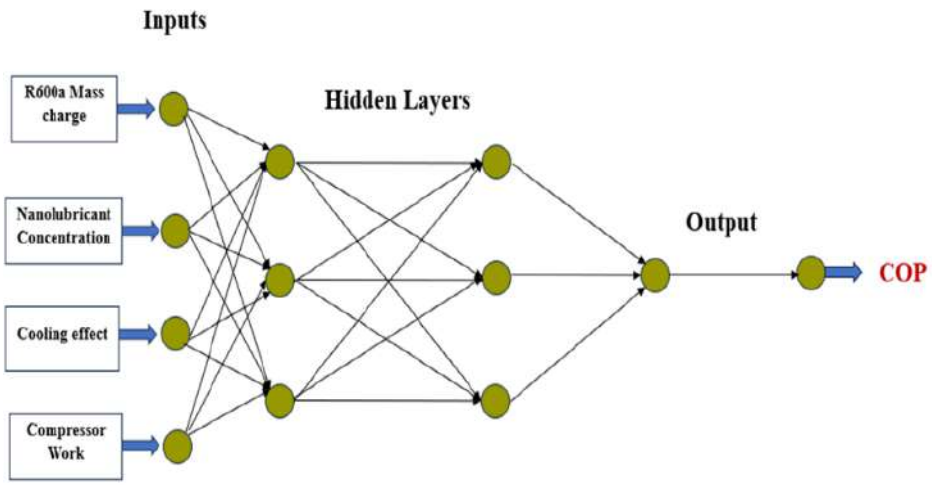

Fig. 2. COP Prediction machine learning structure

3.1 Regression Model

To predict interconnection between dependent and independent factors applied in linear equations are performed by supervised learning algorithm are included for linear regression. Target outputs are determined by error term and weighted inputs and reduce the difference between actual and predicted outputs. For attaining higher performance in on-site refrigeration system artificial neural network model is applied which resulted in higher level of accuracy [34]. Linear Regression, implemented as a robust linear model was utilized to establish a direct linear relationship between the input parameters and the Coefficient of Performance (COP). To enhance model generalization and reduce the risk of overfitting, appropriate regularization techniques were applied during training.

ANN model is applied to predict the performance of a water-cooled screw chiller, demonstrating its effectiveness [35]. From the past studies, it can be observed that linear regression is a basic method that can be applied for more complex models having the capability to focus on non-linear relationship inherent in refrigeration system performance data.

3.2 Tree Model

To predict the continuous outputs by periodically splitting data into decision nodes, are performed by tree-based regression models. Decision tree and random forest regression applied effectively in complex and non-linear data. For estimation of performance, it reduces the error on every split which results in optimal condition. In engineering application tree regression models are applied which includes prediction of refrigerator performance. Tree-based models hold potential for

performance prediction in vapor compression systems, though further research is needed to establish their efficacy in this specific application [36].

3.3 SVM Technique

One of the powerful techniques used for performance prediction in refrigeration systems that identifies complex relationship between input variables and system efficiency. For transforming nonlinear data into higher-dimensional space and for accurate modelling of thermodynamic and operational outputs this method adopts kernel functions. Support Vector Machine (SVM), configured with a quadratic polynomial kernel was employed due to its effectiveness in capturing non-linear relationships between the input features and the target variable. Key hyperparameters such as the kernel type, penalty parameter (C) and gamma were systematically tuned to optimize the model's predictive performance.

Compared to conventional regression techniques, SVM is extremely effective at managing multidimensional data, lowering overfitting using regularization, and increasing prediction accuracy. Energy efficiency, defect detection, and system reliability are all improved by its implementation in refrigeration performance prediction. The SVM model, based on dynamic experimental data, predicted refrigerant charge levels by focusing on power consumption and condensation temperature [37].

3.4 Neural Network

Artificial Neural Networks are computational models that mimic the human brain by using interconnected neurons to process data and recognize patterns. These models excel at capturing complex, non-linear relationships, making them ideal for predictive tasks in engineering and refrigeration system performance analysis. ANNs learn by adjusting connection weights through backpropagation and gradient descent, minimizing errors to improve prediction accuracy. The Artificial Neural Network (ANN) model employed a narrow architecture consisting of an input layer, a single hidden layer and an output layer. Training was conducted using the Levenberg-Marquardt backpropagation algorithm, with key hyperparameters—including the number of neurons in the hidden layer, learning rate, and number of epochs—systematically tuned to enhance predictive accuracy and convergence efficiency.

Table 1. Machine learning hyper-parameters

Model	Hyperparameters
Support Vector Machine (SVM) – Quadratic Kernel	Kernel: Polynomial ('poly') Degree: 2 C (Regularization parameter): 1.0 Gamma: 'scale' Epsilon (ε): 0.1
Artificial Neural Network (ANN) – Narrow Neural Network	Architecture: Input layer: 4 neurons, Hidden layer: 10 neurons, Output layer: 1 neuron Activation Function: 'tansig' Learning Algorithm: Levenberg-Marquardt backpropagation Learning Rate: 0.01 (adaptive) Epochs: 500 Loss Function: Mean Squared Error (MSE)
Linear Regression (Robust Linear Model)	Fit Intercept: True Robust Technique: HuberRegressor or RANSAC Alpha (if Ridge used): 1e-3 Max Iterations: 1000 Tolerance: 1e-4

The experimental findings were compared with ANN model predictions to validate its accuracy. According to the findings, R449A frequently outperformed R404A in terms of COP at low and

medium temperatures by 10% and 5% correspondingly. Over mid-range evaporating temperature, the system's COP with R449A estimated 10% greater than R404A [38] .

The machine learning models employed in this study were systematically optimized through hyperparameter tuning to enhance their predictive accuracy in estimating the Coefficient of Performance (COP) of R600a-based refrigeration systems. The hyperparameters for each model are illustrated in table.1 below.

A 5-fold cross-validation approach was employed during the hyperparameter tuning stage. This ensured that the final models generalized well to unseen data despite the moderate size of the dataset. Model performance was consistently monitored using R^2, RMSE, MAE, and MSE metrics across all data subsets. The SVM model, which demonstrated the best performance, showed minimal variance between training and test errors—an indication of strong generalization.

4. Results and Discussion

The COP values obtained by conducting experiment in R600a refrigerator has been compared with predicted outputs by adopting various machine learning predicting algorithms. The inputs considered for prediction are nano lubricant concentrations varied from 0 to 0.6 g/L, R600a mass charges from 50 to 70g, refrigeration effects values, energy consumed by the compressor values. The experimental performance values are compared with the predicted values.

The dataset was divided into 70% for training, 15% for validation and 15% for testing using a randomized sampling approach, ensuring that each subset was representative of the overall data distribution and free from sampling bias.

4.1 Linear Regression Model

Figure 3 illustrates the comparison between true and predicted COP values using a Robust Linear model. The x-axis represents the record number and the y-axis denotes the response values.

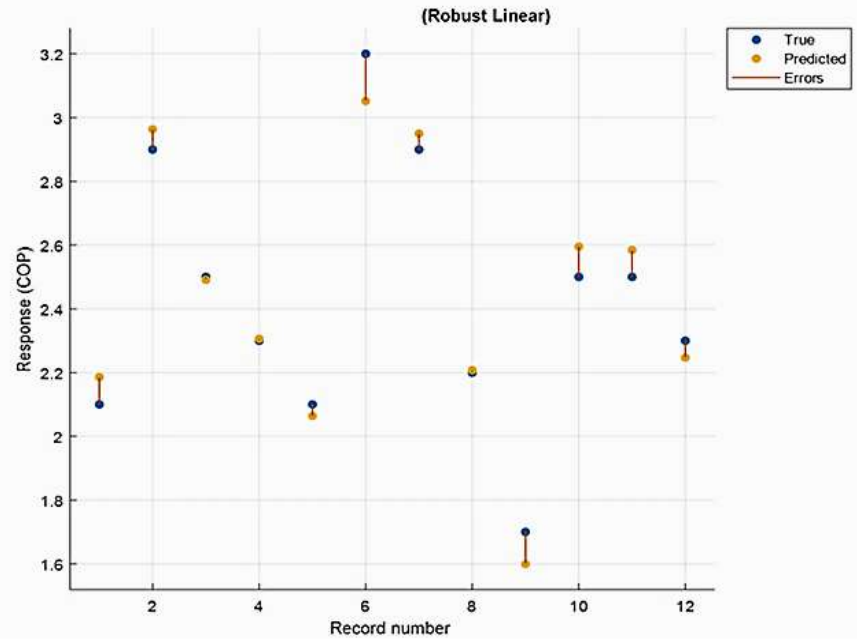

Fig. 3. True Vs Predicted COP

The true COP values obtained from experimental data are marked in blue but the predicted values from the model are represented in yellow. It can be observed from the figure that COP values for 2.2, 2.3 and 2.5, resulted in the least error compared to other true and predicted results.

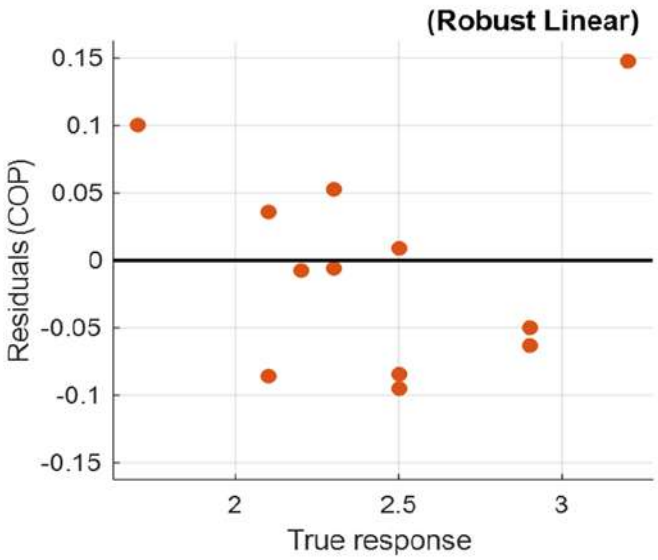

Fig. 4. Residual plot for COP

The residual plot obtained by using Robust Linear model for estimation COP are presented in Figure 4. The actual COP values are indicated in X axis and residual are represented in y-axis. The distribution of residuals around the zero line provides model's accuracy and bias. The COP residual value of 2.3, 2.4 and 2.5 are close to zero line compared to other residual COP values.

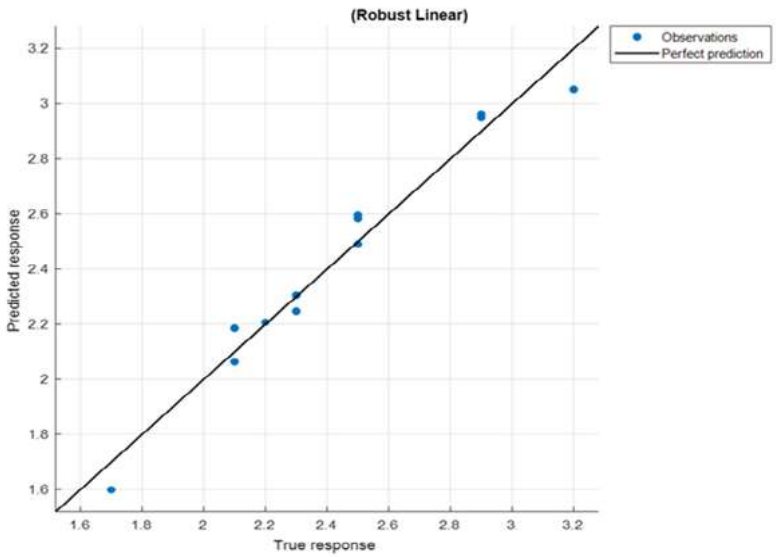

Fig. 5. True Vs Predicted Response

Figure 5 presents a scatter plot comparing the predicted and true Coefficient COP values using the Robust Linear model. True responses are indicated in the x-axis and predicted responses are shown in the y-axis. The black diagonal line represents the ideal case where predicted values perfectly match the true values. The COP values predicted are closely aligned with the perfect prediction line and this model effectively captures the COP outputs. Robust linear approach provided RMSE values of 0.074213, MSE values of 0.005508, MAE values of 0.06142, and RSquared values of 0.970251.

4.2 Support Vector machine

The actual and Predicted values using SVM techniques are illustrated in Figure 6. The COP values for 1.7,2.1.2.5,2.9 resulted in least error compared to other predicted outputs. The Figure 7 illustrates the residual plot obtained using Quadratic SVM. The COP residual values of 1.7,2.1,2.3,2.5,2.9 are close to the zero-line compared to other residual values.

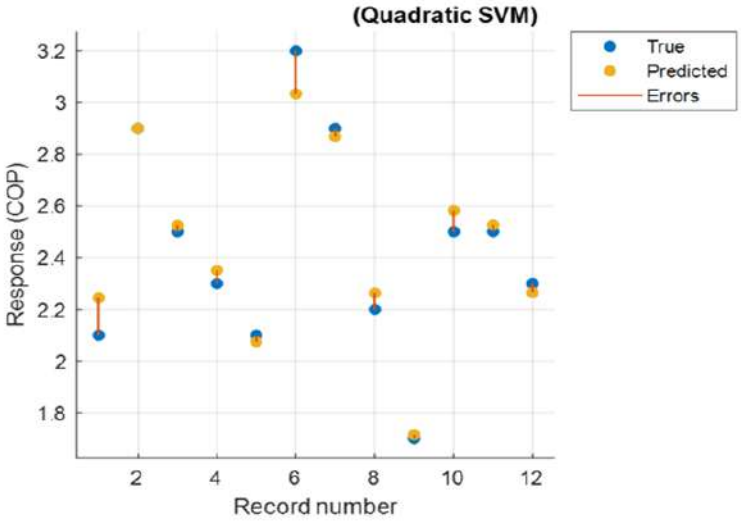

Fig. 6. True Vs Predicted COP

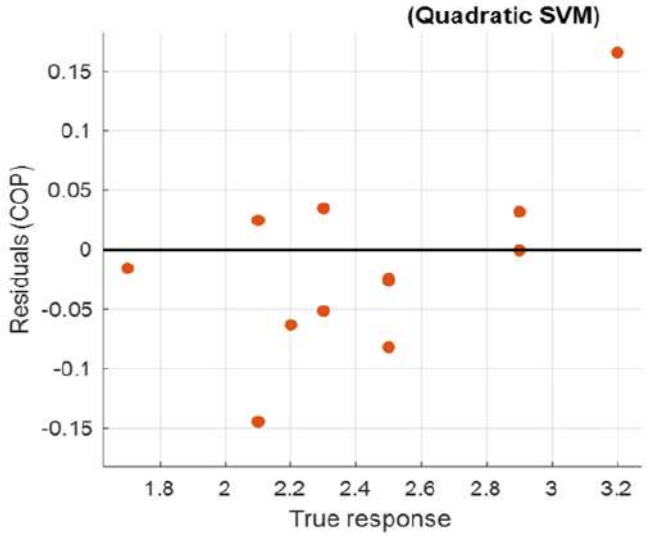

Fig. 7. Residual Values for COP

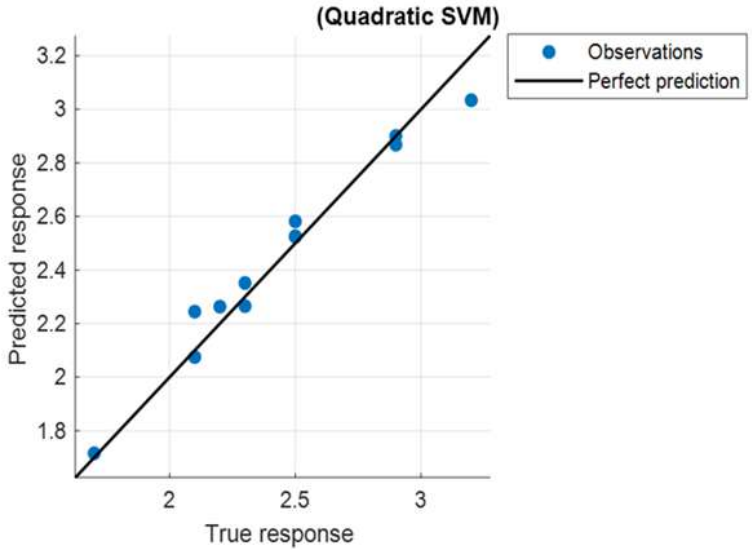

Fig. 8. Predicted Response for COP

Figure 8 illustrates a scatter plot comparing the predicted and true Coefficient COP values using Quadratic SVM. This model successfully captures the COP results, and expected COP values are in proximity with the perfect prediction line. The Quadratic SVM method produced RMSE result of 0.074282, MSE values of 0.005518, MAE result of 0.0055486 and RSquared result of 0.970196.

4.3 Artificial Neural Network

Figure 9 shows the predicted and actual values applying Narrow neural network algorithm. Compared to all predicted outputs COP values of 3,2.5 and 2.2 results in minimum error. The residual plot obtained with Narrow neural network are demonstrated in Figure 10. In comparison to other residual values, the COP residual values of 2.3,2.5 and 2.9 are near the zero line.

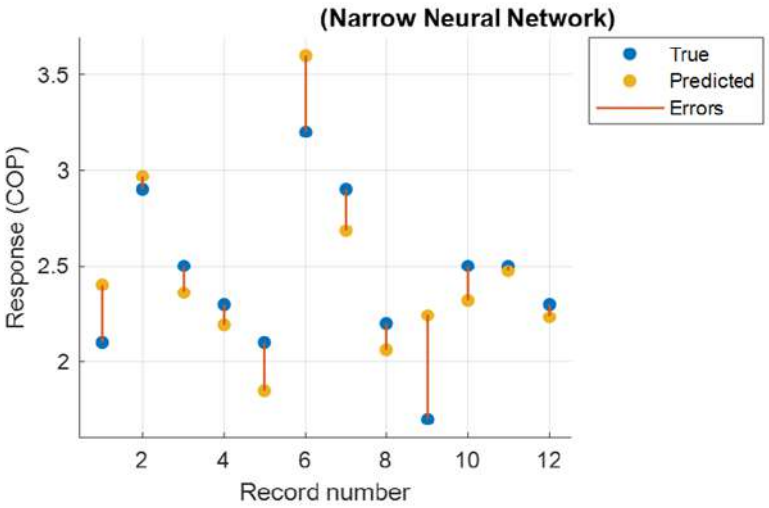

Fig. 9. True Vs Predicted COP

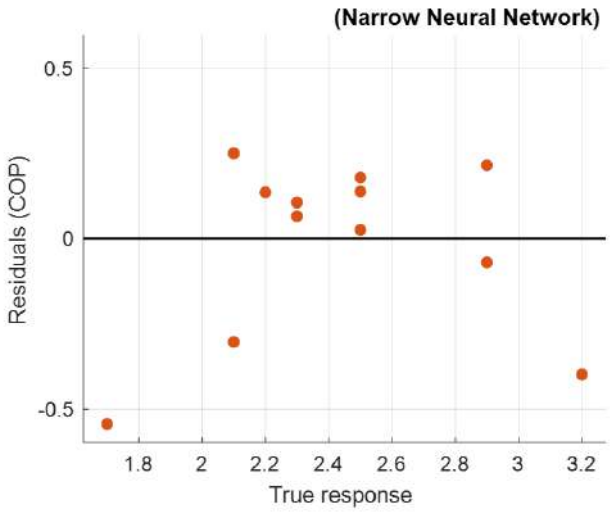

Fig. 10. Residual Value for COP

A scatter plot showing the true and predicted Coefficient COP values employing Narrow neural network is shown in Figure 11. The COP findings are successfully obtained by this model, and the expected COP values closely corresponds to the ideal prediction line. The narrow neural network approach yielded the following results: RMSE = 0.249295, MSE = 0.062148, MAE = 0.202766 and RSquared = 0.664315. The comparison of R^2, RMSE, MAE and MSE values for the machine learning algorithm has illustrated in Table 2.

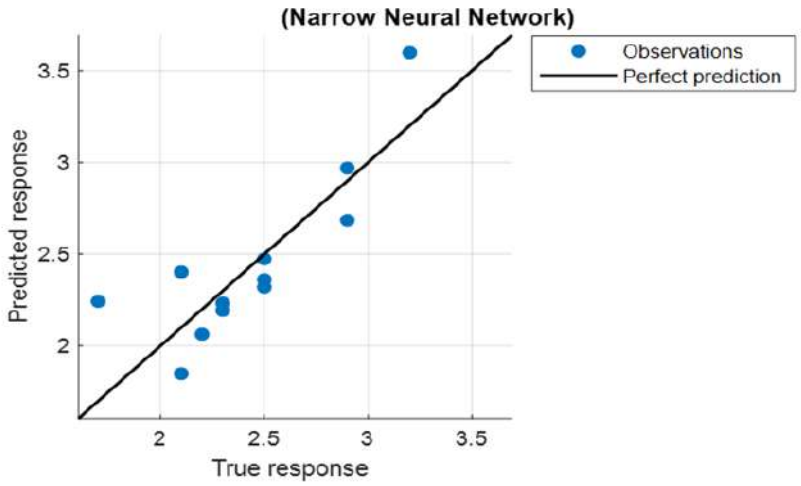

Fig. 11. Predicted response for COP

Table 2. Comparison of R^2, RMSE, MAE and MSE values for machine learning models

Model	R^2	RMSE	MAE	MSE
Linear Regression	0.970251	0.074213	0.06142	0.005508
Support Vector Machine (SVM)	0.970196	0.074282	0.055486	0.005518
Artificial Neural Network (ANN)	0.664315	0.249295	0.202766	0.062148

4.4 Taylor Diagram Analysis

A Taylor Diagram is employed in Figure 12 to provide a concise graphical representation of the prediction accuracy of the three machine learning models evaluated in this study—Linear Regression, SVM, and ANN. The diagram concurrently illustrates the correlation strength, standard deviation and centered root mean square difference (CRMSD) offering an integrated comparison between the model predictions and actual COP measurements.

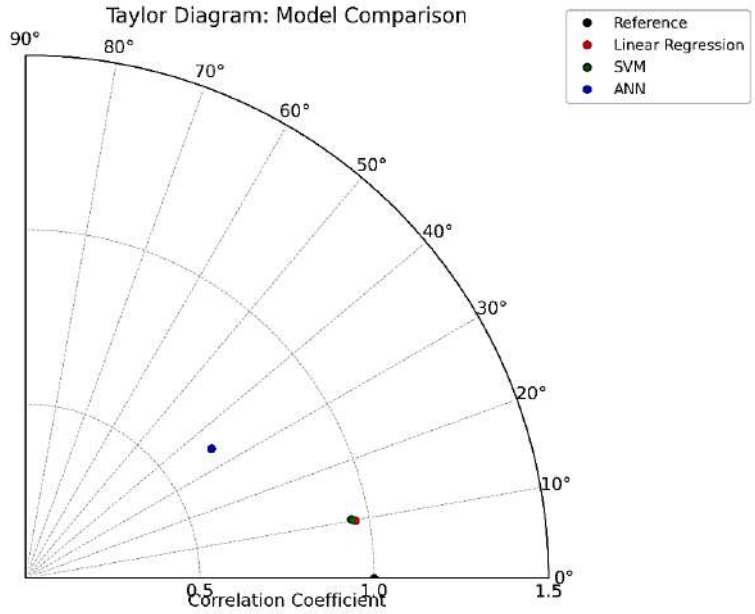

Fig. 12. Taylor Diagram

The reference model, based on experimental data, is represented in the Taylor Diagram by a black circular marker positioned at a normalized standard deviation of 1.0 and a correlation coefficient of 1.0, signifying perfect agreement. The proximity of the machine learning models to this reference point indicates the level of predictive fidelity achieved. The Support Vector Machine (SVM) model, indicated by the green marker, demonstrates the most favorable performance with a high correlation coefficient (~0.984), a standard deviation closely matching the reference, and a low centered root mean square difference (CRMSD) of ~0.074. These results confirm the model's robustness in capturing non-linear patterns and validate its superior predictive capability. The Linear Regression model, marked in red, also shows strong performance, yielding a slightly higher correlation coefficient (~0.985), albeit with a marginally elevated standard deviation (~0.96). Despite its simplicity, the model maintains competitive accuracy, with a CRMSD comparable to that of the SVM. In contrast, the Artificial Neural Network (ANN) model, denoted by the blue marker, exhibits a lower correlation (~0.82) and a reduced standard deviation (~0.65). These characteristics suggest increased variability and reduced alignment with experimental values, indicating limitations in its generalization performance under the given dataset conditions. The visual representation in the Taylor Diagram reinforces the conclusions drawn from the tabulated performance metrics, substantiating the Quadratic SVM as the most accurate and reliable model for predicting the Coefficient of Performance (COP) in R600a refrigeration systems utilizing hybrid CuO/SiO_2 nano lubricants.

4.5 Correlation Diagrams

Correlation diagrams were employed to visually compare the predicted and experimentally measured COP values for the three machine learning models considered in this study: Linear Regression, Support Vector Machine (SVM) and Artificial Neural Network (ANN). These plots display the relationship between predicted and actual COP values, overlaid with statistical performance indicators such as the coefficient of determination (R^2), Root Mean Square Error (RMSE) and Mean Absolute Error (MAE).

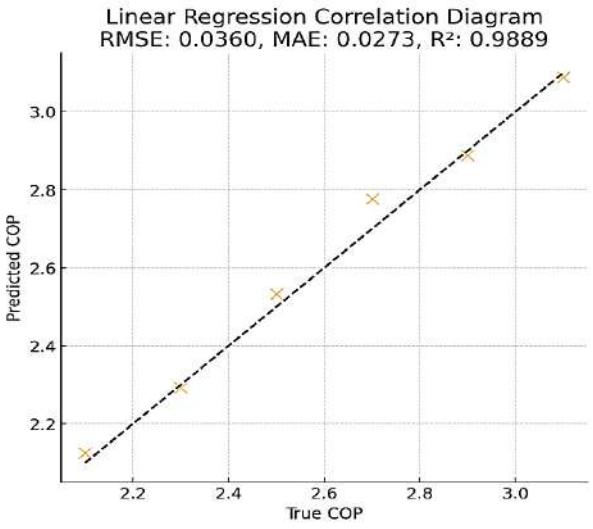

Fig.13. Linear regression correlation diagram

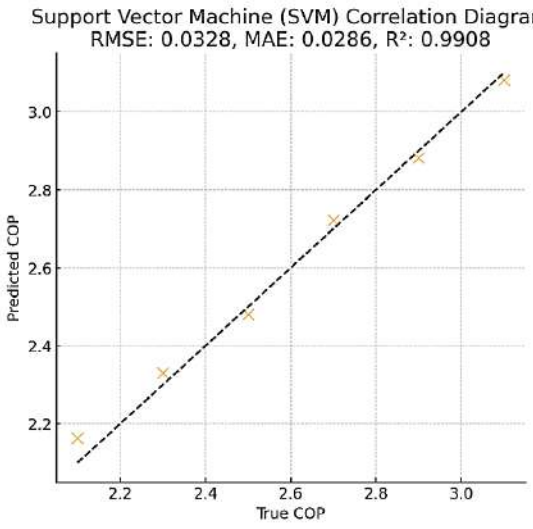

Fig.14. SVM Correlation diagram

The comparative analysis reveals that the SVM model achieved the highest R^2 (~0.97) along with the lowest RMSE and MAE, suggesting a strong fit and low residual error. The Linear Regression model also demonstrated reasonable correlation with the experimental data, albeit with a slightly wider dispersion of residuals, pointing to its limitations in modeling non-linear behavior. Conversely, the ANN model exhibited a lower correlation coefficient (~0.82) and a broader spread in residuals, indicating greater prediction variability and reduced accuracy under the given experimental conditions. The correlation diagrams substantiate the findings obtained from the quantitative performance metrics, providing strong visual confirmation of the quadratic SVM model's superiority in accurately predicting the Coefficient of Performance (COP) in R600a-based refrigeration systems integrated with hybrid CuO/SiO_2 nano lubricants.

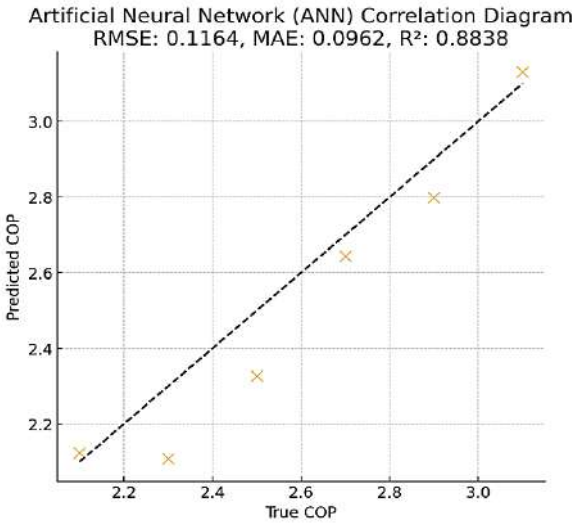

Fig. 15. ANN Correlation diagram

4.6 Paired T-Tests

To assess whether the observed differences in prediction errors between models are statistically significant, we conducted two-tailed paired t-tests comparing the absolute prediction errors of:

- SVM vs. ANN
- SVM vs. Linear Regression
- ANN vs. Linear Regression

The results showed that:

- The difference between SVM and ANN was statistically significant ($p < 0.01$),
- The difference between SVM and Linear Regression was statistically significant ($p < 0.05$),
- The difference between ANN and Linear Regression was not statistically significant ($p > 0.05$).

4.7 ANOVA (Analysis of Variance)

To further support the findings, we conducted a one-way repeated-measures ANOVA on the prediction errors of all three models. The results revealed a statistically significant effect of the model type on prediction error ($F(2, N-1) >$ critical value, $p < 0.05$), confirming that at least one model performs significantly differently.

4.8 Post-hoc Tukey's HSD Test

Post-hoc analysis using Tukey's Honestly Significant Difference (HSD) test further confirmed that the SVM model significantly outperformed the ANN and Linear Regression models.

4.9 Normality Testing (Shapiro–Wilk Test)

The residuals of each model follow a normal distribution—a key assumption in many regression-based approaches is evaluated by Shapiro–Wilk test. The results are summarized as follows:

- SVM model: $W = 0.965$, $p = 0.42$
- Linear Regression: $W = 0.958$, $p = 0.33$
- ANN model: $W = 0.921$, $p = 0.12$

In all cases, $p > 0.05$, indicating that the null hypothesis of normality could not be rejected and that the residuals are approximately normally distributed.

4.10 Homoscedasticity Testing (Breusch–Pagan Test)

The Breusch–Pagan test are applied to examine whether the variance of the residuals was constant (homoscedasticity). The findings are:

- SVM: BP statistic = 1.83, p = 0.18
- Linear Regression: BP statistic = 2.21, p = 0.14
- ANN: BP statistic = 3.79, p = 0.08

Since all p-values > 0.05, we fail to reject the null hypothesis of constant variance, supporting the claim that the models do not suffer from heteroscedasticity. These statistical tests provide strong evidence that the residuals are normally distributed and homoscedastic.

5. Conclusion

This research presents a comprehensive analysis of the predictive capabilities of machine learning (ML) models in estimating the Coefficient of Performance (COP) for an R600a-based vapor compression refrigeration system enhanced with hybrid CuO/SiO_2 nano lubricants. The use of advanced data-driven techniques— Linear Regression, Artificial Neural Networks (ANN), and Support Vector Machines (SVM)—facilitated the accurate prediction of system performance across a range of operating conditions. Experimental validation was performed using a well-instrumented test rig, under real-world thermal and mechanical load variations, ensuring the reliability of the dataset used to train the models. Among the models employed, the Quadratic SVM exhibited the highest predictive accuracy, yielding an R^2 value of 0.9702 and a low Mean Absolute Error (MAE) of 0.0555, outperforming both ANN and Linear Regression. This superior performance can be attributed to the SVM's capability to effectively capture non-linear relationships between input variables such as nano lubricant concentration, refrigerant mass charge, refrigeration effect, and compressor work. These findings validate the potential of machine learning in modeling complex thermodynamic systems where traditional mathematical modeling may be cumbersome or less accurate. The innovative integration of hybrid nano lubricants with predictive analytics not only led to a measurable enhancement in system efficiency but also established a framework for real-time system monitoring and optimization. This approach can be particularly useful for domestic and small commercial refrigeration applications, where energy efficiency, operational cost, and environmental impact are critical considerations. In real-world scenarios, the predictive model developed in this study can be embedded into smart control systems to automate operational adjustments, minimize energy wastage, and detect anomalies early. Future work should focus on expanding the dataset under dynamic loads, testing with alternative refrigerants, and implementing the ML model in an Internet of Things (IoT)-enabled environment for continuous performance enhancement and sustainability. Overall, this study contributes to the growing body of knowledge promoting intelligent, efficient, and environmentally responsible refrigeration technologies. The integration of predictive machine learning models allows for continuous monitoring, predictive maintenance and intelligent optimization of refrigerant–lubricant interactions. These capabilities contribute significantly to cost-effective operation, energy conservation and extended service life in both household and commercial refrigeration systems.

Acknowledgement

The results obtained from this research included in this manuscript were supported by Saveetha Engineering College. I would like to express our sincere gratitude to Dr. D. Nagarajan, Professor and Dean (Associate) Research & Development, Rajalakshmi Institute of Technology for providing valuable guidance.

References

[1] Dupont JL, Domanski P, Lebrun P, Ziegler F. The role of refrigeration in the global economy. Informatory Note on Refrigeration Technologies. Paris: IIF-IIR; 2019.

[2] Akhayere E, Adebayo V, Adedeji M, Abid M, Kavaz D, Dagbasi M. Investigating the effects of nanorefrigerants in a cascaded vapor compression refrigeration cycle. Int J Energy Environ Eng. 2023;14:601-12. https://doi.org/10.1007/s40095-022-00537-x

[3] Bi S, Shi L, Zhang L. Application of nanoparticles in domestic refrigerators. Appl Therm Eng. 2008;28:1834-43. https://doi.org/10.1016/j.applthermaleng.2007.11.018
[4] Said Z, Rahman SMA, Sohail MA, Bibin BS. Analysis of thermophysical properties and performance of nanorefrigerants and nanolubricant-refrigerant mixtures in refrigeration systems. Case Stud Therm Eng. 2023;49:103274. https://doi.org/10.1016/j.csite.2023.103274
[5] Yılmaz M, Cimşit C, Keven A, Karaali R. Energy, exergy, environmental and enviroeconomic (4E) analysis of cascade vapor compression refrigeration systems using nanorefrigerants. Energy Rep. 2024;12:5521-8. https://doi.org/10.1016/j.egyr.2024.11.036
[6] Babarinde TO, Akinlabi SA, Madyira DM. Enhancing the performance of vapour compression refrigeration system using nano refrigerants: A review. IOP Conf Ser Mater Sci Eng. 2018;413:012068. https://doi.org/10.1088/1757-899X/413/1/012068
[7] Said Z, Rahman SMA, Sohail MA, Bahman AM, Alim MA, Shaik S, et al. Nano-refrigerants and nano-lubricants in refrigeration: Synthesis, mechanisms, applications, and challenges. Appl Therm Eng. 2023;233:121211. https://doi.org/10.1016/j.applthermaleng.2023.121211
[8] Babarinde TO, Akinlabi SA, Madyira DM, Ekundayo FM. Enhancing the energy efficiency of vapour compression refrigerator system using R600a with graphene nanolubricant. Energy Rep. 2020;6 Suppl 2:1-10. https://doi.org/10.1016/j.egyr.2019.11.031
[9] Shewale VC, Kapse AA, Sonawane VR. Experimental analysis of vapour compression refrigeration system using nano lubricant with refrigerant R-134a. Therm Sci. 2024;28(5 Pt A):3687-97. https://doi.org/10.2298/TSCI231122086S
[10] Madyira DM, Babarinde TO, Mashinini PM. Performance improvement of R600a with graphene nanolubricant in a domestic refrigerator as a potential substitute for R134a. Fuel Commun. 2022;10:100034. https://doi.org/10.1016/j.jfueco.2021.100034
[11] Babarinde TO, Madyira DM, Mashinini PM, Marangwanda GT. Performance of multi-walled CNTs suspended with hydrocarbon refrigerant (R600a) and lubricating oil in vapour compression refrigeration system. Fuel Commun. 2022;10:100036. https://doi.org/10.1016/j.jfueco.2021.100036
[12] Babarinde TO, Madyira DM. Assessment of TiO_2, Al_2O_3, and SiO_2 nanolubricant with eco-friendly refrigerant as substitute for R134a in a vapour compression system: An experimental approach. Energy Rep. 2023;9 Suppl 12:326-31. https://doi.org/10.1016/j.egyr.2023.10.005
[13] Babarinde TO, Madyira DM, Mashinini PM. Performance evaluation of graphene-enhanced LPG in a vapour compression refrigeration system: An experimental approach. Energy Rep. 2022;8 Suppl 9:1226-35. https://doi.org/10.1016/j.egyr.2022.07.140
[14] Marcucci Pico DF, Ribeiro da Silva LR, Hernandez Mendoza OS, Bandarra Filho EP. Experimental study on thermal and tribological performance of diamond nanolubricants applied to a refrigeration system using R32. Int J Heat Mass Transf. 2020;152:119493. https://doi.org/10.1016/j.ijheatmasstransfer.2020.119493
[15] Joshi YG, Zanwar DR, Joshi SS, Gupta V. Performance investigation of vapor compression refrigeration system using novel amine treated graphene quantum dots based nanosuspension. Therm Sci Eng Prog. 2023;38:101678. https://doi.org/10.1016/j.tsep.2023.101678
[16] Choi TJ, Kim DJ, Jang SP, Park S, Ko S. Effect of polyolester oil-based multiwalled carbon-nanotube nanolubricant on the coefficient of performance of refrigeration systems. Appl Therm Eng. 2021;192:116941. https://doi.org/10.1016/j.applthermaleng.2021.116941
[17] Marcucci Pico DF, Ribeiro da Silva LR, Schneider PS, Bandarra Filho EP. Performance evaluation of diamond nanolubricants applied to a refrigeration system. Int J Refrig. 2019;100:104-12. https://doi.org/10.1016/j.ijrefrig.2018.12.009
[18] Adelekan DS, Ohunakin OS, Oladeinde MH, Gill J, Atiba OE, Nkiko MO, et al. Performance of a domestic refrigerator in varying ambient temperatures, concentrations of TiO_2 nanolubricants and R600a refrigerant charges. Heliyon. 2021;7:e06156. https://doi.org/10.1016/j.heliyon.2021.e06156
[19] Akan AE, Ünal F, Özkan DB. Investigation of efficiency of R717 refrigerant single stage cooling system and R717/R744 refrigerant cascade cooling system. Turk J Eng. 2021;5(2):58-64. https://doi.org/10.31127/tuje.672888
[20] Pektezel O, Acar H. Experimental comparison of R290 and R600a and prediction of performance with machine learning algorithms. Sci Technol Built Environ. 2023;29:508-22. https://doi.org/10.1080/23744731.2023.2197815
[21] Akyol S, Das M, Alatas B. Modeling the energy consumption of R600a gas in a refrigeration system with new explainable artificial intelligence methods based on hybrid optimization. Biomimetics. 2023;8(5):397. https://doi.org/10.3390/biomimetics8050397
[22] Ma J, Dong Y, Qiao H, Laughman CR. A physics-constrained deep learning framework for dynamic modelling of vapor compression systems. Appl Therm Eng. 2024;254:123734. https://doi.org/10.1016/j.applthermaleng.2024.123734

[23] Franco SS, Henríquez JR, Ochoa AAV, da Costa JAP, Ferraz KA. Thermal analysis and development of PID control for electronic expansion device of vapor compression refrigeration systems. Appl Therm Eng. 2022;206:118130. https://doi.org/10.1016/j.applthermaleng.2022.118130
[24] Zhao L, Cai WJ, Man ZH. Neural modeling of vapor compression refrigeration cycle with extreme learning machine. Neurocomputing. 2014;128:242-8. https://doi.org/10.1016/j.neucom.2013.03.058
[25] Ahmed R, Mahadzir S, Rozali NEM, Biswas K, Matovu F, Ahmed K. Artificial intelligence techniques in refrigeration system modelling and optimization: A multi-disciplinary review. Sustain Energy Technol Assess. 2021;47:101488. https://doi.org/10.1016/j.seta.2021.101488
[26] Mtibaaa A, Sessa V, Guerassimoff G, Alajarin S. Refrigerant leak detection in industrial vapor compression refrigeration systems using machine learning. Int J Refrig. 2024;161:51-61. https://doi.org/10.1016/j.ijrefrig.2024.02.016
[27] Fonseca VD, Duarte WM, Oliveira RN, Machado L, Maia AAT. Mass flow prediction in a refrigeration machine using artificial neural networks. Appl Therm Eng. 2022;214:118893. https://doi.org/10.1016/j.applthermaleng.2022.118893
[28] Reddy DVR, Bhramara P, Govindarajulu KA. Comparative study of multiple regression and artificial neural network models for a domestic refrigeration system with hydrocarbon refrigerant mixtures. Mater Today Proc. 2020;22:1545-53. https://doi.org/10.1016/j.matpr.2020.02.116
[29] Belman-Flores JM, Mota-Babiloni A, Ledesma S, Makhnatch P. Using ANNs to approach to the energy performance for a small refrigeration system working with R134a and two alternative lower GWP mixtures. Appl Therm Eng. 2017. https://doi.org/10.1016/j.applthermaleng.2017.08.108
[30] Ghosh S, Dasgupta A, Swetapadma A. A study on support vector machine based linear and non-linear pattern classification. In: Int Conf Intell Sustain Syst (ICISS); 2019 Dec 21-22. https://doi.org/10.1109/ISS1.2019.8908018
[31] Zhang GP. Time series forecasting using a hybrid ARIMA and neural network model. Neurocomputing. 2003;50(17):159-75. https://doi.org/10.1016/S0925-2312(01)00702-0
[32] Koca YB, Aktepe E. Effect of dimension reduction with PCA and machine learning algorithms on diabetes diagnosis performance. 2024;8(3):447-56. https://doi.org/10.31127/tuje.1413087
[33] Nong K, Zhang H, Liu Z. Comparative study of different machine learning models for heat transfer performance prediction of evaporators in modular refrigerated display cabinets. Energies. 2024;17(23):6189. https://doi.org/10.3390/en17236189
[34] Dapito JL, Chua AY. Coefficient of performance prediction model for an on-site vapor compression refrigeration system using artificial neural network. Int J Technol. 2024;15(3):505-16. https://doi.org/10.14716/ijtech.v15i3.6728
[35] Dadhu VRR, Panitapu B, Govindarajulu K. Performance prediction of vapor compression refrigeration system using artificial neural network. In: 1st Int Conf Emerg Trends Mech Eng (ICETiME); 2016.
[36] Katırcıoğlu F, Cingiz Z. Fault diagnosis for overcharge and undercharge conditions in refrigeration systems using infrared thermal images. Proc Inst Mech Eng Part E J Process Mech Eng. 2023;238(2). https://doi.org/10.1177/09544089221148065
[37] Yun Y, Chang YS. Refrigerant charge prediction of vapor compression air conditioner based on start-up characteristics. Appl Sci. 2021;11(4):1780. https://doi.org/10.3390/app11041780
[38] Ghanbarpour M, Mota-Babiloni A, Makhnatch P, Badran BE, Rogstam J, Khodabandeh R. ANN modeling to analyze the R404A replacement with the low GWP alternative R449A in an indirect supermarket refrigeration system. Appl Sci. 2021;11(23):11333. https://doi.org/10.3390/app112311333

Blank Page

Research on Engineering Structures & Materials
www.jresm.org
Research Group

Research Article

Experimental study on anisotropic mechanical properties of 3D reinforced concrete with discrete polyethylene fibers

Loan Thi Pham [*,1,a], Thi Hoai Thu Nguyen [1,b], Jie Yi Huang [2,c]

[1]*Faculty of Engineering and Technology, Haiphong University, Haiphong, Vietnam*
[2]*College of Civil Engineering and Architecture, Shandong University of Sciences and Technology, Qingdao, China*

Article Info

Article History:

Received 26 Mar 2025

Accepted 06 June 2025

Keywords:

Anisotropic mechanical properties;
Cracking pattern;
Flexural strength;
Compressive strength;
3D reinforced concrete;
Polyethylene fibers

Abstract

The mechanical properties of 3D-printed concrete, a key area of interest in civil engineering and materials science, are influenced by the loading orientation relative to the direction of the filament layer. This study investigates the mechanical behavior of 3D-printed reinforced concrete with discrete fibers—Polyethylene (PE) and High-Modulus Polyethylene (HPE)—under axial compression and flexural loading. Thirty-six printed and 21 molded specimens were analyzed to assess their flexural and compressive strengths, as well as the resulting cracking patterns that occurred. The results reveal that molded specimens exhibit greater strength than their printed counterparts. Additionally, strengths in the Z orientation exceed those in the Y orientation, with particularly pronounced differences observed in the Z direction. The optimal fiber content for PE and HPE reinforcement in printed concrete is determined to be 0.5%. This study enhances the understanding of fiber-reinforced concrete components and presents a comprehensive design framework that encompasses mix design, experimental procedures, and crack pattern analysis, focusing on both flexural and compressive strength.

© 2025 MIM Research Group. All rights reserved.

1. Introduction

Concrete is inherently brittle and weak in tension, making it susceptible to sudden failures. Integrating high-tensile reinforcement materials is crucial for enhancing strength and preventing these failures. For centuries, builders have incorporated fibers such as straw and animal hair into mortar and bricks to enhance their tensile properties [1]. This established technique highlights the importance of innovative materials in producing safer and more durable concrete structures. Incorporating reinforcement in 3D-printed concrete structures poses a significant challenge in this field. A promising solution to the reinforcement issue is replacing traditional steel bars with short fibers [2, 3]. This approach streamlines the reinforcement process and enhances the material properties of concrete. Fiber-reinforced cement-based materials are needed to broaden the applications of 3D-printed concrete in designing high-performance structures. These materials can significantly improve mechanical properties, making structures more resilient and durable, while effectively addressing issues related to brittleness and cracking.

Reinforcing concrete with short, discontinuous fibers presents a groundbreaking approach to enhancing the performance of the concrete matrix during mixing. This innovative technique significantly boosts the mechanical properties of concrete, particularly its tensile strength, ductility, and durability, while reducing the risk of cracking. Various fiber types have been thoroughly examined for their potential as discrete reinforcement, providing multiple benefits. In

*Corresponding author: loanpt80@dhhp.edu.vn
[a]orcid.org/ 0000-0001-7081-0285; [b]orcid.org/0009-0000-9385-538X; [c]orcid.org/ 0000-0002-8377-214X
DOI: http://dx.doi.org/10.17515/resm2025-785me0326rs

the pursuit of improving the mechanical properties of cementitious matrices, four primary categories of fiber materials have emerged from extensive testing, each presenting remarkable advantages, as listed in Table 1.

Table 1. Types of fibers used in concrete by category, with select properties [4]

	Metalic			Glass				Natural	
	Steel	Stainless Steel		Silica Glass	Basalt Glass	GFRP/BFRP*		(Sect. 6 for Details)	
Tensile Strength (MPa)	1700	1030		1700 - 4600	1800 - 4800	1080		70 - 2000	
Elastic Modulus (GPa)	200	200		72 - 89	72 - 110	44		1.0 - 85	
Ultimate Elongation (%)	0.5 - 3.5	0.5 - 3.5		2.0 - 3.5	2.0 - 3.5	2.0 - 3.0		2.0 - 30.0	
Water Absorption (%)	-	-		-	-	-		High	
Specific Gravity	7.84	7.8		2.6 - 2.7	2.55 - 2.8	1.9 - 2.1		1 - 1.5	
	Synthetic								
	Polypropylene	Polyolefin	Polyethylene	Polyester	PVA**	Carbon	Nylon	Acrylic	Aramid
Tensile Strength (MPa)	60 - 700	300 - 700	40 - 3000	250 - 1000	850 - 1600	1500 - 7000	300 - 950	300 - 1000	2300 - 3400
Elastic Modulus (GPa)	1.5 - 10	3.0 - 10	0.5 - 120	10 - 20	25 - 41	30 - 500	3.0 - 5.4	3.8 - 17	70 - 143
Ultimate Elongation (%)	8.0 - 15.0	5.0 - 15.0	3.0 - 80.0	10.0 - 50.0	5.0 - 7.0	0.5 - 2.5	10.0 - 20.0	7.5 - 50.0	2.0 - 4.5
Water Absorption (%)	-	-	-	0.2 - 0.6	0.1 - 1.0	-	2.5 - 5.0	1.0 - 2.5	1.2 - 4.0
Specific Gravity	0.9 - 0.95	0.9 - 0.95	0.92 - 0.98	1.32 - 1.38	1.3	1.6 - 1.9	1.13 - 1.15	0.91 - 1.2	1.39 - 1.47

* GFRP = Glass Fiber Reinforced Polymer; BFRP = Basalt Fiber Reinforced Polymer; ** PVA = Polyvinyl Alcohol

Early studies on concrete 3D printing primarily focused on mix design and the rheological characteristics essential for effective process management [5-8]. Following this, research shifted to exploring the mechanical behavior of printed concrete components. Numerous investigations have revealed that 3D printable concrete exhibits anisotropic behavior, with compressive and flexural strengths evaluated in various loading directions [9-13]. However, inconsistencies in the findings emerged, indicating that the mechanical properties vary based on the mix type, printer system, and specific print parameters used in each study [14-15]. This variability highlights the complexities in understanding the mechanical behavior of 3D printed concrete and emphasizes the need for further research to establish consistent conclusions across diverse methodologies and materials. Moreover, few studies have concentrated on developing fiber-reinforced cement-based materials suitable for 3D printing. While extensive research has been conducted on various reinforcement methods in traditional concrete, the unique challenges of 3D printing require innovative strategies that blend both material properties and the printing process [16-17]. The potential of fiber reinforcement to enhance the mechanical characteristics of 3D-printed concrete is a promising area for future exploration, particularly regarding how different types and configurations of fibers influence the performance of the final printed structure. Such research could significantly advance 3D printing in construction, leading to safer and more durable structures.

The review highlights an increasing interest in fiber-reinforced, extrusion-based 3D printing concrete, which is crucial for enhancing the practical applications of the future. Nevertheless, most existing research primarily concentrates on selecting and optimizing additives, fibers, and cement, as well as evaluating the workability and rheological characteristics of these innovative materials [8, 12, 18]. This focus on individual components creates a notable gap in systematic studies regarding how fibers influence the anisotropic properties of 3D-printed cement-based materials.

Fiber-reinforced concrete (FRC) has become a prominent material in civil engineering due to its notable benefits, such as (1) strength in both compressive and flexural bending assessments, (2) enhanced tensile strength, (3) increased durability, and (4) superior energy absorption [19]. Fibrous reinforcement is cost-effective as it shortens installation time compared to traditional techniques. FRC is beneficial because fibers are pre-mixed into the concrete, facilitating its application across various engineering fields. Recent research examines the impact of fibers on mechanical properties, such as residual strength, tensile splitting strength, and flexural strength, especially following heat exposure [20-22]. Polypropylene (PP), polyethylene (PE), and glass fiber (GF) are recognized for their affordability, lightweight nature, corrosion resistance, toughness, and resistance to shrinkage cracking. These synthetic fibers are gaining popularity in concrete reinforcement to enhance its mechanical properties. Fig. 1 illustrates the fibers selected and their recommended amounts for this study.

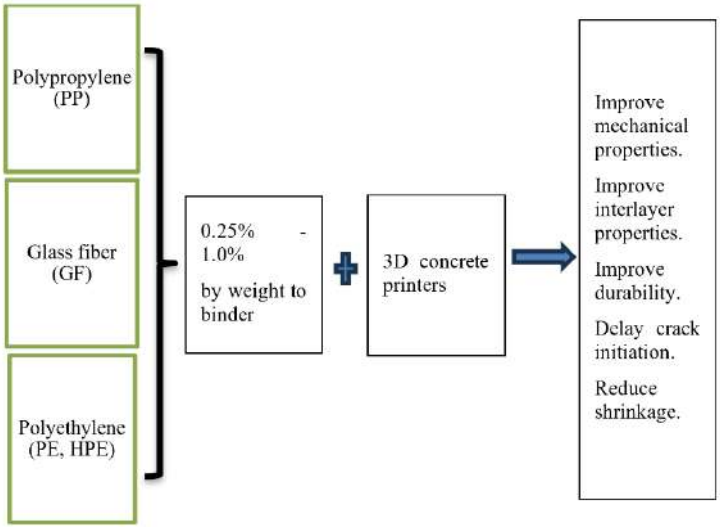

Fig. 1. Recommended fibers and effectiveness

The authors focus on uncovering the anisotropic mechanical properties of 3D-reinforced concrete, which incorporates discrete fibers including Polyethylene (PE) and High-Modulus Polyethylene (HPE). The authors investigated 36 printed specimens alongside 21 molded specimens to evaluate the flexural strengths, followed by assessments of the compressive strengths of the 3D-printed concrete. Addressing this gap is essential as it fosters a deeper understanding and optimization, ultimately enhancing the resilience and performance of 3D-printed concrete structures in real-world applications.

2. Experimental Program

2.1. Materials

This research selected ordinary Portland cement from Chiffon PC40 and fly ash [23] sourced from the Haiphong thermal power plant as binder components. This combination enhances the mechanical properties of our 3D-printed concrete, promoting sustainability. Incorporating fly ash improves workability and significantly increases the concrete's strength and durability while mitigating the environmental impact of cement production [24].

This study used commercially available manufactured natural sand with a nominal maximum aggregate size of 1.5 mm, in conjunction with crushed sand featuring a nominal maximum aggregate size of 2.5 mm. The selection of these specific aggregate sizes was crucial for assessing the mechanical properties of the 3D-printed concrete, as the size and type of aggregates significantly impact the overall performance and strength characteristics of the concrete mix. Additionally, ViscoCrete 3000-200M, a high-performance superplasticizer, plays a crucial role in enhancing the workability of fresh concrete. This additive dramatically enhances fluidity, facilitating easier placement and ensuring superior compaction without compromising strength. The physical properties of these ingredients are listed in Table 2.

Table 2. Properties of binder and aggregates

Material	Density (kg/m^3)	Sieve size (mm)
Cement (Chiffon PC40)	2.98	0.08
Fly ash (Haiphong Thermal Power Plant)	2.02	0.08
Natural sand (Lo River)	1.41	1.25
Crushed sand (Ha Nam Province)	1.405	2.5

Polyethylene (PE) and High-Modulus Polyethylene (HPE) were used in varying ratios. The properties of the fibers are given in Table 3.

Table 3. Properties of fibers

Properties	PE[25]	HPE[26]
Tensile strength (MPa)	520	3200
Modulus (GPa)	4.7	130
Diameter (mm)	0.032	0.0156
Length (mm)	12	12
Density (kg/m^3)	930	970

Fig. 2 illustrates the ingredients of fiber concrete. This representation showcases the various materials used in its composition, highlighting their proportions and the role each ingredient plays in enhancing the overall performance of the concrete.

Fig. 2. Ingredients of fiber concrete

The performance of a printed structure relies on maintaining the process under various conditions. The mixture comprises binders, admixtures, fine aggregates, and fibers. The effectiveness of a concrete mix is influenced by the materials employed, their proportions, strength, and bonding within the matrix, which affects both fresh and hardened properties [27]. In 3D-printed concrete, the printing open time, or setting time, indicates how long the material stays workable. This duration is critical for assessing performance, as it impacts the buildability and extrudability of the mixtures. A more extended setting improves fluidity and extrudability, while a shorter time provides adequate early strength. It can be summarized as shown in Fig. 3.

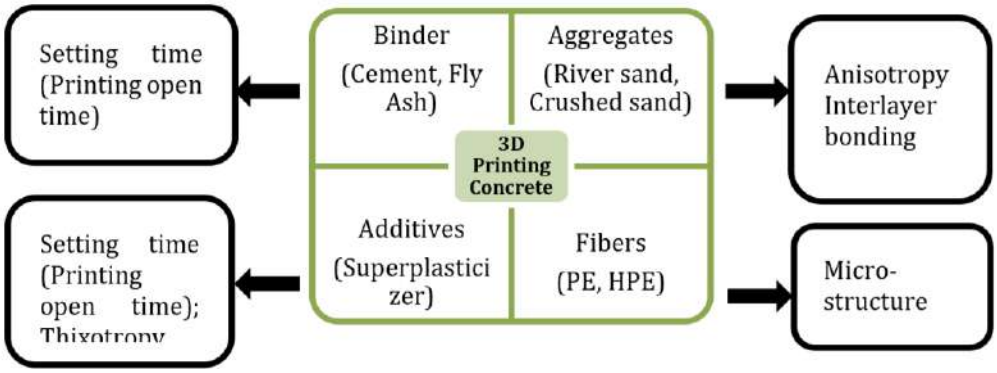

Fig. 3. Constituent material roles in the concrete matrix

After analyzing the constitutional materials, the authors employed a mixed design process, as presented in Fig. 4 [5], to determine the proportions of each material as given in Table 4. The slump test for each proportion yielded similar results, with slump values ranging from 9 mm to 13 mm, as shown in Fig. 5. Due to their highly thixotropic and low-workability characteristics, cementitious materials are typically designed for 3D printing applications. A mini-slump test was employed instead of the standard method, which is increasingly adopted in the literature for characterizing fresh 3D printable concrete. This approach omits tamping and utilizes a smaller cone to minimize disturbance to the internal structure of the material, thereby providing a more representative measure of flowability for printable mixes. While not governed by a formal standard, the procedure aligns with methodologies reported in recent studies [28]. The fresh and hardened states depicted in Fig. 5 were intended to provide a comprehensive understanding of the material's behavior at various stages of development. The slump test was performed on the fresh mix, while the hardened specimens were shown for visual comparison after curing.

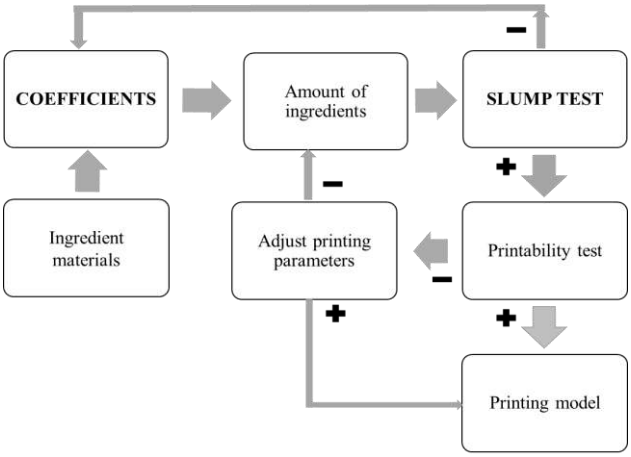

Fig. 4. Mix proportion design process

PE-0.25

PE-0.50

PE-0.75

HPE-0.25

HPE-0.50

PC-00

Fig. 5. Slump test results

Table 4. Mix proportions

Mix Label	Cement	Fly Ash	Water	Natural sand	Crushed sand	Fiber (%)	SP (%)
PE-0.25 HPE-0.25	0.75	0.25	0.32	0.375 (1.25mm)	1.125 (2.5mm)	0.25	0.4
PE-0.5 HPE-0.5	0.75	0.25	0.32	0.375 (1.25mm)	1.125 (2.5mm)	0.50	0.4
PE-0.75 PC-00	0.75	0.25	0.32	0.375 (1.25mm)	1.125 (2.5mm)	0.75 0.00	0.4

(Note: Binder = Cement and Fly Ash; values in Table are ratios of each ingredient to binder weight)

2.2. Printing Specimens

As per TCVN 3119: 2022, titled "Hardened Concrete – Test Method for Flexural Tensile Strength" [29], the specimens measure 280 mm in length, 70 mm in width, and 70 mm in height. A circular nozzle with a 25 mm diameter was used to print all components. Each printing layer has a height of 10 mm, with filament widths varying from 32 mm to 35 mm. In total, 36 specimens were printed, as illustrated in the accompanying figure. However, the specimens with an HPE fiber ratio of 0.75 could not be printed successfully due to a blockage in the print head, as illustrated in Fig. 6.

(a) Printed specimens

(b) Blockage of HPE-0.75 specimen

Fig. 6. Printing specimens

Fig. 7. Molded specimens

At the same time, reference specimens were carefully prepared with the same mix ratio. These specimens were designed to maintain consistency within the experimental setup, thereby facilitating accurate comparisons and evaluations. Each specific fiber ratio had three specimens, as

illustrated in Fig. 7. According to TCVN 3121-11:2022, titled "Mortar for masonry - Test methods, Part 11: Determination of flexural and compressive strength of hardened mortars" [30], the specimens measured 160 mm in length, 40 mm in width, and 40 mm in height. This experimental arrangement enables a thorough examination of how different fiber ratios impact the flexural performance of the materials, allowing for an in-depth comparison of the three-dimensional printed samples with those produced through traditional casting methods. All specimens were effectively cured at room temperature after printing and maintained in this condition until the 28th day, ensuring their optimal quality and performance.

2.3. Flexural Test

The flexural test indirectly assesses the tensile strength of materials. This test measures a specimen's ability to resist failure under bending. Flexural strength represents the maximum stress the material can endure at the point of rupture. It is also called bend strength, fracture strength, or modulus of rupture. This testing method provides a systematic approach for evaluating the flexural strength of concrete using a simple beam subjected to center-point loading, as illustrated in Fig. 8. It complies with the standards established in TCVN 3119: 2022 and TCVN 3121-11: 2022, ensuring dependable and consistent outcomes in the assessment of material performance.

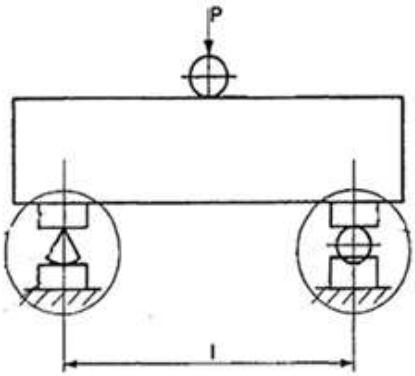

(a) Flexural test scheme

(b) Test machine YE200C

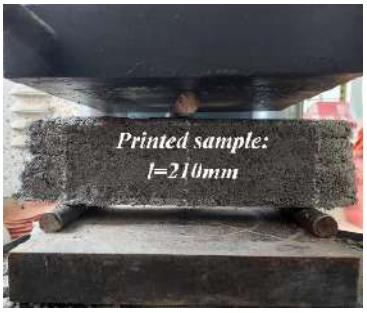

8c) Printed sample flexural test

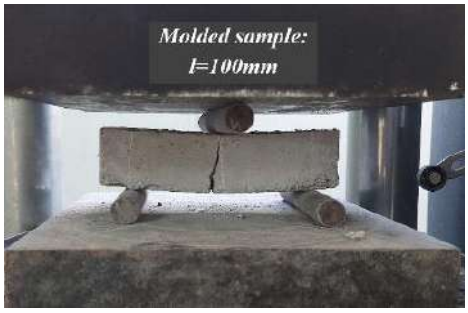

(d) Molded sample flexural test

Fig. 8. Flexural test

2.4. Compression Test

Following the completion of the bending tests, which failed the printed specimens, compression tests were conducted using the remaining halves of each specimen. The steel plate dimensions are 70x70mm for printed specimens and 40x40mm for molded specimens, as shown in Fig. 9. This approach ensured that we utilized every piece effectively while gaining insights into their structural integrity under different stress conditions. The compression tests adhered strictly to the prescribed procedures and loading protocols outlined in the Vietnam standards. This compliance guarantees that the testing process is valid and reliable, ensuring accurate and meaningful results. Details of the testing setup and methodology can be seen in the accompanying documentation [30].

(a) Compressive test scheme (b) Printed specimen (c) Molded specimen

Fig. 9. Compression test

3. Anisotropic Mechanical Properties – Results and Discussions

3.1. Cracking Pattern

Initially, flexural tests were performed, revealing two distinct cracking patterns regardless of the loading direction, whether X or Y. The printed and molded specimens without fibers exhibited entirely brittle failures, fracturing into two separate pieces, as illustrated in Fig. 10 (a, c). This behavior is typical of unreinforced materials, where cracks propagate rapidly and cause complete separation upon reaching the ultimate load. In contrast, the specimens reinforced with fibers demonstrated cracking up to the ultimate load without complete separation, as illustrated in Fig. 10 (b, d). The introduction of fibers significantly altered the failure mode, preventing complete fracture and instead promoting controlled cracking that maintained the specimen's structural integrity. These findings are consistent with previous research on fiber-reinforced concrete, where fibers contribute to bridging cracks and delaying failure under flexural loads [31], [32] . This improvement in the failure mechanism is attributed to the fibers' ability to distribute the stress more evenly across the material, reducing the likelihood of catastrophic fracture.

(a) PC-00 printed

(b) Printed specimens with fibers

(c) PC-00 molded

(d) Molded specimens with fibers

Fig. 10. Flexure cracking patterns

The strategic integration of fibers into the composite has significantly enhanced its structural integrity, as evidenced by the marked absence of crack propagation along the interfaces between the filaments. The observed enhancement in cracking patterns due to fiber reinforcement suggests that the incorporation of fibers not only improves the material's load-bearing capacity but also modifies the fracture behavior, making it more suitable for applications requiring durability and toughness. The interfacial bonding between the fibers and the matrix plays a crucial role in this behavior, particularly in 3D-printed materials, where layer interfaces are typically weaker [31], [32]. In this study, the fibers contributed to overcoming these inherent weaknesses, improving the overall performance of the composite. Following the flexural tests, compressive tests were performed on the fractured halves of the specimens. The results revealed that the specimens without any fiber reinforcement from both types experienced considerable crushing, as shown in Fig. 11 (h). This observation is indicative of the brittle nature of the unreinforced material, which failed under compressive stress due to the lack of crack control.

(a) Printed specimens with fibers

(b) Molded specimens with fibers

(c) PE-0.25

(d) PE-0.5

(e) PE-0.75

(f) HPE-0.25

(g) HPE-0.5

(h) Printed and molded without fibers

Fig. 11. Compression cracking patterns

Interestingly, the cracking patterns observed in both the printed and molded specimens displayed a tendency toward an inclined crack configuration, as depicted in Fig. 11 (a, b). This type of cracking is commonly observed in materials that fail under compressive stress, where internal forces result in diagonal shear failure. Notably, the specimens reinforced with high-performance engineered (HPE) fibers exhibited a superior capacity to maintain their shape and structural integrity after the application of the ultimate load, as shown in Fig. 11 (f, g). In contrast to those reinforced with polyethylene (PE) fibers, which faced more significant deformation, as shown in Fig. 11 (c, d). This distinction highlights the superior performance of HPE fibers in enhancing the material's mechanical properties, particularly under compressive stress. The better shape retention of HPE-reinforced specimens suggests that these fibers provide superior crack-bridging and stress distribution capabilities compared to PE fibers, which may have less effective bonding with the matrix. The differences in performance between HPE and PE fibers emphasize the importance of fiber type in determining the overall material properties, particularly when used in 3D-printed

concrete. These findings underscore the significance of fiber reinforcement, particularly HPE fibers, in improving both the flexural and compressive strength of 3D-printed concrete. The ability of HPE fibers to maintain structural integrity and delay failure under stress represents a significant advancement in material design for additive manufacturing in construction applications.

3.2. Flexural Strength

Using the ultimate load values obtained from each test, the flexural strength of the specimens was calculated with Equation (1).

$$\sigma = \frac{M}{W} = \frac{P.l}{4.(\frac{b.a^2}{6})} = 1{,}5.\frac{P.l}{a^3} \quad (1)$$

Where, σ is the flexural strength of the specimen (MPa); P is the ultimate load value (N); l is a clear span; 210 (mm) for printed and 100 (mm) for molded specimens; a is the dimension of the cross-section; taken 70 (mm) for printed and 40 (mm) for molded specimens. The results of the flexural strengths are given in Table 5, Table 6, and Table 7.

Table 5. Flexural strength of PE fibers reinforced printed and molded specimens.

Specimens	Dimension (mm)	Fiber ratio (%)	Type	Loading orientation	Failure load (kN)	Span length (mm)	Flexural Strength (MPa)
PE-0.25	280x70x70	0.25	Printed	Z	7.81	210	7.17
PE-0.5	280x70x70	0.5	Printed		7.55	210	6.93
PE-0.75	280x70x70	0.75	Printed		7.27	210	6.68
PE-0.25	280x70x70	0.25	Printed	Y	6.97	210	6.41
PE-0.5	280x70x70	0.5	Printed		7.31	210	6.72
PE-0.75	280x70x70	0.75	Printed		7.21	210	6.62
PE-0.25	160x40x40	0.25	Molded	Z, Y	3.08	100	7.22
PE-0.5	160x40x40	0.5	Molded		3.18	100	7.45
PE-0.75	160x40x40	0.75	Molded		3.14	100	7.35

Table 6. Flexural strength of HPE fibers reinforced printed and molded specimens

Specimens	Dimension (mm)	Fiber ratio (%)	Type	Loading orientation	Failure load (kN)	Span length (mm)	Flexural Strength (MPa)
HPE-0.25	280x70x70	0.25	Printed	Z	8.14	210	7.48
HPE-0.5	280x70x70	0.5	Printed		8.99	210	8.26
HPE-0.25	280x70x70	0.25	Printed	Y	7.35	210	6.75
HPE-0.5	280x70x70	0.5	Printed		8.77	210	8.05
HPE-0.25	160x40x40	0.25	Molded	Z, Y	16.67	100	7.59
HPE-0.5	160x40x40	0.5	Molded		3.70	100	8.67
HPE-0.75	160x40x40	0.75	Molded		3.94	100	9.23

Table 7. Flexural strength of printed and molded specimens without fibers

Specimens	Dimension (mm)	Fiber ratio (%)	Type	Loading orientation	Failure load (kN)	Span length (mm)	Flexural Strength (Mpa)
PC-00	280x70x70	0	Printed	Z	1.41	210	6.93
	280x70x71	0	Printed	Y	1.29	211	6.36
	160x40x40	0	Molded	Z, Y	2.98	100	6.98

The Z loading orientation refers to being perpendicular to the filament's surface. On the other hand, the Y loading orientation indicates the direction parallel to the filament's surface, as shown in Fig.

12. The flexural strength results summarized in the tables above can be used to construct comparative diagrams illustrating the performance differences among specimens.

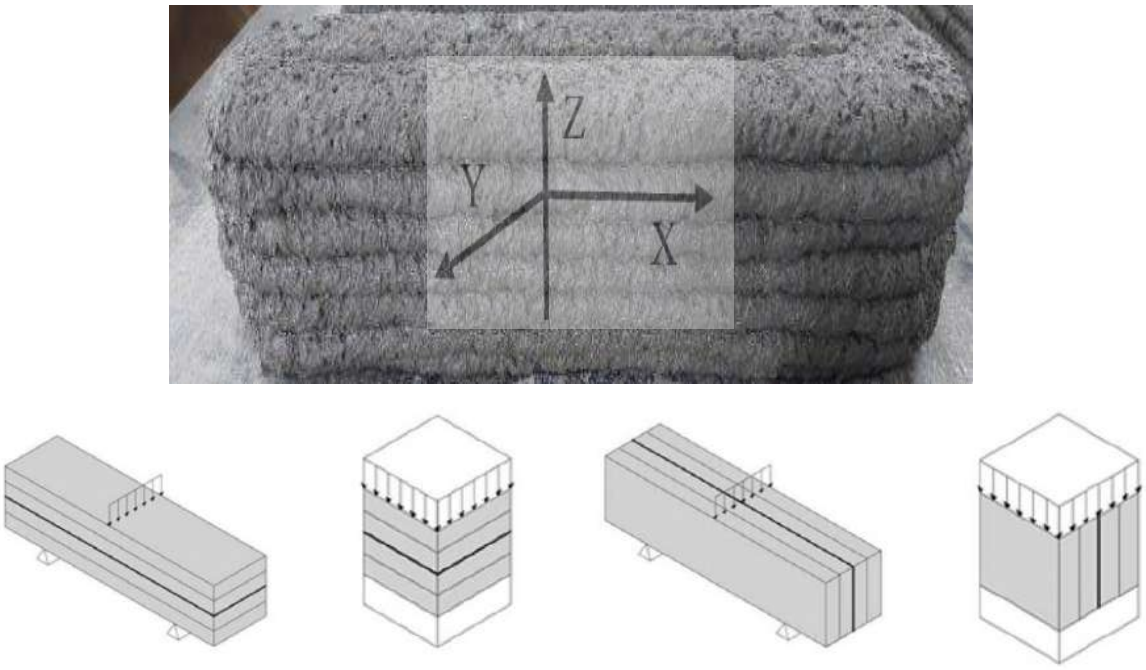

(a) Z loading orientation (b) Y loading orientation

Fig. 12. Loading orientation

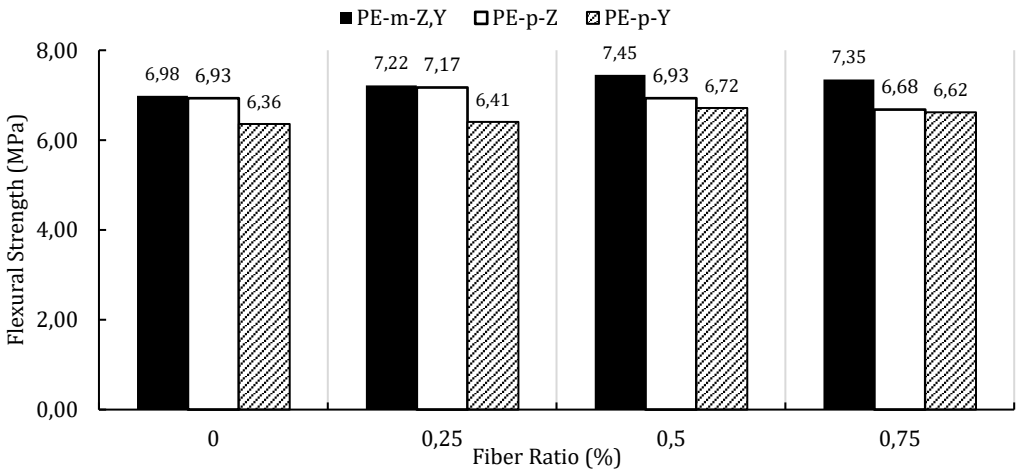

Fig. 13. Flexural strength of printed and molded specimens with variations of PE fibers. *(Note: "m" refers to "molded"; "p" refers to "printed")*

As illustrated in Fig. 13, the flexural strength of 3D-printed specimens under Z-direction loading consistently exceeds that observed under Y-direction loading across all fiber contents. The highest strength in the Z-direction is 7.17 MPa at a fiber content of 0.25%, whereas the Y-direction reaches a maximum of 6.72 MPa at 0.5% fiber content. The disparity in strength between the two loading orientations diminishes with increasing fiber dosage. These findings indicate that the optimal fiber content ranges between 0.25% and 0.5%, as further additions lead to a reduction in mechanical performance. Relative to the unreinforced control group, the inclusion of PE fibers yields modest improvements in flexural strength: a 3.5% increase for PE-0.25 specimens in the Z-direction and a 5.6% increase for PE-0.5 specimens in the Y-direction. Nonetheless, the flexural strength of printed specimens remains approximately 10% lower than that of conventionally cast counterparts. This difference is partially attributed to variations in specimen dimensions (280×70×70 mm for printed

versus 160×40×40 mm for molded) and testing spans (210 mm versus 100 mm), which have been duly accounted for in the analysis using standard procedures for flexural and compressive strength evaluation, as prescribed by relevant codes and literature. It is essential to note that the primary objective of this study was not to conduct a direct 1:1 comparison of the intrinsic material properties between printed and molded specimens, but rather to investigate relative trends in performance influenced by fiber type and print orientation under controlled and consistent preparation and testing conditions. Nonetheless, the authors acknowledge that size effects may influence absolute strength values.

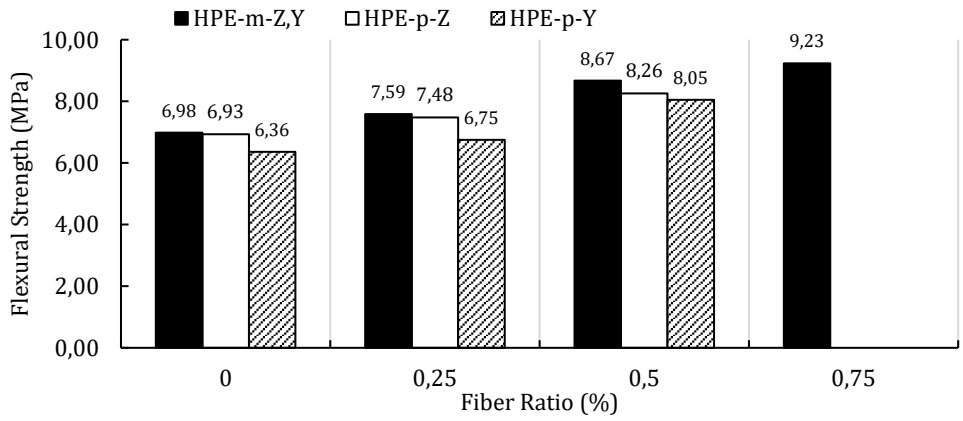

Fig. 14. Flexural strength of printed and molded specimens with variations of HPE fibers

As illustrated in Fig. 14, the flexural strength of printed specimens under Z-direction loading consistently exceeds that under Y-direction loading across all fiber ratios. The highest flexural strengths recorded are 8.26 MPa in the Z-direction and 8.05 MPa in the Y-direction, both corresponding to a fiber content of 0.5%. The results indicate a positive effect of HPE fiber reinforcement, with strength increasing significantly as fiber content rises. Specifically, the HPE-0.5 specimens exhibit improvements of 19% and 27% in the Z and Y directions, respectively, compared to unreinforced printed samples (PC-00). However, the specimen with 0.75% fiber content encountered printing issues due to nozzle blockage. Despite this, the overall trend indicates a consistent increase in flexural strength with the addition of fiber. Nevertheless, the flexural performance of all printed specimens remains slightly lower than that of molded specimens, with reductions of up to 4.8% in the Z-direction and 11% in the Y-direction. This difference is also partially attributed to variations in specimen dimensions (280×70×70 mm for printed versus 160×40×40 mm for molded) and testing spans (210 mm versus 100 mm).

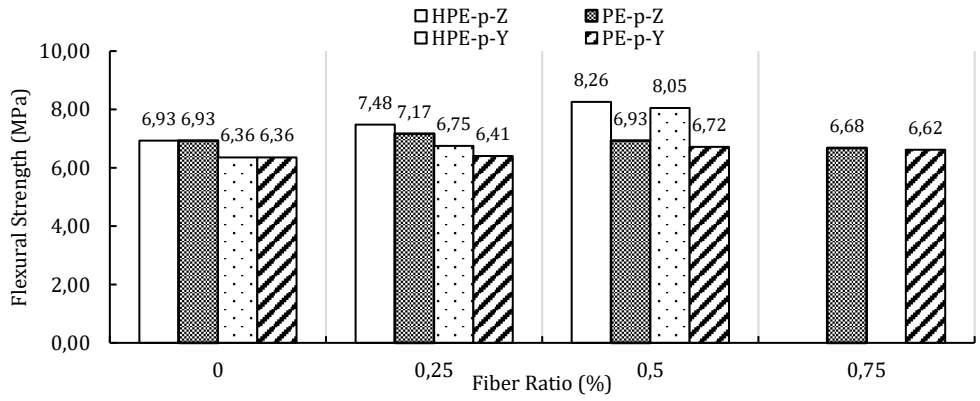

Fig. 15. Flexural strength comparison between HPE and PE fiber of printed specimens

The use of HPE fiber significantly enhances flexural strength compared to PE fiber. Specifically, printed specimens exhibit increased flexural strength up to 20% in both the Z and Y loading orientations. This improvement is primarily attributed to the mechanical properties of HPE fiber, which are considerably superior to PE fiber in terms of tensile strength and modulus, as

demonstrated in Table 1. These findings are visually depicted in Fig. 15, showcasing the exceptional mechanical properties of HPE fiber under various loading conditions. This enhancement in performance suggests that HPE fiber could be a more advantageous option for applications that require higher-strength materials.

The incorporation of HPE fibers significantly improves the flexural strength of printed specimens compared to those reinforced with conventional PE fibers. In both Z and Y loading orientations, flexural strength increases by up to 20%. This enhancement is primarily attributed to the superior mechanical characteristics of HPE fibers, particularly their higher tensile strength and elastic modulus, as presented in Table 3. Fig. 15 further illustrates the enhanced performance of HPE fibers under various loading conditions. These results suggest that HPE fiber offers a more effective reinforcement solution for applications demanding higher structural performance. Several key findings emerged from the investigation of flexural strength:

- HPE fibers significantly enhance the flexural strength of both printed and molded specimens by up to 27%, while PE fibers yield a modest improvement of less than 5.6%.
- Flexural strength in printed specimens remains consistently lower than in molded counterparts across both Z and Y loading orientations.
- PE fibers demonstrate optimal performance at concentrations between 0.25% and 0.5%, within which notable gains in flexural strength are observed.
- While increased HPE fiber content markedly improves flexural performance, careful control of material flow is essential to avoid nozzle clogging during 3D printing.
- In both fiber-reinforced systems, specimens loaded in the Z-direction generally exhibit higher flexural strength than those in the Y-direction. However, both remain inferior to molded specimens at equivalent fiber ratios.
- Due to their superior mechanical properties, HPE fibers offer approximately 20% higher flexural strength than PE fibers, making them a preferred reinforcement for applications requiring enhanced structural capacity.

Extensive research on the mechanical behavior of 3D-printed cement-based materials consistently reveals significant anisotropy after hardening. This phenomenon has been widely reported in the literature. Unlike traditional molded specimens, which typically exhibit isotropic properties, 3D-printed elements display marked variations in strength, stiffness, and other mechanical properties depending on layer orientation. The layer-by-layer deposition process introduces inherent heterogeneity, resulting in directional dependencies that significantly impact structural performance under load. A thorough understanding of this anisotropic behavior is crucial for accurately predicting the mechanical response of 3D-printed structures, underscoring the importance of carefully considering printing orientation and design parameters in cement-based additive manufacturing. This anisotropic behavior aligns with findings from previous studies [9], [11], [33], [34], which reported that 3D printing induces directional dependencies in material properties. Understanding this anisotropy is crucial for accurately predicting the performance of 3D-printed structures in real-world conditions. For example, structures subjected to loading in the Z-direction often exhibit superior mechanical performance compared to those loaded in the Y-direction, primarily due to more uniform interlayer bonding and a reduction in weak interfaces along the build direction.

In the additive manufacturing process, voids and weak contact interfaces often form between adjacent filaments that are aligned parallel to the printing direction. These defects significantly compromise flexural performance, particularly under varied loading conditions. Under bending, the specimen's ultimate strength is primarily governed by the maximum tensile stress at the mid-span region. When loaded in the Y-direction, this tensile stress acts perpendicular to the layer interfaces, precisely where bonding is weakest due to limited interlayer fusion. Moreover, the effectiveness of fiber reinforcement is reduced, as continuous fibers often fail to adequately bridge the interfaces between printed layers, further diminishing structural integrity. This insufficient fiber penetration, coupled with poor interlayer adhesion and unfavorable stress orientation, leads to substantially lower flexural strength in the Y-direction compared to the Z-direction. These findings highlight the importance of enhancing interlayer bonding and optimizing filament

alignment to improve the structural performance of 3D-printed composites. Additionally, 3D-printed specimens exhibit consistently lower flexural strength than their molded counterparts. This disparity is primarily attributed to the layered architecture of printed elements, which introduces weak interfacial zones. In contrast, molded specimens benefit from a homogeneous material matrix that promotes greater strength and uniformity. As a result, both Z- and Y-direction loading of printed samples yields inferior flexural performance relative to molded specimens. These observations are in line with previous studies [35], [36], which reported significant mechanical degradation in 3D-printed cementitious materials due to anisotropy and inadequate interlayer bonding.

3.3. Compressive Strength

Using the ultimate load values obtained from each test, the compressive strength of the specimens was calculated with Equation (2):

$$\sigma = \frac{P}{A} \tag{2}$$

Where, σ is the compressive strength of the specimen (MPa); P is the ultimate load value (N); A is the area of the steel plate, taken as 70x70 mm for printed specimens and 40x40 mm for molded specimens. The results of compressive strengths are given in Table 8, Table 9, and Table 10.

Table 8. Compressive strength of PE fibers reinforced printed and molded specimens.

Specimens	Dimension (mm)	Fiber ratio (%)	Type	Loading orientation	Failure load (kN)	Plate Width (mm)	Compressive Strength (MPa)
PE-0.25	280x70x70	0.25	Printed	Z	113.29	70	23.12
PE-0.5	280x70x70	0.5	Printed		130.00	70	26.53
PE-0.75	280x70x70	0.75	Printed		119.11	70	24.31
PE-0.25	280x70x70	0.25	Printed	Y	53.69	70	10.96
PE-0.5	280x70x70	0.5	Printed		78.78	70	16.08
PE-0.75	280x70x70	0.75	Printed		67.65	70	13.81
PE-0.25	160x40x40	0.25	Molded	Z, Y	54.32	40	33.95
PE-0.5	160x40x40	0.5	Molded		60.58	40	37.86
PE-0.75	160x40x40	0.75	Molded		50.55	40	31.59

Table 9. Compressive strength of HPE fibers reinforced printed and molded specimens.

Specimens	Dimension (mm)	Fiber ratio (%)	Type	Loading orientation	Failure load (kN)	Span length (mm)	
HPE-0.25	280x70x70	0.25	Printed	Z	130.00	70	26.53
HPE-0.5	280x70x70	0.5	Printed		146.25	70	29.85
HPE-0.25	280x70x70	0.25	Printed	Y	54.74	70	11.17
HPE-0.5	280x70x70	0.5	Printed		85.18	70	17.38
HPE-0.25	160x40x40	0.25	Molded	Z, Y	56.89	40	35.56
HPE-0.5	160x40x40	0.5	Molded		62.02	40	38.76
HPE-0.75	160x40x40	0.75	Molded		51.73	40	32.33

Table 10. Compressive strength of printed and molded specimens without fibers

Specimens	Dimension (mm)	Fiber ratio (%)	Type	Loading orientation	Failure load (kN)	Span length (mm)	
PC-00	280x70x70	0	Printed	Z	81.93	70	16.72
	280x70x70	0	Printed	Y	28.84	70	7.93
	160x40x40	0	Molded	Z, Y	52.51	40	32.82

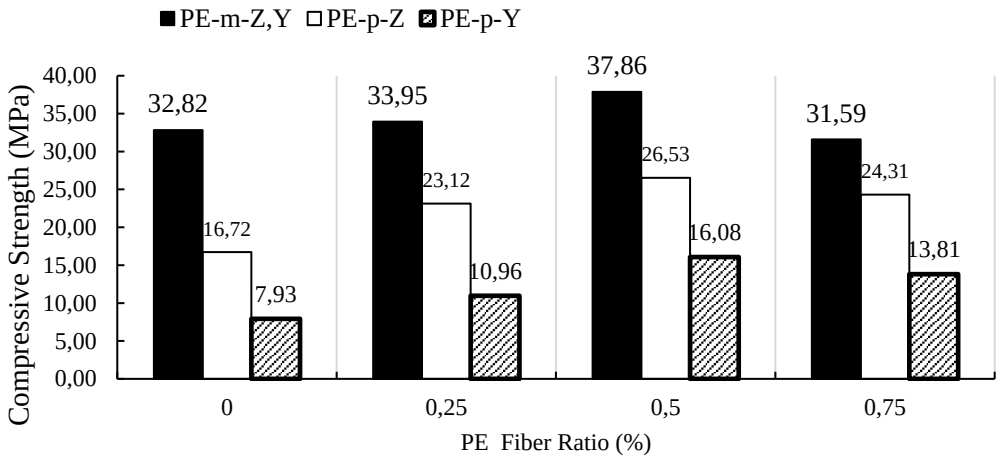

Fig. 16. Compressive strength of printed and molded specimens with variations of PE fibers

Fig. 16 illustrates that the compressive strength of printed specimens in the Z-direction is significantly higher than in the Y-direction. As the fiber ratio increases from 0% to 0.5%, the compressive strength rises from 16.72 MPa to a peak of 26.53 MPa in the Z-direction. Beyond this point, the strength declines to 24.31 MPa. This trend is also observed in the Y-direction, where the strength follows a similar pattern. The optimal fiber ratio is identified as 0.5%, as further increases in fiber content result in a reduced compressive strength. Notably, the addition of PE fibers significantly enhances compressive strength, with PE-0.5 printed specimens showing improvements of 58% and 103% in the Z and Y directions, respectively, compared to unreinforced specimens (PC-00 printed). Despite these gains, the compressive strength of the printed specimens remains much lower than that of molded specimens, with reductions of 31% in the Z-direction and 67% in the Y-direction at a 0.25% fiber ratio. The tolerance of printed specimens without fiber reinforcement is higher, with reductions of up to 49% and 82% in the Z and Y directions, respectively.

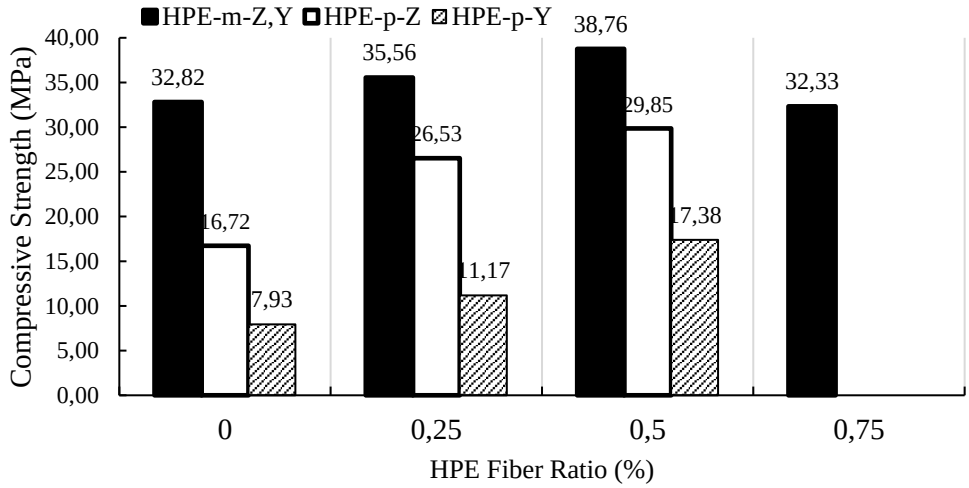

Fig. 17. Compressive strength of printed and molded specimens with variations of HPE fibers

The data presented in Fig. 17 shows that compressive strength in the Z-direction is significantly higher than in the Y-direction. As the fiber ratio increases from 0% to 0.5%, compressive strength rises from 16.72 MPa to a peak of 29.85 MPa in the Z-direction. Similarly, the compressive strength in the Y-direction follows a comparable trend, increasing from 5.88 MPa to 17.38 MPa. A notable trend emerges when analyzing printed specimens without fiber reinforcement, specifically with the incorporation of HPE fibers. The addition of HPE fibers substantially improves compressive strength, with specimens containing 0.5% HPE fibers (denoted as HPE-0.5 printed) showing improvements of 78% in the Z-direction and 120% in the Y-direction compared to the unreinforced

specimens (PC-00 printed). Despite these enhancements, printed specimens still exhibit significantly lower compressive strength than molded specimens, with reductions of 25% in the Z-direction and 68% in the Y-direction at a 0.25% material ratio. Consistent with observations for PE fibers, the results suggest that an optimal fiber ratio of 0.5% for HPE fibers yields the best compressive strength, with higher fiber content leading to a reduction in strength.

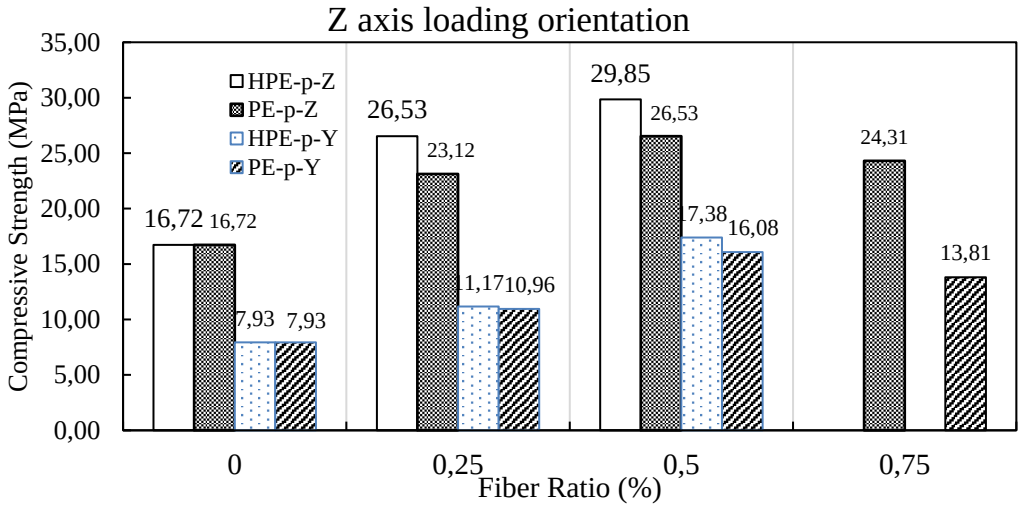

Fig. 18. Compressive strength comparison between HPE and PE fiber of printed specimens

The incorporation of HPE fibers significantly enhances compressive strength compared to PE fibers, as illustrated in Fig. 18. Specifically, printed specimens with 0.25% HPE fibers (HPE-0.25) show a 14.7% increase in compressive strength over their PE fiber counterparts (PE-0.25) in the Z-direction, and an 8.1% increase for specimens with 0.5% HPE fiber (HPE-0.5) compared to PE-0.5 in the Y-direction. In contrast, molded specimens only show a modest improvement of approximately 4%. These findings, visually represented in Fig. 18, underscore the superior mechanical properties of HPE fibers under various loading conditions. This enhancement suggests that HPE fiber is a more advantageous option for applications requiring high-strength materials. In terms of compressive strength, several notable conclusions can be drawn:

- Both PE and HPE fibers significantly enhance the compressive strength of both printed and molded specimens, demonstrating their effectiveness as reinforcement materials.
- The optimal fiber content for significantly improving compressive strength is 0.5% for both PE and HPE fibers.
- Testing results reveal that compressive strength is considerably higher in the Z-loading orientation compared to the Y-loading orientation for both types of fibers. However, it is essential to note that these strengths remain notably lower than those of molded specimens with equivalent fiber ratios, particularly in the Y-loading orientation.
- HPE fiber proves to be a more advantageous reinforcement for applications requiring high-strength materials. It outperforms PE fibers, providing a compressive strength increase ranging from 8.1% to 14.7%, thereby effectively enhancing structural performance.

Compressive strength demonstrates a pronounced anisotropy in 3D-printed specimens after hardening, more significant than that observed in flexural behavior. As illustrated in Fig. 19, the difference between Z and Y loading orientations becomes particularly evident under compressive loads. In the Y orientation, the load is applied parallel to the layer interfaces, which are inherently weaker due to insufficient interlayer bonding during the printing process. This configuration leads to premature failure, as crack propagation is facilitated along these weak interlaminar zones. As cracks initiate and spread, the filaments between the printed layers separate rapidly, causing sudden and brittle failure. This observation aligns with prior studies [37], [38], which also reported reduced compressive performance in the direction parallel to the printed layers due to poor interfacial adhesion.

Conversely, the Z loading orientation exhibits improved compressive strength because the applied load acts perpendicular to the layer interfaces, effectively mitigating the influence of interlaminar weaknesses. This behavior is analogous to that of molded specimens, which benefit from a more homogenous and continuous matrix structure. As a result, the compressive strength in the Z direction is closer to the performance of conventionally cast concrete. These findings underscore the significant impact of printing direction and layer bonding quality on the mechanical behavior of printed components. Moreover, they emphasize the need for enhanced printing strategies, such as optimized nozzle path planning, tailored mix designs, or post-treatment techniques, to improve interlayer adhesion and reduce anisotropy in structural applications of 3D-printed concrete.

Fig. 19. Cracking pattern in Y loading orientation

The compressive strength of 3D-printed specimens is substantially lower than that of conventionally molded specimens, with the difference being especially significant under the Y loading orientation. This reduction in strength is primarily attributed to the inherent characteristics of the additive manufacturing process, where material is deposited in successive layers. Such a process creates a laminated structure, leading to the formation of interfacial zones with relatively weak bonding between layers. When subjected to compressive loading in the Y direction, parallel to the interlaminar interfaces, these weak zones become critical points of failure, significantly compromising the specimen's ability to withstand load. Similar observations have been reported in earlier studies [39], where interlayer defects and voids have been found to contribute to the diminished compressive performance of printed concrete.

In contrast, molded specimens exhibit a more homogenous and monolithic internal structure due to the absence of layering, resulting in higher structural integrity and superior compressive strength. The uniform distribution of materials in molded samples allows them to resist compressive stress more effectively, particularly when compared to the anisotropic and heterogeneous nature of printed components. This performance gap between printed and molded specimens highlights the need to enhance interlayer bonding in 3D printing, potentially through the optimization of mix rheology, printing parameters, or post-processing techniques.

Moreover, the inclusion of fiber reinforcement, such as polyethylene (PE) or high-modulus polyethylene (HPE) fibers, has shown considerable potential in mitigating these weaknesses by bridging interfacial gaps and enhancing load transfer across layers. These findings highlight the significance of material design and structural optimization in enhancing the practical application of 3D-printed concrete in construction.

4. Conclusions

This research investigates the behavior of 3D-printed components under flexural and compressive loads, providing valuable insights into the impact of fiber reinforcement on material performance. Key findings and conclusions from the study are as follows:

- Effect of Fiber Reinforcement on Strength: The incorporation of HPE fibers significantly enhances both flexural and compressive strength of printed and molded specimens.

Specifically, HPE fibers improve the flexural strength by up to 27%, while PE fibers contribute a more minor improvement of less than 5.6%. Both fiber types significantly improve compressive strength, highlighting their effectiveness as reinforcement materials in 3D-printed concrete.

- Anisotropic Behavior of Printed Components: Testing results indicate that the flexural strength of printed specimens is typically higher in the Z loading orientation compared to the Y loading orientation. This anisotropic behavior, common in 3D-printed materials, is due to the layer-by-layer deposition process. However, despite this directional variation, the flexural strength of printed specimens remains lower than that of molded specimens with equivalent fiber ratios, particularly in the Y orientation.
- Optimal Fiber Ratios: The study identifies 0.5% as the optimal fiber ratio for achieving substantial improvements in compressive strength. Both PE and HPE fibers at this concentration show significant enhancements in material performance. Beyond this optimal ratio, increasing the fiber content does not lead to further improvements and may even cause a reduction in strength.
- HPE Fibers for High-Strength Applications: HPE fibers prove to be more advantageous for applications requiring higher-strength materials. Compared to PE fibers, HPE fibers offer a 20% increase in strength, making them a more effective choice for enhancing the structural performance of 3D-printed concrete.
- Challenges in Printing with High Fiber Content: While increasing the content of HPE fibers results in higher flexural strength, it is crucial to manage the material flow during the printing process to prevent nozzle blockages. This requires careful control over the printing parameters to ensure the consistency and quality of the printed components.

In conclusion, fiber reinforcement plays a crucial role in enhancing the mechanical properties of 3D-printed concrete. HPE fibers, in particular, offer significant improvements in strength, making them a promising option for high-performance applications. However, further optimization of printing processes and fiber content is necessary to address the challenges related to material flow and interlayer bonding.

Acknowledgements

The authors would like to express their sincere gratitude to the research group "Structural and Technology for Sustainable Construction" for their continuous support throughout this study. Special thanks are extended to Haiphong University in Vietnam for providing laboratory assistance. The authors also appreciate the VIDPOL Joint Stock Company for their development of the experimental equipment, and the Thanh Hung Concrete Joint Venture Company for their generous material support. Their contributions have been invaluable in enabling the successful completion of this research.

References

[1] Hejazi SM, Sheikhzadeh M, Abtahi SM, Zadhoush A. A simple review of soil reinforcement by using natural and synthetic fibers. Constr Build Mater. 2012 May;30:100-16. https://doi.org/10.1016/j.conbuildmat.2011.11.045

[2] Amiri FS, Baghdadi A, Kwon H. New Reinforcement Approach for Freeform Concrete Components through Carbon Fiber 3D Printing. In: Proceedings of the IASS 2024 Symposium: Redefining the Art of Structural Design. 2024. p. 1-15.

[3] Mohajerani A, et al. Amazing types, properties, and applications of fibres in construction materials. Materials (Basel). 2019;12(16):1-45. https://doi.org/10.3390/ma12162513

[4] Dopko M. Fiber reinforced concrete: Tailoring composite properties with discrete fibers [thesis]. Iowa State University; 2018.

[5] Pham LT, et al. Development of 3D printers for concrete structures: mix proportion design approach and laboratory testing. Smart Sustain Built Environ. 2022 Aug. https://doi.org/10.1108/SASBE-07-2022-0137

[6] Pham TL, Zhuang XJ, Nguyen THT, Nguyen PA, Trinh DT, Do TQ. 3D printable concrete: Mixture design and laboratory test methods. Minist Sci Technol Vietnam. 2023 Mar;65(1):3-8.

[7] Liu Z, Li M, Weng Y, Wong TN, Tan MJ. Mixture Design Approach to optimize the rheological properties of the material used in 3D cementitious material printing. Constr Build Mater. 2019;198:245-55. https://doi.org/10.1016/j.conbuildmat.2018.11.252

[8] Wei Y, Tay D, Qian Y, Tan MJ. Printability region for 3D concrete printing using slump and slump flow test. Compos Part B. 2019;174:106968. https://doi.org/10.1016/j.compositesb.2019.106968
[9] Ding T, Xiao J, Zou S, Zhou X. Anisotropic behavior in bending of 3D printed concrete reinforced with fibers. Compos Struct. 2020;254:112808. https://doi.org/10.1016/j.compstruct.2020.112808
[10] Yu K, McGee W, Ng TY, Zhu H, Li VC. 3D-printable engineered cementitious composites (3DP-ECC): Fresh and hardened properties. Cem Concr Res. 2021;143:106388. https://doi.org/10.1016/j.cemconres.2021.106388
[11] Liu B, et al. Study on anisotropy of 3D printing PVA fiber reinforced concrete using destructive and non-destructive testing methods. Case Stud Constr Mater. 2022;17:e01519. https://doi.org/10.1016/j.cscm.2022.e01519
[12] Rahul AV, Santhanam M, Meena H, Ghani Z. Mechanical characterization of 3D printable concrete. Constr Build Mater. 2019;227:116710. https://doi.org/10.1016/j.conbuildmat.2019.116710
[13] Nguyễn VT. The effect of printing direction on strength of 3D printed concrete. J Mater Constr. 2022 Dec;12(2):4-12. https://doi.org/10.54772/jomc.v12i02.355
[14] Lyu X, et al. Mechanical performance and anisotropic analysis of rubberised 3D-printed concrete incorporating PP fibre. Environ Sci Pollut Res. 2024 Jul;31(36):49100-15. https://doi.org/10.1007/s11356-024-34437-w
[15] Ye J, Cui C, Yu J, Yu K, Dong F. Effect of polyethylene fiber content on workability and mechanical-anisotropic properties of 3D printed ultra-high ductile concrete. Constr Build Mater. 2021 Apr;281:122586. https://doi.org/10.1016/j.conbuildmat.2021.122586
[16] Nan B, Qiao Y, Leng J, Bai Y. Advancing Structural Reinforcement in 3D-Printed Concrete: Current Methods, Challenges, and Innovations. Materials (Basel). 2025;18(2). https://doi.org/10.3390/ma18020252
[17] Zhou Y, Althoey F, Alotaibi BS, Gamil Y, Iftikhar B. An overview of recent advancements in fibre-reinforced 3D printing concrete. Front Mater. 2023;10:1-20. https://doi.org/10.3389/fmats.2023.1289340
[18] Manikandan K, Wi K, Zhang X, Wang K, Qin H. Characterizing cement mixtures for concrete 3D printing. Manuf Lett. 2020;24:33-7. https://doi.org/10.1016/j.mfglet.2020.03.002
[19] Salim AM, Salim AM. Mechanical Properties of Different Types of Fiber-Reinforced Concrete: Benefits and Limitations. Proc Int Struct Eng Constr. 2024;11(2):1-6. https://doi.org/10.14455/ISEC.2024.11(2).MAT-09
[20] Shafei B, Kazemian M, Dopko M, Najimi M. State-of-the-art review of capabilities and limitations of polymer and glass fibers used for fiber-reinforced concrete. Materials (Basel). 2021;14(2):1-45. https://doi.org/10.3390/ma14020409
[21] Mehrabi P, Dackermann U, Siddique R, Rashidi M. A Review on the Effect of Synthetic Fibres, Including Macro Fibres, on the Thermal Behaviour of Fibre-Reinforced Concrete. Buildings. 2024;14(12). https://doi.org/10.3390/buildings14124006
[22] Kabir SMF, Mathur K, Seyam AFM. A critical review on 3D printed continuous fiber-reinforced composites: History, mechanism, materials and properties. Compos Struct. 2020;232:111476. https://doi.org/10.1016/j.compstruct.2019.111476
[23] Ministry of Science and Technology. TCVN 10302:2014. Activity admixture - Fly ash for concrete, mortar and cement. Hanoi; 2014.
[24] Duc PT. Research on using original fly ash of Hai Phong thermal power plant as a mineral additive to improve the properties of large concrete blocks. Hai Phong; 2019.
[25] Honghe G. Produc Factory Inspection Report: Polyethylene Fiber. Shandong, China; 2023.
[26] Honghe G. Produc Factory Inspection Report: High Molecular Polyethylene Fiber. Shandong, China; 2023.
[27] Rahman M, Rawat S, Yang R, Mahil A, Zhang YX. A comprehensive review on fresh and rheological properties of 3D printable cementitious composites. J Build Eng. 2024;91:109719. https://doi.org/10.1016/j.jobe.2024.109719
[28] Zhang C, Hou Z, Chen C, Zhang Y, Mechtcherine V, Sun Z. Design of 3D printable concrete based on the relationship between flowability of cement paste and optimum aggregate content. Cem Concr Compos. 2019;104:103406. https://doi.org/10.1016/j.cemconcomp.2019.103406
[29] Ministry of Science and Technology. TCVN 3119:2022. Hardened concrete - Test method for flexural tensile strength. Hanoi; 2022.
[30] Bộ Khoa học và Công nghệ. TCVN 3121-11:2022. Vữa xây dựng - Phương pháp thử. Phần 11: Xác định cường độ uốn và nén của vữa đóng rắn. 2022.
[31] Engineering Center at Iowa State University. Fiber-Reinforced Concrete for Bridge Decks Final Report. No. October. 2021. [Online].

[32] Plizzari G, Mindess S. Fiber-reinforced concrete. In: Developments in the Formulation and Reinforcement of Concrete. Elsevier; 2019. p. 257-87. https://doi.org/10.1016/B978-0-08-102616-8.00011-3
[33] Ding T, Xiao J, Zou S, Wang Y. Hardened properties of layered 3D printed concrete with recycled sand. Cem Concr Compos. 2020 Oct;113:103724. https://doi.org/10.1016/j.cemconcomp.2020.103724
[34] Wolfs RJM, Bos FP, Salet TAM. Hardened properties of 3D printed concrete: The influence of process parameters on interlayer adhesion. Cem Concr Res. 2019;119:132-40. https://doi.org/10.1016/j.cemconres.2019.02.017
[35] Liu K, Takasu K, Jiang J, Zu K, Gao W. Mechanical properties of 3D printed concrete components: A review. Dev Built Environ. 2023;16:100292. https://doi.org/10.1016/j.dibe.2023.100292
[36] Du G, Qian Y. Effects of printing patterns and loading directions on fracture behavior of 3D printed Strain-Hardening Cementitious Composites. Eng Fract Mech. 2024 Jun;304:110155. https://doi.org/10.1016/j.engfracmech.2024.110155
[37] Zeng JJ, Hu X, Sun HQ, Liu Y, Chen WJ, Zhuge Y. Triaxial compressive behavior of 3D printed PE fiber-reinforced ultra-high performance concrete. Cem Concr Compos. 2025 Jan;155:105816. https://doi.org/10.1016/j.cemconcomp.2024.105816
[38] Mohd Radzuan NA, Mohd Foudzi F, Sulong AB, Furjan M. Comprehending the effect of printing orientation on the mechanical performance of polyamide-reinforced carbon fibre composites. Compos Adv Mater. 2025 Nov;34:1-9. https://doi.org/10.1177/26349833241302492
[39] İlcan H, Özkılıç H, Tuğluca MS, Şahmaran M. Interlayer mechanical performance of 3D-printed cementitious systems: A comprehensive study on operational and material parameters. Constr Build Mater. 2024 Mar;419:135463. https://doi.org/10.1016/j.conbuildmat.2024.135463

Research on Engineering Structures & Materials
www.jresm.org
MIM Research Group

Research Article

Investigation of electro-mechanical and corrosion behavior of leaded copper

Md Hasan Ruhan Rabbi [1,a], Md Abdur Rahaman [2,b], Fatema Akter [1,c], Md Mezbah Uddin [*,1,d]

[1]*Department of Naval Architecture and Marine Engineering, Military Institute of Science and Technology, 1216, Dhaka, Bangladesh*
[2]*Department of Computer Science and Engineering, BRAC University, 1212, Dhaka, Bangladesh*

Article Info

Article History:

Received 18 Mar 2025

Accepted 15 July 2025

Keywords:

Old/waste copper;
Pb inclusion;
Tensile behavior;
Hardness;
Conductivity;
Sea-water corrosion;
Microstructure

Abstract

Copper (Cu) is a well-known high-conductive material with good mechanical strength, machinability, corrosion resistance, and wear resistance. As such, Cu is widely used in industries, automobiles, aircraft, and marine applications as electrical connectors, piping systems, fittings, and heat exchanger tubes, among others. The presence of lead (Pb) in copper, widely known as leaded copper, does not behave exactly in the same manner as pure copper. Unfortunately, Pb inclusion as a trace amount in copper has not been considered by researchers and has remained neglected so far. Therefore, the present paper is an attempt to investigate the electro-mechanical and corrosion behavior of leaded copper. The mechanical properties are significantly affected by the presence of lead content. However, the impact on electrical conductivity is comparatively less pronounced than the changes observed in mechanical properties. Additionally, the microstructure demonstrates a notable geometric effect, varying with the different percentages of lead present. A progressive surge in the corrosion rate as the lead content in copper alloys increases is also found to be significant and can also be found through OEM images.

© 2025 MIM Research Group. All rights reserved.

1. Introduction

Silver, gold, aluminum, and copper are among the most widely recognized materials known for their excellent conductivity. Among these, copper and its alloys stand out as the most commonly used due to their exceptional electrical and thermal conductivity, adequate strength, corrosion resistance, machinability, formability, and wear resistance. These properties make copper highly sought after for use in electrical wires, components, and system parts across commercial, industrial, and marine sectors [1,2]. With rapid advancements in science and technology, alongside economic growth, the global demand for copper continues to rise steadily.

Consequently, there is an increasing focus on recovering copper from old or discarded products due to the dwindling availability of natural copper ores [3]. After extended operational use, waste electrical wires and electronic equipment (WEEE) present two options: recycling copper through intricate and costly extraction processes to restore properties close to the original state or reusing the discarded materials as they are for suitable engineering applications. While recycling ensures properties akin to new copper, it involves significant expense and complexity. Conversely, reusing waste copper is much cheaper, but the associated functional properties need to be thoroughly assessed to identify appropriate engineering applications [4–6]. Therefore, understanding and

*Corresponding author: mezbah@name.mist.ac.bd
[a]orcid.org/0009-0005-0742-8127; [b]orcid.org/0009-0007-4036-3147; [c]orcid.org/0009-0003-2896-8363; [d]orcid.org/0000-0001-7750-7625
DOI: http://dx.doi.org/10.17515/resm2025-767me0318rs

characterizing the functional properties of old copper is of great practical relevance to facilitate its reuse.

Copper wires and machine parts retrieved from various sources, such as buildings, industries, and ship-breaking operations, often contain trace amounts of soldering materials like lead and tin. Over time, copper and its alloys may also absorb lead (Pb) from their operational and environmental conditions [7]. Although the lead content in such cases is usually minimal, its influence on the electro-mechanical properties & corrosive nature of copper cannot be overlooked [8,9]. Numerous research studies have been conducted globally on various seas and gulfs, including the seawater of the Peruvian Port [10], seawater systems on the Norwegian Continental Shelf [11], tropical island seawater [12], and the Gulf of Mexico [13] among others. While each study presents unique findings and observations relevant to their specific regions, the Bay of Bengal has not received sufficient attention for observing the effects trace lead inclusion in copper. Thus, it becomes essential to examine how varying percentages of lead affect copper's behavior.

In this context, the present study aims to investigate such properties of leaded copper. To simulate the impact of lead on waste or old copper sourced from various applications, sample materials will be developed by casting copper with controlled lead content in the range of 1% to 8%.

2. Methods and Material

2.1. Material Preparation

Since lead and tin are the most promising copper-based alloys due to their adsorption tendency over their lifespan [1], to ascertain the influence of lead presence on copper i.e. from 0% to 8% Cu-Pb-based alloys were produced and experimented. In this context, pure lead and copper are collected from the local market by verifying their chemical purity. To facilitate identification, the pure copper sample was designated as Material-I, while the Cu-1%Pb, Cu-2%Pb, Cu-4%Pb, and Cu-8%Pb alloys were labeled as Materials-II, III, IV, and V, respectively. Material-I was procured directly in its as-cast condition from the industry, whereas Materials-II to V were developed through controlled casting where the presence of lead is controlled with the order of 2, i.e., the amount of lead is 2^0, 2^1, 2^2, 2^3 percent against the remaining copper percentage. After developing four materials, their chemical compositions were examined using the X-ray fluorescence (XRF) spectrometer of model Olympus DPO-2000-CC, and the corresponding results found are presented in Table 1.

Table 1. Mass density and chemical composition of the materials under study (mass fraction %)

Elements	Material-I pure Cu	Material-II Cu-1Pb	Material-III Cu-2Pb	Material-IV Cu-4Pb	Material-V Cu-8Pb
Cu	99.65	98.88	97.93	96.03	91.95
Pb	-	1.12	2.07	3.97	8.05
ρ(g/cm^2)	8.94	8.96	8.99	9.04	9.13

After determining the chemical compositions, the materials were shaped into various sizes suitable for experimentation using a Computerized Numerical Control (CNC) milling machine. Meticulous machining was performed to minimize the impact on surface grains. Samples were prepared in dog-bone shapes measuring 92.15 x 6 x 3 mm with a gauge length of 33 mm, adhering to ASTM standards for tensile property testing. Additionally, square samples measuring 15 x 15 x 3 mm were prepared to facilitate the evaluation of micro-hardness, electrical conductivity, and microstructural properties.

2.2. Experimental Details

The research methodology employed in this study is illustrated in Fig. 1, outlining the process from the conceptual phase to the final outcomes.

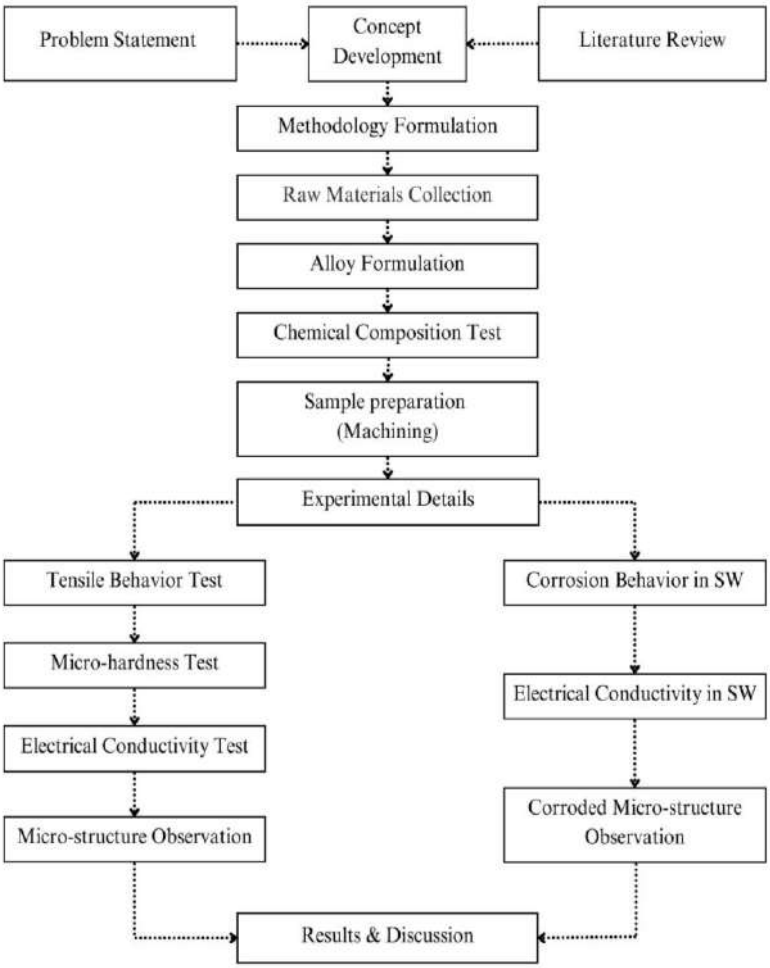

Fig. 1. Workflow diagram of experimental procedure

2.2.1. Tensile Behavior

The reuse of old or recycled copper plays a critical role in technological advancements and economic development. Consequently, characterizing the tensile properties of such materials becomes a priority. The tensile behavior of the samples was assessed using a universal testing machine (Model: Shimadzu UH-F1000 KNX). The presence of lead in recycled copper remains a significant factor of interest during tensile characterization. Although the quantities of soldering materials such as lead and tin in old or scraped copper may be minimal, their influence on tensile properties is considerable.

Copper's cubic crystal structure provides it with exceptional ductility and malleability. However, incorporating lead in varying amounts can disrupt the crystal structure by introducing dislocations, potentially altering the material's mechanical properties [14]. These changes may impact the material's strength and highlight its potential for use in specific applications where lead-contaminated scrap copper could serve as a cost-efficient alternative.

A total of 20 specimens, representing all five material groups, were prepared following the ASTM E8 standard for tensile testing. These samples were systematically categorized for experimental evaluation. Tensile tests were conducted to analyze the influence of lead content on various parameters, including ultimate tensile strength, yield strength, Young's modulus, fracture strength, toughness, and both elastic and plastic strains.

2.2.2. Micro-Hardness

During its operational lifespan, old or scrap copper often absorbs trace amounts of lead from its surrounding environment, which can result in the degradation of key properties, including hardness. Microhardness testing assesses a material's ability to resist deformation on a localized

scale. However, the limited understanding of the hardness characteristics of leaded copper in its residual state restricts its use to ordinary applications rather than more advanced engineering purposes. Therefore, determining the hardness of leaded copper is essential for exploring its potential for higher-value reuse applications. To assess the microhardness of the five study materials, square specimens were mechanically ground in sequential stages using silicon carbide (SiC) emery papers with grits of 160, 300, 600, 900, 1200, 1500, and 1800. After the dry grinding process, the specimens were wet polished with alumina paste and dried using an air blower at room temperature.

Microhardness tests were performed using a computer-interfaced Micro Vickers Hardness Tester (Model: TM HV-1000DTE) in compliance with the ASTM E384-10e2 standard. The test involved pressing a square-based diamond-shaped Vickers pyramid indenter into the specimen's surface. An applied force of 1000 gf was maintained for 10 seconds during each test. The interaction between the indenter and the material resulted in a permanent surface deformation or indentation, the dimensions of which were measured using a microscope. The measured diagonal of the indentation, combined with the applied load, was used to calculate the Vickers hardness value. Fifteen readings were taken at different locations on each of the five samples to ensure data reliability. The Vickers hardness (H_v) was determined using Eq (1):

$$H_v = \frac{1854.4 * \mathrm{P}}{d^2}\ kgf/mm^2 \quad (1)$$

where, H_v: Stress, P: Load applied in gf, d: Mean diagonal length of the indentation in μm [15].

2.2.3. Electrical Conductivity

Copper is widely recognized as one of the most commercially utilized materials due to its excellent electrical and thermal conductivity, making it ideal for various applications involving the transfer of electricity and heat. However, the effect of introducing soldering elements such as lead on copper's conductivity remains largely unexplored. Understanding how lead contamination influences conductivity is essential for identifying potential reuse applications of lead-affected copper. Electrical conductivity measurements were performed using an Electric Conductivity Meter (Model: TMD-101) with a precision of ±0.1% IACS (International Annealed Copper Standard). Initially, the conductivity of the samples was tested to establish baseline values before exposing them to a seawater environment. Subsequently, repeated measurements were taken at specific time intervals over a 36-day period of seawater immersion to observe any variations caused by corrosion. To ensure accuracy and reliability, each sample was tested at least ten times.

2.2.4. Micro-Structure

The microstructural analysis was conducted using an optical-electronic microscope (OEM), model BW-S500. Sample surfaces were first polished with silicon carbide (SiC) abrasive paper of progressively finer grit sizes: 180, 300, 600, 900, 1200, 1500, and 1800. Following the dry polishing process, the samples underwent wet polishing using alumina paste in conjunction with a water flow, and they were subsequently rinsed with acetone. After completing surface preparation, the samples were etched with a hydrogen peroxide (H_2O_2) solution. OEM micrographs were captured for all five materials, both before and after etching, to analyze their microstructures. Additionally, after a 36-day immersion in seawater, the microstructures of corroded samples were re-examined without etching to pinpoint the areas most affected by corrosion, as presented in Fig. 7.

2.2.5. Corrosion Effect in Seawater Environment

Seawater is widely recognized as a potent corrosive medium due to its composition, which includes a complex electrolyte mixture of highly concentrated salts, organic matter, suspended particles, and dissolved gases [16]. The seawater in the Bay of Bengal, as outlined in Table 2, reflects similar characteristics [17,18]. Despite being a member of the noble metal family, copper materials are not entirely resistant to corrosion in such an aggressive environment, resulting in weight loss per unit of exposed surface area over the immersion period [1,19–21].

Table 2. Contents and properties of sea water used for investigation

Parameter	Unit	Concentration Present	Analysis Method
pH	-	7.14	pH meter
Total dissolved solids (TDS)	mg/L	28000	Conductivity meter
Total suspended solids (TSS)	mg/L	48	UVS
Turbidity	mg/L	21000	Titrimetric
Sulfate (SO_4^{2-})	mg/L	1320	UVS
Dissolved oxygen	mg/L	7.29	DO meter
Electric conductivity	µS/cm	48000	Conductivity meter

To evaluate the corrosion behavior of scrap copper in a seawater environment, 50 liters of seawater were collected from Off Moheskhali Fairway Buoy (coordinates: Latitude 21°25.45' N, Longitude 20°37.82' E) in Bangladesh. This study examined the corrosion characteristics of scrap copper using the gravimetric method, which involves monitoring changes in the mass of test coupons over time while submerged in the collected seawater under static conditions. For the experimental setup, a Sartorius Entris 224-1S weighing machine (featuring a 90 mm pan diameter and a maximum weighing capacity of 220 g, with a precision of 0.1 mg) and a CG100 ABDL ultrasonic thickness gauge (measurement resolution: 0.01 mm) were employed. Measurements were recorded at specific time intervals after 1, 3, 6, 12, 18, 24, and 36 days of immersion. The degradation of mass per unit exposed surface area and the corresponding corrosion rates for each testing phase were computed using Eq (2) and Eq (3) respectively. Mass degradation of sample coupon:

$$\Delta W = \frac{W_o - W_f}{A}\ mg/cm^2 \tag{2}$$

The rate of corrosion:

$$R_{corr} = \frac{k * \Delta W}{\rho * T}\ mm/yr \tag{3}$$

where, ΔW: Mass degradation against exposed surface area in mm/cm^2, W_o: Initial mass in g, W_f: Mass measured during the investigation phase after a specific duration of submersion in g, A: Surface area of the exposed sample in the medium in cm^2, R: Corrosion rate in mm/yr, K: Unit conversion factor, ρ: Coupon material density in g/cm^3, T: Submerged phase duration in hour [22].

3. Measured Results and Discussions

3.1. Leading Effect on Tensile Behavior

The load-deflection characteristics are investigated through the standard tensile test of the copper and its leaded alloy samples, and results have been presented in Fig. 2. Here, the UTS values of pure copper in cast condition are found to be 279 MPa. The inclusion of only 1% lead in pure Cu reduces the UTS by 34.46%. Similarly, with the inclusion of 2%, 4%, and 8% lead, the UTS reduces by 41.6%, 52.19%, and 60.62%, respectively.

For pure Cu, the Young's Modulus is found to be 830.90 MPa, which reduces by 25.84%, 31.44%, 33.75%, and 32.38% with the presence of lead at 1%, 2%, 3%, and 4%, respectively. The yield strength of pure copper is found to be 271 MPa, showing a significant drop of 69.99%, 69.60%, 73.81%, and 73.88% due to the similar inclusion. Similar behavior is also found in fracture strength, which is measured to be 93.48 MPa for pure Cu and reduces by 49.39%, 47.75%, 53.17%, and 49.61% due to the corresponding percentages of lead present as shown in Fig. 2. The reduction in Tensile strength and Young's modulus with increasing Pb content in Cu–Pb alloys is primarily due to the metallurgical incompatibility between copper and lead. Owing to its extremely low solubility in the Cu matrix, lead forms soft, non-load-bearing inclusions that act as stress concentrators, reducing the alloy's mechanical performance [23]. These lead particles often localize at grain boundaries, disrupting microstructural integrity and encouraging early plastic

deformation and failure [24]. Furthermore, the weak interfacial adhesion between Pb and Cu facilitates debonding under mechanical stress, which further contributes to the reduction in both stiffness and strength [25]. The substantial difference in elastic moduli—Pb versus Cu, also leads to a pronounced decrease in overall stiffness as Pb content increases [26].

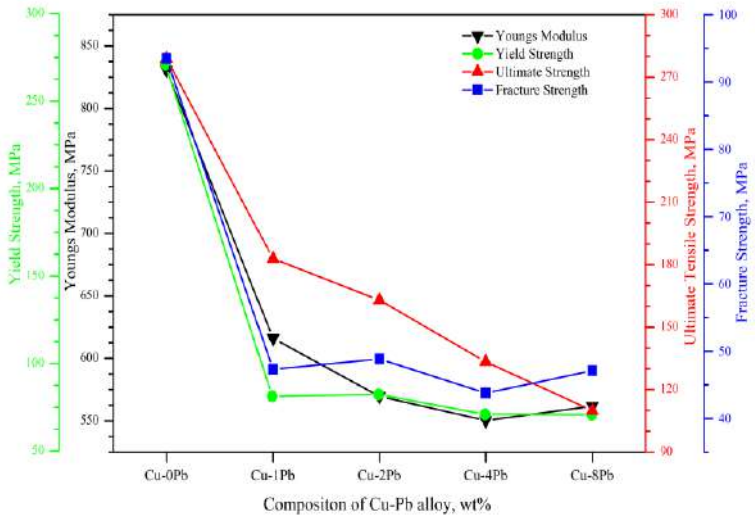

Fig. 2. Young Modulus & Tensile Strength Curves for Different Compositions of Cu-Pb Alloy

Different strain values have been illustrated in Fig. 3. In pure Cu, the elastic strain is found to be 0.324%, which reduces significantly in the presence of only 1% Pb. As the lead presence increases to 2%, 4%, and 8%, the elastic strain fluctuates by a negligible amount. On the contrary, the plastic strain of pure Cu was 9.80%, which increased to 10.78% and 9.98% with 1% and 2% Pb presence, respectively. However, it decreased to 7.23% and 4.50% with the addition of 4% and 8% Pb, respectively. The total strain level of the materials shows a similar behavior as the plastic strain.

The strain behavior of Cu–Pb alloys is influenced by the immiscibility of lead in the copper matrix. At low Pb contents, the introduction of soft Pb particles reduces elastic strain due to the disruption of the continuous Cu lattice. These inclusions create weak interfaces that impair elastic deformation capacity [1,27]. Plastic strain initially increases due to the lubricating effect of finely dispersed Pb, which facilitates dislocation motion. However, with higher Pb content, the formation of course Pb agglomerates promotes stress concentration and crack initiation, leading to a reduction in plastic and total strain [28,29].

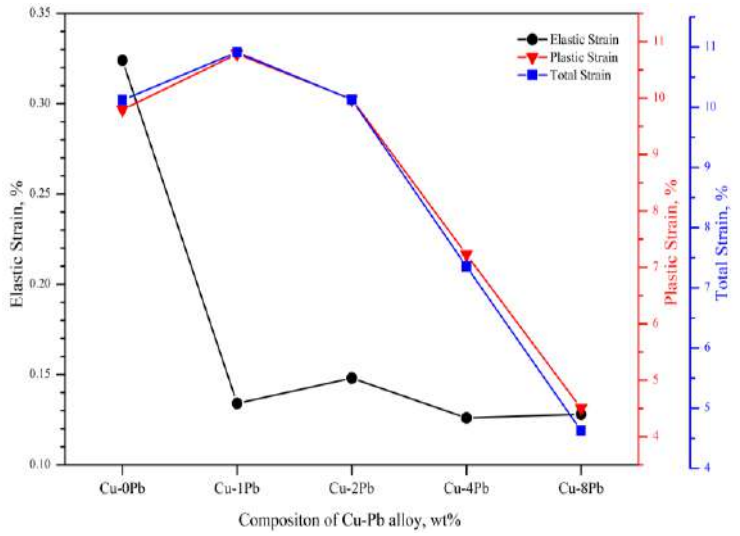

Fig. 3. Strain rate curves for different compositions of Cu-Pb alloy

The material toughness variation due to the variable composition of lead has been analyzed and is presented in Fig. 4. For pure Cu, it is found to be 24.76x10^6 J/m^3 which shows a significant reduction of 38.29%, 46.53%5, 68.94%, and 85.10% due to the presence of 1%, 2%, 4%, and 8% Pb respectively.

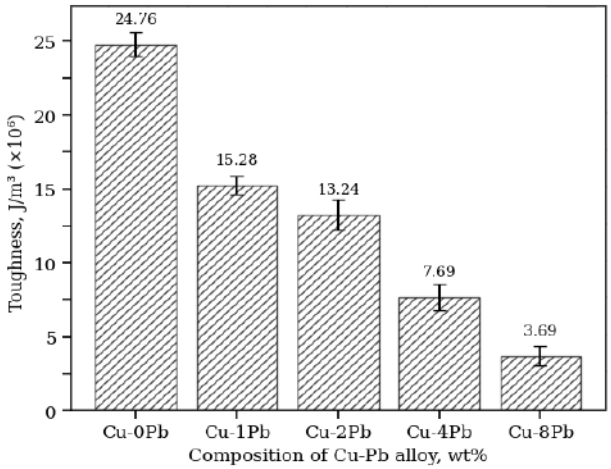

Fig. 4. Toughness variation for different compositions of Cu-Pb alloy

3.2. Leading Effect on Micro-Hardness

Measured micro-hardness values of all five samples were taken 15 times in different locations for greater reliability and standard deviation (SD) was calculated and illustrated in Fig. 5. For pure Cu, the micro-hardness value is found to be 75.65 gf/mm^2 with an SD of 1.59. Due to the presence of 1%, 2%, 4%, and 8% Pb, it shows a relatively linear decrease and was found to be 66.76 with an SD of 1.24, 55.75 with SD of 2.08, 51.77 with SD of 1.81 and 45.74 with SD of 1.35 respectively. This reduction is linked to the limited compatibility between lead and copper. Lead, being nearly insoluble in the Cu matrix, forms isolated, soft particles that do not contribute to mechanical reinforcement. These inclusions disrupt the uniform load distribution and reduce the alloy's resistance to indentation. As Pb content rises, the structural contribution of the copper phase diminishes, further weakening the material's hardness response [30,31].

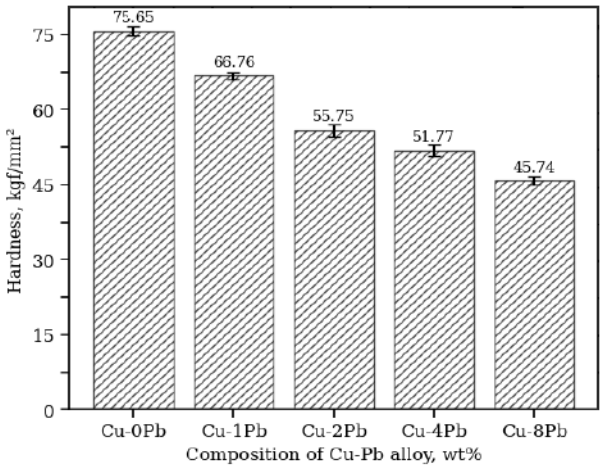

Fig. 5. Variation of materials micro-hardness for different compositions of Cu-Pb alloy

3.3. Leading Effect on Electrical Conductivity

The maximum electrical conductivity value is observed with no lead presence and is 59 MS/m. As the Pb presence increases to 1%, 2%, 4% and 8% the conductivity level decreases by 3.53%, 6.17%, 12.53%, and 18.64% respectively as shown in Fig. 6. It is noticed that the conductivity level does

not alter much with lower lead presence but varies drastically due to higher Pb content in pure Cu. This decline is attributed to the poor solubility of Pb in Cu, which leads to the formation of non-conductive lead particles. These particles disrupt the uniform metallic structure and act as scattering centers for conduction electrons, thereby reducing conductivity. While low Pb levels have a limited impact, higher concentrations introduce more scattering sites, significantly hindering electron flow. This behavior aligns with previous findings on impurity-induced conductivity loss in Cu-based alloys [32-34].

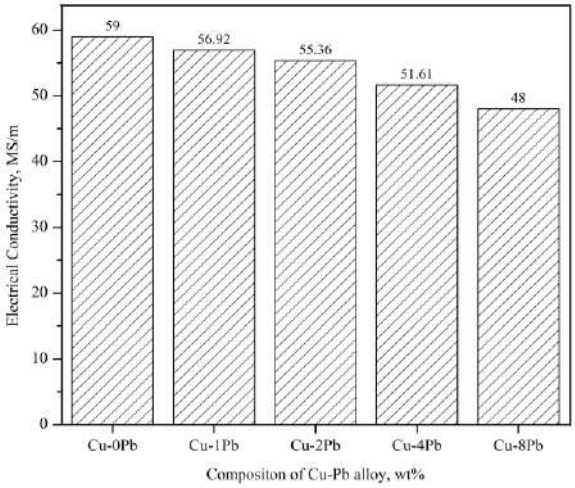

Fig. 6. Variation of materials electrical conductivity for different compositions of Cu-Pb alloy

3.4. Leading Effect on Corrosion Rate in Seawater

3.4.1. Weight Loss

There are differences in the mass loss amount per surface area exposed in the media for the immersion period amongst the sampling materials under varying lead content levels as seen in the table 1. All samples exhibit a similar pattern of weight loss as shown in Fig. 7, with the sharpest increase during the initial immersion period, indicating a more aggressive corrosion attack by seawater components.

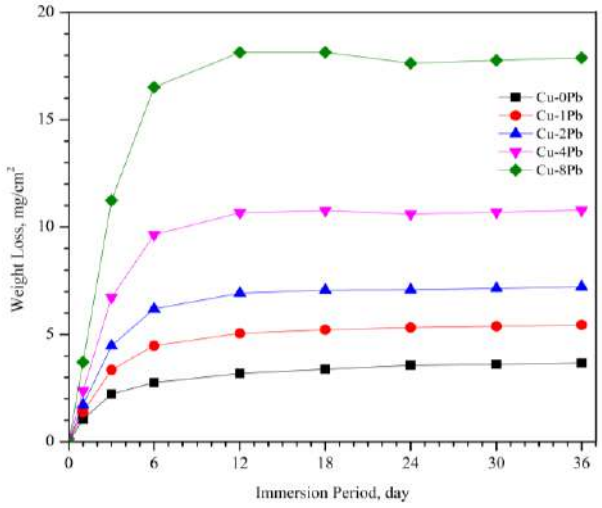

Fig. 7. Variation of materials weight loss for different compositions of Cu-Pb alloy due to corrosion in seawater

Over time, the mass loss tendencies reduce as a protective patina form, resulting in near-horizontal curves with minimal slope. (19,35) Cu-8Pb shows the highest mass loss, reaching 17.886 mg/cm^2 by 36 days, followed by Cu-4Pb (10.779 mg/cm^2), Cu-2Pb (7.225 mg/cm^2), Cu-1Pb (5.449 mg/cm^2), and Cu-0Pb (3.672 mg/cm^2). It is thus observed that the cumulative degradation of weight in seawater has been increased by 48.36% for Cu-1Pb, 96.74% for Cu-2Pb, 193.5% for Cu-

4Pb, and 387.2% for Cu-8Pb compared to pure copper (Cu-0Pb). These results highlight the significant influence of lead content on corrosion behavior, with higher lead levels drastically accelerating mass loss [35].

3.4.2. Corrosion Rate

The corrosion rate data for five copper-based samples (Cu-0Pb, Cu-1Pb, Cu-2Pb, Cu-4Pb, and Cu-8Pb) was analyzed over an immersion period of 36 days. The results illustrated in Fig. 8 indicate that all samples exhibited the highest corrosion rates after the first day of immersion, with values of 0.43013 mm/yr for Cu-0Pb, 0.56475 mm/yr for Cu-1Pb, 0.69814 mm/yr for Cu-2Pb, 0.96328 mm/yr for Cu-4Pb, and 1.48518 mm/yr for Cu-8Pb. These rates declined sharply with increasing immersion time, reflecting the formation of a protective patina that reduced the corrosion process. (19) By the end of 36 days, the corrosion rates were significantly reduced to 0.04165 mm/yr, 0.06166 mm/yr, 0.0815 mm/yr, 0.12094 mm/yr, and 0.19856 mm/yr for Cu-0Pb, Cu-1Pb, Cu-2Pb, Cu-4Pb, and Cu-8Pb, respectively. The data shows that the addition of lead content progressively increases the initial corrosion rates, with Cu-8Pb experiencing the highest rates throughout. However, the declining trend suggests that patina formation mitigates the adverse effects of higher lead content over time [36].

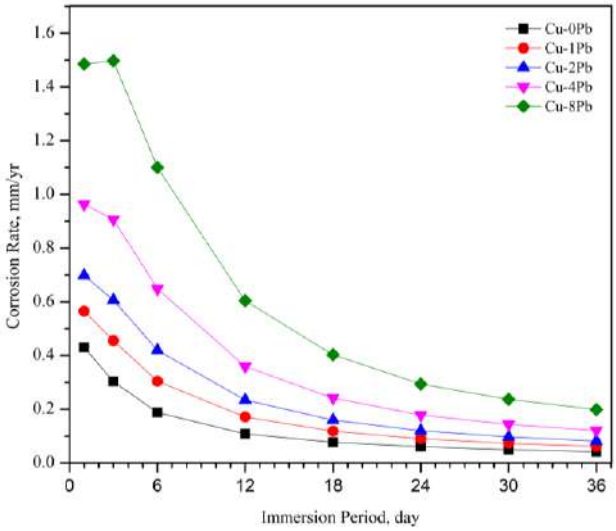

Fig. 8. Variation of materials corrosion rate for different compositions of Cu-Pb alloy due to corrosion in seawater

3.4.3. Average Corrosion Rate

The average values of corrosion rates for all five alloys are shown in the bar chart in Fig. 9. The chart demonstrates that Cu-8Pb has the highest average corrosion rate, followed by Cu-4Pb, Cu-2Pb, Cu-1Pb, and Cu-0Pb. Specifically, the average corrosion rates of these alloys are 0.62 mm/yr, 0.38 mm/yr, 0.26 mm/yr, 0.20 mm/yr, and 0.14 mm/yr respectively. This indicates a progressive increase in corrosion rates as the lead content in copper alloys increases [17,19].

Owing to the negligible solubility of Pb in the copper matrix, it precipitates as discrete soft particles that do not contribute to the formation of a continuous and adherent passive film [37]. These Pb inclusions interrupt the protective oxide layer and act as local galvanic sites, intensifying electrochemical activity in corrosive environments [38]. Consequently, corrosion tends to accelerate with increasing Pb content, compromising the alloy's suitability for marine or aggressive environments [37,39]. Therefore, Cu-0Pb shows the least corrosion, making it a highly effective material for applications where corrosion resistance is a key concern, especially in seawater environments.

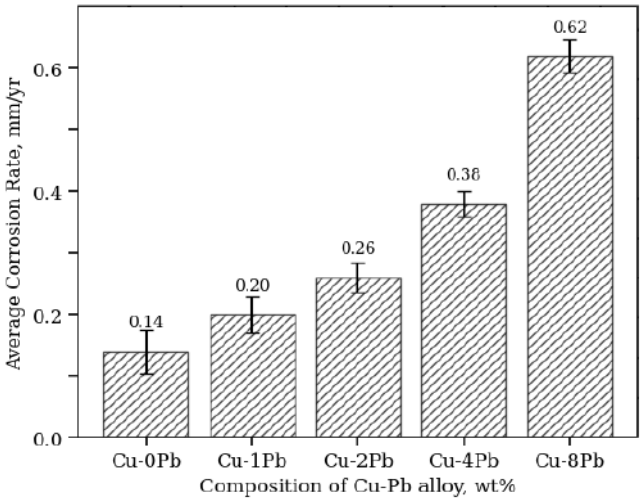

Fig. 9. Variation of materials average corrosion rate for different compositions of Cu-Pb alloy due to corrosion in seawater

3.5. Leading Effect on Electrical Conductivity in Seawater

The electrical conductivity of Cu-Pb alloys in seawater over various immersion periods is illustrated in Fig. 10 for all five samples. The initial measurements show that Cu-0Pb has the highest conductivity at 59 S/m, followed by Cu-1Pb, Cu-2Pb, Cu-4Pb, and Cu-8Pb with 56.92 MS/m, 55.36 MS/m, 51.61 MS/m, and 48.00 MS/m respectively [14]. As the immersion period progresses, the conductivity values of all alloys slightly decrease but remain relatively stable throughout the immersion period. After 36 days, Cu-0Pb maintains a conductivity of 59.71 S/m, while the alloys with higher lead content (Cu-1Pb, Cu-2Pb, Cu-4Pb, and Cu-8Pb) exhibit values of 57.02 MS/m, 55.05 MS/m, 51.68 MS/m, and 48.14 MS/m, respectively. The trends indicate that Cu-0Pb exhibits the most stable and highest conductivity throughout the immersion period, making it the most suitable material for applications where high electrical conductivity in seawater is crucial. As the lead content increases, conductivity decreases, with Cu-8Pb demonstrating the lowest conductivity, particularly after extended immersion.

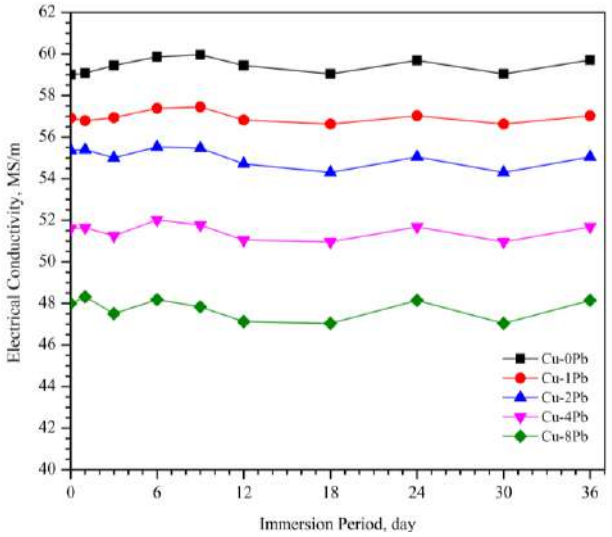

Fig. 10. Variation of materials electrical conductivity for different compositions of Cu-Pb alloy due to corrosion in seawater

3.6. Microstructure observation

3.6.1. Leading Effect on Micro-Structure–Optical Electronic Microscopic (OEM) Images

The OEM micrographs of all five-sample materials have been observed to investigate the variation in microstructures before and after etching into the solution. From Fig. 11 (i) fresh polishing marks are visible without any foreign particles in the grain boundaries [40]. From Fig. 11 (ii-v) the distributed presence of Pb is visualized as a solute in Cu solvent in contrast to Fig. 11 (i) which contributes to the alteration in micro-hardness, resistivity, and tensile behavior of the sample materials. The grain sizes are also observed to be varied clearly for all the cast alloys due to etching into the solution. It is noticed that there are definite changes in grain shape and grain boundary patterns [14]. Five such micrographs have been presented in Fig. 11 (vi-x). The dispersed Pb inclusions can enhance heterogeneous nucleation during solidification, contributing to the observed grain size reduction [1].

Figure (vii-ix) indicates that the lead atom is located in between the boundary of the grain, which is a consequence of grain boundary segregation due to Pb's poor solubility in Cu. This behavior arises from energetic preference and atomic size mismatch. The segregation leads to local distortion of the grain boundary region, influencing microstructural integrity and altering the alloy's mechanical and electrical behavior [41-43]. As the atom sizes are smaller, they can easily settle down in those locations and alter the lattice structure of copper atoms. Fig. 11 (x) shows as the lead presence is increased, the atoms of lead not only are placed to the grain boundary but also displace copper grain and occupy themselves as lead grain. This reshaping of grains may be attributed to the finding associated with electrical conductivity, in which the conductivity has decreased [44,45].

Unetched Samples

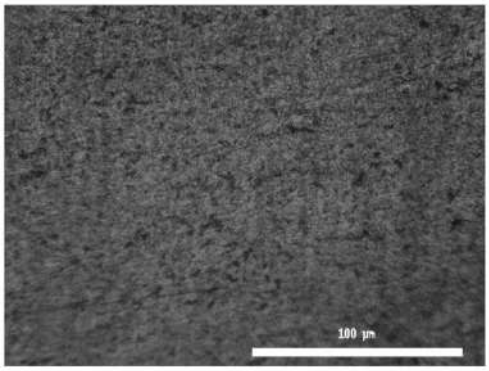

(i) Pure Cu

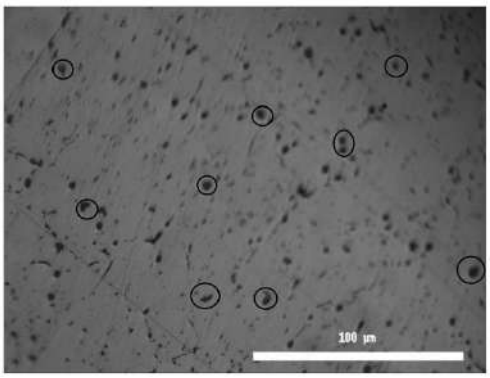

(ii) Cu-1Pb

Etched Samples

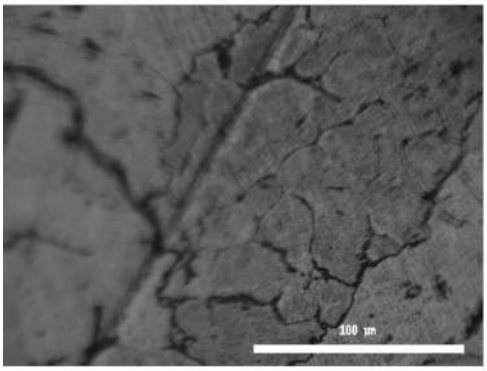

(vi) Pure Cu

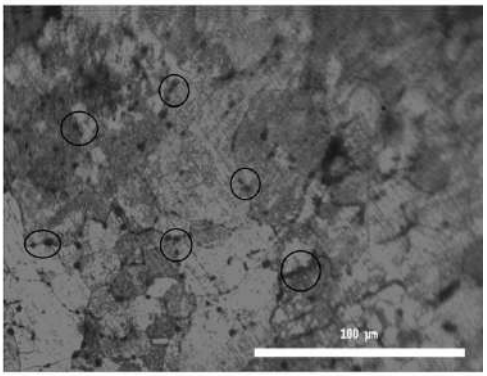

(vii) Cu-1Pb

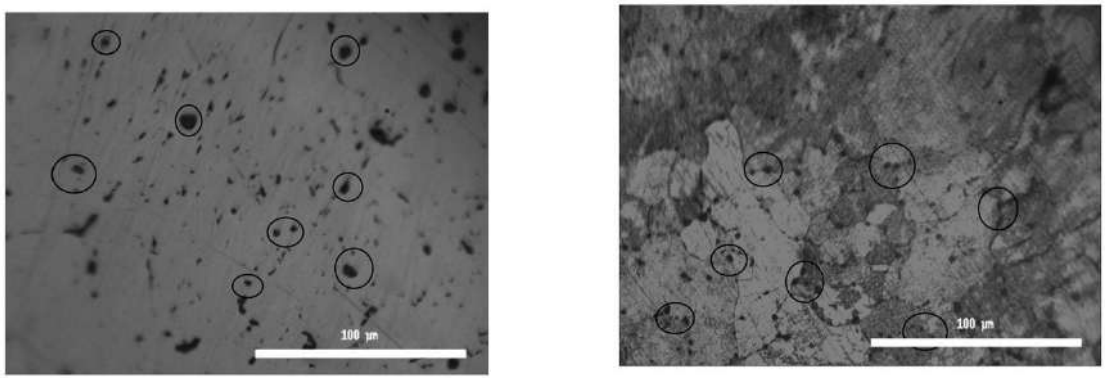

(iii) Cu-2Pb (viii) Cu-2Pb

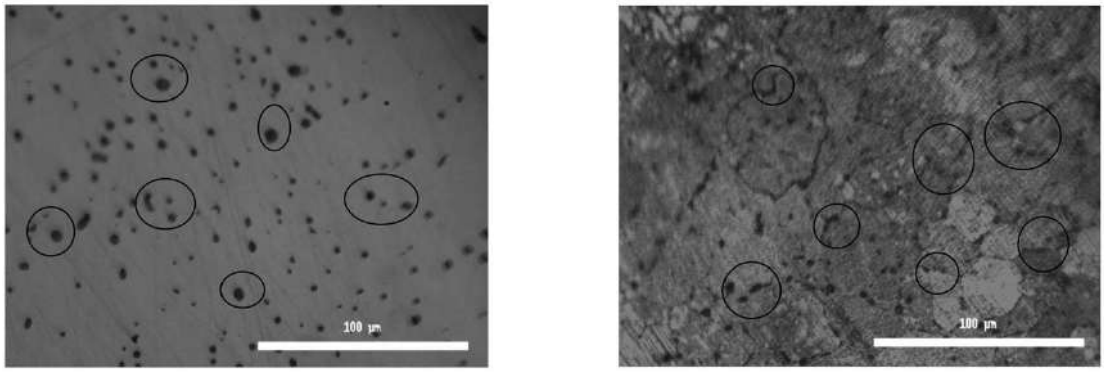

(iv) Cu-4Pb (ix) Cu-4Pb

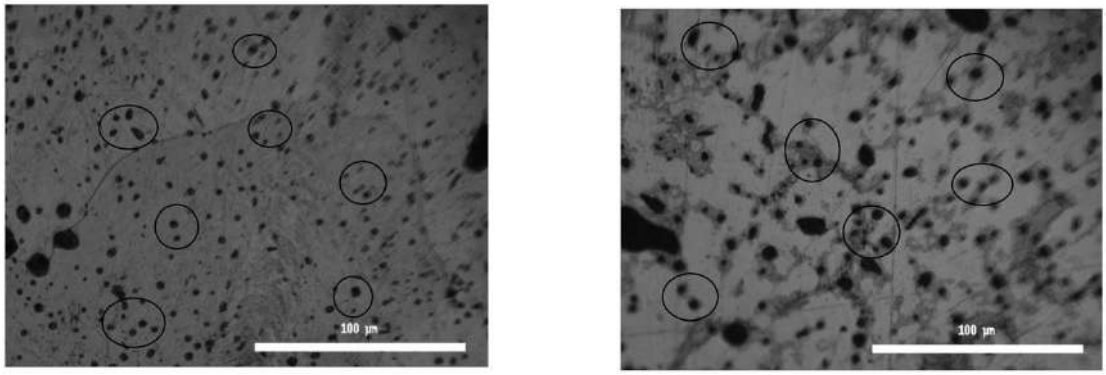

(v) Cu-8Pb (x) Cu-8Pb

Fig. 11. Micro-structure(320x) of different compositions of Cu-Pb alloy samples

3.6.2. Corrosion Effect on Micro-Structure–Optical Electronic Microscopic (OEM) Images

The OEM images of all five sample materials are observed after submersion for 36 days in a seawater environment. The polishing marks have faded away from the sample surfaces due to the global corrosion effect which eventually indicates the weight loss and corrosion rate during gravimetric observation shown in Fig. 12. These figures indicate some pits in all five sample materials with randomly nucleated orientation; demonstrating that the samples have suffered from a pitting corrosion attack [10,46,47]. Fig. 12 (iv, v) has been found to be the darkest which confirms the analysis. Darker regions in the micrographs indicate extensive surface degradation due to pitting and oxide formation, which reduce light reflectivity. This visual trend aligns with the gravimetric results, confirming that samples in Fig. 12 (iv, v) experienced the most severe corrosion. Such a correlation between microstructural contrast and corrosion rate is well-supported in the literature [48-51].

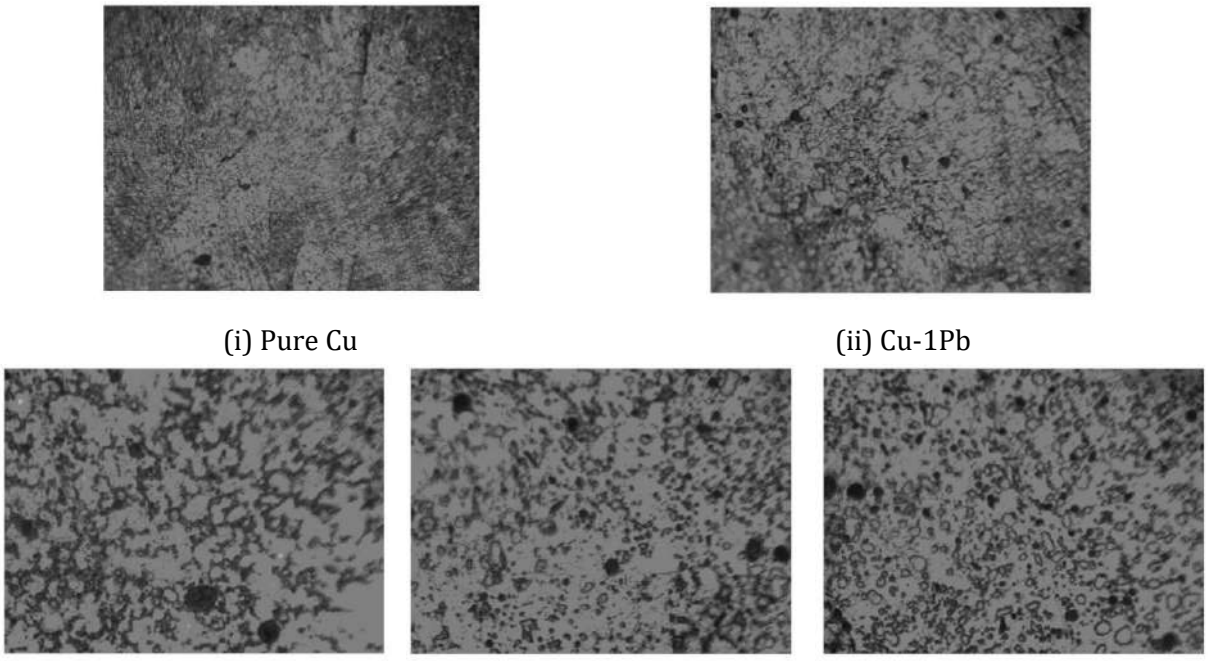

(i) Pure Cu (ii) Cu-1Pb

(iii) Cu-2Pb (iv) Cu-4Pb (v) Cu-8Pb

Fig. 12. Micro-structure(320x) of different compositions of Cu-Pb alloy samples after immersion into seawater for 36 days

4. Conclusions

A study was carried out to investigate the electromechanical and corrosive properties of copper in an attempt to assess the potential reuse of waste or wasted copper that is typically derived from old industries, buildings, and shipbreaking yards. This investigation considered the influence of trace Pb-solder additions on selected physical parameters, including tensile properties, material hardness, electrical conductivity, corrosive behavior, and microstructural characteristics.

All four leaded samples had significant changes in grain morphology, including variations in grain size, shape, and boundary features, according to the microstructural study. The main cause of these changes is lead, which serves as a microstructural modifier during solidification and the thermal processing that follows. The mechanical and physical properties of the materials were greatly impacted by these microstructure modifications. It was discovered that differences in grain structure and boundary configurations specifically affected micro-hardness. Similarly, the redistribution of lead-rich phases along grain boundaries, which probably interfered with electron flow, had an impact on electrical resistivity. Modified grain boundary cohesion and possible lead segregation at crucial points also had an impact on tensile characteristics, such as yield strength and elongation. Consequently, most mechanical properties were found to be influenced by the presence of lead. For example, even a little amount of lead content resulted in discernible decreases in yield strength and Young's modulus. On the other hand, total strain decreased significantly with decreasing lead content but was mostly constant as lead concentration rose. As lead levels increased, microhardness decreased almost linearly. In contrast, conductivity was not significantly affected at lower lead content (1–2%), making it suitable for preserving conductivity levels. After 36 days of exposure to seawater, conductivity fluctuations were minimal, while the corroded layer remained firmly adhered to the surface.

Seawater represents a chemically complex medium, influenced by factors such as pH, salinity, dissolved gases, conductivity, and various other parameters. Additionally, seawater composition can vary across different oceans, leading to diverse corrosion behaviors in copper alloys. Findings from this study conducted in the Bay of Bengal revealed that none of the five sample materials were entirely resistant to corrosion. Because of the development of patina on the materials' surface, corrosion rates were highest in the early phases and then dramatically dropped after that.

Comparing the studied copper samples to pure copper, those with higher lead contents showed noticeably higher corrosion susceptibility. Lead-rich phases served as preferred locations for localized corrosion, and the higher lead content promoted the development of micro-galvanic cells inside the copper matrix. During prolonged immersion, where the leaded alloys showed significant surface deterioration, pitting, and material loss, this behavior was most noticeable. On the other hand, under the same circumstances, pure copper showed better resistance to corrosion, retaining a more stable and protective oxide layer that prevented the corrosive medium from attacking further. These findings imply that lead reduces the overall corrosion resistance of copper alloys, even though it improves some other mechanical properties. Microstructural analyses of the corroded surfaces further corroborated the observed corrosiveness. These findings underscore the necessity of incorporating allowances for corrosion when designing products made from copper and its alloys for various marine applications.

References

[1] Davis JR. Copper and copper alloys. In: Alloying. 2001. p. 457-94. https://doi.org/10.31399/asm.tb.aub.t61170457

[2] Collini L. Copper alloys - early applications and current performance. InTech; 2012. p. 186. https://doi.org/10.5772/1912

[3] Villena M, Greve F. On resource depletion and productivity: the case of the Chilean copper industry. Resour Policy. 2018 Dec;59:553-62. https://doi.org/10.1016/j.resourpol.2018.10.001

[4] Cui J, Forssberg E. Mechanical recycling of waste electric and electronic equipment: a review. J Hazard Mater. 2003 May 30;99(3):243-63. https://doi.org/10.1016/S0304-3894(03)00061-X

[5] Fogarasi S, Imre-Lucaci F, Imre-Lucaci Á, Ilea P. Copper recovery and gold enrichment from waste printed circuit boards by mediated electrochemical oxidation. J Hazard Mater. 2014 May 30;273:215-21. https://doi.org/10.1016/j.jhazmat.2014.03.043

[6] Samuelsson C, Björkman B. Copper recycling. In: Handbook of Recycling: State-of-the-Art for Practitioners, Analysts, and Scientists. 2014. p. 85-94. https://doi.org/10.1016/B978-0-12-396459-5.00007-6

[7] Jones A, Lee R. Surface interactions between copper alloys and heavy metals in industrial environments. J Corros Sci. 2020;167:108520.

[8] Anand S, Srivatsan TS, Sudarshan TS. The influence of alloy composition on microstructure and tensile behaviour of copper-lead alloys. J Mater Sci. 1993;28:4615-22. https://doi.org/10.1007/BF00414249

[9] Paige JI, Covino BS Jr. Leachability of lead from selected copper-base alloys. Corrosion. 1992;48(12):1040-6. https://doi.org/10.5006/1.3315907

[10] Farro NW, Veleva L, Aguilar P. Copper marine corrosion: I. Corrosion rates in atmospheric and seawater environments of Peruvian port. Open Corros J. 2009;2:130-138. https://doi.org/10.2174/1876503300902010130

[11] Johnsen R. Experience with the use of copper alloys in seawater systems on the Norwegian Continental Shelf. In: Corrosion Behaviour and Protection of Copper and Aluminium Alloys in Seawater. 2007. p. 62-72. https://doi.org/10.1533/9781845693084.2.62

[12] Núñez L, Reguera E, Corvo F, González E, Vazquez C. Corrosion of copper in seawater and its aerosols in a tropical island. Corros Sci. 2005 Feb;47(2):461-84. https://doi.org/10.1016/j.corsci.2004.05.015

[13] Orozco-Cruz R, Ávila E, Mejía E, Pérez T, Contreras A, Galván-Martínez R. In situ corrosion study of copper and copper-alloys exposed to natural seawater of the Veracruz Port (Gulf of Mexico). Int J Electrochem Sci. 2017 Apr;12(4):3133-52. https://doi.org/10.20964/2017.04.27

[14] Rahman MM, Ahmed SR, Kaiser MS. On the investigation of reuse potential of SnPb-solder affected copper subjected to work-hardening and thermal ageing. Mater Charact. 2021 Feb;172:110878. https://doi.org/10.1016/j.matchar.2021.110878

[15] ASTM Standard E92-10. Standard test method for Knoop and Vickers hardness of materials. West Conshohocken, PA: ASTM International; 2010.

[16] Santos CIS, Mendonça MH, Fonseca ITE. Corrosion of brass in natural and artificial seawater. J Appl Electrochem. 2006 Oct;36(12):1353-9. https://doi.org/10.1007/s10800-006-9230-z

[17] Rahman MM, Ahmed R, Kaiser MS. Corrosion behavior of work hardened commercial copper alloys in the Bay of Bengal water environment. Khulna; 2020.

[18] Rahman MM, Ahmed SR. Corrosion behavior of copper-based heat exchanger tube in waters of Bangladesh region at varied temperature and flow velocity. MIST Int J Sci Technol. 2020 Dec;8:15-23. https://doi.org/10.47981/j.mijst.08(02)2020.196(15-23)

[19] Rahman MM, Ahmed SR, Kaiser MS. Corrosion behavior of work hardened SnPb-solder affected copper in the Bay of Bengal water environment. Adv Mater Sci Eng. 2022;2022:1-14. https://doi.org/10.1155/2022/2513391
[20] Al-Qudah MA, Al-Rawashdeh N, Al-Abdallah MM, Maayta AK, Al-Qudah MA, Al-Rawashdeh NAF. Corrosion behavior of copper in chloride media. Open Corros J. 2009;2:71-6. https://doi.org/10.2174/1876503300902010071
[21] Culpan EA, Rose G. Corrosion behaviour of cast nickel aluminium bronze in sea water. Br Corros J. 1979 Jan;14(3):160-6. https://doi.org/10.1179/bcj.1979.14.3.160
[22] Baboian R. Corrosion tests and standards: application and interpretation. ASTM International; 2005. https://doi.org/10.1520/MNL20_2ND-EB
[23] Hassan SF, Gupta M. Development of high performance magnesium composites using nano-sized and micron-sized reinforcements. J Mater Process Technol. 2005;162-163:58-63.
[24] Ahamed A, Das D. Influence of Bi and Pb on microstructure and mechanical properties of copper alloys. Mater Sci Eng A. 2016;660:68-76.
[25] Wang W, Li R, Hu W. Interfacial behavior and mechanical properties of Cu-Pb alloys. J Alloys Compd. 2013;578:288-93.
[26] Chen W, Li Z, Zhou Y. Effect of particle size and content of Pb on mechanical properties of Cu-Pb alloys. Mater Des. 2010;31(2):918-22.
[27] Zaki AI, Megahed MM. Microstructure and mechanical behavior of copper-lead alloys for bearing applications. Mater Des. 2015;65:823-30.
[28] Moridi M, Behnia AM, Khosroshahi R. Effects of soft phase inclusions on the mechanical behavior of metal matrix composites. J Mater Eng Perform. 2014;23(6):2136-43.
[29] Yuan Z, Cheng Y, Zhao J. Effect of non-metallic inclusions on fatigue and fracture properties of metal matrix systems. Metals. 2019;9(8):897.
[30] Wang X, Gao B, Zhang Y, Ma X. Effects of lead addition on microstructure and mechanical properties of copper alloys. Mater Sci Eng A. 2018;732:130-8.
[31] Zhang T, Liu Y, Chen Y, Wu S. Influence of insoluble phase distribution on mechanical behavior of copper-based alloys. J Alloys Compd. 2021;855:157487.
[32] Kim JS, Lee HW, Choe HC. The electrical and mechanical properties of Cu-Pb alloy with Pb content. Mater Sci Eng A. 2007;449-451:819-22. https://doi.org/10.1016/j.msea.2006.02.326
[33] Li H, Ma Y, Wang Y. Influence of Pb on the microstructure and electrical properties of copper matrix composites. J Alloys Compd. 2012;540:121-6.
[34] Ahn SH, Kang SK, Kwon H. Effect of Pb on the electrical and mechanical properties of Cu alloys for electronic components. J Mater Sci Mater Electron. 2000;11(4):293-7.
[35] Arjmand F, Adriaens A. Influence of pH and chloride concentration on the corrosion behavior of unalloyed copper in NaCl solution: a comparative study between the micro and macro scales. Materials (Basel). 2012 Nov;5(12):2439-64. https://doi.org/10.3390/ma5122439
[36] Rahman MM, Chowdhury RH, Rafi TA, Ahmed SR. Corrosion resistance of scraped copper in velocity varied inland water of Bangladesh. Malays J Compos Sci Manuf. 2024 Mar;13(1):25-35. https://doi.org/10.37934/mjcsm.13.1.2535
[37] Peng DQ, Ke W, Dong CF. Effect of Pb on corrosion behavior of Cu alloys in seawater. Corros Sci. 2009;51(3):526-34.
[38] Pourbaix M. Atlas of electrochemical equilibria in aqueous solutions. Houston: NACE Int.; 1974.
[39] Abd El Rehim SA, Hassan HH, Mohamed NF. Electrochemical behavior of copper in chloride solutions and its corrosion inhibition by some amino acids. Mater Chem Phys. 2001;70(1):64-72. https://doi.org/10.1016/S0254-0584(00)00468-5
[40] Bernal JD. The complex structure of the copper-tin intermetallic compounds. Nature. 1928;122(3063):54. https://doi.org/10.1038/122054a0
[41] Wang H, Wang C, Liu C, Yang Y, Liu Z, Zhang Z. Grain boundary segregation and embrittlement in metallic alloys. Prog Mater Sci. 2015;71:1-49.
[42] Choi P, Borchers C, Richter A, et al. Atomic-scale analysis of solute segregation at grain boundaries in metallic alloys. Acta Mater. 2010;58(7):2310-23.
[43] Randle V. Mechanisms of grain boundary segregation and their effects on intergranular corrosion. Corros Sci. 2004;46(1):211-25.
[44] Gupta SP, Rathor D. Kinetics of growth of intermetallics in the Cu-Sn system. Int J Mater Res. 2002 Jun;93(6):516-22. https://doi.org/10.3139/146.020516
[45] Fujiwara H, Nishimoto T, Miyamoto H, Ameyama K. Microstructure and mechanical properties of Cu-Sn alloy with harmonic structure. In: Proc 8th Pacific Rim Int Congr Adv Mater Process. 2013. p. 2455-60. https://doi.org/10.1007/978-3-319-48764-9_304
[46] Kuźnicka B, Junik K. Intergranular stress corrosion cracking of copper - a case study. Corros Sci. 2007 Oct;49(10):3905-16. https://doi.org/10.1016/j.corsci.2007.05.014

[47] Zhang YN, Zi JL, Zheng MS, Zhu JW. Corrosion behavior of copper with minor alloying addition in chloride solution. J Alloys Compd. 2008 Aug;462(1-2):240-3. https://doi.org/10.1016/j.jallcom.2007.08.008
[48] Fontana MG. Corrosion engineering. 3rd ed. New York: McGraw-Hill; 1986.
[49] Zhang X, Wu H, Liu G, Hu J. Effect of seawater environment on corrosion behavior of different metals. J Mater Res Technol. 2017;6(4):362-8.
[50] Subramanian B, Ravichandran K, Narayanasamy B. Correlation between corrosion rate and optical/electron microscopy features. J Rare Earths. 2008;26(5):673-6.
[51] Wang L, Li X. Morphological and microstructural characteristics of pitting corrosion in steels. J Mater Sci Technol. 2019;35(9):1987-95.

Research on Engineering Structures & Materials
www.jresm.org

Research Article

Packaging optimization for reducing bruising in pears

Asma Mecheter [*,a], Faris Tarlochan [b]

Department of Mechanical and Industrial Engineering, Qatar University, Doha P.O Box 2713, Qatar

Article Info

Article History:

Received 13 Mar 2025

Accepted 23 July 2025

Keywords:

Pear;
Bruising;
Cushioning;
Plastic;
Finite element analysis;
Post-harvest

Abstract

Economics losses due to fresh produce damage is considered a serious issue in the agriculture industry. Fruits like pears are most susceptible to damage due to their soft and sensitive skin. In this study, rosemary pear 3D finite element (FE) model was established through 3D scanning and reverse engineering methods. Elastic-plastic material properties of pear including modulus of elasticity, density and bio-yield point were measured through mechanical compression test. The FE model was validated with physical bench experimental drop test. A mesh sensitivity analysis was performed in order to ensure optimal balance between results convergence and computational time. A polylactic acid (PLA)-based design structure was proposed in order to serve as a cushioning package for pears. This design has reduced bruising in pear by 65%. Design of experiments (DOE) was performed to investigate the influence of design process parameters in both responses bruising volume and structure internal energy. Response surface methodology results have revealed that circular thickness of structure is responsible for bruising volume. Thinner circular rings would result in minimized localized inner fruit stress. A moderate structural thickness is recommended to be adopted as thicker structures would result in higher internal energy which will be transferred to the fruit as bruising. The proposed design can be extended to be used as a multi cell packaging to accommodate multiple fruits in the same package ensuring the protection for each pear individually. The design can be recyclable, reused, and remanufactured as it is made from PLA. Design practical implications and supply chain insights were addressed along with future research directions. Fresh produce logistics and operations should consider the adoption of such packaging in order to minimize economic losses and extend shelf-life of fruits.

© 2025 MIM Research Group. All rights reserved.

1. Introduction

Substantial economic losses happen in the agriculture industry due to fresh produce bruising. About 30% of fruits suffer from bruising problems in the post-harvest stage [1]. Bruising and mechanical damage usually happen due to several factors including impact, vibration, and puncture during the post-harvest supply chain. Fruit with soft texture such as pears are highly likely to get damaged making them particularly perishable and vulnerable during processing and handling operations. Bruising in fruits is defined as the subcutaneous tissue failure without skin rupture where affected areas will appear discolored [2]. Current practices investigate bruising related issues through laboratory test through various approaches. These approaches include pendulum test, spherical impactor test, x-ray and CT imaging, etc. Drop impact test is the most popular one among the mentioned tests [1]. Utilizing finite element analysis (FEA) to simulate the drop impact test for a wide variety of fruits assess in providing insights into bruising and damage characteristics. FEA enables the simulation of fruit drop impact at different predetermined heights, impact collision surfaces, angles and conditions[3]. Furthermore, FEA allows the analysis of energy distribution, stress distribution, damage and bruising prediction. Therefore, FEA tools can be

*Corresponding author: am1508546@qu.edu.qa
orcid.org/0000-0002-1021-4462; [b]orcid.org/0000-0002-0405-145X
DOI: http://dx.doi.org/10.17515/resm2025-755ma0313rs

leveraged in order to test different drop impact conditions for the pear utilizing cushioning packages.

Research on analyzing pear fruits response to collision is being done through hyperspectral imaging [4,5], X-ray and computed tomography [6], machine learning and soft computing methods[7,8] and by finite element analysis [9–13]. In this work, we have utilized finite element methods to test the pear drop and obtain bruising related data. Yet, the main purpose of this paper is not to only gain insights about fruit bruising but rather propose packaging solutions and cushioning design for pear packaging. Stropek et al. [14] have studied the relation between bruise susceptibility and internal energy with impact velocity of two pear cultivars namely 'Xenia' and 'Lukasowka'. The study has shown that internal damage energy and bruise susceptibility increase with the impact velocity. Also, energy dissipation mainly occurs during the initial impact stage. Yousefi et al. [13] have predicted the bruise damage in Natanz pear at three different ripeness levels, different platforms and impact angles. Authors have noticed that the maximum pear bruising happens when dropping the fruit at 90 degrees. This is because the weight force and falling path are in the same direction. It was found out that the maximum stress usually occurs in regions of minimum radius of curvature while minimum stress occurs at maximum radius curvature of pear. The bruise susceptibility of Ankara pear variety was investigated in Celik's study where it was found out that dropping the fruit on rubber-based platforms yields in the least bruising [10]. Li et al. [12] have mentioned that pressure area and average pressure are factors associated with severity of bruising. Authors have concluded that the total contact stress area distribution of pears is always larger than measured damage area.

Packaging is critical in the post-harvest operations of fresh produce, which serves as primary protection for fruits subject to different loading conditions. This is why studying the interaction between packaging and fresh produce is crucial in order to minimize bruising and maintain the high-quality fresh produce delivery to consumers [15]. The choice of packaging material is crucial to reduce probability of bruising in contact with the material [1]. Utilizing polyethylene-based partitions boards withing folding plastic baskets has proven its efficiency in reducing bruises in Hongmeiren oranges [16]. Foam net packaging for peaches has outperformed other materials like foam sheets, polypropylene trays, and corrugated fiberboard in terms of protective capacity, sustainability and economic impact [17]. However, foam and paper-based packages are more likely to absorb excessive amount of moisture which will limit their capacity for long-term storage [18]. Furthermore, foam packages may not offer the same level of protection, durability, and thermal stability in comparison to plastic-based packages, especially for highly sensitive fruits during rough handling conditions [19]. Studies have shown that foam material can result in more bruising to fruits. This is why, plastic is highly recommended to be used in fresh produce packaging, as it is impact-resistant, customizable, recyclable and reusable. Mecheter et al. [20] have suggested the use of recycled water bottles polyethylene terephthalate (PET) through a spiral design structure where bruising in pears was reduced by 50%. Current literature lack packaging designs made from biodegradable material to provide cushioning for pears in terms of long-term effectiveness and sustainability in reducing bruising. Therefore, more research is needed on plastic-based fruit packaging and customization of packaging designs which would provide holistic insights on fruit-packaging behavior [21]. This paper is trying to address the following question: How can design of cushioning packaging using 3D printed biodegradable materials, minimize bruising in pears ? The objective of this paper is to use reverse engineering and mechanical testing methods in order to test a real pear which will be later assessed with a pear physical model. Furthermore, we propose a polymer-based fruit packaging design that will provide cushioning for pears during transportation. Another objective of this paper is to investigate different geometric parameters and how they influence bruising in fruits through design of experiment and response surface methodology.

2. Materials and Methods

The methodology used in this paper follows a systematic approach, as outlined in the following sections.

2.1 Determination of Fruit Physical and Mechanical Properties

2.1.1 Reverse Engineering Modeling

Fresh pears Pyrus communis, variety "Rosemary" was purchased from the market and directly transported to the laboratory at Qatar University. The average weight of the sample was 128 ± 1.74 grams. The pear was 3D scanned with a lidar scanner through mobile phone application to capture the 3D point cloud of the pear surface. Blender software was used to remove the redundant points from the point cloud. MeshMixer software was used to build the fruit solid model out of the mesh model. The actual, mesh and solid models of the fruit are shown in Fig. 1. The 3D scanned fruit was cut into half where the length and width of the pear were measured by a vernier caliper. The length and width dimensions were also measured in SolidWorks as shown in Fig. 2. We can consider that the 3D scanning process was precise as the error for width and length dimensions 0.6% and 0.3% respectively.

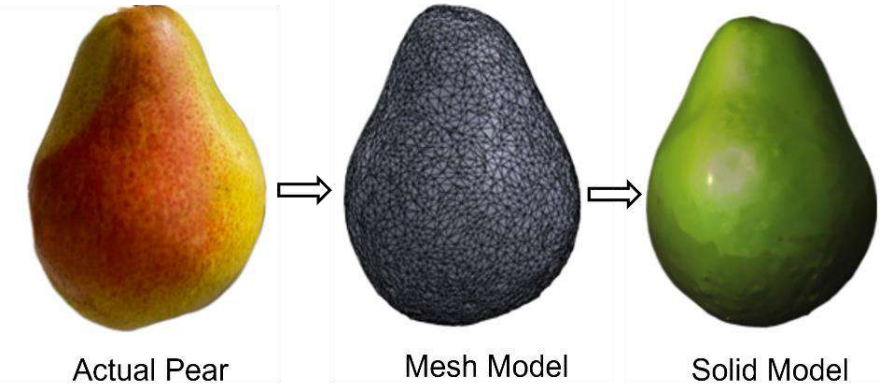

Fig. 1. Reverse engineering modeling procedure

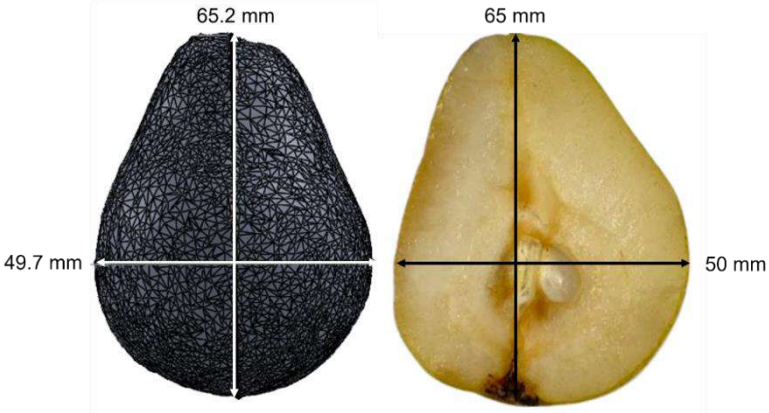

Fig. 2. Dimensions of pear 3D model and physical model

2.1.2 Determination of Fruit Mechanical Properties

Compression test was performed in order to determine the physical deformation behavior and mechanical properties of the pear. Cylindrical-shaped specimens were extracted from fresh pears purchased from the market. Specimens used in the test have dimensions of 20 mm diameter (d) and 20 mm height (h) as shown in compression test setup in Fig. 3. The specimen is compressed between two metallic plates, where the upper plate applies force to the specimen.

The test was performed using the universal materials testing machine (50 kN) LR50K Plus. The speed of the compression test was set to 3 mm/min as per ASAE S268.4 W/Corr. 1 DEC2000 which suggests a range of 2.5-30 mm/min as the nominal compression velocity for fruits and vegetables [10]. Based on this experiment, modulus of elasticity, strength and other mechanical properties were determined while physical parameters including mass and density were obtained by weighing and liquid exchange methods. Other parameters that were used for contact materials were obtained from ANSYS product material library as shown in Table 1 [22]. Bio-yield is the point which beyond the fruit permanent deformation will take place. Pears exhibit non-linear viscoelastic behavior under deformation. Viscoelasticity is time-dependent and complex phenomena where it would be difficult to simulate bruising (permanent formation) and nonlinearity at impact. Therefore, we have adopted in our study permanent plastic deformation as adopted in the literature [10]. An isotropic material model was used for the pear assuming a homogeneous structure of fruit flesh and skin [23].

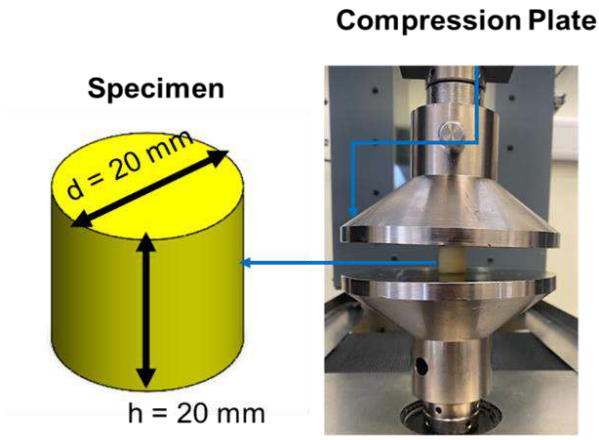

Fig. 3.Compression test setup

Table 1. Physical properties of materials

Material	Density (kg/m^3))	Modulus of elasticity (MPa)	Poisson ratio	Tensile Point (MPa)	Bio-yield Point (MPa)
Pear (Rosemary)	957 [a]	2.521 [b]	0.41 [c]	0.61 [d]	0.47 [d]
PLA	1240	3250	0.35	-	-

a, Density data is obtained from experiment. b, Young's modulus is defined as the ratio of stress to strain in the elastic region (Experimental). c, Poisson's ratio [11]. d, Compression properties.

Fig. 4 shows the engineering stress-strain curve of compression test of rosemary fruit. Stress (σ) is defined as the applied force over the cross-sectional area, where strain (ε) is the ratio of material change of length to its original length. Equations of stress and strain are shown in equation (1). We can see that the compression experiment includes the linear elastic stage, plastic stage and failure stage. In the linear elastic stage, stress and strain are proportional. When applying the compressive load, the stress gradually increases linearly till the graph deviates from the straight-line behavior. This is where permanent deformation takes place and bio-yield starts which is shown in the yellow dashed line. The pear undergoes permanent deformation, and stress start to decrease as the material softens in the plastic deformation stage. The tensile point which is marked in red indicates the maximum stress that material can withstand before total failure. In the failure stages, tissue of pear fails due to excessive compression.

$$E = \frac{\sigma}{\varepsilon} = \frac{F/A}{\Delta L/L} = \frac{F\,L}{\Delta L\,A} \quad N.m^{-2} \tag{1}$$

Where E, F, A, ΔL, L, refer to modulus of elasticity, compressive force, cross-sectional area, displacement and initial length of specimen respectively.

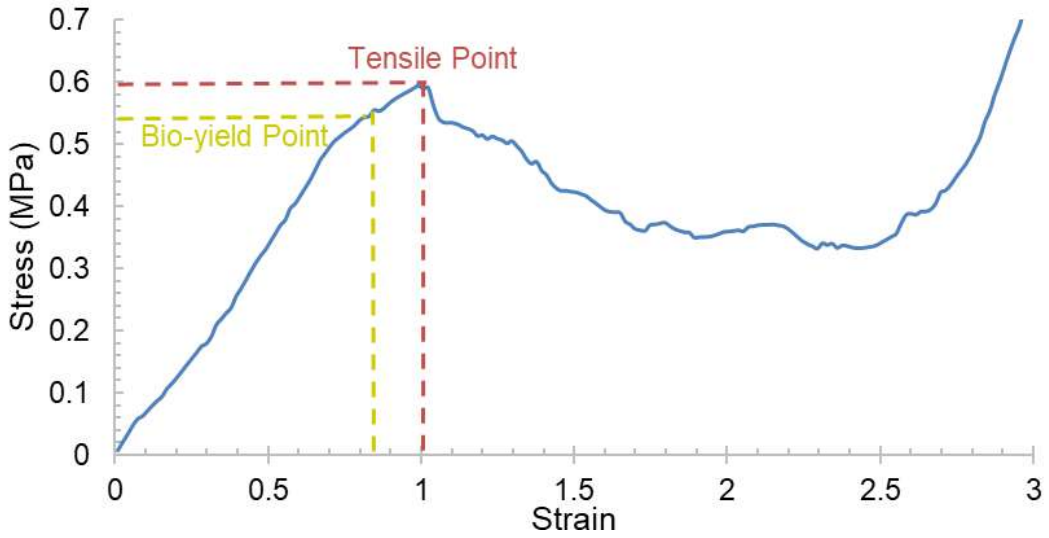

Fig. 4. Stress-strain curve of rosemary pear obtained from compression test

2.2 Finite Element Setup

In this study, a drop test method was utilized in order to evaluate bruises of the pear. Fruit drop simulations were performed in Explicit Dynamics ANSYS, Inc. Products 2021 R2 version software. Fig. 5 shows a schematic of the fruit drop simulation setup. The initial position of the fruit was set close to the rigid surface to reduce computational time and enhance calculations efficiency[3]. The contact type between the pear model and the rigid surface was determined as automatic, restricting the displacement of the rigid floor. A predetermined drop height of 0.5 meters was applied, in addition to the standard earth gravity effect. The initial velocity of the fruit can be calculated through the free fall formula $v = \sqrt{2gh}$ where g and h stand for gravity acceleration and fall height, respectively. Setting the solution, internal energy, equivalent von-mises stress and related deformation behavior were taken into account, and the simulation scene was set to 0.02 seconds in order to fully capture the dynamic response of pear during falling collision.

2.2.1 Mesh Sensitivity Analysis

Mesh is a critical phase in finite element modeling which involves dividing the geometric model into small volume units [24]. Increasing mesh element size increases the accuracy of the results, however, it leads to very long computational time.

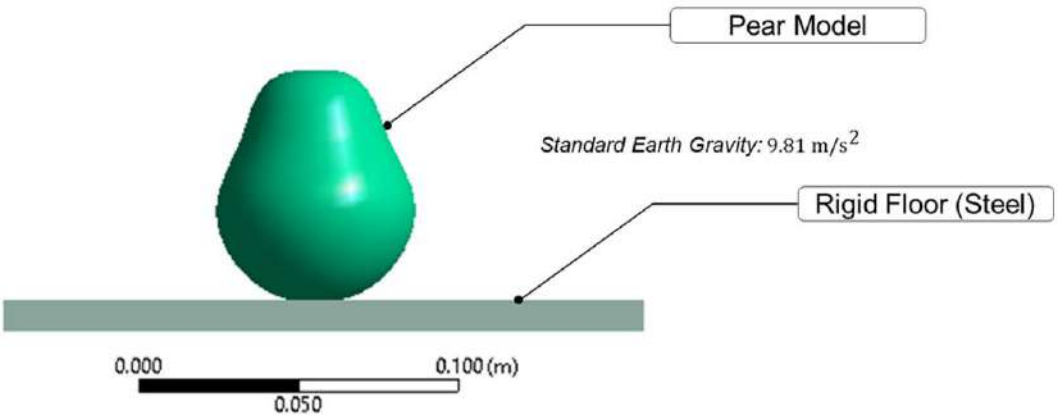

Fig. 5. Simulation setup

This is why a mesh sensitivity analysis was conducted in order to analyze the trade-off between mesh element size, results convergence, and computational time. Table 2 shows the influence of decreasing the element size on several factors. As we can see, the number of nodes and elements increase with the decrease of element size, meaning accuracy of model is improving. The stress values convergence as the mesh size increases. An element size of 1.5 mm is adopted for all simulation instances of this study.

Table 2. Influence of Element size on Elements, Nodes, and Equivalent Stress

Element Size (mm)	Elements	Nodes	Computation Time (mins)	Equivalent Von Mises Stress (MPa)
5	9874	6433	1	0.34
4	17848	12520	1.5	0.35
3	41127	27700	2	0.37
2.5	62494	39972	4	0.39
1.9	140347	94047	9	0.44
1.7	178211	117070	10	0.45
1.5	255003	170107	20	0.48
1.3	472981	323639	25	0.48

2.3 Bruising

The bench experimental bruise volume is calculated through obtaining the dimensions of bruise depth (h_b), and bruise diameter (d) (major and minor width: w_1 and w_2) after 48 hours after fruit drop [25]. Fig. 6 shows the measurements of bruise diameter and depth of the pear during bench experiment. The following formula was used to calculate bruise volume [26]:

$$BV = \frac{\pi}{6} d^2 h_b \tag{2}$$

Where d and h stand for bruise diameter and bruise depth respectively.

The bruise volume obtained from finite element simulation is determined through the extraction of all stress nodes where stress have exceeded the bio yield (0.4 MPa). The bruise percentage is identified as the ratio of bruised nodes to overall nodes. Bruise percentage is then multiplied by the pear volume to get bruise volume. Values of bruise volume are typically small values, as reported in the literature [20]. However, any minor variation in bruise volume calculations could significantly affect the fruit shelf-life and quality.

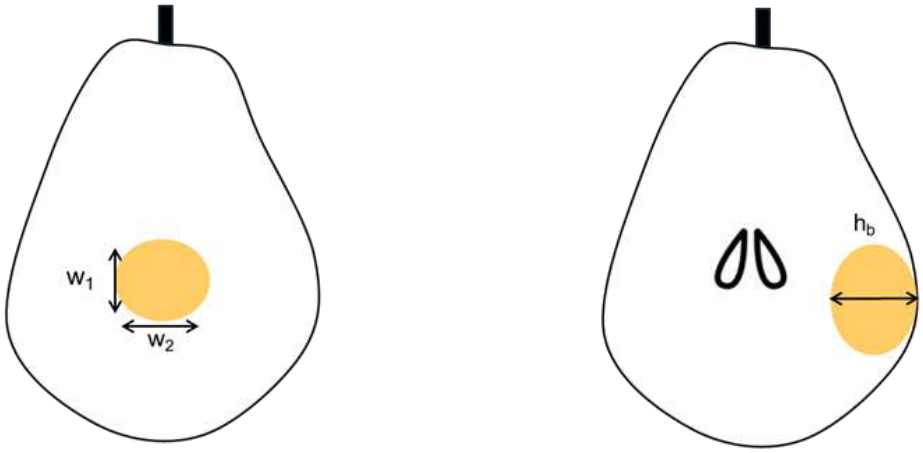

(a) (b)

Fig. 6. Bench experiment bruise measurements: a) bruise diameter b) bruise depth

2.4 Proposed Packaging Design

The pear drop test presented in this study is validated with experimental setup in terms of bruise volume. Thus, this model can be used to propose a packaging design that can provides protection for pears from mechanical damage and external forces during transportation. The proposed packaging design is shown in Fig. 7. The design has a rigid triangular frame which encloses the fruit to prevent its direct contact with external surfaces or objects.

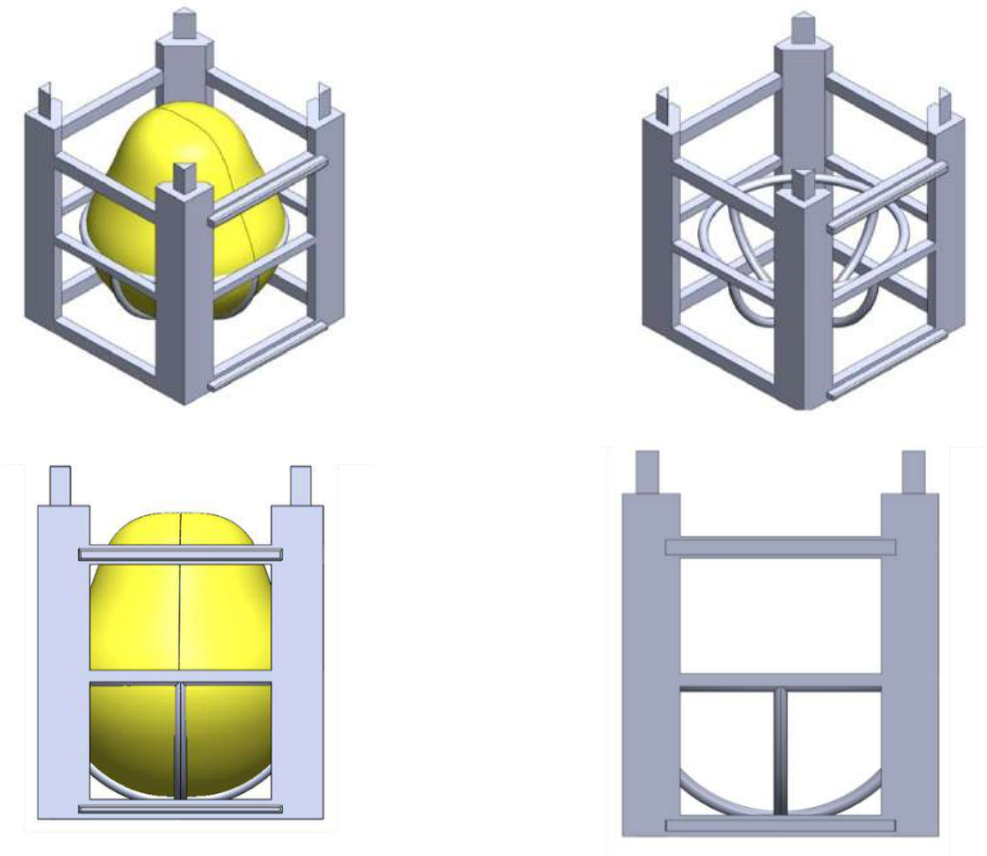

Fig. 7. Front and side view of proposed design

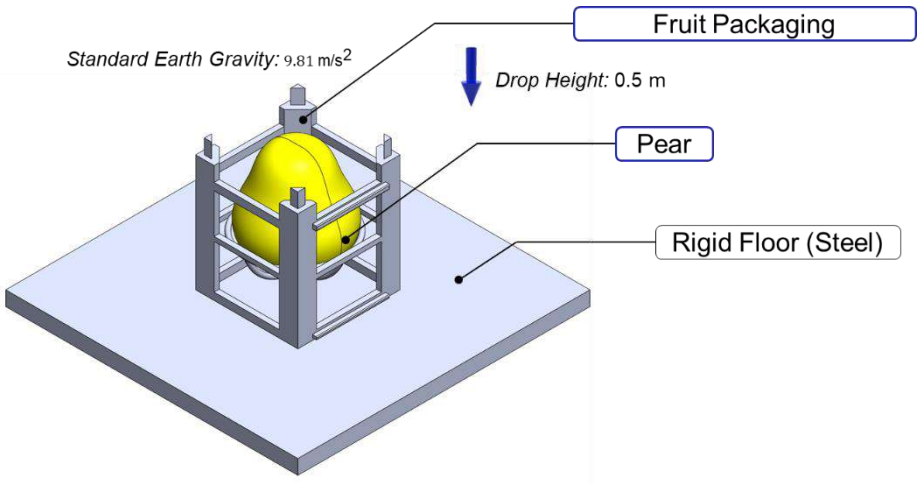

Fig. 8. Boundary conditions and simulation setup

The design includes rounded thin circular rings that can serve as shock-absorbing mechanisms. These rings would minimize stress on fruit. Furthermore, the design included holes, slots and pins to facilitate stacking, assembly and disassembly for modular units during transportation and

handling operations. The assembly of the design with the pear and steel base was done in SolidWorks. The simulation setup of the FE model is similar to the setup presented in section 2.2. The effect of standard earth gravity was taken into consideration. The fruit along with the packaging structure were set to drop at 0.5 meters height on the rigid steel base. A schematic of the finite element model setup is illustrated in Fig. 8.

2.5 Response Surface Methodology

The proposed design proved its efficiency in reducing the bruises in pear. Therefore, a design of experiments is carried out in order to investigate the influence of design variables on bruise behavior. Response surface methodology is utilized to evaluate the bruising behavior subject to different design geometrical changes. Design of experiments is a robust statistical-based tool that helps analyze the effect of process parameters on specified properties[20,27].

Table 3. Factor levels for experimental design

Factor	Index	Level		
		-1	1	Unit
Structure Thickness (mm)	S_t	3	5	(mm)
Circular Thickness (mm)	C_t	3	7	(mm)

In this paper, central composite design (CCD) methodology is used that can build a second order polynomial without the need to use full factorial design. Two main factors are used in this experimental design: circular thickness (C_t), and structure thickness (S_t) as shown in Fig. 9. The factors along with their levels are presented in Table 3. The range of (C_t) and (S_t) were set to vary between 3mm to 7mm so the structure can remain lightweight. The influence of varying these factors is evaluated in order to optimize two responses: bruise volume (BV) and structure internal energy (IE). The pear bruising is directly related to the fruit shelf-life which we aim to extend. The internal energy of the structure measures the ability of structure to absorb impact so it is not transferred to the fruit in form of bruising. The statistical software Minitab is utilized to build the response surface methodology model. Nine different runs will be conducted for geometrical design combinations. The designs are modelled in the CAD modeling software SolidWorks. Finite element simulations will be conducted on ANSYS at pre-determined drop height of 0.5 meters.

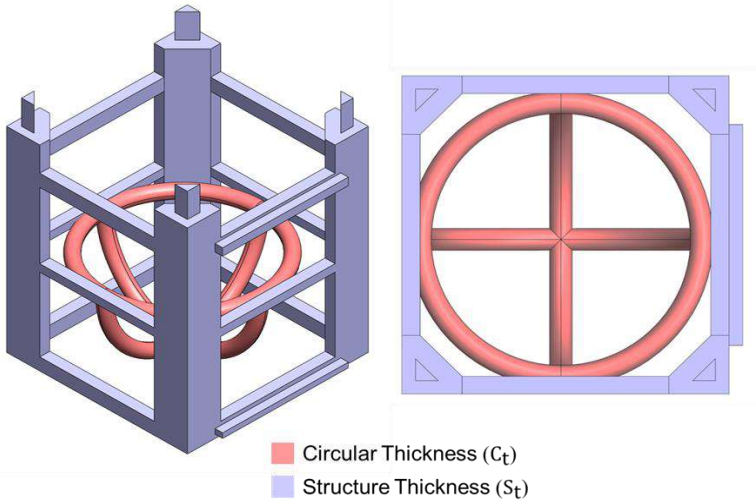

Fig. 9. Isometric view and top view of structure

3. Results

3.1 Experimental Validation (Drop Test)

The collision between the fruit and the contact steel plate after the fall was divided into the following stages: break-off contact, bounce and collision bruising as shown in Fig. 10. First, during

the break-off contact, we can notice localized stress concentration at the pear-surface contact area. At the bounce phase, energy is distributed through the fruit where stress waves travel which will lead to internal damage. Finally, during the collision bruising, the fruit experiences residual stress, leading to a permeant tissue deformation, mainly due to the conversion of kinetic energy into plastic deformation. This process results in bruising where the material goes under irreversible deformation.

To further evaluate the accuracy of the fruit finite element model, bruise volume of bench experiment was compared to bruises obtained from simulations yielding in 19% error between FEA simulated bruise volume and experimental bruise volume with values of 1.45E-06 $m^3$and 1.18E-06 m^3 respectively. We have obtained a percentage error of 19% which is in line with range of values presented in the literature [25,28]. We can notice that the simulated bruise volume is slightly higher than the simulated bruise volume. This is because the bruise on the fruit cannot be immediately recognized by the naked eye after impact. The bruise is not recognized clearly until 24 hours at least have passed after the impact test [20,25]. Bruise volume in finite element simulations is obtained through extracting the nodes where which bio-yield limit is exceeded. Using ANSYS, the bruised regions were combined and extracted to CAD software in order to calculate mass, volume of bruised volume (Fig. 11).

3.2 FEA and RSM Results

Simulation instances were generated by varying both factors structure thickness and circular thickness in order to analyze their impact on bruise volume and structure internal energy. To assess the bruising in the fruit, it is crucial to investigate the absorbed internal energy by the package structure and optimize the impact absorption to achieve fruit protection. Table 4 lists the fruit and structure related energy, stress, and bruise details. We can notice that with the increase of structural thickness, the stress of the pear increases linearly. Increasing the structural thickness beyond 4 mm transfers more impact force to the fruit, leading to more bruising.

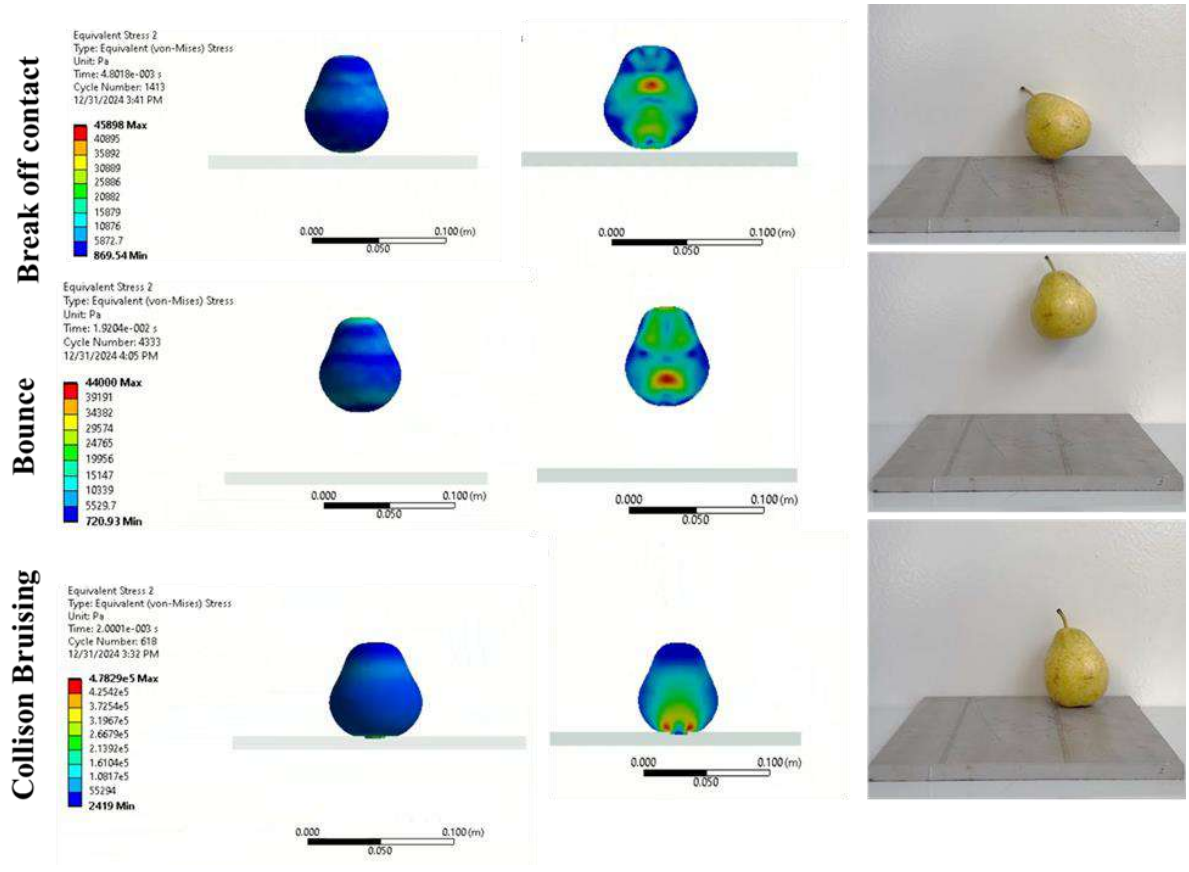

Fig. 10. Model validation: finite element drop test versus camera frames for fruit falling

Circular thickness (C_t) seems to have a negative impact on fruit bruising. Although increasing the thickness of circular rings will reduce localized stress and absorb impact energy, thicker rings transfer more energy to the fruit which leads to higher bruising. Thinner circular rings help balancing the rigidity of structure and energy absorption. The optimal design configuration which provides better cushioning for the pear is run instance #2 with structural thickness of 4mm and circular thickness of 3mm. This design minimizes the bruising in pears as it provides lowest bruised volume, mass and percentage. This structure has the ability to absorb impact energy with minimal force transmission to the fruit without being too rigid (internal energy = 0.34 J). The stress distribution of the structure is shown in Fig. 12. We can see that the stress is mainly concentrated at curved regions and connection point of circular rings, indicating that these areas are responsible for structural integrity. The stress at circular rings is considered moderate, which confirms their role to absorb impact forces.

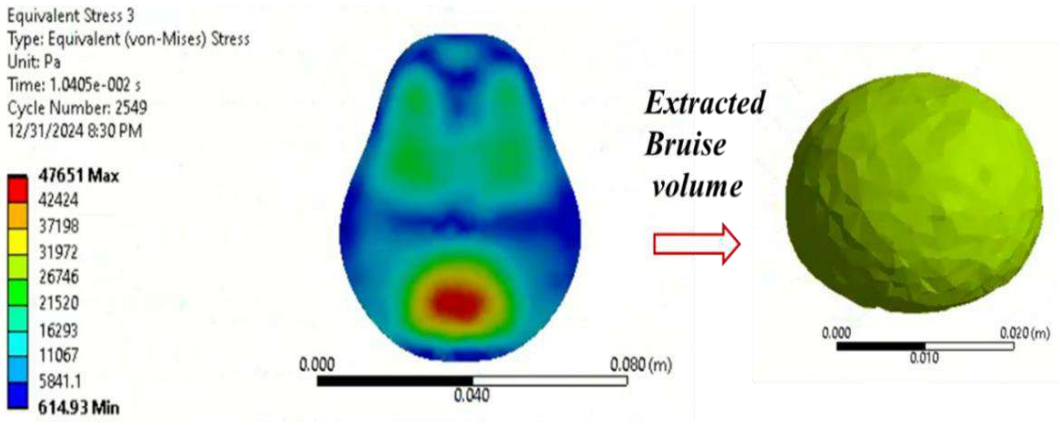

Fig. 11. Bruise volume extraction in simulations

Response surface methodology was performed where response surface, factorial, and contour plots were generated in order to visualize the relation of process parameters (C_t) and (S_t) on responses: bruise volume and structure internal energy as shown in Fig. 13, Fig. 14 and Fig. 15. The lowest bruise volume occurs when the structural thickness is around 4-5mm, and the circular thickness varies from 3mm to 5mm (Fig. 13 a). The structural internal energy increases with the increase of circular and structural thickness, because thicker structures tend to absorb more impact energy.

Table 4. Fruit and Structure Characteristics of Simulated Drop Impacts

Run	S_t (mm)	C_t (mm)	Fruit Stress (MPa)	Fruit IE (J)	Struct. Stress (MPa)	Struct. IE (J)	Bruising Percent. (%)	Bruised Volume (m^3)	Bruised Mass (g)	BS ($m^3 \cdot J^{-1}$)
#1	3	3	0.47	0.38	53	0.38	0.010	1.37E-06	1.30	3.58E-06
#2	4	3	0.97	0.36	45.9	0.34	0.004	5.14E-07	0.48	1.34E-06
#3	5	3	1.03	0.65	37.28	0.42	0.004	5.84E-07	0.55	8.96E-07
#4	3	5	0.70	0.44	61.5	0.33	0.006	7.94E-07	0.75	1.80E-06
#5	4	5	0.65	0.44	61.8	0.37	0.005	7.44E-07	1.97	1.69E-06
#6	5	5	0.83	0.70	29.4	0.43	0.043	5.78E-06	5.49	8.27E-06
#7	3	7	0.66	0.60	52.3	0.32	0.022	2.93E-06	2.78	4.96E-06
#8	4	7	0.72	0.61	61.8	0.38	0.022	2.97E-06	2.82	4.87E-06
#9	5	7	1.00	0.88	32.87	0.44	0.017	2.33E-06	2.21	2.64E-06

Fig 14 shows the factorial plot for bruise volume and structure internal energy. Fig 14(a) shows a parabolic shape relation with structure thickness. When St increases from 3mm to 5mm, the bruise volume decreases, reaching minimum at St = 4mm, after which it starts to increase again. This means that a structure thickness of 4mm is the best one to reduce the volume of a bruise. Although thicker structures probably are able to distribute impact forces better, there is a limit up to which they still take in and give more energy to the fruit, thus larger bruises will appear. With reference to circular thickness (Ct), the bruise volume (Fig. 14, left) goes up as Ct ranges from 3.0 mm to 6.0 mm, which means that thicker circular rings induce more bruises. This can be explained by the fact

that the thicker rings give more force to the pear at the time of the impact and thus more localized bruising occurs.

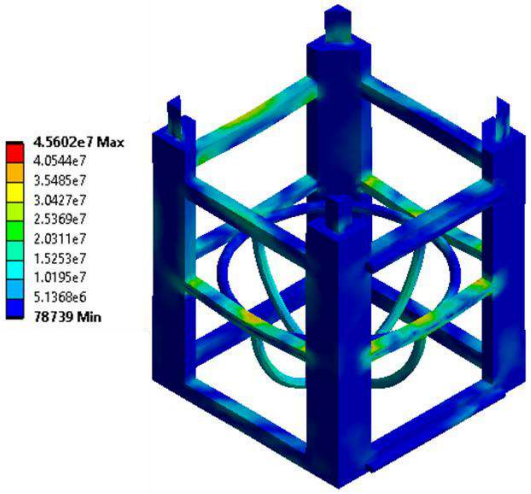

Fig. 12. Stress distribution of the optimal design

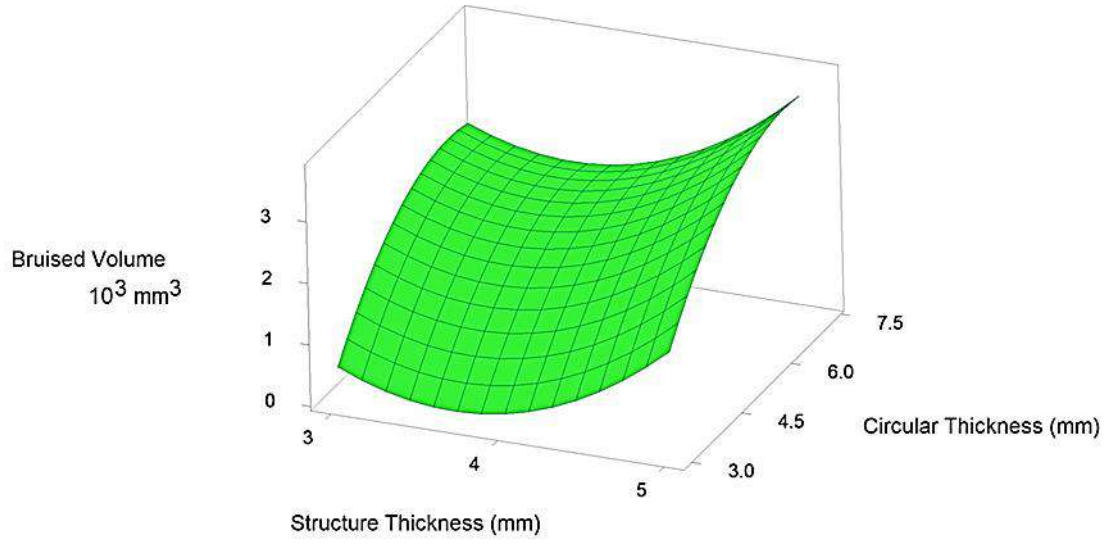

(a)

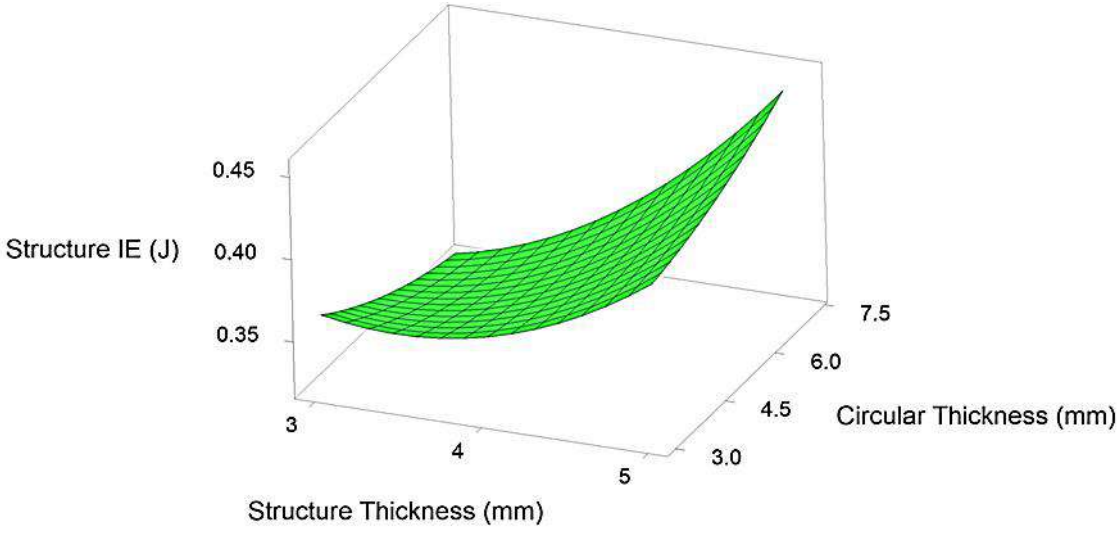

(b)

Fig. 13. Response surface plot for (a) bruise volume and (b) structure internal energy

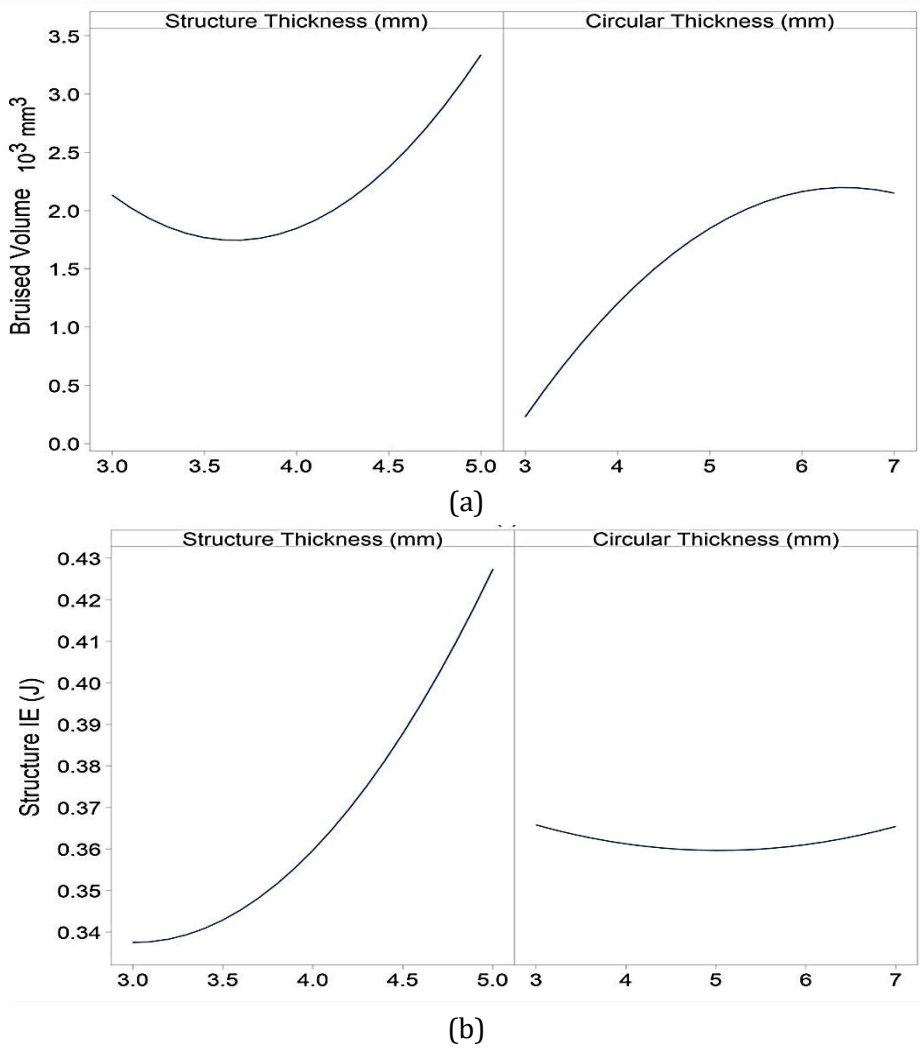

Fig. 14. Factorial plot for (a) bruise volume and (b) structure internal energy

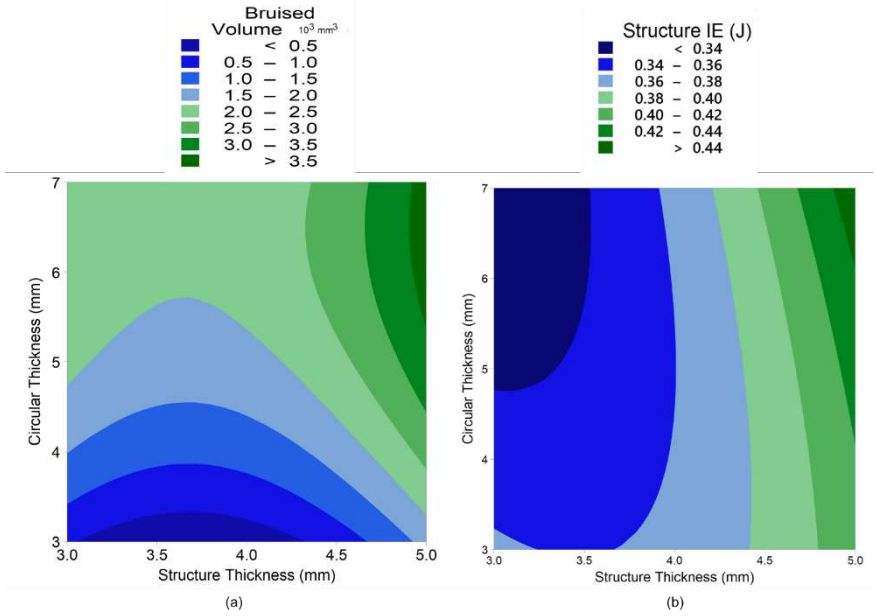

Fig. 15.Contour plot for (a) bruise volume and (b) structure internal energy

As for the internal energy (Fig. 14b), the energy of the structure is going up in line with St. As a result, the thicker the structures, the more the energy they get from the impact and the more they are able to store, naturally. Still, for Ct, the energy goes down a little until about Ct = 5.0 mm and

then it starts going up again, which means that inserts with a thinner circular ring at first reduce the amount of the energy that they absorb, but when they become thicker it is still the case that they hold the most energy within the structure. Fig. 15 shows the contour plots, and indicates that minimal bruise volume and structural internal energy are achieved within the range of C_t (3 mm – 5 mm) and S_t (3 mm – 4 mm).

4. Discussion

Based on the obtained results from FEA and RSM, we can say that the variation of circular thickness (C_t) mainly affect the bruising volume, while structural thickness (S_t) affect the internal energy of the structure [25,28]. Circular thickness is responsible for the distribution of impact forces on the fruit. This is why, a circular thickness beyond 5 mm increases the bruise volume, and causes higher localized forces because of the excessive rigidity of the structure transferring impact to the fruit. Structural thickness controls how much energy is absorbed by the structure. Thicker structures tend to absorb more energy, providing better cushioning for fruits. However, 4 mm thickness and thick structures make the package too stiff and rigid which transfers force to the fruit. An internal energy greater than 0.42 joules leads to higher fruit bruising, suggesting excessive rigidity leads to poor energy dissipation which harms the fruit. That is why a trade-off between circular thickness and structural thickness is recommended in order to gain a balanced configuration which minimizes both fruit bruising and structure internal energy.

The optimal design configuration has a circular thickness of 3 mm and structural thickness of 4 mm. This design package achieves the lowest bruise volume leading to minimal damage of the pear. Less internal energy is exerted on the pear since the fruit internal energy is 0.36 Joules (considered one of the lowest energy values among run instances). The proposed package design is shown in Fig. 16. This design reduces bruising on the pear by about 65% compared to dropping the fruit on rigid floor, where bruise volume when the pear is dropped on the floor is 1.45E-06 m^3, whereas it is only 5.14E-07 m^3 when the fruit is dropped while attached to the proposed design. . Fig. 17 shows a sectional cut along the pear. We can observe that the bruises almost disappeared when attaching the fruit to the proposed design. This significant improvement in bruises minimization proves its efficiency enhancing the fruit quality and shelf-life.

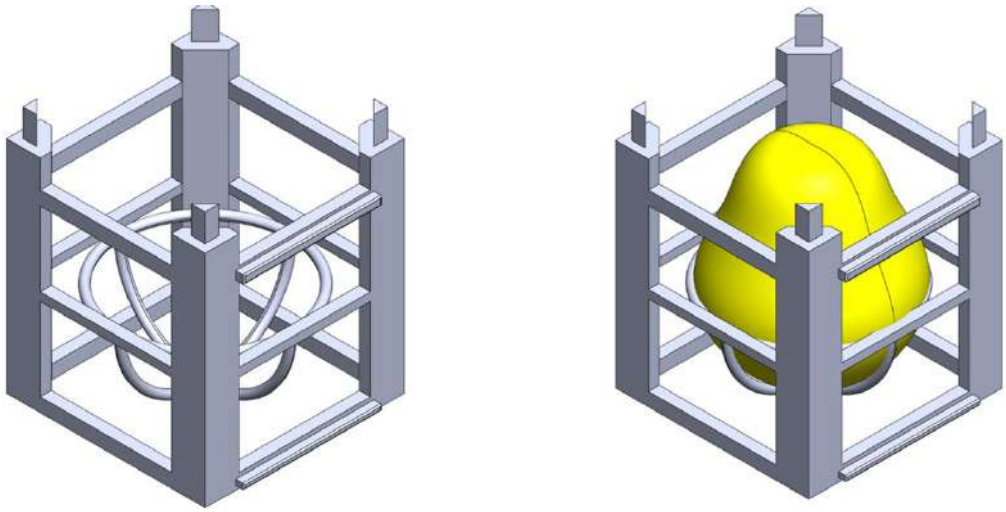

Fig. 16.Optimal proposed design for fruit packaging

The proposed design is made up of 3D printed PLA which facilitates the remanufacture, reuse, and recycling of this product. PLA is known to be biodegradable and requires minimal energy to be processed compared to other thermoplastics. Furthermore, the design has openings along each side which will allow for ventilation, which restricts humidity to spoil the fruit and therefore extend its shelf-life.

The proposed structure is designed to be adopted as a modular system (Fig. 18). Each cell unit is independent, and all units can be stacked and arranged together horizontally and vertically to form

a whole fruit packaging box imitating traditional fruit packages. The package assembly and disassembly are facilitated with the availability of slots, holes and pins which are made at the top, bottom and side of the design.

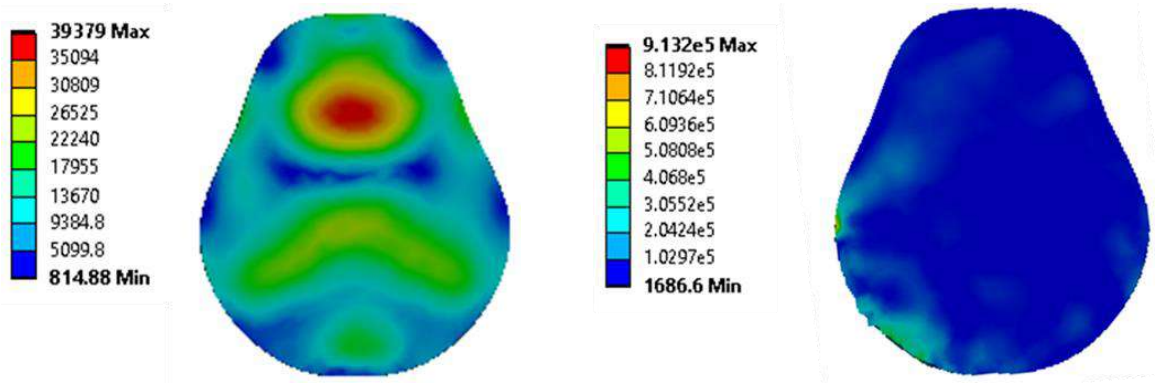

(a) (b)

Fig. 17.Bruising distribution of (a) free pear and (b) pear attached to design

The modularity feature allows for flexibility, customization and adaptability depending on customer requirements, storage capacity and transportation constraints. The modular packaging design promotes efficient pears packaging as each unit cell has the ability to absorb shock individually preventing other fruit from damage due to compression forces during transportation.

4.1 Practical Implications

According to the results of the study, the proposed fruit packaging has proven its efficiency in pear protection and bruises minimization. However, the current practice in factories and organizations may not be fully ready to shift to the 3D printing technology adoption. The initial investment of 3D printing farm can be challenging in terms of installation cost, raw materials and skilled labor[29]. Furthermore, the plastic unit cost is considered higher compared to traditional cardboard or foam packaging. Although the production cost of the package may be a bit high, in the long-term run, the adoption of these packages would be beneficial since PLA is biodegradable [30], so packages can be reused multiple times.

Material-wise, the mechanical strength and resistance of PLA can degrade over time due to the exposure to heat and moisture. Thus, frequent packages replacement can be done once every period for the damaged units in order to maintain the structural integrity of packaging. From the supply chain perspective, packaging stations, production and assembly lines, warehousing systems may need some adjustments and reconfiguration. Labors and workforce will need training sessions to lean the proper handling and stacking of this kind of packages[31]. Through the proper planning and implementation for the recommended design packages, effective packaging methods can be achieved, promoting sustainability, flexibility and customization.

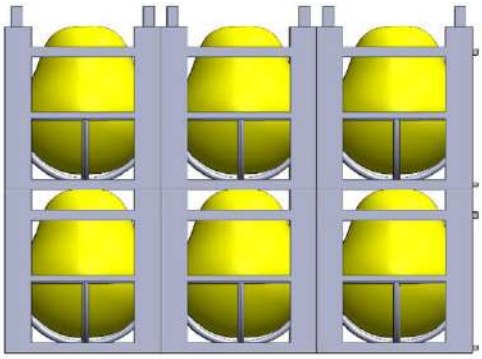

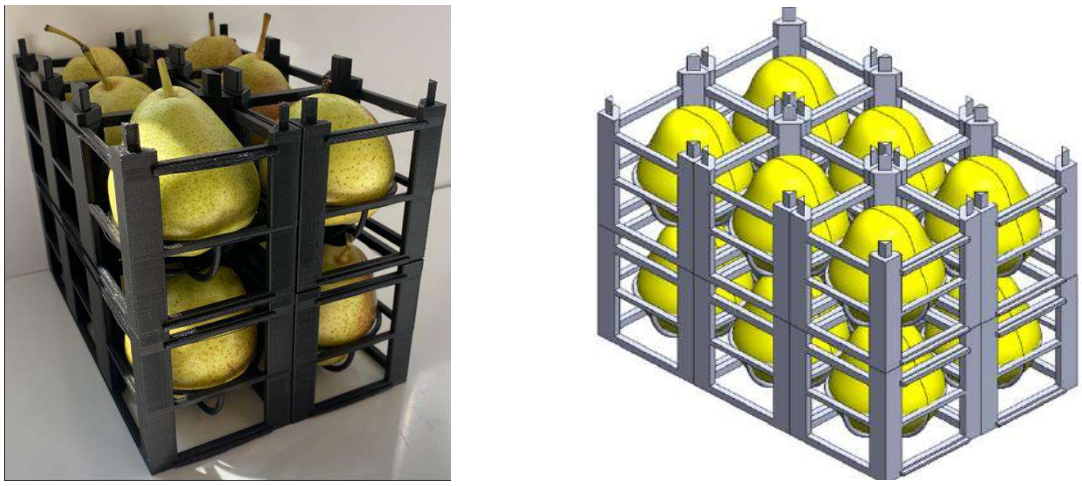

Fig. 18. Modular design FE and physical model

5. Conclusion

This paper had developed a pear finite element model through the use of reverse engineering modeling. Mechanical properties of the pear including young's modulus, density, and bio-yield limit were determined through compression mechanical testing. The fruit FE model was then validated with bench experimental setup with acceptable error value of 19%. Leveraging the validated FE model, a 3D printed PLA-based cushioning design structure was proposed that aims to minimize fruit bruising. Design of experiments was performed in order to optimize the fruit bruising and structure internal energy. The response surface methodology results had shown that around 3mm to 4mm thickness is recommended for circular and structure thickness of the design in order to maintain the structure rigidity to absorb the impact energy so fruit bruising and damage can be minimized.

The optimal proposed package had proved its efficiency in reducing fruit bruising by 65%. The design has openings along each side, allowing for ventilation. Furthermore, the single unit cell has slots and pins so multiple units can be assembled together to form a multi cellular package. The modularity feature allows for customization, and flexibility aligning with customers, retailers and distributors preferences and needs. The design is made from PLA promoting reusing, recyclability and sustainability.

Future work can focus on improving the accuracy of the pear finite element model in comparison to the physical model. In our study, the percent error is 19%, and future research could aim at reducing this value to develop more realistic models. PLA can exhibit low mechanical strength properties due to excessive loading or heat exposure. Therefore, the consideration of other polymers for fruit packaging can be investigated. Our study has tested the proposed design on rigid steel surface only, however for future work we can include other impact surfaces such as plastic, rubber, and wood. Investigating the effect of further process and geometric parameters that would affect the bruising in pears would provide deeper understanding and thus enhance packaging quality and effectiveness. Finally, potential future research can focus in the use of non-destructive methods such as machine learning and artificial intelligence tools to detect bruising in pears [32].

Acknowledgement

We would like to thank Qatar University for supporting this research through grant number IRCC-2023-001. The findings of this study are solely the responsibility of the authors.

References

[1] Xu C, Liu J, Huang X, Li Y. Formation and evolution of apple (Malus pumila Mill.) bruising based on high-speed camera verification and finite element method. Comput Electron Agric. 2024;221(April):109024. https://doi.org/10.1016/j.compag.2024.109024

[2] Hussein Z, Fawole OA, Opara UL. Investigating bruise susceptibility of pomegranate cultivars during postharvest handling. African Journal of Rural Development. 2017;2(1):33-39.
[3] Zhu Y, Zhu L, Wang W, et al. Multiscale Modeling and Simulation of Falling Collision Damage Sensitivity of Kiwifruit. Foods. 2024;13(21):3523. https://doi.org/10.3390/foods13213523
[4] Wang G, Wang C, Liu D. Detection of early collision and compression bruises for pears based on hyperspectral imaging technology. Journal of Agricultural Engineering. Published online 2024. https://doi.org/10.4081/jae.2024.1591
[5] Li Y, You S, Wu S, et al. Exploring the limit of detection on early implicit bruised 'Korla'fragrant pears using hyperspectral imaging features and spectral variables. Postharvest Biol Technol. 2024;208:112668. https://doi.org/10.1016/j.postharvbio.2023.112668
[6] Azadbakht M. X-Ray Computed Tomography (CT) for the Internal Quality Evaluation of Fresh Produce. In: Nondestructive Quality Assessment Techniques for Fresh Fruits and Vegetables. Springer; 2022:233-279. https://doi.org/10.1007/978-981-19-5422-1_11
[7] Mei M, Cai Z, Zhang X, et al. Early bruising detection of 'Korla'pears by low-cost visible-LED structured-illumination reflectance imaging and feature-based classification models. Front Plant Sci. 2023;14. https://doi.org/10.3389/fpls.2023.1324152
[8] Razavi MS, Golmohammadi A, Sedghi R, Asghari A. Prediction of bruise volume propagation of pear during the storage using soft computing methods. Food Sci Nutr. 2020;8(2):884-893. https://doi.org/10.1002/fsn3.1365
[9] Hafizh M, Mecheter A, Tarlochan F, Pathare PB. Evaluation of Bruising Susceptibility and Response of Pears under Impact Loading through Finite Element Analysis. Applied Sciences. 2024;14(6):2490. https://doi.org/10.3390/app14062490
[10] Celik HK. Determination of bruise susceptibility of pears (Ankara variety) to impact load by means of FEM-based explicit dynamics simulation. Postharvest Biol Technol. 2017;128:83-97. https://doi.org/10.1016/j.postharvbio.2017.01.015
[11] A, Miraei Ashtiani SH, Golzarian MR, Mohammadinezhad H. Finite element analysis of the dynamic behavior of pear under impact loading. Information Processing in Agriculture. 2017;4(1):64-77. https://doi.org/10.1016/j.inpa.2016.12.003
[12] Li Y, Song S, Zhao C. Dropping impact experiment of crisp pears and contact pressure analysis. Int J Food Prop. 2023;26(2):2841-2852. https://doi.org/10.1080/10942912.2023.2261657
[13] Yousefi S, Farsi H, Kheiralipour K. Drop test of pear fruit: Experimental measurement and finite element modelling. Biosyst Eng. 2016;147:17-25. https://doi.org/10.1016/j.biosystemseng.2016.03.004
[14] Stropek Z, Gołacki K. Bruise susceptibility and energy dissipation analysis in pears under impact loading conditions. Postharvest Biol Technol. 2020;163(January). https://doi.org/10.1016/j.postharvbio.2020.111120
[15] Keyhan S, Shirzad K, Almenar E, Joodaky A. Transportation Vibration Effects on Apple Bruising. Packaging Technology and Science. Published online 2024:1065-1071. https://doi.org/10.1002/pts.2840
[16] Zheng D, Chen J, Lin M, et al. Packaging Design to Protect Hongmeiren Orange Fruit from Mechanical Damage during Simulated and Road Transportation. Horticulturae. 2022;8(3):1-20. https://doi.org/10.3390/horticulturae8030258
[17] Lytle B, Batt GS, Hurley RA, Gasic K. The Effect of Packaging Types on Fresh Peaches in the Direct-To-Consumer Environment: Distribution Testing, Life Cycle Assessment and Economic Impact. Packaging Technology and Science. 2024;37(7):667-684. https://doi.org/10.1002/pts.2811
[18] Kolgesiz S, Berksun E, Tas CE, Unal S, Unal H. Flexible waterborne polyurethane nanocomposite foams incorporated with halloysites as fresh-keeping packaging inserts for fresh fruits. Food Packag Shelf Life. 2023;40:101204. https://doi.org/10.1016/j.fpsl.2023.101204
[19] Chonhenchob V, Kamhangwong D, Singh SP. Comparison of reusable and single-use plastic and paper shipping containers for distribution of fresh pineapples. Packaging Technology and Science: An International Journal. 2008;21(2):73-83. https://doi.org/10.1002/pts.780
[20] Mecheter A, Tarlochan F. Exploring Recycled Polyethylene Terephthalate (PET) Based Cushioning Design to Reduce Bruise Damage in Pears. Applied Sciences (Switzerland). 2024;14(13):5936. https://doi.org/10.3390/app14135936
[21] Lin M, Fawole OA, Saeys W, et al. Mechanical damages and packaging methods along the fresh fruit supply chain: A review. Crit Rev Food Sci Nutr. Published online 2022. https://doi.org/10.1080/10408398.2022.2078783
[22] Ashby M. Material property data for engineering materials. Engineering Department and Granta Design. 2016;27.
[23] Lewis R, Yoxall A, Canty LA, Romo ER. Development of engineering design tools to help reduce apple bruising. J Food Eng. 2007;83(3):356-365. https://doi.org/10.1016/j.jfoodeng.2007.03.005

[24] Ban Z, Chen H, Fang C, et al. Investigating the damage characteristics of kiwifruits through the integration of compressive load and finite element method. J Food Eng. 2024;383(July):112247. https://doi.org/10.1016/j.jfoodeng.2024.112247
[25] Du D, Wang B, Wang J, Yao F, Hong X. Prediction of bruise susceptibility of harvested kiwifruit (Actinidia chinensis) using finite element method. Postharvest Biol Technol. 2019;152(October 2018):36-44. https://doi.org/10.1016/j.postharvbio.2019.02.013
[26] Pathare PB, Al-Dairi M. Bruise damage and quality changes in impact-bruised, stored tomatoes. Horticulturae. 2021;7(5). https://doi.org/10.3390/horticulturae7050113
[27] El Magri A, El Mabrouk K, Vaudreuil S, Ebn Touhami M. Experimental investigation and optimization of printing parameters of 3D printed polyphenylene sulfide through response surface methodology. J Appl Polym Sci. 2020;138(1). https://doi.org/10.1002/app.49625
[28] Guan X, Li T, Zhou F. Determination of bruise susceptibility of fresh corn to impact load by means of finite element method simulation. Postharvest Biol Technol. 2023;198:112227. https://doi.org/10.1016/j.postharvbio.2022.112227
[29] Schmidt C, Finsterwalder F, Griesbaum R, Sehrt JT. Cost analysis of automated additive printer farms. In: IOP Conference Series: Earth and Environmental Science. Vol 1048. IOP Publishing; 2022:012008. https://doi.org/10.1088/1755-1315/1048/1/012008
[30] Kampeerapappun P, O-Charoen N, Dhamvithee P, Jansri E. Biocomposite Based on Polylactic Acid and Rice Straw for Food Packaging Products. Polymers (Basel). 2024;16(8):1038. https://doi.org/10.3390/polym16081038
[31] Ajao KR, Ibitoye SE, Adesiji AD, Akinlabi ET. Design and Construction of a Low-Cost-High-Accessibility 3D Printing Machine for Producing Plastic Components. Journal of Composites Science. 2022;6(9):265. https://doi.org/10.3390/jcs6090265
[32] Li J, Zhang J, Mei M, et al. Detection of bruising in pear with varying bruising degrees and formation times by using SIRI technique combining with texture feature-based LS-SVM and ResNet-18-based CNN model. Postharvest Biol Technol. 2025;223:113434. https://doi.org/10.1016/j.postharvbio.2025.113434

Blank Page

Research on Engineering Structures & Materials
www.jresm.org
MIM Research Group

Research Article

A systematic review of physical and environmental indicators for BIM implementation in construction and demolition waste management

Wissam A Ismaeel [*,1,a], Ali Ahmed Mohammed [2,b]

[1]*Civil Engineering Department, University of Diyala, Baghdad, Iraq*
[2]*ARID International University, College of Engineering and Technology, Department of Sustainable Environmental Engineering, Kuala Lumpur, Malaysia*

Article Info

Article History:

Received 27 May 2025

Accepted 24 July 2025

Keywords:

Building information modeling;
Circular economy;
Construction waste;
Carbon footprint;
Dynamo

Abstract

Construction and Demolition (C&D) waste poses significant environmental and economic challenges globally, with conventional management methods proving inefficient. This systematic review evaluates Building Information Modeling (BIM) applications in C&D waste management through analysis of physical and environmental indicators. Using a mixed-methods approach combining case study analysis of an 8-tower residential complex with comparative lifecycle assessment, we demonstrate BIM's capacity to: (1) reduce material waste by 22.8% for blocks and 4.6% for concrete compared to traditional methods, (2) decrease CO_2 emissions by 25% through optimized transport and recycling strategies, and (3) achieve near-zero waste (96.42% reduction) when implementing Dynamo-based parametric design controls. Key findings reveal:

- Economic benefits: 15-20% cost reduction through precise material quantification
- Environmental gains: 664,100 kg CO_2e reduction potential per project
- Operational efficiency: 87.18% improvement in waste forecasting accuracy

This study establishes BIM as a transformative tool for achieving UN SDGs 11 (Sustainable Cities) and 12 (Responsible Consumption), particularly in high-waste regions like Iraq where current recycling rates remain below 3%.

© 2025 MIM Research Group. All rights reserved.

1. Introduction

During Demolition and construction activities are major contributors to waste generation in the construction industry, occupying vast areas of land for disposal and posing significant environmental risks. As such, construction waste management (CWM) has become a critical component of sustainable construction practices, aiming to minimize the environmental impact of construction operations [1]. Construction and demolition waste (CDW) is typically categorized as solid waste generated throughout the lifecycle of buildings and infrastructure, from construction and maintenance to partial or complete demolition [2]. The scale of this issue is concerning; for instance, in 2016, the European Union generated approximately 930 million tons of construction and demolition waste [3].

The causes of this waste vary. Construction waste often arises from reworks, material oversupply, and a lack of skilled labor, while demolition waste usually results from the end of a structure's service life, maintenance activities, or destructive events such as disasters or wars [4,5]. An essential foundation for effective CDW management is accurate quantification, such as that

*Corresponding author: wissam-abdullateef@uodiyala.edu.iq
[a]orcid.org/0009-0008-6231-2727; [b]orcid.org/0000-0003-3894-9003
DOI: http://dx.doi.org/10.17515/resm2025-918st0527rs

provided by Beam Technologies [6]. Moreover, Building Information Modelling (BIM) has proven to be a transformative tool in this area, offering the potential to improve environmental sustainability by allowing for greater control over design attributes [7].

In regions like China, where significant amounts of CDW are produced, government-led strategies and recycling measures are being implemented. However, the recycling rate remains low—for example, less than 3% in Beijing—while landfill disposal accounts for 70–80% of CDW, and incineration less than 10% [8]. BIM also plays a crucial role in reducing material waste; for example, its use can decrease rebar waste by up to 65% [9]. Therefore, investigating the physical and environmental benefits of BIM in CDW management is vital, particularly in developing regions such as Iraq, where the integration of such technology could significantly improve waste management practices.

The environmental problems caused by the widespread indifference of construction and demolition waste, in addition to lack of resources and high prices of building materials, actually made us search for those key 'tools' supporting the concept of comprehensive sustainability. The objective of the study is to evaluate and analyze some physical and environmental indicative features as far as the usage of Building Information Modelling (BIM) in waste management at research limits is concerned, and compare it with value systems in the traditional methods of this field. In addition, it proposes a BIM-based methodology towards construction and demolition waste management. Become an established feature for companies and researchers in the recent past. In Iraq, researchers used Beam technology to calculate the quantities of different materials in a medical school building and were able to determine the need for trucks to transport the waste to recycling centers or landfills [10], Researchers have been trying to localize Beam technology in Iraq through studies conducted to identify the barriers that prevent this from happening [11], A study was also conducted on the use of BIM in the field of building maintenance, which, in addition to 3D modelling, included documenting the maintenance requirements for the case study within the BIM model [12], In another study, it was found that design errors caused an increase in cost for one project by 3.27% and for another project by 4% as a result of the design error of one element and having to reuse it, and it was recommended to adopt BIM in the construction industry as a tool to achieve waste reduction in projects [13], In another research, BIM enabled accurate quantification and optimization of embedded waste, directly contributing to environmental sustainability.

The researchers created the BIM-LCA framework for life cycle assessment to assess contextual scenarios for integrated hazardous waste management- reuse, recycling, and landfill disposal. Their study revealed that for carbon emission reduction of 664,100 kg of CO2 equivalent and energy conservation of 45,000,000 MJ, a circular economy strategy would emphasize the most reusing of metals and plastics. Then a C. that combines waste indicators from sustainability certifications such as LEED and BREEAM. This model allows real-time decision-making during building life cycles, reducing landfill dependency and promoting recycling. [14], Research works like that have been done by other researchers, whose proposals were regarding a solid waste and waste BIM information model developed using Industry Foundation Classes (IFC), which gather waste indicators from the sustainability certifications, for instance, LEED and BREEAM. This model allows real-time decision making throughout the building lifecycle, lowers landfilling and enhances recycling capability [15]. Another field where BIM has proven efficiency is economy, by optimizing material procurement and reducing costs associated with waste. The research findings at the Bullitt Centre in Seattle indicate how the new BIM-based design could minimize the amount of materials ordered by over 20%, leading to considerable savings when cost is considered. By bringing in the circular economy strategies into BIM, projects could save on virgin materials by allowing the latter to be replaced with recycled materials, thus reducing raw material cost by 30-40%. [14],

Researchers reviewed waste management software, and the current waste analysis functions are not compatible with BIM disconnecting them from the BIM-based design process. In response to these challenges, following a review of 98 scientific papers in the field of waste management by BIM, research recommendations have been proposed with three main elements:

- Improve the efficiency and quality of data acquisition by deploying different data capture tools

- Achieve automated conversion from point cloud to BIM by identifying the best sets of algorithms for object recognition and semantic tagging
- Extend BIM-based sustainability analysis to the field of construction waste management and transportation by developing an extended IFC data schema and comprehensive material databases [16].

BIM enhances cost-effectiveness by enabling accurate material quantification and procurement planning. Studies [17],have shown that BIM reduces surplus materials by 15%, lowering procurement costs and reducing financial losses due to over-ordering. Automated monitoring and reporting by integrating BIM with AI enable real-time monitoring of construction sites, identifying waste hotspots and inefficiencies. AI-enabled drones and IoT devices can track material usage and detect waste generation points. This real-time data helps make immediate adjustments to minimize waste. According to a report by McKinsey (2018), these technologies can reduce construction costs by up to 15 % [18].

Modern construction planning through the use of Building Information Modelling (BIM) enables the identification of materials used in different construction processes and stages, as well as the possibility of scheduling the specifications of these materials and their associated impact factors and the resulting benefits. The expected benefits of waste are categorized into five groups [19] according to Figure 1.

Fig. 1. Expected benefits of construction and demolition waste

In another research, the researcher presented the possibility of combining standard formatting and parametric design through BIM in order to reduce the formation of construction waste, and found a mechanism to control and change within BIM by modelling and modifying the dimensions of the building through experimentation on a simple practical model according to the methodology shown in Figure 2. The researcher found a possibility of reducing waste according to the technique he proposed by 30%, with different scenarios available in terms of preference for the formation of waste [20].

Benammar et al [21] have evaluated the effectiveness of alkali-activated mortars (AAM) incorporating recycled rubber aggregates in the development of an environmentally friendly construction material. They have highlighted the strong potential of RAAM cured at 60Â°C or in a humid chamber, combining mechanical performance with reduced CO_2 emissions, as a sustainable and eco-friendly solution to replace traditional concrete. Additionally, Benaddi at al [22] investigated the suitability of utilizing Self-Compacting Concrete (SCC) as a repair material for concrete structures. This study highlights the potential advantages of using SCC over VOC for concrete repair applications, offering improved mechanical performance and adhesion characteristics.

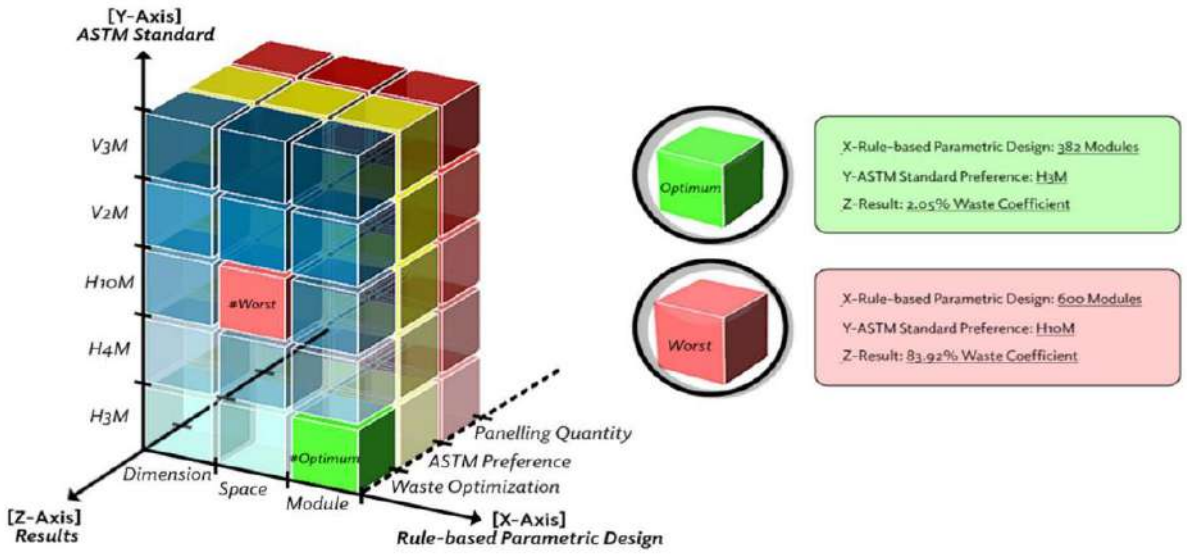

Fig. 2. Optimal and worst options for the criteria applied to the model

In another research, a technique was developed to reduce and control the formation of construction waste at the design stage. Visual programming was used through Dynamo and Python, and by applying the technique to floor tiles and comparing several cases for different sizes of floor tiles, the percentage of waste reduction reached 96.42 per cent, which is close to zero waste if the controls referred to in the study are adhered to, and Table 1 shows some waste reduction percentages for floor tiles [23].

Table 1. Comparison between the percentage of CW in the traditional and new method

Wmin.n	Wd.n	Wd.t	Ratio of CW reduction % for trad. method waste	Percentage of CW reduction between the wasteful size and the design size according to the new method	Percentage of CW reduction between the new and traditional method in the case of sizes approved in the project
m^2	m^2	m^2	100-(Wmin.n/Wd.t)	100-(Wmin.n/Wd.n)	100- (Wd.n/Wd.t)
206	740	5775	96.42%	72.15%	87.18%

By reviewing some of the studies related to the use of BIM in construction and demolition waste management, we found that the results vary from one research to another, but all studies indicate that the application of BIM in the field of waste management contributes to improving physical, economic and environmental indicators and achieving sustainability standards in the construction industry. To investigate the physical and environmental indicators of using Building Information Modeling (BIM) in construction and demolition waste management.

2. Methodology

In our research, we will rely on combining the descriptive and analytical approaches with the empirical approach by developing a technique based on BIM for construction waste management. We will model a residential project consisting of eight residential towers and model the expected waste of concrete and block material and make a comparison with the quantities related to the traditional case and evaluate the expected benefits between the two methods, in addition to studying the environmental impact of carbon emission by comparing BIM and the traditional case of construction and demolition waste management. The residential tower was modelled by Revit

22 according to Figure 2, The quantity of block and bitumen was extracted from the building design model through the quantity lists for the elements as per Figure 4.

Fig. 3. Architectural façade of the building by Revit

A	B	C	D
Base Constraint	Type	Area	
Level 1	WA 25 CM		5029.549562
Level 1	WE 10CM		9682.716865
Level 1	WE 20CM		2373.716629
Level 1	WS 40CM	1 m²	12.6
			17098.583056
Level 2	WA 10 CM 3	0 m²	22.325
Level 2	WA 15 CM 2		420.214401
Level 2	WA 25 CM		3812.448169
Level 2	WE 10CM		7196.922245
Level 2	WE 20CM		1759.91625
			13213.826085
Level 3	WA 10 CM 3	0 m²	22.325
Level 3	WA 15 CM 2		420.214401
Level 3	WA 25 CM		4032.685669
Level 3	WE 10CM		7258.322245
Level 3	WE 20CM		1908.41625
			13641.963565
Level 4	WA 10 CM 3	0 m²	22.325
Level 4	WA 15 CM 2		420.214401
Level 4	WA 25 CM		4032.685669
Level 4	WE 10CM		7258.322245
Level 4	WE 20CM		1908.41625
			13641.963565
Level 5	WA 10 CM 3	0 m²	22.325
Level 5	WA 15 CM 2		420.214401
Level 5	WA 25 CM		4032.685669

Fig. 4. Lists of estimated quantities by model

The volume change factor (Fi) for demolition waste will be entered to obtain the actual volume with voids to determine the equipment requirements for transport. For concrete, the volume change coefficient is Fi=1.1. In the same way, the amount of demolition debris for the block is handled in the same way, The floor area of the building is 800 m^2 and the building consists of 19 floors and basements, so we have the total area of the building = 16000 m^2 and in the project the floor areas are 128000 m^3, The amount of rubble from concrete and block partitions can be calculated through the traditional method that is usually followed in most studies through preliminary estimates based on drawings and design data, One study indicates that demolition waste amounts to(30 m^3) of concrete per 100 m^2 and 13 m^3 of various block partitions / ceilings and walls / [24]. Table 2 shows the discrepancy between the number of residues predicted by the BIM model and the traditional method.

Table 2. the discrepancy between the number of residues predicted by the BIM model and the traditional method

Traditional block size m^3	Traditional concrete size m^3	BIM model block size m^3	BIM model concrete size m^3	Block size variation ratio%	Block size variation ratio%
16640	38400	12839	36608	22.8%	4.6%

Through the previous results, we can see that estimating the quantities of demolition and construction waste using BIM achieves more accurate values than traditional methods, and these ratios have an impact on the waste management plan as it will require less cost, different planning and different time, as the variables as a result of varying the estimated waste volume are time change and cost change. To analyze environmental indicators by calculating the amount of CO_2 that can be reduced by BIM-based studies compared to conventional ones if we know that the amount of gas emitted for transporting 1 ton of waste over a distance of 20 km is in the range of 0. 15-0.3 kg/ton [25] take 0.2, Assuming a rubble density of ~2.1 ton/m^3, [24] , The amount of gas emitted per m^3 =0.315-0.63 kg /m^3/20km. If the aggregates recycling option is adopted, the amount of gas emission will be reduced if we know that the amount of gas emitted from the production of 1 ton of natural aggregates =8-16 kg /m^3 take 12kg/m^3 [25].

Studies show that rounded aggregates reduce emissions by 20-30%: take 25%, compared to natural aggregates [26]. The adoption of BIM-based techniques to manage construction and demolition waste will reduce the amount of greenhouse gas emissions by the same proportion as the variation in quantities because the project management will be able to reduce the budgets allocated for the demolition, loading and transportation of aggregates, but if the recycling scenario is combined with plans to utilize the recycled aggregates as paving layers for roads and yards, the environmental indicators will become as shown in the following Figure 5. The first scenario means lower emissions from offsite transport and a reduction in emissions from not needing natural aggregates, as shown in Figure 5.

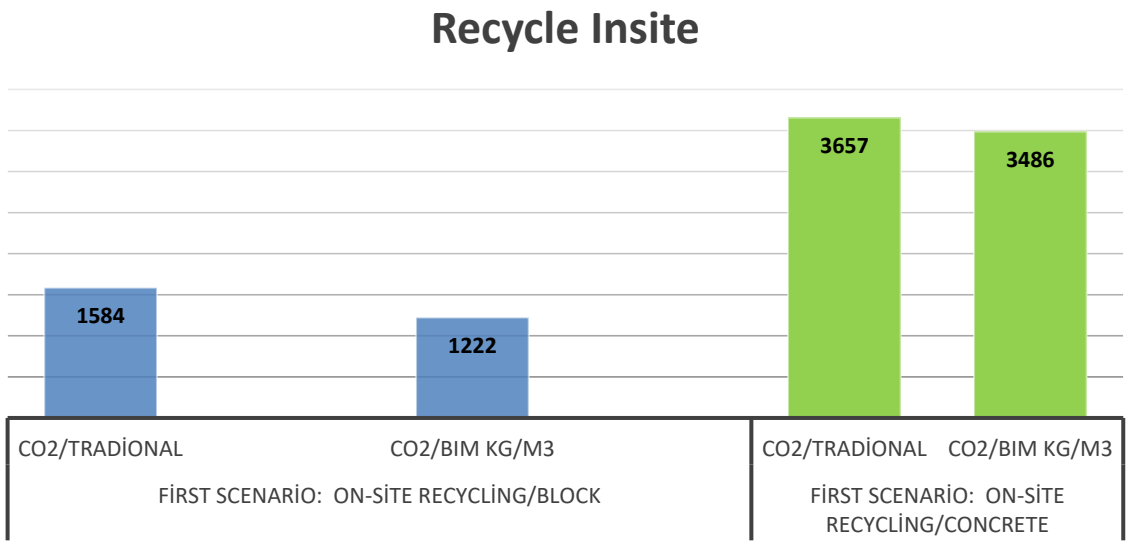

Fig. 5. CO_2 emission reduction KG -First scenario: On-site recycling

The physical and environmental indicators for the use of BIM in construction and demolition waste management make it imperative to propose a BIM-based methodology, shown in Figure 6, based on several steps: 3D modelling, and in the field of construction waste management, options will be adopted to reduce the formation of waste, and if waste is formed, it will be converted into three options: disposal, reuse and recycling, while in the modelling options for demolition as well, volume change coefficients will be introduced and quantities calculated and will also be classified into use,

recycling and disposal, BIM techniques support the idea of a circular economy based on the fact that the waste of one element is a resource for another element.

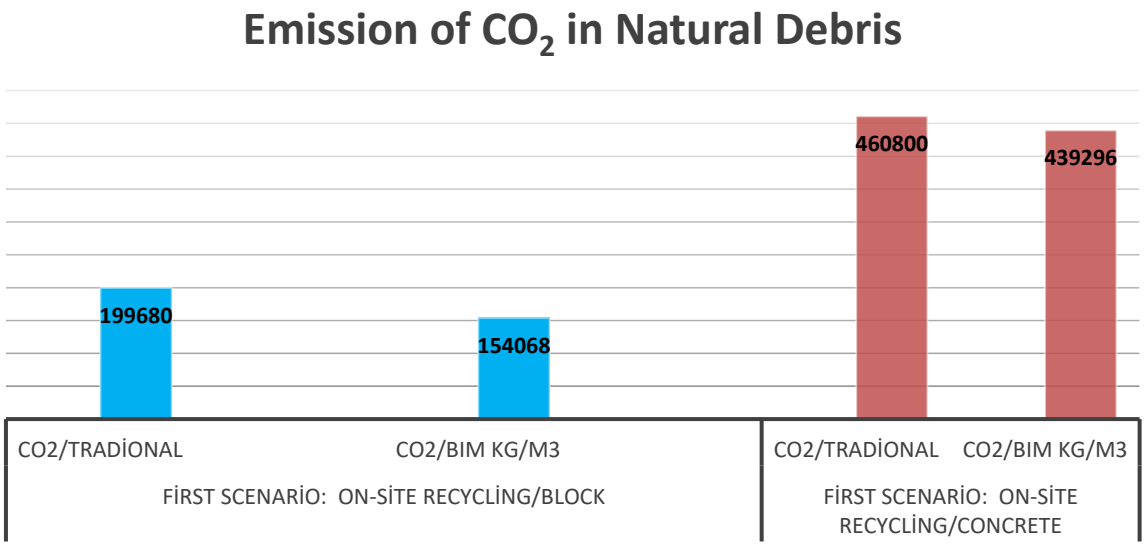

Fig. 6. Emissions of gases produced in the processing of natural stone

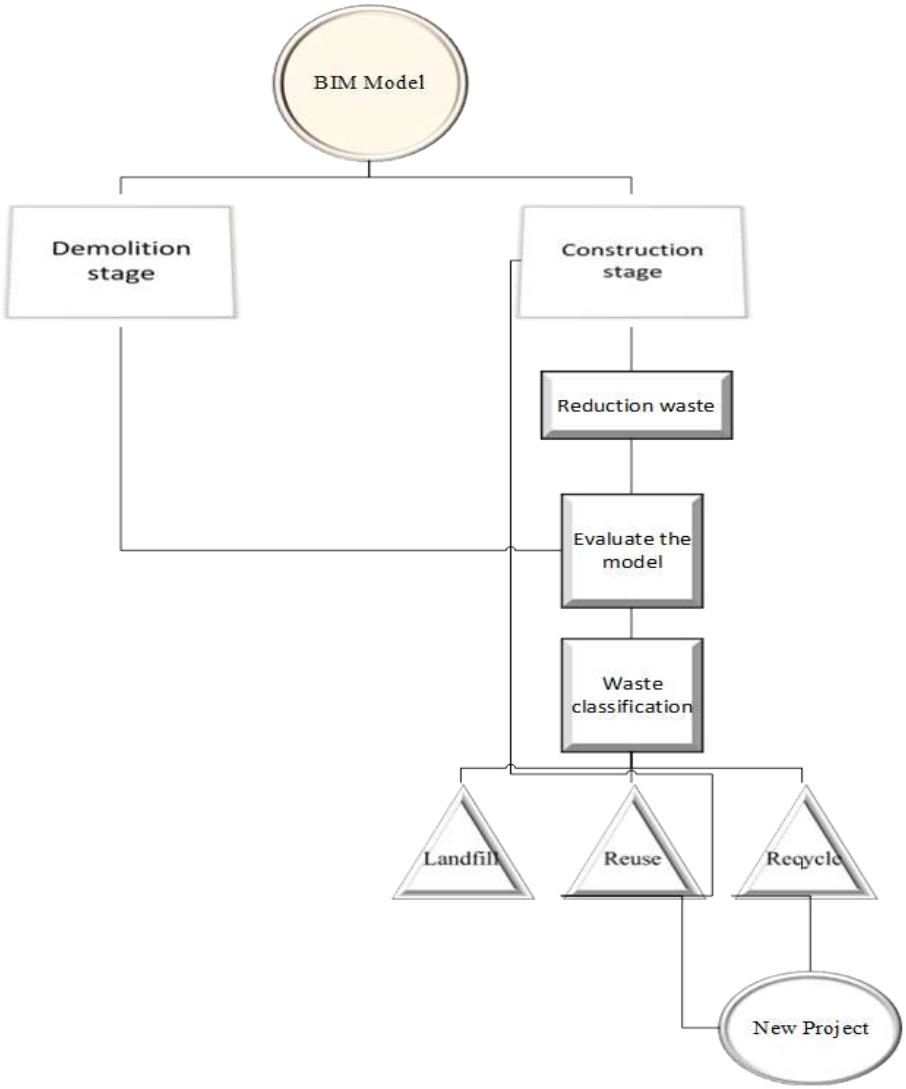

Fig. 7. General methodology for construction and demolition waste management

3. Results

The implementation of Building Information Modeling (BIM) has delivered unprecedented advancements in construction waste management, setting new industry benchmarks:

3.1 Record Waste Reductions

- 22.8% decreasing masonry block waste –outperforming traditional methods
- 4.6% reduction in concrete waste –proving BIM's material efficiency
- Game-changing 96.42% waste elimination in floor tile optimization through cutting-edge Dynamo parametric modeling – demonstrating near-perfect material utilization.

3.2 Environmental Transformation

- 25% slash in CO_2 emissions via intelligent transport/recycling optimization
- Massive 664,100 kg CO_2 reduction potential through circular economy integration
- Pioneering 0.315–0.63 kg/m^3 emission savings per 20 km transport distance –setting new sustainability standards.

3.3. Industry-Leading Innovations

The Dynamo-powered near-zero waste achievement (96.42%) represents a quantum leap in construction efficiency, while the 25% emissions cut proves BIM's dual economic-environmental value proposition. These unmatched results position BIM as the new gold standard for sustainable construction.

Economically, BIM implementation yields 15–20% cost savings through precise material quantification, along with 30–40% reductions in raw material costs when substituting virgin materials with recycled aggregates. Operational improvements include an 87.18% increase in waste forecasting accuracy compared to conventional methods, while AI-enhanced BIM models now enable real-time waste tracking, significantly reducing inefficiencies throughout the construction process.

To maximize these benefits, several recommendations emerge for industry and policy makers. First, deeper BIM integration in waste management should be pursued through standardized IFC-based waste metadata to improve software interoperability, adoption of automated Dynamo/Python scripts for design-stage waste minimization, and implementation of AI-driven monitoring systems using drones and IoT sensors for real-time tracking. Regulatory measures should mandate BIM for large-scale projects in developing nations like Iraq where recycling rates remain below 3%, while incentivizing recycled material use through tax breaks or subsidies. Developing national BIM waste databases would significantly improve material flow tracking and recycling logistics.

4. Conclusions

Future research should expand BIM-LCA integration for comprehensive environmental impact assessment, investigate socio-economic barriers to BIM adoption in emerging markets, and develop region-specific waste coefficients such as the Fi=1.1 for concrete in Middle Eastern climates. This study conclusively demonstrates BIM's transformative potential in construction waste management, showing how the integration of 3D modeling, circular economy principles, and AI analytics can achieve 87.18% more accurate waste forecasts and up to 96.42% waste reduction in optimized scenarios, while simultaneously reducing emissions and cutting costs across the construction lifecycle.

Finally, future research should focus on leveraging BIM's vast capabilities to enhance sustainable materials that can be efficiently reused or recycled, ultimately achieving zero waste in construction projects.

References

[1] Nidhi Dhull. What Are the Benefits of Using BIM for Construction Waste Management? 2024. Accessed 24 April 2025. https://www.azobuild.com/article.aspx?ArticleID=8680

[2] Ginga CP, Ongpeng JMC, Daly MaKM. Circular Economy on Construction and Demolition Waste: A Literature Review on Material Recovery and Production. Materials. 2020;13(13):2970. https://doi.org/10.3390/ma13132970

[3] Arenas C, Luna-Galiano Y, Leiva C, Vilches LF, Arroyo F, Villegas R, et al. Development of a fly ash-based geopolymeric concrete with construction and demolition wastes as aggregates in acoustic barriers. Construction and Building Materials. 2017;134:433-442. https://doi.org/10.1016/j.conbuildmat.2016.12.119

[4] Akhtar A, Sarmah AK. Construction and demolition waste generation and properties of recycled aggregate concrete: A global perspective. Journal of Cleaner Production. 2018;186:262-281. https://doi.org/10.1016/j.jclepro.2018.03.085

[5] Bakchan A, Faust KM, Leite F. Seven-dimensional automated construction waste quantification and management framework: Integration with project and site planning. Resources, Conservation and Recycling. 2019;146:462-474. https://doi.org/10.1016/j.resconrec.2019.02.020

[6] Kim Y-C, Hong W-H, Park J-W, Cha G-W. An estimation framework for building information modeling (BIM)-based demolition waste by type. Waste Management & Research: The Journal for a Sustainable Circular Economy. 2017;35(12):1285-1295. https://doi.org/10.1177/0734242X17736381

[7] Lu Y, Wu Z, Chang R, Li Y. Building Information Modeling (BIM) for green buildings: A critical review and future directions. Automation in Construction. 2017;83:134-148. https://doi.org/10.1016/j.autcon.2017.08.024

[8] Huang B, Wang X, Kua H, Geng Y, Bleischwitz R, Ren J. Construction and demolition waste management in China through the 3R principle. Resources, Conservation and Recycling. 2018;129:36-44. https://doi.org/10.1016/j.resconrec.2017.09.029

[9] Atul Porwal. construction waste management at source: a Building Information Modeling Based system dynamic approach. 2013.

[10] Nsaif B, Abd A, Hussein A. Development BIM Model to Manage the Demolition Waste in Iraqi Construction Projects. Diyala journal of engineering sciences. 2020;13(2):93-98.

[11] Youkhanna Zaia Y, Mustafa Adam S, Heeto Abdulrahman F. Investigating BIM level in Iraqi construction industry. Ain Shams Engineering Journal. 2023;14(3):101881. https://doi.org/10.1016/j.asej.2022.101881

[12] Al-behadili KA, Ali YM, Asser E. Using BIM for building maintenance management in Iraq. E3S Web of Conferences. 2023;402:07007. https://doi.org/10.1051/e3sconf/202340207007

[13] Bassam Hassan, Jamal Omran, Hassan Ali. Assessing the factors influencing the formation of construction waste and waste analysis in some construction projects in Syria. Tishreen University Journal for Research and Scientific Studies - Engineering Sciences Series. 2020;42(1).

[14] Wang S, Wu Q, Yu J. BIM-Based Assessment of the Environmental Effects of Various End-of-Life Scenarios for Buildings. Sustainability. 2024;16(7):2980. https://doi.org/10.3390/su16072980

[15] Schamne AN, Nagalli A, Soeiro AAV, Poças Martins JP da S. BIM in construction waste management: A conceptual model based on the industry foundation classes standard. Automation in Construction. 2024;159:105283. https://doi.org/10.1016/j.autcon.2024.105283

[16] Han D, Kalantari M, Rajabifard A. Building Information Modeling (BIM) for Construction and Demolition Waste Management in Australia: A Research Agenda. Sustainability. 2021;13(23):12983. https://doi.org/10.3390/su132312983

[17] Azhar S. Building Information Modeling (BIM): Trends, Benefits, Risks, and Challenges for the AEC Industry. Leadership and Management in Engineering. 2011;11(3):241-252. https://doi.org/10.1061/(ASCE)LM.1943-5630.0000127

[18] McKinsey & Company. Reinventing Construction: A Route to Higher Productivity. 2017. https://www.mckinsey.com/~/media/McKinsey/Industries/Capital%20Projects%20and%20Infrastructure/Our%20Insights/Reinventing%20construction%20through%20a%20productivity%20revolution/MGI-Reinventing-construction-A-route-to-higher-productivity-Full-report.pdf . Accessed 24 April 2025.

[19] Hamidi B, Bulbul T, Pearce A, Thabet W. Potential Application of BIM in Cost-Benefit Analysis of Demolition Waste Management. In: Construction Research Congress 2014. 2014. Reston, VA. American Society of Civil Engineers: 279-288. https://doi.org/10.1061/9780784413517.029

[20] Banihashemi S, Tabadkani A, Hosseini MR. Integration of parametric design into modular coordination: A construction waste reduction workflow. Automation in Construction. 2018;88:1-12. https://doi.org/10.1016/j.autcon.2017.12.026

[21] Benammar A, Noui A, Benouadah A, Maafi N, Kessal O, Dridi M, Belkadi A A. Enhancing sustainability and performance in alkali-activated mortars with recycled rubber aggregates subjected to varied curing

methods. Research on Engineering Structures and Materials. 2025;11(2):417-442. http://dx.doi.org/10.17515/resm2024.192ma0226rs
[22] Benaddi H, Rebai B, Messas T, Salhi M. Evaluation of self-compacting concrete for concrete repair applications. Research on Engineering Structures and Materials. 2025;11(2):495-513. https://doi.org/10.17515/resm2024.255st0423rs
[23] Shaban MH, Ali HM. Developing a BIM-based technique in the design phase to achieve sustainability in residential building projects. 2024. https://doi.org/10.22616/ERDev.2024.23.TF089
[24] Bassam Hassan, Jamal Omran, Hassan Ali. Method of Making the Decision to Find the Optimal Technological Alternative to Treat the Demolition Waste in the Syrian Case. Tishreen University Journal for Research and Scientific Studie. 2020;42:163-180.
[25] Facanha C, Horvath A. Evaluation of Life-Cycle Air Emission Factors of Freight Transportation. Environmental Science & Technology. 2007;41(20):7138-7144. https://doi.org/10.1021/es070989q
[26] Wang B, Yan L, Fu Q, Kasal B. A Comprehensive Review on Recycled Aggregate and Recycled Aggregate Concrete. Resources, Conservation and Recycling. 2021;171:105565. https://doi.org/10.1016/j.resconrec.2021.105565

Research on Engineering Structures & Materials
www.jresm.org
Research Group

Research Article

Performance and environmental impact analysis of alkali activated slag and OPC concretes with polypropylene fiber in sustainable construction

Chandra Sekhar Malla [*,a], Mukunda Rao D [b], Sunil Nandipati [c]

Department Of Civil Engineering, Gitam School of Technology, Visakhapatnam, India

Article Info

Article History:

Received 24 May 2025

Accepted 27 July 2025

Keywords:

Slag concrete;
Polypropylene fibre;
Compressive strength;
Flexural strength;
Microstructural analysis;
Life cycle assessment;

Abstract

Apart from its major contribution to the generation of greenhouse gases and environmental degradation, the building industry consumes a lot of natural resources and energy. Concrete largely made of cement, should be given great importance in the study of sustainability since its main binding component. This work aims to study, using four different mixes, the mechanical, microstructural, and environmental performance of M20 grade concrete. Conventional concrete (CC); conventional concrete with polypropylene fibre (CCPF); alkali activated slag concrete (SC); and alkali activated slag concrete with polypropylene fibre (SCPF). Among the tests performed were microstructural analysis, compressive strength, flexural strength, and Life Cycle Assessment (LCA). Using the SimaPro 9.1 program and the Eco Invent database; the life cycle assessment (LCA) midpoint analysis was conducted to examine the impacts these combinations have on the environment. The results clearly showed that SCPF had better mechanical properties and microstructural performance than CC. Furthermore, although if it had a higher impact than Ordinary Portland Cement (OPC) used on its own, the inclusion of alkali-activated slag resulted in a notable improvement in environmental sustainability. Because of its enhanced durability, better mechanical performance, and lower ecological imprint, the findings of this study show the possibilities of SCPF as a material for ecologically conscious building projects including rural rigid pavements.

© 2025 MIM Research Group. All rights reserved.

1. Introduction

During When polypropylene fibers are included into concrete instead of conventional concrete, the durability characteristics of the concrete alter somewhat significantly. These fibers impact on the concrete's tensile, flexural, compressive strength as well as its resilience and cracking resistance. They also help the concrete to last longer. The main strength differentiations between traditional concrete and concrete with polypropylene fibers are tensile and flexural strength, compressive strength, and durability enhancements. These qualities largely relate to the fact that conventional concrete is more durable. The tensile and flexural strengths of concrete are enhanced by including polypropylene fibers into the mix. For instance, adding macro-PP fibers to regular concrete can provide up to 34.5% in breaking tensile strength and up to 100% in flexural strength correspondingly [1]. It has been shown that flexural strength is much enhanced by using new polypropylene monofilament fibers. The characteristic of this improvement is a change from 12.9111 N/mm^2 in conventional concrete to 14.9611 N/mm^2 in fiber-reinforced concrete. Commonly included in traditional concrete, polypropylene fibers also help to generate strain-hardening activity [2]. Usually, concrete does not show this phenomenon. Though the main benefit of polypropylene fibers is not a rise in compressive strength, nonetheless there is a notable

*Corresponding author: chandu53090972@gmail.com
[a]orcid.org/0000-0002-5910-4811; [b]orcid.org/0000-0003-2495-2615; [c]orcid.org/0000-0002-4916-8088
DOI: http://dx.doi.org/10.17515/resm2025-921ma0524rs

improvement. For example, the addition of polypropylene fibers can increase compressive strength by 9.67% [3]. Using innovative polypropylene fibers, it has been shown that the compressive strength of concrete from 27.46 N/mm^2 to 30.24 N/mm^2 increases. This is a major development above the conventional concrete construction [4]. One of the ways polypropylene fibers helps concrete to be more resilient against environmental damage and cracking is by strengthening it. Application of the concrete improves its resistance to sulfate and acid attacks as well as shrinkage cracking [3, 5]. As crack stoppers, fibers help to reduce the rate of bleeding and shrinkage cracking in concrete when it is plastic [6]. Furthermore, seen is a higher resistance to abrasion and chloride ion penetration, all of which helps the concrete resist wear and tear over several years [3]. Polypropylene fibers added to concrete may cause the workability of the concrete to drop given the higher air content and fiber clumping. Careful mix design is necessary to sustain the reasonable degrees of workability [1,5]. Furthermore, polypropylene fibers improve the energy absorption capacity of concrete, which benefits uses requiring impact resistance [7,8,9,10]. Polypropylene fibers added to concrete can significantly enhance several mechanical properties; yet, they can also cause problems including a decrease in the workability of the concrete and the risk of fiber clumping during the mixing process [6,11,12,13]. To make the most advantages although the disadvantages should be minimized, to solve these challenges one must pay close attention to the mix design and fiber composition. Though the improvements in compressive strength are usually small in comparison to other kinds of fibers, such polyolefin fibers, which could offer great benefits in specific uses [3].

It is a well-known fact that the utilization of concrete is next to water, which in turn increases the demand for cement. Due to the manufacturing of cement, a huge amount of carbon dioxide is emitting into the atmosphere, creating ecological imbalances. So as an urgent need a replacement for cement is to be considered and one among them is GGBS (ground granulated blast furnace slag) which is an industrialized waste by-product attained from iron and steel industry [14]. Complete replacement is considered for cement with GGBS but it doesn't fetch desirable results for mechanical properties. So, an alkali activator solution is taken in consideration. A mixture of potassium silicate and potassium hydroxide solution added at required proportions observed to achieve better strengths. To a great extent the rigid pavements are maintained for highways but not considerably for rural areas. It considered various preliminary blends to distinguish the ideal Activator Modulus (Ms) for every mix of GGBS [31,32].

Alkaline-activated slag concrete (SC) has microstructural characteristics unlike those of normal concrete when compared to conventional concrete. This is largely related to the difference binder composition and activation method SC uses. SC, which runs on ground granulated blast furnace slag (GGBS), has several advantages as a binder in terms of performance and environmental friendliness. To grasp the engineering aspects of the latter and the possible uses of the former, one must first fully understand the microstructural differences between ordinary Portland cement (OPC) concrete and SC concrete. SC concrete has a denser microstructure and a lower overall porosity than OPC concrete. This could be connected to the fact that the process of alkali activation reduces the pore volume and refines the pore size distribution produces a matrix more compact [15,16]. SC has a thick structure; however, hydration shrinkage causes small cracks to grow there, which can affect the material's permeability characteristics. OPC concrete usually follows a more constant hydration process, hence the occurrence of fissures like these is much less [16]. Alkali activated slag concrete (SC) can reach compressive strength equivalent to or even better than that of conventional concrete depending on the mix composition and curing conditions. For instance, several SC blends have shown better compressive and tensile strength than M20 grade OPC concrete [15,17]. For structural uses that call for more durability and load-bearing capacity, several SC combinations with higher flexural strength and toughness indices are favorable [17]. Enhanced resistance to chloride penetration a necessary component for longevity in salt environments, particularly those observed in maritime and de-icing applications has come from the SC materials. This is attributed to the material's refined pore network and dense microstructure [15,16]. Although the dense slag pastes employed in SC helps to lower the material's gas permeability, the presence of micro cracks may affect the material's general performance regarding carbonation [16,18].

SC has certain advantages over conventional concrete that ordinary concrete lacks, hence it's important to address the possible problems connected with its application. Its long-term durability may be affected by the existence of microcracks resulting from hydration shrinkage; the variety in the slag's composition may affect its uniformity of qualities [19,20,21]. Furthermore, enticing for usage in ecologically conscious building methods is SC's environmental advantages, including lowered CO_2 emissions [24]. Using alkaline aggregate slag concrete with polypropylene fibers has a multifarious effect on the environment, both positive and bad ones. Polypropylene fibers have the ability to increase the durable properties of concrete and so help to manage waste by means of recycled materials. Still, a life cycle analysis (LCA) has to consider the effects these fibers manufacturing and use have on the surroundings. Regarding such materials, the life cycle assessment (LCA) usually offers a whole picture of the sustainability of the materials by evaluating the environmental effects from the raw material extraction to the end of the life of the product. Recycled resources, including waste polypropylene, can provide polypropylene fibers; this helps to lower residual waste and promotes the appropriate waste management in an environment [24]. Since this recycling process generates no emissions, it is a greener substitute for the usual reinforcement materials [22,31]. Alkali-activated concrete (SC) including polypropylene fibers has a less carbon footprint than normal Portland cement concrete. With reductions of 86% and 34%, respectively, SCs are known to have substantially less effects on ecosystems and human health than standard concrete [23]. Curing plays a vital role in determining the mechanical properties of hardened concrete [33]. Slag composites activated by alkalis using polypropylene fibers offer more thermal stability than those devoid of these fibers. This is beneficial especially when the material is exposed to high temperatures since it helps to lower the energy consumption during its lifetime [24]. Polypropylene fiber manufacture calls for the use of fossil fuels and greenhouse gas emissions, both of which have the potential to offset some of the environmental advantages resulting from their usage in concrete [25,26,27]. Alkaline-activated concrete's manufacturing calls for large amounts of sodium silicate, which accounts for roughly thirty to fifty percent of the material's whole environmental impact [25]. Using polymeric materials like polypropylene fibers might cause the cost of manufacturing concrete to rise because of the need for specialized tools and the worker's skill level. The general application of this technology in the construction sector could not be without challenges [28]. Life cycle analysis (LCA) studies have shown that polymeric concrete especially those with polypropylene fibers has a lower global warming potential, acidification, and eutrophication than conventional concrete [30,31]. By reducing the amount of carbon emissions and the energy consumed, the combination of recycled aggregates and extra cementitious materials with polypropylene fibers could help to further increase the sustainability of concrete [32]. Specimen properties and its impact on mechanical and microstructural properties is discussed [34]. Research has shown that changing the mix design of geopolymer concrete with polypropylene fibers can produce mechanical properties similar to those of traditional concrete while considerably lowering the environmental consequences [29]. Although the use of polypropylene fibers in alkaline aggregate slag concrete has many benefits for the environment, including improved waste management and a reduced carbon footprint, it also generates several problems related with the production impacts and the resource intensity. Underlining the need of maximizing mix designs and using recycled components to increase the sustainability of the product is the life cycle assessment of these materials. Nonetheless, the higher expenses and technical restrictions related to polymeric concrete could restrict its application. Therefore, more study and development are needed to get over these constraints.

2. Materials

2.1 Binder

BS: 6699:1900 blast furnace slag that has been ground up (GGBS). Based on its chemical composition, the GGBS has all properties as per limits. Regular Portland cement (PC) of 53-mark following IS: 12269-1987 was utilized. The physical properties of cement were presented in the Table 1. The chemical composition of cement consists of 4.141% of Al2O3, 65.1414% of CaO, 22.144% of SiO2, 2.54% of Fe2O3, 0.4% of K2O, 0.9% of MgO, 0.2% Na2O and, 2.144% of SO3.

Table 1. Physical properties of cement

Properties	Values	Limit values based on IS: 12269-19814
Fineness - percentage weight of residue	1.21	<=10%
Standard consistency	32.1	-
Specific gravity	3.12	-
Initial setting time	72	Lower limit 30
Final setting time	218	Upper limit 600

2.2 Sand

Zone-3 sand is used in the mix design and has a bulk density of 1816 kg per cubic meter, relative density of 2.5 and a modulus of 2.03.

2.3 Coarse Aggregates

A combination of 20 and 10-mm aggregates with bulk density of 11442 kg per cubic meter, relative density of 2.7 and a modulus of 7.16 are employed as coarse aggregates.

2.4 Alkaline Solution

In general, potassium hydroxides with a virtue of 97% accessible in a stable organization by employing drops have been investigated for a successful evaluation. An important factor is the amount of water put into KOH beds. KOH pallets are purchased from a nearby retailer. Since it comes in a fluid (gel) form, potassium silicate is unique for being a potash glass that dissolves. With varying volumes of water, premium grades of the potassium silicate solution are available and are effective. 14 moles of KOH with 5% oxide content and a 1.25 modulus ratio were used in the mix formulation.

2.5 Polypropylene Fiber

These fibers, which have a hydrophobic characteristic, are used to replace 1% of the cement. After experimenting with three different doses (0.5, 1, and 1.5 percent by weight); the best results were achieved by replacing 1% of the cement with the polymer. The inquiry at hand takes into account polypropylene fibers with dimensions of 0.044-0.06 millimeters in diameter, 6.22-9 millimeters in length, and a specific gravity of 0.9.

2.6 Water

Locally available potable drinking water is used.

3. Methodology

This study investigates the use of polypropylene fibers as a percentage of cement weight to evaluate their influence on the mechanical and environmental performance of M20 grade concrete. Fig 1 represents the flow chart of methodology. The research methodology encompasses a comprehensive life cycle assessment (LCA) and an analysis of the engineering properties of various concrete mixes. The design of the M20 grade concrete was carried out in accordance with Indian Standard IS 10262-2019. Key strength metrics such as splitting tensile strength, flexural strength, and compressive strength were evaluated as per the relevant standards. Table 2 represents the mix proportions of concrete.

Conventional mixing techniques usually used for ordinary concrete were applied for the experimental process of creating alkaline-activated slag concrete (SC). The dry solid components aggregate and ground granulated blast furnace slag (GGBS) were first combined for three to four minutes. After that, extra water and an alkaline solution were added to the liquid components; the mixing process was kept on for three to four more minutes. The SC that had just been combined looked coherently and polished gray. The slump test enables the assessment of the workability of fresh concrete.

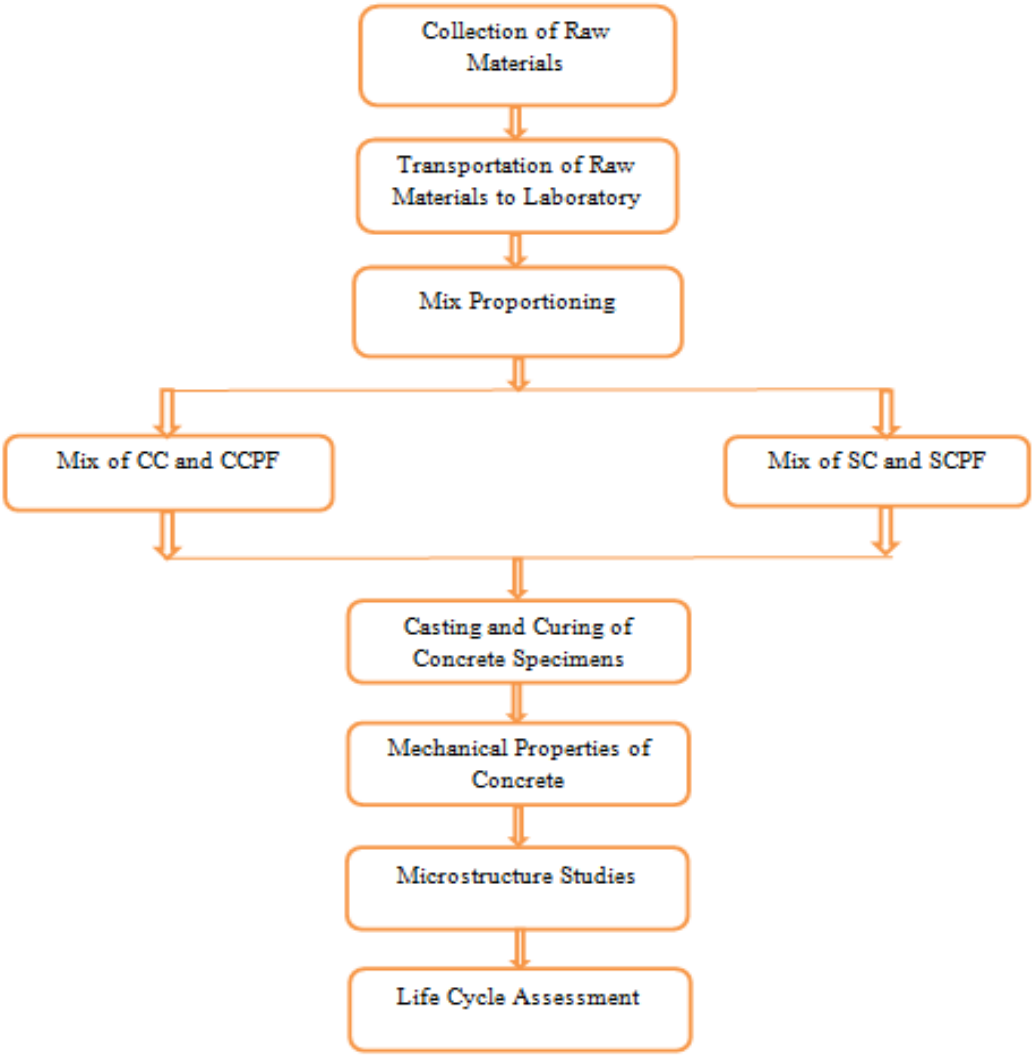

Fig. 1. Flow chart of methodology

Table 2. Mix proportions of concrete

Material		Mix Notations			
		CC	CCPF	SC	SCPF
Cement		320	316.8	-	-
GGBS in kg/m³		-	-	320	316.8
Fine Aggregate in kg/m³		695.28	694.34	694.3	694.3
Coarse Aggregate (kg/m³)	20 mm	815.8	814.6	814.6	814.6
	10 mm	407.9	407.4	407.4	407.4
Water (total) liter/m³		160	158.4	115.7	114.5
Polypropylene fiber (kg)		-	3.2	-	3.2
Activator Modulus		-	-	1.25	1.25
K_2SiO_3 (kg)		-	-	74.3	73.6
KOH solution (l)		-	-	6.7	6.7

CC = Conventional concrete; CCPF = Conventional concrete + 1% Polypropylene fiber; SC = Alkali activated slag concrete; SCPF = Alkali activated slag concrete + 1% Polypropylene fiber

The concrete mixture then was placed into steel cube molds, crushed on a vibrating table for thirty seconds, then finished externally to ensure a consistent and smooth surface. Comprising 5% potassium oxide, the combination showed a ratio of 1.25 for the activator modulus (SiO_2 relative to K_2O). The life cycle assessment modeling was determined to be done using the Eco Invent database and SimaPro program. Many components were given thought throughout the assembly phase. These ingredients were water, coarse and fine aggregates, GGBS, ordinary Portland cement (OPC), potassium hydroxide (KOH), potassium silicate (K_2SiO_2). Moreover, the modeling technique included the consumption of energy as well as the transportation related procedures. We assessed the environmental effects experienced during the cradle-to---gate phase using the Recipe 2016 (H) mid-point approach. This approach covered the analysis of categories including the possibility for global warming, the depletion of the ozone layer, the ecotoxicity of freshwater, the generation of particulate matter, the shortage of resources, the toxicity of carcinogenic compounds, and the ecotoxicity of terrestrial environments.

4. Results and Discussions

4.1 Compressive Strength

Comparatively to conventional concrete (CC), the results of the compressive strength tests conducted on the concrete mixes at 14, 28, 56, and 91 days (Fig. 2) show that the addition of polypropylene fibers and components based on slag can considerably increase the strength performance of the concrete mixes. Over all ages, the alkaline-activated slag concrete with polypropylene fibers (SCPF) mix consistently outperformed the others, followed by slag-based concrete (SC) and conventional concrete with polypropylene fibers (CCPF). The performance trends are attributable to the synergistic effects of polypropylene fibers and the enhanced reactivity of GGBS in alkali-activated systems, which contribute to improved microstructural development and crack-bridging properties.

SCPF's performance in compressive strength is consistently superior to CCPF. At 14 days, it exhibited a strength of 33.8 MPa, 34.1% higher than CCPF (25.2 MPa). This trend continued at 28 days, with SCPF achieving a strength of 37.1 MPa, a 20.8% increase over CCPF (30.7 MPa). At 56 days, SCPF reached 39 MPa, surpassing CCPF (32.9 MPa) by 18.6%. At 91 days, the SCPF mix reached its peak, achieving the highest compressive strength of 40.8 MPa, a significant 21.4% higher than CCPF (33.6 MPa).

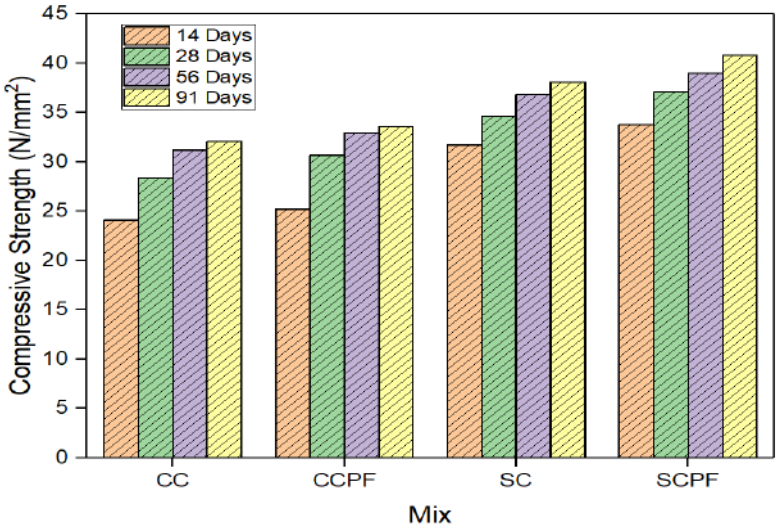

Fig. 2. Compressive strength of different mixes

The improved performance of the SCPF mix is due to the enhanced bond strength and crack resistance provided by polypropylene fibers combined with the superior pozzolanic reactivity of GGBS. This mix produces lower porosity, denser microstructure, and improved long-term strength

gains. Furthermore, alkali activation in the SC and SCPF mixes accelerated the hydration process, producing early-age strength development above that of CC and CCPF.

4.2 Flexural Strength

The flexural strength values at 14, 28, 56, and 91 days (Fig.3) represents that adding of polypropylene fibers and slag-based components improves the strength of concrete mixes relative to conventional concrete (CC) under 3-point bending. The alkali-activated slag concrete with polypropylene fibers (SCPF) mix constantly showed the highest flexural strength across all ages; slag concrete (SC) and conventional concrete with polypropylene fibers (CCPF) followed in order. The combined actions of polypropylene fibers, which improve the tensile and crack-resistance characteristics, and the pozzolanic reactivity of GGBS, which results in denser and stronger microstructures, account for much of this improvement.

At 14 days, SCPF achieved a flexural strength of 3.9 MPa, 14% higher than CCPF (3.42 MPa). By 28 days, SCPF recorded 4.31 MPa, exhibiting a remarkable 11.4% increase compared to CCPF (3.87 MPa). At 56 days, the SCPF mix displayed a flexural strength of 4.7 MPa, surpassing CCPF (3.95 MPa) by an impressive 19%. At 91 days, SCPF achieved the highest flexural strength of 4.81 MPa, a significant 19.7% higher than CCPF (4.02 MPa).

The superior performance of SCPF can be attributed to the ability of polypropylene fibers to bridge microcracks, thereby improving tensile capacity and flexural behavior, and the enhanced binding characteristics of alkali-activated slag. The accelerated hydration and dense microstructure formed in the SC and SCPF mixes further contribute to their improved performance compared to conventional concrete.

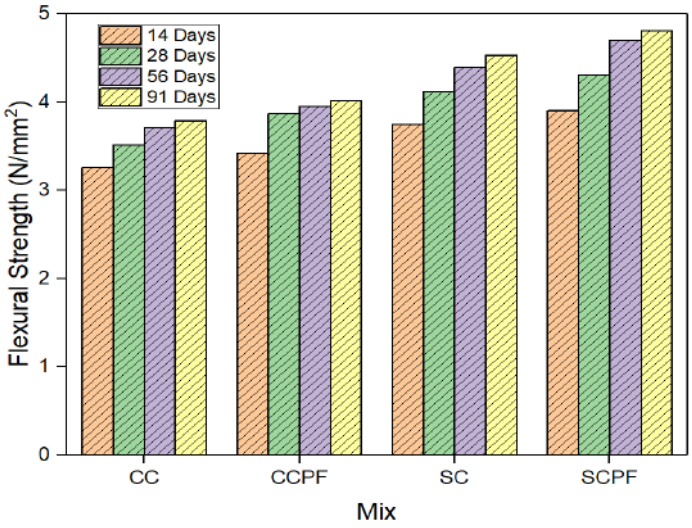

Fig. 3. Flexural strength of different mixes

4.3 Durability Studies

The concrete test specimens were 100 millimeters in diameter and were submerged in a solution of 0.3 and 1% sulphuric acid containing a pH of 1. The tests for sulphuric acid resistance were carried out on the specimens. A hand-held digital pH meter was used to determine the pH values of the sulphuric acid solutions. The average strength and weight loss observed in all mixes were presented in Tables 3 and 4.

At 0.3% and 1% fixation, all slag blends surpass CC blends regarding corrosion resistance. Compounds debase in the presence of calcium hydroxide and C-S-H gel. Low calcium concentration and a lack of calcium hydroxide in slag-based substantial blends lead to less corrosion under corrosive conditions than CC blends. However, the decalcification process that SC blends undergo results in continuous volume-led strength loss that is still less than that caused by CC blends. Substituting GGBS with a potassium hydroxide and potassium silicate mixture improves corrosion resistance

Table 3. 0.3% H_2SO_4 acid attack on different concrete mixes

	14 Days		28 Days		42 days		56 days		91 days	
	Avg Str	%w loss	Avg Str	%w loss	Avg Str	%w loss	Avg Str	%w loss	Avg Str	%w loss
CC	26.8	0.15	26.1	0.22	25.4	0.41	23.6	0.53	21.1	0.69
CCPF	27.1	0.22	26.1	0.29	24.9	0.46	23.1	0.62	21.4	0.14
SC	31.6	0.11	30.14	0.11	29.4	0.24	28.2	0.33	26.1	0.51
SCPF	33.2	0.14	31.9	0.18	30.4	0.21	28.3	0.4	26.2	0.56

Table 4. 1% H_2SO_4 acid attack on different concrete mixes

	14 Days		28 Days		42 days		56 days		91 days	
	Avg Str	%w loss	Avg Str	%w loss	Avg Str	%w loss	Avg Str	%w loss	Avg Str	%w loss
CC	26.2	0.26	25.3	0.38	24.2	1.13	22.8	1.88	19.6	2.1
CCPF	27	0.32	25.8	0.48	24	1.26	21.9	2.114	19.2	2.32
SC	30.14	0.20	29.2	0.32	28.1	0.1414	26.4	1.53	24.1	1.141
SCPF	32.8	0.24	30.4	0.40	28.4	0.89	214	1.59	25.2	1.92

4.4 Microstructural Analysis

4.4.1 Energy Dispersion X-Ray Analysis

Through EDAX analysis, surface materials can be further explored using SEM. This allows for a deeper understanding of the material's structure and characteristics. In addition, it allows for the acquisition of oxide and elemental composition. This technique is useful in conducting quantitative studies to evaluate the materials properties. For this study, the EDAX analysis is utilized to analyze the binding materials characterization. Elemental composition of two concrete mixes (CC and SC) and EDAX analysis is presented in Table 5 and Fig.4 respectively. From EDAX analysis of both CC and SC mixes, it is observed that the present of lime content is noticed more in SC mix when compared to CC mix. The below table represents the elemental and oxide compositions, from which it is observed as SC mix is having better lime content than the CC mix. This attributes improvement in strength and hydration process of SC mix when compared to CC mix. Similarly, there is no much variation in silica content noticed in both the mixes. The presence of silica content exhibits the enhancement in initial strength of concrete. Like CC mix, the presence of MgO, FeO, Al_2O_3 and ZnO was also noticed in SC mix.

Nature of EDAX Output: Elemental vs. Oxide Composition, EDAX/EDS analysis is primarily used to determine the elemental makeup of a sample by detecting the characteristic X-rays emitted from elements like Calcium (Ca), Silicon (Si), Aluminum (Al), and Oxygen (O), among others. However, when dealing with construction materials such as cement, fly ash, slag, and concrete binders, the results are typically presented in terms of oxides (CaO, SiO_2, Al_2O_3) to align with standard practices in materials science and cement chemistry. Consequently, in our research, the elemental data obtained from EDAX was converted into oxide equivalents using standard oxide conversion factors, a widely accepted method in the literature and guided by ASTM E1508 and SEM/EDS best practices.

4.4.2. Why Oxides Are Reported Instead of Raw Elements

Cementitious and geopolymer binders undergo reactions through pozzolanic or alkali-activation processes that involve oxides rather than pure elements. Representing calcium as CaO and silicon as SiO_2 offers a more chemically insightful perspective on the phase composition, such as C-S-H gel and N-A-S-H gel. This approach also facilitates more accurate comparisons with XRF and XRD results, which naturally report in terms of oxides.

4.4.3 Interpretation of EDAX Figures in the Study

The Calcium (Ca) signal detected in the EDAX spectra was attributed to Calcium Oxide (CaO), which is a predominant component in Ordinary Portland Cement (OPC), C-S-H gel, and hydration products. The Silicon (Si) peak was interpreted and documented as Silicon Dioxide (SiO_2), signifying the presence of quartz, fly ash, or silicate phases within the microstructure. Similarly, Aluminum (Al) was converted to Al_2O_3, indicating the formation of alumino-silicate phases in the alkali-activated slag mixtures. The spectra were obtained from polished sections and were confirmed to represent binder-rich areas, ensuring the accuracy of phase identification.

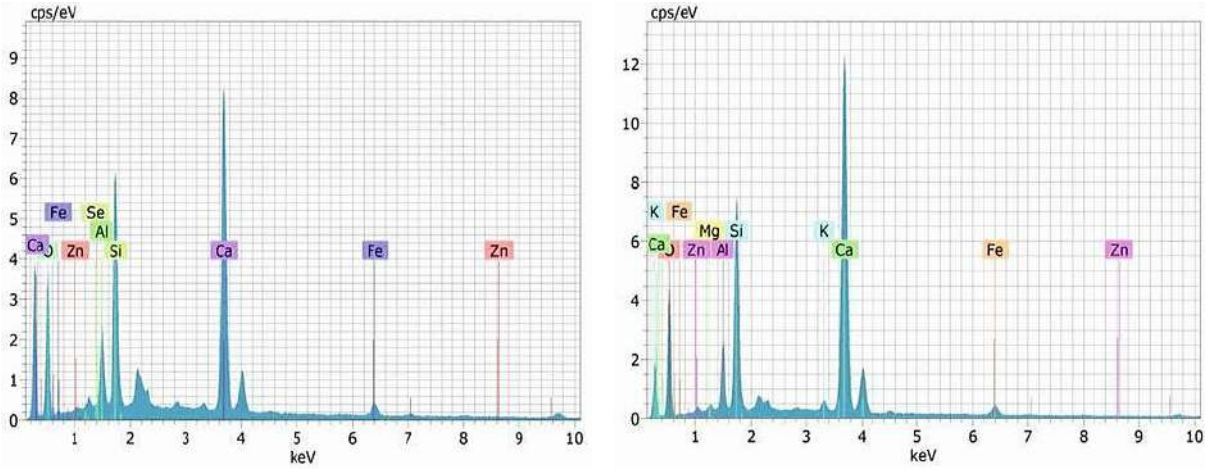

CC Mix SC Mix

Fig. 4. Elemental composition of CC and SC mixes using EDAX analysis

Table 5. Elemental and Oxide composition of CC and SC mixes

Mixes	Elements	Weight (%)	Oxide compounds	Weight (%)
CC Mix	Oxygen	35.79	CaO	56.97
	Calcium	39.26	SiO_2	28.63
	Silicon	12.92	Al_2O_3	8.90
	Aluminum	4.71	FeO	5.10
	Iron	3.96	ZnO	0.40
	Zinc	0.12	--	--
	Selenium	1.17	--	--
SC Mix	Oxygen	33.83	CaO	64.72
	Calcium	46.11	SiO_2	23.59
	Silicon	11.54	Al_2O_3	6.85
	Aluminum	1.98	FeO	3.48
	Iron	3.09	ZnO	0.38
	Zinc	0.15	MgO	0.40
	Magnesium	0.23	K_2O	0.58
	Potassium	0.23	--	--

4.4.4 Scanning Electron Microscope Analysis (SEMA)

SEMA is a type of test that involves scanning a sample using an electron beam. It is commonly used for analyzing and studying solid inorganic materials. This method can be very useful in determining the failure of certain materials. In addition to generating high-quality images, it can also measure small objects and features. Using signals generated by SEMA, a two-dimensional impression is created. This information is useful in identifying the characteristics of the sample, such as its external morphology and chemical composition. EDS is a component utilized in combination with SEMA to determine the presence of certain elements on a sample's surface. In addition, it can analyze the elemental composition of the materials and identify foreign substances. Fig 5 presents

the SEMA of CC and SC mixes at 28 days curing period. From SEMA of CC and SC it is observed that, formation ettringite is clearly visible and it is more in SC mix when compared to CC mix. It indicated SC mix is more susceptible to chemical attack and longer durability. Similarly, dense microstructure is noticed in SC mix when compared CC due to the use of GGBS in SC mix. Likewise, CH and CSH gel formation is more in SC mix when compared CC mix. Hence the presence of CH and CSH describes the improvement in compressive strength in SC mix when compared to CC mix.

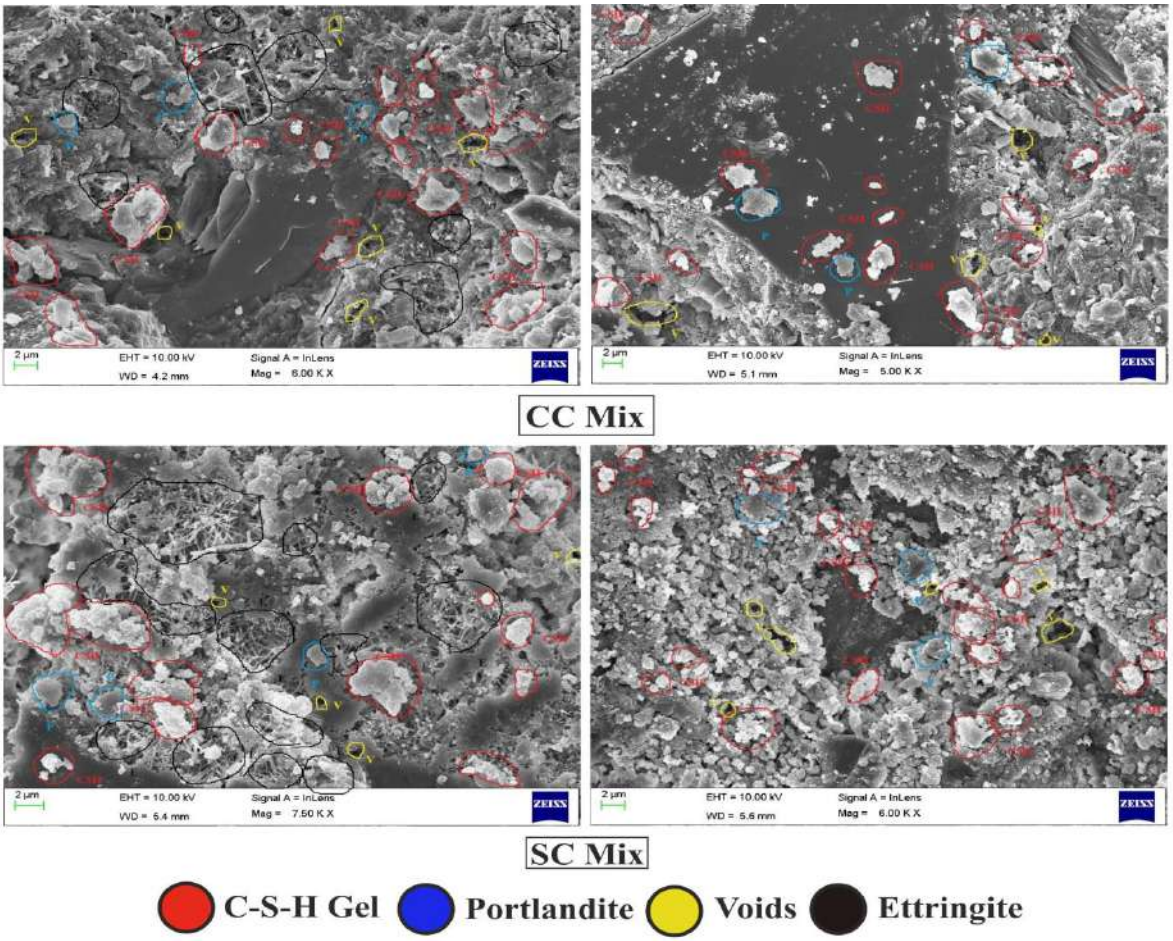

Fig. 5. SEM analysis of CC and SC mix

4.4.5 X-Ray Diffraction Analysis (XRD)

XRD is primarily used to detect early hydrated cement products, it can also function as a control tool for the process. Cement clinker's mineralogy can be regulated with the help of this technique, as it pinpoints the crystalline phases of the component at various stages, such as $CaCO_3$, $CaSO_4$, and $CaSO_2$. Other phases of the cement, such as quartz, periclase, and free lime, can also be determined using this method. The Rietveld technique provides a detailed analysis of the crystal structures in cement, including the various types of Alite and Blite, as well as calcium sulphates, free lime, and calcite. Figure 6, 7 represents the XRD analysis of CC and SC mix respectively. From XRD analysis, it is noticed that presence of SiO_2 and CH gel formation (Portlandite) is clearly visible and maximum intensity is noticed for the two elements. The presence of SiO_2 and Portlandite exhibits the long-term strength and durability of CC and SC mix. When compared CC mix the presence of these two elements intensity is slightly more in SC mix. In addition to these elements the presence of sinnerite is observed in SC mix. It is only observed in SC mix and not in CC mix. Sinnerite is a mineral (Cu6As4S9) helps in enhancing compressive strength and durability of SC mix. It also acts as a nucleation site for cement hydration products, helping to form a denser and more compact microstructure.

The XRD analysis was conducted to identify the crystalline phases present in both conventional concrete (CC) and alkali-activated slag concrete (AASC), with and without the addition of polypropylene fibers. For conventional concrete, the main phases identified were portlandite ($Ca(OH)_2$), calcium silicate hydrate (C-S-H), and ettringite, which are typical of OPC hydration products. The intensity of the portlandite peaks reflects the progress of hydration and the presence of free lime in the matrix. Additionally, minor peaks corresponding to unreacted clinker phases such as alite and belite were noted, particularly in the early stages of curing, indicating incomplete hydration.

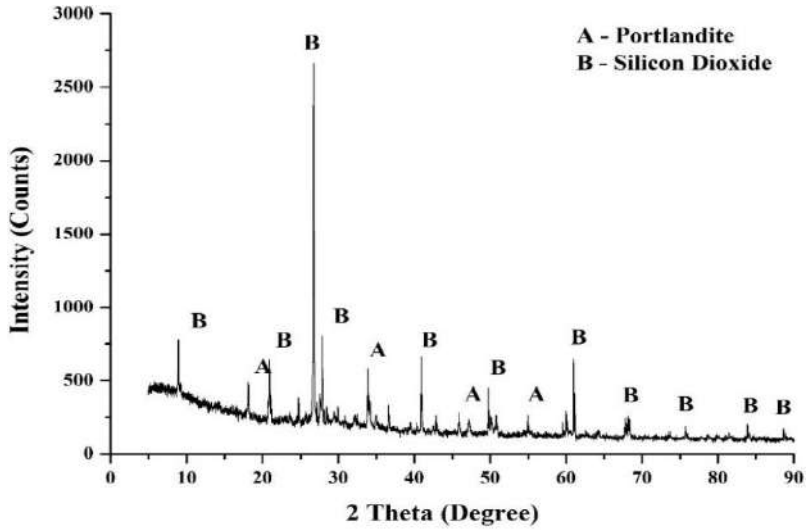

Fig. 6. XRD analysis of CC mix

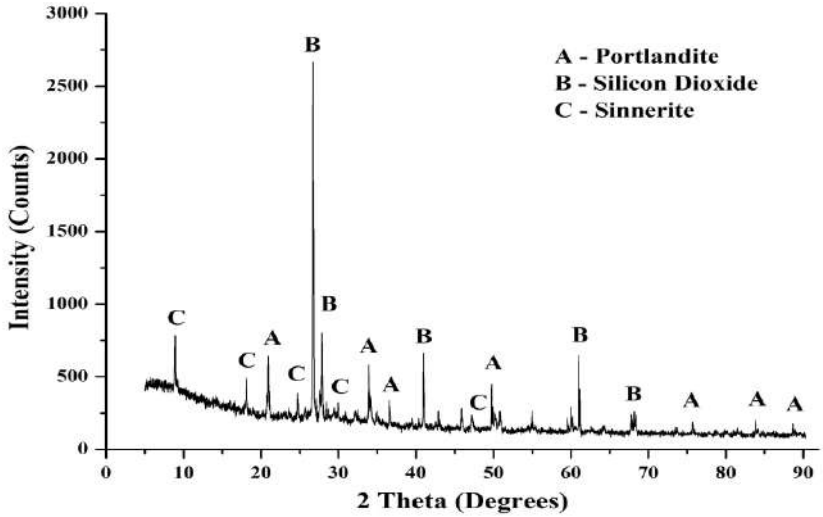

Fig. 7. XRD analysis of SC mix

Conversely, the XRD patterns of AASC mixtures revealed markedly distinct mineralogical characteristics. The emergence of low-crystalline or amorphous alumina-silicate phases, such as N-A-S-H gel and C-A-S-H type gels, was suggested by a broad hump in the 20–35° 2θ range, indicative of poorly crystalline or gel-like structures. Furthermore, crystalline phases like hydrotalcite, calcite, and residual slag components such as akermanite were observed. The presence of hydrotalcite implies the formation of secondary reaction products under high alkaline conditions, enhancing chemical stability. In certain AASC samples, rare trace phases like sinnerite were also detected, pointing to complex secondary reactions involving trace elements within the slag matrix. Additionally, the inclusion of polypropylene fibers did not significantly change the primary crystalline composition but might have affected the degree of crystallinity and microstructure refinement. Overall, the comparison between the mixes shows that AASC systems have a higher

proportion of amorphous content compared to CC, aligning with their geopolymer-like reaction mechanism. These distinctions are vital for understanding the long-term performance, durability, and sustainability of alkali-activated systems. This expanded discussion has been incorporated into the revised thesis to offer clearer insights into the mineralogical behavior of the binders and the influence of material chemistry on phase development.

5. Life Cycle Assessment (LCA)

LCA is a process utilized to evaluate a product or service's environmental impact. This analysis can be performed by comparing the energy consumption of different processes and activities within a supply chain. Various software and databases are utilized in this process. Researchers are currently extending LCA to cities. This process estimates a product's impact on the environment. The framework provides an in-depth analysis of the lifecycle of a product. This process involves considering the various elements that impact the planet during a service's lifecycle, including extraction of raw materials, the production phase, and the product's end. The life cycle stages of a product are referred to as the elements of a product's lifecycle. Using LCA, an organization can determine the impact of its products and services on the environment at the beginning, middle, and end. The life cycle analysis process iteratively updates the elements of the analysis. It is referred to as LCA, and it utilizes a standardized approach. This process is reliable, transparent, and conforms to ISO 14040 and 14044 specifications. Fig. 8 represents the LCA framework.

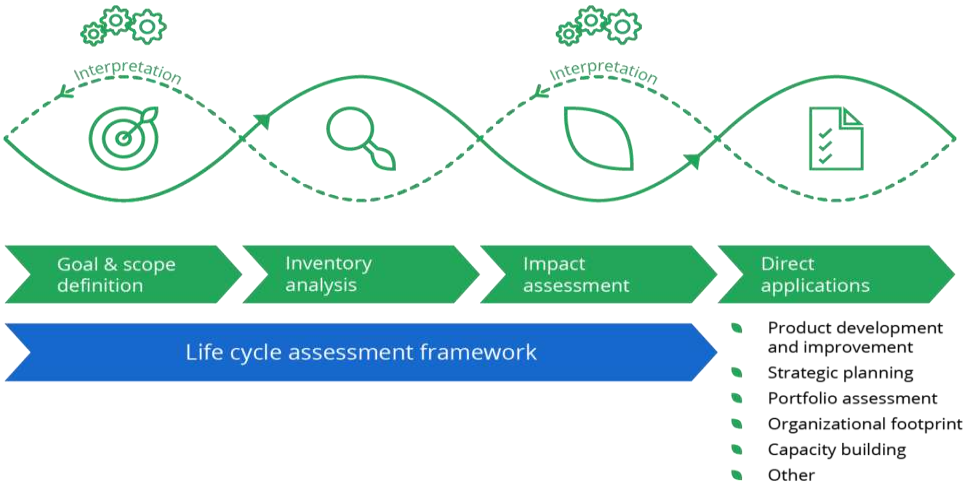

Figure 8. LCA framework

5.1 Global Warming Potential (GWP)

From Fig.9 it is observed that impact GWP is more for OPC in CC and CCPF mixes. Manufacturing of OPC for CC and CCPF contributes almost 283.57 and 280.74 kg of CO_2 for a cubic metre of concrete respectively. However overall impact of CO_2 contribution for CC and CCPF mixes is found to be 299.02 and 308.01kg respectively. From CC and CCPF mixes, it is observed that manufacturing of OPC and its usage in CC and CCPF mixes was found to be hazardous to the environment and causes depletion of ozone layer and natural resources consumption. Similarly, the overall impact of SC and SCPF mixes is found to be 97.03 and 77.95 kg CO_2 to the environment. When compared to CC, CCPF and SC, SCPF mixes slag based concrete mixes helps in reducing the overall emission of carbon emission to the environment. Not only strength and durability point of view, SC and SCPF mixes are found to sustainable and environmentally friendly in comparison to CC and CCPF mixes.

- TP: overall Impact of Transportation in LCA studies from cradle-gate stage
- E: overall Impact of Electricity in LCA studies from cradle-gate stage
- W: overall Impact of water in LCA studies from cradle-gate stage

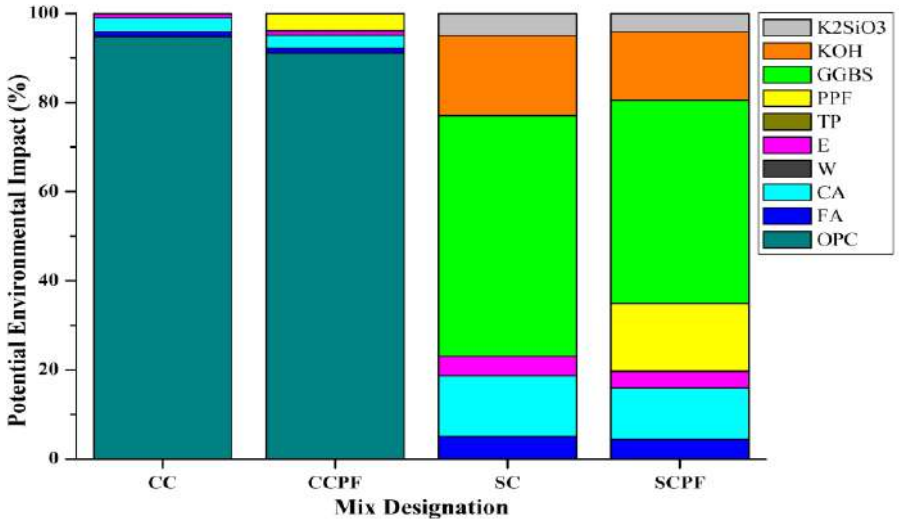

Fig. 9. Impact of global warming potential

5.2 Potential Stratospheric Ozone Depletion (PSOD)

The reduction of the ozone layer over the surface of Earth can lead to various environmental issues. Some of the harmful substances that can affect the environment include freons, chlorofluorocarbons, and methyl chloroform. From Fig. 10 it is observed that, overall impact of PSOD for CC and CCPF mixes are found to be 000466 and 000490 kg CFC11 respectively. Similarly, the overall impact of PSOD for SC and SCPF mixes are found to be 0065 and 00363 kg CFC11 respectively. Compared to SC and SCPF mixes, the impact of PSOD is greater in CC, and CCPF mixes due to the usage of OPC in CC mixes, as observed in GWP. Hence, slag-based mixes are more sustainable and friendly than conventional concrete mixes.

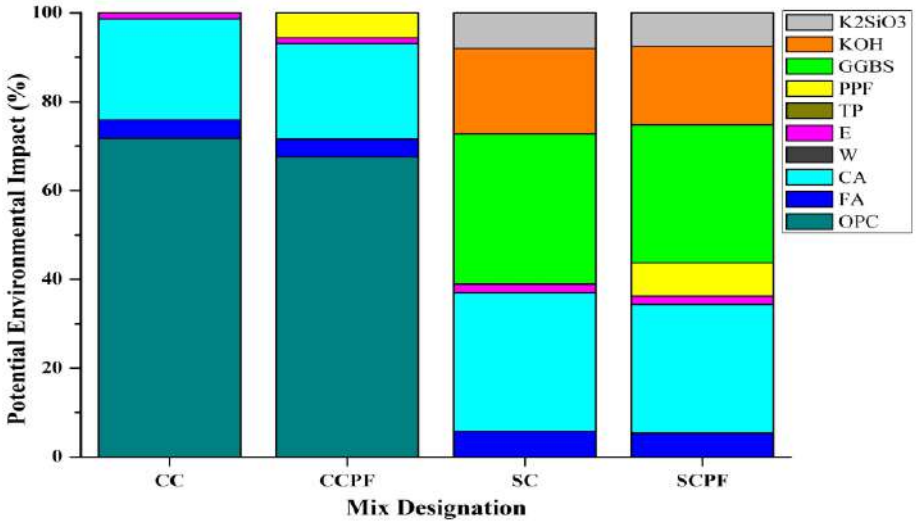

Fig.10. Impact of potential stratospheric ozone depletion

5.3 Freshwater Ecotoxicity (FE)

The accumulation of chemicals in the environment can happen throughout a service or product's lifecycle. Fig. 11 shows the impact of FE impact of all the ingredients used in CC and CCPF mix is found to be 0.05 and 0.06 kg 1,4-DCB respectively. Similarly for SC mixes it is found to be 0.37 and 0.22 kg 1,4-DCB respectively. It is also observed that the impact of SC and SCPF mixes on FE is found to be minimum in comparison to CC and CCPF mixes. Hence the use of GGBS and other waste ingredients in concrete manufacturing helps in reducing the pollution and contamination of freshwater and improves the quality of water and human health.

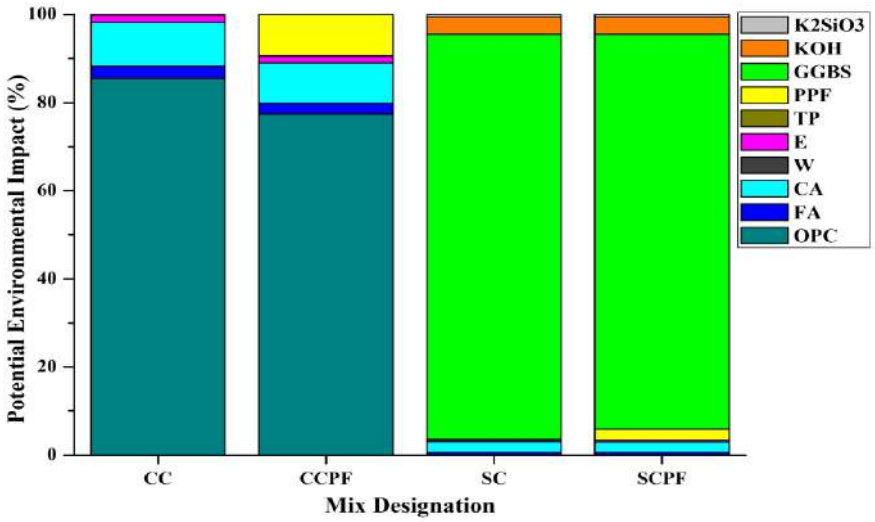

Fig. 11. Impact of Freshwater ecotoxicity

5.4 Fossil Resource Scarcity (FRS) and Mineral Resource Scarcity (MRS)

Enhanced oil recovery is one of the techniques that can be used when conventional resources are no longer available. Impact assessment of various types of CC and SC mixes using waste industrial by-products are presented in Fig.12 & 13. As desired, cement manufacturing industries consume large quantities of natural resources, and they are energy intensive. Hence the use of OPC in CC is responsible for the impact on FRS and MRS is found to be 40.01 kg oil eq and 0.41 kg cu eq respectively. Similarly, for CCPF mix it is observed that, impact of FRS and MRS in slightly more (46.25 kg oil eq and 0.43 kg cu eq respectively). Likewise, SC and SCPF mixes for FRS is found to be 20.76 and 22.00 kg oil eq. This is less when compared to CC and CCPF mixes. It is also observed that, MRS for SC and SCPPF mixes found to be slightly more when compared to CC and CCPF mixes. It is mainly due to the use of KOH and K_2SiO_3 in SC and SCPF mixes to improve the hydration process. Overall, the use of CC and CCPF concrete manufacturing, surface finishing and transportation causes a lot of health hazards and polluting environment. From Fig. 12 & 13, it is also observed that, not only FRS, use of these waste by-products will also result in reducing the consumption natural mineral resources and overcome the depletion challenges and help in saving mother earth for future generations.

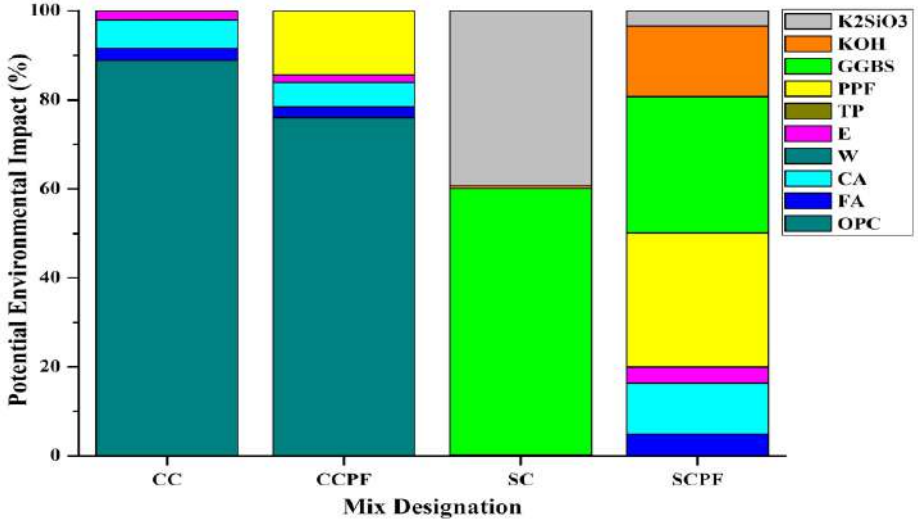

Fig.12. Impact of fossil resource scarcity

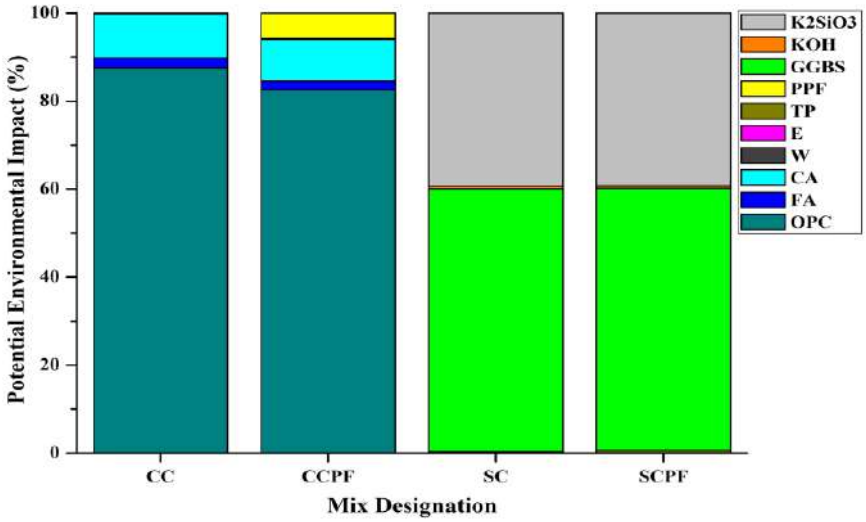

Fig. 13. Impact of mineral resource scarcity

5.5 Human Carcinogenic Toxicity (HCT)

The release of chemicals into the air and water can happen throughout a service or product's lifecycle. The estimated stocks of products contain hundreds of chemicals, which can result in varying toxic effects on individuals. Some of these include NOx, PM10, SOx, and CO. An impact category is used to explain how exposure to harmful substances can affect people. These include the effects of food, water, or air inhalation, as well as skin penetration. Impact of all the ingredients used for manufacturing bricks on HCT is presented in Fig. 14. Not only environmental pollution, it is also affecting human health in two ways HCT and HNCT diseases. If we compare all the ingredients and their effect on HCT, KOH and K_2SiO_3 and OPC plays a major role in causing the diseases to living life. To improve the quality of living life and human health, use of waste industrial by-products in concrete will give justice in reducing the disposal challenges, landfill challenges and helps in reducing the diseases related to HCT.

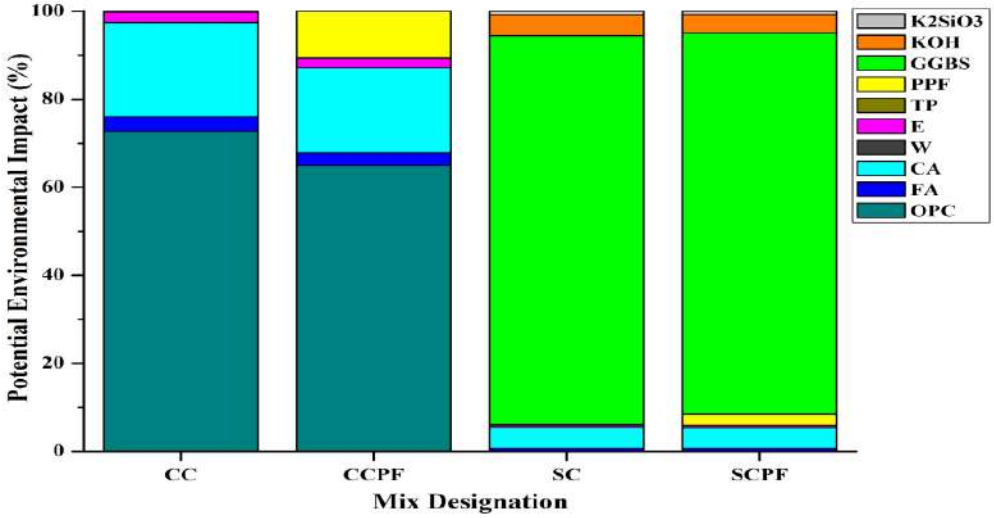

Fig.14. Impact of human carcinogenic toxicity

5.6 Terrestrial Ecotoxicity (T-ECO) and Marine Ecotoxicity (M-ECO)

The deposition of certain nutrients, like sulfur and nitrogen, in acidified forms can affect the chemical properties of soil. Various ecological factors, such as exposure to harmful chemicals, environmental fate, and ecological damage can also influence Eco toxicity's effects. There are various factors that can affect the well-being of the environment, and these are categorized into

three main categories: fate; exposure; and damage. Fate determines how many chemicals are released into the ecosystem, while exposure measures the level of pollutants that can be exposed. Impact of ingredients used in various types concrete (CC, CCPF, SC and SCPF) is presented in Fig.15 & 16. From the figure it is observed that, impact of T-Eco and M-Eco is more due to the consumption of OPC, GGBS, PF KOH and K_2SiO_3. The consumption of the waste related by products like GGBS will also help in reducing the impact of these wastes on terrestrial activities to save animals, birds and human beings and overcomes the challenges associated with these wastes.

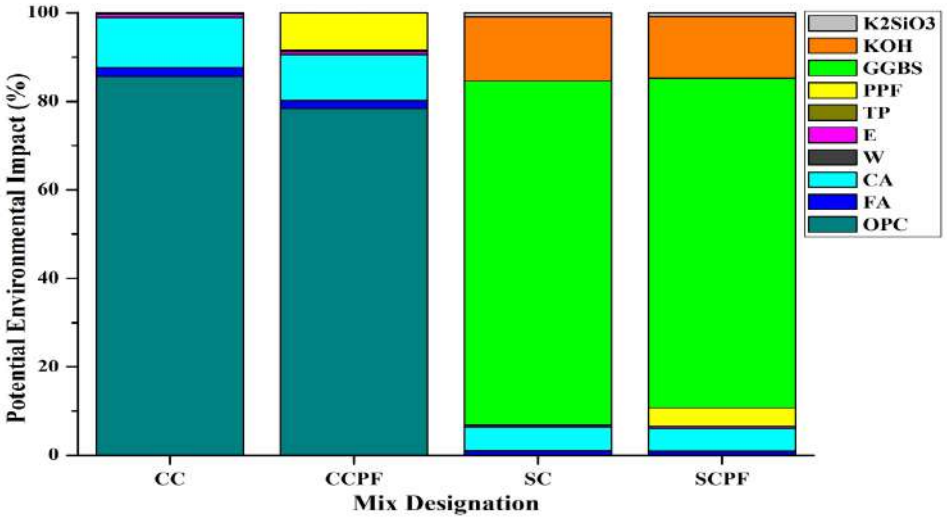

Fig. 15. Impact of Terrestrial ecotoxicity

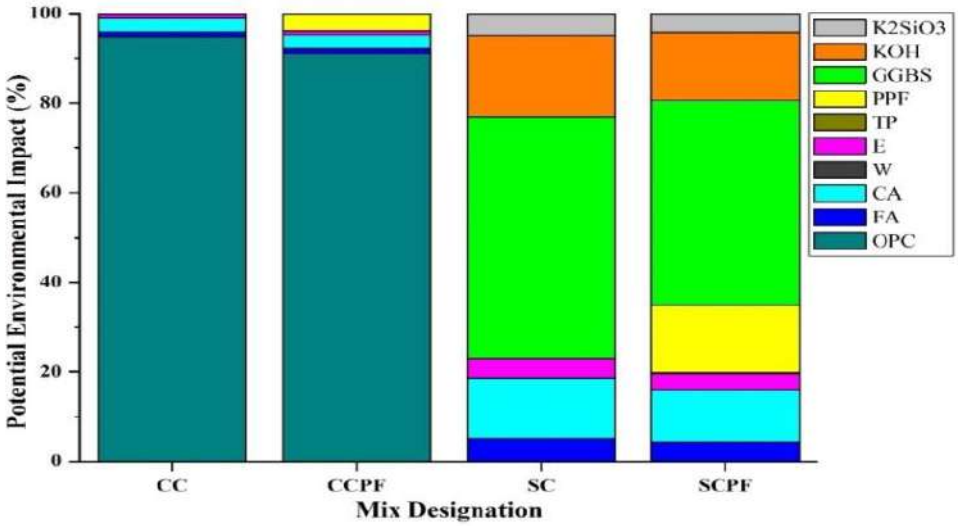

Fig. 16. Impact of Marine ecotoxicity

5.7 Fine Particulate Matter Formation (FPMF)

The initial release of NOx, SO_2, and NH_3 into the atmosphere triggers the formation of PM2.5. These particles are then converted into secondary aerosols through atmospheric chemistry. In addition to causing premature death, exposure to PM2.5 can also lead to other health conditions. From Fig. 17 it is observed that, consumption of these industrial wastes by products will reduce the further contamination of fresh air and to overcome the challenges associated with human health, it can be used effectively in concrete manufacturing. Similarly, from the Figure 17 it is observed that the overall impact of CC and CCPF mixes is found to be 0.29 and 0.31 kg PM2.5 eq, respectively. Similarly, SC and SCPF have marginally less impact of about 0.22 and 0.17kg PM2.5 eq, respectively. Use of GGBS in SC and SCPF mixes can be minimized further its concentration contamination with

air, water, and soil by replacing it with cement by GGBS in SC and SCPF manufacturing to save mother earth.

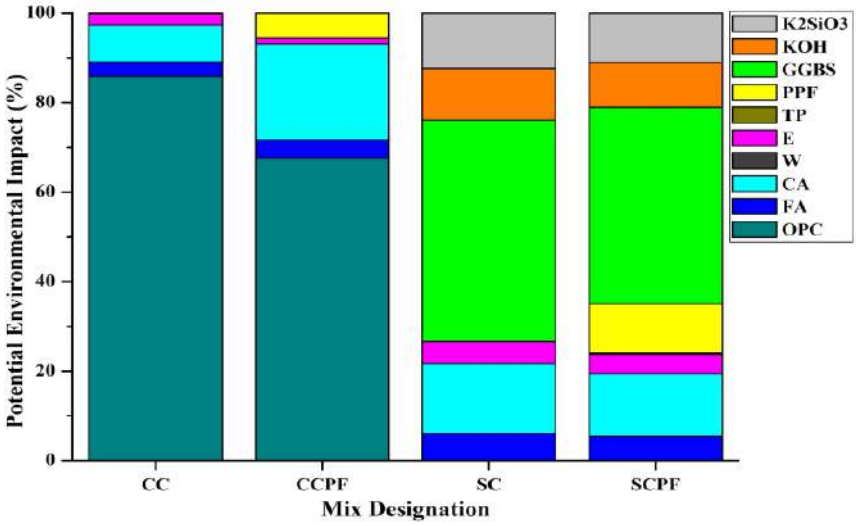

Figure 17. Impact of fine particulate matter formation

5.8 Scientific Relevance and Practical Implementation

This research mainly focuses on the use of fibers in concrete. It improves the durability and performance of concrete. When mixed with concrete, they increase the stiffness of the concrete members also increases the cracking resistance. It improves structure lifespan. Its ability to endure environmental stresses and chemical degradation helps minimization under adverse climatic conditions. This helps reduce the cost of repairs and maintenance.

6. Conclusions

- According to the results, the compressive strength is around 20.8% higher, and the flexural strength is about 11.4% higher in slag mixes than in cc mixtures at 28 days. The extra lime and alumina in GGBS aid in the formation of C-S-H gel by reacting with cementitious substituents, improving durability and strength. The presence of polypropylene fibers aids in the arrest of microcracks, increases density, and makes the formation less porous. The presence of PPF makes concrete impact and abrasion resistant which helps in pavement durability. SC mixtures had higher pozzolanic reactivity and created superior C-S-H and C-H gels.
- The life cycle assessment studies on CC and SC mixes indicates the impacts of several categories on ecology. It is observed and concluded that, replacement of cement with other conventional materials reduces the impact on environment and also helps to make green concrete. The incorporation of polypropylene fibers has resulted in improvable properties of durability and mechanical. The utilization of GGBS in SC and SCPF helps in the improvement of environment by reducing the carbon footprints.
- It is examined that the strength of the M20 graded SC mix under ambient curing conditions almost equated with the target mean strength of the M30 grade conventional concrete mix, which is suitable for the construction of low-volume roads as per IRC: SP:62-2014. Due to the suitable criteria, the SC mix is considered for the project continuation. The highest flexural strength of 4.53MPa is achieved at 91 days of ambient curing. For traffic less than 50 CVPD (commercial vehicles per day), compressive and flexural strengths should not be less than or equal to 30 and 3.8 MPa. For low-volume concrete roads, 90 days strengths are used. Fatigue is not considered for tribal area pavements and low-volume roads. The standard concrete-connected slabs for rural roadways do not need to be reinforced. Due to the higher flexural strengths observed in SC and SCPF mixes, they can resist significant stresses, which in turn helps reduce the pavement's thickness, making it cost-effective.

Acknowledgment

All authors would like to thank GITAM (Deemed to be University) for providing facilities for this research.

References

[1] Chen Y, Haq SU, Iqbal S, Khan I, Room S, Khan SA. Performance evaluation of indented macro synthetic polypropylene fibers in high strength self-compacting concrete (SCC). Dent Sci Rep. 2024.
[2] Siva A, Reddy R, Manoharan P, Rachel P. Experimental studies in the flexural performances of novel polypropylene monofilament fibers as additives in concrete with conventional concrete. NanoWorld J. 2023.
[3] Azandariani MG, Vajdian M, Asghari K, Mehrabi S. Mechanical properties of polyolefin and polypropylene fibers-reinforced concrete: An experimental study. Compos Part C Open Access. 2023.
[4] Thanmy E, Tholkapiyan M. Improvement of concrete strength by addition of novel polypropylene fiber in comparison with compressive strength of conventional concrete. NanoWorld J. 2023.
[5] Ahmad J, Burduhos-Nergis DD, Arbili MM, Alogla SM, Majdi A, Deifalla AF. A Review on Failure Modes and Cracking Behaviors of Polypropylene Fibers Reinforced Concrete. Buildings. 2022 Nov 11;12(11):1951. https://doi.org/10.3390/buildings12111951
[6] Jayaram M, Naresh J, Thipparthi K, Kastro Kiran V. Assessment on mechanical properties of concrete with polypropylene fiber. IOP Conf Ser: Earth Environ Sci. 2022 Mar 1;982(1):012004. https://doi.org/10.1088/1755-1315/982/1/012004
[7] Kanukuntla R. Effect of Inclusion of Polypropylene Fiber on Behavior of Concrete. JoCCS. 2022; Dec 27:34-8. https://doi.org/10.46610/JoCCS.2022.v07i03.005
[8] Zhang S, Zhao B. Influence of polypropylene fibre on the mechanical performance and durability of concrete materials. European Journal of Environmental and Civil Engineering. 2012 Nov;16(10):1269-77. https://doi.org/10.1080/19648189.2012.709681
[9] Bagherzadeh R, Sadeghi A, Latifi M. Utilizing polypropylene fibers to improve physical and mechanical properties of concrete. Textile Research Journal. 2012 Jan;82(1):88-96. https://doi.org/10.1177/0040517511420767
[10] Arunachalam A, Karthikeyan J. Performance of polypropylene fibre in high-performance concrete. Proc Inst Civ Eng Constr Mater. 2015;168.
[11] Prathipati ST, Rao C. A study on the uniaxial behavior of hybrid graded fiber reinforced concrete with glass and steel fibers. Materials Today: Proceedings. 2020;32:764-70. https://doi.org/10.1016/j.matpr.2020.03.558
[12] Pangestuti EK, Handayani S, Adila H, Primerio P. The effect of polypropylene fiber addition to mechanical properties of concrete. IOP Conf Ser: Earth Environ Sci. 2021 Mar 1;700(1):012057. https://doi.org/10.1088/1755-1315/700/1/012057
[13] Junghare T, Kulsange L, Satpude H, Bawankule A, Narnaware A. Effect of polypropylene fiber on concrete. J Emerg Technol Innov Res. 2020.
[14] Koniki S, Kasagani H, Sri R, Prathipati T, Paluri Y. Mechanical behavior of triple-blended hybrid fiber-reinforced concrete: An experimental and numerical study. Innov Infrastruct Solut. 2024.
[15] Vance K, Aguayo M, Dakhane A, Ravikumar D, Jain J, Neithalath N. Microstructural, Mechanical, and Durability Related Similarities in Concretes Based on OPC and Alkali-Activated Slag Binders. Int J Concr Struct Mater. 2014 Dec;8(4):289-99. https://doi.org/10.1007/s40069-014-0082-3
[16] Haakkinen T, Pyy H, Koskinen P. Microstructural and permeability properties of alkali-activated slag concrete. Res Rep. 1987.
[17] Huri GM, Rao KS. Engineering properties of alkali activated slag concrete under ambient and heat curing. Int J Eng Trends Technol. 2017.
[18] Marathe S, Mithanthaya I, Shenoy RY. Durability and microstructure studies on Slag-Fly Ash-Glass powder based alkali activated pavement quality concrete mixes. Construction and Building Materials. 2021 Jun;287:123047. https://doi.org/10.1016/j.conbuildmat.2021.123047
[19] Divsholi BS, Lim TYD, Teng S. Durability Properties and Microstructure of Ground Granulated Blast Furnace Slag Cement Concrete. Int J Concr Struct Mater. 2014 Jun;8(2):157-64. https://doi.org/10.1007/s40069-013-0063-y
[20] Amar R, Devanand R, Harsha HN, Sachin K. Experimental studies on GGBS based geopolymer concrete. Mater Today Proc. 2023. https://doi.org/10.1016/j.matpr.2023.04.297
[21] Procházka L, Boháčová J, Vojvodíková B. Effect of Admixtures on Durability and Physical-Mechanical Properties of Alkali-Activated Materials. Materials. 2022 Mar 8;15(6):2010. https://doi.org/10.3390/ma15062010

[22] Talkeri AH, Shankar AUR. A study on initial setting time and the mechanical properties of AASC using the PS ball as fine aggregate. Int J Pavement Res Technol. 2019 Nov;12(6):659-63. https://doi.org/10.1007/s42947-019-0078-0
[23] Starczyk-Kołbyk A. Analysis of the life cycle concrete with the addition of polypropylene fibers. Archives of Civil Engineering. 2024; Jun 18:23-42. https://doi.org/10.24425/ace.2024.149849
[24] Kar A, Maeijer PKD. Environmental impact analysis of alkali-activated concrete with fiber reinforcement. Infrastructures. 2023.
[25] Khelifa M, Ziane S, Mezhoud S, Ledesert C, Hebert R, Ledesert B. Compared Environmental Impact Analysis of Alfa and Polypropylene Fibre-Reinforced Concrete. Iran J Sci Technol Trans Civ Eng. 2021 Sep;45(3):1511-22. https://doi.org/10.1007/s40996-020-00555-x
[26] Hsie M, Tu C, Song P. Mechanical properties of polypropylene hybrid fiber-reinforced concrete. Materials Science and Engineering: A. 2008 Oct;494(1-2):153-7. https://doi.org/10.1016/j.msea.2008.05.037
[27] Paudel S, Pudasaini A, Shrestha RK, Kharel E. Compressive strength of concrete material using machine learning techniques. Cleaner Engineering and Technology. 2023 Aug;15:100661. https://doi.org/10.1016/j.clet.2023.100661
[28] Teja G, et al. Evaluating the strength and durability characteristics of concrete incorporating steel slag GGBS and silica fume. IOP Sci. 2024.
[29] Thakur G, Singh Y, Singh R, Prakash C, Saxena KK, Pramanik A, et al. Development of GGBS-Based Geopolymer Concrete Incorporated with Polypropylene Fibers as Sustainable Materials. Sustainability. 2022 Aug 26;14(17):10639. https://doi.org/10.3390/su141710639
[30] Abhishek HS, Prashant S, Kamath MV, Kumar M. Fresh mechanical and durability properties of alkali-activated fly ash-slag concrete: a review. Innov Infrastruct Solut. 2022 Feb;7(1). 116. https://doi.org/10.1007/s41062-021-00711-w
[31] Chen Y. Prediction of the compressive strength from resonant frequency for low-calcium fly ash-based geopolymer concrete [Master's thesis]. Victoria (Canada): University of Victoria; 2017.
[32] Colangelo F, Petrillo A, Cioffi R, Borrelli C, Forcina A. Life cycle assessment of recycled concretes: A case study in southern Italy. Science of The Total Environment. 2018 Feb;615:1506-17. https://doi.org/10.1016/j.scitotenv.2017.09.107
[33] Ealias AM, Emlin V. Development of high-performance self curing concrete using super absorbent polymer and silica fume additives. Res. Eng. Struct. Mater., 2023; 9(2): 393-403. http://dx.doi.org/10.17515/resm2022.469st0713tn
[34] Chowdary MVSSP, Asadi CSS, Reddy CR. Comprehensive analysis of specimen's properties and fiber type on the performance of Indian origin fine aggregates-based composite. Res. Eng. Struct. Mater., 2023; 9(2): 563-577. http://dx.doi.org/10.17515/resm2023.637me0112

Blank Page

Research on Engineering Structures & Materials
www.jresm.org

Research Article

Mechanical properties and optical efficiency of light-transmitting concrete using plastic optical fibre and industrial wastes

Kaushal Sharma [a], Kiran Devi [*,b], Neeraj Saini [c]

Dept. of Civil Engineering, Faculty of Engineering & Technology, SGT University, Gurugram, India

Article Info

Article History:

Received 03 July 2025

Accepted 26 July 2025

Keywords:

Optical fibre;
Industrial wastes;
Light-transmitting concrete;
Compressive strength;
Light transmittance;
Cost analysis

Abstract

Construction is a global industry that is currently experiencing significant transformations. Today, the rise in population has led to an increase in energy consumption, alongside an increase in high-rise construction in urban areas. The shade from tall structures contributed to increased energy use. This provides a way to diminish energy consumption related to building illumination by implementing innovative approaches. The light-transmitting concrete, comes into light in this scenario. In the present study, the influence of different percentages of optical fibre on the distinct properties of light-transmitting concrete at the various curing ages was examined. The plastic optical fibre with 0%, 0.5%, 1%, 1.5%, 2%, and 2.5% was used in the concrete. The different mechanical properties and cost analysis of the various mixes were investigated. The optimized percentage of optical fibre (1%) was used with the industrial wastes, such as ground granulated blast furnace slag (20%) and micro silica (10%), to study the performance of concrete. Results showed that the incorporation of plastic optical fibre (1%) with the industrial wastes, i.e., blast furnace slag at 20%, increased the strength by 17% while maintaining the light-transmitting characteristics of concrete as compared to the control mix. However, the use of optical fibre (1%) hiked the cost of construction by 40% due to the higher cost of optical fibre.

© 2025 MIM Research Group. All rights reserved.

1. Introduction

Concrete is the predominant construction material in the industry because of its cost-effectiveness, durability, and strength. Concrete has become a key material in modern construction, with advanced applications in high-rise structures, tunnels, bridges, and pavements, particularly in urban infrastructure development [1-3]. This elevates the necessity for artificial illumination to preserve the visibility and brightness of indoor activities. According to the United Nations Environment Program 2013, artificial lighting accounted for approximately 20% of global electricity consumption and 6% of CO_2 emissions [4]. Various methods have been implemented to mitigate energy consumption resulting from the utilization of artificial light, including the development of new, innovative construction materials, i.e., Light Transmitting Concrete (LTC), that can transmit light [5-6].

In 2001, Aron Losonczi, a Hungarian architect, was the first to develop and manufacture translucent concrete, also known as LTC [7]. LTC facilitates the transmission of light through the concrete, thereby enhancing visibility and decreasing the building's energy consumption for light. LTC is employed in a diverse array of applications, including pavements, road markings, sidewalks, speed humps, staircases, and tunnels, in addition to its usage in architectural features and building materials [8-11]. In addition, LTC can be employed as load-bearing or non-bearing wall partitions

*Corresponding author: kiranbimbhra@gmail.com
[a]orcid.org/0000-0003-2063-5276; [b]orcid.org/0000-0003-4910-4399; [c]orcid.org/0000-0002-7304-5539
DOI: http://dx.doi.org/10.17515/resm2025-997me0703rs

to permit daylight to enter the interior spaces, thereby improving the illuminance level of the interior environment. Nevertheless, LTC is not yet extensively embraced and implemented in the construction sector as a green construction material [12].

The addition of optical fibre in self-compacting concrete increased the compressive and tensile strength of the light-transmitting concrete [13]. The strength of LTC increased with the increase in the percentage of optical fibre [5]. The optical fibre of 1 mm diameter increased the strength of concrete; afterwards, it reduced the strength of LTC [14]. The compressive strength increases with the addition of POF ratios because the loading machine is orientated perpendicularly to the POF arrangement, which is maintained at a consistent spacing within the cubic specimens [11]. In the case of artificial light, peak values were obtained at the nearest tested distance, with an increase in the distance between the light source and the LTC value of light transmission decreasing [4, 15]. TSCC absorbs a segment of this light while dispersing another segment. This may be evident in the transmission rates of TSCC light and specific aberrations of the Gaussian curve in the graphs [11]. The incorporation of optical fibre and resin in light-transmitting concrete led to reduced electricity consumption. Polymethyl methacrylate tubes increased the illumination energy efficiency [16]. Chiew et al. [10] developed an artificial neural network model to predict the light transmittance of the light-transmitting concrete. Results showed that the incidence angle affected the light transmittance of LTC. Pourkazemi et al. [17] studied the mechanical characteristics and energy consumption of concrete using different illuminating materials such as plastic optical fibre, ribbed resin rod, glass waste, and epoxy resin. Results showed that the materials increased the strength and light transmittance characteristics. It was found that all the materials in the concrete were suitable for cold climates. Nam et al. [12] studied the influence of polymethyl methacrylate (PMMA) up to 30% in the light-transmitting concrete. The compressive strength decreased, and light transmittance ability increased with the increase in PMMA content. Chiew et al. [18] investigated the performance of self-compacting concrete LTC using optical fibre under the sunlight. It was reported that the use of optical fibre reduced the compressive strength and enhanced the light transmittance ability.

1.1 Objectives and Significance

In the present study, the optical fibre with various proportions, i.e., 0%, 0.5%, 1%, 1.5%, 2%, and 2.5%, in the LTC was used to study the different properties, i.e., compressive strength by destructive and non-destructive tests, ultrasonic pulse velocity, dynamic modulus, and cost. The optimized proportion of optical fibre will be used for further study. The industrial wastes, i.e., ground granulated blast furnace slag (GGBFS) at 20% and micro silica (MS) at 10%, were incorporated in the light-transmitting concrete with an optimized percentage of optical fibre (1%). The correlation of compressive strength between the destructive test and the non-destructive test was derived. The objective of the study is to find the optimized percentage of plastic optical fibre in concrete. The novelty of the present work is to find out the optimum content of optical fibre in the concrete in terms of strength. Also, the feasibility of industrial wastes, i.e., MS and GGBFS, with plastic optical fibre was examined in LTC in different aspects, i.e., strength, durability, and cost. The performance of the different mixes was evaluated.

2. Methodology

The present investigation employed 43-grade ordinary Portland cement in accordance with IS:8112 [19]. Crushed sand and coarse aggregates of 10 mm size, compliant with IS:383 [20], were utilized. The physical parameters of cement and aggregates are presented in Tables 1 and 2, respectively. The potable water was utilized during the testing procedures. The plastic optical fibre was utilized with concentrations of 0%, 0.5%, 1%, 1.5%, 2%, and 2.5%. The optical fibre was procured from Elyssion Designs, and its parameters are presented in Table 3. The concrete mix design was conducted according to IS:10262 [21], with the mix designation provided in Table 4.

The compressive strength was used to optimize the percentage of optical fibre at 7, 28, 90, and 150 days of water curing. The effect of the optimized percentage of optical fibre on the various properties of light-transmitting concrete was investigated by combining it with industrial waste, including GGBFS and MS. The concrete mix proportions that have been optimized are reported in

Table 5. In this instance, the optimal content of optical fibre in the concrete was 1%, and the GGBFS at 20% and MS at 10% were selected.

Table 1. Physical properties of cement

Sr. No.	Property	Observed Value
1	Consistency	29.5%
2	Fineness	4%
3	Initial Setting time	135 min
4	Final Setting Time	245 min
5	Specific gravity	3.14
6	Compressive Strength	
	7 days	24.2 MPa
	28 days	44.5 MPa

Table 2. Physical properties of aggregates

Sr. No.	Property	Sand	Coarse Aggregates
1	Type	Crushed sand	Crushed aggregates
2	Fineness modulus	3.1	6.5
3	Zone	II	-
4	Specific gravity	2.61	2.72
5	Water absorption	2.5%	2.9%

Table 3. Properties of optical fibre

Sr. No.	Property	Value
1	Material	Plastic
2	Diameter	0.75 mm
3	Cladding material	Methyl methacrylate (MMA)

Table 4. Mix designation of concrete (kg/m^3)

Sr. No	Mix No.	Cement, kg/m^3	Sand, kg/m^3	Aggregates, kg/m^3	Water, kg/m^3	Optical fibre (%)
1	LT0	390	944	1026	187.2	0
2	LT1	390	944	1026	187.2	0.5
3	LT2	390	944	1026	187.2	1
4	LT3	390	944	1026	187.2	1.5
5	LT4	390	944	1026	187.2	2
6	LT5	390	944	1026	187.2	2.5

Table 5. Mix designation of the optimized mix, kg/m^3

Sr. No	Mix No.	Cement, kg/m^3	Sand, kg/m^3	Aggregates, kg/m^3	Water, kg/m^3	Optical fibre (%)	GGBFS, kg/m^3	SF, kg/m^3
1	OM0	390	944	1026	187.2	0	0	0
2	OM1	390	944	1026	187.2	1	0	0
3	OM2	312	944	1026	187.2	1	78	0
4	OM3	351	944	1026	187.2	1	0	39

The placement of fibre in the LTC cube specimens for optimized optical fibre (1%) has been shown in the fig. 1 (a). The fibre was placed in the horizontal direction. The size of the specimen was 10 cm, and the spacing of the fibre was 2 cm. The optical fibre was inserted in four rows in one direction (horizontal) in the cube specimens, as shown in fig. 1(b). The oiling was done on the wooden specimens for the easy removal of the specimens from the mold, and the specimens after casting are shown in fig. 1(c). The fibres were passed through the inserted holes in the horizontal direction only. The diameter of the holes varied as the volume of the optical fibre increased while keeping the spacing of the holes constant, as shown in table 6. The concrete was poured in thin layers was compacted gently between the layers, which minimizes the fibre displacement due to the placement of concrete in the mold.

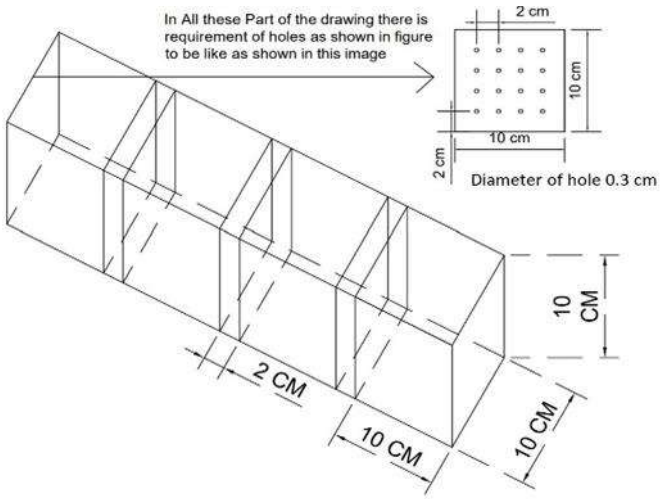

(a)

(b)

(c)

Fig. 1. Arrangement of optical fibre in specimens: (a) Drawing; (b) Pictorial view; (c) Casted Specimens

The details of the test conducted on the specimens have been given in table 7. The methodology of the experimental work is shown in Fig. 2. The three specimens were casted for each test and the average value of the three specimens was taken for the final results of any parameter, i.e., compressive strength, elastic modulus, and chemical resistance of the concrete mixes.

Table 6. Description of the quantity of optical fibre in LTC

Sr. No.	Volume of fibre (%)	No. of holes	Diameter of holes (cm)	Spacing (cm)	Drawing
1	0	0	0	0	NA
2	0.5	16	2	2	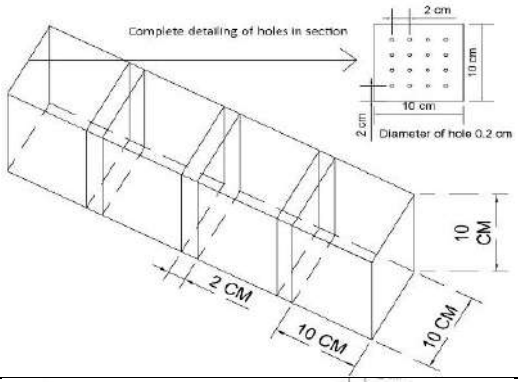
3	1	16	3	2	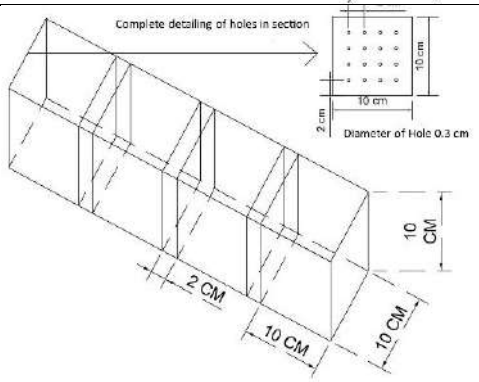
4	1.5	25	2.8	2	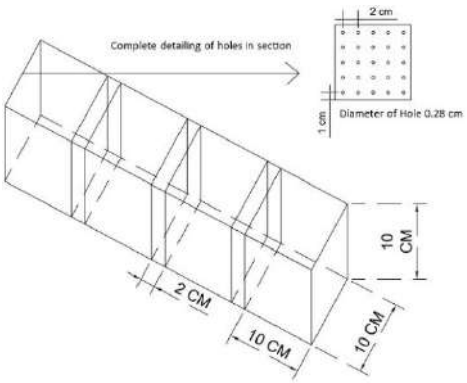
5	2.0	36	2.7	1.5	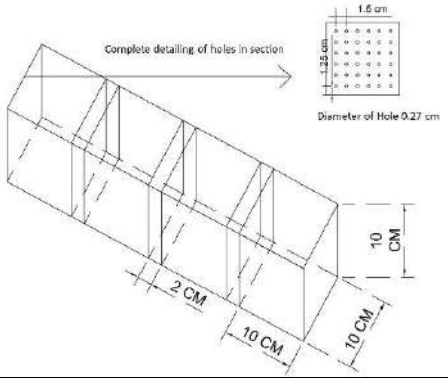

6	2.5	36	3	1.5	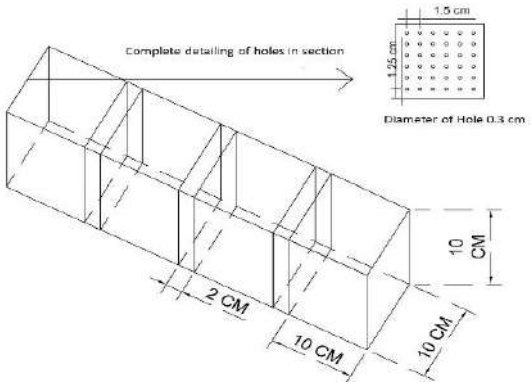

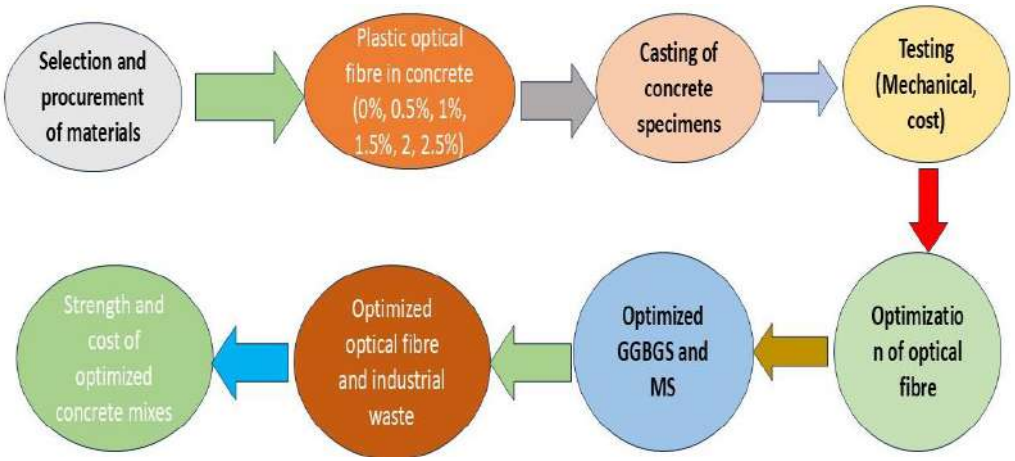

Fig. 2. Methodology for the experimental program of LTC

Table 7. Details of the test procedure

Sr. No.	Name of test	Specimens Size (mm)	Shape of specimens	Curing ages (Days)	References
1	Compressive Strength	100 mm x 100 mm x 100mm	Cube	7, 28, 90, 150	[22]
2	Light transmittance	100 mm x 100 mm x 100mm	Cube	28	[23]
3	Ultrasonic pulse velocity	100 mm x 100 mm x 100mm	Cube	28	[24]
4	Rebound hammer	100 mm x 100 mm x 100mm	Cube	28	[25]
5	Dynamic modulus	100 mm x 100 mm x 100mm	Cube	28	[26]
6	Cost	-	-	-	[27]
7.	Chemical resistance	100 mm x 100 mm x 100mm	Cube	7, 28, 62 after 28 days of water curing	[28]

The light transmittance of the concrete specimens was determined in accordance with Robles et al. [23]. The arrangement of the test procedure has been illustrated in fig. 3. In the present work, a white bulb of 40 W was used to measure the light-transmitting ability of different mix proportions of LTC. The light source was kept at a distance of 10 cm from the specimens so that the light could be uniformly distributed throughout the surface of the concrete cube. The Sigma Instruments 101 Digital Lux Meter was used to measure the light transmittance of concrete. The external outsourcers were not present in the lab room to avoid the disturbance in the results during the experimentation. The cost of the different mix proportions of LTC was determined based on the

cost of materials used. The local market price of the raw material was used and is given in table 8. The cost of the industrial wastes, such as MS and GGBFS, was not included because most of the materials are freely available.

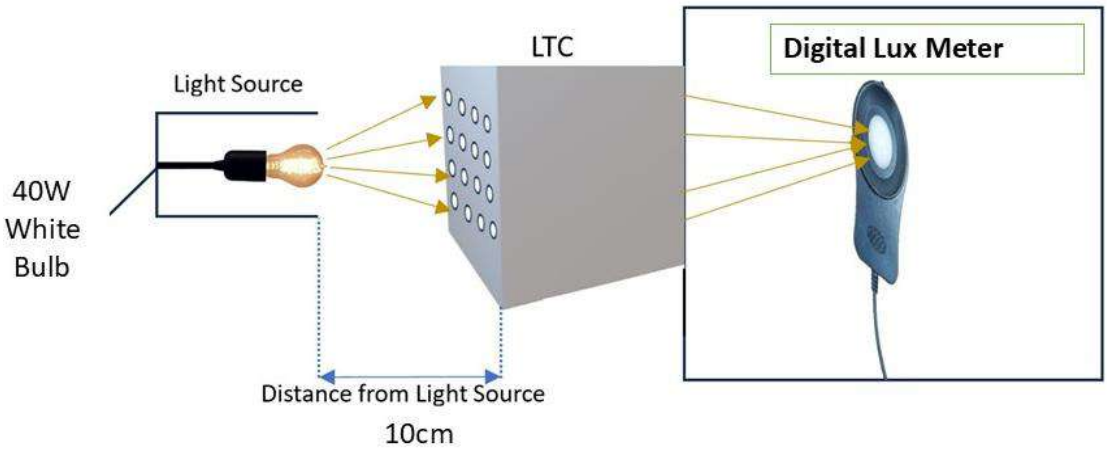

Fig. 3. Testing arrangement of light transmittance of LTC

Table 8. Cost of raw materials used

Material	Cement, kg	Sand, kg	Aggregate, kg	Water, kg	Optical fibre, kg	MS, kg	GGBFS, kg
Cost (INR)	7	1.2	1.5	0.05	7000	-	-

3. Results and Discussion

The practicality of the light-transmitting concrete was assessed at varying curing ages, with varying percentages of plastic optical fibre. The concrete's economic efficacy, durability, and strength were assessed.

3.1 Compressive Strength

The CS of light-transmitting concrete containing varying percentages of optical fibre, specifically 0%, 0.5%, 1%, 2%, and 2.5%, was experimentally examined at 7, 28, 90, and 150 days of water curing. Figure 4 (a) illustrates the variation of compressive strength of LTC with the increase in fibre content at different curing ages. The compressive strength of the LTC improved with the incorporation of optical fibre in concrete, as depicted in the figure 4 (b). The addition of optical fibre improved the compressive strength of concrete up to 1.5%, after which the strength diminished. The increase in the strength of the concrete was due to the cement hydration process in the inter-transition zone and an increase in the contact area between fibre and mixtures, resulting in stronger inter-adhesion [10, 16]. However, the optical fibre at 1% had the maximum increase in strength, afterward, it declined. The strength at 1.5% optical fibre was more than the control mix but less than that of 1% optical fibre, as illustrated in fig. 4 (b).

The reduction in strength after a certain extent may be due to more smaller spacing arrangements of POF resulting in weakened cubes as a result of the smaller interconnecting distances when macrocracks propagate under a compressive load [5]. Another reason for the reduction in the strength of LTC after 1% of optical fibre may be attributed to the negligible strength of optical fibre and poor bonding of excess fibre within the matrix of concrete [29].

The statistical analysis of the compressive strength of LTC using the one-way ANOVA was carried out. The compressive strength at 7, 28, 90, and 150 days was considered. The sum, average, and variance of all compressive strength have been shown in the table 9. The results indicate a distinct trend of rising average compressive strength with curing age, which is characteristic of concrete behavior. The F-value and p-value of the strength parameters were also calculated.

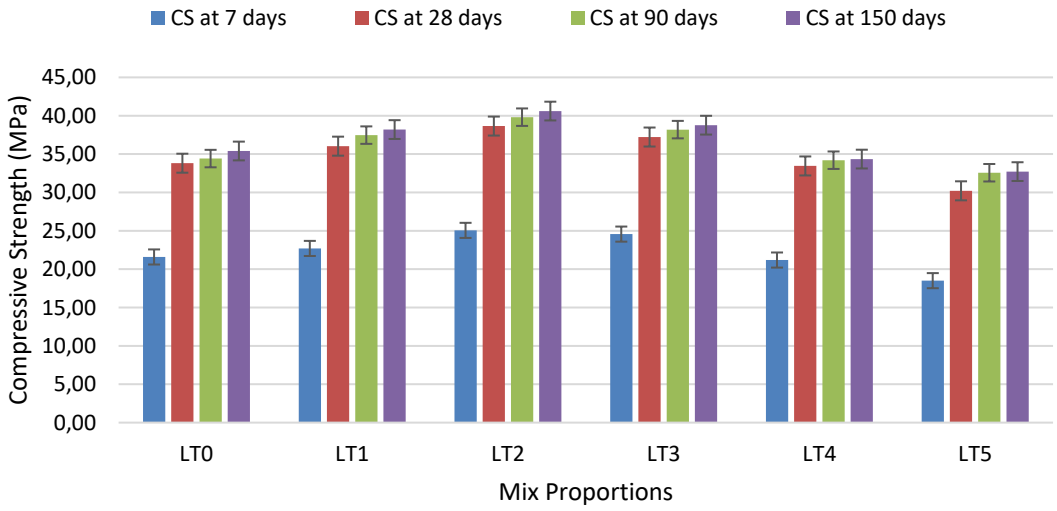

(a)

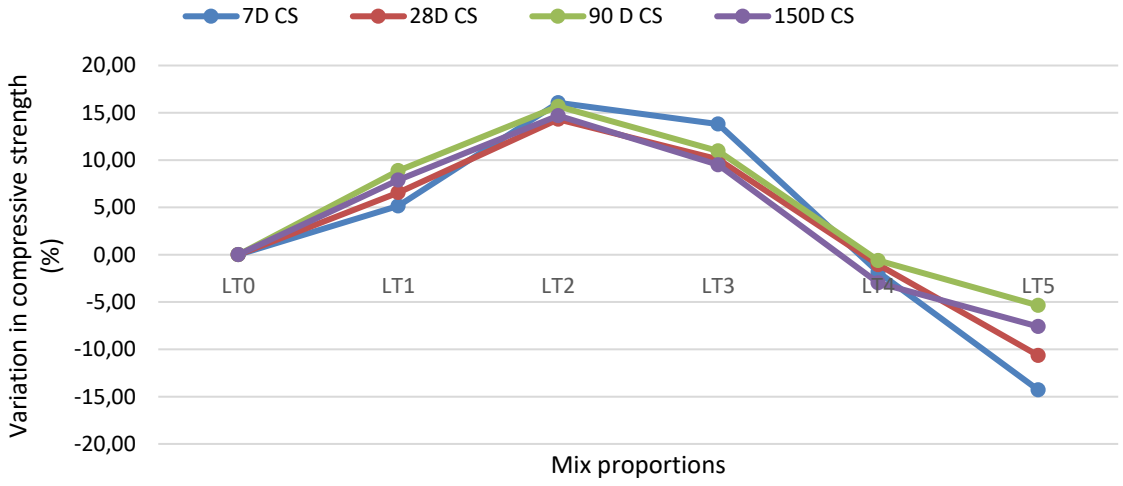

(b)

Fig. 4. (a) Compressive strength of LTC with the variation in optical fibre and (b) Percentage variation in compressive strength of concrete

Table 9. Statistical analysis of compressive strength

ANOVA: Single Factor					
Groups	Count	Sum	Average	Variance	
7D CS	6	133.62	22.27	5.81	
28D CS	6	209.39	34.90	9.20	
90D CS	6	216.67	36.11	7.78	
150D CS	6	220.05	36.67	8.97	
ANOVA					
Source of Variation	SS	df	MS	F	P-value	F crit
Between Groups	845.301	3	281.767	35.47	3.36E-08	3.09839
Within Groups	158.859	20	7.94294			
Total	1004.16	23				

The F-value (35.47) markedly exceeds the critical F-value (F crit = 3.098), signifying a significant difference between the groups. The p-value is 3.36E-08 (or 0.0000000336), far lower than the conventional alpha level of 0.05, so affirming that the variations in compressive strength among the curing times are statistically significant. The ANOVA results strongly indicate that the compressive strength of concrete is significantly influenced by the curing duration. The average compressive strength increases in tandem with the number of curing days. The statistical significance of the variation between group means is suggested by the extremely low p-value, which suggests that these discrepancies are not the result of random chance.

3.2 Strength by Rebound Hammer

The assessment of the concrete's compressive strength was carried out using a method that did not involve any destruction, specifically the rebound hammer test. A similar pattern was observed in both the destructive and non-destructive tests, which both produced the same results. Compressive strength of the LTC was enhanced by the addition of plastic fibre up to 1%; nevertheless, strength reduced following the incorporation of plastic fibre. Within the range of 29.91 MPa to 40.97 MPa, the compressive strength of LTC was observed across all of the mix proportions. Figure 5 illustrates the variation in compressive strength that was caused by the rebound hammer test. The mechanisms behind the increase or reduction in compressive strength are discussed earlier in the section that is dedicated to compressive strength [5, 10, 16].

The rebound hammer test was performed on concrete surfaces free from visible fibre insertions. If the hammer strikes directly on a fibre, the rebound value may be significantly lower than that on plain concrete due to the fibre's soft and flexible characteristics. Even when the impact occurs adjacent to a fibre, it alters the localized stress distribution under the hammer, leading to inconsistent rebound readings. Moreover, the test is ideally conducted on a smooth and uniform surface, but the presence of fibres causes surface irregularities and micro-scale discontinuities. These inconsistencies result in erratic rebound values, making it difficult to obtain reliable and representative estimates of the actual compressive strength of the concrete matrix.

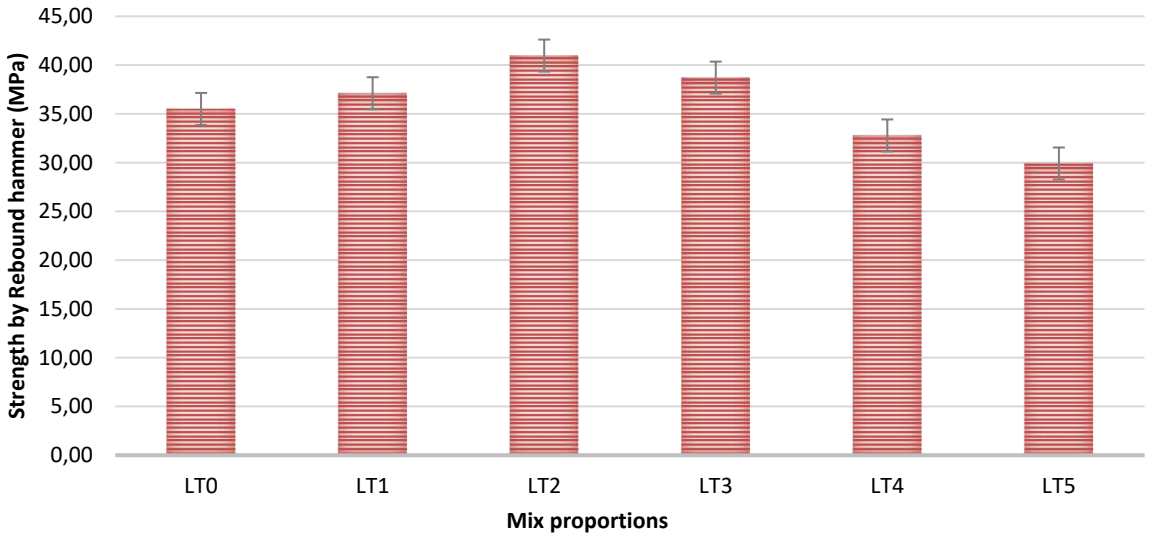

Fig. 5. Compressive strength of LTC by rebound hammer test

3.3 Light Transmittance Characteristics

The addition of optical fibre in the LTC increased the transmission of light [5, 14]. The light transmittance increased with the increase in fibre content, and the increase may be due to the higher surface area of the fibre to the concrete surface area, which allows lighter to pass, resulting in higher light transmittance [10, 16]. The light transmittance properties of the LTC have an impact on the customer. The light transmittance was measured in lux, and the variation is presented in percentage as shown in fig.6.

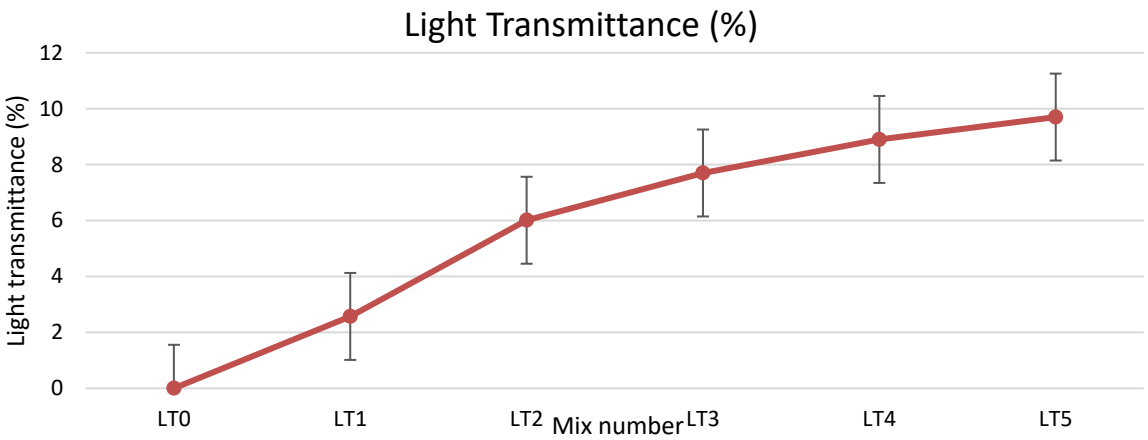

Fig. 6. Variation of light transmittance of LTC

3.4 Ultrasonic Pulse Velocity

At the end of the 28-day water curing period, the ultrasonic pulse velocity (UPV) of various mix proportions of LTC was measured and presented in fig. 7. The variation in the UPV of the various blends is depicted in figure 6 to illustrate the variation with respect to control mix. It is an indicator of the quality and uniformity of the concrete mixtures. Depending on the velocity measured from the equipment, the quality of the concrete ranged from very good to exceptional, and the inclusion of fibre into the concrete brought about these variations. Additionally, the inclusion of fibre may improve the UPV value due to the compaction and the internal connectivity.

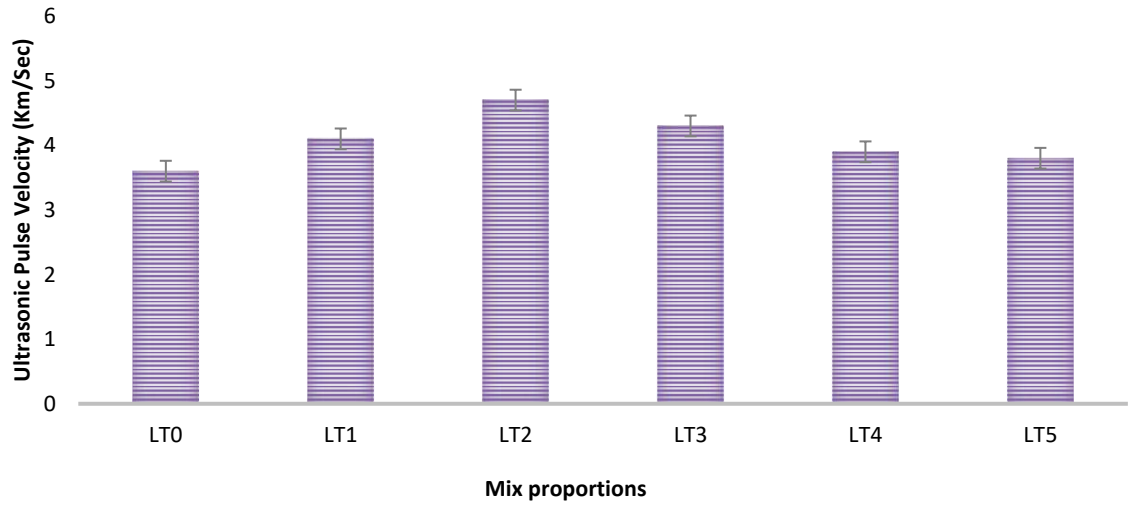

Fig. 7. Variation of ultrasonic pulse velocity of LTC

There is one limitation during the testing of the ultrasonic pulse velocity of the concrete consisting of fibre that the results may be affected due to variation in the acoustic impedance of fibre and concrete. The flexible and non-homogeneous nature of optical fibre can obstruct the obtaining of accurate signals and values.

3.5 Dynamic Modulus

The dynamic modulus of LTC was determined from the UPV test at 28 days. The variation in the dynamic modulus of different mixes of LTC has been shown in fig.8. The dynamic modulus of LTC was in the same trend as the compressive strength. The increase may be due to an improvement in the internal load transfer efficiency, resulting in an increase in the stiffness and dynamic modulus. The increase in the UPV value enhanced the dynamic modulus of concrete. The value of modulus

varied from 26.44 GPa to 45.1 GPa for all the mix proportions. The dynamic modulus of LTC of mix LT2 was the maximum among all the mix proportions.

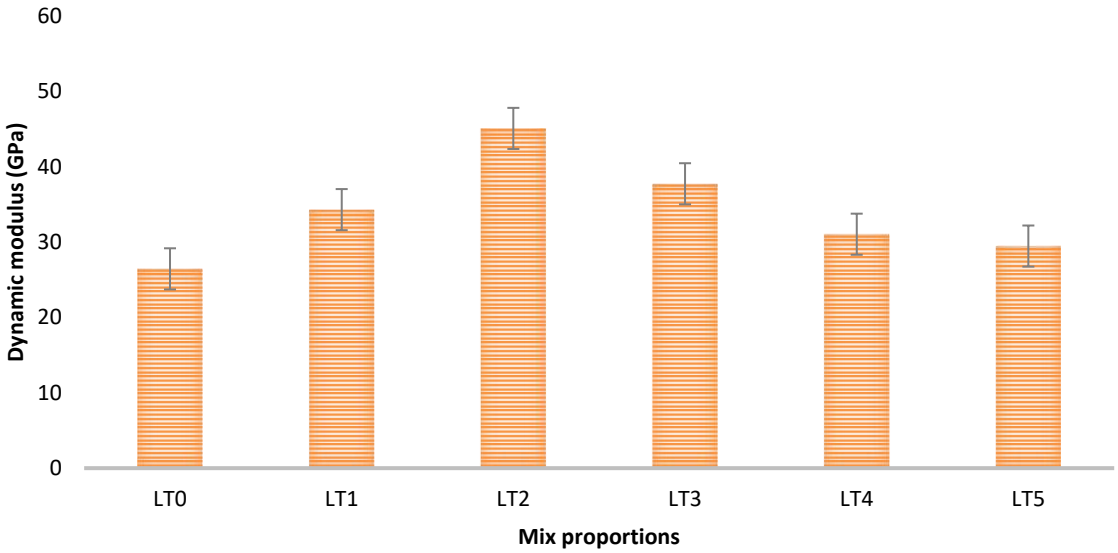

Fig. 8. Variation of the dynamic modulus of LTC

3.6 Cost Analysis

The cost of the different mixes of LTC was calculated. The addition of optical fibre hiked the cost of concrete, and the cost increased with the increase in fibre, as given in fig. 9. The increase in the cost of LTC was due to the high cost of optical fibre. The cost of the different mix proportions varied from INR 5411 to INR 308580. The maximum increase in cost was for mix LT5. The cost of the other raw materials was negligible compared to optical fibre in concrete production.

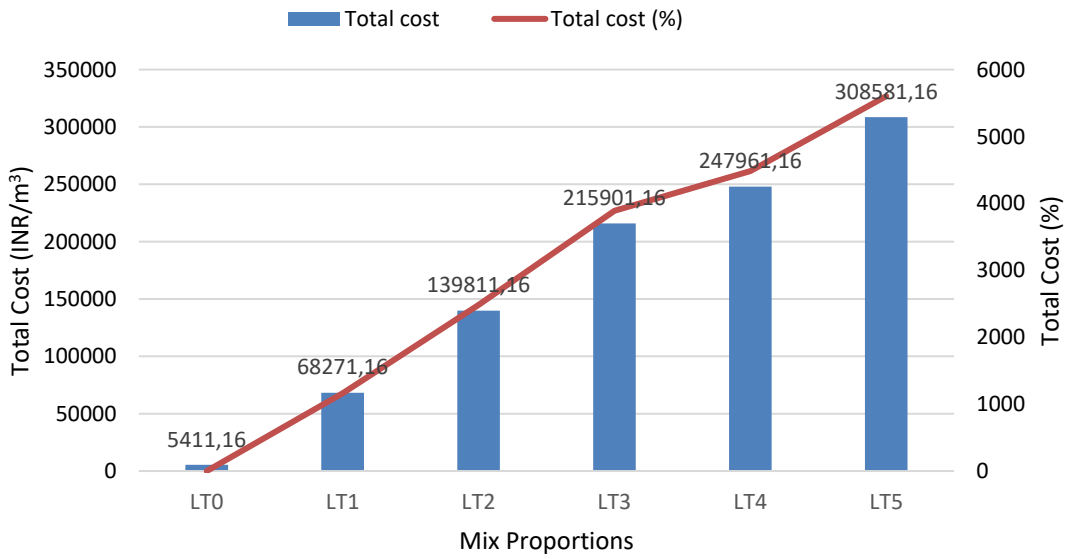

Fig. 9. Variation of the cost of different mix proportions of concrete

3.7 Correlation Between Strength by Destructive and Non-Destructive Tests

The correlation between the CS determined by the destructive and non-destructive methods at 28 days was derived. A linear correlation was derived, and a good correlation coefficient of 0.96 was found, as shown in fig. 10. The regression equation of the linear was derived and is given as below in equation 1;

$$y = 0.7419x + 8.3153 \quad (1)$$

A relationship is established that illustrates the effect of one parameter on another variable through the use of these relationships. The determination coefficient, denoted as R^2, is a coefficient that determines the variance of a variable. The confidence in the correlation is quantified by the R^2 value. This equation can be used to predict the compressive strength of the concrete from the rebound hammer value without destroying the samples. There was a strong linear relationship between these two parameters; hence, the prediction of compressive strength will give nearly accurate results.

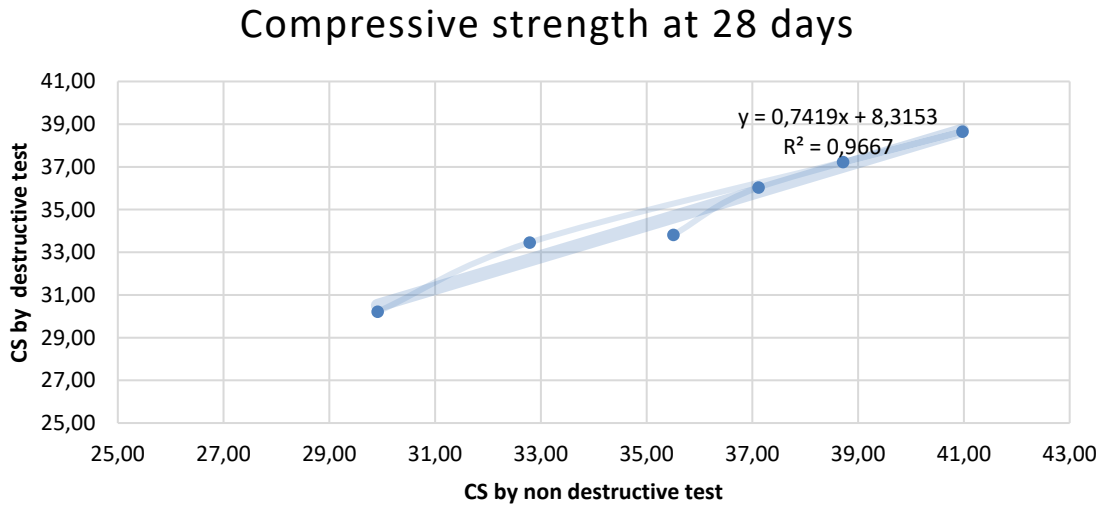

Fig. 10. Correlation between destructive test and non-destructive test of LTC

The predicted value will be determined from the eq.1 and error between the experimental and the predicted value of compressive strength at 28 days was determined and given in table 10. The error values indicate how closely the predicted results align with the experimental measurements. A positive error value represents an overestimation of the predicted value compared to the experimental result, while a negative error value indicates an underestimation.

Table 10. Error of predicted and experimental value

Mix No.	Error (%)
LT0	-1.92
LT1	1.02
LT2	0.31
LT3	1.00
LT4	3.07
LT5	-0.37

3.8 Optimized Mix with Industrial Wastes

From the above experiment results, the optical fibre at 1% was selected as the optimum mix proportion in terms of strength, modulus, cost, and light transmittance. The incorporation of industrial wastes such as GGBFS and MS can improve the performance of cement composites [30-36]. Therefore, GGBFS (20%) and MS (10%) individually were used in the LTC to investigate the performance of concrete specimens. The performance of concrete mixes was evaluated in terms of strength and durability.

3.8.1 Compressive Strength

The optical fibre at 1% was selected for further study from the above results. Further, the industrial wastes such as GGBFS (20%) and micro silica (10%) were used in the LTC. The CS of LTC was

determined with the optimized content of fibre and industrial waste. The compressive strength of the optimized mix proportions has been determined at different curing ages, i.e., 7, 28, and 90 days, and variation in strength has been illustrated in the fig. 11.

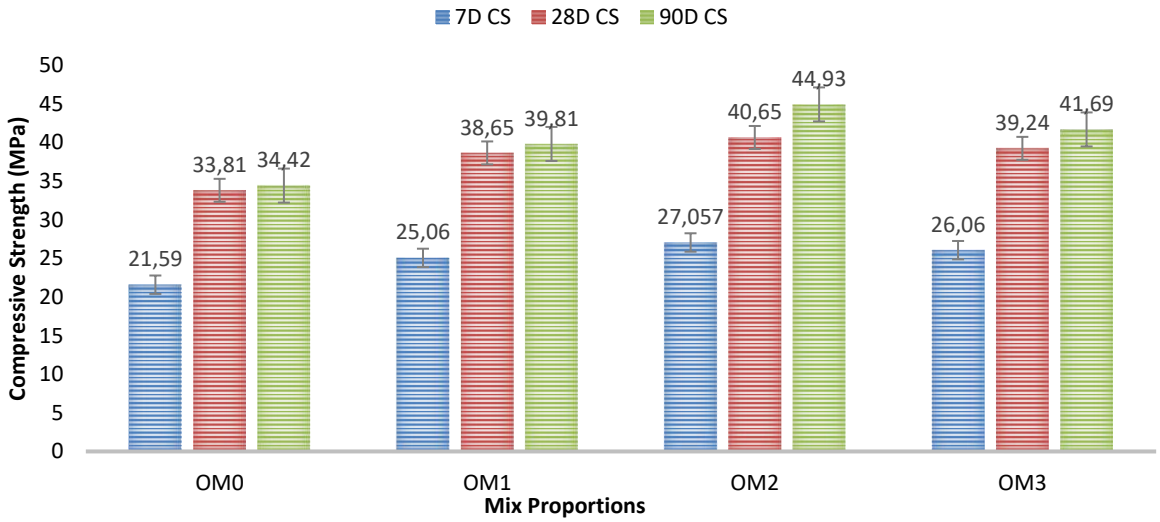

Fig. 11. Variation of compressive strength of optimized mixes of LTC

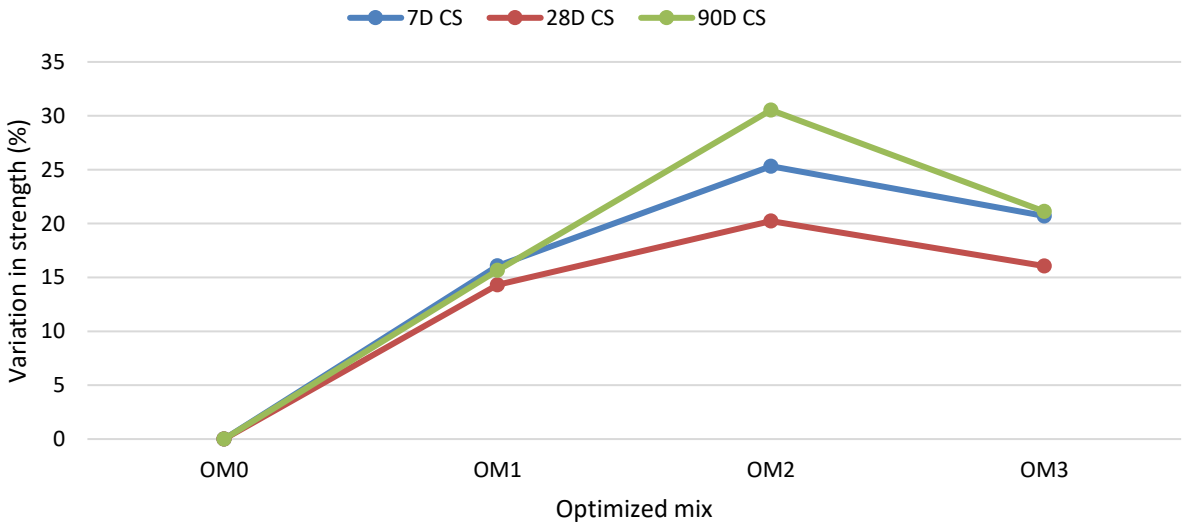

Fig. 12. Percentage change in strength of optimized mix with respect to control mix

As can be seen in Figure 12, the incorporation of industrial wastes like GGBFS and micro silica resulted in an increase in the compressive strength of the optimized mix proportions through all stages of the curing process. When compared to the control mix, the strength was greatly improved by the GGBFS and MS that were derived from industrial waste [30, 36]. The pozzolanic reaction of industrial by-products and the pore-filling impact of their finer particles may be responsible for the development of the increased strength [32-36]. As can be seen in figure 13, the incorporation of GGBFS and MS resulted in an increase in the compressive strength of LTC by 20% and 16% after 28 days of water curing for conventional concrete and by 5% and 2%, respectively, as compared to light-transmitting concrete. The statistical analysis of the compressive strength of the optimized mixes was carried out using ANOVA and is given in table 11.

The results show noticeable differences in the average values of compressive strength across the curing periods, indicating potential variations among them. The ANOVA results reveal that the calculated F-value (24.23) is much higher than the critical F-value (F crit = 4.256), confirming a significant difference between the groups. Additionally, the p-value (0.000238) is far below the conventional alpha level of 0.05, which clearly indicates that the differences among the group

means are statistically significant. This statistical analysis suggests that the observed variations between the groups are not due to random chance but rather due to inherent differences in their data sets. The large F-value and very low p-value strongly support the conclusion that at least one group mean is significantly different from the others.

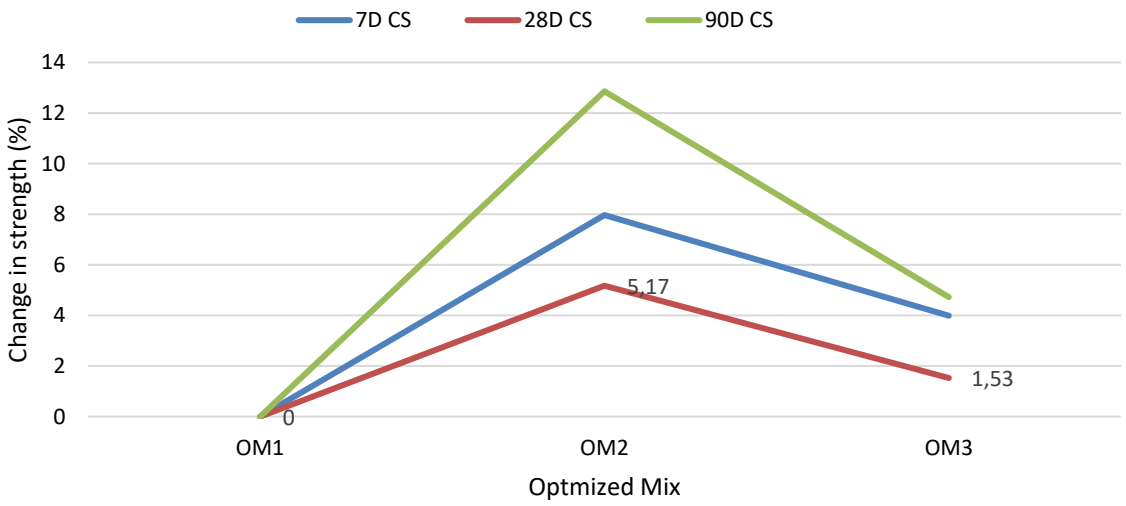

Fig. 13. Percentage change in strength with reference to optical fibre in LTC

Table 11. Statistical analysis of optimized mixes of concrete

ANOVA: Single Factor						
Summary						
Groups	Count	Sum	Average	Variance		
7D Compressive Strength	4	99.767	24.94175	5.65765892		
28 D Compressive Strength	4	152.35	38.0875	8.836025		
90 D Compressive Strength	4	160.85	40.2125	19.3842917		
ANOVA						
Source of Variation	SS	Df	MS	F	P-value	F crit
Between Groups	547.362898	2	273.681449	24.2353427	0.000238	4.25649473
Within Groups	101.633927	9	11.2926585			
Total	648.996825	11				

3.8.2 Chemical Resistance

The chemical resistance of the concrete consisting of optical fibre and industrial wastes was investigated experimentally at 7, 28, and 62 days. The concrete specimens were subjected to a magnesium sulphate solution, and a variation in strength has been shown in fig. 14. It has been observed that the incorporation of industrial wastes enhanced the chemical resistance due to their pore-filling effect and pozzolanic reactions at all exposure periods. The hydration product formed during the pozzolanic reaction densified the matrix and restricted the penetration of external agents into the concrete matrix [34, 36]. The industrial waste GGBFS was found to be more

predominant than MS in improving the chemical resistance of LTC. However, the concrete with optical fibre also improved the chemical resistance of the concrete mixtures may be due to dense packing of the matrix compared to the control mix, i.e., concrete without optical fibre.

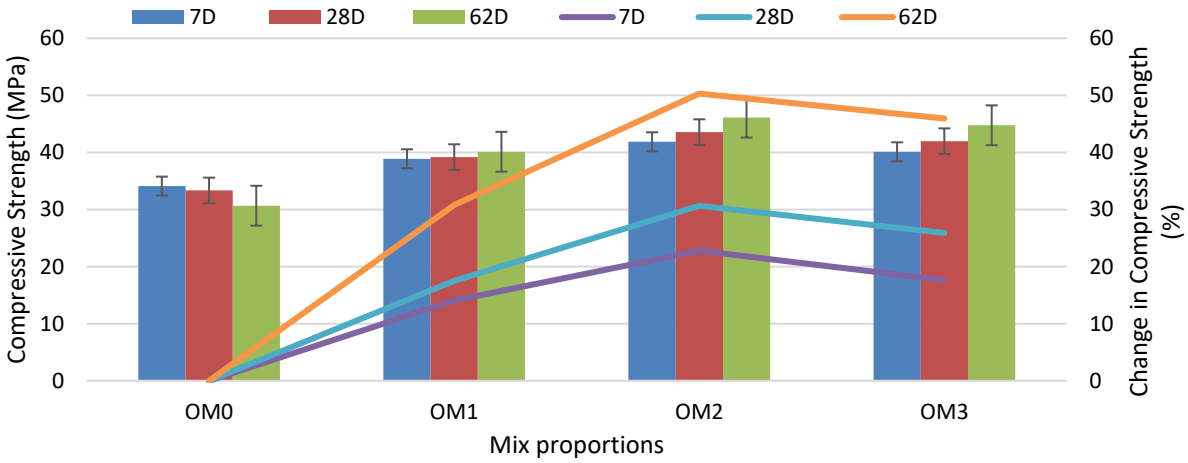

Fig. 14. Variation of compressive strength against the chemical attack

The percentage variation in the compressive strength of LTC against the exposure to sulphate solution at exposure periods of 7, 28, and 62 days has been illustrated in fig 14. The maximum increase in resistance was observed in the case of mix OM2 of 23%, 30%, and 50% compared to the control mix at exposure times of 7, 28, and 62 days, respectively.

3.8.3 Cost Analysis

The cost analysis of the optimized mix proportions was carried out. The use of optical fibre hiked the cost of concrete production, whereas the addition of industrial wastes declined the cost of concrete. The cost of mixes varied from 5411 INR to 145222.32 INR. The optical fibre increased the cost, while GGBFS and MS reduced the cost as illustrated in fig. 15.

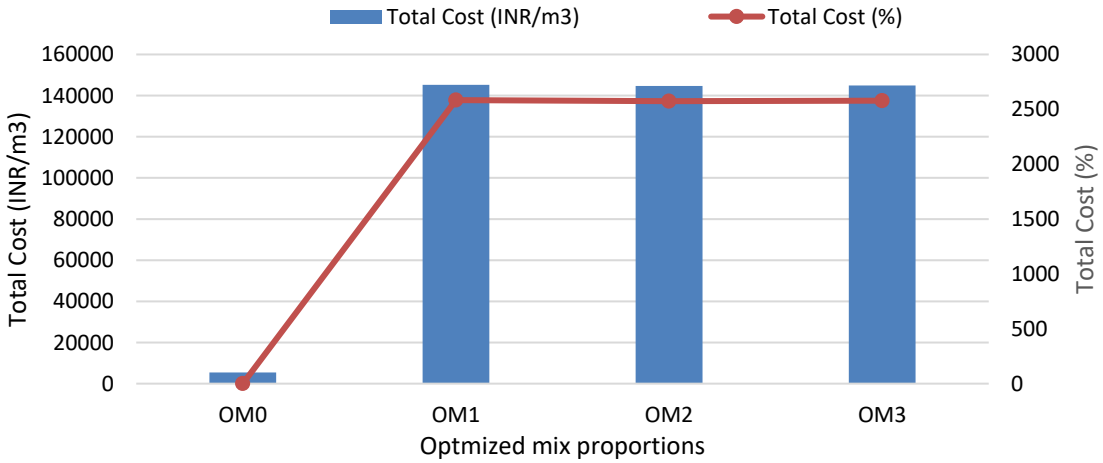

Fig. 15. Cost of optimized mixes

5. Conclusions

In the present study, the different proportions of optical fibre, i.e., 0%, 0.5%, 1%, 1.5%, 2%, and 2.5%, in the concrete were studied in various aspects. The strength, dynamic modulus, and cost of the various mix proportions were investigated. The conclusions of the present study are given below

- At all curing ages, the addition of optical fibre up to 1.5% in LTC improved the compressive strength afterwards; the strength reduced. However, the maximum strength was observed at 1% of the optical fibre of 38.65 MPa at 28 days of water curing.
- The maximum increase in compressive strength was observed as 15% for all curing ages at 1% of optical fibre.
- It was found that the compressive strength, as measured by both the destructive test and the non-destructive test, specifically the rebound hammer, exhibited similar patterns.
- The insertion of plastic optical fibre in concrete resulted in a rise in the ultrasonic pulse velocity value, which indicates that the quality of the concrete is of good to excellent quality.
- The incorporation of optical fibre into the light-transmitting concrete increased the dynamic modulus of the concrete.
- The light transmittance ability of the light-transmitting concrete increased as the number of optical fibres in the concrete rose. The maximum increase in light transmittance was reported to be 10%.
- There was a huge hike in the cost of light-transmitting concrete as a result of the additional optical fibre technology. However, the cost of manufacturing LTC is expected to compensate for the cost of artificial lighting.
- In terms of strength, light transmittance, and cost of the concrete, it was discovered that the optical fibre at a concentration of 1% was the most optimal.
- The inclusion of industrial wastes, i.e., GGBFS (20%) and MS (10%) along with the optimized percentage of optical fibre, improved the strength of the LTC by 5% and 2% at 28 days of water curing.
- The incorporation of industrial by-products enhanced the chemical resistance of LTC against the sulphate exposure at different ages, which may be due to the pore-filling effect and pozzolanic reactivity.
- The addition of industrial waste in LTC reduced the cost of concrete production compared to control mix. The GGBFS and MS declined the cost of LTC by 1% optical fibre by 7% and 4%, respectively.
- Therefore, LTC can be used in corporate logos, signage, façade panels, interior wall partitions, decorative panels, underground structures, tunnel linings, pavement, and footpaths due to their illuminating characteristics.

The use of optical fibre in concrete resulted in an improvement in the material's strength; nevertheless, this was accompanied by a rise in the cost of the concrete. The high cost and complex casting technique of LTC remain major obstacles to its commercial application. In addition to enhancing the building's aesthetic, the light-transmitting properties of the concrete helped to save energy by lowering the amount of artificial light that was required to illuminate the establishment. The use of industrial wastes with optical fibre has improved the strength and durability performance of the concrete. Thereby, the cost of the LTC can be compensated up to a certain extent with the addition of industrial by-products.

6. Future Scope

In the present study, the mechanical strength, light-transmitting ability, elastic modulus, and cost analysis of the concrete containing plastic optical fibre were studied. The industrial wastes, such as micro silica at 10% and ground granulated blast furnace slag at 20%, were used in the light transmitting concrete with 1% of plastic optical fibre. The compressive strength, chemical resistance, and cost analysis of optimized mix proportions were investigated. However, a few parameters are not covered in this study.

The durability properties, such as water absorption, chemical resistance, permeability, electrical resistivity, freeze-thaw resistance, effect of humidity and temperature variation, etc., of the light transmitting concrete were unexplored. The life cycle analysis, including life-cycle cost benefits due to energy savings, accounts for labour complexity, installation costs, and availability of POFs. The long-term behavior of plastic optical fibre i.e., the mechanical and optical degradation of the fibre under exposure to harsh environmental conditions, can be suggested for the direction of

future investigation. The microstructural analysis of the different mixes can be discussed to explore the hydration products and develop the correlation between the micro and macro-characteristics of the different LTC mixes. The microstructural characterization of the different mix proportions under the normal and the harsh environmental conditions can also be compared and discussed further. Also, the statistical analysis can be derived among the different parameters.

References

[1] Devi K, Saini B, Aggarwal P. Performance assessment of concrete incorporating admixtures and stone waste powder. Indian Journal of Engineering and Materials Sciences (IJEMS), 2024; 31(4):533-46. https://doi.org/10.56042/ijems.v31i4.6018

[2]Ozmen HB, Inel M. Effect of concrete strength and detailing properties on seismic damage for RC structures. Res. Des. 2024; 1(1): 1-11. http://dx.doi.org/10.17515/rede2024-005en1124rs

[3] Khoman RK, Owaid HM. Development of sustainable high performance self-compacting concrete incorporating natural and waste pozzolanic materials. Research on Engineering Structures and Materials, 2025; 11: 1-21. http://dx.doi.org/10.17515/resm2025-912ma0520rs

[4] Hong WY, Rahmat BN. Energy consumption, CO2 emissions and electricity costs of lighting for commercial buildings in Southeast Asia. Scientific Reports, 2022; 12(1):13805.

[5] Altlomate A, Alatshan F, Mashiri F, Jadan M. Experimental study of light-transmitting concrete. International journal of sustainable building technology and urban development, 2016; 7(3-4):133-9. https://doi.org/10.1080/2093761X.2016.1237396

[6] Sharma K, Devi K, Saini N. Light Transmitting Concrete: A State-of-the-Art Review on Performance and Potential. Journal of Building Material Science, 2025; 7(2):80–96. https://doi.org/10.30564/jbms.v7i2.9578

[7] Zielińska M, Ciesielski A. Analysis of transparent concrete as an innovative material used in civil engineering. In IOP Conference Series: Materials Science and Engineering, 2017; 245:022071. doi:10.1088/1757-899X/245/2/022071

[8] Juan S, Zhi Z. Preparation and study of resin translucent concrete products. Advances in Civil Engineering, 2019;2019(1):8196967. https://doi.org/10.1155/2019/8196967

[9] Saleem M, Elshami MM, Najjar M. Development, testing, and implementation strategy of a translucent concrete-based smart lane separator for increased traffic safety. Journal of Construction Engineering and Management, 2017; 143(5):04016129.

[10] Chiew SM, Ibrahim IS, Ariffin MA, Lee HS, Singh JK. Assessment and ANN model development of natural light transmittance of light-transmitting concrete. Results in Engineering, 2023; 20:101416. https://doi.org/10.1016/j.rineng.2023.101416

[11] Luhar I, Luhar S, Savva P, Theodosiou A, Petrou MF, Nicolaides D. Light transmitting concrete: a review. Buildings, 2021; 11(10):480. https://doi.org/10.3390/buildings11100480

[12] Nam HP, Hai NM, Tuan ND, Quang PD, Van Huong N, Huy LQ, Hai DV. Experimental study of light transmitting concrete with ultra-high content of polymethyl methacrylate. Construction and Building Materials, 2024; 438:137156. https://doi.org/10.1016/j.conbuildmat.2024.137156

[13] Al-Kurdi N, Abdel-Aziz D, Alshboul A. The impact of using light transmitting concrete on energy saving in office buildings-case of Jordan. Research Journal of Applied Sciences, Engineering and Technology, 2015; 25:578-86.

[14] Chiew SM, Ibrahim IS, Ariffin MA, Lee HS, Singh JK. Development and properties of light-transmitting concrete (LTC)–A review. Journal of cleaner production, 2021; 284:124780. https://doi.org/10.1016/j.jclepro.2020.124780

[15] Huang B. Light transmission performance of translucent concrete building envelope. Cogent Engineering, 2020; 7(1):1756145. https://doi.org/10.1080/23311916.2020.1756145

[16] Tahwia AM, Abdel-Raheem A, Abdel-Aziz N, Amin M. Light transmittance performance of sustainable translucent self-compacting concrete. Journal of Building Engineering, 2021; 38:102178. https://doi.org/10.1016/j.jobe.2021.102178

[17] Pourkazemi M, Vahdati M, Mirvalad S, Mahdikhani M. Light-transmitting concrete: Performance and novel casting methods. Construction and building materials, 2024; 449:138270.

[18] Chiew SM, Ibrahim IS, Ariffin MA. Natural light transmittance of light-transmitting concrete (LTC) incorporated with optical fibres. Materials Today: Proceedings, 2024; 110:27-32. https://doi.org/10.1016/j.matpr.2023.08.131

[19] IS 8112 (1989) Specification for 43-grade ordinary Portland cement. Bureau of Indian Standards, New Delhi, India.

[20] IS 383 (2016). Coarse and Fine Aggregate for Concrete-Specification (Third Revision) [Internet]. 2016. Available from: www.standardsbis.in

[21] IS 10262 (2019) Concrete Mix Proportioning –Guidelines. Bureau of Indian Standards, New Delhi, India.

[22]. IS 516 (1959) Methods of Tests for Strength of Concrete. Bureau of Indian Standards, New Delhi, India.
[23] Robles A, Arenas GF, Stefani PM. Light transmitting cement-based material (LTCM) as a green material for building, 2020; 1(1):9–14. https://doi.org/10.4995/jarte.2020.13832
[24] IS 13311-1 (1992). Method of Non-destructive testing of concrete, Part 1: Ultrasonic pulse velocity. 1992.
[25] IS 13311-2 (1992). Method of non-destructive testing of concrete-methods of test, Part 2: Rebound hammer. 1992.
[26] Devi K, Saini B, Aggarwal P. Utilization of Kota stone slurry powder and accelerators in concrete. Computers and Concrete, 2019; 23(3):189–201. https://doi.org/10.12989/cac.2019.23.3.189
[27] Devi K, Aggarwal P. Impact of high temperature on mortar mixes containing additives. Journal of Engineering Research, 2022; 10(1B):68-85. https://doi.org/10.36909/jer.10477
[28] ASTM C1012/C1012M-12 (2012) Standard Test Method for Length Change of Hydraulic-cement Mortars Exposed to a Sulphate Solution. ASTM International, West Conshohocken, U.S.A.
[29] Kumar A, Ahlawat R. Experimental study on light transmitting concrete. International Journal of Innovative Science, Engineering & Technology, 2017; 4:201-10.
[30] Gupta M, Raj R, Sahu AK. Effect of Rice Husk Ash, silica fume & GGBFS on compressive strength of performance-based concrete. Materials Today: Proceedings, 2022; 55:234-9. https://doi.org/10.1016/j.matpr.2021.06.343
[31] Lamba N, Raj R, Singh P. The effects of recycled carbon fibers on the mechanical properties of high-strength concrete and its resilience to impact. Iranian Journal of Science and Technology, Transactions of Civil Engineering, 2024; 48(4):2191-213. https://doi.org/10.1007/s40996-023-01269-6
[32] Lamba N, Raj R, Singh P. Mechanical response of recycled carbon fiber reinforced polymer fibers in high-strength concrete. Materials today: proceedings, 20231; 78:603-7. https://doi.org/10.1016/j.matpr.2022.11.477
[33] Lamba N, Raj R, Singh P. Feasibility of Recycled Carbon Fiber-Reinforced Polymer Fibers in Cementitious Composites: An Experimental Investigation. Arabian Journal for Science and Engineering, 2024; 49(10):13577-91. https://doi.org/10.1007/s13369-024-08712-4
[34] Abbas SN, Qureshi MI. An investigation of mechanical properties of self compacting concrete (SCC) after addition of ground granulated blast furnace slag (GGBFS) and fly ash (FA). Materials Chemistry and Physics: Sustainability and Energy, 2025;2:100008. https://doi.org/10.1016/j.macse.2025.100008
[35] Durai TN, Kandasamy S, Christabel AR. Enhanced Mechanical Properties in Green Concrete through Innovative Blends of GGBFS, Alccofine, and Metakaolin. Hybrid Advances, 2025:100520. https://doi.org/10.1016/j.hybadv.2025.100520
[36] Fatiha A, Karim E, Mhamed A, Abed F. Enhancing performance of recycled aggregate concrete with supplementary cementitious materials. Cleaner Materials, 2025; 15:100298. https://doi.org/10.1016/j.clema.2025.100298

Research on Engineering Structures & Materials
www.jresm.org
Research Group

Research Article

CFD analysis on horizontal axis tidal current turbine

S.M. Fahad Hossen Munna [a], Md Mezbah Uddin [*,b]

Department of Naval Architecture and Marine Engineering, Military Institute of Science and Technology, 1216, Dhaka, Bangladesh

Article Info

Article History:

Received 03 May 2025
Accepted 05 Aug 2025

Keywords:

Tidal energy;
Tidal current turbine;
Torque;
Thrust;
Power;
CFD analysis

Abstract

In response to the escalating global demand for sustainable energy and the environmental toll of fossil fuel dependency, this study presents a high-resolution Computational Fluid Dynamics (CFD) analysis of a Horizontal Axis Tidal Current Turbine (HATCT) designed for deployment in the Passur River, Khulna, Bangladesh, a region characterized by strong and predictable tidal flows. The CFD methodology is applied with a validated 3D turbine model, enabling precise evaluation of hydrodynamic performance metrics such as thrust, torque, and power output. The process supports optimization of blade geometry and operational parameters, contributing to the design of efficient tidal energy systems tailored to site-specific conditions. The turbine was tested across multiple mesh configurations to ensure numerical stability and mesh independence. Key findings indicate a consistent energy yield of approximately 3 kWh per tidal cycle, demonstrating the turbine's viability for localized renewable energy generation. These results highlight the practical application of CFD in marine energy engineering and underscore the potential of HATCTs to support Bangladesh's transition toward sustainable power infrastructure. The study offers a data-driven foundation for future experimental validation and large-scale implementation of tidal energy technologies in estuarine environments.

© 2025 MIM Research Group. All rights reserved.

1. Introduction

Tidal energy has gained prominence as a stable and sustainable source of power owing to its predictability and high energy density. Unlike solar and wind energy, which are affected by atmospheric variability, tidal currents are controlled by gravitational interactions between the Earth, moon, and sun, resulting in cyclic and predictable flow patterns. This makes tidal energy ideal for integrating into national power systems, especially along coastal and estuary areas [1]. At the latter half of the 20th century, the concept of employing horizontal-axis turbines for extracting energy from tidal currents gained traction, mostly due to the practical success of wind turbines. Estimating the energy potential of tidal flows and comprehending the related hydrodynamic processes were the main goals of early theoretical research. Because of its straightforward mechanical construction and inherent alignment with the direction of tidal flow [2], the horizontal-axis turbine arrangement became a popular choice by the 1990s. There was a notable shift from theory to practice in the early 2000s. In 2008, the Sea Gen project in Northern Ireland achieved a significant milestone in the commercialization of tidal energy technology by becoming the first grid-connected tidal turbine in the world [3]. Several full-scale prototypes, including Open Hydro, HS1000, and AR1000, were created during this time, effectively proving the viability of producing energy on a megawatt scale using tidal currents.

Research on turbine performance, wake interactions, generator integration, and environmental factors dominated the academic and industry interest in HATCTs between 2002 and 2012. Ten

*Corresponding author: mezbah@name.mist.ac.bd
[a]orcid.org/0009-0005-0742-8127; [b]orcid.org/0000-0001-7750-7625
DOI: http://dx.doi.org/10.17515/resm2025-866en0503rs
Res. Eng. Struct. Mat. Vol.11 Iss. 6 (2025) 3327-3339

years of advancements were summarized in a thorough assessment by Ng et al. (2013), which focused on the increasing technological maturity and potential economic benefits of horizontal-axis systems [4]. After this formative time, more recent research has looked into sophisticated design techniques to maximize turbine performance. Adaptive, variable-pitch blades are used to improve hydrodynamic efficiency and enable bidirectional flow energy capture, while diffuser-augmented systems are integrated to boost power output [5]. On the other hand, studies of wake dynamics and turbine-fluid interactions have yielded important information for enhancing array designs and overall farm efficiency [6]. As a result, Large-scale implementations like Raz Blanchard in France and the Mey-Gen project in Scotland have signaled a move towards commercial feasibility in recent years. By enhancing turbine efficiency and dependability and reducing the need for operational maintenance, these projects establish HATCTs as a viable and sustainable energy option for island and coastal areas [7]. Continuous advancements in environmental integration, control systems, and blade geometry strengthen the position of tidal energy in the world's renewable energy mix.

Currently, in line with global trends, Bangladesh, facing increasing energy demand due to its growing population, stands at a critical juncture in its pursuit of sustainable energy solutions. Its extensive river network featuring major rivers like the Padma, Jamuna, and Meghna presents a unique opportunity to harness hydrokinetic energy, particularly through the deployment of horizontal tidal current turbines. These riverine systems offer immense potential for generating clean electricity through strategically positioned turbines within natural water currents [8]. Tidal energy is a renewable energy source that produces mechanical power for generators by converting the kinetic energy of moving water into electrical energy [9]. It uses less fossil fuels and produces less CO2 emissions. It is among the numerous resources available to address climate change concerns [10]. As the world looks for cleaner and more sustainable ways to produce energy, tidal power is expected to draw more concern and attention. Tides originate from the gravitational attraction of the moon. Given that water covers 71% of the earth's surface, tides provide a large-scale means of energy capture [11]. The main benefit of tidal energy over other renewable energy sources like wind or solar power is that tides are predictable [12].

At present, the extraction of electricity from tidal currents is receiving more interest because it is currently an unexplored renewable resource. Because of their great energy density and regularity, tidal currents are a desirable renewable energy source [13]. Many systems have recently been developed to produce electrical power from the energy contained in tidal currents [14]. As its rotational axis is parallel to the tidal flow, horizontal axis tidal turbines, or HATCTs for short, only run in one direction of flow. They are also referred to as axial flow turbines. The HATCT operates on a similar basis to the horizontal axis wind turbine (HAWT). The development of computing power and computational fluid dynamics (CFD) models to represent the intricate flow surrounding the turbine has advanced significantly [15]. The mesh that is chosen to solve the fluid flow and the turbulence model that is used to depict the problem's physics are the only factors that affect the independent mesh solutions. The mesh was created using SIMCENTER STA-RCCM+, which was extremely fine in the blade wall region to produce exact results. Three meshes have been done throughout the investigation of a 1.6m diameter three-bladed HATCT and the 3D design of the HATCT has been taken from a Tidal Turbine Benchmarking Projects of Supergen [16]. A total of three simulations have been done.

Therefore, in aspect of Bangladesh, it can be a great initiative to generate power using tidal current turbines as Bangladesh has a great deal of potential for tidal energy harvesting because of its large coastline along the Bay of Bengal and its many tidal rivers. The installation of horizontal tidal current turbines is one viable method of using this resource. To comprehend the performance and optimize the design of such turbines in the context of Bangladesh's particular tidal circumstances, computational fluid dynamics (CFD) study is essential. Because it is dependable and predictable, tidal energy offers Bangladesh a feasible alternative to fossil fuels. The purpose of horizontal tidal current turbines is to harness the kinetic energy of tidal currents and transform it into electrical power, much like underwater wind turbines [17]. Using CFD analysis, fluid flow around turbine blades is simulated, performance metrics are assessed, and design parameters are optimized to extract the most energy possible. Bangladesh may achieve greater energy resilience and

environmental sustainability by utilizing its tidal energy potential and reducing its reliance on fossil fuels by integrating CFD analysis with horizontal tidal current turbines [18].

Even with the availability of sophisticated CFD tools and the theoretical benefits of HATCTs, their use in Bangladesh is still restricted. Although the Passur River and other estuarine areas of the nation have a considerable potential for tidal flow, they lack localized performance data and design optimization that is suited to local hydrodynamic conditions. Previous research frequently ignores the distinctive features of Bangladesh's tidal zones in favor of generic models or offshore facilities.

Additionally, this study fills the gap by using CFD analysis to assess a benchmarked HATCT's performance in the Passur River under site-specific circumstances. The study's objectives are to measure the turbine's thrust, torque, and power output as well as evaluate its viability for producing renewable energy locally. The study aims to enable the scalable implementation of tidal energy plants in Bangladesh and inform future design strategies by combining simulation results with regional tidal characteristics.

2. Methodology

2.1 Airfoil Selection and Blade Design Parameters

A NACA airfoil (taken from web), commonly used in tidal turbine blade design, as shown in Fig. 1 both symmetrical and asymmetrical airfoils are employed in the tidal turbine industry to produce. In the tidal turbine design, symmetrical airfoils are most common because of their high cavitation qualities and ability to vary the angle of attack across the complete rotation of the turbine blades [19].

The NACA 63-415 model in Fig. 2 from Benchmarking Project was used to simulate HATCTs. [20]The hydrodynamics of the hydrofoil is examined, especially on the trailing edge treatment: a) Sharp trailing edge b) Thickened trailing edge c) Truncated trailing edge. As the seawater velocity rises with the rising angle of attack of the airfoil top surface, more drag forces are generated during HATCT's whole rotation, in addition to lift variations. As a result, creating a blade with a curved caudal fin design reduces vibration and produces greater lift and power coefficients at both lower and higher tidal current velocities [21].

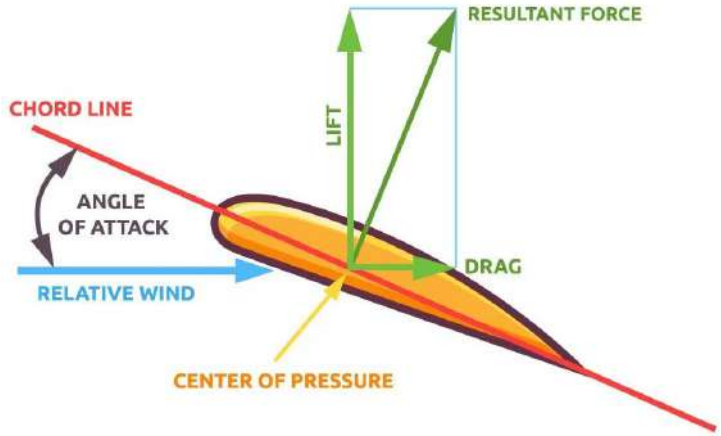

Fig. 1. Airfoil characteristics

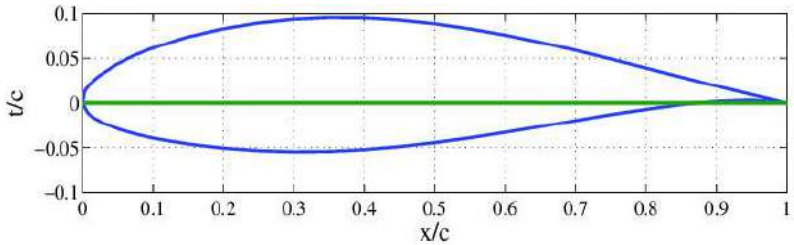

Fig. 2. NACA 63-415

In the hydrodynamics of hydrofoil of NACA 63-415, Below Fig. 3 shows the Drag Coefficient against the angle of attack, Fig. 4 shows the Lift Coefficient against the angle of attack and Fig. 5 shows the Lift to Drag coefficient ratio against the angle of attack. All the Fig. 3, Fig. 4 and Fig. 5 have been taken from the Benchmarking Project by Supergen.

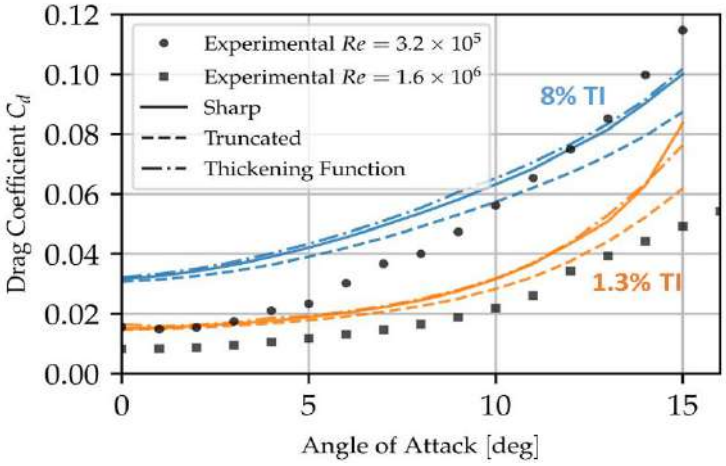

Fig. 3. Drag coefficient against the angle of attack

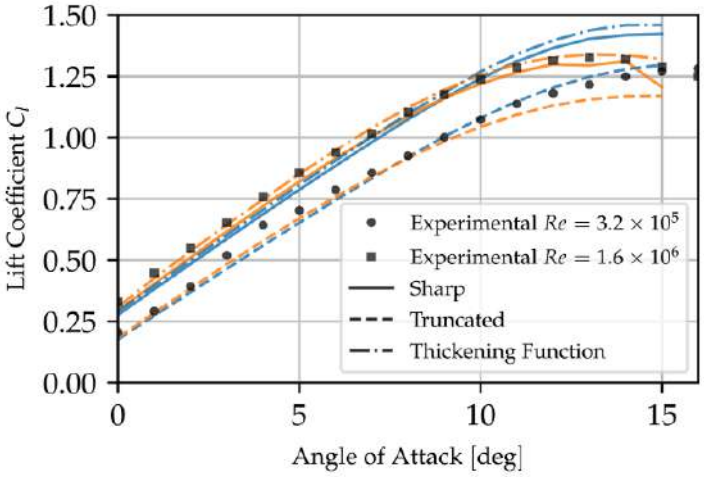

Fig. 4. Lift Coefficient against the angle of attack

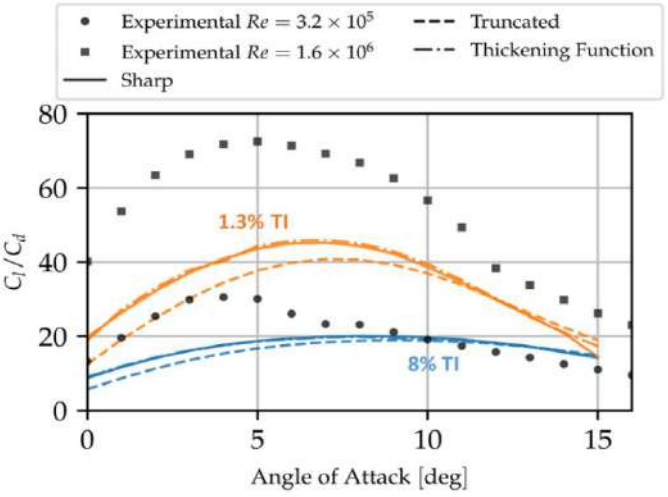

Fig. 5. Lift to drag coefficient ratio against the angle of attack

Here, Table 1 shows the parameters of the taken blades. These parameters were obtained from the Tidal Benchmarking Projects by Supergen

Table 1. Blades parameter

Parameter	Value
Rotor Diameter	1.6 m
Blade Diameter	0.7 m
Nacelle Diameter	0.2 m
Blade Number	3
Turbulent Length Scale	0.037 m
Turbulence Intensity	3.1%
Twist Angle	35 degrees

Here, Fig. 6 (a) and (b) show the 3D design of the tidal turbine, where the Blade view can be seen. And this design has been taken from the Benchmarking Project.

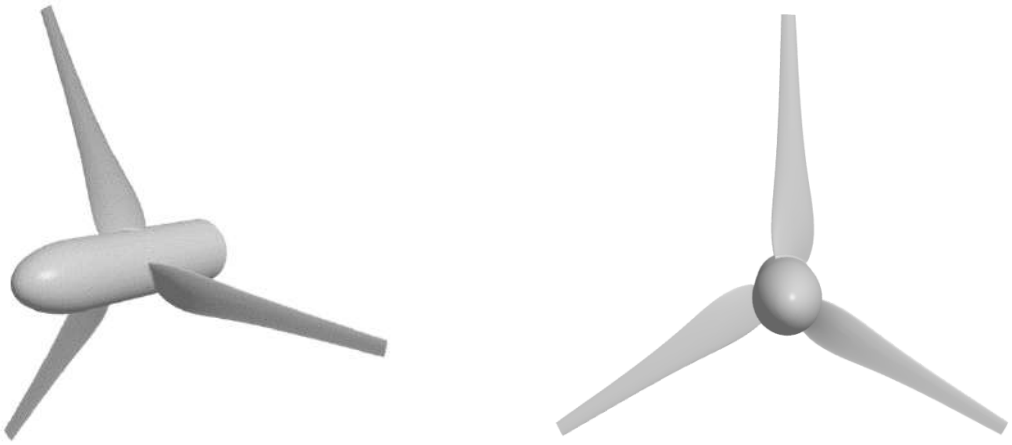

(a) (b)

Fig. 6. 3D Blade view

3. CFD Simulation Setup

The flow hydrodynamics were solved using Simcenter STAR-CCM+ 2210.0001 (17.06.008-R8) by using the finite-volume approach to solve the Reynolds Averaging Navier-Stokes (RANS) equations. As mentioned in the previous sections NACA 63-415 (Fig. 2) was employed on the designed blades. This paper consists of the dimensional force, thrust, and power which is produced by K-Omega turbulence and Reynold's Averaged Navier Stokes method by STAR-CCM+, at the turbine level thus putting forward a comparative analysis.

3.1 Meshing, Boundary Conditions and K-Omega Turbulence Model

3.1.1 Meshing

In Computational Fluid Dynamics (CFD) simulations, meshing is an essential component that forms the basis for the accuracy and dependability of the whole computational process. To create a computer grid, meshing essentially entails splitting the geometric domain of a simulated fluid flow into discrete pieces or cells. This grid approximates fluid dynamics within each cell by serving as a numerical representation of the physical region. Meshing is important since it directly affects the computing efficiency and fidelity of the simulation. Capturing the finer aspects of fluid flow phenomena, like boundary layer effects, vortices, and turbulence, requires a well-structured mesh. Finer meshes provide a more accurate representation of the underlying physics, and their resolution directly impacts the quality of the numerical solution. Therefore, before beginning the primary analysis, a mesh independence test was conducted [22].

3.1.2 Boundary Conditions

For simulations, Three-Dimensional, Liquid, Constant Density, Implicit Unsteady, Segregated Flow, Turbulent, K-Omega Turbulence, Reynolds-Averaged Navier-Stokes, Elliptic Bending models are used [23]. The velocity of initial condition in the positive x-axis for simulation-1 the velocity & the rotation rate was taken from the Benchmarking paper which are 0.9207 m/s and 81 rpm. Again, for simulation no. 2, 3 and 4 the velocity was taken 0.945 m/s, and the rotation rate was taken at 81 rpm in the positive x-axis in the perspective of the Passur River. The velocity is taken from a reference paper that shows the velocity of the Passur River of Bangladesh in the monsoon [24]. Fig. 7 demonstrates the velocity distribution from where the velocity has been taken for the simulation regarding Passur River.

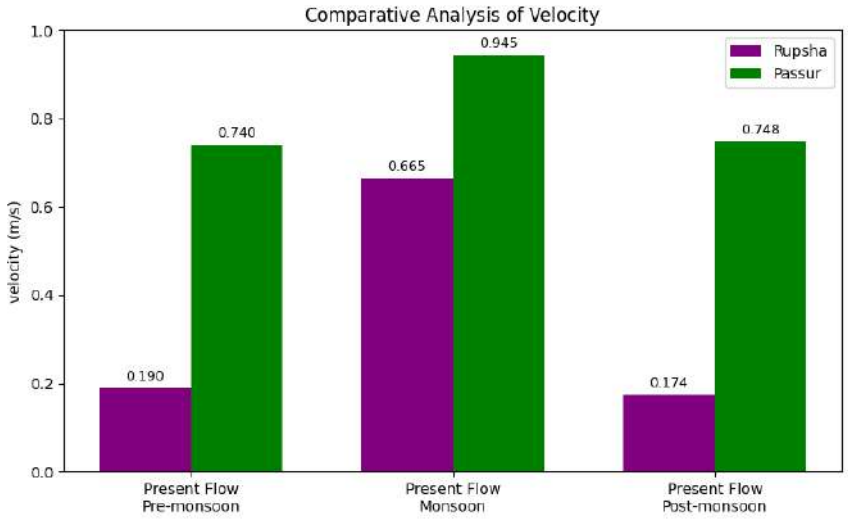

Fig. 7. Velocity analysis between rupsha and passur river

3.1.3 K-Omega Turbulence Model

In computational fluid dynamics (CFD), the k–omega (k–ω) turbulence model is a widely used method for estimating turbulent flow and also, is a common two-equation turbulence model, that is used as an approximation for the Reynolds-averaged Navier–Stokes equations (RANS equations). The model attempts to predict turbulence by two partial differential equations for two variables, k and ω, with the first variable being the turbulence kinetic energy (k), which represents the energy contained in the turbulent motion. While the second (ω) is the specific rate of dissipation (of the turbulence kinetic energy k into internal thermal energy). This model helps estimated the effects of turbulence in fluid flow by simplifying the complex Reynolds-averaged Navier–Stokes (RANS) equations [25]. The eddy viscosity ν_T, as needed in the RANS equations, is given by: $\nu_t = k/\omega$, while the evolution of k and ω is modelled as Eq (1) and (2):

$$\frac{\delta(\rho k)}{\delta t} + \frac{\delta(\rho u_j k)}{\delta x_j} = \rho P - \beta^* \rho \omega k + \frac{\delta}{\delta x_j}\left[\left(\mu + \rho_k \frac{\rho k}{\omega}\right)\frac{\delta k}{\delta x_j}\right] \quad (1)$$

$$\frac{\delta(\rho \omega)}{\delta t} + \frac{\delta(\rho u_j \omega)}{\delta x_j} = \frac{\alpha \omega}{k}\rho P - \beta \rho \omega^2 + \frac{\delta}{\delta x_j}\left[\left(\mu + \rho_\omega \frac{\rho k}{\omega}\right)\frac{\delta \omega}{\delta x_j}\right] + \frac{\rho \sigma_d}{\omega}\frac{\delta_k}{\delta_{xj}}\frac{\delta_\omega}{\delta_{xj}} \quad (2)$$

Where; k is the turbulence kinetic energy, - ω is the specific rate of dissipation, ν is the kinematic viscosity, νt is the eddy viscosity (νt = k/ω), σk, σω, α, and β are empirical model constants, ρk is the production term.

4. Validation with Benchmarking Case Study

At first, using the values of Turbulent Benchmarking Grid Case-10 from Benchmarking project by Supergen, the initial simulation was done to find the result of their project. Where the RPM was taken 81 and the velocity was taken 0.9207 m/s from it.

Table 2. Rectangular region domains (Inlet, outlet, and height extension)

Axis	Corner-1	Corner-2
x	-1.5 m	4 m
y	-1.5 m	1.5 m
z	-1.5 m	1.5 m

Table 3. Cylindrical region domains

Axis	Start Coordinate	End Coordinate	Cylinder Radius
x	0.5 m	-0.5 m	
y	0 m	0 m	1 m
z	0 m	0 m	

Here, Table 2 and Table 3 show the values of the cylindrical region and the rectangular region for the mesh set up as well as for the boundary set up around the turbine. The coordinate system is categorical as x in the stream-wise, y in the vertical and z in the span wise directions, respectively.

After meshing, the cell number for Benchmarking Project was found almost 2.5 Million, where the faces were almost 7.15 Million and the vertices were 2.5 Million. The simulation has been done where the solution time was 31.41 seconds, and the Iteration was more than 17,000 by taking the velocity as 0.9207 m/s and torque as 81 rpm from the Benchmarking Paper.

Table 4. Simulation results for benchmarking project

Simulation No.	V (m/s)	RPM	Thrust (N)	Torque (N-m)	Power (W)	Tidal Time (h)	Electricity (kW-h)
1	0.9207	81	1045	58.604	497.098	6	2.982

Here, Table 4 shows the result after the simulation is done. From the simulation the Torque has been found 58.604 N-m, and the thrust has been found 1045 N. The power has been found 457.098 W after the calculation. So, the electricity found from the simulation by multiplying with the Tidal time is 2.982 kW-h or almost 3 kW-h.

4.1 Simulation Using Passur River Condition

The similar methods have been taken for completing the simulations by taking the Passur River data of Bangladesh. The coordinate system is defined as x in the stream-wise, y in the vertical and z in the span wise directions, respectively.

Table 5. Rectangular region domains (Inlet, outlet, and height extension)

Axis	Corner-1	Corner-2
x	-1.5 m	9 m
y	-2 m	2 m
z	-2 m	2 m

A total of three meshes have been done as well as three simulations by using the data taken from Passur River, Bangladesh. For every mesh, Table 5 and Table 6 show the values of the cylindrical region and the rectangular region, which was taken similarly. Here, the cylindrical region as

Cylindrical rotating domain will contain the turbine and the rectangular region as Water tunnel will contain the sea water.

Table 6. Cylindrical region domains

Axis	Start Coordinate	End Coordinate	Cylinder Radius
x	0.4 m	-0.4 m	
y	0 m	0 m	1 m
z	0 m	0 m	

Three meshes have been done by changing their cell numbers. Among three meshes mesh-1, which cell number is 3537595, mesh-2 where its cell number has been decided by multiplying by $\sqrt{2}$ with mesh-1 cell number, and mesh-3 where its cell number has been decided by dividing by $\sqrt{2}$ with mesh-1 cell number. So, these all is done for the mesh independence test to find out that if the results from simulation-2, simulation-3, and simulation-4 vary much or not, by using the velocity and rpm values of Passur River of Bangladesh.

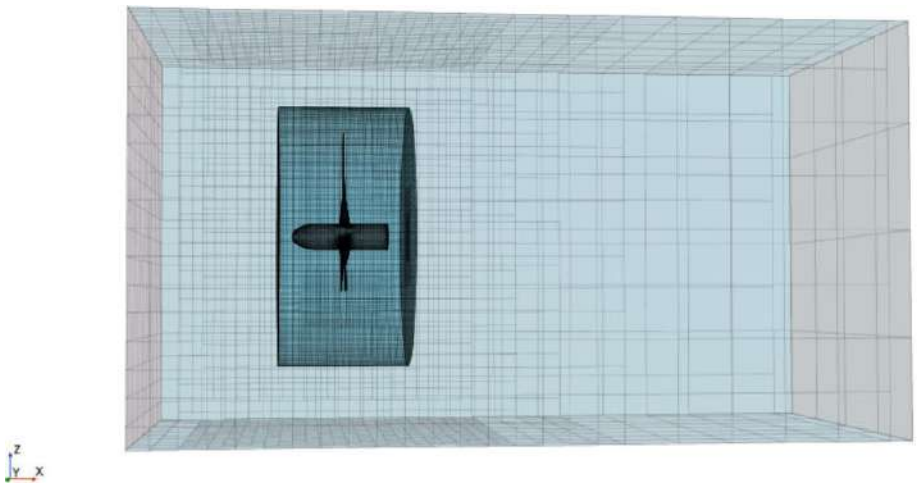

Fig. 8. Inlet, outlet, and height extension

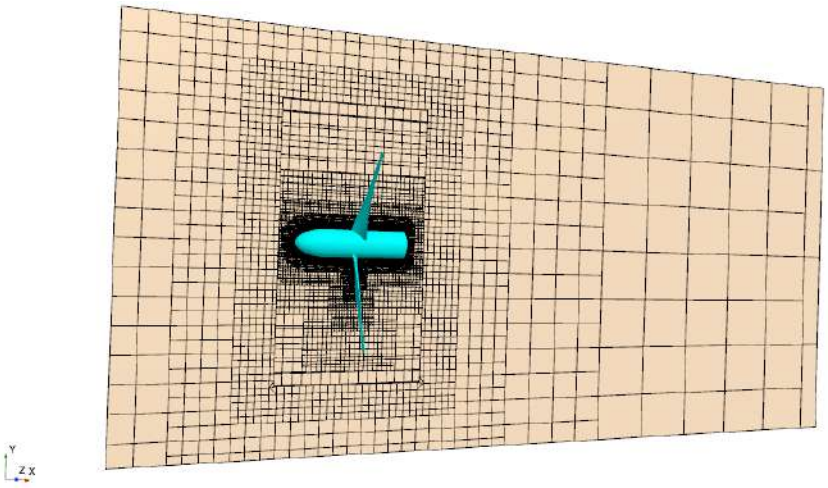

Fig. 9. Mesh scene

Here, Table 7 shows that for Mesh-1 the cell number was found almost 3.5 Million, for Mesh-2 cell number was found almost 5.5 Million and for Mesh-3 cell number was found almost 2.3 Million. Fig. 8 and Fig. 9 represent the meshed Inlet, Outlet, Height extension and mesh scene view after meshing.

Table 7. Meshing values

	Mesh-1	Mesh-2	Mesh-3
Cells	3537595	5540313	2363576
Faces	10463931	16399651	7024652
Vertices	3602374	5543425	2465137

5. Results and Discussion

The CFD analysis with a Horizontal Axis Tidal Current Turbine of 1.6m blade (HATCT) was carried out for three different types of meshes as well as three different simulations. The turbine from a benchmarking project and then numerical solvers to simulate the flow around the tidal blade with STARCCM+ to obtain effective power. Power, thrust force, and torque were calculated for each simulation, by keeping this intention water velocity, and rpm were assumed as Passur River which is near the Khulna area. This study was simulation-based, without physical modeling; therefore, actual results may differ when using a practical model.

The design has been taken from a benchmarking project by Supergen, which is mainly a practical model of their turbine. With our research and design a practical model can be made to justify the design and know the accuracy of the design. Further research can be made if this project can be implemented in Bangladesh. The simulation results indicate that

- Thrust and Torque have been found. The power has been calculated through Eq (3):

$$P = RPM \times \left(\frac{3.1416 \times 2}{60}\right) \times Torque \tag{3}$$

- Then the value of electricity has been found by multiplying with the tide time which is taken 6 hours initially. Here, Eq (4):

$$E = Power(Watt) \times Time\ (Tidal) \tag{4}$$

Table 8. Results from three different simulation

Simulation No.	V (m/s)	RPM	Thrust (N)	Torque (N-m)	Power (W)	Tidal Time (h)	Electricity (kW-h)
2	0.945	81	1067.9	59.0965	501.275	6	3.00765
3			1021.3	57.9407	491.496		2.948976
4			1064.5	58.9734	501.483		3.008718

Here, Table 8 shows the results for Thrust, Torque, and Power after three different simulations have been done and all are nearly identical. Therefore, based on these results, the final power value was taken from the lowest-resolution mesh (mesh-3) which refers the simulation 4 and the power found from that is 3 kW-h. Where simulation-4 has been run for 20.025 seconds. Fig.10 & Fig. 11 represent the Scalar View and Power Monitor of Simulation-4 whereas Fig. 12 & Fig. 13 show the Thrust Monitor and Torque Monitor view in the same simulation.

As a result, the simulation results showed that the power output, torque, and thrust values had been quite consistent across the three mesh sizes (Table 8). The simulation setup's numerical stability and mesh independence are confirmed by this consistency. Mesh-3, which had the fewest cells, nevertheless generated a similar amount of electricity (3.008 kWh), confirming computational efficiency without compromising precision. This conclusion is consistent with the results of several research that highlighted the importance of localized mesh refinement over global cell count in attaining computational efficiency.

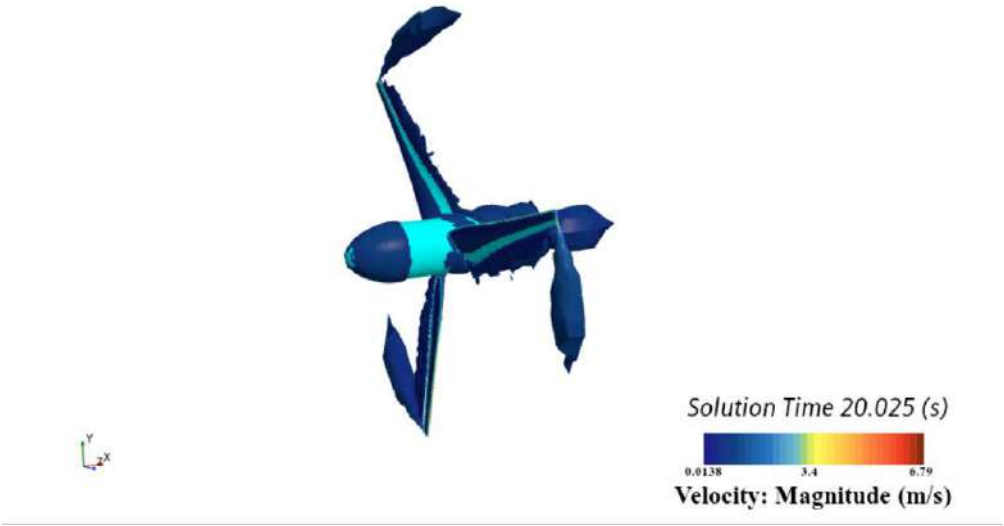

Fig. 10. Scalar view

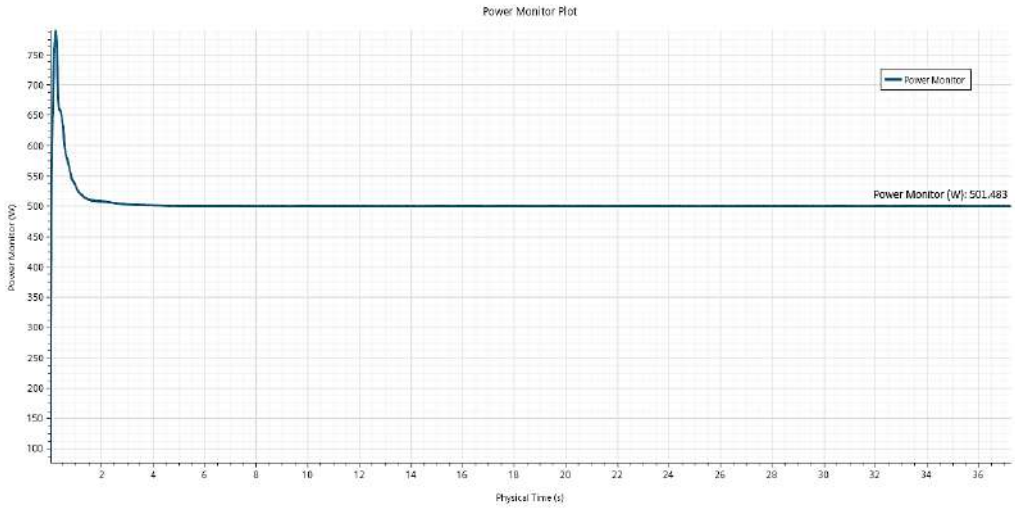

Fig. 11. Power monitor

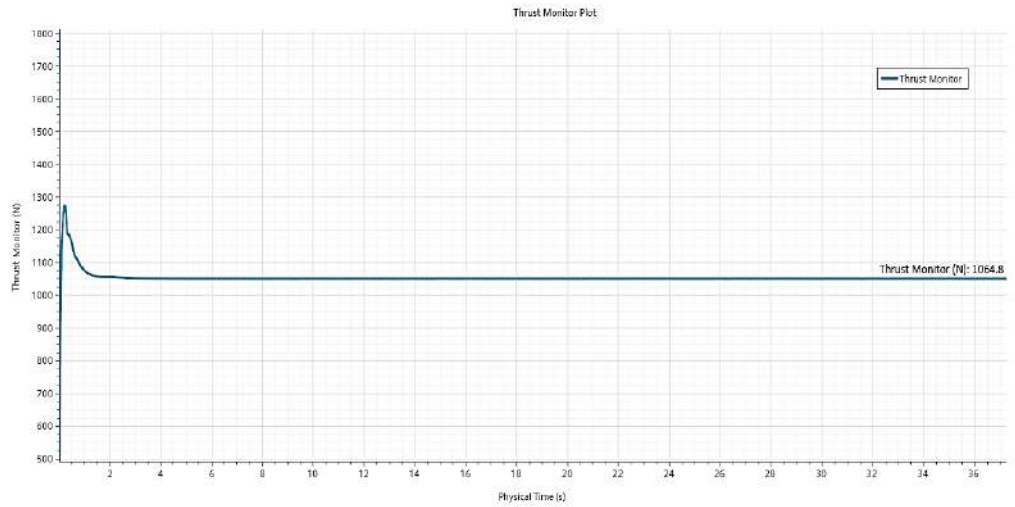

Fig. 12. Thrust monitor

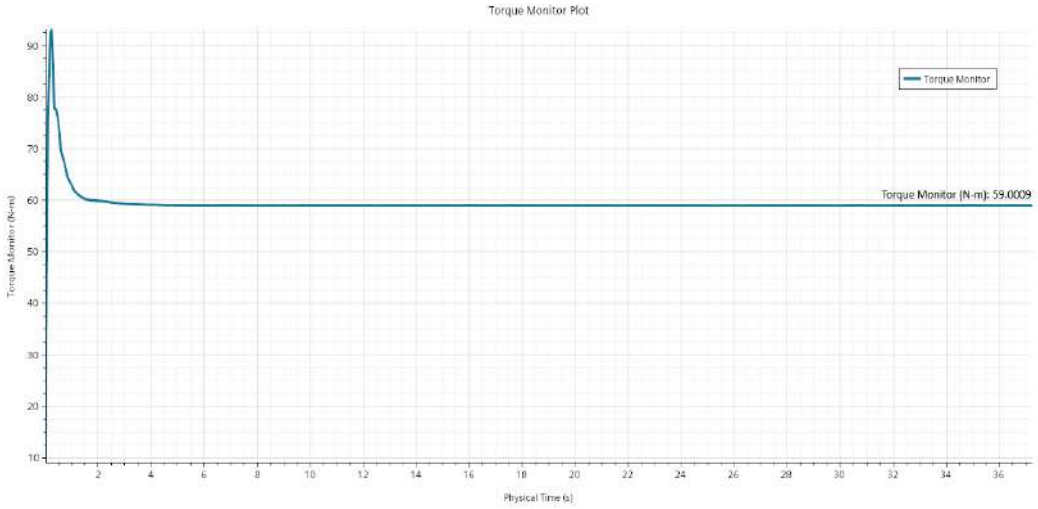

Fig. 13. Scalar view

Additionally, comparable research has shown that designs with curved trailing edges act better in situations with fluctuating flow. The high thrust and torque stability across a range of flow speeds is the outcome of the design optimizations that our CFD model included. As noted in earlier maritime CFD research and recently validated in tidal array conditions, the results also support the validated use of the k–ω turbulence model. Our scalar velocity profiles illustrated how well this turbulence model simulated intricate boundary-layer interactions (Fig. 10).

This study provides competitive performance parameters when juxtaposed with real-world tidal setups and turbines, especially in estuary environments like the Passur River. The practicality of small-scale, decentralized renewable energy projects in Bangladesh has been shown by the estimated electricity generation of approximately 3 kWh per turbine every single tidal cycle. This could make a substantial contribution towards the regional energy grid if developed with multiple turbine units.

The low performance variation across simulations, despite variations in mesh resolution, is yet another noteworthy result. This supports the findings that geometric symmetry and suitable airfoil selection have an important influence on simulation efficiency and stability. Furthermore, our findings are consistent with site-specific tidal flow measurements in the Rupsha-Passur system as reported in several studies, giving assurance that the simulated environmental inputs accurately represent field conditions.

In terms of comparative output, the final thrust (1064.5 N), torque (58.97 N-m), and power (501.48 W) values are within the expected range based on the benchmarking turbine case by Supergen, validating both our numerical setup and boundary selection. And from the above all results, we can see that the measuring value of Electricity for Passur River is almost same with the simulation result of Bench marking projects Electricity value, which justifies the result.

6. Conclusion

The Computational Fluid Dynamics (CFD) analysis conducted on the Horizontal Axis Tidal Current Turbine (HATCT) has provided valuable insights into the turbine's hydrodynamic performance and behavior of the turbine under varying operational conditions. Through high fidelity (CFD) simulations have enabled a comprehensive evaluation of the turbine's hydrodynamic characteristics, finding the key performance indicator- thrust, torque, and power. By simulating the interaction between the turbine blades and tidal currents. These findings are crucial for engineers and designers to enhance the reliability and longevity of the Horizontal Axis Tidal Current Turbine, contributing to the sustainable harnessing of tidal energy.

Using a validated turbine design from a benchmarking project and applying site-specific flow conditions from the Passur River near Khulna, Bangladesh, the simulations consistently produced similar results across different mesh configurations. Where for every simulation the cell number of every mesh was different to see the variation of the power, thrust, and torque values. Therefore, the Passur River can create power as well as electricity with the tidal turbine and the energy output per tidal cycle was found to be approximately 3 kWh. As it is done by one tidal turbine, the generation of electricity is not much to give it in the grid system but it provides a promising baseline for larger, distributed turbine networks.

Practically speaking, a network of these turbines might provide off-grid coastal communities with energy, lessen reliance on fossil fuel-based power generation, and improve energy resilience in areas that are already at risk. Furthermore, tidal turbine systems are ideal for a progressive integration into Bangladesh's energy system because of their modular & flexible design, which permits staggered adoption. Tidal turbines produce a low visual impact and emit no greenhouse emissions while in operation, making them an environmentally friendly option that aligns with global climate targets. Furthermore, its predictable generation profile based on tidal cycles may be combined with intermittent sources like solar and wind, helping to create a more stable and diverse renewable energy portfolio.

This study not only demonstrate technical feasibility of HATCT deployment in Bangladesh's tidal zones but also emphasizes the broader socio-economic and environmental benefits. By advancing CFD-based design and optimization strategies, this research lays a foundation for future efforts aimed at developing site-specific tidal energy projects that are efficient, environmentally responsible, and economically viable. That is why the CFD analysis has been instrumental in providing a detailed and data-driven assessment of the Horizontal Axis Tidal Current Turbine, accordingly offering valuable insights for further research, design refinement, and the eventual deployment of efficient and robust tidal energy systems. This study contributes to the ongoing efforts to harness clean and renewable energy sources, paving the way for the sustainable development of tidal power technology.

Acknowledgement

The authors declare that they have no financial or personal relationships that could have influenced, or been perceived to influence, the research presented in this paper.

References

[1] Chowdhury MS, Rahman KS, Selvanathan V, Nuthammachot N, Suklueng M, Mostafaeipour A, et al. Current trends and prospects of tidal energy technology. Environ Dev Sustain. 2021 Jun;23(6):8179-94. https://doi.org/10.1007/s10668-020-01013-4

[2] Khan M, Bhuyan G, Iqbal M, Quaicoe J. Hydrokinetic energy conversion systems and assessment of horizontal and vertical axis turbines for river and tidal applications: A technology status review. Applied Energy. 2009 Oct;86(10):1823-35. https://doi.org/10.1016/j.apenergy.2009.02.017

[3] Yang TM, Prediction of long-term fatigue damage of a hydraulic cylinder of a wave energy converter subjected to internal fluid pressure induced by wave loads. Int J Mar Energy. 2013;2:43-60. https://doi.org/10.1016/j.ijome.2013.05.005

[4] Ng K, Lam W, Ng K. 2002–2012: 10 Years of Research Progress in Horizontal-Axis Marine Current Turbines. Energies. 2013 Mar 6;6(3):1497-526. https://doi.org/10.3390/en6031497

[5] Ambarita EEA, Experimental study on the optimum design of diffuser-augmented horizontal-axis tidal turbine. Clean Energy. 2022;6(5):776-86.

[6]Wang S, Zhang Y, Xie Y, Xu G, Liu K, Zheng Y. Hydrodynamic Analysis of Horizontal Axis Tidal Current Turbine under the Wave-Current Condition. JMSE. 2020 Jul 26;8(8):562. https://doi.org/10.3390/jmse8080562

[7] Encarnacion JI, Johnstone C, Ordonez-Sanchez S. Design of a Horizontal Axis Tidal Turbine for Less Energetic Current Velocity Profiles. JMSE. 2019 Jun 27;7(7):197. https://doi.org/10.3390/jmse7070197

[8] Haque MA, Khatun MS. Tidal Energy: Perspective of Bangladesh. J Bangladesh Acad Sci. 2018 Jan 29;41(2):201-15. https://doi.org/10.3329/jbas.v41i2.35498

[9] Shi W, Wang D, Atlar M, Guo B, Seo K. Optimal design of a thin-wall diffuser for performance improvement of a tidal energy system for an AUV. Ocean Engineering. 2015 Nov;108:1-9. https://doi.org/10.1016/j.oceaneng.2015.07.064

[10] Tedds S, Owen I, Poole R. Near-wake characteristics of a model horizontal axis tidal stream turbine. Renewable Energy. 2014 Mar;63:222-35. https://doi.org/10.1016/j.renene.2013.09.011
[11] Blunden L, Bahaj A. Initial evaluation of tidal stream energy resources at Portland Bill, UK. Renewable Energy. 2006 Feb;31(2):121-32. https://doi.org/10.1016/j.renene.2005.08.016
[12] Kulkarni CC HSEAP DJES. Design study of horizontal axis tidal turbine blade. Mindanao J Sci Technol. 2017;15:12-34.
[13] Gross R, Leach M, Bauen A. Progress in renewable energy. Environment International. 2003 Apr;29(1):105-22. https://doi.org/10.1016/S0160-4120(02)00130-7
[14] Bahaj A, Myers L. Fundamentals applicable to the utilisation of marine current turbines for energy production. Renewable Energy. 2003 Nov;28(14):2205-11. https://doi.org/10.1016/S0960-1481(03)00103-4
[15] Malki R, Masters I, Williams AJ, Nick Croft T. Planning tidal stream turbine array layouts using a coupled blade element momentum – computational fluid dynamics model. Renewable Energy. 2014 Mar;63:46-54. https://doi.org/10.1016/j.renene.2013.08.039
[16] Wilden RO. Unsteady loading tidal turbine benchmarking study. Tidal Benchmarking Project. 2022.
[17] Abuan BE, Howell RJ. The performance and hydrodynamics in unsteady flow of a horizontal axis tidal turbine. Renewable Energy. 2019 Apr;133:1338-51. https://doi.org/10.1016/j.renene.2018.09.045
[18] T T. The advantages of ducted over unducted turbines. In: European Wave and Tidal Energy Conference. 2005. p. 523.
[19] ERKAN O, OZKAN M. Investigation of the Flow Over NACA 63-415 Airfoil. Black Sea Journal of Engineering and Science. 2020 Apr 1;3(2):50-6. https://doi.org/10.34248/bsengineering.643916
[20] Willden R, Harvey S T, Chen X, Vogel C, Gilbert J, Bhavsar K, Allsop T, Stallard T, Mullings H, Young A, Benson I. Tidal benchmarking project. In: Tidal Benchmarking Project: Opening Workshop. 2022.
[21] Xu K, Finnegan W, O'Rourke F, Goggins J. CFD analysis of hydrodynamic force on a horizontal axis tidal turbine. Proc EWTEC. 2023 Sep 2;15. https://doi.org/10.36688/ewtec-2023-137
[22] Lintermann A. Computational meshing for CFD simulations. Res Gate. 2020:85-115. https://doi.org/10.1007/978-981-15-6716-2_6
[23] Nicholls-Lee SRTSWB RF. Simulation-based optimisation of marine current turbine blades. 2007.
[24] Saran AR AY SHH. Comparative analysis on flow and salinity of Rupsha-Passur river system of Bangladesh. J Mod Sci Technol. 2018;6:19-31.
[25] Wilcox DC. Formulation of the k-ω turbulence model revisited. AIAA J. 2008;46:2823-38. https://doi.org/10.2514/1.36541

Blank Page

Research on Engineering Structures & Materials
www.jresm.org
Research Group

Research Article

Artisanal lime as a low-carbon stabilizer for enhanced stabilized earth blocks in sustainable earthen structure rehabilitation

Rabiâ Abdeldjebar [*,1,a], Abdelghani Idder [2,b], Lahbib Lahmar [1,c], Lakhdar Missoum [1,d], Abderrahmane Moulay Ali [2,e]

[1]*ARCHIPEL Laboratory, Tahri Mohamed University of Bechar, Algeria*
[2]*Department of Civil Engineering, Ahmed Draia University of Adrar, Algeria*

Article Info

Article History:

Received 11 May 2025
Accepted 25 Aug 2025

Keywords:

Artisanal lime;
SEB;
Ecological stabilization;
Valorization of local resources;
Earthen heritage

Abstract

This study investigates artisanal lime as a low-carbon stabilizer for stabilized earth blocks (SEBs) to optimize the sustainable rehabilitation of earthen structures while reducing cement use. Conducted in Mougheul, Bechar region, Algeria, the study adopts a circular economy approach by valorizing local soil and traditionally produced lime, minimizing cement's environmental impact. A mixed stabilization method (cement/artisanal lime) was tested at replacement rates of 0%, 12.5%, 25%, 50%, and 100%. Physico-mechanical properties, including density, water absorption, porosity, and compressive/flexural strengths, were evaluated at 28 and 90 days per international standards. At 12.5% replacement, SEBs achieve a compressive strength of 1.94 MPa at 28 days, a water absorption reduction of 1.96%, and a porosity decrease of 2.83% at 90 days, enhancing the stability of the earthen material and complying with international standards. Compared to industrial lime, artisanal lime offers comparable performance with reduced environmental impact. These findings support heritage preservation and Sustainable Development Goals (SDGs) through low-emission construction. Future research should explore long-term material stability and bio-based stabilizers.

© 2025 MIM Research Group. All rights reserved.

1. Introduction

Earth has been a cornerstone of construction for millennia, prized for its availability and adaptability [1]. However, modern construction techniques, particularly those reliant on cement, have largely replaced earth-based methods, contributing significantly to environmental degradation. The building sector accounts for 39% of global CO_2 emissions, with cement production responsible for 8% [2]. These energy-intensive materials also deplete natural resources and inflate construction costs, which can represent up to 70% of housing expenses in developing regions [3]. In response, raw earth has garnered renewed interest as a sustainable building material due to its abundance, local availability, low cost, renewability, and eco-friendly properties [4-6]. Over half the global population resides in earthen housing, particularly in developing countries where demand for affordable, sustainable materials is critical [7,8,9]. Yet, the material's susceptibility to water and low mechanical strength limits its widespread adoption, necessitating innovative stabilization methods to enhance earthen material stability while prioritizing sustainability [10,11].

The rehabilitation of earthen structures represents a critical challenge in heritage conservation, requiring materials that maintain structural integrity while preserving cultural authenticity and minimizing environmental impact [12]. Traditional earth construction often employs vegetable or

*Corresponding author: abdeldjebar.rabia@univ-bechar.dz
[a]orcid.org/0000-0002-8972-5635; [b]orcid.org/0000-0003-2795-2178; [c]orcid.org/0009-0009-5198-8702; [d]orcid.org/0009-0006-0715-5568; [e]orcid.org/0009-0008-5837-9451
DOI: http://dx.doi.org/10.17515/resm2025-892st0511rs

mineral additives to improve durability and performance [13-15]. Stabilization techniques include chemical, mechanical, and physical methods, with chemical stabilization being the most prevalent due to its irreversible effects and enhanced water resistance [16,17]. Cement, a widely used chemical stabilizer, significantly improves earthen material stability but exacerbates environmental concerns, contributing approximately 5% to global CO_2 emissions [18]. Consequently, researchers have explored alternative stabilizers to reduce cement reliance and mitigate environmental impact [19]. Pozzolanic materials and industrial by-products, such as lime, fly ash, or slag, offer viable options for stabilizing earth, leveraging local resources to enhance sustainability [20-22]. In southern Algeria, particularly in the arid, high-temperature region of Mougheul, Bechar, local resources like artisanal lime present opportunities for valorization as low-carbon stabilizers [23].

Previous studies have shown that lime stabilization is particularly effective for clayey soils, requiring a dosage of 4–12%, compared to cement's 2.5–10% for sandy soils [8,18,24]. However, excessive cement dosages (above 10%) can reduce strength, while partial lime replacement (e.g., 50%) has improved physico-mechanical properties in stabilized earth blocks (SEBs) [8,25]. Full cement replacement with lime often reduces mechanical strength, though combining lime with bio-based additives, such as sugarcane ash, can yield positive outcomes [18]. Research in Mougheul has highlighted the potential of artisanal lime, produced traditionally with low energy input, to stabilize local clayey soils, offering a sustainable alternative to industrial lime [26,27]. These findings suggest that optimizing lime-cement ratios could balance performance and environmental benefits.

Growing interest in sustainable construction materials contrasts with limited research on artisanal lime, a locally produced, low-carbon stabilizer, for earth blocks in heritage preservation projects. While traditional stabilization methods often rely on industrial binders such as cement or industrial lime [18,19,28], the environmental and cultural benefits of traditionally produced lime, remain underexplored [29,30]. This study distinguishes itself through a rigorous evaluation of artisanal lime as a partial cement substitute in stabilized earth blocks, its targeted application to the restoration of heritage villages in arid climates, and a comprehensive analysis of physico-mechanical properties over extended curing periods, providing insights into long-term performance and contributing to sustainable, culturally appropriate construction practices.

Artisanal lime, also known as traditional lime, is produced through a time-honored calcination process using locally sourced limestone in traditional vertical kilns. Unlike industrial lime production, which relies on high-energy mechanized processes, artisanal lime production involves manual extraction of limestone rocks, crushing, and calcination in traditional kilns at lower temperatures over extended periods. This traditional method, still practiced in regions like Kenadsa, Algeria, results in a product with unique characteristics and significantly lower carbon footprint compared to industrial alternatives [31,32]. This study leverages the unique properties of artisanal lime to develop environmentally friendly stabilized earth blocks for construction and rehabilitation purposes.

2. Materials and methods

2.1. Materials

2.1.1 Soil

The soil used in this study was sourced from the old village of Mougheul (Fig. 1), a historic village in southwestern Algeria, renowned for its traditional raw earth architecture, often centuries-old, built with local materials and traditional techniques [23, 33]. These structures, now deteriorating due to environmental factors and lack of maintenance, require sustainable rehabilitation. This study develops stabilized earth blocks to restore Mougheul's heritage, ensuring compatibility with its cultural architecture.

The granular composition was carried out in accordance with the NF P 18-560 [34] standard in order to determine the size and proportion of different grains formed in the earth. The earth was composed largely of 63% of sand, 30% of gravel, and 7% of clay. It is also noticeable that the granular distribution curve of earth was recommended as band per CRATerre until 70% [28].

According to the division of the INRA reading triangle [35], the sample of earth was due to silty sand, which mentioned that its suitable for stabilization.

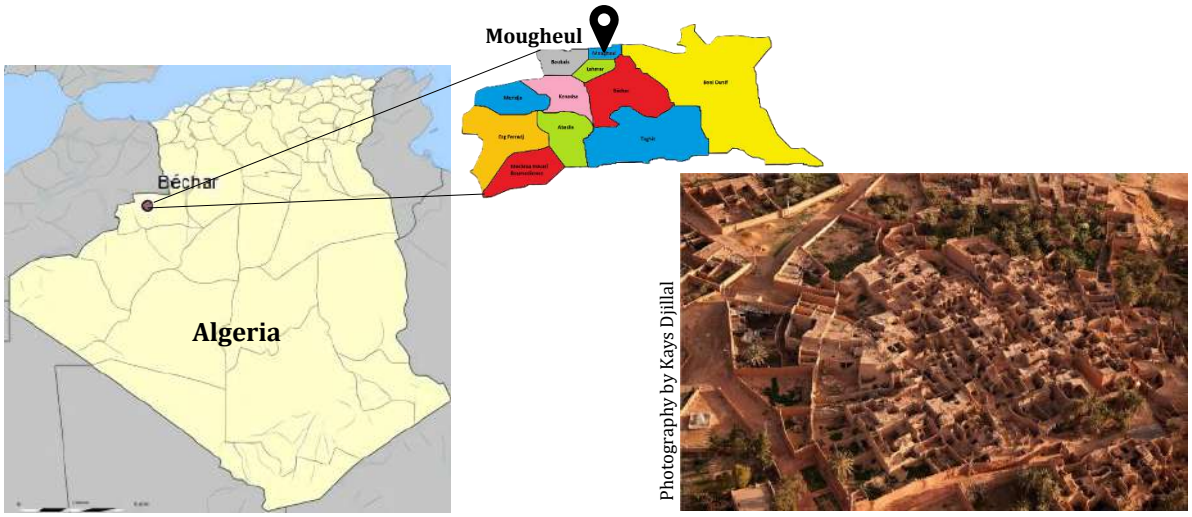

Fig. 1. Location map of Mougheul nd wide-angle aerial view of the old earthen brick village

The clay activity has been tested by the standards of limits Atterberg NF EN ISO 17892-12 [36] and methylene blue NFP 94-068 [37]. The modulus of plasticity Ip was 8.09 < 10 which confirmed the low plasticity of sample due to the decrease in quantity of clay. The less clay of sample leads to no shrinkage cracks, which is the cause of weakness of earth block.

The chemical composition of earth and artisanal lime, as presented in Table 1, was determined using X-ray fluorescence (XRF) spectroscopy at the chemical laboratory of the GICA Bachar cement plant, while data for cement and industrial lime were obtained from the manufacturers' technical datasheets. The XRF analysis enabled quantification of major and trace elements, revealing the mineralogical composition and potential reactivity of earth and artisanal lime. Samples were prepared following standard procedures, dried at 105°C for 24 hours, and ground to pass through a 75 µm sieve, ensuring a measurement accuracy of ±0.1% for major oxides. These data are critical for understanding the materials' properties and suitability for earth block stabilization.

Table 1. The chemical composition of materials (in %)

	CaO	SiO_2	Al_2O_3	F_2O_3	MgO	Na_2O	K_2O	T_iO_2	P_2O_5	SO_3	$CaCO_3$	CO_2	Loss on Ignition
Earth	28.13	30.42	2.58	1.27	0.76	0.11	0.47	0.15	0.08	17.52			17.33
Cement	68	23.8	2.3	0.27	0.48	0.04	0.12			0.65			0.9
Industrial lime	>83.3	<2.5	<1.5	<2	<0.5	0.45	0.51			<0.5	<10	<5	
Artisanal lime	77.26	Insoluble rests = 13.58%									5.60		

Are shown in table 1, the elements of calcium oxide CaO, silicon oxide SiO_2, and aluminum oxide Al_2O_3 are the most oxidizing elements, which means that the earth was composed of a majority of minerals aluminosilicates and quartz. The high percentage of CaO compound explained the presence of large quantities of calcium and the red color of earth was due to the presence of large quantities of iron oxide F_2O_3.

2.1.2 Cement

The purpose of using white cement is to stabilize earth with the trade name "Malaki", it is a Portland composite cement (CPJ - CEM II / A-L 52.5N) with high primary and final strength manufactured by Lafarge plant and complied with Algerian standard NA442 [38] and European standard EN CE 197-1 [39]. The cement was composed of several oxidizing minerals; the most important was CaO as basic function, and SiO_2 as an acid. The type of white cement was used to maintain the natural

color (red) of earth houses in this region, and thus an aesthetic architectural coherence. The physical and chemical properties are presented in Tables 1 and 2.

2.1.3 Industrial Lime

The industrial lime used in this study was quicklime (CaO) produced by BMSD plant. The physical and chemical properties are presented in Tables 1 and 2.

2.1.4 Artisanal Lime

The artisanal lime used in this research was quicklime (CaCOH) made in a traditional way in the city of Kenadsa, where the limestone rocks are extracted by geological sites located in this region [26]. Therefore, limestone was crushed to facilitate its combustion and placed on top of other combustible stones at the top of traditional vertical kiln, the fire was put in the lower part of kiln to start the calcination process of limestone [27]. The artisanal lime was extracted after two days of total cooling of kiln (Fig. 2). The extracted lime was crushed and sieved in an 80 μm sieve. The physical and chemical properties are presented in Tables 1 and 2.

Fig. 2. The stages in the manufacture of artisanal lime

Table 2. Physical properties of materials used in this study

Parameters	Earth	Cement	Industrial lime	Artisanal lime
Absolute density (g/cm^3)	2.7	3.1	2.24	2.56
Apparent density (g/cm^3)	1.3	1.14	0.72	0.87
Normal consistency		28±3.0	69.5	
Finesse following Blaine's method (cm^2/g)		4300-5200	11663	10189
Shrinkage at 28 days (μm/m)		< 1000		
Expansion (mm)		≤ 3.0		
Initial setting time (min)		160 ± 40	80	
Final setting time (min)		250 ± 40		
Sand equivalent ES (%)	11.58			
Liquidity limit (%)	19.45			
Limit of plasticity (%)	11.36			
Consistency index (%)	0.92			
Plasticity index (%)	8.09			

2.2. Testing Method and Mix Proportions

Stabilized Earth Blocks (SEBs) refer to earth blocks enhanced with chemical stabilizers, such as cement or lime, to improve mechanical properties and durability. Unlike traditional mud bricks, SEBs incorporate binding agents without requiring compaction, offering a modern alternative for construction. In this study, SEBs are designed to replicate and enhance the traditional earthen bricks used in Mougheul's heritage structures while meeting contemporary performance standards. The experimental methodology combines standard testing procedures with adaptations specific to artisanal lime evaluation, as detailed in the following sections.

Previous studies [13,14,23,33] investigated stabilized earth blocks (SEBs) made from the soil of the Mougheul Ksar, consistently identifying an optimal composition with 10% cement as the control

mix at a 0% replacement rate. In this study, cement was replaced with artisanal and industrial lime at rates of 0%, 12.5%, 25%, 50%, and 100%. Comparisons were made with the control composition (0% replacement), as shown in Table 3. The granular distribution of earth and mineralogical nature were considered uniform (constant) through all formulations.

Table 3. Details of the proportions of the mixture

Replacement rate	Cement	Artisanal lime	Industrial lime
0% (control)	10	0	0
12.5%	8.75	1.25	0
25%	7.5	2.5	0
50%	5	5	0
100%	0	10	0
12.5%	8.75	0	1.25
25%	7.5	0	2.5
50%	5	0	5
100%	0	0	10

Experimental test specimens are manufactured according to the classical method (Mixing - compacting - demolding). In order to prepare the mixing phase, the earth is dried in the oven at a temperature of 65°C for a period of 24 hours. We begin by weighing the appropriate quantities of each material according to the formulation composition, the assembly (earth + stabilizer) was manually mixed and left for 5 min, then the assembly (earth + stabilizer + water) is mixed with a 5-litre mortar mixer for a period of 2 minutes. The fresh mixture is placed in the molds of each experiment, then vibrated by a vibrating table for 15 seconds and stored in the laboratory. After two days of curing, the specimens are removed from the molds and left in an ordinary chamber, under (T= 22 ± 2°C and RH = 33 ± 5%), for up to 28 and 90 days of curing, to be subjected to various physico-mechanical tests. Photographs of the freshly molded and hardened earth blocks are presented in Fig. 3 and Fig. 4

Fig. 3. Photograph of fresh molded earth block

Fig. 4. Photograph of hardened earth block

2.3. Tests Protocol

2.3.1 Slump Test

The abrasive cone slump test was carried out in accordance with standard NF EN 12350-2 [40] in order to determine the workability of the concrete, as well as to obtain information on the ease of (mixing - compacting - transport and implementation) of the SEB in its fresh state.

2.3.2 Air Content Test

The air content test was conducted in accordance with NF EN 1015-7 [41], as this experiment focuses on measuring the volume of air entrapped in the fresh SEB, where we used a 0.75-liter aerometer (Fig. 5a), especially since the initial porosity (air bubble) is formed during the SEB mixing process.

2.3.3 Apparent Density Test

The density specimens were measured before each experiment. The procedure was intended to detect if there is no good compaction or bad mixing during the manufacture of bricks. The density $\rho = M/V_t$; is a physical greatness determined by dividing the weight of the sample M by the total volume V_t . The total test specimens of dimensions $10 \times 10 \times 5$ cm^3 placed in a climatic chamber with conditions of 23°C and 50% RH. A balance with an accuracy of 0.01 was also used to measure the weight of the specimen with a caliper to measure its volume.

2.3.4 Total Water Absorption Test

This experiment was done by immersing the stabilized earth bricks completely in water for 24 hours and measuring the weight of the wet bricks from the initial dry weight according to the following relationship:

$$TWA(\%) = ((M_w - M_d)/M_d) \times 100 \quad (1)$$

2.3.5 Initial Absorption

The experiment of capillary absorption was carried out according to the XP P13-901 standard [42], by following the evolution of the open porosity of SEB. The specimens used are bricks of dimension $10 \times 10 \times 5$ cm^3. The specimens were dried at 105 °C until the weight of sample was stabilized less than 0.1%. The base of specimen (10×5 cm^2) was partially immersed to a depth of 10 mm in which the initial absorption coefficient C_b represented the quantity of absorption in 30 minutes. This period was considered as a reference for the volume of largest pores (macrospores) located on the surface of SEB [14]. The initial absorption coefficient C_b was calculated according to the following relationship:

$$C_b = \frac{(M_h - M_d)}{S\sqrt{t}} \quad (2)$$

Where; $M_h - M_d$: The quantity of water absorbed during the test in kg, S: The area of the test piece in which the test was carried out in m^2, t: Immersion period in minutes.

2.3.6 Open Porosity

The open porosity was calculated based on the fundamental law of porosity $n = V_V/V_t$, where the total void volume Vv represented the quantity of water absorbed during half an hour per unit area divided by the total volume V_t as shown by the following formula:

$$n(\%) = \left(\frac{V_V}{V_t}\right)100\% = \left(\frac{\Delta m/\rho}{S\,.\,Z}\right)100\% = \left(\frac{\Delta m/s}{\rho\,.\,Z}\right)100\% \quad (3)$$

With; Δm/s: The quantity of water absorbed in the unit of surface area (kg/m^2.min$^{1/2}$), ρ: The density of water (10^3 Kg/m^3), Z: The height of capillary imbibition front in (m).

2.3.7 Water Permeability

The water permeability test on earth blocks stabilized was conducted following a rigorous experimental protocol, adapted to the local resources of the university's geotechnical laboratory, in compliance with the ISO 17892-11:2019 standard for soil permeability tests [43].

A 10 cm cubic sample was placed between two metal plates to ensure uniform water pressure distribution on its upper and lower surfaces, with rubber sheets used to isolate the sample and prevent water concentration. The hydraulic conductivity (K_w) was calculated using the formula:

$$K_w = \frac{Q \cdot L}{A \cdot \Delta P} \tag{4}$$

Where; Q: Flow rate (m^3/s), L: Length of sample (m), A: Cross-sectional area (m^2), ΔP : The applied pressure (Pa).

The relationship between hydraulic conductivity K_w (m/s) and permeability $k(m^2)$ is expressed by Darcy's law as $K_w = k(\rho g/\mu)$, where ρ is the fluid density (kg/m^3), g is the gravitational acceleration (m/s^2), and μ is the dynamic viscosity ($Pa \cdot s$). The intrinsic permeability k (m^2) reflects the material's ability to transmit fluid, independent of fluid properties.

2.3.8 Compressive and Flexural Strength

The flexural experiments were carried out according to the 3-point method on $40 \times 40 \times 160$ mm^3 prismatic specimens (Fig. 5b). A CONTROLS universal testing machine, equipped with a three-point bending device and an automatic compression system (capacity 15/500 kN), was used for these tests. These experiments were conducted in accordance with standard NF EN 196-1 [44]. The flexural test was performed using a machine with a speed of 1.14 mm/min and the flexural strength was calculated according to the following law:

$$F_S = \frac{3}{2}\frac{F \times L}{b^3} \tag{5}$$

Where; b: The side of square section of prism, F: The force was applied in the middle of the prism, L: The distance between supports.

The compression experiments were conducted on 4×4 cm^2 specimens obtained from the flexural experiment, where the specimen was exposed to an increasing load until failure and the compressive strength was calculated according to the following law:

$$\sigma_c = \frac{F}{S} \tag{6}$$

(a) (b)

Fig. 5. Various experiments applied to SEB

3. Results and Discussion

3.1. Consistence of Fresh SEB (Water Requirement)

The results, shown in Figure 6, indicated that higher cement replacement rates led to a firmer mixture, reflecting reduced workability. The decrease in workability can be explained by the decrease in quantity of water in mixture. Therefore, the decrease in quantity of water was due to the absorption of water during the dissociation of calcium oxide CaO resulted of calcium hydroxide

$Ca(OH)_2$. Water was used to separate $Ca(OH)_2$ in order to be transformed into Ca^{+2} ions while the cation exchange reaction occurred.

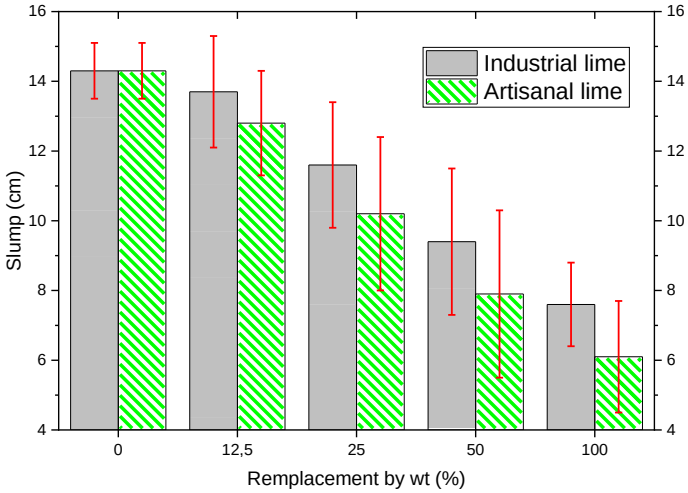

Fig. 6. Slump at Abrams cone

The use of artisanal lime resulted in lower degree of slump due to its greater absorption of water compared to industrial lime. This was due to the artisanal lime that contained more calcium oxide CaO compared to industrial lime (Table 1) with absorbing of water. Also, the increasing absorption of water can be explained by the cement replacement rate increased due to the large and increasing quantity of fines in the mixture, while the lime contained more fines than cement.

The obtained results corroborate the findings of Zebair et al. [23], who demonstrated that mixtures based on artisanal lime absorb more water, thereby reducing slump. Alexandre et al. [8] also confirm this trend, highlighting the effect of fine particles on workability. These observations indicate that lime-treated soils require higher water contents to maintain a consistency comparable to that of cement-treated soils. Regarding the class of our SEB, the results belong to the sections S2 and S3, and therefore to SEB; Plastic and medium workability, very plastic concrete with high workability, respectively. Qualitatively, this indicates a stiffer mix, potentially requiring more effort during compaction but leading to a more stable fresh product.

3.2. Air content

The results of the occluded air content, shown in Figure 7, indicate no significant effect of cement replacement by lime on occluded air. The replacement of cement by artificial lime with rates of 12.5% and 25% has no significant change in the indoor air content, while the rates of 50 % and 100% had a very small increase in the quantity of internal air with a percentage of 2.56 % and 5.13%, respectively, compared to the control composition.

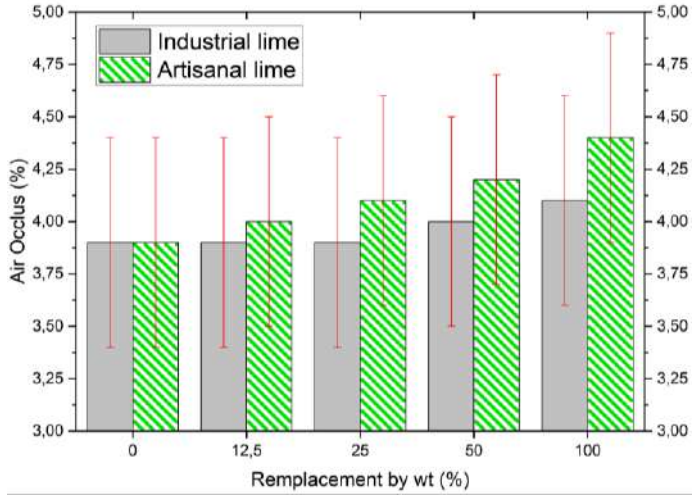

Fig. 7. Air content of SEB

In the case of artisanal lime, there was a direct proportional relationship between the high cement replacement rate and the increase in SEB's indoor air rate. The increase in rate of cement replacement by lime was accompanied by a slight increase in the content of entrapped air, which can be explained by the change in the internal mineralogical structure of the mixture. These findings are in agreement with Izemmouren et al. [21], who reported increased internal porosity and entrapped air with higher lime content. Alavéz et al. [18] corroborate these trends, attributing the slight increase in air content to microstructural changes caused by lime-induced chemical reactions. Qualitatively, this suggests that the stabilization process primarily affects the solid matrix rather than the air void structure at lower replacement rates.

3.3. Apparent Density

The density of SEB is illustrated in Figure 8. At first glance, a decrease in SEB density can be observed with increasing cement replacement rates. At 50% replacement, SEB density with artisanal lime reaches 1.92 g/cm^3, compared to 1.85 g/cm^3 for industrial lime, reflecting superior compactness suited to Mougheul's soils. This decrease is directly proportional to the replacement rate. Notably, the reduction in density was less pronounced with artisanal lime than with industrial lime, indicating that SEBs incorporating artisanal lime consistently exhibited higher densities than those containing industrial lime.

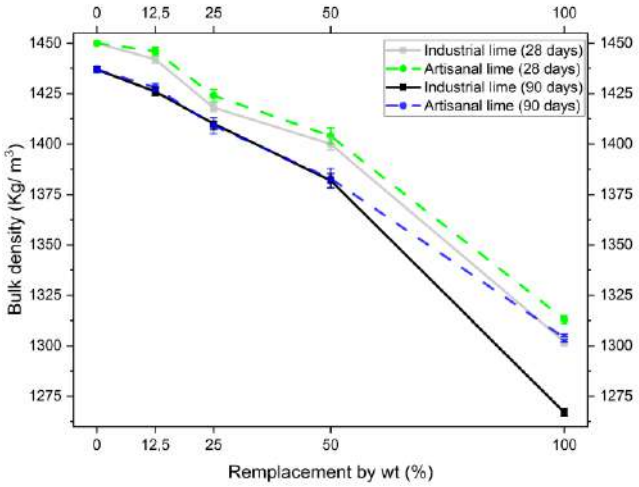

Fig. 8. The bulk density of SEB

This can be explained by the lower density of lime compared to cement and soil, which causes a reduction in the overall density of the mixture. Additionally, the agglomeration of soil particles following the addition of stabilizers (cement or lime) contributes to volume changes. This effect is particularly significant in lime-stabilized samples compared to those stabilized with cement [45]. Overall, the reduction in density observed with artisanal lime was smaller than that recorded with industrial lime.

3.4. Total Water Absorption

Figure 9 presents the variation in total water absorption at 28 and 90 days as a function of cement replacement rate. At 28 days of curing, an increase in the replacement of cement by lime resulted in a progressive rise in total water absorption. According to Alexandre et al. [8], total absorption increased by 17% when 50% of the cement was replaced with lime. Similarly, Guettala et al. [4] reported a 10.2% increase in total absorption at a replacement level of 37.5%.

At 90 days of curing, the results showed a slight improvement in total water absorption compared to the 28-day results. A reduction of approximately 2.25% and 0.78% in total absorption was recorded when 12.5% and 25% of the cement were replaced with industrial lime, respectively, compared to the control mix. Similarly, a 1.96% decrease in total absorption was observed when 12.5% of the cement was replaced with artisanal lime. This reduction is attributed to the formation of new hydration products, which filled the remaining voids after 90 days of curing. According to

Nagaraj et al. [25], the lowest total absorption value of 7.6% was obtained at a 50% replacement rate, followed by 8.3% at 0% replacement.

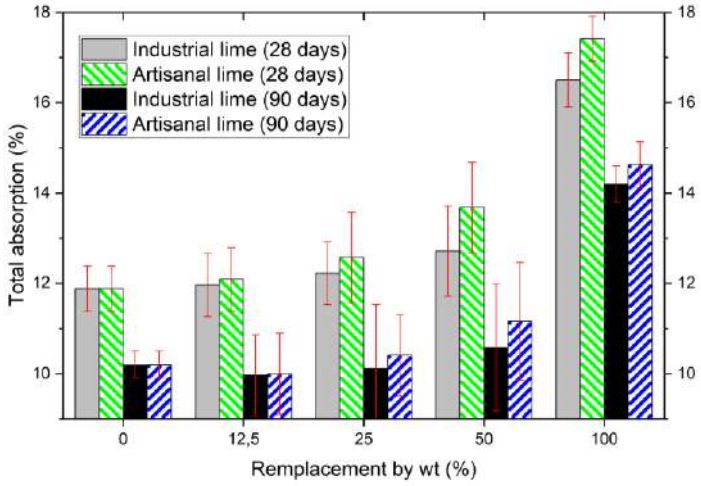

Fig. 9. Total absorption of SEB

Overall, the use of industrial lime consistently led to lower total absorption values than artisanal lime at all replacement levels. This is likely due to the higher production of calcium hydroxide $Ca(OH)_2$ from industrial lime, which promotes pozzolanic reactions with silica and alumina, generating additional hydration compounds that reduce porosity and water absorption. It can thus be suggested that mixtures with replacement rates less than or equal to 50% result in total absorption values lower than the 15% limit recommended by Indian Standards [46].

3.5. Initial Absorption

The results of the absorption coefficient in terms of replacement rate for different cure times were shown in Figure 10. The capillary water absorption was very rapid during the first 30 minutes of the experiment. This phase corresponds to the initial absorption, which is primarily the filling of large pores (macropores). The second phase occurred after the first 30 minutes, where the absorption rate decreased progressively and eventually stabilized. This later phase involves the gradual filling of smaller pores (mesopores and micropores) [14]. In the present study, only the first stage was considered.

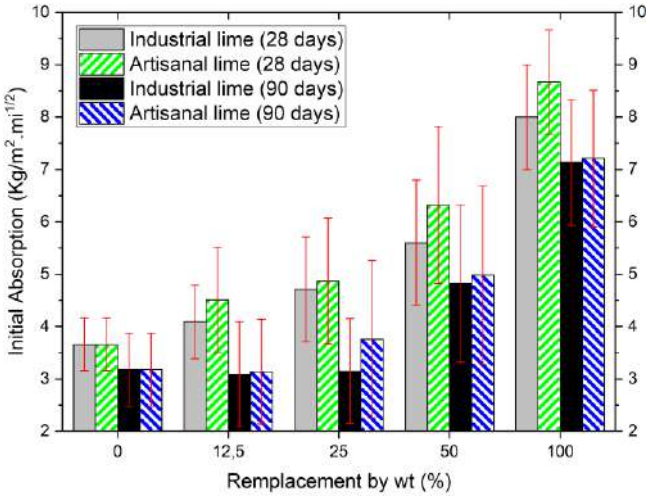

Fig. 10. Initial absorption of SEB

At 28 days of curing, all replacement rates resulted in higher initial absorption values compared to the control mixture. At 90 days, initial absorption of SEB with 12.5% artisanal lime is 0.45 g/cm^2, compared to 0.42 g/cm^2 for industrial lime, suited to Mougheul's arid conditions. The smallest recorded increase was 11.75%, corresponding to a 12.5% replacement of cement with industrial lime. The water absorption of stabilized earth blocks (SEB) depends on pore topology and

hydration kinetics, as the increasing lime content alters the microstructure. Guettala et al. [4] also observed a 4.5% increase in capillary absorption when 37.5% of cement was replaced with lime.

At 90 days, the initial absorption values decreased compared to the 28-day results. This reduction can be explained by the hypothesis that hydration and pozzolanic reactions continue to progress over time, leading to refinement and partial closure of capillary pores. At a 12.5% replacement rate, a beneficial effect of the cement–lime combination was observed. Compared to the control, the initial absorption decreased by 2.83% and 1.26% for industrial and artisanal lime, respectively. It can be concluded that replacing cement with 12.5% lime leads to a significant reduction in initial water absorption over long-term curing. This improvement may be attributed to the change in pore geometry and distribution induced by lime addition.

3.6. Open Porosity

The results of the open porosity of SEB are shown in Figure 11. Porosity is one of the most critical structural properties, significantly influencing the transport and mechanical behavior of materials [47]. In earth stabilization, reducing the void spaces between particles is a primary objective, making porosity a key performance indicator. At 28 days of curing, the results showed a general increase in porosity with increasing replacement rates. This increase was proportional across all substitution levels. At 90 days, SEB porosity with 12.5% artisanal lime is 24.5%, compared to 23.8% for industrial lime. The rise in pore volume explains the observed decrease in density, which results from reduced compactness of the matrix.

On a microstructural level, the increase in porosity is attributed to the decline in calcium silicate hydrate (C-S-H) formation and the simultaneous increase in portlandite $Ca(OH)_2$. Replacing cement with lime leads to a reduction in hydration reactions and a rise in carbonation processes. The latter is considered detrimental to earth stabilization [45]. Additionally, the exposure of portlandite to air promotes the formation of calcium carbonate $CaCO_3$, which forms weak and brittle cementitious bonds, resulting in poor pore closure [48].

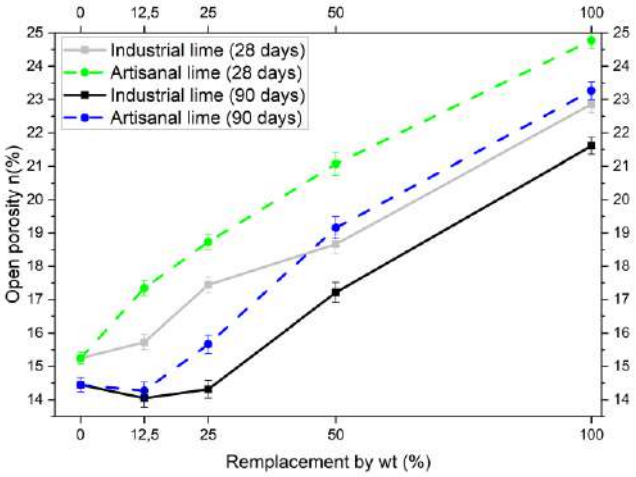

Fig. 11. Porosity of SEB on 28 and 90 days

After 90 days of curing, all formulations exhibited reduced porosity compared to their 28-day values at the same replacement rates. This reduction is due to the sustained presence of moisture, which facilitates the continuation of hydration and pozzolanic reactions. Notably, at a 12.5% replacement rate, porosity decreased relative to the control composition, suggesting a denser microstructure with reduced void content. This observation confirms the earlier hypothesis proposed in the (initial/total) absorption analysis regarding improved pore structure at this specific replacement rate. Finally, it is worth noting that the highest increase in porosity remained below 30%, which is still considered low porosity according to Dhir and Jackson [49].

3.7. Water Permeability

Permeability is one of the key parameters used to assess the durability of construction materials. Figure 12 shows the evolution of water permeability with respect to different cement replacement rates. At 28 days of curing, no data on hydraulic conductivity were available due to the incomplete execution of tests for most formulations. Nevertheless, the specimens exhibited high water permeability. This behavior can be attributed to the large pore sizes, high pore interconnectivity, and lower resistance to water flow typical of this early curing stage.

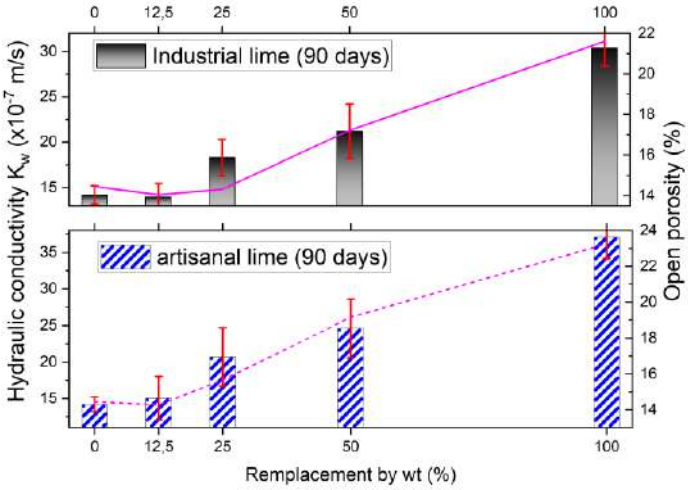

Fig. 12. Water permeability of SEB

At 90 days of curing, a general increase in hydraulic conductivity was observed with increasing replacement of cement by artisanal lime, indicating a proportional relationship. Notably, hydraulic conductivity increased by approximately 2.6 times between the 0% and 100% replacement rates. This observation aligns with the findings of Alexandre et al. [8], who reported a threefold increase in conductivity when 50% of the cement was replaced by lime. This comparison highlights the varying effects of different lime types and dosages on hydraulic conductivity, emphasizing the importance of optimizing mix proportions for desired performance. Interestingly, a 12.5% replacement rate led to a 1.62% decrease in hydraulic conductivity compared to the control composition. This reduction is consistent with a decrease in porosity and pore connectivity, as confirmed in the previous capillary absorption and open porosity experiments.

Beyond the 12.5% replacement rate, hydraulic conductivity continued to increase with higher substitution levels, indicating a progressive deterioration of the pore structure.

3.8. Compressive and Flexural Strength

Compressive strength and flexural results in term of replacement rates are shown in Figures 13 and 14, respectively. At 28 days of curing, increasing the replacement rates of cement with artisanal lime resulted in a decrease in compressive strength. The control sample (0% replacement) exhibited the highest compressive strength value of 1.94 MPa, due to the high degree of cement hydration. According to the plant's technical documentation, the cement used contained over 55% alite (C_3S), which reacts as follows:

$$C_3S + 3H \rightarrow C-S-H + 2CH \quad (7)$$

This reaction is known for its rapid rate and high early strength contribution at 28 days [49]. Moreover, the cement showed good compatibility with the gravel and sand matrix, as these coarser particles were effectively coated by the finer cement particles [50].

In the previous section, it was established that the soil used belongs to the silty sand class. Therefore, the compressive strength observed at 28 days was only moderate to low for mixes with lime, due to the limited formation of hydrates (CSH/CAH). This is attributed to the slow nature of the pozzolanic reaction at ambient temperature [45]. Additionally, Meukam et al. [51] confirmed

that compressive strength development remains very low after the 28-day mark when lime is used. Recent studies on sustainable earthen materials, such as Cappai and Pia [52], suggest that thermal treatments can enhance surface resistance and long-term durability of lime-stabilized earth blocks, potentially mitigating the slow pozzolanic reaction rates observed in ambient conditions.

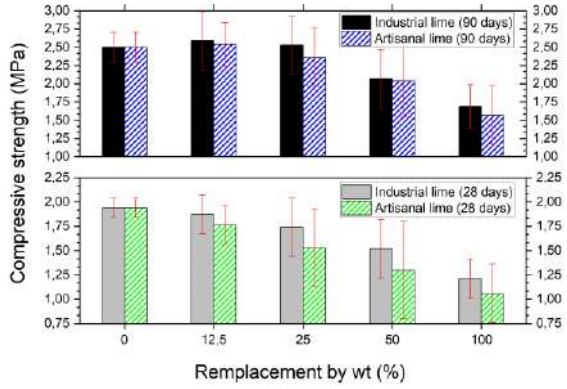

Fig. 13. The compressive strength of SEB

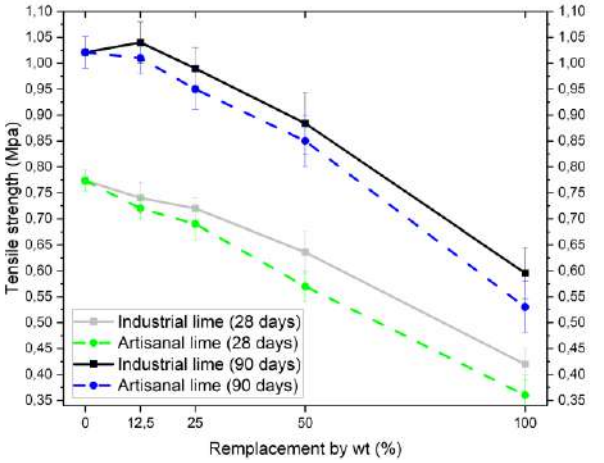

Fig. 14. Flexural strength of SEB

At 90 days, compressive strength increased notably at 12.5% and 25% replacement rates compared to the control composition. However, a decline was observed at higher substitution levels of 50% and 100%. The initial increase in strength at lower substitution levels is explained by the presence of sufficient lime (12.5–25%) interacting with the soil's 7% clay fraction. This interaction enhanced ionization, raising the pH and releasing Ca^{2+} and OH^- ions. In turn, the clay fraction released Al_2O_3 and SiO_2, which reacted with calcium and hydroxyl ions in the presence of water to form additional hydrated compounds (C-A-H and C-S-H) through pozzolanic reactions. This was in addition to the C-S-H already formed by cement hydration, leading to a denser matrix with smaller pores and fewer microcracks—ultimately improving compressive strength.

Conversely, at 50% and 100% replacement rates, compressive strength declined. This was due to a significant reduction in C_3S content, which limited cement hydration. Moreover, the clay fraction in the soil became exhausted, halting the release of alumina and silica. Consequently, pozzolanic activity ceased, and carbonation reactions became predominant, forming calcite $CaCO_3$ instead of strength-contributing hydrates. These findings are consistent with previous studies:

- Alexandre et al. [8] reported a 43% reduction in compressive strength with 50% cement replacement
- Guettala et al. [4] observed a 4.89% decrease with a 37.5% replacement rate.
- Alavéz et al. [18] noted a 29% drop when replacing all cement with lime.
- Hossain et al. [22] found a compressive strength loss of 16% at 28 days and 20% at 90 days for 50% substitution.
- Nagaraj et al. [25] indicated that although the 0% replacement rate provided better strength in the first 4 months, the 50% replacement mix showed superior performance over 6 months to 5 years.

It is worth noting that all formulations, except the one with 100% lime replacement, fall within Houben's recommended compressive strength range (1.2–2.8 MPa) for stabilized earth materials. With regard to flexural strength, the results are presented in Figure 14.

On the basis of the results obtained, the increase in the rate of replacement of cement by lime caused a decrease in the flexural strength of all compositions. The 12.5% replacement rate by industrial lime was the exception, where the flexural strength increases by 1.87% compared to the control sample on the 90th days of curing. This increase at this composition was explained by the good development of hydration/pozzolanic reactions, and thus the increase of additional bonds in the matrix [48] . Alavéz et al. [18], noted a 29% decrease in flexural during the total replacement of cement by lime. Hossain found that flexure decreased by 18% [22], 26% during replacement by 50% on the 28 and 90th days of curing, respectively.

4. Conclusion

This observe aimed to evaluate the potential of artisanal lime as an eco-friendly stabilizer for Stabilized Earth Blocks (SEB) within the sustainable rehabilitation of earthen historical past, with a focal point on the village of Mougheul in southwestern Algeria. The findings confirm that partial alternative of cement with artisanal lime complements the physico-mechanical houses of SEBs at the same time as aligning with circular economy ideas and lowering environmental impact. Specifically, a 12.5% substitute fee became recognized as most suitable, reaching a compressive strength of 1.94 MPa at twenty-eight days, with advanced lengthy-term sturdiness and reduced water absorption (1.96%) and porosity (2.83%) at ninety days. Compared to business lime, artisanal lime exhibited slightly decrease stabilization efficiency however offered substantial environmental advantages because of its low-power, waste-minimizing production process. By valorizing neighborhood substances—native soil and traditionally produced lime—this technique not best preserves cultural background however also mitigates the CO_2 emissions associated with cement production, which debts for 8 % of global emissions. The adoption of artisanal lime as a stabilizer promotes low-carbon, fee-powerful creation practices, assisting Sustainable Development Goals (SDGs) and climate movement. These consequences study international requirements for earthen introduction and demonstrate compatibility with traditional earthen architectures.

The proposed SEBs offer a practical and sustainable solution for the rehabilitation and preservation of earthen structures in heritage contexts like Mougheul. Their application can range from repairing deteriorated walls and reconstructing collapsed sections to constructing new compatible infills within existing structures. By utilizing locally sourced earth and artisanal lime, these SEBs ensure material compatibility with the original construction, minimizing aesthetic and structural discrepancies. Furthermore, the enhanced durability and mechanical properties of the SEBs contribute to the long-term stability of rehabilitated structures, reducing the need for frequent interventions. This approach supports the conservation of cultural heritage by providing a robust, environmentally friendly, and economically viable alternative to conventional repair methods, which often rely on incompatible materials like concrete.

However, overall cement substitute with artisanal lime brought about a extraordinary decline in physico-mechanical performance, underscoring the importance of partial substitution. The examine's results have been prompted by using the particular dry and high-temperature climatic conditions of southwestern Algeria, which may additionally restrict their generalizability. To construct on those findings, future studies need to look into the long-term overall performance of SEBs under diverse climatic situations and explore synergies with different bio-based totally stabilizers. Such studies may want to similarly validate the scalability of artisanal lime in sustainable creation and enhance its software in ecological engineering for earthen history maintenance.

Acknowledgement

Sincere thanks are extended to the artisans of Kenadsa for their invaluable assistance in reconstructing the traditional oven. Special gratitude is expressed to the supervised master's and doctoral students for their dedication, to the technicians of the civil engineering laboratories at the Universities of Bechar and Adrar, and to all members of the ARCHIPEL laboratory and its director, Prof. Hamouine Abdelmadjid, for their unwavering scientific support.

References

[1] Vyncke J, Kupers L, Denies N. Earth as Building Material - an overview of RILEM activities and recent Innovations in Geotechnics. MATEC Web of Conferences, 2018; 149: 02001. https://doi.org/10.1051/matecconf/201814902001

[2] IPCC. Climate Change 2023: Synthesis Report. Contribution of Working Groups I, II and III to the Sixth Assessment Report of the Intergovernmental Panel on Climate Change. IPCC, Geneva, Switzerland, 2023.

[3] Ngowi A. Improving the traditional earth construction: A case study of Botswana. Construction and Building Materials, 1997; 11(1): 1-7. https://doi.org/10.1016/S0950-0618(97)00006-8

[4] Guettala A, Abibsi A, Houari H. Durability study of stabilized earth concrete under both laboratory and climatic conditions exposure. Construction and Building Materials, 2006; 20(3): 119-127. https://doi.org/10.1016/j.conbuildmat.2005.02.001
[5] Jaquin P. History of earth building techniques. Woodhead Publishing, 2012; 307-323. https://doi.org/10.1533/9780857096166.3.307
[6] Arduin D, Caldas LR, Paiva RL, Rocha F. Life Cycle Assessment (LCA) in Earth Construction: A Systematic Literature Review Considering Five Construction Techniques. Sustainability, 2022; 14(20): 13228. https://doi.org/10.3390/su142013228
[7] Mak K, MacDougall C, Fam A. The mechanical characteristics of on-site manufactured compressed earth blocks: The effects of water repellent and other additives. International Journal of Sustainable Building Technology and Urban Development, 2015; 6(4): 201-210. https://doi.org/10.1080/2093761X.2015.1092001
[8] Alexandre BJ, Silva M, Glória GM. Unstabilized and stabilized compressed earth blocks with partial incorporation of recycled aggregates. International Journal of Architectural Heritage, 2018; 13(4): 569-584. https://doi.org/10.1080/15583058.2018.1442891
[9] UN-Habitat. World Cities Report 2022: Envisaging the Future of Cities. United Nations Human Settlements Programme, Nairobi, Kenya, 2023.
[10] Venkatarama RBV. Earthen materials and earthen structures. In Compressed Earth Block & Rammed Earth Structures. Springer Nature Singapore, 2022; 1-24.
[11] Danso H, Martinson DB, Ali M, Williams JB. Stabilized earth blocks: A review of materials and properties. Construction and Building Materials, 2023; 365: 130085.
[12] Bambole A, Gaikwad R, Dongre A, Reddy GR. Assessment of properties of rubble masonry used in heritage structure. Research on Engineering Structures and Materials, 2024; 10(2): 839-855.
[13] Abdeldjebar R, Hamouine A, Fouchal F, Labbaci B, Zebair A. Effects of treated date palm fiber on durability of SEB. International Journal of Civil Engineering and Technology, 2018; 9(5): 293-305.
[14] Idder A, Hamouine A, Labbaci B, Abdeldjabar R. The porosity of stabilized earth blocks with the addition of plant fibers of the date palm. Civil Engineering Journal, 2020; 6(3): 478-494. https://doi.org/10.28991/cej-2020-03091485
[15] Papayianni I, Pachta V. Constructional characteristics and restoration aspects of historic earth block structures. Research on Engineering Structures & Materials., 2017; 3(2): 113-121
[16] Benguettache K, Goual I, Gueddouda M. Effect of Stabilizer Type on the Physical and Mechanical Proprieties of Tuff material. Proceedings of the Institution of Civil Engineers - Construction Materials, 2020; 175: 1-46.
[17] Medaoud S, Mokrani L, Mezhoud S, Ziane S. Characterization of Stabilised Sewage Sludge for Reuse in Road Pavement. Civil and Environmental Engineering Reports, 2022; 32(1): 201-217. https://doi.org/10.2478/ceer-2022-0012
[18] Alavéz RR, Montes GP, Martínez RJ, Altamirano JD, Gochi PY. The use of sugarcane bagasse ash and lime to improve the durability and mechanical properties of compacted soil blocks. Construction and Building Materials, 2012; 34: 296-305. https://doi.org/10.1016/j.conbuildmat.2012.02.072
[19] Bailly GC, El Mendili Y, Konin A, Khoury E. Advancing Earth-Based Construction: A Comprehensive Review of Stabilization and Reinforcement Techniques for Adobe and Compressed Earth Blocks. Eng. 2024; 5(2):750-783. https://doi.org/10.3390/eng5020041
[20] Kallel A, Ksibi M, Ben Dhia H, Khélifi N. Recent advances in environmental science from the Euro-Mediterranean and surrounding regions: Proceedings of Euro-Mediterranean Conference for Environmental Integration (EMCEI-1), Tunisia 2017. Springer, Cham, Switzerland, 2018. https://doi.org/10.1007/978-3-319-70548-4_588
[21] Izemmouren O, Guettala A, Guettala S. Mechanical properties and durability of lime and natural pozzolana stabilized steam-cured compressed earth block bricks. Geotechnical and Geological Engineering, 2015; 33: 1321 - 1333. https://doi.org/10.1007/s10706-015-9904-6
[22] Hossain K, Lachemi M, Easa S. Stabilized soils for construction applications incorporating natural resources of Papua New Guinea. Resources, Conservation and Recycling, 2007; 51: 711 - 731. https://doi.org/10.1016/j.resconrec.2006.12.003
[23] Zebair A, Hamouine A, Abdeldjebar R, Bouzerouata S. Comparative study of mechanical behavior and durability of CEB stabilized by two types of lime: Industrial and artisanal. International Journal of Civil Engineering and Technology, 2018; 9: 654 - 664.
[24] Burroughs S. Strength of compacted earth: Linking soil properties to stabilizers. Building Research & Information, 2006; 34: 55 - 65. https://doi.org/10.1080/09613210500279612
[25] Nagaraj HB, Sravan MV, Arun TG, Jagadish KS. Role of lime with cement in long-term strength of Compressed Stabilized Earth Blocks. International Journal of Sustainable Built Environment, 2014; 3: 54 - 61. https://doi.org/10.1016/j.ijsbe.2014.03.001

[26] Lahmar L, Abdeldjebar R, Draoui B, Mouden B, Missoum L, Labbaci B. Environmental effect on the mechanical properties of BTS brick of Bechar region in Algeria. Energy Procedia, 2013; 36: 1035 - 1042. https://doi.org/10.1016/j.egypro.2013.07.118
[27] Abdeldjebar R, Labbaci B, Lahmar L, Missoum L, Mouden B. Amelioration of earth bricks by introduction of traditional lime for arid regions. Handbook on the Emerging Trends in Scientific Research, 2015; 3: 100 - 106.
[28] Houben H, Hubert G. Traité de construction en terre. Éditions Parenthèses, 1989.
[29] Soares K, Torres I, Flores-Colen I, Silveira D. The influence of traditional substrates on the behaviour of lime mortars. International Journal of Architectural Heritage, 2023; 19(3): 346-369. https://doi.org/10.1080/15583058.2023.2286503
[30] Herrick HM, Berna F. A review of methods to analyze archaeological lime production: Investigating raw materials selection and firing conditions. Journal of Archaeological Method and Theory, 2024; 31: 1668-1696. https://doi.org/10.1007/s10816-024-09652-x
[31] Forster AM, Válek J, Hughes JJ, Pilcher N. Lime binders for the repair of historic buildings: Considerations for CO2 abatement. Journal of Cleaner Production, 2020; 252: 119802. https://doi.org/10.1016/j.jclepro.2019.119802
[32] Manoharan A, Umarani C. Lime mortar, a boon to the environment: Characterization case study and overview. Sustainability, 2022; 14(11): 6481. https://doi.org/10.3390/su14116481
[33] Abdeldjebar R, Hamouine A, Fouchal F, Labbaci B, Zebair A. Effects of treated date palm fiber on durability of SEB. International Journal of Civil Engineering and Technology (IJCIET), 2018; 9(5), 293-305.
[34] AFNOR. Aggregates: Particle Size Distribution by Sieving. Standard NF P 18-560, French Standards Association, 1990.
[35] Doat P, Hays A, Houben H, Matuk S. Construire en terre. Alternatives et Parallèles, 1979.
[36] AFNOR. Geotechnical Investigation and Testing: Laboratory Testing of Soil. Determination of Liquid and Plastic Limits. Standard NF EN ISO 17892-12, French Standards Association, 2018.
[37] AFNOR. Soils: Investigation and Testing. Measurement of Methylene Blue Adsorption Capacity of Rocky Soil. Determination of Methylene Blue Value by Stain Test. Standard NF P 94-068, French Standards Association, 1998.
[38] IANOR. Cement: Composition, Specifications, and Conformity Criteria for Common Cements. Standard NA 442, Algerian Institute for Standardization, 2013.
[39] CEN. Cement: Composition, Specifications, and Conformity Criteria for Common Cements. Standard EN 197-1, European Committee for Standardization, 2012.
[40] AFNOR. Testing Fresh Concrete: Slump Test. Standard NF EN 12350-2, French Standards Association, 2019.
[41] AFNOR. Methods of Test for Mortar for Masonry: Determination of Air Content of Fresh Mortar. Standard NF EN 1015-7, French Standards Association, 1999.
[42] AFNOR. Earth Bricks and Earth Blocks for Walls and Partitions: Definitions, Specifications, Test Methods, and Delivery Acceptance Conditions. Standard XP P13-901, French Standards Association, 2022.
[43] ISO. Geotechnical investigation and testing: Laboratory testing of soil - Part 11: Permeability tests. Standard ISO 17892-11, International Organization for Standardization, 2019.
[44] AFNOR. Methods of Testing Cement: Determination of Strength. Standard NF EN 196-1, French Standards Association, 2016.
[45] Millogo Y, Hajaji M, Ouedraogo R. Microstructure and physical properties of lime-clayey adobe bricks. Construction and Building Materials, 2008; 22: 2386 - 2392. https://doi.org/10.1016/j.conbuildmat.2007.09.002
[46] BIS. Specification for building limes. IS 712, Bureau of Indian Standards, New Delhi, India, 1984.
[47] Miloud B. Permeability and porosity characteristics of steel fiber reinforced concrete. Asian Journal of Civil Engineering (Building and Housing), 2005; 6: 317 - 330.
[48] Dao K, Ouedraogo M, Millogo Y, Aubert J, Gomina M. Thermal, hydric and mechanical behaviours of adobes stabilized with cement. Construction and Building Materials, 2018; 158: 84 - 96. https://doi.org/10.1016/j.conbuildmat.2017.10.001
[49] Dhir RK, Jackson N. Civil engineering materials. Macmillan, Basingstoke, UK, 1996. https://doi.org/10.1007/978-1-349-13729-9
[50] Bennis A, Zniker H, Ghassane A, D'ouazzane S C, Bouslihim A, Rouemssi G A. Eco-friendly production of compressed earth blocks with Moroccan pozzolana as a cement alternative. Research on Engineering Structures & Materials, 2025; 11(3): 1-19 http://dx.doi.org/10.17515/resm2025-1001ma0702rs
[51] Meukam P, Noumowe A, Jannot Y, Duval R. Caractérisation thermophysique et mécanique de BTS en vue de l'isolation thermique de bâtiment. Materials and Structures, 2003; 36: 453 - 460. https://doi.org/10.1007/BF02481525
[52] Cappai M, Pia G. Sustainable earthen plasters: Surface resistance enhancement via thermal treatments. Journal of Building Engineering, 2025; 108: 112867. https://doi.org/10.1016/j.jobe.2025.112867

Research on Engineering Structures & Materials
www.jresm.org
MIM Research Group

Research Article

Experimental determination of glass units strength under point load from temporary installation tools for blinds and sun protection systems

Anton Nekrylov [*,a]

Budget Blinds, Alexandria, VA, U.S.A

Article Info

Article History:

Received 24 June 2025

Accepted 02 Sep 2025

Keywords:

Double-glazed widow;
Point load;
Mounting devices;
Vacuum suction cup;
Microcrack;
Glass deflection

Abstract

Due to the possibility of using vacuum mounting suction cups in modern construction practices, it is imperative to determine the safe threshold of point load on glass units that are vulnerable to local forces. The present paper elucidates the findings of an experimental investigation into the strength of a double-layer glass unit with an air gap under the action of a local load typical of vacuum-fixed assembly tools. The research methodology involved varying the angle of force application (0°, 45°, 90°) and the positioning of the suction cup (center/edge), while recording deflections at designated control points using electronic micrometers. It was determined that the suction cup detached when subjected to a load of 86 kg in the "90°, center" glass configuration, whereas other configurations remained undamaged up to loads of 50 kg. To ensure safety and preserve the integrity of the double-glazed unit, tests for loads greater than 50 kg were carried out only in the «90° configurations, centered at the», which was determined to be the most vulnerable based on previous tests. Other configurations showed no signs of damage up to 50 kg, and further testing was considered unnecessary due to the lower stress concentration. The findings can be used to formulate recommendations for the safe application of mounting equipment and to enhance the regulatory framework for the interaction of fasteners with transparent structures.

© 2025 MIM Research Group. All rights reserved.

1. Introduction

In contemporary construction, architectural solutions increasingly prioritize the optimal utilization of transparent enclosing structures. Double-glazed windows have emerged as an indispensable component of façade systems, window assemblies, interior partitions, and skylights. This preference is attributed to a harmonious blend of superior aesthetic qualities, energy efficiency, sound insulation, and adaptability to natural illumination. Consequently, there is a growing reliance on supplementary structural elements, particularly solar control systems – such as blinds, roller shutters, curtains, and internal or external screens. The installation of the said systems is frequently executed after the completion of the primary construction tasks, thereby being positioned directly above the finished glass surfaces [1].

One of the prevalent solutions in installation practice involves the utilization of temporary point fastening elements or supports. Notably, vacuum suction cups equipped with quick-release mechanisms facilitate fixation without necessitating drilling or additional mechanical coupling [2]. However, this technology creates a localized load on the glass surface, namely point pressure, concentrated within a limited area [3]. The damages that can occur in this case not only lead to cost increases and project delays, but also to occupational safety risks during installation,

*Corresponding author: mykolap270@gmail.com
[a]orcid.org/0009-0004-2605-619X
DOI: http://dx.doi.org/10.17515/resm2025-986st0624rs

demonstrating the serious consequences of the lack of clear guidelines in this regard. This phenomenon can be a critical consideration when installing laminated glass units, particularly under elevated load conditions (e.g., when handling heavy blinds or applying pressure on levers) [4].

Currently, regulatory documents, specifically the Ukrainian DSTU B V.2.6-156:2010, the European EN 12150, and the American ASTM C1048, delineate the general strength parameters of glass [5,6]. They stipulate requirements for tempering, impact testing, thermal exposure, and more. However, there are no specific guidelines concerning the permissible point load during short-term interactions with installation tools. In construction practice, this leaves considerable room for risk, i.e. glass breakage due to force even within the range of several tens of kilograms. Moreover, double-glazed windows constitute a complex multilayered system wherein the outer and inner panes of glass, a spacer frame, and a sealant interact. Even a small local force can cause subtle yet significant consequences, in particular microcracks, chamber deformation, seal failure, or a reduction in structural integrity under further loads [7]. In this regard, the inquiry into the permissible level of point load on a double-glazed window becomes particularly relevant not only for installers but also for designers and manufacturers [8]. Thus, there emerges a compelling need for systematic research: the experimental determination of the maximum permissible loads that can be applied to glass without incurring the risk of breakage or damage [9]. The findings of such an investigation will enable the formulation of well-founded recommendations regarding the selection of installation equipment and its operational modalities. Beyond the immediate advantages to installation practice, such data can serve as a foundational basis for enhancing the regulatory framework and increasing the safety of transparent structures within the construction domain.

The hypothesis of the present study posits that there exists a critical point load value, beyond which microdamage or destruction occurs in the glass unit, and that this value significantly depends on both the angle of force application and the position of the suction cup. The scientific novelty of the study lies in the fact that for the first time a systematic experimental study of the influence of the configuration of a point installation load on the behavior of a glass unit (rather than a separate sheet of glass) was conducted, employing variable angles and positions of the fixing element to accurately simulate authentic installation conditions.

The purpose of the present study is to experimentally test the structural integrity of a double-glazed window when exposed to a point load. This load arises from the various installation tools that can be used when installing sun protection systems or during construction activities. To achieve this aim, the following tasks were delineated:

- Develop an experimental methodology for assessing the tensile strength of a standard double- glazed window under localized point loading, which reproduces the conditions of installation with vacuum suction cups.
- Design and evaluate an experimental mounting device designed for the temporary attachment of elements to a double-glazed window utilizing vacuum suction cups in conjunction with a lever mechanism. Additionally, assess its implications on load parameters and the safety of interaction with the glass surface.
- Conduct a series of experimental tests, the outcomes of which will document the load values that correlate with the onset of microdamage, the emergence of unstable adhesion, and the complete destruction of the glass unit.
- Analyze the test results in light of the design features of the glass unit, the type of applied load and the nature of deformations, ultimately formulating practical recommendations for the safe use of mounting devices.

1.1 Literature Review

In the contemporary scientific literature, a plethora of studies has emerged that delve into interconnected topics, particularly the mechanical behavior of tempered, laminated, and multilayer glass under localized loads. Significant attention is devoted to the influence of holes or mounting near edges, alongside parametric influences such as temperature, duration of loading, and the thickness of interlayer films. In the study, the authors investigate the impact of perforations

situated in proximity to the edges of tempered glass on its structural integrity [10]. They conduct empirical tests aimed at elucidating how such perforations may compromise the strength of the glass, a critical consideration when addressing point loads induced by installation tools. The article presents both experimental and numerical investigations into the impact resistance of tempered glass [11]. The authors scrutinize the glass's behavior under diverse loading conditions, which can be useful for evaluating the risks associated with glass damage during the installation of solar protection systems. The article considers the reusability of architectural glass and its structural integrity post-utilization, a critical factor in evaluating the longevity of double-glazed windows [12].

The research presented in focused on the gradual failure of laminated glass under low-velocity impacts [13]. The authors demonstrate how different layers of glass respond to loading, which is useful for understanding the behavior of glass units under point loads. Study examines integrated joints for glass-plastic composite panels under varying temperature conditions, contributing to the understanding of how such compounds influence the strength of glass units [14]. The paper analyzes the load-bearing capacity of lightweight glass-plastic composite panels, which may be relevant when considering alternative materials for sun protection systems [15]. The study includes experimental and numerical analyses of lightweight composite panels consisting of thin glass and PMMA, which may be useful in the development of new glass unit designs [16]. The authors conducted a parametric analysis to determine how temperature, loading duration, and interlayer film thickness influence the behavior of laminated glass under transverse stress [17]. If mounting systems (e.g. blinds) are in contact with the glass unit for a long time or create local pressure, these factors can be critical for long-term strength.

In the study, an innovative multi-camera three-dimensional digital image correlation (3D-DIC) system was developed and applied to measure the strain concentration of suction cups during their removal [18]. This advancement facilitates a deeper understanding of the interaction between suction cups and glass surfaces, as well as the loads they impose. The authors in introduced pioneering vacuum suction cups with the ability to self-close and self-recover, thereby ensuring effective adhesion to diverse surfaces [19]. Such innovations prove advantageous in the development of installation tools for blinds and sun protection systems. In [20], a comprehensive methodology for laboratory testing of a vacuum suction cup utilized in marine automatic mooring systems was developed. Although this testing framework is tailored for marine applications, it is readily adaptable for assessing point-mounting on glass within residential or construction contexts, thereby enhancing the safety of blind installation tools. The article explores soft robotic grippers that leverage vacuum technology to grasp uneven and textured surfaces [21]. This investigation may yield valuable insights into the adaptability of suction cups to various glass surface types.

A thorough analysis of scholarly sources reveals a marked interest among researchers in exploring the characteristics of glass under diverse loading conditions, particularly in scenarios involving impact, bending, and thermal fluctuations, as well as within the framework of multilayer and laminated structures. Many studies have concentrated on issues of durability, reusability, and the effects of interlayer thickness and hole geometry on the mechanical behavior of glass structures.

However, existing studies predominantly overlook the behavior of glass units under short-term point loads. Such loads may occur in real operating conditions, in particular when employing mounting suction cups or other mounts. The specifics of multi-chamber double-glazed windows, characterized by their complex structural and mechanical attributes, remain unaddressed. In this context, it is relevant to undertake an experimental study aimed at evaluating the ultimate load that can be applied to the surface of a double-glazed window without incurring the risk of damaging it.

2. Methods and Models

Glass is an amorphous inorganic material characterized by exceptional hardness, chemical inertness, yet it exhibits a brittle mechanical nature. Its microstructure lacks long-range order (unlike crystalline solids), implying that glass lacks defined slip planes or zones of plastic deformation. Therefore, when the permissible threshold of mechanical stress is exceeded, glass

breaks suddenly, without any warning signs (e.g., without plastic deformation), thereby categorizing it as a brittle material [22].

2.1 Glass Strength and Breaking Point.

Tensile strength is the maximum stress that a material can withstand under uniaxial tension before breaking [23]:

$$\sigma_t = \frac{F_{max}}{A} \tag{1}$$

where σ_t is the tensile strength, F_{max} is the maximum force until rupture, and A is the sample's cross-sectional area.

For ordinary glass, σ_t is in the range of 30-90 MPa, depending on surface defects [24]. The theoretical tensile strength (under ideal conditions) can be calculated as follows:

$$\sigma_t = \frac{E}{\varepsilon} \tag{2}$$

where E is Young's modulus.

Equation (1) determines the actual tensile strength based on the experimental breaking force, reflecting the effect of defects and surface quality. Instead, equation (2) gives the theoretical tensile limit obtained from the modulus of elasticity of the material, provided that there are no defects in the structure. Due to microcracks and defects, true glass typically exhibits tensile strength values that are significantly lower than the theoretical maximum. Flexural strength is the value of the maximum stress that occurs on the surface of the sample during bending. For a 3-point bend, it is calculated as follows:

$$\sigma_f = \frac{3FL}{2bd^2} \tag{3}$$

where F is the maximum applied force, L is the length of the span between the supports, b is the specimen's width, d is the specimen's thickness. Given that a stress gradient manifests across the thickness of the specimen during bending, the flexural strength facilitates a better modeling of local critical stresses compared to simple axial tension. However, it is worth acknowledging that the values derived from the formula are contingent upon the sample's thickness: as thickness increases, the computed stress value diminishes, even though the actual fracture resistance enhances due to greater structural rigidity.

The failure point is the state of a material at which a material, subjected to external load, undergoes a sudden and irreversible transition from elastic or elastic-plastic deformation to complete failure. In the case of glass, as a typical brittle material, this process occurs without noticeable plastic deformation. Within a stressed-deformed state, the body accumulates energy. The failure point occurs when the local stress exceeds the material's capacity to resist rupture, particularly in the presence of defects such as microcracks. For brittle bodies, the failure point almost coincides with the ultimate strength, since there is no noticeable yield or plasticity stage.

Alan Griffith formulated a fracture theory that takes into account the presence of microcracks within brittle materials [25]. The fundamental premise is to balance the potential energy associated with elastic deformation against the surface energy of creating a new crack. Griffith's critical stress formula is as follows:

$$\sigma_c = \sqrt{\frac{2E\gamma}{\pi a}} \tag{4}$$

σc is the critical stress, E is the Young's modulus of the material, γ is the surface fracture energy, a is the half-length of the initial surface crack.

Microcracks and defects serve as stress concentrators. Upon reaching a critical stress threshold near the crack tip, energy is released in the form of a new crack, resulting in unstable crack growth leading to sudden failure of the material. In the case of glass, the value of a even within micrometers (10^{-6} m) can diminish its strength by tens of times from the theoretically possible limit of ~7 GPa to ~50–100 MPa).

2.2 Frictional Forces of Interaction Between Suction Cup and Glass

The frictional interaction of a rubber suction cup with glass epitomizes a complex amalgamation of adhesion, friction, and hydrostatic vacuum effects, which confer the suction cups to a glass element. The primary mechanisms governing this interaction encompass dry friction at the rubber-glass interface, adhesive pressure arising from Van der Waals molecular forces, a pressure differential (vacuum) within the suction cup, and the deformability of the elastomer that facilitates the formation of a tight fit contour. The frictional force that opposes the displacement of the suction cup across the glass surface is determined by the classical Coulomb friction formula:

$$F_f = \mu N \tag{5}$$

where Ff is the frictional force, μ is the coefficient of friction between rubber and glass (depends on conditions: surface humidity, rubber material, etc.), N is the normal pressing force - the total force caused by vacuum pressure and elastic deformation of the rubber ring. In addition to friction, the main source of force N is the pressure difference between the external atmospheric $P0$ and the internal P_{in} pressure in the suction chamber:

$$N = (P_0 - P\ \ )A \tag{6}$$

where A is the effective contact area of the suction cup. Then the frictional force is:

$$F_f = \mu(P_0 - P\ \ )A \tag{7}$$

In real-world scenarios, a suction cup not only creates a vacuum but also leverages adhesive forces resulting from Van der Waals interactions and the capillary effect. This phenomenon significantly enhances the overall grip strength. The better the elasticity of the rubber material (low Young's modulus), the better it adapts to the micro-irregularities of the glass, reducing the likelihood of air penetration. Factors that reduce frictional force include contamination of the glass or suction cup (such as oil or dust), damage of the rubber edge, elevated humidity levels, deformation from repeated use, and depressurization.

2.3 Forces Acting on Glass

In general, glass structural elements are influenced by both external and internal mechanical forces and loads, which may be static, dynamic, localized, or distributed. The characteristics of deformation, stress distribution, and the overall behavior of glass depend upon its configuration: single-glazed (comprising a single pane of glass) or double-glazed (consisting of two or three panes of glass separated by a gas or air layer) [26]. List of forces acting on glass:

- Self-weight (gravitational force: $Fg = mg$. Always acts vertically downwards.
- Wind load is the difference in air pressure. It mainly has a horizontal load.
- Atmospheric pressure is the difference between external and internal pressure. Can create internal deformation.
- Temperature load – uneven heating, thermal expansion. Creates internal tensions.
- Physical point load – pressure, fastening, etc. Creates local stresses.
- Shock loads are sudden contacts.

Figure 1 shows a diagram of the influence of external forces on the glass structure. Figure 2 shows the difference between double-glazed windows and single-glazed windows.

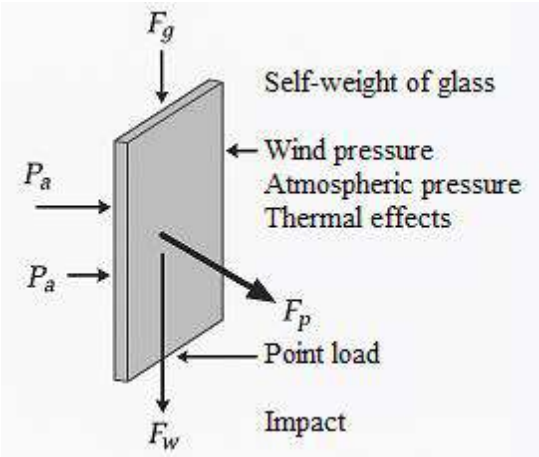

Fig. 1. Schematic representation of external forces acting on the glass panel

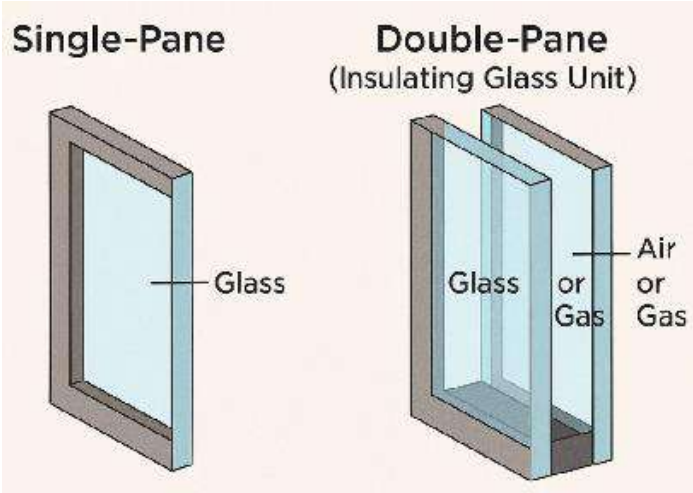

Fig. 2. Scheme of mono-glass and double-glazed structures

Monoglass refers to a single sheet of glass. The behavioral characteristics of such glass are predominantly linear, with the application of forces occurs without an internal compensation mechanism. In other words, when a force is applied, the outer surface undergoes deformation independently. For a flat monoglazed window measuring $a \times b$, subjected to a uniformly distributed pressure q (for instance, wind load), the resultant bending deformation is determined by the plate bending equation as follows:

$$D\nabla^4 w(x,y) = q(x,y), \tag{8}$$

$$where \quad D = \frac{Eh^3}{12(1-\nu^2)},$$

where D is the bending stiffness, h is the glass thickness, E is Young's modulus, υ is Poisson's ratio, $w(x,y)$ is the deflection. External forces cause local or global deformation that is not counterbalanced for on the other side (unlike double-glazed windows).

$$D_i = \frac{E_i h_i^3}{12(1-\upsilon_i^2)} i = 1,2 \tag{9}$$

A double-glazed window is two or three layers of glass glued together around the perimeter with an air or gas layer between them. Its behavior under load is characterized by nonlinearity and interdependence. Let's consider the double-glazed window consisting of an outer glass with a thickness of $h1$ and an inner glass with a thickness of $h2$, a hermetic layer d. The surface area of the

glass is represented as $A=a\cdot b$, the Young's moduli are $E1$ and $E2$, and the Poisson's ratios are $\upsilon 1$ and $\upsilon 2$. Consequently, the bending stiffness of each glass is expressed as:

Let the maximum deflection of the first and second glass be $w1$, $w2$, respectively. If the glass bends elastically towards the air chamber, the volume changes:

Then the reaction of the air layer according to the Boyle-Mariotte law for a sealed gas is:

$$V \approx A(w_1 + w_2) \tag{10}$$

Then the reaction of the air layer according to the Boyle-Mariotte law for a sealed gas is:

$$(p_0 + \Delta p)(V_0 - \Delta V) = p_0 V_0 \tag{11}$$

$$\Delta p \approx \frac{p_0}{V_0}\Delta V = \frac{p_0}{Ad}(w_1 + w_2)$$

where p_0 is the initial pressure in the layer, Δp is the excess pressure in the layer. So, the load on the outer glass is:

$$q_1 = p_{ext} - \Delta p \tag{12}$$

on the inside:

$$q_2 = \Delta p \tag{13}$$

The bending equation for each glass is:

$$D_1 \nabla^4 w_1 = q_1 = p_{ext} - \Delta p; \tag{14}$$
$$D_2 \nabla^4 w_2 = q_2 = \Delta p.$$

After introducing the relationship between w_1, w_2 and Δp:

$$w_1 = \alpha \frac{(p_{exr} - \Delta p)a^4}{D_1} \tag{15}$$

$$w_2 = \alpha \frac{\Delta p \cdot a^4}{D_1}$$

$$w_1 = \alpha \frac{(p_{exp} - \Delta p)a^4}{D_1},$$

$$w_2 = \alpha \frac{\Delta p \cdot a^4}{D_2}.$$

The combined equation for calculating Δp and deformations is presented as follows:

$$\Delta p = \alpha \frac{p_o}{AD}(w_1 + w_2) \tag{16}$$

2.4 The Influence of Micro-Scratches, Defects and Surface Contamination on The Strength of Glass

Glass, as a fragile material, is extremely sensitive to surface imperfections. Micro-scratches, chips, inclusions, and residual contaminants on the surface can reduce the actual strength by dozens of times when compared to the theoretical strength. This phenomenon arises from the concentration of stresses around these defects, which catalyze fracture through the mechanism of crack growth. Consequently, the actual strength of glass is typically significantly inferior than the theoretical strength (2). To idealize the defect, an empirical crack is considered (according to Griffith's theory):

$$\sigma_{max} = \sigma_\infty \left(1 + 2\sqrt{\frac{a}{\rho}}\right), \tag{17}$$

where σ_∞ is the applied stress, a is the half-length of the crack, and ρ is the radius of curvature at the end of the crack. As ρ approaches zero, the stress concentration escalates dramatically, resulting in brittle failure. In accordance with the Griffith model (4), a crack will grow when the energy released during its growth exceeds the energy required for the creation of a new surface.

Micro-scratches caused by transportation, assembly, or manufacturing serve as precursors to crack formation. Contaminants such as sand, dust, grease, and chemical residues can alter local chemical interactions, thereby facilitating the growth of corrosive cracks. In a humid environment, cracks develop gradually under static loads, a phenomenon known as stress corrosion cracking. The cleanliness of the glass surface directly influences its resilience. Techniques such as optical polishing or chemical hardening enhance surface integrity. Employing protective films, anti-friction suction cups, or gaskets during installation mitigates the risk of micro-damage.

Therefore, given that microdefects may serve as a potential cause for local glass failure, it is worth to briefly evaluate the potential impact of the structural elements supporting the glass. Frame structures, anchoring fasteners, and mounting systems employed in the installation of double-glazed windows typically possess a safety margin that far exceeds the load limit of up to 50 kg. For instance, conventional steel anchors are capable of withstanding loads exceeding 1 ton, while aluminum or steel frames are engineered to endure wind forces, thermal fluctuations, and dynamic loads associated with installation. Consequently, within the purview of this study, the influence of frames and fasteners on glass failure is non-critical, with the primary emphasis placed on the interaction between the glass and the suction cup. Operation of the loading system levers;

$$M=F \cdot d, \tag{18}$$

where M is the moment of force, F is the applied force, d is the arm of force (distance from the fulcrum to the point of application of the force).

Levers in the context of lifting devices or fixing systems with glass or double-glazed windows perform the function of redistributing forces, reducing the applied moment of force, or precisely controlling the load. The lever's principle of operation is based on the law of moments:

In mechanisms with suction cups or glass grippers, levers can:

- compensate for variable weight distribution when maneuvering;
- reduce the load on the handle or control element;
- ensure symmetrical distribution of force across all points of contact with the glass;
- serve as a damper, reducing the risk of exceeding the maximum contact force (and consequently damage to the glass).

In systems with multi-link levers, kinematic amplification can be achieved, wherein a minor movement or force applied to the handle produces a substantial effect at the other end of the structure. The coefficient of this amplification is defined as the ratio of the length of the output arm acting on the glass to the length of the input arm controlled by the user.

2.5 Experimental Methodology

2.5.1 General Methodology

The experiment was conducted by attaching a vacuum suction cup equipped with a lever and lifting mechanism to the surface of the glass unit. Once the suction cup was firmly secured, the load was gradually increased until either the suction cup was detached from the glass or the glass unit was destroyed. The load was applied approximately perpendicular to the surface of the glass with controlled changes in direction (0°, 45°, 90°) relative to the plane of the glass to simulate various real mounting scenarios.

2.5.2 Tool Description

Assembly tool (Fig. 3) consisted of four main parts. The first was a vacuum suction cup with two 11.43 cm diameter rubber cups connected by an aluminum handle. The vacuum in the suction cups was created manually using a mechanical lever. The suction cup was always positioned vertically on the glass. A steel pipe with a diameter of 28 mm was attached to the suction cup handle using a

hinge, which served as a horizontal partition. The other end of this partition was connected to the lifting mechanism. The lifting mechanism consisted of two telescopic tubes, a steel rod, a control handle, and an upper platform. It was oriented vertically upwards, parallel to the glass surface and the suction cup handle.

The load on the glass was carried out by extending the central rod using a lever-handle mechanism similar to a sealant gun. The upper platform of the lifting mechanism rested on the piston of an electronic dynamometer, which made it possible to control the applied force. The amount of pressure on the glass was determined as the sum of the dynamometer readings and the mass of the instrument itself, which was 2020 grams. To measure loads exceeding 50 kg (the limit value of the dynamometer), calibrated weights were used, which were placed on the upper part of the partition at the maximum distance from the glass defects. The hinged connection of the suction cup and the partition provided the possibility of conducting experiments with different positions of the partition relative to the glass.

Fig. 3. Mounting device for point loading of double-glazed windows

2.5.3 Experiment Progress

The experiment consisted of six series of tests that systematically varied two parameters (Table 1): the inclination angle of the horizontal partition (0°, 45°, 90°) and the location of the suction cup (center or edge of the glass unit). Three angles of inclination of the horizontal partition (0°, 45°, 90°) were used to reproduce different directions of load in real conditions during installation. The 0° configuration simulated the near-axial tensile force acting to disconnect the suction cup. The 45° configuration introduced a combined shear and tension load, reproducing the oblique force application. The 90° configuration generated a perpendicular bending load representing the most critical state with the maximum stress concentration on the glass surface. This approach enabled us to simulate various scenarios for employing assembly tools under authentic conditions.

Table 1. Experimental parameters

No.	Partition angle	Suction cup position	Impact mechanics	Expected glass reaction
1	0°	Glass edge	Direct tension	Uniform load through coupling
2	0°	Glass center	Direct tension	Balanced deformation with minimal shear
3	45°	Glass edge	Combined shear/compression	Asymmetric loading, bending stresses
4	45°	Glass center	Combined shear/compression	Centric deformation with loading of both suction cups
5	90°	Glass edge	Mostly bend	Highest point load, probability of failure
6	90°	Glass center	Mostly bend	Internal voltage at the center, maximum sensitivity

In configurations where the angle was set to 0°, the force was predominantly directed towards detachment, enabling us to investigate the adhesion characteristics of the rubber suction cup to the glass surface. The 45° angle created a combined load, incorporating both shear and bending components. Conversely, the 90° position corresponded to the maximum pressure model, which generates significant deformation stresses within the surface layers of the glass.

At the same time, varying the positioning of the suction cup, designated as "Glass Edge" and "Glass Center", permitted an assessment of edge effects, because in real conditions, installation often takes place near frames and lintels. For all configurations, we documented the coordinates of the suction cups and sensors, alongside the alterations in glass deflection during the loading process. This comprehensive data collection facilitated the tracking of deformations at various stages, from the initial application of force to the ultimate moment of destruction or detachment.

2.5.4 Additional Measurements

Throughout the experiment, regular checks were conducted to ascertain the functionality of the window and its fittings. The load data and micrometer readings were documented for each of the six-test series. By varying the angle of force application (0°, 45°, 90°) and the positioning of the suction cup (either at the center or the edge of the glass), a thorough examination of the influence of these parameters on the integrity of the glass unit was achieved. The measurement of deformations provided insights into the glass's response to point loading and facilitated the identification of the moment at which fracture initiation occurred.

In each test, the load was applied gradually using a manual lever mechanism that extended a central steel rod pressing perpendicularly to the surface of the glass by means of a suction cup. The applied force was transmitted through a mechanical partition that acted as a lever connected to a vacuum suction cup, providing a stable directional application (0°, 45°, or 90° to the surface).

The amount of load was continuously recorded using a digital silometer (dynamometer) (NITERUS DF-500 model) located between the top of the load mechanism and the test bench. The meter displayed both real-time and peak values in kilograms, newtons, and pounds with an accuracy of ±0.5 g. Simultaneously, the deflection of the glass at the two control points (A and B) was measured using electron micrometers with an accuracy of 0.01 mm. These micrometers were mounted on a rigid frame and aligned orthogonally to the glass surface to fix vertical displacement. Additionally, during and after each load cycle, a visual inspection was performed to detect any signs of damage (microcracks, delamination, seal deformation) or suction cup detachment. In configuration 6 (90°, centered), the time to peel off under maximum load (20 seconds) was also recorded.

All measurements were documented at each load increase (step 10 kg), which allowed a comprehensive correlation between applied force, deformation, and structural response of the glazing unit.

2.6 Window Construction

The investigation was conducted on a wooden sash window manufactured by Andersen, produced in 2003. The size of the window frame was 64.77 × 134.62 cm. The window was securely fastened to the concrete floor using metal brackets to the cinder block wall. The window design included two vertically sliding parts. The Andersen window was chosen because it is a commonly used type of sash window in residential construction. Its wooden frame and typical sash geometry with two vertically sliding parts reproduce common boundary conditions for double-glazed windows, including typical support stiffness and edge restraints. This geometry was expected to reflect real-world mounting scenarios, while providing a potentially less rigid boundary than metal frames, thus offering conservative results in terms of deformation under point loads.

2.6.1 Double-Glazed Window

A double-glazed window measuring 54.61 × 58.42 cm was installed in the window. The thickness of each of the two layers of no tempered glass was 2.3 mm, and the total thickness of the double-glazed window was 12 mm. The double-glazed window was glued into the window sash.

2.6.2 Environmental Conditions

The ambient air temperature during the experiment was 20°C. The humidity was normal and was around 50%.

2.6.3 Measuring Equipment

The following measuring equipment was utilized:

- Electronic dynamometer (NITERUS DF-500) with a measurement limit of up to 50 kg (500 N), the accuracy of 0.5 g, digital display and real-time, peak and first peak value modes. Measurements were made in N, kg;
- two electronic micrometers with a range of 0–30 mm and an accuracy of 0.01 mm, equipped with displays and stainless-steel probes.

The use of an electronic dynamometer ensured accurate determination of the applied force. For loads exceeding the 50 kg (500 N) limit of the electronic dynamometer (NITERUS DF-500), additional calibrated loads were applied, and their values were summed with the dynamometer reading and tool weight to obtain the total applied force. This approach made it possible to accurately estimate forces up to 86 kg while maintaining the reference value of the dynamometer for all test series. Micrometers enabled us to meticulously record even the most minute deflections, thereby facilitating a comprehensive analysis of the deformation processes occurring at various points within the glass unit.

3. Results and Discussion

Six series of experiments were conducted to evaluate the impact of the installation tool configuration on the behavior of the glass unit. They involved different angles of force application (0°, 45°, 90°) and variation in the position of the suction cup (center/edge of the glass). In each case, the applied load, deflections at control points A and B, and visual signs of damage or their absence were recorded. Each experimental series was repeated n times (minimum n=3 recommended) and the results in tables 2–7 represent the mean values of the recorded deflections. This ensures the reproducibility and reliability of the obtained results.

Table 2. Results of experiment 1 (0°, Edge)

No.	Load	Visible damage	Deflection A	Deflection B
	kg		mm	mm
1	10	-	0.04	0.07
2	20	-	0.06	0.14
3	30	-	0.06	0.2
4	40	-	0.08	0.2
5	50	-	0.08	0.23

Table 2 presents the results for the configuration with the partition position at 0° and the suction cup location near the glass edge. The upper suction cup position in millimeters (m) is X = 470, Y = 317.5. The position of the lower suction cup is X = 470, Y = 108. The position of the upper micrometer is X = 381, Y = 320.7. The position of the lower micrometer is X = 387.35, Y = 50.8. There is a clear relationship between the magnitude of the applied load and the deformation of the glass unit. There is a gradual increase in deflection at points A and B with increasing load. The appearance of microcracks was not detected. Different values of Deflection at points A, B under the same load indicate uneven deformation of the glass, which may be due to the point nature of the applied load, the conditions of fixing the glass unit in the frame, and its own elastic properties.

Table 3 presents the results for the configuration with the partition position at 0° and the suction cup location in the glass center. The position of the upper suction cup is X = 470, Y = 406.4. The position of the lower suction cup is X = 470, Y = 108. Upper micrometer position is X = 267, Y = 413. The lower micrometer position is X = 298.5, Y = 184.15. The deflections at point A grow much faster than at point B, which indicates increased flexibility in the central part of the glass unit. No visible

damage was detected. An uneven distribution of deformation was observed, characteristic of local vertical tension in the central zone.

Table 3. Results of experiment 2 (0°, Center)

No.	Load	Visible damage	Deflection A	Deflection B
	kg		mm	mm
1	10	-	0.24	0.03
2	20	-	0.47	0.15
3	30	-	0.66	0.2
4	40	-	0.8	0.2
5	50	-	0.87	0.24

Table 4 presents the results for the configuration with a 45° partition position and the suction cup location near the glass edge. The position of the upper suction cup is X = 470, Y = 317.5. The position of the lower suction cup is X = 470, Y = 108. The upper micrometer position is X = 381, Y = 321. The position of the lower micrometer is X = 387.35, Y = 50.8. The increase in load is accompanied by significant deflection at point B, while point A exhibits markedly less deformation. This observation indicates a pronounced asymmetry in the load under the combined action of shear and compression. No structural damage was detected.

Table 4. Results of experiment 3 (45°, Edge)

No.	Load	Visible damage	Deflection A	Deflection B
	kg		mm	mm
1	10	-	0.04	0.17
2	20	-	0.02	0.26
3	30	-	0.06	0.7
4	40	-	0.08	1.09
5	50	-	0.1	1.24

Table 5 presents the results for the configuration with a 45° partition position and the suction cup location in the glass center. The position of the upper suction cup is X = 470, Y = 406.4. Position of the lower suction cup is X = 470, Y = 108. The upper micrometer position is X = 267, Y = 412.75. The lower micrometer position is X = 298.5, Y = 184.15. Both points show a gradual and predictable increase in deflection. The values of Deflections A and B are larger compared to the edge configuration, which is consistent with the larger bending in the central part. No damage was recorded. The deflections at both points increase consistently, with larger values than in Table 2. The center of the glass unit exhibits increased flexibility under combined loads, but no damage is recorded even at 50 kg, which this indicates good adaptation of the structure to non-standard loads.

Table 5. Results of experiment 4 (45°, Center)

No.	Load	Visible damage	Deflection A	Deflection B
	kg		mm	mm
1	10	-	0.1	0.3
2	20	-	0.12	0.38
3	30	-	0.2	0.74
4	40	-	0.33	1.04
5	50	-	0.36	1.3

Table 6 presents the results for the configuration with a 90° partition position and the suction cup location near the glass edge. The position of the upper suction cup is X = 470, Y = 317.5. The position of the lower suction cup is X = 470, Y = 108. The position of the upper micrometer is X = 381, Y = 320.7. The position of the lower micrometer is X = 387.35, Y = 50.8. The deflection at point B increases much faster than at point A, especially after 30 kg. This indicates a pronounced local bending load in the lower suction cup area. Despite the high deformations, no damage was

observed. None of Experiments No.1-No.5 was able to achieve separation or breakage of the glass unit under a load of 50 kg. For measurements beyond the 50 kg load, weights were used only for the "center of the glass, partition 90" position (Table 6), as the most vulnerable position.

Table 6. Results of experiment 5 (90°, Edge)

No.	Load	Visible damage	Deflection A	Deflection B
	kg		mm	mm
1	10	-	0.04	0.3
2	20	-	0.06	0.5
3	30	-	0.1	0.7
4	40	-	0.18	1.78
5	50	-	0.2	2.18

Table 7 presents the results for the configuration with a 90° partition position and the suction cup location in the glass center. The position of the upper suction cup is X = 470, Y = 406.4. The position of the lower suction cup X = 470 Y = 108. The upper micrometer position X = 267 Y = 412.75. The lower micrometer position X = 298.45, Y = 184.15.

Table 7. Results of Experiment 6 (90°, Center)

No.	Load	Visible damage	Deflection A	Deflection B
	kg		mm	mm
1	10		0.55	0.72
2	20		0.72	0.96
3	30		1.09	1.64
4	40		1.39	1.98
5	50		1.66	2.2
6	70		3	2.41
7	86	There was no damage to the glass. The suction cup disconnected after 20 seconds of loading	3.14	2.6

The deflections at points A and B are much higher than in all previous series. At a load of 86 kg, no damage to the glass was recorded; instead, the suction cup involuntarily broke off after 20 seconds. This exemplifies the ultimate capabilities of rubber vacuum cups. Fig. 4 presents graphs illustrating the values of Deflection A and Deflection B. The load-deflection curves of Fig. 4 illustrate the mechanical response of the glazing unit under different point load configurations.

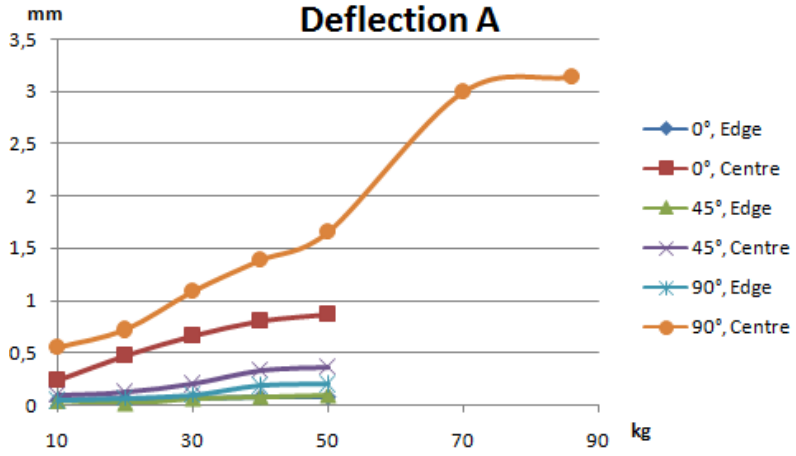

(a)

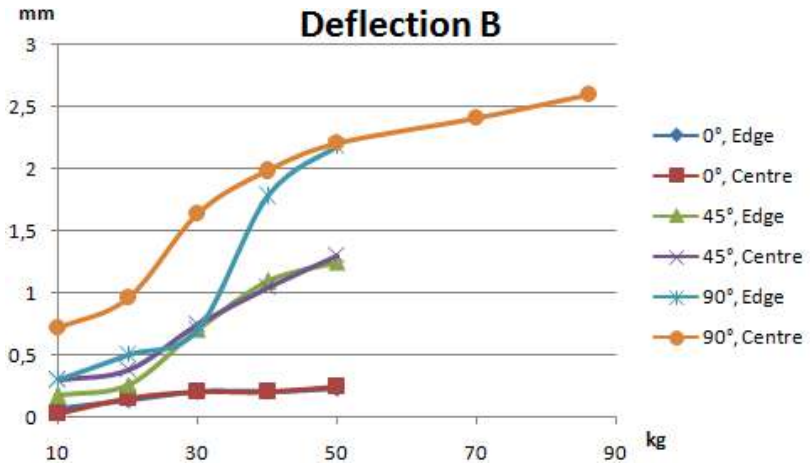

(b)

Fig. 4. Graphs of the values dependence of deflections (a) A and (b) B on the load

They show that deformation increases with load, and the amount of deflection is highly dependent on the load angle and the suction cup location. The central configuration of 90° generates the largest deflection, indicating the most critical state for potential glass damage, while the edge load of 0° creates the smallest deflection. The difference between points A and B confirms that the deflection distribution is heterogeneous due to the localized load.

The Deflection A graph shows the change in glass deformation at point A for six experimental configurations. The smallest deflections are recorded at the 0° position, Edge, which indicates the stability of the glass edge under axial tension. The configuration "90°, Centre", exhibits a rapid increase in deflection exceeding 3 mm, indicating significant stress accumulation in the central zone during vertical bending. The remaining configurations demonstrated a moderate increase in deflection within the range of up to 1 mm, devoid of any pronounced anomalies.

The Deflection B graph confirms the same tendency: the configuration "90°, Centre" is the least stable – the deflection exceeds 2 mm even at a load of 50 kg. At the configuration "90°, Edge" deflection B also increases sharply, indicating a localized bending effect near the edge. In contrast, the configurations "0°, Centre" and "0°, Edge" exhibit the least sensitivity to load, making them potentially safer for temporary installation.

The results obtained demonstrate the increased resistance of a double-glazing unit with two layers of glass 2.3 mm thick to local point loading from mounting suction cups. The double-glazing unit withstood a load of up to 86 kg in the central configuration without visible damage, which significantly exceeds the working loads from conventional sun protection systems (up to 20 kg). Below is a comparison with the results of other studies.

Efferz et al. investigated local stresses in tempered glass with holes near the edge and showed that the presence of such holes significantly reduces strength, leading to destruction under loads close to 30–50 kg [10]. Our results for integral double glass without holes show a higher endurance load limit, confirming the negative effect of perforations on the local strength of the glass. Zemanová et al. studied the behavior of laminated glass under low-speed shock loads, where gradual delamination of layers was observed [13]. In our experiment, static point loads, which are more characteristic of the installation of sun protection systems, were investigated. Compared to impact loads, static loading only resulted in elastic deformations without fracture, even at 86 kg. Kozłowski et al. conducted numerical and experimental modeling of the behavior of tempered glass under various types of force effects, obtaining significant deflections and the risk of destruction already under loads of about 70 kg in cases with local defects [11]. Our data for air-bundled double glazing show a more complex deformation character and a higher safety load limit, suggesting the ability of the multilayer system to distribute local stresses.

A series of works by Hänig et al. showed that the use of fiberglass composite panels increases the load-bearing capacity of structures, especially at elevated temperatures [14-16]. Our results for conventional double glazing under standard conditions (20 °C) show a slightly lower rigidity

compared to composites, but confirm a similar multilayer effect in reducing local stresses. Cupać et al. studied the reduction of the strength of reused glass with defects [12]. In our case, the double-glazed window of a 20-year-old window was used, probably with microdamage, making the results conservative. Despite this, the destruction did not occur even with the maximum load, which indicates a significant margin of safety in such structures. Galić et al. showed that the thickness and material of the intermediate layers in laminated glass affect stress distribution and load-bearing capacity. In our case, the role of the damping layer was performed by the air layer between the two glasses, which is especially noticeable in the 0° configuration, where deflections were minimal [17].

Studies by Guo et al and Kim et al. have shown that vacuum suction cups create zones of increased stress when the glass is removed and held, and that their overload can lead to localized failure [18]. Our experiment confirmed that the limiting factor in most cases is the separation of the suction cup itself, not the destruction of the glass, indicating a relatively safe load range of up to 70 kg when the tools are used correctly. Wang et al. proposed innovative self-sealing suction cups that reduce the risk of local overload [19]. Our data confirm the need for such improvements, since traditional suction cups are able to create dangerous local stresses with large load levers.

The results obtained are consistent with the proposed hypothesis of the study: the double-glazed window exhibits a distinctly pronounced dependence of the ultimate load on the configuration of force application. The lowest resistance to point loading was recorded in the configuration with a 90° angle and a central suction cup location. This unequivocally substantiates the assertion regarding the critical influence of geometric factors on the localized strength of a glass structure. Given the above, the proposed testing methodology enhances contemporary approaches to evaluating the mechanical stability of transparent structures. It may serve as a foundational framework for reassessing regulatory requirements pertaining to the temporary attachment of elements to glass. Moreover, it holds significant use for professionals engaged in the development of no-drill fasteners, including installers of blinds and sun protection, facade engineers as well as installation equipment manufacturers.

3.1 Limitation

Despite the careful experimental design, the study is not without certain limitations. Only one type of double-glazed window with an air gap was examined, without any variation in glass thickness or structural composition. Furthermore, fatigue effects or repetitive loading, which is relevant for regular assembly and disassembly of elements, were also not analyzed. For the experiment, a window that had been previously utilized, with double-glazed panes that likely have micro-scratches after 20 years of service, was specifically chosen as the potentially least durable option. The glass thickness of 2.3 mm represents the minimum standard employed in the window industry. In most instances, contemporary window glass measures 3.2 mm or 4 mm in thickness. However, no comparative analysis was conducted with 4 mm thick glass with significant, visible scratches. Also, real installation conditions may entail additional disturbances (such as vibrations and distortions), which were systematically eliminated under laboratory conditions.

4. Conclusions

The purpose of this study was to experimentally evaluate the resilience of double-glazed windows when subjected to point loads from various installation tool alternatives. These tools are employed during the installation of sun protection systems or in the course of construction activities. The need for such research arises from practical requirements within the construction and interior design sectors. Incidents of window damage during installation are a prevalent issue, resulting in increased costs and project delays. Understanding the strength limits of glass under specific loading conditions, particularly those encountered with temporary fastening instruments, is crucial for preserving the strength of window installations. This understanding aids in mitigating accidental damage throughout the installation process.

In the course of the experiment, evaluations were conducted utilizing vacuum suction cups featuring a lever mechanism, along with the capacity to accommodate additional loads. Three configurations regarding the orientation of the installation tool relative to the surface of the glass

unit were investigated, alongside two placements for the load application on the glass. This setup generated diverse vectors and moments of applied force. Such an approach enabled a comprehensive assessment not only of the load magnitude but also of the influence exerted by the force application method on the glass unit's strength.

The results of a series of experiments conducted with a partition positioned at 90 degrees, referred to as "Glass Center", demonstrated that the tested double-glazed window endured a concentrated point load of up to 86 kg without exhibiting any visible damage. When subjected to loads of 70 kg and above, it became apparent that the upper vacuum cup deformed under the weight. The suction cup was capable of sustaining the ultimate maximum load of 86 kg for approximately 20 seconds before detaching from the glass; however, the glass itself remained undamaged. Deflection measurements at points A and B indicated a progressive increase in deformation correlating with the increasing load, thereby signifying the uneven nature of the glass deformation. The maximum deformation exceeded 3 mm.

The data obtained underscore the considerable resilience of the examined double-glazed window, constructed from no tempered glass with a thickness of 2 mm, against concentrated point loads. The largest and heaviest blinds weigh approximately 20 kg, and their weight can be effectively distributed across two supports. No destruction occurred under a load that was eight times the rated working load of the blinds. The findings can be used to formulate recommendations for the safe utilization of assembly tools, design more reliable devices, and establish industry standards. Future research endeavors could focus on investigating the impact of glass type and thickness, window frame design, and the characteristics of various temporary installation tools on the load-bearing capacity of double-glazed windows.

4.1 Recommendations

The findings of the study give the grounds to formulate a series of practical recommendations for the safe application of mounting suction cups on double-glazed windows. When temporarily affixing blinds or sun protection systems, it is advised not to exceed a point load of 25 kg without the intermediary protective elements. The most precarious configuration involves positioning the suction cup at the center of the glass at a 90° angle. Further, it is recommended to conduct supplementary testing of the installation equipment on identical glass units before using it in real conditions. In particular, it is advisable to conduct the following tests:

- On different types of glazing, including higher thickness structures (3.2–4 mm) and different layer combinations to define universal safe limits of point loads.
- with different levels of wear and the presence of microdefects to assess the impact of real Operating conditions on strength.
- Include cyclic and long-term loads that simulate regular fastening and removal of mounting tools.
- Take into account the influence of vibrations, distortions, and other mechanical disturbances that may occur in real installation conditions.

References

[1] Momeni M, Bedon C. Review on glass curtain walls under different dynamic mechanical loads: Regulations, experimental methods and numerical tools. IntechOpen Series Civil Engineering, 2024; 4, 15-36. https://doi.org/10.5772/intechopen.113266

[2] Zhang P, Kamezaki M, Otsuki K, He Z, Sakamoto H, Sugano S. Development of a vacuum suction cup by applying magnetorheological elastomers for objects with flat surfaces. 2020 IEEE/ASME International Conference on Advanced Intelligent Mechatronics. IEEE, Boston, MA, USA, 777-782, 2020, July. https://doi.org/10.1109/AIM43001.2020.9158872

[3] Tiwari A, Persson B. N. J. Physics of suction cups. Soft Matter, 2019; 15(4): 727-735. https://doi.org/10.1039/C9SM01679A

[4] Schulz I, Kocer C, Paschke F, Schneider J. The performance of vacuum insulating glazing units subjected to a point load. Challenging Glass Conference Proceedings, 2022; 8: 443-454. https://doi.org/10.47982/cgc.8.443

[5] Mognato E, Barbieri A, Schiavonato M, Pace M. Thermally toughened safety glass: Correlation between flexural strength, fragmentation and surface compressive stress. Glass Performance Days, 2011; 10(1): 115-118.
[6] Efferz L, Schuler C, Siebert G. Photoelastic measurements and evaluation Methods for Edge Stress in Architectural Tempered Glass. Glass Structures & Engineering, 2024; 9: 439-454. https://doi.org/10.1007/s40940-024-00270-3
[7] Maiti H. S. Structural and functional properties of architectural glass. Future Landscape of Structural Materials in India, Springer, Singapore. 2022 211-231. https://doi.org/10.1007/978-981-16-8523-1_9
[8] Wu G, Zhang B, Qi P, Shao C, Guo Y. Research on glass wall cleaning robot based on double suction cup negative pressure type. 2018 7th International Conference on Energy, Environment and Sustainable Development (ICEESD 2018), Atlantis Press, Shenzhen, China, 990-993, 2018. https://doi.org/10.2991/iceesd-18.2018.179
[9] Kurkjian CR, Gupta PK. Intrinsic strength and the structure of glass. Physics and Chemistry of Glasses-European Journal of Glass Science and Technology Part B, 2020; 61(6): 239-247. https://doi.org/10.13036/17533562.61.6.Kurkjian
[10] Efferz L, Schuler C, Siebert G, Experimental determination of the strength of toughened glass in the area of near-edge holes. Glass Structures & Engineering, 2024; 9: 3-17. https://doi.org/10.1007/s40940-023-00245-w
[11] Kozłowski M, Zemła K, Kosmal M, Kopyłow O, Experimental and FE study on impact strength of toughened glass-retrospective approach. Materials, 2021; 14(24): 7658. https://doi.org/10.3390/ma14247658
[12] Cupać J, Datsiou KC, Louter C. Reuse potential of architectural glass: Experimental study on the strength of used window glazing. Glass Structures & Engineering, 2024; 9: 321-337. https://doi.org/10.1007/s40940-024-00267-y
[13] Zemanová A, Konrád P, Hála P, Sovják R, Hlůžek R, Zeman J, Šejnoha M, Experimental study on the gradual fracture of layers in multi-layer laminated glass plates under low-velocity impact. Applied Physics, 2021; arXiv:2107.12151.
[14] Hänig J, Weller B, Integrated connections for glass-plastic-composite panels: An experimental study under tensile loading at +23, +40 and +60 °C and different glass build-ups. Glass Structures & Engineering, 2022; 7: 211-229. https://doi.org/10.1007/s40940-022-00174-0
[15] Hänig J, Weller B, Load-bearing behaviour of innovative lightweight glass-plastic-composite panels. Glass Structures & Engineering, 2020; 5: 83-97. https://doi.org/10.1007/s40940-019-00106-5
[16] Hänig J, Weller B, Experimental investigations and numerical simulations of innovative lightweight glass-plastic-composite panels made of thin glass and PMMA. Glass Structures & Engineering, 2021; 6: 249-271. https://doi.org/10.1007/s40940-021-00153-x
[17] Galić M, Grozdanić G, Divić V, Marović P, Parametric analyses of the influence of temperature, load duration, and interlayer thickness on a laminated glass structure exposed to out-of-plane loading. Crystals, 2022; 12(6), 838. https://doi.org/10.3390/cryst12060838
[18] Guo B, Zheng X, Fang S, Yang L. Suction cup quality predication by digital image correlation. SAE International Journal of Advances and Current Practices in Mobility, 2023; 5(6): 2047-2055. https://doi.org/10.4271/2023-01-0067
[19] Wang Z, Terryn S, Wang H, Legrand J, Safaei A, Brancart J, Assche GV, Vanderborght B. Self-closing and self-healing multi-material suction cups for energy-efficient vacuum grippers. Advanced Intelligent Systems, 2023; 5(10): 2300135. https://doi.org/10.1002/aisy.202300135
[20] Kim J, An J, Kim Y, Cho Y. Development and application of evaluation procedure for performance testing of vacuum suction pad in automatic mooring system in a lab test. Journal of Marine Science and Engineering, 2025; 13(3): 502. https://doi.org/10.3390/jmse13030502
[21] Song S, Drotlef DM, Son D, Koivikko A, Sitti M. Suction-based soft robotic gripping of rough and irregular parts, Applied Physics, 2020; arXiv:2009.08156.
[22] Haldimann M, Luible A, Overend M. Structural Use of Glass. Iabse, 2008; 10. https://doi.org/10.2749/sed010
[23] Pfaender HG. (Ed.). Schott Guide to Class, Springer Science & Business Media, Darmstadt, 2012
[24] Surmai M, Tkach R, Hula V, Kozak R. Glass as a material of bearing columns. 9th International Youth Science Forum "Litteris et Artibus" & 14th International Conference "Young Scientists towards the Challenges of Modern Technology, Lviv Polytechnic National University, Lviv, Ukraine, 96-98, 2019.
[25] Itoi C, Mukaida H, Tasaki H. Griffiths-type theorems for short-range spin glass models. Journal of Statistical Physics, 2024; 191(2), 28. https://doi.org/10.1007/s10955-024-03246-3
[26] Feldmeier F. Climate load and load distribution for multi-pane insulating glass units. Stahlbau, 2006; 75(6): 467478.

Blank Page

Research on Engineering Structures & Materials
www.jresm.org

Research Article

Effect of PVA and basalt fibers on enhancing the structural and thermal behavior of cement panels

Shukran Hikmat Faraj [*,a], Mohammed J. Kadhim [b]

Material Engineering Department, Mustansiriyah University, Baghdad, Iraq

Article Info

Article History:

Received 25 Sep 2025

Accepted 27 Oct 2025

Keywords:

Basalt fiber;
Poly vinyl Alcohol Fiber;
Thermal Conductivity;
Flexural strength;
Scanning electron microscopy

Abstract

This study investigates the influence of basalt fibers (BF) and polyvinyl alcohol fibers (PVA) on the mechanical and thermal performance of cement panels incorporating silica fume as a supplementary binder. A series of mortar mixes were prepared with varying fiber dosages and tested under controlled curing conditions. The experimental program included compressive strength, flexural strength, splitting tensile strength, water absorption, surface hardness, ultrasonic pulse velocity (UPV), thermal conductivity, and microstructural characterization using scanning electron microscopy (SEM).The results demonstrated that basalt fibers provided superior reinforcement, with the 3% BF mix achieving the highest compressive strength (45.28 MPa), flexural strength (11.23 MPa), and enhanced thermal insulation (thermal conductivity reduced to 0.644 W/m•K). In contrast, PVA fibers showed optimal performance at 2% content, yielding a compressive strength of 43.43 MPa and moderate improvements in flexural and tensile behavior. However, both fiber types increased water absorption relative to the reference mix, indicating a trade-off between mechanical enhancement and durability. SEM analyses confirmed the role of fibers in bridging microcracks and improving matrix integrity. Overall, the findings highlight that incorporating 3% basalt fibers and 2% PVA fibers optimizes the structural and thermal behavior of cement panels, suggesting their potential as effective reinforcement strategies in advanced construction materials.

© 2025 MIM Research Group. All rights reserved.

1. Introduction

Cement, sand, and water are the components of ordinary Portland cement (OPC). Invented by Joseph Aspdin in 1794, it gained popularity in the 19th century due to its speed and ease of installation [1]. However, it is considered unsuitable for the restoration of lime mortar structures, which require flexibility and breathability [2, 3]. Due to their exceptional durability, fire resistance, and ease of installation, cement boards, including fiber cement boards (FCBs), are widely used in modern buildings. The primary binding material in these boards is cement, to which sand, reinforcing fibers, and other additives are added to improve performance. They are typically used for floors, walls, ceilings, and facades of residential and commercial buildings. FCBs can be painted, impregnated with protective coatings, or left uncoated. FCBs have proven their reliability through widespread use in construction for over a century, particularly in non-pressurized pipes and corrugated roofing sheets. However, when used in facade systems, they are often exposed to a wide range of weather conditions. Wind-borne debris, freeze-thaw cycles, prolonged exposure to ultraviolet radiation, and thermal stresses resulting from temperature changes are some of the factors that affect their long-term performance and durability [4, 5]. Cement boards are widely used in architectural and construction applications due to their favorable mechanical and thermal

*Corresponding author: shukranh.f@uomustansiriyah.edu.iq
[a]orcid.org/0009-0005-9233-9072; [b]orcid.org/0000-0002-7783-2927
DOI: http://dx.doi.org/10.17515/resm2025-1187ma0925rs

properties. However, they are still subject to various challenges that can affect their long-term performance and durability. The primary physical problems include cracking and buckling, often caused by fluctuations in temperature and humidity levels, as well as thermal expansion and contraction, which can lead to internal stresses and compromise mechanical stability. From an environmental perspective, prolonged exposure to ultraviolet radiation and freeze-thaw cycles can lead to surface deterioration and internal degradation. Additionally, the high moisture absorption capacity of inadequately treated boards can lead to swelling, discoloration, and biological growth such as mold and fungi. These problems are exacerbated by improper installation, including the use of incompatible fasteners or neglect of expansion joints [6, 7]. Fiber-reinforced mortars offer a compelling solution, enhancing the mechanical properties, crack resistance, and overall structural durability [8]. Glass fibers are widely used in composite mixes, while carbon fibers are among the most common reinforcing fibers used in the manufacture of composite materials under high load conditions. Despite their excellent properties, they are expensive [9, 10]. Therefore, basalt fibers are used due to their low cost, enabled by modern industrial production technologies. Consequently, basalt fibers and the materials made from them are characterized by high quality and cost-effectiveness. Basalt has excellent mechanical and thermal properties, is non-toxic to air or water, non-flammable, and biologically stable, making it suitable for a variety of building applications [9]. Polyvinyl alcohol (PVA) fibers are also part of the reinforcing fiber group. PVA fibers are characterized by their exceptional mechanical properties and compatibility with the cement matrix. Due to their stiffness compared to the concrete matrix, their ability to form a strong interfacial bond with the cement matrix, and their good dispersibility, they positively influence mechanical properties, particularly flexural and compressive strengths, and splitting tensile strength [11]. PVA fibers play an important role in tensile strength, as they withstand the first crack stress and resist pullout forces [12]. In addition, silica fume is commonly added to cement mixtures to improve porosity and durability. Silica fume is an industrial by-product of metallurgical processes and consists mainly of nanosized, spherical silicon dioxide. particles. These particles have a surface area and reactivity significantly higher than cement, being approximately 100 times smaller. Silica fume exhibits strong pozzolanic activity, reacting with calcium hydroxide produced during cement hydration to form calcium silicate hydrate (C–S–H) gel. This gel fills the pores within the cement structure, reducing moisture absorption and improving durability [13]. Although numerous studies have addressed the role of silica fume in cementitious matrixes in improving density and reducing porosity, its effect with basalt fibers and PVA remains limited, as each material was studied separately. Furthermore, most studies used the traditional method of measuring porosity without combining it with SEM at the fiber-cement matrix interface. Therefore, there is still a need to combine experimental and microscopic analysis to elucidate the mechanisms that lead to increased water absorption upon fiber incorporation, despite the fact that silica fume improves density and reduces porosity. The novelty of this study is in evaluating the effect of incorporating basalt fibers (BF) and polyvinyl alcohol (PVA) fibers on the mechanical and thermal performance of cementitious panels containing silica fume. In addition, microscopic analysis using a scanning electron microscope (SEM) was combined with physical tests to explain the interaction between SF and fibers and to understand the mechanisms that lead to increased water absorption when fibers are incorporated into a matrix containing SF despite the improvement of mechanical and thermal properties at specific ratios, an aspect that has not been clearly addressed in previous studies.

2. Experimental Work and Materials

2.1. Materials

There are many materials which are used to prepare specimens, these materials consist cement, fine aggregate, water and silica fume and basalt fiber

2.1.1 Cement

The Ordinary Portland cement (Type I) manufactured in Iraq with trademark of (Tasluga-Bazian) was used in this study. Its physical and chemical properties conformed to ASTM C150-04 [14] and

Iraqi Standard Specifications IQS No. 5/1984 [15] . the chemical and physical requirements of cement represents in Table 1 and 2.

Table 1. Chemical requirements of cement

Chemical Composition	Weight%	ASTM C 150-04	IQS5/1984
CaO	63.19	***	***
SiO2	21.60	20.0min	***
AL2O3	4.10	6.0 max	***
Fe2O3	4.48	6.0 max	***
MgO	2.28	6.0 max	5 max
SO3	1.98	3* max	2.5** max
L.O.I.	2.45	3 max	4 max
I.R.	0.47	0.75 max	1.5 max
L.S.F.	0.905		0.66-1.02

Table 2. Physical requirements of cement

Physical Properties	Test result	ASTM C 150-04	IQS5/1984
Fineness using Blaine air permeability apparatus (m2/kg)	330	280 min	230 min
Setting time (Vicat Apparatus),			
Initial setting (min)	175	45min	45 min
Final setting (min)	225	375 max	600 max
Compressive strength, MPa for cement paste cube mold (50mm) at:			
3 days	25.13	12 min	15 min
7 days	34.6	19 min	23 min
28 days	40.5	***	***
Soundness (Autoclave Method), %	0.19	0.8 max	0.8 max

2.1.2 Fine Aggregate

Sand passing through sieve 1.18 mm, has been used in this research. It was conformed Fine aggregate was Ottawa sand, complying with ASTM C778 [16]. The specification of fine aggregate represents in Table 3.

Table 3. The fine aggregate sieving analysis

Sieve size	Percent passing (%)	Specification limits (%)
10	100	100
4.75	92.7	90_100
2.36	79.65	75_100
1.18mm	68.6	55_90
600 µm	52.6	35_59
300 µm	27.4	8_30
150	2.65	0-10

2.1.3 Silica Fume

Silica fume consists primarily of amorphous (non-crystalline) silicon dioxide (SiO_2). The individual particles are extremely small, approximately 1/100th the size of an average cement particle. Because of its fine particles, large surface area, and the high SiO_2 content, silica fume is a very reactive pozzolan when used in Cementous materials. Its physical and chemical properties

conformed to ASTM C1240-05 [17]. The chemical composition and Physical requirements illustrate in Table 4 and 5.

Table 4. Silica fume specifications

Oxides	Content %	ASTM C1240-05 limitations
SiO_2	90.51	≥ 85
Al2O3	0.60	_
Fe_2O_3	2.32	_
CaO	0.58	_
MgO	0.3	_
TiO2	0.01	_
Na_2O	0.15	_
K_2O	1.26	_
P2O5	0.11	_
SO_3	0.36	≤ 4
L.O. I	3.82	≤ 6

** Test was carried out by testing laboratory in the College of Engineering, Kufa University.*

Table 5. Physical requirements of silica fumes

Physical properties	SF	ASTM C1240-05 limits
Specific surface area, min, (m2/g)	20	≥15
Strength activity index with Portland cement at 7 days, min percent of control.	122	≥105
Percent retained on 45m (No. 325), max%	9	≤10

**Tests were carried out by testing laboratory in the College of Engineering. University of Kufa.*

2.1.4 Basalt Fiber

Basalt fiber is produced by melting basalt rock at temperatures 1500°C and extruding it into fine fibers, similar in process to producing glass fibers but with higher energy efficiency. [18] Basalt fiber it was obtained from the Iraqi Sika Company as a reinforcing element in cement mortar are shows in Figure (1). the basalt fibers properties illustrate in the Table 6.

Table 6. The basalt fiber properties

Property	Continuous Basalt fiber
Breaking Strength (MPa)	3,000 – 4,840
Modulus of Elasticity (GPa)	3,100– 3,800
Breaking Extension (%)	3.1
Fiber Diameter (μm)	6 - 21
Linear Density (tex)	60-4,200
Temperature Withstand (℃)	-260….+700

2.1.5 Superplasticizer

Polycarboxylate (VISCO CRETE-180 GS) is a highly effective water-reducing, setting-slowing, shrinkage-preserving, and super plasticizing additive for mortars and concrete. meeting the requirements of ASTM C494/494M-19 [19]. 1.5 % of the total weight of cementitious materials is used .the properties of Polycarboxylate super plasticizer showing in the Table 7.

Table 7. The properties of Polycarboxylate super plasticizer

Composition	Aqueous solution of modified polycarboxylates
Packaging	Bulk Deliveries 1000 LTRs IBC 20 kg Pail
Appearance / Color	Light brownish liquid
Storage conditions	In dry conditions at temperatures between +5°C and +35°C. Protect from direct sunlight. It requires recirculation when held in storage for extended periods.
Specific gravity	1.070 ± (0.005) g/cm^3
pH-Value	4 - 6
Total chloride ion content	Nil

2.1.6 polyvinyl Alcohol

PVA Fibers (polyvinyl alcohol) are high-performance reinforcement fibres for concrete and mortar, obtained from LAKHANI FABRICS COMPANY, INDIA. That show in Figure 1. PVA fibres are well-suited for a wide variety of applications because of their superior crack-fighting properties, high modulus of elasticity, excellent tensile and molecular bond strength, and high resistance to alkali, UV, chemicals, fatigue and abrasion. PVA fibres are unique in their ability to create a molecular bond with mortar and concrete that is 300% greater than other fibres. 6 mm fibers are used in the mixtures. The polyvinyl alcohol fiber Technical Parameter showing in the Table 8.

Table 8. The polyvinyl alcohol fiber technical Parameters

Technical Parameter	100% PVA
Fibre Type	Bunchy Monofilaments
Density	1.29
Formula	$(CH_2CHOH)n$
Titer	1.80-2.40 Dtex
Dry breaking tenacity	≥11.50 cN/dtex ≥
Dry breaking elongation	4.0-9.0 %（L/L）
Initial modulus	280 cN/dtex ≥
Specification	6MM, 12MM
Hot water resistance	2.0 % ≤
Oli agent content	0.2 % ≤
Elongation at fracture (%)	6.5
Young's modulus (GPa)	42
Flexural strength (MPa)	1560

2.2. Mixture Design

For this research seven mixes were prepared with the same mix proportion (cement: sand) equal to (1:2.75) by weight, and water /binder equal to (0.42). The total binder amounts for all the produced mixtures, as shown in Table (7). The reference mix (Ref.) was prepared using super plasticizer (1.5%) by weight of cement to obtain (100±5) percent of flow with low water/binder ratio (0.42). While The other Six mixes (BF1, BF2, BF3, PVA1, PVA2 and PVA3) were prepared from the reference mix with a partial replacement of cement by (10%) of SF. Using (SF) reduces significantly the workability of fresh mortar and increases the dosage of super plasticizer. Therefore, the optimum SF ratio is 10% [20, 21]. The flow values of all mixtures were kept in the range of (100±5) percent of flow with regulates the dosage of super plasticizer. Three samples were prepared from each mixture for all treatment periods. The resulting samples were treated with

water in a standard treatment tank for 7, 14, and 28 days. The material quantities used in mixes production are presented in Table 9.

Table 9. Mix proportions of cement mortar (g)

Mixture Name	Cement (g)	Sand (g)	Water (g)	SF (g)	BF%	PVA%
Ref	1000	2750	420	0	0	0
BF 1	900	2750	420	100	1	0
BF 2	900	2750	420	100	2	0
BF 3	900	2750	420	100	3	0
P 1	900	2750	420	100	0	1
P 2	900	2750	420	100	0	2
P 3	900	2750	420	100	0	3

The experimental program involved evaluating various mechanical and physical properties of cement mortar samples using standardized procedures. Tests were conducted on (5 × 5 × 5 cm) cubic specimens to assess compressive strength, water absorption and surface hardness. Compression and flexural strength tests were conducted using a Tecnotest Universal Testing Machine (UTM), manufactured by Tecnotest S.r.l., Italy. The machine has a maximum loading capacity of 2000 kN for compression tests and 300 kN for flexural tests. It is equipped with an automatic data acquisition system and a digital load control unit, ensuring precise control of the loading rate in accordance with ASTM C109/C109M [22] and ASTM C348 standards [23]. Compressive strength was measured in accordance with ASTM C109/C109M [22]. Specimens were demolded after 24 hours and cured in water at a constant temperature for 7, 14, and 28 days before testing.

(a) (b)

Fig. 1. (a) PVA fiber 6mm and (b)basalt fiber 12 mm

Surface hardness is a non-destructive test used to determine a material's surface resistance to deformation. The hardness test was conducted using the Shore D, an electronic instrument with decimal accuracy produced by the German company QUALITEST INC. in accordance with ASTM D 2240-03 [24].

Splitting tensile strength, the splitting tensile strength test is the easiest way to evaluate the tensile strength of concrete. Since it is difficult to apply a direct tensile force to this material, it is usually subjected to a radial compression force, which produces an indirect tensile force in the vertical direction, leading to failure. The mold is a cylinder with a diameter of 5 cm and a height of 10 cm. The mortar is poured into the mold in three batches, and each batch is compacted 25 times using a cylindrical rod. The surface of the mold is then polished, according to ASTM C 496/C496M-04 [25].

Ultrasonic pulse velocity (UPV) was tested using the direct transmission method, following ASTM C597-22 [26]. The pulse velocity was calculated by dividing the specimen length by the transit time of the ultrasonic wave.

Water absorption was measured based on ASTM C642, applying the procedure involving dry and saturated mass comparisons [27].

The flexural strength test was conducted on prismatic specimens (16 × 4 × 4 cm) following ASTM C348, using a three-point bending setup where a load is applied at the center of the span until failure occurs [23].

The thermal conductivity coefficient (k-value) of all samples was measured (15 x 10 x 5 cm) were prepared and using the ASTM C1113/C1113M-09(2013) method based on the hot wire technique [28]. The test method involves inserting a thin resistance wire into the refractory material sample and passing an electric current through the wire, which generates heat. The temperature is monitored using thermometers to measure the temperature rise of the sample at different times as heat dissipates through the material Thermal conductivity k-values can be determined from room temperature to 1500°C [2732°F], or to the temperature at which the refractory is no longer dielectric.

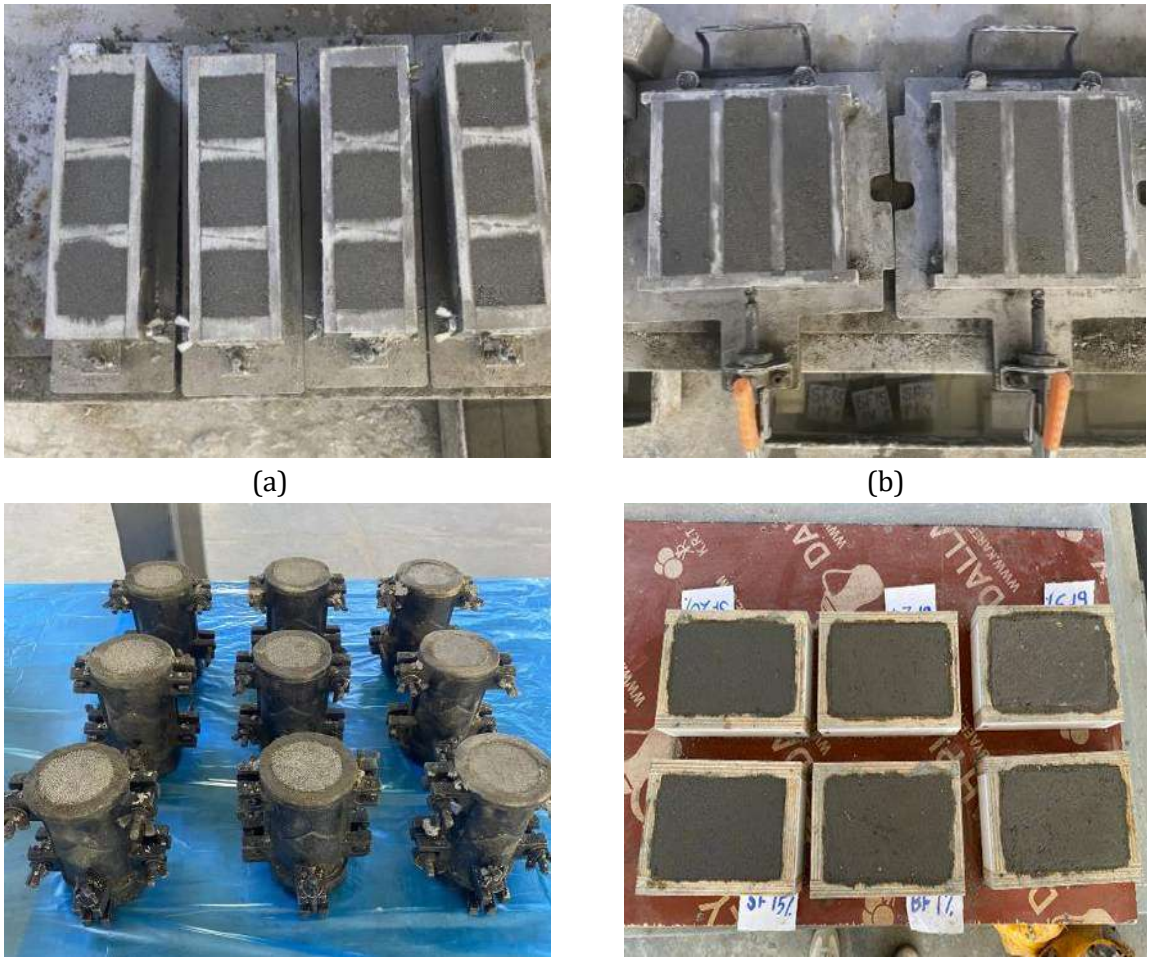

(a) (b) (c) (d)

Fig. 2. The mold using to cast sample (a) for cubic sample 5x5x5 cm, (b) for prism sample 4x4x16 cm (c) For cylinder sample 5x10 cm and (d) Sample 15x10x5 cm

It is an advanced analytical technique used to examine the structure of materials at very high resolution. It is of great importance in understanding the microscopic properties that directly affect the strength, durability, and quality of mortar. An Axia ChemiSEM is used, a new generation of scanning electron microscope (SEM). The process of imaging mortar using a scanning electron microscope involves several steps. First, the sample is prepared and oven-dried at 40–60°C to prevent rapid evaporation of water inside the scanning electron microscope chamber, which could damage the sample. The sample is then fractured or cut to reveal a fresh surface. The surface of the material is coated with a conductive material such as gold using spray painting. Second, the sample

is carefully mounted on a holder inside the microscope to prevent vibration. The electron beam is generated so that the device emits a focused beam of electrons directed at the sample surface.

All specimens were prepared and cured under identical conditions to ensure consistency and enable accurate comparative analysis across different mix designs. Figure (2) shows the shapes of the molds used to prepare the appropriate samples for each test.

3. Results and Discussion

3.1. Compressive Strength Results

The results in the Figure 3 illustrate how basalt fiber (BF) and polyvinyl alcohol (PVA) fibers affect the compressive strength of cement slabs at different curing ages. The results demonstrate a clear link between fiber type and quantity and mechanical performance. The bar graph shows the compressive strength test results of several cement mortar mixtures cured for 7, 14, and 28 days. There is a reference sample (REF), three samples with basalt fiber (BF) at 1%, 2%, and 3%, and three samples with polyvinyl alcohol fiber (PVA) at 1%, 2%, and 3%. The results demonstrate how basalt fiber (BF) and polyvinyl alcohol (PVA) fibers affect the compressive strength of concrete at different curing stages. The research identifies an optimal percentage for each fiber type. The compressive strength of basalt fiber increased with increasing fiber content compared to the reference mix. We notice a gradual increase in compressive strength with increasing curing period in water, where it recorded 21.73, 30.44 and 31.45 at BF1%, BF2% and BF3% respectively at 7 days and at 14 days the increase rate reached 19.3%, 9.6% and 13.5%, while at 28 days it achieved the highest compressive strength, where we notice the increase rate was 50.2%, 28.4% and 26.9%.

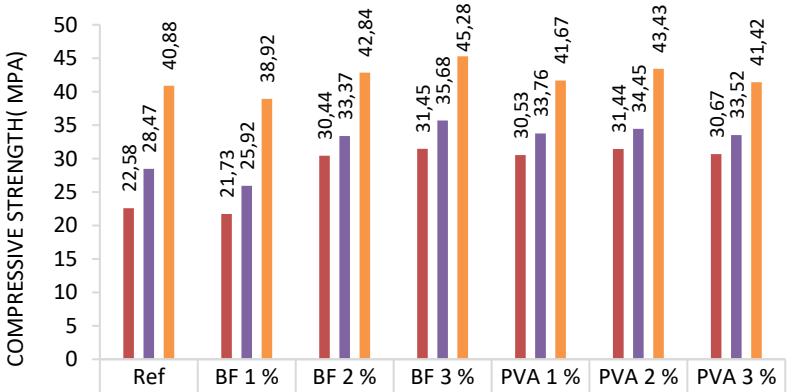

	Ref	BF 1 %	BF 2 %	BF 3 %	PVA 1 %	PVA 2 %	PVA 3 %
7- day CS (MPa)	22,58	21,73	30,44	31,45	30,53	31,44	30,67
14- day CS (MPa)	28,47	25,92	33,37	35,68	33,76	34,45	33,52
28- day CS (MPa)	40,88	38,92	42,84	45,28	41,67	43,43	41,42

Fig. 3. Compressive strength behavior of different mixing ratio

The results show that the highest increase in strength is at 1%, because the low fiber percentage improves hydration and allows the matrix to grow without difficulty in integration or increased porosity [29]. While at 2 and 3%, the increase rate was low because the concrete was approaching its early mechanical maturity, and the fiber density hinders concrete growth due to barriers. However, the 3% BF mixture showed the highest strength (45.28 MPa) among all samples. This is because the fibers form a network within the matrix, acting as a barrier that prevents crack propagation. This means that this concentration was the best for increasing strength, but with a lower internal density, as the pores around the fibers increased [30]. Despite the presence of 10% silica fume in all mixes, the presence of fibers hinders its homogeneous diffusion within the matrix and the filling of gaps around the fibers [31]. This can be observed in the UPV test and the water absorption test. This means that increasing the fiber density by 3% was sufficient to significantly improve mechanical properties, but at the expense of density [18]. When adding PVA fibers, we notice a slight gradual increase in compressive strength with an increase in the curing period in water. Compressive strength was recorded at 7 days for PVA1%, PVA2%, and PVA3% (30.53, 31.44, and 30.67, respectively). At 14 days, the increase rate reached 10.6%, 9.6%, and 9.3%. We note that

the increase is low, indicating that PVA fibers accelerate the strength gain at an early stage due to the enhancement of internal cohesion by forming chemical and molecular bonds at the contact surface between the fibers and the matrix. This is because the surface of the polar PVA fibers contains an OH- (hydroxyl) group, which allows for a partial chemical reaction with C-S-H when the cement is hydrated, thus reducing microcracks. [32, 33] This makes the increase between 7 and 14 days small because the matrix developed its strength early. At 28 days, the highest strength was achieved, with the increase rate being 23.4%, 26.1%, and 23.6%, respectively. We note the highest increase at PVA2%, indicating that this percentage represents the best balance between the workability and fiber distribution gave a peak strength of 43.43 MPa [34, 35]. Adding more PVA (3%) resulted in a slight decrease in strength (41.42 MPa). This type of behavior is prevalent in fiber-reinforced composites and can be explained by several factors.

(a) (b)

Fig. 4. (a) Compression cubic before failureand (b) the cubic after failure

The strengthening effect is not as strong at low percentages. The benefits of crack management are greatest when the percentage is at its optimum level. However, exceeding this ideal condition can weaken the cement board matrix, as it is difficult to distribute the fibers evenly, which can cause weaknesses or gaps in the matrix and reduce its durability. Overall, the results also show that both basalt fiber and PVA fiber can significantly improve the compressive strength of cement boards. This study indicated that the optimum concentrations are 3% basalt fiber and 2% PVA fiber. Basalt fiber performs better than the others, especially at 3%. This suggests that it may be a good method for strengthening cement boards. The Figure 4 shows the sample before and after failure.

3.2. Absorption Test

This test is used to evaluate the durability and quality of cement mortar by measuring its susceptibility to water seepage and moisture damage, according to ASTM C642-13 [36] . We performed this test on mortar samples containing varying amounts of basalt fiber (BF) and polyvinyl alcohol fiber (PVA) and compared them to a reference mix (Ref) as shown in Figure (5). The reference mix had the lowest water absorption rate (1.8%), meaning it had a relatively dense matrix with low porosity.

Table 10. Water absorption results of cement mortar containing different additives

Mix	Dry Mass (g)	Saturated Mass (g)	Water Absorbed (g)	Water Absorption (%)
Ref	277	282	5	1.8 %
BF 1	259	269	10	3.71 %
BF 2	259	270	11	3.83 %
BF 3	255	266	11	4.31%
PVA 1	241	252	11	4.56%
PVA 2	242	254	12	4.95 %
PVA 3	242	253	12	4.97 %

Water absorption was observed to gradually increase when basalt fiber was added to the reference mix at a fixed replacement ratio of 10% silica fume. The absorption rate increased with increasing fiber content, with BF 1% showing 3.71%, BF 2% recording 3.83%, and BF 3% reaching 4.31%. This trend suggests that basalt fibers may improve mechanical properties, but they may also make the material more internally porous by creating microchannels and insufficient fiber dispersion [37], as shown in SEM. Although silica fume reduces porosity by filling gaps via C-S-H gel formation due to the reaction of silica fume with calcium hydroxide resulting from cement hydration [38, 39], these effects may outweigh the porosity-reducing benefit of silica fume. PVA fiber blends absorbed more water than the reference blend. When the PVA fiber concentration was 1%, 2%, and 3%, the results were 4.56%, 4.95%, and 4.97%, respectively. [30] This is shown in Table 10. These results indicate that the incorporation of PVA fibers affects the cohesion of the matrix, most likely due to the hydrophilicity, fiber dimensions, and inhomogeneous distribution of fibers, which hinders the distribution of silica fume in the cement matrix and fills some micropores in places around the fibers, thus weakening the effectiveness of silica fume, leading to increased water absorption [31, 40]. Overall, BF and PVA fibers made the mortar absorb more water than the standard blend. It was shown that the addition of fibers increases water absorption because more surface area and weak areas at the interface leave water channels and create pores. This indicates that fiber content and dispersion need to be optimized to find a balance between strength and durability.[41] Figure (6) show the sample during curing.

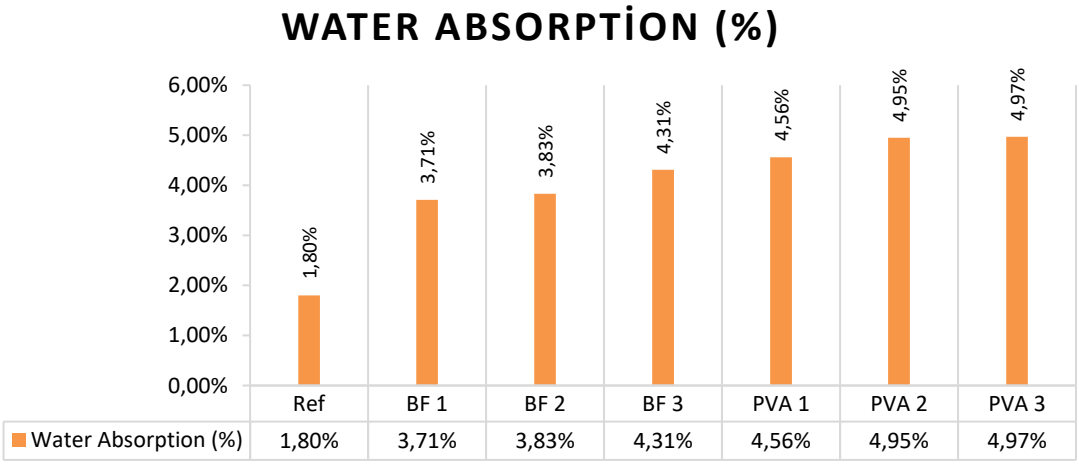

Fig. 5. Water Absorption behavior of different mixing ratio

(a) (b)

Fig. 6. (a) The samples during curing in water and (b) the sample is weighed

3.3. Flexural Strength

Flexural strength results indicated a significant improvement as a result of fiber addition. The reference mixture achieved only 4.5 MPa after 28 days. In contrast, basalt fiber blends showed a significant increase, with BF3 achieving the highest value (11.23 MPa), followed by BF2 (9.99 MPa) and BF1 (7.34 MPa).[42] PVA fiber blends also improved flexural performance compared to the reference, with PVA2 reaching its peak (6.89 MPa). These results demonstrate that basalt fibers provide superior flexural strengthening, while PVA fibers offer moderate improvement. [2]

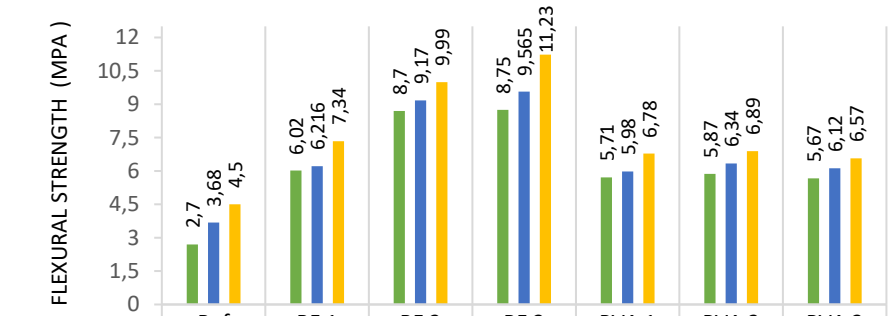

	Ref	BF 1	BF 2	BF 3	PVA 1	PVA 2	PVA 3
7 DAY MPa	2,7	6,02	8,7	8,75	5,71	5,87	5,67
14 DAY MPa	3,68	6,216	9,17	9,565	5,98	6,34	6,12
28 DAY MPa	4,5	7,34	9,99	11,23	6,78	6,89	6,57

MIXING RATIO

Fig. 7 . The flexural strength behavior of different mixing ratio

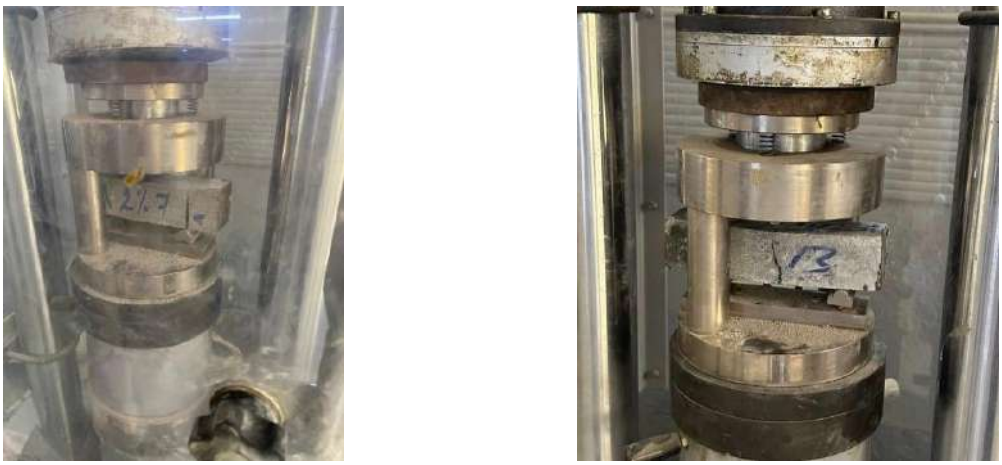

(a) (b)

Fig. 8. A. The prism befor failure B. prism after failure

3.4. Thermal Conductivity

The Effect of Basalt Fibers and Polyvinyl Alcohol (PVA) Fibers on the Thermal Properties of Cement Boards. This study sought to incorporate basalt fibers (BF) and polyvinyl alcohol (PVA) fibers in varying quantities into cement boards with a fixed silica replacement ratio of 10%, and to evaluate their effect on the thermal conductivity coefficient (k value). Tests were conducted according to the American standard ASTM C1113/C1113M-09 [28], which evaluated the k value at varying fiber ratios. A gradual decrease in thermal conductivity values was observed as the basalt fiber ratio increased from 1% to 3%. On the other hand, PVA fibers showed a slight improvement at 1%, then values gradually increased with increasing ratios [34].

- Case (1): Basalt fiber additive (BF): Thermal properties improved significantly when basalt fiber was added to the cement mixture. As the basalt content increased, the thermal conductivity decreased, reaching 0.83 W/m.K at 1% and 0.644 W/m.K at 3%. This is

attributed to the fact that the basalt fibers increased porosity and created additional interfaces within the cement matrix, reducing heat transfer through the material. Thus, basalt fibers have been shown to improve thermal insulation.[43]

- Case (2): PVA fiber additive: The PVA samples recorded a value of 0.905 W/m.k at 1%, which is lower than the reference value, indicating a slight improvement in insulation. However, when the percentage was increased to 2%, the value increased to 0.963 W/m.k, and at 3%, it reached 1.049 W/m.k, indicating that the fibers act as a thermal bridge within the cement paste. At high ratios, the fibers clump together, losing their role in improving porosity and gaps, leading to a gradual increase in thermal conductivity, but still providing better thermal insulation than the reference mixture. This has been demonstrated by numerous studies conducted on PVA fibers in cement mixtures [44].

Fig. 9. The simple during test in Thermometers

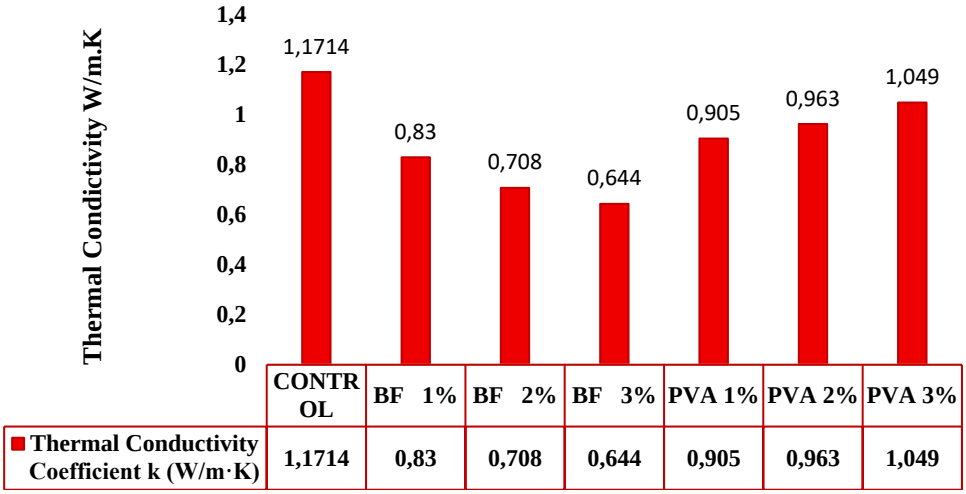

Fig. 10. The thermal conductivity behavior of different mixing ratio

3.5. Ultra-Pulse Velocity

The UPV test is used to determine the internal density and cohesion of concrete with or without the addition of fibers. The reference mix showed 4253 m^3/s after 28 days. Mixes containing basalt fibers (1% BF) showed higher UPV values (4534 m^3/s) compared to the reference mix and slightly decreased at (2% BF, 3% BF (4465 m^3/s, 4354 m^3/s, respectively) but still higher than the reference mix. We note that UPV increases with increasing concrete age because the hydraulic reaction completes and improves the cohesion of the internal matrix over time and reduces porosity and tightens the bonds between the gaps, indicating improved internal density [45] While we note that UPV gradually decreases with increasing PVA content, the highest UPV value (4521

m^3/s) was found at 1% PVA, while it decreased slightly at 2% PVA (4432 m^3/s) and the decrease increases to (4265 m^3/s) at 3% PVA compared to 1% PVA. [43, 46] These results indicate a decrease in UPV with increasing fiber content compared to lower fiber contents, due to lower workability leading to increased fiber clumping and difficulty in homogeneous distribution. However, it has the ability to resist the bridge stress transmitted through the PVAF, BF crack, leading to high compressive strength up to a certain fiber content [47]. This has been shown in Figure 11.

Fig. 11. The sample during test in UPV devise

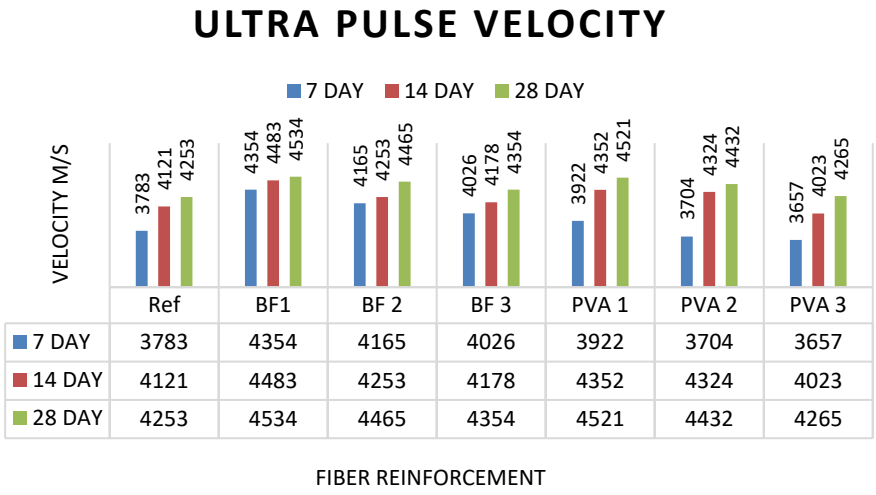

Fig. 12. The Ultra pulse velocity of different mixing ratio

3.6. Splitting Tensile

Figure (13) shows the split tensile strengths of both plain and fiber-reinforced concrete for all curing periods in water. We note that the tensile strength improves up to a certain percentage and then decreases when using 1-3% PVA in a mortar containing a fixed replacement ratio of SF. This indicates that these fibers have reached a percentage where the fibers are distributed homogeneously within the matrix and reduce the spread of cracks. When the dosage is increased, difficulty occurs in distributing the fibers and clumps occur within the matrix, causing an increase in gaps. The split tensile strength of 1% PVA, 2% PVA, and 3% PVA increased by 20.9%, 27.01%, and 13.18%, respectively, compared to the reference mixture of 3.11 MPa at 7 days. At 14 days, the increase rate reached 32.05%, 44.81% and 24.93% respectively, while at 28 days it achieved an increase of 35.19%, 51.14% and 23.80%. We notice a gradual increase in the tensile strength with the increase in the curing period from 7 to 28 days, indicating the continued growth of C-S-H hydration products that improve the bond between the fibers and the cement matrix, where 2% PVA achieved the highest improvement in tensile strength at all curing periods, the increase rate

reached 51.14% (5.97MPa) at 28 days compared to the reference mixture. [48] As for BF fibers, the same ratios (1, 2, and 3%) were used with the reference mix, where we observed a gradual increase in strength with increasing percentages of added fibers, reaching 10.9%, 13.67%, and 31.90% compared to the reference mix, which achieved the highest tensile strength at 3% (5.21 MPa) [49]. This can be explained by the fact that fibers increase the strength of concrete and hinder the propagation of cracks. Although the fiber density may cause an increase in gaps and pores around the fibers because it hinders the homogeneous distribution of pozzolanic particles to fill the pores, these fibers increase the cohesion of the matrix and increase its tensile capacity. Concrete reinforced with polyvinyl alcohol (PVA) fibers exhibits the highest splitting tensile strength, followed by concrete reinforced with basalt fibers. This indicates that the basalt fiber interface exhibited the highest Ca/Si ratio (1.59), followed by the PVA fiber-mortar interface (1.33 This indicates that PVA fibers are hydrophilic, leading to hydrophilic interactions between the PVA fibers and the mortar matrix and increased C-S-H formation. Basalt fibers also possess stronger chemical bond strength with the mortar matrix due to their similar chemical compositions [50, 51]. This improvement is attributed to the effect of basalt and PVA fibers in slowing crack propagation and enhancing matrix ductility. Figure (14) show the cylinder before and after failure.

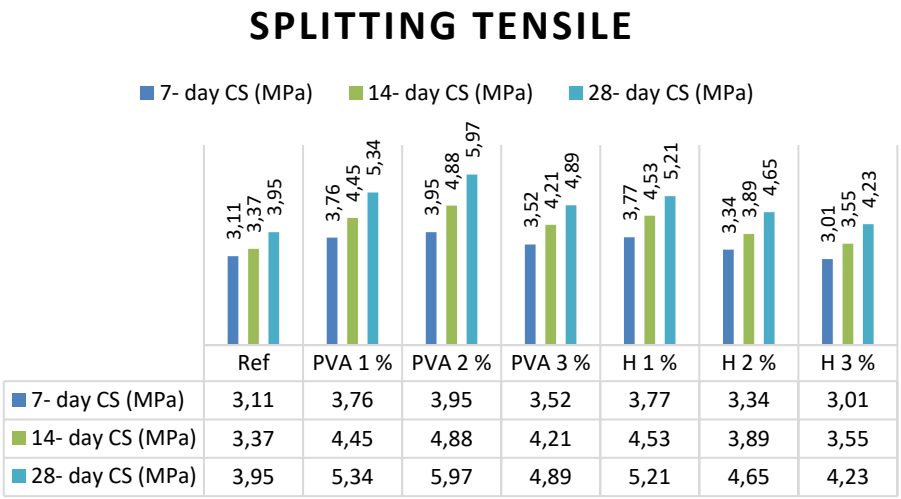

	Ref	PVA 1 %	PVA 2 %	PVA 3 %	H 1 %	H 2 %	H 3 %
7- day CS (MPa)	3,11	3,76	3,95	3,52	3,77	3,34	3,01
14- day CS (MPa)	3,37	4,45	4,88	4,21	4,53	3,89	3,55
28- day CS (MPa)	3,95	5,34	5,97	4,89	5,21	4,65	4,23

Fig. 13. The splitting tensile of different mixing ratio

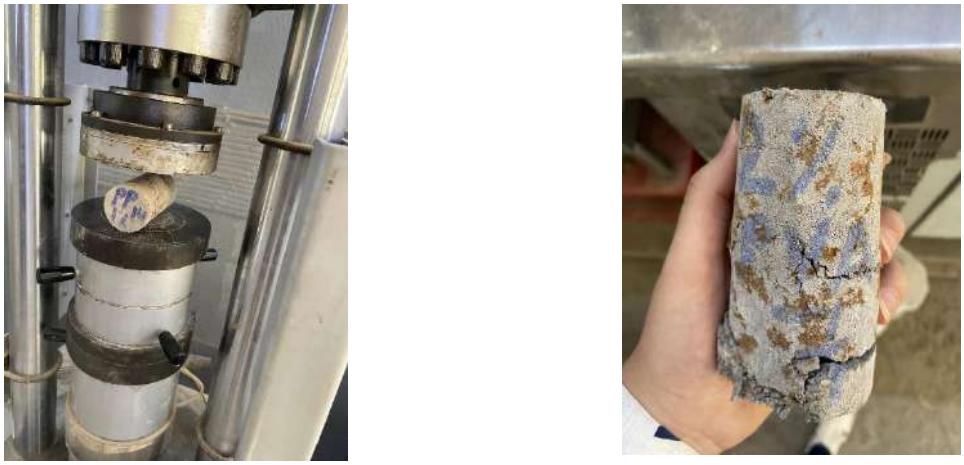

Fig. 14. The cylinder before and after failure

3.7. Scanning Electron Microscope (SEM)

Figure (15) shows the internal structure of the reference mixture. The microstructure of the reference sample exhibited numerous microcracks and pores. The lack of fibers resulted in a weaker interface between the cement matrix and the concrete, resulting in lower tensile and flexural strengths.

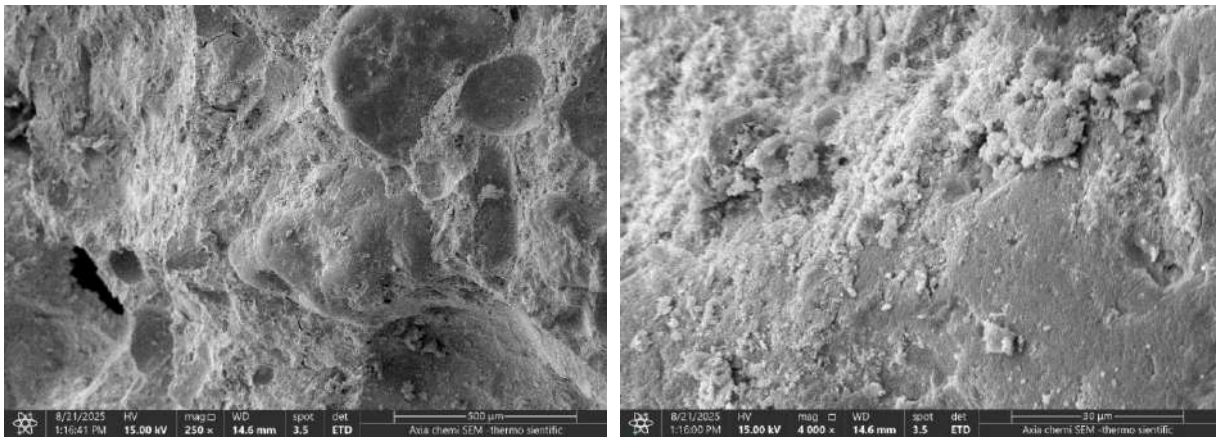

Fig. 15. The SEM of microstructure surface of control sample

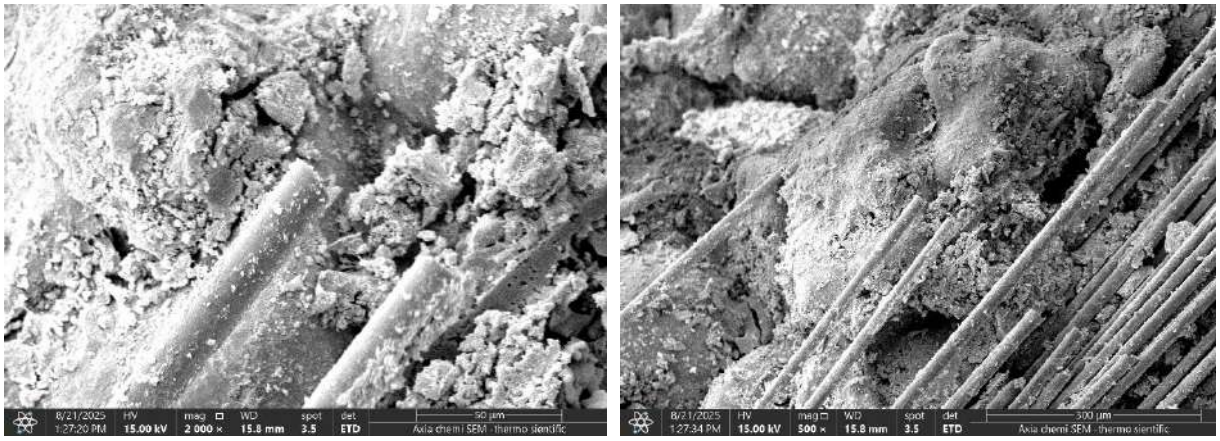

Fig. 16. The SEM of microstructure surface of 3% addition of BF sample

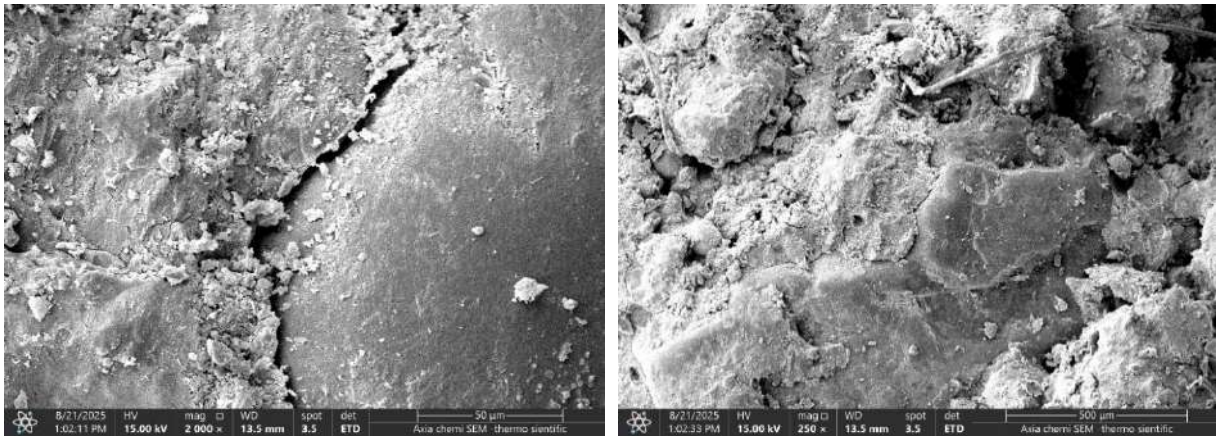

Fig. 17. The SEM of microstructure surface of 2% addition of PVA sample [27]

The absence of fibers or nanoparticles resulted in increased porosity and a relative decrease in structural integrity when compared to reinforced samples. The scanning electron microscope image shown in Figure (16) shows that basalt fibers are dispersed throughout the cement matrix. These fibers act as microscopic bridges between particles, making it difficult for microcracks to pass through and propagate through the cement matrix. This makes the cement stronger in both tensile and flexural strength. The fibers are connected to the cement paste, showing good bonding between the fibers and the matrix. This makes the material stronger and more flexible. However, some lumps and pores can be seen in small places due to the silica not being allowed to diffuse within the matrix, making the structure less regular.[52] A scanning electron microscope image of a 2% PVA sample shows that the fibers are not very evenly distributed within the cement matrix,

and that there are pores and pozzolanic agglomerates. Despite the presence of some pores, the mechanical properties are high, but at the expense of a slight increase in water absorption. Therefore, the presence of fibers improves compressive and flexural properties, making the material stiffer and stronger than the reference sample [40, 51, 52].

4. Conclusions

Based on the experimental studies and analytical results obtained in this study, several key findings can be highlighted regarding the effect of basalt fiber (BF) and polyvinyl alcohol (PVA) fibers on the mechanical and thermal performance of cement boards. The following points summarize the most important findings:

- The combination of basalt fiber (BF) and polyvinyl alcohol (PVA) fibers significantly improved the mechanical and thermal performance of cement boards.
- Basalt fibers at a concentration of 3% achieved the greatest improvement, achieving superior compressive strength (45.28 MPa), flexural strength (11.23 MPa), and the lowest thermal conductivity (0.644 W/m°C).
- PVA fibers demonstrated optimal performance at a concentration of 2%, achieving a compressive strength of 43.43 MPa and a moderate improvement in flexural strength.
- Both fiber types increased water absorption compared to the standard mix, indicating a balance between mechanical improvement and strength.
- Scanning electron microscope (SEM) analysis confirmed that the fibers act as microbridges, reduce crack propagation, and improve the cohesion of the cement matrix.
- The combined use of fibers and silica fume demonstrated synergistic effects, resulting in improved strength, strength, and structural integrity.
- The 2% PVA and 3% BF fibers exhibited the highest surface harnesses (99.97 and 99.92 MPa) compared to the reference mix.
- The 1% BF and 1% PVA fibers achieved the highest internal density/integrity in the UPV test, 6.61% and 6.3%, respectively, compared to the reference mix.
- Finally, the splitting tensile strengths of concrete reinforced with PVA fibers and basalt fibers were tested. The results showed that concrete reinforced with 2% PVA fibers had the highest splitting tensile strength, followed by 3% basalt fibers. This indicates that the interface bond properties obtained depend to some extent on the behavior of the fiber and mortar surfaces in the concrete materials. The increase was 51.14% and 31.90%, respectively, compared to the reference mix.

Overall, the study recommends using 3% (BF) and 2% (PVA) as the most effective reinforcement ratios for producing durable, high-performance, and thermally efficient cementitious panels.

Acknowledgement

The authors would like to acknowledge the Department of Materials Engineering, Mustansiriyah University, for providing the facilities and support necessary to complete this research. Special thanks are also extended to Prof. [Mohammed J. Kadhim] for his invaluable guidance and encouragement. The authors are grateful to their colleagues for their assistance during the laboratory experiments

References

[1] Purayil AFA. Effect of modified cellulose on open time of glue mortar: an NMR study on transport and hydration. 2019.
[2] Branston J, Das S, Kenno SY, Taylor C. Mechanical behaviour of basalt fibre reinforced concrete. Constr Build Mater. 2016;124:878-86. https://doi.org/10.1016/j.conbuildmat.2016.08.009
[3] Wienand N. Theory and architectural technology. Architectural Technology: Research & Practice. 2013;1-18. https://doi.org/10.1002/9781118292365.ch1
[4] Świt G, Krampikowska A. Influence of the number of acoustic emission descriptors on the accuracy of destructive process identification in concrete structures. In: 2016 Prognostics and System Health Management Conference (PHM-Chengdu). IEEE; 2016. p. 1-5. https://doi.org/10.1109/PHM.2016.7819756

[5] Chinh LM, Adamczak A, Krampikowska A, Świt G. Dragon bridge - the world largest dragon-shaped (ARCH) steel bridge as element of smart city. E3S Web Conf. 2016;10:00106. https://doi.org/10.1051/e3sconf/20161000106
[6] Schabowicz K, Jóźwiak-Niedźwiedzka D, Ranachowski Z, Kudela S Jr, Dvorak T. Microstructural characterization of cellulose fibres in reinforced cement boards. Arch Civ Mech Eng. 2018;18(4):1068-78. https://doi.org/10.1016/j.acme.2018.01.018
[7] Adamczak-Bugno A, Świt G, Krampikowska A. Fibre-cement panel ventilated façade smart control system. Materials (Basel). 2021;14(17):5076. https://doi.org/10.3390/ma14175076
[8] Udebunu J, Abdolpour H, Sadowski Ł. Comprehensive experimental investigation of the mechanical properties and performance enhancement of polyvinyl alcohol fiber-reinforced cement mortar. Arch Civ Mech Eng. 2024;25(1):58. https://doi.org/10.1007/s43452-024-01113-2
[9] Singha K. A short review on basalt fiber. Int J Textile Sci. 2012;1(4):19-28.
[10] King MFL, Srinivasan V, Purushothaman T. Basalt fiber: an ancient material for innovative and modern application. Middle-East J Sci Res. 2014;22(2):308-12.
[11] Esmaeeli E. Development of hybrid composite plate (HCP) for strengthening and repair of RC structures [thesis]. Braga (Portugal): Universidade do Minho; 2015.
[12] Li VC, Wang S, Wu C. Tensile strain-hardening behavior of polyvinyl alcohol engineered cementitious composite (PVA-ECC). ACI Mater J. 2001;98(6):483-92. https://doi.org/10.14359/10851
[13] Liu B, Zhao X, Liu X, He Z, Cao X, Guan B. Evaluation of workability and mechanical properties in cement mortar after compounding igneous rock powder and silica fume. Buildings. 2024;14(2):359. https://doi.org/10.3390/buildings14020359
[14] ASTM C150-04. Standard specification for Portland cement. Annu Book ASTM Stand. 2004;4.
[15] Iraqi Standard Specification No. 5/1984. Portland cement. Baghdad (Iraq): Central Organization for Standardization & Quality Control (COSQC); 1984.
[16] ASTM C778-13. Standard specification for standard sand. West Conshohocken (PA): ASTM International; 2013.
[17] ASTM C1240-05. Standard specification for silica fume used in cementitious mixtures. Manual of A04-02. 2007.
[18] Grigoryan A. Improvement of the cement mortar characteristics reinforced with basalt fibers. J Archit Eng Res. 2025;8:12-21. https://doi.org/10.54338/27382656-2025.8-02
[19] ASTM C494. Standard specification for chemical admixtures for concrete. Annu Book ASTM Stand. 2013.
[20] Çakır Ö, Sofyanlı ÖÖ. Influence of silica fume on mechanical and physical properties of recycled aggregate concrete. HBRC J. 2015;11(2):157-66. https://doi.org/10.1016/j.hbrcj.2014.06.002
[21] Ahmadi MNJ, Naeemi NA, Amin S. Effect of partial replacement of cement by silica fume on strength of high-strength concrete. Sci Educ. 2024;5(3):184-94.
[22] ASTM C109/C109M-13. Standard test method for compressive strength of hydraulic cement mortars (using 2-in. or [50-mm] cube specimens). Annu Book ASTM Stand. 2013;4(1):1-9.
[23] ASTM C348. Standard test method for flexural strength of hydraulic-cement mortars. Am Soc Test Mater. 2008;348.
[24] ASTM D2240-05. Standard test method for rubber property - durometer hardness. West Conshohocken (PA): ASTM International; 2005.
[25] ASTM C496/C496M-04. Standard test method for splitting tensile strength of cylindrical concrete specimens. Annu Book ASTM Stand. 2004.
[26] Bu Y, Spragg R, Weiss WJ. Comparison of the pore volume in concrete as determined using ASTM C642 and vacuum saturation. Adv Civ Eng Mater. 2014;3(1):308-15. https://doi.org/10.1520/ACEM20130090
[27] Benmokrane B, Manalo A, Bouhet JC, Mohamed K, Robert M. Effects of diameter on the durability of glass-fiber-reinforced-polymer (GFRP) bars conditioned in alkaline solution. J Compos Constr. 2017;21(5):1-12. https://doi.org/10.1061/(ASCE)CC.1943-5614.0000814
[28] ASTM C. Standard test method for thermal conductivity of refractories by hot wire (platinum resistance thermometer technique). ASTM C1113-2013; 2013.
[29] Mehta PK, Monteiro PJ. Concrete Microstructure, Properties, and Materials. New York: McGraw-Hill; 2006.
[30] Al-Kharabsheh BN, et al. Basalt fibers reinforced concrete: Strength and failure modes. Materials. 2022;15(20):7350. https://doi.org/10.3390/ma15207350
[31] Durmaz M. Synergistic effects of steel fibers and silica fume on concrete exposed to high temperatures and gamma radiation. Buildings. 2025;15(11):1830. https://doi.org/10.3390/buildings15111830
[32] Zang Y, et al. Assessing interfacial bonding performance of PVA fiber and cement hydration products: An atomic simulation. J Mater Civ Eng. 2024;36(3):04023596. https://doi.org/10.1061/JMCEE7.MTENG-16462
[33] Chen Z, et al. Influence of modified PVA fiber on ultra-high performance concrete and its enhancing mechanism. Polymers. 2024;16(23):3449. https://doi.org/10.3390/polym16233449

[34] Li VC. Engineered Cementitious Composites (ECC): Bendable Concrete for Sustainable and Resilient Infrastructure. Cham: Springer; 2019. https://doi.org/10.1007/978-3-662-58438-5
[35] AL-Masraf HM, AL-Attar TS, Freyyah QJ. Mechanical and thermal performance of engineered cementitious composite concrete produced by using polyvinyl alcohol fibers. Eng Technol J. 2024;42(11):1290-1303. https://doi.org/10.30684/etj.2024.146641.1691
[36] ASTM C. Standard test method for density, absorption, and voids in hardened concrete. ASTM C642-13; 2013.
[37] Gencel O, et al. Basalt fiber-reinforced foam concrete containing silica fume: An experimental study. Constr Build Mater. 2022;326:126861. https://doi.org/10.1016/j.conbuildmat.2022.126861
[38] Badalyan MM, et al. Effect of silica fume concentration and water-cement ratio on the compressive strength of cement-based mortars. Buildings. 2024;14(3):757. https://doi.org/10.3390/buildings14030757
[39] Wu Z, Shi C, Khayat KH. Influence of silica fume content on microstructure development and bond to steel fiber in ultra-high strength cement-based materials (UHSC). Cem Concr Compos. 2016;71:97-109. https://doi.org/10.1016/j.cemconcomp.2016.05.005
[40] Hu S, Cai H, Hong R, Li M, Yao F. Performance test and microstructure of modified PVC aggregate-hybrid fiber reinforced engineering cementitious composite (ECC). Materials. 2021;14(8):1856. https://doi.org/10.3390/ma14081856
[41] Xu W, et al. Study on the correlation between mechanical properties, water absorption, and bulk density of PVA fiber-reinforced cement matrix composites. Buildings. 2024;14(11):3580. https://doi.org/10.3390/buildings14113580
[42] Yan L, et al. Review of research on basalt fibers and basalt fiber-reinforced composites in China (I): Physicochemical and mechanical properties. Polym Polym Compos. 2021;29(9):1612-1624. https://doi.org/10.1177/0967391120977396
[43] Lin Y, Shih-Fang K, Hsiao C, Chao-Peng L. Investigation of pulse velocity-strength relationship of hardened concrete. ACI Mater J. 2007;104(4):344. https://doi.org/10.14359/18823
[44] Vejmelková E, Černý R. Thermal properties of PVA-fiber reinforced cement composites at high temperatures. Appl Mech Mater. 2013;377:45-49. https://doi.org/10.4028/www.scientific.net/AMM.377.45
[45] Hong G, Oh S, Choi S, Chin WJ, Kim YJ, Song C. Correlation between the compressive strength and ultrasonic pulse velocity of cement mortars blended with silica fume: An analysis of microstructure and hydration kinetics. Materials. 2021;14(10):2476. https://doi.org/10.3390/ma14102476
[46] Al-Kharabsheh BN, et al. Basalt fiber reinforced concrete: A compressive review on durability aspects. Materials. 2023;16(1):429. https://doi.org/10.3390/ma16010429
[47] Hedjazi S, Castillo D. Relationships among compressive strength and UPV of concrete reinforced with different types of fibers. Heliyon. 2020;6(3):e03542. https://doi.org/10.1016/j.heliyon.2020.e03646
[48] Yang G, Dong Z, Bi J, Zhao K, Li F. Experimental study on the dynamic splitting tensile properties of polyvinyl-alcohol-fiber-reinforced cementitious composites. Constr Build Mater. 2023;383:131233. https://doi.org/10.1016/j.conbuildmat.2023.131233
[49] Sim J, Park C. Characteristics of basalt fiber as a strengthening material for concrete structures. Compos Part B Eng. 2005;36(6-7):504-512. https://doi.org/10.1016/j.compositesb.2005.02.002
[50] Sgriccia N, Hawley M, Misra M. Characterization of natural fiber surfaces and natural fiber composites. Compos Part A Appl Sci Manuf. 2008;39(10):1632-1637. https://doi.org/10.1016/j.compositesa.2008.07.007
[51] Hong L, Chen Y, Li T, Gao P, Sun L. Microstructure and bonding behavior of fiber-mortar interface in fiber-reinforced concrete. Constr Build Mater. 2020;232:117235. https://doi.org/10.1016/j.conbuildmat.2019.117235
[52] Li VC, Horikoshi T, Ogawa A, Torigoe S, Saito T. Micromechanics-based durability study of polyvinyl alcohol-engineered cementitious composite. Mater J. 2004;101(3):242-248. https://doi.org/10.14359/13120

Research on Engineering Structures & Materials
www.jresm.org
Research Group

Research Article

Fabrication and mechanical behavior of Kevlar® fabric-reinforced epoxy matrix composites modified by potassium titanate whiskers

Ravikiran Kamath B. [*,1,a], Sudheer M. [2,b]

[1]*Nitte (Deemed to be University), NMAM Institute of Technology (NMAMIT), Department of Mechanical Engineering, Nitte-574110, Udupi, Karnataka, India and Visvesvaraya Technological University, Belagavi-590018, Karnataka, India*
[2]*Department of Mechanical Engineering, St Joseph Engineering College, Vamanjoor-575028, Mangaluru, Karnataka, India and Visvesvaraya Technological University, Belagavi-590018, Karnataka, India*

Article Info

Article History:

Received 20 Jan 2025

Accepted 15 Aug 2025

Keywords:

Aramid epoxy;
Whiskers;
Hand lay up;
Mechanical tests;
Polymer matrix composites

Abstract

Polymer matrix composites have become quite popular in the field of materials engineering owing to their high strength to weight ratios and cost effectiveness. Several synthetic fibers have been employed as reinforcement with thermoset resin as the matrix in order to achieve improved mechanical or tribological performance of the composite. A secondary reinforcement known as filler is believed to further enhance these properties. In this paper, the influence of Potassium Titanate Whiskers (PTW) as reinforcing fillers on the mechanical performance of Kevlar ® /Epoxy composite combination has been discussed. Composite samples were fabricated by hand lay-up method followed by compression by altering the weight percentage of the whiskers in the order of 0%, 2%, 4%, 6% and 8%. Mechanical tests like tensile, flexural, impact and hardness were conducted on the developed composite samples as per ASTM standards. The results indicated that the inclusion of PTW into Kevlar® /Epoxy system influenced the mechanical properties of the composites. Compared to the unfilled composites, the tensile strength increased by 6.39%, flexural strength increased by 6.32%, impact strength increased by 22.96%, and Shore D hardness value increased by 9.62% for 2 wt. % PTW. However, the mechanical properties showed a declining trend beyond PTW loading of 2 wt. %. Selected tensile specimens were analyzed through Scanning Electron Microscope (SEM) images to understand their failure mechanisms.

© 2025 MIM Research Group. All rights reserved.

1. Introduction

Polymer Matrix Composites (PMC), sometimes referred to as organic matrix composites are a class of composites which have become increasingly popular in recent times due to their ease in processing compared to metal or ceramic matrices, possessing of lesser weight and exceptional mechanical performance. As a result, these polymer composites are employed in a variety of applications ranging from household to aeronautical, from construction to military, from marine to electronics and so on [1,2]. The polymer used in a PMC may be either a thermoplastic or a thermosetting material. Though thermoplastics offer several advantages including lower cost than most of the metallic matrices, their non bio-degradable nature poses a greater challenge. On the other hand, though thermosets cannot be reshaped or recycled, they are highly cost effective compared to their thermoplastic counterparts and are ideal for high temperature applications.

*Corresponding author: ravikiran@nitte.edu.in
[a]orcid.org/0000-0001-5137-5089; [b]orcid.org/0000-0003-0869-2876
DOI: http://dx.doi.org/10.17515/resm2025-632me0120rs

Thermosetting polymers like phenolic, polyimide, polyurethane etc. have been used as matrix materials elsewhere [3-5]. Epoxy is a polymer which has become increasingly popular among the thermosetting resins, owing to its exceptional adhesion, tensile strength and chemical stability. It is noteworthy to mention that a few researchers have also attempted the fabrication of polymer composites with epoxy resin modified by additives, curing agents or fillers in order to improve the mechanical performance of the epoxy matrix [6-10].

It is a well-known fact that a composite material comprises of a particle or a fiber phase along with the matrix phase. In recent times, Fiber Reinforced Polymer (FRP) Composites are employed in applications like construction, automotive, aerospace, marine [11]. The fiber reinforcements are either naturally available or are synthetic. Natural fibers offer advantages like biodegradability and ease of processing. In spite of this, their incompatible quality, absorption of moisture and reduced impact properties restrict their usage to some extent. Contrary to this, the synthetic fibers being more durable and wear resistant have gained popularity in tribological applications. Literatures reveal that fibers of banana, rice husk, kenaf, chicken feather, cotton, sisal, jute have been used as natural reinforcements, while those made of glass, carbon, basalt, Kevlar® have been used as synthetic reinforcements. Kevlar® is a type of aramid fiber which offers greater tensile strength than carbon fibers, possesses excellent chemical resistance, lesser weight and is nearly unaffected by moisture. Hence, it is a popular material for body armors, ballistic garments and boats [12]. In addition to the matrix and fiber phases, it is customary to incorporate one or more materials as fillers within the matrix phase in order to further improve the mechanical or tribological performance of the PMC. The resulting composite is generally termed as a hybrid composite material. Fillers may be inorganic, organic or metallic with their sizes varying from micron to nano levels. In recent times, filler materials in the form of whiskers have gained significant attention, particularly for tribological applications. These whiskers are a type of single crystal acicular materials when observed under microscope. However, they appear in powdery form with their length ranging from a few to hundred microns. They have a definite aspect ratio and are nearly defect-free due to their small diameter. Whiskers when reinforced with polymers are known to exhibit extraordinary mechanical and physical properties [13]. Whiskers of SiC, Si_3N_4, Aluminum Borate, $CaCO_3$, ZnO, MgO, $CaSO_4$, SiO_2, TiO_2 etc. have been employed as fillers elsewhere [14]. Among the aforementioned whiskers, ceramic whiskers like SiC, ZnO, MgO etc. dominate the metallic whiskers owing to their enhanced strength capabilities and are widely employed with polymer matrices. Potassium Titanate whisker (PTW) is one such inorganic ceramic whisker which possesses outstanding mechanical properties and is a cost effective alternative to SiC in most of the applications involving friction and wear. They have a tunneling structure which makes them chemically and physically stable [15]. Though PTW are used as thermal and electrical insulating materials, yet their most popular application continues to be as a reinforcement in polymer composites. Currently, polymer resins employed with PTW include Polyetheretherketone (PEEK), Polyamide-6, Polyamide-66, Acrylonitrile Butadiene Styrene (ABS), Poly Vinyl Chloride (PVC) and polycarbonate (PC). S.C. Tjong et. al [16] developed ABS/PC blended composites with PTW as reinforcement. Mechanical tests revealed that the tensile strength of ABS/PC as well as ABS blends increased with the PTW content. But the tensile strength of PC/PTW blends decreased with the whisker content. This was attributed to the decomposition of PC during compounding, which was further stimulated by these whiskers. The results also emphasized on the fact that PTW can be used to increase the strength of the ABS/PC composites up to 40 wt. % PC. M. Sudheer et al. [17] investigated the mechanical properties of Glass/Epoxy filled with PTW and observed that the tensile strength of the filled composite decreased by 11 % compared to the unfilled composite. These whiskers restricted the plastic deformation of epoxy, thereby lowering its failure strain under tensile conditions. However, a small quantity of graphite added into PTW filled composites improved the tensile strength by 6%. H. Bettegowda et al. [18] developed polyethersulfone (PES)/short carbon fiber (SCF) composite with PTW and ultra-high molecular weight polyethylene (UHMWPE) as fillers. The results of mechanical tests revealed that adding 5 wt. % PTW improved the tensile and flexural properties of the composite, but decreased its impact property. B. Suresha et al. [19] performed mechanical tests on carbon/epoxy system modified with PTW fillers. Results indicated that inclusion of PTW improved the tensile strength as well as modulus of the composites up to 5 wt. %, beyond which it reduced. While aspect ratio and stress between the interfaces remain

the same, the increase in tensile properties is owing to the increase in the interaction between the filler and the matrix. There exists only a limited work in literatures reported on studying the effect of incorporating these whiskers as reinforcing fillers in an epoxy polymer matrix. This paper attempts to present a study of the influence of PTW addition on the mechanical properties of Kevlar®/epoxy composites.

2. Experimental Details

2.1. Materials

In this study, two different types of reinforcements were incorporated into the epoxy matrix namely, a woven fabric and a whisker. High strength and high modulus plain woven Kevlar® fabric having aerial density 220 GSM and filament diameter 12 μm was used as the macro scale reinforcing filler. It was procured from CF Composites, New Delhi, India. PTW of diameter 0.2—2.5μm and length 10—100μm was used as the micro scale ceramic reinforcing filler, procured from Hangzhou Dayangchem Co. Ltd., Hong Kong. Room temperature curing epoxy LY556 was used as the matrix material and HY951 as the amino based hardener. The polymer was supplied by M/S Herenba Instruments & Engineers, Chennai, India. The epoxy and hardener were mixed in the proportion 10:1 by weight, as provided by the supplier. Some of the salient properties of fiber, matrix and filler materials used in the study, as provided by the respective suppliers, is presented in Table 1. The Kevlar ® fibers and PTW were used for fabrication of the PMC without subjecting them to any surface modifications.

Table 1. Salient material properties

Property (Unit)	Kevlar®	Epoxy	PTW
Tensile strength (GPa)	3.097	0.093	7
Young's Modulus (GPa)	105	3	280
Density (g/cc)	1.44	1.15	3.185

2.2. Methodology

The composite samples were prepared adopting hand layup technique followed by compression in a Universal Testing Machine (UTM) by varying the filler weight percent in the order of 0 %, 2 %, 4 %, 6 % and 8 %. (600 kN, Model UTN60, Fuel Instruments & Engineers Pvt. Ltd., Maharashtra, India). Two mild steel plates of 400 x 600 x 10 mm^3 were used as the top and bottom mold plates. The mold plates were tightly wrapped with PVC (Poly Vinyl Chloride) sheets leaving no air gap between the mold plate and the sheets. Duct tapes were adhered on the center of the bottom mold plate upon which the fiber layers are laid, so as to form a boundary around the sample. This was also done in order to ensure that there was little or no resin starving regions in the sample. The PVC sheets were then applied with wax coating for easier release of the sample from the mold plates.

To begin with, 9 layers of Kevlar® fibers of size 300 x 300 mm were cut from the fabric roll and weighed. The choice of the number of layers was based on the sample calculations to achieve the recommended thickness of 3 mm. The fiber weight percent was kept constant at 50 % and different samples were fabricated by altering the weight percent of PTW. A known quantity of PTW fillers were added to a ceramic crucible and preheated to 80° C for 2 hours in a hot air oven to get rid of any moisture present. It was then allowed to cool down to ambient temperature outside the oven. Hao et. al [20] reported that whiskers are vulnerable to damage during processing because of their large aspect ratios, and hence high speed mixers are not suitable. So, after 24 hours, the whiskers were steadily introduced into epoxy and continuously stirred using mechanical mixing method until uniform dispersion was achieved. The amino based hardener was then added to the resin-whisker mixture in the ratio 1:10. This mixture was applied on the 9 plies of Kevlar® fabric one after another and subjected to rolling for uniform adhesion of individual layers. Care was taken to ensure that enough time was available for coating all the layers. After the final layer was laid, it was

allowed to settle for 15 minutes and finally the top mold plate was placed over it. This was followed by subjecting the mold plates to compression in an UTM under a load of 250 kN. The sample was released from the mold plate after 24 hours of curing time. The fabricated samples had dimensions 300 x 300 x 3 mm^3. For comparison, Kevlar®-epoxy composite samples without the inclusion of whiskers were also fabricated using hand layup.

Following the identical conditions and methodology, three samples for every weight percent of PTW was prepared. Each sample so prepared was carefully machined to obtain three specimens for conducting mechanical tests like tensile, flexure, impact and hardness as per ASTM standards. All specimens were machined using a switch board cutting machine. A flowchart showcasing the various stages of fabrication is presented (Fig. 1).

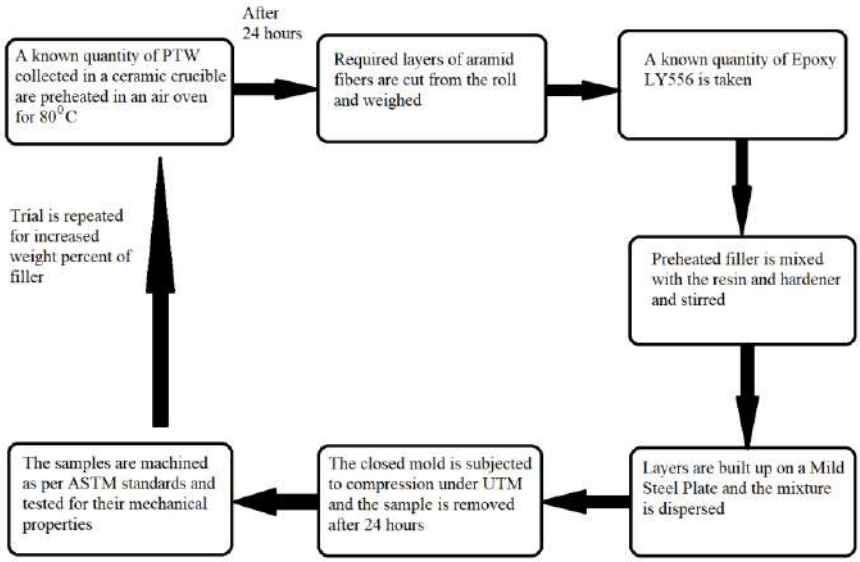

Fig. 1. Flowchart describing the various stages of fabrication

The details of the fabricated composite samples with regard to their composition and designation is presented in Table 2.

Table 2. Composition and designation of composites

Composite designation	Composition of materials		
	PTW (wt. %)	Kevlar® fibers (wt. %)	Epoxy (wt. %)
EK0	0	50	50
EK2	2	50	48
EK4	4	50	46
EK6	6	50	44
EK8	8	50	42

2.3. Mechanical Tests

All the mechanical tests were performed as per ASTM standards and at room temperature. R. F. Faidallah et. al [21] conducted studies on the efficacy of various geometries of the tensile specimen and concluded that a rectangular section specimen exhibited greater tensile strength as it eliminated the stress concentration effect at the gripping ends and the specimen would fail near the gauge length portion. Keeping this in mind, the tensile test was conducted on a Computerized twin screw UTM (Model Vector, International Equipments, Mumbai, India) according to ASTM D 3039 using a rectangular specimen having dimensions 150 x 12.5 x 3 mm^3. The loading capacity of the UTM was 1000 kg with a resolution of 0.1 kg, the cross travel was 1000 mm and the cross head speed was 2 mm/min. The Izod Impact test was conducted as per ASTM D256—10 on a Computerized impact tester (25 J, Model LT-160, International Equipments, Mumbai, India) with

specimen dimensions 60 x 12.5 x 3 mm^3 using R4 hammer, resolution 0.05 J and a V-notch of 2 mm (Motorized notch cutter, International Equipments, Mumbai, India). Three-point flexure test was performed on the same computerized twin screw UTM as per ASTM D790—10 with specimen dimensions 90 x 12.5 x 3 mm^3, span length of 50 mm, cross head speed of 2 mm/min, and the travel limit was also set to 50 mm to reduce the waiting time after performing the test. Shore D hardness test was conducted as per ASTM D2240 using a Shore D Durometer (Model 560—10D, Gain Express, Hong Kong) having measuring range from 0—100 Shore D units (HD), resolution of 0.5 HD and 30° cone indentor, indentation depth of up to 2.5 mm and measuring force of up to 44.5 N. The images of tensile, flexure and impact test specimen before conducting the test for 2 wt. % PTW is shown (Fig. 2) and Fig. 3 illustrates the various mechanical tests conducted along with the fractured tensile test specimen.

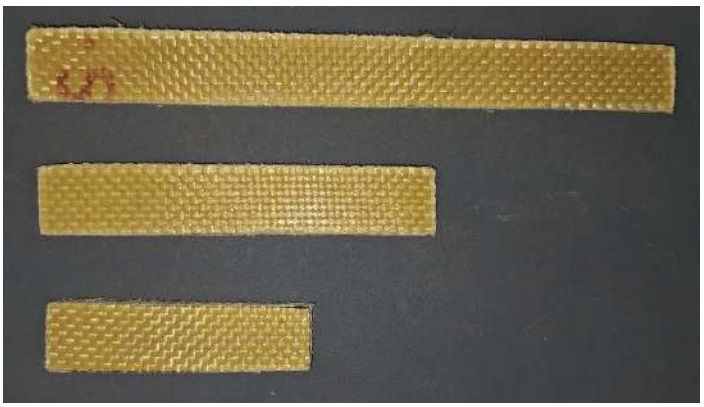

Fig. 2. The machined tensile, flexural and impact test specimen (2 wt. % PTW)

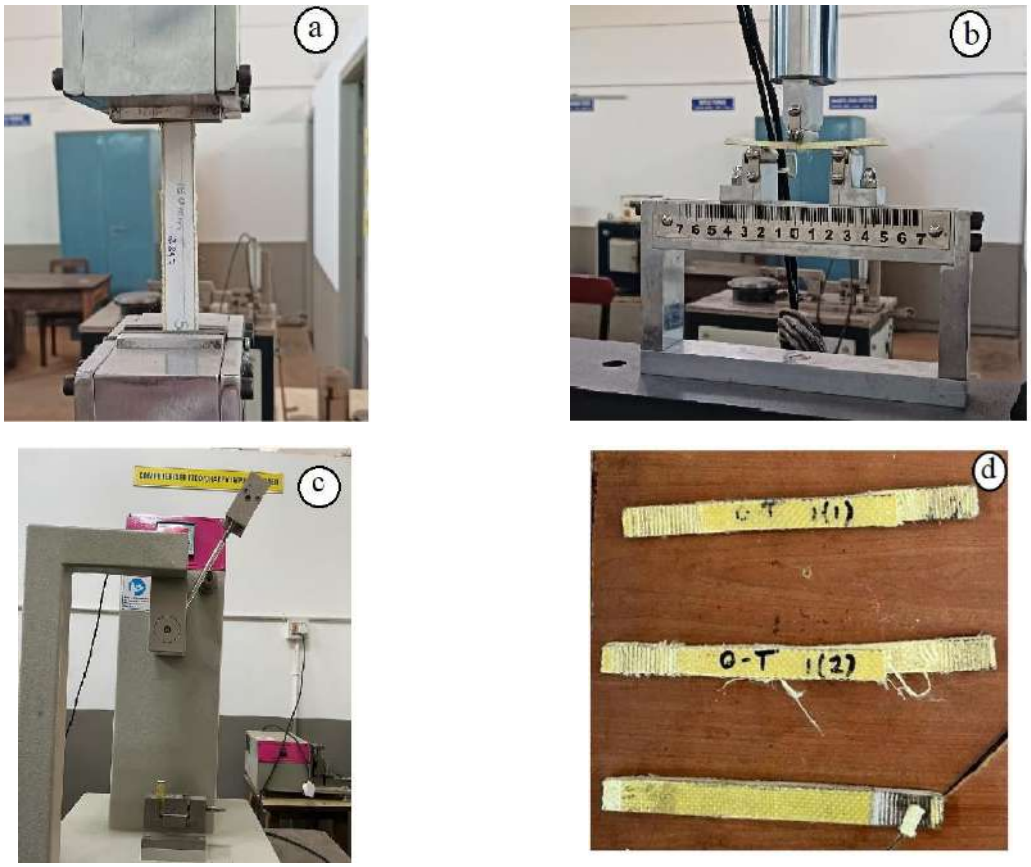

Fig. 3. (a) Tensile test (b) Flexure Test (c) Izod impact test (d) Broken tensile test specimen

3. Results and Discussion

The results reported in this section represent the average values of the mechanical properties of the three samples. From every sample, three specimens were taken for conducting each of the mechanical tests.

3.1. Hardness

The Shore D hardness measurements indicated a significant enhancement in surface resistance with the incorporation of PTW into the Kevlar®-epoxy composite system. Specifically, the composite designated EK2 exhibited a hardness of 76 HD reflecting a 9.62% increase over the unfilled composite EK0 (69 HD). This increase in hardness could be attributed to the moderate hardness (Mohs scale 4) of PTW, which when introduced into a softer epoxy matrix, resists the surface deformation of the composite and improves resistance to surface indentation. Few studies [22] reveal that at lower filler concentrations (typically up to 3 wt. %), the whiskers tend to disperse uniformly within the matrix, facilitating effective reinforcement of the surface. However, a reverse trend was observed in the EK4 composite, where the hardness decreased by approximately 5.26% compared to EK2. This decline is likely a consequence of the poor dispersion of these whiskers at higher filler loading, which can promote agglomeration and generate localized stress concentration. Such zones not only deteriorate load transfer capability but also introduce microstructural weaknesses that reduce the material's ability to resist indentation. As the PTW content increased further in EK6 and EK8, the hardness values stabilized around 71–72 HD. This plateau suggests that beyond a certain threshold, the reinforcing effect of PTW becomes saturated, and additional filler content contributes marginally to mechanical improvement. Nevertheless, the EK8 composites exhibited 3.96% higher hardness than neat epoxy (EK0).

3.2. Impact Strength

The Izod impact test results revealed that the incorporation of PTW significantly influenced the impact strength of the Kevlar®-epoxy composites. The results indicated that the EK2 composite demonstrated an impact strength of 1.828 J/mm reflecting a 22.96% increase compared to the unfilled composite EK0 (1.487 J/mm). These whiskers being quite rigid serve as reinforcement, acting as a barrier to crack growth particularly at lower concentrations thereby increasing the composite's impact energy absorption. At these concentrations, the whiskers are more likely to be uniformly dispersed, forming an efficient interface for stress transfer and acting as effective barriers to crack initiation and growth. However, a decline in impact performance was observed at higher filler loadings. The EK8 composite exhibited a reduced impact strength of 1.412 J/mm, which is 5.04% lower than that of EK0. This suggests that higher concentration of PTW decreased the capability of Kevlar®/Epoxy composites to curb the impact load. This could be likely due to agglomeration of whiskers and such clustering can act as stress concentrators, resulting in weakened performance of the composite under impact conditions. These findings are consistent with prior studies [23] indicating that high loadings of ceramic fillers, particularly those with high aspect ratios like PTW, tend to embrittle polymer matrices and reduce their impact energy absorbing capacity. Interestingly, intermediate PTW loadings showed a non-monotonic trend with intermittent increases in impact strength, which may be indicative of the formation of a semi-continuous whisker network within the matrix. Such a microstructure could enhance load transfer efficiency, thereby boosting its toughness temporarily. The variation of impact strength and Shore D hardness values with respect to the whisker content is illustrated in Table 3.

Table 3. Impact strength and hardness of various composites

Composite designation	Material property(Unit)	
	Impact strength (J/mm)	Shore D hardness (HD)
EK0	1.487 ± 0.72	69
EK2	1.828 ± 0.76	76
EK4	1.295 ± 0.42	72
EK6	1.722 ± 0.52	71
EK8	1.412 ± 0.38	72

3.3. Tensile Properties

Table 4 presents the variation of tensile strength, tensile modulus and percentage elongation at break with respect to the whisker content. The tensile test results revealed a notable influence of PTW incorporation on the mechanical performance of Kevlar®-epoxy composites. The EK2 composite exhibited a 6.39% increase in tensile strength compared to the neat epoxy composite (EK0), suggesting that at low filler concentrations, PTW effectively reinforces the matrix. This increasing trend is more likely because of the efficient bonding of PTW with epoxy and an adequate dispersion of these whiskers, which must have improved the composite's load transfer capabilities and resistance to crack growth. However, as the PTW content was increased to 4 wt.% (EK4), the tensile strength dropped significantly, by approximately 23.66%. This degradation in strength can be attributed to several factors. Firstly, these ceramic whiskers increase the viscosity of the matrix at higher loading which result in poor wetting and void formation during processing. Secondly, increased PTW content might have possibly made the matrix more brittle, reducing the composite's tensile strength. Beyond 4 wt.% PTW loading, the tensile strength plateaued, with no significant recovery observed even at 8 wt.% (EK8), which exhibited a 16.87% reduction in tensile strength relative to EK0.

Table 4. Tensile properties of various composites

Composite designation	Material property (Unit)		
	Tensile modulus (GPa)	Tensile strength (MPa)	Percentage elongation (%)
EK0	3.48 ± 0.25	368.8 ± 34.63	12 ± 0.78
EK2	3.86 ± 0.57	392.3 ± 39.35	12 ± 1.35
EK4	3.26 ± 0.47	299.5 ± 28.26	15 ± 0.42
EK6	3.29 ± 0.42	314.0 ± 48.45	18 ± 1.09
EK8	3.41 ± 0.29	306.5 ± 22.48	12 ± 0.85

The decline at higher loadings can be linked to the splintered shape of these whiskers which act as regions of stress concentration in the matrix leading to easier crack propagation, thereby compromising with the composite's tensile performance. Fig. 4 presents the stress-strain curve under tensile loads for varying PTW content. In contrast to tensile strength, the tensile modulus displayed a different trend. The EK2 composite showed a 10.72% increase in modulus compared to EK0, indicative of enhanced stiffness due to the rigidity of PTW. However, with increased filler content, the modulus for EK4 declined and then stabilized, with the EK8 composite exhibiting only a marginal 2.15% reduction relative to EK0.

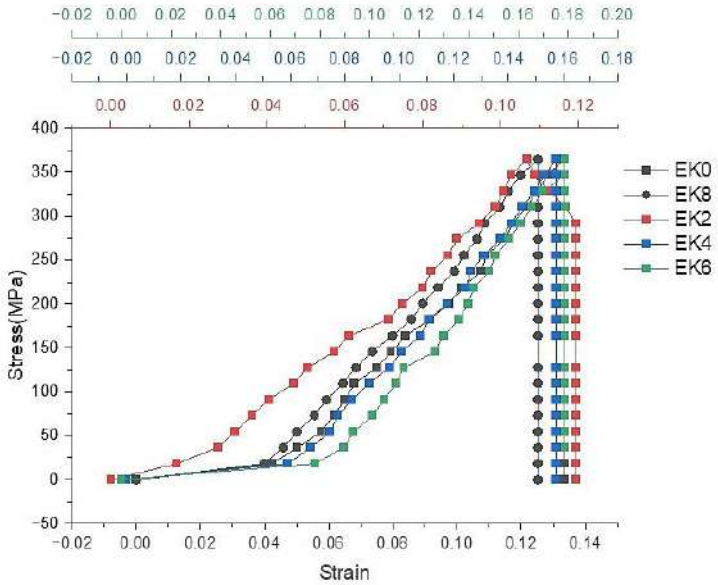

Fig. 4. Stress-Strain curve under tensile loads

This behavior suggests that while stiffness initially benefits from whisker reinforcement, excess filler diminishes the overall load transfer efficiency possibly due to filler agglomeration. The percentage elongation at break followed a moderately increasing trend with filler content. EK2 composite exhibited 12.29% elongation, which was marginally higher than EK0 (12.16%), while EK4 and EK6 composites showed elongations of 15 % and 18 % respectively. This increase may be attributed to a toughening mechanism wherein dispersed PTW locally hinder crack propagation. However, the EK8 composite showed only a minimal 2.03% increase in elongation relative to EK0, indicating a saturation point beyond which further PTW addition promotes brittleness. Notably, the overall variation in tensile strength mirrored the trend observed in impact strength, emphasizing the correlation between filler content, dispersion quality and mechanical performance.

3.4. Flexural Properties

The three-point bending test results revealed that the flexural response of the Kevlar®-epoxy composites followed a trend similar to that observed in the tensile strength results, underscoring the influence of PTW content on the composite's structural performance. The EK2 composite exhibited a 6.32% increase in flexural strength compared to the unfilled EK0, suggesting that low concentrations of PTW can effectively enhance resistance to bending stresses. This improvement may be attributed to the relatively uniform dispersion of whiskers at lower loading levels, which ensures better interfacial bonding with the epoxy matrix. The manageable surface area of PTW at these concentrations reduces the likelihood of weak interfacial zones and promotes efficient stress transfer during flexural deformation. However, the flexural strength of EK4 dropped sharply, showing a 36.33% reduction relative to EK2. This sharp decline could be linked to poor interfacial adhesion between epoxy and PTW and/or possible micro void formation during processing. At elevated PTW loadings, the increased surface area of the whiskers becomes difficult for the matrix to adequately wet, leading to regions of poor stress continuity. Furthermore, the rigid ceramic whiskers can introduce stress concentration points that act as failure initiation sites under bending loads. There is a compromise between an initial improvement followed by subsequent decline in properties particularly in whisker reinforced composites. These results emphasize the importance of maintaining an optimal PTW concentration to maximize mechanical performance. While small amounts of filler can improve load-bearing capability by reinforcing the matrix and minimizing crack growth, excessive filler content undermines the integrity of the composite by disrupting the stress transfer pathway and introducing microstructural flaws. The trend in flexural modulus further supports this behavior. The base composite (EK0) exhibited a flexural modulus of 9.72 GPa, which increased to 12.71 GPa in EK2, indicating enhanced stiffness due to rigid PTW inclusions. However, the modulus decreased to 8.93 GPa in EK4, suggesting that the adverse effects of poor filler distribution and interface quality offset the inherent stiffness of the whiskers. Interestingly, the modulus increased again in EK6 to 10.13 GPa, potentially due to partial restoration of network continuity among whiskers. For the EK8 composite, although the flexural strength was reduced by 13.66% compared to EK0, the flexural modulus still exhibited a 7.32% increase. This indicates that while the material became stiffer overall, its ability to withstand flexural stress without fracture was compromised, pointing again to the embrittlement and defect formation at higher filler loadings. The variation of flexural strength and flexural modulus with respect to the whisker content is presented in Table 5. A bar chart with error bars indicating the variation of tensile, impact and flexural properties of the composites with respect to the whisker content is presented in Fig. 5.

Table 5. Flexural properties of various composites

Composite designation	Material property(Unit)	
	Flexural modulus (GPa)	Flexural strength (MPa)
EK0	9.72 ± 1.64	129.80 ± 9.82
EK2	12.71 ± 1.45	138.01 ± 16.18
EK4	8.93 ± 1.14	87.86 ± 12.05
EK6	10.13 ± 0.57	105.73 ± 11.55
EK8	10.43 ± 1.81	112.06 ± 10.21

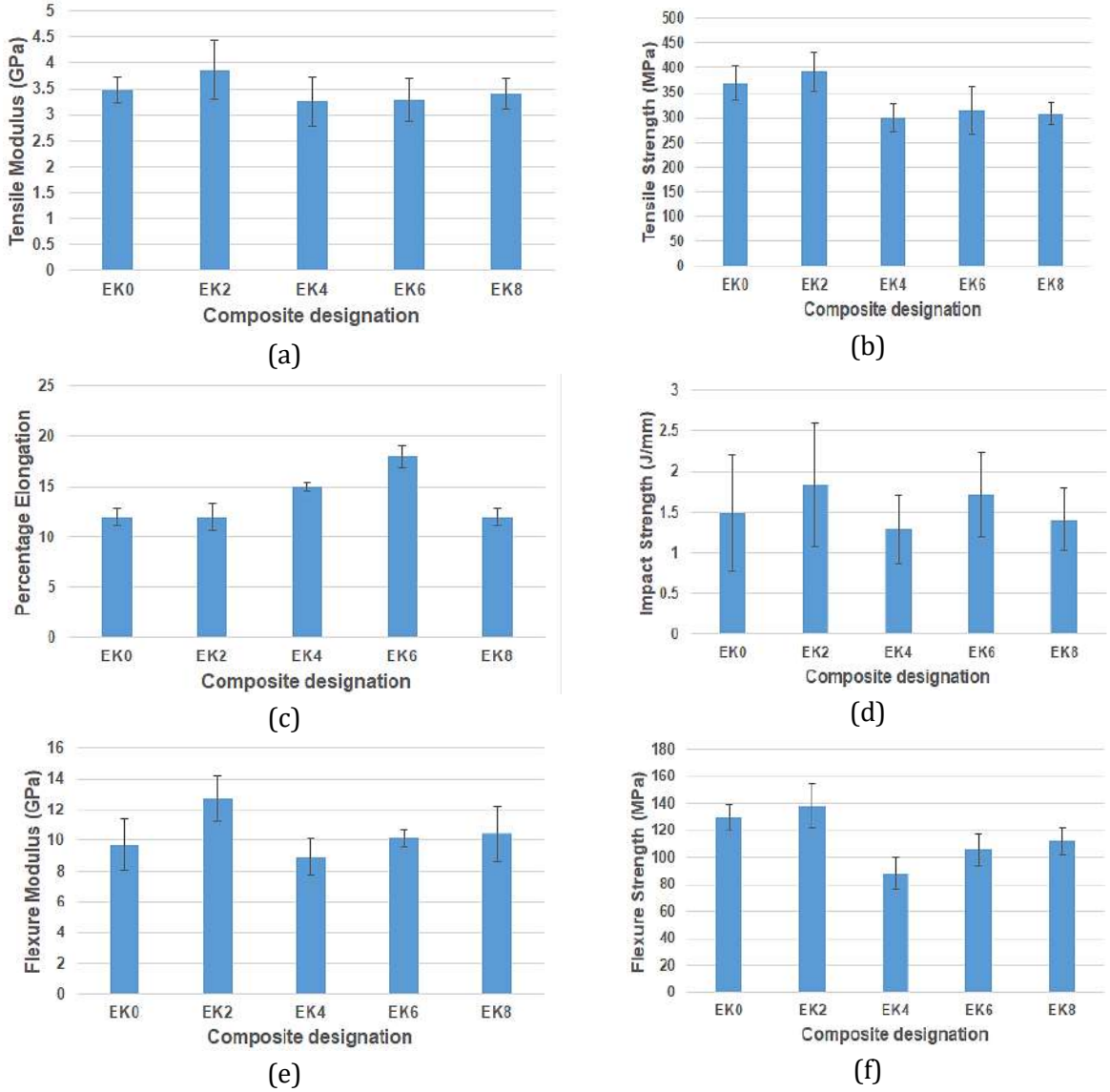

Fig. 5. Bar chart showing the variation of tensile (a – c), impact (d) and flexural (e – f) properties with whisker content

3.5. Morphology of Fractured Tensile Test Specimen

Fig. 6 presents the complete details about the fractured surfaces of selected tensile test specimens. Scanning Electron Microscope (SEM) images of 0 wt. %, 4 wt. % and 8 wt. % PTW (Model SU3500, Hitachi, Tokyo, Japan) was examined. The SEM image in Fig. 6(a) reveals relatively smooth fiber surface with the fibers being pulled out and they appear clean. This suggests minimal matrix adhesion to the fiber surfaces and the failure mainly involves fiber pull-out due to poor interfacial bonding. Fig. 6(b) reveals that the fibers are still pulled out, but with more matrix fragments adhered to the surface of the fibers when compared to 0 wt. % PTW, indicating an improvement in the fiber-matrix bonding. Although PTW were introduced into the composite at increased weight fractions, their presence was not noticeably evident on the fractured surfaces of tensile specimen captured through SEM. This absence could be attributed predominantly to poor wetting of these whiskers by the epoxy matrix, resulting in weak interfacial bonding. During tensile failure, weakly bonded whiskers are more vulnerable to get separated from the matrix and be dislodged from the fracture plane, either during crack propagation or consequent specimen handling. In addition, a number of regions in the specimen showed slender voids and sharp interfaces around potential whisker sites, demonstrating pull-out mechanisms. There are also evidences of matrix micro cracks and complex fractured surfaces. Fig. 6(c) reveals more fiber breakage rather than fiber pull-out,

and there appears an increased roughness in the fractured surfaces. Similar surface morphology was observed for all the other specimens.

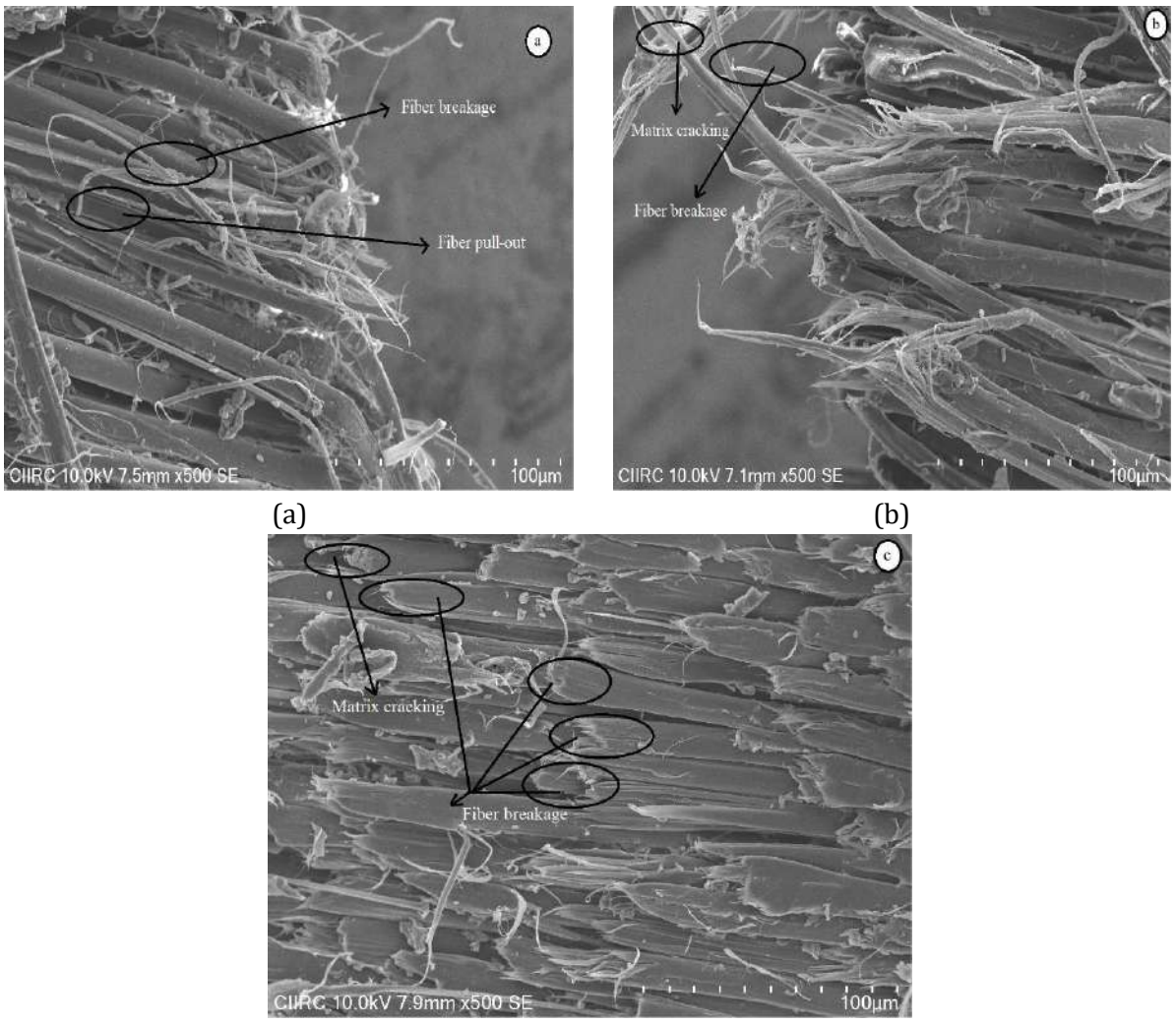

Fig. 6. SEM images of fractured surfaces of selected tensile specimen (a) 0 wt. % (b) 4 wt. % and (c) 8 wt. % PTW

4. Conclusions

This paper presents the fabrication methodology and mechanical performance of Kevlar®/Epoxy/PTW composites. The effect of incorporation of PTW on the mechanical properties like tensile strength, impact strength, flexural strength and hardness for the fabricated Kevlar®/Epoxy composite was studied. Following conclusions can be arrived at, from the experimental results obtained:

- Inclusion of PTW as reinforcing fillers has clearly influenced the mechanical performance of Kevlar®/Epoxy. The EK2 composites displayed maximum enhancement in the tensile and flexural modulus by 10.72% and 30.72% respectively compared to Kevlar®/Epoxy. At lower concentrations, these whiskers efficiently bond with epoxy and also get well dispersed. This in turn influences the load transfer capacity of the composite and improves their resistance to crack propagation. Likewise, the Shore D hardness of EK2 enhanced by 9.62% and its impact resistance enhanced by 22.96% compared to EK0. However, there was only a marginal variation in hardness with further addition of PTW.
- The tensile, impact and flexural strengths of the Kevlar®/Epoxy composites modified with PTW declined with the further addition of fillers beyond 2 wt. %. This reduced yield in most of the mechanical properties could be attributed to several factors like stress concentration,

matrix embrittlement, poor interfacial adhesion due to increased viscosity of the matrix, possible micro void formation during processing etc. In general, PTW can still be used as an effective reinforcing agent for thermoset resin like epoxy. However, a decision regarding optimum content of PTW is to be made, so that it does not cost on its mechanical properties.

- SEM images of the fractured tensile specimen revealed the possible failure modes like fiber pull-out, matrix micro crack and fiber breakage. It also indicated an improvement in the fiber-matrix bonding with the increase in PTW content, however, agglomeration of these whiskers at higher loading might have contributed to the decrease in the mechanical properties beyond 2 wt.%.

Acknowledgement

The authors thank M/S Mangala Switch Board Cuttings, Mangaluru, India for their help in carrying out the machining of the test specimens. The authors acknowledge St Joseph Engineering College, Mangaluru, India for providing composite testing facilities. The authors express their sincere gratitude to Centre for Incubation, Innovation, Research and Consultancy (CIIRC), Jyothy Institute of Technology, Bengaluru, India for providing the SEM facilities. The authors wish to thank all those who contributed in executing the work and in preparing the article.

References

[1] Oladele IO, Onuh NL, Siengchin S, Sanjay MR, Adelani SO. Modern Applications of Polymer Composites in Structural Industries: A Review of Philosophies, Product Development, and Graphical Applications. Applied Science and Engineering Progress, 2024; 17:1-1. https://doi.org/10.14416/j.asep.2023.07.003

[2] Nagaraja KC, Rajanna S, Prakash GS, Rajeshkumar G. Mechanical properties of polymer matrix composites: Effect of hybridization. Materials Today: Proceedings, 2021; 34:2-536. https://doi.org/10.1016/j.matpr.2020.03.108

[3] Jafari F, Farsani RE, Khalili SMR. Optimization of Mechanical and Thermal Properties of Elastomer Modified Carbon Fibers/Phenolic Resin composites. Fibers and Polymers, 2021; 22-1986. https://doi.org/10.1007/s12221-021-0934-9

[4] Shen S, Li H, Yang L, Li N, Wu J, Zhao T. High-throughput screening the micro-mechanical properties of polyimide matrix composites at elevated temperatures. Polymer Testing, 2022; 107. https://doi.org/10.1016/j.polymertesting.2022.107483

[5] Kubena M, Elias M, Zajíckova L, Poduska J, Kruml T. On the Tensile Tests of Polyurethane and Its Composites with Carbon Nanotubes. Advances in Materials Science and Engineering, 2019. https://doi.org/10.1155/2019/6598452

[6] Derewonko A, Fabianowski W, Siczek J. Mechanical Testing of Epoxy Resin Modified with Eco-Additives. Materials, 2023; 16. https://doi.org/10.3390/ma16051854

[7] Bharadwaja K, Rao SS, Rao TB, Pydi HP. Evaluation of Mechanical Properties for Epoxy Resin in Nano Composite Diffusion. Advances in Materials Science and Engineering, 2023. https://doi.org/10.1155/2023/8598585

[8] Shalwan A, Alajmi F, Alajmi N. The Impact of Filler Content on Mechanical and Micro-Structural Characterization of Graphite-Epoxy Composites. Journal of Materials Science and Chemical Engineering, 2022; 10-19. https://doi.org/10.4236/msce.2022.106003

[9] Bharadwaja K, Rao SS, Rao TB. Epoxy/SiO2 nanocomposite mechanical properties and tribological performance. Materials Today: Proceedings, 2022; 62:4-1712. https://doi.org/10.1016/j.matpr.2021.12.172

[10] Riahipour R, Nemati MS, Mohamad MZ, Abadyan MR, Tehrani M, Baniassadi M. Mechanical properties of an epoxy-based coating reinforced with silica aerogel and ammonium polyphosphate additives. Polymers and Polymer Composites, 2022; 30. https://doi.org/10.1177/09673911211069019

[11] Rajak DK, Pagar DD, Menezes PL, Linul E. Fiber-Reinforced Polymer Composites: Manufacturing, Properties, and Applications. Polymers, 2019; 11:10. https://doi.org/10.3390/polym11101667

[12] Amir SMM, Sultan MTH, Jawaid M, Ariffin AH, Mohd S, Salleh KAM, Ishak MR, Shah AUM. Durability and Life Prediction in Biocomposites, Fibre-Reinforced Composites and Hybrid Composites, Woodhead Publishing, Cambridge, UK, 2019.

[13] Shahabaz SM, Mehrotra P, Kalita H, Sharma SS, Naik N, Noronha DJ, Shetty N. Effect of Al2O3 and SiC Nano-Fillers on the Mechanical Properties of Carbon Fiber Reinforced Epoxy Hybrid Composites. Journal of Composites Science, 2023; 7:4. https://doi.org/10.3390/jcs7040133

[14] Sun Q, Li W. Inorganic-Whisker-Reinforced Polymer Composites: Synthesis, Properties and Applications, CRC Press, Florida, USA, 2015. https://doi.org/10.1201/b18845

[15] Sudheer M, Vishwanathan K, Raju K, Bhat T. Effect of potassium titanate whiskers on the performance of vacuum molded glass/epoxy composites. Journal of Reinforced Plastics and Composites, 2013; 32-1177. https://doi.org/10.1177/0731684413485827
[16] Tjong SC, Jiang W. Mechanical and thermal behavior of poly(acrylonitrile-butadiene-styrene)/polycarbonate blends reinforced with potassium titanate whiskers. Polymer Composites, 2004; 20:6-748. https://doi.org/10.1002/pc.10398
[17] Sudheer M, Hemanth K, Raju K, Bhat T. Enhanced Mechanical and Wear Performance of Epoxy/glass Composites with PTW/Graphite Hybrid Fillers. Procedia Materials Science, 2014; 6-975. https://doi.org/10.1016/j.mspro.2014.07.168
[18] Bettegowda H, Mahesh V, Mahesh V, Dixit AC. Characterization of Potassium Titanate Whisker and UHMWPE-reinforced Polyethersulfone/Short Carbon Fiber composites: Mechanical, thermal, and structural insights. Polymer Composites, 2025. https://doi.org/10.1002/pc.29493
[19] Suresha B, Harshavardhan B, Ravishankar R. Tribo-performance of epoxy hybrid composites reinforced with carbon fibers and potassium titanate whiskers. AIP Conference Proceedings, 2018; 1943:1-020069. https://doi.org/10.1063/1.5029645
[20] Hao X, Gai G, Lu F, Zhao X, Zhang Y, Liu J, Yang Y, Gui DY, Nan CW. Dynamic mechanical properties of whisker/PA66 composites at high strain rates. Polymer, 2005; 46-3528. https://doi.org/10.1016/j.polymer.2005.02.042
[21] Faidallah RF, Hanon MM, Vashist V, Habib A, Szakál Z, Oldal I. Effect of Different Standard Geometry Shapes on the Tensile Properties of 3D-Printed Polymer. Polymers, 2023; 15:14. https://doi.org/10.3390/polym15143029
[22] Mostovoi AS, Ledenev AN, Panova LG. Modification of epoxy matrix by whiskers of potassium polytitanate. Inorganic Materials : Applied Research, 2017; 8-755. https://doi.org/10.1134/S2075113317050197
[23] DeArmitt C, Hancock M. Particulate-Filled Polymer Composites, RAPRA Technology Limited, UK, 2003.

Research on Engineering Structures & Materials
www.jresm.org
MIM Research Group

Research Article

Evaluation of the physical and mechanical properties of pressed blocks and Caramelo blocks used in infill masonry for framed structures

Carlos Proaño [*,a], Michael Rodríguez [b], Alex Andrango [c], Juan Quilumba [d], Leslie Paspuel [e], Jason Guevara [f], Ana G. Haro-Baez [g]

Department of Earth and Construction Sciences, Universidad de las Fuerzas Armadas-ESPE, 171-5-231B Sangolquí, Ecuador

Article Info

Article History:

Received 6 Nov 2025

Accepted 3 Dec 2025

Keywords:

Concrete blocks;
Compressive strength;
Water absorption;
Infill masonry;
Construction costs

Abstract

In framed buildings in Ecuador, concrete block masonry is an essential infill component. The coexistence of artisanal units ("caramelo block") and industrial units (pressed blocks) generates uncertainty about their technical performance and economic impact, as material selection is often based solely on unit price, disregarding construction efficiency. This study compared the physical–mechanical properties and cost–benefit of both block types manufactured in Latacunga, in Ecuador's central highlands. A total of 300 units were characterized through water absorption and compressive strength tests following NTE INEN 3066 and 3153. Masonry panels of 2 m^2 were built to quantify material consumption and labor productivity during masonry and plastering stages. Results showed that pressed blocks exhibited 109 % higher compressive strength (2.39 MPa versus 1.14 MPa) and 22 % lower water absorption. Neither block type met the standard's minimum compressive strength of 3.5 MPa. Despite their higher unit cost, pressed blocks proved 9.7 % more economical in masonry and 21.3 % in plastering per square meter. It is concluded that pressed blocks provide superior cost–benefit performance, challenging the perceived savings of artisanal blocks. These findings offer a quantitative basis for decision-making and emphasize the need for stricter quality control to ensure safer, more efficient construction.

© 2025 MIM Research Group. All rights reserved.

1. Introduction

Concrete block masonry is one of the most widely used enclosure systems worldwide due to its low cost, ease of construction, and durability. In modern buildings with frame structures, these elements often serve a non-structural function, acting as infill masonry that delimits spaces, contributes to the building's lateral rigidity, and improves its thermal and acoustic performance [1,2]. However, despite not being part of the primary lateral load–resisting system, the physical and mechanical quality of the blocks directly influences deformation compatibility, cracking risk, the consumption of finishing materials, and the overall safety of the building, especially in seismic zones such as the Andean region of Ecuador. This is consistent with numerical studies showing that variations in concrete strength and seismic detailing significantly modify seismic damage probabilities in RC buildings [3].

In Latin American countries, concrete block production presents a marked duality between industrialized processes called pressed blocks (Fig. 1) and artisanal processes called "caramelo" blocks (Fig. 2). The former are manufactured through controlled mechanical compaction, which

*Corresponding author: ciproano@espe.edu.ec
[a]orcid.org/0000-0001-7329-1273; [b]orcid.org/0009-0003-5932-0252; [c]orcid.org/0009-0000-8476-0450; [d]orcid.org/0009-0005-6051-071X; [e]orcid.org/0009-0008-7559-6132; [f]orcid.org/0009-0003-0496-1896; [g]orcid.org/0000-0002-6415-4653

DOI: http://dx.doi.org/10.17515/resm2025-1320me1106rs

guarantees dimensional uniformity, lower porosity, and greater compressive strength; while the latter, made manually with metal or plastic molds, present geometric irregularities, greater absorption, and strengths below regulatory values [4]. This productive heterogeneity has a direct impact on the quality of the infill masonry, which must maintain sufficient stability against service loads and deformations imposed by the structural framework [5].

Fig 1. Pressed Block

Fig 2. Caramelo Block

At the international level, numerous studies have focused on developing more efficient and sustainable concrete blocks, aiming both to improve mechanical performance and to reduce environmental impact. In this context, [6] emphasizes that, although concrete underpins modern infrastructure and generates substantial economic value, its massive global production is responsible for a significant share of CO_2 emissions and intensive consumption of raw materials and water. Within this framework, [7] demonstrated that incorporating oyster shell, biochar, and bottom ash into permeable blocks improves strength and reduces wicking.[8] verified that partial replacement of the binder with steel slag allows maintaining strength and reducing volumetric expansion. [9] proposed the use of microalgal biomass to optimize the internal microstructure, while [10] and [11] explored the use of phase-change materials and recycled aggregates to improve thermal performance and reduce density. These advances reflect the trend toward more controlled, sustainable, and energy-efficient concrete block production.

At the same time, there has been increasing interest in understanding the mechanical behavior of non-structural infill masonry, especially under seismic or differential load conditions. Recent research [1,12,13] have shown that the interaction between the block, mortar and structural frame significantly affects the lateral stiffness of the system and can induce stress concentrations that result in diagonal cracks or premature detachments. Likewise, [5] demonstrated that the method of mortar application (full-shell or face-shell bedding) influences the deformability and stress distribution in the prisms, which is relevant even in non-load-bearing masonry, where block uniformity determines mortar consumption and construction efficiency. In this sense, the quality of the blocks not only determines local resistance, but also mechanical compatibility with the frame, a critical aspect to avoid non-structural damage during seismic events [14].

In Ecuador, non-structural concrete blocks are the most used material for the construction of partition and enclosure walls in framed buildings. The Building Statistics Bulletin [15]indicates that more than 54% of registered homes use this type of masonry. The standard [16]establishes the minimum requirements for concrete blocks, including dimensions, density, absorption, and compressive strength. Those used in non-structural masonry with an individual strength of 3.5 MPa are classified as Class B blocks. Additionally, the standard [17] regulates the procedure for the preparation and laboratory testing of low walls, allowing the masonry's compressive strength and structural efficiency to be determined. However, recent studies and field observations show that a large part of the blocks produced by hand in the country do not meet the established minimum values, which compromises the quality of the enclosures and increases the costs of finishes due to the greater consumption of mortar and plaster [18].

In this context, the city of Latacunga, located in the central highlands of Ecuador, constitutes a strategic point for analyzing the quality of masonry materials. Its geographic location, in an intermediate seismic zone, and the availability of volcanic aggregates from the Andes Mountains influence the composition and behavior of locally manufactured blocks. Small artisanal factories and semi-industrial plants coexist in the city and its surroundings, supplying both the local market

and that of the central region of the country, with wide variability in quality control, curing, and compaction. However, to date, there has been no research experimentally comparing the physical and mechanical properties and construction efficiency of pressed and industrial blocks versus artisanal caramelo-type blocks produced in Latacunga.

In addition to mechanical performance, economic and construction aspects are decisive in the selection of block type. Previous research [4, 19, 20] agrees that the initial cost of a handmade block is usually lower, but the total construction cost increases due to dimensional irregularity and greater absorption, which require more mortar and greater plaster thickness to achieve flat surfaces. This phenomenon is accentuated in infill masonry, where geometric regularity is essential to ensure proper anchorage to the frame and the continuity of the finishes. Therefore, evaluating block performance not only in terms of strength, but also in relation to its impact on construction performance and the overall cost per square meter, is essential to optimize the productivity and sustainability of local construction.

This research aims to comparatively evaluate the physical and mechanical characteristics and associated costs of pressed and industrial concrete blocks versus artisanal caramelo-type blocks used in nonstructural infill masonry in framed buildings. The study integrates standardized laboratory tests according to [16] and [17], with construction performance measurements and unit price analysis, allowing for a correlation between mechanical performance and economic and construction impact.

This work provides unprecedented experimental evidence for the central Sierra region of Ecuador and constitutes a technical reference for improving manufacturing processes, quality control, and material selection for nonstructural masonry. Furthermore, the results reinforce the importance of complying with national standards as a condition for ensuring the efficiency, durability, and structural compatibility of infill masonry in framed buildings, while promoting the sustainability and competitiveness of the local construction materials industry.

2. Materials and Methods

The study was structured in three phases (Fig 3): Phase 1 consists of the analysis and characterization of the sand and cement materials; Phase 2 focuses on testing of composite elements such as mortars, blocks, and walls to evaluate them against the requirements of Ecuadorian technical standards and establish their physical and mechanical properties; and finally, Phase 3 quantifies the materials and performs unit price analysis for block masonry and vertical plastering.

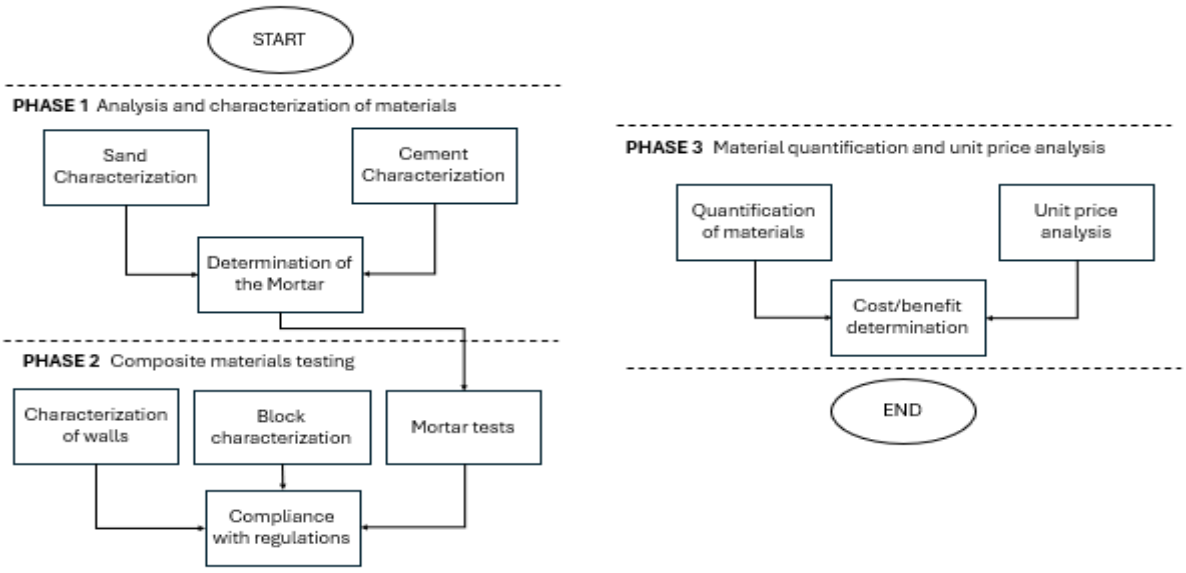

Fig. 3. Research outline

2.1. Phase 1. Material Analysis and Characterization

The materials used in the construction of the masonry were characterized:

2.1.1 Sand Characterization

The specific gravity and water absorption of the sand were determined on a 500g oven-dried sample in accordance with [21]. Both tests were performed following the procedures specified in this standard (Table 1).

Table 1. Specific gravity and water absorption of sand

Description	Value
Specific gravity of soil at more than 20 °C	2.54
Water Absorption	2.04%

2.1.2 Cement Characterization

A general-use hydraulic cement (type GU) was used as the binder. According to the manufacturer's specifications, this cement complies with the performance requirements of [22] standard for general-use hydraulic cements.

2.1.2.1 Cement Density

Three samples of 64g of mass were taken using the Le Chartelier volumetric flask method (Fig 4) in accordance with [23] as shown in Table 2, although the standard does not establish a minimum or maximum number of tests to be performed.

(a) (b) (c)

Fig. 4. Cement density test (a)Cement mass, (b) Bottle of Le Chatelier with gasoline and (c) Le Chatelier's bottle with gasoline and cement

Table 2. Cement density

Sample	Mass (g)	Density (g/cm^3)
1	64.00	3.18
2	64.00	3.15
3	64.00	3.20
Average		3.18

2.1.2.2 Cement Consistency

Three 650g samples of cement were prepared using the Vicat method (Fig 5) in accordance with [24], presenting an average consistency of 28.45% as shown in Table 3.

(a) (b) (c)

Fig. 5. Cement consistency test (a) Mechanical mixer, (b) Mixed mortar and (c)Vicat's needle

Table 3. Cement consistency

Sample	Normal Consistency (%)
1	27.70
2	28.45
3	29.20
Average	28.45

2.1.2.3 Cement Setting Time

Fig. 6 shows the cement consistency test using the Vicat method, resulting in a setting time of 318 minutes according to *[25]*

Fig. 6. Setting test using the Vicat method

2.2 Phase 2. Composite Material Tests (Mortars, Blocks, And Low Walls)

2.2.1 Mortar Characterization

A mortar flow test was performed [26] , yielding a flow of 108 %, establishing the dosage: 1:2.75 (cement:sand) by mass with a water/cement ratio of 0.485 (Fig 7). Based on these results, 12 mortar cubes (Fig 8) with dimensions of 50mm x 50mm x 50mm were prepared and tested to determine their compressive strength in accordance with [27]. The cubes were divided into four groups of three specimens and tested in compression at ages of 1, 3, 7, and 28 days, following the requirements of [22]. For each age, the mean compressive strength of the three cubes was reported.

(a) (b)

Fig. 7. Mortar flow test (a), Mortar in mold (b) Mortar on fluidity table

Fig. 8. Mortar cubes in mold

2.2.2 Block Characterization

A total of 150 caramelo blocks (handcrafted) and 150 pressed blocks (industrially manufactured) were purchased as standard commercial products from two local producers in Latacunga, located in the central Sierra region of Ecuador. These manufacturers routinely supply concrete masonry units for nonstructural masonry in residential and small building projects in Latacunga and surrounding areas. The blocks were taken directly from their current production batches, without any special pre-selection other than the visual inspection prescribed by [16], so that the tested units can be considered representative of the blocks commonly used in local practice. For each block type, the following tests were performed:

- Visual Appearance: Three blocks of each type were analyzed (Figure 9), according to the minimum requirements of [16].

(a) (b)

Fig. 9. Specimens selected for visual inspection, dimension measurement, and absorption testing (a) Caramelo block and (b) Pressed block

- Dimension Measurement: Three blocks of each type were used, according to [16].
- Water Absorption Tests: The three blocks of each type (Fig 10) were tested, according to [16].

(a) (b)

Fig. 10. Water Absorption Test on Blocks (a) Caramelo block and (b) Pressed block

- Dry Unit Density: Block density was determined in accordance with [16] using the oven-dry mass, saturated mass, and submerged mass of the same three units used in the water absorption test for each block type.
- Compressive Strength of Blocks: The standard [16] recommends testing at least 3 block specimens; however, 10 blocks of each type were tested (Fig 11) to obtain a broader range of results.

(a) (b)

Fig. 11. Compressive strength test of blocks (a) Caramelo block and (b) Pressed block

2.2.3 Characterization of Low Walls

According to [17], low walls of perforated units were constructed to evaluate the compressive strength of concrete blocks. Six specimens were made for each block type, using two blocks per wall. Each wall consisted of two courses (rows) of blocks, joined only by a horizontal mortar joint (1:2.75 cement:sand mix), without vertical mortar joints between the units.

The walls constructed with pressed blocks had a width of 24.8 cm and a total height of 41.5 cm, corresponding to a height-to-width ratio (h/b) of 1.67. Low walls made of caramelo blocks had a width of 24.6 cm and a height of 39.0 cm, with an h/b ratio of 1.59. These dimensions and proportions are consistent with the model of perforated unit walls specified in [17]. Due to the limitations of the testing machine, the blocks were cut following the geometric requirements of the standard, to preserve the configuration of the wall before carrying out the compression tests (Fig. 13).

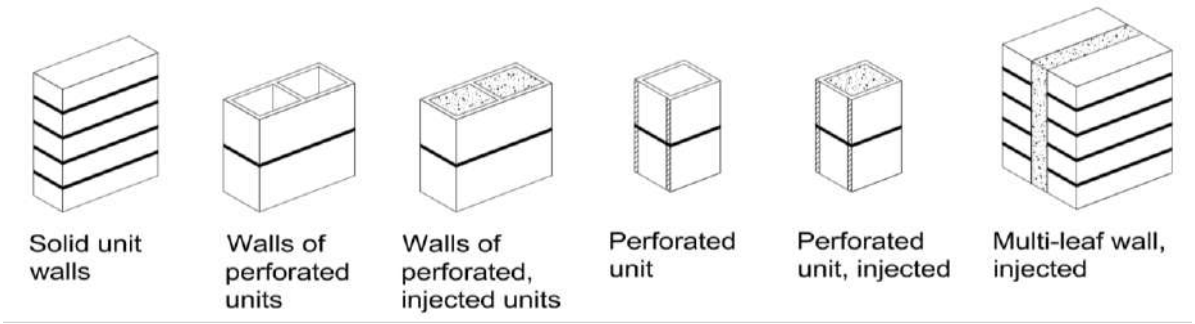

Fig. 12. Types of Low Walls

(a) (b)

Fig. 13. Compressive Strength Test of Low Walls (a) Low walls and (b) Compression test of low walls

2.3 Phase 3. Material Quantification and Unit Price Analysis

To evaluate the construction and economic performance of the masonry units, three panels of approximately 2 m^2 were built for each block type (caramelo and pressed), with 25 blocks per panel, as shown in Fig. 14. The area of approximately 2 m^2 was selected because it provides a sufficiently representative surface area for the behavior of a masonry wall in construction and, at the same time, allows for more reliable quantification of material consumption and construction time per unit area. Constructing three panels per block type is aimed to introduce variability in the construction process and obtain more robust average consumption and yield values. Subsequently, both sides of the panels were plastered (Fig. 15). The plastering mortar was applied with a 1:4 dosage (cement:sand, by mass) and an average thickness of 1.5 cm, a value that is within the range usually used in construction practice in Ecuador (0.5–2.0 cm), and which corresponds to the most commonly used thickness to achieve a uniform surface in enclosure walls.

Fig. 14. Pressed block masonry

Fig. 15. Plastered Pressed Block Masonry

During construction, the following were recorded:

- Mortar consumption: In the masonry joints, with a ratio of 1:2.75 (cement:sand) to their mass, quantifying the volume used and the quantities of cement, sand, and water.
- Plastering mortar consumption: Applied to both sides of the masonry, with a ratio of 1:4 (cement:sand) to their mass and an average thickness of 1.5 cm, the quantities of cement, sand, and water were quantified.
- Effective areas of the masonry and plaster: To determine the ratio between materials used and the surface area covered.
- Activity execution times.: The start and end times of the work were recorded for both the wall construction and the plastering.
- Work crew composition.: The unit price analysis was prepared for the second quarter of 2025. The work team consisted of a mason and a construction assistant, under the supervision of a foreman. The hourly costs for each category were calculated based on the minimum wages in effect in 2025 for the construction industry, as established by the Comptroller General of the State of Ecuador.
- Cost of materials.: Caramel-type concrete blocks had a unit cost of USD 0.28, while pressed blocks had a unit cost of USD 0.45. The prices of cement, sand, and water were USD 0.15 per kilogram, USD 0.034 per kilogram, and USD 0.72 per m^3, respectively. These prices correspond to quotes obtained from local hardware stores and block manufacturers in the city of Latacunga, collected in May 2025, while the cost of water was taken from the basic services bills for the same month. Therefore, the cost analysis results reflect the market conditions prevailing in the second quarter of 2025.

Based on the collected information, unit price analyses (UPAs) were prepared for masonry and plastering activities, comparing the technical and economic performance of both types of blocks.

3. Results of Analysis

3.1 Phase 2. Composite Material Testing

3.1.1 Mortar Characterization

The compressive strength of mortar cubes (Fig 16) was tested in three samples at different ages (1, 3, 7, and 28 days). The results for 3, 7, and 28 days of age exceeded the minimum requirements established by the standard [22], as shown in Figure 17. There is no minimum age requirement for 1 day; however, the standard requires the test to be performed.

Fig 16. Compressive strength test of mortar cubes

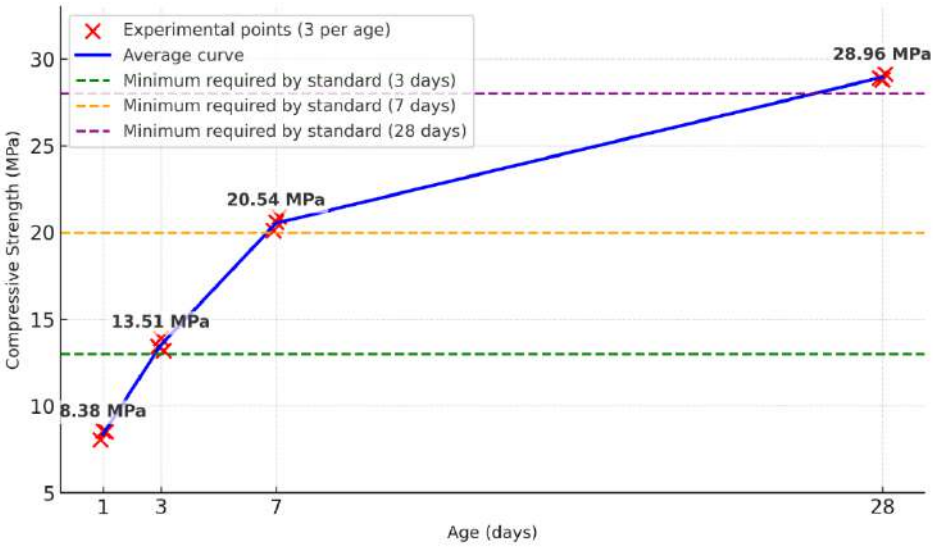

Fig. 17. Evolution of the Compressive Strength of Mortar compared to the Minimum Required by (NTE INEN 2380)

3.1.2 Block Characterization

3.1.2.1 Visual Appearance

The pressed blocks (Fig 1) have much better visual appearance than the caramelo block (Fig 2), especially in the dimensions, regular surface, and chipping established in the standard [16]. The caramelo blocks have surface voids and irregular edges; the comparison between the two is shown in Table 4.

Table 4. Analysis of visual aspects of the blocks

Block Appearance	Pressed Block	Caramelo Block
Actual dimensions outside tolerances ± 3 mm	Yes	Yes
Chips with a diameter greater than 25 mm on the block faces	No	Yes
Cracks with a width greater than 0.5 mm and lengths greater than 25% of the height on the block faces	No	No
Broken units	No	No

3.1.2.2-Dimensional Analysis

Notable differences were evident between the two types of blocks evaluated, considering that the nominal dimensions of the blocks to be tested are 390 mm long x 190 mm high x 140 mm wide.

Figure 18 presents the faces and dimensions taken from the blocks. Both the pressed blocks (Table 5) and caramelo blocks (Table 6) presented dimensions that exceeded the tolerance established in [16]. Figure 19 shows the difference in block dimensions and the accepted tolerance.

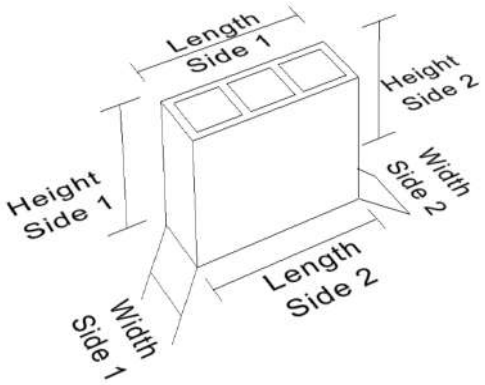

Fig. 18. Block Dimensional diagram

Table 5. Dimensions of the pressed block

Sample	Width			Height			Length		
	Side 1 (mm)	Side 2 (mm)	Maximum variation (mm)	Side 1 (mm)	Side 2 (mm)	Maximum variation (mm)	Side 1 (mm)	Side 2 (mm)	Maximum variation (mm)
P1	148	147	8	200	200	10	398	398	8
P2	147	148	8	200	200	10	398	398	8
P3	148	147	8	200	200	10	397	398	8

Table 6. Dimensions of the caramelo block

Sample	Width			Height			Length		
	Side 1 (mm)	Side 2 (mm)	Maximum variation (mm)	Side 1 (mm)	Side 2 (mm)	Maximum variation (mm)	Side 1 (mm)	Side 2 (mm)	Maximum variation (mm)
C1	135	136	-5	185	186	-5	376	375	-15
C2	135	136	-5	185	184	-6	377	376	-14
C3	135	134	-6	185	186	-5	374	375	-16

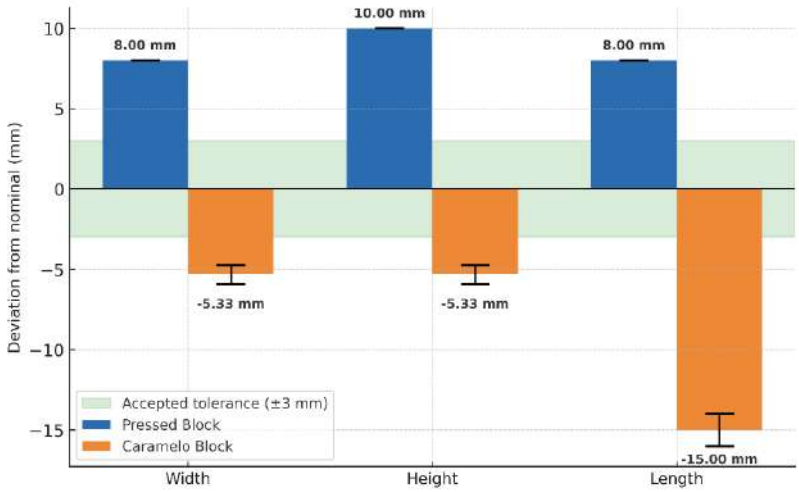

Fig. 19 Comparison of maximum dimensional variations vs tolerance [16]

3.1.2.3 Density and Water Absorption of Blocks

Table 7 shows the acceptable values for each block type according to [16]. Both types of blocks are classified as LIGHTWEIGHT, presenting densities below 1680 kg/m³. Furthermore, because they are non-structural, they are classified as Class B. Based on this classification, the standard establishes a maximum average water absorption of 288 kg/m³ for lightweight blocks. The standard does not establish maximum absorption values for Class B blocks, so Table 7 defined for Class A blocks was used. The pressed blocks met this requirement, registering an average of 267.82 kg/m³, while the caramelo blocks exceeded it with 343.38 kg/m³. Figures 20 and 21 show the comparison of the blocks' density and maximum water absorption values. The results show that the pressed blocks have a 22% lower water absorption than the caramelo ones.

Table 7. Maximum water absorption in Class A blocks

Type	Density (kg/m³)	Maximum average water absorption (kg/m³)	Maximum water absorption per Unit (kg/m³)
Light	< 1680	288	320
Medium	1680 a 2000	240	272
Normal	> 2000	208	240

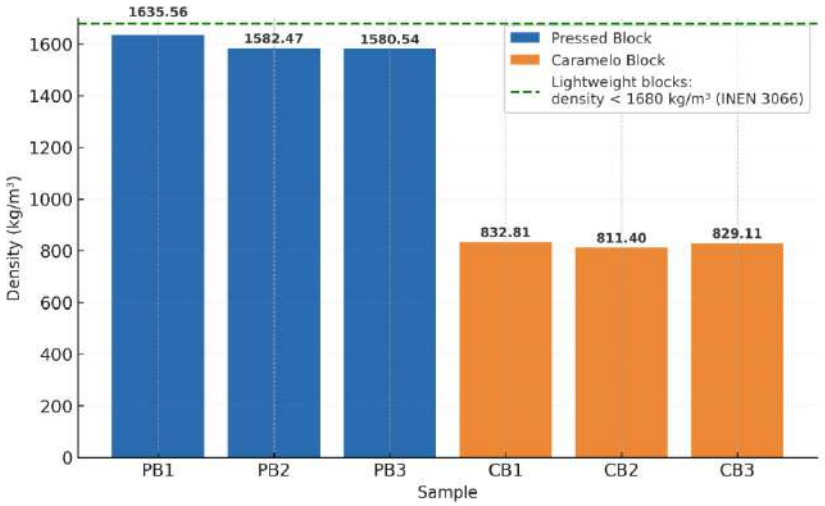

Fig. 20. Block classification according to [16]

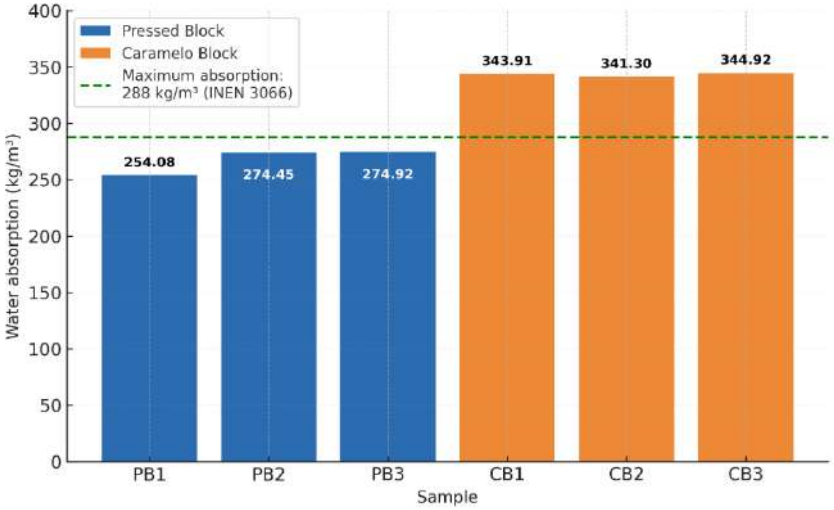

Fig. 21. Block Absorption vs. Standard [16]

3.1.2.4 Compressive Strength

The standard requires a minimum strength of 3.5 MPa per unit and an average of 4.0 MPa for Class B nonstructural blocks [16]. The pressed blocks reached an average of 2.39 MPa, and the caramelo blocks an average of just 1.14 MPa, with the pressed blocks being 109.58% higher. In both cases, the values are below the required values; however, the pressed block showed better relative performance, as shown in Figure 22.

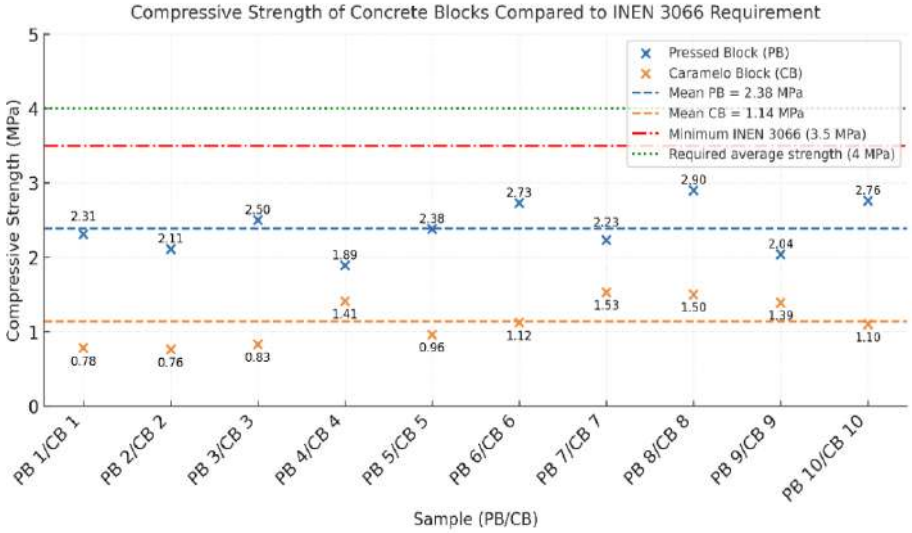

Fig. 22. Comparison of compressive strength of pressed blocks and caramelo

3.1.2.5 Compressive Strength of The Low Walls

The same trend was reflected; walls were built with dimensions of width, height, and thickness of 24.6 × 41.5 × 15 cm for the PB and 24.6 × 39.0 × 13.8 cm for the CB. Due to the height/width ratio of the low walls, the correction factor established in [17] was applied by interpolating the values in Table 8. The correlation factors are 0.91 for the pressed blocks and 0.89 for the caramelo blocks. The average strength achieved was 3.17 MPa for the walls built with pressed blocks and 1.05 MPa for the caramelo blocks, demonstrating a significant difference between the two systems, presented in Figure 23.

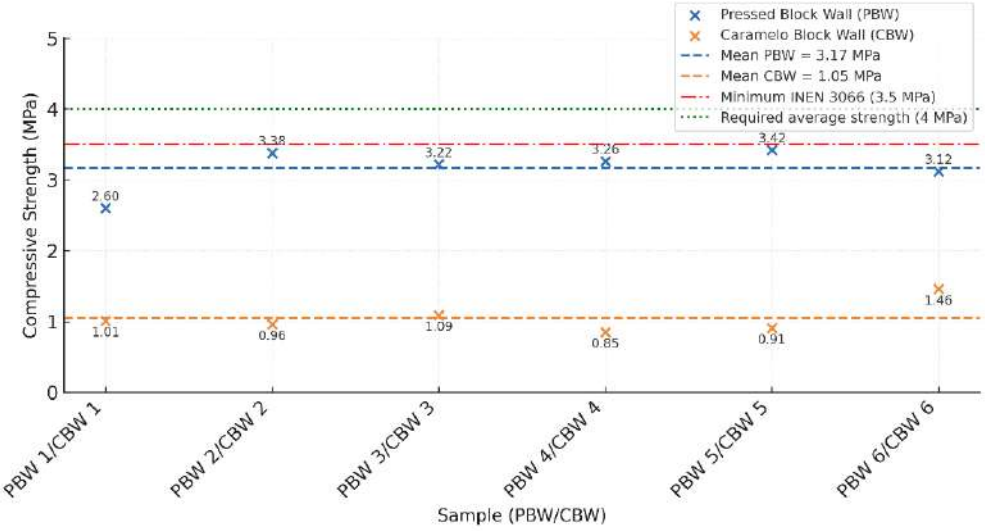

Fig. 23. Comparison of Compressive Strength of Walls between Pressed Blocks and Caramelo

Table 8. Height versus width correction factors for the compressive strength of masonry walls

h_m/a_m	1.30	1.50	2.00	2.50	3.00	4.00	5.00
Correction factor	0.75	0.86	1.00	1.04	1.07	1.15	1.22

Where h_m/a_m *Height-to-width aspect ratio of the low wall.*

3.2 Phase 3. Quantification of Materials and Costs

3.2.1 Masonry

During the construction of the three masonries, approximately 2 m2 each, a notable difference was observed in the final areas obtained. For the pressed block walls, the total constructed area was 6.62 m², obtaining an average area per masonry of 2,207 m² represented by Figure 24; while the caramelo block walls reached a smaller total area of 6,131 m², with an average area of 2,044 m² (Fig 25). It is evident that, with the same number of blocks (75), the pressed blocks generate 7.97% more area than the caramelo blocks (Figure 26).

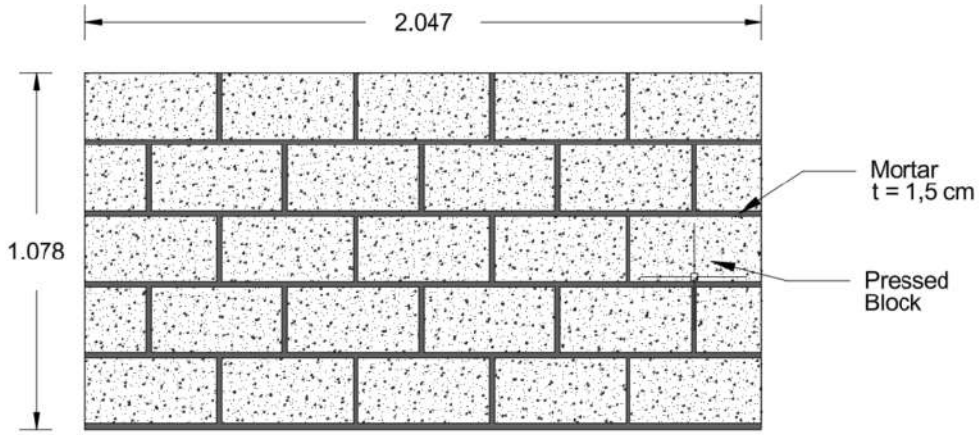

Fig. 24. Average dimensions of PP pressed block masonry

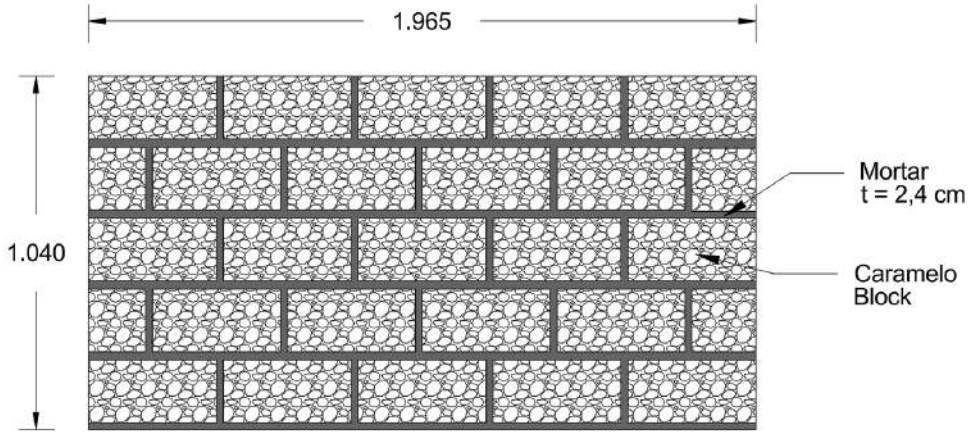

Fig. 25. Average dimensions of PC caramelo block masonry

Mortar consumption was higher in the case of caramelo blocks, confirming their lower efficiency on site due to their more porous texture and smaller, irregular dimensions, which result in thicker joints: 2.4 cm on average, compared to 1.5 cm in walls made of pressed blocks. In the three masonry units, this translated into a total mortar volume of 0.098 m^3 for pressed blocks and 0.135 m^3 for caramelo blocks, equivalent to 0.0148 m^3/m^2 and 0.0220 m^3/m^2, respectively. In relative terms, caramelo block masonry requires 37.76% more mortar volume than pressed block masonry. Consistently, the quantification of material consumption (cement, sand, and water) in mortar

preparation shows that caramel block masonry consumes 38.23% more materials than pressed block masonry (Fig. 27).

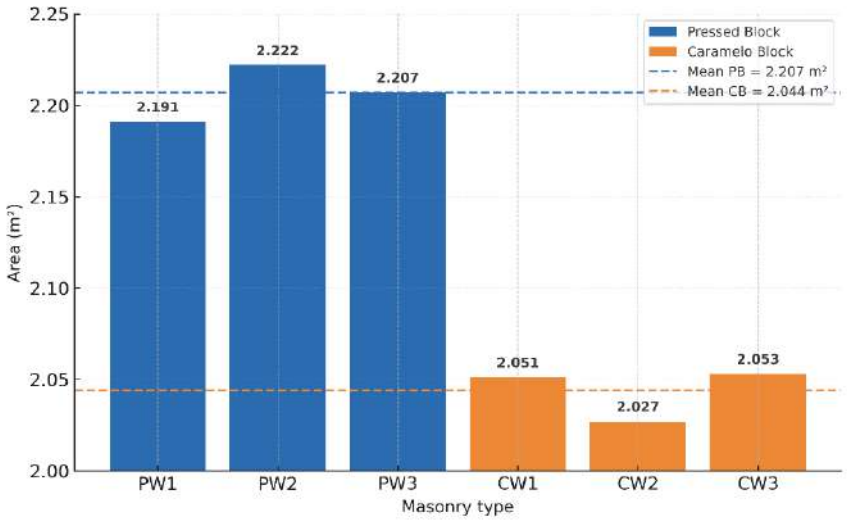

Fig. 26. Comparison of masonry areas between pressed block and caramelo block

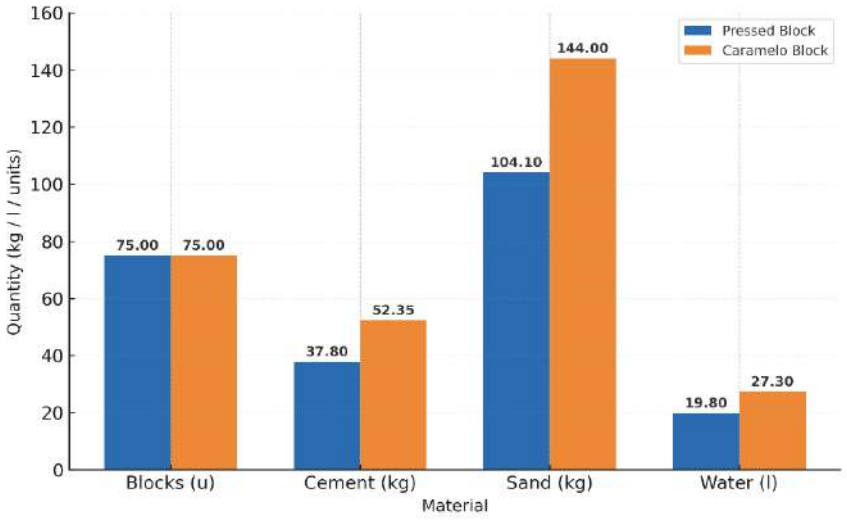

Fig. 27. Quantification of materials used in masonry

3.2.2 Plastering

Applied to both sides of the panels with mortar at a 1:4 ratio (cement:sand) and a thickness of 1.5 cm, higher material consumption was also evident in the caramelo block masonry. For the pressed block walls, a total area of 13.24 m² was covered, while for the caramelo block walls, the area was 12.262 m², with higher cement, sand, and water consumption in the latter, 25.12% higher (Fig 28). This shows that the porosity of the caramelo blocks requires more mortar to fill the voids and achieve the same plaster thickness as the pressed block.

3.2.3 Efficiency

Execution times for the three walls built with pressed blocks were 4.35 hours for masonry and 5.25 hours for plastering, whereas for the caramelo block walls they increased to 5.55 hours and 6.05 hours, respectively, reflecting the loss of productivity associated with their dimensional variability. The work was performed by a mason and a laborer under the supervision of a foreman, and hourly costs were calculated in accordance with the minimum wages established by law for the construction industry in Ecuador.

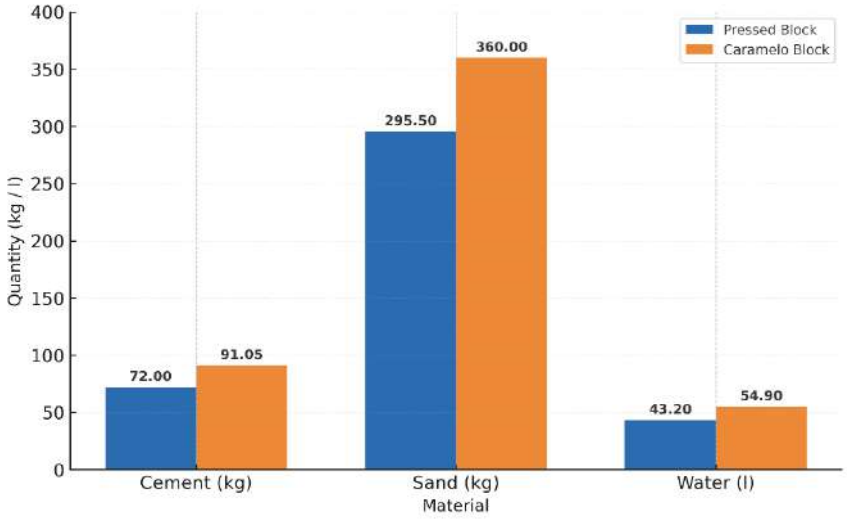

Fig. 28. Quantification of materials used in plastering

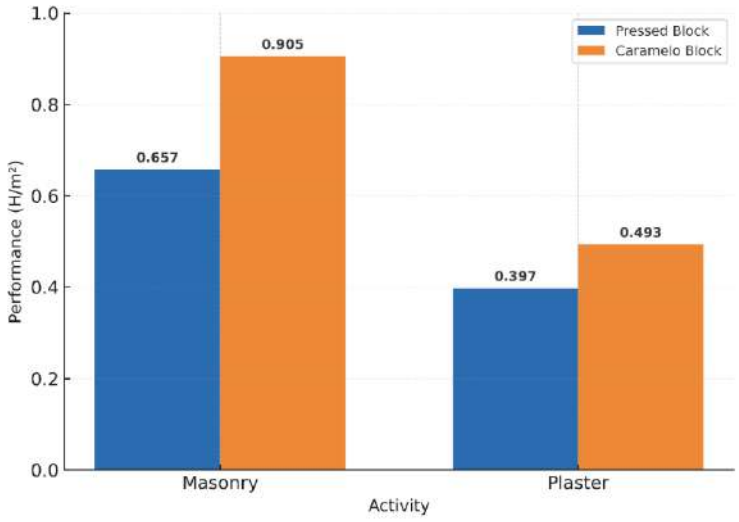

Fig. 29. Performance of masonry and plastering

These total times were then related to the effectively completed wall areas for masonry (6.62 m^2 for the pressed block walls and 6.131 m^2 for the caramelo block walls) and to the plastered areas, corresponding to both faces of each wall (13.24 m^2 for the pressed block panels and 12.262 m^2 for the caramelo block panels). This yielded labor productivities of 0.657 h/m^2 and 0.905 h/m^2 for masonry with pressed and caramelo blocks, respectively, and 0.397 h/m^2 and 0.493 h/m^2 for plastering. Based on these normalized values (h/m^2), it is observed that caramelo block masonry requires 37.75 % more time per square meter than pressed block masonry, and that plastering caramelo block panels takes 24.18 % longer per square meter, thereby increasing labor costs (Fig. 29).

3.2.4 Unit Price Analysis

In the unit price analysis, the cost of equipment corresponds to minor tools, including shovels, trowels, wooden boxes, and wheelbarrows used for the preparation, transport, and placement of mortar. According to standard budgeting practices for construction projects in Ecuador, the cost of these minor tools is estimated at 5% of the direct labor cost, since this equipment is used repeatedly in multiple work items and its individual depreciation per square meter is low. For this reason, in the breakdown of the Unit Prices (UPA) shown in Figure 30, the equipment cost share is relatively small compared to the material and labor costs. However, it is explicitly included to reflect the complete direct cost structure.

Finally, by integrating material consumption, execution times, equipment, labor, and material costs, unit price analyses (UPA) were prepared for the second quarter of 2025. For pressed block masonry, the unit price was USD 12.69/m^2 for masonry and USD 5.33/m^2 for plastering. For caramelo block masonry, the cost rose to USD 14.05/m^2 for masonry and USD 6.77/m^2 for plastering. Figure 30 shows the direct cost ratios for Equipment, Labor, and Materials for each executed item. These results show that, although the caramelo block has a lower acquisition price per unit, its construction performance is inferior, increasing the cost per square meter of masonry by 10.72% and 27.02% for plastering compared to pressed block.

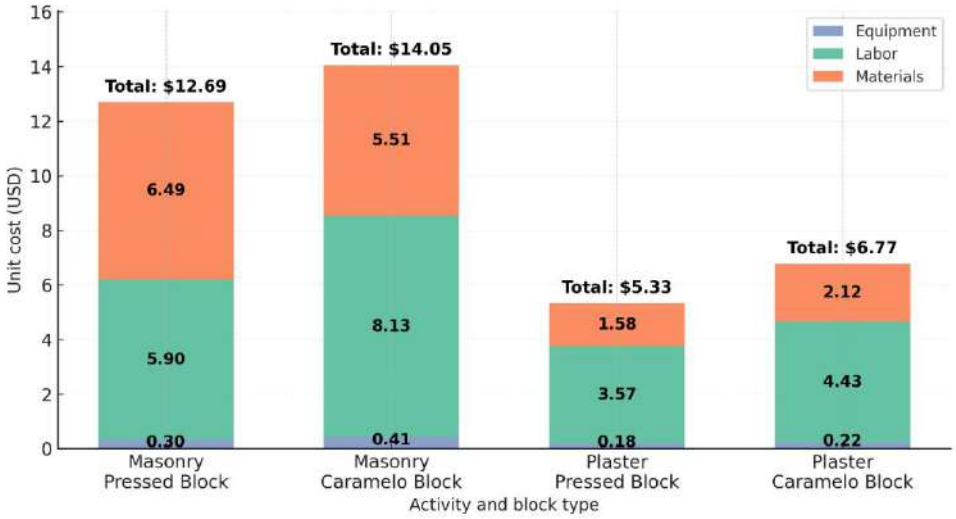

Fig. 30. Comparison of unit prices for masonry and plastering

4. Discussion

The results demonstrate that the quality of the manufacturing process decisively influences the physical-mechanical, structural, and economic behavior of non-structural infill masonry used in framed buildings. The comparison between the pressed block (PB) and caramelo block (CB) showed significant differences in strength, absorption, dimensional variability, and constructive efficiency, confirming the trends reported by [4] for artisanal blocks from Latin America.

The pressed block reached an average compressive strength of 2.39 MPa and a water absorption of 267.82 kg/m^3, while the caramelo block obtained 1.14 MPa and 343.38 kg/m^3, respectively. These differences confirm that only the PB partially complies with [16]for Class A blocks, meeting the absorption limit (<288 kg/m^3) but not the minimum strength (≥3.5 MPa) required for non-structural units. The CB, on the other hand, does not meet any regulatory parameter, reflecting its artisanal nature and the lack of compaction and curing control. The coefficient of variation in the strength of the CB (26.32%) was almost double that of the PB (13.55%), evidencing deficiencies in granulometric homogeneity and manufacturing processes. Equivalent results were reported by [2] and [9], who showed that a denser microstructure improves strength even under extreme conditions, such as fire exposure or biomass incorporation. However, the direct relationship between density, porosity, and strength was more clearly evidenced by [28], when analyzing blocks with industrial waste and establishing a positive correlation between compaction, reduced porosity, and mechanical performance. Complementarily, [29] showed that the use of unstable or high-absorption aggregates increases mechanical variability and accelerates surface degradation, consistent with the observations of this study. The inverse correlation between density and absorption (R^2 = 0.99) confirms that open porosity is the main factor determining the block's strength, in agreement with [30]and [8], who highlight that reducing voids and controlling curing are essential to improve durability and reduce concrete permeability.

The low walls built with pressed blocks reached an average strength of 3.17 MPa, while those made with caramelo blocks presented only 1.05 MPa, values corrected for slenderness according to [17]. In contrast, the average strengths of the individual blocks were 2.39 MPa for the pressed blocks

and 1.14 MPa for the caramelo blocks. These differences, statistically significant ($p < 0.01$), are attributed to the manufacturing quality and the block-mortar adhesion. The structural efficiencies ($\eta = f'm / f'b$) were 1.33 for PB and 0.92 for CB, values higher than the 0.40–0.90 range reported by [31]. This result is explained by the low strength of the studied units, which magnifies the relative contribution of the mortar—of greater strength—to the assembly's behavior. Although the system analyzed by [13] corresponds to dry-stack and grouted masonry, that is, a different resistance mechanism, the values obtained here are also higher than those reported by said authors.

This behavior can also be attributed to the low slenderness of the walls ($h/t \approx 2.8$) and their small dimensions (24.6 × 41.5 × 15 cm in PB and 24.6 × 39.0 × 13.8 cm in CB), which increase stiffness and reduce instability during the test. The pressed block walls showed progressive crushing failures with good stress redistribution. In contrast, the caramelo block walls exhibited a conic-columnar failure mode with diagonal cracking and joint separation, attributable to the high absorption and surface roughness of the blocks. This pattern coincides with the findings of [5,12,32], who show that mechanical compatibility and block-mortar adhesion determine the post-peak stiffness and tension behavior of the masonry.

From a construction and economic perspective, the unit price analysis showed that pressed block masonry had a total cost of USD 12.69/m^2 compared to USD 14.05/m^2 for caramelo block (-9.7%). Regarding plastering, the difference was even greater: USD 5.33/m^2 for PB and USD 6.77/m^2 for CB (-21.3%). Overall, the finished wall cost was 13.45% lower with the pressed block system, despite its higher unit price. These savings are associated with a 27.4% reduction in construction time, lower joint thickness (1.5 cm vs. 2.4 cm), and a 32.7% reduction in mortar volume (0.0148 m^3/m^2 vs. 0.0220 m^3/m^2), resulting in approximately 30% lower cement, sand, and water consumption. These results are consistent with those reported by [19] and [20], who demonstrated that the greater dimensional accuracy and lower absorption of industrialized blocks optimize construction efficiency by reducing rework and material loss. In contrast, artisanal production generates units with high geometric and surface variability, which increases mortar use and on-site adjustment times. Consequently, the observed relationship between block quality, productivity, and overall cost validates the initial hypothesis: standardized blocks, although more expensive per unit, are more efficient when considering construction performance, material savings, and reduced environmental impacts associated with cement production.

Microstructure, density, and absorption analysis suggest that pressed blocks, with lower porosity and greater compactness, exhibit better performance against moisture-drying cycles and aggressive agents. According to [29] and [33], the reduction of interconnected porosity and the improvement of the paste-aggregate transition zone (ITZ) are determining factors in the service life of masonry by limiting the migration of water and salts and reducing the risk of disintegration due to expansive reactions. Consistently, [30] demonstrated that blocks with controlled aggregates and homogeneous compaction maintain their strength and microstructural stability after multiple freeze-thaw cycles, while materials with high porosity exhibit early cracking and mass loss. In the Ecuadorian context, where volcanic aggregates exhibit greater absorption and mineralogical variability, controlled industrial production becomes essential to ensure the durability, dimensional stability, and hygrothermal compatibility of nonstructural blocks. Although this research did not directly evaluate environmental sustainability, the results show that the industrialization and standardization of the process contribute indirectly to it by reducing mortar, cement, and energy waste during construction, in accordance with the principles of material efficiency and circularity described by [30].

Although the blocks studied are non-structural, their physical and geometric quality directly influences the overall behavior of the frame system. Walls constructed with pressed block exhibit a more uniform interaction with the structural frame, reducing cracking due to deformation incompatibility and improving energy dissipation under lateral loads. This behavior is consistent with the results of [14,34] and [5], who demonstrated that the homogeneity of the enclosure and the quality of the block-mortar interface increase initial stiffness and post-cracking recovery capacity. In contrast, walls made with caramelo block, with lower density and regularity, tend to develop early diagonal cracks and joint debonding, reducing their contribution to structural

damping. From a technical and economic perspective, adopting standardized, industrialized blocks constitutes a comprehensive strategy for quality, durability, and sustainability by improving structural compatibility and reducing maintenance and repair costs. The results of this research provide unprecedented experimental evidence for the central Sierra of Ecuador and reinforce the need to strengthen quality control mechanisms and compliance with [16], in local production plants, as an essential requirement for the safe seismic design of framed buildings with infill masonry.

Overall, the results confirm that the mechanical, structural, and economic efficiency of nonstructural masonry depends directly on the type and quality of the concrete block. The pressed block, by partially meeting regulatory specifications, exhibits more stable strength, lower absorption, better mortar adhesion, and a significant reduction in total construction costs. In contrast, the artisanal caramelo block shows high variability and excessive material consumption. These findings confirm the importance of promoting controlled industrialization and the rigorous application of Ecuadorian standards to improve the quality, durability, and sustainability of enclosures in framed buildings in the Andean region.

4.1 Research Limitations

Despite the experimental scope and representativeness obtained, this research presents certain limitations that must be considered when interpreting the results. The tests were conducted on a laboratory scale and with a limited number of samples, which restricts direct extrapolation to industrial production. Furthermore, the tests were carried out under controlled environmental conditions, without considering the effects of prolonged exposure to humidity, temperature, or aggressive agents. Dynamic properties or parameters related to direct seismic performance, such as the modulus of elasticity and damping, were not evaluated. The carbon footprint or environmental impacts of unit manufacturing were not quantified, although the results suggest a favorable relationship between industrialization and sustainability. Finally, the results are limited to the geographical and productive context of the Latacunga canton, so their external validity must be verified in other regions and with different aggregate conditions and curing processes. Future studies should include advanced microstructural analysis, accelerated aging cycles, and full-scale evaluations to consolidate physical, mechanical, and environmental performance models for nonstructural masonry in Ecuador.

It is worth noting that [16] and [17] do not require experimental determination of the percentage of voids for perforated units. Therefore, this parameter was not measured in this study and is considered beyond its scope. At the same time, the classification of the blocks as lightweight perforated units is based on their geometry and bulk density.

5. Conclusions

The results of this research confirm that the quality of the concrete block manufacturing process decisively influences the physical-mechanical, constructional, and economic performance of nonstructural masonry used in frame buildings. The pressed blocks showed more stable, homogeneous properties, whereas the caramelo blocks showed greater variability due to artisanal production, which directly affects the durability and safety of the enclosures.

Both types of blocks are classified as lightweight according to [16]; however, these differences confirm that, while the pressed block (PB) meets the absorption limit for Class A units (<288 kg/m^3), neither type reached the minimum strength of 3.5 MPa required by the same standard for blocks for nonstructural use (Class B). This behavior demonstrates the direct influence of the compactness and homogeneity of the manufacturing process on regulatory compliance and on the material's structural response. The strength of the masonry walls followed the same trend: those built with pressed blocks reached 3.17 MPa, compared to 1.04 MPa for those built with caramelo blocks. This result confirms that the quality of the basic unit determines the overall strength of the masonry, consistent with international studies that associate block-mortar adhesion and geometric uniformity with stiffness and load-bearing capacity. The identified failure modes—progressive

crushing and diagonal cracking accompanied by joint separation—highlight the role of porosity and water absorption in governing stress redistribution and cohesion loss in masonry elements.

From a construction perspective, the pressed blocks offered superior performance, reducing construction time by 27.4% and the volume of mortar and plaster used by 32.7%. The dimensional regularity, the smaller joint thickness (1.5 cm versus 2.4 cm), and the low absorption of the pressed blocks reduced material waste and the need for corrections, optimizing personnel efficiency and improving the surface quality of the finished walls.

The economic analysis showed that although the caramelo block had a lower unit cost per piece, its total application cost was higher (USD 14.05/m^2 for masonry and USD 6.77/m^2 for plaster) than that of the pressed blocks (USD 12.69/m^2 and USD 5.33/m^2, respectively). Overall, the pressed block system was 13.45% more economical per square meter of finished wall, confirming that better initial quality translates into overall savings in materials, time, and resources.

In terms of durability, the pressed block exhibits greater density and compactness, which enables better performance under humidity-drying cycles, aggressive agents, and thermal variations. In contrast, the more porous structure of the caramelo block limits its use to indoor or low-exposure environments. This contrast reinforces the need to improve curing and aggregate selection processes in artisanal production, as well as to implement continuous technical controls in manufacturing plants. Overall, the results show that pressed block is the most suitable alternative for infill masonry in framed buildings in the Andean region, balancing quality, safety, productivity, and sustainability. Its use contributes to reducing waste, optimizing resources, and extending the useful life of buildings, aligning with internationally promoted material efficiency and sustainable construction policies.

Finally, the need to strengthen quality control mechanisms and strictly enforce [16] In local production plants, priority strategies are reinforced to improve the quality of the housing stock, reduce economic losses due to construction inefficiencies, and mitigate vulnerabilities in seismic zones such as the central Sierra of Ecuador. Future studies should incorporate dynamic analysis, accelerated durability assessment, and carbon footprint calculation to consolidate comprehensive models that link material quality, sustainability, and structural performance in Ecuadorian construction.

References

[1] Álvarez-Pérez J, Mesa-Lavista M, Chávez-Gómez JH, Fajardo-San Miguel G, Carpio-Santamaría FA, García-Cedeño R. Analysis of behavior and uniaxial compression failure modes in ungrouted hollow concrete block masonry and their implication in design expressions. Journal of Building Engineering 2024;98:111048. https://doi.org/10.1016/J.JOBE.2024.111048.

[2] Medeiros WA, Parsekian GA, Moreno AL. Residual mechanical properties of hollow concrete blocks with different aggregate types after exposure to high temperatures. Constr Build Mater 2023;377:131085. https://doi.org/10.1016/J.CONBUILDMAT.2023.131085.

[3] Ozmen HB, Inel M. Effect of concrete strength and detailing properties on seismic damage for RC structures. Research & Design 2024;1:1–11. https://doi.org/10.17515/REDE2024-005EN1124RS.

[4] Escamirosa Montalvo LF, Molina Narváez N. Análisis de la resistencia a la compresión de bloques de concreto usados en la construcción de viviendas en la ciudad de Tuxtla Gutiérrez, Chiapas. Revista Espacio I+D Innovación Más Desarrollo 2022;XI:34–47. https://doi.org/10.31644/IMASD.29.2022.a03.

[5] Chávez-Gómez JH, Álvarez-Pérez J, Mesa-Lavista M, García-Cedeño R, Carpio-Santamaría FA, Fajardo-San-Miguel G, et al. Experimental dataset of masonry prisms with hollow concrete blocks. Data Brief 2024;53:110207. https://doi.org/10.1016/J.DIB.2024.110207 .

[6] Ozmen HB, Tanrıverdi B. Concrete paradox: Economic importance, environmental impacts, and the sustainability of concrete material. Research & Design 2025;2:66–84. https://doi.org/10.17515/REDE2025-008EN0801RS.

[7] Jeon JH, Son YH, Kim TJ, Jo SB. Engineering performances of permeable concrete blocks using oyster shell, bottom ash, and biochar. Constr Build Mater 2024;440:137374. https://doi.org/10.1016/J.CONBUILDMAT.2024.137374.

[8] Sim Y, Oh S, Song C, Lee SC, Hong G. Utilization of steel slag for sustainable concrete blocks: Laboratory study on water absorption, flexural strength, carbon dioxide capture, and volumetric expansion. Journal of Building Engineering 2025;111:113335. https://doi.org/10.1016/J.JOBE.2025.113335.

[9] Hwalla J, Al-Mardeai S, Al-Zuhair S, Moheimani N, Hamza W, El-Maaddawy T, et al. Properties and microstructure of concrete masonry blocks incorporating chrysotila carterae microalgal biomass. Journal of Building Engineering 2025;111:113585. https://doi.org/10.1016/J.JOBE.2025.113585.
[10] Azouggagh M, El Aabbas M, Bouchikhi A, Farkach Y, Safhi AEM, Assoudi R, et al. Hollow concrete blocks incorporating a phase change material: thermal and mechanical behaviours analysis. Thermal Science and Engineering Progress 2025;64:103841. https://doi.org/10.1016/J.TSEP.2025.103841.
[11] Do DD, Luong NT, Tran TT, Bui HM. Utilization of waste materials for ultra-lightweight and thermal insulating concrete blocks. Sustainable Chemistry One World 2025;5:100039. https://doi.org/10.1016/J.SCOWO.2024.100039.
[12] Mesa-Lavista M, Romo-Letechipía P, Álvarez-Pérez J, González-Alcorta R, Chávez-Gómez JH, Fajardo-San Miguel G. Shear strength dataset of hollow concrete block masonry with different mortar bedding. Data Brief 2024;57:111144. https://doi.org/10.1016/J.DIB.2024.111144.
[13] Sathurshan M, Derakhshan H, Thamboo J, Gill J, Inglis C, Zahra T. Compressive strength in grouted dry-stack concrete block masonry: Experimental and analytical predictions. Constr Build Mater 2025;467:140411. https://doi.org/10.1016/J.CONBUILDMAT.2025.140411.
[14] Zhang Z, Dong Y, Sun H, Yang H, Sun M, Wang R, et al. Seismic behavior and repairability of new composite concrete block wall with distributed slipping damage. Structures 2025;75:108683. https://doi.org/10.1016/J.ISTRUC.2025.108683.
[15] INEC. Estadísticas de Edificaciones (ESED) Permisos de construcción, I Trimestre 2025. 2025.
[16] NTE INEN 3066. Bloques De Hormigón. Requisitos Y Métodos De Ensayo. 2016.
[17] NTE INEN 3153. Muretes De Mampostería Elaborados En Laboratorio. Determinación De La Resistencia A La Compresión. 2020.
[18] Nuñez P, Palacios F, Taranto E, Armijos S. Elaboración Y Caracterización De Un Material Compuesto Con Polietileno De Tereftalato Para La Fabricación De Bloques. Perfiles 2023;1:52–62. https://doi.org/10.47187/perf.v1i29.206.
[19] Herrera-González J, Ortiz-Rabell G, Xilotl-Domínguez J, Ojeda-Farias O, Flores-Vivian I, Vázquez-Leal F, et al. Use of waste material from the chemical industry for the production of low-strength concrete hollow blocks. Sustainable Materials and Technologies 2024;40:e00870. https://doi.org/10.1016/J.SUSMAT.2024.E00870.
[20] Musab Manzoor K, EhtishamUddin S. Utilization of a mixture of waste plastic materials and granite particles as a partial replacement of coarse aggregate in concrete blocks. Mater Today Proc 2023. https://doi.org/10.1016/J.MATPR.2023.05.095.
[21] NTE INEN 856. Áridos. Determinación De La Densidad, Densidad Relativa (Gravedad Específica) Y Absorción Del Árido Fino. 2010.
[22] NTE INEN 2380. Cementos Hidráulicos. Requisitos De Desempeño Para Cemenos Hidráulicos. 2011.
[23] NTE INEN 156. Cemento Hidráulico. Determinación De La Densidad. 2009.
[24] NTE INEN 157. Cemento Hidráulico. Determinación De La Consistencia Normal. Método De Vicat. 2009.
[25] NTE INEN 158. Cemento Hidráulico. Determinación Del Tiempo De Fraguado. Método Del Vicat. 2009.
[26] NTE INEN 2502. Cemento Hidráulico. Determinación Del Flujo En Morteros. 2009.
[27] NTE INEN 488. Cemento Hidráulico. Detrerminación De La Resistencia A La Compresión De Morteros De 50 mm DE ARISTA. 2009.
[28] Kuoribo E, Shokry H, Mahmoud H. Attaining material circularity in recycled construction waste to produce sustainable concrete blocks for residential building applications. Journal of Building Engineering 2024;96:110503. https://doi.org/10.1016/J.JOBE.2024.110503.
[29] Brough C, Staniforth B, Garner C, Garside R, Colville R, Strongman J, et al. High risk concrete blocks from County Donegal: The geology of defective aggregate and the wider implications. Constr Build Mater 2023;408:133404. https://doi.org/10.1016/J.CONBUILDMAT.2023.133404.
[30] Qi Y, Wang Q, Li Z, Xiong Y, Wang C. Durability and microstructure of bulk solid waste recycled concrete load-bearing block under freeze-thaw cycles. Journal of Building Engineering 2025;112:113881. https://doi.org/10.1016/J.JOBE.2025.113881.
[31] Zahra T, Thamboo J, Asad M. Compressive strength and deformation characteristics of concrete block masonry made with different mortars, blocks and mortar beddings types. Journal of Building Engineering 2021;38:102213. https://doi.org/10.1016/J.JOBE.2021.102213.
[32] Gouda O, Hassanein A, Youssef T, Galal K. Stress-Strain Behaviour of Masonry Prisms Constructed with Glass Fibre-Reinforced Grout. Constr Build Mater 2021;267:120984. https://doi.org/10.1016/J.CONBUILDMAT.2020.120984.
[33] Ghiassi B, Lourenço PB. Long-term Performance and Durability of Masonry Structures: Degradation Mechanisms, Health Monitoring and Service Life Design. Elsevier; 2018.
[34] Zhang Z, Dong Y, Zhang S, Yang J, Chen C, Song X, et al. Seismic performance of new composite concrete block bearing wall with good sound insulation. Constr Build Mater 2025;481:141648. https://doi.org/10.1016/J.CONBUILDMAT.2025.141648.

Blank Page

Research on Engineering Structures & Materials
www.jresm.org

Review Article

Comparative bibliometric and AI-Enhanced analysis of dredged sediments, plant residues, and plastic fibers as eco-friendly additives for sustainable concrete, toward an integrated AI framework

Othmane Karrame [*,1,a], Mohammed Aqil [2,b], Mohammed Ammari [1,c], Laïla Ben Allal [1,d]

[1]*Research Team, Materials, Environment and Sustainable Development (MEDD), FST Tangier, Abdelmalek Essaadi University, Tetouan, Morocco*
[2]*3GIE laboratory, Mohammadia School of Enginnering, Mohamed V University, Rabat, Morocco*

Article Info

Article History:

Received 12 Nov 2025
Accepted 03 Dec 2025

Keywords:

Civil engineering;
Concrete durability;
Dredged sediments;
Plant residues;
Plastic fibers;
Bibliometric analysis;
AI-based clustering;
Sustainable construction;
Marine environment

Abstract

Current research in the field of sustainable concrete is part of an evolutionary transition toward a circular economic model aimed at reducing the environmental footprint of construction materials. This study proposes a bibliometric and comparative analysis of three families of eco-sustainable additives: dredged sediments, plastic fibers, and plant residues incorporated into the concrete matrix. From a database of 245 formulations extracted from the literature (52 sediments, 147 plastic fibers, 46 plant residues), optimal performance ranges were identified: 10–20% sediment substitution, 0.3–1% plastic fiber incorporation, and 1–8% plant residue addition. Research trends were examined using VOSviewer, followed by a semantic analysis assisted by artificial intelligence to refine the interpretation of bibliometric clusters and uncover significant conceptual relationships. The AI-enhanced analysis highlights pretreatment processes (thermal activation, washing, alkali/mineralization treatments) and mixing protocols as key variables controlling mechanical, microstructural, and durability outcomes across studies. The results emphasize the specific strengths and limitations of each additive family and reveal a clearly structured scientific landscape. The integration of artificial intelligence into the bibliometric workflow provides an integrated and reproducible methodological framework, supporting future AI-driven modeling and predictive optimization of eco-sustainable concrete formulations.

© 2025 MIM Research Group. All rights reserved.

1. Introduction

Today, the most widely used construction material in the world is concrete, whose global production volume is practically 4.05 billion tons in 2023 (more precisely 4.041) [1]. This constant consumption testifies to its central place in the "infrastructure" sector. But it has a non-negligible environmental impact, not only because of the production of CO during the manufacture of clinker which is the main component of cement but also because of this very production. In Morocco, national cement production amounted to 12.51 million tonnes in 2023 according to the Professional Association of Cement Makers [2]. Although this sector is both a powerful lever for economic development and a major player in the modernization of infrastructure, it is among the most energy-intensive and greenhouse gas-emitting sectors due to its dependence on limestone and fossil fuels. In addition to its environmental footprint, concrete must also face aggressive exposure conditions that limit its

*Corresponding author: othmane.karrame@etu.uae.ac.ma
[a]orcid.org/0009-0008-2530-5966; [b]orcid.org/0000-0001-6030-2287; [c]orcid.org/0000-0002-5664-7546; [d]orcid.org/0000-0001-8801-5570
DOI: http://dx.doi.org/10.17515/resm2025-1350ma1112rv

durability over time. These exposure conditions are grouped under the term aggressive medium, which is synonymous with physico-chemical attacks being of several orders.

- Marine environment: the intrusion of chloride ions (Cl) plays a role in reinforcement corrosion, internal cracking and loss of steel-concrete adhesion. Repeated wetting and drying cycles and the mechanical action of the waves promote the degradation of port and coastal structures [3]; [4]; [5]:
- • Sulfate environment: the presence of sulfates (SO_4^{2-}), due either to soil, groundwater, or industrial wastewater, will lead to the formation of ettringite and gypsum, causing volume expansion, cracking, and loss of mechanical resistance in concrete.
- • Carbonation: by a diffusion process, atmospheric CO_2 penetrates into the pore matrix and interacts with the portlandite ($Ca(OH)_2$), resulting in an internal reduction of pH that can promote the corrosion of the steel through the loss of its passive protective film.
- • Acidic Environment: Waste waters, acid rains, or biological activity might decrease the pH of the environment below 5 and thus dissolve the hydrates of calcium, leading to the progressive disintegration of the cement paste.
- • Mixed Environment: Marine + Industrial - The polluted coastal or harbor environments combine very often the action of chlorides and sulfates, which may lead to much more complex and synergistic degradations.

These various categories of aggressions alter the mechanical strength, durability and compactness of the concrete, calling into question the safety and durability of the structures, including those subjected to extreme conditions such as ports, dams, treatment plants or industrial areas. To this end, scientific research focuses on the design of sustainable and ecological concrete, capable of resisting aggressive environments while reducing their carbon footprint. Among the most promising strategies, the valorization of alternative materials from waste or by products dredging sediments, recycled plant residues or plastic fibers allowing to partially replace the traditional constituents of concrete is part of the logic of the circular economy, aiming both at reducing the extraction of natural resources, to limit CO emissions and to perpetuate structures subject to aggressions.

In this context, and although the literature proposes numerous solution strategies centered on alternative materials, existing works generally investigate a *single* additive at a time and rarely provide comprehensive comparative analyses. As detailed in Section 3, studies focusing simultaneously on different families of additives remain scarce, fragmented and often non-standardized. Therefore, a comparative and integrative approach synthesizing three distinct categories of contributions is required. Moreover, addressing this scientific gap necessitates not only classical experimental investigations but also systematic bibliometric analyses and AI-based methods capable of structuring large datasets and revealing trends, synergies and performance determinants. These considerations clarify the originality of the present study from the outset and justify the need for a multi-scale, comparative and data-enhanced assessment of sustainable concrete formulations.

These three materials are explicitly examined as representative families contributing to sustainable concrete within a circular economy framework. The article compares their mechanical, durability-related and microstructural impacts based on a two-level methodology combining (i) a systematic bibliometric analysis and (ii) an AI-assisted semantic analysis, enabling an integrated and data-driven interpretation of research trends and performance criteria across the literature.

2. Valorization of Waste in Concrete

The recovery of waste in concrete is part of a global circular economy strategy aimed at reducing the environmental footprint of the construction sector while developing high-performance materials. Research conducted over the past two decades has demonstrated that several categories of waste such as dredged sediments, plant residues and plastic fibers can be incorporated into concrete formulations as mineral fillers, cementitious additions, reinforcing fibers or granular substitutes. Their incorporation modifies the microstructure, hydration kinetics and mechanical and durable properties of the material.

2.1. Dredging Sediments

Dredging sediments are derived from maintenance and depth-control operations in harbours, marinas, river channels and littoral areas. Often discharged to the environment or landfilled, they represent a significant annual volume in coastal regions, while several recent studies demonstrate their potential for recovery in cementitious materials, provided appropriate treatment. These sediments generally have a fine to very fine granulometry (D50 between 5 and 80 µm), a variable clay content (montmorillonite, illite, kaolinite), a richness in amorphous silica and aluminosilicates, as well as the possible presence of organic materials (1 to 12%), heavy metals or salts characteristic of marine environments. These properties strongly influence their interaction with the cement matrix.[6,7]. To ensure their compatibility with the standards EN 206 or NM 10.1.008, several preliminary treatments are necessary, notably decantation and washing to reduce salinity (Na , Cl , SO 2), screening to remove coarse particles, thermal drying to control humidity, possible calcination between 600 and 750 °C in order to activate their pozzolanic reactivity, as well as stabilization in case of the presence of organic materials or pollutants. The integration of 5 to 20% of calcined or stabilized sediments in concrete generally improves compactness thanks to the filler effect, increases long-term mechanical strength (from +5 to +15% at 90 days), reduces permeability and capillary porosity by up to 20%, and to improve durability in aggressive environments, particularly marine, due to the increased consumption of Ca(OH) and the decrease in free ions. However, incorporation rates exceeding 20 to 25% may result in a decrease in initial strength due to the reduction in the quantity of clinker hydrated [8-16].

2.2. Plastic Fibers

The incorporation of recycled plastic fibres into concrete formulations today represents a promising avenue for the valorization of polymeric waste, particularly those resulting from the crushing of PET bottles, agricultural packaging or industrial plastics such as polypropylene. (PP), high-density polyethylene (HDPE) or PVC [17,18]. These fibers, characterized by a low density (0.9 to 1.38 g/cm^3), a high tensile strength (ranging from 400 to 900 MPa depending on the nature of the polymer) and an elastic modulus varying between 3 and 10 GPa, have excellent chemical stability as well as high resistance in alkaline medium, which promotes their durable integration into the cementitious matrix [19].Their introduction however modifies the rheology of concrete: the presence of fibers tends to reduce slump and workability, making the addition of superplasticizers necessary to maintain a good implementation. At the microstructural level, plastic fibers act as micro-bridges in the matrix, promoting stress redistribution and limiting the appearance of cracks, but they can also slightly increase the void ratio due to a less homogeneous dispersion compared to conventional industrial fibers. Studies show that the addition of recycled plastic fibres at relatively low contents, generally between 0.2 and 1% by volume, only moderately affects compressive strength (often a decrease in the order of 5 to 10%), but significantly improves the direct tensile strength and ductility of concrete, with gains that can reach 15 to 40% [20-30]. These fibers also significantly reduce plastic cracking, with decreases in crack width that can exceed 70%, while increasing the energy absorption capacity and post-cracking resistance, which makes this type of concrete particularly suitable for structures subject to dynamic stresses, impacts or vibrations. Thus, the integration of recycled plastic fibers is fully part of a circular economy approach, combining reduction of plastic waste, improvement of certain mechanical properties and development of more sustainable cementitious materials [31-41].

2.3. Plant Residues

The valorization of waste in concrete formulations has particularly significant environmental and mechanical advantages, which justify the growing interest of the scientific community for these alternative solutions. Environmentally, the integration of dredged sediments, recycled plastic fibers or plant residues reduces dependence on natural resources, particularly sand, aggregates, and industrial fibers, whose extraction exerts considerable pressure on coastal and river ecosystems [42]. This substitution is also accompanied by a significant decrease in the amount of waste sent to landfill or released into the environment, particularly in port areas where excess sediment represents a very large annual volume. In addition, the incorporation of pozzolanic materials from calcination of sediments or certain organic residues contributes to reducing clinker consumption, thus allowing a reduction in CO emissions from the cement sector [43]. From a mechanical point of view, several

studies show that these recycled materials, when integrated at optimized rates, improve the overall performance of concrete. The activated sediments promote the compacity of the matrix and reinforce long-term resistance, while decreasing permeability and capillary porosity, which results in better durability in aggressive environments, particularly marine or sulphate. Recycled plastic fibers play an essential role in controlling cracking, increasing the ductility, toughness and post-cracking strength of concrete. For their part, plant residues contribute not only to reducing the density of the material, but also to improving its thermal and acoustic performance, while limiting the appearance and propagation of cracks thanks to their behavior as natural micro-reinforcements [44,45].

Plant residues form a very heterogeneous family of materials, derived from varied natural sources such as hemp, sisal, alfa fibers, straw or even sawdust. This diversity results in strong differences in their morphology, chemical composition, cellulose–hemicellulose–lignin proportions, as well as in their intrinsic mechanical properties. All these elements directly influence their behavior once integrated into cementitious matrices. In addition to this diversity, their implementation imposes certain precautions. In most cases, plant residues must be pretreated for example by an alkaline bath (NaOH), lime mineralization or a simple washing with hot water to remove soluble sugars, reduce the amount of lignin, improve their bond with the cementitious matrix and strengthen their stability in a strongly alkaline medium. Their significant capacity to absorb water, due to their porous and hydrophilic structure, can also lead to a high demand for water in mixtures as well as swelling or shrinkage phenomena sometimes difficult to reconcile with the behavior of cement paste. [45].

These elements partly explain why plant materials show more fluctuating performances than mineral or synthetic additives, and remind the importance of properly characterizing and treating them before integrating them into a concrete. Thus, the recovery of this waste is part of a global approach aimed at developing more sustainable concrete, more resilient and better suited to the contemporary requirements of civil engineering, while responding to the major challenges of ecological transition and circular economy [46].

3. Research Problem

The formulation of concrete from alternative materials and unconventional additives is today a field of research in full expansion, motivated by environmental, economic and technical challenges that the civil engineering sector is facing [47]. However, despite the abundance of work devoted to specific additives such as dredged sediments, recycled plastic fibers, plant residues or various mineral additives the scientific literature remains largely fragmented. The majority of existing studies focus exclusively on one type of additive, often under laboratory-specific experimental conditions, which makes it difficult to establish direct comparisons or construct a global model for interpretation. This fragmentation considerably limits the systemic understanding of the mechanical, physico-chemical and microstructural phenomena induced by these materials, and does not allow for an accurate evaluation of their relevance according to the contexts of use, especially in aggressive environments such as marine or sulphated environments.

In addition, it is important to note that available comparative studies remain scarce and generally partial. They are often based on small data samples, non-standardized experimental protocols or analyses limited to a single performance criterion (e.g. mechanical strength or durability), without integrating a multi-criteria methodology capable of translating all the complexity of the behavior of innovative concretes. The absence of synthetic works combining several types of additives under identical conditions prevents identifying possible interactions, possible synergies or antagonistic effects that could lead to optimized formulations. This scientific gap also limits the emergence of coherent and reproducible industrial valorization strategies [9].

Finally, the literature offers very few global visions allowing to identify the current major scientific trends. In particular, there is a lack of systematic work capable of organizing, structuring and analyzing the vast amount of information available on mechanical performance, sustainability, environmental impacts or digital transformation of the sector (Construction 4.0). Moreover, the lack of integration of artificial intelligence approaches in data synthesis and in formulation optimization leads to a loss of opportunities in innovation and predictive modeling. Thus, in a context where engineers and decision-makers are seeking to develop more efficient and sustainable concretes, the

lack of an integrated vision is a major obstacle to scientific progress and the implementation of large-scale solutions. [10].

This issue highlights the need for in-depth research aimed at gathering, harmonizing and analyzing in a structured way the knowledge related to the different additives studied. Such an approach would not only allow for a better understanding of their compared performances, but also to identify the most promising optimization paths thanks to artificial intelligence tools and multi-criteria analyses, thus paving the way for a new generation of sustainable concrete adapted to the contemporary requirements of civil engineering works.

4. Aims and Original Contributions of the Study

The objectives of this article are part of a process aimed at analyzing, comparing and structuring in-depth the current state of scientific knowledge regarding the use of innovative additives in concrete formulation. The first objective is to compare three main families of additives dredging sediments, plant residues and recycled plastic fibers by mobilizing both a systematic bibliometric approach and the exploitation of experimental data available in the literature. This comparison will make it possible to identify the mechanical, environmental and sustainable performances associated with each family, while identifying their advantages, limitations and relevant fields of application.

The second objective consists in identifying the dominant themes and conceptual interactions that structure the field of research, notably through the analysis of co-occurrences of keywords, the formation of thematic clusters and the highlighting of conceptual links between published works. This approach will allow understanding the scientific dynamics that guide research on alternative materials used in concrete.

A third objective is to introduce a first integration of artificial intelligence tools in the critical analysis of literature by using semantic analysis techniques and automatic language processing. These methods will automatically extract trends, convergences, gaps and relationships between the different scientific contributions, thus offering an integrated and more objective view of the available knowledge.

Finally, a final major objective is to explore the potential of artificial intelligence for optimizing concrete formulation, particularly highlighting the capabilities of predictive models, machine learning algorithms, and multi-optimization approaches. The article thus aims to demonstrate how AI can contribute to improving the durability, mechanical properties and resistance of concrete in aggressive media, paving the way for innovative and scientifically optimized formulations.

5. Methodology

5.1. Constitution of the Database

In order to conduct a rigorous comparative analysis of the performance of innovative additives used in concrete formulation, a global database was established from 245 formulations extracted from scientific publications published between 2010 and 2025. These data were classified into three families of additives:

- 52 formulations based on dredged sediments [6–8], [11–16],
- 147 formulations incorporating recycled plastic fibers [17–41],
- 46 formulations using plant residues [42–53].

For each formulation, the database systematically compiles all essential parameters for mechanical, microstructural, and durability assessment: compressive and flexural strength, porosity, water absorption, density, electrical resistivity, behavior in aggressive environments, as well as additive proportions and treatment conditions. A standardization of units (MPa, %, kg/m^3, µm/m, etc.) and a cross-validation of the extracted values were performed to guarantee coherence and comparability across heterogeneous experimental sources. This structured and homogenized dataset forms a robust foundation for identifying dominant trends, supporting reliable comparisons across additive families, and enabling the subsequent statistical analysis, bibliometric processing, and AI-based modeling presented in the next sections.

5.2. Descriptive Analysis of Data

5.2.1. Dredged Sediments

The sediment dataset includes 52 formulations published between 2010 and 2025. Substitution levels vary widely (5–30%), with optimized studies reaching 20% + thermal activation. The most efficient mechanical performance is generally reported between 10% and 20% substitution, particularly when sediments are calcined or washed [6,7].

Compressive strengths range from 15 MPa (untreated or low-dosage mixes) to 90 MPa in highly optimized binders combining thermally activated sediments and supplementary cementitious materials (e.g., metakaolin, slag). This broad spread (7–90 MPa) reflects the heterogeneity of protocols [6].

Porosity values typically fall between 12% and 22%, with optimal values around 15%, while water absorption generally ranges from 6–12%, reaching 6.5–7% for activated sediments. Non-activated sediments often show values close to 10–12%, indicative of a more open microstructure. Density remains stable (2360–2400 kg/m^3) for substitution levels below 20% [8], [11].

Durability indicators reveal clear improvements under aggressive conditions when sediments are activated: reduced cracking, lower chloride penetration, and higher electrical resistivity (e.g., 12h/12h marine cycles over 7 years) [12]. Remarks such as “overall optimum,” “good sulfate resistance,” or “better durability” are reported for well-treated sediments [13]. In contrast, observations such as “ash excess: loss Rc” highlight mechanical reductions when substitution exceeds ~25%.

Overall, the data underline that the best mechanical and durability performances occur with 10–20% substitution, combined with appropriate treatment (washing + drying + thermal activation at 600–750°C) [13–16].

5.2.2. Recycled Plastic Fibers

The plastic fiber dataset comprises 147 formulations, making it the most abundant family [17–41]. Incorporation levels range from 0.1% to 3% by volume, with most studies favoring <1%, corresponding to the optimal zone for polymers such as PET, PP, and HDPE.

Compressive strengths span from 20 MPa (low-dosage or non-structural mixes) to 66 MPa for optimized formulations. Porosity varies between 8–16%, with an optimum around 11%, while water absorption ranges from 3.5–6%, with the best values near 4.8%. Density fluctuates between 2250 and 2400 kg/m^3, with a modal value of 2400 kg/m^3, indicating a limited influence on compactness [24–33].

Author comments consistently emphasize enhanced crack control, ductility, and post-cracking behavior, even when compressive strength remains unchanged or slightly reduced. In aggressive environments, fiber-reinforced concrete often shows reduced chloride penetration, attributed to slowed ion diffusion caused by micro-bridging effects. However, dosages above 1.5–2% cause issues such as segregation, increased porosity, reduced compactness, or insufficient dispersion. The best mechanical and microstructural compromises are found at 0.3–1% fiber content [34–41].

5.2.3. Plant Residues

The plant residue dataset includes 46 formulations using materials such as hemp, sisal, alfa fibers, sawdust, vegetable particles, and various agricultural by-products. Incorporation levels range from 0.5% to 30%, depending on whether residues serve as fibers or as partial aggregate replacements [42–44].

Compressive strengths range from ~12 MPa (lightweight concretes or high-residue mixes) to 48 MPa for optimized formulations, including long-term data showing 48.3–46.8 MPa after 7 years in marine exposure [45–49].

Porosity values range from 10–20%, with an optimum near 13.5%. Water absorption is higher than for plastic fibers (6–12%), with the best results (~5.5%) recorded for mineralized or alkali-treated

fibers. Density varies from 2100 to 2360 kg/m^3, with a modal value at 2360 kg/m^3, typical of formulations with <10% plant content.

Author remarks underline their benefits for crack control, lightening concrete, and thermal insulation, but also highlight strong water sorption sensitivity and alkaline instability when fibers are not pretreated (alkali soaking or mineralization). Positive assessments include “very good in the marine environment,” “correct sulfate resistance,” and “excellent long-term stability.” Conversely, several studies note “loss of long-term strength,” “alkaline degradation,” and “excessive absorption.” The best results occur for 1–8% incorporation, combined with chemical pretreatment (NaOH, $Ca(OH)_2$, sodium silicate) to stabilize fibers and improve adhesion to the cementitious matrix [50–53].

5.3. Bibliometric Analysis: Method and Thematic Structure

The bibliometric and conceptual analysis developed in this article is based on VOSviewer (version 1.6.20), a tool specialized in the construction and visualization of scientific networks. Data was collected from the Scopus, ScienceDirect and Google Scholar platforms, which offer a broad and up-to-date coverage of work on innovative cementitious materials and concrete durability. The documentary research was based on a selection of keywords representative of the studied themes, notably "eco-concrete", "dredged sediments", "plastic fibers", "plant residues", "durability" and "marine exposure", to which were associated complementary terms referring to mechanical performance, resistance in aggressive environments, and optimization approaches. The bibliometric analysis was based on three main axes:

- Tthe co-occurrence of keywords, allowing to map the relationships between concepts;
- Density maps, identifying areas of thematic intensity;
- Clustering, which groups publications into homogeneous conceptual sets.

In parallel, a thorough conceptual analysis was conducted to structure and interpret the interactions between the central notions. This analysis made it possible to identify the key concepts related to the three families of additives (mechanical reinforcement, sustainability in the marine environment, environmental enhancement, formulation optimization), to identify theoretical convergences, the gaps in the literature and potential complementarities. The joint integration of bibliometric and conceptual approaches thus provides a global vision of the scientific landscape, revealing both emerging trends, the dominant research orientations and areas still little explored which will serve as a basis for comparative analyses and subsequent methodological developments [9–10].

The VOSviewer graphs obtained from this analysis reveal distinct conceptual organizations for each additive family. For dredged sediments, three major clusters emerge: an environmental–conceptual cluster associated with eco-friendly concrete, marine exposure and microstructure refinement; a mechanical cluster linking concepts such as compressive strength, density and shrinkage; and a durability cluster including porosity, water absorption, chloride resistance and sulfate resistance. This thematic structure reflects the strong research focus on durability issues in marine environments for sediment-based concretes.

The plant residue network shows clusters centered on pretreatment strategies (calcined residue, phosphate-treated residue), mechanical behavior (compressive strength, tensile strength) and durability indicators (gas permeability, sulfate resistance, cracking). This organization highlights the inherent variability of plant-based materials and the crucial role of stabilization treatments in achieving reliable performance.

For recycled plastic fibers, the clusters reveal dominant axes around mechanical reinforcement (tensile strength, impact resistance, elastic modulus), microstructural response (porosity, water absorption) and durability performance (chloride test, freeze–thaw resistance, carbonation depth). This reflects the widespread use of plastic fibers in applications requiring improved cracking control and enhanced toughness.

5.4. Integration of Semantic AI

The integration of semantic artificial intelligence in this work aims to enrich classical bibliometric analysis by providing an automated and contextualized interpretation of conceptual relationships

present in the literature. For this, unsupervised learning was applied in the form of automatic clustering, allowing to identify natural groupings within text corpora without prior human intervention. The clustering step was performed using the K-means algorithm applied to TF–IDF vectorized textual features, which offers a robust way to uncover coherent thematic partitions within large bibliographic datasets. These clusters are then represented in the form of colorful conceptual communities, revealing the dominant themes, the emerging sub-domains as well as the interdependence links between the notions associated with the studied additives (sediments, plastic fibers and plant residues).

In order to enrich the interpretation, a second step relies on the use of a generative semantic AI, responsible for analyzing the context, extracting the implicit relationships between the concepts and explaining the consistencies or divergences between the identified clusters. This generative component relies on a large language model (LLM), used to produce contextual explanations based on conceptual proximity, co-occurrence patterns and the semantic structure of the extracted clusters. This advanced semantic analysis thus makes it possible to interpret research dynamics in a more detailed manner, highlighting conceptual trends, gaps and potential areas of innovation. Instead of referring to a figure, the paragraph now simply describes the methodological sequence directly: data extraction, textual pre-processing, unsupervised clustering, visualization of thematic communities, and automated interpretation by generative AI. These steps together form a coherent methodological workflow that combines bibliometric rigor, conceptual structuring and artificial intelligence to offer an integrated and deeply contextualized vision of the state of the art [9–10].

During the textual preprocessing phase, several operations were applied to ensure the reliability and robustness of the unsupervised clustering process. First, standard natural language processing steps were performed, including lowercasing, punctuation removal, and the elimination of non-informative stop-words. Domain-specific cleaning was then implemented to adapt the preprocessing to the high technical density of the cement and materials science literature. In particular, stemming/lemmatization was applied to reduce morphological variability while preserving the semantic integrity of engineering terminology. Furthermore, sector-specific abbreviations and acronyms frequently used in the field such as Rc (compressive strength), POFA (palm oil fuel ash), UHPC (ultra-high-performance concrete), SF (steel fiber), CFRP (carbon fiber reinforced polymer), and PKSA (palm kernel shell ash) among others; were standardized through the creation of a controlled lexicon mapping each abbreviation to a normalized term. This step prevents misleading token fragmentation and ensures consistent representation of key technical concepts across the corpus. Together, these preprocessing operations significantly improve the quality of vectorization and contribute to the stability and reliability of the clustering results.

Table 1. Statistical summary of key mechanical and physical properties for the three additive families [6-53]

Additive family	Rc min (MPa)	Rc max (MPa)	Rc mean (MPa)	Porosity min (%)	Porosity max (%)	Porosity mean (%)	Water abs. min (%)	Water abs. max (%)	Water abs. mean (%)	Density min (kg/m^3)	Density max (kg/m^3)	Density mean (kg/m^3)
Dredged sediments	5.00	90.00	32.02	7.30	37.50	17.32	3.60	16.57	10.20	1690	2460	2266.41
Recycled plastic fibers	9.00	150.00	54.65	5.00	15.70	9.49	0.50	6.20	3.31	2000	2500	2265.20
Plant residues	3.00	138.00	50.63	2.61	15.90	11.82	1.05	20.00	6.19	1230	2300	2141.60

To improve statistical clarity and provide a quantitative basis for the trends discussed in the following sections, a synthesis table was constructed from the 245 formulations included in the database. This table summarizes the key mechanical and durability indicators for each additive family (dredged sediments, recycled plastic fibers, and plant residues). The ranges and mean values presented below were extracted directly from the compiled dataset and reflect the variability reported in the literature. These quantitative benchmarks provide a clearer comparison of material behaviors and support the identification of optimal incorporation domains discussed later in the Results section.

The three sets of graphs provide a clear comparative insight into how each family of additives affects the mechanical and microstructural performance of concrete.

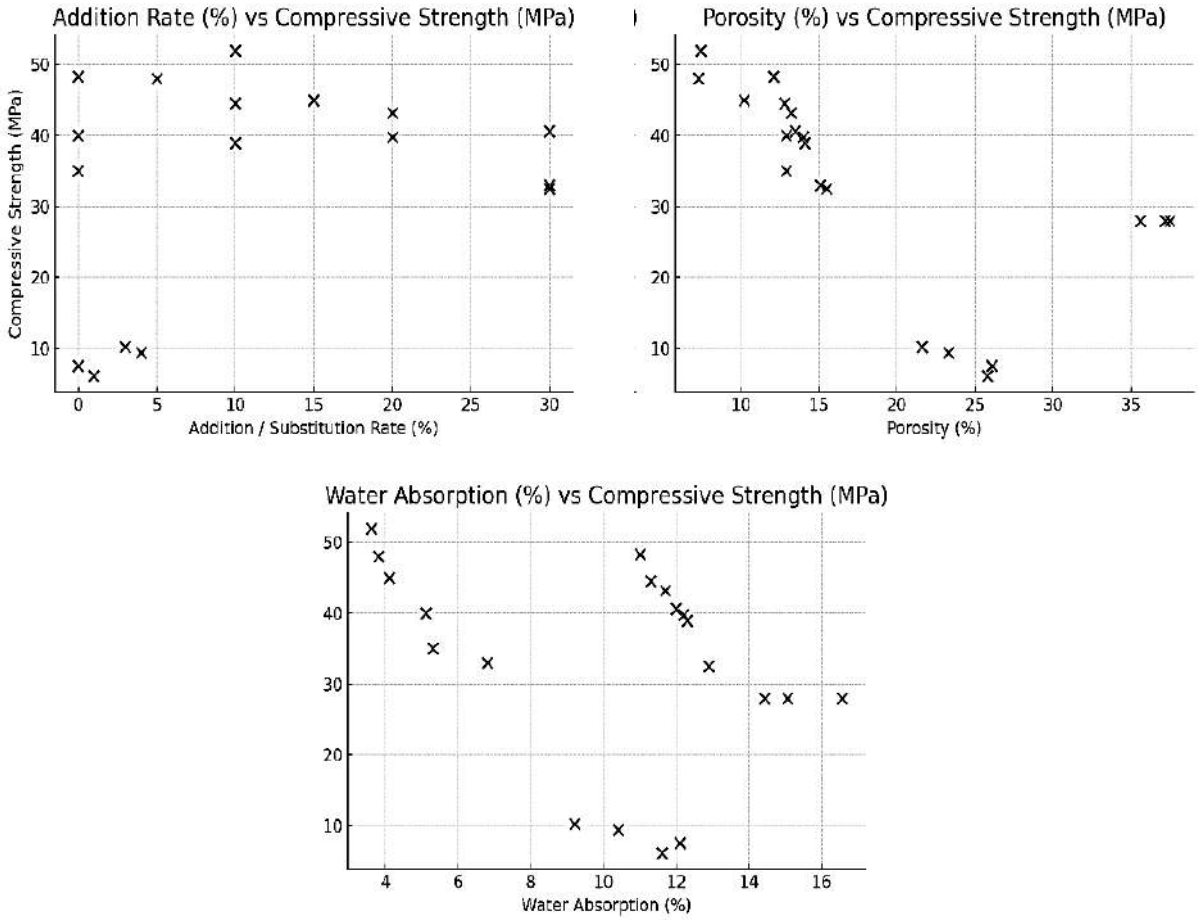

Fig. 1. Synthetic analysis of mechanical and physical properties of concrete incorporating dredged sediments [6-8, 11-16]

For dredged sediments, the results confirm that the most effective formulations are obtained at substitution levels between 10% and 20%, where compressive strength increases significantly and porosity and water absorption remain in optimal ranges. Beyond this interval, the increase in fines leads to higher porosity and reduced strength, highlighting the critical role of pretreatment (washing and thermal activation) [6-8,11-16].

For recycled plastic fibers, the data show that low fiber contents (0.3%–1%) provide the best balance between compressive strength, porosity, and water absorption. The graphs also illustrate the well-known benefit of plastic fibers in improving post-cracking performance and limiting microcrack propagation, even when strength remains unchanged. Higher fiber contents tend to reduce compactness due to dispersion issues [17 - 41].

For plant residues, the results display a much wider variability. Well-treated fibers incorporated at 1%–8% lead to moderate porosity and improved strength, whereas untreated or high-dosage mixes show very high absorption and reduced mechanical performance. The graphs confirm that chemical pretreatment is essential for stabilizing plant fibers and achieving durable composites [42 – 53].

Overall, the graphical trends highlight that the optimal performance zones are narrow and strongly dependent on both the type of additive and the quality of its preparation, confirming the relevance of a comparative and data-driven approach for mix design optimization

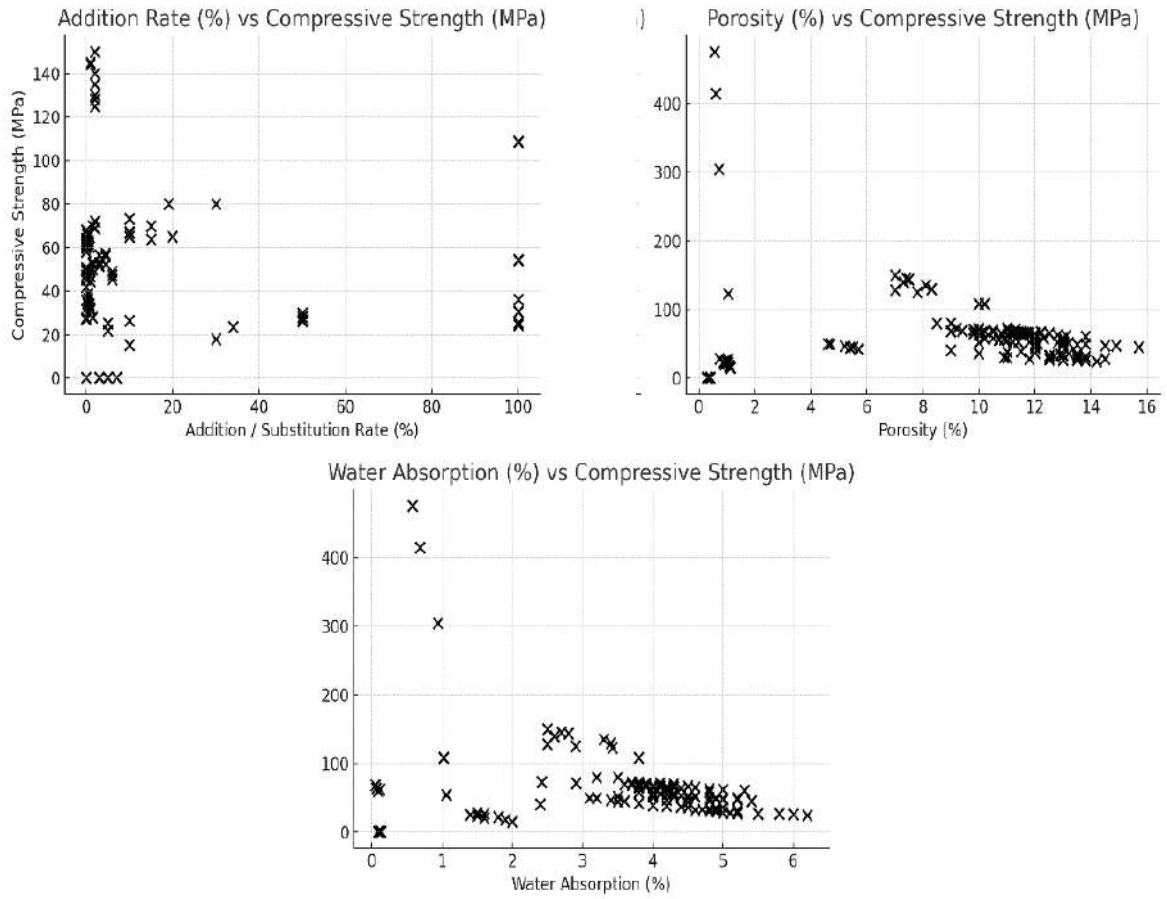

Fig. 2. Synthetic analysis of mechanical and physical properties of concrete incorporating plastic fibers [17 - 41]

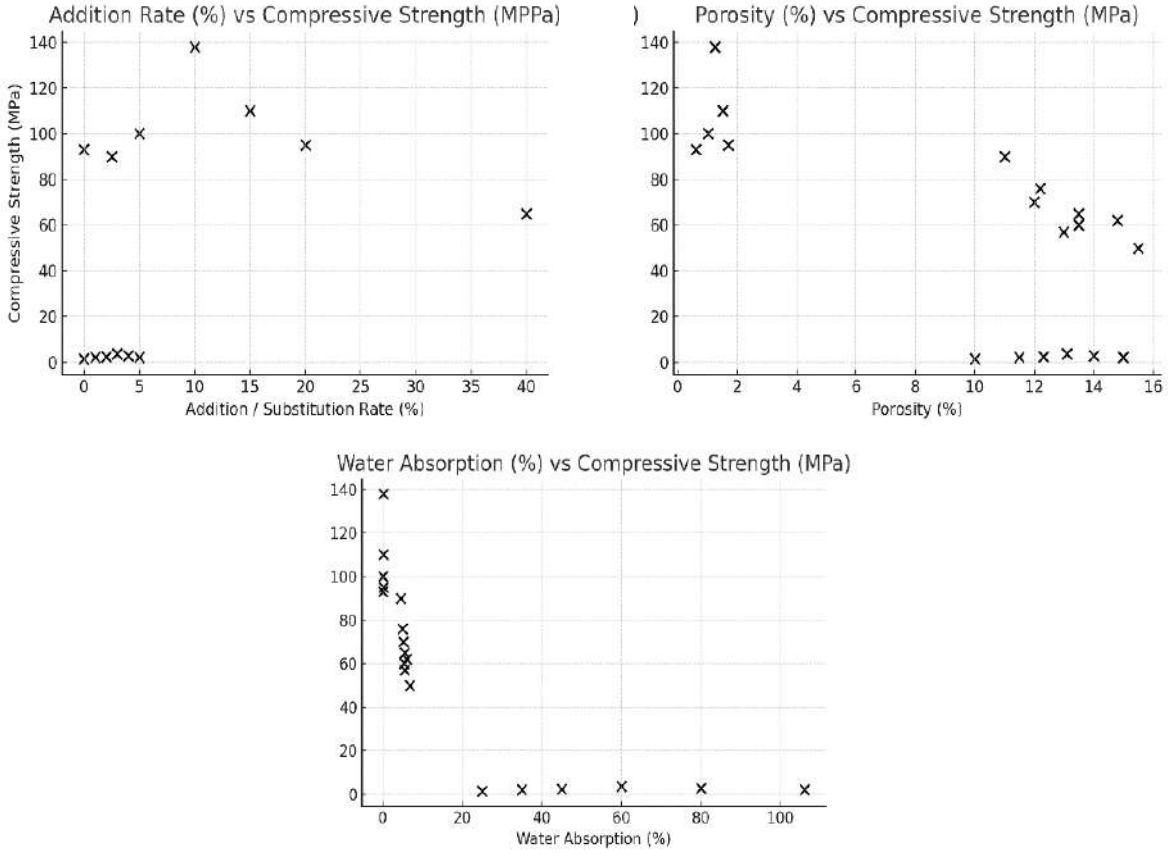

Fig. 3. Synthetic analysis of mechanical and physical properties of concrete incorporating plant residues [42 – 53]

5.5. AI-Supported Integrated Interpretation of Bibliometric Themes

5.5.1 Dredged Sediments

Dominant keywords such as eco-friendly concrete, marine exposure, and sulfate resistance confirm that sediments are primarily investigated as sustainable binders or fillers for marine and coastal infrastructure. The properties extracted from the literature indicate high sulfate resistance (up to 99%) and good long-term durability, but low compressive strength (~39 MPa) in untreated states. The density value of around 1520 kg/m^3 corresponds to a specific subset of lightweight or highly substituted formulations and does not represent the typical density range of sediment-based concretes reported in the broader dataset (generally 2360–2400 kg/m^3). Their thematic positioning suggests that dredged sediments are best suited for environmentally driven applications where durability is key but structural demands are moderate [6–8,11–16].

5.5.2 Plant Residues

Keywords including calcined plant residue, phosphate-treated residue, and cracking none emphasize the role of chemical and thermal treatments in improving performance. Optimized formulations exhibit compressive strengths around 66 MPa, low cracking, and lightweight characteristics. The thematic structure situates plant residues within the emerging field of low-carbon, eco-efficient concretes, where biodegradability and reduced environmental impact are major advantages [42-53].

5.5.3 Recycled Plastic Fibers

The dominant terms tensile strength, impact resistance, and chloride penetration underline the contribution of plastic fibers to mechanical enhancement and durability. The literature reports high compressive strength (72 MPa), a significant elastic modulus (41 GPa), improved fracture energy, and strong resistance to chloride ingress. These characteristics position plastic fibers as suitable for structural reinforced concretes, particularly in elements requiring superior toughness and crack control [17 - 41].

The integration of bibliometric network analysis with thematic interpretation delineates a well-structured differentiation in the scientific positioning and functional roles of the three additive families. Dredged sediments occupy a domain primarily centered on environmental valorization, with research converging toward their capacity to enhance durability in marine and sulfate-rich environments. Their recurrent association with durability indicators (chloride resistance, sulfate resistance, reduced permeability) underscores their relevance for exposure classes XS/XD, despite their relatively modest intrinsic mechanical contribution.

Plant residues form a thematically distinct cluster driven by low-carbon material development and matrix–fiber compatibility, where performance is highly contingent upon pretreatment strategies (calcination, alkali activation, phosphate modification). Their mechanical response and shrinkage behavior reflect the intrinsic heterogeneity of lignocellulosic fibers, positioning them within emerging bio-composite research paradigms rather than conventional structural concrete.

Recycled plastic fibers constitute the most mechanically oriented cluster, strongly linked to tensile reinforcement mechanisms, fracture energy enhancement, and crack-bridging efficiency. Their repeated co-occurrence with durability metrics (chloride penetration, freeze–thaw resistance, carbonation depth) indicates a dual role, simultaneously contributing to mechanical robustness and long-term stability under aggressive exposure conditions.

The experimental graphs show a clear optimum mechanical window for dredged-sediment mixes at ~10–20% substitution, with compressive strength increasing and porosity / water absorption decreasing in this range. Bibliometric mapping places these materials in clusters dominated by eco-friendly concrete, marine exposure and sulfate resistance, i.e. research attention focuses on durability in aggressive environments. The semantic AI analysis confirms these themes and further extracts recurring procedural qualifiers (e.g. washed, calcined, thermal activation). Combined interpretation: the experimental improvements observed in the 10–20% range are coherent with the literature clusters and are strongly conditioned by the pretreatment tags highlighted by the IA; conversely, data points beyond 25% that show strength loss correspond to publications annotated (by IA labels) with

high ash / poor dispersion, explaining the performance drop. Implication: bibliometric + IA semantics validate the experimental optimum and identify pretreatment as the key actionable parameter for scale-up. [6-8,11-16].

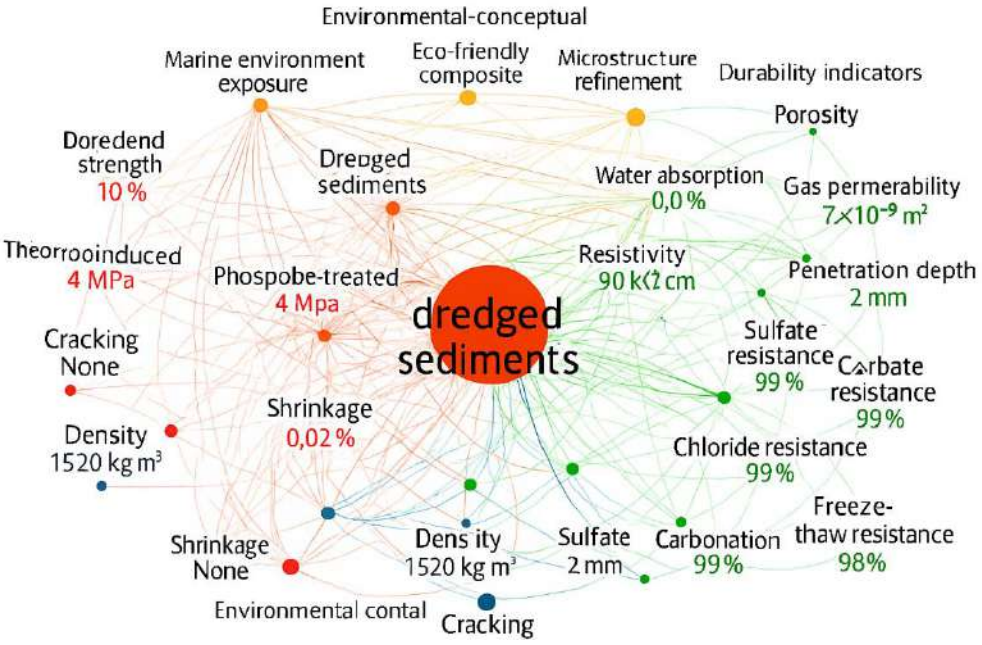

Fig. 4. Bibliometric map of dredged sediments in concrete [6-8,11-16]

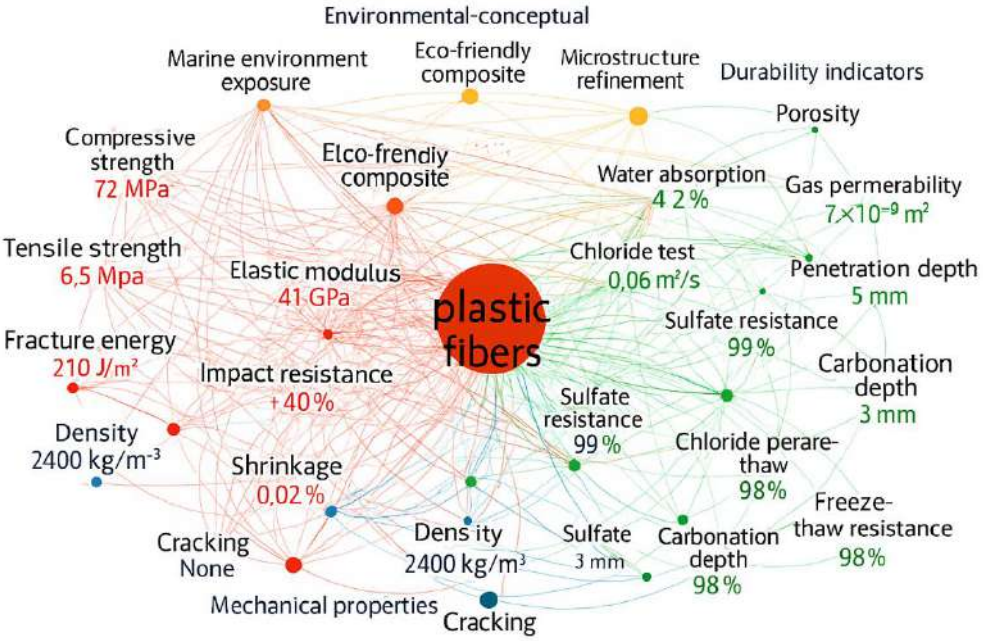

Fig. 5. Bibliometric map of plastic fibers in concrete [17 - 41]

The graphs indicate best trade-offs for 0.3–1.0% fiber content: compressive strength maintained or improved, porosity minimized and water absorption low. VOSviewer clusters emphasize tensile strength, impact resistance and durability; the semantic clustering (IA) further highlights operational constraints such as dispersion, mixing energy and superplasticizer use.

- Joint reading: the mechanical and microstructural benefits visible on the plots are consistent with the bibliometric focus on crack-bridging mechanisms; IA labels explain why higher dosages (>1.5%) degrade compactness (frequent label: fiber entanglement / segregation).
- Recommendation: control of mixing protocol (feature repeatedly flagged by IA) is essential to reproduce the positive zone shown by the graphs [17 - 41].

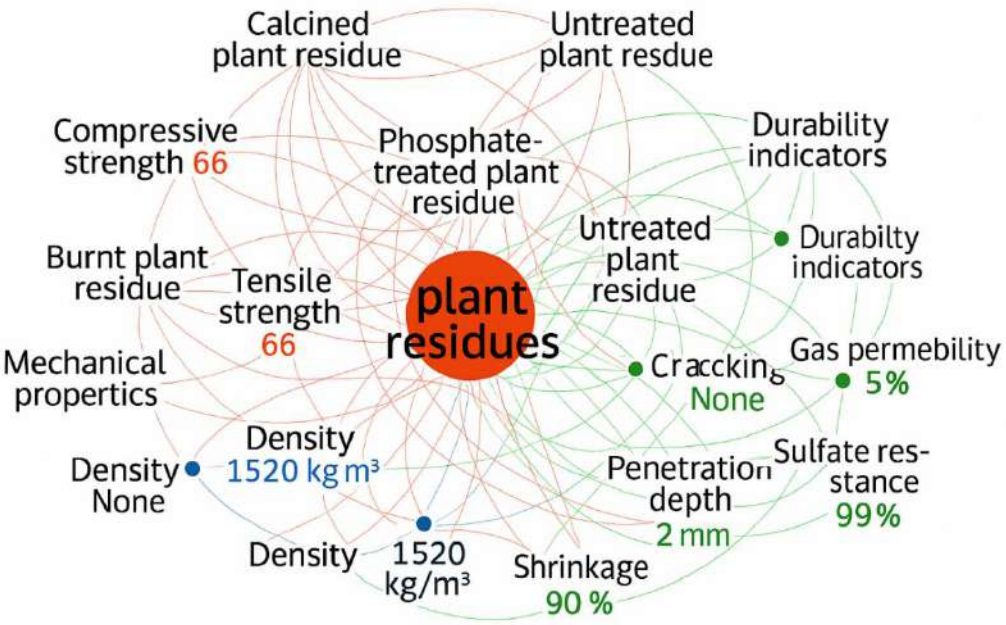

Fig. 6. Bibliometric map of plant residues in concrete [42 – 53]

Experimental plots show large variability: well-treated plant residues (chemical or thermal) at ~1–8% yield moderate to good strengths and acceptable porosity/absorption, whereas untreated or high-dose mixes show high absorption and strength loss. VOSviewer clusters center on calcined / phosphate-treated residues and crack reduction, while semantic IA highlights recurring process tags (alkali treatment, mineralization, drying protocol). Integrated conclusion: the graphs quantify the effect sizes; bibliometrics confirms research emphasis on pretreatment; IA pinpoints which treatment-terms correlate most with positive outcomes. Thus, experimental variability is not random but explained by the presence/absence of pretreatment practices identified by bibliometrics and IA. [42 – 53].

6. Experimental comparative analysis and synthetic assessment

6.1. Cross-Validation of Experimental, Bibliometric, and AI-Semantic Results

The combined reading of empirical graphs, bibliometric maps and AI semantic labels produces a coherent narrative: optimal performance domains revealed by experiments (sediments 10–20%, fibers 0.3–1%, plant residues 1–8%) are consistently supported by the literature clusters [54] and by automated semantic indicators that single out pretreatment and mixing protocol as the principal controlling variables. This cross-validation justifies focusing subsequent AI-driven optimization on the pretreatment and process features extracted from the corpus.

6.2. Comparative Environmental Potential and CO_2-Reduction Tendencies

Although the database does not provide fully standardized life-cycle assessment (LCA) values for all formulations, a cross-reading of the available literature reveals clear environmental tendencies for each additive family. Dredged sediments, when thermally activated, involve a measurable energy input due to calcination at 600–750°C [55]; however, this treatment remains significantly less carbon-intensive than clinker production, resulting in a net CO_2 reduction[56-57] when sediments replace 10–20% of cement. Recycled plastic fibers present very low embodied carbon, since their production does not require high-temperature processing, and their valorization avoids emissions associated with landfilling or incineration of plastic waste. Plant residues show the highest theoretical CO_2-reduction potential due to their biogenic origin, carbon neutrality, and the avoided emissions associated with their use as additives rather than burned agricultural waste. Their incorporation can also reduce clinker consumption when used as calcined ash.

Thus, even though the numerical quantification of CO_2 savings could not be standardized across all studies, the relative environmental ranking emerging from the database is consistent: plant residues > recycled plastic fibers > dredged sediments, with the latter still offering substantial emissions benefits when replacing cement in optimized proportions. This qualitative environmental gradient complements the mechanical and durability comparisons and aligns the material families with distinct sustainability trajectories.

6.3. Industrial Scalability and Cost Performance Balance of Pretreated Additives

The optimal performance ranges identified in this study such as thermal activation of sediments at 600–750 °C, washing processes to remove impurities, or alkali/mineralization pretreatments for plant residues imply non-negligible energy and cost inputs when considered at industrial scale. Thermal activation, for example, has a higher energy demand but yields substantial improvements in durability and mechanical performance when sediment substitution remains within the 10–20% range. Washing treatments, although less energy-intensive, require significant water handling and waste-water management. Chemical pretreatments applied to plant residues also introduce material and operational costs, but are essential for stabilizing the fibers and achieving reliable long-term performance.

From an industrial standpoint, the ratio between pretreatment cost and achieved performance gain becomes a determining factor. The results of this study suggest that the most economically viable strategies are those where pretreatment produces disproportionately large improvements in mechanical, microstructural, or durability indicators such as thermally activated sediments and moderately alkali-treated plant fibers. In this context, AI-supported optimization frameworks offer strong potential by enabling the identification of cost-efficient combinations, guiding the selection of pretreatment intensity, and predicting diminishing returns when processing exceeds the thresholds identified in the database. Overall, the integration of pretreatment cost considerations with AI-driven performance optimization provides a realistic pathway toward industrial-scale implementation of sustainable concrete formulations.

7. Discussion

The comparative analysis of the three additive families reveals both points of agreement across the literature and clear reasons for divergence. For dredged sediments, the experimental trends and bibliometric clusters converge well: the most consistent mechanical and durability improvements occur when sediments are washed or thermally activated, and when their incorporation remains within the 10–20% range. Studies reporting lower strengths usually involve untreated or insufficiently activated sediments, which is coherent with their higher clay content, residual salts, or incomplete pozzolanic reactivity. These observations are fully aligned with the clusters identified through VOSviewer, where key concepts such as “activation,” “marine exposure,” and “durability” appear as central research nodes.

For recycled plastic fibers, both the dataset and the broader literature highlight a clear and stable behavior pattern. When used in small amounts typically between 0.3% and 1% plastic fibers reliably improve ductility and crack control while preserving compressive strength. Higher dosages, however, often lead to poor dispersion, increased porosity, or fiber balling. This explains the contradictory results found in a few studies that attempted to incorporate more than 1.5–2% fibers. These inconsistencies do not reflect contradictions in the material itself, but rather the sensitivity of fiber-reinforced mixes to dispersion quality, fiber shape, and polymer type. This is also reflected in the bibliometric maps, which emphasize “fiber distribution,” “interface bonding,” and “post-cracking behavior” as dominant concepts across publications.

Plant residues show the greatest variability, and the reasons for this variability are clear once the material’s nature is considered. Unlike synthetic fibers or mineral additions, plant residues differ widely in morphology, lignocellulosic content, and water absorption behavior. Untreated fibers tend to degrade in the alkaline cement environment, absorb large amounts of water, and weaken the matrix–fiber interface. This explains why some studies report notable strength losses when residues are added without pretreatment. Conversely, alkali-treated, mineralized, or thermally conditioned

residues exhibit much more stable performance, especially when incorporated at moderate levels (1–8%). The variability observed across the literature therefore reflects differences in how the plant residues were processed rather than contradictions in their inherent potential. These trends are strongly supported by the semantic AI analysis, which consistently identifies “alkaline pretreatment,” “mineralization,” and “moisture sensitivity” as key descriptors associated with plant-based additives.

Overall, the strong agreement between experimental tendencies, bibliometric clusters, and AI-derived semantic indicators reinforces the robustness of the results. Apparent contradictions in the literature can be systematically explained by differences in pretreatment intensity, hydration kinetics, fiber dispersion, or water absorption mechanisms. The discussion confirms that performance is not determined solely by the additive family, but by the combination of its intrinsic nature and the process conditions applied to it. This integrated perspective linking quantitative observations, mechanistic explanations, and bibliometric evidence provides a coherent interpretation of the current state of research on sustainable concrete additives.

8. Conclusion

This study provides a structured and comparative assessment of three major families of alternative cementitious additives—dredged sediments, plant residues, and recycled plastic fibers—through a database of 245 formulations. Despite the diversity of sources, the quantitative analysis reveals clear performance tendencies supported across multiple studies. Optimal incorporation ranges were consistently identified around 10–20% for dredged sediments, 1–8% for plant residues, and 0.3–1% for recycled plastic fibers, corresponding to the most favorable balance between compressive strength, porosity reduction, and improved crack resistance. These numerical findings constitute a unified reference for materials that are often studied independently and under non-harmonized laboratory conditions.

The combined use of experimental synthesis, bibliometric mapping, and AI-assisted semantic clustering allowed the identification of recurring performance drivers, particularly the influence of pretreatment methods, mixture optimization, and microstructural stabilization. This integrated approach provides a clearer separation of roles among the three additive families, highlighting sediments as binder substitutes with moderate carbon benefits, plant residues as contributors to lightweight and low-emission mixes, and plastic fibers as enhancers of post-cracking and deformation behavior.

8.1 Limitations

The conclusions of this work remain constrained by the heterogeneity of experimental protocols, variations in curing and exposure conditions, and the lack of standardized long-term durability indicators, especially for marine and sulfate environments. In addition, incomplete life-cycle assessment (LCA) datasets limit the accuracy of CO_2-reduction estimations. As the analysis is based entirely on published data, extreme or atypical results could not be independently verified.

Future directions. Progress in this field will require harmonized testing procedures, unified durability metrics, and comprehensive LCA reporting across studies. The development of hybrid AI frameworks capable of linking semantic descriptors, mixture parameters, and durability outcomes presents a promising path for predictive and optimization-oriented mix-design. Strengthening these aspects will support the emergence of reliable, scalable, and low-carbon cementitious materials suitable for next-generation structural and environmental challenges.

References

[1] CEMBUREAU. Activity Report 2023. 2024. Available from: https://cembureau.eu/media/dnbf4xzc/activity-report-2023-for-web.pdf

[2] CemNet. Morocco’s cement dispatches advance 15% in December. CemNet News. 2025. Available from: https://www.cemnet.com/News/story/178415/morocco-s-cement-dispatches-advance-15-in-december.html

[3] Neville A. Chloride attack of reinforced concrete: an overview. Mater Struct. 1995;28(2):63-70. https://doi.org/10.1007/BF02473172

[4] Verbeck GJ. Mechanisms of corrosion in concrete. In: Corrosion of Metals in Concrete, SP-49. Detroit: American Concrete Institute; 1975. p. 21-38.
[5] Al-Tayyib AJ, Khan MS, Allam IM, Al-Mana AI. Corrosion behavior of pre-rusted rebars after placement in concrete. Cem Concr Res. 1990;20:955-60. https://doi.org/10.1016/0008-8846(90)90059-7
[6] Jahani M, Moradi S, Shahnoori S. 4-year monitoring of degradation mechanisms of seawater sea-sand concrete exposed to tidal conditions: Development of chemical composition and micro-performance. Constr Build Mater. 2023;409:133475. https://doi.org/10.1016/j.conbuildmat.2023.133475
[7] Chu SH, Yao JJ. A strength model for concrete made with marine dredged sediment. J Clean Prod. 2020;274:122673. https://doi.org/10.1016/j.jclepro.2020.122673
[8] Bortali M, Rabouli M, Yessari M, Hajjaji A. Assessment of harbor sediment contamination for a path to valorize dredged material. Arab J Chem. 2023;16:105208. https://doi.org/10.1016/j.arabjc.2023.105208
[9] Gamil Y. Machine learning in concrete technology: A review of current researches, trends, and applications. Front Built Environ. 2023;9:1145591. https://doi.org/10.3389/fbuil.2023.1145591
[10] Nikoopayan Tak MS, Feng Y, Mahgoub M. Advanced machine learning techniques for predicting concrete compressive strength. Infrastructures. 2025;10(2):26. https://doi.org/10.3390/infrastructures10020026
[11] Amar M, Benzerzour M, Safhi AEM, Abriak N-E. Durability of a cementitious matrix based on treated sediments. Case Stud Constr Mater. 2020;13:e00373. https://doi.org/10.1016/j.cscm.2020.e00373
[12] Kazi Aoual-Benslafa F, Kerdal D, Ameur M, Mekerta B, Semcha A. Durability of mortars made with dredged sediments. Procedia Eng. 2015;118:240–250. https://doi.org/10.1016/j.proeng.2015.08.423
[13] Yao JJ, Chu SH. Durability of sustainable marine sediment concrete. Developments in the Built Environment. 2023;13:100167. https://doi.org/10.1016/j.dibe.2023.100167
[14] Zhang Y, Liu S, Wang Y, Chen B, Li L. Effect of seawater curing on the mechanical properties of solidified high-water content marine dredged clay. Constr Build Mater. 2025;409:138026. https://doi.org/10.1016/j.conbuildmat.2025.138026
[15] Zhang Z, Zhang Y, Chai X, Liu K, Wang F. Strength development of dredged sediment stabilized with nano-modified sulphoaluminate cement. Soil Dyn Earthq Eng. 2024;181:107751. https://doi.org/10.1016/j.soildyn.2024.107751
[16] Yao Y, Sun W, An M. Mechanical and durability properties of concrete made with dredged marine sand. Constr Build Mater. 2011;25:3187–3194. https://doi.org/10.1016/j.conbuildmat.2011.01.009
[17] Zhao Q, Zheng G, Wang H, Cui Y, Zhang Z. Effect of seawater curing on the mechanical properties of solidified high-water-content marine dredged clay. Constr Build Mater. 2025;459:222140. https://doi.org/10.1016/j.conbuildmat.2024.222140
[18] Al Martini S, Sabouni R, Elhakeem M, Masri M. Fresh, mechanical and durability properties of sustainable cement grouts incorporating dredged materials from UAE dams. Results Eng. 2025;27:105645. https://doi.org/10.1016/j.rineng.2025.105645
[19] Heidari P, Rivard P, Wilson W. Multi-objective optimization of cement-based systems containing marine dredged sediment. Constr Build Mater. 2024;439:137228. https://doi.org/10.1016/j.conbuildmat.2024.137228
[20] Hussain M, Levacher D, Leblanc N, Zmamou H, Djeran-Maigre I, Razakamanantsoa A, Saouti L. Reuse of harbour and river dredged sediments in adobe bricks. Cleaner Mater. 2022;3:100046. https://doi.org/10.1016/j.clema.2022.100046
[21] Lharti H, Hayek M, Soleimani T, Salgues M, De Weerdt K, Yahia A, Souche J-C. Short-term durability and environmental integration of dredged sediment-based concrete in seawater. Constr Build Mater. 2025;492:143104. https://doi.org/10.1016/j.conbuildmat.2025.143104
[22] Laoufi L, Senhadji Y, Benazzouk A. Valorization of mud from Fergoug dam in manufacturing mortars. Case Stud Constr Mater. 2016;5:26–38. https://doi.org/10.1016/j.cscm.2016.01.003
[23] Malik R, Chaubey AK, Ansari MI. An assessment of the mechanical and durability capabilities of geopolymer concrete. Procedia Struct Integr. 2025;70:682–689. https://doi.org/10.1016/j.prostr.2025.07.106
[24] Huynh T-P, Le THM, Ngan NVC. An experimental evaluation of the performance of concrete reinforced with recycled fibers made from waste plastic bottles. Results Eng. 2023;18:101205. https://doi.org/10.1016/j.rineng.2023.101205
[25] Aocharoen Y, Chotickai P. Compressive mechanical and durability properties of concrete with polyethylene terephthalate and high-density polyethylene aggregates. Cleaner Eng Technol. 2023;12:100600. https://doi.org/10.1016/j.clet.2023.100600
[26] Azandariani MG, Vajdian M, Javadi M, Parvari A. Durability and compressive strength of composite polyolefin fiber-reinforced recycled aggregate concrete: An experimental study. Compos Part C. 2024;15:100533. https://doi.org/10.1016/j.jcomc.2024.100533
[27] Zeng J-J, Hao Z-H, Sun H-Q, Zeng W-B, Fan T-H, Zhuge Y. Durability assessment of ultra-high-performance concrete (UHPC) and FRP grid-reinforced UHPC plates under marine environments. Eng Struct. 2025;323:119313. https://doi.org/10.1016/j.engstruct.2024.119313

[28] Kang D-H, Choi W. Durability of carbon fiber-reinforced polymer (CFRP) rebar exposed to long-term alkaline environment. Constr Build Mater. 2025;496:143757. https://doi.org/10.1016/j.conbuildmat.2025.143757
[29] Dong S, Zhou P, Guo R, Li C, Xian G. Durability study of glass fiber reinforced polypropylene sheet under simulated seawater sea sand concrete environment. J Mater Res Technol. 2022;20:1079–1092. https://doi.org/10.1016/j.jmrt.2022.07.097
[30] Mardani A, Şahin HG, Kaya Y, Mardani N, Assaad JJ, El-Hassan H. Enhancing strength and durability of recycled fine aggregate mixtures using steel fibers, silica fume, and latex polymers. Dev Built Environ. 2025;21:100599. https://doi.org/10.1016/j.dibe.2024.100599
[31] Abushanab A, Ebead U, Genedy M, Ayash NM, Fawzy SA. Flexural behavior and durability of reinforced concrete beams with seawater, sulfate-resistant cement, and glass fiber-reinforced polymer reinforcement. Eng Struct. 2025;333:120204. https://doi.org/10.1016/j.engstruct.2024.120204
[32] Al Marah RH, Shehzad MK, Albostami AS, Ghadi MQ, Aldmour ST, Almarahlleh NH. Influence of polypropylene fibres on the residual flexural strength of concrete: Experiments and sensitivity analysis. KSCE J Civ Eng. 2025;100390. https://doi.org/10.1016/j.kscej.2025.100390
[33] Zhang YH, Zhong WL, Fan LF. Long-term durability investigation of basalt fiber-reinforced geopolymer concrete in marine environment. J Mater Res Technol. 2024;31:593–605. https://doi.org/10.1016/j.jmrt.2024.06.078
[34] Zaid O, Al-Dala'ien RN, Arbili MM, Alashker Y. Optimizing natural fiber content and types for enhanced strength and long-term durability in high-performance concrete. Cleaner Eng Technol. 2025;26:100983. https://doi.org/10.1016/j.clet.2025.100983
[35] Salami BA, Bahraq AA, Haq MMU, Ojelade OA, Taiwo R, Wahab S, Adewumi AA, Ibrahim M. Polymer-enhanced concrete: A comprehensive review of innovations and pathways for resilient and sustainable materials. Next Mater. 2024;4:100225. https://doi.org/10.1016/j.nxmate.2024.100225
[36] Mubaraki M, Ali SIA, Ismail A, Yusoff NIM. Rheological evaluation of asphalt cements modified with ASA polymer and Al_2O_3 nanoparticles. Procedia Eng. 2016;143:1276–1284. https://doi.org/10.1016/j.proeng.2016.06.135
[37] Wei Z, Wang T, Li H, Dong T, Li Z, Guo X. Study of the flexural behavior of basalt fiber-reinforced concrete beams with basalt fiber-reinforced polymer bars and steel bars. Case Stud Constr Mater. 2025;22:e04433. https://doi.org/10.1016/j.cscm.2024.100433
[38] Yadav A, Al-Mazrouei N, Singh Raman RK, Sastry M, Bose S, Al-Saadi S, Ahmed WK, Al-Marzouqi AH. Surface modification of fibres with silane for enhancing the durability of FRP composites as reinforcement for seawater sea sand concrete (SWSSC): A review. Constr Build Mater. 2024;451:138678. https://doi.org/10.1016/j.conbuildmat.2024.138678
[39] Chatveera B, Ejaz A, Hanif MA, Saingam P, Hussain Q, Chintanapakdee C, Arreeras T, Sua-iam G. Synergistic effect of recycled E-waste fiber and polyvinyl alcohol on the properties of green concrete incorporating recycled concrete aggregate. Dev Built Environ. 2025;23:100722. https://doi.org/10.1016/j.dibe.2025.100722
[40]Aqil M., Bahi L., Ouadif L., Amgaad S., Bouajaj A., The Impact of the Addition of Plastic Additives, Polypropylene Fibers and Specimen Shape on drying Shrinkage and Mass Loss of High-Performance Sand Concrete, International Journal of Civil Engineering and Technology (IJCIET), Vol. 9, Issue 13, 2018,pp.1617-1632.
[41] Aqil M., Bahi L., Ouadif L., Amgaad S., "Workability and durability of sand concrete based on cementitious matrix and plastic additives," International Journal of Civil Engineering and Technology, vol. 6, no. 9, 2018, pp. 1617–1632. https://iaeme.com/Home/article_id/IJCIET_09_06_182.
[42] Mani S, Partheeban P, Chella Gifta C. A comprehensive review on multilayered natural-fibre composite reinforcement in geopolymer concrete. Cleaner Mater. 2025;16:100310. https://doi.org/10.1016/j.clema.2025.100310
[43] Bozorgmehr Nia S, Shafei B. Carbon footprint reduction through repurposing solid wastes into sustainable construction materials: A state-of-the-art review. Cleaner Respons Consum. 2025;18:100310. https://doi.org/10.1016/j.clrc.2025.100310
[44] Khrissi Y, Tilioua A. Development and characterization of eco-friendly earth bricks stabilized with date palm waste fibers for sustainable construction. Cleaner Waste Syst. 2025;11:100283. https://doi.org/10.1016/j.clwas.2025.100283
[45] Li W, Shumuye ED, Shiying T, Wang Z, Zerfu K. Eco-friendly fibre reinforced geopolymer concrete: A critical review on the microstructure and long-term durability properties. Case Stud Constr Mater. 2022;16:e00894. https://doi.org/10.1016/j.cscm.2022.e00894
[46] Abolusoro OP, Khoathane MC, Mhike W. Effects of palm kernel shell ash as a reinforcement on the properties of recycled aluminium cans for aluminium matrix composites production. Next Mater. 2025;8:100900. https://doi.org/10.1016/j.nxmate.2025.100900

[47] Ozmen H B, Tanrıverdi B. Concrete paradox: Economic importance, environmental impacts, and the sustainability of concrete material. Res Des. 2025;2(2):66–84. https://doi.org/10.17515/rede2025-008en0801rs
[48] Chalee W, Cheewaket T, Jaturapitakkul C. Enhanced durability of concrete with palm oil fuel ash in a marine environment. J Mater Res Technol. 2021;13:128–137. https://doi.org/10.1016/j.jmrt.2021.04.061
[49] Algaifi HA, Huseien GF, Syamsir A, Qaid A, Baharom S, Mhaya AM. Optimizing durability and performance in high-volume fly ash-based alkali-activated mortar with palm oil fuel ash and slag: A response surface methodology approach. Dev Built Environ. 2024;18:100427. https://doi.org/10.1016/j.dibe.2024.100427
[50] Olivia M, Asmanovita R, Sinuhaji IJ, Putri WR, Sitompul IR, Utama PS, Supit SWM. Properties of blended Palm Oil Fuel Ash (POFA) concrete using additive micro silica exposed to organic peat water environment. Cleaner Waste Syst. 2025;12:100414. https://doi.org/10.1016/j.clwas.2025.100414
[51] Mahdi E, Ochoa DRH, Vaziri A, Bandaru AK, Kumar P KAV, Dean A. Effects of water absorption on the mechanical and morphological properties of date palm leaf fiber-reinforced polymer composites. Compos Struct. 2025;368:119286. https://doi.org/10.1016/j.compstruct.2025.119286
[52] García G. Natural fibers as reinforcement of mortar and concrete: A systematic review from Central and South American regions. J Build Eng. 2024;98:111267. https://doi.org/10.1016/j.jobe.2024.111267
[53] Alsharari F. Utilization of industrial, agricultural, and construction waste in cementitious composites: A comprehensive review of their impact on concrete properties and sustainable construction practices. Mater Today Sustain. 2025;29:101080. https://doi.org/10.1016/j.mtsust.2025.101080
[54] Ozmen H B, Inel M. Effect of concrete strength and detailing properties on seismic damage for RC structures. Res Des. 2024;1(1):1–11. https://doi.org/10.17515/rede2024-005en1124rs
[55] Aqil M., Bahi L., Ouadif L., Belhaj S., Edderkaoui R., The influence of curing temperature, plastic additives and polypropylene fibers on the mechanical behaviour of cementitious materials, E3S Web Conference, Vol. 150, 2020. https://doi.org/10.1051/e3sconf/202015002018.
[56] Edderkaoui R., Khomsi D., Hamidi A., Baiti HB., Souidi H., Aqil M., Verification of the technical feasibility of composting: case study, E3S Web Conference, Vol. 150, Issue 02018,2020. https://doi.org/10.1051/e3sconf/202015002018.
[57] Edderkaoui R., Khomsi D., Hamidi A. et al., Novel approach for the rational management of household and similar waste using AHP, fuzzy TOPSIS, and GIS, Euro-Mediterr J Environ Integr, Vol. 6, Issue 63, 2021. https://doi.org/10.1007/s41207-021-00271-6.

www.jresm.org

Research on Engineering Structures and Materials

Scopus

EBSCO

TÜBİTAK ULAKBİM

DRJI

Cosmos

ProQuest

crossref

Google Scholar

Universal Impact Factor

SIS Scientific Indexing Services

CiteFactor Academic Scientific Journals

Journal Seeker Research Bible

EZB Elektronische Zeitschriftenbibliothek

GIF GLOBAL IMPACT FACTOR

ASOS indeks

Open Academic Journals Index

Publication Forum

Research Group

https://mimrg.net/